IFireSS

21st - 23rd | Rio de Janeiro
JUNE, 2023 | BRAZIL

PROCEEDINGS

Editors:
Aline Lopes Camargo, Ângela Gaio Graeff, Carla Neves Costa, Deives Junior de Paula, Fabrício Longhi Bolina, Gabriela Lins Albuquerque, Hermes Carvalho, João Paulo C. Rodrigues, João Victor Dias, Paulo von Kruger, Ricardo A. M. Silveira, Saulo José Almeida, Tiago Ancelmo Pires

Organizers

CIB   UF*M*G   12 90   UNIVERSIDADE Ð COIMBRA   albrasci

IFireSS 2023 - International Fire Safety Symposium

Rio de Janeiro - Brazil

June 21st to 23rd, 2023

Aline Lopes Camargo
Itecons, Univ. de Coimbra – Portugal

Ângela Gaio Graeff
UFRGS - Federal University of Rio Grande do Sul, Brazil

Carla Neves Costa
UNICAMP - State University of Campinas, Brazil

Deives Junior de Paula
IPT - Institute of Technological Research - Brazil and IteCons – UC, Portugal

Fabrício Longhi Bolina
UNISINOS - University of Vale do Rio dos Sinos, Brazil

Gabriela Lins Albuquerque
USP - University of São Paulo, Brazil

Hermes Carvalho
UFMG - Federal University of Minas Gerais, Brazil

João Paulo Correia Rodrigues
UC - University of Coimbra, Portugal and UFMG - Federal University of Minas Gerais, Brazil

João Victor Fragoso Dias
UFES - Federal University of Espírito Santo, Brazil

Paulo von Kruger
UFMG - Federal University of Minas Gerais, Brazil

Ricardo A. M. Silveira
UFOP – Federal University of Ouro Preto, Brazil

Saulo José Almeida
UNICAMP - State University of Campinas, Brazil

Tiago Ancelmo Pires
UFPe - Federal University of Pernambuco, Brazil

Proceedings of IFireSS 2023 - International Fire Safety Symposium

Aline Lopes Camargo, Ângela Gaio Graeff, Carla Neves Costa, Deives Junior de Paula,Fabrício Longhi Bolina, Gabriela Lins Albuquerque, Hermes Carvalho, João Paulo Correia Rodrigues, João Victor Fragoso Dias, Paulo von Kruger, Ricardo A. M. Silveira, Saulo José Almeida, Tiago Ancelmo Pires.

Primeira edição.
Junho, 2023

Preface

The Organising and Scientific committees of IFireSS 2023, as well as CIB W-14 Commission - Fire Safety, would like to thank your participation in the International Fire Safety Symposium – IfireSS – 2023, in Rio de Janeiro, Brazil. The city of Rio de Janeiro allowed the creation of a unique and fantastic environment for the realization of this event.

The Symposium contributed to the exchange of ideas and knowledge in the area of Fire Safety and assisted in planning future research activities for the area.

The Symposium has had participants from different countries around the world and covered a wide variety of research areas including: Structural Fire Safety; Mechanical and Thermal Properties of Materials; Fire Chemistry, Physics and Combustion; Fire Reaction; Fire Safety in Vehicles and Tunnels; Fire Risk Assessment; Smoke Control Systems; Firefighting and Evacuation; and Fire Regulations, Standardization and Construction Trends.

The articles presented at this Symposium were of high quality, in different areas of fire safety, and these proceedings reflect that fact. They will serve as the basis for developments in the field, research projects and technical standards. The in-person or online presentations were superb and resulting in discussions of a high level for the area.

The Organizing and Scientific Committees of IFIRESS 2023 and CIB W14 Commission

Committees

Organizing Committee

Chairmen

Hermes Carvalho
UFMG - Federal University of Minas Gerais, Brazil

João Paulo Correia Rodrigues
UC - University of Coimbra, Portugal and UFMG - Federal University of Minas Gerais, Brazil

Members

Aline Lopes Camargo, UFMG - UC - University of Coimbra, Portugal
Ângela Gaio Graeff, UFRGS - Federal University of Rio Grande do Sul, Brazil
Carla Neves Costa, UNICAMP - State University of Campinas, Brazil
Deives Junior de Paula, IPT - Institute of Technological Research - Brazil and IteCons – UC, Portugal
Fabrício Longhi Bolina - UNISINOS - University of Vale do Rio dos Sinos, Brazil
Gabriela Lins Albuquerque - USP - University of São Paulo, Brazil
João Victor Dias, UFES - Federal University of Espírito Santo, Brazil
Luciano Rodrigues Ornelas de Lima, UERJ - State University of Rio de Janeiro, Brazil
Paulo von Kruger, UFMG - Federal University of Minas Gerais, Brazil
Ricardo A. M. Silveira – UFOP – Federal University of Ouro Preto, Brazil
Saulo José Almeida, UNICAMP - State University of Campinas, Brazil
Tiago Ancelmo Pires, UFPe - Federal University of Pernambuco, Brazil

Scientific Committee

Chairmen

Dhionis Dhima
CSTB – Centre Scientifique et Technique du Bâtiment, France

João Paulo Correia Rodrigues

UFMG - Federal University of Minas Gerais, Brazil

Venkatesh Kodur
MSU – Michigan State University, USA

Wan-ki Chow
The Hong Kong Polytechnic University, China

Members

Abdelhamid Bouchaïr - Clermont University, France
Ahmed Kashef - National Research Council, Canada
Albert Simeoni - Worcester Polytechnic Institute, USA
Ali Nadjai - Ulster University, UK
Amarildo Benzane - National Police Academy, Mozambique
Ananth Ramaswamy - Indian Institute of Science, India
Antonio Bilotta - Naples Federico II University, Italy
Bin Zhao - Centre Technique Industriel de la Construction Métallique – CTICM, France
Brian Meacham - Meacham Associates, USA
C S Manohar - Indian Institute of Science, India
Colleen Wade - Fire Research Group Limited, New Zealand
Cristian Maluk Zedan - Semper, UK
Daniel Brandon - Research Institutes of Sweden, Sweden
Dionysios Kolaitis - National Technical University of Athens, Greece
Ehab Zalok - Carleton University, Canada
Eleni Asimakopoulou - Central Lancashire University, UK
Emidio Nigro - Naples Federico II University, Italy
Eslami Mohammadreza - University of California at Berkley, USA
Gaurav Srivastava - Indian Institute of Technology- Gandhi Nagar, India
George Hadjisophocleous - Carleton University, Canada
Gert Van der Berg - Fire safety consulting, The Netherlands
Guan-Yuan Wu - Central Police University, Taiwan
Haiyan Zhang - South China University of Technology, China
Jean-Christophe Mindeguia - Bordeaux University, France
Jean Marc Franssen - Liège Unversity, Belgium
John Adam Gales - York University, Canada
Jose Luis Torero Cullen - University College London, UK
Keerthi Ranasinghe - Warringtonfire, UK
Kees Both - Etex Group, Belgium
Kevin La Malva - Code Unlimited, USA
Kostiantyn Afanasenko - National University of Civil Defence, Ukraine
Liang Yi - Central South University, China
Linda Makovicka Osvaldova - Zilina University, Slovakia
Longhua Hu - University of Science and Technology of China
Luke Bisby - Edinburgh Univesrsity, UK
M. Z. Naser - Clemson University, USA
Mamoru Kohno - Tokyo University of Science, Japan
Maxime Audebert - National School of Engineers of Saint-Etienne , France
Ming Wai Lee - City University of Hong Kong, China
Nicolas Pinoteau - Centre Scientifique et Technique du Bâtiment, France

Norman Werther - Technical University of Munich, Germany
Panos Kotsovinos - ARUP, UK
Patrick van Hees - Lund University, Sweden
Paulo Vila Real - University of Aveiro, Portugal
Peihong Zhang - Northeastern University, China
Petr Kuklik - Czech Technical University in Prague, Czech Republic
Ricardo Hallal Fakury – Federal University of Minas Gerais, Brazil
Rita Fahy - National Fire Protection Association, USA
Roberto Felicetti - Politecnico di Milano, Italy
Ruben Van Coile - Ghent University, Belgium
Samuel L. Manzello - REAX Engineering, USA
Tomaž Hozjan - Ljubljana University, Slovenia
Tuula Hakkarainen - VTT, Finland
Vasant Matsagar - Indian Institute of Technology- Delhi, India
Yuanhua He - Civil Aviation Flight University of China, China
Yulianto Sulistyo Nugroho - Universitas Indonesia, Indonesia

Organization and Sponsorship

Organizers

Partners

Sponsors

Contents

Fire Safety of Structures   259

xii

Keynote Speeches

FIRE SPRINKLER PROTECTION – MODERN CHALLENGES AND SOLUTIONS FOR WAREHOUSES

Yibing Xin

FM Global (yibing.xin@fmglobal.com)

Keywords: Sprinkler, Suppression, Fire Protection, Storage, Commodity

1. FIRE HAZARDS AND CHALLENGES IN MODERN WAREHOUSES

Among all types of commercial properties and buildings, warehouses often have the highest quantity of combustibles per unit of footprint (i.e., fuel loading), and thus present very challenging scenarios for fire protection. Failure to achieve adequate protection may result in significant fire safety concerns and catastrophic property losses. Traditionally, commodities have been stored in warehouses directly on the floor or on rigid racks to maximize the space utilization, and handled by forklifts that require certain aisle space to operate. This results in the widely used double-row rack storage (Fig. 1a), where protection challenges primarily come from the storage height and commodity type. This has motivated the continuous development of large-orifice sprinklers.

Figure 1: Warehouse storage illustrations: (a) double-row rack storage; (b) on-end roll paper storage; (c) open-top plastic containers stored in racks.

Modern warehouses are constantly evolving with emerging challenges that require innovative sprinkler solutions. As examples, this work will focus on three specific fire hazards in today's warehouses: (1) open-top combustible container (OTCC) storage in racks (Fig. 1c); (2) high storage of on-end hard-surface paper rolls (Fig 1b); and (3) top-loading automatic storage and

retrieval system (TL-ASRS). When a fire occurs among the OTCCs placed on racks, the water discharged from ceiling sprinklers is collected by the containers resulting in very little wetting of the lower portion of the storage. Consequently, fires can spread beyond the coverage area of activated sprinklers. In contrast, fires from on-end storage of hard-surface paper rolls can also impede water penetration through strong upward fire plumes, and become uncontrolled via paper exfoliation that exposes fresh fuels. As to TL-ASRS, the densely arranged storage tends to prevent adequate downward water transport, whereas the narrow gaps between adjacent container units preclude use of in-rack sprinklers. Clearly, these challenging fire scenarios in modern warehouses demand innovative and cost-effective solutions.

2. DEVELOPMENT OF COST-EFFECTIVE SOLUTIONS

OTCC fires are challenging largely due to the limited downward water transport to the lower portion of the storage. To address this problem, in-rack sprinklers may be deployed in a very dense manner, which inevitably leads to high cost of fire protection. To overcome the water transport issue, the container structure can be modified to allow for adequate water cascading from one tier to another. This work will assess options of container modification and the corresponding protection performance using ceiling sprinklers.

To counteract the tremendous fire plume generated by on-end paper roll fires, this work explores the use of large-orifice sprinklers to produce high momentum water sprays. In this study, a unique challenge is the limitation of testing lab capabilities, especially when the roll storage height exceeds that of the lab. Therefore, an innovative testing method is developed to evaluate sprinkler protection performance beyond current lab capabilities.

The unique storage arrangement of TL-ASRS, especially the narrow gaps between adjacent columns, does not allow for installation of in-rack sprinklers. In addition, the human occupied storage facility is also not suitable for many gaseous agent-based suppression systems. As a result, this work evaluates ceiling sprinkler protection options in conjunction with carefully selected final extinguishment measures. The final extinguishment is crucial to TL-ASRS fires due to the limited access for firefighting activities that are traditionally used as the last resort to achieve complete fire extinction.

3. FUTURE DEVELOPMENT OF SMART SPRINKLER TECHNOLOGY

Traditional sprinkler technology has many limitations, such as slow activation, sprinkler skipping and lack of proactive response to fire spread. Looking into future, a new generation of SMART (Simultaneous Monitoring, Assessments and Response technology) sprinkler is being developed and commercialized. This work will provide a review of state-of-the-art on SMART sprinkler, expected to be increasingly used to address challenges of modern warehouse fires.

Behaviour of Timber Structures in Case of Fire

Dhionis DHIMA[a]

Keywords: fire reaction, fire resistance, timber structures, timber-concrete composite structures, fire extinction.

1. INTRODUCTION

Currently the use of wood as the main construction material is becoming more and more popular not only for 1 to 3 storey buildings, but also for mid-rise and high-rise buildings. In addition, in the context of reducing carbon emissions, buildings with wood seem interesting because this allows the transition to a low-carbon, circular and sustainable economy. But, this should not lead us to ignore the risks that wood as a combustible material presents to fire safety. For that reason several researchs are carried out in the world, in order to identify the best construction techniques so that the wooden buildings provide at least the same fire safety as the other types of buildings made up of concrete or steel structures. The combination of these three main building materials is one of the paths taken more and more by construction builders to take advantage of the qualities of each material.

However, unprotected structural timber constitutes an additional fuel load compared to concrete and steel. In fire situation its combustion and/or charring can lead to the collapse of the building if measures preventing these phenomena are not taken. For a wooden structure, the two aspects, reaction and resistance to fire, are interesting because the first favors the ignition of fire and contributes to its development, and the second characterizes its capacity to ensure its function of resistance and/or compartmentation in a fire situation.

In this paper, several experimental results allowing to identify the contribution of wooden structures on the development of the fire, are given. Calculation methods for wooden structures, assemblies included, as well as those for composite timber-steel and timber-concrete structures are presented. Finally, technical conclusions and possible solutions, based on experimental and numerical results, for the safety of buildings made of timber structures, are also presented.

2. Description

The presentation begins by recalling the context why it is interesting to know the fire behavior of wooden structures. This can be simply summarized by "Willingness to build with more wood and reduction of the carbon footprint". Then the regulatory codes, the fire safety objectives and the criteria that allow to satisfy them, are recalled.

In order to have an overview of where wooden structures stand in relation to concrete and steel structures in a fire situation, the durations of fire resistance of five beam and frame structures are compared. These structures have been dimensioned according to the standards EN 1992-1-1, EN 1993-1-1 and EN 1995-1-1 [1].
The contribution of wooden structural elements to the development of fire, inside [2, 3, 4, 5] and outside [6] of a building, is illustrated using several results of experimental studies based on real compartment fires. These

---

[a] CSTB, Centre Scientifique et Technique du bâtiment (dhionis.dhima@cstb.fr).

studies make it possible to identify the most important parameters that contribute to the development of the fire, the effect of partial or complete protections on its duration, and in particular, the durations of the temperature stages above 1000°C. The two most important parameters are the density of the fuel load and the opening factor of the fire compartment. Concerning the vertical propagation of the exterior of a building, the role of wooden facades is presented and the most important parameters are identified [7, 8, 9]. The contribution to the fire development of the beams and columns of a mixed timber-steel-concrete structure of an open car park tested and modeled in fire is also presented [9, 10]. Regarding fire resistance, simplified and advanced calculation methods for timber structures [12] and their assemblies [13, 14, 15, 16], as well as those for mixed timber-steel [17] and timber-concrete structures [18, 19, 20, 21, 22] are presented.

Encouraging experimental results, relating to the evolution of the compressive strength of wooden specimens and to the reversibility of this resistance after cooling, complete the presentation relating to the fire resistance of timber structures.

The conclusions of a parametric FSE (Fire Safety Engineering) study based on small, medium and large scale fire tests [3, 23, 24] and modeling [25], in order to predict under what conditions flame extinction can occur are also presented.

The technical conclusions based on the analysis of presented experimental studies and the application of the FSE are accompanied by some proposals for probable solutions which would make it possible to achieve the levels of security fixed by safety objectives.

Concerning the complete encapsulation of wooden structural elements, some solutions proposed and applied in France are given [26].

3. CONCLUSION

The analysis of the large-scale experimental results and the application of FSE by exploiting the experimental results at several scales make it possible to design technical solutions which could lead to the extinction of the flames during a fire, and consequently to a high probability to satisfy the fire safety objectives of a building.

It is essential to improve the models that simulate the development of fire and to carry out more research in order to take into account the effect of the wind on the extinction of flames and smoldering fires.

However, the complete encapsulation of the elements of timber structures and the use of sprinklers can easily satisfy the safety objectives for the duration of the fire. These solutions are known and are relatively simple to implement.

7. REFERENCES

[1]   O. Parissier : "La sécurité incendie des structures bois en comparaison avec les autres matériaux de construction", Mémoire de diplôme d'Ingénieur, Polytech Clermont-Ferrand, Septembre 2008.

[2]   A. R. Medina Hevia: "Fire resistance of partially protected cross-laminated timber rooms", these de doctorat, Carleton University Ottawa, Canada, 2014.

[3]   G. Auguin: "Essais de résistance au feu sur maquettes reconstituant un local avev certaines parois en bois apparent", Efectis-France, 22-000161-GAU, France.

[4]   D. Brandon: "Fire Safe implementation of visible mass timber in tall buildings – compartment fire testing", RISE Report 2020:94.

[5]   R. McNamee, J. Zehfuss, I. A. I. Bartlett, M. Heidari, F. Robert, L. A. Bisby: "Enclosure fire dynamics with a cross-laminated timber ceiling et Enclosure fire dynamics with a combustible ceiling", Fire and materials, 01 September 2020.

[6]   A. Frange, M. Fontana: "Fire Performance of Timber structures under Natural Fire Conditions", 8th IAFSS, septembre 18-23, 2005 Beijing, China.

[7]   I. Kotthoff, B. Bart, R. Wiederkehr: Holzanwendung im Fassadenbereich. Naturbrandversuche in Merkers (D) vom 15. bis 18. Oktober Grossbrandversuche V1 bis V12 an der MFPA Leipzig. Kurzdokumentation. Unter Mitarbeit von R. Wiederkehr, B. Bart, I. Kotthoff, D. Kehl, H. Kolb, J.

[8]   M. Teibinger, I. Matzinger and P. Schober: "Experimental study of the fire performance of wooden facades", ATEC Web of Conferences 9, 02004 (2013), DOI: 10.1051/matecconf/20130902004, published by EDP Sciences, 2013.

[9]   D. Dhima, J-M. Gaillard: "Experimental Study of Fire Behaviour of Wooden Facades", Fire Science and Technology 2016, The Proceedings of 10th Asia-Oceania Symposium on Fire Science and Technology, p 193-203, October 2016.

[10] D. Pardon: "Essai de parking de stationnement largement ventilé (PSLV) pour la société Arbonis", CSTB/DSSF/EA2R/26062803, 20 juillet 2017, France.

[11] P Lardet, M. Manthey: "Opération « Treed It » - Parc de stationnement, Ingénierie du comportement au feu des structures", Rapport d'étude 26062803/D, 07 septembre 2020, CSTB, France.

[12] prEN 1995-1-2 : Design of timber structures – Part 1-2: Structural fire design, 2023-05-09.

[13] M. Audebert, D. Dhima, M. Taazount, A. Bouchaïr: "Behaviour of dowelled and bolted steel-to-timber connections exposed to fire", Engineering Structures, Vol. 39, p. 116-125, 2012.

[14] M. Audebert, D. Dhima, M. Taazount, A. Bouchaïr: "Experimental and numerical analysis of timber connections in tension perpendicular to grain in fire", Fire Safety Journal, vol 63, p 125-137, 2014.

[15] M. Audebert, D. Dhima, A. Bouchaïr, A Frangi: "Review of experimental data for timber connections with dowel-type fasteners under standard fire exposure", Fire Safety Journal 107 (2019) 217-234.

[16] M. Audebert, D. Dhima, A. Bouchaïr, N. Pinoteau: "Simplified Design Method for Fire Resistance of Timber Connections", Journal of structure engineering, 12 December 2021, DOI: 10.1061/(ASCE)ST.1943-541X.0003137.

[17] A. Béreyziat A.: "Étude du comportement thermomécanique de poutres mixtes acier-bois en situation d'incendie", thèse de Doctorat, Centrale Lyon - ENISE 19 septembre 2022, St. Etienne, France.

[18] A. Frangi et all.: "Fire Design of Timber-Concrete Composite Slabs with Screwed Connections", Journal of Structural Engineering, ASCE, Vol. 136, No. 2, 2010.

[19] XP CEN/TS 19103 : Eurocode 5 : Conception et calcul des structures en bois - Calcul des structures mixtes bois-béton - Règles communes et règles pour les bâtiments, Janvier 2022.

[20] NF EN 1995-1-1 : Conception et calcul des structures en bois - Partie 1-2 : Généralités - Règles communes et règles pour les bâtiments, Novembre 2005.

[21] V. SCHERER: Master's Thesis in Structural Engineering Timber-Concrete Composite Structures – "Contribution for a Fire Design Model for the new Eurocode 5", ETH Zurich, 1st Semester 2018.

[22] R. Avenel, A. Malara: "Rapport d'essais n° DSSF 21-02350/B concernant un «plancher mixte bois/béton»", CSTB, France, 05/03/2021.

[23] G. Giovannelle: "Essais au feu sur une maquette de local comprenant des parois en bois apparent" , Rapport CSTB-DSSF/EA2R/26088892, 31 mai 2022, France.

[24] R. Mole-Antoniazza: "Modélisations numériques des essais moyennes échelles", Rapport d'étude CSTB-DSSF/26088892, 31 mai 2022, France.

[25] M. Duny and El M. Koutaiba: "Etude paramétrique des conditions d'auto-extinction du bois structural dans un local", ADIVBOIS, CSTB et EFECTIS France, Rapport d'étude CSTB 26085000, 3 février 2023, France.

[26] D. Dhima: "Etude bibliographique relative aux structures en bois basée sur des résultats expérimentaux", Rapport d'étude, CSTB, 14 septembre 2022, France.

Explosions

EFFECT OF STANDOFF DISTANCE ON RESPONSE OF STEEL SECTIONS SUBJECTED TO NEAR-FIELD DETONATIONS

Dravesh Yadav a   **Gaurav Srivastava b,***

ABSTRACT

Extreme loading conditions generated by explosions that may result from terrorist attacks, transportation, and storage of energetic materials can cause devastating consequences for structures and their occupants. Blast-induced effects can be broadly classified into two distinct categories, 1) far-field detonation and 2) near-field detonation. Threats involving terrorist attacks using large amounts of explosives, kept at some distance from the structures, come under far-field detonation. A possible threat tactic is to detonate small quantities of explosives in contact with critical load-bearing structural members to compromise the stability of the structure, leading to its partial or complete collapse, which can be defined as near-field detonation. In the near-field region, the blast loading is affected by local phenomena such as the expansion of the detonation products and after-burn. These phenomena are not observed in far-field blast loading. This study investigates the response of steel sections subjected to blast loads due to near-field detonations. A combination of the Material Point Method (MPM) and Implicit Continuous-fluid Eulerian (ICE) method within the Uintah-Computational Framework (UCF) was used for simulations. These methods are based on a coupled Eulerian-Lagrangian formulation. Pressure, temperature, and velocity profiles generated from the explosion on the sections were also investigated.

Keywords: TNT, MPM-ICE, Uintah, Ignition and Growth Model, near-field detonation.

ᵃ Indian Institute of Technology Gandhinagar, India (dravesh.yadav@iitgn.ac.in)**.**

ᵇ,* Indian Institute of Technology Gandhinagar, India (gauravs@iitgn.ac.in)**,** Corresponding author.

1. INTRODUCTION

Over the past few decades, terrorist attacks have become more frequent, with explosive attacks accounting for more than 50% of all incidents in the last two decades, as per data from the National Consortium for the Study of Terrorism and Response to Terrorism. Notable attacks like the 9/11 attack on the Twin Towers of the World Trade Center and attacks on several bridges significantly impact the design of structures worldwide. The failure of the structure depends on the amount and location of explosives [1].

High-occupancy buildings are easy targets for terrorist attacks that might result in a total or partial structural collapse with the greatest fatalities. Blast-induced events can be majorly classified into two categories: "near-filed" and "far-field" detonations [2]. Small bag packs or a parcel can reach the targets, but due to several such incidents, near-field detonations have become a major threat to the structures. The experimental and analytical investigation of near-field blast response is challenging because the loading is dominated by high-pressure, high-temperature detonation products rather than a diffracting shock wave as in far-field detonations [3]. The need to accurately predict the blast loads and structural response in near-field detonations has become significantly important for the security of buildings and critical infrastructures. Design charts such as those available in UFC 3-340-02 [4] can not be used in near-field detonations because they can not capture the amplitudes of the incident and reflected peak overpressures and the effect of the expanding detonation products on the overpressure histories [5].

One of the critical factors that affect the response of steel sections to near-field detonations is the standoff distance, which is the distance between the explosive charge and the target structure. The effect of the standoff distance on the response of steel sections has been the subject of extensive research in recent years, as it can significantly impact the design and safety of structures in high-risk areas. Several studies have been performed to characterize the near-filed blast and to investigate the response of structures to the near-filed blast loading [5]–[8]. Jinwon et al. [5] numerically modeled the detonations of explosives and characterized their effect in the near-field. Most of the CFD models assume that all the energy released from the explosive is released upon detonation and is used to drive the shock front forward. This assumption does not hold for under-oxidized explosives such as TNT. Afterburning is a process that occurs in these situations. As the shock wave expands into the atmosphere, the detonation products can consume oxygen from the surrounding air and oxidize. Afterburning does not affect peak overpressure significantly but can increase impulse [5]. Remennikov et al. [2] investigated the response of steel plates subjected to near-field detonation and proposed a simplified model for predicting the damage from near-field loading. Zarkrisson et al. [8] numerically simulated the blast loading in near-field scenarios and its application on steel plates. Fan et al. [9] numerically investigated the load induced by cylindrical charge parameters for near-field explosion and observed that the pressure in the axial direction was greater than that in the radial direction. The opposite was observed for the far-field detonations. The behavior of blast load is different for near-field detonation than for far-field detonations. CFD tools must be used to characterize the response of structures subjected to near-field detonation [5].

Understanding the effect of the standoff distance on the response of steel sections is critical in designing structures to withstand blast loading and protect human lives and critical assets. The current study numerically investigates the effects of near–field blast loading on steel sections. The model was verified and validated for overpressure at different standoff distances and the response of steel plates subjected to near-filed detonation. Further, the effect of standoff distance on displacement, pressure profiles, velocity profiles, and temperature profiles were investigated.

2. SIMULATION METHODOLOGY

Uintah Computational Framework (UCF) was used as the underlying framework for simulations [10]. It consists of several components. The main components used for the model are 1) The Material Point Method (MPM), 2) The Implicit, Continuous fluid Eulerian algorithm (ICE), and 3) The combined Fluid-Structure Interaction algorithm (MPMICE). MPM was used to model the steel plate, while ICE was used to model the explosion from the charge. The quasi-meshless MPM can model large deformations, material contact, fracture, etc. [11]. Each grid cell in the cell-centered ICE model carries the thermodynamic variables, which are calculated by an iterative pressure solution, volume, temperature, and kinetic attributes like velocity. The complicated flow behaviour of combustion gas interactions in surface flames, convective flames, and detonation product gas expansions can be modeled using ICE. The main component used in the current study is MPMICE, which is a combination of both MPM and ICE. The use of MPMICE made it possible to simulate fluid-solid interactions as well as flow and deformation.

2.1 Equations of state

To model, the reactants and products in case of explosions equation of states (EOSs) are required. EOSs give the relationship between pressure, volume, and energy. In the current study, JWL EOS was used to model the reactant, and ideal gas EOS was used to model the products. The JWL EOS calculates the average bulk pressure, which is given as follows:

$$p = Ae^{-R_1V} + Be^{-R_2V} + \omega C_v T \tag{1}$$

where, p is bulk pressure; V is relative volume; A, B, R_1, R_2, and w are material constants. The parameters for the detonation of reactants were taken from the literature [12].

2.2 Reaction model

The ignition and growth model [13] was used to model the detonation from the explosive. The governing equation for the model is given by:

$$\frac{dF}{dt} = I(1-F)^b \left(\frac{\rho}{\rho_o} - 1 - a\right)^x + G_1(1-F)^c F^d p^y + G_2(1-F)^e F^g p^z \tag{2}$$

Where, F is the fraction of the chemical energy released, t is time in μs, ρ and ρ_o are current and initial densities, respectively, p is pressure, and $I, G_1, G_2, a, b, c, d, e, g, x, y, z$ are constants. In this model, the shock front ignites a portion of the explosive. The reaction rate is controlled by surface area and pressure. The amount of hotspot generation leads to rapid consumption of explosive material. The parameters for TNT were taken from the literature [12].

2.3 Material model

Johnson-Cook plasticity and damage models were used to model the behavior of steel plates. The model is applicable for modeling the material behaviour of metals under high strain rates and temperatures. The model parameters for XLERPLATE Grade 350 were taken from the literature [14].

3. VERIFICATION AND VALIDATION STUDIES

3.1. Example 1 (Verification of TNT explosion)

Fan et al. [9] numerically modeled the overpressure of TNT spherical charge. A TNT charge of 1 kg was taken, and only 1/8th part was modeled due to symmetry. Symmetric boundary conditions at x-, y-, and z- faces with Neumann boundary conditions being applied at x+, y+, and z+ faces. The resolution was 20 mm, with four particles on each side of each cell. The overpressure profiles at 1 m, 2 m, and 3 m from the point of detonation were calculated at 0º angle. Figure 1 shows a comparison of pressure profiles from simulation and reference. It was observed that the arrival time of peak pressure is slightly lower than that of the results obtained from the reference [9]. The values of peak pressures obtained from the present simulation are higher at 2 m and 3 m standoff distances than that from reference results [9]. The overpressure reaches below ambient pressure after a certain time, which is termed the negative overpressure phase. In the negative overpressure phase, the structure is subjected to a suction force. The negative phase overpressure histories are also considered for the overall performance of the structures. The presented model in this study can capture the negative overpressures as well.
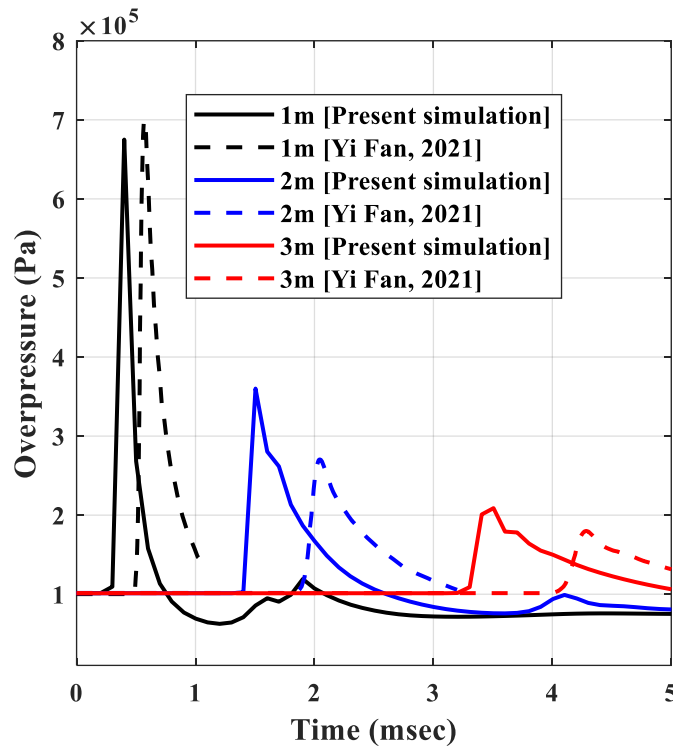
Figure 1: Simulated and reference pressure-time history at different standoff distances for 1kg TNT [reference simulation did not capture negative pressure].

3.2. Example 2 (Validation of steel plate response)

Remennikov et al. [2] experimentally investigated the response of steel plates for near-field detonation and provided a simplified model for predicting the damage caused by near-field blast loading. Figure 2 shows the test rig for explosive loading of steel plates. The overall dimensions of the rig were 1000 mm x 1000 mm x 800 mm. The effective surface area of the plate exposed to the blast source was 700 mm x 700 mm, and the plate was 10 mm thick. Figure 3 shows the schematic of the model. Only 1/4th part of the plate was modeled due to symmetry. A spherical charge of 1 kg TNT was taken, and a steel plate (XLERPLATE Grade 350) was modeled at a 110 mm standoff distance. Symmetric boundary conditions were applied on y- and z- faces. The plate was fixed at y+ and z+ faces. The effective exposed area was taken for the simulation. Figure 4 shows the deflected shape of the plate from the experiment (3D scanned image) and simulation. The shape of the deformed plate from the simulation is similar to that obtained from the experiment. Figure 5 shows the comparison of the displacements at the center of the plate from the present simulation and displacements obtained from the experiment and numerical model of Remennikov et al. [2]. The results obtained from the experiment are the final deformations calculated from the 3D image. Initially, the displacement obtained from the present simulation was lower than that obtained from the numerical model in reference [2], but after a certain time, the final displacement does not have a significant difference.

11
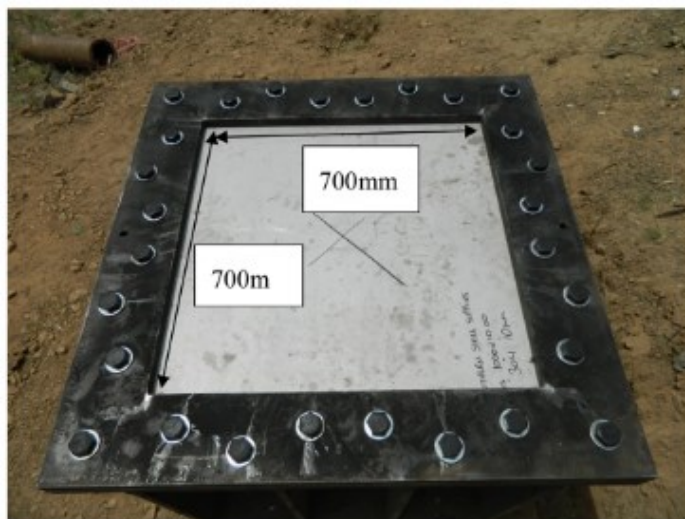
Figure 2: Plate dimensions and test rig used in the experiment [2].
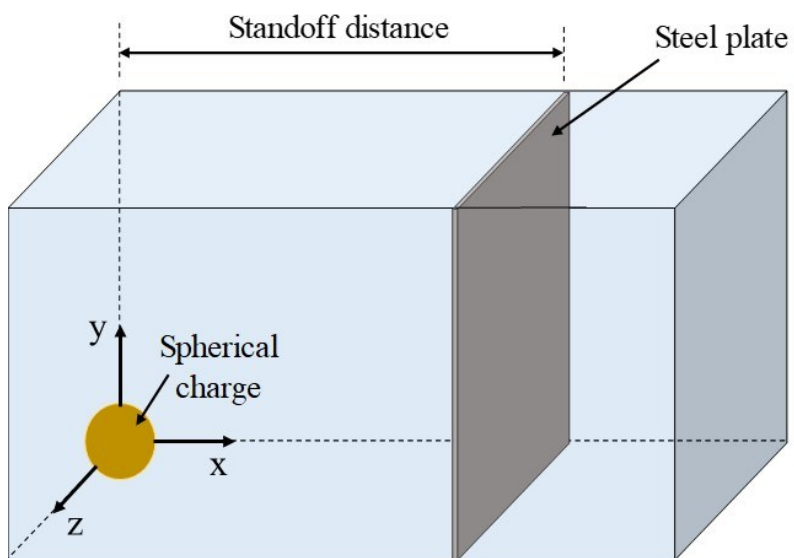
Figure 3: Schematic of the model for validation study (for example 2).

(a)   (b)
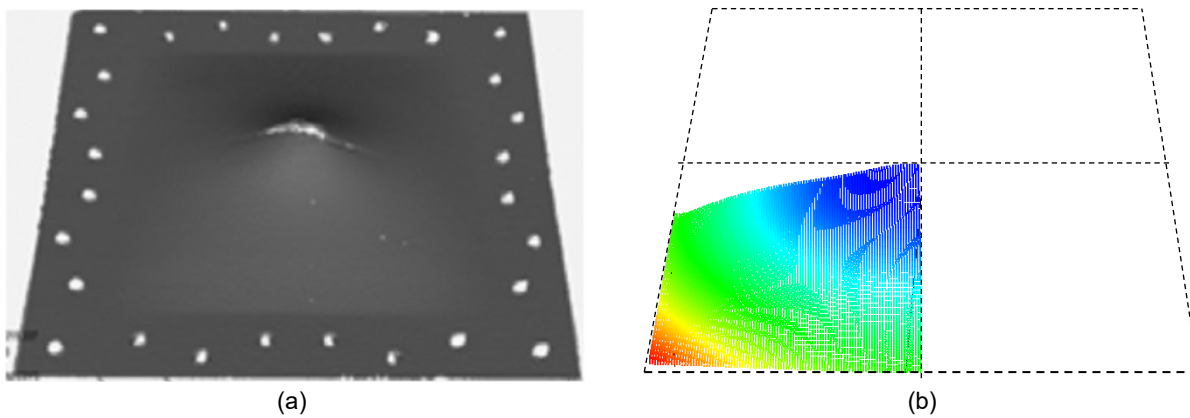
Figure 4: Deformed shape of steel plate, (a) experiment [2] and (b) present simulation.
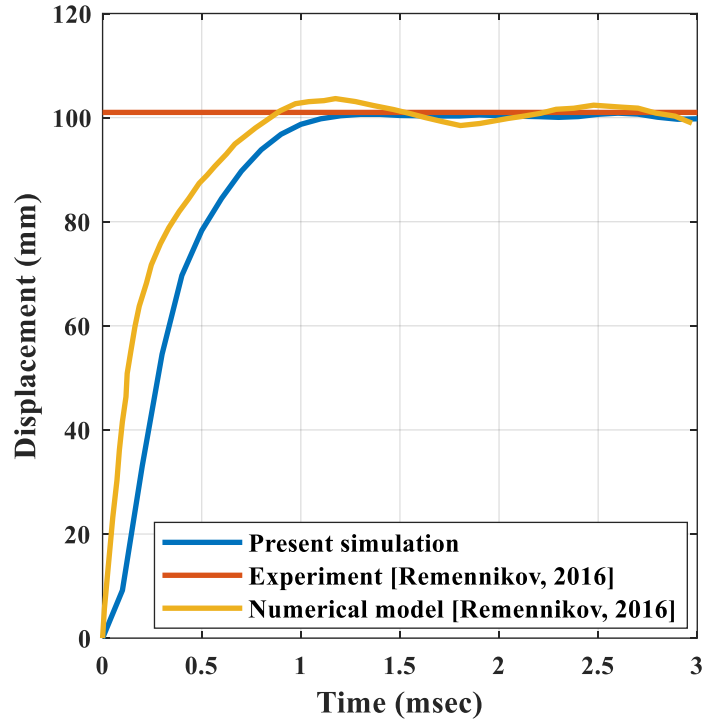
Figure 5: Comparison between displacement at the center of the plate from simulation and reference [2].

4. RESULTS AND DISCUSSIONS

This section investigates the effect of standoff distance on displacement, overpressure, velocity, and temperature profile. A TNT spherical charge of 1 kg was taken for all the simulations, and a steel plate of 1000 mm x 1000 mm x 10 mm was taken. The steel material taken was XLERPLATE Grade 350. The material models are the same as discussed in section 2. Eight different standoff distances were taken, ranging from 100 mm to 1050 mm, to investigate the effect of near-field detonation.

4.1 Displacement of steel plate

Figure 6 shows the maximum displacement in the x-direction with time. The displacement is maximum (about 130 mm) at 100 mm standoff distance and decreased exponentially as the standoff distance increased. The value of displacement is about 30 mm (minimum) at a standoff distance of 1050 mm. The observed phenomena were expected, as the target is moved away from the explosive charge the blast load generated due to the overpressure reduces. It was observed that in the region from 300 mm to 600 mm distance the difference in displacement id about 10 mm. And further the rate of decrease of displacement increases for 800 mm and 1050 mm standoff distances.

4.2 Overpressure profiles near the center of the steel plate

Figure 7 shows the overpressure profiles for different standoff distances. In the Figure, the y-axis is overpressure in MPa near the center of the plate, and the x-axis denotes the time in msec. It was observed that the peak overpressure for 100 mm standoff distance was about 250 MPa and reduced as the standoff distance was increased. The arrival time also increases as we increase the standoff distance. Secondary and tertiary shock waves were observed in pressure profiles. These were due to the successive reflection of the shock wave of the air/explosive interface shortly after detonation.

13
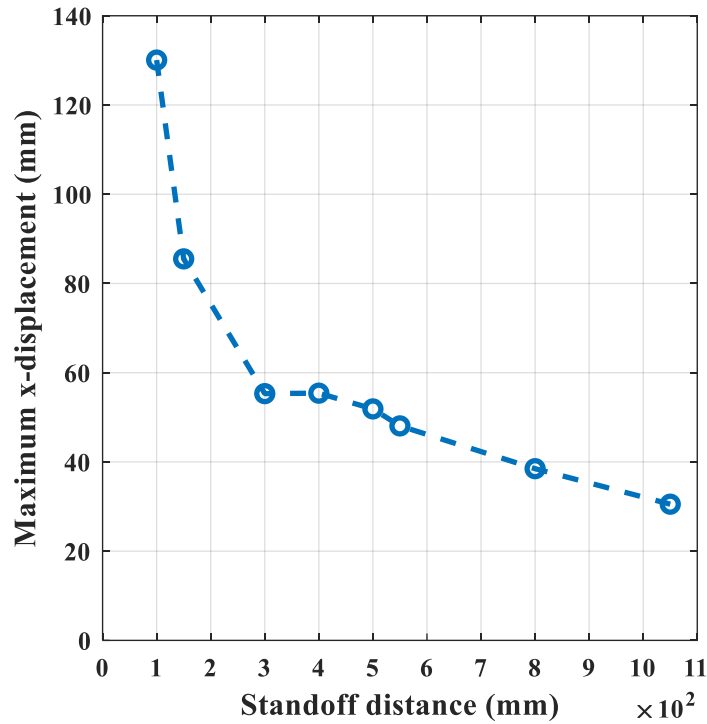
Figure 6: Maximum x-displacement for different standoff distances after 2 msec.

4.3 Gas and plate velocity profiles at the center of the plate

Figure 8 shows the velocity profiles. In the Figure, the left y-axis represents the gas velocity near the center of the plate, and the right y-axis represents the particle velocity at the center of the plate. It can be observed that the gas velocity is initially positive, but as the overpressure reaches the plate, it changes its direction due to the reflection from the plate. The particle velocity is always in positive x-direction with a maximum value for 100 mm standoff and decreases as the standoff distance is increased. The reflected and particle velocities are highest for 100 mm standoff distance and decreases as the standoff distance was increased. The maximum particle velocity was about 300 m/sec.

4.4 Temperature profiles at the center of the plate

Figure 9 shows the temperature profiles. The maximum temperature observed was about 9000 K. It was observed that the occurrence of peak temperature was after the arrival time of peak overpressure. The temperature values decreased as the standoff distance increased, and it has a minimum value of 1500 k for a 1050 mm standoff distance.

14
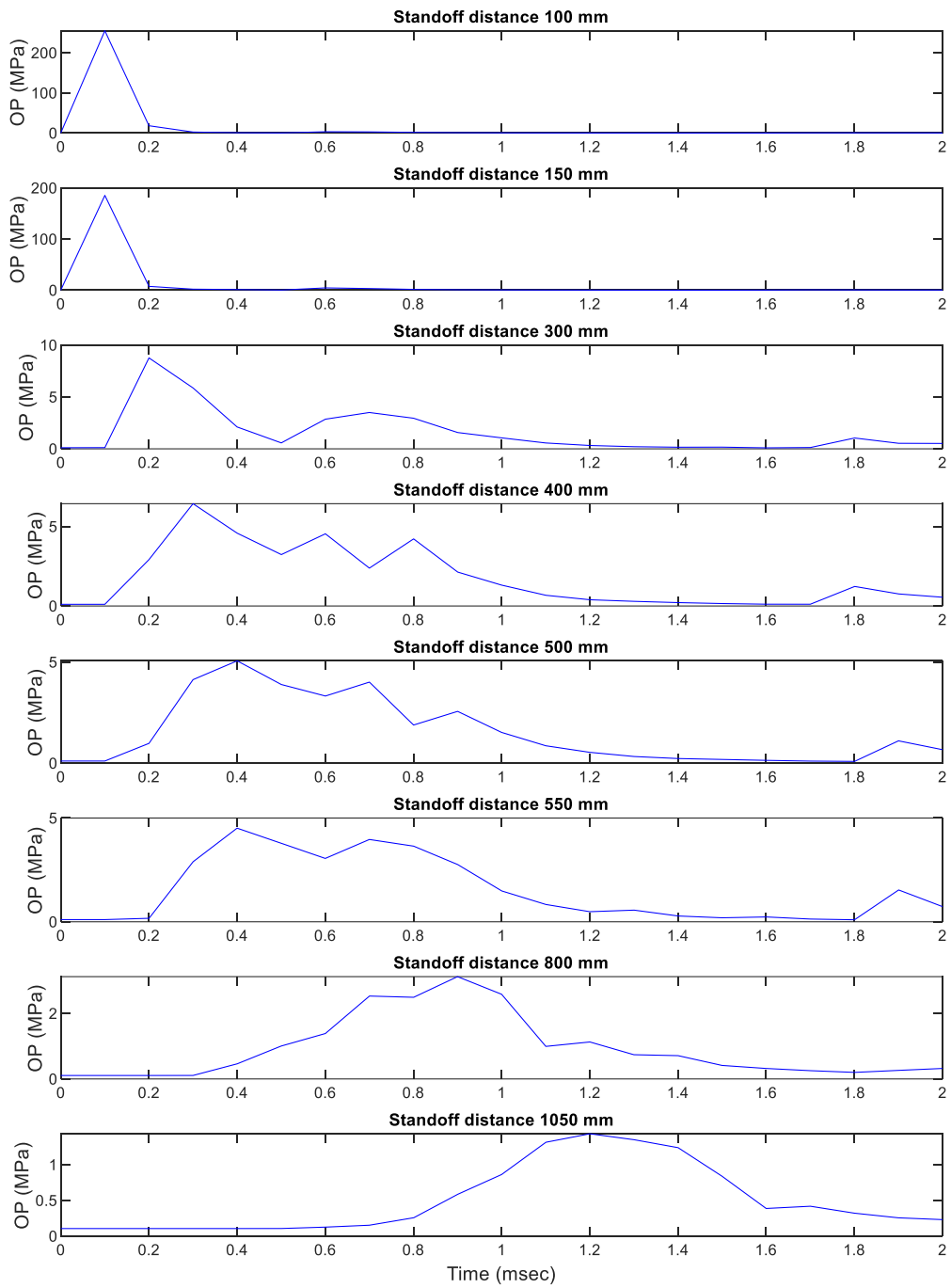
Figure 7: Pressure-time histories for different standoff distances.
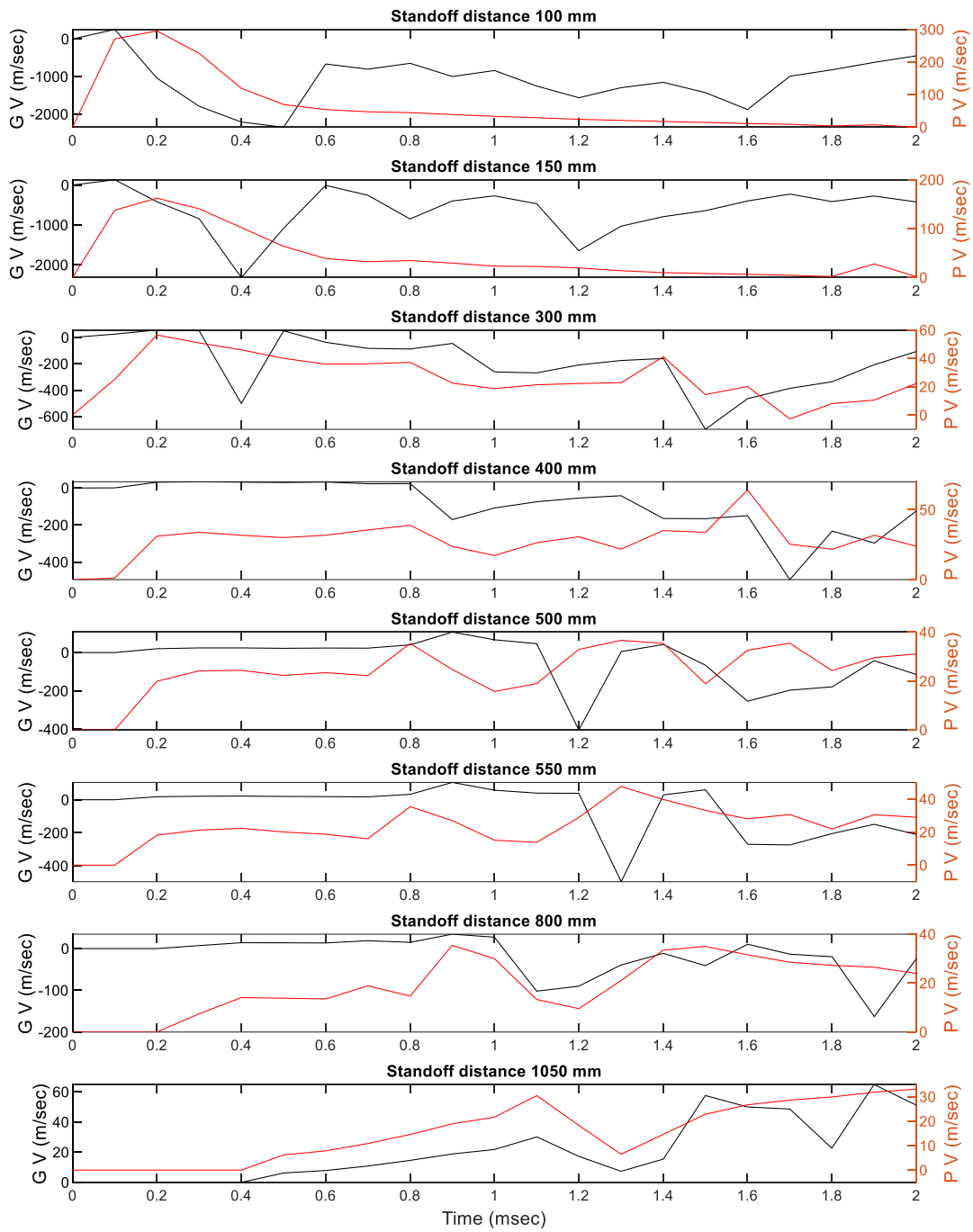
Figure 8: Velocity profiles of gas (near the center of the steel plate) and particle (at the center of the plate).
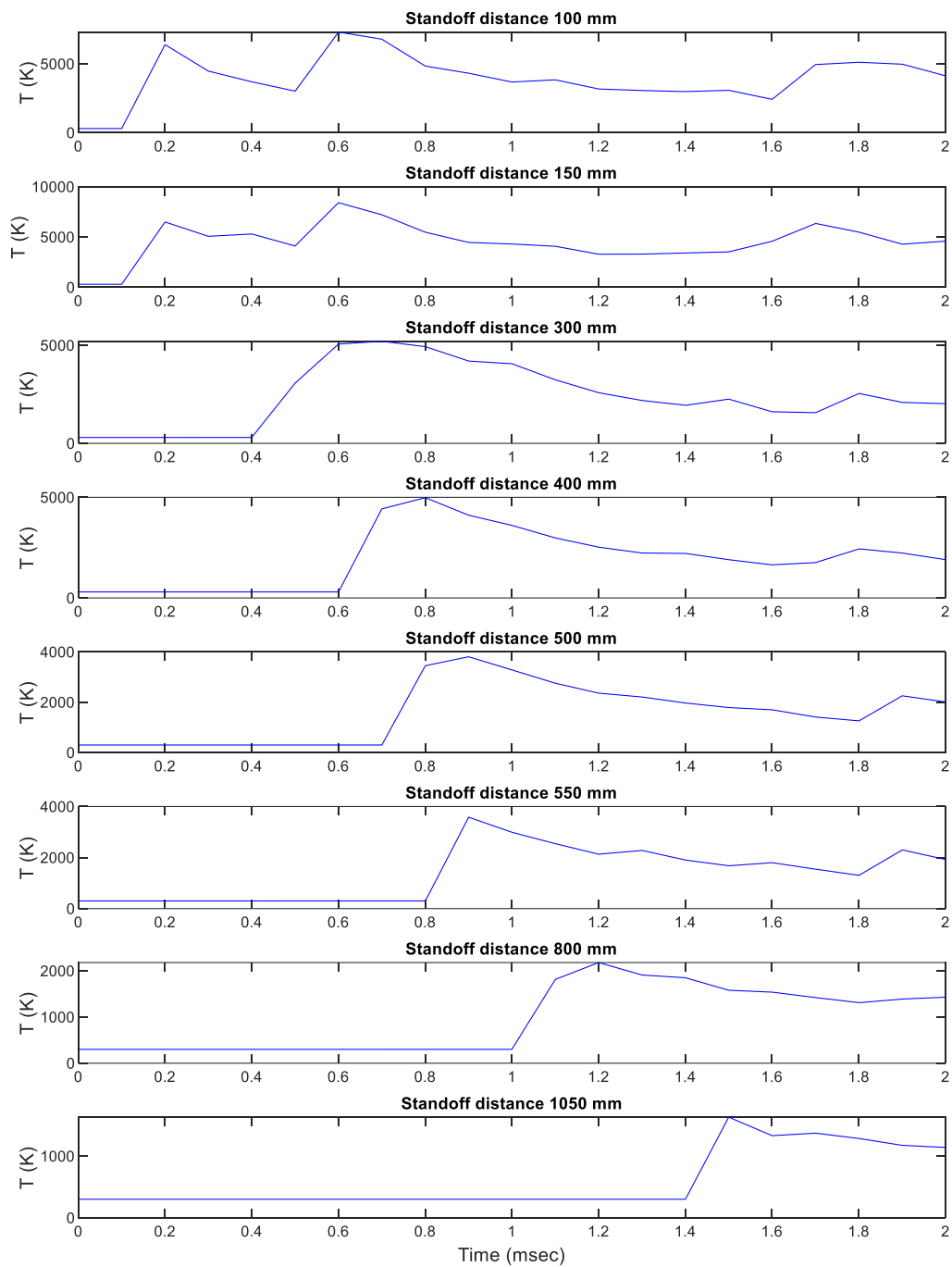
Figure 9: Temperature profiles for different standoff distances.

5. CONCLUSIONS

In this work, the effect of standoff distances on the response of steel sections was investigated. It was observed that as the standoff distance increases, the displacement decreases. The peak overpressure is maximum for 100 mm standoff distance and decreased significantly as the standoff distance increased. The gas velocity was calculated near the center of the plate, and it was observed that initially, the velocity is positive, which denotes that the velocity is in the positive x-direction, but after the pressure profile reaches the plate, the velocity changes its direction to negative x-direction. The particle velocity at the center of the plate was calculated, and it was observed that the particle velocity is always in the positive x-direction. The temperature near the center of the plate was calculated, and it was observed that for smaller standoff distances (100 mm and 150 mm), the temperature was about 8000 K and decreased significantly with an increase in standoff distance. Further, it was found that the time to reach the peak temperature was lower than the time to reach the peak pressure.

Overall it can be concluded that the overpressure, velocity, and temperatures induced due to near-field detonations affected the plate significantly. The proposed numerical model is capable of modeling the coupled response of the structure due to blast loading as most of the previous models are capable of uncoupled study of blast loading on structures. Further, the effect of near-field detonations can be studied for different sections with varying masses of the charge.

References

[1] S. Lukić and H. Draganić, "Blast Loaded Columns—State of the Art Review," Applied Sciences, vol. 11, no. 17, p. 7980, Aug. 2021.

[2] A. Remennikov, T. Ngo, D. Mohotti, B. Uy, and M. Netherton, "Experimental investigation and simplified modeling of response of steel plates subjected to close-in blast loading from spherical liquid explosive charges," International Journal of Impact Engineering, vol. 101, pp. 78–89, Mar. 2017.

[3] A. M. Remennikov and B. Uy, "Explosive testing and modelling of square tubular steel columns for near-field detonations," Journal of Constructional Steel Research, vol. 101, pp. 290–303, Oct. 2014.

[4] "UFC 3-340-02 Structures to Resist the Effects of Accidental Explosions," 2005.

[5] J. Shin, A. S. Whittaker, D. Cormie, and W. Wilkinson, "Numerical modeling of close-in detonations of high explosives," Engineering Structures, vol. 81, pp. 88–97, Dec. 2014.

[6] R. B. Wegener and J. B. Martin, "Predictions of permanent deformation of impulsively loaded simply supported square tube steel beams," International Journal of Mechanical Sciences, vol. 27, no. 1–2, pp. 55–69, Jan. 1985.

[7] S. Fujikura, M. Bruneau, and D. Lopez-Garcia, "Experimental Investigation of Multihazard Resistant Bridge Piers Having Concrete-Filled Steel Tube under Blast Loading," J. Bridge Eng., vol. 13, no. 6, pp. 586–594, Nov. 2008.

[8] B. Zakrisson, B. Wikman, and H.-Å. Häggblad, "Numerical simulations of blast loads and structural deformation from near-field explosions in air," International Journal of Impact Engineering, vol. 38, no. 7, pp. 597–612, Jul. 2011.

[9] Y. Fan, L. Chen, Z. Li, H. Xiang, and Q. Fang, "Modeling the blast load induced by a close-in explosion considering cylindrical charge parameters," Defence Technology, p. S2214914722000290, Feb. 2022.

[10] J. R. Peterson, J. C. Beckvermit, T. Harman, M. Berzins, and C. A. Wight, "Multiscale modeling of high explosives for transportation accidents," ACM International Conference Proceeding Series, no. July, 2012.

[11] B. Banerjee, J. E. Guilkey, T. B. Harman, J. A. Schmidt, and P. A. McMurtry, "Simulation of impact and fragmentation with the Material Point Method," 11th International Conference on Fracture 2005, ICF11, vol. 5, no. May 2014, pp. 3485–3490, 2005.

[12] J. G. Bennett, K. S. Haberman, J. N. Johnson, and B. W. Asay, "A constitutive model for the non-shock ignition and mechanical response of high explosives," Journal of the Mechanics and Physics of Solids, vol. 46, no. 12, pp. 2303–2322, Dec. 1998.

[13] B. W. White and C. M. Tarver, "Ignition and growth modeling of detonation reaction zone experiments on single crystals of PETN and HMX," presented at the Shock Compression of Condensed Matter - 2015: Proceedings of the Conference of the American Physical Society Topical Group on Shock Compression of Condensed Matter, Tampa Bay, Florida, USA, Tampa Bay, Florida, USA, 2017, p. 030001.

[14] D. Mohotti, P. L. N. Fernando, D. Weerasinghe, and A. Remennikov, "Evaluation of effectiveness of polymer coatings in reducing blast-induced deformation of steel plates," Defence Technology, vol. 17, no. 6, pp. 1895–1904, Dec. 2021.

Occurrence of Dust Explosions followed by fire in reinforced concrete silos

Paulo Palmeira Machado 1[a], Carla Neves Costa 2[b],

(a) Universidade Estadual de Campinas, Doctorate Student (p192242 @dac.unicamp.br)
(b) Universidade Estadual de Campinas, Civil Engineering professor Faculdade de Engenharia Civil, Arquitetura e Urbanismo (carlac @fec.unicamp.br)

ABSTRACT

Dust explosions are the combustion of thin particles suspended in the air of closed environments, in this way, silos are favorable environments for the occurrence of such events. Dust explosions can occur in any silo with combustible products suspended in air at a sufficiently high concentration. Several studies point out that the energy generated by dust explosions is enough to cause fires in silos and burn all the stored product, in addition to the structural damage, especially if there is no ventilation in the silo Several researchers have already defined critical parameters that define the possibility of a dust explosion, such as particle size and dust concentration. The primary explosions are capable of generating secondary explosions that increase fire probability. It is important to notice that if there is no explosion, fire is less likely to occur. Although there is not a lot of papers treating about probability of occurrence of fires after dust explosion in reinforced concrete silos, some researchers developed simple mathematical equations to enable statistical analysis. This statistical analysis is undoubtedly an important step to a risk assessment in silos, and other structures and other performance based methods. After fire ignition, there are a lot of published papers simulating fire and structure resistance, specially using Monte Carlo or other distribution to simulate values of fire.

Keywords: Dust explosions, fire, reinforced concrete, silos

1. INTRODUCTION

Dust explosions are the combustion of thin particles suspended in the air of closed environments, in this way, silos are favorable environments for the occurrence of such events. Dust explosions can occur in any silo with combustible products suspended in air at a sufficiently high concentration. Several studies point out that the energy generated by dust explosions is enough to cause fires in silos and burn all the stored product, in addition to the

structural damage, especially if there is no ventilation in the silo. The objective of this paper is to investigate the probability of dust explosion and the probability of this explosion to cause a fire, in addition to the factors that influence the probability of occurrence of these fires. For this, a literature review and statistical data collection of fire in silos developed to.

Silo fires caused by dust explosions are a serious and potentially deadly hazard that can occur in industries that handle large quantities of dry materials such as grain, feed, and cement (National Fire Protection Association, 2018). According to the U.S. Chemical Safety and Hazard Investigation Board (CSB), dust explosions are one of the leading causes of fires and explosions in the food and agriculture industry (CSB, 2016).

The conditions necessary for a dust explosion to occur include the presence of a combustible dust, an ignition source, and sufficient oxygen (National Fire Protection Association, 2017). Different types of materials have different levels of combustibility, with some materials being more problable to dust explosions than others. For example, grain and other food products, wood products, are all known to be prone to dust explosions (National Institute for Occupational Safety and Health, 2018).

2. DUST EXPLOSIONS AND FIRE

The National Fire Protection Association (NFPA) defines a dust explosion as "a fire that results from the rapid combustion of particles that are finely divided, generally smaller than 500 microns in diameter, and suspended in air or some other oxidizing atmosphere" (NFPA, 2022). These explosions can be dangerous and destructive, resulting in injuries, fatalities, and significant damage to property and equipment.

Dust explosions occur when a cloud of combustible dust particles is ignited and rapidly combusts, creating a powerful explosion. Several factors can contribute to the ignition and spread of a dust explosion, including the concentration of dust particles, the size and shape of the particles, and the presence of an ignition source.

According to the NFPA, five conditions must be present for a dust explosion to occur: fuel (combustible dust), oxygen, an ignition source, dispersion of dust particles, and confinement of the dust cloud (NFPA, 2022). When these conditions are met, an explosion can occur.

Fires can occur after a dust explosion due to the high temperatures generated by the explosion and the presence of flammable materials in the area. When a dust explosion occurs, the rapid combustion of the combustible dust particles can create extremely high temperatures, which can ignite flammable materials, leading to a fire.

According to the National Fire Protection Association (NFPA), fires can be a secondary hazard of dust explosions, and combustible materials, such as packaging materials or equipment, can become fuel for a fire following an explosion (NFPA, 2022). In addition, the high temperatures generated by a dust explosion can damage surrounding structures and equipment, creating additional fuel sources for a fire.

The intensity of fires in silos can vary based on the type of product stored. The stored product can affect the ignition and combustion characteristics, as well as the heat release rate and smoke production during a fire. Some products, such as wood pellets and straw, are more prone to combustion due to their low ignition temperature and high surface-to-volume ratio (Kleineidam et al., 2017). Other products, such as wheat and corn, are less prone to combustion but can still pose a fire risk if stored improperly (Dunn, 2017).

In addition to the type of product stored, other factors can also affect the intensity of fires in silos, including the size and configuration of the silo, the temperature and humidity conditions, and the presence of ignition sources (Kleineidam et al., 2017).

In general, silos storing agricultural products such as hay, straw, or corn can be particularly susceptible to fires due to the high moisture content and potential for spontaneous combustion (Tamburrino et al., 2020). Grain dust explosions can also occur in grain silos, which can lead to fires.

There are several models that have been developed to predict the probability of a dust explosion occurring in a given situation, based on factors such as the type and concentration of the dust, the size and shape of the space in which the dust is present, and the ventilation and ignition sources present in the area. Some commonly used models for predicting the probability of a dust explosion include:

1. The "maximum explosion pressure" model: This model estimates the maximum pressure that could be generated by a dust explosion in a given space based on the properties of the dust and the size and shape of the space.
2. The "Kst" model: The Kst model is based on the maximum explosion pressure model and estimates the probability of a dust explosion occurring based on the dust's ability to generate pressure.
3. The "Pmax" model: The Pmax model is also based on the maximum explosion pressure model and estimates the probability of a dust explosion occurring based on the maximum pressure that could be generated by the dust in a given space.
4. The "dusting explosion index" model: The dusting explosion index model estimates the probability of a dust explosion occurring based on the dust's ability to disperse and mix with air.

Zhang et. al developed a review of literature on the factors that influence a dust explosion, and together with this literature review they developed a statistical method to predict dust explosion probability. The authors took into account the following parameters: minimum ignition energy (MIE); minimum explosion concentration (MEC); minimum ignition temperature of a dust cloud (MITc); maximum burst pressure (Pmax); maximum rate of pressure increase ((dP/dt)max); and explosion index (KSt).

Several researchers have already defined critical parameters that define the possibility of a dust explosion, such as particle size and dust concentration. According to Amyotte (2013), the particle size is the most important factor for determining a dust explosion, and this is because the smaller the particle, there is an increase in the surface area of the grains, and with this, an increase in the dust reactivity, and if combustion takes place between a gaseous oxidant and solid fuel then there are more possible sites for the chemical reaction on the surface of each particle.

Zhang et. al (2018) conclude that factors such as dust dispersion, ignition energy, dust concentration, oxygen and combustible agents favor the occurrence of dust explosions, while factors such as particle size, humidity and inert density would reduce the probability of occurrence of dust explosions. dust explosions.

Hassan et al (2014) developed a flowchart with a method to determine the probability of a dust explosion occurring, the flowchart is presented in Figure 1. The method consists of using 5 steps: step 1-risk identification; 2-data collection from databases, or from experimental works; 3-data analysis, with the classification of parameters, statistical analysis and determination of the PDF curve; 4-probabilistic modeling; 5-Graphing for quick visual identification. Hassan et al (2014) determined a equation (1) to calculate the probability of dust explosion occurrence:

$$P = 0,5[(Diameter \times MEC) + (MEC \times MIT) + (MIT \times MIE) + (MIE \times LOC) \times (LOC \times Diameter)]S_f \times S_n \tag{1}$$

Addai et al. (2016) developed a method to estimate Minimum Ignition Temperature (MIT) for hybrid mixtures. They observed that MIT value increased when dust amount was below Minimum Explosible Concentration, meaning that, if there is no dust explosion, the ignition of a fire is less likely to occur.

3. RELIABILITY IN SILOS

Failure probability is the defined as the number of times that silo fails divided by the total number of analysis. This kind of article is already published by some authors, like Van Coile et. Al (2017), Yaping (2013), Shpilberg (1977).

Van Coile et. Al (2017) developed a fluxogram to define if there is a structural failure. The author defines that after ignition, it is necessary to consider the probability of failure of users to suppress the fire before flashover, the probability of the sprinklers to fail and the probability of fire brigade to fail to suppress the fire before flashover. After all this probabilitys it is necessary to consider fire growth and structure capability to resist to fire action.

To apply Van Coile et al (2017) fluxogram to a silo, after the dust explosion there is the probability of a fire starting, and to this, it is necessary to reach minimum energy of explosion, so, it is possible to use Monte Carlo to make a distribution of Explosion Energy depending on the . If users, fire brigade and sprinklers are unable to suppress fire, then the structure will be verified by equation (2):

$$f(x) = g(x) - h(x) = R - S \tag{2}$$

Where f(x) is reliability function, g(x)=R=resistance, h(x)=S=Solicitation. With a Monte Carlo analysis its possible to calculate probability of failure of structure based in these factors and values.

Figure 1 - Probability of dust explosion (flowchart)

4. CONCLUSIONS

Although there is not a lot of papers treating about probability of occurrence of fires after dust explosion in reinforced concrete silos, some researchers developed simple mathematical equations to enable statistical analysis. This statistical analysis is undoubtedly an important step to a risk assessment in silos, and other structures and other performance based methods.

However there is no article published about fire probability after a dust explosion, it is proposed to do the analysis as a future paper, since it is an important step to a performance based design, since its necessary to calculate the probability of occurrence of fire and its intensity. After fire ignition, there are a lot of published papers simulating fire and structure resistance, specially using Monte Carlo or other distribution to simulate values of fire.

5. REFERENCES

[1]   ZHANG, Jiangshi; XU, Peihui; SUN, Longhao; ZHANG, Wenyue; JIN, Jianghong. Factors influencing and a statistical method for describing dust explosion parameters: a review. Journal Of Loss Prevention In The Process Industries, [S.L.], v. 56, p. 386-401, nov. 2018. Elsevier BV. http://dx.doi.org/10.1016/j.jlp.2018.09.005.

[2]   HASSAN, Junaid; KHAN, Faisal; AMYOTTE, Paul; FERDOUS, Refaul. A model to assess dust explosion occurrence probability. Journal Of Hazardous Materials, [S.L.], v. 268, p. 140-149, mar. 2014. Elsevier BV. http://dx.doi.org/10.1016/j.jhazmat.2014.01.017.

[3]   AMYOTTE, Paul. Introduction. An Introduction To Dust Explosions, [S.L.], p. 1-7, 2013. Elsevier. http://dx.doi.org/10.1016/b978-0-12-397007-7.00001-x.

[4]   U.S. Chemical Safety and Hazard Investigation Board (CSB) (2016). Dust Explosions in the Food and Agriculture Industries. Washington, D.C.: U.S. Chemical Safety and Hazard Investigation Board.

[5]   HSE. (2021). Dust explosions. Retrieved from https://www.hse.gov.uk/explosions/dust-explosions.htm

[6]   National Institute for Occupational Safety and Health (NIOSH). (n.d.). Dust Explosion Scenarios and Case Studies. Retrieved from https://www.cdc.gov/niosh/topics/explosions/case-studies.html

[7]   European Process Safety Centre. (n.d.). Dust Explosion Hazard Estimation Tools. Retrieved from https://www.epsccentre.org/hazard-estimation-tools/dust-explosions/

[8]   European Process Safety Centre. (n.d.). Pmax. Retrieved from https://www.epsccentre.org/hazard-estimation-tools/dust-explosions/pmax/

[9]   National Fire Protection Association. (2022). NFPA 652: Standard on the Fundamentals of Combustible Dust. Retrieved from https://www.nfpa.org/codes-and-standards/all-codes-and-standards/list-of-codes-and-standards/detail?code=652

[10]   Dunn, D. (2017). Fire in the Grain. Fire Engineering, 170(8), 85-87.

[11]   Kleineidam, J., Dittrich, H., Kalkbrenner, F., Kinateder, M., & Eichberger, A. (2017). Fire behavior of pellets and granules in storage and transport. In International Symposium on Fire Investigation, Science and Technology. Springer, Cham.

[12]   Tamburrino, A., Giuseppe, A., Calabrese, A., & Currò, F. (2020). Fire risk assessment of agricultural silos: Comparison between HAZID and HAZOP methodologies. Process Safety Progress, 39(4), e12146. https://doi.org/10.1002/prs.12146

[13] DustSafetyScience. Incidents. April 2023. https://dustsafetyscience.com/category/incidents/

[14] Van Coile, R., Balomenos, G.P., Pandey, M. D. An Unibiased Method for probabilistic Fire Safety Engineering, Requiring a Limited Number of Model Evaluations. Fire Technology, 53(5), 1705-1744, 2017.

[15] Yaping, He. Probabilistisc fire-risk-assessment function and its application in fire resistance design. Procedia Engineering, 2013

[16] Shpilberg, David C. The probability Distribution of Fire Loss Amount. The journal of Risk and insurance Association. Vol. 44, n. 1, 103-115, 1977.

Firefighting

A SMOKE SENSOR VIA CNN FOR REAL-TIME VICTIM DETECTION IN SMOKY INDOOR ENVIRONMENTS

Sebastian Gelfert[1]

ABSTRACT

Searching for victims in smoky indoor environments is a challenging task during firefighting missions. This is due to the fact that firefighters have limited visibility in smoke and existing search strategies require time to find the missing victim. Nowadays, fire departments are also equipped with remote-controlled mobile robots with embedded sensor technology, which are navigated by operators outside the danger zone and are used to search for victims. Operators also reach their mental limits, as it is difficult to judge changing smoke conditions within the image displayed on the human-machine interface. In this paper, a novel approach that uses artificial intelligence to display the smoke intensity in a smoky indoor environment on a human-machine interface to support operators of a remote-controlled mobile robot is presented. Thereby, a deep learning model is trained on a reference system to determine and visualize the smoke intensity on the interface. Experiments show that this approach enables efficient visualization of the smoke intensity.

Keywords: Computer vision, deep learning, mobile robot, optical camera, smoke intensity, smoky environment, SSD, victim detection.

1. INTRODUCTION

The increasing number of apartment fires over the last years caused a tremendous loss of human life (20,755 fire deaths in 2020 [1]). Due to the furnishing in the home area, the combustion process causes a large amount of smoke, which increases the time needed for firefighters to search for victims and at the same time significantly complicates the search process. [2]. Mobile robots that are remote-controlled by operators outside the danger zone have gained a lot of interest in the past, as they assist firefighters during search and rescue missions [3]. This assistance is needed due to the fact that firefighters' cognitive fatigue reduces their efficiency during long search missions [4]. Also, today's intelligent imaging systems are an integral part of mobile robots, especially for victim detection in hazardous environments [5]. A key role during the search for victims with mobile robots is assigned to the operator [2]. By using a human-machine interface (HMI), the operator is required to navigate the mobile robot inside the building as well as assess whether or not a victim is in the indoor environment [2]. Because of this stressful situation and the associated cognitive fatigue of the operator, the operator potentially fails to recognize victims due to the smoke as well as the additional navigation of the mobile robot [4]. In summary, it is therefore necessary to provide the operator with further information of the indoor environment such as smoke intensity. Figure 1 shows a schematic illustration of the smoke intensity visualized on the HMI.

---

[1] Department of Electrical & Electronic Engineering, Munster Technological University; Cork, Ireland (sebastian.gelfert@mycit.ie).

This paper is an early work for victim detection in smoky indoor environments. The main contribution of this work is a novel approach that qualitatively determines the smoke intensity in a smoky indoor environment using a trained CNN model and an optical camera equipped on a remote-controlled mobile robot. The smoke intensity is visualized to the operator's HMI.

Figure 1: Visualization of the smoke intensity on the HMI

The paper is structured as follows: In section 2, the related work on this topic is discussed. The methodology of determining the smoke intensity shows section 3. In section 4, the experimental outline and obtained results of the experiment are demonstrated. Finally, a conclusion of the work and directions for future work is provided in section 5.

2. RELATED WORK IN SMOKE DETECTION

In this section, the related work in smoke detection is presented.

Khan et al. [6] present a smoke detection and segmentation framework for hazy and clear real-world surveillance settings based on a convolutional neural network (CNN). The authors [6] employ an efficient CNN architecture (EfficientNet) with better accuracy and also segment the smoke regions. As a result, Khan et al. [6] increase the accuracy up to 3% and decreases the false positive rate (FPR) by 0.46%.

A novel hybrid approach to assess precise as well as fast identification of smoke in video sequences is given by Gagliardi et al. [7]. The approach combines a feature detector based on Kalman filtering and a CNN. First, the algorithm automatically selects a specific region of interest within the image for gray colored moving objects. Second, the CNN verifies the presence of smoke in the proposed region of interest. The authors [7] compare their approach with existing metrics on several video datasets and demonstrate the improvement of their approach.

A special application of smoke detection in a normal and foggy IoT environment is investigated by Khan et al. [8]. The authors [8] use the VGG-16 CNN architecture. Experiments show better results in terms of accuracy, FPR as well as efficiency compared to other CNN models.

He et al. [9] propose a smoke detection method for normal and foggy environments. The approach combines an attention mechanism, a feature-level module as well as a decision-level fusion module. Through comparative experiments with an existing and self-created dataset, He et al. [9] show higher accuracy and precision compare to other existing CNN approaches.

Saponara et al. [10] introduce a real-time video-based smoke and fire detection system which uses YOLOv2 CNN. The training process of the YOLOv2 CNN is executed with a fire and smoke image dataset in outdoor and indoor scenarios. The trained data is tested with fire and smoke and negative videos in several outdoor (for instance storage area) environments as well as indoor (for instance container, home, office) environments and is compared to other CNN methods. The YOLOv2 CNN method achieves promising results in terms of accuracy in comparison to the state-of-the-art CNNs.

Another special application of fire smoke detection in a wildland forest is presented by Zhang et al. [11]. The authors [11] uses a Faster R-CNN to detect smoke in forest environments and produce synthetic forest smoke training images by inserting simulative and real smoke into forest environment images. The trained system is verified with real forest smoke images and the performance of simulative smoke show better results.

Zhao et al. [12] investigate the impact of using additional infrared bands for fire smoke detection from landsat images with a CNN model when wildfires occur. Thereby, the authors [12] design a lightweight CNN model (Variant Input Bands for Smoke Detection) and show in a case study that the trained CNN model could effectively detect fire smoke mixed with cloud over limited geographic areas.

Also, Almeida et al. [13] propose a novel lightweight CNN model for wildfire detection through RGB images. The CNN architecture is applicable with aerial images by unmanned aerial vehicles (UAV) as well as video surveillance systems. The CNN model achieves an accuracy of 98.97% and a F1 score of 95.77%.

In the work of Lin et al. [14], the authors [14] develop a joint detection framework based on Faster R-CNN and 3D CNN. The two frameworks show high performance in smoke location and recognition. The authors [14] achieve a detection rate of 95.32% and a FPR of 0.39% for smoke video sequences.

Zeng et al. [15] address an improved detection method based on CNN to detect fire smoke. The authors [15] verify the CNN models Faster R-CCN, Single Shot MultiBox Detector (SSD), Region-based Fully Convolutional Networks (R-FCN) and improve the detection effect by replacing the feature extractor with a novel feature extraction network (for instance MobileNet, ResNet V2, Inception V2, Inception ResNet V2). Experiments demonstrate that the mean average precision (mAP) reaches 56.04% on the smoke detection dataset.

Also, Cheng [16] uses Faster R-CNN for smoke detection in images. During an experimental verification, Cheng [16] demonstrates the improvement of accuracy and the decrease of the FPR.

Nguyen et al. [17] present a novel smoke detection method by using surveillance cameras in indoor environments. The method consists of two stages. First, motion regions between consecutive frames are located by using optical flow. Second, a CNN is used to detect smoke in this region. The method is evaluated with an own image dataset as well as a real video sequence. The proposed method achieves better accuracy compared to the state-of-the-art methods.

Also, Pincott et al. [18] develop and evaluate a vison-based CNN (Faster R-CNN) approach for indoor fire and smoke detection. Based on indoor fire and smoke videos, the trained CNN model achieves up to 92.37% correct fire detections, but smoke detection did not perform well. In 2022, Pincott et al. [19] present a second work with the objective, to study two existing CNN models (Faster R-CNN Inception V2 and SSD MobileNet V2) and design a vision-based indoor fire and smoke detection system. Tests show that the Faster R-CNN Inception V2 model achieves better results in terms of accuracy and detection compared to the SSD MobileNet V2 model.

Dhiman et al. [20] propose a firefighting robot that uses CNN to detect fire. The authors [20] achieve an accuracy of fire detection up to 98.25%. Also Guo et al. [21] present a firefighting robot that uses a Faster R-CNN model to detect indoor fire in noisy images. The authors [21] obtain a precision of up to 99.8%.

Another approach of fire detection with a firefighting robot is presented by Li et al. [22]. The work proposes a thermal image flame detection with YOLOv4-F based on YOLOv4-tiny CNN model. Experiments show that the accuracy of the proposed YOLOv4-F CNN model is 5.75% higher and the mAP rises by 7.02%, compared to the YOLOv4-tiny, YOLOv5-s and YOLOv7-tiny CNN models.

Furthermore, Tephila et al. [23] address a firefighting robot that uses deep learning to detect fire. The authors [23] use a combination of Imagenet and Alexnet and achieve a fire detection accuracy of up to 97.75%.

An efficient fire detection based on a CNN model in video surveillance applications is proposed by Muhammad et al. [24]. The efficient CNN architecture, inspired by the SqueezeNet architecture, is used to detect fires. The architecture has the advantage that it uses smaller convolutional kernels with lower computational requirements.

Tests show that due to the increased depth, the proposed solution achieves an accuracy that is comparable to other more complex CNN models. Also, Muhammad et al. [25] present a second work. In this work, the authors [25] propose another efficient CNN model for fire detection in uncertain surveillance scenarios. Experiments also show better performance of the CNN model compared to state-of-the-art CNN models.

An et al. [26] propose a dynamic convolution YOLOv5 CNN-based fire detection approach. First, the approach uses the K-mean++ algorithm to optimize anchor box clustering. Second, the dynamic convolution is introduced into the convolution layer of YOLOv5. Third, the pruning of the network heads of YOLOv5's neck and head is carried out to improve the detection speed. During experiments, the authors [26] verify that the dynamic convolution YOLOv5 fire detection method reaches higher performance (recall, precision, F1 score) than the YOLOv5 method. Also, in comparison to other CNN models, the precision and F1 score is improved.

Chowdhury et al. [27] introduce a hybrid model for fire detection. The vision-based fire detection model uses the color and motion attributes of fire in the frame. In the second part, a physical MQ-2 smoke sensor is used to recognize smoke and gas in the environment caused by the fire. Experiments show that the system has an accuracy of up to 86.67%. Also Zhang et al. [28] use a vision-based systems and a physical MQ-2 smoke sensor in their work. On the other hand, Jobert et al. [29] present a novel optical smoke sensor.

Li et al. [30] propose a deep-learning fire source localization algorithm with temperature and smoke sensor data fusion according to the stages of the combustion process. Experiments show that the root mean squared error of the model localization reaches 0.63, 0.08 and 0.17 in three stages.

Fritsche et al. [31] discover that real smoke and fog, generated by a fog machine, is physically different, but emphasize that the attenuating influence on vision measurement is basically comparable.
Summarizing the smoke detection approaches in the literature [6] - [31] no research, by the best knowledge of the author, is known that determines the smoke intensity in real-time in a smoky indoor environment using an optical camera as well as a CNN model.

3. METHODOLOGY OF SMOKE INTENSITY MODEL

This section describes the, by the author of this work, proposed methodology for determining the smoke intensity in smoky indoor environments. Figure 2 illustrates the methodology in a flowchart.
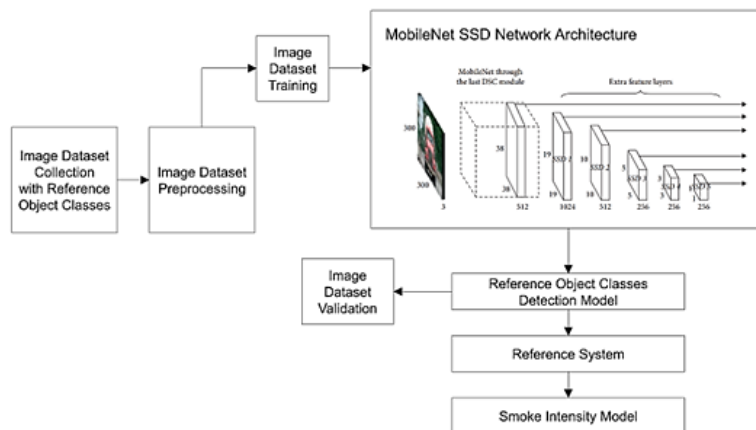
Figure 2: Flowchart of smoke intensity model

Since no image dataset is available for the smoke intensity model, first it has to be crated with reference object classes. After preprocessing (for instance removal of outliers) and training the image dataset on a MobileNet SSD network architecture, a reference object classes detection model is provided. On the one hand, the generated model is validated on an image dataset and is the input for the reference system on the other hand. Based on the reference system, the smoke intensity model is derived.

3.1 – Image Dataset Collection

Since there is no image dataset available, an own image dataset is generated in this research work. The image dataset consists of a collection of reference object classes taken with an optical camera and a sensor for illumination. The optical camera (model Rapoo) is a high resolution device (1,920×1,080 px) with a viewing angle of 80° and a frame rate of 30 fps. It is connected to a single-board computer via serial interface (USB) and positioned statically in space. The scene with the reference object classes consists of a neutral background but is combined with different lighting conditions. These lighting conditions are characterized for instance by lateral sunlight or shadowing. In total, 193 RGB images (640x480 px) are captured, also without reference object classes for true negative predictions.

3.2 – Reference Object Classes

The reference object classes used in this research work has the characteristics that they are unique from other objects in the scene. In Figure 3 example images of the novel image dataset, captured with the optical camera, are illustrated.

Figure 3: Examples of the reference object classes in different positions captured with the optical camera

Figure 3 shows that the reference object classes are represented by a combination of letters and shapes, which differ from conventional shapes in a scene.

3.3 – Image Dataset Preprocessing

Three steps are taken to preprocess the image datasets. In the first step, images that are not suitable for training are removed from the image dataset (blur, reference objects cropped, outliers). Second, the image dataset is annotated[1] (XML format) by the individual letters and numbers. Third, the image dataset is randomly sorted into a training (90%) and a validation (10%) batch. The random split is applied with the library Split Folders[2].

3.4 – Image Dataset Training

After preprocessing the image dataset, the data is trained on a Single Shot MultiBox Detector (SSD) MobileNet network architecture[3]. The deep learning model is pretrained on the COCO dataset[4]. The used MobileNetV2[5] is an appropriate architecture for devices with low computational power. It consists of two layers, whereby the first layer is a depthwise convolution and performs lightweight filtering by applying a single convolutional filter per input channel and the second layer is a 1×1 convolution, which is responsible for building new features through computing linear combinations of the input channels [32]. In order to prevent the training of overfitting, the image dataset is trained over 30,000 steps. The result of the training is a reference object classes detection model in different regular environmental conditions based on RGB images.

---

[1] https://github.com/tzutalin/labelImg/

[2] https://pypi.org/project/split-folders/

[3] https://github.com/tensorflow/models/blob/master/research/object_detection/g3doc/tf1_detection_zoo.md

[4] https://cocodataset.org/

[5] https://github.com/tensorflow/models/blob/master/research/object_detection/g3doc/tf1_detection_zoo.md

3.5 – Image Dataset Validation

For the assessment of the performance of the trained model, a validation image dataset is used and its results are presented in a precision recall (PR) diagram as well as in a receiver operating characteristics (ROC) diagram. Figure 4 illustrates the validation results of the trained MobileNet SSD network architecture in a PR diagram with its F1 score and average precision AP.
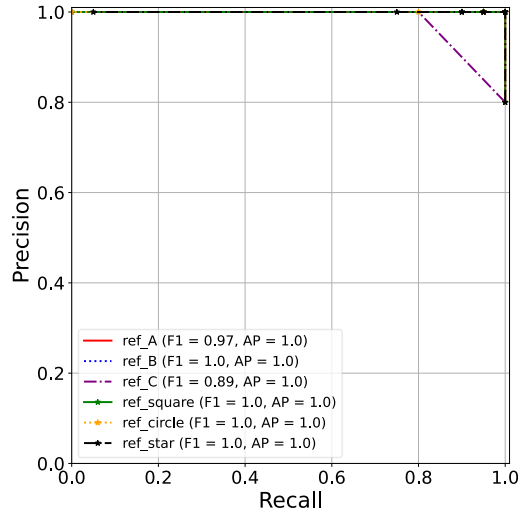
Figure 4: PR diagram with F1 and AP

The PR curves of the reference object classes show a high precision and recall. On all reference objects, F1 has a value greater than 0.89 (ideal model: 1.0), which indicates a balance of precision and recall. The mean average precision of the reference object classes has a value of 0.83 (ideal model: 1.0). The results indicate a high accuracy of the victim detector.

Figure 5 illustrates the validation results of the trained MobileNet SSD network architecture in a ROC diagram with the value of the area under the curve (AUC).
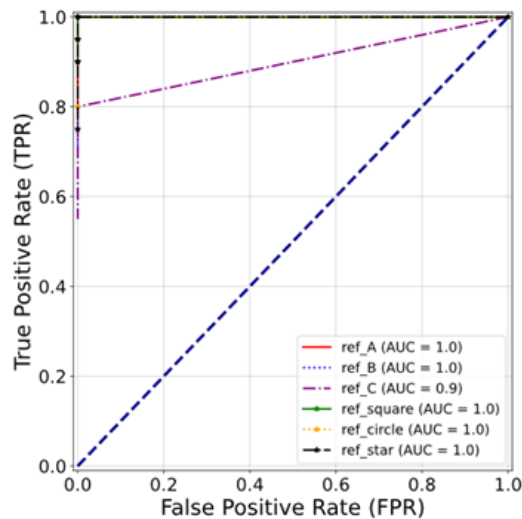
Figure 5: ROC diagram with AUC

The ROC curves of the reference object classes show that the curves are located above the dashed diagonal line (AUC = 0.5). AUC has a value greater than 0.9 (ideal model: 1.0). The result points out that there is a chance

greater than 90% that the MobileNet SSD network architecture can distinguish between a positive class and a negative class.

3.6 – Reference System

The reference system represents the basis for the smoke intensity model and is established with an experimental reference study. The study determines the correlation of an increasing smoke intensity to the detection rates of the reference object classes and applies them to the smoke intensity model. Figure 6 illustrates the experimental reference setup for the study. It consists of a 1,000 mm long smoke chamber with an optical camera, the reference object classes and filled with artificial smoke from a fog machine.
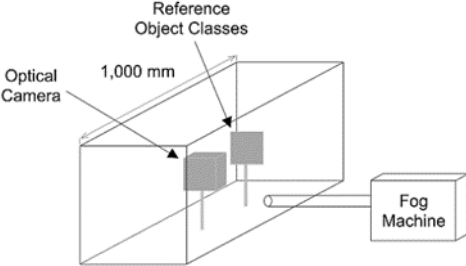
Figure 6: Experimental reference setup

Figure 7 shows the plotted result of the experimental reference study of each reference object class in a detection rate (ordinate) time (abscissa) diagram. Frame 1 represents no smoke and frame 3187 represents high smoke (increasing smoke level).
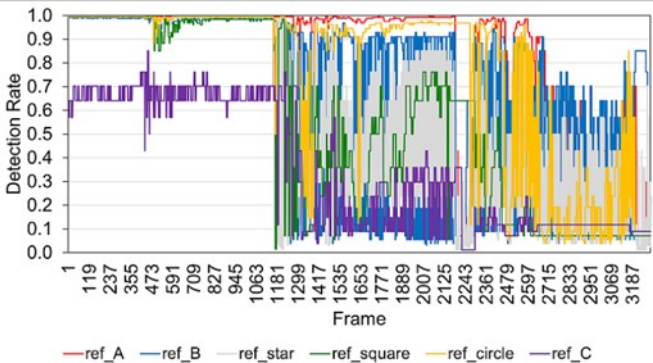
Figure 7: Detection rate (ordinate) time (abscissa) diagram

It can be summarized that the detection rate of the reference object class ref_C decreases at frame range 1,100 – 1,200 (low smoke level), where on the other hand the detection rate of the reference object class ref_A decreases at frame greater than 2,500 (high smoke level).

3.7 – Smoke Intensity Model

Based on the results of the reference system, a smoke intensity model is described in the format of an algorithm. Figure 8 illustrates the algorithm of the smoke intensity model.

35

```
Algorithm Smoke Intensity Model
 1: Input: Detection rates of reference object classes (scores)
 2: if detection_scores ref_C > 0.5, then
 3:        output description no smoke;
 4: end
 5: if detection_scores ref_C < 0.5 and ref_A > 0.8, then
 6:        output description low smoke;
 7: end
 8: if detection_scores ref_C < 0.5 and ref_A < 0.8, then
 9:        output description high smoke;
10: end
11: Output: Smoke Level → no smoke, low smoke, high
     smoke visualized on human-machine interface
```

Figure 8: Smoke intensity model

4. EXPERIMENTAL EVALUATION

In this section, the experimental evaluation of the smoke intensity model is conducted with an optical camera mounted on a mobile robot in a smoky indoor environment with varying smoke intensity sending its environmental information to the human-machine interface and visualizes the smoke intensity on it. First, the experimental setup is described and second, the obtained results of the experiment are discussed.

4.1 – Experimental Setup

Figure 9 illustrates the experimental setup for the evaluation of the smoke intensity model.
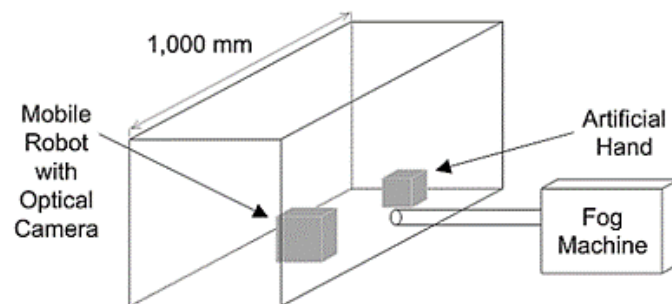
Figure 9: Experimental setup

The experimental setup consists of a 1,000 mm long smoke chamber (transparent body) in which the smoke experiment is performed. The smoky environment is implemented with artificial smoke from a fog machine. Although real smoke and artificial smoke are physically different, Fritsche et al. [31] describe in their research work that the attenuating influence on vision is basically the same. Furthermore, an artificial hand is positioned in the smoke chamber, to ensure a visual contrast to the surrounding area. The mobile robot (see Figure 10) is positioned statically in space and equipped with an optical camera and the reference object classes in front of it. The optical camera is connected to a single-board computer (Raspberry Pi 4 Model B, 8 GB) via serial interface (USB). In order to conduct the experiment in real-time, the CNN model on the single-board computer is converted into a TFLITE format. The mobile robot has the following main specifications: size 275×255×315 mm, weight 4 kg, speed 0.5 m/s, drive unit 4× 12VDC motors. It can be controlled remotely and the information are visualized in real-time on a human-machine interface (Figure 10) to the operator outside the danger zone.
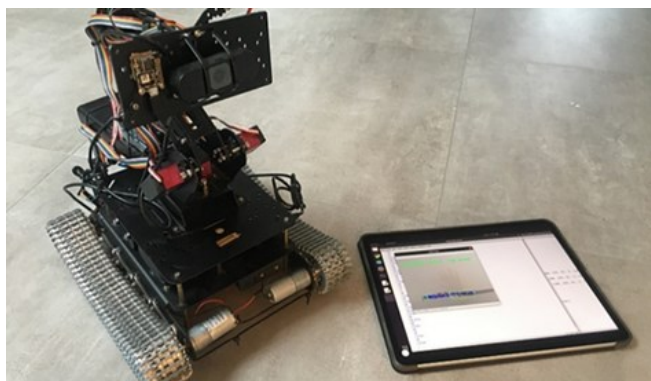
Figure 10: Mobile robot with human-machine interface

The experimental evaluation is conducted as follows: The mobile robot is positioned stationary in the smoke chamber. The smoke chamber is then continuously filled with artificial smoke by the fog machine. The frames of the optical camera are continuously plotted and transmitted in real-time to the human-machine interface and the smoke intensity (no smoke, low smoke, high smoke) is visualized.

4.2 - Experimental Results

Figure 11 illustrates example frames (frame rate top left) of the human-machine interface captured with the optical camera on the mobile robot in the smoke chamber with increasing smoke intensity.

(a) No smoke   (b) Low smoke   (c) High smoke
Figure 11: Results of smoke intensity experiment with increasing smoke intensity

The following results can be drawn from the data:
•   The smoke level in a scene can be determined based on the variation of the detection rates of selected reference object classes.
•   An optical camera is sufficient for smoke level determination, no physical smoke sensor required.
•   The artificial hand is used as a reference to represent changing smoke intensity in a scene.

5. CONCLUSIONS

In this paper, a novel smoke sensor for victim detection in smoky indoor environment based on a MobileNet SSD network architecture is developed and evaluated. The smoke sensor (optical camera, no physical smoke sensor) is based on a smoke intensity model and supports operators outside the danger zone during victim detection by providing the operator with a visualization of the smoke intensity in the smoky indoor environment. Experiments demonstrate a promising approach for victim detection. In summary, remote-controlled mobile robots can be equipped with the smoke intensity model and can visualize the smoke intensity in real-time on a human-machine interface outside the danger zone. This allows an efficient and time-limited victim detection mission. In future research work, the smoke intensity model will be validated in a more complete environmental setup carried out with a real rescue scenario (for instance, victim body, several heat sources, background temperature higher than the victim body, collapsed and cluttered environment, darkness). Additionally, an improvement of the smoke intensity model with a finer subdivision of the smoke intensity is researched as well as an algorithm that provides additional thermal image information on the human-machine interface to the operator above a defined smoke intensity.

REFERENCES

[1] CTIF, "World Fire Statistics 2020," *https://www.ctif.org/,* 2020.

[2] J. Casper and R. R. Murphy, "Human-robot interactions during the robot-assisted urban search and rescue response at the World Trade Center," *IEEE Transactions on Systems, Man, and Cybernetics,* vol. 33, p. 367–385, 2003.

[3] R. R. Murphy and J. L. Burke, "Up from the Rubble: Lessons Learned about HRI from Search and Rescue," *Proceedings of the Human Factors and Ergonomics Society Annual Meeting,* vol. 49, p. 437–441, 2005.

[4] Y. S. Dadwhal, S. Kumar and H. K. Sardana, "Data-Driven Skin Detection in Cluttered Search and Rescue Environments," *IEEE Sensors Journal,* vol. 20, p. 3697–3708, 2020.

[5] M. Coombes, W. Eaton and W. H. Chen, "Machine Vision for UAS Ground Operations," *Journal of Intelligent and Robotic Systems,* vol. 88, p. 527–546, 2017.

[6] S. Khan, K. Muhammad, T. Hussain, J. D. Ser, F. Cuzzolin, S. Bhattacharyya, Z. Akhtar and V. H. C. de Albuquerque, "DeepSmoke: Deep learning model for smoke detection and segmentation in outdoor environments," *Expert Systems with Applications,* vol. 182, p. 115125, 2021.

[7] A. Gagliardi, F. de Gioia and S. Saponara, "A real-time video smoke detection algorithm based on Kalman filter and CNN," *Journal of Real-Time Image Processing,* vol. 18, p. 2085–2095, 2021.

[8] S. Khan, K. Muhammad, S. Mumtaz, S. W. Baik and V. H. C. de Albuquerque, "Energy-Efficient Deep CNN for Smoke Detection in Foggy IoT Environment," *IEEE Internet of Things Journal,* vol. 6, p. 9237–9245, 2019.

[9] L. He, X. Gong, S. Zhang, L. Wang and F. Li, "Efficient attention based deep fusion CNN for smoke detection in fog environment," *Neurocomputing,* vol. 434, p. 224–238, 2021.

[10] S. Saponara, A. Elhanashi and A. Gagliardi, "Real-time video fire/smoke detection based on CNN in antifire surveillance systems," *Journal of Real-Time Image Processing,* vol. 18, p. 889–900, 2020.

[11] Q.-X. Zhang, G.-H. Lin, Y.-M. Zhang, G. Xu and J.-J. Wang, "Wildland Forest Fire Smoke Detection Based on Faster R-CNN using Synthetic Smoke Images," *Procedia Engineering,* vol. 211, p. 441–446, 2018.

[12] L. Zhao, J. Liu, S. Peters, J. Li, S. Oliver and N. Mueller, "Investigating the Impact of Using IR Bands on Early Fire Smoke Detection from Landsat Imagery with a Lightweight CNN Model," *Remote Sensing,* vol. 14, p. 3047, 2022.

[13] J. S. Almeida, C. Huang, F. G. Nogueira, S. Bhatia and V. H. C. de Albuquerque, "EdgeFireSmoke: A Novel Lightweight CNN Model for Real-Time Video Fire–Smoke Detection," *IEEE Transactions on Industrial Informatics,* vol. 18, p. 7889–7898, 2022.

[14] G. Lin, Y. Zhang, G. Xu and Q. Zhang, "Smoke Detection on Video Sequences Using 3D Convolutional Neural Networks," *Fire Technology,* vol. 55, p. 1827–1847, 2019.

[15] J. Zeng, Z. Lin, C. Qi, X. Zhao and F. Wang, "An Improved Object Detection Method Based On Deep Convolution Neural Network For Smoke Detection," in *2018 International Conference on Machine Learning and Cybernetics (ICMLC),* 2018.

[16] X. Cheng, "Research on Application of the Feature Transfer Method Based on Fast R-CNN in Smoke Image Recognition," *Advances in Multimedia,* vol. 2021, p. 1–7, 2021.

[17] V. T. Nguyen, C. H. Quach and M. T. Pham, "Video Smoke Detection For Surveillance Cameras Based On Deep Learning In Indoor Environment," in *2020 4th International Conference on Recent Advances in Signal Processing, Telecommunications & Computing (SigTelCom),* 2020.

[18] J. Pincott, P. W. Tien, S. Wei and J. K. Calautit, "Development and evaluation of a vision-based transfer learning approach for indoor fire and smoke detection," *Building Services Engineering Research and Technology,* vol. 43, p. 319–332, 2022.

[19] J. Pincott, P. W. Tien, S. Wei and J. K. Calautit, "Indoor fire detection utilizing computer vision-based strategies," *Journal of Building Engineering,* vol. 61, p. 105154, 2022.

[20] A. Dhiman, N. Shah, P. Adhikari, S. Kumbhar, I. S. Dhanjal and N. Mehendale, "Firefighting robot with deep learning and machine vision," *Neural Computing and Applications,* vol. 34, p. 2831–2839, 2021.

[21] J. Guo, Z. Hou, X. Xie, S. Yao, Q. Wang and X. Jin, "Faster R-CNN Based Indoor Flame Detection for Firefighting Robot," in *2019 IEEE Symposium Series on Computational Intelligence (SSCI)*, 2019.

[22] S. Li, Y. Wang, C. Feng, D. Zhang, H. Li, W. Huang and L. Shi, "A Thermal Imaging Flame-Detection Model for Firefighting Robot Based on YOLOv4-F Model," *Fire,* vol. 5, p. 172, 2022.

[23] M. B. Tephila, P. M. Aswini, S. Abhinandhan and K. K. Arjun, "Deep Learning and Machine Vision based Robot for Fire Detection and Control," in *2022 4th International Conference on Inventive Research in Computing Applications (ICIRCA)*, 2022.

[24] K. Muhammad, J. Ahmad, Z. Lv, P. Bellavista, P. Yang and S. W. Baik, "Efficient Deep CNN-Based Fire Detection and Localization in Video Surveillance Applications," *IEEE Transactions on Systems, Man, and Cybernetics: Systems,* vol. 49, p. 1419–1434, 2019.

[25] K. Muhammad, S. Khan, M. Elhoseny, S. Hassan Ahmed and S. Wook Baik, "Efficient Fire Detection for Uncertain Surveillance Environment," *IEEE Transactions on Industrial Informatics,* vol. 15, p. 3113–3122, 2019.

[26] Q. An, X. Chen, J. Zhang, R. Shi, Y. Yang and W. Huang, "A Robust Fire Detection Model via Convolution Neural Networks for Intelligent Robot Vision Sensing," *Sensors,* vol. 22, 2022.

[27] N. Chowdhury, D. R. Mushfiq and A. E. Chowdhury, "Computer Vision and Smoke Sensor Based Fire Detection System," in *2019 1st International Conference on Advances in Science, Engineering and Robotics Technology (ICASERT)*, 2019.

[28] M. Zhang, Y. U. Wan-Jun, N.-M. Cang, Y. Tian, J.-Y. Tang and M. Zhang, "Research on Indoor Fire Early Warning System Based on Video Image and Smoke Sensor," in *2020 5th International Conference on Intelligent Informatics and Biomedical Sciences (ICIIBMS)*, 2020.

[29] G. Jobert, M. Fournier, P. Barritault, S. Boutami, J. Auger, A. Maillard, J. Michelot, P. Lienhard, S. Nicoletti and L. Duraffourg, "A Miniaturized Optical Sensor for Fire Smoke Detection," in *2019 20th International Conference on Solid-State Sensors, Actuators and Microsystems & Eurosensors XXXIII*, 2019.

[30] L. Li, J. Ye, C. Wang, C. Ge, Y. Yu and Q. Zhang, "A Fire Source Localization Algorithm Based on Temperature and Smoke Sensor Data Fusion," *Fire Technology,* vol. 59, p. 663–690, 2023.

[31] P. Fritsche, B. Zeise, P. Hemme and B. Wagner, "Fusion of radar, LiDAR and thermal information for hazard detection in low visibility environments," in *2017 IEEE International Symposium on Safety, Security and Rescue Robotics*, 2017.

[32] M. Sandler, A. Howard, M. Zhu, A. Zhmoginov and L.-C. Chen, "MobileNetV2: Inverted Residuals and Linear Bottlenecks," in *Proceedings of the IEEE Conference on Computer Vision and Pattern Recognition (CVPR)*, 2018.

.

FLASHOVER CHARACTERISTICS IN CONFINED SPACE UNDER LOW PRESSURE

Yuanhua HE 1a,*; Zitong LI 2b;Jingdong WANG 3c; Di ZHANG 4d, and Jiaxin LIANG 5e,*

ABSTRACT

In order to reveal the inherent mechanism of the flashover in aircraft cargo compartment under low pressure, a series of fire flashover experiments were conducted in a 1/4 volume FAA standard aircraft cargo compartment at 96 kPa and 60 kPa. The ignition of single-walled corrugated cardboard is chosen as the criterion of flashover. The influence of different fire sizes and fuel types on flashover is studied by comparing the average temperature of smoke layer, the radiation heat flux at floor level and the heat release rate of the fire source. The critical condition and behavior of flashover are analyzed. The results show that the flashover occuring under low pressure requires higher temperature and radiation heat flux. The increase of size of fire source raises the possibility and severity of flashover occurrence. After the minimum fire size for flashover is reached, continuous increase of the fire source size will bring the flashover forward. The average temperature of the smoke layer and the radiation heat flux at floor level required for flashover are about 450°C and 14 kW/m^2. In addition, the minimum fire size for flashover is directly proportional to their evaporation heat and inversely proportional to their combustion heat.

Keywords: Low pressure; Confined space; Flashover; Critical condition; Heat release rate.

1 INSTRUCTIONS

Flashover is a transitional stage of fire in confined space, in which all the combustibles reaches the ignition points almost at the same time. And the flame spread rapidly on all the surfaces of the combustibles, leading to the fire in the whole space[1]. Aircraft cargo compartment is a typical confined space with various combustibles, large fire load and poor ventilation. Once a fire happens, combustible smoke will quickly accumulate on the ceiling, and flashover occurs which will seriously threaten the human lives and properties[2-5]. According to the statistics of aviation accidents, aircraft cargo fire accidents occur frequently and are extremely harmful. In 2007, China Airlines No. 120 suddenly caught fire and burned the No. 2 engine on the right wing of the aircraft, and the cabin exploded after the 198 s, and the aircraft began to burn in full. In 2013, when Asiana Airlines Flight 214 landed at

---

1a,* Professor. College of Civil Aviation Safety Engineering. Civil Aviation Flight University of China, Guanghan 618300, China. e-mail:921306013@qq.com. Corresponding author.

2b Student. College of Civil Aviation Safety Engineering. Civil Aviation Flight University of China, Guanghan 618300, China. e-mail:1291728194@qq.com.

3c Student. College of Civil Aviation Safety Engineering. Civil Aviation Flight University of China, Guanghan 618300, China. e-mail:1473887854@qq.com.

4d Student. College of Civil Aviation Safety Engineering. Civil Aviation Flight University of China, Guanghan 618300, China. e-mail:572469108@qq.com.

5e,* Student. College of Civil Aviation Safety Engineering. Civil Aviation Flight University of China, Guanghan 618300, China. e-mail:985119695@qq.com.

San Francisco International Airport, the tail of the aircraft hit the airport breakwater, the plane caught fire instantly and an explosion occurred about 3 minutes later, killing a total of 307 passengers and crew members in this air crash. Oxygen is thin at low pressure, and the development process and law of fire are different from those at atmospheric pressure, and the time and scale of deflagration will also be different. High-altitude airport is a typical low-pressure environment, with altitudes of more than 2438 meters. High-altitude airports around the world are mainly distributed in China, Nepal, Peru and other countries. Studying the development of flashover in aircraft cargo compartment will help reduce the input of rescue personnel and equipment to a great extent, improve the safety of the adjacent airspaces, and greatly decrease the casualties and damage to properties caused by the flashover.

Flashover in confined space under atmospheric pressure has widely been studied by researchers. Chow [6] applied a zone model to investigate the flashover in confined space with different ventilation areas and analyzed the average upper and lower layer temperature, the smoke layer interface height, the mass flow rates for intake air and outgoing smoke and other important parameters. Xing et al [7] used Fire Dynamics Simulator (FDS) software to show the flashover process in the carriage of electric multiple units (EMU) and found that a power function relationship between the heat release rate (HRR) of the initial ignition source and the time of flashover occurrence. Kumar et al [8] conducted a full scale compartment flashover study using plywood board as lining material on walls and determined the peak heat release rate, flashover conditions and gas concentrations in transient condition and compared with tenability limits of fire hazards.

Some researchers have also been focusing on the studies of fire under low pressure. A famous study conducted by the Swiss scholar Wieser et al [9] in 1997 was carried out in a mobile test room of 6 m × 2.8 m × 2.1 m. The pressure was chosen to be 97 kPa and 71 kPa, and the parameters such as combustion mass loss, gas concentration, and smoke density were measured. The results showed that as the pressure decreased, the fire developed and the smoke density decreased more slowly. However, the ceiling temperature of the smoke layer and CO concentration were slightly affected by the atmospheric pressure. Thereafter, Liu et al [10] investigated the effect of low pressure on the combustion characteristics of early fires and analyzed the change of HRR and smoke concentration of the fire source. It was found that the HRR of the fire source would be reduced under low pressure, which provides some guide for the design and application of fire detection system in highland area. Li et al [11] conducted n-Heptane tanks and wood cribs fire experiments in two laboratories under different pressures and found significant differences in the combustion characteristics such as flame temperature,thermal radiation flux, and fuel mass loss . For the same burning surface area, the burning rate, radiation heat flux and flame temperature were lower under low pressure than under atmospheric pressure, but the combustion time was longer. Xin [12] studied the combustion characteristics of n-Heptane pool fire and gasoline pool fire at different pressures in a simulated low-pressure cargo compartment, and measured the combustion characteristics such as mass loss rate of the fire source and flame temperature.

Flashover happening in buildings have gain more attention at present. Some flashover researches can be found on aircraft cabin rather than cargo compartment. At the same time, current fire research under low pressure started late and haven't been largely investigated, let alone those on large-size space. In 1985, Sarkos et al[13] of the FAA carried out a flashover experiment on a C-133 full-size aircraft cabin for the first time. The results showed that the location of the fire source has a crucial impact on the occurrence of flashover. The closer the fire source to the cabin door, the lower the possibility of flashover. Wang et al[14] simulated the flashover on C-133 with its dimension provided by the FAA using a computational fluid dynamics fire-field model to predict the occurrence time of the flashover. In 2016, Zhang et al[15]analyzed the factors of flashover initiation based on the BFD curve parameter model, and found that the opening factor, the fuel load and fire development coefficient can directly affect the occurrence time of flashover. However, due to the large differences in the structure, fuel types and ventilation conditions between the aircraft cabin and the cargo compartment, the data of the aircraft cabin flashover cannot be directly applied to the cargo compartment. Therefore, this paper uses 1/4 volume FAA standard aircraft cargo compartment to establish a flashover experiment platform and tests the effects of different sizes and types of fire source on flashover, in order to reveal the inherent mechanism of flashover in aircraft cargo compartment, optimize the aircraft cargo compartment design, improve firefighting capability and reduce the casualties and property losses caused by flashover.

2 EXPERIMENTAL DESIGN

2.1 Experimental platform

The experiment's aircraft cargo compartment was a 1⁄4 FAA standard aircraft cargo compartment [16] with a inner dimension of 4.16 m × 2.03 m × 1.67 m with a front-opening vent A (1.2 m × 0.8 m). Several types of fuel were added as combustibles to a square steel pan of variable sizes that was positioned in the middle of the cargo compartment floor. A high-precision electronic balance (kunhong KM-11) was placed under the steel pan to measure the mass loss of the fuel during combustion. A 3cm thick thermal isolation blanket positioned between the steel pan and the balance in order to safeguard it. The electronic balance had a range of 60 kg, an accuracy of 1 g and a frequency of 1 Hz. Two single-wall corrugated cardboard boxes with a size of 45.7 cm × 45.7 cm × 45.7 cm and a distance of 40 cm between them were positioned 50 cm from the left edge of the steel pan and comply with FAA guidelines for solid fire experiments in aircraft cargo compartments. Two radiation heat flux meters, R1 and R2, were placed on two sides of the boxes to measure the radiant heat flux received by the floor, with an accuracy of ±3 % and a range of 0-200 kW/m^2. The existing flashover theory is generally based on two-region models, that is, the restricted space can be divided into the upper smoke layer area and the lower cold smoke layer area, among them, the thermal property parameters in the smoke layer are the focus of the investigation. Therefore, eight sets of thermocouple trees (1-T~8-T) were arranged to measure the temperature of the smoke layer.The three corners of the cargo compartment were used to position the thermocouple trees 1-T, 3-T, and 8-T. At the centre of each wall, the thermocouple trees 2-T, 4-T, 6-T, and 7-T were positioned. The centre of the steel pan was directly above the thermocouple tree 5-T. Ten centimetres separated each thermocouple tree from the wall. Six thermocouples were mounted from the cargo compartment ceiling downward on each tree. The temperature of the 50 cm thick layer of smoke in the ceiling of the cargo compartment was measured using thermocouples spaced 10 cm apart. All of the K-type thermocouples used in the experiment had a diameter of 1 mm, a measurement range of -100°C to 1300°C, and an accuracy of 1°C. The flashover experimental platform, thermocouples and radiation heat flux metres are arranged as shown in Figure 1.
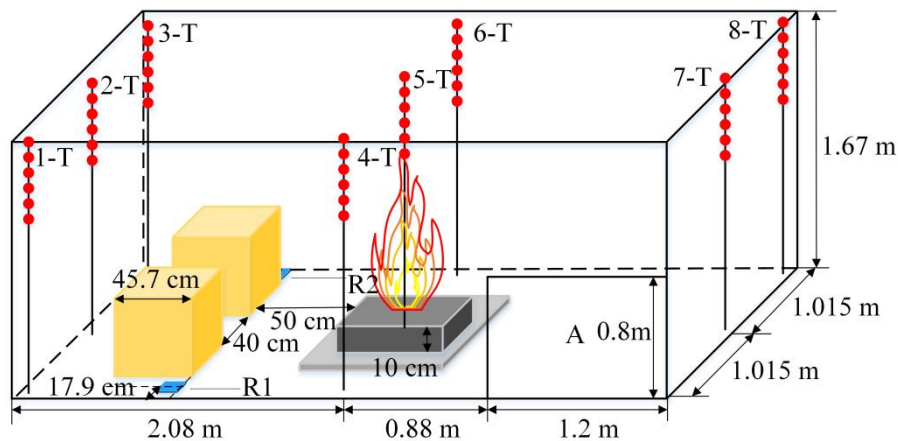
Figure 1: Platform Layout for the flashover experimental and measurement stations

2.2 Experimental working conditions and procedures

Previous research indicated that factors such as space size, opening vent size, wall material, fuel type, and the size and position of the fire source all had an impact on flashover. This research focuses on the impacts of pressure, steel pan size, and fire source type on flashover in order to simulate the flashover situations in confined space under atmospheric pressure and low pressure. This research focuses on the effects of fuel type and fire size at two atmospheric pressures, 96 kPa at the Civil Aviation Flight University of China, Guanghan, and 60 kPa at the Kangding airport. n-Heptane, Aviation Kerosene and Anhydrous Ethanol are selected for the fuel; the oil pan is selected by a square oil pan that complies with FAA MPS liquid fire standard, the size of the fire source ranged from 20 to 60 cm, and the thickness of fuel remains 1 cm. The experimental working conditions are shown in Table 1.

At present, the generally accepted criterions of flashover are: (1) the temperature of the ceiling smoke layer in confined space reaches 600°C; (2) the radiation heat flux at floor level in confined space reaches 20 kW/m^2; (3) All combustibles in the confined space are ignited.It should be noted that although criterion (1) and (2) have high

accuracy and primarily target indoor wood decoration materials and furniture components in building fires, their indicators are unquestionably high when the primary combustibles in an aircraft's cargo compartment are cardboard, fabric, and other materials. As a result, this paper chooses criterion (3) as the criterion for flashover in aircraft cargo compartment in accordance with the concept of flashover. The time in the experiments begins when the fuel in the steel pan ignites, followed by the ignition of a single piece of single-wall corrugated cardboard, which is considered to represent the occurrence of flashover, and the experiment is complete until the flame is entirely extinguished. To maintain the uniformity of the experimental settings, the cargo compartment is next cooled and ventilated while waiting for the temperature to reach room temperature.Each set of tests was performed at least three times in order to increase the dependability of the data from the studies.

Table 1:Test cases

Working condition number	Fuel types	Atmospheric pressure (kPa)	size of fire source (cm)
1-10	n-Heptane	96/60	20 / 30 / 40 / 50 / 60
11-20	Aviation Kerosene	96/60	20 / 30 / 40 / 50 / 60
21-30	Anhydrous Ethanol	96/60	20 / 30 / 40 / 50 / 60

3 EXPERIMENTAL RESULTS

3.1 Flashover process analysis

Figure 2 displays the temperature variations on the smoke layer during a typical flashover operation (60 kPa, 50 cm Aviation Kerosene pool fire). The average temperature of the smoke layer and the radiation heat flux at floor level started to steadily rise after the Aviation Kerosene in the steel pan was ignited. The two single-wall corrugated cardboards start to pyrolyze with black smoke while thermal smoke continues to build up on top of the cargo compartment. In the 295s, the flashover takes place as the cardboard begins to burn beneath the smoke layer's thermal radiation. The average temperature of the smoke layer is 545°C, and the radiation heat flux absorbed by the floor is 19.5 kW/m^2. After that, both the average temperature and the radiation heat flux climb significantly, reaching 643°C and 29.4 kW/m^2, respectively. Due to the limited amount of combustible material in the cargo compartment, full combustion following flashover only lasts for a brief period of time. As the combustible material burns out, the flashover enters the fading stage, and the average temperature of the smoke layer and the radiation heat flux received by the compartment's floor gradually decrease.
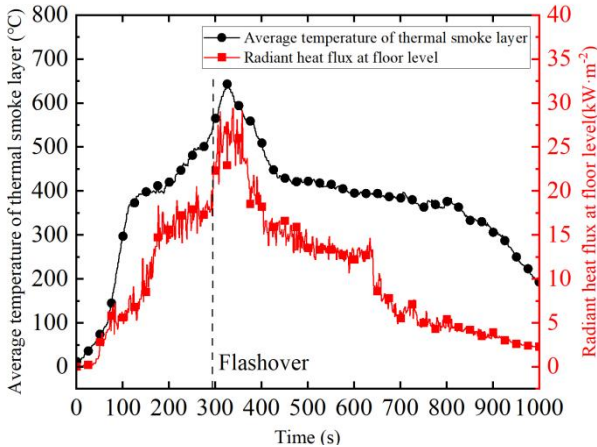
Figure 2: Variation of the average temperature of smoke layer and radiation heat flux at floor level in typical flashover process (50 cm Aviation Kerosene)

Along with Figure 3, the four stages of flashover in the confined space—incipient, growth, full developed, and decayed—can be easily identified. Prior to 295 seconds, the flashover is in the incipient stage, during which the flame scale slowly enlarges, the combustible smoke from combustion builds up at the top of the cargo

43

compartment, the temperature of the smoke layer rises, and the cardboard starts to pyrolyze and emit black smoke under the influence of thermal radiation on the smoke layer, as shown in Figure 3(a) to Figure 3(d). Figure 3(e) illustrates what happened when flashover occurred at 295 seconds when the cardboard was ignited by the flame and heat radiation of the smoke layer. Immediately following flashover, the temperature of the smoke layer rises sharply, and the flashover then enters the full developed stage with further expansion of the flame scale, during which the temperature of the smoke layer, the radiation heat flux at floor level reached the top, as shown in Figure 3(f). As the combustibles in the compartment burn out, the flashover enters the fading stage, which causes the temperature in the cargo compartment to decrease, as seen in Figures 3(g) and Figure 3(h).

| (a) t=10 s | (b) t=60 s | (c) t=120 s | (d) t=200 s |

| (e) t=295 s flashover initiation | (f) t=320 s | (g) t=600 s | (h) t=850 s |
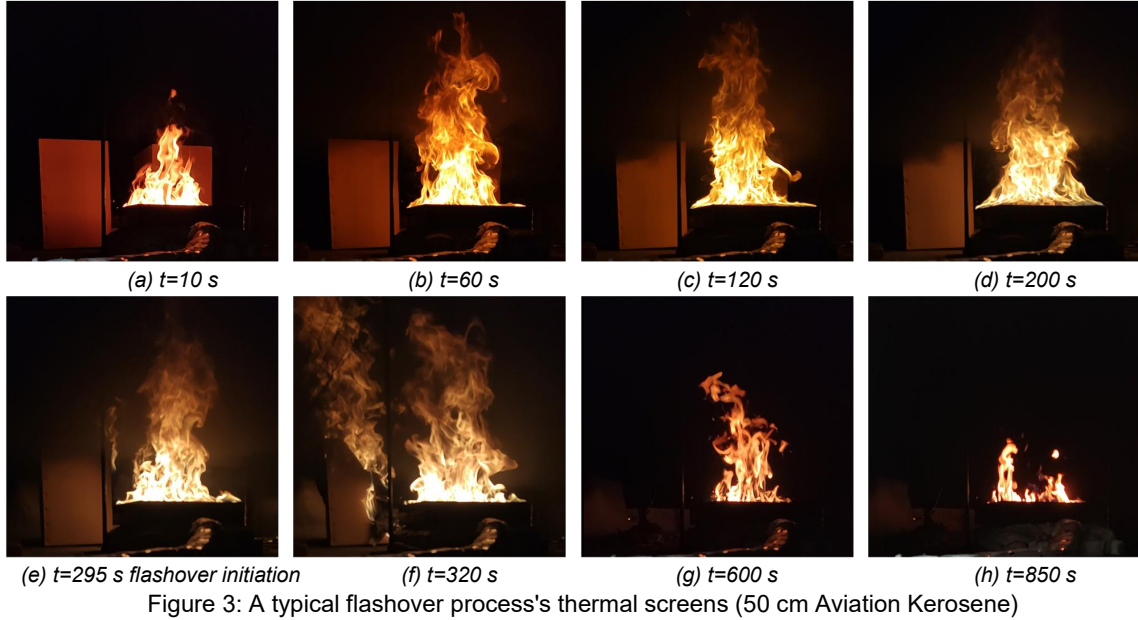
Figure 3: A typical flashover process's thermal screens (50 cm Aviation Kerosene)

The mass loss rate of the fuel is calculated by using the thermal weight loss data collected by the electronic scale, and the heat release rate of the fuel in the combustion process can be calculated by using formula (1):

$$\dot{Q} = \dot{m}h_c \tag{1}$$

$\dot{Q}$ represents the heat release rate of the fire source, $\dot{m}$ represents the mass loss rate of the fuel, and h_c represents the heat of combustion of the fuel, is taken as 4.797×10^4 kJ/kg [17]. The combustion efficiency in the restricted space of this paper is 100%. Firstly, considering that the 1/4FAA standard cargo compartment used in the crash experiment, although it is a confined space, the space volume is large, about 14 m^3. A vent with an area of about 1 m^2 is set near the fuel ignition source, which to a certain extent ensures that the air in the cabin is sufficient and is convenient for the full contact between fuel and oxygen. In addition, when ventilation is not taken into account, it is assumed that the experiment is carried out in a completely confined space, through the calculation of oxygen consumption during fuel combustion at 60 kpa, it is found that under the temperature condition of 100 °C, the oxygen consumption of fuel combustion is only 2.5 %. Therefore, It is almost assumed that the fuel can be fully burned in this confined space.

The changing oxygen concentration inside the experimental aircraft cargo compartment during the experiment is obtained through the fuel mass loss. According to the volume distribution and the average temperature of smoke layer, the estimated temperature of the whole aircraft cargo compartment during the experiment is about 100°C. Therefore, the gas molar volume under 60kPa condition is calculated using the ideal gas equation. The oxygen content inside the experimental aircraft cargo compartment during the experiment is the difference between the 21% oxygen content in the air and the oxygen consumed during fuel combustion. The oxygen concentration can be obtained by the ratio of the oxygen content to the total gas content in the experimental aircraft cargo compartment formula (2).

$$C_{t+1} = \frac{V_{wc}}{V_{em}}\left(\frac{0.21V_{em}}{V_{wc}} - \frac{km_{i+1}}{M_{Ak}}\right) \tag{2}$$

Where, V_{wc} represents the gas molar volume, V_{em} represents the experimental aircraft cargo compartment volume (14 m^3), k represents the molar ratio of fuel to oxygen during complete combustion (k is 12.5 in this case), and M_{Ak} represents the molar mass of Aviation Kerosene. Due to the short time intervals between the adjacent points of the measured fuel mass loss rate, the oxygen concentration (C_{t+1}) inside the experimental

chamber during that time period is approximated as the oxygen concentration at time (t_{i+1}).The variation of oxygen concentration during the experiment is shown in Figure 4.
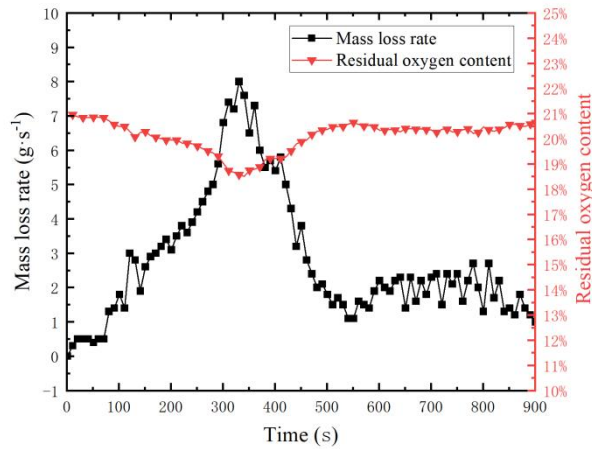
Figure 4: Oxygen concentration under the temperature condition of 100 °C

As shown in Figure 4, it can be observed that under the conditions of 60 kPa and 100°C, when the fuel combustion reaches the maximum heat release rate, the oxygen concentration is the lowest, accounting for 18.5 % of the air. In this case, the oxygen consumed by fuel combustion is only 2.5 %, while in the actual experiment, the experimental aircraft cargo compartment has a vent to facilitate the flow of oxygen, indicating that the oxygen consumed by fuel combustion is less than 2.5%. Therefore, the paper considered that the fuel combustion completely.

Figure 5 depicts the variation of mass loss rate and heat release rate of the fuel during the combustion process of a 50 cm Aviation Kerosene pool fire. The combustible gas continues to evaporate after the fuel is ignited under the influence of heat radiation from the flame and the smoke layer to sustain the combustion. While the combustion process continues, the temperature of the smoke layer rises gradually, the flame height continually climbs, and the heat radiation received by the fuel also gradually rises. As a result, the fuel's mass loss rate and heat release rate both rise steadily over time. The cardboard ignites and radiates heat outward, causing an abrupt increase in the heat feedback received by the fuel, which causes the mass loss rate and heat release rate of the fuel to change abruptly and increase quickly. At this point, the mass loss rate and heat release rate of the fuel have reached the critical point that can trigger a fail-safe. The fuel's mass loss rate and heat release rate reached their maximums at 8.0 g/s and 348.00 kW, respectively, as the combustion intensified further. Subsequently, as the effective combustion area shrank, the remaining fuel was gradually consumed and the combustion entered the extinction stage, and the fuel's mass loss rate and heat release rate also gradually decreased.
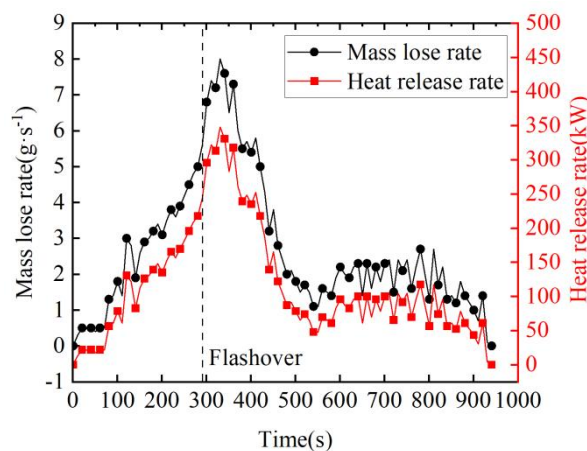
Figure 5: Mass loss rate and heat release rate of fuel in typical flashover process (50 cm Aviation Kerosene)

To express the mass loss rate per unit area, previous studies[18-20] have proposed pressure model $\dot{m}'' \sim fcn(p^2D^3)$ and radiation model $\dot{m}'' \sim fcn(p^2D)$ based on the ambient pressure p and the diameter of the fire source D. The equivalent diameter of the oil pool was calculated by $D_{eq} = 2L/\sqrt{\pi}$,because a square oil pool with a side length of L was used in this experiment. To confirm the relationship between thermal convection and thermal radiation during the pool fire combustion process of this experiment, the experimental data have been plotted using the corresponding relationship between the two models as shown on Figure 6.

（a）pressure model   （b）radiation model
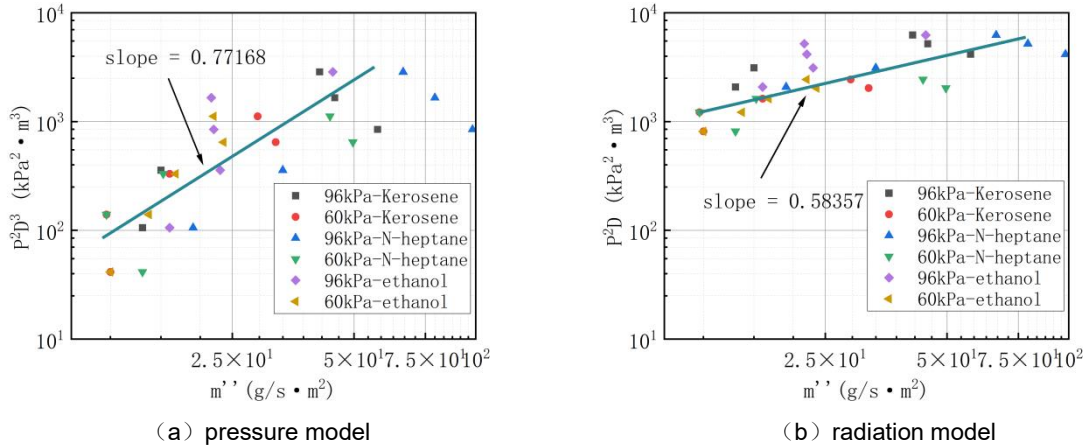
Figure 6: Relationship between mass loss rate per unit area and the pressure model and radiation model

The horizontal axis in the figure represents the mass loss per unit area of pool fires, denoted $\dot{m}'' = \dot{m}'/L^2$, while the vertical axis represents pressure model $p^2D_{eq}^3$ and radiation model p^2D_{eq} for two different types of pool fires at different ambient pressures. It can be seen that the degree of dispersion of the 96 kPa and 60 kPa data sets is more pronounced in the pressure model shown in Figure 6 (a). The radiation models shown in Figure 6 (b) give a clearer representation of the experiments in the different groups, with the discrete data points clustered around the curves. In summary, under the experimental conditions, the radiation model has been verified to be better at correlating the unit area mass loss rate of the pool fire than the pressure model. Therefore, the expression for the radiation model of the mass loss rate per unit area can be given as $\dot{m}'' \propto (p^2D_{eq})^{\frac{1}{0.58357}}$.

3.2 The effect of different sizes of fire source on flashover

Table 2 displays the flashover ignition time for various fuel source sizes at 96 kPa and 60 kPa. The crucial steel pan size needed to induce flashover at 96 kPa is 40 cm for n-Heptane and Aviation Kerosene pool fires and 60 cm for 100% ethanol pool fires. For n-Heptane and Aviation Kerosene pool fires, the critical steel pan size needed to initiate flashover at 60 kPa is 50 cm, while anhydrous ethanol pool fires require no flashover ignition. Due to the thin oxygen content in low pressure environments, which prevents pool fires from burning completely, the critical steel pan size needed to trigger flashover is larger. It is crucial to raise the size of the steel pan in order to increase the area where the fire source and oxygen come into contact, and then to increase the size of the fire scale in order to cause the confined space fire to develop into flashover.

Table 2: Flashover time at different sizes of fire sources

Sizes of fire source (cm)	Atmospheric pressure (kPa)	n-Heptane	Aviation Kerosene	Anhydrous Ethanol
20	96	-	-	-
	60	-	-	-
30	96	-	-	-
	60	-	-	-
40	96	118、127、132	161、154、166	-
	60	-	-	-
50	96	76、86、83	97、108、105	-
	60	221、232、227	295、281、277	-
60	96	55、52、50	68、66、74	148、162、156
	60	153、171、165	232、213、214	-

The variation of temperature on the upper smoke layer is one of the most significant elements determining the development of flashover, according to researchers who conducted comprehensive experimental and theoretical investigation of thermal balance and thermal instability of fire in confined spaces. The study of each thermocouple individually is more difficult because there are so many of them. Therefore, based on the idea of regional models, assuming that the temperature, density, and smoke concentration of the same height of thermal layer is uniform. Using the state averaging equation to compute the average temperature, the equation as indicated in equation (3)[21]:

$$T_{av} = \frac{H_r - H_i}{\int_{H_i}^{H_r} \frac{1}{T} dy}$$

(3)

Formula (4) is created by discretizing the denominator in formula (3):

$$\int_{H_i}^{H_r} \frac{1}{T} dy = \sum_{j=1}^{L} \frac{h_{j+1} - h_j}{T_{j+1} - T_j} \ln\left(1 + \frac{T_{j+1} - T_j}{T_j}\right)$$

(4)

H_r H_i are the thermocouple height of the top and bottom, respectively, T_i are the arithmetic mean of the temperature measured by the thermocouple at the height h_i.

Figures 7 and 8 illustrate how the average temperature of the smoke layer in the upper section of the cargo compartment varies for various size fire sources at 96 kPa and 60 kPa, respectively, using an Aviation Kerosene pool fire as an example. The average smoke layer temperature in the confined space grew with the size of the steel pan at 96 kPa air pressure when the steel pan d 40 cm, although it never went above 200 °C. When d was raised to 40 cm, flashover happened 161 seconds after ignition. The smoke layer's average temperature rose quickly, rising from 456 °C to a peak of 631 °C in just 37 seconds. After 68 seconds of ignition, flashover happened when d reached 60 cm, and in the 44 seconds that followed, the average temperature rose from 449 °C to a peak of 723 °C. The moment of flashover happened earlier and the peak of the average temperature of the smoke layer also increased as the size of the steel pan was expanded further. The average temperature of the smoke layer in the confined space steadily rises at 60 kPa when the steel pan size is 50 cm, but it never rises above 200 °C. When d reaches 50 cm, flashover happens 295 seconds after ignition. The flashover happens after 232 seconds when d reaches 60 cm. When atmospheric pressure dropped, the flashover happened later and the peak average temperature of the smoke layer also dropped.
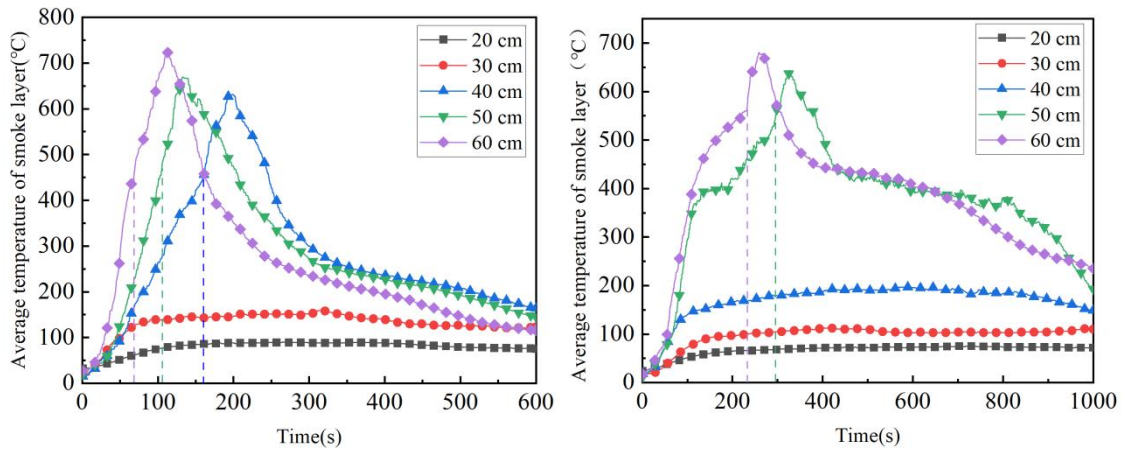
Figure 7 and Figure 8: Average temperature of smoke layer of Aviation Kerosene with different sizes
(at 96 kPa, at 60 kPa)

Figures 9 and 10 show the variation of radiation heat flux at floor level in the Aviation Kerosene pool fire of different sizes at 96 kPa and 60 kPa atmospheric pressure, respectively. At 96 kPa, when the steel pan size d < 40 cm, the radiation heat flux at floor level in the confined space increased with the increase of the steel pan size, but never exceeded 3.5 kW/m². When d increased to 40 cm, the radiation heat flux at floor level increased rapidly from 14.3 kW/m² before flashover to the peak of 32.4 kW/m² after flashover within 16 s. When d reached 60 cm, the radiation heat flux at floor level increased rapidly from 14.0 kW/m² to the peak of 43.0 kW/m² in 47 s. By continuing to increase the steel pan size, the moment of ignition was advanced and the peak of radiation heat flux at floor level was increased. At 60 kPa, when the steel pan size d < 50 cm, the radiation heat flux at floor level in the confined space increased gradually with the increase of the steel pan size, but never exceeded 5 kW/m². When d increased to 50 cm, the flashover occurred in 295 s. When d reached 60 cm, the flashover occurred in 232 s. With the decrease of atmospheric pressure, the peak of the radiation heat flux at floor level decreased.
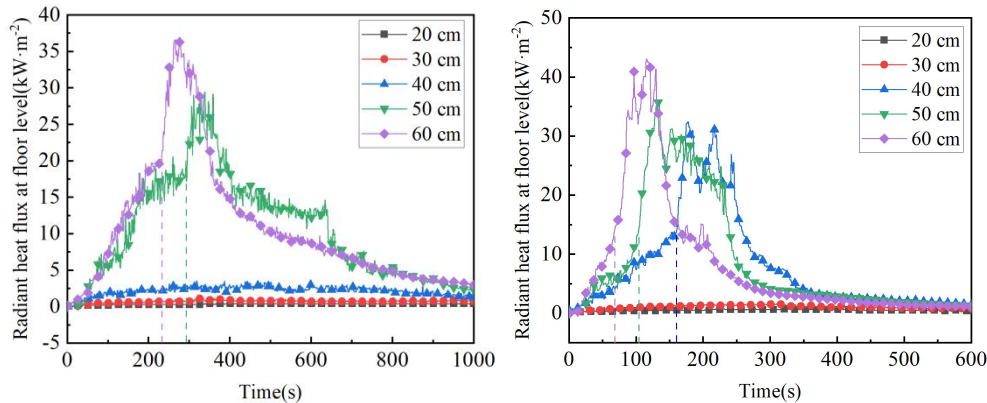
Figure 9 and Figure 10: radiation heat flux at floor level of Aviation Kerosene fires with different sizes
(at 96 kPa, at 60 kPa)

Figures 11 and 12 demonstrate the heat release rates of Aviation Kerosene pool fires of various sizes at 96 kPa and 60 kPa pressure, respectively. The change trends of the average smoke layer temperature and the radiation heat flux at floor level are essentially similar with these figures. As the fire source size increased from 20 cm to 60 cm at an air pressure of 96 kPa, the peak heat release rate increased from 26.1 kW to 643.80 kW. At an air pressure of 60 kPa, the peak heat release rate increased from 17.4 kW to 387.15 kW. The sudden increase in heat release rate is the result of a combination of the flame, smoke layer, thermal steel pan, and thermal radiation from the wall facing the fuel.
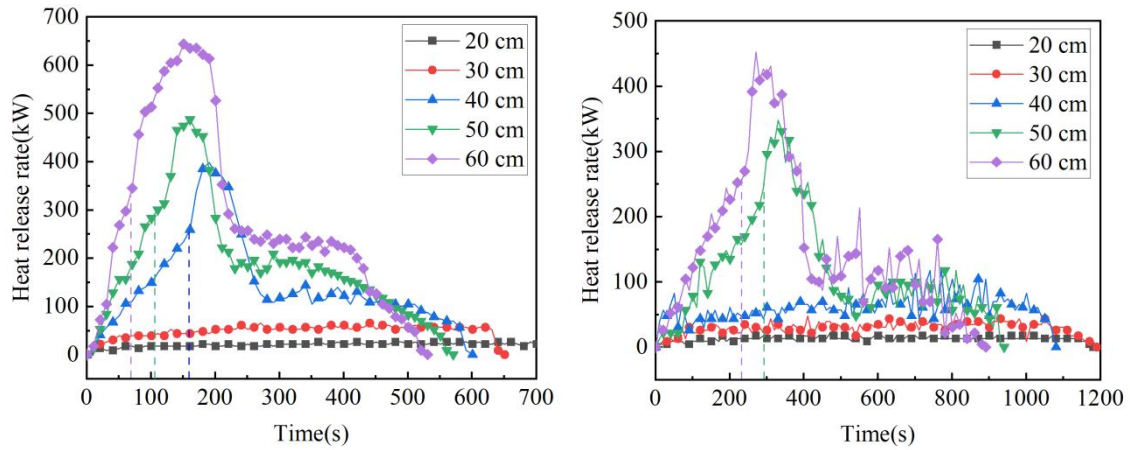
Figure 11 and Figure 12: Heat release rate of Aviation Kerosene fires with different sizes(at 96 kPa, at 60 kPa)

In accordance with the aforementioned trends, which are not shown here, are also the average temperature of the smoke layer, the radiation heat flux at floor level, and the rate at which the various sizes of the fire source released heat during the combustion process of the n-Heptane and Anhydrous Ethanol pool fires. The average temperature of the smoke layer, the radiation heat flux at floor level, and the fire source's rate of heat release will all rise as the fire source's size increases, improving the likelihood and severity of flashover.

3.3 The effect of different types of fuel on flashover

The thermal property factors h_e (evaporation heat) and h_c (combustion heat), which are determined by the types of fuel, have a significant impact on how a fire develops in a confined space. The thermal property parameters of the various fuel types are shown in Table 3 with the minimal size needed to generate flashover at atmospheric pressure[22]. The relationship between the minimal size of fire source D_{fmin} needed for the flashover and the thermal property parameters of the fuel will be shown by conducting a comparative investigation of the evaporation heat and combustion heat of the three types of liquid fuels in formula (5):

$$D_{f\min} \propto \left(\frac{\Delta h_{vap}}{\Delta h_c} \right)$$
(5)

That is, the minimum size of fire source required for flashover is directly proportional to the evaporation heat of the fuel, and inversely proportional to the combustion heat of the fuel.

Table 3 : Thermophysical parameters of fuel and minimum size of fire source needed for flashover(96 kPa)

Fuel types	Evaporation heat (kJ / kg)	Combustion heat (kJ / kg)	Minimum size of fire source (cm)	Flashover occurrence time (s)
n-Heptane	318	47970	40	127
Aviation Kerosene	342	43500	40	161
Anhydrous Ethanol	926	29700	60	156

While studying the impact of fuel type on flashover under atmospheric and low pressure, chose 60 cm to be used as the minimum fire size due to the need of 60 cm for Anhydrous Ethanol pool fire flashover at atmospheric pressure.

Figures 13 and 14 depict the changes in the smoke layer's average temperature over the course of combustion for the three liquid flue at 96 kPa and 60 kPa pressure. It is discovered that the n-Heptane pool fire is the first to start a flashover at 52 seconds under the identical steel pan size. The floor's radiation heat flux is 14.3 kW/m^2, with a peak of 45.2 kW/m^2, and the smoke layer's average temperature is 457 °C, with a peak average temperature of 727 °C. The second Kerosene pool fire started a flashover at 68 seconds and involved aviation fuel. The floor receives a radiation heat flux of 14.0 kW/m^2 on average from the smoke layer, with a peak flux of 43.0 kW/m^2 and an average temperature of 723 °C for the smoke layer. At 156 seconds, the anhydrous ethanol pool fire was the most recent to experience flashover. At this time, the smoke layer's average temperature was

49

454 °C, its highest average temperature was 671 °C, and the floor's radiation heat flux was 14.2 kW/m^2 with a peak of 40.0 kW/m^2.
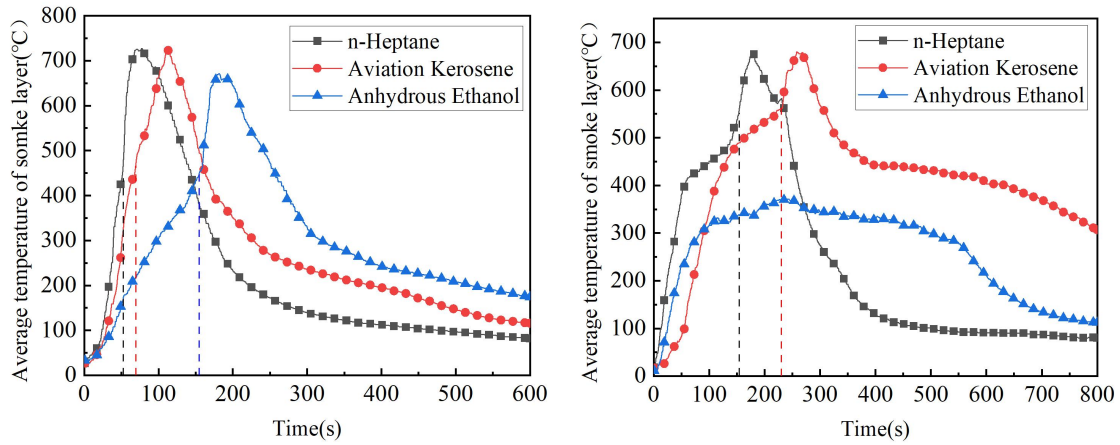
Figure 13 and Figure 14: Average temperature of smoke layer of different fuels (60 cm, at 96 kPa and 60 kPa)

According to Figures 15 and 16, the n-Heptane pool fire was the first to experience flashover at 60 kPa at 153 seconds. At this time, the smoke layer's average temperature was 547 °C, 90 °C higher than the temperature at 96 kPa; the peak average temperature was 52 °C. lower than that at 96 kPa, the peak is 36.8 kW/m^2, which is 8.4 kW/m^2 lower than that at 96 kPa, and the radiation heat flux at floor level is 19.9 kW/m^2, which is 5.6 kW/m^2 higher than that at 96 kPa. The second is a Kerosene pool fire in aviation. The floor is receiving a radiation heat flux of 20.2 kW/m^2, 6.2 kW/m^2 more than at 96 kPa, and the highest reach of 36.9 kW/m^2, 6.1 kW/m^2 less than at 96 kPa. The average temperature of the smoke layer is 562 °C, 113 °C higher than at 96 kPa; the peak average temperature is 43 °C lower than at 96 kPa. The fire in the anhydrous ethanol pool at 60 kPa did not result in a flashover, and the smoke layer's greatest average temperature was only 371 °C. Moreover, the floor's highest radiation heat flux was only 6.6 kW/m^2.
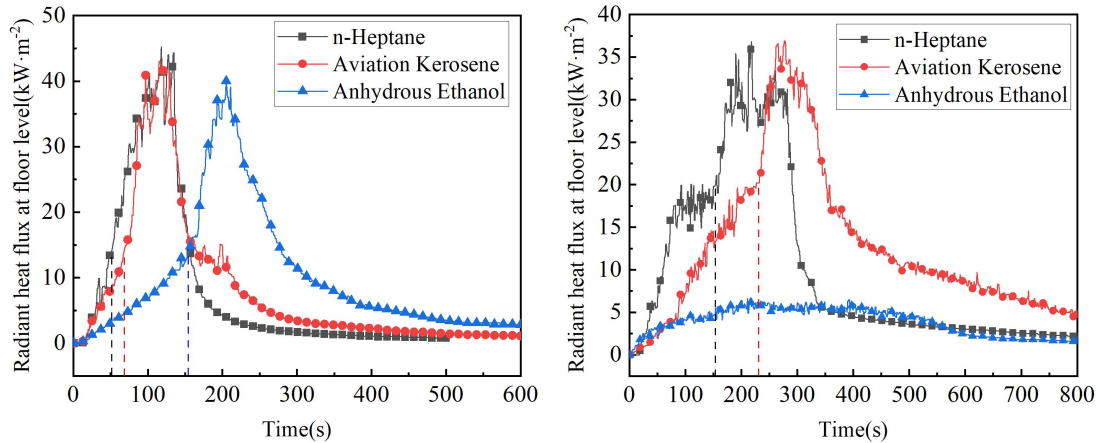
Figure 15 and Figure 16: radiation heat flux at floor level of different fuels (60 cm, at 96 kPa and 60 kPa)

Figures 17 and 18 show the variation in heat release rates for three liquid fuels during combustion for two different air pressures. The trend is generally consistent with that in the average smoke layer temperature and the radiation heat flux at floor level, but anhydrous ethanol's heat release rate and total heat release are significantly less than those of n-Heptane and Aviation Kerosene because of the evaporation heat of anhydrous ethanol.

50
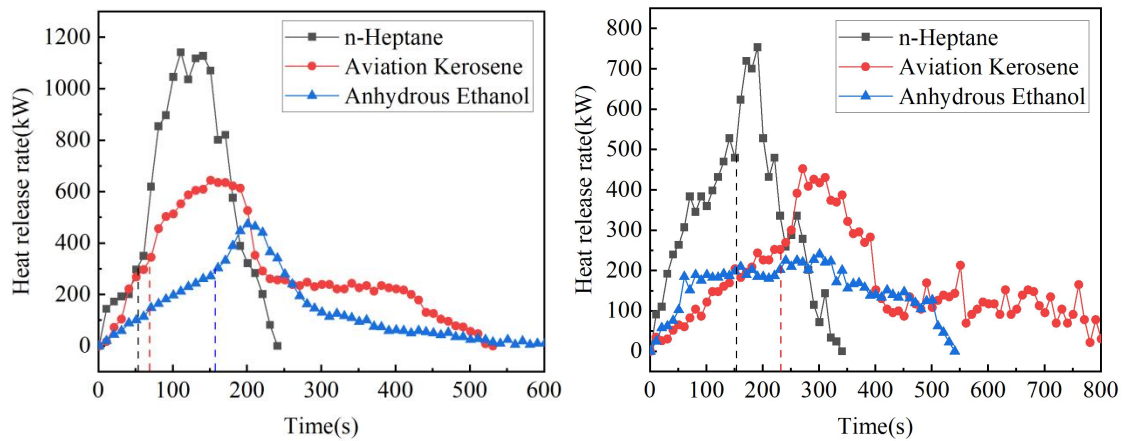
Figure 17 and Figure 18: Heat release rate of different fuels (60 cm, at 96 kPa and 60 kPa)

4 CONCLUSIONS

(1) To induce a flashover under low pressure, a larger critical steel pan size and other essential conditions are needed. The fire source is ignited and begins to burn under the influence of oxygen fuel, which results in the production of a significant quantity of heat, which is the inherent mechanism of the process of the flashover in confined space under 60 kPa atmospheric pressure. The temperature of the upper smoke layer will rise as thermal smoke from combustion builds up in the upper portion of the enclosed space. At the same time, the radiation heat flux absorbed by the floor will also rise, which will cause the cardboard to pyrolyze. The cardboard ignites under the influence of oxygen and flashover occurs when the floor receives radiation heat flux of 19.6 kW/m^2 and the average temperature of the smoke layer reaches 551 °C. Moreover, the average temperature of the smoke layer and the radiation heat flux absorbed by the floor rise more slowly at 60 kPa due to the fire source's insufficient burning, which lengthens the time needed to commence flashover.

(2) As the size of the fire source grows, so do the average smoke layer temperature, the radiation heat flux at floor level, and the rate at which the fuel releases heat, which raises the likelihood and severity of flashover. If the fire is kept growing after it reaches the minimum size necessary to start a flashover in the cargo compartment, the flashover will start sooner. The minimum ignition size needed to start a flashover is inversely related to the heat of fuel combustion and directly proportional to the heat of fuel evaporation. The n-Heptane pool fire is the first to cause a flashover when the size of the fire sources is the same, followed by the Aviation Kerosene pool fire, and the anhydrous ethanol pool fire is the least likely to do so. In addition, the n-Heptane pool fire had greater average smoke layer temperatures, radiation heat flux at floor level, and heat release rates than the Aviation Kerosene and Anhydrous Ethanol pool fires.

(3) The size of the confined space can be increased. Considering that the full-size bombardment experimental platform is more expensive, more dangerous, more difficult,therefore, only 1/4 FAA standard aircraft cargo compartment was used in this study, and the size of the confined space can be considered to increase in the future, even to conduct full-size flashover experiments.Other types of fire sources can be added and the size of the oil pan can be increased. Due to the limited time, only three liquid fire sources were used in this study, and other types of liquid or solid fire sources and larger oil pan sizes can be considered in the future to conduct flashover experiments.

REFERENCES

[1]National Fire Protection Association. *NFPA 921 Guide for fire and explosion investigations*[M]. Quincy: Natl Fire Protection Assn, 2017.

[2]Cong Li,Yina Yao,Zhenxiang Tao,Rui Yang,Hui Zhang. *Influence of depressurized environment on the fire behaviour in a dynamic pressure cabin* [J]. Applied Thermal Engineering,2017,125.

[3]Cong Li,Rui Yang,Yina Yao,Zhenxiang Tao,Quanyi Liu. *Factors affecting the burning rate of pool fire in a depressurization aircraft cargo compartment* [J]. Applied Thermal Engineering,2018,135.

[4]Zhenxiang Tao,Rui Yang,Cong Li,Yina Yao,Ping Zhang,Hui Zhang. *An experimental study on fire behavior of an inclined ceiling jet in a low-pressure environment* [J]. International Journal of Thermal Sciences,2019,138.

[5]Quanyi LIU, Zhongzheng SUN, Zhihao LV, et al. *Experimental study of the burning characteristics of typical aircraft cabin materials at various pressures* [J]. Journal of Tsinghua University (Science and Technology), 2019, 59 (06): 432-437.

[6]CHOW W K. *Study on the flashover criteria for compartmental fires* [J]. Journal of Fire Sciences, 2016, 15 (2): 95-107.

[7]Wendian XING, Mingnian WANG, Qi LI. *Study on influence of combustion characteristics of initial ignition source on flashover in EMU carriage* [J]. Journal of Safety Science and Technology, 2018, 14 (05): 36-42.

[8]KUMAR A A, KUMAR R, ANSARI A A. *Room corner fire growth studies of plywood lining material under fully ventilated condition [*J]. Journal of The Institution of Engineers (India) Series A, 2021, (2): 1-7.

[9]Wieser D, Jauch P, Willi U. *The influence of high altitude on fire detector test fires*[J]. Fire Safety Journal, 1997, 29(2): 195-204.

[10]Yong LIU. *Research on the influence of highland environment on early combustion characteristics of fire and fire detection*[D]. University of Science and Technology of China, 2006.

[11]Li Z H, He Y, Hui Z, et al. *Combustion characteristics of n-Heptane and wood crib fires at different altitudes*[J]. Proceedings of the Combustion Institute, 2009, 32(2): 2481-2488.

[12]Xin CAI. *Experimental study on the effect of high altitude and low pressure conditions on the performance of fine water mist fire extinguishing*[D]. University of Science and Technology of China, 2009.

[13]SARKOS C, HILL R. *Evaluation of aircraft interior panels under full-scale cabin fire test conditions*[C]// American Institute of Aeronautics and Astronautics. 23rd Aerospace Sciences Meeting. Dallas, Texas: AIAA Press, 1985: 393.

[14]WANG Z, JIA F, GALEA E R, et al. *Computational fluid dynamics simulation of a post-crash aircraft fire test* [J]. Journal of Aircraft, 2013, 50 (1): 164-175.

[15]Qingsong ZHANG, Guangtao SONG, Hanpeng QI. *Simulation study on the effect of the aircraft cabin structure on the flashover* [J]. Journal of Safety and Environment, 2016, 16 (06): 126-128.

[16]Federal Aviation Administration. Reinhardt J W. *Minimum performance standard for aircraft cargo compartment Halon replacement fire suppression systems (2012 Update)* [S]. DOT/FAA/TC-TN12/11,2012. https://www.fire.tc.faa.gov/pdf/tc-tn12-11.pdf.

[17]Zhihao LV. *Study on the characteristics of fine water mist field and fire suppression effectiveness in cargo hold of civil aircraft* [D]. Civil Aviation Flight University of China, 2020.

[18]De Ris JL.Wu PK,Heskestad G.Radiation fire modeling.Proc Combust Inst 2000;28(2):2751-9.

[19]Ris JD,Murty Kanury A,Yuen MC.Pressure modeling of fires.Symp (Int)Combust 1973:141):103344.

[20]Yao W, Hu X, Rong J, et al. Experimental study of large-scale fire behavior under low pressure at high altitude[J]. Journal of fire sciences, 2013, 31(6): 481-494.

[21]Y. He. On Experimental Data Reduction for Zone Model Validation[J]. Journal of Fire Sciences,1997,15(2).

[22]Peihong ZHANG,Xing TANG,Xiangliang TIAN,Chang LIU,Maohua ZHONG. *Experimental study on the interaction between fire and water mist in long and narrow spaces*[J]. Applied Thermal Engineering,2016,94.

Fire Chemistry, Physics and Combustion

ANALYSIS OF THE POSSIBILITY OF IGNITION OF VARIOUS MATERIALS BY SHORT-CIRCUIT SPARKS

Kostiantyn A. Afanasenko[a,*]

ABSTRACT

The paper studies the possibility of various substances ignition with an electric ignition source, namely, a short circuit, depending on different parameters. The comparative analysis of fires causes depending on the approach of their conditional classification is given. Among others, ignition sources of electrical origin are highlighted.

An analysis of the fires causes statistical data collection used by various countries is carried out. It has been established that when using different approaches to their collection, the number of electrical ignition sources varies from 15 to 27%. And up to 50% of them are short circuits. The main characteristics of a short circuit and its fire hazard are considered. It has been established that in the event of a short circuit an intense scattering of sparks (drops of molten metal) is observed.

The paper considers the methods for calculating the flight times of a various metals spark in various aggregation states and the possibility of igniting combustible materials by them. Found that a drop of molten copper will be a ignition source for textiles, rubber and fabric with dimensions larger than 2.9 mm; a drop of molten steel will be the ignition source for solid combustible materials with dimensions larger than 2.6 mm.

Keywords: short-cirquit, ignition cource, sparks.

1. ANALYSIS OF THE FIRES CAUSES AND FIRES STATISTICS

Fires at critical infrastructure facilities usually have serious consequences. As a result, people can be injured, and serious damage can be caused to both businesses and the environment.

[a,]National University of Civil Defence of Ukraine, Address: 94 Chernyshevska Str. Kharkiv 61023 Ukraine, email address: armfree0@gmail.com, **Corresponding author**.

At the same time, the causes (ignition sources) of fires at such objects can be divided into 4 groups: open fire, thermal features of mechanical energy, thermal features of chemical reactions, thermal features of electrical energy. The latter, according to statistics, can reach up to 25% of the total.

1.1 Analysis of typical fires causes

Fires causes of can vary in a fairly wide range. The authors [1] identifies the following classification of the fires causes:
1. Arson.
2. Production equipment failure, violation of the technological process: defects in the design, manufacture and installation of production equipment; violation of technological regulations; electrostatic discharge; destruction of moving parts and parts, getting into moving mechanisms of foreign parts; malfunction of the devices cooling system, surfaces friction; malfunction, lack of spark-extinguishing equipment; other malfunctions of production equipment.
3. Violation of fire safety rules during installation and operation of electrical installations: lack of design and production of electrical installations, the electrical network short circuit; violation of the design rules of electrical installations and electrical networks; violation of the rules of electrical installations technical operation; violation of fire safety rules during the operation of electrical household appliances.
4. Violation of fire safety rules during electric gas welding works.
5. Explosion.
6. Self-ignition of substance and materials.
7. Violation of fire safety rules during the installation and operation of furnaces: improper arrangement and malfunction of heating furnaces and chimneys; violation of fire safety rules during the operation of furnaces.
8. Violation of fire safety rules during installation and operation of heat-generating units and installations: lack of design and manufacture of heat-generating units and equipment; violation of the installation rules of heat-generating units and equipment; violation of fire safety rules during the operation of heat-generating units and equipment.
9. Violation of fire safety rules during operating household gas, kerosene, and gasoline appliances.
10. Careless handling of fire: smoking carelessness; carelessness during fire works (heating pipes, engines and other equipment with an open fire); another reason for careless handling of fire.
11. Mischief of children with fire.
12. Lightning discharge.
13. Undetermined cause.
14. Other reasons.

Thus, identifying the main causes of fires (ignition sources) and determining the degree of their danger is an urgent task.

1.2 Statistical data on ignition sources as fires causes

An ignition source is an object that emits thermal energy sufficient for ignition (combustion initiation is an exothermic process that includes redox transformations of substances and materials and is characterized by the presence of volatile products and light radiation) [2].

According to the nature of origin, ignition sources are classified as follows:
– open fire, heated combustion products and surfaces heated by them;
– thermal features of mechanical energy;
– thermal features of electrical energy;
– thermal features of chemical reactions (open fire and combustion products are separated from this group into an independent).

If all fires in Ukraine to be taken for 100%, then fires caused by "violation of fire safety rules during installation and operation of electrical installations" amount to an average of about 25 % annually from the total number of fires; fires due to "electrostatic discharge" and "lightning discharge" account for about 1% of the total number of fires. Analysis of various statistics shows that the approach to data collection is quite different.

For example, in Canada, during the fires causes data collection, all fires are taken into account, including ecosystems, residential, non-residential buildings, etc. [3]. With this approach, the number of electrical ignition sources can reach 15%. (figure 1).
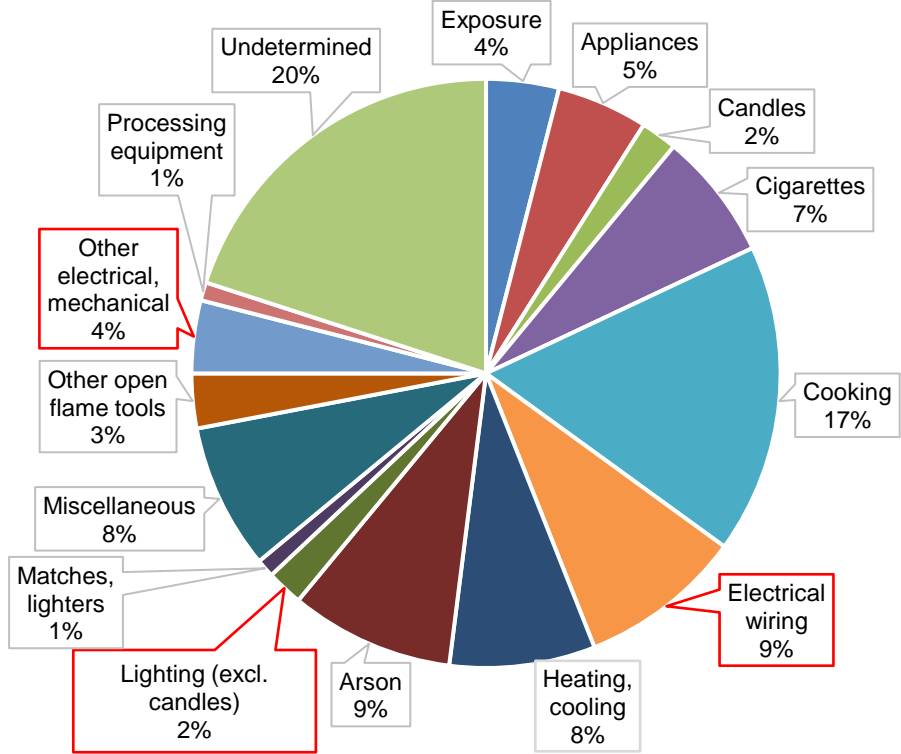
Figure 1: Statistics on the fires causes during 2005-2014 in Canada [3]

However, the statistics of the causes of fires in Great Britain (Table 1) [4] allow us to assess the sources of ignition at industrial enterprises and critical infrastructure facilities. And in this case, the number of electric ignition sources increases to 27%.

Table 1. Average year fire statistics 2010-2020 in England (including Critical Infrastructure Facilities) [4]

Year	Total	Smokers' materials	Cigaretts, lighters	Matches	Cooking appliances	Space heating appliances	Central and water heating appliances	Blowlamps, welding and cutting equipment	Electrical distribution	Other electrical appliances	Candles	Other/ Unspecified
2010/11	20755	1079	726	1295	2742	696	120	380	2613	2720	145	8239
2011/12	20321	1152	737	1321	2491	571	104	401	2432	2585	125	8402
2012/13	16506	852	653	834	2298	547	125	319	2464	2393	142	5879
2013/14	16527	878	619	834	2123	464	135	342	2462	2248	123	6299
2014/15	15562	802	711	762	2136	448	105	334	2288	2177	105	5694
2015/16	16026	949	853	860	2045	415	101	310	2255	2061	113	6064
2016/17	15868	851	919	782	1970	434	104	292	2359	1823	106	6228
2017/18	15616	883	823	703	1943	440	115	267	2186	1820	103	6333
2018/19	15032	922	519	526	1847	379	90	273	2232	1669	90	6485
2019/20	14334	853	517	486	1713	431	98	241	2 223	1628	85	6059
2020/21	11916	735	368	346	1273	376	71	204	1 703	1164	59	5617
Total	178463	9956	7445	8749	22581	5201	1168	3363	25217	2 288	1196	71299
Persent		5,58	4,17	4,90	12,65	2,91	0,65	1,88	14,13	12,49	0,67	39,95

The analysis of the given data shows that the number of ignition sources of electrical origin, depending on the method of statistical data collection, can vary within 15-27%. Thus, determining the danger of electrical origin ignition sources is an urgent task.

2. CLASSIFICATION OF THE ELECTRICAL ORIGIN IGNITION SOURCES

Literature analysis shows three groups of electrical origin ignition sources [5, 6, 7]:

1. Electric spark (arc). There are sparks and arcs arising as a result of the thermal action of short-circuit, electric sparks (drops of metal) created during electric welding, arising from the destruction of the bulbs of electric incandescent lamps or as a result of the static electricity charges.
2. Heating of substances, nodes and surfaces of technological equipment.
3. Discharges of atmospheric electricity. There is a difference between a direct lightning strike and secondary lightning strikes.

Also, the power lines heating in case of overvoltage and leakage currents should be attributed to the heat features of electrical energy.

At the same time, a short circuit, as a cause of fires, reaches up to 50% of the total number of electrical ones.

2.1 Thermal action of short-circuit

The danger of short circuits is explained by the thermal effect of electric current, which is quantitatively expressed by the Joule-Lenz law.

According to Ohm's law, as the resistance R decreases, the current I increases in square, so the amount of heat Q released in the conductor when a short-circuit current occurs increases sharply.

A short-circuit, the effect of which is not limited in time, leads to the melting of conductors and the occurrence of sparks and arcs, so it can be a cause of fires of nearest combustible materials.

2.2 Electric sparks (drops of metal)

When a short circuit occurs, sparks occur in 100% of cases. Electric sparks and arcs occur when an electric current passes through the air. Electric sparks (drops of metal) are formed, in the case of short circuits of electrical conductors. The size of the hot particles of metal at short circuit of electric wiring can reach 3 mm. At the same time, when they expand, they are in a molten state, which increases their danger. However, when released into the environment, they gradually cool down.

With a short circuit, sparks fly in all directions, and their speed does not exceed 10 m/s. The area of particle flight in the event of a short-circuit depends on the height of the wire, the initial speed of the particle flight, the angle of departure and is probabilistic in nature (Fig. 2).

For the height of the location of the wire 10 m the probability of hitting particles at a distance 9 m is 0.06; 7 m – 0.45; 5 m – 0.92; for the height of the location 3 m the probability of hitting particles at a distance 8 m is 0.01; 6 m – 0.29; 4 m – 0.96; and for the heights 1 m the probability of scattering of particles on6 m - 0.06; 5 m - 0.24; 4 m – 0.66 and 3 m – 0.99.

It should be noted that during a short-circuit, electric sparks, as a rule, have time to form before the protection devices are triggered, and therefore the probability of ignition of flammable substances and materials during a short-circuit is sufficient.
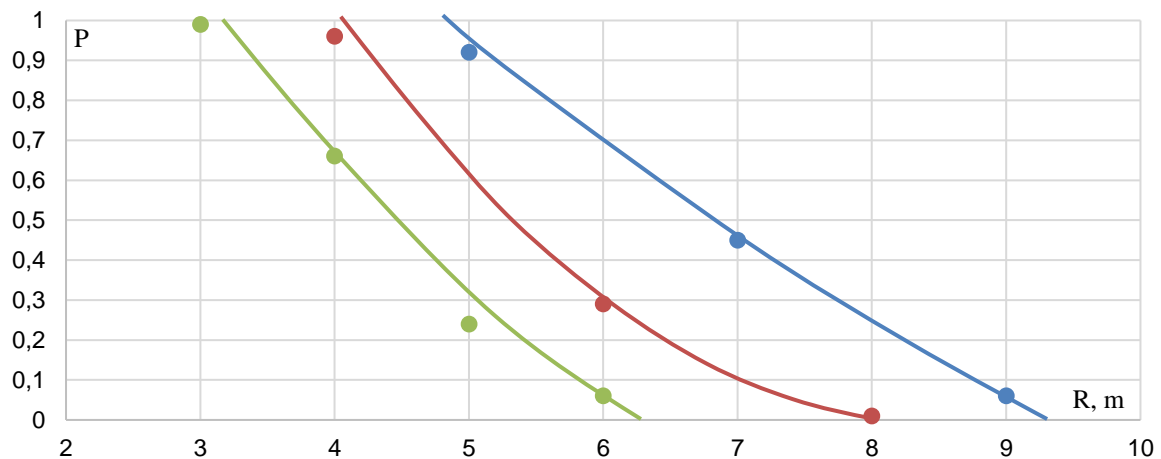
Figure 2. The probability (P) of hitting metal particles depending on the height of their formation and distance to the object (R, m)

Thus, if there is a probability of a drop of metal hitting the surface of a combustible substance, its ignition is possible. Therefore, there is a need to determine the ignition capacity of such a drop depending on the external conditions and physical and chemical properties of the materials of the drop and the combustible substance.

2.3 Calculation of igniting ability of a metal drop

The temperature of the heated particles depends on the type of metal and cannot be lower than its melting temperature. Thus, the temperature of aluminum particles during a short circuit reaches +2500 ºC [8, 9].

The amount of heat that a particle (drop) of metal can give to a combustible environment before reaching its self-ignition temperature is calculated in the following sequence.

The average flight speed of a drop of metal in free fall is calculated by the formula:

$$\omega_{dr} = 0{,}5 \cdot \sqrt{2 \cdot g \cdot H}, [m/s], \tag{1}$$

where g=9.81 – Is the acceleration of free fall;
H – Is the height of the drop.

The volume of a drop of metal is calculated by the formula:

$$V_{dr} = \frac{\pi \cdot d_{dr}^3}{6} = 0{,}524 \cdot d_{dr}^3, [m^3], \tag{2}$$

where d_{dr} – is the diameter of the drop, [m].

The mass of the drop is calculated according to the formula:

$$m_{\text{кD}} = V_{dr} \cdot \rho_{dr}, [kg] \tag{3}$$

where ρ_{dr} – Is densityof metal, [kg/m³].

Further calculations will be made for three metals used in electrical products (including cable products): steel, aluminum and copper [10]. Fig. 3 shows the dependence of the drop mass depending on its diameter and the metal of which it is composed.
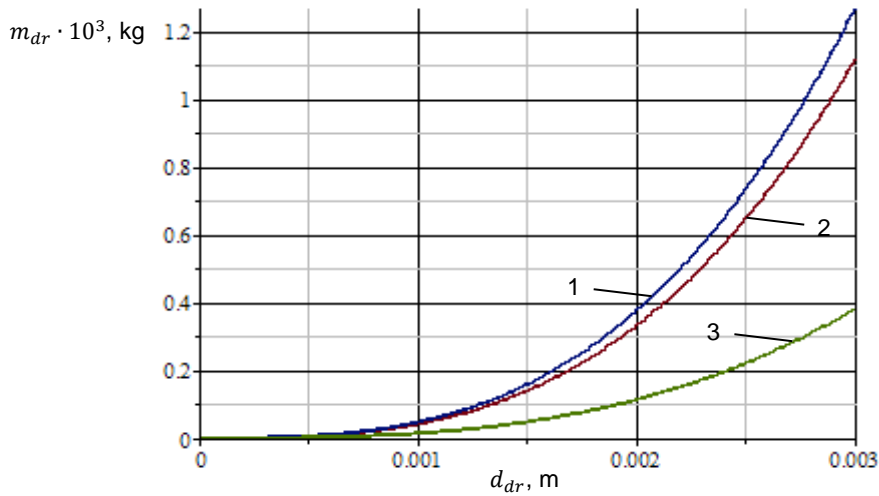
Figure 3. Dependence of the drop mass depending on its diameter and the metal of which it is composed.
1 – copper, 2 –steel, 3 – aluminum.

Depending on the duration of the drop's flight, three states of its aggregate are possible: liquid, crystallization state, and solid.

The flight time of a drop in a liquid state is calculated by the formula:

$$\tau_{liq} = \frac{C_p \cdot m_{dr}}{\alpha \cdot S_{dr}} \cdot ln\frac{T_{start} - T_0}{T_{melt} - T_0}, [s] \tag{4}$$

where C_p –specific heat capacity of the metal melt, [J/(kg·K)]; S_{dr} – surface area of the drop, [m²]; T_{start} – temperature of the drop at the beginning of the flight, [K]; T_{melt} – metal melting point temperature, [K]; T_0 – ambient temperature, [K]; α –heat transfer coefficient, [W/(m²·K)].

The drop heat transfer coefficient is calculated in the following sequence:
a) calculate the Reynolds number (the Reynolds number is a dimensionless quantity, is one of the characteristics of the movement of a viscous liquid and determines the ratio of inertial forces to viscous forces) according to the formula:

$$Re = \frac{\omega_{кр} \cdot d_{кр}}{r}, \tag{5}$$

where $r = 15.1 \cdot 10^{-6}\ m^2/s$ – coefficient of kinematic viscosity of air at a temperature of +20 ℃;
b) calculate the Nusselt criterion (the Nusselt criterion characterizes the average intensity of convective heat exchange between the surface of the body and the free or forced flow of liquid or gas) according to the formula:

$$Nu = 0{,}62 \cdot \sqrt{Re}, \tag{6}$$

c) calculate the heat transfer coefficient according to the formula:

$$\alpha = \frac{Nu \cdot \lambda_{air}}{d_{dr}}, [W/(m^2 \cdot K)], \tag{7}$$

where $\lambda_{air} = 0{,}022$ W/(m · K) – air thermal conductivity coefficient.

If $\tau \leq \tau_{liq}$, then the final temperature of the drop is calculated by the formula:

$$T_{final} = T_0 + (T_{start} - T_0) \cdot \exp\left(-\frac{\alpha \cdot S_{dr}}{C_p \cdot m_{dr}}\right), [K]. \tag{8}$$

The drop flight time, during which its crystallization occurs, is determined by the formula:

$$\tau_{cryst} = \frac{m_{dr} \cdot C_{cryst}}{\alpha \cdot S_{dr} \cdot (T_{liq} - T_0)}, [s], \tag{9}$$

where C_{cryst} – the specific metal crystallization heat, [J/kg].

With the help of the above formulas, the time of flight of a molten metal drop was calculated depending on external conditions. Graphical interpretation of calculations is shown in Figure 4.

If , then the final temperature of the drop is calculated by the formula:$\tau_{liq} < \tau \le (\tau_{liq} + \tau_{cryst})$

$$T_{final} = T_{liq}, [K], \tag{9}$$

To assess the degree of danger in work, the flight time of a drop of metal in a molten state was calculated (Fig. 5) .
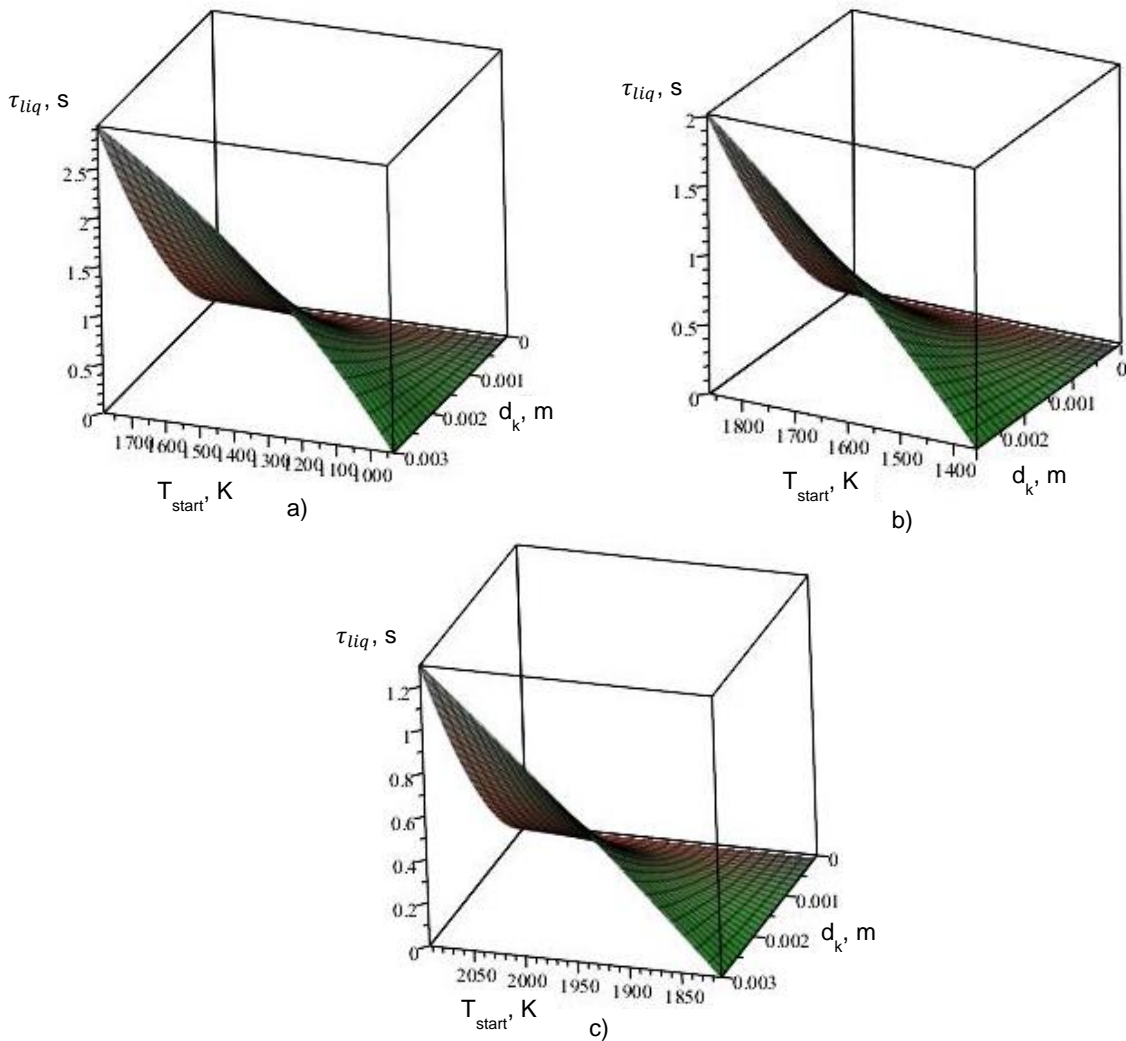
Figure 4. Dependences of the flight time of a metal drop in a molten state on the initial temperature and drop diameter: a) Aluminum; b) Copper; c) Steel.
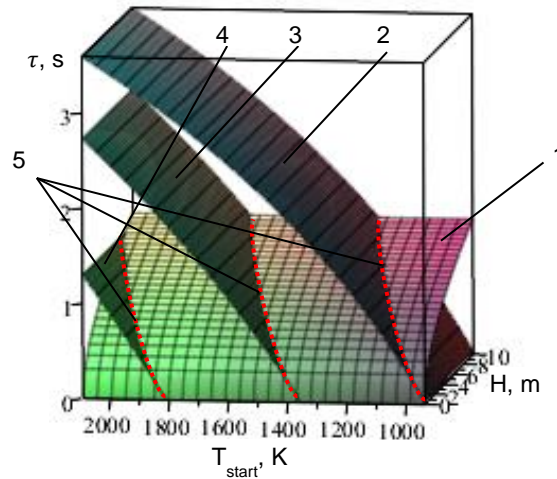
Figure 5. Dependences of the flight time of a metal drop in a molten state on the initial temperature, flight height, and average flight time. 1 – average flight time; 2 – aluminum; 3 – copper; 4 – steel; 5 – the time of the drop falling in the molten state.

Analysis of Fig. 5 shows a comparison of the time the drop remains in the molten state with the flight time of the drop from a certain height. In accordance with the received calculation data, it can be concluded that when falling from a height of up to 8 m, drops of all metals will be in a molten state.

If , then the final temperature of the drop in the solid state is calculated by the formula: $\tau > (\tau_{liq} + \tau_{cryst})$

$$\text{T}_{final} = \text{T}_0 + (\text{T}_{fuse} - \text{T}_0) \cdot \exp\left\{-\frac{\alpha \cdot S_{dr}}{C_{dr} \cdot m_{dr}} \cdot [\tau - (\tau_{liq} + \tau_{cryst})]\right\}, [K], \qquad (9)$$

where C_{dr} – the specific heat capacity of the metal, [J/(kg·K)].

The next stage of the work was to analyze the possibility of ignition from a metal drop in a molten state of various solid combustible materials, such as plastic, wood, textiles and rubber.

The amount of heat that a drop of metal gives off to the solid material on which it fell is calculated by the simplified formula [11, 12, 13]:

$$W = V_{dr} \cdot \rho_{dr} \cdot C_{dr} \cdot (T_{final} - \text{T}_{SI}) \cdot \text{K}, [J], \qquad (10)$$

where T_{SI} – the self-ignition temperature of the combustible material, [K]; K – coefficient equal to the ratio of the heat given off to the combustible material to the energy stored in the drop. It is allowed to take K=1.

Some characteristics of the fire hazard of solid combustible materials are given in the table 3.

Table 3. Some fire hazard characteristics of solid combustible materials [14, 15, 16]

Name of the material	Self-ignition temperature of the substance (T_{SI}), [K]	Minimum ignition energy (W_{Ign}), [mJ]
Polyethylene	690	70
Rubber	613	30
Textile	633	25
Wood	603	40-60

Calculations of the energy transferred by metal drops to combustible materials were carried out according to the above formulas (Fig. 6).
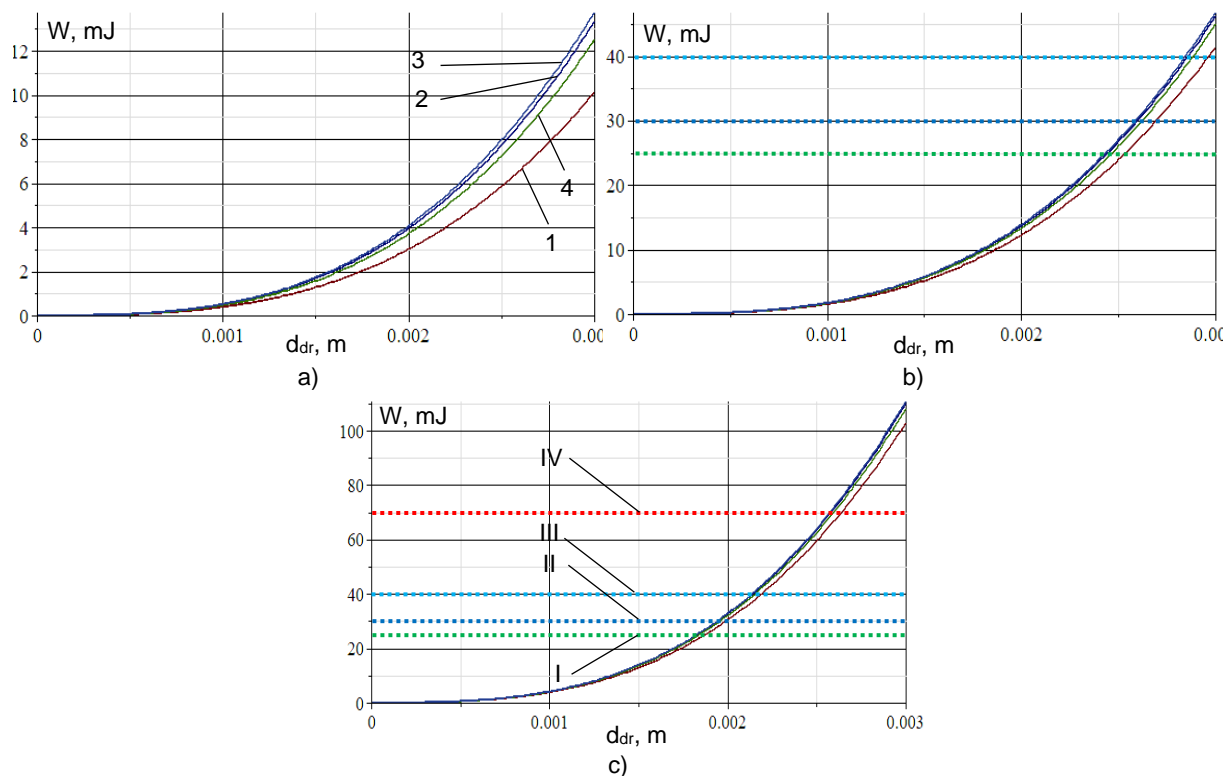
Figure 6. Calculated energies of a metal drop in the molten state depending on the diameter of the drop for: a) aluminum, b) copper, c) steel. Transmitted energy: 1 – polyethylene; 2 – rubber; 3 – textiles; 4 - tree. Minimal ignition energy: I – textile; II – rubber; III – wood; IV – polyethylene.

Analysis of the data shown in Fig. 6 allows us to conclude that when drops of molten aluminum fall on combustible materials, ignition will not occur.

At the same time, a drop of molten copper will be a source of ignition for textiles, rubber and fabric with dimensions greater than 2.9 mm.

And a drop of molten steel will be the source of ignition for all listed solid combustible materials with dimensions greater than 2.6 mm.

3. CONCLUSIONS

1. The work examines the statistics of fires in several countries, highlights the peculiarities of statistical data collection. It has been established that the share of electrical ignition sources can be up to 27% at industrial facilities and critical infrastructure facilities.

2. The nature of a short circuit as a source of ignition has been studied. It was established that in the case of a short circuit, drops of molten metal are splashed, which can cause ignition of various materials.

3. The method of calculating the parameters of metal drops when they occur during a short circuit is considered. It has been established that when drops of molten aluminum fall on combustible materials, ignition will not occur. At the same time, a drop of molten copper will be a source of ignition for textiles, rubber and fabric with dimensions larger than 2.9 mm. A drop of molten steel will be the source of ignition for all listed solid combustible materials with dimensions larger than 2.6 mm.

4. REFERENCES

[1] Manzello, S.L. (2020). *Fire Causes. Encyclopedia of Wildfires and Wildland-Urban Interface (WUI) Fires.* Springer, Cham. 334 p. https://doi.org/10.1007/978-3-319-52090-2_300122

[2] Liberman, M.A. (2021). *Combustion Physics.* Springer Cham, 618 p.

[3] Campbell, J.; Jones, T. (2017). *Fire statistics in Canada, Selected Observations from the National Fire Information Database.* Canadian Centre for Justice Statistics for the Canadian Association of Fire Chiefs 2005 to 2014, New Brunswick, 82 p.

[4] Lader, D. (2021). *Detailed analysis of fires attended by FRSs, England.* Tables 0601.

[5] Martinka, J. (2022). *Fire Hazards of Electrical Cables.* Springer Nature Switzerland AG, 102 p.

[6] Nejtková, M.; Makovicka Osvaldova, L.; Markert, F.; Zelinka, S. (2020). *Behaviour of Wooden Materials Exposed to Electrical Ignition Sources,. Wood & Fire Safety. WFS 2020.* Springer, Cham. p. 191-196. https://doi.org/10.1007/978-3-030-41235-7_29

[7] Korytchenko, K.; Krivosheyev, P.; Dubinin, D.; Lisniak, A.; Afanasenko, K.; Harbuz, S.; Buskin, O.; Nikorchuk, A.; Tsebriuk, I. (2019). *Experimental research into the influence of twospark ignition on the deflagration to detonation transition process in a detonation tube, Eastern-European Journal of Enterprise Technologies*, vol. 4, (5-100), p. 26-31. DOI: 10.15587/1729-4061.2019.175333

[8] Wang, Y., Zhang, Z. (2011). *The Approximate Method of Three Phase Short-Circuit Current Calculation Based on the Per-Unit Value Form of Ohm's Law. Advances in Computer Science, Environment, Ecoinformatics, and Education. CSEE 2011. Communications in Computer and Information Science,* vol 217, p. 203-209. https://doi.org/10.1007/978-3-642-23339-5_37

[9] Petryshchev, A.; Milko, D.; Borysov, V.; Tsymbal, B.; Hevko, I.; Borysova, S.; Semenchuk, A. (2019). *Studying the physical-chemical transformations at resourcesaving reduction melting of chromenickelcontaining metallurgical waste. Eastern-European Journal of Enterprise Technologies*, vol. 2, no. 12–98. p. 59–64. DOI: 10.15587/1729-4061.2019.160755

[10] Sadkovyi, V.; Andronov, V.; Semkiv, O.; Kovalov, A.; Rybka, E.; Otrosh, Y.; Udianskyi, M.; Koloskov, V.; Danilin, A.; Kovalov, P. (2021). *Fire resistance of reinforced concrete and steel structures*, PC TECHNOLOGY CENTER, p. 1-166. DOI: 10.15587/978-617-7319-43-5

[11] Korytchenko, K.V., Tomashevskyi, R.S., Varshamova, I.S., Dubinin, D.P., Lisnyak, A.A., Lipovyi, V.O. (2019). *Numerical simulation of initial pressure effect on energy input in spark discharge in nitrogen. Problems of Atomic Science and Technology*, vol. 122 no. 4, p. 116-119.

[12] Abramov Y.; Basmanov O.; Salamov J.; Mikhayluk A. (2018). *Model of thermal effect of fire within a dike on the oil tank. Naukovyi Visnyk Natsionalnoho Hirnychoho Universytetu,* vol. 2. p. 95–100. DOI: 10.29202/nvngu/2018-2/12

[13] Abramov, Y.; Basmanov, O.; Oliinik, V.; Khmyrov, I.; Khmyrova, A. (2022). *MODELING THE CONVECTIVE COMPONENT OF THE HEAT FLOW FROM A SPILL FIRE AT RAILWAY ACCIDENCE, EUREKA, Physics and Engineeringthis,* vol. 2022(6), p. 128–138.

[14] Gooch, J.W. (2007). *Self-ignition temperature. Encyclopedic Dictionary of Polymers.* Springer, New York, NY. 869 p. https://doi.org/10.1007/978-0-387-30160-0_10245

[15] Zhang, X.; Xi, G. (2008).*New experimental technique to determine coal self-ignition duration. Front. Energy Power Eng. China,* vol. 2, p. 479-483 https://doi.org/10.1007/s11708-008-0058-6

[16] Grüneberger, P.; Winklhofer, E. (2019). *Charge temperature evaluation in self-ignition events. Automot. Engine Technol.,* vol. 4, p. 93–99 https://doi.org/10.1007/s41104-019-00046-w

INFLUENCE OF DIFFERENT CLAY MINERALS STRUCTURES ON THE FIRE RETARDANCY OF INTUMESCENT POLYMERS

Ana Lucia S. Ventapane a, *; Simone P. S. Ribeiro b; Regina S. V. Nascimento c; Alexandre Landermann d**

ABSTRACT

A series of clay minerals was added to a polymeric matrix of poly (ethylene-co-butyl acrylate), EBA-30, containing an intumescent formulation of ammonium polyphosphate (APP) and pentaerythritol (PER), in order to investigate the effect of the crystalline structure on the flame retardancy of the polymer composites. The clay minerals mica, kaolinite (Kaol), palygorskite (Pal) and K-feldspar (K-Fsp) were tested in this work with and without the intumescent formulation. The results from limiting oxygen index (LOI) and cone calorimeter analyses showed that while Pal with the intumescent formulation led to the highest LOI values and a heat release rate (HRR) close to zero, indicating a synergistic effect with the intumescent formulation and the polymer matrix, K-Fsp showed the lowest impact on the synergism performance with a higher value for the HRR peak. The heating microscopy showed a higher stability of the intumescent layer with the addition of Pal then with the addition of K-Fsp, showing that that the crystalline structure of Pal led to a better interaction with the polymer matrix and to a greater synergism in the composites.

Keywords: Clay minerals; Crystalline structure; Flame retardant; Intumescent formulation.

[a],* Chemical Institute, Federal University of Rio de Janeiro – IQ/UFRJ,149 Athos da Silveira Ramos Avenue, Rio de Janeiro, RJ 21941909 BRAZIL, other contact details (analuciaventapane@pos.iq.ufrj.br)**, Corresponding author.

[b] Chemical Institute, Federal University of Rio de Janeiro – IQ/UFRJ (spsilva@iq.ufrj.br)**.

[c] Chemical Institute, Federal University of Rio de Janeiro – IQ/UFRJ (rsandra@iq.ufrj.br)**.

[d] Civil Engineering Program, Federal University of Rio de Janeiro – COPPE/UFRJ (alandes@coc.ufrj.br)**.

1. INTRODUCTION

Considering the vast applicability of polymers in the daily life, their high flammability is a huge disadvantage for these materials. Therefore, different approaches to increase flame retardancy of polymeric materials has been studied [1]. Flame retardant additives, such as intumescent formulations, have been presented as eco-friendly and less toxic compared to other flame retardants such as organohalogen counterparts, which are carcinogenic and bioaccumulative [2]. In general, intumescent formulations are composed of an acid source, a carbonaceous compound and a blowing agent that in the presence of a heat source forms an expanded carbonaceous layer, named char. This intumescent layer is responsible for preventing the transfer of heat, of oxygen and combustible gases during the burning of the material ceasing the flame [3]. However, the intumescent formulations do not achieve the desired flame retardancy properties, thus, a strategy to increase the intumescent formulation efficiency is the use of synergistic agents [4]. Montmorillonite is a well-established clay mineral synergistic agent in the literature mainly due to its advantages such as low cost and easy access. Some authors have shown that structural characteristics of the montmorillonite, such as the increase of its interlamellar spacings can affect its synergistic action in the intumescent formulations [5]. Montmorillonite, due to its structure can catalyze the Diels-Alder and esterification reactions that contribute to the formation of the char, as a consequence, increasing the thermal properties and reducing the hear release rate of the material [6]. Nonetheless the sole use of montmorillonite on the polymer matrix does not lead to any improvement of the flame retardant properties of the composites [7].

Despite of their structure, the evaluation of the effect of other clay materials on the flame retardancy of polymers is not common in the literature. Due to this fact, this study aims to investigate, through structural analysis, if there is a synergistic action of other clay minerals, when added to the intumescent formulation, on the flame retardancy of polymer materials. Therefore, this study intends to investigate the effect of the crystalline structure of different clay minerals such as mica, kaolinite (Kaol), palygorskite (Pal) and also K-Felspar (K-Fps) on the flame retardancy performance of polyethylene-co-butyl acrylate (EBA-30) on intumescent formulation composed by ammonium polyphosphate (APP) as an acid source and blowing agent and pentaerythritol (PER) as a carbonaceous compound was employed.

Those clay minerals, K-Fsp and the polymeric materials were characterized using thermogravimetric analysis (TGA). The textural analysis of the clay minerals was evaluated using B.E.T isothermals. X-ray fluorescence (XRF) analysis were performed to determine the composition of the minerals present in the clay minerals and K-Fsp samples. The material's flammability was evaluated by limit index oxygen (LOI) and cone calorimeter technique. The LOI measures were performed to measure the minimum oxygen content necessary to sustain the burning process and the cone calorimeter measured the heat release rate of the material. With the heating microscopy was possible to verify the thermal stability of the char.

2. EXPERIMENTAL

2.1 Materials and processing

The polymer matrix used was a poly (ethylene-co-butyl acrylate), supplied by Arkema, under the commercial name of Lotryl 30BA02, hereafter referred to as EBA-30. The intumescent formulation was composed by ammonium polyphosphate (APP), supplied by Clariant with the commercial name of Exolit 422 and pentaerythritol (PER) supplied by Sigma – Aldrich. In the polymeric sample production, the intumescent formulation was used in a 30 wt.% of APP: PER in a ratio of 3:1 respectively where according to the literature, a maximum of the flame retardant properties is observed for polyethylene materials in this proportions [8]. The minerals mica, Kaol, Pal and K-Fps were supplied by União Brasileira de Mineração (UBM). These minerals were supplied as powders, except for mica, that was supplied in the laminar form. The mica had to be milled with a mortar and pestle, and then introduced in a Puverisette 14 mill model with the rotation of 10,000 RPM. All clay minerals and K-Fsp materials were dried in a temperature of 70 °C for 14 hours before being processed. In the composites production, the clay minerals were used in a 3 % of the total mass of the composite. Better flame retardant properties are observed in this concentration according to the literature [9].

The polymers and additives were mixed in a Haake Rheochord 900 rheometer equipped with a Romix chamber 600 roller blared rotor, at 140 °C under 50 RPM. The mixture was then pressed in a Carver press at 150 °C with a load of 9000 kgf to obtain 100 mm X 100 mm X 3 mm specimens for flammability tests.

2.2 Characterization

The clay minerals and K-Fsp were analyzed utilizing a PerkinElmer 7 high temperature thermogravimetric analyzer (TGA). The analysis was performed under the following conditions: 10 mg sample in platinum capsules submitted to a temperature ramp from 30 °C to 850 °C under a heating rate of 10 °C/min. As the purge gas it was used a synthetic one with a 20 mL/min flux.

For textural analysis a Micromeritics, model ASAP 2010 (Accelerated Surface Area and Porosimetry), was used. This analysis measures the samples specific area using the B.E.T. (Brunauer – Emmet – Teller) method, through N_2 adsorption and desorption isothermals at 77 K.

For the determination of the chemical composition of the minerals present in the mica, Kaol, Pal, and K-Fsp samples it was used a Rigaku RIX 3100 X-ray fluorescence (XRF) with a rhodium source and X-ray spectroscopy for detection. The samples were analyzed in the form of pellets with a mass of approximately 500 mg. Before analysis, the samples were dried and calcinated in a muffle at 450 °C for 150 minutes.

2.3 Flammability evaluation

The LOI test is normalized according to ISO 4589-2 standard method which determines the minimum oxygen content necessary to sustain a burning process in an oxygen and nitrogen gas mixture atmosphere. A fire testing technology (FTT) apparatus was employed using 100 mm × 6.7 mm × 3 mm specimens of the polymers and composites produced. The measurements are accurate to ± 1 LOI unit.

The cone calorimetry is standardized by the ISO 5660-1 (2002) and allows the determination of a quantitative measurement of heat release rate (HRR), expressed in kW/m^2. This technique best reproduces fire conditions in a laboratory bench scale experiment [10]. The analyses were performed using a mass loss cone calorimeter MLCC, model FTT-0014/2012. Samples measuring 100 mm X 100 mm X 3 mm were exposed horizontally to a 50 kW heat flux which corresponds to the heat released during well-developed fires [11].

The heating microscopy can be used to monitor the intumescent layer of the material [12]. The heating microscopy analyses were executed with a Leitz heating microscope, model 1A, and the images were captured by a Samsung SDC 415 ND camera which provides the visualization of the sample behavior under heating. The samples used were 3 mm sided cubes.

3. RESULTS AND DISCUSSION

3.1 Characterization

The data of mass loss obtained from the TGA curves for the clay minerals and K-Fsp are shown in Table 1.

Table 1: Percentages of mass loss of mica, Kaol, Pal and K-Fsp obtained by thermogravimetric analysis in a temperature range variating from 100 °C to 800 °C.

Sample	Temperature (°C)							
	100	200	300	400	500	600	700	800
Mica	0%	0%	1%	1%	1%	1%	1%	2%
Kaol	0%	0%	1%	1%	4%	10%	11%	11%
Pal	7%	9%	10%	11%	14%	15%	20%	20%
K-Fps	0%	0%	0%	0%	0%	0%	0%	0%

The palygorskite clay mineral presented a 7% mass loss at 100 °C which indicates the presence of humidity in the material. Another mass loss at 200 °C can be associated with the presence of water in their structural channels

[13]. Except for Pal, around of 200 °C, none of the other samples showed mass losses, and this suggests that the other samples did not have humidity in their structures. In the range from 200 °C to 400 °C, a mass loss is observed for Pal which can be attributed to the presence of water at the edges of the material and the possible presence of organic matter inside the structure [13]. A loss of material structure can occur after 400 °C. Between 400 °C and 700 °C Kaol and Pal presented a mass loss which can be attributed to a dihydroxylation process of the material that occurs in this range temperature. For Kaol, meta kaolinite can be formed. [14] After 700 °C mica showed a brief mass loss due to the dihydroxylation process. K-Fsp showed high thermal stability up to 800 °C, which may indicate that there is no presence of organic matter in the material [13,14].

The determination of the chemical composition of clay minerals and K-Fsp was performed by X-ray fluorescence (XRF) analysis. The results are shown in Figure 1.
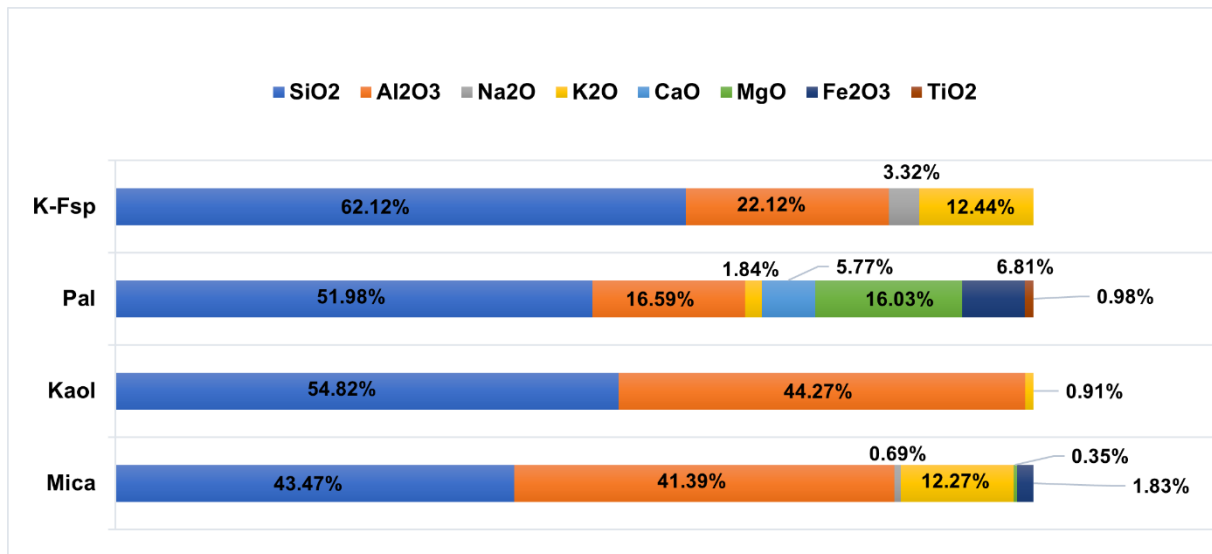
Figure 1: Chemical compositions of Mica, Kaol, Pal and K-Fsp

K-Fsp has the higher silicon content in the structure, and also aluminium by the reason of the formation of an aluminosilicate tetrahedral. The potassium content present in the structure is due to the fact that it is the compensation cation. The presence of sodium is possibly other minerals on the sample [13]. Pal has a high percentage of silicon, aluminium and magnesium content, it has a tetrahedral units of silicon and octahedral sheets of aluminium and magnesium in its structure. The presence of iron indicates an isomorphic substitution in the octahedral sheets [15]. The presence of potassium is generalized because it substituted an exchangeable cation inside the formed pores and the channels. The presence of calcium and titanium is not expected in the Pal crystalline structure. The presence of a considerable percentage calcium indicates another mineral content in the sample and the presence of titanium indicates an impurity in the material [13]. Kaol presented high percentages of only silicon and aluminum due to its crystalline structure form without interlayer compensation cations. The lower concentration of potassium could be related to the presence of other minerals in the sample [13]. Mica presented a rich content of silicon and aluminium in its structure. The potassium content present in the structure is due to the compensation cation in its interlayer. The presence of iron is usually due to very few isomorphic substitutions that do not change the structure of the clay mineral. A small percentage of magnesium can indicate that the mineral is a muscovite type [13].

B.E.T isotherms were used to determine the specific surface areas of mica, Kaol, Pal and K-Fsp which are presented in Table 2. Pal differed greatly from others that present small areas, presenting a high specific area, due to its highly porous structure formed by channels [14].

Table 2: Mica, Kaol, Pal and K-Fsp specific areas

Sample	Specific area - B.E.T. (m² /g)
Mica	1.5
Kaol	6.5

Pal	98.8
K-Fsp	0.8

3.2 Flammability evaluation

Figure 2 exhibits the LOI values obtained for the clay minerals and K-Fsp materials.
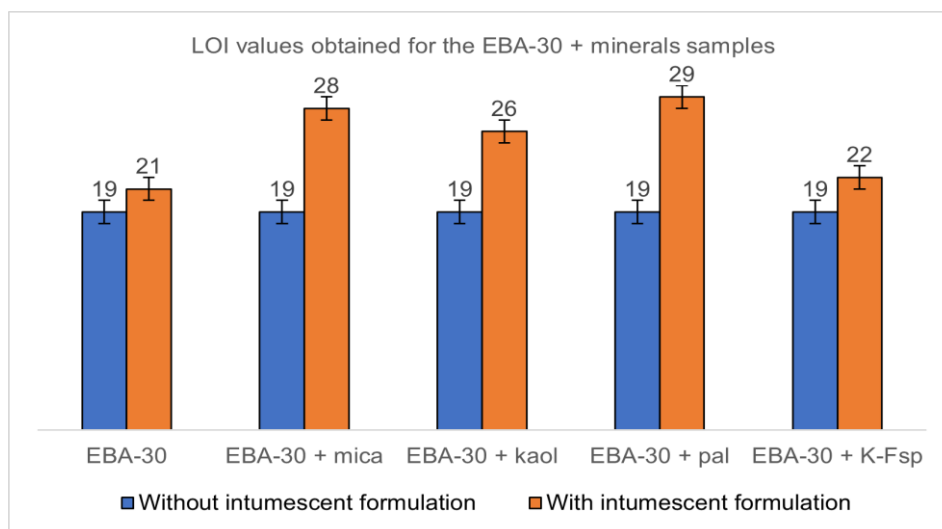
Figure 2: Limiting oxygen index (LOI) values obtained for the EBA-30 and minerals samples, with and without intumescent formulation.

It is possible to observe that the sole addition of clay minerals or of K-Fsp to the polymeric matrix did not increase the fire retardant properties since the values remained at 19%. The same behavior was observed with the sole use of montmorillonite without an intumescent formulation in EBA-30 matrix. [16] With the intumescent formulation, without the clay minerals, the LOI value extended to 21%. Nonetheless, the addition of the clay minerals mica, Kaol and Pal with APP/PER in EBA-30 matrix the values obtained for LOI were 28%, 26% and 29 % respectively. Therefore, a synergistic effect is observed for the materials tested. On the other hand, K-Fsp did not demonstrate a synergistic effect in the intumescent formulation. As the experimental LOI error is ± 1, the value of K-Fsp LOI is the same for the EBA-30 with intumescent formulation. Feldspar is a tectosilicate and has a three dimensional structures composed by aluminum silicates with a partial substitution of silicon by aluminium [13]. The K-Fsp structures added to EBA30 + APP/PER did not increase the LOI value of the polymeric materials. The LOI value obtained for the EBA-30 + APP/PER + mica sample was 28%, and considering the experimental error, it is a similar value to the obtained in the previous work, of a LOI of 29%, which was obtained for sodic montmorillonite, Cloisite Na [17]. This occurred due to the fact that mica has a similar structure to the one of montmorillonite, composed of a 2:1 structure consisting of an octahedral sheet of $Al_2(OH)_6$ bonded between two tetrahedral sheets of SiO_4. The large difference between mica and montmorillonite is the potassium as a compensation cation in the intermediate layer and the non-expansiveness of the lamellae, limiting their interlamellar space to 10.1 Å. [13]

The EBA-30 + APP/PER + Kaol sample generated an LOI result of 26%. Kaolinite has a 1:1 structure with a tetrahedral sheet of SiO_4 and an octahedral sheet of $Al_2(OH)_6$ bonded together. Kaol does not have compensation cations and its interlayer space is 7.15 Å, therefore, the penetration and interaction of organic compounds is more difficult [13]. In addition, while mica and montmorillonite can use the two tetrahedral sheets of SiO_4, both on the external and internal faces of the material, the reactions between Kaol and the intumescent formulations would occur primarily on the external faces of the clay minerals. On the internal faces the interaction is only with a SiO_4 sheet, still conferring some degree of improvement to the system. [13] The best LOI result value obtained for the EBA-30 + APP/PER + Pal sample was 29%, the same value obtained in a previous work for sodic montmorillonite, Cloisite Na [17]. Pal is a phyllosilicate of aluminum and magnesium, with fibrous morphology consisting of parallel ribbons in 2:1 layer containing two octahedral sheets of magnesium with partial replacement by aluminum and iron pressed between a tetrahedral sheet of SiO_4 [18]. The same results obtained for Pal and montmorillonite suggests that the spatial arrangement of SiO_4 tetrahedral sheets and $Al_2(OH)_6$ octahedral sheets does not have an influence on the synergy effect measured by the LOI, but the interaction of the organic material with the clay mineral can

influence the synergism. As seen in Table 2, Pal has a large specific surface area due to its channels and pores [15]. Consequently, this channels and pores can be used for the catalysis of the reactions. Pal can act as a catalyst in petroleum polymerization [19]. Then, considering the highly porous structure, Pal could possibly be catalyzing char-forming reactions such as the APP and PER esterification reactions in a similar way to the ones with montmorillonite [16]. As seen in Figure 1, Pal has other elements such as Fe, Mg and Ca in its chemical composition, which do not seem to have an influence on the synergistic action, since mica does not have high concentrations of these metals in its composition and has similar LOI results. These results lead to the conclusion that the crystalline structure have an influence on the synergistic action of the material.

The peak of the heat release rate (pHRR) and the ignition time of the polymeric materials without intumescent formulation, containing only clay minerals and K-Fsp, are shown in Table 3.

Table 3: pHRR and time ignition values of the samples without the intumescent formulation.

Sample	pHRR (kW/m^2)	Time ignition (s)
EBA-30	830	180
EBA-30 + mica	620	350
EBA-30 + kaol	840	180
EBA-30 + Pal	660	250
EBA-30 + K-Fsp	660	310

Except for Kaol, the addition of clay minerals and K-Fsp increased the ignition time of the polymeric material compared to the result for the raw polymer. The decrease in pHRR of mica and Pal clay minerals and K-Fsp is also observed when compared to the raw polymer. This effect was not observed for Kaol sample. Due to the thermal stability of clay minerals and their composition, some authors mention that clay minerals, such as montmorillonite can form a protective layer that works as a physical barrier that prevents the transfer of heat, oxygen and combustible gases in the material, resulting in the reduction of the pHRR [20]. However, LOI tests with clay minerals and K-Fsp showed no change in their results, which indicates that despite the formation of a barrier, it was not very protective, since the material was still highly flammable.

The peak heat release rate (pHRR) and ignition time of the polymeric materials containing the intumescent formulation and clay minerals or K-Fsp are shown in Table 3.

Table 3: pHRR and ignition time values of the samples with the intumescent formulation.

Sample	pHRR (kW/m^2)	Ignition time (s)
EBA-30	830	180
EBA-30 + APP/PER	450	80
EBA-30 + APP/PER + mica	230	150
EBA-30 + APP/PER + Kaol	280	115
EBA-30 + APP/PER + Pal	0	0
EBA-30 + APP/PER + K-Fsp	290	125

Table 3 shows that the addition of the intumescent formulation reduced the ignition time of the material, however, it generated a rate of about half of the one of pure polymer. With the addition of all clay minerals tested and of K-Fsp, there was a considerable reduction in the peak of heat release rate as compared to the material containing only the intumescent formulation. The highest value among the clay minerals reached about half of the pHRR value for the EBA-30 + APP/PER. This suggests that mica, Kaol, Pal and K-Fsp had a good performance reducing the inflammability of the composite. This effect was also detected by the LOI, except for K-Fsp, as shown in Figure 2. Among the other samples tested, K-Fsp presented the highest peak of heat release rate and despite generating an increase in the reported ignition time, among the clay minerals, K-Fsp obtained the lowest ignition time. Kaol had the second highest peak of heat release rate and mica had the third highest value, which was about 25% of the value of the pHRR obtained for the pure polymer.

The composite with the clay mineral Pal, as shown in Table 3, oscillated close to zero for the values of pHRR and consequently the ignition time, for all three specimens of the triplicate. Pal when exposed to a heat flux of 50 kW/m^2,

which corresponds to the heat released during developed fires [21], did not ignite. Palygorskite, was also responsible for the highest LOI value shown in Figure 2, and, considering the experimental error, a value of 30% LOI is commercially desired. The results suggest the occurrence of a strong synergistic action between the mineral clay and the APP/PER intumescent formulation in the EBA-30 matrix, which can be related to the fact that, due to its larger surface area, Pal would be strongly catalyzing the esterification and Diels-Alder reactions between APP and PER that generate char precursors and therefore avoiding the collapse of the char structure at higher temperatures [16,22].

Heating microscopy images obtained for the EBA-30 + APP/PER samples containing the best and worst results from LOI and cone calorimetry clay minerals Pal and K-Fsp in three different temperatures from 35 °C, 300 °C and 790 °C are shown in Figure 3.

	30 °C	300 °C	790 °C
EBA-30 + APP/PER			
EBA-30 + APP/PER + pal			
EBA-30 + APP/PER + K-Fsp			
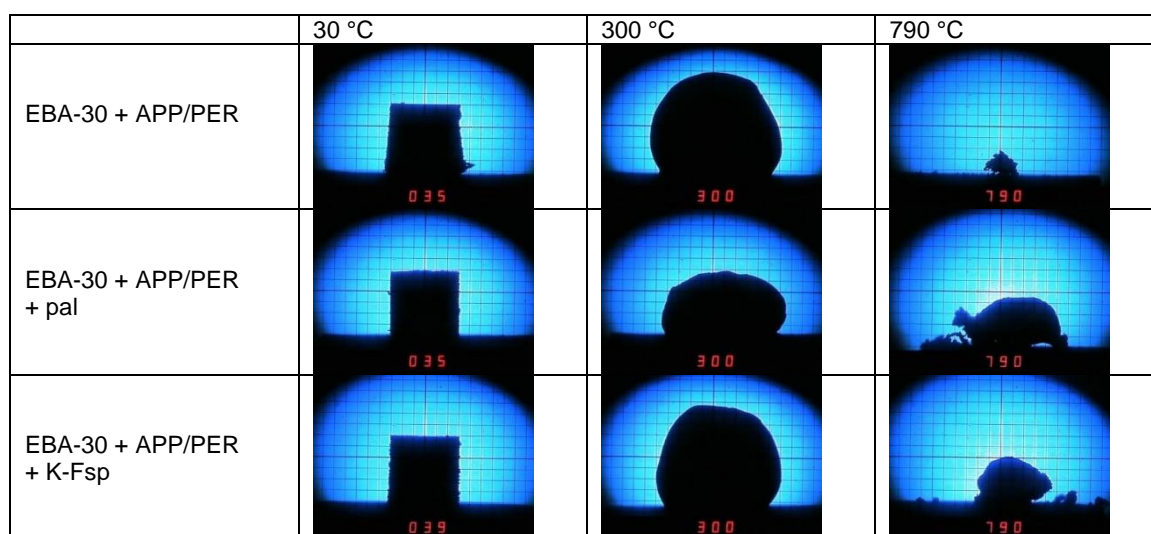
Figure 3: Images of the EBA-30 + APP/PER+ mineral specimens obtained through heating microscopy.

The evidence that the intumescent process occurred in the material is observed by a volumetric expansion at 350 °C. It is possible to observe that Pal produced a larger and more structured residue than K-Fsp at 790 °C. This fact can explain the higher LOI value recorded for the sample containing Pal and the lower for the one containing K-Fsp. It was reported in a previous work that the addition of montmorillonite maintained the P–O–C bond and the crystalline cells of polyaromatic structures connected by polymeric chain fragments at temperatures above 430 °C, and that the clay mineral in the polymeric structure gave flexibility and thermal stability to the structural layers at high temperatures [16]. Other authors suggest that the intumescent char generates an increase in thermal stability with the formation of an organic aluminosilicophosphate from clay minerals and intumescent formulation structures during the burning process. [8] The same mechanism may be occurring with the addition of the Pal and K-Fsp, thus increasing the thermal stability of the materials.

4. CONCLUSIONS

The flammability test showed that the addition of mica, Pal, K-Fsp and Kaol without the intumescent formulation to the EBA-30 copolymer did not increase the polymeric matrix flame retardant properties. However, when added in a small amount with an intumescent APP/PER mixture, a synergistic effect was detected through TGA, heating microscopy, LOI and cone calorimeter analysis. All the clay minerals presented better synergistic action than the K-Fsp, indicating that the clay mineral structure plays an important role in the measured flame-retardant properties. Among the clay minerals studied, Pal presented the greatest synergistic action with the intumescent formulation in the EBA-30 matrix showing that it could possibly be catalyzing the char formation reactions. On the other hand, the material containing APP-PER and K-Fsp presented the poorest flame-retardant properties. In conclusion, the crystalline structure of the clay minerals appears to affect the synergy with APP/PER in EBA-30.

REFERENCES

[1] Bar, M.; Alagirusamy, R.; Das, A. (2012). *Flame retardant polymer composites*, Fibers and Polymers, vol.16, no. 4, p. 705-717.

[2] Xu, Q.; Wu, L.; Yan, X.; et al. (2021). *Halogen-free flame retardant polypropylene fibers with modified intumescent flame retardant preparation, characterization, properties and mode of action*, Polymers, vol.13, no. 15, p. 2553.

[3] Alongi, J.; Han, Z.; Bourbigot, S. (2015). *Intumescence: tradition versus novelty*, Progress in Polymer Science, vol. 51, p. 28-73.

[4] Estevão, L.R.M.; Le Bras, M.; Delobel, R.; et al. (2005). *Spent refinery catalyst as a synergistic agent in intumescent formulations: influence of the catalyst's particle size and constituents*, Polymer Degradation and Stability, vol.88, no. 3, p. 444-445.

[5] Ribeiro, S.P.S.; Martins, R.C.; Cescon, L.S.; et al. (2019). *NMR evaluation of montmorillonite's d-spacings on the formation of phosphocarbonaceous species in intumescent systems*, Journal of Applied Polymer Science, vol.136, no. 42, p. 48053.

[6] Martins, R.C.; Rezende, M.J.C.; Nascimento, M.A.C.; et al. (2020). *Synergistic action of montmorillonite with an intumescent formulation: the impact of the nature and strength of acidic sites on the flame retardant properties of polypropylene composites*, Polymers, vol.12, no. 12, p. 2781.

[7] Ribeiro, S.P.S.; Estevão, L.R.M.; Pereira, C.; et al. (2009). *Influence of clays on the flame retardancy and high temperature viscoelastic properties of polymeric intumescent formulations*, Polymer Degradation and Stability, vol.94, no. 3, p. 421-431.

[8] Bourbigot, S.; Le Bras, M.; Breant, P.; et al. (1996). *Zeolites: new synergistic agents for intumescent fire retardant thermoplastic formulations criteria for the choice of the zeolite*, Fire Mater, vol.20, no. 3, p. 145-154.

[9] Estevão, L.R.M.; Le Bras, M.; Delobel, R.; et al. (2004). *Structure property relationship in intumescent polymeric formulations containing waste zeolite based material as a synergistic agent*, European Polymer Journal, vol.40, no. 7, p. 1503-1513.

[10] Babrauskas, V. & Peacock, R. D. (1992). *Heat release rate: the single most important variable in fire hazard*, Fire Safety Journal, vol.18, no. 3, p. 255-272.

[11] Schartel, B.; Bartholmai, M.; Knoll, U. (2006). *Some comments on the main fire retardancy mechanism in polymer nanocomposites*, Polymers for Advanced Technologies, vol.17, no. 9, p. 772-777.

[12] Estevão, L.R.M.; Nascimento, R.S.V. (2002). *The use of heating microscopy in the study of intumescent in waste catalyst containing polymer systems*, Polymer Degradation and Stability, vol.75, no. 3, p. 517-533.

[13] Grim, R. E. (1953). *Clay Mineralogy*. Soil Science, 317 p.

[14] Theng, B. K. G. (1974). *The Chemistry of Clay Organic Reactions*. Rank Precision Industries, 632 p.

[15] Galan, E. (1996). *Properties and applications of palygorskite-sepiote clays*, Clay Minerals, vol.31, p. 443-453.

[16] Ribeiro, S.P.S.; Estevão, L.R.M.; Pereira, C.; et al. (2013). *Mechanism of action of different d-spacings clays on the intumescent fire retardance of polymers*. Journal of Applied Polymer Science, vol.130, no. 3, p. 1759-1771.

[17] Ribeiro, S.; Estevão, L.R.M.; Nascimento, R.S.V. (2008). *Effect of clays on the fire-retardant properties of a polyethylenic copolymer containing intumescent formulation*. Science, Technology & Advanced, vol. 9, no. 2.

[18] Huang, J.; Liu, Y.; Liu, Y; et al. (2007). *Effect of attapulgite evidence pore size distribution on soybean oil bleaching*, Journal of the American Oil Chemist's Society, vol. 84, no. 7, p. 687-692.

[19] Konta, C.; Hurlbut, C.S. (1995). *Clay and man: clay raw materials in the service of man*, Applied Clay Science, vol. 10, no. 4, p. 275-335.

[20] Kiliris, P.; Papaspyrides, C.D. (2010). *Polymer/layered silicate (clay) nanocomposites: an overview of flame retardancy*, Program of Polymers and Science, vol. 35, no. 7, p. 905-958.

[21] Shartel, B.; Barthomai, M.; Knoll, U. (2005). *Some comments on the use cone calorimeter data*, Polymers Advanced & Technology, vol. 88, no. 3, p. 540-547.

[22] Bourbigot, S.; Duquesne, S. (2007). Fire retardant polymers: recent developments and opportunities, Journal of Materials Chemistry, vol. 17, no. 22, p. 2283-2300.

COMPUTATIONAL MODEL OF FIRE BASED ON A FULL-SCALE EXPERIMENT

Bruno C. L. de A. Matos[a], George C. B. Braga[b], Fernando L. da S. Ferreira[c], João Paulo C. Rodrigues[d], Rodrigo B. Caldas[e]

ABSTRACT

Fire, while being one of humanity's great discoveries and improving human life in many ways, also poses dangers when it gets out of control and becomes a fire. To combat these incidents, firefighting departments have been created, constantly evolving their knowledge and techniques to deal more effectively with fires. Therefore, this work aims to present a possible solution for studying fire behavior and developing knowledge about this complex phenomenon to improve prevention and firefighting techniques. The proposed solution is to simulate fires using computational models with specialized software, based on data obtained from full-scale compartmentalized fire experiments.

Keywords: Fire; compartmentalized fire; full-scale test; computational simulation.

1. INTRODUCTION

Since the beginning of humanity, the human being has been trying to understand natural phenomena and one of the greatest discoveries was fire. Even in prehistory, humans were already attempting to control it and throughout human history, fire has been used for various purposes such as protection against animals, cooking, heating, industrial production, lighting, among other uses.

Unfortunately, despite the many advantages that fire brought to human life, it also brought danger. Throughout history, there have been various disasters caused by large fires that have consumed buildings and even entire cities. Recognizing the danger that uncontrolled fire could cause, fire departments were created to combat it.

The fire departments have been constantly evolving, using techniques and tools more suitable and more efficient protective equipment. However, this is only possible through observation and research. Observation, whether in case of firefighting or in post-fire investigation, where the origin and cause of fire are investigated.

As firefighting has evolved, standards have been established for prevention and combat to fires. Research is needed to support these standards and improve firefighting practices, alongside the experience gained from cases of fires.

_____
*(a) University of Coimbra (bruno00matos@yahoo.com.br)
(b) Fire Department of the District Federal, Brazil (george.braga@gmail.com)
(c) University of Coimbra (flsferreira@uc.pt)
(d) University of Coimbra (jpaulocr@dec.uc.pt)
(e) University of Minas Gerais (caldas@dees.ufmg.br)

In fire research, one way to study is through experiments simulating a real fire in a controlled compartment. These studies allow researchers to observe fire behavior and gather information related to compartmentalized fires, such as temperature, duration and intensity.

However, to carry out a full-scale experiment, it is necessary to have specific knowledge, time for planning and execution, financial and human resources for preparing the scenario to be tested. In addition, specific measurement equipment is also required, such as thermocouples, heat flux meters and thermal cameras. In light of this, it is crucial to make the most of every experiment conducted by gathering as much information as possible.

The Military Fire Brigade of the Federal District in Brazil has been constantly developing research in the field of firefighting, focusing on the performance of firefighting during fire combat, as well as the equipment used by them. Furthermore, they conduct fire simulations to improve their understanding of the phenomenon.

Fires are complex physical-chemical phenomena, and when it comes to compartmentalized fires, certain environmental factors are highly relevant, such as volume, floor area, ceiling height, fire load, distribution of the fire load and ventilation. These factors can significantly impact the behavior and intensity of a compartmentalized fire.

Another way to study fires is by using computational models with the support of software that has been developed for this purpose. This type of model enables to change the variables present in a fire, simulate various scenarios and analyze its behavior in a cheaper and faster way compared to a full-scale experiment.

On the other hand, this way also brings some challenges. To carry out a fire simulation using a computational model, it is necessary to have a good understanding of the software, including its limitations, provide input data correctly and finally know how to interpret the results. Thus, computational models currently emerge as a tool to assist in the study of fire behavior, rather than to replace full-scale experiment.

In 2019, a research opportunity arose when a glass manufacturer contacted the Military Fire Brigade of the Federal District, through fire officer, George Cajaty, to test the efficiency of a fire-resistant glass. The main objective of the experiment was to verify the viability of using this glass in glass curtain wall facades, complying with current regulations regarding vertical compartmentalization. As a result, the Military Fire Brigade planned and conducted a full-scale experiment, which was funded by the manufacturer.

2. METHODOLOGY

2.1 Full-scale experiment

To carry out the experiment, it was first necessary to design the building that would be subjected to the fire. The fire officer, Bruno Matos, developed a building project seeking economy, fast construction, fire resistance and structural reuse. Based on this project, two modular buildings were constructed, each with two floors and almost identical, except for the use of fire-resistant glass instead of drywall for the windowsill on the first floor.

The building structure was made of carbon steel with protection provided by a sacrificial layer of fire-resistant gypsum board. The walls of these buildings were made of drywall. The construction process of the buildings can be seen in the photos below (Figure 1).

| a) | b) |

c)

d)

e)

Figure 1: The construction process of the buildings (author)

The fire load used in the experiment was 700MJ/m², based on the Brazilian standard NBR 14432:2001, which considers the building's use as an office. Buildings in Brazil with this type of occupancy often utilize this type of façade, which is also seen in residential buildings. However, since the fire load is higher in offices according to this standard, the worst-case scenario was used. Figure 2 shows the fire load used, represented by wood cribs as fuel.

Figure 2: The fire load, wood cribs. (author)

In terms of compartment ventilation, the structures had two opposing openings, a door and a window. They were strategically positioned to optimize the prevailing wind direction in the area, enabling air to flow in through the door while smoke and flames escape through the window. After all, the goal of the experiment was to study the effect of fire on the glass façade.

Regarding the instrumentation of the experiment, a project was developed with the location of each measurement instrument, thermocouples and heat flux meters, as show in Figure 3. In addition, the best position for cameras, both thermal and common, like GoPro, were also planned. The common camera had to placed in a container with water to withstand the high temperatures it would be subjected. The thermal cameras were positioned to register from the front and side the entire experiment, allowing to observe fire behavior throughout the experiment.

With this instrumentation, the goal was to measure the ambient temperatures in the middle of the compartment and along the layers every 30 cm. The heat release rate was also measured by installing heat flux meters on the wall at a height of one meter. Thermocouples were also installed on the beams and columns next to the window, as well as on the glass and windowsill, on both ground floor and first floor, because would be where the fire was expected to escape.

a)   Floor plan   b)   Section view
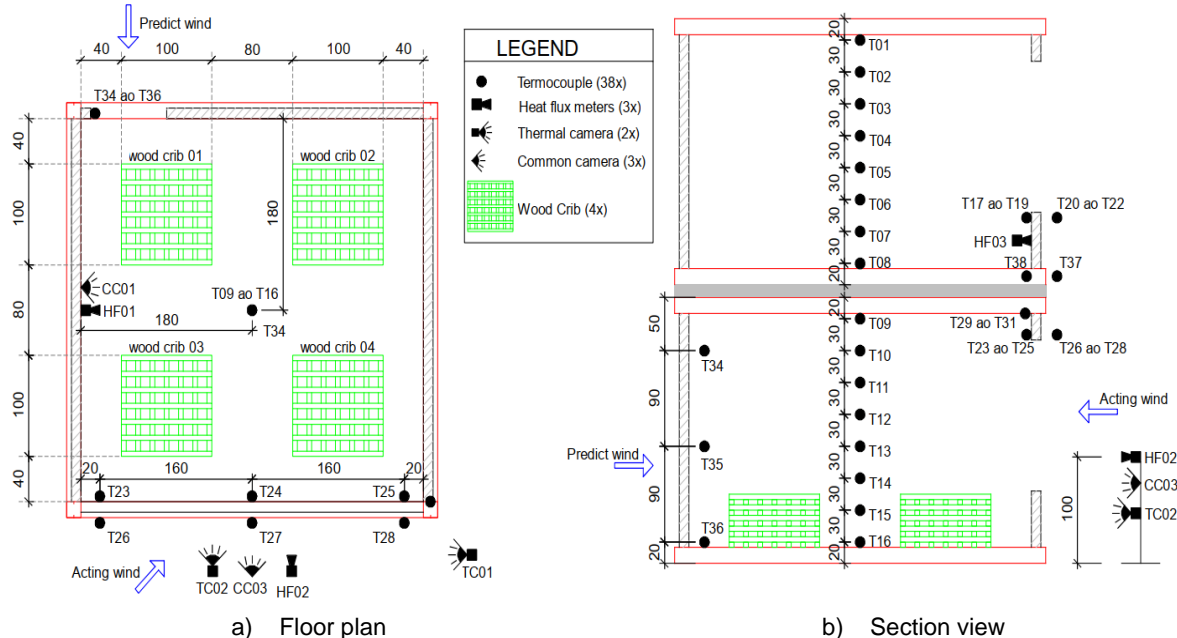
Figure 3: Buildings instrumentation. (author)

2.2 Computational model

The computational model was essential in determining the ventilation strategy and structural design based on the temperatures reached in the simulation.

To use software effectively, it is important to be aware of its possible limitations. For example, when using FDS/ NIST or PyroSim, it is crucial define an appropriate mesh and position obstruction and vents within the cell boundaries.

The FDS/NIST software guide recommends an expression to determine an appropriate mesh size based on the diameter of fire and the heat release rate. However, in this simulation, a refined mesh was necessary due to the use of wood cribs as the fire load. The cribs consisted of wooden bars with a cross-section of 5x5 cm. Therefore, a mesh size of at least 5x5 cm was used in the region of the cribs to ensure an accurate representation of the burning behavior of the wood.

The tables below show the input data used in the computational model, all based on bibliographic references.

Table 1: Building dimensions

Description	Dimensions (m)
Compartment (length x width x height)	3,6 x 3,6 x 2,5
Door (length x width x height)	0,8 x 2,1
Window (length x width x height)	1,4 x 3,6 x 0,7

Table 2: Building construction features

Location	Building material
Walls (thickness = 90 mm)	Drywall (2 x 12,5mm)
Ceiling (thickness = 50 mm)	Composite panel + Gypsum plaster

Table 3: Input parameters of the computational model

Description	Values and references
Reaction	Wood_pine (SFPE handbook, 3rd Ed)
• Specify heat of combustion	1,79E4 kJ/kg
Material	Yellow Pine (Quintiere, Fire Behavior - NIST NRC Validation)
• Density	600 kg/m³
• Specific heat	2,85 kJ/(kg.K)
• Conductivity	0,14 W/(m.K)
• Emissivity	0,9
Material	Gypsum Plaster (Quintiere, Fire Behavior - NIST NRC Validation)
• Density	1440 kg/m³
• Specific heat	0,84 kJ/(kg.K)
• Conductivity	0,48 W/(m.K)
• Emissivity	0,9
Pool Fire (diameter = 20 cm)	Experimental
• HRRPUA	200 kW/m²
Wood crib (1,0 x 1,0 x 0,4) m	SFPE calculation for Kodur Method
• HRRPUA	600kW/m² (superficial area of stick)
• Ignite temperature	384 °C

After running the model, it is necessary to analyze the results carefully. Therefore, the main analyzed data were: the correct fire ignition, ignition and wood consumption, smoke and flame behavior, fire spread through the cribs, temperatures reached in the environment and heat release rate.

a) Before running model   b) During the fire
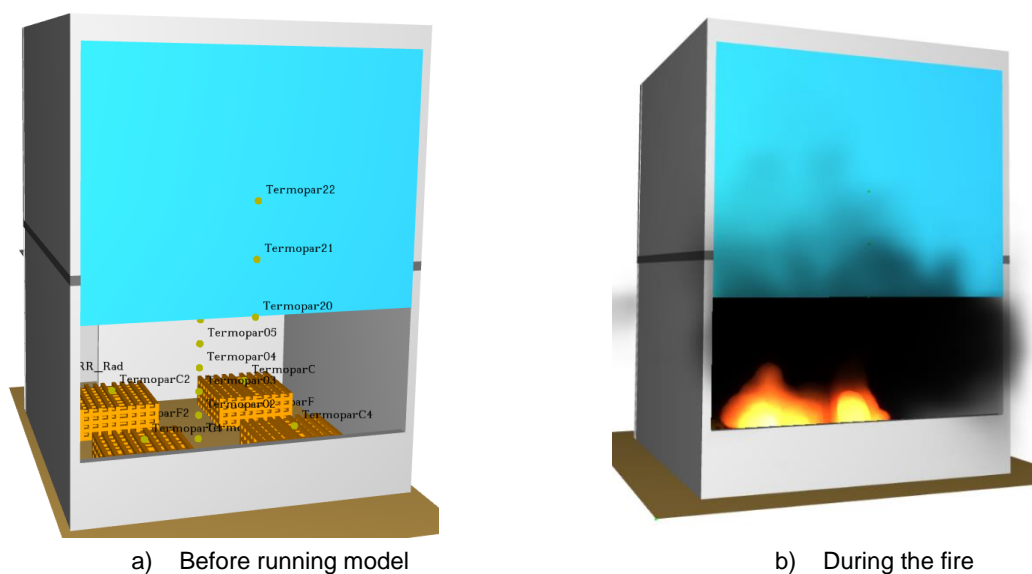
Figure 4: Computational model of fire. (author/Smokeview)

3. RESULTS

Considering the main focus of this study is to use computational models based on full-scale experiments, only the relevant data within the scope of this paper will be presented among all the data obtained from the experiments.

Therefore, the results presented below refers to both experiments and relates to the ground floor compartment, where the fire load was located. The obtained results include temperature-time curves, which were measured by thermocouples located in the center of the compartment and distributed at 30 cm intervals along its height. In addition, the fire intensity was measured using a heat flux meter installed on the wall at 1m of height and photographic records of the building during and after the fire.

a) Experiment 1 - flashover phase of fire.   b) Experiment 2 – The initial phase of fire

Figure 5: Full-scale experiments of fire. (author)
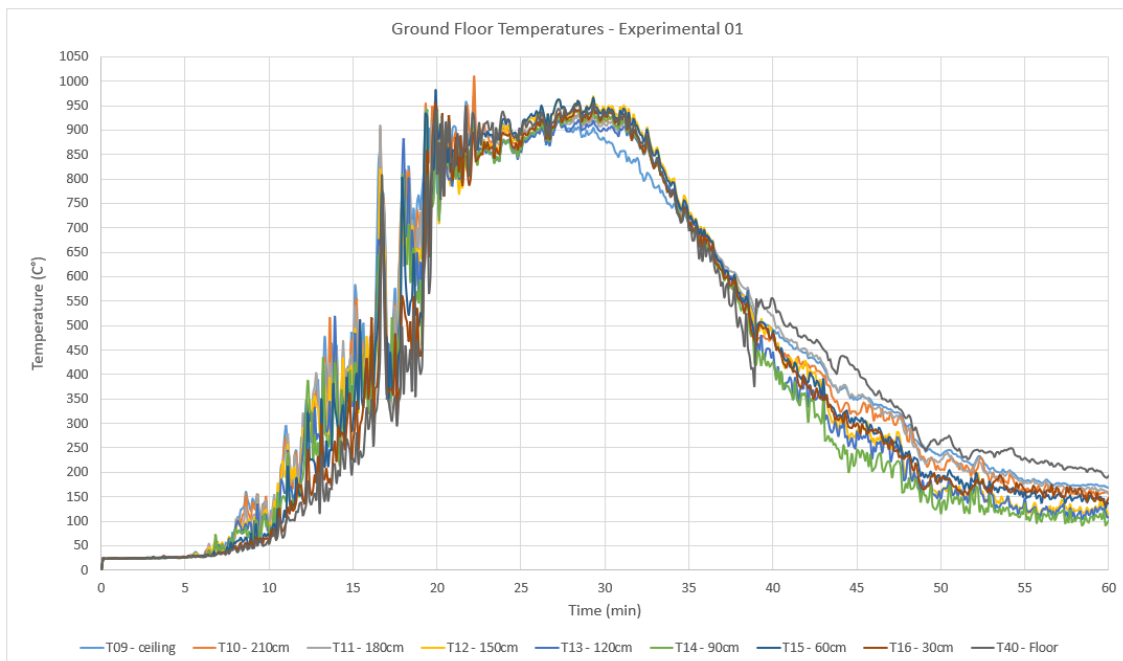
Figure 6: Experiment 1 – Temperatures along the height in the center of the compartment. (author)
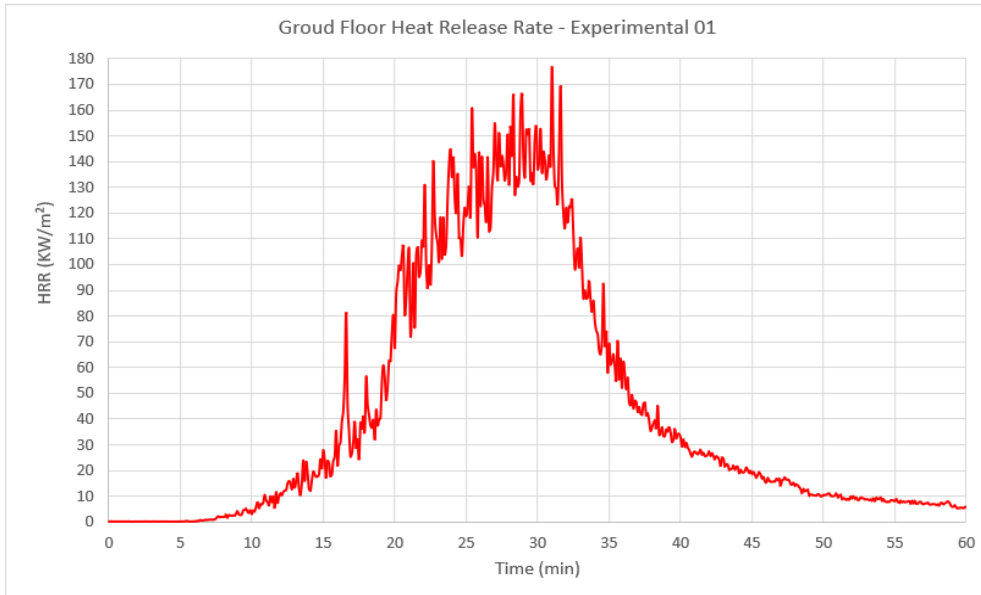
Figure 7: Experiment 1 – Intensity of fire. (author)
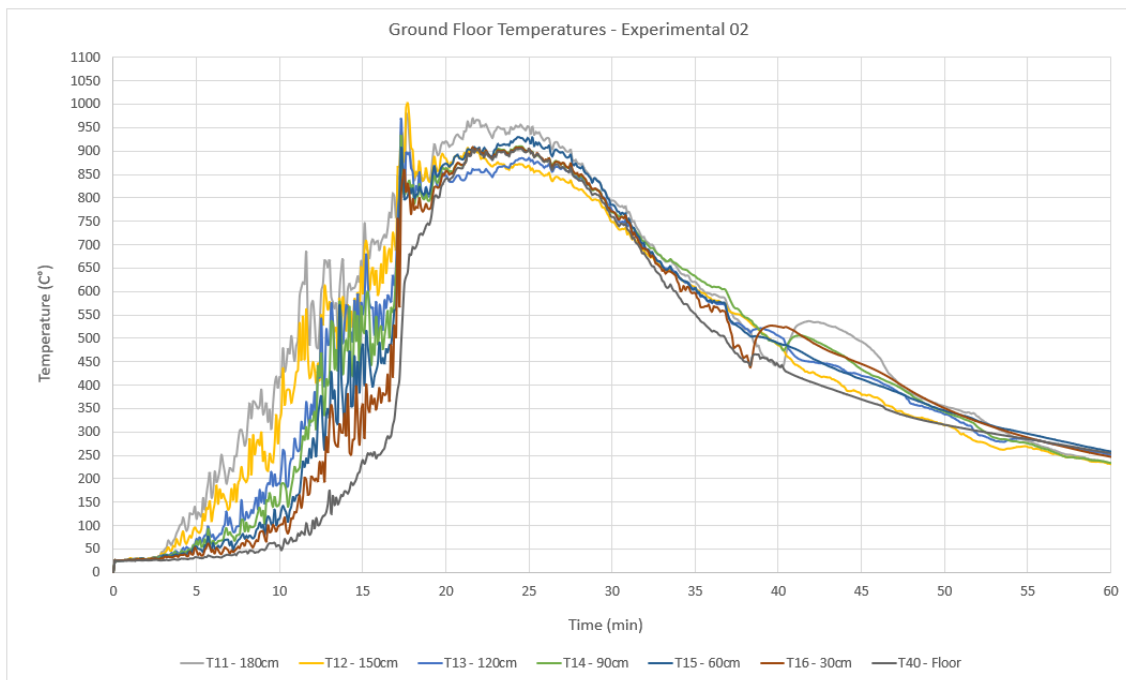
Figure 8: Experiment 2 – Temperatures along the height in the center of the compartment. (author)
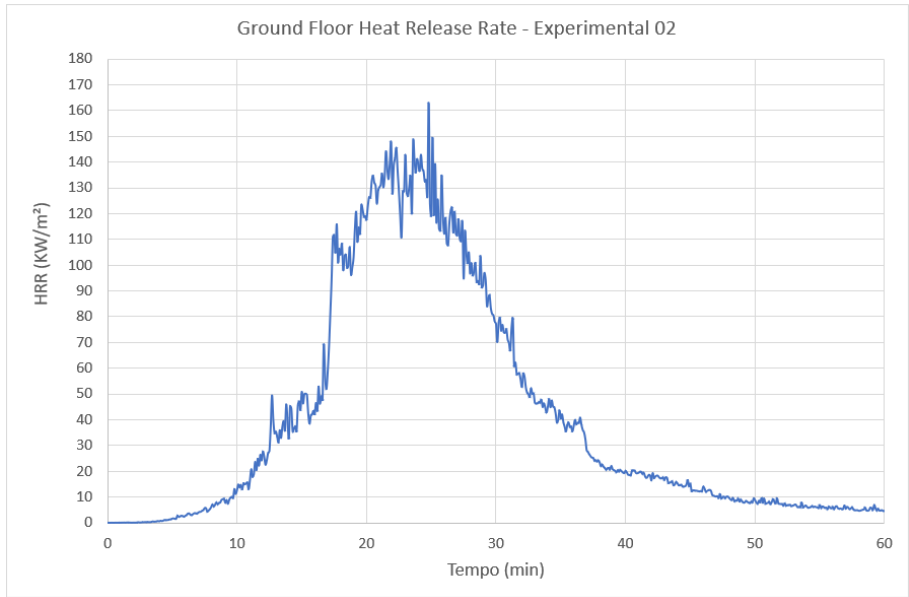
Figure 9: Experiment 2 – Intensity of fire. (author)

a) Experiment 1 - Walls

b) Experiment 1 - Ceiling

c) Experiment 2 - Walls

d) Experiment 2 - Ceiling

Figure 10: Damage to buildings post-fire. (author)

4. RESULTS ANALYSIS

After the presentation of the relevant data regarding the two experiments, some analyses will be presented that may be useful for the computational modeling of compartmentalized fires.

Firstly, it should be noted that on the day of the experiment, the wind changed direction, which is unusual for the region at that time. As a result, during the experiment, the wind was blowing towards the window instead of the door, Figure 3, as had been predict in planning phase. In light of this, the behavior of the fire was analyzed and it was necessary to close the compartment door after 15 minutes in order to increase the fire intensity.

From the temperature-time curves presented for both experiments, Figures 6 and 8, some fire behavior can be observed.

In Experiment 1, where the wind entered through the window, it was observed that during the growth phase, the temperatures reached in the different layers had significant variation, but followed the same increasing trend. This can be explained by the turbulent regime that occurred due to the pressure exerted by the fire from inside out, against the pressure of the wind from outside in. As a result, the environment as a whole was heated uniformly.

As the fuel was consumed and the fire intensity increased, aided by closed door, a flashover occurred. This caused the pressure of the fire to surpass the wind pressure, leading to the fire starting to come out through the window. Consequently, the compartment reached its maximum temperature and remained on this plateau for around 15 minutes. After this plateau, the temperature in the layers of the compartment began to decrease differently but followed the same trend.

Regarding Experiment 2, during the fire growth phase, the temperature in the layers increased at different rates until they reached the maximum temperature plateau, which lasted less than in Experiment 1, around 10 minutes. After this phase, the temperature in the layers began to decrease at the same rate, but at the end of the 60 minutes, the temperatures in the layers were higher than the temperatures in Experiment 1.

After the experiment concluded, a photographic record was taken to document the damage caused to the compartment containing the fire load. Figure 10 shows the difference in damage sustained by the compartments in two experiments, including both on the walls and ceiling. The second experiment resulted in slightly more damage than the first, particularly to the ceiling. This may have been due to influence of the wind during the experiments.

Figure 11 presents a comparative graph of the temperature-curves of experiments 1 and 2, along with the curve obtained from the computational model used before the experiment, as well as curves already established and described in the European and Brazilian standards, namely ISO 834 and Natural Fire Curve.

To represent the temperature-time curves of the fire, the most severe conditions were selected, which were the temperatures recorded by thermocouples in the uppermost layers, near the ceiling.

It is possible to observe on the graph of the Figure 11 the maximum temperatures reached in each curve. Below is a summary table of these results.

Table 4: Maximum temperatures of curves

Curves	Maximum Temperatures (°C)
Real Fire - Experimental 1	967,96
Real Fire - Experimental 2	980,34
ISO 834	945,34
Natural fire	941,47
Computational Model Fire	1082,09
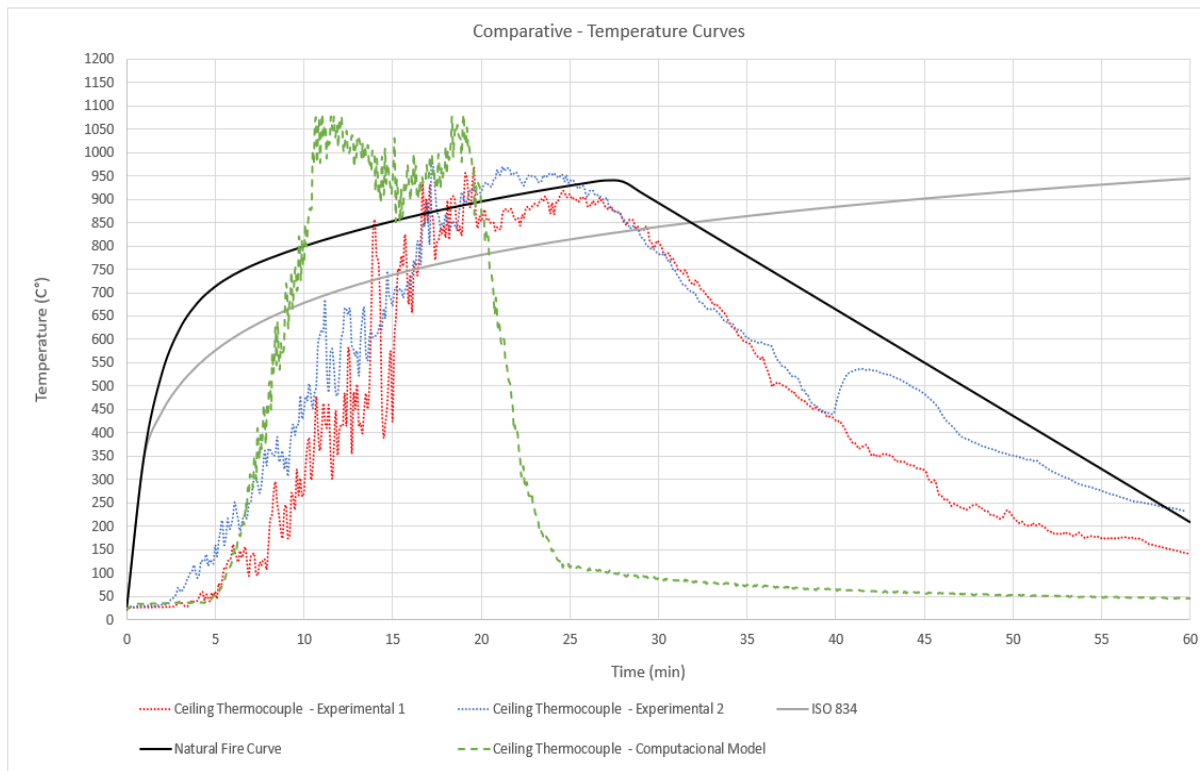
Figure 11: Comparative temperature-time curves. (author)

The graph shows that the experiment curves behaved similarly, with only a slight time lag between them due to wind variation. Specifically, the wind was stronger during the first experiment than during the second, causing the maximum temperature of the fire to occur earlier in the second experiment.

Another observation regarding the two experiments is that the maximum temperature reached in the second experiment was higher than that in the first experiment. This difference can also be attributed to the change in external factor, the wind, as the other variables were identical.

And why does this factor impact the two experiments in this way, considering that the two buildings are identical in terms of the ground floor and fire load? The wind caused a greater air exchange between the external environment, which was at ambient temperature of around 24°C, and the interior of the compartment, influencing both the magnitude and the time required to reach the maximum temperature. Despite the circumstances that can affect an experiment of this type, it is possible to consider that the compartmentalized fire was essentially the same in both cases.

Regarding Figure 11, it can be observed that the maximum temperature reached by the computational model was higher and occurred earlier compared to the maximum temperatures in the experiments.

It's important to note that this model was created prior to the experiments with the purpose of better planning the experiment and designing the building structure to withstand the impact of the fire while still being reusable. The input data used to characterize the model were obtained from international sources, as shown in Table 3. Therefore, it's evident that these data do not exactly correspond to the features of the materials present in Brazil for the experiments.

Take this into account, it was necessary to conduct a separate experiment to further study these materials, with the aim of achieving a closer match between the computational model and the full-scale model of compartmentalized fire. However, this particular study is part of a future work to be published, where the ignition temperature of the wood used in the experiment, as well as the heat release rate of both the ignition source and the wood crib, were determined. The results from this experiment allowed us to provide feedback and improve the previous model.

81

Regarding the temperature-time curves that are already well-stablished and widely used in Brazil and Europe, it can be observed that the natural fire curve closely approximated the curves obtained in the experiments. However, a significant difference was observed during fire growth phase, where the natural fire curve had faster temperature increases, following a logarithmic pattern, whereas the curves from experiments exhibited slower temperature increases, closer to an exponential pattern.

The curves of the experiments showed a higher maximum temperature than the natural fire curve. Additionally, while the natural fire curve had a peak to represent the maximum temperature, the curves from the real fire experiments had a plateau shape.

Concerning the cooling phase, it can be observed that the natural fire curve well describes the behavior of the curves obtained from the experiments, with this phase well represented by a linear decrease.

When it comes to the ISO 834 curve, it was observed that the maximum temperature reached in 60 minutes was lower than the temperatures obtained in the experiments and higher than the temperature predicted in the natural fire curve. Additionally, this curve only obtained the maximum temperature and did not represent the fire behavior as well as the natural fire curve did.

Given the previous analyses, it is understood that the natural fire curve is the best to describe a compartmentalized fire. However, this curve can still be improved both in the fire growth phase and in the phase where the maximum temperature occurs. It is also the scope of another work to be presented in the future, using these data as parameters.

Figure 12 presents a comparison of fire intensities in the presented models. The computational model predicted a more intense fire with its peak occurring earlier than the peaks in the experiments. One factor that contributed to this was the lack of wind in the model, in addition to the material characteristics. This further proves that the computational model needs improvement, by including wind and better defining material characteristics.
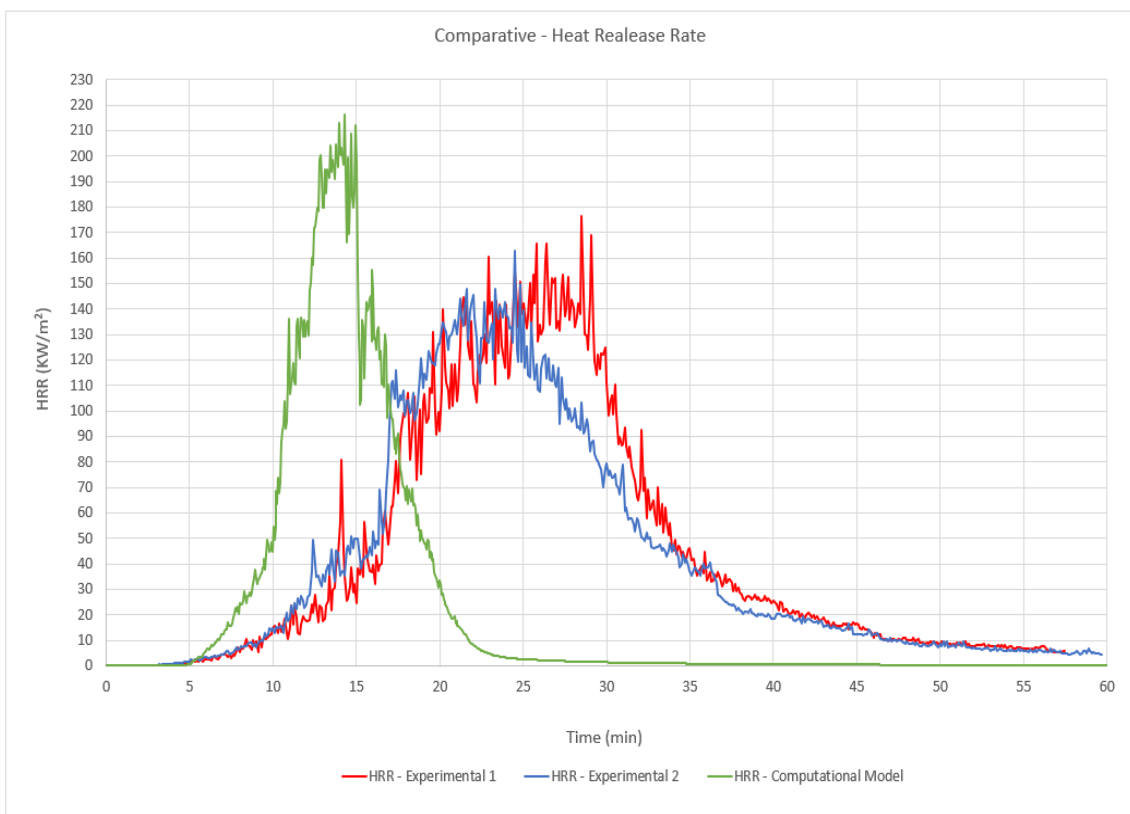
Figure 12: Comparative of intensity of models. (author)

4. CONCLUSIONS

Based on the data and analyses previously conducted, it can be concluded that the experiment complied its purpose by simulating a real fire during one hour using specified fire load, resulting in high temperatures and intensity as required by standard.

From this experiment, it was possible to study the behavior of a compartmentalized fire, verifying that external factors, such as wind, can influence a fire. It was possible to compare the behavior of temperature-time curves of experiments, curves established and widely used in Brazil and Europe, and the computational model curve.

It was noticed that the computational model used to plan the experiments overestimated the expected results. This proves that the data used, although obtained from relevant bibliographies, do not represent the characteristics of the materials used in the experiments and found in Brazil.

On the other hand, this model was useful for the success of the experiment. Therefore, it was the computational model that allowed for the planning of a high-cost experiment. Through this experiment, it was possible to use its data as reference to calibrate the computational model. This enable the model to be used in other computer simulations.

However, this computational model presented needs adjustments in some parameters, such as density and ignition temperature of wood, heat release rate of the wood crib and consideration of wind, so that it can be used in other simulations.

As a suggestion for future works, it is recommended to better characterize the materials to be used in the model, simplify de wood crib, so that the model mesh can have fewer elements and thus reduce the computational cost. Additionally, proposed studies should be carried out to improve the natural fire curve, making it even closer to real fire curves.

REFERENCES

[1] Kodur, V. K. R., & Harmathy, T. Z. (2016). Properties of building materials. SFPE Handbook of Fire Protection Engineering, Fifth Edition. https://doi.org/10.1007/978-1-4939-2565-0_9.
[2] Drysdale, Dougal. (1998). An introduction to fire dynamics, Second Edition.
[3] Quintiere, James G. (1997). Principles of fire behavior, Second Edition.
[4] EUROPEAN STANDARD, Eurocode 1: Actions on structures - Part 1-2: General actions – Actions on structures exposed to fire. Portugal, 2010.
[5] ABNT NBR 14432 – Fire-resistance requirements for building construction elements - Procedure, Brazil, 2001.
[6] ABNT NBR 14323 – Structural fire design of steel and composite steel and concrete structures for buildings, Brazil, 2013.
[7] NIST Special Publication 1019, (2021). Fire Dynamics Simulator User´s Guide, Sixth Edition. https://dx.doi.org/10.6028/NIST.SP.1019.
[8] NIST Special Publication 1018-3, (2021). Fire Dynamics Simulator Tecchnical Reference Guide Volume 3: Validation, Sixth Edition. https://dx.doi.org/10.6028/NIST.SP.1018.

Fire Investigation

PROPOSAL OF LEGAL EVIDENCE AND PROOF COLLECTION METHOD FOR FIRE INVESTIGATIONS

André Luiz Gonçalves Scabbia[a], Caio Cesar Moreira[b], José Luiz Gavião de Almeida[c]

(a) *Instituto de Pesquisas Tecnológicas de São Paulo-IPT (scabbia@ipt.br)*
(b) *Mestrando do Instituto de Pesquisas Tecnológicas de São Paulo-IPT (caio.moreira@ensino.ipt.br)*
(c) *Faculdade de Direito da Universidade de São Paulo (jlgalmeida@hotmail.com)*

ABSTRACT

All expertise must follow the principle of cooperation, as described in the CPC (2015) [1], of Article 6: "*all the subjects of the process must cooperate with each other in order to obtain, in a reasonable time, a fair and effective decision on the merits.*" The investigation requires enforcement with essential requirements and methodology, starting with collection data, consolidation of information, record of notes, photographs, drawings, audio and video recordings, critical and reasoned analysis of data and records, to then reach the conclusions, which will be presented in a document called an expert report or technical report. The methodology recommended by NFPA 921 [2] for fire investigation has seven steps, which the data collection step is the basis of the entire investigation. Given the importance of collect data for the development of an expert engineering works, as well as fire and explosion investigations, the article proposes a method based on the application of the 5W1H tool, as proposed by CARDOSO (2017) [3], which is composed of six questions: What – Who – Why – When – Where – How. Some authors, in a complementary way, use the 5W2H, as How much. The method used here is subdivided into eight steps, that is a mixture of the issues raised in the criminal investigations, NFPA [2] and SCABBIA; MOREIRA & ALMEIDA (2022) [4]. The initial step consists of an exploratory study aimed at identifying typical Risk Scenarios that cause fires or explosions, as established by LEES (2005) [5] and in the ABNT NBR ISO 31000: 2018 [6], considering: (i) context establishment, (ii) risk identification and (iii) risk analysis. In the activity of establishing the context, compare the definitions of how and why to carry out investigations, also using the concepts from Engineering and those expressed in Civil Law, based on different authors (BRANDIMILLER, 1996 [7]; DEL-CAMPO [8], 2008; PRESOTTO et al 2017 [9]. Regarding the place of the accident happened, the publication of SILVA (1992, 1997 and 2001) [10 to 12], RODRIGUES (2000) [13] and the UNIVERSITY OF SHEFFIELD (2007) [14] present a theoretical framework on the dynamic behavior of structures, even after the action of fire, which facilitates the expert or investigator to have a notion of the fire epicenter, and allows to

identify, even in the initial phase, Accidental Hypotheses. The paper of SHIELDS & SILCOCK (1987) [15] present case studies that describe how to do a fire investigation. The model developed by REASON (1990) [16] and adapted by ORTIZ (2018) [17] and ORTIZ & SCABBIA (2022) [18] for questions of investigations allows understanding how risks can materialize in accidents, such as fire and explosions, revealing the faults that can arise in defenses. To conduct a fire and explosion investigation, you can use the principles proposed by DEL-CAMPO (2008) [8], which is based on criminal proceedings, and follow the doctrine of BRANDIMILLER (1996) [7]. It was relevant that the professional (Expert Engineers, Consultants or Investigators) has full knowledge of the subject in which he is evaluating, regardless of his engineering background, in addition to understanding the investigative methodology that always seeks to determine the root cause of the claim. Regardless of the questions that must be answered in the investigation process, the root cause must be sought, even if it takes months to collect data and analyze the information, because you cannot generate a wrong, erroneous and superficial report. All expertise must be based on technical standards and legislation related to the subject of the claim, highlighting that such activity is of paramount importance for clarifying the facts and supporting the principle of full defense in accordance with the Brazilian Federal Constitution.

1. INTRODUCTION

The first step in carrying out an investigation is to apply the 5W1H tool, as proposed by Cardoso (2017), which consists of six questions: What - Who - Why - When - Where - How. Some authors, in a complementary way, adopt the 5W2H, with the use of How much. The adoption of this tool is presented below.

All expertise must follow the Principle of Cooperation, as described in CPC (2015) [1], of Art. 6 All the subjects of the process must cooperate with each other so that a fair and effective decision on the merits is obtained within a reasonable time.

All conclusions must be based on evidence, obtained through data collection, tests carried out in situations similar to those found at the location of the expertise, or available in bibliographical references, which allow generating information and proposing Accidental Hypotheses (HA).

According to ABNT NBR 13752 – Engineering Expertise in Civil Construction, ABNT (1996) [6], "*activity that involves investigating the causes that motivated a certain event or the assertion of rights*".

Jurisdictional provision via technical expertise, engineering, must necessarily have as a starting point the verification of compliance with technical standards and legal obligations of those involved. In the case of fires, verifying compliance with the Technical Instructions of the Fire Department and the existence of AVCB, is a path that leads to satisfactory results.

A general understanding of the process is also necessary, not limited to the questions presented in the judicial process, that is, seeking to meet the objective of the work, which is to determine the root cause of the accident.

These concerns permeate the analysis of Art. 402 of the Civil Code, the notions of guilt and intent or responsibility without these elements, not forgetting the connection of damages with losses, initial and future, by analyzing the effects of the one with a direct result of this or the possibility of using the damages probable damage or what in law has come to be called probable damage or loss of a chance. In addition to Art. 464 of the CPC, the expert evidence consists of an examination, inspection or evaluation. *Paragraph 1. The judge will reject the*

expertise when: the proof of the fact does not depend on the technician's special knowledge; is unnecessary in view of other evidence produced; verification is impracticable.

2. OBJECTIVE

Proposal of legal evidence and proof collection method for fire investigations.

3. METHOD

Preparation of expertise, the risk analysis tools described in the ABNT NBR ISO 31000 standard were adopted.

4. RISK ANALYSIS

When the tasks are distributed according to the 5W1H tool, we have:

4.1. Who

According to IBAPE/SP – Instituto Brasileiro de Avaliações e Perícias de São Paulo "*Such activities must be carried out under the responsibility and exclusive competence of engineers and architects legally qualified by the Regional Councils of Engineering and Agronomy – CREA, and of Architecture and Urbanism – CAU, in accordance with Federal Law 5194 of 21/12/1966 and CONFEA resolutions, and Federal Law 12.378, of 12/31/2010*". In multidisciplinary expertise and in cases where there is involvement of areas of various specializations or modalities, the expert in charge must make use of the assistance of qualified and trained auxiliary professionals in the matters involved, always with the focus that "*Expert - Professional legally qualified, suitable and qualified to perform an expertise*".

Expert work is of interest to individuals or legal entities, public and private, and may be contracted by any of them, including in the administrative or judicial spheres. Its purpose is to clarify facts and protect rights – known as Technical Evidence – and are normally related to Real Estate and Improvements, Machinery and Equipment, Motor Vehicles, Installations, Projects, Technical Documents, as indicated in the NBR ABNT 13752:1996 standard, and accidents involving all these areas, the so-called "claims", regulated by Insurance Companies.

4.2. Where

The accident location.

4.3. How

The first step is to have the release of the site of the accident for the work to be carried out, this may come from a government agency or from interested (authorized) persons.

It should be noted that data obtained before the official release may not have legal validity, and the expert may even be accused of changing the location of the accident, which may lead to legal complications.

When the technical expert goes to work in civil processes involving fires and explosions, he is faced with a place in ruins, altered after the intervention of the Fire Department, Civil Defense and Technical Police, often without access to minimal information (documents, filming, projects), as it may have been destroyed by the accident.

The existence of guidelines, even basic ones, can facilitate meeting the expert's demands, with regard to the dynamics of the process: (i) see and report all details of the claim, (ii) involve all technical assistants, (iii) respond related party questions, all to indicate the root cause of the fire. Currently, there is no standard procedure in Brazil that specifies how to perform the interface between technical expertise and the dispute in which it is inserted.

The expertise can also be carried out years after the accident, but for that it is necessary to have access to the entire process and carry out the analysis of Accidental Hypotheses with the

use of specialists, bibliographical review, tests on paradigm materials or equipment, in the related areas, in order to verify its validity and have sufficient data for root cause determination.

Expert work requires compliance with essential requirements and methodology, starting with data collection, consolidation of information, preparation of records through notes, photographs, drawings, audio and video recordings, critical and substantiated analysis of information and records, to then reach the conclusions, which will be presented in a document called Report or Technical Report.

4.4. Why

Due to the principle of broad defense (Article 5 of the Federal Constitution of Brazil of 1988), the right to react against allegations formulated contrary to its interests is assured to the party, producing evidence, bringing arguments and presenting a defense, with the purpose of influence the conviction and, consequently, the decision to be taken by the judge.

4.5. When

Defining the amount of time to carry out an investigation is not an easy task, either because of the professional's experience or because of the understanding of the information on the object examined.

As a general rule, it can be established that the expertise will require the time necessary to collect all the data, consolidate the information, analyze, evaluate and draw conclusions and, finally, prepare the expert report.

Taking as an example an investigation to determine the origin and cause of fires in commercial buildings in Brazil, a research was carried out on the subject, as part of the master's thesis project at the Institute of Technological Research of the State of São Paulo - IPT , conducted and guided by the Authors, with the participation of 19 professionals, including investigators from criminal institutes (5), investigators from other public bodies (1) and investigators from the private sector (8), which resulted in the following conclusions. See Figure 1.
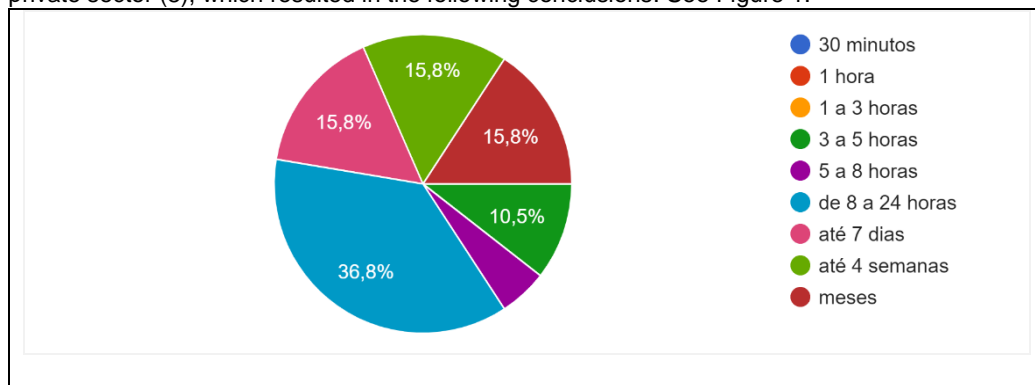
Figure 1: working time (Source: IPT)

4.6. What

Basically the activities are:

(i) Survey and description of all elements that allow the expert to carry out his study and substantiate his conviction and conclusion, including, when applicable, the anamnesis of the case, presented chronologically, identifying the dates of occurrence of the events, photographic report and drawings elucidative.

(ii) Analysis and reasoning, set out in a clear, objective, intelligible manner, covering everything necessary for a perfect understanding of the matter, supported by relevant technical references, standards, bibliography, projects, specifications, memorials, regulations, manuals, legislation, contracts, schedules, budgets, expert opinions, essays, etc.

(iii) When applicable, depending on the objective, nature and type of the investigation, the following should be done: verifying non-compliance with technical standards, using specific methods, with all the necessary and sufficient information to allow the identification of cause and effect, as well as estimating the costs of repairing the problems.

The method adopted will be divided into eight stages. The first step consists of an exploratory study aimed at identifying Risk Scenarios - typical RS that cause fires or explosions, as established by Lees (2005) and in ABNT NBR ISO 31000:2018-Guidelines for risk management, considering: (i) setting the context, (ii) risk identification and (iii) risk analysis. For this purpose, processes will be analyzed, seeking to identify typical Risk Scenarios, as shown in Figure 2.
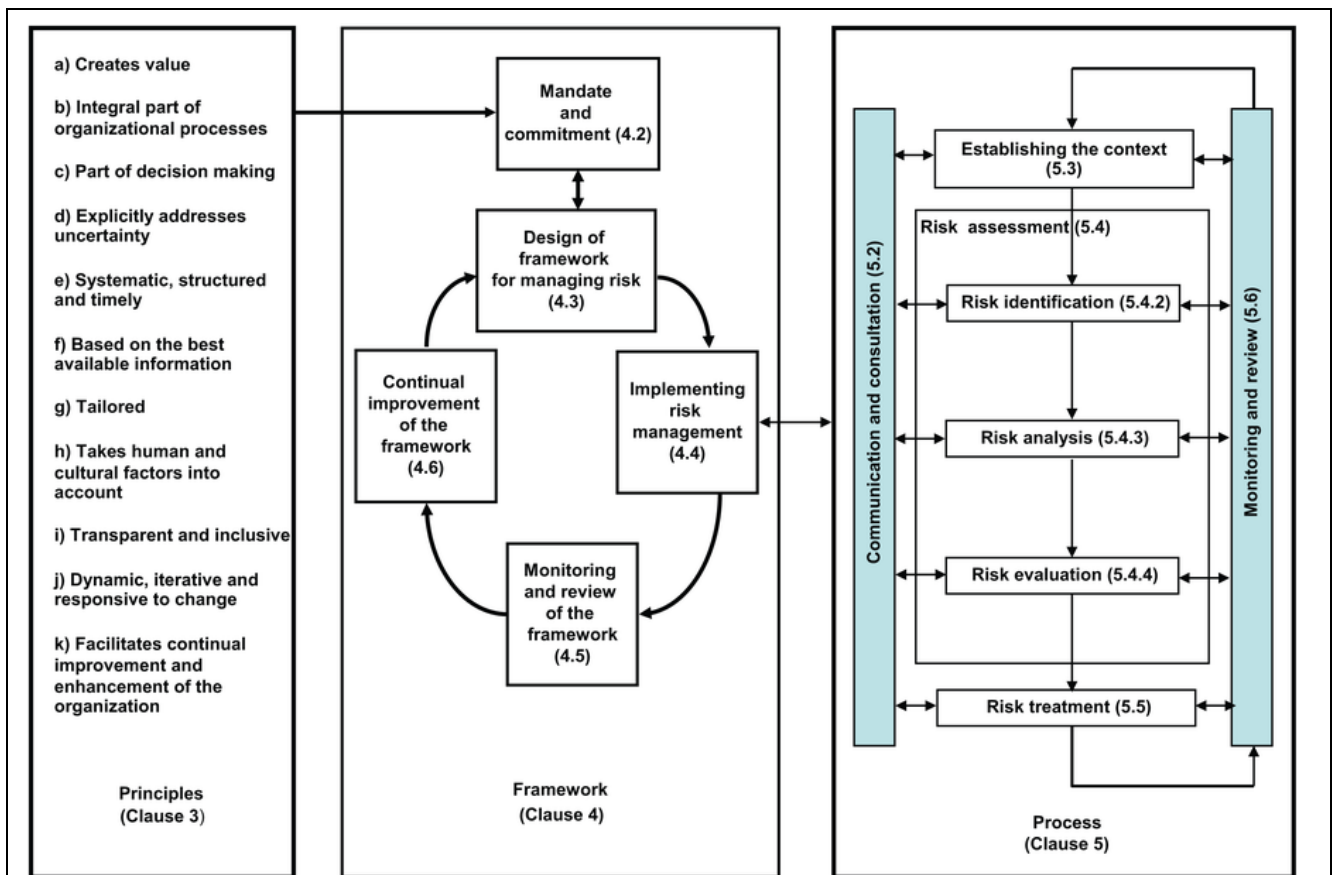
Figure 2: ABNT NBR ISO 31000

In the activity of establishing the context, compare the definitions of how and why to carry out inspections, equally adopting concepts from Engineering and those expressed in Civil Law, based on different authors (BRANDIMILLER, 1996; DEL-CAMPO, 2008; PRESOTTO et al 2017; MIRANDA & SOUZA, 2019).

With regard to the location of the accident, the works by Silva (1992, 1997 and 2001), Rodrigues (2000) and studies by the UNIVERSITY OF SHEFFIELD (2007) present a theoretical framework on the dynamic behavior of structures, including after the action of fire , which makes it easier for the Expert to have an idea of the epicenter of the fire, and allows identifying, even in the initial phase, Accidental Hypotheses of the fire. It is noteworthy that Shields & Silcock (1987) present case studies that describe how to perform a fire analysis.

In matters related to explosion, one has to differentiate its origin, whether it is a physical explosion, that is, rupture of a structure due to overpressure or degradation in its structure; from a chemical explosion, arising from the ignition of an explosive cloud, such as combustibles. For that, one should adopt the works of Goharrokhi (2005), Abbasi & Abbasi (2005), Gholami (2008), Dunjo et al (2011) and Ashok et al (2014), the latter describing risks in sewers, which in situations specifications can generate explosive clouds, liable to ignition.

The model developed by Reason (1990) and adapted by Ortiz (2018) and Ortiz & Scabbia (2022) for expertise issues, allows us to understand how risks can materialize in accidents, such as fire and explosions, revealing the flaws that can arise in the defenses. It is noteworthy that although the defenses work well, failures can always arise, which represent the dynamics of the process. In the Model, the surfaces correspond to the defenses and the holes to the flaws that can appear in the defenses. In the real world, these holes are continually opening and closing at different times and positions. The alignment of faults, on the different defense surfaces, may allow a certain risk to result in the occurrence of a claim, as shown in Figure 3.

Defenses (surfaces) can be divided into four groups: Defense 1 - replacement or reduction; Defense 2 - engineering controls, consisting of operational measures such as the implementation of systems that make the accident more difficult; Defense 3 - administrative measures, defined by operational procedures; and Defense 4 - physical protection measures, basically composed of barriers that make the accident more difficult. See Figure 3.
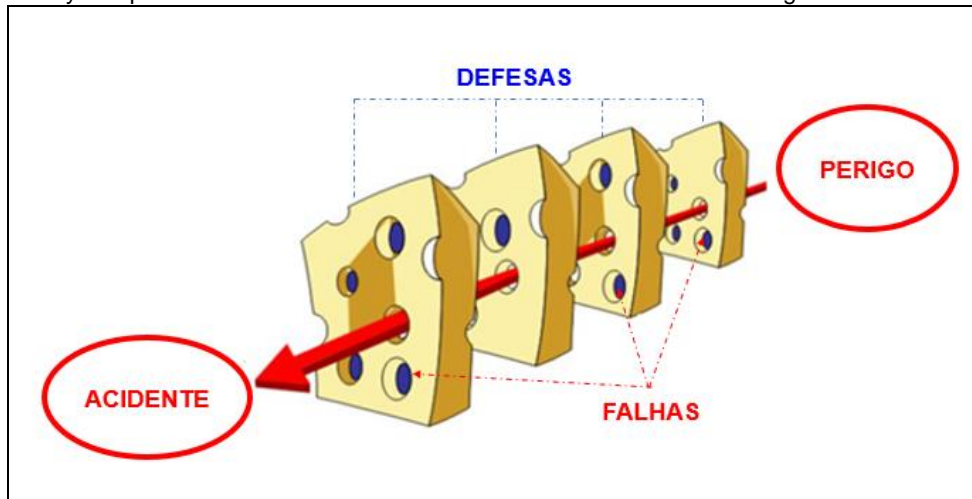
Figure 3 – James Reason method (Source: Adapted for Reason (1990))

Failures in defenses arise for two main reasons:

• Latent conditions, which are failures arising from: (i) inadequate design of operating, inspection or maintenance procedures, (ii) non-compliance with technical standards in the development of projects or (iii) change in the way participants act;
• Active failures, which are represented by unsafe acts committed by people included in the system, for example: counting or exposing cash in public.
The expertise must identify the probable failures that may be related to the root cause of the claims.
To carry out technical expertise of fire and explosion, one can adopt the principles proposed by Del-Campo (2008), which is based on criminal proceedings. See Figure 4, and follow Brandimiller's (1996) doctrine. It should be noted that fires and explosions may be related to accidents at work, an aspect not addressed in the present work. See Figure 4.

5. FINAL CONSIDERATIONS

The guidelines proposed here do not have the format of a model or even a pre-defined pattern to be followed, it is essential to analyze the reality of each case, ensuring answers to all the 5W1H or 5W2H questions, the requirements regarding: habitability, structural safety, fire safety, safety in use and operation.
All expertise must be based on technical standards and legislation related to the subject of the claim, emphasizing that such activity is of paramount importance for clarifying the facts and supporting the principle of ample defense in accordance with the federal constitution.
It proved to be relevant that the professional (Expert) has full knowledge of the matter in which he is evaluating, regardless of his engineering background, in addition to understanding the investigative methodology that always seeks to determine the root cause of the accident.
Regardless of the questions to be answered in the expert process, the root cause must be sought, even if it takes months to collect data and analyze the information, as a wrong, erroneous and superficial piece cannot be generated.

REFERENCES

[1] BRASIL. Código de Processo Civil (2015). Código de Processo Civil Brasileiro. Brasília, DF: Senado, 2015.
[2] National Fire Protection Association. (2021). Guide for fire and explosion investigations. (Standard no. 921). Retrieved from https://www.nfpa.org.
[3] CARDOSO Jr., Jarbas L. Modelo para extração da inteligência coletiva e suporte à decisão em ambientes de colaboração utilizando o referencial 5W1H. 2017. 440 p. Tese (Doutorado) - Escola Politécnica, Universidade de São Paulo, 2017.
[4] SCABBIA, A. L. G.; MOREIRA, C. C.; ALMEIDA, J. L. G. Perícia técnica de engenharia: proposta de método de trabalho. AecWeb, São Paulo, 24 ago. 2022.
[5] LEES, F.P. Lee's Loss Prevention in the Process Industries: Hazard Identification, Assessment and Control. 3rd Edition, Elsevier, Oxford, UK, 2005.
[6] ASSOCIAÇÃO BRASILEIRA DE NORMAS TÉCNICAS - ABNT. Gestão de Riscos – Princípios e diretrizes. NBR ISO 31000. Rio de Janeiro. 2009.

[7] BRANDIMILLER, Primo A. Perícia judicial em acidentes e doenças do trabalho. São Paulo: Senac, 1996.

[8] DEL-CAMPO, Eduardo Roberto Alcântara. Exame e levantamento técnico pericial de locais de interesse à justiça criminal: abordagem descritiva e crítica. 2008. Dissertação (Mestrado em Direito) - Faculdade de Direito da USP, São Paulo, 2008.

[9] PRESOTTO, Maria Izabel Millani; EBERLE, Camila R.; De TONI, Regina; TREVISAN, Francisco. Perícias de engenharia na construção civil – estudo de caso. Curitiba, setembro/2017, edição especial, pp. 1 a 73.

[10] SILVA, Valdir Pignatta. Flambagem Lateral de Vigas de Aço em Regime Elástico - Linear. 1992 155 p. Dissertação (Mestrado) Departamento de Estruturas e Fundações da Escola Politécnica da Universidade de São Paulo. São Paulo, 1992.

[11] SILVA, Valdir Pignatta. Estruturas de aço em situação de incêndio. 1997. 170 p. Tese (Doutorado) Departamento de Estruturas e Fundações da Escola Politécnica da Universidade de São Paulo. São Paulo.

[12] SILVA, Valdir Pignatta. Estruturas de aço em situação de incêndio. São Paulo, Zigurate, 2001.

[13] RODRIGUES J. P. C. Fire Resistance of steel columns with restrained thermal elongation. 2000. 388 p. Tese (Doutorado) Instituto Superior Técnico da Universidade Técnica - Lisboa. Lisboa, Dez. 2000.

[14] THE UNIVERSITY OF SHEFFIELD - STRUCTURAL FIRE ENGINEERING RESEARCH AT. Apresenta atividades de pesquisa. Disponível em: <http://www.fire-research group.shef.ac.uk > Ultimo acesso em: 30 de Julho de 2007.

[15] SHIELDS, T. J. & SILCOCK, G. W. H. Buildings and Fire, Singapur: Longman Scientific & Technical; New York: John Wiley & Sons, 1987.

[16] REASON, J. Human error. New York: Cambridge University Press, 1990.

[17] ORTIZ, Jessé Belline A relação do ser humano com atividades e locais insalubres e perigosos. 2018. 116p. Dissertação (Mestrado) Disponível em: https://sapiens.ipt.br/Teses/2018_HAB_Jesse_Belline.pdf.

[18] ORTIZ, J. B.; SCABBIA, A. L. G. Locais de trabalho com agentes químicos e inflamáveis. AECweb, 31 jan. 2022. Disponível em: https://www.aecweb.com.br/revista/materias/locais-de-trabalho-com-agentes-quimicos-e-inflamaveis/22970. Acesso em: 01 ago. 2022.

INVESTIGATION ON KISS NIGHTCLUB FIRE

Rodrigo   A. Freitas[a],*   **João Paulo C. Rodrigues[b]**

ABSTRACT

This paper aims to study the fire that occurred at Kiss nightclub, in Brazil in 2013. In addition, the paper aims to apply and test fire investigation methodologies proposed by the authors in previous works. Initially, as much building data as possible was gathered, including historical documents and an on-site visit. With the data in hand, hypotheses for the Area of Origin and Point of Origin were elaborated. The study also focused on developing hypotheses for the following causes: fire outbreak, spread, itinerary, data, damage, injured people, and deaths from the fire. Laboratory tests and full-scale tests were performed to help on the investigation and select hypotheses. Finally, based on the evidence, the causes of the fire were organized and classified.

Keywords: fire, investigation, causes, spread, evacuation, injured, nightclub.

1. INTRODUCTION

Unfortunately, several fires in nightclubs have become notorious in the last two decades. One of the most catastrophic fires in US was the Station Nightclub fire (February 2001), which caused around 100 deaths [1]. Other terrible fires occurred in other nightclubs: Canecão Mineiro (Brazil, 2003, seven deaths), Republica Cromañón (Argentina, 2004, 194 deaths), and Lame Horse (2009, Russia, 156 deaths)[1]. All these fires were related to the acoustic covering materials, fireworks, overcrowding, license issues, and systematic violation of local fire safety regulations.

Lamentably, this same pattern repeated itself in Brazil in 2013. Considered the second-most deadly fire in Brazil, the fire incident at the Kiss nightclub had 242 deaths and more than 600 direct victims. This fire has shocked the city of Santa Maria, in the state of Rio Grande do Sul, in Brazil, as well as the fire safety community. This work is a

[a]PhD student in Fire Safety Engineering ─ Departamento de Engenharia Civil da Faculdade de Ciências e Tecnologia da Universidade de Coimbra. Rua Luís Reis Santos. Polo II da Universidade. 3030-788 Coimbra. PORTUGAL. Telephone number: +5561984188017. E-mail: rodrigo.almeida.freitas@gmail.com

[b] BEng and MSc in Civil Eng. - FCT_UC - Coimbra – Portugal, PhD and Habilitation in Civil Eng. - IST_UL - Lisbon – Portugal

part of a comprehensive fire investigation carried out in Kiss nightclub and aims to describe and present the main characteristics of Kiss nightclub that contributed to this devastating fire.

So, it is possible to recognize a consistent tendency in this pattern of fire incidents in nightclubs with live music. Fires in nightclubs deserve a detailed investigation, in a technical and scientific manner, of the threats and vulnerabilities involved in this type of incident. Besides, the lessons that could have been learned to mitigate fires in nightclubs appear not to have been efficiently exposed, parameterized, or implemented. It is questioned in Brazil[1][2][3], to what extent the fire safety standards were actually revised and improved after two similar domestic fires with deaths.

This work aims to carry out a fire investigation at Kiss nightclub. Specifically, it aims to:
1. Identify the causes of the fire at Kiss nightclub, addressing the fire outbreak, its development, propagation, damages, losses, injuries, and deaths.
2. Provide as many facts, circumstances, factors, actions, omissions, and contributions as possible related to the fire incident at Kiss nightclub.
3. Reinforce the multifactorial and multicausal character of the fire incident.

This work was supported by the methodologies briefly illustrated in Figure 2, proposed in 2022 by this author[4]. It is not the purpose of this work to criticize or review the official criminal report or previous studies. It is not the objective of this work to determine culpability, responsibility, or even to establish itself as casual evidence to compose administrative or judicial proceedings.

3. RESULTS

A comprehensive fire investigation must collect and gather as much building data as possible, including those that are not preliminary related to the fire incident. This section presents the main characteristics of the building, including: the architecture, HVAC systems, fire extinguisher protection, emergency signs, emergency lighting, covering materials, and others. It also includes a summary of the documentation and licenses of Kiss nightclub.

3.1 Historical data of the building

Based on city hall documents, the CREA-RS report[5] and testimonials[6], it was possible to gather a history of the construction and operation of the Kiss nightclub, here summarized and illustrated in Figure 1.
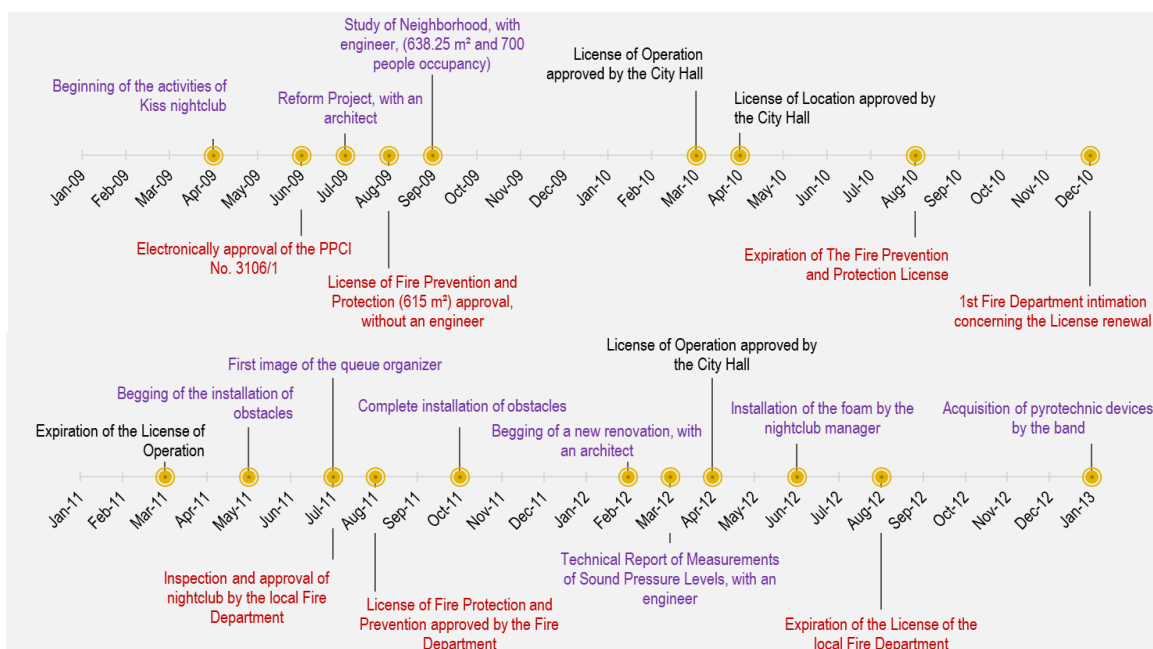
Figure 1: Historical data of the building from 2009 to 2013

94
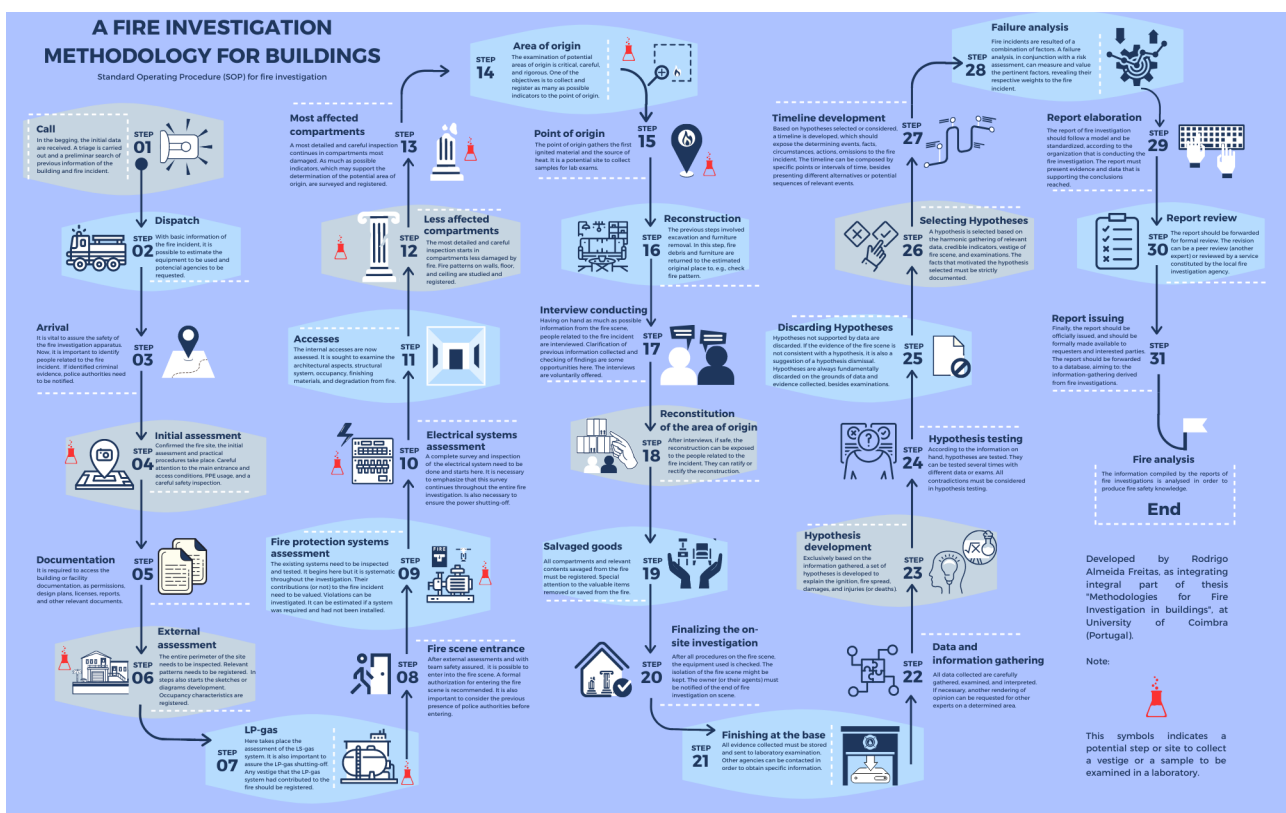
Figure 2: Fire investigation methodologies [4]

3.2 Building systems

The Kiss nightclub was built in masonry, with two floors connected by two open stairs: a ground floor for customers and a mezzanine with restricted access for the employees and music bands. The total area of the club was 640.32 m^2 [6]. Briefly, there were two stages and, as a result, two dance floors, besides two DJ booths. There were two escape routes; the main one was a corridor in the central area of the club, as shown by Figure 3a. Despite the internal vertical walls, the nightclub had several openings among the rooms, making the whole building a single span, with no compartmentation.

a)   b)

Figure 3: Kiss architecture – a) Ground floor b) HVAC system [7]

There were two windows on the façade of Kiss nightclub that were bricked up on the day of the fire. There were no more openings in the building, except the entrance doors and HVAC duct outlets. The HVAC system was consisted of air conditioners, fans, and exhausting ducts (that were closed), as illustrated by Figure 4b. Kiss's finishing materials varied, with the main ones being fabrics (curtains), plastics (televisions, speakers, and some seats), and polyurethane foam (on some walls and ceilings). The ground floor ceiling was formed by gypsum board, and the mezzanine ceiling was formed by a timber roof truss. There were several materials that formed the floor of the club, with emphasis on a raised wooden floor (false floor) on the main dance floor.

There are several Kiss reconstructions available that demonstrate the nightclub compartments. Among these, one carried out by the University of Santa Maria (UFSM)[8] stands out, which was validated by photos of the environments after the fire, as shown by Figure 4 and Figure 5. A YouTube video named "*Kiss: Dispositivo Interativo Digital - Palco e Saída*" [7] illustrate this reconstruction. Such reconstructions are shown here, aiming to present and illustrate the environments and constructive characteristics of Kiss.

a)   b)

Figure 4: Main corridor – a) reconstruction [8] b) after the fire

a)

b)

Figure 5: Second dance floor [8] – a) reconstruction [8] b) after the fire

3.3 Fire safety systems

Kiss nightclub had only the basic fire safety measures: fire extinguisher protection, emergency signs, emergency lightening, and emergency exits. The following ones were not installed in the building: a standpipe system, fire detection, a fire alarm, sprinklers, and a smoke control. There was no fire brigade at the nightclub. There were several obstacles at the exits. Before reaching the final doors, the occupant had to pass a guard set in front of the doors, where there was a retractable horizontal bar. This obstacle was damaged by the weight of the victims' bodies, and it was removed during fire operations, but one can still observe its point of anchoring. This was just one of the existing obstacles, as there were still several queue organizers, steel barriers, guardrails, railings, that partially obstructed the final exit. All these guardrails, the only two emergency signs, and the emergency lights are shown in Figure 6.

The fire extinguisher protection had several violations: some units were stored in a service room, and the unit adjacent to the stage did not work on the day of the incident. There were two types of foam on the stage, one gray and the other yellow; both were pyramidal foam boards (Figure 7a). It is mentioned [6][7] that the foams were purchased at a mattress store. It is observed that the installation of the plates was not uniform (as seen below) but arranged separately, with a space between each installed plate (Figure 7). It was previously assessed that these foams had no fire-retardant properties. The next sections show a set of exams and tests that assessed the foam had a low ability to resist ignition, besides propagating fire and smoke production.

a)

b)

Figure 6: Kiss architecture – a) emergency signs and lightening b) possible victims' allocations [7]

97

| a) | b) |
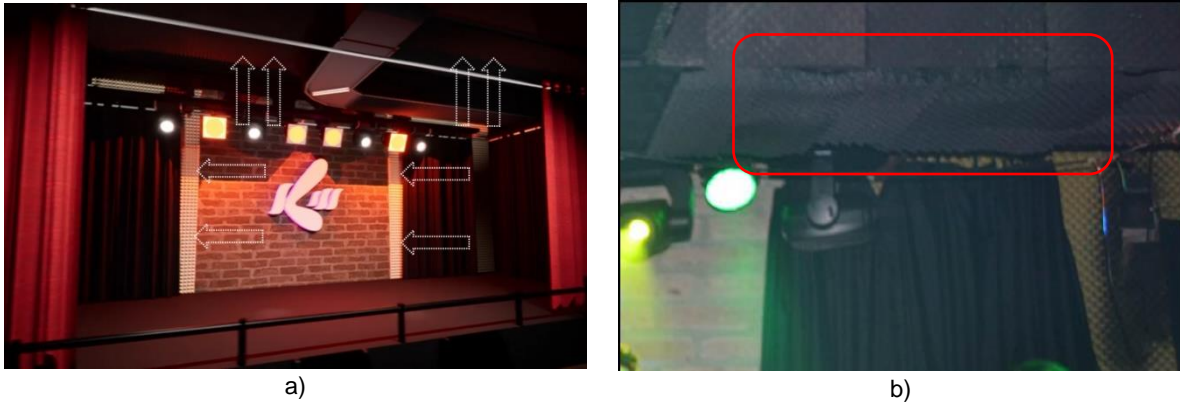
Figure 7: Kiss main stage – a) reconstruction [8] b) on the day of the incident

The state of preservation of the Kiss nightclub, even after 10 years of the incident, allowed us to collect details of emergency exits. With these data on hands, it is possible to draw a comparison between the regulation prescriptions and the characteristics of Kiss's emergency exits. Table 1 briefly exposes the violations of Kiss's emergency exits.

Table 1: Emergency exit violations

	Kiss nightclub conditions	NBR 9077 prescription [9]
Guardrails	Various in the walkways, even one across the discharge.	Walkways must be permanently unobstructed and free.
Doorways	Blocked by other door leaves.	Completely free.
Stairs	Wooden made, without fire resistance.	It must have fire resistance.
Steps design	Step height above 18 cm and step going below 28 cm.	It must be balanced by the formula of Blondel.
Egress width	3.05 meters.	4.40 meters.
Quantity of exit discharge.	Only one discharge.	A minimum of two discharges, as far apart as possible from each other.
Distance to reach an exit	31.76 meters.	10 meters (w/o sprinklers & w/ 1 exit). 20 meters (w/o sprinklers & w/ 2 exits).

3.4 Full-scale testing and laboratory exams

Some full-scale tests and laboratory exams were performed to test hypotheses. To test the flammability and burning of the foam, scenarios were set up inside a container balcony to simulate the fire outbreak. Three samples of different foams available in the Brazilian market were mounted above a dummy holding different pyrotechnic devices. Different scenarios were tested, assessing different fuels and different heat sources.

A foam, purchased at a mattress store and labelled as "generic" sample, notably without fire-retardant properties, similar to the one used at Kiss, was tested as a scenario. To have a comparison scenarios, it was acquired two other foams labeled as official acoustic protection, in which the manufacturer claimed to have fire-retardant properties, including laboratory exams. They were labelled as "A" and "B" samples. Besides, a curtain was also installed next to the foam to check if the fabric could ignite before the foam. Two pyrotechnic devices acquired by the band on the day of the incident were also tested: "silver rain" and Sputnik. To have a comparison scenario, a pyrotechnic device considered potentially safe (because it is classified as indoor) was purchased, called Gerb. Table 2 contains the results of the tests and Figure 8 shows this full-scale test.

Table 2: Scenarios tested

Scenarios	Combustive considered	Source of heat considered	Fire outbreak before the source of heat
1	Generic foam	Outdoor device "silver rain"	yes

2	Generic foam	Indoor device "Gerb"	no
3	Generic foam	Outdoor device "Sputnik"	yes
4	Tested acoustic foam A	Outdoor device "silver rain"	no
5	Tested acoustic foam A	Indoor device "Gerb"	no
6	Tested acoustic foam A	Outdoor device "Sputnik"	no
7	Tested acoustic foam B	Outdoor device "silver rain"	no
8	Tested acoustic foam B	Indoor device "Gerb"	no
9	Tested acoustic foam B	Outdoor device "Sputnik"	yes
10	Fabric curtains	Outdoor device "silver rain"	no
11	Fabric curtains	Indoor device "Gerb"	no
12	Fabric curtains	Outdoor device "Sputnik"	no

a)   b)   c)   d)
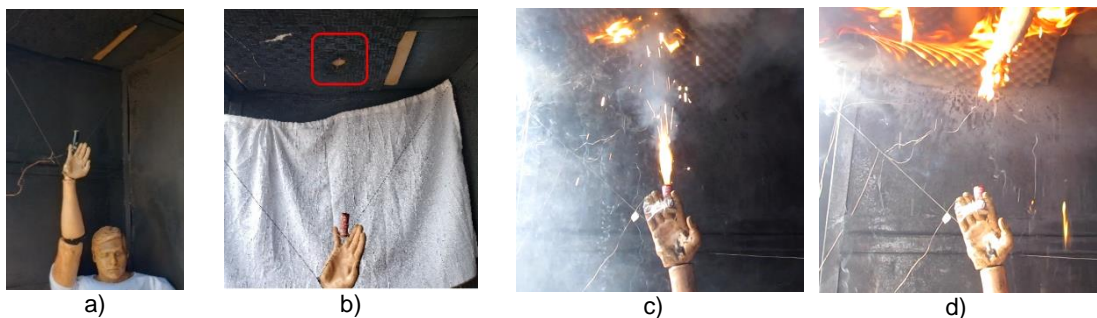
Figure 8: full-scale tests a) dummy with a Gerb, b) After test: acoustic foam A with an outdoor device "Sputnik", c) and d) During the test: generic foam with an outdoor device "Sputnik"

It is observed that in none of the scenarios did the curtain fabric ignite. Then, it was focused on a more detailed study of the foams considered. To present a consistent comparison, post-test information is summarized in Table 3. It is important to note that the Sputnik device presents the worst threat in the fire outbreak. The generic foam, similar to that used at the Kiss nightclub, represents the most vulnerable fuel, and creates the unhealthiest environment for the nightclub's occupants. It is still possible to observe that one of the acoustic foams, which had laboratory reports to attest to fire protection, ended up being ignited when exposed to the device "Sputnik", which demonstrates a potential nonconformity of the fire resistance alleged.

Table 3: Data from Kiss similar foam and acoustic foams

	Generic foam	**Tested acoustic foam A**	**Tested acoustic foam B**
Ignition before the indoor pyrotechnic device "Gerb"	Not observed	Not observed	Not observed
Ignition before the outdoor pyrotechnic device "Silver Rain"	Observed	Not observed	Not observed
Ignition before the outdoor pyrotechnic device "Sputnik"	Observed (+++)	Not observed	Observed (+)
Propagation on foam, after ignition	Observed (+++)	Not observed	Observed (+)
Dripping, after ignition	Observed (+++)	Not observed	Observed (+)
Degradation / mass loss	Generalized (+++)	Punctual, with Sputnik	Generalized (+)
Smoke production, after ignition (OPEN)	Smoke from the foam (+++), with Silver Rain and Sputnik	Just the smoke from the device	Smoke from the foam (+), with Sputnik only

Table subtitle:
(REAL): observations obtained by full-scale testing.
(OPEN): test performed on a balcony of a container, with an open wall, to avoid the accumulation of gases.
(Silver Rain): after being exposed to the Silver Rain device.

Comparative scale, by visual observation:
(+++): greater amount, greater frequency, or greater speed.
(+): smaller amount, lower frequency, or slower speed.

(Sputnik): after being exposed to the Sputnik device.

With a real sample of the foam used in the Kiss nightclub and the foam in which ignition was not observed (acoustic foam A), it was possible to carry out laboratory tests. The objective was to study the rate of mass loss as a function of temperature. Figure 9a illustrates the mass loss of the foam from the Kiss nightclub, which loses approximately 90% of its mass after exposure to 400°C. It is possible to observe the abrupt thermal degradation of the Kiss nightclub foam after 200°C. On the other hand, acoustic foam (Figure 9b), which has fire-retardant properties, loses 90% of its mass only after being exposed to over 600°C of temperature.
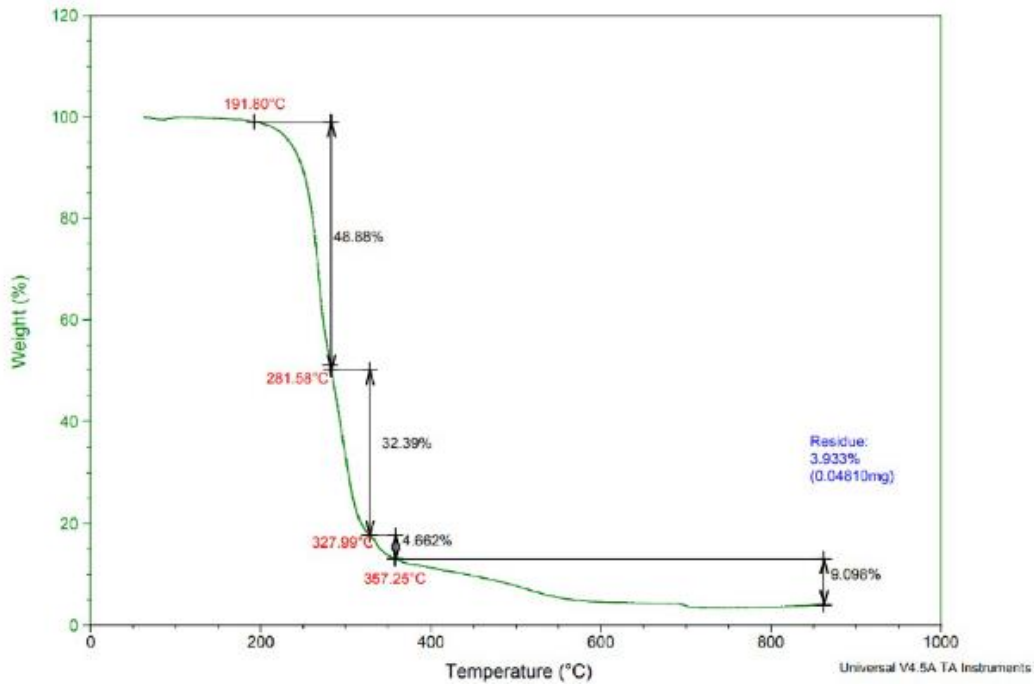
Figure 9: Mass loss exam – Kiss nightclub foam
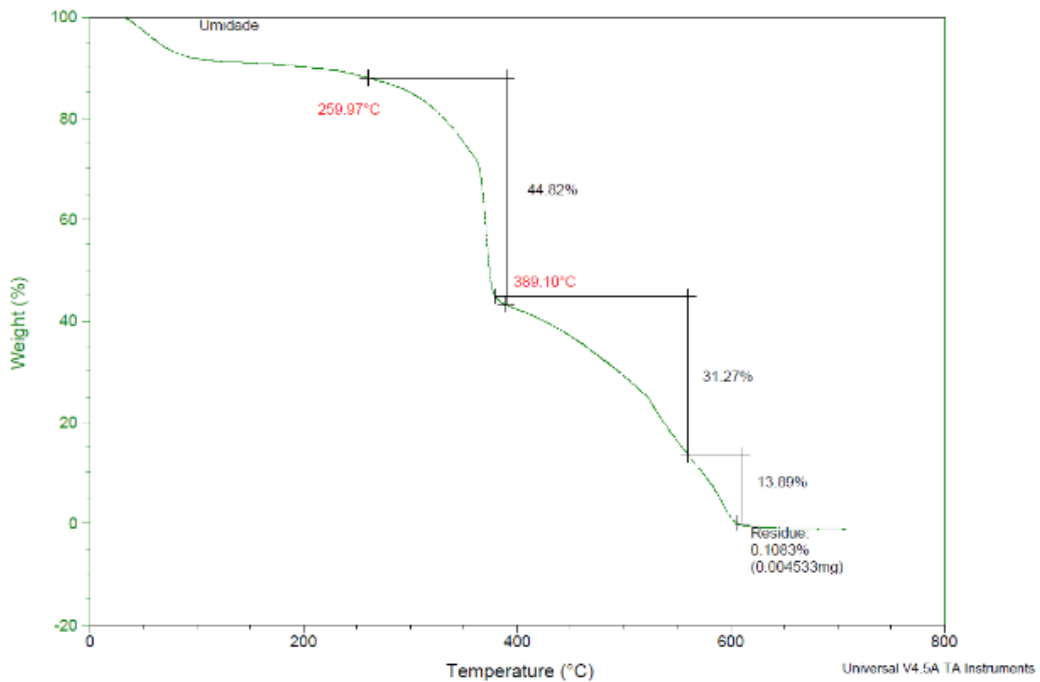
Figure 10: Mass loss exam – certified foam

100

Relevant dripping fire was observed in the burning of the generic foam and in the burning of the acoustic foam B. It was observed that the dripping in the generic foam, similar to that used in the Kiss nightclub, was intense and had a severe impact on the clothing and on the skin of the dummy used, burning both the fabric of the clothing and the rubber cover of the dummy (Figure 11a and b). It is estimated that such dripping was also observed in the FDS/Pyrosim fire simulation (Figure 11c). This dripping fire demands a deeper study, especially because it demonstrates a high potential to cause injuries in humans. Using thermocouples positioned on the dummy's hand and chest, it was possible to measure the temperature of samples of these drippings, which eventually fell on the dummy's hand and chest. Temperature levels are shown in Figure 12 and Figure 13. It was possible to observe temperature values above 400°C on the dummy's hand and above 900°C on the dummy's chest.

| a) | b) | c) |
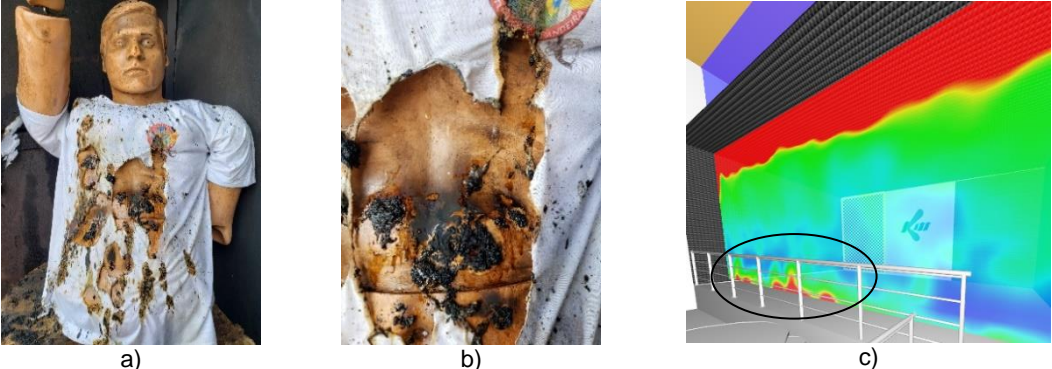
Figure 11: Dripping fire – a) shirt of the dummy after the fire b) skin of the dummy after the fire c) dripping observed in the fire simulation
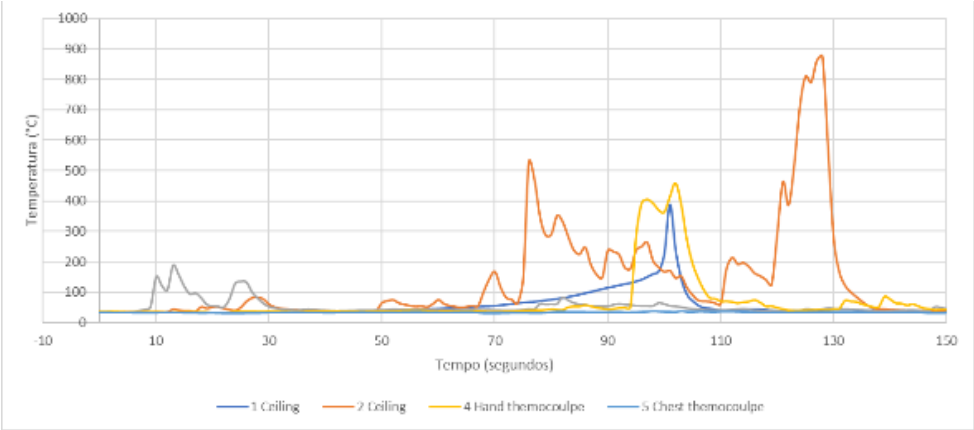
Figure 12: Temperature levels observed in scenario 1
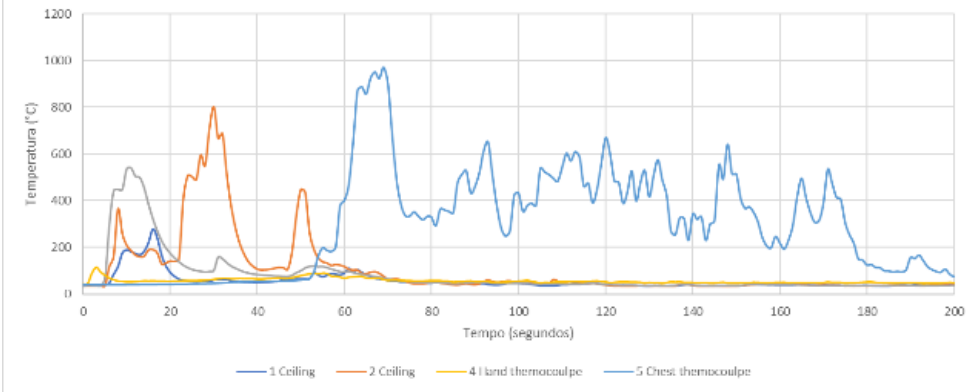
Figure 13: Temperature levels observed in scenario 2

3.4 Computer simulations

After carrying out examinations and tests related to the outbreak of the fire, examinations of the fire propagation within the building were carried out. Thus, a computer simulation of fire was carried out using the FDS/Pyrosim software. The Kiss nightclub model in the FDS is shown in Figure 14a. It is necessary to register that the fire load in the model is represented by the foam that covered the ceiling, side walls, and back walls of the stage. The characteristics of the foam used in the model were based on laboratory tests that sought to identify the physical and chemical characteristics of the real foam at the Kiss nightclub. However, it is not possible to gather all the necessary data with the existing equipment in the laboratories available in Brasilia, Brazil. So, some data from the study of the foam from the fire at The Station nightclub [11][12][13] were used in the model. The finished fire simulation is illustrated in Figure 14b.

a)   b)
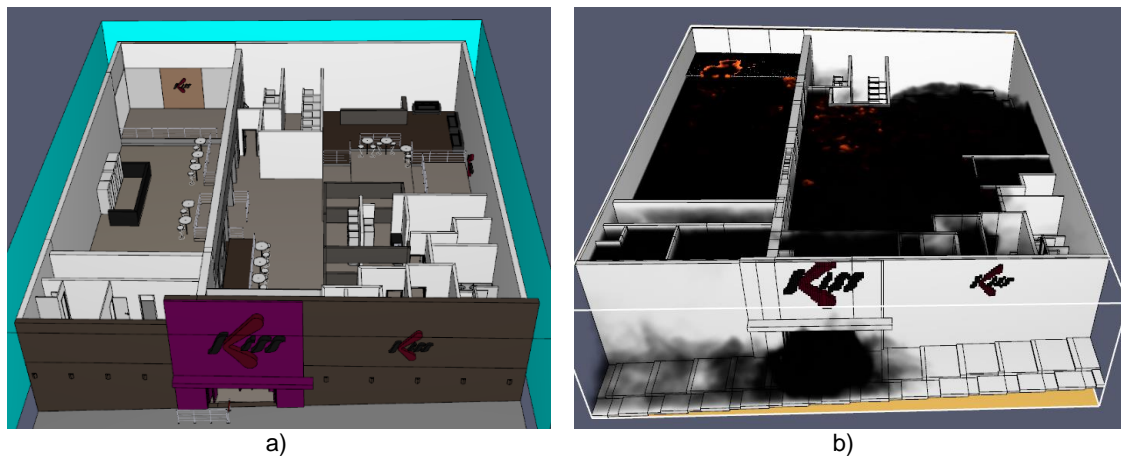
Figure 14: Kiss nightclub – a) architecture on the FDS/Pyrosim simulation b) fire simulation

The simulation results demonstrate the production of smoke in the nightclub until 70 seconds after the fire. Figure 15 and Figure 16 demonstrate the architecture of the nightclub with the overlapping of the mezzanine above the ground floor (i.e., top view); so, the emergency exits on the ground floor do not appear in figures below. In addition to the smoke, it is possible to observe the visible manifestation of flames. After the outbreak of the fire, the smoke fills the stage and later directs itself to the main dance floor. With 50 seconds of fire simulation (Figure 16d), smoke fills the main dance floor, and the flames also direct towards the center of the main dance floor.

a)   b)   c)   d)
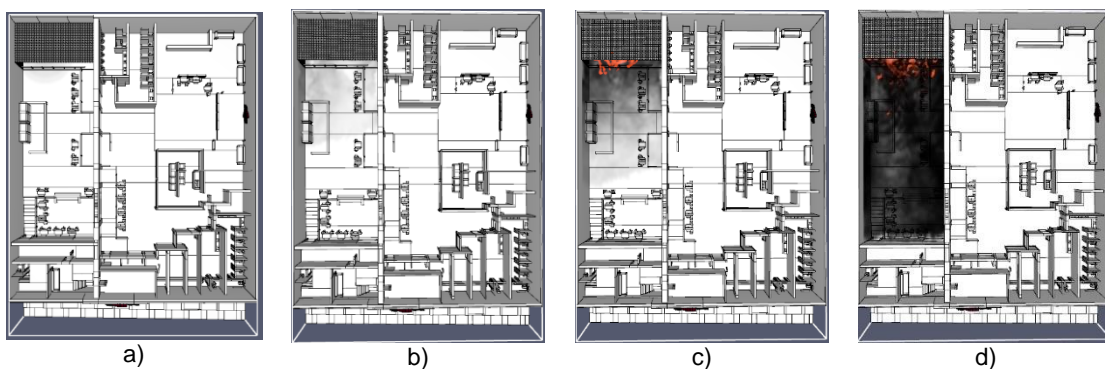
Figure 15: Fire simulation ranging from 20 seconds to 50 seconds
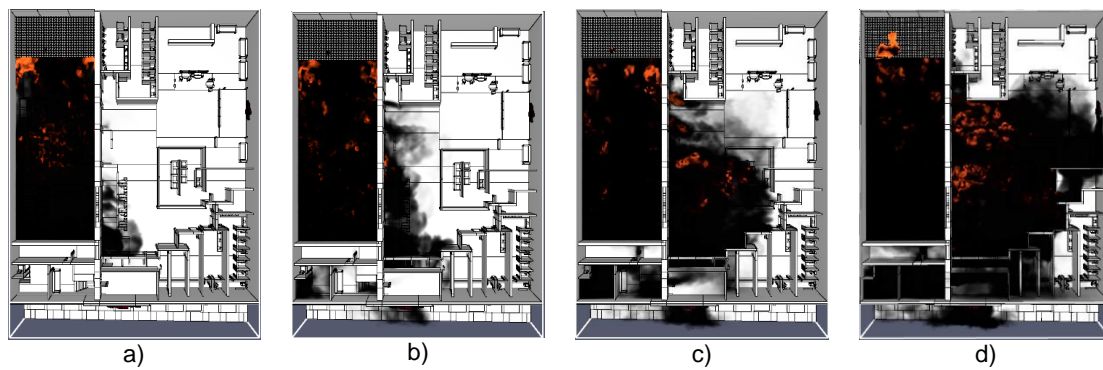
Figure 16: Fire simulation at 60 seconds, 63 seconds, 66 seconds, and 69 seconds

In the computer simulation, the first sign of smoke outside the main dance floor is exactly in the central corridor of the club, in front of the first exit doors. With 63 seconds of simulation (Figure 16b), the flames begin to direct towards the main corridor. 63 seconds later, the smoke seeks the only existing opening of the nightclub, directing itself naturally to where there is more oxygen supply. From that moment on, it is also possible to visualize smoke on the mezzanine. After 66 seconds of simulation, the fire progresses to the bathroom hall and mezzanine. From then on, the fire takes over the secondary dance floor, bathrooms, kitchen, and mezzanine completely.

Considering the existence of a real video of the fire outbreak, the real time of the occurrence of the fire was compared with the simulation time, obtaining reasonable validation for the initial moments of the fire, as shown in Figure 17.
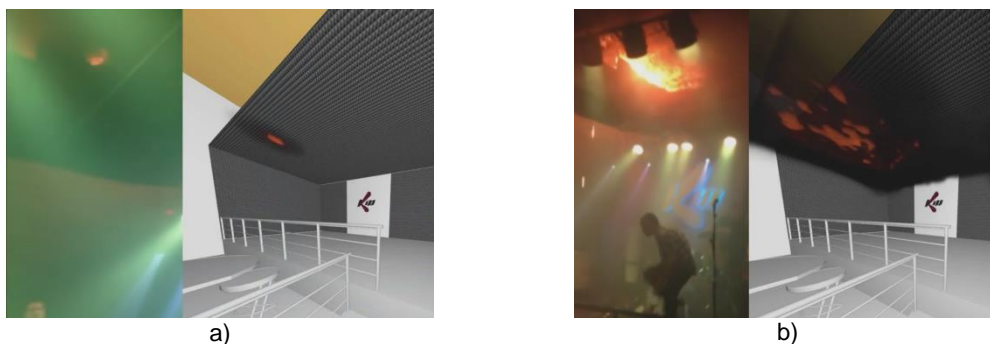
Figure 17: Real fire origin and modelled fire origin – a) at 04 seconds b) at 16 seconds

The simulation was a reconstruction of what happened at the Kiss nightclub during the fire. The relevance of the simulation is to predict the movement of the smoke. Considering that the architecture of the Kiss nightclub was modeled very closely to reality, it is believed that the smoke moved along the same path illustrated in the simulation as in the real fire. Thus, with the simulation, it is possible to gather more evidence that the fire spread from the stage to the main dance floor, from there to the corridor of the main hall, and to the corridor next to the stairs. From there, to the only escape route, to the mezzanine, and, finally, to the entrance hall of the nightclub.

Either the smoke and the fire (high temperatures and heat flux) moved in the same direction in search of oxygenation. In this way, different indicators and evidence were gathered in order to demonstrate that the fire develops from the stage to the main dance floor (Figure 15c). Subsequently, the fire spreads to the escape routes, i.e., to the central corridor and to the corridor next to the stairs leading to the mezzanine (Figure 16b). Finally, the fire spreads to the other compartments, especially the secondary dance floor, the bathroom hall, and the entrance hall (Figure 16d). Other possibilities for the fire's itinerary weren't achieved in this work.

After studying the outbreak and development of the fire, a study of the causes of injuries and deaths was developed. Thus, evacuation models were carried out in order to visualize and understand the movements and flows of the occupants. The first simulation was performed by setting up scenarios with different number of occupants. Kiss nightclub documents and previous studies suggest that the occupancy would be 691[5], 700[5], 769[14][7] or 771[14] people. With conflicting official numbers, an occupancy scenario formed by the simple average of these numbers was adopted, taking this scenario as the compliance occupancy of the building (scenario C). After that,

103

additional scenarios were established according to the occupancy cited by the witnesses. For each scenario, the evacuation time was measured, and later, the results obtained were compared with the scenario of compliance occupancy. The results are shown in Table 4. Scenario F is established by the total number of injured people and deaths, considered the real scenario on the day of the fire.

Table 4: Pathfinder simulations based on occupancy

Scenarios based on the quantity of occupants		Comparison w/ adequate occupancy (%)	1) Actual conditions (seconds)	Comparison w/ adequate time of evacuation (%)
A	691	93%	401,8	100%
B	700	94%	396,5	99%
C	741	compliance occupancy	400,5	---------------
D	769	104%	433,8	108%
E	771	104%	424,5	106%
F	878	118%	480,3	120%
G	1000	135%	555,0	139%
H	1300	175%	680,0	175%
I	1500	202%	non-viable	non-viable

With the simulations in Table 4, it was possible to estimate the impact of the number of occupants in the evacuation. A second simulation was performed to estimate the impact of the violations on the Kiss evacuation. For these simulations, only two scenarios were initially adopted: the scenario with the occupancy in compliance and the scenario with the actual occupancy on the day of the Kiss nightclub fire. In order to assess the corrections of the violations, hypothetical scenarios were evaluated, correcting, at a time, only one violation and, in the end, as many violations as possible. The results are shown in Table 5.

Table 5: Pathfinder simulations based on hypothetical scenarios

Scenarios based on the quantity of occupants		Total time of the complete evacuation (seconds) Relation between the evacuation time of the scenarios considered and the actual scenario (%)					
		1) Actual conditions	Changing only one condition and keeping the other violations				6) No guardrails, adequate egress width, and three discharges
			2) With no guardrails	3) Adequate egress width	4) Two discharges	5) Three discharges	
C	741	400,5 100%	300,0 74,91%	295,8 73,85%	325,0 81,15%	259,5 64,74%	172,5 43,07%
F	878	480,3 100%	417,30 86,88%	353,8 73,66%	386,0 80,37%	315,8 65,75%	252,30 52,53%

Finally, the work of gathering data and information from the fire incident is concluded. Only a summary of the results was presented in this section. It is important to note that more data was gathered, and more tests were performed in addition to those exposed here. The information and results of exams and tests aimed to support the process of elaborating, testing, discarding, and selecting hypotheses for the causes of fire outbreak, spread, and for the causes of injuries and deaths, which will be discussed in the next section.

5. DISCUSSION OF RESULTS

An accident has many explanations. The occurrence of an accident should not be attributed to a single cause or factor. The aim of this section is to point out, in a clear, reasoned, and evidence-based process, the most relevant causes of the Kiss nightclub fire. Hypotheses were formulated, tested, discarded, and selected based on the data collected in the building, on the information from documents, and on the results of exams and tests. Not all results could be exposed in this work.

The methodology applied here is based on the Scientific Method, hypothesis testing, and evidence presentation, according to Figure 2. Besides the evidence considered, the "what if" technique was also applied to support the classification of causes, especially by considering whether removing or modifying one factor would mitigate or eliminate a given cause. According to the selected hypotheses, a set of causes was proposed, as seen below.

5.1 Causes for the fire outbreak

It was possible to determine the following causes of the fire outbreak at Kiss nightclub:

- Absence of fire-protective coating and covering materials.
- Absence of technical responsibility (engineer or architect) in Fire Protection.
- Omissions and inappropriate actions by the nightclub management.
- Inadequacy of the government inspection.
- Inappropriate use of pyrotechnic devices.
- Inadequacy of the fire extinguishers' protection.
- Inadequacy of the fire safety regulation.
- Insufficient performance of the existing fire-protective coating and covering materials.

5.2 Causes for fire propagation/itinerary and for fire damage/losses

It was possible to reach the following causes of the fire propagation/itinerary and for fire damage/losses

- Incomplete active fire protection.
- Omissions and inappropriate actions by the nightclub management.
- Inadequacy of the government inspection.
- Absence of fire-protective coating and covering materials.
- Absence of technical responsibility (engineer or architect).
- Absence of smoke control.
- Inadequacy of the fire extinguishers' protection.
- Absence of fire detection and alarm.
- Inadequacy of the fire safety regulation.
- Inadequacy of the firefighting operations.
- Absence of compartmentation.
- Insufficient performance of the existing fire-protective coating and covering materials.

5.3 Causes for injuries and deaths

It was possible to reach the following causes of the injured people and deaths:

- Inadequacy and insufficiency of emergency exits.
- Omissions and inappropriate actions by the nightclub management.
- Absence of fire-protective coating and covering materials.
- Overcrowding.
- Inadequacy of the government inspection.
- Absence of smoke control.
- Absence of fire detection and alarm.
- Inadequacy of the fire safety regulation.
- Inadequacy of the rescue operations.
- Absence of technical responsibility (engineer or architect).
- Absence, inadequacy, or lack of adherence to a Protocol of Integrated Operations or Plan of Mutual Assistance.
- Inadequacy of the exit signs.
- Inadequacy of the emergency lighting.
- Absence of compartmentation.
- Insufficient performance of the existing fire-protective coating and covering materials.

6. CONCLUSIONS

The final goal of a fire investigation is to reveal the facts, circumstances, factors, conditions, actions, omissions, vulnerabilities, and threats related to a fire incident, besides identifying the causes of the fire. Thus, this work

presented such demands, pointing out eight causes for the fire outbreak, twelve causes for the development, spread, damage, and losses, and fourteen causes of injuries and deaths. It is observed that there were multiple situations that escalated this fire incident. This work supported the idea that a fire event does not result from a single cause and, consequently, reinforced the multifactorial and multicausal character of fire disasters.

The importance of using consistent fire investigation methodologies was highlighted in this work. Through the methodologies used, the Scientific Method and the elaboration and testing of hypotheses were valued. In addition, the methodologies promoted statements based on a harmonious set of evidence.

It is critical to reduce the repetition of fire disasters through the fire investigation. In this sense, with the use of methodologies, this work reveals deficiencies in regulation, performance, and inspection of the fire safety system. It brings opportunities to improve Fire Safety Science and Engineering, in addition to implementing and maintaining knowledge management for building fire investigations.

REFERENCES

[1] Duval, R. F. (2006). NFPA Case Study: nightclub fires. National Fire Protection Association, Fire Investigations Department. Accessed on August 10th 2021, at: https://www.springfieldmo.gov/DocumentCenter/View/10224/NFPA-Case-Study-Nightclub-Fires.

[2] Dias, R. S. (2019). Comparação de procedimentos normativos de dimensionamento de saídas de emergência para boates e casas noturnas por meio de simulação computacional e evacuação de pessoas. Trabalho de Conclusão de Curso não publicado. Graduação em Engenharia Civil da Universidade Federal do Rio Grande do Sul. Porto Alegre, Brasil. Accessed on August 8th, 2022, at: https://www.lume.ufrgs.br/handle/10183/206100.

[3] NFPA (2013). O beijo da morte. O devastador incêndio da boate Kiss ressalta mais uma vez como as deficiências normativas contribuem para estas armadilhas mortais a nível mundial. NFPA Journal Junho de 2013, ano 15, número 2, 18-25 Accessed on August 10th 2021, at: https://www.nfpajla.org/pt/arquivos/lugares-de-reunioes-publicas-discotecas/993-el-beso-de-la-muerte.

[4] Freitas, R.A., Rodrigues, J.P.C. A fire investigation methodology for buildings. Architecture, Structures and Construction 2, 269–290 (2022). https://doi.org/10.1007/s44150-022-00057-6.

[5] Regional Council of Engineering and Agronomy (CREA) of Rio Grande do Sul. Analysis of the accident at Kiss nightclub. Santa Maria, RS. Technical report: Special Committee of the CREA-RS. Porto Alegre, Brazil. Accessed on August 10, 2021, at: http://www.crea-rs.org.br/site/documentos/documentos10/RELATORIO%20COMISSAO%20ESPECIAL%20FINAL.pdf.

[6] Estado do Rio Grande do Sul (2013). Relatório final de Inquérito Policial. Incêndio Boate Kiss. Polícia ivil do Estado do Rio Grande do Sul. Santa Maria, Brasil.

[7] Estado do Rio Grande do Sul (2013). Laudo Pericial 12.268/2013. Exame pericial em local de incêndio com vítimas fatais. Instituto Geral de Perícias. Incêndio Boate Kiss. Polícia Civil do Estado do Rio Grande do Sul. Santa Maria, Brasil.

[8] UFSM (2021). A Kiss antes do incêndio. Dispositivo interativo digital resultante da reconstrução 3D da boate foi coordenado por professora da UFSM e é utilizado como ferramenta no julgamento da tragédia. Universidade Federal de Santa Maria. Revista Arco. Accessed on September, 10th, 2022, at: https://www.ufsm.br/midias/arco/a-kiss-antes-do-incendio/

[9] ASSOCIAÇÃO BRASILEIRA DE NORMAS TÉCNICAS (2001). NBR 9077. Saída de Emergência em edifícios. Rio de Janeiro, Brazil.

[10] CBMDF (2022). Relatório de Análise Química. Diretoria de Investigação de Incêndio. Corpo de Bombeiros Militar do Distrito Federal. Brasília.

[11] Grosshandler, W., Bryner, N., Madrzykowski, D. and Kuntz, K. (2005), Report of the Technical Investigation of The Station Nightclub Fire (NIST NCSTAR 2), Vol. 1, National Construction Safety Team Act Reports (NIST NCSTAR), National Institute of Standards and Technology (NIST), Gaithersburg, MD, USA [online]. Accessed on August 7th, 2021, at: https://tsapps.nist.gov/publication/get_pdf.cfm?pub_id=100988.

[12] Grosshandler, W., Bryner, N., Madrzykowski, D. and Kuntz, K. (2005), Report of the Technical Investigation of The Station Nightclub Fire: Appendices (NIST NCSTAR 2), Vol. 2, National Construction Safety Team Act Reports (NIST NCSTAR), National Institute of Standards and Technology (NIST), Gaithersburg, MD, USA [online]. Accessed on August 7th, 2021, at: https://tsapps.nist.gov/publication/get_pdf.cfm?pub_id=100989.

[13] Hennemann, G.G., Bolina, F.L., Manica, G.C. et al. Investigation on the causes and consequences of Kiss nightclub fire in Brazil. Archit. Struct. Constr. 2, 291–309 (2022). https://doi.org/10.1007/s44150-022-00032-1.

[14] Hennemann, G. G. (2019). Análise crítica do incêndio da boate Kiss segundo simulação computacional. Trabalho de Conclusão de Curso não publicado. Graduação em Engenharia Civil da Universidade do Vale do Rio dos Sinos. São Leopoldo, Brasil.

LARGE EDDY SIMULATIONS OF FLAME MORPHOLOGICAL CHARACTERISTICS OF PAIR OF UNEQUAL POOL FIRES

Siva K Bathina, a,*

Sudheer Siddapureddy, b

ABSTRACT

When two or more fires are located close enough to interact with each other then those are termed multiple pool fires (MPF). Generally, fire accidents with unequal pool diameters are as common and responsible as equal pool diameters. Moreover, the flame morphological characteristics of unequal pool fires are asymmetric compared to equal pool sizes. Therefore, to explore the asymmetric characteristics of MPF with unequal pool sizes, large eddy fire simulations are performed using a fire dynamic simulator. In the simulations, the diameters of large (D_l) and small (D_s) are 0.3 m and 0.2 m are considered respectively and the distance between the pools (S = 0, 0.1, 0.2, 0.3, 0.4, 0.5, 0.6 m) and their burning rates were varied. The results showed that, with the increase in burning rate from S = 0.6 to 0.2 m, the flame heights of D_s and D_l increased to 39% and 24.5% respectively which can be confirmed that the flame height of D_s has greater influence than D_l. Meanwhile, it is noticed that, a maximum of 7°of flame tilt of D_s which is greater than D_l of all studied cases. It is also observed that the rate of air entrainment of D_l was higher than D_s.

Keywords: multiple pool fires; unequal pool sizes; Large-eddy simulations; flame height; air entrainment.

1. INTRODUCTION

Hydrocarbon fuels, such as crude oil, LNG, and kerosene, require a lot of storage and transportation to be processed and produced in the energy and chemical industries [1,2]. These fuels, on the other hand, are flammable and explosive that is easily ignited and create explosions disaster, such as pool fires [3,4], vapour cloud explosions (VCE) [5,6], boiling liquid expanding vapour explosions (BLEVE) [6], and so on. Once any of the above-mentioned events turn out of control, the entire plant will experience a domino effect, resulting in massive economic loss and

a* Indian Institute of Technology Dharwad, India (bathinasivakumar.004@gmail.com), Corresponding author,

b, Indian Institute of Technology Dharwad, India (sudheer@iitdh.ac.in)..

causalities [7,8]. Among the various forms of fire accidents, pool fire is the most common form of accident in storage and process industries [3,9] and is defined as the pool of liquid burning on a horizontal surface (liquid/water) where fuel and air get mixed by buoyancy control resulting in combustion [10]. When these discrete pool fires burn at close enough distance to interact with each other, such a phenomenon is called the formation of multiple pool fires (MPF) [11]. The formation of MPF is common in the material, mining, and transportation industries. Several fire accidents caused by MPFs have been reported globally since the 1950s, attracting increasing attention from the fire community [12]. In the petrochemical sector, for example, the unintentional ignition of a fuel tank can readily ignite nearby fuel tanks, resulting in a large-scale multiple pool fire. The interaction among fires usually results in a significant increase in burning rate and flame height when compared to a single fire. As a result, MPF may cause flames to merge, resulting in disastrous results by altering heat feedback and air entrainment. For an instance, on October 29, 2009, a fuel leak at Indian Oil Corporation caused 11 pool fires with flames visible from a distance of 30 kilometres, taking the lives of 12 people [3]. The understanding of the formation and progression of pool fire accidents has a significant impact on fire rescue, safety evacuation, and extinguishing [13]. Meanwhile, it is a crucial fundamental problem in the area of combustion and flame that has been researched for decades [13–17]. As a result, understanding fire interaction mechanisms is both fundamental and practical for assessing potential fire hazards.

In the early 1960s, Huffman et al. [11] performed multiple open pool fire experiments and observed that the distance between the fire sources decreases beyond a certain limit, and the individual fires start burning more intensively with the increase in flame height. Following that, various experimental studies revealed the various interacting effects that distinguish the MPF from standalone pool fire (SPF) [18–25]. However, most of these MPF studies were performed with equal pool sizes. But, MPF accidents comprised of unequal pool sizes as common as pools with identical sizes. Recently, Wan et al. [23] set up a pair of various unequal circular pool fire configurations to study the effect of pan diameters in the configuration and their inter-spacings on burning rate and heat feedback components. They observed that for a given fire group mass burning rate of the small pool increases monotonically with the decrease in distance between the fires whereas in the case of the large pool, the burning rate first increases and then decreases with a decrease in distance between the fires. To the best of authors' knowledge, the flame morphological studies and the air entrainment of unequal pool fires are remained as knowledge gap.

In this work, numerical study of a pair of unequal n-heptane circular pool fires was carried out. The pan diameters for the pair of unequal pool sizes are 0.3 and 0.2 m are considered. This work aimed at the flame interactions, flame height, and air entrainments caused by unequal pair of pool fires with various separation distances in an open space. The details of the numerical studies are described in the subsequent section.

2. NUMERICAL MODELLING

Of the different strategies available for modelling MPFs, Computational Fluid Dynamics (CFD) has arisen as a ground-breaking one with the possibility to deal with their complexities. In the present work, numerical simulations are performed using Fire Dynamic Simulator (FDS) V 6.7.5. FDS is intendedly developed to calculate the smoke flow and heat transfer from and to the fire [26]. It consists of large-eddy simulations (LES) and direct numerical simulation (DNS) models. The present work is simulated using a LES model which offers less time demand than DNS. FDS solves the various models like hydrodynamic, pyrolysis and gas-phase combustion, species transport, and radiation transport to obtain flame properties like the evaporation of liquid fuel, temperature, gas velocities, species concentration, and other pertinent variables within each grid cell. The hydrodynamic model solves the Navier-Stokes equation with an emphasis on smoke and heat transfer from the flame[27]. Turbulence and turbulent viscosity are treated by employing large-eddy simulation and Deardorff's models respectively. Combustion is assumed as mixing controlled and an infinite fast reaction of lumped species i.e., diffusion of air and fuel species is controlled by mixing time, and the chemical reaction between the air and fuel species occurs infinitely fast. In FDS, three lumped species are considered and those are air, fuel, and products. Fuel, products are solved explicitly and the air is considered a background species.

FDS studies are successfully applied in MPFs scenarios to study the flame merging and effect of fire array size, separation distances, and heat release rates [28]. Yu et al. [29] performed numerical studies using large eddy simulation (LES) and studied the flame merging based on the Iso-surface at 99% of HRR and air entrainment restriction ignoring the radiation heat feedback (by maintaining the constant HRR irrespective of the distance between the pans in a fire array) effect for different fire arrays. Recently, Wang et al. [30] performed LES of flame interactions of unequal heat release rate (HRR) of two identical propane pool fires in an open space

2.1 Simulation setup

A computational domain is considered with a dimension of 2.4 m (*W*) × 2.4 m (*L*) × 3.2 m (*H*) in a Cartesian coordinate system. A uniform structured grid ($\delta x = \delta y = \delta z$) is considered for all the cases. The width, length, and height of the computational domain are chosen so that they do not influence the air entrainment into the computational domain. Except for ground, all other boundaries are set to an 'OPEN' atmosphere. The ground is set to 'INERT' as shown in Figure 1. The initial temperature is set to 20℃. The simulations are run until the flame properties converged to a steady-state. All simulations are run for a period of 30 s. The necessary thermochemical properties of n-heptane fuel for the simulation are mentioned in Table 1.
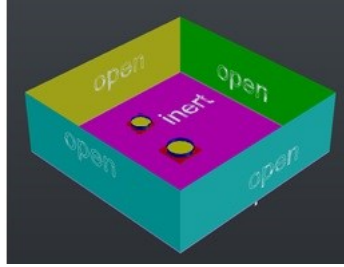
Figure 1 Geometrical model and boundary conditions

Table 1 Thermochemical properties of n-heptane used in the present work

S. No	Property	Symbol	Value [31]
1	Heat of combustion (kJ/kg)	ΔH_c	44600
2	Heat of vaporization (kJ/kg)	ΔH_v	320
3	Boiling Point (°C)	T_b	98.5
4	Emissivity (-)	ε_l	0.9
5	Density (kg/m^3)	ρ_l	675
6	Specific heat (kJ/kg K)	C_{pl}	2.24
7	Conductivity (W/m K)	k_l	0.14

In this work, a pair of n-heptane unequal circular pools were considered with the diameters of D_l = 0.3 m and D_s = 0.2 m, where D_l and D_s are large and small pool diameters respectively. According to the Blinov and Khudyakov [32] experimental data, the pool diameter in the present study comes under the radiative-dominated regime (conduction dominated $D < 10$ cm, convection dominated $10 \leq D < 20$ cm, and radiation dominated $D \geq 20$). The separation distance from edge to edge (*S*) between the two unequal pool fires were *S* = 0, 10, 20, 30, 40, 50, and 60 cm considered. Noted that the chosen pan diameters, separation distances and their burning rates were considered based on the previously reported experimental data [30]. The details of the simulated cases are shown in Table 2.

Table 2 List of simulation cases

Case	Mass burning rate (kg/m^2 s) of D_s [23]	Mass burning rate (kg/m^2 s) of D_l [23]	*S* (cm) [23]
1	0.0477	0.0380	0
2	0.0464	0.0445	10
3	0.0419	0.0416	20
4	0.0338	0.0378	30
5	0.0316	0.0364	40
6	0.0279	0.0357	50
7	0.0222	0.0356	60

2.2 Grid independency analysis

To accomplish reliable results from a CFD analysis, one needs to give more emphasis on the size of the grid cell. The resolution of the flow field of the fire depends on the number of the grid (*δx*) cells that span the characteristic

diameter (D^*). It is expressed as a non-dimensional form as shown in Eq. 1. Eq. 1 represents not only the impact of the grid size but also the fire size.

$$D^* = \left(\frac{\dot{Q}}{\rho_\infty C_p T_\infty \sqrt{g}}\right)^{2/5}$$

(1)
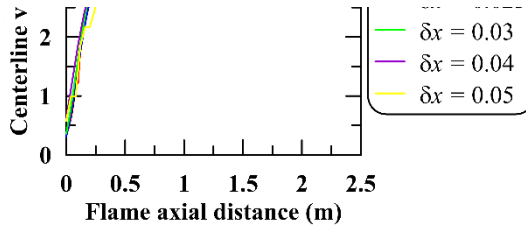
e rate (HRR), ρ_∞ is the density of ambient air, T_∞ is the ambient ity. The more the number of grid cells occupies the characteristic obtained. If the D^* is relatively smaller than the physical diameter oarse grid and vice-versa. The grid resolution i.e., the ratio of ould be in the range of 4 to 16. Therefore, six grid sizes of 0.015, 05 m were considered. A test case (= 0) of two unequal fires with 0 separation distance between the fires was considered and applied to all the above-mentioned grid sizes. Using the six grid sizes, the flame properties like centerline temperature and velocity distributions of the test case were studied. The results of the grid independency analysis are shown in Figure 3.
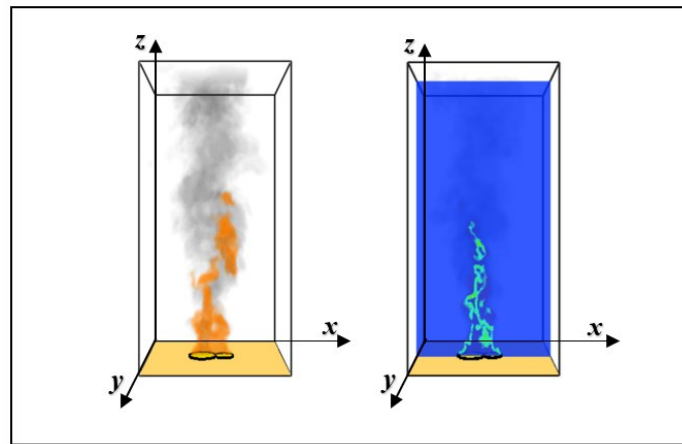
Figure 2 Test case: two unequal pools with 0 separation distance
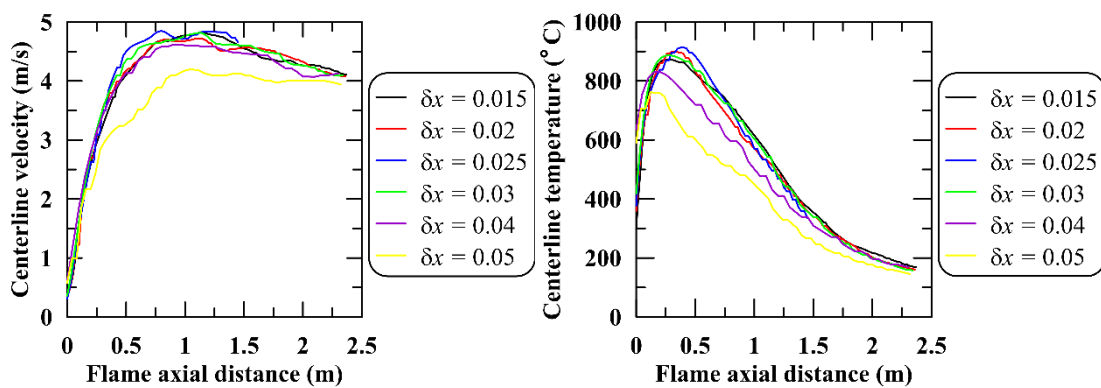
Figure 3 Grid independence analysis of centerline temperature and velocity distributions

It is noticed from Figure 3 that with the relatively large grid size, a large deviation can be noticed in the temperature and velocity distributions. As the grid size decreases, the trends of the temperature and velocity distributions reach uniform. Moreover, beyond the grid size of 0.025 m, the variation in the temperature and velocity distribution of various grid sizes tends minimal. Therefore, 0.025 m was chosen as the grid size for further numerical studies.

111

3. RESULTS AND DISCUSSIONS

3.1 Flame height

In this work, flame height is computed based on the Iso-surface temperature at 330 ℃ [33]. To calculate the flame height, Iso-surface data for the last 10 s of the steady-state data is averaged. Moreover, the averaged Iso-surface data is used to reconstruct the Iso-surface at 330 ℃ using the MATLAB® programme. The generated Iso-surfaces for different separation distances with D_l = 0.3 m and D_s = 0.2 m are shown in Figure 4. If the S is 0, then the two unequal pool flames merge completely together just above the burner and form as single fire whose height is termed as merging flame height.

S = 0

S = 0.1

S = 0.2 m

S = 0.3 m

S = 0.4 m

S = 0.5 m

S = 0.6 m
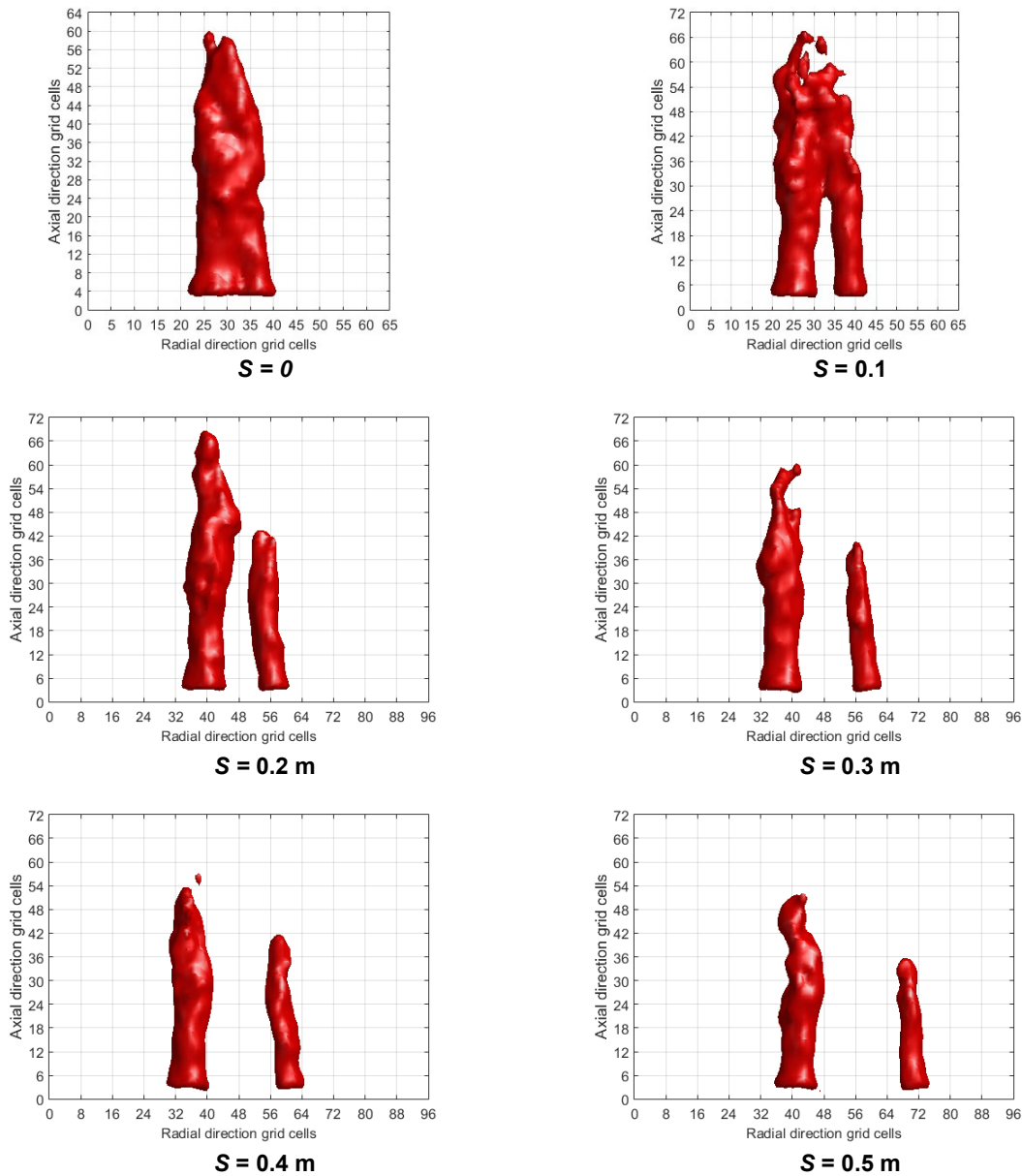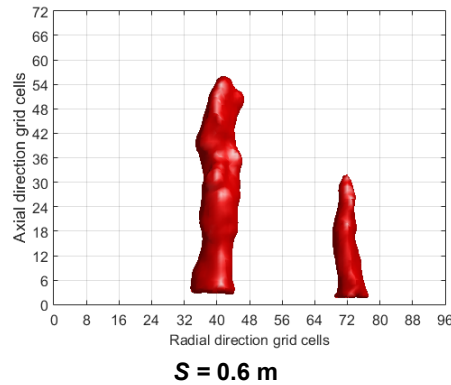
Figure 4 Flame height of Iso-surface at 330 ℃

With the increase in S, the flame height of two unequal pools decreases and reaches to form two single standalone flames. Table 3 shows the variation in the flame height of D_s and D_l with S. It is evident from the Figure 4, at $S = 0$ m, two flames are completely merged and form a single fire. As the S increases to 0.1 m, the flames are still in partial contact and interacting with each other at the flame axial height of 0.625 m from the pool base. At $S = 0.1$ m, the flame height is termed as interacting flame height. Beyond $S = 0.1$ m, the flame heights of two unequal pools reduce monotonically.

Table 3 Flame heights of D_s and D_l

S.No	S (m)	Mass burning rate (kg/m² s) of D_s [23]	Mass burning rate (kg/m² s) of D_l [23]	Flame height of D_s (m)	Flame height of D_l (m)
1	0	0.0477	0.0380	1.425 (merging flame height)	
2	0.1	0.0464	0.0445	1.625 (interacting flame height)	
3	0.2	0.0419	0.0416	1	1.65
4	0.3	0.0338	0.0378	0.95	1.425
5	0.4	0.0316	0.0364	0.975	1.275
6	0.5	0.0279	0.0357	0.825	1.225
7	0.6	0.0222	0.0356	0.725	1.325

This is due to flame height being directly related to the HRR. When the HRR is increased concerning S, the flame height of the D_l and D_s also increases. However, the flame height of the D_s has the greater influence on the burning rate rather than the flame height of D_l. It is observed from Table 3 that with the increase in burning rate from $S =$ 0.6 to 0.2 m, the flame heights of D_s and D_l increased to 39% and 24.5% respectively which can be confirmed that the flame height of D_s has greater influence than D_l.

3.2 Flame interactions

The burning rates of pool fires with equal pool sizes are identical with respect to pool spacing [21,34,35]. However, pool fires of unequal pool sizes having different burning rates with respect to S led to asymmetrical flame interactions. This can be attributed to the asymmetrical behaviour of air entrainment and heat feedback of unequal pools. In the literature, the flame interactions due to variation in the pressure field that existed between the pools are divided into three stages [34]: I) standalone flames, II) interacting flames, and III) completely merged flames. The interactions of flames from the standalone stage to the completely merged stage are shown in Figure 4. When the distance between the two pools is smaller than the threshold value than those two flames form as a single flame. The pressure field that existed between and around the two unequal pool fires with various S is shown in Figure 5.

113

S = 0

S = 0.1

S = 0.2 m

S = 0.3 m

S = 0.4 m

S = 0.5 m

Figure 5 Pressure distribution for various separation distances

It is observed from Figure 5 that a relatively low-pressure field was generated between the two pools and a relatively high-pressure field was generated at the outer field of the two flames until S = 0.2 m. Due to this, the two flames start deflecting inward and interact with each other. Beyond S = 0.2 m, a positive pressure field was set up between the two pools and grows in the flame axial direction. This upward-growing positive pressure field between the pools leads to flames behaving as single flames without interacting with each other.

3.3 Flame tilt

es is different from the two pool fires having equal pool sizes. In ween the flame centre to the vertical direction that is drawn from ained by connecting the line passing through the peaks of each rofiles with various S are shown in Figure 6. Moreover, as an temperature contours was demonstrated in Figure 4 for the case e 4 that, the tilt angle of the θ_{D_s} is greater than the θ_{D_l}, where θ_{D_s} ge pool diameters respectively. The reason for this phenomenon eveloped at the outer sides of the two flames. As was shown in that the D_s and D_l were located at right and left sides of the computational domain. Furthermore, the burning rate of D_l is greater than D_s from S = 0.6 to 0.3 as shown in Table 2. Having D_l higher burning rates, a relatively high-pressure field was generated at the outer side of the D_l compared to D_s as shown in Figure 5. This relatively high-pressure field at the D_l side supports the flame to be not deflected to the higher extends. At the same time, having smaller flame heights and relative low pressure field of the D_s leads to flame to be deflected to greater extends compared to tilt of D_l. While for the cases of S = 0.2 and 0.1 m, the given burning rates of both pools are almost identical for the corresponding case, hence the pressure field developed at the outsides of the two pools is almost uniform which leads to a symmetric flow field. As a result, identical flame tilt angles from both pools can be observed as shown in Figure 6 for S = 0.2 and 0.1 m.

S = 0

S = 0.1

S = 0.2 m

S = 0.3 m

S = 0.4 m

S = 0.5 m

116

Figure 6 Temperature contour profiles of two unequal pool fires at various separation distances

3.4 Air entrainment

The size and shape of a pool fire, as well as the amount of soot produced and the composition of combustion products, are all influenced by air entrainment [36]. It is reported that the air entrainment in the entire burning region of the pool fire is independent of HRR and is mainly controlled by fluid dynamic interactions of flames [37]. At any height, the integrated air entrainment rate into the fire plume is obtained by placing the device QUANTITY='MASS FLOW' [26]. In this study, this device is placed and oriented in a positive 'Z' direction and it measures the net integrated mass flux ($\dot{m} = \int \rho \boldsymbol{u} \cdot ds$, where ρ is the air density, $\boldsymbol{u}$ is the velocity vector, ds is the planner surface area) through the given planar area. The rate of air entrainment of D_l and D_s with various separation distances are depicted in Figure 7. It is noticed from the Figure 7 that the rate of air entrainment of the D_l is greater than the D_s and rate of air entrainment of D_l for all S is almost uniform until their individual flame heights. While in the case of D_s, except for $S = 0$, the air entrainment rate is almost uniform until their individual flame heights. A significant air entrainment restriction can be noticed with 0 separation distance. The reason is that being a small pool diameter (D_s), air entrainment was restricted by large pool diameter (D_l).
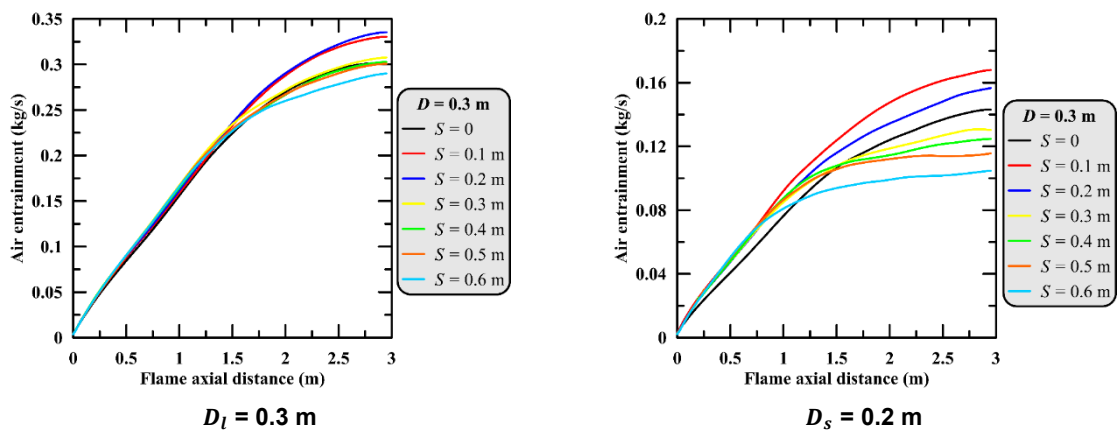
Figure 7 Rate of air entrainment of D_l and D_s with various separation distances

It is also observed from Figure 7 that beyond the individual flame heights of D_l and D_s, the variation in air entrainment rate can be seen with various S. A strong entrainment restriction is observed in the plume (beyond flame height) zone similar to the flame zone with 0 separation distance and the restriction becomes weaker with the increase in separation distance for both the pool diameters.

4. CONCLUSIONS

In this work numerical investigations are performed on the asymmetric flow characteristics of two unequal n-heptane circular fires of unequal heat release rates in open space. The MBR combination and burner separation distance are varied. The major conclusions are summarized as follows:

The flame height of two unequal fires is as follows: At S = 0 m, two flames are completely merged and form a single fire. As the S increases to 0.1 m, the flames are still in partial contact and interact with each other at the flame axial height of 0.625 m from the pool base. At S = 0.1 m, the flame height is termed as interacting flame height. Beyond S = 0.1 m, the flame heights of two unequal pools reduce monotonically. The flame heights of D_s and D_l increased to 39% and 24.5% respectively as the spacing between the pools is decreased from 0.6 m to 0.2m. A maximum of 7°of flame tilt of D_s which is greater than D_l of all studied cases. It is also observed that the rate of air entrainment of D_l was higher than D_s.

ACKNOWLEDGEMENTS

REFERENCES

[1]   M. Masum Jujuly, A. Rahman, S. Ahmed, F. Khan, LNG pool fire simulation for domino effect analysis, Reliab. Eng. Syst. Saf. 143 (2015) 19–29. https://doi.org/10.1016/j.ress.2015.02.010.

[2]   Y. Yang, G. Chen, P. Chen, The probability prediction method of domino effect triggered by lightning in chemical tank farm, Process Saf. Environ. Prot. 116 (2018) 106–114. https://doi.org/10.1016/j.psep.2018.01.019.

[3]   S. Vasanth, S.M. Tauseef, T. Abbasi, S.A. Abbasi, Multiple pool fires: occurrence, simulation, modeling and management, J. Loss Prev. Process Ind. 29 (2014) 103–121. https://doi.org/10.1016/j.jlp.2014.01.005.

[4]   M. Muñoz, E. Planas, F. Ferrero, J. Casal, Predicting the emissive power of hydrocarbon pool fires, J. Hazard. Mater. 144 (2007) 725–729. https://doi.org/10.1016/j.jhazmat.2007.01.121.

[5]   S. Zhang, Q. Zhang, Influence of geometrical shapes on unconfined vapor cloud explosion, J. Loss Prev. Process Ind. 52 (2018) 29–39. https://doi.org/10.1016/j.jlp.2018.01.004.

[6]   A.M. Birk, Shock waves and condensation clouds from industrial BLEVEs and VCEs, Process Saf. Environ. Prot. 110 (2017) 15–20. https://doi.org/10.1016/j.psep.2017.06.017.

[7]   N. Alileche, D. Olivier, L. Estel, V. Cozzani, Analysis of domino effect in the process industry using the event tree method, Saf. Sci. 97 (2017) 10–19. https://doi.org/10.1016/j.ssci.2015.12.028.

[8]   V. Cozzani, M. Campedel, E. Renni, E. Krausmann, Industrial accidents triggered by flood events: Analysis of past accidents, J. Hazard. Mater. 175 (2010) 501–509. https://doi.org/10.1016/j.jhazmat.2009.10.033.

[9]   D. Wu, Z. Chen, Quantitative risk assessment of fire accidents of large-scale oil tanks triggered by lightning, Eng. Fail. Anal. 63 (2016) 172–181. https://doi.org/10.1016/j.engfailanal.2015.11.029.

[10]   C. Gong, L. Ding, H. Wan, J. Ji, Z. Gao, L. Yu, Spatial temperature distribution of rectangular n-heptane pool fires with different aspect ratios and heat fluxes received by adjacent horizontal targets, Fire Saf. J. 112 (2020) 102959. https://doi.org/10.1016/j.firesaf.2020.102959.

[11]   K.G. Huffman, J.R. Welker, C.M. Sliepcevich, Interaction effects of multiple pool fires, Fire Technol. 5 (1969) 225–232. https://doi.org/10.1007/BF02591520.

[12]   H. Persson, A. Lzonnermark, Tank fires : review of fire incidents 1951-2003, 2004. https://www.sp.se/sv/units/risesafe/safety/fire/Documents/Skydd/SP_report2004_14.pdf.

[13]   S. Sudheer, L. Kumar, B.S. Manjunath, A. Pasi, G. Meenakshi, S. V. Prabhu, Fire safety distances for open pool fires, Infrared Phys. Technol. (2013). https://doi.org/10.1016/j.infrared.2013.09.006.

[14]   D.J. Rasbash, Properties of fires of liquids, Fuel 35, 1965.

[15]   H. Koseki, Combustion properties of large liquid pool fires, Fire Technol. 25 (1989) 241–255. https://doi.org/10.1007/BF01039781.

[16]   S.. P. Sudheer S.V., Measurement of flame emissivity of gasoline pool fires, Nucl. Eng. Des. 240 (2010) 3474–3480. https://doi.org/10.1016/j.nucengdes.2010.04.043.

[17]   S. Sudheer, S. Prabhu, Characterization of hexane pool fires using infrared thermography, J. Fire Sci. 31

(2013) 143–165.

[18] J.R. Vincent, S.R. Gollahalli, An Experimental Study of the Interaction of Multiple Liquid Pool Fires, J. Energy Resour. Technol. 117 (1995) 37. https://doi.org/10.1115/1.2835318.

[19] M.A. Delichatsios, A correlation for the flame height in group fires, Fire Sci. Technol. 26 (2007) 1–8. https://doi.org/10.3210/fst.26.1.

[20] S. Zhang, N. Liu, J. Lei, X. Xie, Y. Jiao, R. Tu, Experimental study on flame characteristics of propane fire array, Int. J. Therm. Sci. 129 (2018) 171–180. https://doi.org/10.1016/J.IJTHERMALSCI.2018.02.024.

[21] Y. Jiao, W. Gao, N. Liu, J. Lei, X. Xie, L. Zhang, R. Tu, Interpretation on fire interaction mechanisms of multiple pool fires, Proc. Combust. Inst. 37 (2019) 3967–3974. https://doi.org/10.1016/j.proci.2018.06.049.

[22] F. Ge, A. Simeoni, J. Ji, H. Wan, Experimental study on the evolution of heat feedback in multiple pool fires, Proc. Combust. Inst. 38 (2021) 4887–4895. https://doi.org/10.1016/J.Proci.2020.06.050.

[23] H. Wan, L. Yu, J. Ji, Experimental study on mass burning rate and heat feedback mechanism of pair of unequal circular pool fires of heptane, in: Proc. Combust. Inst., Elsevier Ltd, 2021: pp. 4953–4961. https://doi.org/10.1016/j.proci.2020.07.079.

[24] N. Liu, Q. Liu, J.S. Lozano, L. Zhang, Z. Deng, B. Yao, J. Zhu, K. Satoh, Multiple fire interactions: A further investigation by burning rate data of square fire arrays, Proc. Combust. Inst. 34 (2013) 2555–2564. https://doi.org/10.1016/j.proci.2012.06.098.

[25] S.K. Bathina, S. Sudheer, Experimental investigation of flame height and air entrainment of n-heptane double open pool fires, Exp. Heat Transf. (2022) 1–11.

[26] K.B. McGrattan, S. Hostikka, R. McDermott, J. Floyd, C. Weinschenk, K. Overhold, Fire dynamics simulator: user's guide (version 6.7.5). NIST special publication 1019, 2020. http://fire.nist.gov/fds.

[27] R.G. Rehm, H.R. Baum, Equations of motion for thermally driven, buoyant flows, J Res Natl Bur Stand. 83 (1978) 297–308. https://doi.org/10.6028/jres.083.019.

[28] W.G. Weng, D. Kamikawa, Y. Fukuda, Y. Hasemi, K. Kagiya, Study on flame height of merged flame from multiple fire sources, Combust. Sci. Technol. 176 (2004) 2105–2123. https://doi.org/10.1080/00102200490514949.

[29] L. Yu, H. Wan, Z. Gao, J. Ji, Study on flame merging behavior and air entrainment restriction of multiple fires, Energy. 218 (2021) 119470. https://doi.org/10.1016/j.energy.2020.119470.

[30] Z. Wang, L. Yu, J. Ji, Numerical Investigation on the Asymmetric Flow Characteristics of Two Propane Fires of Unequal Heat Release Rate in Open Space, Fire Technol. (2021) 1–23. https://doi.org/10.1007/s10694-021-01111-3.

[31] M.J. Hurley, D.T. Gottuk, J.R. Hall Jr, K. Harada, E.D. Kuligowski, M. Puchovsky, J.M. Watts Jr, C.J. WIECZOREK, Others, SFPE handbook of fire protection engineering, (2016) 94–107. https://doi.org/10.1177/0734904116630559.

[32] V.I. Blinov, G.N. Khudyakov, Diffusion burning of liquids. Army Engineer Research and Development Labs Fort Belvoir VA, (1961). http://www.dtic.mil/docs/citations/AD0296762.

[33] B. Rengel, C. Mata, E. Pastor, J. Casal, E. Planas, A priori validation of CFD modelling of hydrocarbon pool fires, J. Loss Prev. Process Ind. 56 (2018) 18–31. https://doi.org/10.1016/j.jlp.2018.08.002.

[34] K.G. Huffman, J.R. Welker, C.M. Sliepcevich, Interaction effects of multiple pool fires, Fire Technol. (1969). https://doi.org/10.1007/BF02591520.

[35] H. Wan, Z. Gao, J. Ji, Y. Zhang, K. Li, L. Wang, Effects of pool size and spacing on burning rate and flame height of two square heptane pool fires, J. Hazard. Mater. 369 (2019) 116–124. https://doi.org/10.1016/j.jhazmat.2019.01.111.

[36] X.C. Zhou, J.P. Gore, H.R. Baum, Measurements and prediction of air entrainment rates of pool fires, Symp. Combust. 26 (1996) 1453–1459. https://doi.org/10.1016/S0082-0784(96)80366-3.

[37] M.A. Delichatsios, Air entrainment into buoyant jet flames and pool fires, Combust. Flame. 70 (1987) 33–46. https://doi.org/10.1016/0010-2180(87)90157-X.

Fire in Industrial Buildings

STRUCTURAL FIRE BEHAVIOUR OF PROTECTED TUBULAR STEEL COLUMNS IN INDUSTRIAL WAREHOUSES UNDER STANDARD AND SIMULATED FIRE CONDITIONS

Pegah Aghabozorgi[1]*; Luís Laim[2]; Aldina Santiago[3]; Nuno Cândido[4]

ABSTRACT

This paper aims to compare the influence of different fire scenarios, namely standard and simulated fire conditions, on the fire performance of a load-bearing column assembly from a steel industrial warehouse protected with gypsum-based fire protection mortars during a fire event. The steel column fire performance was evaluated using the heat transfer and thermo-mechanical analysis implemented in FE software. To conduct the thermal analysis on the steel column, three distinct fire design models were defined: the ISO 834 standard temperature-time curve, a zone model, and a computational fluid dynamics model. Afterwards, an optimization was performed in terms of the fire protection thickness to compare the minimum required thickness for each specified fire model, i.e., simulated fire curves and the standard fire curve. The findings indicated that the use of the simulated fire models in the design process might have the potential to reduce the costs of fire protection materials, as they may provide more realistic fire curves in appropriate fire safety measurements. Finally, a parametric study was carried out to assess the impact of other variable factors, such as load ratio and column cross-section, on the behaviour of protected steel column assemblies at elevated temperatures.

Keywords: computational fluid dynamics, finite element method, fire safety, steel columns, fire protection mortars.

1. INTRODUCTION

Fire safety engineering is a multi-disciplinary field aiming to evaluate building designs according to a specified fire model. Due to the current trend towards a performance-based fire design, correctly identifying fire models becomes a must to ensure a safe and optimal solution to risk mitigation. Therefore, the fire model has an essential role in assessing the behaviour of steel structures exposed to fire. The fire design can be obtained from different methods, including the standard fire curve and the natural fire models. The standard fire curve is typically based on ISO 834 standard temperature-time curve [1], prescribed by the European International Standards, or parametric fire curves (EN 1991-1-2) [2], following a uniform temperature-time relationship representing the temperature evolution of the gases surrounding the element as a function of time. In contrast, the natural fire model presents the effective heat flow transferred through the fire spread into the element. In this method, the fire-driven fluid flow can be simulated

---

[1]* ISISE, ARISE, Department of Civil Engineering, University of Coimbra, Portugal, (pegah.aghabozorgi@gmail.com), corresponding author.

[2] ISISE, ARISE, Department of Civil Engineering, University of Coimbra, Portugal, (luislaim@uc.pt).

[3] ISISE, ARISE, Department of Civil Engineering, University of Coimbra, Portugal, (aldina@dec.uc.pt).

[4] OneSource, Consultoria Informática, Lda, Coimbra, Portugal, (ncandido@onesource.pt).

with some fire dynamic simulator programs such as the zone model code CFAST (Consolidated Model of Fire Growth and Smoke Transport) [3] and the computational fluid dynamics (CFD) model using Fire Dynamics Simulator (FDS) code [4]. There are various studies which have evaluated these two methods and compared their differences in the temperature distribution of the structural steel members [5], [6]. The comparison of the results showed that the natural fire scenario is more realistic than the standard fire curves prescribed by the European International Standards, and in the majority of the cases, it targets more economical and safe solutions [5].

Steel warehouses are widely used in various industries such as manufacturing, construction, chemical, commercial, etc. However, fires in steel warehouses can be dangerous due to the high temperature rise, intensifying the risk of structural collapse. Therefore, the application of appropriate protective measures and fire-resistant design is essential to minimize damage to the building, ensuring the safety of its occupants, and maintain the structure's integrity during a fire. Among various fire protection methods available for protecting steel warehouses from fire, gypsum-based mortars with silica micro and nano-particles (SMNP) were selected in this study due to their proven effectiveness in improving the fire resistance rating of structural steel members in some previous research conducted by the authors [7], [8].

It is worth mentioning that fire dynamics in large enclosures, such as industrial warehouses, have different behaviours than fires in small and medium-sized enclosures (fire compartments). Whereas homogeneous temperatures of the gas are assumed in the fire compartments, significant non-uniform temperature distribution in both the vertical and horizontal direction may be observed in large enclosures [9]. The measurement of the non-uniform temperature distributions resulting from localized fire has been the topic of many studies over the past decades [10]–[13]. Therefore, simple time-temperature fire curves are usually used in the fire design of compartments, and CFD models would be better to be used in large enclosures (Figure 1). Few investigations have been recently taken on fire damage and the impact of fire conditions on the large-space enclosures when subjected to non-uniform elevated temperatures caused by fire. For example, Woźniczka presented a performance-based analysis of a steel warehouse hall storing recyclable materials under an advanced fire scenario developed by a CFD model, and the measured fire resistance was 30 minutes for the steel hall roof without fire protection [14]. Eremina et al. evaluated the fire resistance limit of a modern warehouse building with or without fire-retardant coating for both standard temperature mode and possible real fire mode using the simulation of real fire development in FDS software [15]. They have also shown that the effectiveness of fire-retardant intumescent coating characteristics was dependent on the actual fire condition [16].

When a fire outbreaks in a large compartment such as an industrial warehouse, the load-bearing members are usually exposed to localized fire. Given that steel columns are the main load-carrying elements of warehouse buildings governing the collapse of these structures, assessing their fire performance under a fire scenario representing the real fire behaviour in a large compartment is of great importance. Therefore, some investigations started to focus on the thermo-mechanical behaviour analysis of load-bearing columns under localized fires to assess the fire performance of large space buildings [17]. An experimental study was also carried out by Piroglu et al. [18] on unprotected structural steel members of an industrial factory exposed to fire to make an appropriate assessment of their mechanical properties after exposure to the fire. Moreover, Ambroziak et al. [19] performed some experimental and numerical calculations to assess the fire impact on the strength and durability of real structural elements of a warehouse building after a fire. Despite all the investigations currently done in this field, research concerning the specifics of the design and performance of steel warehouse buildings, especially when protective measures are adopted under fire-driven fluid flow, is still a critical concern for structural engineers and fire safety experts.

To deal with this concern, firstly, the thermal performance of enhanced gypsum-based mortars protecting steel column assemblies taken from a realistic prototype warehouse building in a fire situation is assessed based on experimental and thermo-mechanical numerical analyses [20] developed in ABAQUS software. Secondly, the impact of different thermal actions is also numerically investigated, including ISO 834 standard temperature-time curve [1] and advanced temperature-time curves [2]. The last one is estimated by the CFAST code [4] and a CFD model using the Fire Dynamics Simulator (FDS) code, where fire-driven fluid flows are simulated. Finally, a parametric study is conducted to assess the influence of other parameters, such as load ratio and the cross-section of the column.
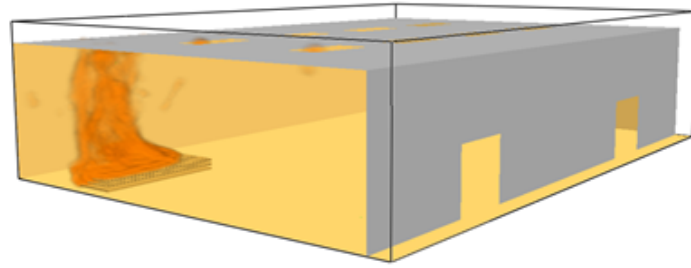
Figure 1: Computational fluid dynamic simulation of a fire scenario in large enclosures

2. 2. DEVELOPMENT OF FE ANALYSIS MODELS

FE models were developed in the commercial software Abaqus to examine the influence of different fire models on the structural behaviour of steel columns in warehouse buildings. The process firstly involved subjecting each FE model to three different analyses: heat transfer analysis, linear buckling analysis, and thermo-mechanical analysis. The heat transfer analysis, as the first step, was set to determine the temperature distribution along the length of the member when exposed to a fire. The calculated temperature distribution was then utilized as an input in the nonlinear stress analysis model to explore the structural behaviour of the element under the same condition. From the linear analysis, the initial geometric imperfections were applied to the specimen with the magnitude of L/1000 and b/200 for global and local imperfection, respectively. While in the nonlinear quasi-static analysis, thermo-mechanical actions were applied to the imperfect column to obtain the failure mode and critical temperature of the specimen.

2.1 Model Description

An industrial one-story steel warehouse, shown in Figure 2 (a), was considered as a case study. The floor area of this large compartment was set to be 30m x 20m with two doorways of 3m x 3m (on the same longest facade). One column of this warehouse was selected to study its thermo-mechanical behaviour when placed in this large-space compartment under different fire actions using CFD-FEM couplings for instance. The columns were square hollow sections (SHS) 150mm x 150mm x 8mm with 6 m height. They were insulated with one layer of gypsum-based fire protection mortars with SMNP. A schematic of the column with its cross-sectional geometry is presented in Figure 2 (b). Considering that the column assemblies are entirely inside the compartment, the fire curves were applied on all four sides of the column.

The standard temperature-time curve, which is used in standard fire tests for rating structure elements, is characteristic of a fully developed fire in a compartment. It is often referred to as the ISO 834 temperature-time curve and is given by Equation (1), where T_g is the gas (compartment) temperature and t is the time [in minutes] from the beginning of the fire.

$$T_g = 20 + 345 \lg(8t + 1) \tag{1}$$
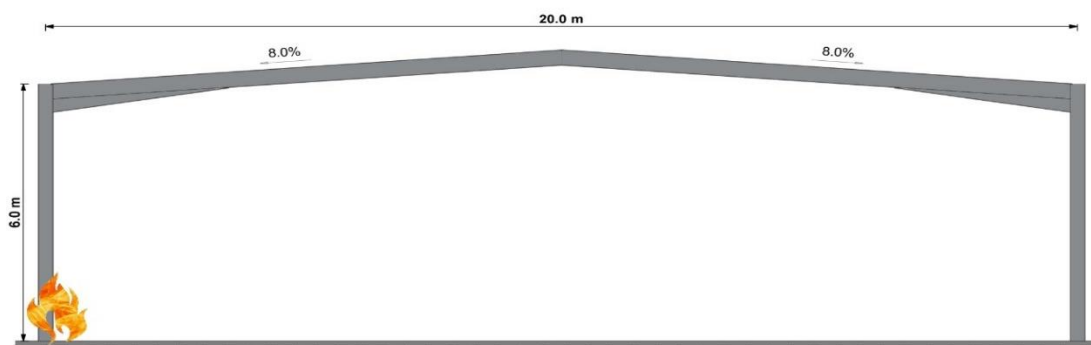
(a)
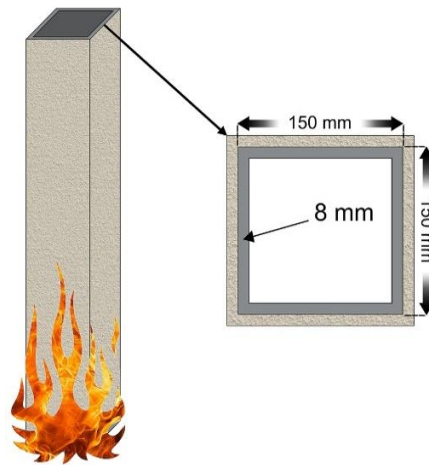
(b)

Figure 2: Prototype warehouse building model to be analyzed (a) with a schematic of the column cross-section with fire protection (b)

2.2 FE Model

The FE models of the column with the fire protection mortars were created using 3D finite elements with SHELL elements (S4R and DS4 in Abaqus). The columns were, in practice, simply supported at one end and fully restrained at the other end. They were subjected to axial compression of 442.82 KN, which is 50% of the design buckling load value at an ambient temperature according to EN 1993-1-1 [21]). As observed in the FE model (Figure 3), a reference point is defined at the centroid of the cross-section to be tied to the cross-section at each end through coupling constraints. The concentrated force is applied to the reference point where defined at the top end of the column. At the base end, all translational and rotational degrees of freedom were restrained, i.e. U1=U2=U3=UR1=UR2=UR3=0. But at the loading end, three degrees of freedom were restrained; i.e., lateral and transverse translational and longitudinal-axis rotational (U1=U2=UR3=0).
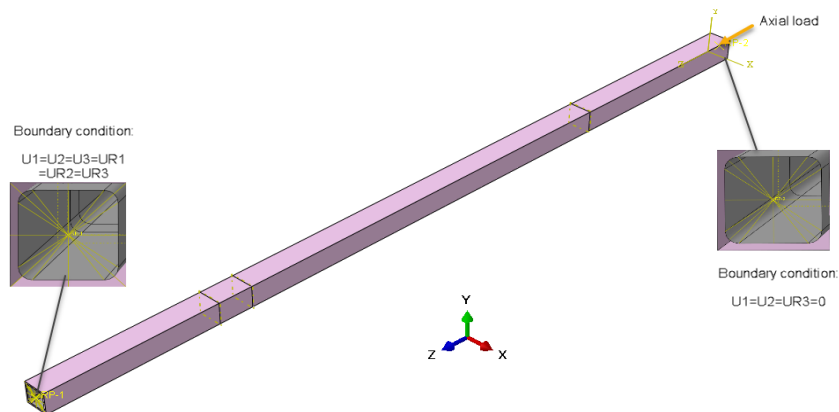
Figure 3: Numerical FE model, Boundary conditions and loading position

Moreover, based on a sensitivity analysis conducted earlier [22], a mesh size of 10 mm on the cross-section of the column was employed in this study for all the above-mentioned analyses.

2.3 Material properties

The steel columns were composed of S355 structural steel. The thermal and mechanical behaviour of both the steel tube and fire protection mortars were varied with respect to the temperature. Therefore, in order to achieve a more accurate prediction of the structural fire behaviour of the protected steel column, this variation in temperature should be employed in the FE analysis. For the steel properties, Eurocode 1993-1-2:2005 [23] was used as a reference to

124

specify temperature-dependent material properties of the steel at varying temperatures in this case study. The true stress-strain curves were included in the material definition to consider the large-deformation effect of steel. A nonlinear isotropic material model based on Von Mises yield criterion with Young's modulus E = 210 GPa and yield stress $\sigma_y = 355$ MPa was assumed at the ambient temperature. Figure 4 depicts the effective thermal properties of the gypsum-based fire protection mortars used in FE analysis, which were determined based on the previous experiments developed by the authors [8]. The steel density is 7850 Kg/m^3, and the Poisson's ratios are 0.3 and 0.2 for the steel and the fire protection mortar, respectively.

(a) Specific heat

(b) Bulk density

(c) Thermal conductivity
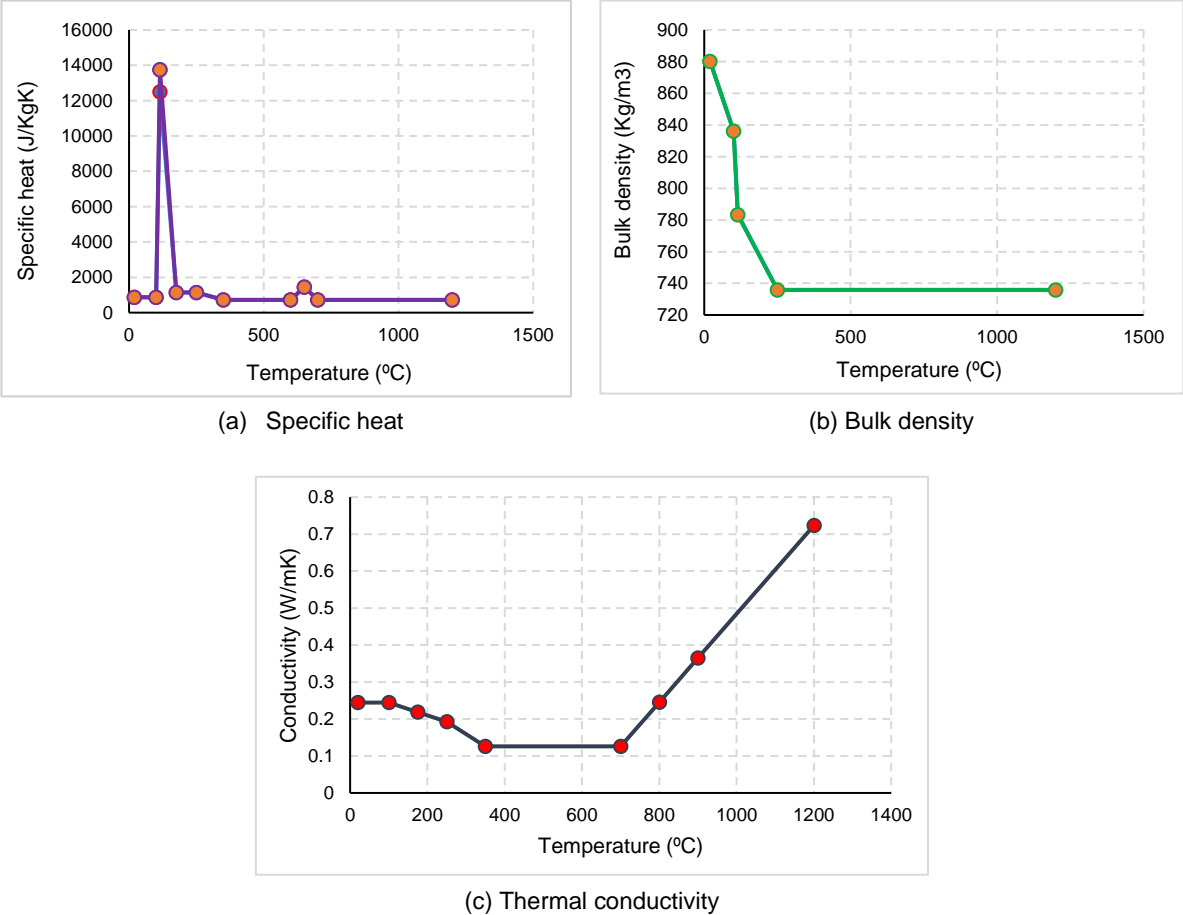
Figure 4: Thermal properties of enhanced gypsum-based mortars with SMNP

3. DEVELOPED NATURAL FIRE MODELS IN INDUSTRIAL WAREHOUSE BUILDING

For a natural fire-based design, various factors, including the fire load type and size, the fire-zone size, the number of vents, the room construction, the combustion model, the radiation model, and ventilation conditions, are considered for instance. In this study, an appropriate design fire was carefully selected to be used as an input in computing the temperature distribution inside the studied enclosure. Two fire models from the same fire scenario were selected, the two-zone model and the FDS model version 6 were used to simulate the impact of the fire on the building. This study focused on analyzing the effect of a localized fire rather than a generalized fire, as it is typically the case in industrial warehouses. The following hypotheses were considered for the fire scenario: a fast fire growth rate, fire load density of 1755 MJ/m2, fire area of 36 m2 (at the compartment corner), heat combustion 17500 kJ/kg, wood as burning material, and a maximum heat release rate of 37 MW (EN 1991-1-2 [2]). A 20cm concrete slab was assumed for floor and 0.04 m coverings with high thermal resistance were selected for the ceiling and walls.

3.1 2-zone model

To predict the development of the gas temperature in the warehouse, a two-zone model simulation was conducted using the fire modelling software CFAST [24] version 7.7.0.

The obtained results for the gas temperature-time curves from the simulation were plotted in Figure 5. According to this figure, the CFAST fires heat up slower compared to the ISO 834 temperature-time curve; instead, it peaks at higher temperatures for hot-air zones. The different thermal actions were compared based on the Ingberg Method (areas under the time-temperature curves). From CFAST simulation the following maximum temperatures were reached: 597ºC for the cold air layer, 899ºC for the hot air layer and 1500ºC for the plume temperature at the ceiling level.

(a) (b)
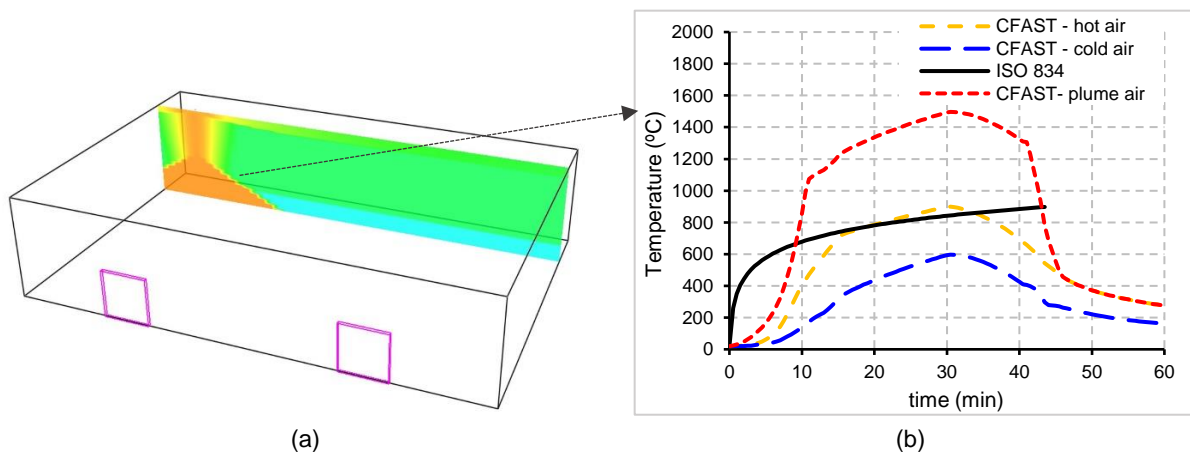
Figure 5: A comparison of the gas temperature around the corner obtained through the fire simulation of a steel warehouse in CFAST software environment (b) with the ISO 834 temperature-time curve

3.2 FDS model

Fire Dynamic Simulator (FDS) [25] is a common tool for describing fluid behaviour during a fire event. It allows the users to do the fire simulation with more detail. As a result, much more information needs to be specified to describe the fire and system boundaries making it a time-consuming procedure [26]. Figure 6 displays the gas temperature-time curves obtained from the simulation in the FDS software environment. Although the ISO 834 temperature-time curve heats up faster within the first minutes of fire, the FDS fire stays mostly at higher temperatures when oxygen concentrations are high (see Figure 6).

(a) (b)
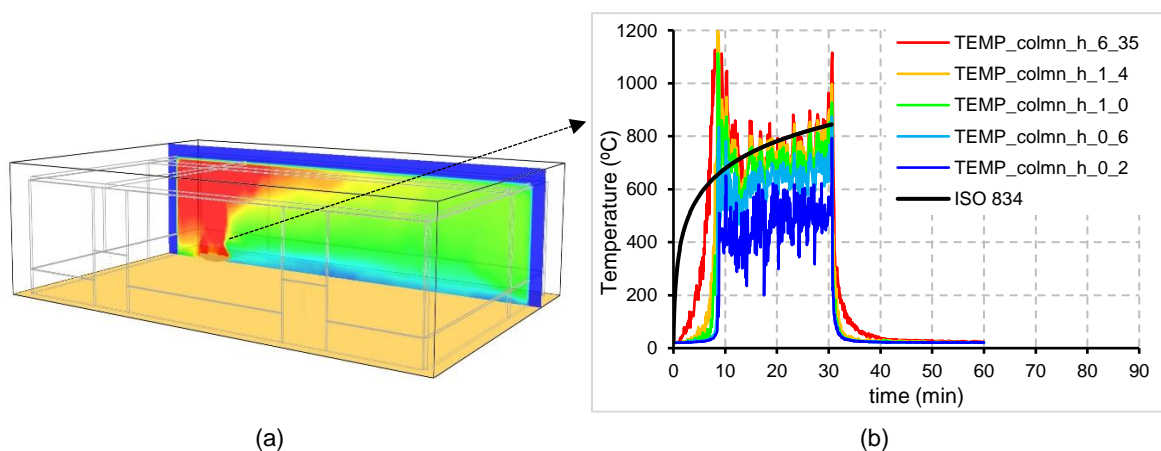
Figure 6: A comparison of the gas temperature around the corner obtained through the fire simulation of a steel warehouse in FDS software environment (b) with the ISO 834 temperature-time curve

4. COMPARISON OF THE RESULTS FOR DIFFERENT FIRE CONDITIONS

Based on the developed FE models described in section 2.2, a comparison was made between the analysis results obtained using an ISO 834 temperature-time curve and those obtained by fire simulation models developed in previous sections (3.1 and 3.2). In the following, an optimization is implemented to identify and compare the optimal thickness of the fire protection mortar in terms of failure time and fire resistance rating during exposure to different fire scenarios. The findings were aimed at ensuring the optimum fire safety level by evaluating the influence of fire conditions on fire protection measures. It is worth mentioning that the accuracy of the FE model has been assessed earlier using the experimental data obtained from fire resistance test as described in reference [20], [22]

Figure 7 and Figure 8 show the axial displacement-maximum temperature curve and vertical displacement of the steel tube column with the fire protection mortar for the 50% axial load level and over one-hour exposure to the natural fire curve obtained using the two-zone model software CFAST. Note that the maximum thickness required for the failure of the column is highlighted in red in all the figures except in Figure 8, as it is not reached for the assumed thicknesses. A huge difference is observed for the optimal thickness and the critical temperature of the steel column between two CFAST fire curves evaluated in this study; one with the hot air temperature exposed to the column at the hot air zone ($CFAST$ I) and the other for the plume air temperature ($CFAST$ II). This huge difference is due to the high temperature (in the range of 1400-1500ºC) of the plume layer at minute 30 of fire exposure, implying the significant influence the plume can have on the fire safety design measurement of the large-space compartment with a localized fire. The optimal thickness is taken using the iterative process for each specified fire protection thickness in the Abaqus, which is around 1-5-2 mm when $CFAST$ I fire curve is applied, while this value is 24-25 mm for $CFAST$ II time-temperature curve. For this case study, it can be concluded that the optimal thickness required for the steel assemblies from the warehouse is overestimated when using the ISO 834 temperature-time curve, provided that the increased temperature arising from the plume air in the hot zone layer is disregarded.

The results from the analyses for the maximum thickness the failure happens are summarized in Table 1, which include the maximum temperature at the column surface (θ_{cr}), the critical time at the failure point (t_{cr}), and fire protection thickness (t_{FP}). It should be noted that ISOI, ISOII, and ISOIII are ISO 834 temperature-time curves corresponding to fire duration of 60 min, 43.5 min, and 30.6 min, respectively. As it is clear from Figure 7 to Figure 12, the optimal thickness is achieved through an iterative process. Accordingly, the optimal thickness for natural fire curve FDS is not reached as the column has been over a short fire period, but the maximum temperature measured on the steel column is significantly smaller than the maximum temperature predicted by the standard ISO temperature-time curve. The analysis results clearly indicate that considering the standard fire curve in the fire safety design of the large space compartment may lead to the underestimation of the actual fire resistance limit of the metal structures, depending on the existing fire scenario.

Table 1:The analysis results on the fire protection optimization of steel the columns under different fire conditions

Fire condition	t_{FP} (mm)	θ_{cr} (ºC)	t_{cr}(min)
$CFAST$ I	1.5	662.928	39.437
$CFAST$ II	24	625.163	54.892
ISO I	10.5	585.952	58.461
ISO II	5.5	583.593	42.62
ISO III	2	582.728	30.109
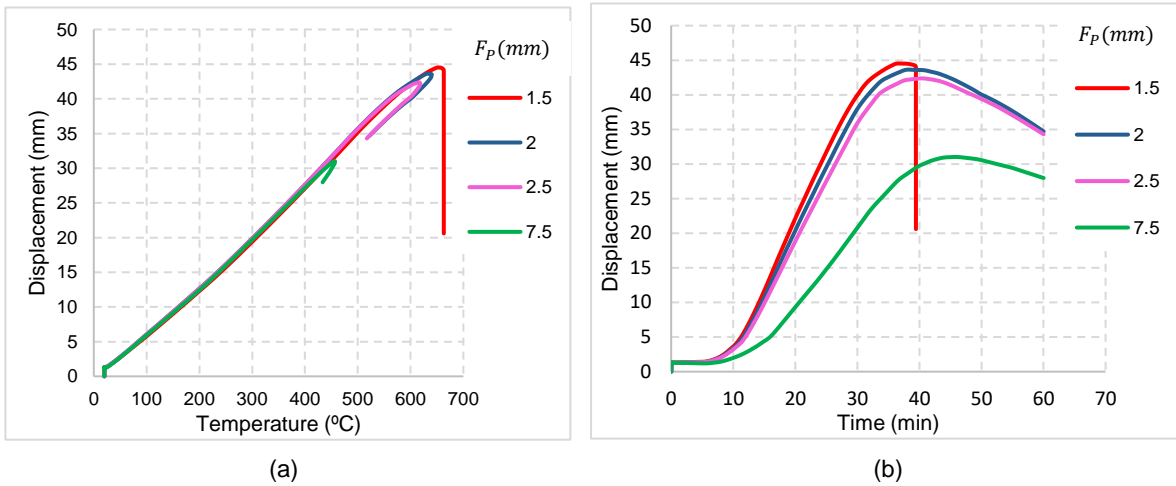
Figure 7: Temperature evolution and (a) and axial displacement-temperature curve (b) of the steel column for different fire protection thickness (F_P) subjected to one-hour $CFAST$ I fire.
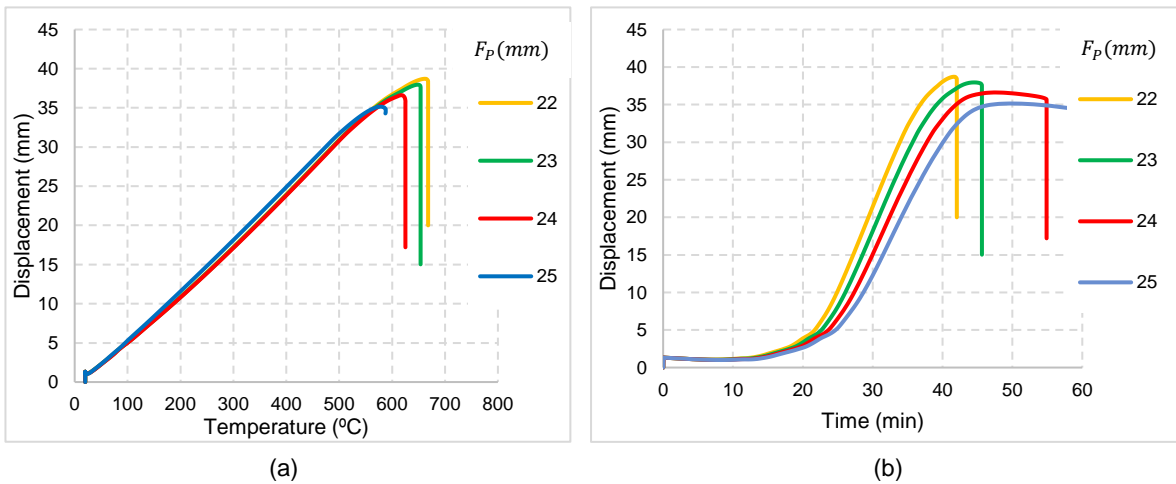
Figure 8: Temperature evolution and (a) and axial displacement-temperature curve (b) of the steel column for different fire protection thickness (F_P) subjected to one-hour $CFAST$ II fire.
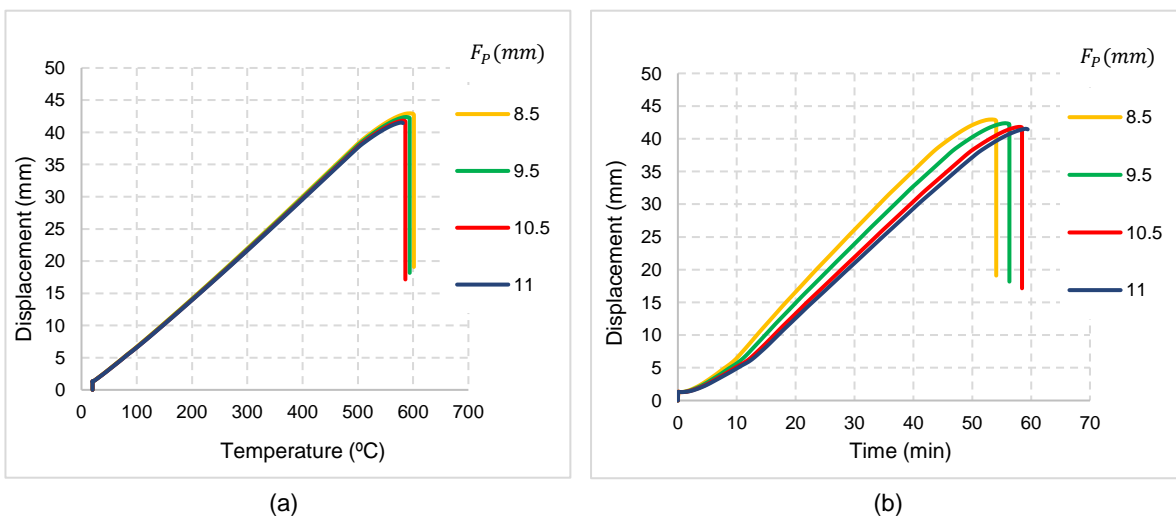
Figure 9: Temperature evolution and (a) and axial displacement-temperature curve (b) of the steel column for different fire protection thickness (F_P) subjected to one-hour ISO fire.
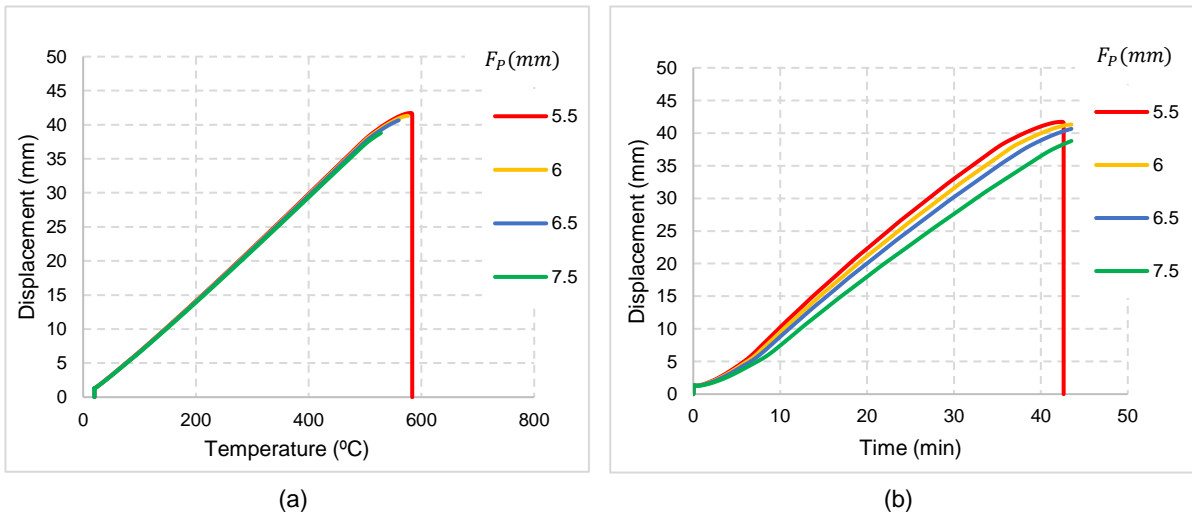
Figure 10: Temperature evolution and (a) and axial displacement-temperature curve (b) of the steel column for different fire protection thickness (F_P) subjected to 43.5 min ISO fire (equivalent time of fire exposure for CFAST).
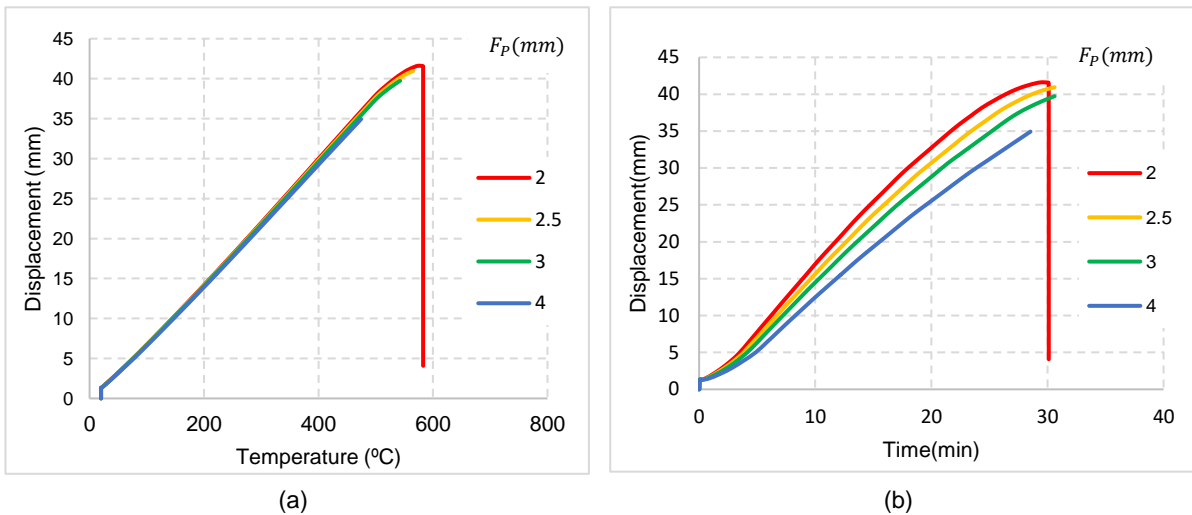
Figure 11: Temperature evolution and (a) and axial displacement-temperature curve (b) of the steel column for different fire protection thickness (F_P) subjected to 30.6 min ISO fire (equivalent time of fire exposure for CFAST).
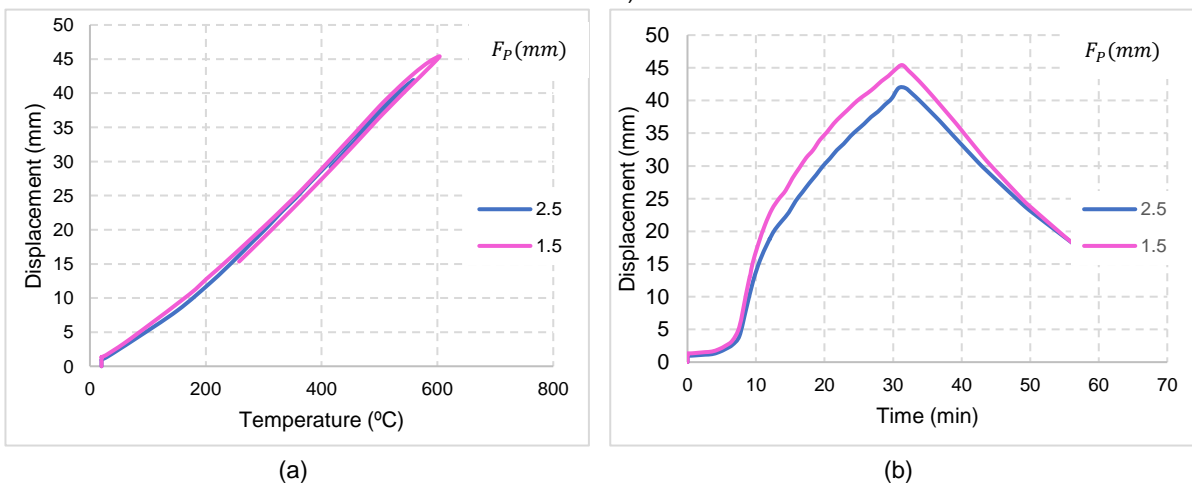
Figure 12: Temperature evolution and (a) and axial displacement-temperature curve (b) of the steel column for different fire protection thickness (F_P) subjected to FDS fire.

129

Figure 13 shows the deformed shape of the protected column at the ultimate load and elevated temperature with the corresponding failure mode, i.e., local-global failure mode.
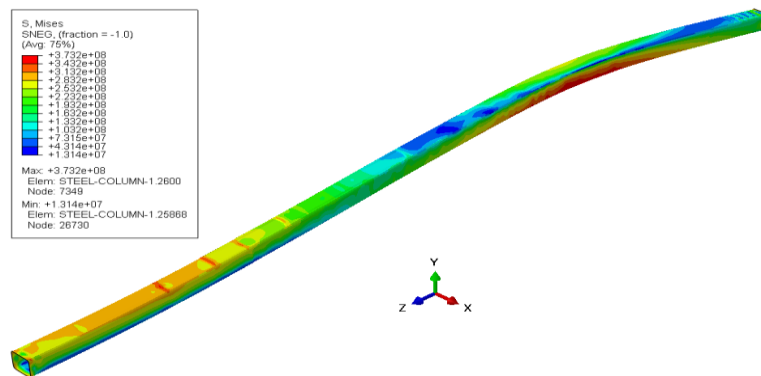
Figure 13: Deformed configuration of the steel column assemblies at failure point

5. PARAMETRIC STUDIES

Figure 14 shows the effect of the cross-section on the displacement-temperature response of the column for 50% load level. The columns had 6 m length and were protected with 10.5 mm fire protection mortar; the thickness was slightly higher than the optimal fire protection calculated for a one-hour ISO 834 temperature-time curve. It is observed that the I-sections HE260B have a higher fire resistance rating than the Square hollow sections (SHS) for all the load levels evaluated in this parametric study, i.e., 50LL, 30LL or 15LL. The differences between the critical temperature and the fire resistance rating for either different cross-sections or load levels are detailed in Table 2: both the fire resistance and the critical temperature are increased up to around 10 % for the I-section column and at different load levels compared to the column with the SHS section 150mm x 150mm x 8mm. This may be consequence of using a load level as a function of the design load bearing capacity of the columns, instead of the respective actual ultimate load.

Error! Reference source not found. shows the failure time-dependence to the load ratio applied on the SHS column during the nonlinear analysis. As the load increased, the failure happened earlier. Therefore, increasing the load level would decrease the critical time and the temperature on the column surface, but this decrease in the critical temperature is recorded higher for I-section HE260B.

Table 2: Main design parameters for parametric studies of the FE model

	50 LL		**30 LL**		**15 LL**	
	θ_{Cr}	T_{Cr}	θ_{Cr}	T_{Cr}	θ_{Cr}	T_{Cr}
HE260B	711.879	73.981	743.552	80.154	849.389	96.336
SHS	662.91	67.717	698.996	72.4595	777.387	88.7
DIFF (**%)**	7.38	9.25	6.37	10.62	9.26	8.6

130
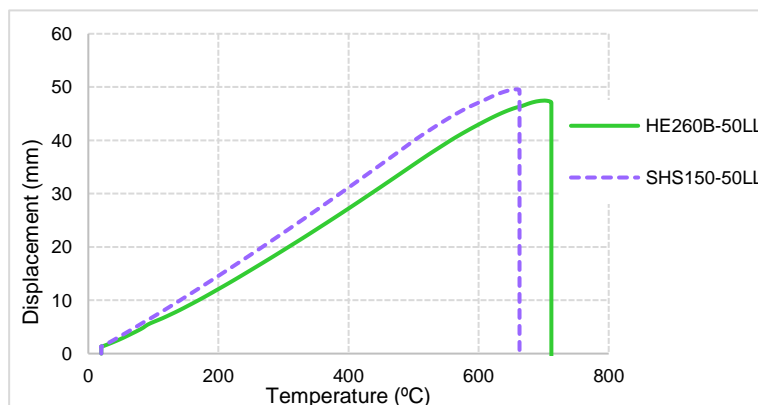
Figure 14: Axial displacement-temperature curve for different cross-sectional configuration of protected steel column.
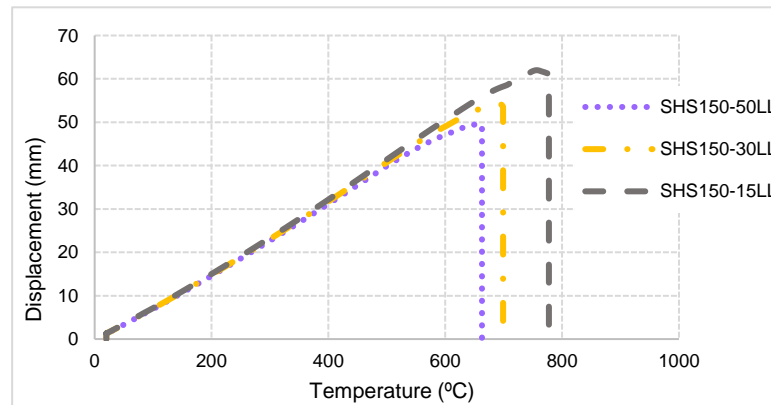
Figure 15: Axial displacement-temperature curve of the protected SHS steel columns for different loading rates.

6. CONCLUSIONS

This paper uses numerical simulations to investigate the behaviour of axially compressive protected column assemblies of an industrial metal warehouse under different fire actions. Some significant conclusions drawn from the present numerical results are summarized as follows:

- Fire models can have a great influence on the fire safety design of industrial metal warehouses. The optimal fire protection thickness computed using a natural fire scenario was much thinner than that predicted by a standard fire scenario.
- The choice of a different cross-sections such as I-sections may end in different critical temperatures, and as a result improving the fire resistance rating of the protected column assemblies from the warehouse buildings, at least up to 10%.
- An increase from 15% to 50% in load ratio speeds the failure of the column at lower temperatures leading to decreasing the fire resistance of the columns until 30%.

7. ACKNOWLEDGEMENTS

8. REFERENCES

[1]   ISO. (1999). ISO 834-1 Fire resistance tests -Elements of building construction, Part 1: General requirements, *International Organization for Standardization, Geneva, Switzerland*, 1999.

[2]   EN 1991-1-2. (2002). Eurocode 1 : Actions on structures - Part 1-2 : General actions - Actions on structures exposed to fire. Brussels, Belgium, European Committee for Standardization, 2002.

[3]   Jones, W.; G. Forney; R. Peacock; P. Reneke. (2000). A technical reference for CFAST: an engineering tool for estimating fire and smoke transport, *NIST Technical Note*, 2000.

[4]   National Institute of Standards and Technology (NIST), "FDS-SMV: Fire Dynamics Simulator (FDS) and Smokeview (SMV),.."

[5]   Zehfuss, J.; D. Hosser. (2007). A parametric natural fire model for the structural fire design of multi-storey buildings, *Fire Saf J*, vol. 42, no. 2, pp. 115–126, 2007, doi: 10.1016/j.firesaf.2006.08.004.

[6]   Szumigała, M.; Ł. Polus. (2015). A comparison of the rise of the temperature of an unprotected steel column subjected to the standard fire curve ISO 834 and to a natural fire model in the office, *Engineering Transactions*, vol. 63, no. 2, pp. 157–170, 2015.

[7]   Laím, L.; A. Santiago; H. Caetano; D. Craveiro; A. Shahbazian. (2022). Numerical analysis and structural fire design of protected SHS steel columns with thermally enhanced gypsum-based mortars, vol. 54, 2022, doi: 10.1016/j.jobe.2022.104629.

[8]   Caetano, H.; L. Laím; A. Santiago; L. Durães; A. Shahbazian. (2022). Development of Passive Fire Protection Mortars, *Applied Sciences*, vol. 12, no. 4, p. 2093, 2022, doi: 10.4324/9781315232140-14.

[9]   Xu, Q.; G. Q. Li; Y. C. Wang; L. Bisby. (2020). An experimental study of the behavior of intumescent coatings under localized fires, *Fire Saf J*, vol. 115, no. November 2019, p. 103003, 2020, doi: 10.1016/j.firesaf.2020.103003.

[10]   Pallares-Muñoz, M. R.; I. Paya-Zaforteza; A. Hospitaler. (2021). A new methodology using beam elements for the analysis of steel frames subjected to non-uniform temperatures due to fires, *Structures*, vol. 31, no. January, pp. 462–483, 2021, doi: 10.1016/j.istruc.2021.02.008.

[11]   Du, Y.; G. Q. Li. (2012). A new temperature-time curve for fire-resistance analysis of structures, *Fire Saf J*, vol. 54, pp. 113–120, 2012, doi: 10.1016/j.firesaf.2012.07.004.

[12]   Malendowski, M.; A. Glema. (2017). Development and Implementation of Coupling Method for CFD-FEM Analyses of Steel Structures in Natural Fire, *Procedia Eng*, vol. 172, pp. 692–700, 2017, doi: 10.1016/j.proeng.2017.02.082.

[13]   Yan, X.; T. Gernay. (2021). Numerical modeling of localized fire exposures on structures using FDS-FEM and simple models, *Eng Struct*, vol. 246, 2021, doi: 10.1016/j.engstruct.2021.112997.

[14]   Woźniczka, P. (2019). Performance-Based Analysis of Older-Type Large-Space Hall in Fire, *Archives of Civil Engineering*, vol. 65, no. 1, pp. 17–29, 2019, doi: 10.2478/ace-2019-0002.

[15]   Eremina, T.; D. Korolchenko; D. Minaylov. (2022). Experimental Evaluation of Fire Resistance Limits for Steel Constructions with Fire-Retardant Coatings at Various Fire Conditions, *Sustainability (Switzerland)*, vol. 14, no. 4, 2022, doi: 10.3390/su14041962.

[16]   Eremina, T.; D. Korolchenko; D. Minailov. (2020). Assessment methods for fire durability of intumescent fire protection coatings, *IOP Conf Ser Mater Sci Eng*, vol. 960, no. 3, 2020, doi: 10.1088/1757-899X/960/3/032038.

[17]   Ferraz, G.; A. Santiago; J. P. Rodrigues; P. Barata. (2016). Thermal Analysis of Hollow Steel Columns Exposed to Localised Fires, *Fire Technol*, vol. 52, no. 3, 2016, doi: 10.1007/s10694-015-0481-2.

[18]   Piroglu, F.; M. Baydogan; K. Ozakgul. (2017). An experimental study on fire damage of structural steel members in an industrial building, *Eng Fail Anal*, vol. 80, no. July 2016, pp. 341–351, 2017, doi: 10.1016/j.engfailanal.2017.06.051.

[19]   Ambroziak, A.; P. Piotrkowski; T. Heizig. (2019). Assessment of technical condition and repair of steel structure elements on the example of fire damage in a warehouse building, *MATEC Web of Conferences*, vol. 284, p. 02001, 2019, doi: 10.1051/matecconf/201928402001.

[20]   Laím, L.; A. Santiago; H. Caetano; D. Craveiro; A. Shahbazian. (2022). Numerical analysis and structural fire design of protected SHS steel columns with thermally enhanced gypsum-based mortars, vol. 54, 2022, doi: 10.1016/j.jobe.2022.104629.

[21]   1993-1-1, E. Eurocode 3 : Design of steel structures - Part 1-1: General rules and rules for buildings.

[22]   Aghabozorgi, P.; A. Santiago; L. Laím; N. Cândido. (2022). Proceedings of the 12th International Conference on Structures in Fire (SiF 2022), in *A parametric study of tubular steel columns protected with gypsum-based mortars under fire load using finite element modelling*, 2022, pp. 693–702.

[23]   1993-1-2, E. (2005). "Design of steel structures. General Rules. Structural Fire Design" European Committe for Standardization, Brussels, Belgium., 2005.

[24]   Peacock, R. D.; P. A. Reneke; G. P. Forney. (2017). CFAST-Consolidated Model of Fire Growth and Smoke Transport (Version 7) Volume 2 : User ' s Guide, *Nist*, vol. 2, no. Version 7, 2017.

[25]   McGrattan, K.; R. Mcdermott; S. Hostikka; J. Floyd. (2010). Fire Dynamics Simulator (Version 5) User ' s Guide, *Nist Special Publication*, no. Version 5, 2010.

[26]   Molkens, T.; B. Rossi. (2021). *On the Simulation of Real Fire for Post Fire Resistance Evaluation of Steel Structures*, vol. 57, no. 2. Springer US, 2021. doi: 10.1007/s10694-020-01025-6.

A REVIEW OF THE COLLAPSE OF INDUSTRIAL STEEL BUILDINGS IN CASE OF FIRE
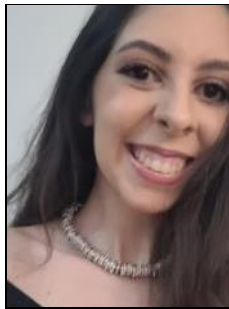
**Maria Luiza C.
Moreira [a,*]**

**João Paulo C.
Rodrigues [b]**

ABSTRACT

Fires in industrial buildings have been increasing in recent years and, with great destructive potential due to the high fire loads inside, can endanger occupants and property. In this sense, regulations stand out, such as the French standard, which prescribes that an eventual collapse of this type of structure must occur towards its interior, considered a safe failure mode. Hence, it becomes relevant to study the fire behavior of these structures. Therefore, this work aims to review the literature that addresses the fire behavior of industrial buildings in steel structures with aspects related to experimental tests, numerical analysis, fire modeling, as well as structural behavior. In this sense, discuss studies analyzing the structure's failure mode and the influence of fire load and protection in this type of building. Also, as a crucial factor in the structure's collapse, the formation of plastic hinges and their position, depending on the fire extent, will be discussed.

Keywords: fire behavior; industrial; steel structure; research; fire.

1.   INTRODUCTION

Industrial fires are a reality that is present in a representative manner in several countries, causing a high loss of human life and patrimony. According to a report elaborated by National Fire Protection Association (NFPA) [1], in the US, between 2011 and 2015, an average of 37,910 fires in industrial and manufacturing buildings was reported annually.

Within this context, building design considering fire becomes relevant since fire causes substantial changes in the material's properties and induces thermal elongation. In a structure, due to the restraining imposed by the surrounding elements, such as elongation, generates an increase in stresses that can lead to the occurrence of instabilities [2].

---

[a]***** Universidade Federal de Minas Gerais, marialuizacalderaro@ufmg.br**,** Corresponding author**.**

[b,] Universidade de Coimbra, Portugal and Universidade Federal de Minas Gerais, Brazil, jpaulocrod@ufmg.br.

Regarding fire dynamics, industrial buildings differ from other types of buildings, an aspect that must be considered in fire safety design. According to Cosgrove [3], the development of fire in industrial halls has, in general, its evolution as represented in Figure 1.
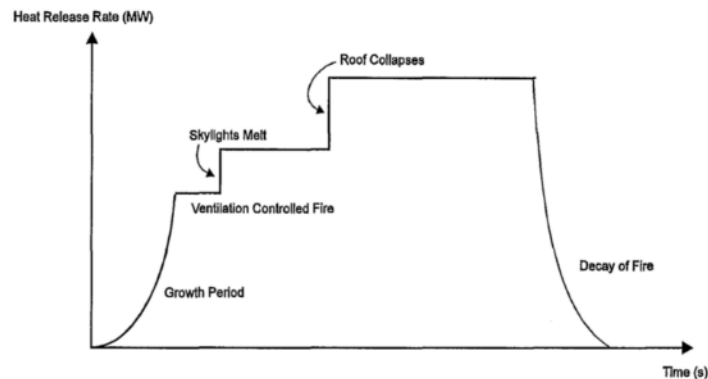
Figure 1 Fire Development Profile for Single Story Building [3]

Three phases are verified: fire growth, steady-state condition, and decay. In the first one, growth occurs until flashover or fuel burning. Then, in the second phase, the fire can be governed by the effect of ventilation or the fuel available for burning. In this phase, the skylights and roofs begin to burn, which will feed the fire through the entry of oxygen. Once all the fuel has been consumed, the fire enters a third phase, the decay phase.

Bong [4] argues that in a larger industrial building, there are changes in the dynamics and behavior of fire. Due to the higher compartment volume and higher ceilings, in the initial stages, the fire plume will enter a large volume of the cold air layer. With the fire development, the cold air will continue to enter the ceiling jet and will not have the conditions required to cause flashover.

Therefore, as seen in Figure 1, the fire is initially controlled by fuel availability. Because of that, it has a non-uniform temperature distribution, being more severe in the ignition region. Thus, the structure within this area will be more affected and more likely to suffer from instabilities in compressed elements [4].

Steel undergoes changes in its microstructure at high temperatures, reducing its strength and stiffness. Thus, it will be more susceptible to fire action and subject to instabilities and even the collapse of the structure. Industrial buildings, due to regulatory requirements, must have inward collapse mode. And therefore, numerical and experimental studies have been conducted to evaluate the behavior of these structures and to guarantee safe failure mode. This point is relevant for the safety of neighboring buildings, firefighters, and people around the building.

In this sense, this research will provide an overview of the fire behavior of steel structures in industrial buildings, aspects related to fire modeling, numerical analysis, and experimental tests conducted in this field.

2. STUDIES ON OVERALL STRUCTURAL BEHAVIOR

2.1. Fire Modeling

To predict physical properties within a compartment in a fire situation, such as temperature, gas concentration, or internal pressure, experimental tests and numerical simulations for fire modeling can be carried out. As tools to numerically predict those properties, mathematical formulations can be used through stochastic or deterministic methods.

Stochastic models, for instance, are based on probabilistic models to predict fire evolution. Deterministic models, however, obtain the solution from mathematical formulations governing the physical and chemical behavior of fire [5]. This approach is more frequently implemented in software and, has as an example, the two-zone models and the field models.

The field model is based on the computational fluid dynamics (CFD) model and describes fire dynamics with higher precision. In this model, the geometry is discretized in volume elements. The theoretical basis consists in solving transport equations, considering the conservation of mass, momentum, and energy, combined with physical models of turbulence, combustion, and radiation [6,7] (Figure 2).
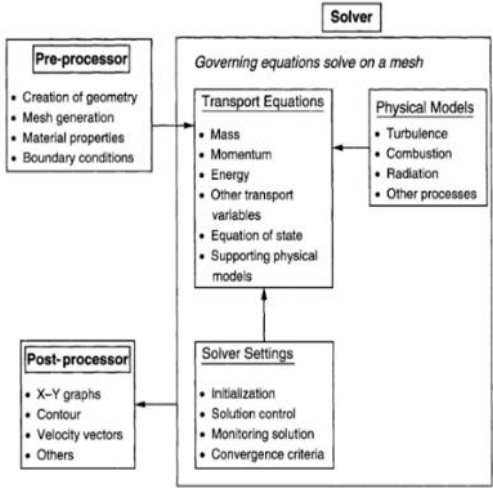
Figure 2 CFD analysis parameters [6]

A numerical and experimental study conducted by Vigne et al. [8] aimed to study the smoke dynamics in a cubic atrium measuring 20 meters, using experimental tests and numerical simulation in FDS (Fire Dynamics Simulator), software developed by NIST for analysis of fire dynamics in CFD (Figure 3).

(a) (b) (c)
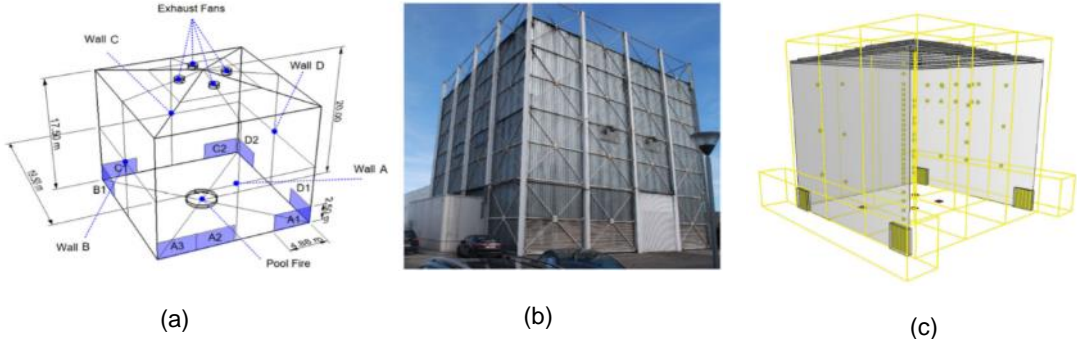
Figure 3 (a) Geometrical sketch (b) Built structure (c) Numerical model on FDS [8]

The authors aimed to evaluate how the existence of four heat sources, ignited at different times, collaborate to fire development. Four pans with a diameter of 0.92 m filled with n-heptane and a combined heat release rate of 5.2 MW were used (Figure 4). The temperature was measured inside the compartment with the installation of 59 thermocouples.

(a) (b)
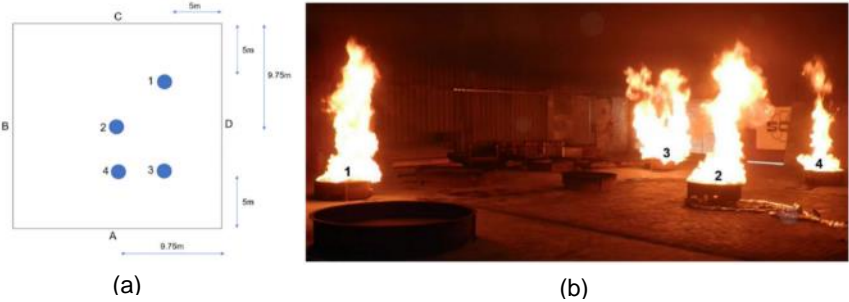
Figure 4 (a) Pan positions (b) Pan ignition during experiment [8]

135

Initially, regarding the analysis to numerically simulate fire spread, the experiment performed by Vigne et al. [8] was compared to other experiments with a single heat source, with the result data presented in Table 1.

Table 1 Comparison of single and multiple heat sources experimental results [8]

| t (sec) | Single Heat Source | | | | Multiple Heat Sources | |
| | Experiment 1 | | Experiment 2 | | | |
	HRR (MW)	Smoke Layer Interface Height (m)	HRR (MW)	Smoke Layer Interface Height (m)	HRR (MW)	Smoke Layer Interface Height (m)
270	5.20	4.30	5.30	4.80	3.40	3.90

The authors concluded that multiple heat sources resulted in a more severe environment inside the compartment. Experimental data analysis detected a drastic drop in the smoke layer interface height, reaching 3.90 meters in 270 seconds, a thicker layer than compared with a single heat source experiment, as seen in Table 1.

Furthermore, because the heat sources had different ignition times, at 270 seconds, the measured HRR was up to 55.88% lower than the single heat source cases, and yet the smoke layer interface height was 23.08% thicker. This fact demonstrates a higher capacity for smoke production, explained by the higher turbulence and airflow in this situation. In addition, a layer of smoke with lower temperatures (about 50°C difference) and less uniformity was observed.

And therefore, it highlights the importance of evaluating more complex fire conditions and the assessment of fire spread, which directly impacts the subsequent structural behavior.

Similarly, Chao et al. [2] compared the results of experimental tests and numerical simulations for fire modeling. In this case, the authors aimed to analyze the beam fire-thermal-structural behavior. And therefore, initially determining the fire spread, experimentally and numerically. Based on the results obtained, perform a thermomechanical analysis to study the structural behavior.

The apparatus used for the experimental tests and the FDS model is seen in Figure 5. Illustratively, the flame was obtained numerically and experimentally, as seen in Figure 5c. And therefore, it is possible to observe the influence of mesh refinement on the results.

(a)   (b)

(c)
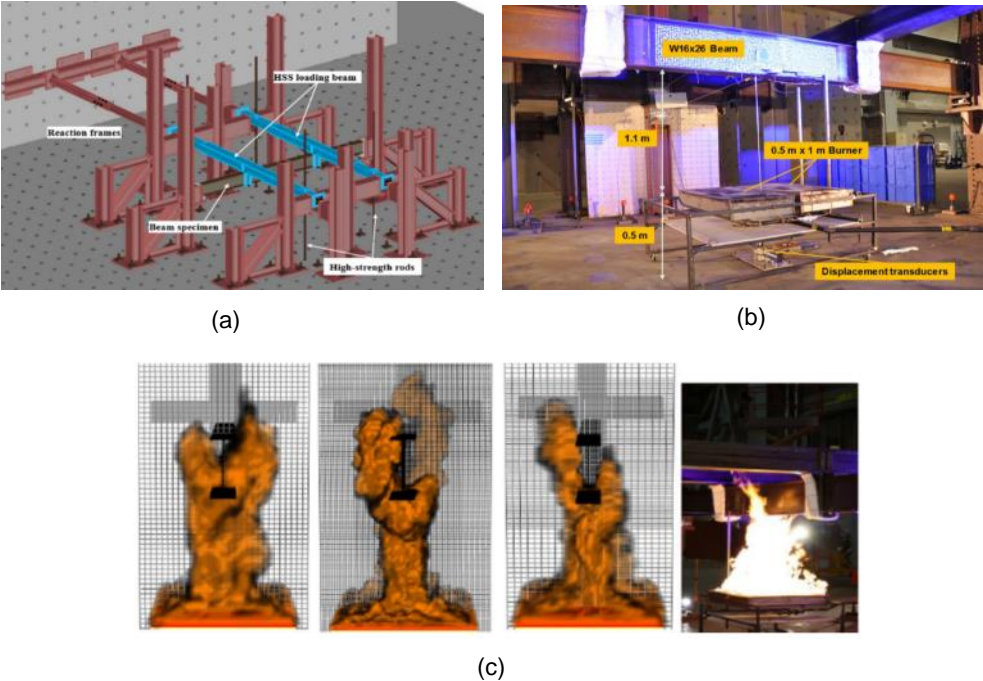
Figure 5 (a) Test apparatus numerical modeling (b) Test structure c) Comparison of flame results in numerical simulation on FDS with different mesh sizes and during test [2]

The performed experiments, according to Chao et al. [2], have measuring uncertainties, with an estimated error of approximately ±12%. The FDS, software used, predicts good results and, according to [9], percentage differences within the uncertainty of the test. Therefore, a valid tool for fire modeling.

2.2. Fire Resistance of the structure

The increase in temperatures significantly impacts the physical properties of steel, such as strength and stiffness. And therefore, fire is a critical situation for the structure's integrity [10].

In this sense, as required by the Arrêté du 17 août 2016 [11], in industrial buildings, aiming for the safety of people around, firefighters and to contain the fire spread to neighboring buildings, an eventual collapse of the structure must be inward.

Newman et al. [12] explained the behavior of symmetrical pitched portal frames. In the initial moments of the fire, there is the heating and consequent elongation of the rafters, causing a small deflection of the eaves towards the outside, combined with an upward deflection of the apex. As the fire progresses, an increase in bending moments in the elements and the formation of plastic hinges can be observed, with the probable positions shown in Figure 6a.

Proceeding the rafter's collapse, the condition shown in Figure 6b will resemble a catenary. This behavior induces inward movement of the tops of the columns and an overall collapse of the structure.
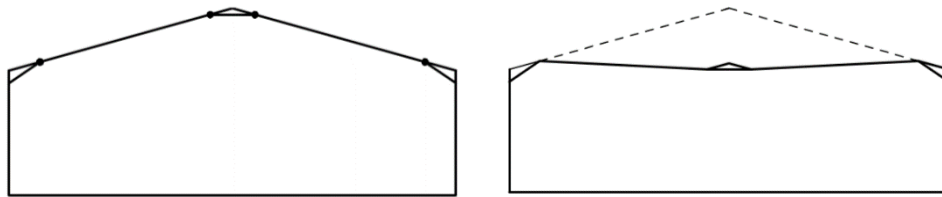
Figure 6 a) Fire induced plastic hinges probable positions b) Rafter collapses to eaves level [12]

The behavior observed by Newman et al. [12] is described by the subsequent authors based on numerical analyzes and experimental tests.

2.2.1. Numerical analysis on the prediction of fire behavior of steel frames

To evaluate the failure mode of the structure in a fire situation, Vassart [13] analyzed 2D frames. During heating, are mainly two phases. Within the first was observed elongation of the heated elements, causing a progressive increase in internal forces due to the restraining provided by the colder elements. As the structure continues to heat, it reaches the second phase with excessive deformations and consequent collapse (Figure 7).
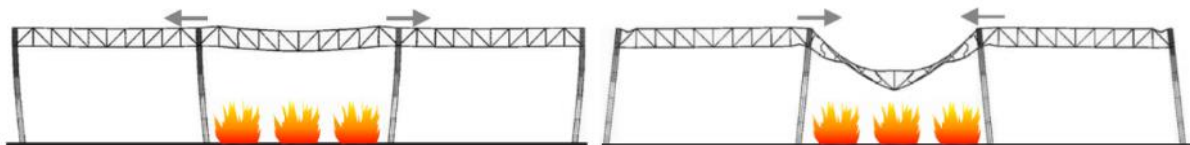
Figure 7 Fire induced horizontal displacements [13]

Similar behavior was obtained by Ali et al. [14]. Parametric analyzes carried out evaluated the behavior of a 2D steel frame. For this purpose, static structural analysis was initially performed at an ambient temperature. Then,

based on the deformed structure, inserted the temperature variation. The effect of geometric and material non-linearity and fluency were also considered.

The analyzes were validated with previous experimental tests, presenting a 10% error. In Figure 8, it is possible to observe the failure modes of a 2D steel frame, with emphasis on Types I and II. Type I collapse mode occurs due to the initial heating of the girders, causing elongation of the element and lateral displacement at the ends of the columns towards the outside. As the heating continues, formed plastic hinges. From that point on, there is a substantial increase in the beam's deflections, generating a catenary and favoring the collapse of the structure towards the interior.

Type II occurs when the fire is closer to one of the end columns. Due to the fire location, the girders do not heat enough for the catenary to form. With an increasing temperature, there is a loss of stiffness in the columns until their buckling. In this type of failure, there is a prevalence of lateral displacement of the structure and, consequently, the collapse towards the outside.
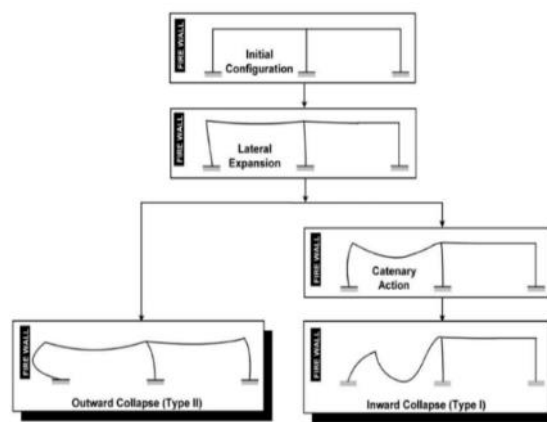
Figure 8 Types of failure on single-story steel frames [14]

Through parametric analysis of the frame shown in Figure 8, the authors evaluated the influence of the fire load position, loading, and column cross-section. As the extent of the fire changes, there is a modification in the structure's failure mode (Type I or Type II) and, in addition, results in a greater lateral displacement when the whole structure is exposed to fire.

The authors concluded that the load increase collaborated to reduce the time until collapse. 102 minutes with a load of 1.5 kN/m, 49 minutes for 12.5 kN/m, and 26 minutes for 25 kN/m. In addition, this alteration also caused a reduction in the maximum lateral displacement, and the collapse occurred at lower temperatures. Overall, the authors explained the earlier formation of plastic hinges as a consequence of greater stress on the structural elements.

In addition, the authors concluded that the height of the building also influences the collapse time and maximum lateral displacement. The higher the frame, the shorter the time until beam or girder failure and the smaller the horizontal displacements. Fluency is also relevant, particularly when increasing the building's height. Considering a 6 meters high frame, the lateral displacements were up to 4% higher with the creep considered. As for 9 to 12 meters, up to 12%.

Analyzing the behavior of 3D frames, Bong [4] studied a steel structure with a floor plan of 30 x 40 meters and cross sections of the elements shown in Figure 9.
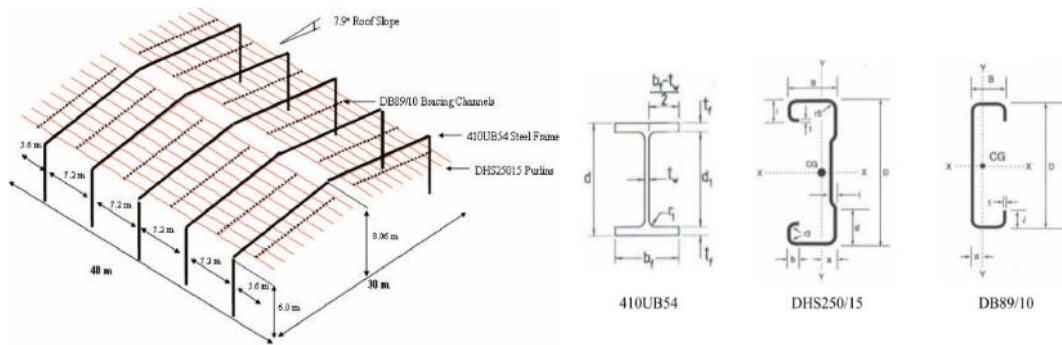
Figure 9 Steel Structure Design [4]

The structure was analyzed in the Finite Element Method to evaluate the influence of different column support conditions and axial and out-of-plane constraints.

Table 2 Analysis parameters [4]

Analysis number	Description of location and severity of fire	Support conditions	Purlin Axial Restraints	Mode of Failure	Simulation End Time* (minutes)
(1)	Fully developed fire	Fixed	Yes	Catenary	18.5
(2)		Pinned	Yes	Sway	19.6
(3)	Localised fire near centre of building	Fixed	Yes	Catenary	60.0
(4)		Pinned	Yes	Sway	60.0
(5)	Localised fire near end of building	Fixed	Yes	Catenary	60.0
(6)		Pinned	Yes	Sway	60.0
(7)	Fully developed fire	Fixed	No	Inwards	14.9
(8)		Pinned	No	Sway	14.1
(9)	Localised fire near centre of building	Fixed	No	Catenary	60.0
(10)		Pinned	No	Sway	60.0
(11)	Localised fire near end of building	Fixed	No	Inwards	20.5
(12)		Pinned	No	Sway	18.5
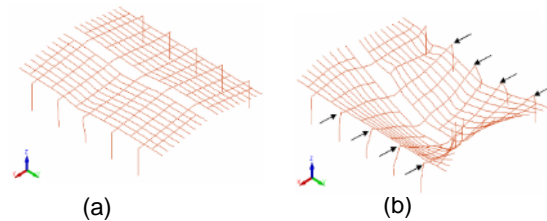
Figure 10 Simulation Results – Structure collapse (a) Analysis 3, t = 60 min (b) Analysis 7, t = 14.92 min [4]

The author highlights the results from the analysis carried out with the contained fire (Figure 10a) and fully developed fire (Figure 10b). With the fire located in only a portion of the building, the load is transferred, so the members with lower temperatures act, supporting the warmer and less resistant members, allowing the structure to endure more time.

Another conclusion of the analysis is that the columns' support condition also influences the collapse mode of the structure, as pinned supports tend to collapse towards the outside. In addition, as seen in Figure 10b, representing analysis 7, with pinned supports, there is greater verticality of the columns, and the collapse occurs mainly on the roof.

To assess the influence of plastic hinges on the structure's collapse mode, O'Meagher et al. [15] carried out a series of numerical analyzes, considering several structural heating conditions and how they influence the collapse. The situations considered comprise the entirely heated structure (Situation G) and partially heated due, for example, to the presence of protection (Situations A – F) in Figure 11.
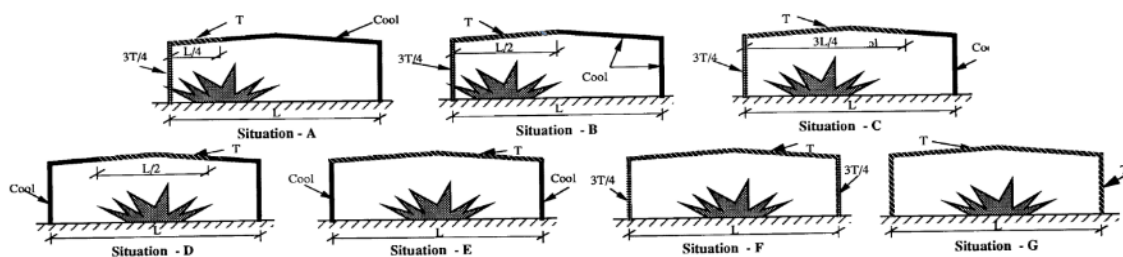
Figure 11 Heating situations analyzed [15]

The situations described in Figure 11 were analyzed, varying the span, wind force, and restrained stiffness. As a result, when the rafter is partially heated, plastic hinges form close to or in the division between the cold and heated parts.

For comparative purposes, the results are shown in Figure 12, and data are summarized in Table 3.
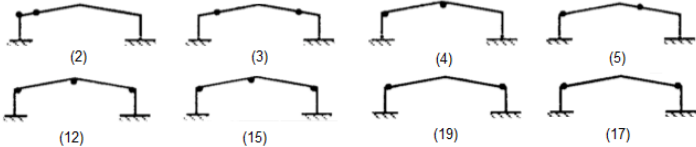
Figure 12 Analysis Results - Plastic Hinges [15]

Table 3 Analysis Parameters

Case	Situation	Wind Force (kN)
2	A	3.0
3	D	3.0
4	B	3.0
5	C	3.0
12	F	-
15	E	-
19	G	-
17	G	-

The authors considered the outward collapse mode to be unacceptable. Among the 20 analyses, cases 17 and 19 showed an unsafe failure mode and, in a real situation, they should be evaluated. In both cases, this analysis refers to situation G, in which the entire structure is heated. In this sense, it is concluded that the protection, even if partially, prevents the collapse in an unsafe way.

In addition, it is also possible to observe that the presence of a resistant moment at the base also contributes to the collapse occurring inwards. In cases 17 and 18, shown in Table 4, this consideration allows a safe failure mode.

Table 4 Influence of Base Restraint in Failure Mode

Case	Situation	Span (m)	Wind Force (kN)	Base restraint (kN/rad) x10^{-3}	Formation of plastic hinges and failure mode acceptance	
17	G	17	-	-		Unacceptable
18	G	17	-	1500		Acceptable

In a 3D frame, the failure mode analysis, in addition to the variables already mentioned, also includes the fire extent within the building. In this sense, different structural behaviors are expected if the fire is concentrated in a region or taking over the entire area. In the case shown in Figure 13, the fire is contained in the right portion of the building. Due to the higher temperatures present in the region, the structure begins to fail. After its collapse, this portion will function as an "anchor" for the rest of the structure. Additionally, it dictates that an eventual global collapse of the structure occurs safely, toward the interior.
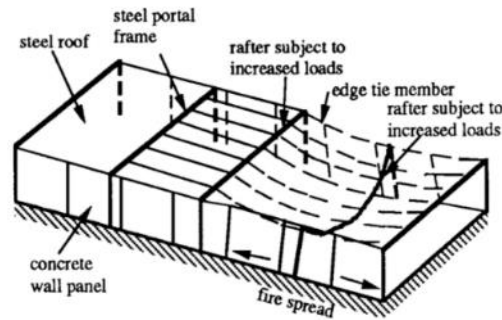
Figure 13 Building behavior to fire [15]

2.2.2. Experimental and numerical evaluation

In a study carried out by Lou et al. [16], experimental tests and numerical analysis were carried out on a 3D frame of 12 x 6 meters and 5.4 meters high, and a fire compartment with 4 x 6 meters, located on the left portion of the building (Figure 14a).
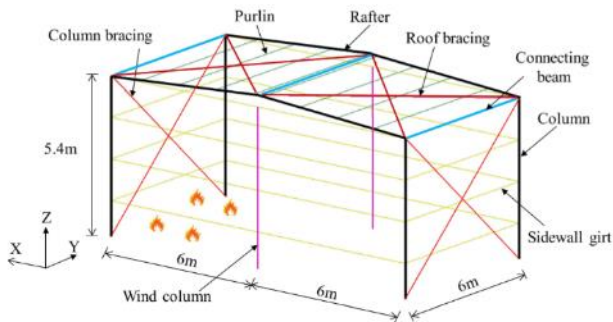
Member	Symbol	Cross section (mm)	Yield strength (MPa)
Frame column	Z1~Z4	H200 × 150 × 6 × 8	345
Wind column	KFZ1, KFZ2	H200 × 150 × 6 × 8	
Rafter	L5~L8	H200 × 150 × 6 × 8	
Column bracing	–	Φ16 × 3	
Roof bracing	–	Φ16 × 3	235
Purlin	–	C140 × 60 × 20 × 3	
Connecting beam	LG1~LG3	Φ125 × 5	
Wall girt	–	C140 × 60 × 20 × 3	

(a)

(b)

Figure 14 (a) Structural frame layout (b) Elements cross sections [16]

In the experiment, was measured the temperatures and deformations in the structure and coating. The test lasted 33 minutes. At 5 minutes, the fire was already severe, with visible deformation in the facade and roof. At 10 minutes, flames were coming out the windows, and significant deformation of the coating was already visible. At 20 minutes, the structure began to collapse due to the buckling of the columns. At this time, the surrounding gas was at 900°C.

141

The tested structure did not effectively collapse as it was supported by the firewall. In numerical analysis, the structure was taken to collapse, observing by the lateral displacement a tendency to collapse towards the outside (Figure 15b).

(a)   (b)

Figure 15 (a) Structure post-fire (b) Numerical simulation displacement results [16]

As observed in the test, the structural elements exposed to the fire were seriously compromised and perceived instabilities, but it was proven that there was no failure in the connections.

In addition, due to the fire load position, a non-uniform distribution of temperatures was observed in the thermocouple readings. That contributed to the behavior obtained in the numerical analysis of the prevalence of horizontal displacements in structural collapse. In addition, through measurements, it was verified that the temperature rises in the upper layer differed from that predicted by ISO 834 [17], being up to 300°C higher. On the other hand, the parametric curve of EN1993-1-2 [18] was 200°C below test measurements.

Such outward collapse behavior was explained by Ali et al. [14]. There are two structural collapse modes, the interior, and exterior. The first occurs when the heating of the beams causes a catenary and consequent displacement of the top of the columns, resulting in a collapse towards the interior. The second situation is more likely to occur when the fire is closer to a column or a corner. Thus, with heating and lateral displacement, without an excessive increase in beam deflection, there is a tendency for lateral displacements to prevail, causing collapse towards the outside.

The structural failure mode was studied by Roy et. al [19]. The authors conducted experimental tests in a cold-formed steel structure shed (Figure 16). Through numerical analysis in Abaqus, it was concluded that the software predicted the failure mode and the collapse temperature of the structure with accuracy, with a difference lower than 1%.

(a)   (b)

Figure 16 Structural design (a) 3D view (b) Front view elevation [19]

Due to the non-uniform fire load distribution in the building and the protection of only one wall with Gypsum boards, the structure collapsed asymmetrically but towards the interior (Figure 17).

(a)

(b)

Figure 17 Structure during experiment (a) non-symmetrical collapse (b) Inward structural collapse
(t = 38 min) [19]

The structure collapsed at 21:30 minutes of testing, with a temperature and 622.5 ºC due to buckling. Plastic hinges were formed on the steel studs, represented schematically in Figure 18. It is also possible to observe the asymmetric collapse due to the protection in only one of the walls.
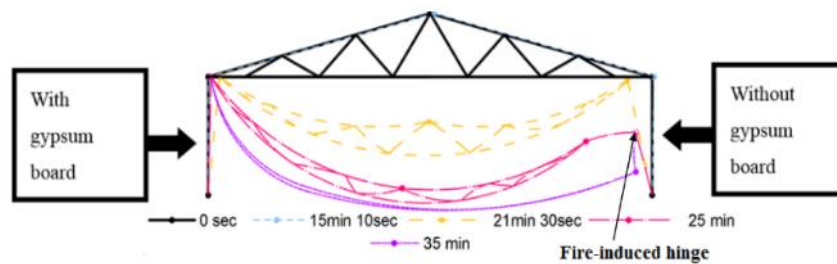
Figure 18 Structural deformation as a time function [19]

The structure was also analyzed with Abaqus, considering non-linearity and elastoplastic behavior. The authors partially modeled the original structure, containing two trusses and their respective supporting walls to represent its central portion.

The numerical analysis predicted the collapse of the structure at 22 minutes (2.33% above that observed in the experimental test) and at 628.2 ºC (0.92% higher), as shown in Figure 19a. The deformation of the structure was also compared, and the behavior observed in the experimental test was satisfactorily predicted by numerical analysis (Figure 19b).

(a)

(b)

Figure 19 (a) Structure deformation obtained by numerical analysis (b) Experimental and
numerical structural deformation comparison [19]

143

As conclusions of the study, the steel structure with cold-formed profiles behaved as expected. Despite the non-uniform fire load distribution, the collapse occurred towards the interior due to the south wall, protected with Gypsum panels. Additionally, the collapse of roof trusses, formation of plastic hinges, and instabilities in the structure also occurred. The numerical analysis conducted satisfactorily predicted the structural behavior, as well as the failure mode and collapse temperature. Thus, a valid tool for studying the behavior of this type of structure in a fire situation.

Chao et al. [2] also performed numerical and experimental studies. After analyzing the fire spread experimentally and in CFD, using FDS (Figure 5), the authors evaluated the failure behavior upon loading. To this end, was measured the beam's mid-section vertical displacement in both static and transient analysis (Figure 20). Lateral torsional buckling was responsible for failure in both analyses.

(a)   (b)
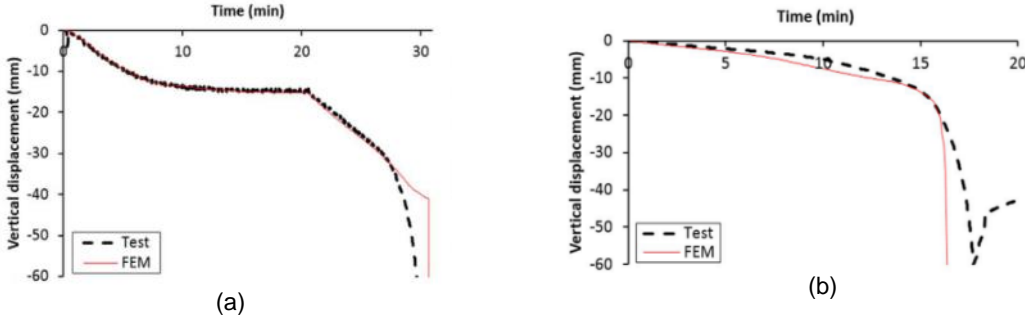
Figure 20 Vertical displacement predicted and measured (a) Static analysis (b) Transient analysis [19]

In Table 5, it is possible to verify the difference between the measured and predicted for both analyses. Errors lower than 10% were obtained, a satisfactory result according to the authors and within the uncertainties of experimental tests.

Table 5 Time, temperature and failure load comparison for static and steady-state analysis regarding experimental and numerical analysis [19]

	Numerical	Experimental	Difference
Static analysis			
Failure Time (s)	30.80	30.60	0.7%
Failure Temperature (°C)	635	654	-2.9%
Failure Load (kN)	102	100	2%
Steady-state analysis			
Failure Time (s)	16.50	17.7	-6.8%
Failure Temperature (°C)	640	706	9.3%

2.3. Effect of protection on fire behavior

Protective materials can be utilized in structural steel elements to limit the structure loss of resistance and stiffness. Their principle is to delay the increase in steel temperatures, prevent the structure from collapsing, and also have an impact on its failure mode.

To assess the effect of protection on the structural integrity, Roy et. al [19], in their experimental test, previously mentioned in Section 2.2.2, used 15mm Gypsum panels on the south wall of the compartment (Figure 16a). The post-test condition for both protected and unprotected walls can be seen in Figure 21.

Figure 21 Influence of protection on the structure integrity. a) Northern wall, without Gypsum protection b) Southern wall with Gypsum boards [19]

As concluded by the author, the protection delayed the measured temperature by 45% and collapse time by 46%. And, in the protected wall, the elements remained vertical. Therefore, adding protection to even just one wall allowed the structure to collapse inwards. In its absence, [19] states that the collapse would occur in an unsafe mode to the exterior of the building.

3. FINAL CONSIDERATIONS

A literature review on the fire behavior of industrial steel buildings was conducted. Among the most relevant aspects dealt with, the failure mode of the structure stands out, which, prescribed in countries like France, states that the collapse must occur towards the interior to protect people around and the fire crew working to put out the flames. As a relevant contribution, the study by O'Meagher et al. [15], through a series of numerical analyses, studied the formation of plastic hinges in the structure. The results helped to understand their prevailing position, linked to a safe failure mode. Therefore, as reviewed, the protection can be used as a mechanism not only to delay the structural heating and resistance loss but also to guarantee an inward collapse. That statement was verified by studies in both rolled and cold-formed steel. That is a pertinent design aspect and is required by several countries. In Brazil, however, a regulation in this field is still lacking, and the study of failure modes and structural collapse is relevant to support a future standard.

REFERENCES

[1] R. Campbell, "Fires in Industrial and Manufacturing Properties," 2018. [Online]. Available: www.nfpa.org/101

[2] C. Zhang, H.-X. Yu, L. Choe, J. Gross, and G.-H. Li, "Simulating the fire-thermal-structural behavior in a localized fire test on a bare steel beam," *Eng Struct*, vol. 163, pp. 61–70, May 2018, doi: 10.1016/j.engstruct.2018.02.036.

[3] B. W. Cosgrove, "Fire design of single storey industrial buildings," University of Canterbury, 1996.

[4] M. W. Bong, "Structural fire performance of steel portal frame buildings," University of Canterbury, 2005.

[5] M. L. Janssens, *Introduction to Mathematical Fire Modeling*, 2nd Edition. CRC Press, 2000. doi: 10.1201/9781482279009.

[6] J. Tu, G. H. Yeoh, and C. Liu, *Computational fluid dynamics: a practical approach*. Butterworth-Heinemann, 2018.

[7] G. Cox, "Turbulent closure and the modeling of fire by using computational fluid dynamics," *Philosophical Transactions of the Royal Society of London. Series A: Mathematical, Physical and Engineering Sciences*, vol. 356, no. 1748, pp. 2835–2854, Dec. 1998, doi: 10.1098/rsta.1998.0300.

[8] G. Vigne, W. Węgrzyński, A. Cantizano, P. Ayala, G. Rein, and C. Gutiérrez-Montes, "Experimental and computational study of smoke dynamics from multiple fire sources inside a large-volume building," *Build Simul*, vol. 14, no. 4, pp. 1147–1161, Aug. 2021, doi: 10.1007/s12273-020-0715-1.

[9] K. McGrattan, "Verification and validation of selected fire models for nuclear power plant applications, volume 7: Fire Dynamics Simulator (FDS)," *Final Report, NUREG-1824, EPRI*, vol. 1011999, 2007.

[10] G. Băetu, T.-F. Gălăţanu, and S.-A. Băetu, "Behavior of Steel Structures under Elevated Temperature," *Procedia Eng*, vol. 181, pp. 265–272, 2017, doi: 10.1016/j.proeng.2017.02.388.

[11] França, *Arrêté du 17 août 2016 relatif à la prévention des sinistres dans les entrepôts couverts soumis à autorisation sous la rubrique 1510, y compris ceux relevant également de l'une ou plusieurs des rubriques 1530, 1532, 2662 ou 2663 de la nomenclature des installations classées pour la protection de l'environnement*. França, 2016, p. 11. Accessed: Feb. 23, 2023. [Online]. Available: https://www.legifrance.gouv.fr/loda/id/JORFTEXT000033117556/?isSuggest=true

[12] W. Simms and G. Newman, "Single storey steel framed buildings in fire boundary conditions," 2002.

[13] O. Vassart *et al.*, *Fire Safety of Industrial Halls and Low-rise Buildings: Realistic Fire Design, Active Safety Measures, Post-local Failure Simulation and Performance Based Requirements*. EUR 22568, 2007.

[14] H. M. Ali, P. E. Senseny, and R. L. Alpert, "Lateral displacement and collapse of single-story steel frames in uncontrolled fires," *Eng Struct*, vol. 26, no. 5, pp. 593–607, Apr. 2004, doi: 10.1016/j.engstruct.2003.12.007.

[15] A. J. O'MEAGHER, I. Bennetts, P. Dayawansa, I. Thomas, and others, "Design of Single Storey Industrial Buildings for Fire Resistance," *Steel Construction*, vol. 26, no. 2, 1992.

[16] G. Lou, C. Wang, J. Jiang, Y. Jiang, L. Wang, and G.-Q. Li, "Experimental and numerical study on thermal-structural behavior of steel portal frames in real fires," *Fire Saf J*, vol. 98, pp. 48–62, Jun. 2018, doi: 10.1016/j.firesaf.2018.04.006.

[17] ISO, *ISO 834-1:1999 - Fire-resistance tests — Elements of building construction — Part 1: General requirements*. 1999.

[18] CEN, *EN1993-1-2 - Eurocode 3: Design of steel structures - Part 1-2: General rules - Structural fire design*. 2005.

[19] K. Roy *et al.*, "Collapse behaviour of a fire engineering designed single-storey cold- formed steel building in severe fires," *Thin-Walled Structures*, vol. 142, pp. 340–357, Sep. 2019, doi: 10.1016/j.tws.2019.04.046.

NUMERICAL-EXPERIMENTAL INVESTIGATION OF FIRE PERFORMANCE IN INDUSTRIAL BUILDING FAÇADE CLADDING SYSTEMS

Deives J. de Paula[a]; João Paulo C. Rodrigues[b]; Aline L. Camargo[c]; Rúben F. R. Lopes[d]

ABSTRACT

Facades are essential components of buildings that contribute to their aesthetic and functional appearance, but they can also play a significant role in spreading fires, as evidenced by the Grenfell Tower tragedy. To enhance building fire resilience, predicting fire behaviour on facade cladding systems is a critical role. Several studies have used computational fluid dynamics software to investigate the effects of fires on external cladding systems, with a focus on tall and very tall buildings for offices or housing. However, few studies have explored the impacts of forest fires in industrial buildings, which can have direct consequences for industrial activity and result in direct and indirect economic losses. The 2017 Great Forest Fires in Portugal caused extensive damage and revenue losses for over 500 companies. In some industrial sites affected by these fire, sandwich panels with polyurethane (PUR), polyisocyanurate (PIR), and mineral wool cores were used to rebuild the building's external cladding after that. Experimental tests in InduForestFire project were conducted to compare the performance of these sandwich panels in two fire exposure scenarios and fire tests were based on BS-8414-2 test procedure. The results and discussion highlight the importance of fire risk assessment of external cladding systems in industrial sites.

Keywords: wildland industrial interface, facade, industrial building, fire reaction, fire spread

1. INTRODUCTION

Facades are essential parts of the buildings and contribute to their general aesthetic and functional appearance. From a fire safety perspective, they can contribute to fires of significant impact. Between 2007 and 2011, about 423 fires attacked industrial building' external walls in US, with economic losses of 19.4 million dollars. Unfortunately, the Grenfell Tower [1], a renewed building in UK, is an example of a recent tragedy. In 2017, the Grenfell building facade cladding system significantly contributed to the fire spread and their development, causing 72 deaths [1]. Therefore, predicting the fire behaviour of facade cladding systems is fundamental to improve buildings' fire risk resilience. Several numerical-experimental works have used computational fluid dynamics software to study fire dynamics and their effects on external cladding systems [2,3,4,5,6]. However, the parameters for evaluating the fire behaviour of facades are not equivalent between methods, and the test results are not comparable, limiting their application and extension [7]. Additionally, research to assess different facade cladding systems' fire behaviour has increased to harmonise their evaluation through standardised test methods.

Notably, studying fire behaviour on the facades of tall and very tall buildings, whether for offices or housing, is crucial. Forest fires in industrial building interface areas have also revealed severe consequences, emphasising the importance of acceptable facade behaviour towards the fire to reduce the onset of fire in the building system and avoid fire spread. The external cladding of industrial buildings can also be affected by fires with other exposure conditions, such as a fire adjacent to the facade. The 2017 Great Forest Fires in Portugal affected wildland industrial interface areas, with more than 500 affected companies and estimated damage and loss of revenue value of 275

147

M€ [8]. These affected industrial zones were assessed in 2020 and sandwich panels with polyurethane, polyisocyanurate and mineral wool cores were some of the materials used to rebuild the building's external cladding [9]. Few studies report damages in industrial buildings affected by external fires [9,10]. However, some fires have revealed severe consequences to industrial facilities, such as direct and indirect economic losses and a significant impact on manufacturing activity.

After the Greatest Forest Fires of 2017 in Portugal, 77.1 % of the outdoor stored raw materials and finished products burned in all industrial sites. These are usually flammable and are held next to the facades [9]. Nearly 80.6 % of these materials were ignited by embers or direct contact with flames from the forest fires, contributing negatively to the extent of the fire damage to the facades and roofing [9]. The building envelope structures are the first parts affected by external fires (See Figures 1a and 1b).

| a | b |

Fig.1 – Damages in external cladding in industrial buildings affected by 2017' Greatest Forest Fires

A preventative fire safety approach requires an exact knowledge of fire spread on external walls, and different studies have been carried out in the last three decades on this topic [11]. The fire outside a building and immediately next to the external wall cladding can severely impact the façade and depends almost entirely on the quantity of fire load present. In these cases, oxygen from the air is, in excess, sufficiently supplied for the combustion process.

In MFPA [11], Leipzig's studies on different fire sources were determined the Heat Release Rate (HRR) values. These were from 0.4 MW to 2.3 MW (maximum) and were from 0.3 MW to 2.0 MW (average); duration of fire between 25 and 45 min, whereby the time of the exposure to a fully developed fire were between 10 and 25 minutes, and the maximum height of flames were from 2.1 m to 3.8 m. Regarding the flame heights on these fires, the external wall cladding systems, even made from non-combustible materials, cannot prevent the fire from entering the building if these openings are exposed to the fire for 10 to 20 minutes. Moreover, the probability of a fire entering the building increases significantly if the external wall cladding contains flammable material, and the first floor is often affected, too [11]. In this context, the facades' behaviour towards the fire must be adequate to minimise, as much as possible, the primary fire foci, reducing their fire spread probability and avoiding horizontal compartmentation breakage.

Aiming to understand the fire development in external cladding walls in industrial buildings, the experimental tests were conducted in real-scale and outdoor conditions in two different fire exposure scenarios. In scenario A, the fire load was placed inside the building. In scenario B, the fire load was outside and near the facade wall, an equivalent scenario observed in Portugal's industrial buildings affected by external fires. Scenario B was proposed considering Kotthoff and Riemesch-Speerb's [11] research findings about the fire load position outside the building and their relationship with the building' damages by an external fire attack.

This article compares the results of experimental tests with sandwich panels used as external cladding facade systems in industrial facilities. These tests were based on the BS-8414-2 [12] standard, and the references for exposed and internal temperatures were based on BRE 135 [13] Annex B. The observations in the external cladding system' behavior during the tests, including continuous flaming and burning through the wall joints were reported. Furthermore, the numerical model for one sandwich panel type and their deviation between the experimental results for both fire exposure scenarios are discussed in this work.

2. MATERIALS AND METHODS

2.1 Experimental System

2.1.1 Test Apparatus

The test apparatus comprises a structure assembled with steel profiles and a combustion chamber based on BS 8414-2:2015 Annex B [12]. This apparatus was mounted to conduct the tests outdoors in Vila Nova de Poiares, Portugal. Each specimen, i.e. the facade wall system, was installed on this test frame, composed of two vertical faces (main and wing walls), perpendicular to each other, simulating a building corner. Figures 4.a and 4.b present the test specimen dimensions on the test frame, including the thermocouples positions on the fire-exposed side at levels 1 and 2, based on BS-8414-2 [12]. The constructive details of test frame with the combustion chamber and the entire test apparatus are presented in Figures 4.c and 4.d, respectively.

| a | b | c | d |
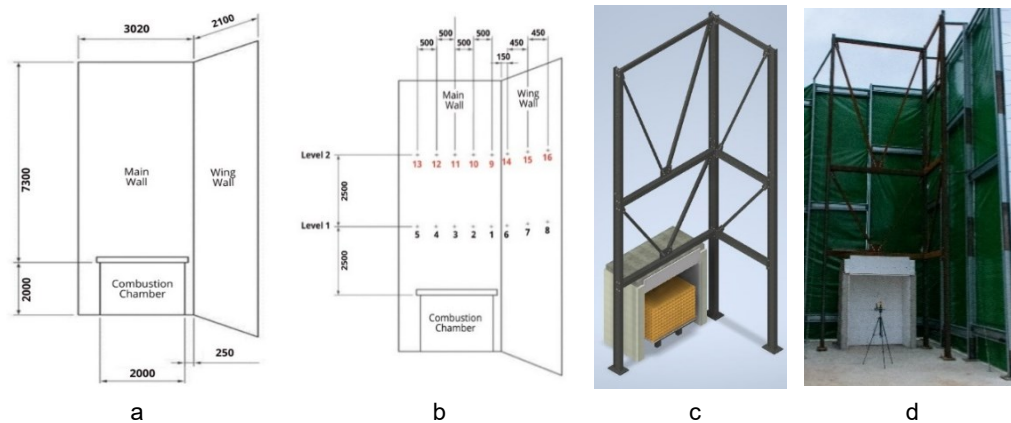
Fig.4 – Experimental system: a. Specimen dimensions; b. Instrumentation position;
c. Corner perspective; d. Test apparatus;

2.1.2 Fire Exposure Scenarios and Fire Load

The fire scenarios on these experimental tests were:

a) Scenario A: internal fire in the building – is considered to be fully developed (post-flashover) in a room, in which the flames escape through a room venting and promote the projection of flames on parts of the façade, exposing the façade wall cladding system to the effects of the fire. Figure 3.b shows the wood crib centred to the combustion chamber and 100 mm away from the floor. These are the conditions established in BS-8414-2 [12];

b) Scenario B: fire external to the building – the proposed scenario simulates an external fire, with its development outdoors, without openings in the wall, reproducing the typical situation of materials (or equipment) stored outside the building and immediately next to the external cladding wall. Some examples of these fire situations in industrial facilities are a fire in a garbage container, a fire in a vehicle, and a fire in stored combustible material. In this scenario, the main wall does not have the combustion chamber opening, and the wood crib is positioned close to the facade walls, 100 mm away from the main wall and 500 mm from the side wall (Fig. 3.c). This fire scenario could also happen in other kinds of occupancies.

Each wood crib was mounted with 250 softwood sticks of *Pinus Pinaster* (wood pine), an available wood species in Portugal with similar heat of combustion of *Pinus Silvestris*. The wood sticks have a square section of side (50 ± 2) mm and lengths of (1500 ± 5) mm and (1000 ± 5) mm, 100 and 150 units of each length, respectively. The wood crib was assembled in alternate layers of long and short sticks, as presented in Figure 4.a. Before starting each test, the wood crib was weighed with an industrial crane scale model Kern HTS 600K200IP. The average wood moisture was determined with the ten softwood sticks randomly measured with a Hydromette HT 65 wood moisture meter, according the following sampling and test frequencies criteria in EN 13183-2 [14].

The wood density in each wood crib was within BS-8414-2 [12] range values (400 to 600 kg/m^3). The moisture content measured at the test moment was a mean value of 12.5 % in all tests. To ignite the heat source, 16 low-density fibreboard strips, with nominal dimensions of (25 x 12 x 1000) mm, soaked in white spirit for 5 minutes before being inserted into the gaps between the wood sticks of the second layer, were used in each test. According

to BS-8414 [12], this heat source releases a total heat output of 4500 MJ over 30 min, reaching a peak heat release rate of (3 ± 0.5) MW.
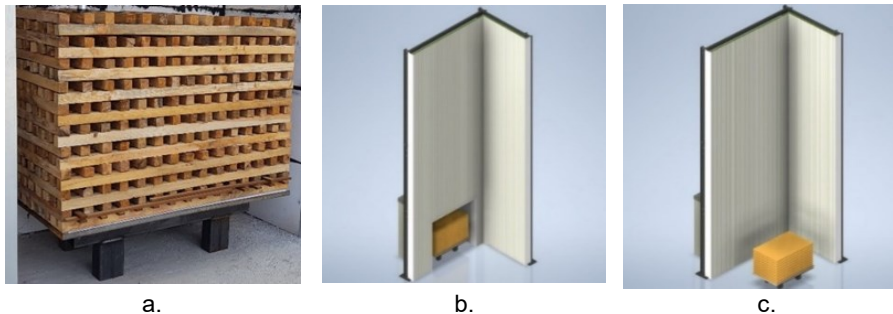
a.   b.   c.
Figure 3 –Fire load and fire exposure scenarios: a. wood crib; b. Scenario A; c. Scenario B

2.1.3 Instrumentation

The temperature profiles on the exposed side were measured with Class 1 K-type probe thermocouples (Chromel/Alumel alloy) according to EN 60584-1 [15], with the hot joints positioned 50 mm from the external face of the test specimen, distributed as presented in Figure 2.b. Sixteen exposed thermocouples were installed, eight per level, with a vertical distance of 4500 mm and 7000 mm, respectively. In addition, eight internal K-type probe thermocouples, the same model as the external, were installed on Level 2 with their hot joints at the midpoint of the insulation core (away 50 mm from the exposed side), spaced 10 mm from the external thermocouples horizontally. Table 1 presents the thermocouple positioning details used in the experimental tests. The data acquisition system was set to record the temperature values every 5 s. The temperature test range for thermocouples is from -40º C to 1000ºC.

Table 1 – Instrumentation identification and position in the experimental tests

TC ID	Level	Height (mm)	Position	Wall
T1 to T5	Level 1	4500	Exposed	Main
T6 to T8	Level 1	4500	Exposed	Wing
T9 to T13	Level 2	7000	Exposed	Main
T14 to T16	Level 2	7000	Exposed	Wing
T9_I to T13_I	Level 2	7000	Internal	Main
T14_I to T16_I	Level 2	7000	Internal	Wing

2.2 Test Specimens and Test Program

In Portugal, industrial buildings usually have a structure with steel elements covered by simple profiled steel sheets. However, sandwich-type panels with different thermal insulation materials are used as cladding when the building has thermal and acoustic comfort requirements. The external façade cladding can also be assembled on-site made of profiled steel sheets and insulation material. These types of external cladding are usually attached to a horizontal substructure composed of omega-type profiles, which are fixed to the main structure of the building.

The test specimens were made of sandwich panels with metallic sheets of cold-profiled S220GD structural hot-galvanised steel sheet according to EN 10346 and EN 10169, with 0.5 mm thickness. The vertical joints of all sandwich panels have the same design, and they have a double tongue and groove, but have different materials to cover the exposed insulation core, with exception of mineral wool panels. In Polyisocyanurate panels, this covering was made of flexible polyethylene tape that also acts as water tightness barrier in the joint.

All sandwich panels tested have a total thickness of 100 mm, 1150 mm width, and height of 9300 mm. Despite of this height based on BS 8414-2 test rig, this height corresponds to the height usually seen in industrial buildings in Portugal. Each tested sandwich panel's insulation core material properties were collected in the manufacturer's datasheet and described in Table 2.

Table 2 – Insulation core material properties of sandwich panels

Sandwich panel insulation core material	Weight (kg.m^{-2})	Thermal Conductibility (W.m^{-1}.K^{-1})	Insulated core density (kg.m^{-3})	Thermal Transmitance (W.m^{-2}.K^{-1})	Thermal Resistance (m^2.K.W^{-1})
Mineral Wool	19.60	0.0420	100	0.33	3.03
Polyisocyanurate	12.53	0.0217	38 to 45	0.22	4.56
Polyurethane	12.53	0.0230	40	0.23	4.35

[†] NPD - No Performance Declared

Table 3 summarises the test program comprising six real-scale experimental tests, three conducted in fire exposure scenario A and another three in scenario B.

Table 3 – Experimental test program

Test ID	Test Specimen Description	Fire Scenario
E1-MW-A	Sandwich Panel with Mineral Wool insulation core	A
E2-MW-B	Sandwich Panel with Mineral Wool insulation core	B
E3-PIR-A	Sandwich Panel with Polyisocyanurate insulation core	A
E4-PIR-B	Sandwich Panel with Polyisocyanurate insulation core	B
E5-PUR-A	Sandwich Panel with Polyurethane insulation core	A
E6-PUR-B	Sandwich Panel with Polyurethane insulation core	B

2.3 Test Procedures

The experimental tests were carried out based on procedures prescribed in the BS-8414-2 [12] and the reference temperature parameters for levels 1 and 2 were based on Annex B of BRE 135 [13]. The measured temperatures in level 1 were used to determine Start Temperature (T_s) and Start Time (t_s). T_s is the level 1 thermocouples' average temperature 600 s (5 min) before ignition, and t_s is when the temperature by any external thermocouple equals or exceeds 200 °C above T_s and remains above for, at least, 30 s. Each experimental test duration was 3600 s (60 min). The fire load was ignited at t=0 s and extinguished after 1800 s (30 min), according to the BS-8414-2 [12]. The measured level 2' temperatures, in each tested specimen, were compared with the following:

- **External Fire Spread (temperature):** when the temperature rises 600 °C above T_s for any external thermocouples at level 2 for a period of at least 30 s, within 15 min of the start time, t_s.
- **Internal Fire Spread (temperature):** when the temperature rises 600 °C above T_s for any internal thermocouples at level 2 for a period of at least 30 s within 15 min of the start time, t_s.

Observations were recorded during and after the fire exposure period, when one or more of them occurred, according the following situations:

- **Internal Fire Spread (Burn-through):** when continuous flaming with duration over 60 s on the internal surface of the test specimen at or above a height of 0.5 m above the combustion chamber opening occurs, within 15 min of the start time, t_s.
- **Fire spread above test specimen:** when the fire propagation above the edges of the specimen occurs anytime during the test, for a period of at least 60 s, after the fire source ignition.
- **Ongoing system combustion:** if this event occurs after extinguishing the fire source (after the first 30 min of the test) and/or during the test period.
- **Detachment of system parts**: If occurs any system collapse, spalling, delamination or flaming debris during the total test period (3600 s).

3. RESULTS AND DISCUSSION

3.1 Experimental Analysis

3.1.1 Environmental Conditions

During the experimental tests, the Kestrel 5500 weather meter was used to measure environmental conditions, including ambient temperature, relative air humidity, wind speed, and wind direction. The weather meter was installed at the height of 1.2 m from the floor, 10 m away from the main wing of the system apparatus, and aligned with the wing wall to minimise the influence of the experiments and obtain accurate outdoor weather data.

Throughout all tests, the measured temperature and humidity values were within the range specified in BS-8414-2 [12]. Table 4 summarises the environmental conditions. The tests were conducted without any fog or precipitation.

Table 4 – Environmental Conditions during experimental tests

| Test ID | Ambient Temperature (ºC) | | Relativity Air Humidity (%) | | Wind Speed and Direction | | | |
| | | | | | Start | | End | |
	Start	End	Start	End	Speed (m/s)	Direction	Speed (m/s)	Direction
E1-MW-A	21.3	22.8	47.0	44.0	1.2	133º SE	0.8	136º SE
E2-MW-B	27.6	28.6	57.1	52.2	1.3	236º SW	1.3	214º SW
E3-PIR-A	26.0	30.0	40.5	36.2	1.1	333º NW	1.3	33º NE
E4-PIR-B	18.7	21.3	83.4	71.9	1.3	36º NNE	0.7	32º NNE
E5-PUR-A	22.0	23.5	67.1	55.7	0.3	186º SSW	1.4	236ºSW
E6-PUR-B	14.1	15.7	84.2	73.1	0.5	25º NNE	1.6	17º NNE

3.1.2 Temperature Profiles and Test Observations

This section presents the average temperature profiles recorded over time in all experimental tests, in front of the facade walls and inside the insulated core. Table 5 presents the Start Temperature (T_s), Start Time (t_s) and the reference values for external and internal fire spread verification in each experimental test, according procedures described in 2.1.4. The observations were collected with recorded videos using audiovisual resources (digital HD video camera recorder) and a thermal detector camera. These observations combined with temperature measurements taken from external and internal thermocouples to characterise the event when applicable. In addition, the situations described in section 2.4 and any other that could be relevant (e.g. flaming inside the joints, wood crib disassembling, etc.) were reported when they occurred in each experimental test. In some tests is indicated the thermocouple ID to clarify the temperature measurement and the event during test (i.e. flaming or fire spread above specimen's top boundary).

Table 5 – Start Temperature (T_s), Start Time (t_s) and external/internal fire spread reference values

| Test ID | Start Temperature T_s (ºC) | Start Time t_s | | External/internal fire spread reference values | |
		Started at (s)	TC ID	Ending at (900 s + t_s) (s)	Temperature (600 ºC + T_s) (ºC)
E1-MW-A	26.5	125	T3	1025	626.5
E2-MW-B	29.0	145	T5	1045	629.0
E3-PIR-A	28.9	130	T3	1030	628.9
E4-PIR-B	20.3	275	T3	1175	620.3
E5-PUR-A	20.2	145	T3	1045	620.2
E6-PUR-B	14.8	255	T3	1025	626.5

3.1.2.1 Tests E1-MW-A and E2-MW-B

In both tests, level 2 external and internal thermocouples measured values that do not exceed the reference temperature value ($T_s + 600$ ºC) from Start Time (t_s) to the next following t_s=900 s.
In the E2-MW-B test, the average temperature at level 2 in exposed thermocouples rose and decreased earlier than the E1-MW-A. These reached a higher value in the first 600 s (10 min) after Start Time (t_s) and almost 180 ºC above the E1-MW-A average temperature for the same level.
In the E2-MW-B test, the average temperature of internal thermocouples rose earlier than the E1-MW-A test and stayed slightly higher for the same test period after the fire source extinguishment. Figure 7 presents level 2 average temperatures in exposed and internal thermocouples from Start Time (t_s) until 3000 s.

During the E1-MW-A and E2-MW-B experimental tests, from the start time to the next 15 min, they were not observed continuous flaming in any parts of the specimen and the fire did not spread above the top boundary of the specimen. Regarding the detachment of system parts after extinguishing the heat source, there was no system collapse, spalling, delamination or flaming debris on the floor around the test area in both tested specimens. In the E2-MW-B test, the wood crib was disassembled at 1455 s; in the E1-MW-A test, this occurred at 1332 s.
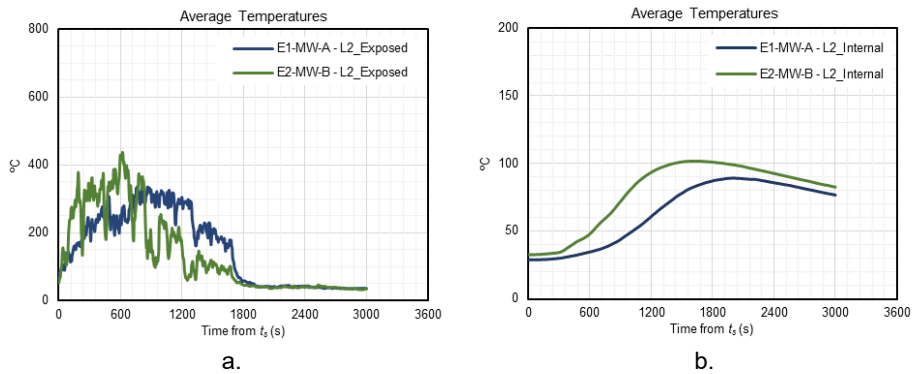
Figure 7 – Average Temperatures at level 2: a. Exposed; b. Internal

3.1.2.2 Tests E3-PIR-A and E4-PIR-B

In the E3-PIR-A test, level 2 external and internal thermocouples measured values that do not exceed the reference temperature value (Ts + 600 ºC) from Start Time (t_s) to the next following $t_{s=}$900 s.

Continuous flaming at vertical joints was observed in this test, starting at 480 s on the main wall (centred with the combustion chamber) and 584 s on the adjacent wall (joint nearest to the corner of the test specimen). Smoke production was observed at the vertical panel joint centred with the wood crib at 1030 s (17 min 10 s) without continuous flaming.

During the E4-PIR-B test, continuous flaming started at 480 s on the main wall and 540 s on the adjacent wall (Fig. 18.a). The temperature in the exposed T9 thermocouple exceeds 620.3 ºC at 690 s (11 min 30 s) and reaches the peak value of 955.1 ºC at 805 s (13 min 25 s). The temperatures in exposed T14 increased in the same way of T9 thermocouple over time and reached the peak of 914 ºC at 805 s (13 min 25 s).
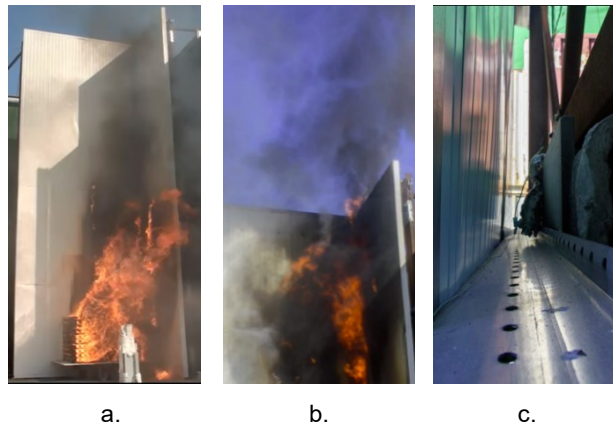
Figure 8 – E4-PIR-B observations

These two exposed thermocouples were positioned near the corner of the test specimen. Level 2 internal thermocouples, in both tests, do not exceed the reference temperature (Ts+600 ºC). After 831 s, the fire spread above the top boundary E4-PIR-B specimen Fig. 8.b) for more than 60 s. At 1515 s (25 min 15 s) the fire penetrated through the panel joint with visible smoke and flames on the unexposed side, and the T9_I temperature was 208 ºC inside the insulation core. Damages on the unexposed side of the E4-PIR-B specimen caused by the flames are presented in Fig. 8.c). Flaming was observed in the panel joints at the corner of the test specimen. In this case, the fire did not penetrate the unexposed side of the side wall. However, smoke production from the insulated core remains after fire load extinguishing, nearest the test specimen corner.

Regarding the detachment of system parts after extinguishing the heat source, there was no system collapse, spalling, delamination or flaming debris on the floor around the test area, in both tested specimens. It was observed in the E4-PIR-B test that the average temperature at level 2 in exposed thermocouples rose and decreased earlier than in the E3-PIR-A test. Still, it reached a higher value in the first 600 s (10 min), almost 250 ºC above the E3-PIR-A average level 2 temperature and still higher until 1200 s, after Start Time (t_s). In the E4-PIR-B test, the average temperature of internal thermocouples after 600 s (10 min) increased earlier than the E3-PIR-A test and

stay higher for the same test period after the fire source extinguishing. Figure 9 presents level 2 average temperatures in exposed and internal thermocouples from Start Time (t_s) until 3000 s.
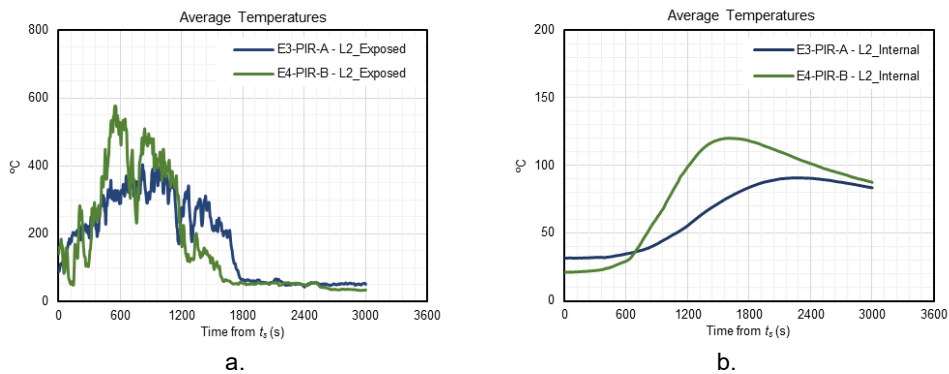
Figure 9 – Average Temperatures at level 2: a. Exposed; b. Internal

3.1.2.3 Tests E5-PUR-A and E6-PUR-B

In the E5-PUR-A test, the temperature at 435 s (7 min 15 s) in T10 and T11 exceeds 620.2 ºC. In the E5-PUR-A test, continuous flaming started at 338 s in the vertical joints of the main wall (Fig. 10.a) and 413 s in the vertical joint of the adjacent wall (Fig. 10.b). After that, the flame spread above the test specimen's top boundary occurred at 592 s meeting the early test termination criteria (Fig. 10.c).

For this reason, the fire source was extinguished at 622 s (10 min 22 s). Flaming at vertical joints was observed in the E6-PUR-B test too, starting at 440 s on the main wall and at 520 s at the corner of the test specimen (Fig. 10.d). The temperatures in exposed thermocouples T9, T11, and T14 exceeded 614.8 ºC at 620 s (10 min 20 s), and at 640 s, the flame spread above the test specimen top boundary, met the early test termination criteria (Fig. 10.e).

In the same way that the E5-PUR-A test, the test was interrupted and the fire source was extinguished at 652 s (10 min 32 s). After extinguishing the fire source, in E5-PUR-A and E6-PUR-B tests, smoke production and persistent flaming at panel joints were observed in the vertical joints of the main and wing walls. The water was used to extinguish the flames on tested specimens for safety reasons.
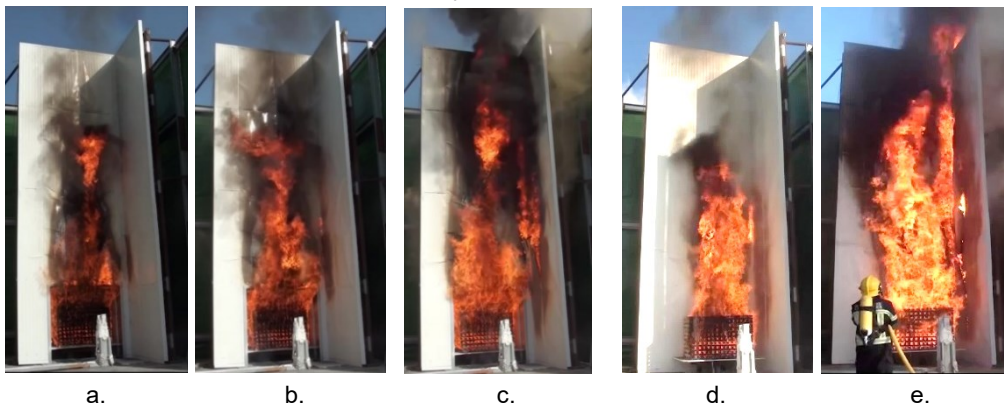
Figure 10 – E5-PUR-A and E6-PUR-B test observations

It was observed in the E6-PUR-B test that the average temperature at level 2 in exposed thermocouples reached a higher value the first 500 s (8 min 20 s), 125 ºC above the E7-PUR-B average level 2 temperature, from Start Time (t_s). In the E6-PUR-B test, the average temperature of internal thermocouples rose earlier than the E5-PUR-A test, 360 s from Start Time (t_s), but not exceeding 40 ºC. After 360 s from the Start Time (t_s), the E5-PUR-A average temperatures of internal thermocouples reached the peak value (50 ºC). Figure 11 presents level 2 average temperatures in exposed and internal thermocouples from Start Time (t_s) until 3000 s.

154
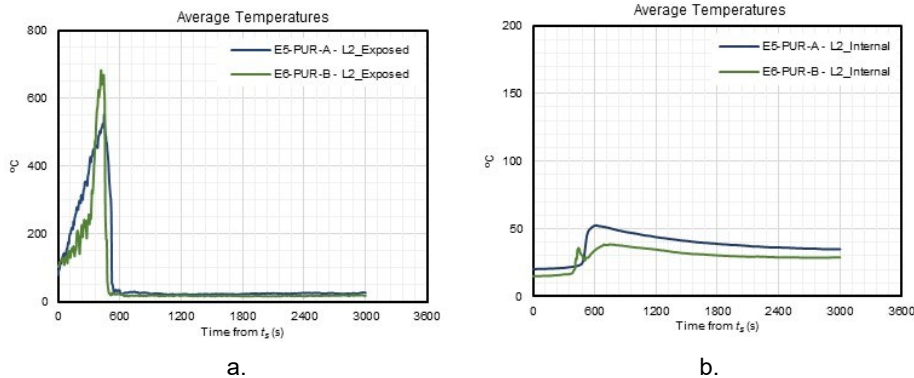
Figure 11 – Average Temperatures at level 2: a. Exposed ; b. Internal

3.1.3 Final Considerations

After evaluating temperature profiles and observations in video data recordings in each experimental test, Table 7 summarises the results according to the parameters and conditions described in section 2.4. It was observed that the temperature profiles during the 900 s after t_s are different between fire exposure scenarios. The level 2 average temperature values were higher in scenario B. They increased earlier than scenario A tests, compared to the first 600 s (10 min) after Start Time (t_s). The exposed thermocouple that influenced t_s determination in all tests was those vertically aligned with the combustion chamber centre (in case, T3), except E2-MW-B, which was positioned far from the corner of the main wall (T5).

Table 7 - Experimental tests summary

Test ID	External Fire Propagation (temperature)	Internal Fire Propagation (temperature)	Internal Fire Propagation (Burn-through)	Fire Spread above test specimen	Ongoing system combustion
E1-MW-A	Not Occurred	Not Occurred	Not Occurred	Not Occurred	Not Occurred
E2-MW-B	Not Occurred	Not Occurred	Not Occurred	Not Occurred	Not Occurred
E3-PIR-A	Not Occurred	Not Occurred	Not Occurred	Not Occurred	Yes (Note 3)
E4-PIR-B	At 690 s	Not Occurred	At 825 s	At 830s	Yes (Note 3)
E5-PUR-A	At 405 s	See Note 1	See Note 1	At 550 s	See Note 1
E6-PUR-B	At 620 s	See Note 1	See Note 1	At 630 s	See Note 1

Note 1: E5-PUR-A and E6-PUR-B tests met the early termination condition.
Note 2: If the time event is appointed, the value is from the ignition of fire load (t=0).
Note 3: After fire extinguishment.

3.2 Numerical Analysis

3.2.1 Numerical Model

The numerical analysis was carried out for the sandwich panel with mineral wool core to verify the average temperature profiles on the facade walls in both scenarios. The Fire Dynamics Simulator [16] software, version 6.7.9, was used to conduct the simulations. The temperatures on the facade's surface were obtained from devices configured in the numerical models considering the shape and dimensions of the specimens presented in the experimental setup, according to the 2.1.1 section. The sandwich panels were simplified as a homogeneous plate with thermal properties in Table 2 for both models.

The heat release rate in the numerical model was adjusted using the HRR evolution curve presented by Anderson *et al.*[4]. The dimensions of the computational calculation grid are 16,000 mm × 20,000 mm × 12,000 mm, sufficient for the test system and the development of the hot gas plume resulting from combustion, with open boundaries for pressure on the sides and top of the computational domain. Each cell in this mesh has dimensions of 125 mm × 125 mm × 125 mm in the fire development area (wood crib and external face of the facade wall) and 250 mm × 250 mm × 250 mm for the rest of the numerical model, resulting in 326,400 cells. These conditions are equivalent to the ones used in Dréan *et al.* [6,7] numerical models. The mesh resolution for practical cost-time simulations with

plumes of hot gases was assessed with the dimensionless ratio $D^*/\Delta x$ criteria proposed in the Technical Reference Guide [17] and was compared with FDS Validation Guide [18] values for similar models.

For the maximum energy released during the test (Q = 3 ± 0.5 MW), the smallest size for the Δx to obtain reliable radiative heat flux results should be near to 150 mm. Thus, the mesh size of 125 mm is adequate to accurately capture the phenomena of combustion and turbulent flow from ignition until the fire is fully developed in simulation. The environmental parameters for numerical modelling were established with atmospheric pressure p_{atm} = 1.013 atm, relative humidity of 40% and wind speed of 0.5 m/s. The ambient temperature was set with 20 ºC, the same value defined for Start Time (Ts). The fire load was ignited at t = 0 s in the simulations.

3.2.2. Comparison between numerical and experimental results

In the numerical modelling, the temperature values from 50 mm from the facade surface were recorded every 5 s. As presented in section 2.3, the level 1 thermocouples were used to determine the Start Time (t_s) and level 2 thermocouples were used to verify the external fire spread parameter. The average temperatures recorded in the experimental tests (red lines) and numerical models (blue lines) at levels 1 and 2 are presented in Figures 12 and 13.

3.2.2.1 Average temperature profiles – E1-MW-A

The values between the numerical model and the experimental test in the levels 1 and 2 average temperature profiles had a different pattern from 150 s to the next 900 s. Until 150 s, the temperatures in level 1 are practically equivalent, but after that, the experimental values increase and stay higher, at least at 100 ºC. The Start Time (Ts) occurred at 120 s in the numerical model and the experimental test. This occurs in experimental test because ambient temperature are higher than numerical model (6 ºC) and wind conditions are slightly different than numerical model for this period. The fire load that was setted up in numerical model could be less severe and less energy were release than the real fire load used in experimental test.
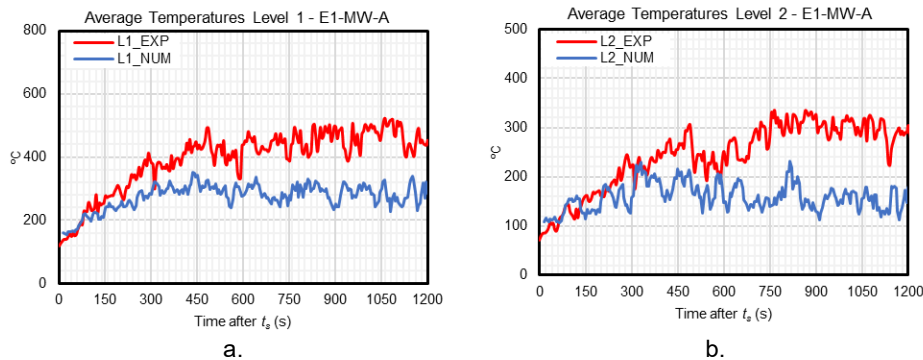
Figure 12 – Average Temperatures at levels 1 and 2 in E1-MW-A test

The temperatures at level 2 in the numerical model were between 120 s and 1020 s and not higher than 620 ºC (Ts + 600 ºC). The maximum and average values were 400 ºC and 250 ºC, respectively. In the experimental test, the temperatures at level 2 were not higher than 626.5 ºC (Ts + 600 ºC), and their maximum and average values were 500 ºC and 350 ºC, respectively. At 1020 s, the fire load reaches an HRR of 2.6 MW in FDS simulation, and these values are within the range BS-8414-2 [12] reference values for fire development during the tests.

3.2.2.2 Average temperature profiles – E2-MW-B

The values between the numerical model and the experimental test in the levels 1 and 2 average temperature profiles differed from 0 s to the next 750 s. Since the ignition of the fire load, the temperatures in level 1 are higher in the experimental test and kept above the numerical ones until 800 s. As a result, the numerical model's Start Time (Ts) occurred at 155 s and the experimental test at 145 s.

The temperatures at level 2 in the numerical model between 120 s and 1020 s were not higher than 620 ºC (Ts + 600 ºC), and the maximum and average values were 450 ºC and 200 ºC, respectively. Therefore, at 1055 s, the HRR obtained in FDS [16] simulation was 3.1 MW and is within the reference values proposed in BS-8414-2 [13]. In the experimental test, the temperatures at level 2 were not higher than 626.5 ºC (Ts + 600 ºC), but the maximum and average values were 500 ºC and 400ºC, respectively, from 150 s to 800 s. After this moment, due to the loss of mass and consequent collapse of the burning wood crib during the test, the average temperature decreased to 200 ºC.
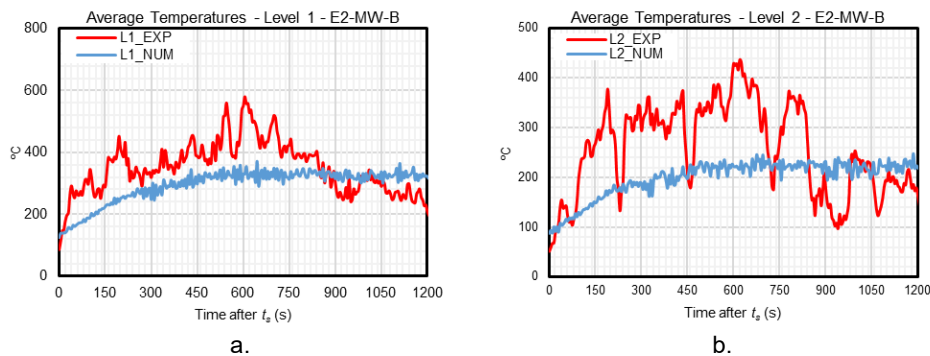
Figure 13 – Average Temperatures at levels 1 and 2 in E2-MW-B test

4. CONCLUSIONS

This research presents fire testing results in three external cladding systems typically applied in industrial buildings in Portugal and compared two possible fire scenarios with the same cladding assembly using a technical basis of a recognised large-scale fire test method [12]. It was observed in this work that the fire development and their effects in tested specimens in scenario A were not the same when comparing scenario B, a real possibility and representative external fire source verified and initially discussed. Scenario A reproduces a frequent condition used in residential and commercial buildings and is the primary fire exposure scenario in the full-scale fire tests [12], also considered in industrial sites. Otherwise, scenario B reproduces a common situation in day-by-day industrial sites in Portugal, which is a realistic approach for this occupation. Therefore, in BS-8414-2 [12] there is no recommendation to adopt an external fire load adjacent and close to the specimen in the test setup rig to conduct the tests.

According to the test summary (Table 7), half of tested specimens met the external fire propagation condition, and 67 % of that was in scenario B. The burn-through occurred in 16.7 % of specimens when the fire penetrated the unexposed side of the wall. The fire spread above the top boundary of specimens occurred in 50% of tests, and 67% of that was in PUR sandwich panels. In the E3-PIR-A and E4-PIR-B tests, the insulation tape added to the edges of the panel and joint promotes ignition and vertical fire propagation through the joint. This situation influenced insulation core material ignition, and fire spread inside from the joint to the panel core. The Kothoff experiment considerations [11] were observed in these tests, when the exposure of external cladding to a fully developed fire between 10 and 25 minutes, the fire entering in external wall cladding.

On the other hand, E2-MW-B and E1-MW-A test specimens with a rock wool core did not have insulation tape at the vertical joints, a non-combustible barrier between panels, and their behaviour against the buoyancy flames from the fire load are better than the other insulated cores. Visible flaming in scenario B occurred between 165 to 205 s after t_s, while in scenario A it only occurred between 185 to 445 s after t_s, in PIR and PUR cores. From 600 s (10 min) to 1200 s (20 min) of fire exposure in scenario B tests (E4-PIR-B and E6-PUR-B) a vertical fire spread on the facade occurred with flame heights higher than 9.3 m, and the fire spreads beyond the top boundary of the tested specimens.

A slight deviation in the Start Time (t_s) between the numerical model and the experimental test in E2-MW-B. This was expected because the heat release rate curve (HRR) considers fire development inside the combustion chamber. This HRR curve was used for both numerical models (E1-MW-A and E2-MW-B) and used the same in previous FDS simulation studies [5]. With the wood crib in E2-MW-B outside and adjacent to the wall, the fire develops with an oxygen-rich air supply. Otherwise, in E1-MW-A, the fire development was governed by the combustion chamber opening, a ventilation-controlled fire. The environment variables (wind speed and ambient temperature) were used in simulations presented here to give an initial data set to compare temperature profiles between the numerical model and experimental test. In future work, a full calibration of the influence of environmental variables in heat release rate and, as a consequence, in temperature profiles, will be discussed further.

Given the results presented here in the experimental tests, an external fire scenario (scenario B) could be more severe than an internal fire scenario (scenario A) and affect the building envelope with higher temperatures in a shorter period. The facades' behaviour towards the fire must be adequate to minimise, as much as possible, the primary fire foci, reducing their fire spread probability and avoiding horizontal compartmentation breakage. For this reason, storage of combustible raw materials outdoors and close to the facades must be avoided in industrial sites and their risk assessment should be part of the fire safety project.

A standard adoption for fire testing of external cladding systems by a public regulation must be carefully studied. If a country intends to define its regulations, the external cladding systems evaluation requirements, severity level and performance acceptance criteria must be defined. Furthermore, this must be done according to the fire safety regulations approach and the objectives that need to be achieved systemically (e.g. the occupant egress time versus external cladding performance).

REFERENCES
[1] McKenna, S.T.; Jones, N.; Peck, G.; Dickens, K; Pawelec, W; Oradei, S; Harris, S; Stec, A. A.; Hull, T.R.; "Fire behaviour of modern facade materials – Understanding the Grenfell Tower fire." Journal of Hazardous Materials, Vol. 368, 2019.

[2] Anderson, J.; McNamee, R. J.; Façade fire tests – Measurements and modeling, MATEC Web of Conferences, 2013, vol. 9. doi: 10.1051/matecconf/20130902003.

[3] Anderson, J.; Boström, L.; McNamee, R.J.; Milovanović, B.; Experimental comparisons in façade fire testing considering SP Fire 105 and the BS 8414-1, Fire and Materials, Aug. 2018, vol. 42, no. 5, pp. 484–492. doi: 10.1002/fam.2517.

[4] Anderson, J.; Boström, L.; McNamee, R.J.; Milovanović, B., Uncertainties in façade fire tests – Measurements and modeling, MATEC Web of Conferences, May 2016, vol. 46. doi: 10.1051/matecconf/20164603002.

[5] Drean, V.; Schillinger, R.; Leborgne, H.; Auguin, G.; Guillaume, E.; Numerical Simulation of Fire Exposed Façades Using LEPIR II Testing Facility, Fire Technology, vol. 54, no. 4, pp. 943–966, Jul. 2018, doi: 10.1007/s10694-018-0718-y.

[6] Drean, V.; Girardin, B; Guillaume, E.; Fateh, T.; Numerical simulation of the fire behaviour of facade equipped with aluminium composite material-based claddings-Model validation at large scale, Fire and Materials, vol. 43, no. 8, pp. 981–1002, Dec. 2019, doi: 10.1002/fam.2759.

[7] White, N; Delichatsios, M.; Fire Hazards of Exterior Wall Assemblies Containing Combustible Components. Verlag New York: Springer; 2015.

[8] Guerreiro, J.; Fonseca, C.; Salgueiro, A.; Fernandes, P.; Iglésias, E. L.; de Neufville, R.; Mateus, F.; Castellnou Ribau, M.; Sande Silva, J.; Moura, J. M.; Castro Rego, F.; Caldeira D. N.; "Avaliação dos incêndios ocorridos entre 14 e 16 de outubro de 2017 em Portugal Continental. Relatório Final. " Comissão Técnica Independente. Assembleia da República. Lisboa, 2018.

[9] R.F.R. Lopes et. al., Resilience of Industrial Buildings to Wildland-Urban Interface Fires, IOP Conf. Ser.: Earth Environ. Sci. Vol. 1101, DOI 10.1088/1755-1315/1101/2/022034, 2022.

[10] Khakzad, N. Impact of wildfires on Canada's oil sands facilities, Nat Hazards Earth Syst Sci, 2018,18:3153–66.

[11] Kotthoff, I.; Riemesch-Speerb, J. Mechanism of fire spread on facades and the new Technical Report of EOTA "Large-scale fire performance testing of external wall cladding systems", MATEC Web of Conferences, vol. 9, 2013, DOI: https://doi.org/10.1051/matecconf/20130902010

[12] BS 8414-2:2015+A1:2017, Fire performance of external cladding systems. Test method for non-loadbearing external cladding systems fixed to and supported by a structural steel frame, British Standards Institution, 2017.

[13] BRE Report 135: Fire performance of external thermal insulation for walls of multi-storey buildings, BRE Trust, 3rd edition, Garston, 2013.

[14] BS EN 13183-2:2002, Moisture content of a piece of sawn timber, Part 2: Estimation by electrical resistance method, British Standards Institution, 2007.

[15] CEN/EN 60584-1:2013, Thermocouples - Part 1: EMF specifications and tolerance, European Committee for Standardization, Brussels, 2013.

[16] McGrattan, K; McDermott, R; Floyd, J; Hostikka, S; Forney, G; Baum, H. Computational fluid dynamics modelling of fire, 2012, Int J Comput Fluid Dyn 26:349–361

[17] McGrattan, K.; McDermott, R.; Hostikka S.; Floyd, J.; Vanella, M.; *Fire Dynamics Simulator – Technical Reference Guide*. NIST Special Publication 1018-1, Sixth Edition, http://dx.doi.org/10.6028/NIST.SP.1018.

[18] McGrattan, K.; McDermott, R.; Hostikka S.; Floyd, J.; Vanella, M.; *Fire Dynamics Simulator – Validation Guide*. NIST Special Publication 1018-3, Sixth Edition, http://dx.doi.org/10.6028/NIST.SP.1018.

Fire Reaction

INFLUENCE OF MINERAL WOOL THICKNESS ON CHANGES IN FIRE RESISTANCE OF LOAD-BEARING STRUCTURES
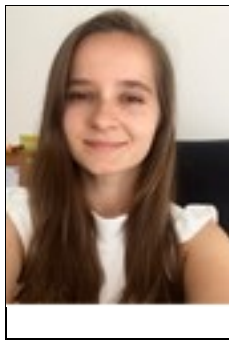
Katarína Košútová
a,*

Linda M. Osvaldová
b

ABSTRACT

The paper deals with the experimental testing of load-bearing sandwich structures in terms of fire resistance. For the experimental study, we created six variants of constructions in which we changed not only the thickness of the mineral wool but also the material composition of the construction itself. The monitored component during testing was mineral wool and the effect of the change in thickness on the resulting fire resistance. Among the composition of the tested load-bearing sandwich constructions are the listed materials. Namely plasterboard construction board, thermal insulation from expanded polyurethane with different surface treatment, mineral wool, new fireproof boards and wooden posts. To determine the behavior of the given materials during fire, we used the EN 1365-1:2013 test method. The temperature of the materials during the fire was monitored by inserted thermocouples. The main goal of our research was to find out whether the thickness of mineral wool has an effect on fire resistance and whether it is possible to achieve higher fire resistance by changing the thickness of mineral wool. We used several scientific and statistical methods to evaluate the obtained data.

Keywords: fire resistance, mineral wool, temperature, experimental testing, fire boards

a,* University of Žilina, Faculty of security engineering, Department of Fire engineering, katarina.kosutova@uniza.sk , Corresponding author.

b University of Žilina, Faculty of security engineering, Department of Fire engineering, linda.makovicka@uniza.sk.

1. INTRODUCTION

Mineral wool ranks among the most frequently used materials for additional insulation of buildings. Mineral wool has excellent fire resistance properties, which are proof that the fire does not spread if exposed to flames. However, we are interested in the question of how this material behaves during fire in combination with other building materials. In the contribution, we are devoted to experimental studies according to EN 1363-1: 2021 and EN 1365 – 1: 2013. In the research, we created six variants of load-bearing sandwich structures, while we changed the thickness of the mineral wool from 80 mm to 40 mm. We did not use mineral wool in the reference sample. In addition to investigating the effect of the thickness of the mineral wool on the fire resistance of the structure, we also monitored the behavior of the load-bearing wall structure itself when thermal insulation from expanded polyurethane was changed. We used two types of thermal insulation when assembling the investigated load-bearing sandwich structures. Namely thermal insulation from expanded polyurethane with an aluminium layer on the surface and thermal insulation from expanded polyurethane with mineral felt on the surface. We used wooden columns as a supporting element in the construction. To close the entire structure, we used a universal plasterboard fireproof board on the side exposed to the fire, and on the opposite side we used new types of fireproof boards. We then subjected the samples to a fire resistance test that lasted 125 minutes. The main goal of our research was to find out whether the thickness of mineral wool has an effect on fire resistance and whether it is possible to achieve higher fire resistance by changing the thickness of mineral wool.

Sandwich panels are also investigated by the authors Haffke, et. al. [1] about their contribution, they point to the lack of knowledge of the fire resistance of assembled sandwich structures. The authors conducted an experimental investigation of the structural and thermal behavior of precast concrete sandwich panels. In which they applied mineral wool as thermal insulation. In total, they tested three sandwich assemblies, where they found the resulting fire resistance REI – 120, M. All tested structures retained their structural and fire-protective functionality due to increased bending stiffness and high thermal insulation ability [1]. The authors Perera, et. al. [2] are engaged in numerical research of constructions composed of different types of plasterboard linings and thermal insulation. In the post, they discuss the fire resistance of modular wall panels with thermal insulation from rockwool, glass-fibre and mineral-wool. The authors claim that the analysis pointed to an insignificant influence of the choice of insulation material between rockwool, glass-fibre and mineral-wool on structural fire resistance [2]. The authors Kontogeorgos, et. al. [3] are engaged in the research of sandwich constructions composed not only of conventional materials but also of phase-changing materials and vacuum insulating materials. In an experimental study, the authors assembled four different sandwich structures, which they exposed to temperatures of up to 900 °C on one side. While the other side was observed under ambient conditions. Different types of plasterboard, thermal insulation and thermal-insulating plaster alternated in the assembled constructions. In the conclusion, the authors state that the use of mineral wool in the construction will ensure the slowing down of the temperature increase [3]. The authors Freitas and Rodrigues [4] also write about the need for awareness about the materials from which buildings are built in their contribution. In the contribution, they analyse the fire from the point of view of the fire investigator [4].

2. MATERIALS AND METHOD

2.1 Materials

In experimental studies, we worked with several variants of load-bearing wall constructions. At the same time, we changed the internal composition of the walls in the examined variants. A permanent element of each variant is the universal plasterboard. The plasterboard used in the research is one of the universal plasterboards with a solid core reinforced with glass fibers. It has increased strength and surface hardness. According to the EN 13501-1 standard, it belongs to the reaction to fire class A2-s1, d0. The coefficient of thermal conductivity λ is 0.142 and the diffusion resistance factor μ is 12.7. Plasterboard has a compressive strength of 6.65 MPa [5]. The next layer in the variants is made of mineral wool. As part of the examined variants, we changed its thickness, which is also analysed problem in our paper. Mineral wool is used as heat, sound, and fire insulation. It is non-flammable, in the event of a fire, there is no development and spread of flame on the surface or the formation of toxic fumes. The reaction to fire class of mineral wool is A1. The coefficient of thermal conductivity λ is 0.035 and the diffusion resistance factor μ is 2.15 [6]. The following are two types of thermal insulation, which abound with different properties. The common feature of the types of thermal insulation used is a polyurethane core. We can observe the difference in the surface treatment of the heat-insulating material. And in the first case, it is an aluminium finish. Such material is chemically

resistant to gasoline, mineral oil, microorganisms, and mold. It does not decompose. In this case, the reaction to fire class is C – s1, d0 and the coefficient of thermal conductivity λ is 0.025 [7]. In the second case, it is a surface treatment composed of mineral felt. Such material is resistant to gasoline, mineral oil, microorganisms, and mold. It does not decompose. In this case, the reaction to fire class is E and the coefficient of thermal conductivity λ is 0.023 [8]. From the side exposed to the flame, the construction of the examined variants is completed by new board fireproof materials. These are boards that replace cement chipboards, plasterboards, OSB boards, fire protection boards and other boards. They abound in properties such as high strength, mechanical resistance, resistance to frost, mold, and pests. They are hydrophobic and belong to fire reaction class A1. The coefficient of thermal conductivity λ is 0.14 and the diffusion resistance factor μ is 8.8 [9]. The load-bearing capacity of the structure is ensured by wooden columns. It is a selected type of glued wood, which is high-performance precisely because of the layering and gluing of individual layers, which ensures a significantly high load-bearing capacity as well as shape stability and rigidity. The reaction to fire class is D – s1, d0 and the compressive strength value is 20 MPa [10]. In the following table 1, we can see the thickness, height and width of the materials used in the tested constructions S1-S6. In figure 1 we can see variants S1, S3 and S5 before the test and placement of 8 thermocouples from the outer side on fireproof board.

Table 1: Thickness, height and width of the materials used in the tested constructions (authors)

Material Marking	Plasterboard SDK	Thermal insulation PUR	Wooden post H	Mineral wool MW	Fireproof board FB
Version S1, S2					
Thickness [mm]	15	160	45	-	12
Height [mm]	1 000	1 000	1 000	-	1000
Width [mm]	600	545	160	-	600
Version S3, S4					
Thickness [mm]	15	160	45	80	12
Height [mm]	1 000	1 000	1 000	1 000	1000
Width [mm]	600	545	160	600	600
Version S5, S6					
Thickness [mm]	15	160	45	40	12
Height [mm]	1 000	1 000	1 000	1 000	1000
Width [mm]	600	545	160	600	600
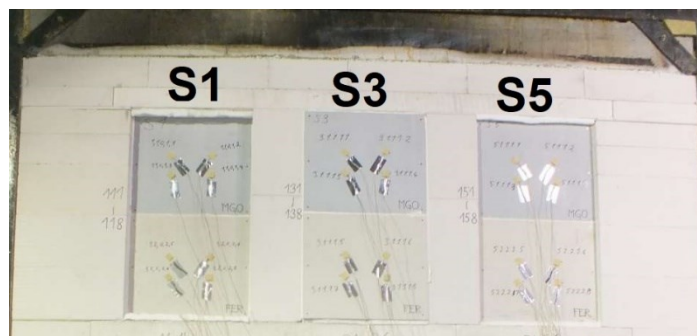
Figure 1: View of the tested specimens: variants S1, S3 and S5 in the
test frame before test (authors)

As we can see in table 1, the change between the assembled constructions occurs in the case of mineral wool thickness S3, S4 and in S5, S6. The location of the mineral wool is chosen from the exposed side behind the plasterboard. The thickness of the mineral wool changes from 80 mm (S3, S4) to 40 mm (S5, S6). As we can see, variant S1, S2 do not contain mineral wool in their composition, so it is a reference sample. Mineral wool was also used in the reference samples, but only in the side parts with a thickness of 20 mm. The variants S3, S4 and S5, S6 are supplemented by a change in the type of thermal insulation. In Figure 2, we can see examples of the material composition of the test structure S3 and its real design. Two thermocouples were placed behind each layer in the centre of the layer equidistant from the top and bottom edges. The specific location of the thermocouples can be seen in Figure 3.
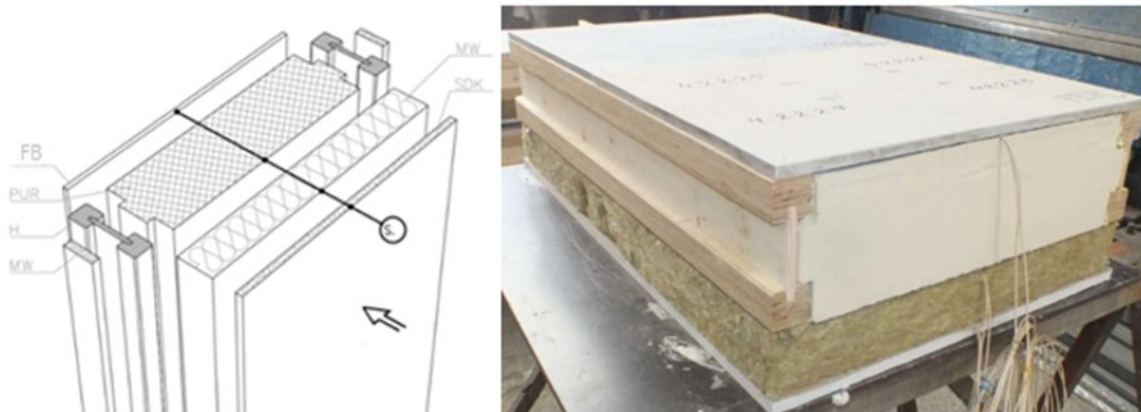
Figure 2: Material composition of the test structure S3 and its real design (authors)

The thermocouples used in the studies were placed according to the standards EN 1363 - 1: 2021 and EN 1365 – 1: 2013. The thermocouples in the furnace space are placed so that they are not in contact with the flames from the burners and that a distance of at least 450 mm from the wall surface is maintained floor or ceiling of the furnace. One of the conditions is that one thermocouple should be placed every 1.5 m^2. It is also necessary to ensure a permanent location of the thermocouples on the test sample, i.e., they must not fall or move during the test. In the case of tested walls with a variable composition, which are assumed to have different insulating capabilities, the increase in average temperature must be monitored separately for individual surfaces. Again, one thermocouple must be placed for every 1.5 m^2, but at least two thermocouples for each separate area [11,12]. The location of the thermocouples and their setup can be seen in the Figure 3. Two thermocouples were used behind each layer. Four thermocouples were used only on the outside of the structure.
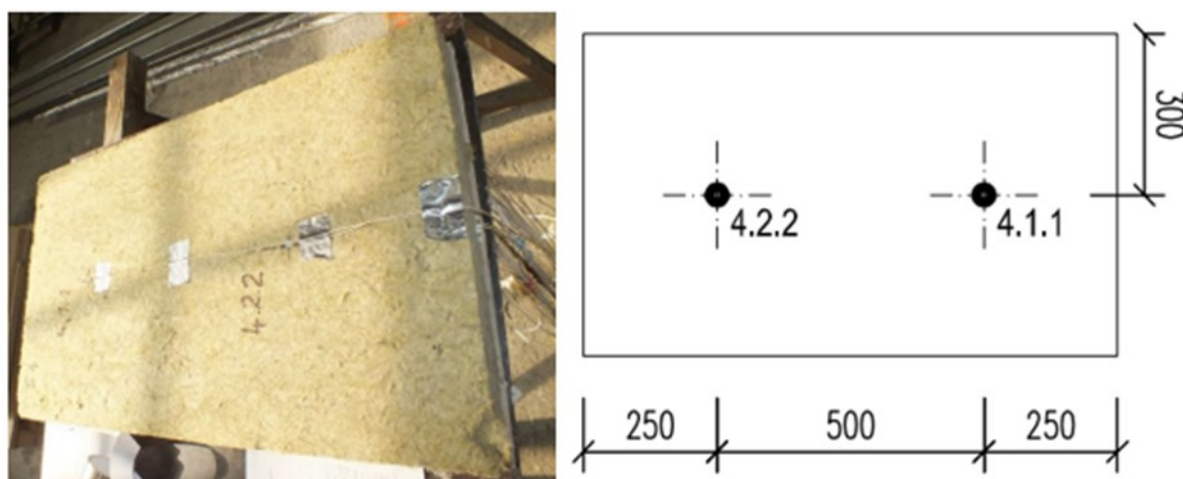
Figure 3: Placement of a thermocouple behind a layer of mineral wool (authors)

2.2 Test method

Each sample in size 1,000 mm height, 600 mm width and 187 mm (S1, S2) or 267 mm (S3-S6) thickness was placed in a frame that serves as an input structure for the test sample. The frame, by its placement in the furnace, ensures heating, pressure, and other conditions. Four gas burners act on the test samples, whose temperature increase in the furnace was calculated according to the standard temperature-time curve [11,12]. The thermal load acted on the test samples from the side where the universal plasterboard fireproof board was located. The observation was carried out during testing, following the criteria specified in the standards. At the same time, smoke development and thermal behavior were monitored. The internal temperature of the test samples behind the mineral wool was observed with two thermocouples. In the figure 4, we can see the progress of the test from the side of

fire. In the left part of the figure 4 is the test sample with added mineral wool of 80 mm thickness (S3) and on the right side we see the reference test sample (S1). Figure 4 left side was captured at 72 minutes of testing, while on sample S1 we noted the formation of cracks from the inside on the plasterboard. Figure 4 right side was captured at 90 minutes, when the decomposition of sample S1 can be seen. In both cases, it is possible to notice that the test structure with added mineral wool of 80 mm thickness (S3) is not damaged by thermal stress on the surface.
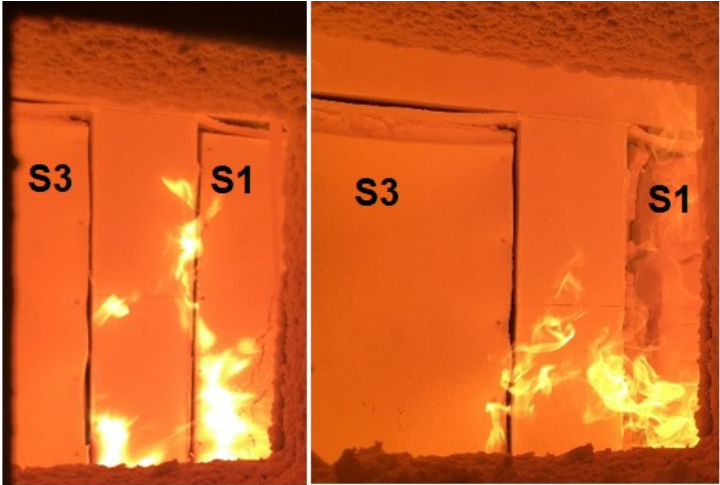
Figure 4: Behavior of the samples S1, S3 during the test from the exposed side, left side was captured at 72 minutes of testing and right side at 90 minutes of the testing (authors)

In Figure 5 below, we can see the outer side of the test structures, while on the left is the reference sample (S1), in the middle is the test sample with added mineral wool of 80 mm thickness (S3) and on the right side of the picture is the test sample with added mineral wool of 40 mm thickness mm (S5). As we can see, the surface temperature of the reference sample varied up to 150 ºC. In the case of the test construction with 80 mm thick mineral wool (S3) added, the surface temperature was lower. And in the case of the test structure with added mineral wool with a thickness of 40 mm (S5), the surface temperature ranged from low to medium high temperatures according to the attached scale. The temperature of the surface of the samples was measured by a thermal camera during the whole 125 minutes of fire resistance testing.
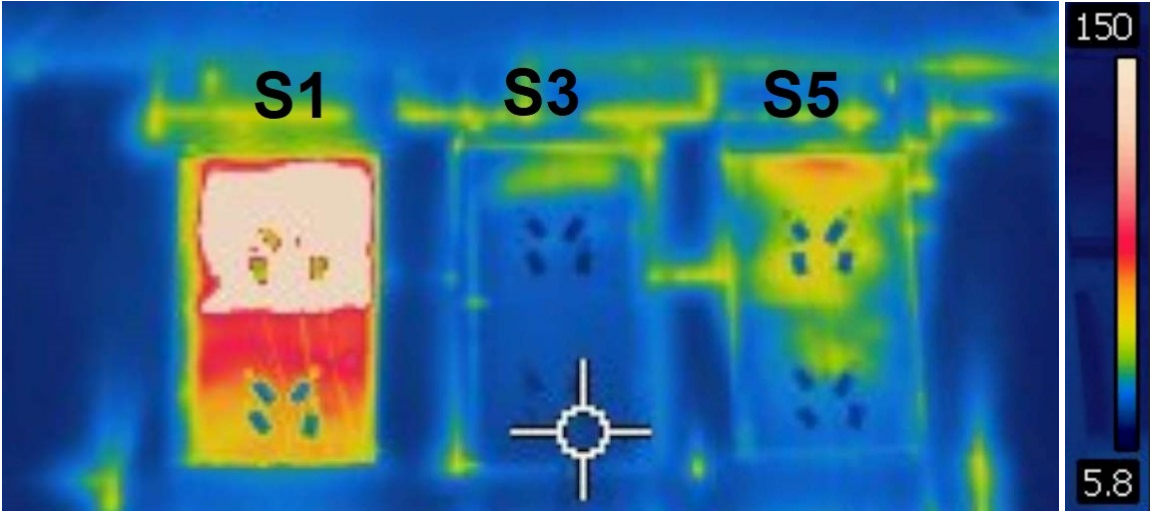
Figure 5: Temperature behavior of the samples S1, S3 and S5 during the test from the non-exposed side (authors)

3. EQUATION AND SYMBOLS

Figure 6 shows the development of temperatures for samples S5 and S6 using mineral wool with a thickness of 40 mm in the construction of the load-bearing wall. Figure 6 shows the temperature values measured by thermocouples located between the mineral wool and the insulation material. An average temperature value was created from the thermocouples, which is used in Figure 6. The constructions of the load-bearing walls S5 and S6 differ in the used thermal-insulating material with different surface treatment. Which was located behind the mineral wool. For the test structure marked S6, heat-insulating material with an aluminium surface treatment and for the test structure marked S5, heat-insulating material with a mineral felt surface treatment. We noticed an increase in temperature in both cases of test constructions from 4 minutes. The temperature in the case of test sample S5 rose by almost 30 ºC/min for 7 minutes, then the temperature rise slowed down to 2 minutes. There was a downward trend from 9 minutes and the temperature decreased by 4 ºC in 14 minutes to 91 ºC. This phenomenon could have been caused by the properties of the universal fire protection board with the combination of a 40 mm mineral wool layer. Over the next 10 minutes, the temperature increased by almost 300 ºC to 419 ºC. During the next 78 minutes, the temperature continuously increased by 1 to 4 ºC/min and in the 113th minute of the test it had a value of 828 ºC. The temperature continued to rise for another 5 minutes to a value of 853 ºC. In the last 7 minutes of the test, a downward temperature trend appeared again, and it decreased to a final value of 839 ºC. The temperature recorded in the final minute of the test behind the previous material, i.e., the universal fireproof board, was 869 ºC. Which means a temperature reduction of 30 ºC behind the added mineral wool. In the case of sample S6, the temperature rises by 58 ºC to 100 ºC after 8 minutes. Again, from minute 9, we observe a decreasing temperature trend of 13 ºC in 14 minutes to a value of 87 ºC. The temperature began to rise more slowly, but from the 27th minute it was already rising rapidly by more than 60 ºC/min. This lasted only a few minutes and from the 38th minute it rises again continuously by 1 to 8 ºC/min. At the test time of 113 minutes, the sample had a temperature of 816 ºC. Compared to the previous sample, it is a temperature decrease of 10 ºC. Subsequently, a downward trend occurred again after 118 minutes to a value of 807 ºC. In the last 7 minutes, the temperature of the test sample started to rise again to the final value of 830 ºC. The temperature recorded in the final minute of the test behind the previous material, i.e., the universal fireproof board, was 822 ºC. The final temperature behind the layer of mineral wool therefore rises by 8 ºC. We can therefore discuss the possible influence of the thermal insulation material from the back side of the mineral wool, since the temperature difference between the S5 and S6 variants is 8 ºC. Furthermore, we note that the test sample with thermal insulation with surface treatment made of aluminium reached higher temperature values during the test for up to 112 minutes compared to the test sample with thermal insulation with surface treatment made of mineral felt. In the last 13 minutes of the test, we observed both a decrease and a slight increase in temperature in both test samples. We rate sample S6 better, composed of layers with mineral wool 40 mm thick and with a heat-insulating layer of expanded polyurethane with aluminium surface treatment. Both test samples did not exceed the desired temperature values from the standard.
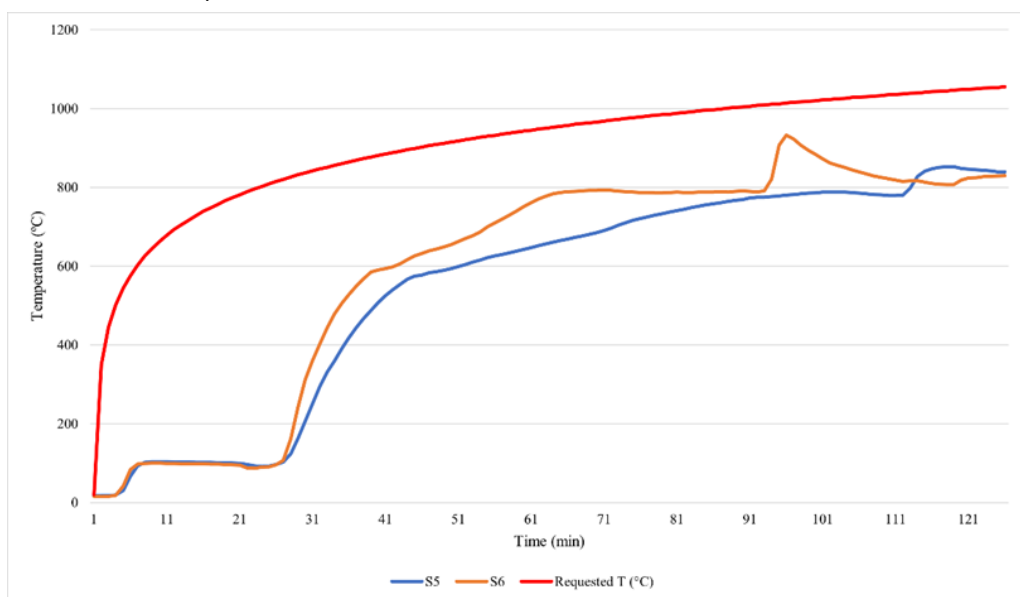
Figure 6: Development of temperatures during the test of samples S5, S6
(authors)

Figure 7 shows the course of development temperatures for samples S3 and S4 using mineral wool with a thickness of 80 mm in the construction of the load-bearing wall. Figure 7 shows the temperature values measured by thermocouples located between the mineral wool and the insulation material. An average temperature value was created from the thermocouples, which is used in Figure 7. The constructions of the load-bearing walls S3 and S4 differ in the used thermal-insulating material with different surface treatment, which was located behind the mineral wool. For the test construction marked S4, thermal-insulating material with an aluminium surface treatment and for the test construction marked S3, thermal-insulating material with a mineral felt surface treatment. We noticed the first increase in temperature in the case of sample S3 from the 6th minute of the test. The temperature increased by 60 ºC to 88 ºC within two minutes. From the 9th minute, as in the previous test samples S5 and S6, we observed a decreasing temperature trend that lasted 19 minutes. During this time, the temperature decreased by 21 ºC to a value of 67 ºC. From the 29th minute of the test, we observed a rise in temperature again. This increase was continuous for a few minutes and subsequently the temperature increased by almost 40 ºC/min. In this way, the temperature rises to 304 ºC within 7 minutes. In the next 78 minutes of the test, the temperature rises by 1 to 10 ºC/min. During the 118-minute test, the temperature was 820 ºC. In the last 7 minutes of the test, the temperature started to decrease. It dropped by 6 ºC to a final value of 814 ºC. The temperature recorded in the final minute of the test behind the previous material, i.e., the universal fireproof board, was 859 ºC. Which means a temperature reduction of 45 ºC. Compared to sample S5 with a layer of mineral wool 40 mm thick, which reached a temperature value of 839 ºC at the end of the test, this is a reduction of the resulting temperature by 15 ºC. In the case of sample S4, we recorded an increase in temperature 2 minutes earlier than in sample S3. The temperature rises in the next 6 minutes by almost 15 ºC to a value of 102 ºC. From the 10th minute of the test, we noticed a drop in temperature. As with sample S3, this decrease lasted until the 28th minute of the test. The temperature value was 80 ºC, which means a reduction of 20 ºC. Which is almost the same course of temperature development as for sample S3. During the next 19 minutes, the temperature continuously increased by almost 20 ºC/min. During the 47 minutes of the test, it had a value of 552 ºC and continued to rise by almost 10 ºC/min. Only after the 107th minute of the test, when it started to gradually decrease from the value of 822 ºC. During the remaining 18 minutes of the test, the temperature decreased to 803 ºC. The temperature recorded in the final minute of the test behind the previous material, i.e., the universal fireproof board, was 885 ºC. Here we see the largest drop in temperature by 82 ºC. Compared to the previous sample S3, the difference in the resulting temperatures is 11 ºC. However, compared to the S6 sample with the same thermal insulation with a surface treatment of aluminium and 40 mm thick mineral wool, it is a temperature difference of 27 ºC. As we can notice in Figure 7, at the 113th minute of the test, the temperatures of the samples leveled off, and while the temperature decreased for the S4 sample, it increased for the S3 sample and subsequently decreased from the 118th minute. However, as a result, the thermally insulated sample S4 with aluminium surface treatment reached a lower temperature than the sample S3. Again, we can discuss not only the positive influence of the thickness of the mineral layer, but also the positive influence of the thermal insulation layer with better fire resistance. Therefore, we better evaluate sample S4, composed of layers with mineral wool with a thickness of 80 mm and with a thermal-insulating layer of expanded polyurethane with a surface treatment of aluminium. Both test samples did not exceed the desired temperature values from the standard.
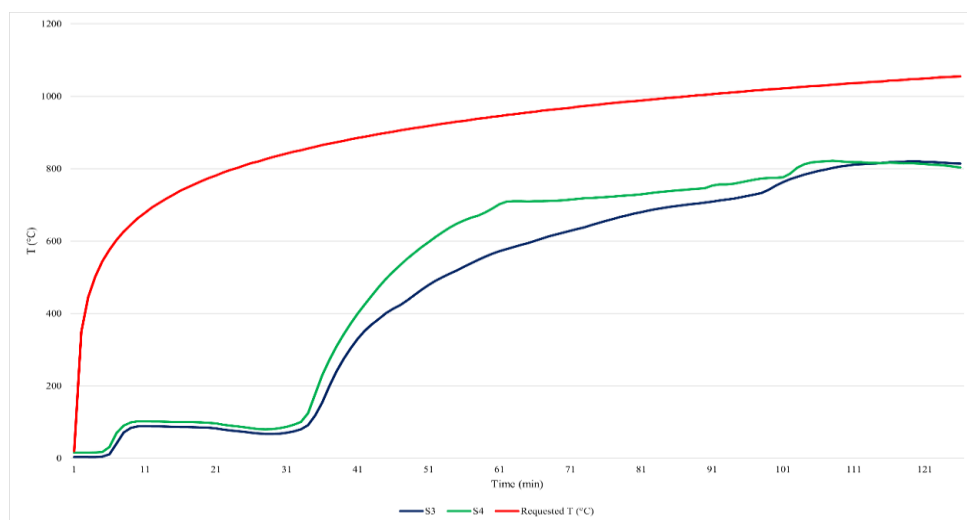
Figure 7: Development of temperatures during the test of samples S3, S4 (authors)

To compare the obtained results, we present Figure 8. As we can see from the figure, all the created sandwich constructions of the load-bearing walls did not exceed the required temperature from the standard. The measured results show that the sample marked S4 has the best fire resistance of the assembled load-bearing sandwich structures. In its composition there is a universal fireproof board, mineral wool with a thickness of 80 mm, behind it a layer of thermal insulation with a polyurethane core with an aluminium surface treatment continues and it is closed by a new type of fireproof boards. The load-bearing capacity of the structure is ensured by wooden columns. At the end of the test, in 125 minutes, this sample reached a temperature of 803 ºC behind the layer of mineral wool. What is the lowest temperature measured in all tested constructions by thermocouples placed behind the mineral wool. An average temperature value was created from the thermocouples, which is used in Figure 8. Sample S3, which had the same thick layer of mineral wool but different thermal insulation, reached a temperature behind the mineral wool layer of 814 ºC at the end of the test. Although, according to the above graph, the sample marked S6 reached the highest temperature during the entire measurement period, at the end a downward trend appeared, which caused the final temperature behind the mineral wool layer to reach 830 ºC. The composition of the S6 sample is a universal fireproof board, mineral wool with a thickness of 40 mm, behind it is a layer of thermal insulation with a polyurethane core with an aluminium surface finish, and it is closed by a new type of fireproof boards. The difference in the composition with the S5 sample is in the thermal insulation with a mineral felt surface finish. In the last 20 minutes, the sample S5 first recorded a decreasing temperature trend and then an increasing one. Which ultimately means that it reached the highest temperature behind the mineral wool layer of all the tested constructions, namely 839 ºC.
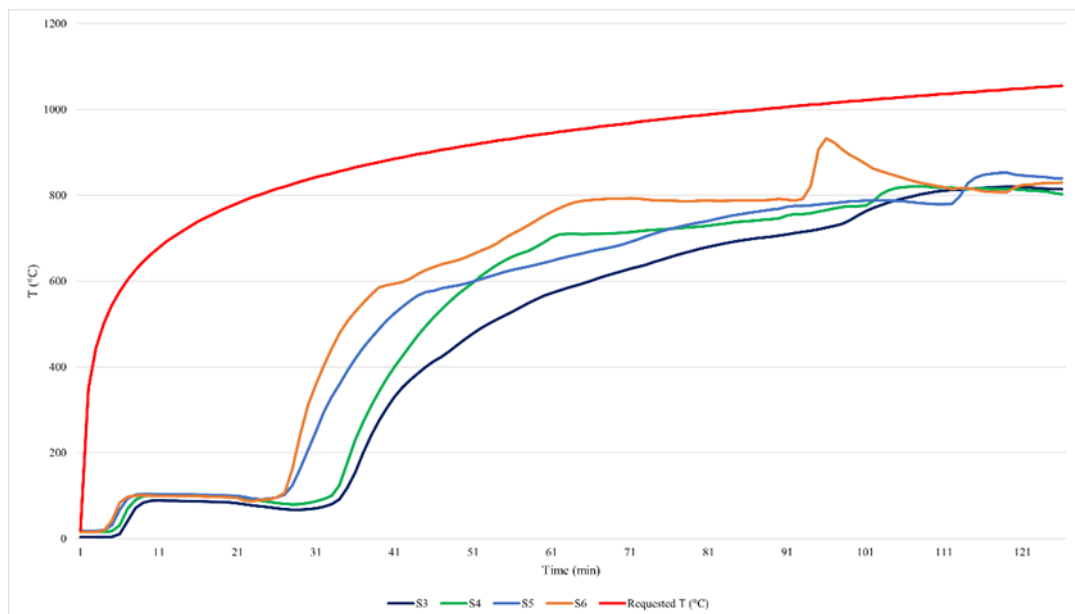
Figure 8: Comparison of temperature development (authors)

4. CONCLUSIONS

By concluding temperature changes during testing and their subsequent comparison, we came to conclusions. Testing alone took 125 minutes. The average starting temperature from the thermocouples was 14.1 °C. During testing, we monitored the course of the temperature change in different parts of the composition of the variants in comparison with the desired temperature according to the EN 1365-1 standard. Subsequently, we compared temperature changes not only between the variants themselves but also between the materials. The influence of the application of mineral wool as well as its thickness on the increase of fire resistance was manifested, which is also documented in Figure 8. For structure S1 (without mineral wool) the highest temperature was measured on the far side of the structure from the fire at 125 min 182 °C, by adding mineral wool 40 mm thick (S5) the annotated temperature dropped to 62 °C, and at 80 mm thick (S3) at 33 °C. By comparing the temperatures measured behind a layer of mineral wool with a thickness of 80 mm and 40 mm between samples S3 and S5, whose structural composition further included thermal insulation with a surface treatment of mineral felt, we found the following. The

test structure marked S3 (mineral wool 80 mm) reached a temperature of 814 °C in 125 minutes of the test. While the temperature recorded in the final minute of the test behind the previous material, i.e., the universal fireproof board, was 859 ºC. Which means a temperature reduction of 45 ºC. The test structure marked S5 (mineral wool 40 mm) reached a temperature of 839 °C in 125 minutes of the test. While the temperature recorded in the final minute of the test behind the previous material, i.e., the universal fireproof board, was 869 ºC. Which means a temperature drop of 30 ºC. As we can see, the difference between the final temperature measured on the reverse side of the reference sample S1 and the final temperature measured on the reverse side of the test sample S3 is 149 ºC. The difference between the final temperature measured on the reverse side of the reference sample S1 and the final temperature measured on the reverse side of the test sample S5 is 122 ºC. From which it follows that the addition of mineral wool with a thickness of 80 mm ensured a higher fire resistance compared to a layer of mineral wool with a thickness of 40 mm. For structure S2 (without mineral wool) the highest temperature was measured on the far side of the structure from the fire at 125 min 153 °C, by adding mineral wool 40 mm thick (S6) the annotated temperature dropped to 123 °C, and at 80 mm thick (S4) at 32 °C. By comparing the temperatures measured behind a layer of mineral wool with a thickness of 80 mm and 40 mm between samples S4 and S6, whose structural composition further included thermal insulation with an aluminum surface treatment, we found the following. The test structure marked S4 (mineral wool 80 mm) reached a temperature of 803 °C in 125 minutes of the test. While the temperature recorded in the final minute of the test behind the previous material, i.e., the universal fireproof board, was 885 ºC. Which means a temperature reduction of 82 ºC. The test structure marked S6 (mineral wool 40 mm) reached a temperature of 830 °C in 125 minutes of the test. While the temperature recorded in the final minute of the test behind the previous material, i.e., the universal fireproof board, was 822 ºC. Which surprisingly means an increase in temperature of 8 ºC. The difference between the final temperature measured on the reverse side of the reference sample S2 and the final temperature measured on the reverse side of the test sample S4 is 121 ºC. The difference between the final temperature measured on the reverse side of the reference sample S2 and the final temperature measured on the reverse side of the test sample S6 is 30 ºC. As we can see from the obtained results, by adding mineral wool with a thickness of 80 mm, we ensured higher fire resistance compared to adding mineral wool with a thickness of 40 mm. We can state that by applying mineral wool, we can significantly increase the fire resistance of the described structure.

ACKNOWLEDGEMENTS

REFERENCES

[1]   Haffke, M.; Pahn, M.; Thiele, C.; Grzesiak, S. (2022). *Experimental Investigation of Concrete Sandwich Walls with Glass-Fiber-Composite Connectors Exposed to Fire and Mechanical Loading.* Applied Sciences, vol. 12, p. 3872.

[2]   Perera, D.; Poologanathan, K.; Gatheeshgar, P.; Upasiri, I. R.; Sherlock, P.; Rajanayagam, H.; Nagaratnam, B. (2021). *Fire performance of modular wall panels: Numerical analysis.* Structures, vol. 34, p. 1048-1067.

[3]   Kontogeorgos, D.; Semittelos, G.; Mandilaras, I.; Founti, M. (2016). *Experimental investigation of the fire resistance of multi-layer drywall systems incorporating Vacuum Insulation Panels and Phase Change Materials*. Fire Safety Journal, vol. 81, p. 8-16.

[4]   Freitas, R.A.; Rodrigues, J.P.C. (2022). A fire investigation methodology for buildings. Architecture, Strucures and Construction, vol. 2, p. 269–290.

[5]   Electronic portal Gipsol, (2023). *Knauf plasterboards*. [online]. Available at: https://gipsol.sk/sadrokartony-knauf

[6]   Knauf Insulation, (2013). *Nobasil MPN*. [online]. Available at: https://cdn1.idek.cz/dek_sk/document/978849634

[7]   Linzmeier, (2020). *Linitherm PGV T*. [online]. Available at: https://www.linzmeier.de/produkte/dach/steildach/linitherm-pgv-t/

[8] Linzmeier, (2020). *Linitherm PAL W.* [online]. Available at: https://www.linzmeier.de/produkte/wand/linitherm-pal-w/

[9] *Magnesium board - a revolutionary breakthrough in the construction industry,* (2023). [online]. Available at: https://www.stavebnik.sk/clanky/horcikova-doska-revolucny-prelom-v-stavebnictve.html

[10] Electronic portal Technomol build, (2023). *Glued wooden structures.* [online]. Available at: https://www.technomol.sk/lepene-drevene-konstrukcie/

[11] EN 1363 - 1: 2021, Fire resistance testing. Part 1: Basic requirements.

[12] EN 1365 - 1: 2013, Fire resistance testing of load-bearing elements. Part 1: Walls.

EXPERIMENTAL FIRE PERFORMANCE OF WOOD BIO-CONCRETES: STUDY ON REACTION TO FIRE AND RESIDUAL STRENGTH

Bruno M. C. Gomes[a]; Amanda L. D. Aguiar [b,*]; Monique A. F. Rocha[c]; Alexandre Landesmann[d]; Nicole P. Hasparyk[e], and Romildo D. Toledo Filho[f]

ABSTRACT

Environmental issues have led to the use of biomass wastes in making cement-bonded construction materials to improve their thermal insulation, and thus build energy-efficient performance. However, the use of biomass in bio-concrete is a cause of concern from the point of view of an accidental fire. Therefore, the present study aims to provide an overview of the flammability of the wood bio-aggregates and bio-concretes using a Mass Loss Cone Calorimeter, and the residual strength of bio-concretes after the cone calorimeter tests. For the production of bio-concretes, volumetric fractions of 40%, 45%, and 50% of wood shavings were used with a cementitious matrix composed of Portland cement and rice husk ash, and fly ash. Cone Calorimeter tests were performed at a heat flux of 50 kW/m^2. In addition, compressive strength tests were carried out in burnt samples. The main results indicate that the incorporation of an inorganic binder involving wood bio-aggregates inhibits ignition and the variation of volumetric fraction of wood shavings in the bio-concrete mixtures did not change the contribution of Heat Release Rate (HRR). After cone calorimeter tests, a reduction of 29% and 15% in the mechanical capacity was observed for WBC40 and WBC45, respectively.

Keywords: Reaction to fire; residual compressive strength; wood bio-aggregates; wood bio-concretes.

[a] Federal University of Rio de Janeiro/COPPE, Brazil (brunocunhaeng@gmail.com).

[b,*] Federal University of Rio de Janeiro/COPPE, Brazil (amanda.aguiar@numats.coc.ufrj.br).

[c] Federal University of Rio de Janeiro/Macaé, Brazil (moniquerocha@macae.ufrj.br).

[d] Federal University of Rio de Janeiro/COPPE, Brazil (alandes@coc.ufrj.br)

[e] Departamento de Segurança de Barragens e Tecnologia, FURNAS-Centrais Elétricas S.A. (nicole@furnas.com.br)

[f] Federal University of Rio de Janeiro/COPPE, Brazil (toledo@coc.ufrj.br)

1. INTRODUCTION

The technologies and building works developed by Civil Engineering bring positive impacts on the quality of life by constructing buildings and infrastructure for the population, which attend to the socioeconomic needs of humanity [1]. However, for this, the industry consumes a large portion of natural resources and thus contributes to environmental degradation through pollution and high rates of greenhouse gases (GHGs) release [2]. Globally, this sector is responsible for the consumption of 60% of raw materials [3], 40% of energy, 12% of water [4], and up to 40% of GHG emissions [5].

In this context, researchers and industries have joined efforts to make the construction field less harmful to the environment through integrated techniques that address waste and sustainability, ensuring that social and economic spheres are also contemplated [6]. On the other hand, the construction industry uses a large amount of non-renewable natural resources that cause environmental degradation through their extraction and pollution [7,8]. One of the solutions to this problem is to reuse plant and agricultural residues that previously did not have an adequate destination and incorporate them into composite materials. These composites are capable of storing the CO_2 sequestered during plant growth [9–13].

Bio-concretes are composite materials whose final characteristics are, in general, linked to the properties of their constituent materials. Generally, those cement composites contain bio-aggregates bound by a cementitious matrix, water, and additives. Cementitious materials act as binders, providing resistance and durability, while bio-aggregate provides lower density, energy absorption capacity, and thermal acoustic insulation [14]. In Brazil, it is estimated that the civil construction industry is responsible for using about 70% of the wood extracted in the country, 54% of which is used raw as rafters and slats, 45% in agglomerates, and 1% in doors, and windows [15]. Thus, due to the high amount of products that need processing, a large amount of wood shavings is generated by carpentry without proper disposal, which makes it possible to use them as bio-aggregates in cementitious composites.

Some chemical components present in wood can negatively affect the performance of bio-concrete, which can reflect on hydration, hardening, and mechanical properties [16]. Vaickelionis and Vaickelioniene [17] state that extractives (resins, fatty acids, terpenes, simple sugars, phenolic compounds) and hemicellulose are mainly responsible for the negative effect on the hydration of bio-concrete, as they can be degraded by the high alkalinity of the cement and release by-products that delay the hydration of the cement. Beraldo *et al.* [18] also state that the presence of sugars and extractives soluble in water or alkali slows down the setting time of the cement. Quiroga *et al.* [19] explain that the presence of inhibitory substances promotes the formation of a membrane around the anhydrous cement grains, which prevents the access of water to them and causes a reduction in the cohesion of the material. Therefore, the bio-aggregates must be submitted to a previous treatment to inhibit these effects and be applied to bio-concretes. One of the solutions found is the treatment in an alkaline solution of calcium hydroxide, which proved to be a more efficient method than the thermal treatment when analyzing the compressive strength of bio-concrete produced with treated wood [20].

Since bio-concrete is a composite that can contain large fractions of plant material in its composition, its chemical composition content affects combustion properties [21]. Thus, it is necessary to know the fire reaction properties of these materials and classify them based on fire safety standards. In the Euroclass system, building materials are divided into seven classes based on their fire reaction properties [9]. The performance and fire scenarios for each class are presented by this manuscript. The highest class, the one with the greatest safety for fire retardant wood products, classified as A2, while low-density fiberboard is assigned to class E. Meanwhile, most products containing natural wood get European class D with known and stable fire performance [22]. In this regard, developing a composite that does not ignite and maintains its level of mechanical performance is one of the challenges faced by bio-based materials [13]. Therefore, this study aims to provide an overview of the flammability of bio-aggregates and wood bio-concretes using a Mass Loss Cone Calorimeter, as well as the residual compressive strength of bio-concretes after cone calorimeter tests.

2. MATERIALS AND METHODS

2.1 Raw materials

In this work, wood shavings (WS) were collected from the state of Rio de Janeiro (Brazil) as residues, which contain a mix of four species: 1. *Manilkara salzmanni*, 2. *Erisma uncinatum warm*, 3. *Cedrela fissilis* and 4. *Hymenolobium petraeum*. This material went through processing to obtain the required characteristics for the production of bio-concrete. First, the WS particles were separated through mechanical sieving, and only the fraction of nominal diameter superior to 1.18 mm was used. After that, this material was treated in calcium hydroxide solution at a concentration of 1.85 g/l [23]. Finally, the treated material was air-dried and homogenized using the method of the elongated pile. The bulk density, moisture content, and water absorption of the treated WS were 530 kg/m³, 19%, and 70%, respectively. In Figure 1-a it is possible to observe the visual appearance of the wood shavings, while in Figure 1-b it is possible to see the micrography of the bio-aggregates without any treatment, and in Figure 1-c the deposition of calcium hydroxide in the particles of wood shavings after alkaline treatment.

a)   b)   c)
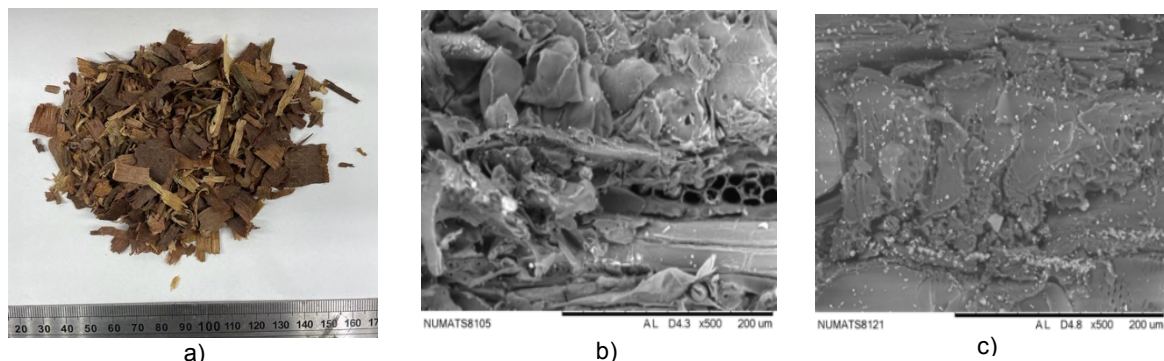
Figure 1: Wood shavings used for the production of bio-concrete: a) Aspect of the bio-aggregate, b) SEM of wood shavings in natural state, and c) SEM of wood shavings after alkaline treatment

In addition to Portland cement Brazilian type CPIIF-40, fly ash and rice husk ash were used as SCMs to reduce cement consumption and CO_2. The chemical composition, determined by X-ray Fluorescence Spectrometry, and the specific density, obtained by a helium gas pycnometer, of these materials are presented in Table 1.

Table 1: Chemical composition and specific mass of cementitious materials

Oxides	Cement	Fly ash	Rice husk ash
SiO_2	12.715%	54.434%	94.305%
Al_2O_3	3.496%	31.133%	0.000%
Fe_2O_3	4.451%	5.350%	0.072%
K_2O	0.596%	3.512%	2.470%
CaO	73.927%	1.815%	1.092%
SO_3	4.013%	1.715%	1.483%
TiO_2	0.000%	1.104%	0.000%
BaO	0.000%	0.553%	0.000%
Tm_2O_3	0.000%	0.135%	0.000%
ZrO_2	0.000%	0.087%	0.000%
MnO	0.094%	0.056%	0.545%
ZnO	0.029%	0.040%	0.000%
SrO	0.348%	0.024%	0.000%
Y_2O_3	0.000%	0.014%	0.000%
CuO	0.028%	0.000%	0.017%
LOI*	9.78%	1.66%	5.19%
Specific Mass	3053 kg/m³	1885 kg/m³	2510 kg/m³

*Loss on ignition

172

2.2 Wood bio-concrete

Three volumetric fractions of WS (40%, 45%, and 50%) was adopted for the production of wood bio-concretes (WBC). The cement matrix was composed, in mass, of 45% of cement (CEM), 25% of rice husk ash (RHA) and 30% of fly ash (FA). As a setting accelerator, calcium chloride (CC) was used in the content of 2% in relation to the mass of cementitious materials of each mixture. The water-to-binder ratio was set at 0.30 for all blends. In addition to cement hydration water (Wh), a compensation water (Wc), referring to the water absorbed by the wood bio-aggregates, was considered to ensure good workability of the bio-concretes. Therefore, total water (Wt) is the sum of hydration water and compensation water. These percentages of materials were based on previous works [24–27]. Table 2 presents the consumption of materials of all blends studied, in kg/m^3.

Table 2: Wood bio-concretes composition, in kg/m^3

WBC	WS	CEM	FA	RHA	CC	Wh	Wc
WBC40	212.00	375.82	250.55	208.79	16.70	250.55	148.40
WBC45	238.50	344.50	229.67	191.39	15.31	229.67	166.95
WBC50	265.00	313.18	208.79	173.99	13.92	208.79	185.50

Production process of bio-concretes followed adaptations of the Brazilian Standard ABNT NBR 16697 [28]. The procedure began with mixing the wood shavings and cementitious materials for 1 minute. After that, total water, previously mixed with calcium chloride, was added progressively over 1 minute. A total mixing time of 4 minutes was necessary to obtain a homogenous bio-concrete. The samples were cast in two layers in prismatic molds of 100 x 100 x 25 mm (length x width x thickness) and each layer was mechanically vibrated on a vibration table (68 Hz) for 10 seconds. After 24 hours, the samples were demolded and stored in a room at a temperature of 22 ± 3 °C and relative humidity of 55 ± 5% until reaching 28 days of age. Figure 2 shows the wood bio-concrete samples before the fire reaction tests.

a)   b)   c)
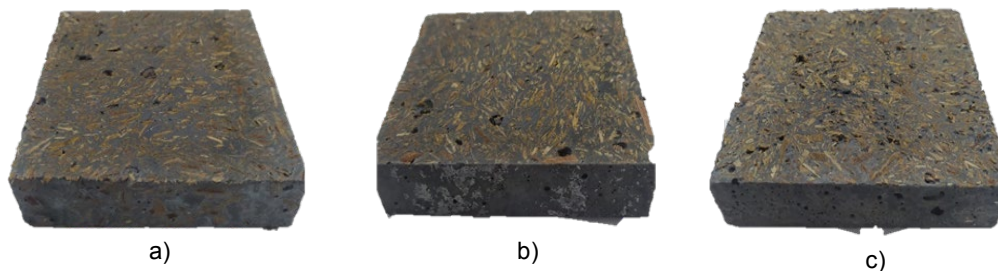
Figure 2: Samples of WBCs before heat flux: a) WBC40, b) WBC45, and c) WBC50

2.3 Cone Calorimeter tests

A Mass Loss Cone Calorimeter (MLCC), model FTT-0014/2012 (Figure 3), was used to perform reaction to fire tests on wood bio-aggregates and wood bio-concretes. The wood bio-aggregates were tested in natural conditions (NW) and treated in (Ca(OH)$_2$) conditions (TW) and the bio-concretes with the volumetric fractions of biomass previously indicated: 40% (WBC40), 45% (WBC45), and 50% (WBC50). A heat flux of 50 kW/m^2 was chosen because it represents a heat flux of a developed fire. Nowadays, this equipment operates the most advanced method to evaluate the reaction to fire properties of a material on a reduced scale. Six samples of each type were tested. All faces of the samples, except for the top face, were wrapped with aluminum foil. The specimens were exposed to the heat flux under the cone located at 25 mm from the sample surface to begin the test.
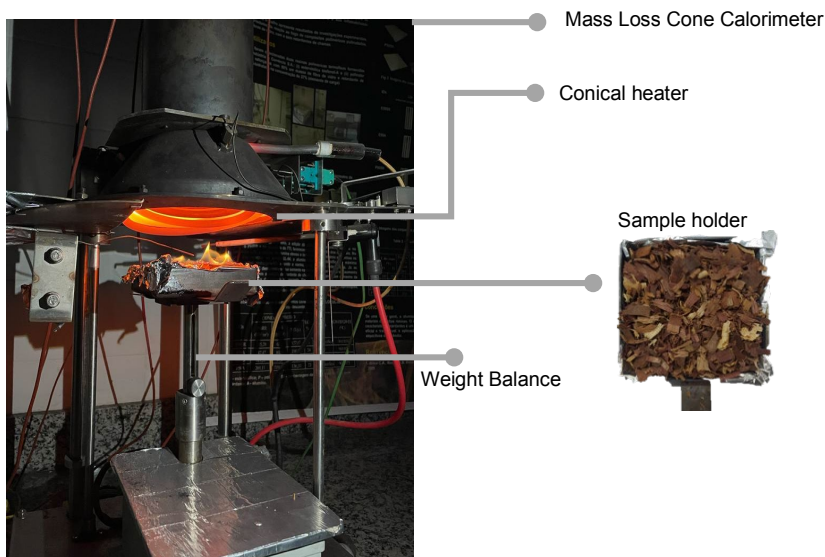
Figure 3: General scheme of the Mass Loss Cone Calorimeter

The test procedure was performed according to the standards ISO 17554 [29] and ISO 13927 [30]. In all tests, the samples were examined in horizontal position up to 2 minutes after the flame ceases, or up to 10 minutes if the sample does not ignite. During the test, the following reaction to fire properties were determined: heat release rate (HRR), peak of HRR (PHRR), medium value of HRR (MHRR), total heat released (THR), total mass loss (TML), effective heat of combustion (EHC), maximum temperature reached (MTR), time to ignition (TTI), and time to flame out (TTF).

2.4 Compressive strength

The bio-concrete compression tests were performed on 6 specimens of each mix. In order to evaluate the residual strength of wood bio-concrete, samples were tested before and after cone calorimeter tests. For this, a Bionix–25 kN (Figure 4-a) was used with a displacement speed of 0.3 mm/min. The samples, after being subjected to the fire reaction tests, were cut in smaller samples with dimensions of 25 x 25 x 50 mm (length x width x height) as shown in Figure 4-b. The mass and dimensions were measured to verify variation in their density after cone calorimeter tests.

a)   b)
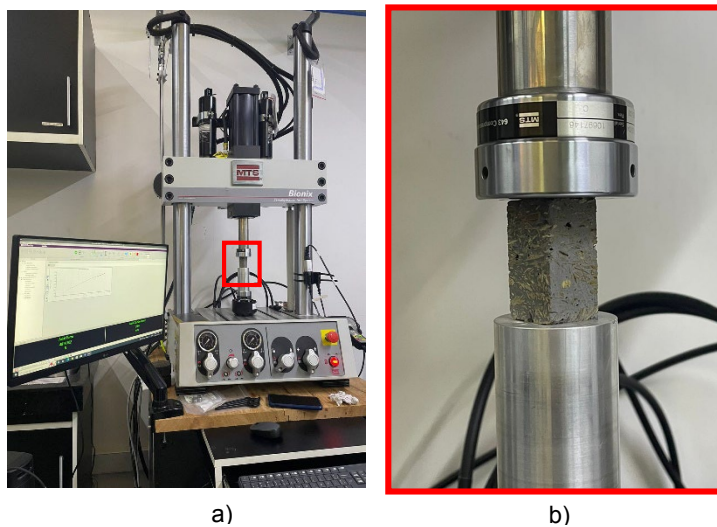
Figure 4: Uniaxial compression test: a) setup, and b) sample

3. RESULTS AND DISCUSSION

ANOVA analysis of all data indicated that all reported in this study, where found to fall within the 95% confidence interval band for having a normal distribution and one analyzed by the Tukey Test method to identify significant difference between the variables.

3.1 Reaction to fire

The main results of the reaction to fire properties are presented in Table 3. In addition, data of thickness and density of the samples were provided.

Table 3: Combustion properties of wood bio-aggregates and wood bio-concretes

		NW	TW	WBC40	WBC45	WBC50
1	Thickness (mm)	25	25	25.5 (3.83)	25.1 (0.56)	24.5 (1.86)
2	Density (kg/m^3)	-	-	1353.5 (1.20)	1322.5 (3.22)	1090.6 (2.11)
3	PHRR (kW/m^2)	93.99 (7.01)	83.74 (11.19)	13.25 (15.97)	13.07 (9.74)	14.32 (5.54)
4	MHRR (kW/m^2)	65.34 (7.51)	57.07 (13.10)	9.64 (18.66)	9.51 (11.46)	11.41 (6.21)
5	THR (MJ/m^2)	22.3 (7.37)	18.6 (13.56)	6.3 (15.08)	5.8 (11.29)	6.9 (5.89)
6	TML (%)	84.14 (4.14)	77.48 (3.71)	11.72 (7.85)	11.73 (5.91)	13.42 (3.89)
7	EHC (MJ/kg)	7.88 (2.98)	7.49 (13.79)	1.57 (18.87)	1.48 (10.65)	1.93 (6.05)
8	MTR (°C)	777 (1.10)	765 (0.28)	477 (2.69)	475 (1.75)	483 (0.77)
9	TTI (s)	21 (14.20)	15 (31.10)	-	-	-
10	TTF (s)	362 (4.04)	348 (9.92)	-	-	-

The coefficient of variation is shown in parentheses.

The heat release rate (HRR) was defined as the heat release per unit area evaluated under a constant heat flux, using Eq. (1).

$$\dot{q}''(t) = \frac{q(t)}{A} = \frac{1.1c}{A} \frac{\Delta Hc}{r_0} \sqrt{\frac{\Delta P}{T_e}} \cdot \left[\frac{X_{O_2}^o - X_{O_2}(t)}{1,105 - 1.5\,X_{O_2}(t)} \right] \tag{1}$$

Where $\dot{q}''$ is the HRR (kW/m^2); q(t) is the heat released (kW); A is the area initially exposed in horizontal orientation (m^2) before the test, and Δ_{hc} is the net heat of combustion (kJ/kg). In fire reaction studies, the heat release rate is the most important parameter considered, required in zone and field models, as it concerns the fire control characteristics and indicates the contribution to the fire development. Figure 5 shows the heat release rate curves measured in samples of wood shavings in their natural state (Figure 5-a) and after alkaline treatment (Figure 5-b). Because of concerns about incorporating plant residues in the production of concrete due to the incompatibility between bio-aggregates and the cementitious matrix [31], the use of methods that reduce the percentage of extractives present in the biomass, which are mainly responsible for delaying cement hydration [18,32], has become an interesting and widely technique for the viability of bio-concrete production [31–34]. In wood bio-concrete, extractives can affect mechanical properties, density and moisture content [35]. In the fire reaction properties, a reduction of approximately 11% on the heat release rate was observed between natural and treated bio-aggregates. It occurs because the alkaline treatment removes the extractives from wood shavings, which are the components that release the most heat during burning [36], with their content reduced the biomass will release less heat.
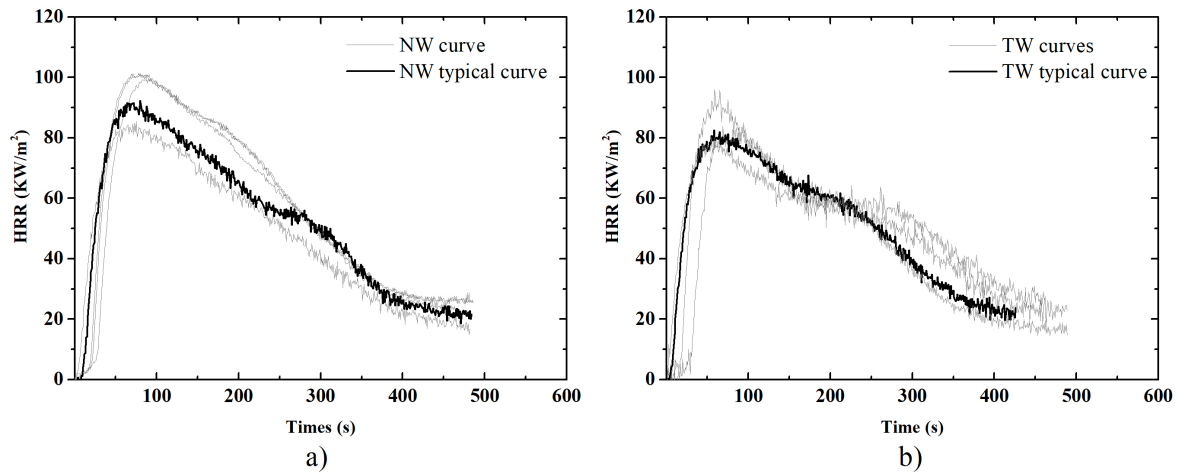
Figure 5: Variation of heat release rate over time: a) NW, and b) TW

In all curves presented in Figure 5, it was observed that the rate of heat release increased suddenly when the specimen was ignited and then dropped after the material was degraded by heat. For studies carried out in wood using Cone Calorimeter, the presence of two peaks in the curves is commonly reported in the literature [37–40]. However, when it comes to particulate material, oxygen levels are higher inside the sample than solid materials. Therefore, the heat can spread faster and maximize the damage caused by fire, reducing the ignition time. The initial peak is mainly caused by ignition followed by the formation of the carbonization layer that occurs in the first seconds of tests. After the occurrence of the first peak, the rate of heat release tends to decrease. When the fire reaction behavior of wood samples in their natural state is evaluated, the samples are not completely burned since a charred layer that forms on the surface of the sample contributes to increasing the residual capacity of the member protecting the interior of the section [41]. As the wood shavings are in particulate format, this protection is minimized and the material is easily degraded, having a lower fire resistance than if evaluated in a solid format.

Figure 6 shows, respectively, the HRR curves over time for the bio-concretes produced with 40, 45, and 50% of bio-aggregates (Figure 6-a, 6-b, 6-c). However, even with different fractions of plant biomass, the variables did not show different statistical behavior among themselves. Two phases are observed in the presented curves. The first release of heat occurs in a more accentuated way, which is caused by the burning of the wood shavings that are on the surface of the sample. The second phase occurs around 300 seconds after starting the test, where there was a stabilization in the heat release rates of the samples that remain practically constant until the end of the test. Table 3, line 3 presents the PHRR values for all variables. The NW samples presented a value of 93.99 kW/m², while the TW samples presented a value of 83.74 kW/m², i.e. about 11% lower than the natural samples. Thus, the removal of extractives from biomasses caused by the alkaline treatment resulted in a reduction in the PHRR values of bio-concretes. When comparing the different bio-concretes, data are not discrepant. For the average values of MHRR (Table 3, line 4), comparing WBC40 with WBC50 it is possible to notice that there was an increase in this property of 18% with the increase of the biomass content. However, all bio-concretes maintain low heat release and no ignition.
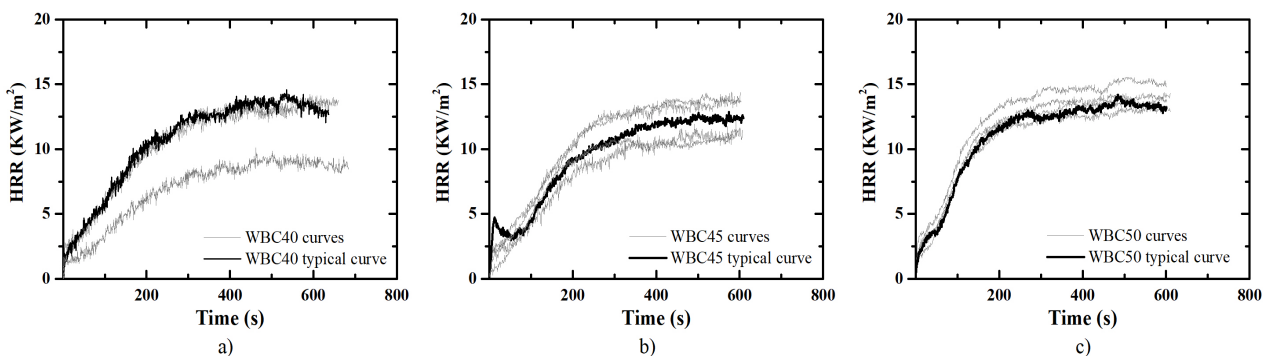
Figure 6: Variation of heat release rate over time: a) WBC40, b) WBC45, and c) WBC50

176

THR refers to the total heat of combustion released by the material during the test. The higher the value of THR, the greater the potential of thermal energy available for the combustion of the material to occur. In Table 3, line 5 the THR values are presented. When comparing bio-concrete with wood particles, it is possible to verify that the cementitious matrix acts on the bio-aggregates as an insulator for the propagation of heat. It provides for the material, in addition to becoming incombustible, decreasing the heat released under the fire conditions.

The total mass loss (Table 3, line 6) corresponds to the variation in mass of the sample during the entire firing process, which is calculated using five-point numerical differentiation equations in cone calorimeter tests [29]. It changes depending on material properties such as the level of pyrolysis, volatilization, and burning under constant heat flux. In addition to being directly related to the HRR, TML is also associated with specific extinguishing area and CO_2 produced during burning. A material that has a lower mass loss rate is indicative of a lower susceptibility for flame propagation. Figure 7-a shows the evolution of the mass loss rate over time for all variables studied and it was highlighted in the final 40 seconds of the evaluated bio-concrete samples.
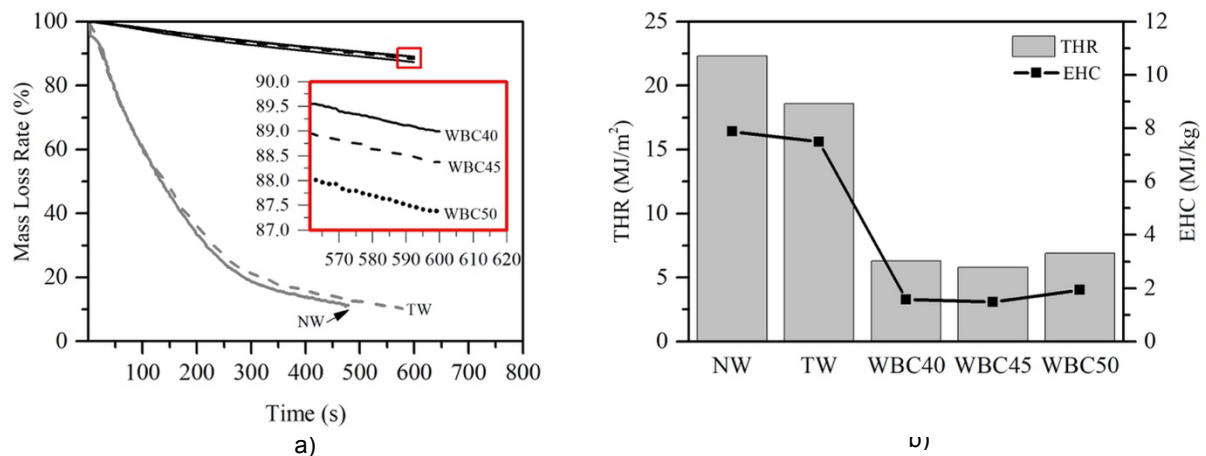
Figure 7: Reaction to fire properties: a) total mass loss over time, and b) total heat release and effective heat of combustion

The cementitious matrix behaved as a thermal insulator for the wood bio-aggregates, making the heat transfer more difficult and turning the composite into an incombustible material. In Figure 7-a, it is possible to observe that the bio-concretes had a small mass loss and the average values presented in Table 3, line 6 did not show discrepancy for the bio-concretes produced with volumetric fractions of 40% and 45%. For WBC50, there was an increase of 14% in TML compare to WBC40 and WBC45 due to the higher content of wood shavings and higher porosity in the matrix. Thus, despite the difference of 10% in the biomass content, the results for these properties did not vary significantly.

Average chemical heat of combustion, determined in the MLCC, is defined as the effective heat of combustion (EHC) [42]. This parameter corresponds to what would be expected in a fire where incomplete combustion occurs, when a material is not completely burned. EHC is a parameter that depends directly on the level of irradiance and time that corresponds to the heat released from the volatile portion during the combustion of the material, which can be calculated using Eq. (2) [43]. Where MLR is the mass loss rate.

$$\text{EHC} = \frac{HRR}{MLR} \qquad (2)$$

Table 3, line 7 presents the mean EHC values found in this study for pilotless ignition conditions. It is possible to notice that the EHC values did not show significant differences for the three studied bio-concretes (See Figure 7-b). Lyon and Janssens [43] state that one of the factors that most contribute to the EHC of materials is fuel chemistry, ventilation rate, and combustion efficiency in the flame. Hull *et al.* [44] also mentioned that the EHC is influenced by fire dynamics and combustion efficiency. For the NW and TW samples, which presented ignition, there was a variation in the EHC values up to 80% when compared to the bio-concretes.

WBC40, WBC45 and WBC50 did not present significant variation in EHC values (1.48 – 1.93 MJ/kg) due to the fact that they did not present ignition and released low heat, the peak value is very close to the average value. On the

other hand, the samples of wood shavings, presented a very pronounced HRR peak, and, therefore, higher values of EHC (7.88 MJ/kg for NW and 7.49 MJ/kg for TW). Ignition time is the time required to establish a sustained flame on the sample surface. This is an important parameter to evaluate the combustion behaviour of materials, since the shorter the ignition time, the more flammable the material. In Table 3, line 9, the ignition time of the NW was 21 seconds and TW samples was 15 seconds (28% lower than NW). For the bio-concretes, there was no ignition.

3.2 Residual compressive strength

Figure 8 shows the average values of residual compressive strength of the studied bio-concretes. Since conventional concrete is a non-combustible material, little attention is paid to its reaction to fire properties. On the other hand, when exposed to heat, the material suffers a degradation and loss of its mechanical properties that affect its compressive and tensile strength, as well as its modulus of elasticity. This occurs because of chemical-physical processes that the material undergoes due to the high temperatures that induce widespread cracking and damage to the matrix and aggregates [45,46].

Fire spalling phenomenon, occurs when there is a sudden detachment of layers or pieces of concrete from the surface of the element when exposed to extreme temperatures in fire situations. When this phenomenon occurs, depending on its magnitude, a significant decrease in the geometry of the cross-section can occur, exposing the reinforcement directly to flames, compromising the structural load capacity [45]. The literature reports two physical mechanisms that are associated with fire spalling: (i) the increase in pore pressure due to water vaporization (a thermo-hygro mechanism) and (ii) the introduction of thermal stresses due to high-temperature gradients (a thermo-mechanical mechanism) [47–49]. For bio-concrete, as it may have a high content of bio-aggregates, thermal degradation of the biomass occurs, decreasing the pore pressure inside the composite. Therefore, the spalling phenomenon does not occur for these materials.

The shrinkage suffered by the cementitious matrix and the carbonization of the vegetal biomass caused the decrease in bio-concrete density, which damaged its microstructure and, therefore, decreased its mechanical performance. As a composite material, when exposed to fire conditions and high temperatures, the bio-aggregate loses mass faster than the cementitious matrix, causing damage in the interface between them. Another point concerns the porosity present in the particles and their internal moisture content. When heated, water is easily eliminated in the form of vapor, which causes damage to the matrix. From Figure 8-a, a decrease of around 29% and 15% for WBC40 and WBC45, respectively after the cone calorimeter test, indicate a weakening of the bio-aggregate/cementitious matrix interface. For WBC50, which has a less resistant matrix, even without the action of the heat flux, the surface burning effect did not affect this mechanical property due to the high porosity that enable the release of heat from the sample, reducing damage caused at the interface due to heat buildup. Aguiar *et al*. [50] showed that increasing the biomass content improves the thermal stability of wood bio-concrete.
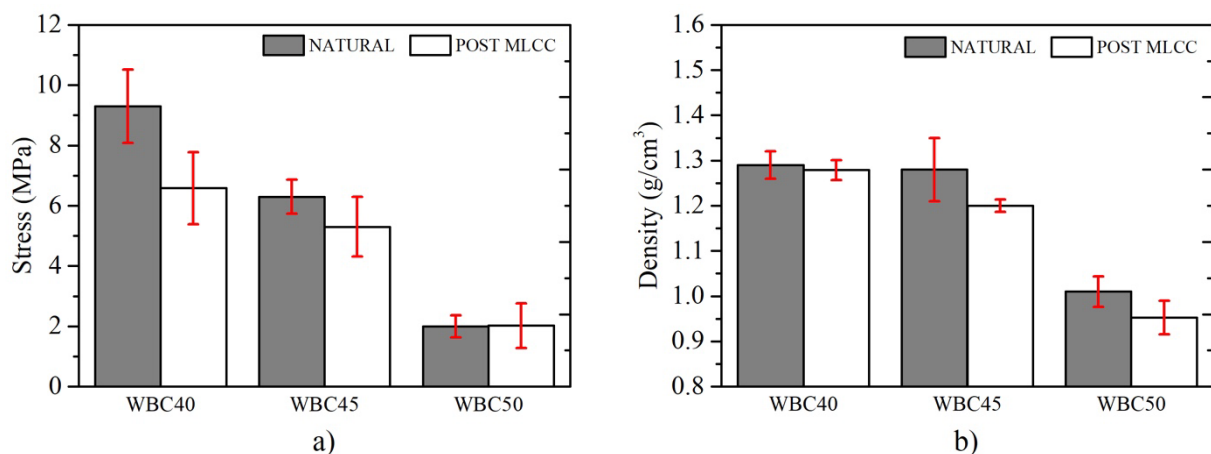
Figure 8: Post MLCC analysis of wood bio-concretes: a) residual compression, and b) density variation

According to the Analysis of Variance statistical tool (ANOVA) and the Tukey test performed, there is a significant difference for the residual compression test when comparing the WBC40 results before and after exposure to fire conditions. The WBC45 and WBC50 samples showed no significant difference. When analyzing the density of the

materials, the shrinkage caused by the heat flux was proportional to the mass loss and therefore the samples did not present statistically significant differences.

4. CONCLUSIONS

This paper investigated the fire behaviour of bio-concrete produced with volumetric fractions of 40, 45, and 50% of wood shavings in a Mass Loss Cone Calorimeter and its post-fire residual compressive strength. Parameters such as time to ignition (TTI), Heat Release Rate (HRR), peak of HRR (PHRR), medium value of HRR (MHRR), total heat released (THR), total mass loss (TML), and effective heat of combustion (EHC) were studied and the following conclusions can be addressed:

- Alkaline treatment, contributed positively to the reduction of PHRR, MHRR, THR, and TML, despite not being indicated as a technique to improve fire reaction parameters. However, due to the high variability found in materials of plant origin and the non-applicability separately of wood shavings, effects of treatment in the reaction to fire properties becomes secondary;
- All analyzed bio-concretes presented a firing process in two stages. The first results from an increased release of heat by burning the bio-aggregate located in the samples surface, and the second by a smaller release of heat from the matrix cement;
- The paste of cementitious materials behaved as an insulating material promoting incombustibility to the composite since no bio-concrete ignited;
- The difference of 10% of bio-aggregate (WBC40 – WBC50) was not enough to bring significant differences in the fire reaction properties of the bio-concretes;
- The conditions similar to a fire caused a reduction of the mechanical capacity of the bio-concretes and a decrease in density for the WBC40 while statistically this behaviour was not significant for the WBC45 and WBC50.

REFERENCES

[1] C. Lee, J.W. Won, W. Jang, W. Jung, S.H. Han, Y.H. Kwak, *Social conflict management framework for project viability: Case studies from Korean megaprojects*, Int. J. Proj. Manag. 35 (2017) 1683–1696.

[2] X. Zhang, Y. Wu, L. Shen, *Embedding "green" in project-based organizations: the way ahead in the construction industry?*, J. Clean. Prod. 107 (2015) 420–427.

[3] I.Z. Bribián, A.V. Capilla, A.A. Usón, *Life cycle assessment of building materials: Comparative analysis of energy and environmental impacts and evaluation of the eco-efficiency improvement potential*, Build. Environ. 46 (2011) 1133–1140.

[4] H. Said, L. Berger, *Future trends of sustainability design and analysis in construction industry and academia*, Pract. Period. Struct. Des. Constr. 19 (2014) 77–88.

[5] H. Son, C. Kim, W.K. Chong, J.S. Chou, *Implementing sustainable development in the construction industry: constructors' perspectives in the US and Korea*, Sustain. Dev. 19 (2011) 337–347.

[6] I.S. Khan, M.O. Ahmad, J. Majava, I*ndustry 4.0 and sustainable development: A systematic mapping of triple bottom line, Circular Economy and Sustainable Business Models perspectives*, J. Clean. Prod. 297 (2021) 126655.

[7] A. Goel, L.S. Ganesh, A. Kaur, *Sustainability integration in the management of construction projects: A morphological analysis of over two decades' research literature*, J. Clean. Prod. 236 (2019) 117676.

[8] H.D. Nguyen, L.D. Nguyen, Y.-Y. Chih, L. Le-Hoai, *Influence of participants' characteristics on sustainable building practices in emerging economies: Empirical case study*, J. Constr. Eng. Manag. 143 (2017) 5017014.

[9] G. Bumanis, M. Andzs, M. Sinka, D. Bajare, *Fire Resistance of Phosphogypsum-and Hemp-Based Bio-Aggregate Composite with Variable Amount of Binder*, J. Compos. Sci. 7 (2023) 118.

[10] M.Y.R. da Gloria, V.M. Andreola, D.O.J. dos Santos, M. Pepe, R.D. Toledo Filho, *A comprehensive*

approach for designing workable bio-based cementitious composites, J. Build. Eng. 34 (2021) 101696.

[11] R. Sonnier, O. Belkhane, L. Ferry, L. Aprin, P. Delot, C. Garcia, A.H. de Menibus, H. Lenormand, M. Potin, *Fire behaviour of hemp, clay and gypsum-based light biobased concretes and renders*, Constr. Build. Mater. 331 (2022) 127230.

[12] Y.R. Herrero, K.L. Camas, A. Ullah, *Characterization of biobased materials, in: Adv. Appl. Biobased Mater.*, Elsevier, 2023: pp. 111–143.

[13] J. Giancaspro, C. Papakonstantinou, P. Balaguru, *Mechanical behavior of fire-resistant biocomposite, Compos. Part B Eng.* 40 (2009) 206–211.

[14] A. Matoski, *Utilizacao de po de madeira com granulometria controlada na producao de paineis de cimento-madeira*, (2013).

[15] M.F.N. dos Santos, B. Rosane Ap G, B.S. Bezerra, H.S.A. Varum, *Comparative study of the life cycle assessment of particleboards made of residues from sugarcane bagasse (Saccharum spp.) and pine wood shavings (Pinus elliottii)*, J. Clean. Prod. 64 (2014) 345–355.

[16] S. Amziane, F. Collet, *Bio-aggregates based building materials: State-of-the-art report of the RILEM technical committee 236-BBM*, Springer, 2017.

[17] G. Vaickelionis, R. Vaickelioniene, *Cement hydration in the presence of wood extractives and pozzolan mineral additives*, Ceram. Silikaty. 50 (2006) 115.

[18] A.L. Beraldo, A.C. de ARRUDA, A.C. STANCATO, C.A.P. SAMPAIO, O.P. FERNANDES FILHO, V.M. LEONEL, *Compósitos à base de resíduos vegetais e cimento Portland, ENCONTRO Bras. EM MADEIRA E EM ESTRUTURAS MADEIRA.* 8 (2002).

[19] A. Quiroga, V. Marzocchi, I. Rintoul, *Influence of wood treatments on mechanical properties of wood-cement composites and of Populus Euroamericana wood fibers, Compos.* Part B Eng. 84 (2016) 25–32.

[20] A.L.D. Aguiar, C.G. Bezerra, L.R. Caldas, A.S. Bernstad, R.D.T. Filho, *Environmental Performance of Wood Bioconcretes with Different Wood Shavings Treatments*, Constr. Technol. Archit. 1 (2022) 69–76.

[21] G. Dorez, L. Ferry, R. Sonnier, A. Taguet, J.-M. Lopez-Cuesta, *Effect of cellulose, hemicellulose and lignin contents on pyrolysis and combustion of natural fibers*, J. Anal. Appl. Pyrolysis. 107 (2014) 323–331.

[22] B.A.-L. Ostman, E. Mikkola, *European classes for the reaction to fire performance of wood products*, Holz Als Roh-Und Werkst. 4 (2006) 327–337.

[23] C.G. Bezerra, S. Oliveira, N.P. Hasparyk, D.O.J. dos Santos, A. de C. Pereira, V.K.C.B.L.M. Balthar, R.D. Toledo Filho, *Caracterização reológica de pastas ternárias para o desenvolvimento de bioconcretos leves de casca de arroz*, Matéria (Rio Janeiro). 28 (2023).

[24] N.A. da Silva, A.L.D. de Aguiar, M.Y.R. da Gloria, R.D.T. Filho, *Bond-Behavior of Bamboo Strips and Bamboo/Wood Bio-Concretes*, in: Proc. 75th RILEM Annu. Week 2021 Adv. Sustain. Constr. Mater. Struct., Springer, 2023: pp. 923–933.

[25] A. Araujo, N. da Silva, T. Sá, L. Caldas, R. Toledo Filho, *Potential of Earth-Based Bamboo Bio-Concrete in the Search for Circular and Net-Zero Carbon Solutions to Construction Industry*, in: IOP Conf. Ser. Earth Environ. Sci., IOP Publishing, 2022: p. 12043.

[26] M.C. Pinto, *Influência da Temperatura e de Tratamentos Alcalinos na Remoção dos Extrativos da Biomassa de Madeira e seus Efeitos na Hidratação de Pastas de Cimento e de Bioconcreto*, (2019).

[27] N.A. da Silva, *Estudo da aderência bambu-bioconcreto*, (2019).

[28] ASSOCIAÇÃO BRASILEIRA DE NORMAS TÉCNICAS. NBR 16697: *Cimento Portland-Requisitos*. 2018., n.d.

[29] ISO 17554:2014, International Organization for Standardization, *"Reaction to fire tests —* Mass loss measurement"., n.d.

[30] ISO 13927. Plastics – Simple heat release test using a conical heater and a thermopile detector. Brussels: CEN – Comité Européen de Normalisation. 2005., n.d.

[31] R.C. Sun, J. Tompkinson, *Comparative study of organic solvent and water-soluble lipophilic extractives from wheat straw I: yield and chemical composition*, J. Wood Sci. 49 (2003) 47–52.

[32] G. Delannoy, S. Marceau, P. Gle, E. Gourlay, M. Guéguen-Minerbe, D. Diafi, S. Amziane, F. Farcas, *Impact of hemp shiv extractives on hydration of Portland cement*, Constr. Build. Mater. 244 (2020) 118300.

[33] A.Q. Dayo, A. Zegaoui, A.A. Nizamani, S. Kiran, J. Wang, M. Derradji, W. Cai, W. Liu, T*he influence of different chemical treatments on the hemp fiber/polybenzoxazine based green composites: Mechanical, thermal and water absorption properties, Mater.* Chem. Phys. 217 (2018) 270–277.

[34] A. Zegaoui, R. Ma, A.Q. Dayo, M. Derradji, J. Wang, W. Liu, Y. Xu, *Morphological, mechanical and thermal properties of cyanate ester/benzoxazine resin composites reinforced by silane treated natural hemp fibers*, Chinese J. Chem. Eng. 26 (2018) 1219–1228.

[35] J. Bodig, B.A. Jayne, *Mechanics of wood and wood composites*, (1982).

[36] M.A. Dietenberger, L.E. Hasburgh, *Wood products: thermal degradation and fire*, Ref. Modul. Mater. Sci. Mater. Eng. (2016) 1–8.

[37] J. Kim, J.-H. Lee, S. Kim, *Estimating the fire behavior of wood flooring using a cone calorimeter*, J. Therm. Anal. Calorim. 110 (2012) 677–683.

[38] O. Grexa, H. Lübke, *Flammability parameters of wood tested on a cone calorimeter*, Polym. Degrad. Stab. 74 (2001) 427–432.

[39] Y.-J. Chung, *Comparison of combustion properties of native wood species used for fire pots in Korea*, J. Ind. Eng. Chem. 16 (2010) 15–19.

[40] B.-H. Lee, H.-S. Kim, S. Kim, H.-J. Kim, B. Lee, Y. Deng, Q. Feng, J. Luo, *Evaluating the flammability of wood-based panels and gypsum particleboard using a cone calorimeter*, Constr. Build. Mater. 25 (2011) 3044–3050.

[41] Q. Xu, L. Chen, K.A. Harries, F. Zhang, Q. Liu, J. Feng, *Combustion and charring properties of five common constructional wood species from cone calorimeter tests*, Constr. Build. Mater. 96 (2015) 416–427.

[42] A. Tewarson, Generation of heat and chemical compounds in fires, Section 3rd, Chapter 5, SFPE Handb. Fire Prot. Eng. Edn), PJ DiNenno, Ed. Natl. Fire Prot. Assoc. Quincy, Massachusetts. (2002).

[43] J. Jiang, J. Li, Q. Gao, *Effect of flame retardant treatment on dimensional stability and thermal degradation of wood*, Constr. Build. Mater. 75 (2015) 74–81.

[44] T.R. Hull, K. Lebek, M. Pezzani, S. Messa, *Comparison of toxic product yields of burning cables in bench and large-scale experiments*, Fire Saf. J. 43 (2008) 140–150.

[45] C. Rossino, F. Lo Monte, S. Cangiano, R. Felicetti, P.G. *Gambarova, HPC subjected to high temperature: a study on intrinsic and mechanical damage*, in: Key Eng. Mater., Trans Tech Publ, 2015: pp. 239–244.

[46] C. Rossino, F. Lo Monte, S. Cangiano, R. Felicetti, P.G. *Gambarova, Concrete spalling sensitivity versus microstructure: Preliminary results on the effect of polypropylene fibers*, in: MATEC Web Conf., EDP Sciences, 2013: p. 2002.

[47] P. Kalifa, F.-D. Menneteau, D. *Quenard, Spalling and pore pressure in HPC at high temperatures*, Cem. Concr. Res. 30 (2000) 1915–1927.

[48] Z.P. Bazant, *Analysis of pore pressure, thermal stress and fracture in rapidly heated concrete*, (1997).

[49] H. Saito, Explosive spalling of prestressed concrete in fire, Bull. Japan Assoc. Fire Sci. Eng. 15 (1966) 23–30.

[50] A.L.D. Aguiar, R.D. Toledo Filho, *Influence of High Temperatures on the Mechanical Properties of Wood Bio-Concretes*, in: Constr. Technol. Archit., Trans Tech Publ, 2022: pp. 61–68.

Fire Risk Assessment

GEOGRAPHIC INFORMATION SYSTEM AND MULTI-CRITERIA ANALYSIS AS A FIRE RISK ASSESSMENT IN HERITAGE SITE

Erika Esteves Lasmar a

Paulo Gustavo von Krüger b

Ana Clara Mourão Moura c

ABSTRACT

The fire prevention in the cultural heritage of protected cities, which can be handled by Fire Engineering, receives as support for a better confrontation of accidents, the complementary use of the Geographic Information System - GIS, with the Multicriteria Analysis Method - MCA, using variables from traditional fire risk analysis methods: Gretener, Chichorro, EbraFire and Arica. These are selected, quantified and weighted according to their greatest contribution to the site's vulnerability.

Knowing deeply the variables that interfere in a process becomes fundamental for decision making. Hence the importance of the form prepared for the technical visits, and later the creation of the attributes table, designed to organize the data of the chosen location.

The advantage of this unique and integrated proposal is the ease of obtaining visual answers, through maps, facilitating the interpretation and understanding of the data collected and judged as more or less vulnerable to a fire.

In this investigation, the analyzes were carried out in the blocks around Praça Tiradentes in Ouro Preto and focused on Portuguese colonial architecture, characterized by the contiguity of the buildings, the use of wood for structure and for clad the floors and roofs of the buildings, indicating the types of buildings that, in most cases, are vulnerable to fire.

Keywords: fire engineering; analysis method; GIS; MCA; technology

---

a Universidade Federal de Minas Gerais, erikalasmar@hotmail.com.

b, Universidade Federal de Minas Gerais, paulovonkruger@gmail.com.

c, Universidade Federal de Minas Gerais, anaclara@arq.ufmg.br.

1. INTRODUCTION

It is commonly known that fires in protected sites cause irreparable losses and that the main actions to combat this type of accident must be aimed at preventing them.

Based on the Fire Engineering vision, according to Claret (2017) [1], a building can be designed so that the action of fire is minimized and controlled. This author considers that specific safety objectives, demonstrated through projects, contribute to minimize and control the fire action.

This article contributes for the Fire Engineering as a possibility of preventing fires in cultural heritage sites, expanding the forms of risk assessment, taking the technological advance of software as an aid. These will support studies in search of greater efficiency in dealing with claims.
The integrated use of the Geographic Information System – GIS, with the Multicriteria Analysis Method – MCA, applied as models for assessing fire risks in sites protected as cultural heritage, constitute a technical improvement in the control of claims.

For the application of the GIS and MCA method, assumptions were created aiming at the elaboration of decision making processes for preventing firefighting, from multiple points of view, based on already known methods, such as Gretener, Chichorro, EbraFire and Arica.

Ouro Preto, in Minas Gerais state, the object of this study, requires the implementation of Fire Engineering to enrich a type of historic urban landscape, recognized as an important cultural asset of contemporaneity.

2. DEVELOPMENT

2.1 Ouro Preto

The relevance of Ouro Preto for the proposed study lies in understanding of the formation of its historical urban landscape, in which each period of its transformation produced an accumulation of forms, leaving the mark of its own time, and can be recognized as a morphological period.

The studies by Pereira Costa and Gimmler Netto (2015) [2] refer to the understanding of the morphogenesis and structure of historical urban landscapes applied in the city of Ouro Preto, Minas Gerais state, and described in this item.

According to the authors, the urban landscape presents historicity insofar as it reveals a greater number of morphological periods in its composition. They understand the concept of historicity as the accumulation of forms produced over time. There are dispersed types of historical urban landscapes, but the most significant examples are in the historic center because it has a higher incidence of occurred facts.

There is great interest in maintaining historical urban landscapes, as this integrates with the concept of contemporaneity and the preservation of urban heritage.

According to Pereira Costa and Gimmler Netto (2015) [2], from 1698, the initial historical landmark was the discovery of gold in the region. This led to the opening of paths and the process of occupation of the territory.

The urban plan is configured by the formation of settlements around temporary chapels, interconnected by the main path (*Caminho Tronco*) and secondary ones, to support the mining activity.

The urban tissue is organized through residential occupations around the chapels, construction of ranches, small sales for the mine workers subsistence.

Despite the wealth that the region boasted, in the beginning the dwellings were built in a provisional and quite simple way, with local materials, since what featured the period was the inconstancy situation in which the explorers lived, whose permanence in the place would be in accordance with the results of gold exploration.

The vernacular typology prevailed, with wood widely used due to its abundance for the proximity to the dense Atlantic Forest. It was used in the basic types of housing, in structures, doors, windows, floors and roofs. Filling the walls with wattle and daub contributed to the thermal control of the dwellings. Clay was also considered as a closing material for the constructions. According to Vasconcelos (1951) [3], the use of stones provided much more protection against the cold climate.

Also according to authors Pereira Costa and Gimmler Netto (2015) [2], in 1711, the settlements of Pilar and Antônio Dias were agglutinated and elevated to the status of village. In 1720, with the creation of the Captaincy of Minas Gerais, Vila Rica becomes its headquarters, constituting the cultural and political center for the colony.

The economic development resulting from the gold exploration is reflected in urban improvements, construction of palaces and public buildings and squares; in artistic expressions, whether in the fine arts, literature, music, especially the religious architecture from Minas Gerais, which was an example of Baroque in Brazil, according to Mello (1985) [4].

At Santa Quitéria Hill, Vila Rica's main square is built, unifying the centrality of the Pilar and Antônio Dias camps for this space, where administrative buildings are implemented: Chamber and Jail Building, Foundry House and Dispatches, Palace of the Governors.

The construction of the square consolidated the continuity of the occupation along the *Caminho Tronco*, transferred to this space the centrality of the villages and transformed the urban form by the densification of the population around it.

The urban plan is expanded by the creation of new streets and alleys, configuring extensive blocks that adapt to the rugged site, both in the Pilar and Antônio Dias regions.

The studies by Pereira Costa and Gimmler Netto (2015) [2], state that in the Imperial Period, 19th century (1822-1889), Vila Rica is elevated to the category of city, as capital of the province. To keep it as a political center and modify the morphology then current, in order to modernize it, there were investments in health, water supply, transport with the creation of new roads and public lighting with street lamps, implementation of university schools (Pharmacy, Normal and Mining).

The urban form is reflected in the subdivision of a few blocks to the west and north of what was then Independency Square (only in 1894 did it become Tiradentes Square).

For the mentioned authors, from 1889 to 2014, the urban tissue is little modified and the uses are formed by single-family residences.

The urban plan is the most persistent morphological element of Ouro Preto. The original plan structured along the *Caminho Tronco* maintains the cultural value of the urban landscape in the present times.

The urban tissue tends to be persistent but is susceptible to accidental destruction by fire or gradual replacements from changing ownership or other functional alterations.

The protection of the cultural value of heritage proposes the study of the situation and the possibilities arising from an accident or incident. The fact is that disasters – or, in this case, fires in cultural heritage sites, always have a conditioning factor, which is the correct maintenance and prevention that precede these episodes. In the case of Ouro Preto, the factors go beyound. They are also found in the urban morphology of the city.

Thus, when analyzing the city of Ouro Preto and establishing prevention and fires fighting plans, one must take into account: the potential risk of a fire by the difficulty to be faced due to the relief, geological formation of the city and by the anthropic processes that have shaped its forms over time; the difficulties of fighting fires in a city with of narrow and steep streets that, in general, slow down the passage of firefighters' vehicles, when they don't completely stop them over; the absence of a more distributed network of fire hydrants; the state of conservation of the buildings and the quantification of the fire load contained therein; expansions or irregular occupations; the risks,

both in the single building and in the community, since the proximity of the buildings can lead to the generalization of the fire.

The analysis debate on the challenges of the historic center of Ouro Preto in relation to fire prevention and combat has conditions that are the correct maintenance and prevention that anticipate these episodes.

Kruger et al (2020) [5] state that, "Ensuring fire safety in historic sites goes beyond the issue of safeguarding the property, reaching the aid in preserving of cultural memory: the intangible property, this being an inseparable part of human life, which is the main object of fire protection."

The spatial cut selected for this article covers the area that remained preserved in the historic center of the city, but it was the one that underwent major modifications to meet the new tourist demands.

2.2 GIS and MCA

For Eastman et al (1995) [6], the technological evolution of GIS has involved three domains of applications: the first, is the use of GIS as an informational database, as a coordination and access to geographic data; the second, is the use of GIS as an analytical tool, which means establishing a logical and mathematical relationship between the map layers and their derivative maps; and the third stage, which is the use of GIS as a tool to support decision making by providing means for actions on the analyzes produced. In our opinion, the third stage is intrinsically related to the second, as it generates the analytical product that indicates spatial potentialities and vulnerabilities.

The spatial analysis of the studied areas, a condition given by the GIS, allows the identification of the vulnerable spaces observed in the duality and in the ability of GIS to "(...) store the geometry of the geographic objects and their attributes (...)", as mentioned by Câmara and Monteiro (2002). [7]

Among the spatial analysis models, the Multicriteria Analysis – MCA stands out. In this juncture, the use of maps to support decision making goes beyond the visualization of geographic space and information, both spatial and non-spatial, and provides a greater understanding of the analyzed location, representing reality and creating scenarios that can assist in decision making.

Moura (2020) [8] explains that, in the systemic approach, the identification of the main variables is to **decompose** reality by listing its characteristics. Once the process of **decomposing** (in subjects, in space and in time) is done, comes the process of **composing**, that is, separating the main variables by models that highlight aspects of this reality to finally **recompose**, that is, applying methods of combining them with a view to a judgment.

Figure 1 illustrates the author's idea.
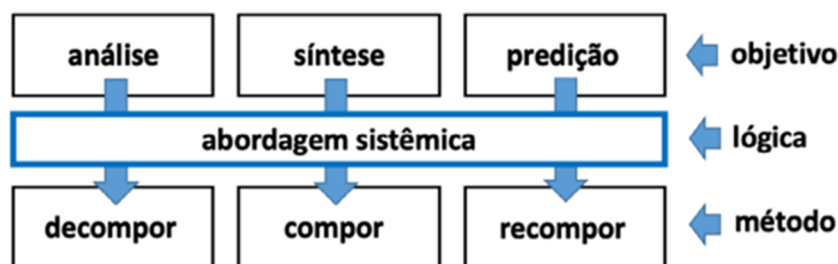
Figure 1: Systemic approach in the processes of analysis and interpretation of territorial reality. Source: Moura, 2020

Given the spatial data analysis capability of GIS, which also allows for data storage and manipulation, one can work in conjunction with MCA. This selects variables/attributes, i.e. alphanumeric codes stored in tables, for example, to form the characterization of a space. It combines the main attributes, usually conflicting information, and relates to the geographic space. In this way, it is possible to verify the existing reality and perform simulations with the aim of testing possibilities for improvements in the results.

In Moura, 2007, [9] it reads the multicriteria analysis procedure "is based on mapping variables by information plan and defining the degree of pertinence of each plan and each of its legend components for the construction of the final result, using weighting factors whenever necessary."

This investigation used the complementary use of GIS and MCA to evaluate the fire risks of a part of the historic center of Ouro Preto, Minas Gerais. The variables were taken from traditional fire risk analysis methods: Gretener, Chichorro, EbraFire and Arica. These were selected, quantified and weighted according to their relative importance in relation to the others.

2.3 Source of variables

The investigative principles contained in the methods of fire risk analysis chosen, show that they treat it in a similar way some issues, but differ in some details. The choice of these methods is justified by the points in which they differ, which leads to a complement between them, and the possibility of obtaining greater assertiveness in the answers obtained in the survey.

1) Gretener's Method: It was the basis for the IT-35 in Minas Gerais state. It was created by engineer Max Gretener, in 1960. Its objective is to quantify fire risk as well as fire safety, according to pre-established evaluation criteria.

The method uses mathematical formulas and statistically based data table analysis at the same time. It mainly analyzes the fire process determining the factors that propagate the fire, evaluates the activation as a function of the occupancy of the unit, and the contribution of safety measures to reducing the risks.

2) **Chichorro Method** - **Holistic Calculation of Fire Risk of Construction and Enabled Optimization of its Reduction in Constructions Works**: is a fire risk assessment model, developed at the University of Porto, arising from the concern of analysis of heritage buildings in urban sites due to the increasing occurrence of fires, some of high severity, and the quantification of the impact that a fire outbreaks in a building may have. The risk of fire in this case is calculated by the product of its probability and its severity. The severity takes into account the total consequences, the capacity of the fire to develop and spread, and the effectiveness of rescue and fire fighting.

3) **EBRAFire Method** - **Existing Building's Risk Assessment for Fire**: also developed in Portugal, it is a method still under development that locates, in detail, where to intervene in a given building in order to raise its fire safety rating. The methodology takes into account that one can act in a way that contributes to the fire safety by correcting the parameters in detail, after detailed analysis. The method also evaluates fire risks in spaces dedicated to events, such as parties, concerts, and others.

4) **Simplified Arica Method** - Fire Risk Analysis in Old Urban Centers: This is an updated version of the Arica Method developed in Portugal in 2004. The Simplified Arica Method is a reorientation of the original method, aiming of facilitate the application of the form and to guide design interventions for existing buildings.

Based on the wording of the updated Decree-Law nº 95/2019, it started using alternative fire safety and non-prescriptive verification methods.

> It is up to the designer to determine the fire safety measures to be implemented in the building, with appropriate justification in the descriptive memory of the fire safety project, using methods of analysis of fire safety conditions or methods of risk analysis, recognized by ANEPC or by method to be published by LNEC. (COELHO et al, 2019) [10]

The 2019 Arica Simplified method, has the goal of assessing fire risk in protected urban centers.
For each Unit of Analysis - UA, the fire safety index is calculated by an equation, in which are considered:
- Global factor related to the start of the UA fire;
- Global factor relating to the development and spread of the AU fire;
- Global factor regarding to the evacuation of the UA;
- Global factor relating to UA firefighting.

For Muculo (2013) [11], these global factors cover all aspects relevant to fire safety, from the safety of occupants, property and the building itself, and are made up of several partial factors.

These methods above are in the form of questionnaires that are answered during technical visits. The results are modified with each improvement intervention installed, according to the guidelines that are given to the owners of the buildings.

The main variables were extracted from these questionnaires and was selected those that could best be answered within the reality of Ouro Preto. Based on them, a new form was created especially for application in this case.

The form was prepared with the objective of also meeting Fapemig's Universal Edital Project, prepared by its coordinator Paulo Gustavo von Kruger.

The second step in this process, better explained in the next item, was to apply the form in the geographic space defined in Ouro Preto. The answers will compound the attribute table used in MCA process.

3. MCA FOR FIRE RISK ASSESSMENT

3.1 Alphanumeric Data

The form is one of the products created with the variables taken from the different methods of fire risk analysis. The goal is to clearly answer questions about the variables. Such answers will feed the attribute table, which corresponds to a second product. The attribute table associates the polygons of the lots with their characteristics, so that an analysis of their current state can be performed. The MCA is the intersection of these information and will be applied in the GIS.

In a macro way, the form created investigates the following information:

1. Development and spread of fire: deals with the type of fire load existing in the building;
2. Effectiveness of rescue and firefighting: this is information about the existence of fire extinguishers, distance to hydrants and Fire Company, accessibility of the building;
3. Evacuation and Safety: are the evacuation routes. Number of passage units, slope of the route, emergency lighting;
4. Fire scene: description of the building in terms of area, ceiling height, and floor scene;
5. Conditions of electrical installations.
6. Characteristics of the buildings: age, facade height, use, number of floors, number of occupants.
7. Construction characteristics: types of materials in masonry, types of floors, information about vertical circulation, state of conservation, ventilation, number of spans with spacing wider than 1.10m, and existence of fire detection and alarm equipment;
8. Types of automatic detection and passive protection required by regulation.
9. Latitude and longitude.
10. Food facilities (kitchen);
11. Gas installations.

The application of the form was carried out in the blocks surrounding Tiradentes Square in Ouro Preto, Minas Gerais state. The figure 2 illustrates the selected geographical space and the corresponding buildings. They are in brown.

Figure 2: Historic center of Ouro Preto. Source [12]: IPHAN / Programa Monumenta, UFMG, 2001/2002.

The application of the form was carried out in the blocks surrounding Tiradentes Square in Ouro Preto, Minas Gerais

3.2 MCA Roadmap

The logic behind the MCA requires a clear definition of the objectives to be achieved. To do this, the variables that account for the characteristics of the area are selected, according to their vulnerability to fire.

Once selected, the integration model is applied to the variables, transforming their behavior into numerical data in an attributes table, to enable comparison of results, defining grades and weights. Grades are assigned by technical knowledge of experts, who rank the legend components of each variable according to the degree of pertinence to the risk. They are defined according to a normalization of 1 and 10, 1 being for a condition of greater vulnerability to fire, recorded as negative, and 10 for a less vulnerable situation, recorded as positive. The cases whose scores were 0 (zero), means the non pertinence of the variable in the building.

The weights have a meaning related to the degree of relevance of each variable to the set of variables.

Moura (2020) explains the normalization of variables and their legend components as follows:

> The next step consists of normalizing the variables and their legend components in two processes: bringing all information into quantitative representation in order to favor map algebra, and specifying minimum and maximum values common to all to allow data of different natures to be combined. (MOURA, 2020) [8]

The weight of evidence is also explained by Moura (2020) as one:

> (...) ranking for a reason for investigation, from the judgment by different weights arbitrated by the researcher according to some decision method. This process is interesting to classify vulnerabilities, potentialities, interests and probabilities, that is, everything that requires a classificatory ranking. (MOURA, 2020) [8]

After the clarifications about the model for evaluating the variables, we started to fill in the attributes table. This was filled in with the data collected in the field and by research conducted among experts in the fire area in relation to the selected variables.

To explain the scores considered for each of the variables, we used technical standards, Fire Department Technical Instructions, previous technical knowledge, and field research:

189

AFAST (Offset) - viewing the defined space on the map;

ACCESS_V_CB (Fire Department Car Access) - viewing the space defined on the map;

T_RES_DESC_CB (Displacement Response Time) - viewing the space defined on the map;

CONCENTRA_CI (Concentration of fire load) - determined by IT-09 of CBMMG and inspected on site;

DIST_HIDRANT (Hydrant Distance) - viewing the space defined on the map;

EQUIP_EFIC_EXT (Equipment for Effectiveness of the Fire Fighting System - extinguishers) - inspected on site;

EQUIP_EFIC_DET (Equipment for Effectiveness of the Fire Fighting System - fire detection) - inspected on site;

ACESS_EDIF (Building Accessibility) - surveyed on site;

ILUM_EM (Emergency Lighting) - inspected on site;

EST_CONSER (Conservation status) - inspected on site;

CIRC_VERT (Vertical circulation) - inspected on site;

IE_NORMAS (Adequacy of electrical installation standards) - determined by ABNT NBR 5410 and inspected on site;

IG_NORMAS (Adequacy of gas installation standards) - determined by ABNT NBR 15526:2016 and inspected on site;

POP_QUANT (Public frequenting the building) - inspected on site;

EVENTS_PROX (Events near) - inspected on site;

PUB_EVENTO (Public attending the space during events) - information provided by the Municipal Secretariat of Tourism, Industry and Commerce and the Research and Study Sector of Ouro Preto/MG.

To explain the weights considered for each of the aforementioned variables, experts in the fire area were invited to make a comparison between the selected variables, through a script of questions, in order to define a ranking of greater vulnerability to fire. Thomas Saaty's method, called AHP – Analytic Hierarchical Process, was used. It proposes a comparison between paired variables and at the same time defines a criterion of importance among them.

In Thomas Saaty's (1988) [13] definition, "With the AHP we have a means of identifying the relevant facts and the interrelationships that exist". And also explains, "It is a three part process which includes identifying and organizing decision objectives, criteria, constraints and alternatives into a hierarchy; evaluating pairwise comparisons between the relevant elements at each level of the hierarchy;"

The figure 3 shows the ranking weights of the selected variables.

Figure 3: Result of variables by Weights of Evidence (presents a classification ranking of the most vulnerable condition, according to the investigation. AHP Method). Source: The authors.

Figure 4 presents, by maps, the results of the studies of each variable applied to the selected blocks of Ouro Preto in relation to vulnerability to fire risk. They are represented by the grades 1 and 10, being 1 for a condition of greater vulnerability to fire (red color) and 10 for a less vulnerable situation (green color). The cases whose scores were 0 (zero) (yellow color), means the non pertinence of the variable to the building.
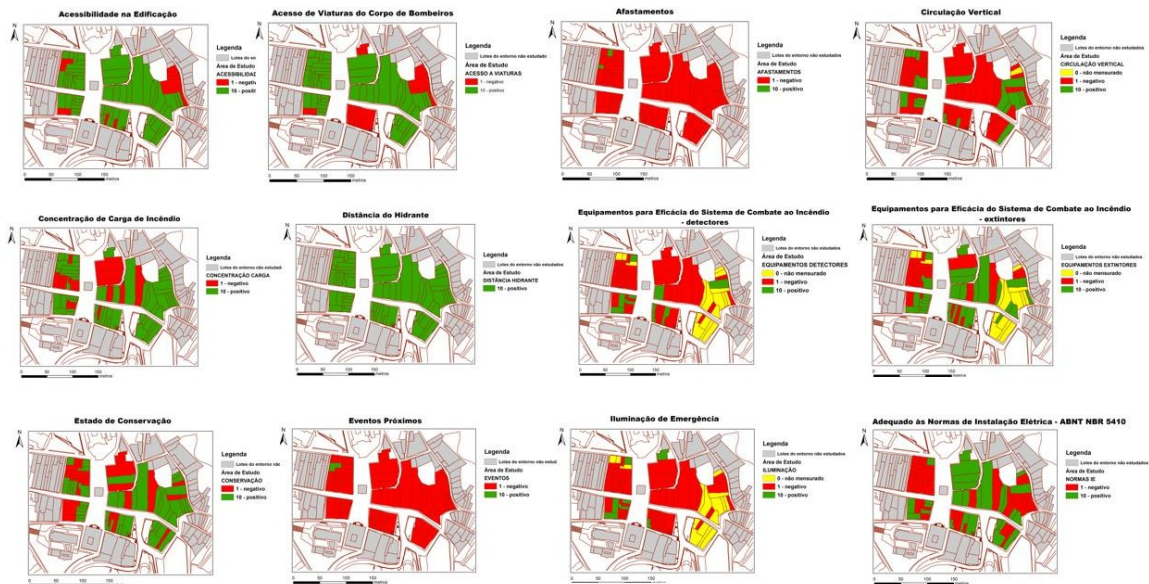
Figure 4: Presents the pertinence of the variables in each block of Ouro Preto. Source: The authors.

Figure 5 represents the combination of the variables from the figure 4 in just one map. In the situation presented, each variable received a score and a weight in relation to its importance to the other. This information, grades and weights, were introduced into the attribute table within the GIS. The result allows a more complete analysis of the situation of vulnerability to fire in the historic center of Ouro Preto.
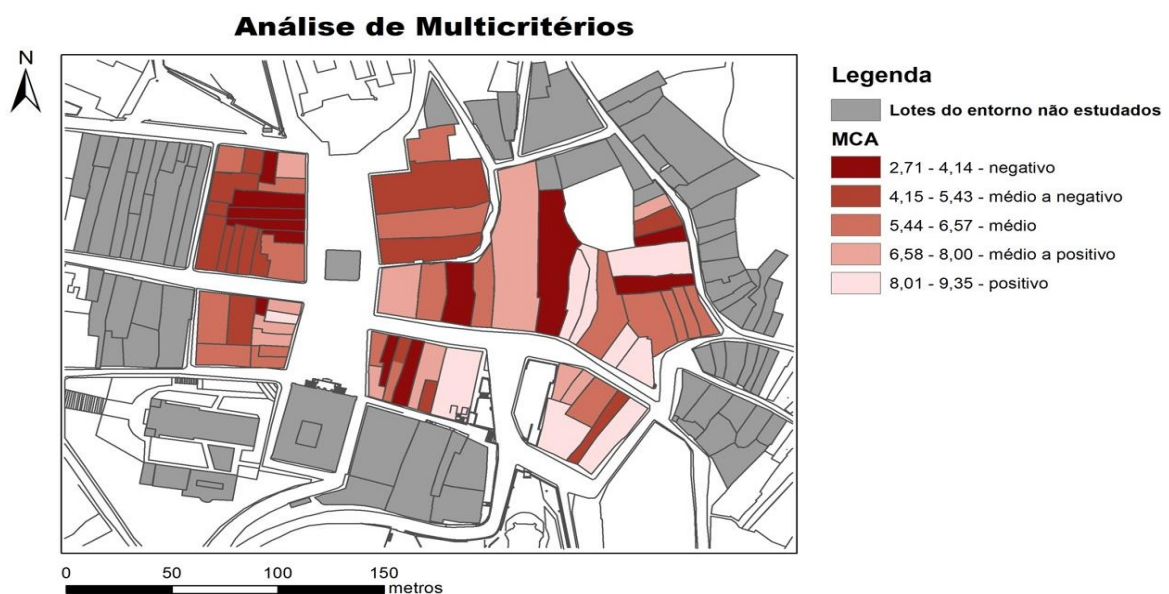
Figure 5: Summary map integrating the variables into the table of attributes entered the GIS. Source:The authors.

191

The gradation of colors on the map corresponds from situations of greater vulnerability to fires to minors, that is, from the strongest to the weakest colors, respectively.

4. CONCLUSIONS

This article is justified by the use of technological advances of the Geographic Information System software - GIS, with the aid of the Multicriteria Analysis Method - MCA, for fire risk analysis in culturally heritage sites. The advantage of its use in relation to the already known methods is the ease of obtaining visual answers, by means of maps, facilitating the interpretation of the data collected in the field.

Despite having used variables from the traditional Gretener, Chichorro, EbraFire and Arica, the elaboration of the GIS + MCA analysis method, intends to constitute a unique proposal for fire risk analysis, in order to facilitate the understanding of the spaces most vulnerable to fire.

The GIS plus MCA analysis method intends to support Fire Engineering, concentrating relevant variables to this process in a single solution, which allows an idea of the reality of the whole studied geographic space, as well as obtaining changes in scenarios according to interferences and improvements that may occur there.

An attributes table was prepared with the variables of the fire risk analysis methods crossing address, lot and block information, with each variable evaluated with a grade and a weight.

The analysis of the scores was obtained by field studies. The weights were obtained by means of evaluations by experts in the fire area on a questionnaire containing the 16 variables. The objective was to create a ranking of importance among them. This whole process is dynamic because the number of variables can increase or decrease depending on the geographic space chosen and the desired context.

The analyses on fires were carried out in the blocks surrounding Praça Tiradentes in Ouro Preto and focused on Portuguese colonial urbanism and architecture, characterized by the street layouts of the old Vila Rica. The contiguity of the buildings, the intense use of wood to structure and clad floors and roofs, demarcated their construction types, which, in most cases, are vulnerable environments to fire.

As a result, a map representing the greater or lesser vulnerability to fire risks of the block to be studied was elaborated.

Must be recognize the possibilities that are opening of computational technologies for fire risk analysis. This proposal is a clear method, with a defensible structure and perfectly reproducible, once explained to other professionals. Moreover, it has a character of adaptability and flexibility, whose variables and weights can be revised. Another important characteristic is its replicability for the rest of Ouro Preto or for other locations, which gives it a character of scalability.

The future developments of the research will be the expansion of the area of application due to adjustments and calibration of the methodological script.

REFERENCES

[1]   Claret, A.M.G. (2017). *Introduction to Fire Engineering for students, architects, engineers, managers and firefighters*, 3iEditora.
[2]   Costa, S.A.P.; Netto, M.M.G. (2015). *Fundamentals of Urban Morphology*, C/Arte.
[3]   Vasconcelos, S. (1915). *Private Architecture in Vila Rica*, UFMG.

[4]   Mello, S. (1985). *Mineiro Baroque*, Brasiliense.

[5]   Kruger, P.G. et al. (2020). Comparative Analysis between fire risk assessment methodologies in Ouro Preto, International Congress on Recovery, maintenance and Restoration of Buildings, v.5, Rio de Janeiro.

[6]   Eastman, J.R.; Jin,W.; Kyem, P.A.K., Toledano,J. (1995). *Raster Procedure for Multi-Criteria/Multi-objective decisions,* Photogrammetric Engineering and Remote Sensing, 539-547p.

[7]   Câmara, G.; Monteiro, A.M.V. (2005). *Basic Concepts in Geoinformation Science*, Introduction to Geoinformation Science, Chapter 2, 2-1-2-35p.

[8]   Moura, A.C.M. (2020). *Conscious Choice in Geoinformation Technologies for Representation, Analysis, Simulation and Proposition for a Territory: Suporting Geodesign*, Geoprocessing in Environmental Analysis, Chapter 1, 11-68p.

[9]   Moura, A.C.M (2017). *Basic Concepts in Geoinformation Science*, Introduction to Geoinformation Science, Chapter 2, 2-1-2-35p.

[10]   Coelho, A.L.; Pedro, L.B.; Vicente, M.; Ferreira, T.M. (2019). *ARICA 2019 – Method for fire afety assessment in existing buildings. Description, scope and conditions of application*, Projeto Reabilitar como Regra, Lisboa, 1-51p.

[11]   Muculo,C.P. (2013). *Fire Risk assessment by the Arica Method to Buildings in Porto*, Master Degree, University of Porto, 136p.

[12]   IPHAN / Programa Monumenta. (2001/2002). *National Inventory of Real Estate Property of the Urban Heritage Sites of Ouro Preto and Mariana,* UFMG.

[13]   Saaty, T.L. (1988). *What is the Analytic Hierarchy Process?* Mathematical Models for Decision Support. NATO ASI Series, Berlin, vol 48.

HOW DOES SOUTH KOREA PROTECTS ITS HERITAGE THROUGH FIRE PREVENTION AND RISK ANALYSIS
– COMPARISON WITH FOUR ESTABLISHED ANALYSIS METHODOLOGIES

Luana O. Gonçalves[1]

Paulo V. Krueger [2],*
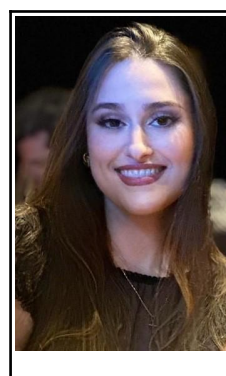
Marina R. Abrantes[3]

ABSTRACT

This work aims to present South Korea's fire prevention method at historic sites making a comparison of four analysis methodologies of the fire risks in historical sites. These analysis methodologies are the following: Ebrafire, Chichorro, Gretener and Multicriteria.

After doing a research of fire risk analysis in some brazilian historical sites in order to find a better way to preserve heritage, it has become interesting to cross brazilian architecture information with asian information, more specifically, south korean. Even though fire risks and disasters happen all over the world, it is interesting to look at it from the perspective of a developed country, which has such modern technology and AI, being one of the most technological countries nowadays.

From that, this work tries to go further in the preservation theme, having the study of fire done in the Brazilian historical places as a base. Bringing the same look, but now, for the South Korean patrimony and heritage, analyzing the methods used to measure the risk of fire and comparing with some methods already known.

Therefore, although the results here are not conclusive, since this research is in the initial phase, it is already possible to verify the similarities and differences between the methods, as well as the prognoses to be given from the analysis carried out by them.

Keywords: : risk assessment methodology; fire risk management; historical sites; South Korea;

[1] Federal University of Minas Gerais Brazil (luaholiveira96@gmail.com)**.**
[2],* Federal University of Minas Gerais Brazil (paulovonkruger@gmail.com)**,** Corresponding author.
[3] Federal University of Minas Gerais Brazil (ninaabrantes1@gmail.com)**.**

1. CONTEXT

In 2008 a fire was started in an important historical place in South Korea: Namdaemun gate, in Seoul, causing severe damage to the 550-year-old structure and, at the time, there were a lot of international comments about the ability of Korea to preserve and take care of their heritage places [13]. Thinking about their historical villages and constructions, made, most of them, of wood (since wood is easily burned and their villages have constructions very close to one another) it has become interesting to know how they manage the fire risk assessment. Another point of interest in South Korea was about the continuing aging citizens, the high rise buildings, the barracks, the shanty towns, the outdoor markets and a lot of concentrated places having so many wooden houses. If there were arson or fire accidents in these areas the damage would be significant. Otherwise, fire prevention in Korea was a small thing in Korea at the end of the 90's, so it has become an interest to understand the prevention of the fire in such a technological country.

On the other hand, in Brazil, in September of 2018 the National Museum in Rio de Janeiro had been almost completely damaged by a fire, destructing almost all the historical collection, built in more than 200 years. Also destroyed the building itself, that was one of the official residence of the king and emperors. It was the most important museum of Brazilian natural history, with more than 20 millions of items in their collection. In another part of the world an historical damage caused by fire happened in 2019 at the famous Notre Dame Cathedral, in Paris. As it can be seen, the fire in the last years caused terrible and irreversible damage to the patrimony around the globe. The technicals and the ways of preventing those fires, especially in historical places, inspired this article, as a way to understand the methods used in South Korea and make a parallel to what is done in the West, especially in Brazil.

Both brazilian normative instruction number one [1] and Korean Framework Act On The Management of Disasters And Safety third article [14] of chapter one defines disaster as a result of an adverse event, natural or man-made, using   human   material   of environmental damage in addition to economic and social damage, which can   be   classified as natural - arising from natural process or natural phenomena - or technological - arising from accidents, dangerous procedures, infrastructure failures or specific human actions - with a small difference that the korean law classifies the last one as social accidents.

In order to base the article, it is necessary to know the main fire risk analysis methods used for the research: Ebrafire, Chichorro, Gretener and Multicriteria which, for summary purposes, will be referred to here as base methods. It is important to remember that these are not universal methods, but widely known resources in the Luso-Brazilian field of fire science that were chosen to make the connection with South Korea based on what was already known.

2. THE BASIS METHODS

Starting from EBRAFire: Existing Building's Risk Assessment for Fire is considered a simple method for calculating Fire Safety[5]. It was created by Universidade Beira Interior, and consists an analysis method where you can interpose to correct the parameters of a given building individually, in order to raise the fire safety rating.

This method assigns a rating to the buildings analyzed, based on fundamental parameters, observed in technical and regulatory standards, and also in empirical events resulting from experience in preventing and fighting fires.[8] The model provides a detailed analysis of the parameters attached to the building's fire safety, with results that are easy to understand.

In addition, it allows an automatic procedure, facilitated by using an Excel© spreadsheet, which the simplified assessment of an existing building regarding its fire safety. This procedure deals with a set of data that can be taken from the observation of one or more existing buildings in a given location[5].

The data used in this method are taken from the building itself under analysis, observing its characteristics and entering the information in a checklist of field thus allowing the assessment of the level of comfort and safety in the face of possible structural fires. Some factors analyzed to get the results are: Duration and speed of Fire Propagation, resulting in the severity of the fire, the susceptible compartments, the means of combat available, the efficiency of fire fighting, the efficiency-severity combination factor, the probability of occurrence of ignitions , the escape conditioning factor, the surrounding environment and security, the risk of exception, the characteristic protection class of the building, the characteristic protection class of the society and the characteristic protection class of the activity/exception.

The Chichorro is a holistic calculation of construction fire risk and enabling optimization of its reduction with shell-work [4]. For the method, the concept of fire risk is the result of the product of the probability of a fire occurring by the severity of its consequences, taking Fire Development and Propagation and Rescue and Fire Fighting Effectiveness factors with equal weight, charting the preservation of built heritage in an equivalent way to

the safeguarding of human life. In this research it was chosen to use version 2.0 of the method, which presents four global Fire Risk factors: the Probability of Fire Occurrence, the Total Fire Consequences, - which may be related to the fire scenario and the horizontal and vertical evacuation routes -, the Development and Propagation of the Fire and the Effectiveness of Rescue and Fire Fighting.

In this method, the acceptable risk depends on several factors and can change over time and based on the age of the building, preparing reference values based on local legislation at the time of creation of the method. Fire Risk is acceptable if its value is less than or equal to unity. As a general rule, in cases where the Fire Risk value is greater than unity, measures must be implemented to mitigate this risk.

Gretener's method is probably the most widespread, adapted and used Fire Risk analysis method, which is based on the analysis of the fire process, determining the factors that promote its development, measuring the activation risks according to the type of occupation and even assessing the contribution of security measures to reducing the risk of fire[8].

It is used to evaluate and compare the Fire Risk level , based on alternative concepts between different types of buildings. The various parameters and respective burdens used to calculate the Fire Risk in this method were obtained based on statistical data and measured by its wide practical application being confirmed by the technical and scientific environment [4]. Gretener considers the existence of three types of buildings, in terms of fire propagation respect: Construction in cells: hinders and limits the horizontal and vertical spread of fire(cells up to 200m2), construction of large surfaces: allows and facilitates the horizontal spread of fire, except the vertical (areas greater than 200 m2, on a single floor) and large volume construction: favors and accelerates horizontal and vertical propagation of the fire (several floors not compartmentalized among themselves).

The effective Fire Risk results from the product between the activation hazard factor and the exposure to hazard. The activation danger quantifies the probability of fire occurrence, depending on two factors, the type of operation of the building and the dangers created by human factors, being found table for different types of buildings. The hazard exposure factor is defined by the quotient between the product of all potential danger factors and the product of all protective factors.

The calculation of the Fire Risk is done for the largest or most dangerous fire compartment. The verification of fire safety is done by comparing the effective Fire Risk with the Permissible Fire Risk, which varies depending on the activities carried out in the building. Finally, the building or compartment that obtains a Fire Risk value lower than the Admissible Fire Risk value is considered safe against fire.

Last but not list, the Multicriteria method was developed at the Federal University of Minas Gerais using the previously mentioned methodologies (Gretener, Chichorro and EBRAFire) and introducing BIM and GIS, constituting a new way of analyzing fire risk management and of a fire prevention and firefighting project in protected buildings and sites, using computational simulations that foresee the risks of the real situation. [9]

The Geographic Information System - GIS is a geographic database of analyzes complex, by integrating data from diverse sources and by creating databases georeferenced, having been used as an auxiliary tool in fire risk prevention methods. [9]

While the Building Modeling Information - BIM is a work methodology that proposes a change of culture and challenges traditional ways of designing projects, building and contracting services in the sectors of Architecture, Engineering, Construction and Operations.

The model produced by BIM facilitates the exchange of information and allows sharing in real time, in addition to integrating work teams in a single software language. It works with parameterized information of materials and equipment of the works, allows simulations of project solutions, contributes to the planning of works, of purchases and for the maintenance of the system, since it has the capacity to store the attributes of the materials used in the work, quantify them by disciplines and still carry out the visualization in 3D.

In short, the method uses computer simulation to emulate a real situation, based on a model that owns a huge database, which in turn corresponds to a simplified representation of reality. Making the Multicriteria an important tool to help research and documentation management, fundamental for the preservation of the heritage.

3.COMPARISONS

3.1 SURROUNDINGS

In [10] there can be seen the attempt to reduce the damages caused by fire, more specifically in Yang Dong village area. The attempts to protect the historic village is basically on the surroundings: preventing forest fires from occurring so it stands for future generations. To protect the current forest environment and residential

arrangement, they evaluate the effect on the flow rate and build a risk map with the results, just as what is done at the upper mentioned methods.

To enhance the importance of considering the surroundings, Kim and Lee did a research study to predict fire behaviors in historical village buildings and structures using a database on the combustion of rice straw and silver grass. The results pointed that if a thatched roof house were to combust completely, then thatched roof houses within a 5.68 m radius of the burnt house are in danger of fire spread, maximizing the fire's damage.[6] A similarity can be seen here: in Ebrafire when a building is considered high risk or when the risk is unknown, the risk is increased, so the neighboring buildings are considered high risk, mainly considering the speed of fire propagation and the difficulty of protecting that area in case of fire nearby.

In comparison with the basis methods, there can be noticed another similarity: they do a mapping of the type of material used in the places, (most of them by wood), measuring how much damage it could bring. One difference that can be noticed is the attention they give while doing the research of the scenario: they do pay attention to wildfires, destructive fire that spreads quickly over woodland or brush and how it can spread to the villages. The basis methods mentioned do count the surroundings, but not specifically the forests. The Ebrafire was created with huge possibilities of forest fires thinking specially on Portugal's cases, where this situation is quite common, to use the same method in Brazil, frequently this situation can be erased, cause most of its historical sites are located in the middle of the city.

In [6], there can be seen the parameters and the questions used to analyze the impact of the fire. Those questions are very similar to the ones used in the methods explained before, such as what kind of fire can happen, what are the chances of that fire happening and if the fire breaks out, how much damage will it do.

As used in the CHICHORRO method, they also have the same basis to calculate the risk: The factors that affect the damage caused by that fire. Fire risk assessment (FRA) is a factor that tries to predict the damage caused by the fire. [4] In terms of assessment, fire risk analysis derives from risk factors for fire and analysis to present the damage caused by accidents and their consequences. The performance of the fire risk assessments goes through various stages, as the programs mentioned, as a way to predict the risks related to the scenario where the fire might happen.

This can be seen also in [12], when the method takes in count several possible scenarios and the measure is based on checking the risk reduction or even re-analyzing.
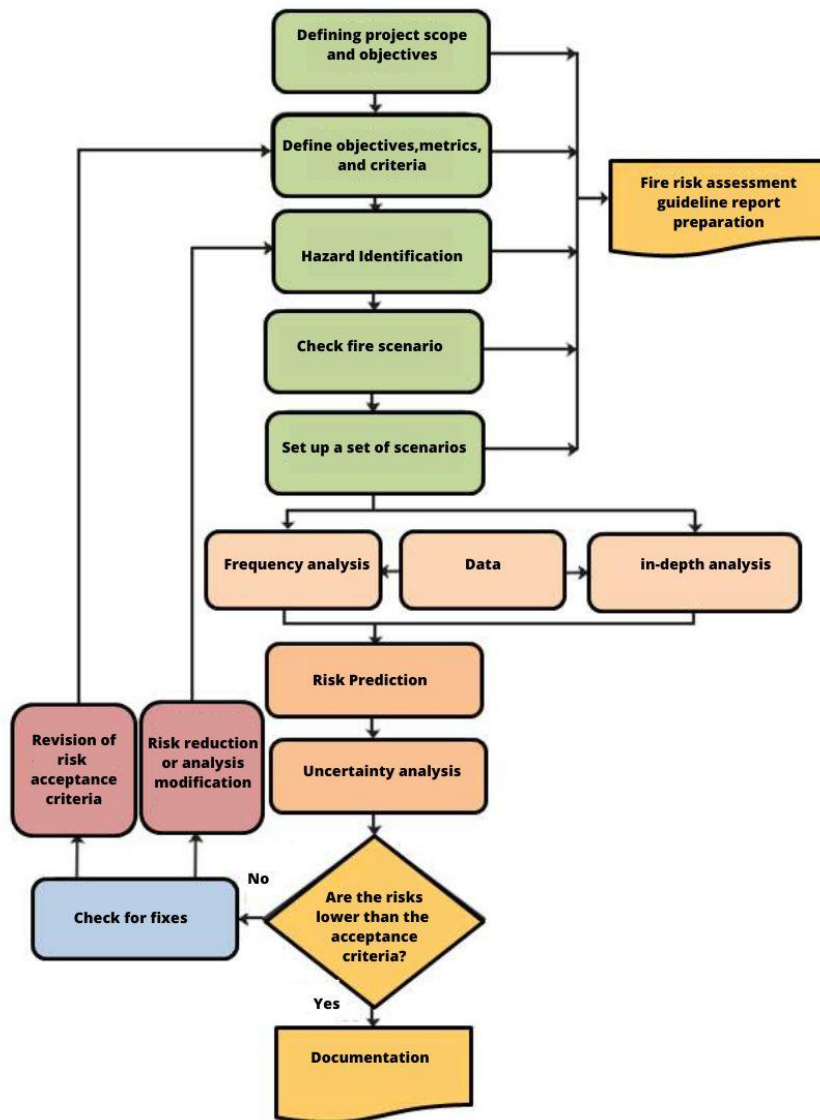
Figure 1: Fire risk assessment process
Source: Adapted from [12]

3.2 ACTIVITIES

The study [11] proposes that the preventive level is more important than the response level among village residents, and the response level should be prioritized over the preventive level in village organization in order to prevent and reduce fire risk and damage in Korean historic villages. It is important to remember that both Chichorro and Gretener has an specific topic related to human activities, asking questions like there are smokers in the building, do people cook, is this a restaurant or does it have a use with high potential fire risk, taking in count the fire load of the equipment and materials.

In Brazil, the Technical Instructions of the Fire Department of each state are responsible for tabulating the possibilities of occupations and assigning a "fire load" to each one of them, that is, the amount of those to measure the heat energies possible to be released by the fire, complete combustion of all combustible materials in a space, including wall coverings, partitions, floors and ceilings.

The method focuses on community‑based activities, categorized by "residents" and "organizations," and is based upon an expert survey and an analytic hierarchy process (AHP) to clarify the weighting of attributes. [11] Such efforts by the Korean government suggest that many fires were caused by human error, and that it has begun to direct its attention to human‑related measures. Furthermore, the government changed the main paradigms of cultural heritage safety systems from protective measures to human‑related proactive measures against fire.

3.3 ESCAPE ROUTES

The distance between the safety center is also something important to evaluate when a risk of fire is being calculated. In the methods used in the west it also has a space to count this criteria, but inserted in different equations. The is also a following steps to be done, such as geocoding the space after identifying the distribution of fire occurrence, use the ArcGis 9.3 space program after estab-lishing the basic space data to perform the nearest proximity analysis and then identify the positional relation of the hot spots after identifying 119 safety center location. [16]

In the bases method, the presence and distance of fire hydrants and the width of roads, the number of accesses to the building and the distance from the Fire Department count as aspects to quantify the fire response, which can lead to a greater risk of fire as the distance between the surveyed points increases.

3.4 BUILDING MATERIALS

Since most Korean historic villages were constructed from materials readily available from the surrounding natural environment, such as trees, mud, stone, and straw, they are highly prone to damage by storms, floods, termites, and fires.

Its important to remember that both Chichorro and Gretener has specific topic called "furniture fire load" - which takes into account the dangers inherent in the content and program of uses of the site, the combustibility, the production of fumes and the danger of corrosion and toxicity - and "real state fire load" - inherent building hazards: floor levels, dimensions of the compartments and the building materials.

In Korea it can been seen a huge effort to analyze the wood and the materials that compose the buildings. They have a description list of wood and their facility to spread fire. It is more specific and judicious, being able to calculate the time more specifically depending on the wood used. [10]

3.5 SPATIALIZATION OF INFORMATION

In the case of the Multicritéria and the reformulated Chichorro and Ebrafire, geographic information systems (GIS or GIS - Geographic Information System) are used to digitally record geographic and topographic characteristics and store this geospatial data in indexed and overlapping layers. [9] This digital information is then converted into specific data formats and stored on computers to create a database of geospatial information.This is combined with data analyzed by Excel© spreadsheet that generate a color legend based on the classification of the building, spatializing the classification and making the surrounding information given in visual elements. [8]

In Korea, the Cheongju City has been transformed into a new urban structure in 2014 when Cheongju City and Cheongwon-gun were integrated. Before a lot of disasters happened in that area, most of them a huge loss of life and property caused by a large-scale fire, studies and safety programs were created to minimize the risks and consequences. A fire distribution map for the years 2011 to 2013 was made, when the fire occurred in Cheongju, in order to analyze the pattern of occurrence. [15]

As seen in the other methods already cited, this program [15] also had a following step to be done. First, using a distance-declining function, points and coordinates were created in order to extract fire hot spots in the city. Second, fire occurrence by substituting the fire frequency (number) and damage distribution Find out the frequency (number) and spatial distribution type of damage amount. Through the correlation between the frequency of fire occurrence and the amount of damage, the regional correlation is explained as a covariate ratio through the correlation coefficient and the coefficient of determination. Third, It's done an autocorrelation analysis on the space to determine the global Moran index (Moran's I) of fire occurrence throughout the space.

In conclusion, this program was done after the fire occurred. Their occurrences helped the research to point to different areas of risk. Usually, in the methods used in the West and listed here, the calculation is done before the incidents. Even though, the programs used are basically the same: Excel data, spatial statistics techniques, density analysis, correlation between fire frequency and damage amount, and spatial autocorrelation by using a geographic information system (ArcGis 9.3) and a spatial statistics program (GeoDa1.6.1).
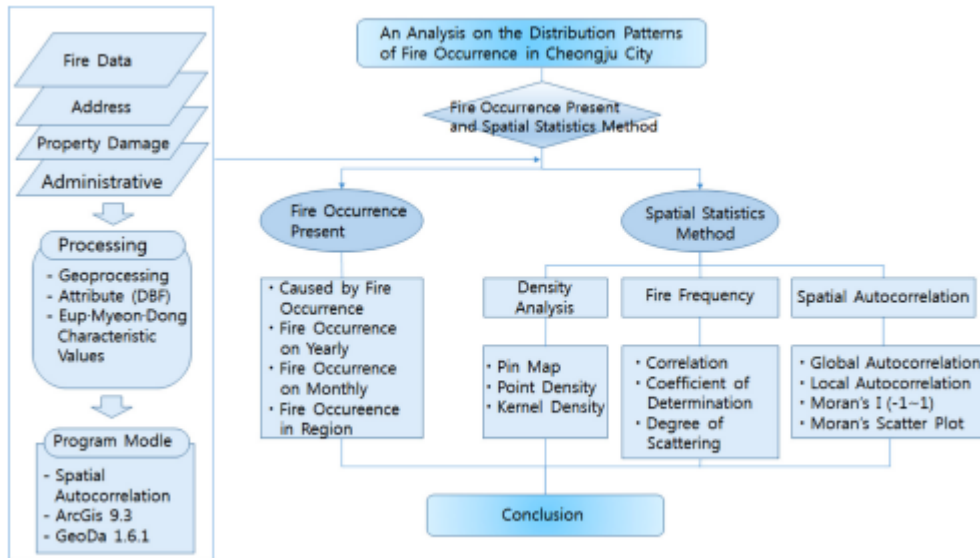
Figure 02: Squeme of the method utilized in Cheongju city area.
Source: [15]

Even though directly approaching and observing is the best and most reliable way to find out about the characteristics of an area or object, it is not a very easy and cheap idea considering big areas and places. A way to solve this problem is combining ways of collecting information: aerial photography, especially using the QGIS software, and making field visits just as is done in other methods.

4.DELIBERATION ABOUT FIRE ROBUSTNESS INDEX (FRI)

It is important to know that there can be some points of limitation in the researches, especially when we try to compare the methods, taking into account its initial phase and the huge distance of the researchers and the analysis site. Koutsomarkos[7] brings some important appointments when it comes to the creation of FRI and, in this case, how to evaluate the methods chosen for the research.

As explained above, every method requires a series of judgments to be made – not just about the method design, but also about the burdens that are allocated to specific attributes and how correlations between them are quantified. Since a risk index is defined by a multi-attribute evaluation to reach a result that aggregates several aspects into a single number, the scoring process is typically undertaken by allocation of points to each attribute. Therefore the foundation of any fire risk index is a points system. In most of the cases, if not all of them, this process includes a group of 'experts' in the field which is responsible to define the weighting based on their collective professional judgment and experience.[7] So, as much as the process is based on scientific methods, the criteria for defining weights can be subjective.

5.CONCLUSIONS

Before the analysis of different ways and studies done in Korea about fire and the proportion of the damage it could have, it can be seen that the methods used in Brazil and western countries are not used in Korea. At least, not properly named. However, the topics used to make the analysis are pretty similar - even sharing common aspects with distinct nomination - , just like the examination of the outside area - the surroundings -, the fire propagation speed, the buildings materials, the escape routes, the amount of damage a fire could bring, the alert signs, etc. It shows that the ways of doing it are compatible, even though, different.

The methods like EBRAFire, Chichorro, Gretener's and Multicriteria combine these specificities and give us a result that is more complete and involves more topics, being able to create a better idea of the entire reality, while the Korean way of doing it is more fragmented. There are studies showing the surroundings, how the fire can spread depending on the material used, all the signs that must have to help the people in case of a fire, and all the other topics. But, with that, it has many solo results that may not be easy to compare and join to have a fuller view of the place condition.

There are both goods and bads in both ways of doing it, but thinking about effective solutions to the problems and the creation of proposals to decrease the damages, having a result that has more topics combined is more useful, cause making a proposals taking in count all the topics combined and related to each other is more effective than to propose different and multiple plans. Cause, just as sad at [11], a fire scenario is a qualitative and chronological description that identifies the important events for the occurrence of fire.

It would be ideal to have in Korea a method that could join all their statistics together, in order to make it easier to propose plans to decrease or even prevent their cities and historical villages, since having a standardized and multidisciplined procedure may be an advantage to assess a large number of similar properties, which is the exactly occupancy pattern in these locations[7]. They consist of very important places and some of them are a UNESCO World Heritage Site. Also Brazil and the western countries could do the same detailed analysis just as South Korea, to know their cities and historical places even better. All of the countries can benefit from a sharing method of prevention of fire.

ACKNOWLEDGEMENTS

REFERENCES

[1]   Brazil. Instrução normativa n. 1, de 24 de agosto de 2012.
[2]   CBMMG (Corpo de Bombeiros Militar de Minas Gerais). Instrução Técnica no 09: Carga De Incêndio nas Edificações e Área de Risco. 2.ed. 2018.
[3]   CBMMG (Corpo de Bombeiros Militar de Minas Gerais). Instrução Técnica no 35: Segurança contra incêndio em edificações que compõem o Patrimônio Cultural. 2.ed. 2018.
[4]   Chichorro, M., FERREIRA, R., CORREIA, A. Risk Assessment of urban fire - Proposal os a Model for Analysis and Management of Existing Building. INTERNATIONAL CONFERENCE on URBAN RISKS. Lisboa. 2016.
[5]   Fernando José da Silva et. al. Int. Journal of Engineering Research and Application. ISSN: 2248-9622, Vol. 10, Issue 12, (Series-II) December 2020, pp.57-65
[6]   Kim, D.H.; Lee, J.H. An Experimental Analysis of Thatched-Roof Materials to Assess Fire Risk in Historical Villages. J. Korean Soc. Hazard Mitig. 2015, 15, 117–122.
[7]   Koutsomarkos, V, et al. 'Tactics, Objectives, and Choices: Building a Fire Risk Index', Fire Safety Journal. (2020). doi: 10.1016/j.firesaf.2020.103241.
[8]   KRUGER, Paulo Gustavo Von et al. (2021) "An Assessment of Fire Hazard in the Historic Town of Ouro Preto based on Four Established Analysis Methodologies", Global Journal of Human-Social Science, 21(B4), pp. 1–8. doi: 10.34257/GJHSSBVOL21IS4PG1.
[9]   Lasmar. E. E. Uso do SIG, do BIM e de métodos de análise e gestão de riscos de incêndio em patrimônio cultural. Master Dissertation. Universidade Federal de Minas Gerais, 2020.
[10] Lee, J.-H. e Kim, D.-H. (2014) "Developing Heat Flux Evaluation and Fire Risk Map for Forest Fires in Yangdong Villages", Journal of Korean Society of Hazard Mitigation. Sociedade Coreana de Mitigação de Riscos. doi: 10.9798/kosham.2014.14.5.19.
[11] Lee, Ji-Hee & Chun, Woo-Young & Choi, Jun-Ho. (2021). Weighting the Attributes of Human-Related Activities for Fire Safety Measures in Historic Villages. Sustainability. 13. 3236. 10.3390/su13063236.
[12] Meacham, Brian J. 건축물의 화재위험성평가(Fire Risk Assessment) 개요 및 관련자료. Korean Fire Protection Association, 12 de março de 2013. 방재정보
[13] Paek, Seunghan, e Dai Whan An. "Reassembling Heritage after the Disaster: On the Sungnyemun Debate in South Korea". Sustainability, vol. 12, no 9, January 2020, p. 3903.
[14] South Korea. Cultural Heritage Protection Act. Korea Legislation Research Institute. 2015
[15] Yeon, G., Kwon, S., & Hwang, H. (2015). An Analysis on the Distribution Patterns of Fire Occurrence in Cheongju City Using the Spatial Statistics Method.
[16] Yeon, Kyung Hwan et al. "An Analysis on 119 Safety Center depending on the Distribution of Fire Occurrence in Chungju-Cheongwon City." (2014).

.

FIRE IN BELT CONVEYORS: A RISK ASSESSMENT APPROACH FOR A FIRE PROTECTION DESIGN

Cassio R. Armani [(a)] *
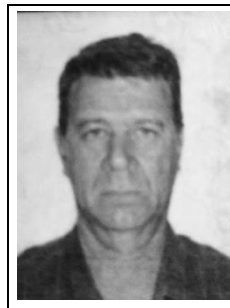
Sérgio Colin [(b)]

Victor S. Moraes [(c)]

ABSTRACT

Belt conveyors are essential equipment found in several types of industrial and logistical processes, including combustible materials such as cereals, sugar, biomass, coal, etc. They are subject to fire hazards due to the operational features of their components and any fire on the conveyors is generally characterized by the flames spread. Despite the lack of statistical data about fires on conveyor belts in Brazil, a substantial number of events was found in the news. This paper also presents the results of a search involving Brazilian and international standards that cover the fire protection for this equipment and they are restricted to some fire precautions. This paper is focused on the problem related to the fire risk in belt conveyors. Its aim is the employment of Bowtie diagram, in such a way that it is possible to understand the failures that can generate a fire event and which barriers can prevent or mitigate the risks. Therefore, it is an approach that should help to visualize the risks and to define the necessary fire prevention and fire protection measures. The method used in the research is the deductive hypothetical.

Keywords: Fire Engineering; Risk assessment; Conveyors.

1. INTRODUCTION

Belt conveyors are related to a vast range of goods transportation in many industry and storage premises, since light to heavy goods and short to long distances. Due to the continuous movement of a belt and other components there are many different hazards including the fire risks. They represent one of the worst consequences and, in addition to the risk to people, they can lead to significant losses and the interruption of a process.

[a] * Universidade Federal de Pernambuco - cassio.armani.pos@ufpe.br - Corresponding author

[b] Universidade Federal de Pernambuco – sergio.colin.pos@ufpe.br

[c] Universidade Federal de Pernambuco – victor.moraes.pos@ufpe.br

For developing this paper, it was necessary to research some fires and to understand the fire risks in all conveyor's components.

The aim of this paper is to research a risk assessment tool and its employment for determining preventive and protective measures against a fire event.

The prescriptive codes and standards are not always a guarantee for a good decision and those who are responsible for a fire design should consider a risk assessment, in such a way that a plan is not restricted to a few numbers of precautions. This paper includes a research about the Brazilian prescriptive laws and national and international standards related to the fire protection for conveyors.

Thus, Bowtie diagram is used to list the likely causes of fire on conveyors and to understand the barriers that should avoid a fire event and the barriers that represent the measures to control a fire.

2. FIRES IN BELT CONVEYORS IN BRAZIL

Although it is difficult to find any statistical data about fires in buildings in Brazil [1], this a survey was conducted to find the most recent fires that occurred in Brazil and that were released by the media.
In Brazil, there is no data available on fires in industrial, goods storage and mining areas, which are the places where belt conveyors are most easily found.

In the search for data, a survey of the fires that occurred in the country in the last decade was carried out, according to table 1.

Table 1: List of fires on belt conveyors

Date	Location	Type of commodity
Oct.18, 2013	Santos – SP	sugar [2]
Aug. 03, 2014	Santos – SP	sugar [3]
Jan. 05, 2017	Cubatão – SP	ammonium nitrate [4]
Mar. 03, 2019	Nova Lima - MG	iron ore [5]
Nov. 27, 2019	Santos -SP	soybeans [6]
Jul. 22, 2020	Paranaguá- PR	grains (harbor) [7]
Sep. 21, 2020	Itabira – MG	gravel [8]
Feb. 19, 2021	Jari – AP	wood biomass [9]
Apr. 25, 2021	Canaã dos Carajás – PA	maintenance work [10]
Oct. 06, 2021	Marabá – PA	copper ore [11]
Jul. 04, 2022	Canaã dos Carajás	iron ore [12]
Sep. 10, 2022	Cubatão – SP	bulk sulfur [13]

Data in table 1 indicate this type of fire is usual and due to the belt material and the transported goods a fire spread is quite common. Besides that, a fire may spread to other structures and premises. Although there is no history of casualties among the employees, there are signs of damage and losses, especially those related to the continuity of business and environmental damages.

Figure 1: Fire in a conveyor in Santos Harbor (Portal G1, 2019) [6]

The list of conveyors fires demonstrates that a minimum level of fire protection hasn't been enough to avoid and to control a fire hazard properly. Any smart owners and managers should look forward to avoiding belt conveyor fires by the best engineering practices which include more than the standards requirements.

3. LEGAL AND REGULATORY ASPECTS

In Brazil, there are state laws and decrees for fire safety regulations, but only five states have provisions on the measures to be adopted on belt conveyors, as follows:
a) Alagoas - Technical Instruction 27 [14], articles 5.3.8 and 6.1.4;
b) Amazonas - Technical Instruction 27 [15], articles 5.3.8 and 5.3.11 e 5.9.4;
c) Minas Gerais - Technical Instruction 43 [16], articles 5.1.9 and 5.2.7;
d) Paraná - Technical Procedure Standard 27 [17], articles 6.7.3, 6.10.1 and 8.2;
e) Rio Grande do Norte - Technical Instruction 27 [18], articles 5.3.8 to 5.3.11 and 5.9.4;
f) São Paulo - Technical Instruction 27 [15], articles 5.3.8 a 5.3.11, 5.9.1, 5.9.4 and 5.9.5.

In short, these documents require an automatic sprinkler system for belt conveyors over 12 m - application rate of 12 l/min/m², heat detection along the entire length of the conveyors, motion sensors and they recommend a cleaning program.

There are two states regulations that stand out with a smaller number of requirements, limited to the requirement of a metallic canopy - for screw conveyors - and to the motion sensors and a cleaning program for belt conveyors in general:
a) Bahia - Technical Instruction 27 [19], articles 5.9.1, 5.9.4 and 5.9.5;
b) Piauí - Technical Instruction 27 [20], articles 5.9.1, 5.9.4 and 5.9.5.

All the mentioned technical instructions have a basic approach for the requirements and the detailed criteria about fire protection for conveyors should to be searched in other standards. There's no provision about a risk assessment for the establishment of fire safety measures, according to the most diverse scenarios that may involve belt conveyors - horizontal, inclined or vertical - regardless of the height and inclination of the equipment.

It was also possible to verify that there isn't any indication for the adoption of the current Brazilian standard, and this is relevant in such an extended country.

Among all the Brazilian standards for fire protection, there is only one that deals with the aspect of fire safety for conveyors - ABNT NBR 16913:2020 – Fire protection of belt conveyors with automatic sprinklers – Requirements [21].

In summary, it establishes as a requirement the installation of automatic sprinkler systems for outdoor and indoor belt conveyors. According to the Brazilian standard, that system is required for outdoor conveyors when their height is greater than 12 m and without access for manual firefighting with fire extinguishers and hoses, or below 12 m height in the following conditions:
   a) fully enclosed conveyor, or
   b) conveyor with combustible coverage, or
   c) multi-level conveyor.

In addition, that standard specifies the type of sprinkler system - wet pipe or pre-action - for installations with an inclination of less than 30° and deluge system for those installations with an inclination greater than 30°.

It also presents the sprinklers flow rate - 95 l/min per sprinkler - wet pipe or previous action - or a rate of 12 l/min/m² - along the conveyor, in the case of a deluge system.

In case of a pre-action or deluge system, a pre-action valve or a deluge valve must be activated after a cable-type linear temperature detector detects a fire.

ABNT NBR 16913 [23] has the predictions about manual firefighting – hoses - for an outdoor and enclosed conveyor, either by means of a fire engine - minimum of 30,000 liters of water - or by means of a standpipe system along the conveyor.

Although ABNT NBR 16913 is a good reference, it is restricted to the protection criteria by an automatic sprinkler system. It also doesn't contain aspects of risk assessment for different fire scenarios, as well as other fire safety measures.

During the research, it was verified that the NFPA 15 - Standard of Water Spray Fixed Systems for Fire Protection [22] – stands out the conditions for protecting conveyors. It contains the criteria on the type of sprinkler (open projector), placed on the surfaces, in order to extinguish fires in the belts, hydraulic oil, over contents of the belts or the engine.

According to NFPA (2017) [22], it is necessary to provide an interlocking system between the fire detection system and engine shutdown.

The water supply must be sufficient to provide both the design flow rate and 946 l/min for hose streams, for a minimum duration of 60 minutes.

The sprinkler system must be sufficient to protect the upper belt, its contents and the lower belt (return), having an application rate of 10.2 l/min/m². The fire sprinkler system must extend over conveyor surfaces where combustible materials are likely to accumulate, the structural parts, and the idler rolls supporting the belt.

NFPA 15 is a world recognized standard, but it doesn't cover other aspects involving fire protection for conveyors.

Another NFPA standard that is related to belt conveyors is the NFPA 650 - Standard for Pneumatic Conveyor Systems for Handling Combustible Particulate Solids [23], but it only deals with the pneumatic conveyors and solid combustible goods. Thus, it has a very restricted application.

Therefore, there is not a NFPA standard dedicated to fire protection for several types of belt conveyors, based on a risk assessment approach and related to other fire protection systems.

There is another international reference – FM Data Sheet 7-11 – from Factory Mutual Insurance Company [24], a well-recognized industrial insurance company and that document is dedicated to the fire protection aspects for conveyors.

According to FM Global, that standard provides criteria about automatic sprinkler systems, which are similar to NFPA 15, but the types of sprinkler system and the flow rates may vary depending on the conveyor orientation, according to Table 2.

Table 2: Sprinkler protection options for outdoor conveyors [24]

| Belt orientation | Sprinkler system type | Sprinkler demand | | | |
		Number of Sprinklers Operating	Flow per Sprinkler, Sprinkler density	Water duration	Hose demand
< 10°	wet, dry, pre-action	5	95 l/min per sprinkler	60 min	246 l/min
10° - 30°	wet, dry, pre-action	7	95 l/min per sprinkler	60 min	246 l/min
> 30°	deluge	All sprinklers on a single system	12 l/min/m² along the length of conveyor	60 min	246 l/min

Besides, the FM DS -7-11 deals with the distribution of portable fire extinguishers - every 15.2 m along the length of the conveyor - and indicates a standpipe system with a minimum flow rate of 380 l/min.

It also has recommendations on protection against explosions, in the case of conveyors transporting combustible solid like grains, coal, wood chips, among others. According to FM DS 7-11, attention should be adopted regarding:
> a) Operations and maintenance;
> b) Control of ignition sources, and
> c) Contingency plan.

FM DS-7-11 is the most comprehensive standard about fire safety on belt conveyors. Despite that, it was noticed a lack of recommendations about a previous risk analysis, which means a search of possible failures that could lead to a fire and ways to prevent it in this type of equipment.

4 RISK ASSESSMENT

Risk is an event that may be calculated as a function of probability and consequence, according to the definition in the ABNT NBR ISO 31000 standard – Risk Management [25]. The following formula is presented by Huang and Xin [26], based on the definition of fire risk as the product of a fire probability and the consequences or damage extension resulting from a fire:

$$FR = \sum_{i=0}^{n} P_{fi} \times C_{fi}$$

where:
FR is the fire risk (casualties per year or losses per year);
P_{fi} is the probability of fire occurrence (losses per year);
C_{fi} is the consequence of the fire (casualties or financial losses); and

n represents the total number of occurrences.

According to Duarte, Leite and Pontes [27], a fire hazard or an explosion hazard is associated with any possible sources of ignition and available fuel. Risk represents the probability of ignition occurring or the probability that a certain amount of fuel is available, considering it is in a flammability range, or the probability of heat and combustion products to compromise the structure.

Risk management is understood as the set of "[...] coordinated activities to direct and to control an organization, regarding to the risks." [25]

Ponte Junior [28] defines a risk management process as follows:

> "... the providing process for technical engineering solutions, considering the involvement of uncertainty, imponderability and subjectivism related to accidents, whether due to the influence of natural forces, design failures, equipment failures, operation failures, management failures or any kind of human error.".

The recognition of any hazard and prospective scenarios involving a fire or an explosion event is necessary so that accidents can be avoided.

Fire risk management applies the same concepts already described, but with a focus on events related to fire, gas leaks and flammable hazardous products, explosions, overheating of machinery and electrical installations, among other risks.

According to Luo and Sun, fire risk management is "essential to decreasing the probability of a fire occurring and mitigating its consequence, once it happened." [29]. Therefore, the fire risk assessment must identify the hazards, quantify the risks and propose measures, in such a way it is possible to achieve the risks decreasing or under control.

Also, according to Luo and Sun, the objectives of fire risk management are:
a) Identify fire hazards;
b) Reduce the risk as far as is feasible, and
c) Decide on fire protections and management plan.

In this context, Duarte, Leite and Pontes [27] say that it is necessary to consider these questions:
- what is at risk?
- what may be protected in the process?
- what is an acceptable risk?

Looking to identify and to measure the risk, there are several techniques (qualitative, semi-quantitative and quantitative) and tools. The Bowtie is a graphic tool, which consists of a method of visualization of a top event, the probable causes, the preventive barriers, the reactive barriers and the consequences of the event.

According to Bortnowski *et al* [30] fire in conveyors may have the following causes:

- blocked idler: the asymmetrical wear of conveyor may result in edges abrasion, which can lead to the blockage idlers. It may be caused by a jamming a rock or a large size grain, or due to the seizure of bearings;

- belt slippage: it is one of the most critical damages to a conveyor and it may be caused by (1) the insufficient belt tension, (2) the wear of the drive pulley lagging or (3) an excessive load on the conveyor.

Tripller and Czylwik [31] say that fires on belt conveyors may be caused by <u>bearing failures</u>. In that case the rollers will heat up and they will become an ignition source to the belt. So, they recommend the provision of a heat detector system under a belt conveyor and on the bearings.

According to Trávníček *et al* [32] explain that the most frequent technical failures are the following:

- <u>drum breakage or displacement</u> – a damage or a displacement may exist because of poor tightening during repairs. Consequently, there's friction against the frame structure and the generation of an ignition source;

- <u>belt displacement or belt slippage</u> – it happens due to the insufficient belt operating conditions, and it may result in the belt friction and the conveyed material ignition;

- <u>pulley breakage or pulley shift</u> – it leads to the friction against the frame structure and the generation of an ignition source;

- <u>bearing damage</u> – any damage to this component may cause increased friction, temperature rise or rupture of the bearing cage and dropping of bearing balls on the combustible material;

- <u>overheated electric motors</u> – that happens due to electrical faults, such as faulty connections at the motor terminal or arcing, and hot weather conditions too.

Once the fire risks are known, it is necessary point out a question: "Are just the laws and standards enough to ensure an effective fire safety for a conveyor?" The answer for this question is implied in table 1.

5 USING A BOWTIE DIAGRAM FOR THE FIRE RISK ASSESSMENT

The Bowtie diagram is a "graphic tool to illustrate an accident scenario, starting from accident causes and ending with its consequences" [33]. According to Mulcahy *et al*, "the first appearance of bowtie diagrams has been attributed to lectures on Hazard Analysis given at The University of Queensland, Australia in 1979" [34], although the exact origin of this technique is not clear.

At the center there is a critical event and on the left-hand side the possible events are listed. On the right-hand side there are all possible consequences to the event.

Between the hazards - possible causes - and the event there is a set of control measures or control barriers. Each cause may correspond to one or more barrier. And between the event and the consequences a set of recover controls or recover barriers are listed, as stated by Alizadeh and Moshasheai [35] and Li [36].

In order to establish the likely causes, it is important to gather information events that have already occurred on this type of equipment or to have the support of one's expertise. Comparing to other risk assessment methods, the Bowtie diagram has the advantage of being a dynamic tool because it can take a new information into account, according to a dynamic environment which is dominant in process safety risk and safety analysis.

Another favorable aspect of the Bowtie method is the visualization of the probable causes and the corresponding mitigation layers, as well as the consequences and the related protection layers.

On the other hand, the Bowtie diagram doesn't show the event in a timeline, as it is possible using the Events Tree analysis. Anyway, Bowtie diagram has proven to be a reliable and efficient tool to analyze accident scenarios and to be used in a process safety analysis and risk management.

This type of approach allows Fire Safety specialists to adopt a holistic view of the problem and not be restricted to legal and regulatory parameters, which in many cases may be insufficient. The analysis of the barriers also favors

the adoption of precautions related to the inspection and maintenance of equipment, which are often forgotten after the implementation of a system.
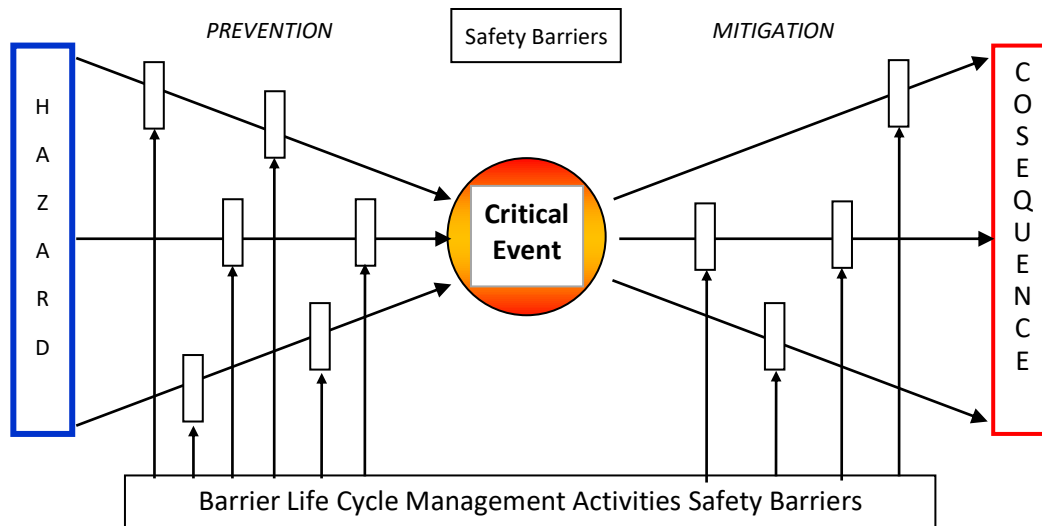
Figure 2: Bowtie model (Li, 2019) [36]

Applying the Bowtie method for a "fire event in belt conveyors", the first step was to identify the hazard – fire – and the event – fire in a belt conveyor. A hazard may be understood as part of the business, but it potentially responsible for damage and losses, and the event occurs when there is not control over the hazard.

Then, it is necessary to list the threats, which represent the potential to cause the event, i.e., a fire in a belt conveyor, in a delivered material or other components. Based on the research, the following causes were listed - damage to the bearings, belt displacement, drum breakage or displacement, pulley displacement, overheated electric engine, hot work and clogged conveyor.

Afterwards it was possible to list the consequences like the belt and other component damage, business interruption or damage in other buildings due to the fire spread.

Once the causes and consequences related to fire in conveyors are known, a brainstorm process may help to correlate the preventive barriers and the causes. It is important to highlight that some of the preventive barriers are found in the prescriptive standards - Brazilian state regulations or in the national or international standards - but many of them depend on the decision over the fire plans and design, as follows:
- hot work permit;
- training for operational procedures;
- regular inspections and maintenance;
- process monitoring cameras;
- indoor and outdoor television circuit;
- monitoring the belt tension, and
- installation of frequency converters for electric motors.

Using the same process, it is not difficult to find the mitigation barriers and the corresponding consequences. So, the question is: "After a fire started in a conveyor what barriers may control or mitigate the event?". Once again, it's possible to verify that some of the barriers are not provided by state regulations or technical standards for all conveyors installed in Brazil, such as:
- sprinkler system;
- linear temperature detection system;
- hose stream system;
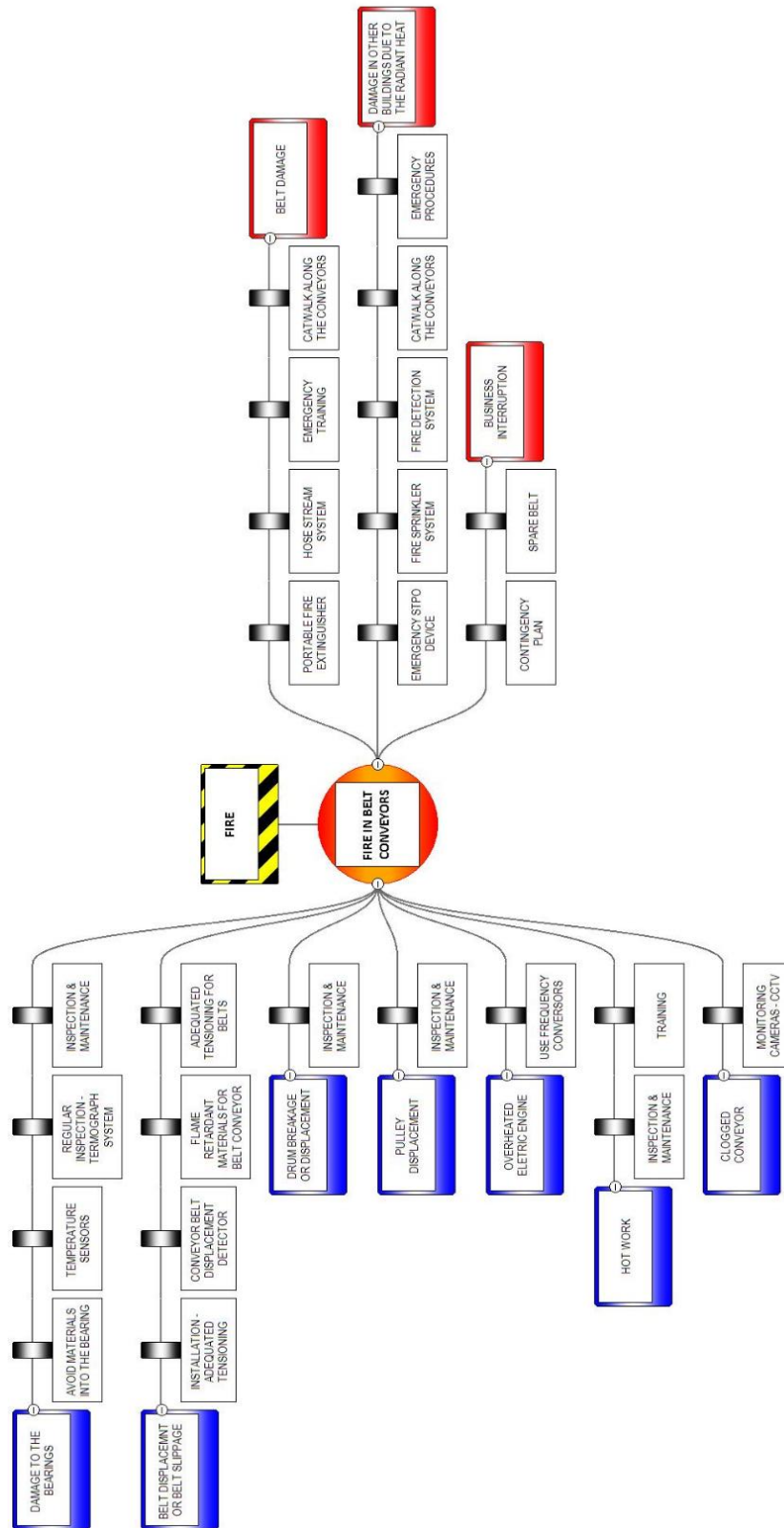
Figure 2: Bowtie diagram for the fire risk involving conveyors

- catwalk parallel to the conveyor;
- emergency stop device, and
- Contingence planning.

There are mitigation barriers that may be found in existing conveyors, but many of them depend on an assessment evaluation. For example, an automatic system is required just for newer equipment and only in 5 Brazilian states, among the 26 states and Federal District. This requirement should be followed just when a conveyor has more than 12 m height, which means that in case of many fires the reactive barrier is represented by portable fire extinguishers and fire hoses.

Figures 3 to 6 show some mitigation barriers for fire in conveyors.

Figure 3: Catwalk to access the conveyor (Componente, 2021) [37]

Figure 4: Sprinklers system (Fabiano, B. et al, 2013) [38]
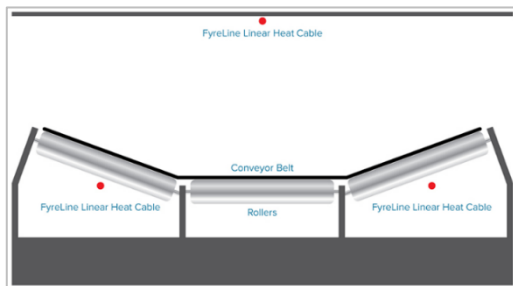
Figure 5: Linear temperature detectors (Eurofire, 2015) [39]

Figure 6: Standpipe system (Equipamento, 2019) [40]

Another relevant issue has to do with the access to the place that there is a fire because in some circumstances the application of extinguishing agent may be very difficult. There are factories in Brazil in which the conveyors system has a parallel catwalk, where portable fire extinguishers and hydrant valves are displaced to the industrial Fire Brigade. Probably this protection is required by the insurance companies as some of them follows the FM Global Ds 7-11.

A contingency planning has an immense value for a company, where the business interruption causes many losses, and it should include the emergency planning, trained personnel, standard procedures and spares components.

3. CONCLUSIONS

Belt conveyor is an equipment of significant importance in the transport of bulk products, and it is present in several processes with an uninterrupted operation. A fire in that equipment may represent thousands or millions of dollars in losses, besides the risk of serious damage to the environment, such as the contamination of soil, air and water.

According to this research, there are different criteria for fire protection in conveyors, comparing the different State legislations and the Brazilian standard. So, similar conveyors installed in different plants in the country may have different levels of fire protection. The Brazilian standard does not include all necessary measures and it is also important to remind that a standard establishes the minimum fire safety requirements, and a good design depends on a broader approach, which includes a risk assessment.

The adoption of FM DS 7-11 is strongly recommended, but it is not required by local laws. Thus, that document is followed by some companies, according to the insurance companies' requirements. Nevertheless, there are some preventive or mitigation barriers, which are not foreseen in FM-DS 7-11.

The present research also demonstrates that in a period of ten years there were at least twelve events in different companies, not including those fires that were not publicized by the press.

Therefore, the prescriptive codes and standards are not always adequate to ensure the best levels of fire protection for a building or equipment and, throughout this research, it became clear that a risk assessment method may lead to better design solutions for new or existing conveyors.

The Bowtie diagram was chosen as a fire assessment tool, and it proved to be a very comprehensive method once the threats and consequences were easily established.

It is very useful for a qualitative analysis, and it permits to identify many risks, considering the different types of conveyors, types of materials to be delivered, conveyors extension and height, among some different scenarios.

Using the Bowtie diagram helped to conclude and to visualize the preventive and the mitigation barriers, in such a way that it may complement the fire safety laws and standards in Brazil.

4. ACKNOLEGMENTS

5. REFERENCES

[1] Corrêa, C., Duarte, D., Braga, G. **Fragilidade da estatística de incêndios estruturais no Brasil**. Guarujá: Editora Científica Digital Ltda., 2021. P. 32-38;

[2] GOMES, F. Incêndio em armazéns da Copersucar em Santos destrói 180 mil t de açúcar. **Portal G1**, 18 Out 2013. Available in: https://g1.globo.com/mundo/noticia/2013/10/incendio-em-armazens-da-copersucar-em-santos-destroi-180-mil-t-de-acucar-1.html. Access on Dec.13 2022;

[3] AMARAL, C. Fogo recomeça no terminal de açúcar do Porto de Santos, SP. **Bom Dia SP.** TV Tribuna. 03 Out 2014. Fogo recomeça no terminal de açúcar do Porto de Santos, SP. Available in: https://globoplay. globo.com/v/3542575/. Access on Dec. 14, 2022;

[4] FREITAS, S. Explosão em fábrica de fertilizantes espalha nuvem de fumaça tóxica. **Jornal Nacional**. 05 Jan 2017 Available in: https://g1.globo.com/jornal-nacional/noticia/2017/01/explosao-em-fabrica-de-fertilizantes-de-sp-espalha-nuvem-de-fumaca-toxica.html. Access on Nov. 30, 2022;

[5] VALE, J. H. Incêndio se alastra e destrói unidade de conservação na Grande BH; veja imagens. **Estado de Minas**. 17 Set 2019. Available in: https://www.em.com.br/app/noticia/gerais/2019/09/17/ interna_gerais, 1085889/incendio-alastra-destroi-unidade-conservacao-grande-bh-veja-imagens.shtml. Access on Nov 30, 2022;

[6] INCÊNDIO atinge terminal de carga no Porto de Santos, SP. **Bom dia SP**. Portal G1. 27 Nov 2019. Available in: https://g1.globo.com/sp/santos-regiao/porto-mar/noticia/2019/11/27/incendio-atinge-terminal-de-carga-no-porto-de-santos-sp.ghtml. Access on Nov 30, 2022;

[7] INCÊNDIO atinge dala na área de transporte de grãos do Porto de Paranaguá. **Bom dia Paraná**. Portal G1 RPC 22 Jul 2020. Available in: https://g1.globo.com/pr/parana/noticia/2020/07/22/incendio-atinge-dala-na-area-de-transporte-de-graos-do-porto-de-paranagua.ghtml Access on Dec.14 2022;

[8] CORREIA transportadora pega fogo na área da Vale em Itabira. Itabira Online. 22 Set 2020. Available in: https://itabiraonline.com.br/2020/09/22/correia-transportadora-pega-fogo-na-area-da-vale-em-itabira/. Access on Dec. 14, 2022;

[9] JARI Celulose, no Amapá, sofre incêndio. **Tissue Online.** 19 Fev 2021. Available in: https://tissueonline. com. br/jari-celulose-no-amapa-sofre-incendio/. Access on Nov. 30, 2022;

[10] INCÊNDIO atinge a Mina do Sossego, em Canaã dos Carajás. **Jornal Liberal**. 26 Apr. 2021. Available in: https: //globoplay.globo.com/v/9466794/. Access on Dec. 03, 2022;

[11] INCÊNDIO paralisa produção de cobre em mina da Vale no Pará. **Seu Dinheiro**. 06 Oct. 2021. Available in: https://www.seudinheiro.com/2021/empresas/vale-vale3-incendio-paralisa-producao-em-mina-do-salobo/. Access on Dec 14, 2022;

[12] INCÊNDIO no S11D da Vale assusta funcionários. **Portal F5**. 04 Jul 2022. Available in: https://portalf5.com. br/2022/07/04/incendio-no-s11d-da-vale-assusta-funcionarios/. Access on Jan. 02, 2023;

[13] INCÊNDIO atinge sistema de transporte de enxofre em terminal portuário em Cubatão, SP. Portal G1. Santos e Região. 10 Set 2022. Available in: https://g1.globo.com/sp/santos- regiao/noticia/2022/09/10/ incendio-atinge-sistema-de-transporte-de-enxofre-em-terminal-portuario-em-cubatao-sp.ghtml. Access on Jan. 02, 2023;

[14] CBMAL. **Instrução Técnica nº 27 – Armazenamento em silos**. Maceió: Corpo de Bombeiros Militar de Alagoas, 2021. Available in: https://saps.cbm.al.gov.br/webroot/downloads/IT%2027_2021% 20 CBMAL%20 -%20Armazenamento%20em%20silos.pdf. Access on Mar. 15, 2023;

[15] CBPMESP. **Instrução Técnica nº 27 – Armazenamento em silos**. São Paulo: Corpo de Bombeiros da Polícia Militar do Estado de São Paulo, 2019. Available in: http://www.ccb.policiamilitar.sp.gov.br/dsci_ publicacoes2/_lib/file/doc/IT-27-19.pdf. Access on Mar. 15, 2023;

[16] CBMMG. **Instrução Técnica nº 27 – Armazenagem em silos**. Belo Horizonte: Corpo de Bombeiros Militar de Minas Gerais, 2020. Available in: https://www.bombeiros.mg.gov.br/storage/files/shares/intrucoes tecnicas /IT_43_1a_Ed_PUBLICADA.pdf. Access on Mar. 15, 2023;

[17] CBMPR. **Norma de Procedimento Técnico nº 27 - Unidades de armazenamento e/ou beneficiamento de produtos agrícolas e insumos Parte 02 – Grãos**. Curitiba: Corpo de Bombeiros Militar do Paraná, 2018. Available in: https://www.bombeiros.pr.gov.br/sites/bombeiros/arquivos_restritos/files/documento/ 2018-12/NPT_027_Parte_02_Graos_24OUTUBRO2018.pdf. Access on Mar.15 2023;

[18] CBMRN. **Instrução Técnica nº 27 – Armazenamento em silos.** Natal: Corpo de Bombeiros Militar do Rio Grande do Norte, 2022. Available in: http://sistemascbm.rn.gov.br/serten/webroot/downloads/ITs_ 2022/IT-27-2022.pdf. Access on: Mar. 15, 2023;

[19] CBMBA. **Instrução Técnica nº 27 – Armazenamento em Silos**. Salvador: Corpo de Bombeiros Militar da Bahia, 2020. Available in: http://www.cbm.ba.gov.br/sites/default/files/2020-07/it_27.2020_silos.pdf. Access on Mar. 15, 2023;

[20] CBMPI. **Instrução Técnica nº 27 – Armazenamento em Silos.** Terezina: Corpo de Bombeiros Militar do Piauí, 2019. Available in: http://www.cbm.pi.gov.br/download/201909/CBM03_9b0250e7f7.pdf. Access on: Mar. 15, 2023;

[21] ASSOCIAÇÃO BRASILEIRA DE NORMAS TÉCNICAS. **ABNT NBR 16913:2020. Proteção contra incêndio de transportadores de correia utilizando sistemas de chuveiros automáticos – Requisitos**. Rio de Janeiro: Associação brasileira de Normas Técnicas, 2020. 9p.;

[22] NATIONAL FIRE PROTECTION ASSOCIATION. **NFPA 15. Standard for water spray fixed systems for fire Protection**. Quincy: National Fire Protection Association, 2017. p.19-20;

[23] NATIONAL FIRE PROTECTION ASSOCIATION. **NFPA 654. Standard for the prevention of fire and dust explosions from the manufacturing, processing, and handling of combustible particulate solids**. Quincy: National Fire Protection Association, 2020. p.6;

[24] FM GLOBAL. **Data Sheet 7-11 – Conveyors**. Johnston: Factory Mutual Insurance Company, 2020. 18p.;

[25] ASSOCIAÇÃO BRASILEIRA DE NORMAS TÉCNICAS. **ABNT NBR ISO 31000:2018. Gestão Riscos – Diretrizes**. Rio de Janeiro: Associação brasileira de Normas Técnicas, 2018. p.1;

[26] HUANG, C.; XIN, J. Fire risk analysis of residential buildings based on scenario clusters and its application in fire risk management. **Fire Safety Journal**, London, nov. 2013, v.62, p. 72-78. Available in: < http://www.sciencedirect.com/science/article/pii/S0379711213001653> Access on: Feb. 08, 2023;

[27] DUARTE, D.; LEITE, M.S.; PONTES, R. Gerenciamento de Riscos de Incêndio. In: ENCONTRO NACIONAL DE ENGENHARIA DE PRODUÇÃO, 1998, Recife. **Anais eletrônicos…** Recife: Associação Brasileira de Engenharia de Produção, 1998. Available in: <http://www.abepro.org.br/biblioteca/ENEGEP1998_ART366.pdf>. Access on: Feb. 11, 2023;

[28] PONTE JUNIOR, G.P. **Gerenciamento de Riscos Baseado em Fatores Humanos e Cultura de Segurança**. 1 ed. Rio de Janeiro: Elsevier, 2014. 200p.

[29] LUO, M.; SUN, X. **Fire Risk Assessment for Super High-rise Buildings**. Procedia Engineering, v.71, May.2014. Available in: http://www.sciencedirect.com/science/ article/pii/S1877705814004895. Access on: Access on: Dec. 10, 2022;

[30] BORTNOWSKI, P.; KAWALEC, W.; KR'OL, R.; OZDOBA, M. Types and causes of damage to the conveyor belt – Review, classification and mutual relations. **Engineering Failure Analysis**. 2022. Available in https://www.sciencedirect.com/science/article/pii/S1350630722004940?via%3Dihub. Access on Mar. 25, 2023;

[31] TRIPPLER, S.; CZYLWIK, A. **Detection of overteated rollers in belt conveyors systems**. Quincy: Fire Protection Research Foundation, 2017. Available in: https://www.nfpa.org/-/media/Files/News-and-Research/Resources/Research-Foundation/Symposia/2017-SUPDET/SUPDET17-Czylwik---Trippler.ashx. Access on Mar. 25, 2023;

[32] TRÁVNÍČEK, P.; KOTEK, L.; JUNGA, P. Prevention of accidents in facilities for the treatment and storage of selected agricultural products. **Safety Science**. n.153, 2022. Available in: https://www.sciencedirect.com/ science/article/pii/S0925753522001394?via%3Dihub. Access on Mar. 25, 2023;

[33] KHAKZAD, N.; KHAN, F.; AMYOTTE, P. Dynamic risk analysis using bow-tie approach. **Reliability Engineering & System Safety**. Vol.104, 2012. p.36-44. Available in: https://www.sciencedirect.com/science/article/pii/S0951832012000695. Access on Mar. 26, 2023;

[34] MULCAHY, M.B.; BOYLAN, C.; SIGMANN, S.; STUART, R. Using bowtie methodology to support laboratory hazard identification, risk management, and incident analysis. **Journal of Chemical Health and Safety**. Vol.24, no. 3, 2017, p.14-20. Available in: https://www.sciencedirect.com/science/article/ pii/ S1871553216300925. Access on Mar. 23, 2023;

[35] ALIZADEH, S.S.; MOSHASHAEI, P. The Bowtie method in safety management system: A literature review. **Scientific Journal of Review**. 2020. p.133-138. Available in https://www.researchgate.net/profile/Seyed-Shamseddin-Alizadeh/publication/339439384_The_Bowtie_method_in_safety_management_ system_ A_literature_review/links/5f2f960e458515b7290fdb73/The-Bowtie-method-in-safety-management-system-A-literature-review.pdf. Access on Mar. 27, 2023;

[36] LI, Y. **A Systematic and Quantitative Approach to Safety Management**. Delft: Delft University of Technology, 2019.p.30. Available in: https://repository.tudelft.nl/islandora/object/uuid:458a384f-6f8a-4fc3-8bc4-c01397b54b59?collection=research. Access on Mar. 26, 2023.

[37] COMPONENTE. Transportadores de Correia. Componente Equipamentos Industriais Ltda, 2021. Available in: https://componente.com.br/. Access on Apr. 09, 2023;

[38] FABIANO, B. et al. Coal dust emissions: From environmental control to risk minimization by underground transport. An applicative case-study. **Process Safety and Environmental Protection. v**ol.92, no. 2, 2014, p.150-159. Available in: https://www.sciencedirect.com/science/article/pii/S0957582013000049. Access on Apr. 03, 2023

[39] EUROFIRE. Using Linear Heat Detection for Conveyor Applications.2015. Available in: https://eurofyre.co.uk /news/using-linear-heat-detection-for-conveyor-applications/. Access on Apr. 10, 2023;

[40] EQUIPAMENTO da Vale pega fogo em Nova Lima e suspeita é de incêndio criminoso. **Estado de Minas**. 16 Abr 2019. Available in: https://www.em.com.br/app/noticia/gerais/2019/03/16/interna_gerais,1038567/equipamento-da-vale-pega-fogo-e-suspeita-e-de-incendio-criminoso.shtml. Access on Apr 03, 2023;

ASSESSING THE IMPACT OF DIFFERENT INSPECTION, TESTING AND MAINTENANCE INTERVALS ON THE RELIABILITY OF AN AUTOMATIC FIXED FIRE PROTECTION SYSTEM.

Henrique Pimenta[a]

(a) FM Global (Henrique.pimenta@fmglobal.com)

1. ABSTRACT

Protection layers are of great importance for risk reduction in any industry occupancy, both to prevent the occurrence of a hazardous event and to mitigate its consequences.

As an example, a fixed automatic fire protection system can considerably reduce the consequences of a fire hazard scenario for people, property damage and business interruption, acting as a strong mitigating layer of protection at most cases. However, it is not always clear how to maintain a minimum reliability of this system so it can be considered as a reliable layer of protection against a fire hazard scenario.

In this work, a typical automatic deluge protection system covering an outdoor unit operation processing ignitable liquids will be considered as a potential mitigative layer of protection against a fire scenario. The study addresses the calculation of the probability of failure on demand (PFD) of the system and its reliability as a function of different inspection, testing and maintenance (ITM) intervals for the fire pump and the isolating valves.

The study clearly shows that the deluge system can only be effectively credited as a reliable mitigative protection layer if the ITM intervals for the fire pump set and isolating valves are performed weekly. In addition, the PFD of the system reaches roughly 72% when the ITM intervals of the fire pump set and the isolating valves are performed at a annually frequency.

Lastly, the study shows that adding redundant and independent subsystems increases the overall system reliability, and the maximum reliability to be achieved in an industry will also depend on the risk improvement appetite of the plant.

Keywords: inspection, testing, maintenance, reliability, fire protection.

1. INTRODUCTION

1.1 Protection layers

It is already well known by the process safety community what are the ways to reduce the risk of a hazardous event that may generate losses, both in terms of people, as well as property and the environment. By the very definition of risk of a certain hazardous event occurring, its reduction can be considered through reducing the probability of

occurrence of this event or mitigation of its consequences, and the agents responsible for this risk reduction related to this specific event are called protection layers.

In addition, according to the CCPS (Center for Chemical Process Safety) and the LOPA theory [3] (Layers of Protection Analysis), one of the core attributes for a protection layer to be considered in a serious process hazard analysis is that it must be reliable. In a quantitative way, and based on the same sources presented above, a reliable protection layer must present a reliability greater than or equal to 90%, or, in other words, it should present a PFD less than or equal to 10%.

1.2 Mitigative protection layers

Mitigative protection layers are those that tend to decrease the risk by acting to reduce its consequences. Usually, these layers will be demanded if any failure occurred in the preventive protection layers that would act in the same risk scenario.

This paper will focus on a specific type of mitigative protection layer, which is the fixed automatic fire protection system, such as a deluge or a wet sprinkler system. Such systems are historically known to be very effective protection layers for reducing the consequences of a fire event, both for people and property.

As an example, reference [1] shows that the death rate per 1,000 reported fires (between 2015 and 2019) in the USA was 89 % lower in properties with sprinklers than in properties with no sprinkler protection.

In addition, in terms of property damage and considering the Latin American region, FM Global loss statistics consistently shows that, a fire in a sprinklered location is about 15 times less severe than in an unsprinklered location. The figure below [2] shows the average loss for non-adequately sprinkler properties in north America and in other parts of the world.
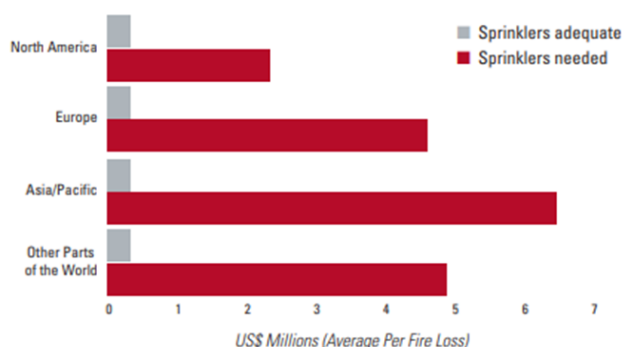
Figure 1 – Effectiveness of Automatic Sprinklers

This effectiveness of automatic sprinkler protection is nothing new for the process safety and loss prevention community, as these mitigative protection layers are already commonly considered in process hazard analyses, such as HazOps and even LOPA.

However, like any other protection layer, automatic fire protection systems have a probability of failure on demand and obviously need adequate ITM to keep their reliability at acceptable levels. ITM tasks for preventive layers of protection such as Basic Process Control Systems (BPCS), Alarm management Safety Instrumented Systems (SIS) seem to be well understood and well applied by the process safety community, especially considering the chemical and petrochemical industry sectors.

However, for an active mitigative protection layer, such as an automatic sprinkler system, field experience says that there seems to be a discrepancy between the ITM frequencies needed to maintain the system with an adequate level of reliability, although there are good references that well discretize the ITM subject for automatic fire protection systems, such as NFPA standards and the FM Global Property Loss Prevention Data Sheets [8].

Therefore, the next section will deal with the fundamental concepts of system reliability, to delve deeper into the issue of minimum reliability (or maximum PFD) suggested for an automatic fire protection system to be credited as a reliable mitigative protection layer.

2. SYSTEM RELIABILITY CONCENPTS

2.1 Reliability

Reliability R is the probability that a component or system will perform the function for which it was designed, during a predefined period, given that it was working or able to operate at the initial instant. Therefore, the reliability equation can be written as follows [4]:

$$R(t) = \Pr(T \geq t | c_1, c_2 \ldots), 0 \leq R(t) \leq 1 \quad (1)$$

Where:
T: failure time (random variable)
t: Predefined period of time
$c_1, c_2 \ldots$: Operational conditions

Therefore, the probability of failure $F(t)$ of this component as a function of time can be defined by:

$$F(t) = \Pr(T \leq t), 0 \leq F(t) \leq 1 \quad (2)$$

$F(t)$ can also be called *unreliability* and, for this paper, will also be synonymous with Probability of Failure on Demand, or PFD (considering that the automatic fire protection system will work in a low demand mode and would actuate once per year or rarer). Finally, from Equations (1) and (2), it is possible to conclude that:

$$R(t) = 1 - F(t) \quad (3)$$

2.2 Failure rate

Failure rate λ is the frequency with which a system or component fails, expressed in failures per unit of time. The failure rate is an important function in reliability analysis since it shows changes in the probability of failure over the lifetime of a component. In practice, for most electrical and mechanical components, λ often exhibits a bathtub shape and is referred to as a bathtub curve, as shown in the figure below:
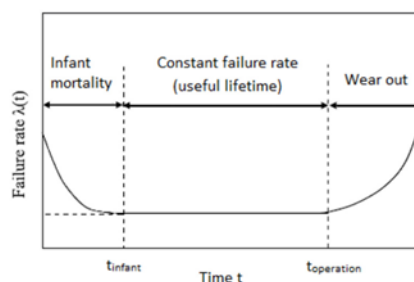
Figure 2 – Example of a bathtub curve

The bathtub curve usually has three different time periods, being them:

- **Infant mortality:** This is an interval characterized by a decreasing failure rate, and it starts from a high failure occurrence. Failures that occur within this time are usually known as systematic failures and are driven by issues in design, manufacturing, or construction.

  Knowing that the higher the failure rate, the greater the probability of failure of a component or system at a given time, the infant mortality curve represents a major problem for the reliability calculations. To minimize the infant mortality curve of a component, this device undergoes a series of tests under extreme conditions before being put on sale, to identify and retain the components most likely to present systematic failures.

- **Useful lifetime:** This region represents the normal operating life of most assets, and it exhibits a reasonably constant failure rate, mainly characterized by random failures of the component. This period of time will be considered when calculating the PFD of a component or system, as will be shown throughout this paper.

- **Wear out:** In this region, there is a gradual increase in failure rate of assets with increasing time, where failures usually occur due to fatigue, wear, gradual deterioration, corrosion, etc. This period basically represents end of life cycle of assets.

2.3 Exponential distribution

The exponential distribution is one of the most used distributions in system reliability analysis. This can be attributed primarily to its simplicity and the fact that it gives a simple, constant failure rate model corresponding to a situation that is often realistic [4]. Therefore, considering the *Useful lifetime* region of a component represented in a bathtub curve (which is normally the longer period compared to the other two ones), this distribution may be adequate for calculating its probability of failure.

In short, for an exponential distribution, the reliability of a component (assuming its constant failure rate) can be calculated by [4]:

$$R(t) = e^{-\lambda t} \ (4)$$

Therefore, the probability of failure on demand of this component can be calculated by:

$$PFD = F(t) = 1 - e^{-\lambda t} \ (5)$$

These concepts and equations will be foundational for the following sections of this paper.

3. CASE STUDY

3.1 Automatic deluge system of a process plant unit operation

Automatic deluge systems are typically recommended for outdoor unit operations that handle significant amounts of ignitable liquids (liquids that may burn when in contact with an ignition source [5]).

As previously mentioned, these systems are considered effective mitigative protection layers against fire scenarios, which may occur in the event of loss of containment of the ignitable liquid in conjunction with some source of ignition nearby. An example of a unit operation provided with an automatic deluge system is shown in the figure below:

Figure 3 - Example of an automatic deluge system in a chemical plant handling ignitable liquids

In addition, an automatic deluge system is usually composed of many mechanical and electrical components and subsystems, connected mainly in series. Among these subsystems, the most important ones are the water tank, fire pump set (including components such as sensing elements for automatic starting of the pump by pressure drop, control panel, battery pack and diesel engine), isolating valves between the water tank piping and the deluge valve and, finally, the deluge system itself (consisting mainly of pilot line, compressed air system, and open nozzles).

Therefore, one possible way to represent the main subsystems of the automatic deluge system is through the following simplified block diagram:
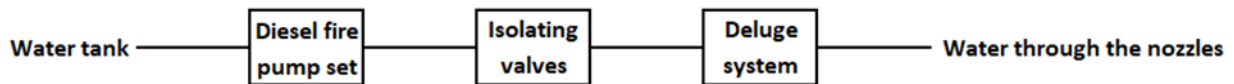
Figure 4 - Water path to fire fighting

Lastly, it is important to assume in this case study that the deluge system was well designed and is in accordance with good engineering practices [9][10]. Therefore, it is assumed that, if the system operates, it will be able to control or even suppress the fire in the unit operation in which it is installed. Therefore, the objective of this study is to focus on the reliability of this system when its action is needed.

3.2 Estimating failure rates for each system block

One of the main goals of this case study is to calculate the PFD of the automatic deluge system, represented by Figure 4. The water tank will not be considered in the PFD calculations for the purposes of this study. The two most common failure modes associated with the water tank are if this tank is empty or if any isolating valves between the tank and the fire pump set are closed. For these two conditions, the deluge system would fail (lack of water to fight the fire) on demand. However, the failure mode referring to a closed isolating valve is already covered in the "Isolating Valves" block and the failure mode referring to the tank being empty is covered in the weekly fire pump ITM checklist, which is part of fire pump set block scope.

For components connected in series, the PFD of the system is the sum of the PFDs of each subsystem or block, which means that if a subsystem has an undetected dangerous failure, the entire system will be impaired.

Therefore, the first step to calculate the PFD of a component or system is to estimate its failure rate, mainly the undetected dangerous failure rate, whose failure will lead to an unsafe condition.

For that, reference [6] presents a database with several failure rates of components related to a fire protection system, including failure rates of a diesel fire pump set, isolating valves and deluge systems.

Finally, for the three blocks presented in Figure 4, their failure rates presented in [6] were compared with the failure rates recorded by FM Global (mainly in the Latin American region) through loss prevention field visits in recent years, to validate the use of the lambdas found in [6]. As expected, the compared failure rates are in the same order of magnitude, and they are presented below:

3.2.1 Diesel fire pump set

The automatic actuation loop of the diesel fire pump set is composed of pressure sensing line, the fire pump control panel, and the final element, which is the diesel engine. In addition to these series-connected components, there are some other critical devices that are part of the fire pump set, such as the battery pack (normally two redundant sets) and solenoid valve in the engine system's cooling line. Each of these components has its own failure rate. However, reference [6] already directly presents the final failure rate of the fire pump set, where this final failure rate con be considered as a function of the failure rates of the components of this block.

Therefore, the considered failure rate for the fire pump set is shown below:

- $\lambda_{FP} = 1.2x10^{-4} \ failures/hour$

3.2.2 Isolating valves

This block represents all isolating valves (usually manual valves) that are part of the fixed fire protection system, that can be found from the outlet of the water tank piping to the last valve located upstream of the deluge valve. Therefore, the failure mode considered for this block is that at least one critical isolating valve that could impair the entire deluge system is in the closed position when such system is triggered. As a conservative approach, the study considers that one closed valve will already impair the entire deluge system. Reference [6] also presents a failure rate for this specific failure mode, which will be considered constant in this study.

The considered failure rate for the isolating valves is shown below:

- $\lambda_V = 6.3x10^{-6} \ failures/hour$

3.2.2 Deluge system

This study considers the deluge system most seen in Brazil, which has a pilot line (pressurized with compressed air) provided with closed sprinklers, where the system actuator is the deluge valve itself, which will open if the pilot line depressurizes. The open deluge nozzles can also be considered part of the actuation system. Each of these components has its own failure rate. However, reference [6] already directly presents the final failure rate of the deluge system, where this final failure rate is a function of the failure rates of the components of this block.

Therefore, the considered failure rate for the deluge system is shown below:

- $\lambda_D = 2.8x10^{-6} \ failures/hour$

The reliability of the deluge system will be calculated considering the three failure rates mentioned above. It is important to note that this is a simplified approach, since a more complex model would present the failure rates of all critical components present in each block in Figure 4. However, it is expected that this simplified approach will present results consistent with reality, since the failure rates presented above were compared with the failure rates recorded by FM Global (mainly in the Latin American region) through loss prevention field visits made in the last years, and such failure rates are in the same order of magnitude.

Lastly, it is assumed that the failure rates of each of the three blocks are constant throughout the useful lifetime of the deluge system.

4. CALCULATING THE PFD FOR EACH SYSTEM BLOCK USING THE EXPONENTIAL DISTRIBUTION

4.1 Differences between ITM interval, Mission time and Useful lifetime

In addition to the failure rate, another important variable for calculating the PFD of a system is the time t present at Equation 5.

Usually, the variable t will be assigned to the component's mission time or ITM interval, where an explanation of each term is found below:

- Mission time: is defined as the period of time between when a device is put into service and when it is replaced or completely refurbished to "as-new" condition.
- ITM interval: is the period of time between ITM. A ITM is an important task to detect previously dangerous failures in the component so that it may be repaired.

Therefore, it is important to establish a relationship between these different concepts of time, also adding the concept of Useful lifetime. In general, the relationship between the three mentioned concepts of time will respect the following inequation:

$$ITM \ interval < Mission \ time < Useful \ liftime$$

In other words, if the mission time is less than or equal to the ITM interval, then there is technically no need to inspect and test the device. If the useful lifetime is less than the mission time, then the assumption of constant failure rates used by all common PFD calculation methods is incorrect, and such calculations are meaningless.

In addition, it is important to know that the useful lifetime is a property of the device in the environment where it is deployed. Therefore, it is not a design choice or a maintenance strategy.

Unlike useful lifetime, mission time is a design decision that is documented in the PFD calculations. Mathematically, whenever ITM coverage is less than 100%, then undetectable dangerous failures can potentially occur that will never be detected by testing. The latent failures will remain in the device until either a demand occurs, or the device is replaced at the end of its mission time.

As shown below, the probability of a latent failure accumulates with time, considering a ITM interval with coverage less than 100%. In this case, only replacing the device will reset the PFD curve to zero.
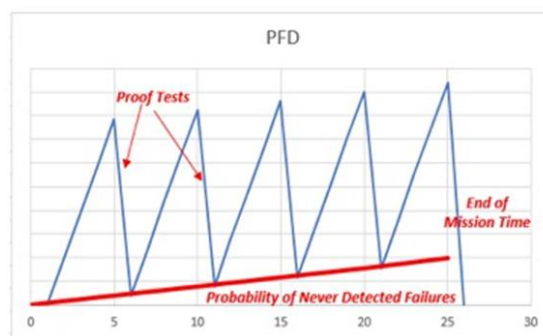
Figure 5 - Differences between ITM (proof tests) interval and mission time [7]

In addition, for this study, a proof test coverage of 95% was considered for the fire pump set and isolating valves, which means that 95% of all possible undetected failures would be revealed during their ITM. The terms Proof testing and ITM are considered interchangeable.

4.2 Establishing ITM intervals and final calculations

For the scope of this study, the ITM intervals of each block in Figure 4 will be used to fill in the time variable t presented in Equation 5.

In addition, the intention of this case study is to present the variations of the total PFD of the system as a function of different ITM intervals adopted.

This study will also assume that the ITM is ideal, where the detected dangerous failure modes of the components are fixed promptly.

Finally, by knowing the failure rates of each block of the system represented in Figure 4, the main variables of this study will be the ITM intervals referring to the fire pump set and isolating valves.

4.2.1 Fire pump set

The fire pump set PFD calculations will be performed as a function of its ITM interval. Ideally, the diesel fire pump (considered in this case study) should be tested weekly by an employee or contractor who knows well the mechanisms of the system, as recommended by [8]. The weekly diesel pump ITM consists of starting it in automatic mode (due to pressure drop) and keep it running for at least 30 minutes. A step-by-step guide of the items to be inspected, tested, and maintained is also presented in [11].

On the other hand, many companies adopt their own test frequencies for their fire pumps, which can often be monthly, semi-annually, or even annually. However, it is important to know that increasing the range of ITM intervals, the PFD of this subsystem will also increase, possibly reaching unacceptable levels of reliability at some point.

4.2.2 Isolating valves

Like the fire pump set, the isolation valves PFD calculations will be performed as a function of their ITM interval. The ITM interval of isolating valves is treated as a visual inspection of these valves, which ideally should be locked with chains in the open position. A step-by-step guide of the items to be inspected, tested, and maintained is also presented in [11].

The recommendation to lock valves with chains [8][11] is a good engineering practice adopted to reduce the probability of having an ICV (improperly closed valve). Another good engineering practice for this case is to use rising stem gate valves as isolation valves whenever possible, as it facilitates the visual inspection to check if the valves are open, decreasing the chance of an inspection error.

In addition, as already specified in this paper, the PFD for this case means the probability of at least one of these isolating valves being closed, which will prevent the flow of water through the deluge system, in case this system is demanded by any fire in the unit operation covered by the automatic deluge system.

Ideally, isolating valves should be inspected on a weekly basis [8][11]. However, many companies adopt their own valve inspection frequencies, which can often be monthly, semi-annually, or even annually. In addition, there are many sites where this valve inspection does not even exist.

4.2.3 Deluge system

For this case study, it is assumed that the deluge system is properly inspected on an annual basis, which is in accordance with good engineering practices [8].

Therefore, the main objective of this case study is to show the increase in the PFD of the system due to the different ITM intervals for the fire pump set and isolation valves.

4.3 Final calculations and assessment of results

To present the final results, the Fire pump set, Isolating valves and Deluge system PDF calculations were made considering the following ITM intervals:

Table 1 – ITM intervals considered for each subsystem

	ITM interval considered		
	Fire pump set	Isolating valves	Deluge system
Point 1	1 week	1 week	12 months
Point 2	1 month	1 month	12 months
Point 3	6 months	6 months	12 months
Point 4	9 months	9 months	12 months
Point 5	12 months	12 months	12 months

From the Table 1 above, the following graph of the evolution of the system's PFD at a function of different ITM intervals for fire pump set and isolating valves could be generated:
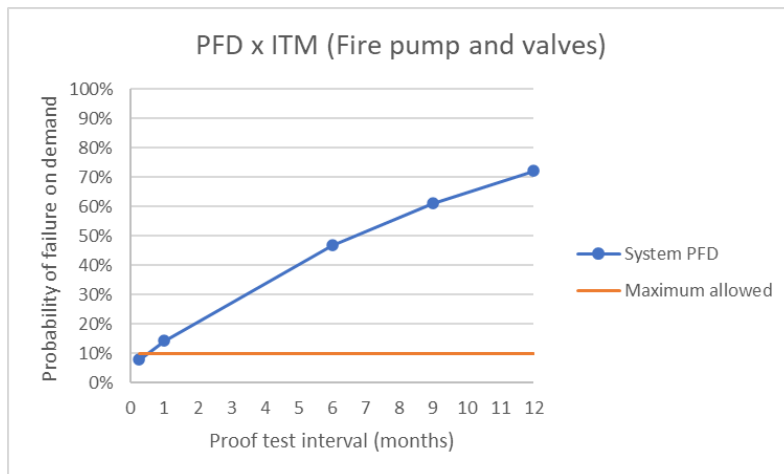
Figure 6 - PFD x ITM interval of fire pump set and isolating valves

In addition, Figure 7 below represents the same PFD curve, but only considering the first two calculated points, to zoom in on the PFD curve between these points:
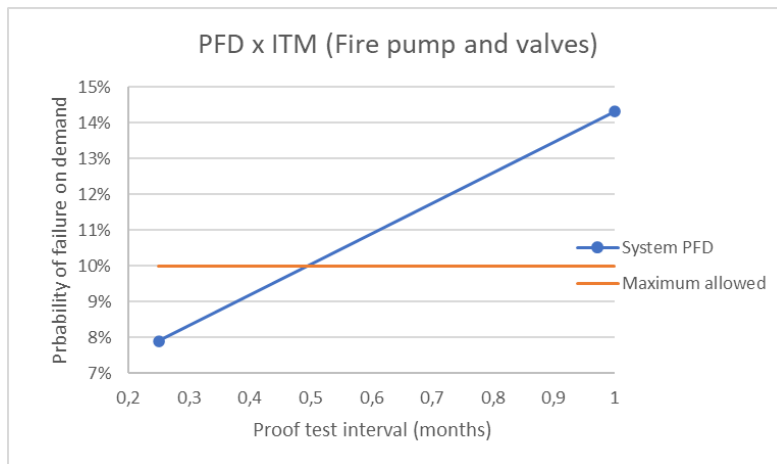
Figure 7 - PFD x ITM interval of fire pump set and isolating valves (1st two points only)

It is possible to notice, therefore, that if the ITM intervals are made on a weekly basis (first point of the curve), the PFD of the system is around 8%, which is consistent with data presented in [1], where an analysis was carried out between 2015 and 2019 regarding fires in properties equipped with a sprinkler system, where the sprinkler systems failed to operate in 8% of the cases.

In addition, the orange horizontal curve presented in the two Figures above is of great importance for this study, since this curve is considered the maximum suggested limit of the PFD allowed for the automatic deluge system to be credited as a reliable mitigative protection layer.

Another way to visualize the results presented is to represent the reliability curve of the system as a function of the ITM intervals. For this curve, only the first two points were computed, to better visualize the results:
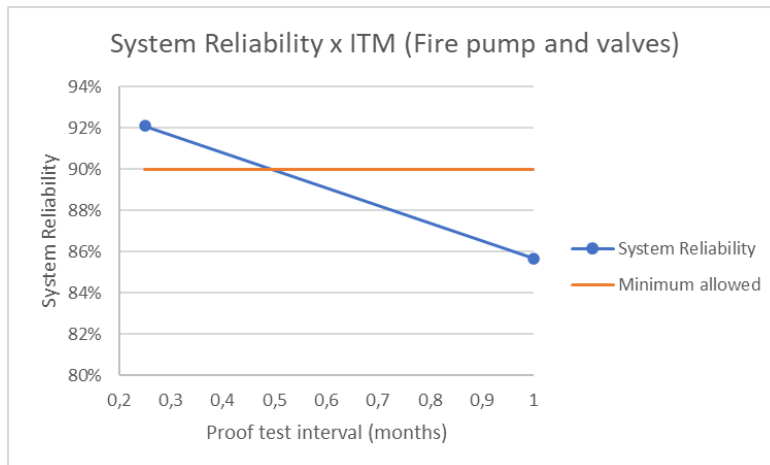
Figure 8 – Reliability x ITM interval of fire pump set and isolating valves (1st two points only)

Therefore, the first and most important conclusion that can be observed is that the deluge system can be effectively credited as a reliable protection layer if the ITM intervals for the fire pump set and isolating valves are performed weekly, where such frequencies are already recommended by good engineering practices [8].

Another conclusion that can be drawn from analyzing the graphs above is that, if the ITM intervals are performed annually (or above that) for the fire pump set and the isolating valves, the PFD of the system reaches 72%. A good correlation with this scenario is to keep a car stationary without starting its diesel engine for a year or more. Experience and intuition say that the probability of this car's engine running after being idle for 1 year is low.

After the analysis above and knowing the failure rates of each block of Figure 4, it is possible to imagine that the fire pump set must have a high contribution to the total PFD of the system. To verify this, the Figure below representing the contribution of each of the three subsystems to the final PFD calculation was generated, again as a function of the ITM interval frequencies of the fire pump set and isolating valves:
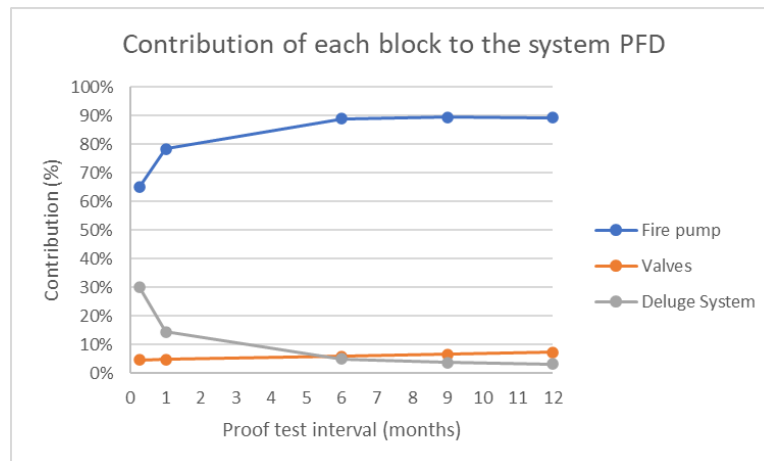
Figure 9 - Contribution of each block to the system PFD

Through the analysis of the Figure above, it is possible to notice the largest contribution in the total PFD comes from the fire pump set, as already expected (more failure modes compared to the other blocks).

4.4 Possible way to increase the reliability of the deluge system

As seen above, the maximum calculated reliability of the case study system, considering the ITM intervals made in accordance with good engineering practices [8], was approximately 92%, which is already an adequate number to credit the deluge system as a reliable mitigative protection layer.

226

However, a possible question that may arise for a company that has an appetite for risk improvement is how to increase the reliability of this system even more.

One possible answer to this question is to add redundant subsystems or components. Below, a simulation will be made of how the reliability of the deluge system would look if a second similar diesel fire pump set were installed in parallel to the first one (assuming that one set is independent of the other and only one fire pump is necessary to guarantee the effectiveness and performance of the fixed fire protection system).

The following simplified block diagram represents the system configuration with a new fire pump set installed in parallel with the first one.
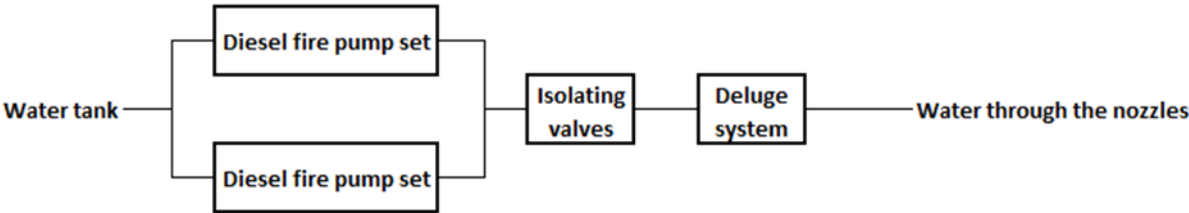
Figure 10 – Water path to fire fighting with two redundant fire pumps

The analysis of the figure above makes it clear that, if there is a dangerous failure in a fire pump set, there is still a path for the water flow to the deluge nozzles, through the second fire pump set installed in parallel. The new system reliability curve (considering only the first two test points, like Figure 8) is presented below:
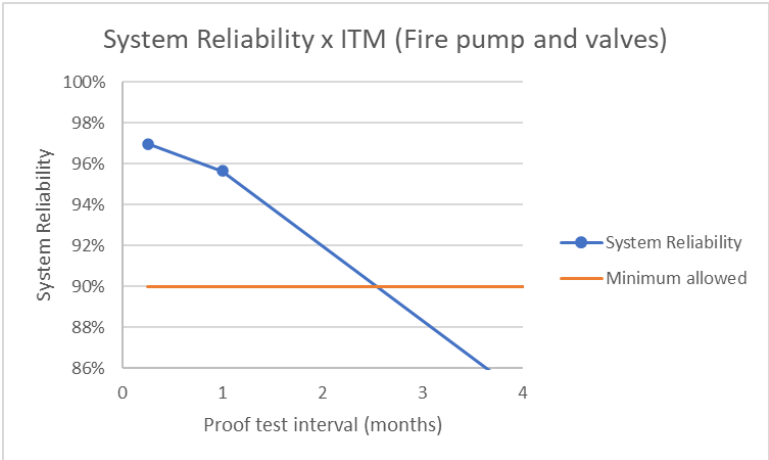
Figure 11 - Reliability x ITM interval of fire pump set and isolating valves (1st two points only) considering two sets of redundant fire pumps

It is possible to notice that the maximum reliability of the system is now around 97%, representing a 5% improvement over the original system. Certainly, the new system is more reliable, but it involved some additional cost of installing a new fire pump set. Therefore, the maximum reliability to be achieved in an industry will also depend on the risk improvement appetite that this plant has and how much the plant is willing to invest so that the system is as reliable as possible.

Lastly, the analysis of Figure 11 also shows that, if the deluge system of this case study has two similar and independent fire pump sets installed in parallel, it would be tolerable to carry out the ITM related to fire pumps and isolating valves monthly. However, it is important to point out that this monthly frequency is not considered a good practice by the fire protection engineering community, but the analysis of the Figure above shows that such a frequency could be tolerable in this specific case.

5. CONCLUSIONS

The main conclusions from the results obtained in this study are shown below (the first three items are based on the deluge system provided with only one fire pump set):

- The deluge system can only be effectively credited as a reliable mitigative protection layer if the ITM intervals for the fire pump set and isolating valves are performed weekly, where such frequencies are already recommended by good engineering practices [8].
- The PFD of the system reaches 72% when the ITM intervals of the fire pump set and the isolating valves are performed once a year.
- The fire pump set provides the greatest contribution to the system's PFD.
- Adding redundant and independent subsystems increases the overall system reliability. In addition, the maximum reliability to be achieved in an industry will also depend on the risk improvement appetite of the plant.
- If the deluge system of this case study has two similar and independent fire pump sets installed in parallel, it would be tolerable to carry out the ITM related to fire pumps monthly, although such frequency is not considered a good practice in the fire protection community.

6. REFERENCES

[1] NFPA Research – *US Experience with Sprinklers.* Marty Ahrens (October 2021).
[2] Understanding the Hazard – *Lack of Automatic Sprinklers*. FM Global (2010).
[3] *Layer of Protection Analysis: Simplified Process Risk Assessment* – a CCPS Concept Book (October 2001).
[4] *Reliability Engineering and Risk Analysis – A Practical Guide (3rd edition).* Mohammad Madarres, Mark P. Kaminskiy, Vasiliy Krivstov.
[5] FM Global Property Loss Prevention Data Sheet 7-32: *Ignitable Liquid Operations* (April 2020).
[6] *A review of sprinkler system effectiveness studies. Fire Science Reviews (2013).* Kevin Frank, Neil Gravestock, Michael Spearpoint and Charles Fleischmann.
[7] *Useful Life, Mission Time, and Proof Tests.* Stephen Thomas.
[8] FM Global Property Loss Prevention Data Sheet 2-81, *Fire Protection System Inspection, Testing and Maintenance (April 2019).*
[9] FM Global Property Loss Prevention Data Sheet 7-14*, Fire Protection for Chemical Plants (July 2019).*
[10] FM Global Property Loss Prevention Data Sheet 2-0, *Installation Guidelines for Automatic Sprinklers (October 2021).*

FIRE PREVENTION IN HISTORIC HERITAGE IN CITY OF OURO PRETO - MINAS GERAIS

**Ana Carolina
Castanheira Pereira**

Paulo Von Kruger

ABSTRACT

During the last decades, many fires occurred in several buildings around the world, a fact that raised awareness of numerous scholars and generated several evolutions regarding the theme of fire safety. However, much still needs to be done to avoid this problem. It can be said that historic buildings need even more attention. Several laws were elaborated with a focus on preventing this problem in new buildings, but the existing ones are often not contemplated by these parameters. This work analyzes buildings in the historic center of Ouro Preto in Minas Gerais in Brasil, this city is declared a national monument and world heritage.

The importance of this historic site is highlighted not only for Brazil but also for the whole world. Having in mind the issue of superficiality in the analysis of fire prevention, three methods of analysis will be used to reach a more complete and reliable result. They are: Chichorro 2.0, simplified Arica and IT35 (global analysis), which will be explained throughout this work. Such methods will be applied in 54 chosen buildings. At the end of this work the results will be presented through tables and maps that will expose the riskiest buildings.

Keywords: Fire, Heritage, Methodologies, Prevention.

1. INTRODUCTION

This article has as main references the final paper: Fire prevention in historical heritage: case study in the city of Ouro Preto, Minas Gerais and the research: Fire risk assessment in historical sites of Minas Gerais: Ouro Preto funded by Fapemig. According to Unesco (2015) preventive risk management is cheaper than rehabilitation expenses. In the case of fires, the preventive assessment is important to protect property and people. This article will focus on the historic town of Ouro Preto in the state of Minas Gerais in Brazil. Ouro Preto is an important city in terms of historical heritage. According to Iphan – world historic heritage – Ouro preto is world heritage, prize awarded by unesco. This article will present 54 buildings analyzed in the city and the results about a risk of fire. Three methods were used to perform the evaluation: Global Analysis from IT35, Chichorro 2.0 And Arica. The Arica and Chichoro are used in Portugal and therefore follow the rules there. Only the first method follows the brazilian rules.

2. METHODOLOGY

The present study is divided into 3 parts:
1. Theoretical foundation,
2. Field research,
3. Guidelines.

Table 1 (Methodology)

Step	Description	Method
1 º step	Theoretical foundation	Documents analysis and talk with residents.
2º step	Field research	Application of methodologies
3º step	Guidelines	Analysis of previous steps and map production with results

(Pereira,2022)

2.1 Theoretical foundation
A quiz with question regarding the structure of the buildings was used to start the talk with the residents. Some important collected information was about gas, number of residents and existence of windows in the kitchen. The quiz was produced by Ignis, a group of students from the Federal University of Minas Gerais.

2.2 Field research
After 1° step, the collected data were applied in the three methodologies. They are: Global Analysis from IT35, Chichorro 2.0 And Arica.

The Global Analysis aims to analyze the risk of fire in old and historic Brazilian buildings. It was carried out together with IPHAN. According to IT35 – technical instruction used in cultural heritage buildings in Minas Gerais – the analysis takes into account: use/occupation, height, dimensions, constructive characteristics and fire load of buildings. The building's fire safety coefficient is obtained by adopting the ratio between the safety factor (S) and the overall fire risk (R).

$$y = S/R \qquad\qquad 01$$

The Arica (Fire risk analysis in old urban centers) is a method developed by Antônio Leça Coelho and Ana Margarida Sequeira Fernandes in 2010 and its application focuses on buildings located in old urban centers. However, it can be used in the evaluation of new buildings. According to Neto, Ferreira and Remor (2020), the methodology was designed to ensure buildings located in historic urban centers do not have a higher degree of risk than the most recent ones. Arica aims to make assessment objective and applicable on an urban scale. This method is based on two types of factors: the global risk factor (A, B and C) and the global effectiveness factor (D).

According to Ferreira (2016) the Chichorro method was developed by Daniel Martins, a master's student at the Faculty of Engineering of the University of Porto, under the guidance of Pr. Miguel Chichorro, professor at the same institution. In this method, the concept of fire risk is translated by means of the product of the fire occurrence probability by the severity of the consequences. The Chichorro 2.0 method, used in this research, is an evolution of the initial method. The improvement of Chichorro was developed by Ferreira, Ricardo (2016), also supervised by Miguel Chichorro. The Chichorro 2.0 method is an evolution of the Chichorro method (holistic calculation of fire risk in construction and enabled optimization of its reduction with works). The Chichorro 2.0 interface was designed to make the application easier and more intuitive. (Pereira, 2022).
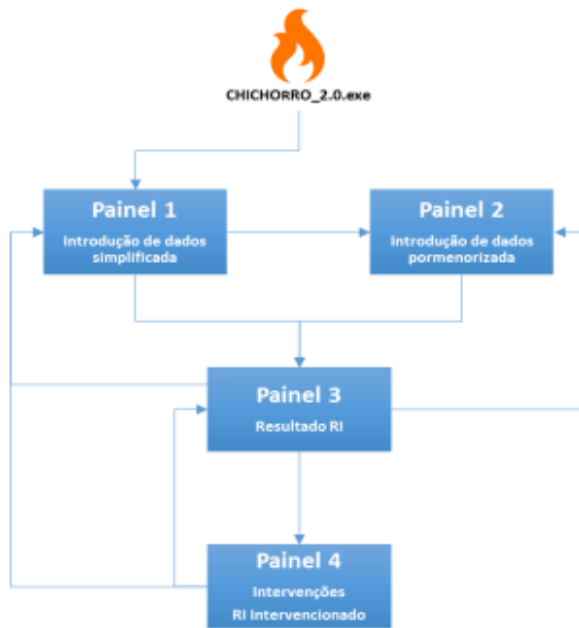
Functional flowchart of the developed software (Ferreira

In the Chichorro 2.0 method, the concept of fire risk is translated through the product of the probability of a fire occurring by the severity of its consequences.

$$RI = P \times G \qquad\qquad 02$$

3. RESULTS

The map below (Figure 1) shows the 54 analyzed buildings.

Figure 1: Buildings analyzed colored in brown (PEREIRA, 2022)

The 3 methodologies were applied Ill buildings. This was done to perform a more reliable analysis. Based on the results obtained, this table was prepared. The results in green mean that the building does not present a risk of fire and the results in red mean that the building presents a risk of fire.

Table 2 (Result)

<div align="right">To be Continued</div>

	Chichorro 2.0	Global Analysis from IT35	Simple Arica
Code	Classification	Classification	Classification
Edification 01	Have security	Have security	Have security
Edification 02	Does not have security	Does not have security	Does not have security
Edification 03	Have security	Does not have security	Have security
Edification 04	Does not have security	Does not have security	Have security
Edification 05	Have security	Have security	Have security
Edification 06	Have security	Does not have security	Have security
Edification 07	Have security	Does not have security	Have security
Edification 08	Have security	Does not have security	Have security
Edification 09	Have security	Does not have security	Have security
Edification 10	Have security	Does not have security	Does not have security
Edification 11	Have security	Does not have security	Have security
Edification 12	Does not have security	Have security	Does not have security
Edification 13	Have security	Have security	Does not have security
Edification 14	Does not have security	Have security	Does not have security
Edification 15	Does not have security	Does not have security	Does not have security
Edification 16	Does not have security	Does not have security	Does not have security
Edification 17	Have security	Does not have security	Does not have security
Edification 18	Does not have security	Does not have security	Does not have security
Edification 19	Does not have security	Does not have security	Does not have security
Edification 20	Have security	Does not have security	Does not have security
Edification 21	Have security	Does not have security	Does not have security
Edification 22	Have security	Does not have security	Does not have security
Edification 23	Have security	Have security	Does not have security
Edification 24	Does not have security	Does not have security	Does not have security
Edification 25	Does not have security	Does not have security	Does not have security
Edification 26	Have security	Does not have security	Does not have security
Edification 27	Have security	Does not have security	Does not have security
Edification 28	Have security	Does not have security	Does not have security
Edification 29	Have security	Does not have security	Does not have security
Edification 30	Does not have security	Have security	Does not have security
Edification 31	Have security	Does not have security	Does not have security
Edification 32	Does not have security	Does not have security	Does not have security
Edification 33	Have security	Does not have security	Have security
Edification 34	Have security	Have security	Does not have security
Edification 35	Have security	Does not have security	Does not have security
Edification 36	Have security	Does not have security	Does not have security
Edification 37	Does not have security	Does not have security	Does not have security
Edification 38	Have security	Does not have security	Does not have security
Edification 39	Have security	Does not have security	Does not have security
Edification 40	Have security	Have security	Have security
Edification 41	Have security	Have security	Does not have security
Edification 42	Have security	Does not have security	Does not have security
Edification 43	Does not have security	Does not have security	Does not have security
Edification 44	Does not have security	Does not have security	Does not have security
Edification 45	Have security	Does not have security	Does not have security

Edification 46	Have security	Have security	Does not have security
Edification 47	Have security	Have security	Does not have security
Edification 48	Does not have security	Does not have security	Does not have security
Edification 49	Does not have security	Have security	Does not have security
Edification 50	Does not have security	Does not have security	Does not have security
Edification 51	Does not have security	Does not have security	Does not have security
Edification 52	Have security	Does not have security	Does not have security
Edification 53	Have security	Have security	Does not have security
Edification 54	Have security	Does not have security	Does not have security

(Pereira,2022)

From the results found, 4 maps were generated. The first three were made with results obtained in each of the methodologies. The last one was a compilation of all the results. The maps were created to facilitate the visualization of which building presents a high risk of fire.

The Figure 2 summarizes the result of the risk assessment of the Chichorro 2.0 method, in which buildings in green have a low risk of fire. Buildings colored in red, on the other hand, have a high or imminent risk of fire, therefore, they received results greater than acceptable.

Figure 2: Buildings with low risk of fire and with very high or imminent risk according to the Chichorro 2.0 methodology (Pereira, 2022).

Figure 3 shows the buildings with low risk of fire and with very high or imminent risk according to the Global Analysis methodology. Green buildings have a low fire risk. Buildings colored in red present a high or imminent risk of fire.

233

Figure 3: Buildings with low risk of fire and with very high or imminent risk according to the Global Analysis methodology (Pereira, 2022).

Figure 4 shows the buildings with low risk of fire and with very high or imminent risk according to the Simple Arica methodology. Green buildings have a low fire risk. Buildings colored in red present a high or imminent risk of fire.

Figure 4: Buildings with low risk of fire and with very high or imminent risk according to the Simple Arica methodology (Pereira, 2022).

And the last map summarizes the results of the 3 methodologies. In green are the buildings that are considered as sage by the 3 methods, in yellow those that are safe according to 2 methods, in orange the ones that ate safe only in one method and in red in none of methods.

Figure 4: Overall result (Pereira, 2022).

4. CONCLUSIONS

Based on what has been presented, we can conclude that this study is of great relevance with regard to preventing fires in historical heritage sites. This paper showed the potential riskiest buildings in the analyzed area in Ouro Preto city. The aim of this work is to point out the least safe buildings. It was also possible to perceive which factor most influence the results of the methodologies used. In the case of Chichorro the houses that are not occupied is potentially safe in relation to the risk of fire. On the other hand, in simplified Arica and Global Analysis not being occupied is considered as an aggravating fact.

Thus, the main outcome of this study is to support the decision on which locations should be prioritized for renovations and investments.

ACKNOWLEDGEMENTS

REFERENCES

[5]   PEREIRA, Ana. Prevenção de incêndios me patrimônios históricos: estudo de caso na cidade de Ouro Preto. 2022.

[5]   FERREIRA, Ricardo Jorge Sousa. Desenvolvimento e implementação numérica do método chichorro de avaliação de risco de incêndio em edifícios. 2016. 206 f. Dissertação (Mestrado Integrado em Engenharia Civil) – Departamento de Engenharia Civil, Faculdade de Engenharia da Universidade do Porto, Porto. 2016. Disponível em: https://core.ac.uk/download/pdf/302948234.pdf. Acesso em: 01 de agosto de 2022

[5]   GERLACK, Mariana de Oliveira. **Análise de risco de incêndio**: Estudo aplicado a escolas de Porto Alegre. 2018. 117f. Monografia (Bacharelado em Engenharia Civil) – Departamento de Engenharia Civil da Escola de Engenharia, Universidade Federal do Rio Grande do Sul, Porto Alegre. 2018. Disponível em: https://www.lume.ufrgs.br/bitstream/handle/10183/189412/001087497.pdf?sequence. . Acesso em: 01 de agosto de 2022

[1]   CORPO DE BOMBEIROS MILITAR DE MINAS GERAIS. **Instrução técnica n. 09**: Carga de Incêndios nas edificações e área de risco. Belo Horizonte: Diretoria de Atividades Técnicas, [2009]. Disponível em: https://www.bombeiros.mg.gov.br/images/stories/dat/it/it%2009.pdf. Acesso em: 15 de novembro de 2022.

[1]   CORPO DE BOMBEIROS MILITAR DE MINAS GERAIS. **Instrução técnica n. 35**: Segurança Contra incêndio em edificações que compõem o patrimônio cultural. 2. Ed. Belo Horizonte: Diretoria de Atividades Técnicas, 2018. Disponível em: https://bombeiros.mg.gov.br/images/stories/dat/it/it_35_seguranca_contra_incendio_em_edificacoes_historicas_%202a_edio.pdf. Acesso em: 15 de novembro de 2022.

[4]   LOURENÇO, Válter Horta. **Avaliação do risco de incêndio de edifícios do centro Histórico de faro** – aplicação do método chichorro a ação do movimento popular urbano. 2019. 158 f. Dissertação (Mestrado em História) – Universidade do Algarve, Instituto Superior de Engenharia, Algarve. 2020. Disponível em: https://sapientia.ualg.pt/handle/10400.1/15535. Acesso em: 20 de outubro de 2022.[5] MOREIRA, Luís Ferreira; KRÜGER, Paulo Gustavo Von; LANZINHA, João Carlos Gonçalves. EBRAFire, a Avaliação e a Classificação dos Edifícios em Segurança Contra Incêndio, 2018.

[4]   NETO, Julio Tozo; FERREIRA, Tiago Miguel; REMOR, Marcelo Bevilacqua. Análise de vulnerabilidade ao incêndio em núcleos urbanos antigos - Os centros históricos brasileiros e a metodologia Arica simplificada. *In*: ASSOCIAÇÃO DOS GEÓGRAFOS BRASILEIROS. **Redução do risco de desastres e a resiliência no meio rural e urbano**. Bauru: AGB, 2020, p. 505-522. Disponível em: https://www.agbbauru.org.br/publicacoes/Reducao2020/Reducao_2ed-2020-28.pdf. Acesso em: 3 de novembro de 2022.

[1]   ORGANIZAÇÃO DAS NAÇÕES UNIDAS PARA A EDUCAÇÃO, A CIÊNCIA E A CULTURAUNESCO. **Gestão de riscos de desastres para o Patrimônio Mundial.** Brasília: UNESCO: IPHAN, 2015. 80 p.

[2]   Escola Politécnica de São Paulo. **Legislação brasileira surgiu após incêndios de grandes proporções em SP.** São Paulo, 2009. Disponível em: https://www.poli.usp.br/noticias/426-legislacao-brasileira-surgiu-apos-incendios-de-grandes-proporcoes-em-sp.html. Acesso em: 1 de dezembro de 2022.

[1]   COELHO, Antônio Leça. Incêndios em Edifícios. Editora ORION, outubro de 2010. DIAS, Luís Andrade de Mattos. Estruturas de Aço – **Conceitos, Técnicas e Linguagem**. Ed. Zigurate. 2015. TECNOBLOG. Tecnoblog: tecnologia que interessa, c2018. Página inicial. Disponível em: <https://tecnoblog.net/>. Acesso em: 05 de jun. de 2021.

[2]   IPHAN – INSTITUTO DO PATRIMONIO HISTORICO E CULTURAL DE MINAS GERAIS. **Centro histórico de Ouro Preto (MG). Disponível em: http://portal.iphan.gov.br/pagina/detalhes/30.**

[4]   VICENTE, R.; MENDES DA SILVA, J. A. R.; VARUM, H.; GUIMARÃES DA COSTA, A.; SUBTIL, A.; SANTOS, C.; SANTOS, M.; FERREIRA, T.; RODRIGUES, A. Avaliação do risco de incêndio urbano. Coimbra: Instituto Pedro Nunes, 2010. 139 p.

[1]   GOUVEIA, Antônio Maria Claret de. Introdução à Engenharia de Incêndio– para estudantes, arquitetos, engenheiros, administradores e bombeiros. Belo Horizonte: 3i editora, 2017. ISBN: 978-85-9548-007-0.

[5]   FERREIRA, Ricardo. Desenvolvimento e implementação numérica do método chichorro de avaliação de risco de incêndios de edifícios. 2016. Página 2

ASSESSING THE DEGREE OF READINESS AT URBAN AREAS WITH ELEVATED FIRE RISK IN PORTUGAL

A. L. Camargo[a],[*], João P. C. Rodrigues[b]

(a) University of Coimbra, CERIS, Itecons, Portugal (aline.camargo@itecons.uc.pt)
(b) Fed. Univ. of Minas Gerais, Brazil; Univ. of Coimbra, CERIS, Portugal (jpaulocr@dec.uc.pt)

Keywords: urban fires; fire risk; degree of readiness; firefighters' resources.

1. INTRODUCTION

Fire is one of the most harmful events in a building or an environment, and it can cause property damage, destruction of heritage, and ultimately the loss of human lives. Therefore, preventing and controlling a fire incident is essential to ensure safety. One of the significant concerns in controlling the fire incident is the degree of readiness of the response forces regarding adequate means and resources to fight fires for the buildings and their premises [1]. To guarantee this degree of readiness is essential to plan the firefighters' resource allocation. This paper proposes to verify the degree of readiness and the resources available considering the risk of urban fires with elevated fire risk in Portugal.

2. URBAN FIRE RISK IN PORTUGAL

The risk of urban fire, including historical sites, will be taken considering the National Risk Assessment (Fig. 1 a and b) elaborated by the Portuguese National Emergency and Civil Protection Authority (ANEPC, Autoridade Nacional de Emergência e Proteção Civil) [2]. Also will be considered the estimated probability of fire (Fig. 1 c) presented in Bispo *et al.* (2022)[3]. ANEPC maps the risk considering the number of residents, buildings built before 1945 and building height. In addition to the risk of urban fire, it also establishes the risk in Historic Sites. The main variables considered in Bispo *et al.* are the population density, the degraded buildings density and consumer buying power.

---
[*] Corresponding author – aline.camargo@itecons.uc.pt, Rua Pedro Hispano, s/n, 3030-289 Coimbra, PORTUGAL
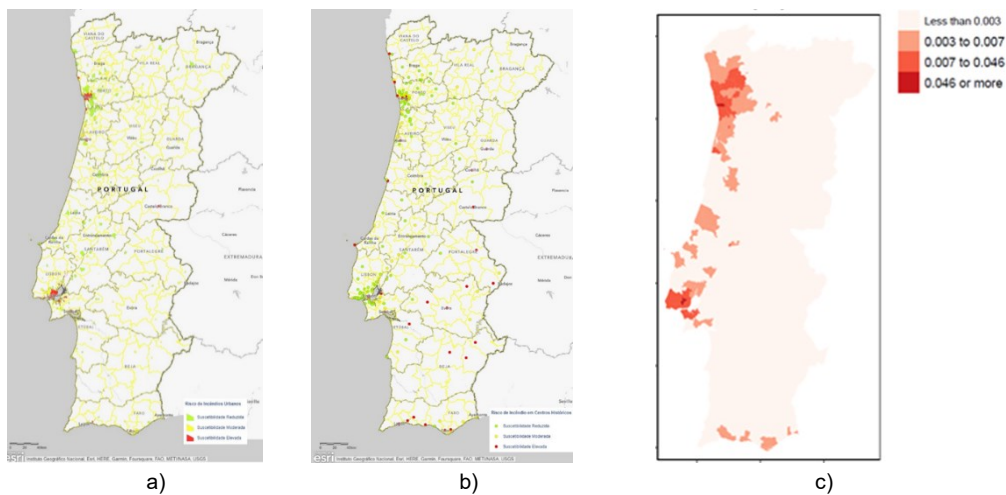
Figure 1. (a) Urban fire risk; (b) fire risk in historic centers; (c) estimated probability of fire occurrence

3. DEGREE OF READINESS

Three factors define the degree of readiness: the distance and/or maximum time to travel, by the regular access routes, between the fire department and the building or enclosure; the technical means (vehicles and equipment) mobilized for immediate dispatch after the alert; and the human resources, in minimum quantity, 24 hours a day on standby [1].

Buildings of the 3rd or 4th category must verify the degree of readiness when applying for the licensing. It means that if at up to 10km (or 10 minutes), there is a firefighter department with an Urban Fire Fighting Vehicle (VUCI), an Ambulance for Rescue (ABSC) and a minimum of seven firefighters available 24 hours a day. Furthermore, if within up to 15km (or 15 minutes), fire departments have the other means (Ladder Vehicle or lifting platform - VE/PE, Urban Tactical Tank Vehicle - VTTU and Tactical Command Vehicle -VCOT, with at least two firefighters for each vehicle). Remember that up to three fire departments can be activated to guarantee these minimum means. If this is not possible, the SCIE designer must adopt the compensatory measures.

Verification of the degree of readiness is done in the SCIE project. After verifying the building risk category, the designer responsible for the SCIE project can verify and explain in the descriptive project memorandum the fulfilment or not of the degree of readiness and already indicate the compensatory measures. When the project goes for evaluation by the authority (ANEPC), it verifies the data provided for the approval or no of the project and building licensing. Suppose the

technician in charge does not establish the level of readiness; the authority verifies it and returns the project to the designer, demanding compensatory measures if applicable.

Ensuring the degree of readiness does not mean that all the minimum means will be sent every time there is an urban fire. The fire department receives from the CDOS the type of occurrence and its location. District Command of Emergency Operations (CDOS) will direct the alarm to the fire department according to the location and description of the occurrence. The Fire Department decides which means to dispatch according to the location, type of occurrence and description of the call. The event alarm does not indicate the building's risk category. However, Emergency Plans for high-risk buildings already determine the measures and means to be considered.

4. CONCLUSIONS

Verify if the Portuguese urban areas with higher fire risk, including the historical sites, are contemplated with the resources necessary to guarantee the degree of readiness, not only in terms of isolated buildings but also as an urban environment.

5. ACKNOWLEDGEMENTS

6. REFERENCES

[1]   Portaria n.º1532/2008 de 29 de dezembro alterada pela Portaria 135/2020 de 2 de Junho, *RegulamentoTécnico de Segurança Contra Incêndio em Edifícios (RT-SCIE),* República Portuguesa, 2008.

[2]   Autoridade Nacional de Emergência e Proteção Civil (2019). *Avaliação Nacional de Risco.* Lisboa, 129 p.

[3]   Bispo, R.; Vieira, F. G.; Bachir, N.; Espadinha-Cruz, P.; Lopes, J. P.; Penha, A.; Marques, F.J.; Grilo, A. (2023). *Spatial Modelling and Mapping of Urban Fire Occurrence in Portugal.* Fire Safety Journal, V. 138, 2023, 103802, ISSN 0379-7112. https://doi.org/10.1016/j.firesaf.2023.103802.

Fire Safety in Vehicles and Tunnels

FIRE IN ROAD TUNNELS IN BRAZIL - STANDARDS

André Luiz Gonçalves Scabbia[(a)], Anthony Edward Pacheco Brown [(b)], José Luiz Gavião de Almeida[(c)]

(a) Instituto de Pesquisas Tecnológicas de São Paulo - IPT (scabbia@ipt.br)
*(b) Coordenador da ABNT CE Túneis - Risiko Analise de Seguranca Ltda - São Paulo, Brasil (*risiko@uol.com.br)
(c) Faculdade de Direito da Universidade de São Paulo (jlgalmeida@hotmail.com))

Keywords: Tunnels, Fire, Legal evidence and proof.

ABSTRACT

From 2003 to 2022, the Fire Safety Special Commission for Transport Systems (CB24) of the Brazilian Association of Technical Standards (ABNT) carried out a continuous improvement on the ABNT Standards [1 to 10] subject to road tunnels, regarding to fire safety premises. Ten standards were prepared, revised and updated, as follows, ABNT NBR 5181, Tunnel Lighting Systems – Requirements, 2021; ABNT NBR 15661, Fire Protection in Road Tunnels, 2021; ABNT NBR 15775, Fire Safety Systems in Tunnels - Tests, Commissioning and Inspections, 2019; ABNT NBR 15981, Tunnel Fire Safety Systems - Tunnel Emergency Signaling and Communication Systems, 2019; ABNT NBR 16484, Fire Safety at Rail Transport Systems – Requirements, 2020; ABNT NBR 16639, Fire Protection in subway and monorail tunnels – Requirements, 2020; ABNT NBR 16736, Fire Protection in road and urban tunnels – Emergency operation in road and urban tunnels – Requirements, 2019; ABNT NBR 16888, Fire safety for freight transport rail systems ─ Requirements, 2020; ABNT NBR 16980, Fire protection to the existing urban tunnels – revitalization requirements, 2021; ABNT NBR 17027 – Fire Protection in submerged tunnels - requirements (press) The ABNT is an independent, private, non-profit and public utility, affiliated to the International Standard Organization (ISO), was founded on 09/29/1940, with the purpose of carrying out the technical standardization in Brazil, providing inputs for Brazilian technological development. The area of road tunnels is handled by Fire Safety Special Commission for Transport Systems, created in 2003, it belongs to the attributions of CB24 - Fire Safety, which was created in Jan. 1990. This Special Commission has been preparing technical standards for the last fifteen years. The Brazilian road development occurred together with the industrial one, since the constant displacement of people and materials became more frequent. However, with the greater road frequency, the most serious accidents also began to occur. Fortunately, in Brazil, the of tunnel fire accidents occurrence is very low and with no fatalities. The draft standard is carried out by the technical committee, in monthly face-to-face meetings, but, at the moment, they are being carried out virtually the Zoom platform. Between 2019 and 2022, three standards were carried out, one of which, ABNT NBR 16888, presents the fire protection requirements for the cargo rail system that is already ~~was~~ published and the other two standards are in the elaboration and editing ~~and~~ phases, respectively. This standard presents the requirements, in addition to the railway, those for workshops, stations, terminals, vehicles and other buildings that make up the cargo rail transport system. Establishes the requirements to carry out the analysis and management of fire risks and emergency and contingency procedures in this cargo rail system. ABNT NBR 16980, Fire protection – existing urban tunnels – revitalization requirements, 2021; considering the existence of old urban

tunnels, the commission decided to draw up a standard for their revitalization, concerning fire safety systems. The standard ABNT NBR 17027 - Protection against fire in submerged tunnels - requirements (press), deals with requirements (qualitative) and criteria (quantitative) necessary for fire safety, although Brazil does not yet have this type of superstructure, the commission prepared this standar before the starting of the design of two submerged tunnels projects..

1 INTRODUCTION
This article verify the risk scenarios detected in accidents that occurred in the last 30 years in tunnels, with fire generation and that are being addressed in national regulations, through technical commissions, in order to create barriers to prevent its occurrence in Brazil, and if it does occur, that it does not generate risk situations for its occupants. It is based on works presented in the past, which are cited in it.

The Technical Commission for the elaboration of draft standards is formed by technicians from transport concessionaires (Ecovias, CCR, Metrô, Vale, MRS, Rumo), manufacturers of electromechanical and fire protection systems, independent consultants, the State Fire Department and researchers (IPT, USP). When it is verified that the proposals for improving fire safety internationally, were defined and implemented in road tunnels, after fire events that occurred in some of these tunnels, and that were associated with the established safety verification elements, it is proven that all of them are being considered for the composition of fire safety and the resumption of commercial operation in road tunnels in Brazil

2 acidentes que indicaram cenários de riscos que devem ser evitados
The following are reports of accidents that occurred, their root causes and proposed mitigating measures, initially studied by Scabbia (2007) [11] and completed by Scabbia & Berto (2021) [12].

2.1 Tunnel - Nihonzaka [11]

Mashimo's report (2002), after the accident, the following specific measures were taken to resume tunnel operations; -it is important to note that, at the time of the fire, this tunnel, like many others, did not have measures aimed at fire protection:
- • • prohibit the circulation of trucks with dangerous cargo;
- • • prohibit overtaking inside the tunnel;
- • • install radars to prevent high-speed traffic;
- • • install Variable Message Signs – PMV at the tunnel entrances (two at each entrance) and two more internally;
- • • join the two tunnels, that is, attach the tunnel affected by the fire to the parallel tunnel (which had the opposite direction), transforming them into unidirectional ones, with four lanes in the same direction;
- • • build emergency bays for cars inside the tunnel;
- • • improve lighting inside the tunnel;
- • • install traffic lights (red/green) at the entrance to the tunnel.

2.2 Tunnel - Caldecott [11]

The National Transportation Safety Board report (1983) Highway Accident Report Adopted: Multiple Vehicle Collisions And Fire Caldecott Tunnel Near Oakland, California (April 7, 1982) adopt the following additional measures:

• inform the driver before his approach to the accident site;

• evaluate and revise, where necessary, emergency procedures;

• develop a system with rapid response to emergencies and train tunnel operators in all phases of the emergency, including in cases of fire, periodically, such that it can demonstrate the capacity of the employees;

• clearly identify the tunnel's emergency exits;

• prohibit lane changes or overtaking inside the tunnel;

• improve conditions for tunnel supervision and performance through the adoption of a communication and fire safety system;

• prohibit dangerous goods from entering the tunnel;

• review federal highway administration and urban transportation administration programs to encourage vehicle segregation to prevent the road from posing an unnecessary risk to the public by sharing the road with moving trucks carrying product dangerous;

• monitor drivers with known medical conditions;

• adopt automatic systems to ensure compliance with these proposals.

2.3 Tunnel – Montblanc [11]

The Report of the Ministère de l'Equipement, des Transports, du Logement (1999) points out the need to consider the following actions to improve fire safety:

• examine the possibility of reducing potential fire risks by controlling transported materials;

• examine the possibility of inspecting vehicles before entering the tunnel;

• install automatic incident detection system (DAI);

• adopt Operations Control Center – single CCO;

• implement a road operation capable of supervising and quantifying the vehicles inside the tunnel, to allow quick and effective action in fire situations;

• ensure that the systems/equipment, mainly the electrical and communication systems inside the tunnel, remain in operation during the occurrence of fire;

• clearly inform users about the occurrence of fire, with visual and sound signals, automatically indicating the emergency exits;

• implement a first-time uninterrupted service, made up of a team of three to five specialists, able to act within 5 minutes of identifying an occurrence;

• adopt a single plan of action, considering both sides (France and Italy)

2.4. Eurotúnel [12]

The report jointly issued by the Bureau d'Enquêtes sur les Accidents de Transport Terrestre (2010) points to the need to adopt the following improvements:

• implement sufficiently reliable devices and procedures, aimed at mitigating the risks associated with the formation of electrical arcs between objects with excessive height, such as truck parts or their payload, and the catenary.
• adjust the automatic fire detection system, making it faster and more reliable for any fire principle;
• review the operating procedure when detecting a fire;
• review procedure for hazard identification and risk assessment;
• review the methodology for controlling work carried out by third parties to the tunnel operator;
• improve procedures related to crisis management, in case of fire in the tunnel, in order to allow the evacuation of passengers in an acceptable period of time and the quick start of fire fighting.

2.5. Tunnel - China (General) [12]
Statistical data on fires between 2000 and 2016 in China by Ren et al. (2019) evaluated 161 fire events, considered large and medium-sized. Among the analyzed cases, 40 events, that is, 24.8%, caused damage to the structure or infrastructure of the tunnel and 11 cases caused deaths inside the tunnels (Figure 1). Actions were recommended regarding the implementation of passive protection measures. Due to the observed damage, the authors made several recommendations for improvements, in line with the recommendations made in the previously reported events.
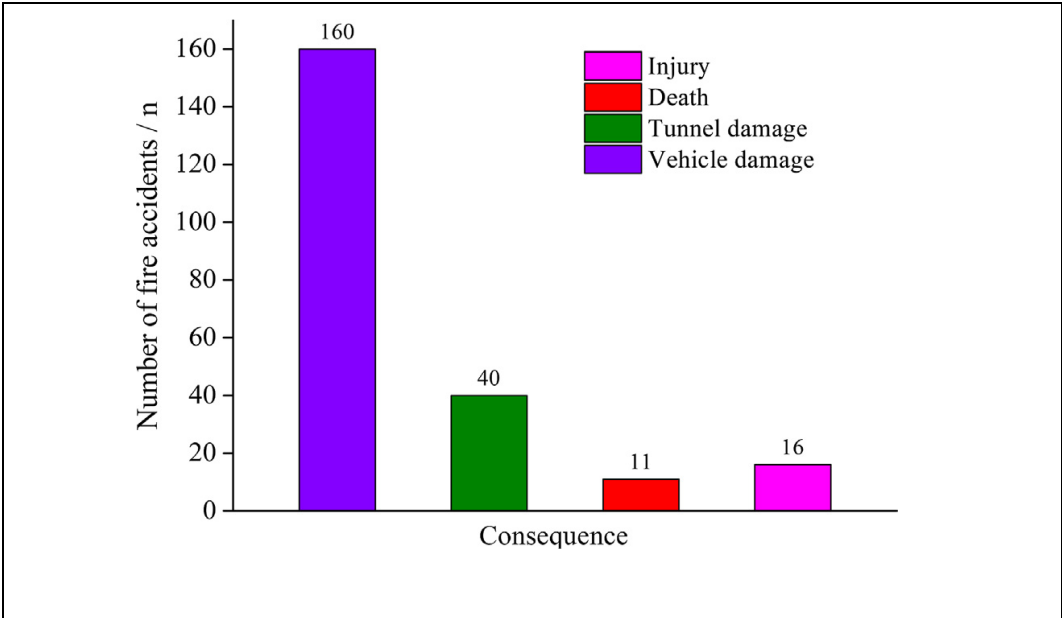
Figure 1 – Accidents in Tunnels - China

2.6. Tunnel – Australia [12]

Casey (2020), Australia has adopted, since 2002, fixed fire fighting systems with water, of the Deluge type, inside some tunnels. In approximately 50% of harmful events, where used the deluge system, the fire was extinguished. In the other events they limited the fire and the operation team carried out the end of combat (Figure 2).
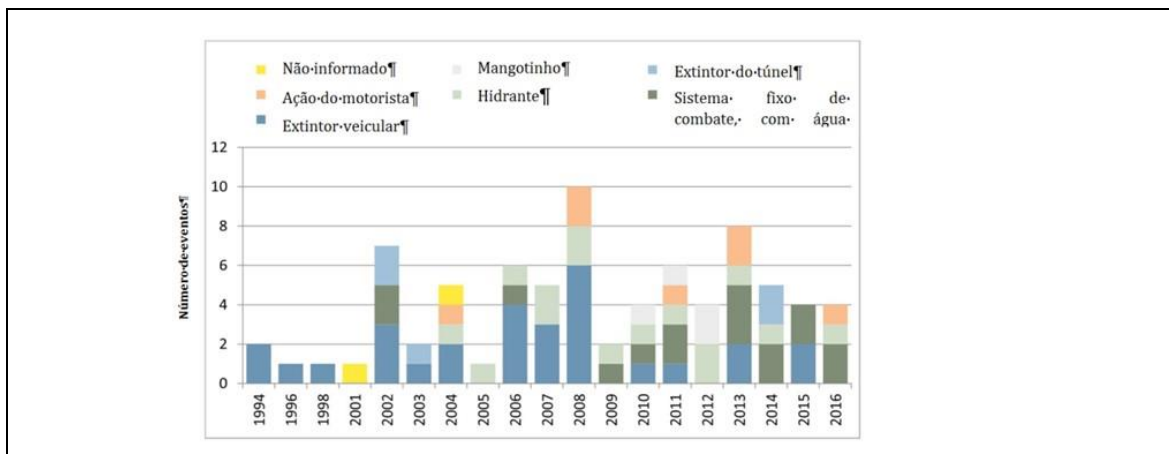
Figure 2 - Events involving the use of fire fighting systems in major tunnels in Australia, between 1994 and 2016. Source: Casey (2020)

Table 1 presents, in a summary, the proposals for improvement that were defined after the fire in some tunnels, associated with the established verification elements, proving that, in some way, all were considered for the composition of fire safety and the resumption of commercial operation. Distributed as follows:

Drivers and users
Control of transported loads
Structural and civil elements
Tunnel operation centralized in CCO
Fire protection systems
   • Tunnel lining fire resistance
   • Reaction to fire
   • Incident or fire detection
   • Ventilation
   • Lighting

- Fire extinguishing
- Emergency exit

Mechanical and electrical-electronic systems
User information systems
Maintenance and periodic updating

Table 1 - Practical improvements after fires

Túnel (historico de eventos retirado da Tabela 1)	Elementos de verificação													
	Condutores e usuários	Controle das cargas transportadas	Elementos estruturais e civis	Operação do túnel centralizada em CCO	Sistemas de proteção contra incêndio							Sistemas mecânicos e eletroeletrônicos	Sistemas de informação aos usuários	Manutenção e atualização periódica
					Resistência ao fogo do revestimento do túnel	Reação ao fogo	Detecção de incidentes ou incêndio	Ventilação	Iluminação	Extinção do fogo	Saída de emergência			
Nihonzaka	x	x	x	x	(*)	(*)	x	x	x	(*)	x	x	x	x
Caldecott	x	x	x	x	(*)	-	x	-	-	-	x	-	x	-
Afeganistão	x	x	x	x	(*)	-	-	-	-	-	-	-	-	-
King's Cross	x	x	x	x	(*)	x	-	x	x	-	-	-	x	x
Palermo - italia	x	x	x	x	(*)	-	-	-	-	-	-	-	x	-
Canal da Mancha (1996)	x	x	x	x	(*)	x	-	-	x	x	-	-	-	-
Mont Blanc	x	x	x	x	(*)	x	x	-	x	-	-	x	x	-
Tauern	x	x	x	x	(*)	-	-	-	-	-	-	-	-	-
Reigersdorf	x	x	x	x	(*)	-	-	-	-	-	-	-	x	-
Canal da Mancha (2015)	x	x	x	x	(*)	-	-	-	-	x	x	x	-	-
China 2000 - 2016	x	x	x	x	x	x	(*)	(*)	(*)	(*)	(*)	(*)	(*)	(*)
Australia (1994 – 2016)	x	x	(*)	x	(*)	(*)	(*)	(*)	(*)	x	(*)	(*)	(*)	(*)

(*) No analised   Scabbia & Berto 2020 [11]

It should be noted that among the verification elements, in addition to fire protection systems, clearly associated with fire control, the other elements predominantly include fire prevention actions.

It is important to note that, for all the accidents shown in Table 3, the need for drivers and users to respond to operational commands is considered. This situation stems from the observation, in the events studied, that, in general, they did not go to the emergency exits, mainly due to the fact that they were not alerted to the severity of

the event. From this point of view, such action has a protective nature and depends on other elements aimed at fire safety.

In all the cases indicated in Table 1, it is considered necessary to define and control the loads present in the tunnels, including the limitation of the toxicity generated when they are ignited. Likewise, the existence, or revision, of operating procedures, with centralized management in an Operational Control Center, are always considered.

The existence of damage to the tunnel structure is also indicated in all the analyzes carried out, as an important problem, although explicit proposals for improvements were included.

Fire protection systems, mechanical and electrical-electronic systems and user information systems are presented at all events, always with a strong recommendation to review, expand or modernize them. Therefore, the process of technological updating of all these systems, throughout the commercial operation of the tunnels, was considered

Scabbia et all (2009) [13], no matter how much automatic control or supervision systems are inserted in the tunnels, these do not replace, but only help the operational teams. During an accident, people inside the tunnel always need support, via duly equipped human intervention.

Table 2 - Relationship between Brazilian standards and proposed verification elements by [12]

Normas	Escopo	Condutores e usuários	Controle das cargas transportadas	Elementos estruturais e civis	Operação do túnel centralizada em CCO	Resistência ao fogo do revestimento do túnel	Reação ao fogo	Detecção de incidentes ou incêndio	Ventilação	Iluminação	Extinção do fogo	Saída de emergência	Sistemas mecânicos e eletroeletrônicos	Sistemas de informação aos usuários	Manutenção e atualização periódica
						Sistemas de proteção contra incêndio									
ABNT NBR 5181	Projeto de iluminação em túneis	x	x	x	x	x	x	x	x	x	x	x	x	x	x
ABNT NBR 15661	Projeto e operação de túneis com trafego de veículos, em ambiente rodoviários e urbanos	x	x	x	x	x	x	x	x	x	x	x	x	x	x
ABNT NBR 15775	Ensaios, comissionamento e inspeções para todos os tipos de túneis	x	x	x	x	x	x	x	x	x	x	x	x	x	x
ABNT NBR 15981	Sistemas de sinalização e de comunicação de emergências em túneis	x	x	x	x	x	x	x	x	x	x	x	x	x	x
ABNT NBR 16484	Projeto e operação de túneis com sistemas de transporte sobre trilhos	x	x	x	x	x	x	x	x	x	x	x	x	x	x
ABNT NBR 16736	Operação em caso de emergência em túneis rodoviários e urbanos	x	x	x	x	x	x	x	x	x	x	x	x	x	x
ABNT NBR 16888	Segurança contra incêndio para sistemas ferroviários de transporte de cargas	x	x	x	x	x	x	x	x	x	x	x	x	x	x
ABNT NBR 16980	Proteção contra incêndio - Túneis urbanos existentes - Requisitos de revitalização (Aprovada em 2021))	x	x	x	x	x	x	x	x	x	x	x	x	x	x
ABNT NBR 17027	Proteção contra incêndio em túneis submersos	x	x	x	x	x	x	x	x	x	x	x	x	x	x

Drivers and users Control of transported loads Structural and civil elements Tunnel operation centralized in CCO Fire protection systems Mechanical and electrical-electronic systems User information systems Maintenance and periodic updating.

5 CONCLUSION

When it is verified that the internationally accepted proposals for improving fire safety, see Table 1, were accepted and implemented in the national standards for road tunnels, see Table 2, it is proven that all of them were considered for the composition of fire safety for commercial operations in road tunnels in Brazil. Not Available agovernmental mechanism for periodic inspection of tunnels, which guarantees compliance, during their use, with the implementation and maintenance of these requirements

REFERENCES

[1] ABNT NBR 5181, Sistemas de iluminação de túneis – Requisitos, 2021

[2] ABNT NBR 15661, Proteção contra incêndio em túneis, 2021

[3] ABNT NBR 15775, Sistemas de segurança contra incêndio em túneis - Ensaios, comissionamento e inspeções, 2019

[4] ABNT NBR 15981, Sistemas de segurança contra incêndio em túneis – Sistemas de sinalização e de comunicação de emergências em túneis, 2019

[5] ABNT NBR 16484, Segurança contra incêndio para sistemas de transporte sobre trilhos – Requisitos, 2020

[6] ABNT NBR 16639, Proteção contra incêndio em túneis metro ferroviários e monotrilho – Requisitos, 2020

[7] ABNT NBR 16736, Proteção contra incêndio em túneis rodoviários e urbanos – Operação de emergência em túneis rodoviários e urbanos – Requisitos, 2019

[8] ABNT NBR 16888, Segurança contra incêndio para sistemas ferroviários de transporte de cargas ─ Requisitos, 2020

[9] ABNT NBR 16980, Proteção contra incêndio – túneis urbanos existentes – requisitos de revitalização, 2021

[10] ABNT NBR 17027 - Proteção contra incêndio em túneis submersos – requisitos (prelo)

[11] SCABBIA, André Luiz Gonçalves. Túneis rodoviários: proposta de avaliação de conformidade para liberação ao uso e operação comercial. 2007. Tese (Doutorado em Dinâmica das Máquinas e Sistemas) - Escola de Engenharia de São Carlos, Universidade de São Paulo, São Carlos, 2007. doi:10.11606/T.18.2007.tde-17012011-125628. Acesso em: 2023-05-08.

[12] SCABBIA, A.L.G. ; BERTO, A.F. Seguranca Contra Incêndio em túneis, Revista Concreto N. 97 - Inspeção e manutenção, 2020.

[13] SCABBIA, ALG et al. Road tunnels: proposal for fire and explosion risk analysis. 2009, Anais.. Budapest: Escola de Engenharia de São Carlos, Universidade de São Paulo, 2009. . Acesso em: 08 maio 2023.

FIRE PERFORMANCE OF R/C AND FRC TUNNELS EXPOSED TO FIRE: COMPARISON BETWEEN LINEAR AND NON LINEAR ANALYSES VIA A SIMPLIFIED 1D APPROACH

Francesco Lo Monte a*

Patrick Bamonte b

ABSTRACT

The mechanical response of reinforced concrete tunnels (R/C) exposed to fire can represent a critical issue in the design phase of this kind of infrastructures, due to the combination of a few negative aspects such as the development of severe fire scenarios, the development of sizable indirect actions and the severe compression state which can foster spalling phenomenon. It follows the need for a reliable evaluation of the fire performance of tunnels exposed to high temperature, considering the decay of the material properties and the evolution of the internal actions. This task is however often complex, since it can need the implementation of non-linear analyses which consider the diffusion of heat in the structural elements, the variation of the mechanical properties of the materials and the interaction between lining and surrounding soil. Such analyses are often performed by means of advanced finite element codes which can perform multi-physics simulations (as for example Abaqus or Safir). On the other hand, in the present study, a simplified approach is described for linear and non-linear analyses of deep R/C tunnels exposed to fire, based on the main assumption of axisymmetric loading and heating. This assumption is generally kept for deep tunnels, in which the ratio between vertical and horizontal pressure is usually not too far from the unit value. The assumption of axisymmetry makes it possible to describe the behavior of the lining via a sectional analysis (1D approach), in which the plane section assumption is kept. Such algorithm can be rather easily implemented in any work sheet or programming code (as for example Matlab, Fortran, or similar). This simplified approach allows to rapidly perform parametric analyses necessary for understanding the role played by different key parameters, and to understand the advantages of performing a non-linear analysis allowing the plasticization of the section.

Keywords: concrete tunnel; simplified approach; axisymmetry; plastic analysis; indirect actions.

---

a,* Department of Civil and Environmental Engineering, Politecnico di Milano (francesco.lo@polimi.it)**,** Corresponding author.

b,* Department of Civil and Environmental Engineering, Politecnico di Milano (patrick.bamonte@polimi.it).

1. INTRODUCTION

The structural behavior of tunnels exposed to fire can represent a critical aspect in the design phase, due to some specific issues which characterize this kind of infrastructures. In particular, the combination of a few negative conditions makes fire a very severe condition. First of all, the characteristics of the fire compartment is generally favorable for the development of rather severe fire scenarios with very high temperatures, even overcoming 1000°C, and prolonged durations [1]. In addition to this, the fuel, potentially consisting in oil and hydrocarbons, brings in a significant fire load and an elevated Heat Release Rate (RRT) as demonstrated by the typical fire curves related to hydrocarbon-based fires (Hydro-Carbon fire curve – HC, or Modified Hydro-Carbon – HCM, Rijkswaterstaat curve – RWS,…).

Secondly, the inherent structural redundancy of the lining in deep tunnels, because of (1) the surrounding soils restraining the overall dilation of the ring and (2) the almost axisymmetry of the problem which restrains any curvature of the lining, favors the development of sizable indirect actions in terms of both compression and bending moment, dramatically modifying the initial state of stress. It is worth noting as the structural sensitivity in case of fire is strictly connected to the specific characteristics of the concrete adopted, this making the definition of the actual mix design to be used (as for example including polypropylene fibers) of primary importance [2-5].

On the base of the main aspects above described, the assessment of the structural performance of the lining in case of fire accidents is rather complex. In particular, too simplified approaches can lead to excessively conservative results with a subsequent need for oversizing reinforcement, thus significantly increasing the overall costs. It follows the need for a reliable evaluation of the fire performance of tunnels exposed to high temperature, considering the decay of the material properties because of the high temperature as well as the evolution of axial force and bending moment in the lining due to the restrained thermal expansion.

Such purpose, however, needs on most cases the implementation of (sequentially) coupled thermo-mechanical analyses considering the non-linear response of the materials. This often requires the need for advanced finite element codes which can perform multi-physics simulations (as for example Abaqus or Safir) [6], but at the cost of more onerous geometrical modeling (usually requiring the explicit introduction of rebars and their interaction with the surrounding concrete) and analysis burden (with calculation time in the order of hours for a single ring of lining).

To this end, in order to have a much simpler and faster tool, in the present study, a simplified approach is described for the linear and non-linear analysis of deep reinforced concrete (R/C) tunnels exposed to fire. Such approach is based on the main assumption of axisymmetric loading, as often kept for deep tunnels in which the ratio between vertical and horizontal pressure can be close to the unit value. It is worth noting, however, that the state of bending and compression induced by fire is generally dominating with respect to the initial stress state of the lining, this smoothing down the effects related to initial lack of axisymmetry.

The great importance given to the assumption of axisymmetry comes from the fact that, in such case, the overall behavior of the lining can be described through the sectional response, in which the plane section assumption can be kept. This allows for the implementation of rather simple, but effective, algorithms which can be implemented in any work sheet or programming code.

2. BEAM THEORY IN HEAT-EXPOSED MEMBERS

In order to recall the main kinematics of a lining exposed to fire, the general case of a slab exposed to heating on one side only is reported in Figure 1, where the typical temperature and stresses distribution within the depth are shown for a given fire duration. Stresses can be divided in (a) self-equilibrated stresses induced by the internal sectional constrain to thermal expansion of the hot layers (green line in figure) and (b) load-induced stresses (in blue line in the figure) where load can be both due to external forces or indirect actions, this latter for example be caused by the external restrain of the overall thermal expansion of the structural member. Thermal stresses are caused by the dilation of the hottest layer this being restrained by the inner cold core of the slab, thus introducing compression next to the exposed surface and tension in the inner part, so to guarantee translational equilibrium, while compression rises in the cold side to guarantee rotational equilibrium. Obviously, the resultant of thermal stress is zero in terms of both axial force and bending moment.
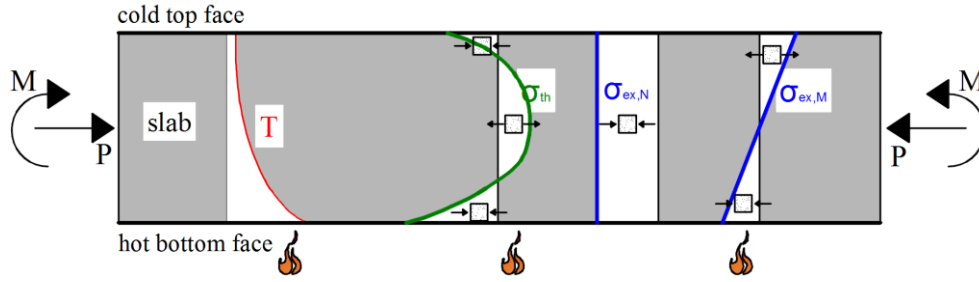
Figure 1: Slab heated at the bottom face: profiles of temperature, thermal stress and load-induced stress.

The same kinematics involves tunnel linings in which, however, bending is totally prevented by the axisymmetry of the problem, thus leading to the introduction of a bending moment M bringing tension at the cold side and compression at the hot layer. Furthermore, sectional elongation (thus the circumferential elongation) of the lining is more or less efficiently limited by the presence of the surrounding soil, which reacts with an overpressure increasing the compression in the lining itself. It is worth underling as bending moment magnitude is linked to the flexural stiffness of the lining (thus on its thickness), while the axial force magnitude is driven by the stiffness of the soil.

As abovementioned, if the axisymmetry assumption is maintained, the tunnel lining response during a fire can be expressed via a sectional approach, in which the plane section hypothesis is kept, as also currently performed at SLS/ULS or in seismic conditions. Such assumption is very powerful, since makes it possible to describe the total strain profile through a linear equation depending on two parameters only (in case of simple bending), which can be easily evaluated enforcing the two equilibrium conditions (namely, translational and rotational ones). In the following, total strain at the geometrical barycenter ε_0 and sectional total curvature χ will be chosen as reference parameters, thus leading to the well-known kinematic equation $\varepsilon_{tot}(y,t) = \varepsilon_0(t) + \chi \cdot y$, where compression is considered positive (and, consequently, shortening positive) with the reference system reported in Figure 2. The mechanical strain $\varepsilon(y,t)$ can be thus expressed as difference between total strain and thermal strain, $\varepsilon(y,t) = \varepsilon_{tot}(y,t) - \varepsilon_{th}(y,t) = \varepsilon_0(t) + \chi \cdot y - \varepsilon_{th}(y,t)$.

The equilibrium can be then enforced by introducing the linear relation between mechanical strain and stress $\sigma = \varepsilon \cdot E$, this allowing also to consider non-linear mechanical behavior if a secant approach is adopted by defining an effective secant modulus $E = \bar{\sigma}/\bar{\varepsilon}$:

$$\begin{cases} N = \int \sigma dA = \int E(\varepsilon_0 + \chi y - \varepsilon_{th}) dA \\ M = \int \sigma y dA = \int E(\varepsilon_0 + \chi y - \varepsilon_{th}) y dA \end{cases} \Rightarrow \begin{cases} N = (\varepsilon_0 + \chi e_{k,G} - \varepsilon_{th,0})\widehat{EA} \\ M = (\varepsilon_0 e_{k,G} - \varepsilon_{th,0} e_{th,G})\widehat{EA} + \chi \widetilde{EI} \end{cases} \quad (1)$$

N and M are considered applied to the geometrical center (barycenter) of the section and the following definitions have been introduced: effective axial stiffness $\widehat{EA} = \int E dA$, effective static moment $\widehat{ES} = \int Ey dA$, effective flexural stiffness $\widetilde{EI} = \int Ey^2 dA$, average thermal strain $\varepsilon_{th,0} = \int E\varepsilon_{th} dA/\widehat{EA}$, average thermal curvature $\chi_{th} = \int E \cdot \varepsilon_{th}/y \cdot y^2 dA/\widetilde{EI}$, eccentricity of the thermal stress resultant with respect to the barycenter $e_{th,G} = \int E\varepsilon_{th} y dA/\int E\varepsilon_{th} dA = \chi_{th}/\varepsilon_{th,0} \cdot \widetilde{EI}/\widehat{EA}$ and distance of the stiffness center with respect to the geometrical barycenter of the section $e_{k,G} = \widehat{ES}/\widehat{EA}$.

It is now rather interesting to express the strain at the barycenter and the sectional curvature, ε_0 and χ, as the sums of two contributions, namely, the value at the beginning of the fire duration, $\varepsilon_{0,in}$ and χ_{in}, and their following variation $\Delta\varepsilon_0$ and $\Delta\chi$. The generalized forces are represented in Figure 2, where it can be noticed the presence of 3 components of axial force. The first one, $N_{in} = (\varepsilon_{0,in} + \chi_{in}e_{k,G})\widehat{EA}$ is applied at the center of stiffness k_G and it represents the initial axial force applied before of the fire, the second one, $N_{th} = -\varepsilon_{th,0}\widehat{EA}$ is applied at center of application of $\varepsilon_{th,0}$ and is the value of the axial force if the element is perfectly-restrained against thermal expansion ($\varepsilon_0 = \chi = 0$), and the third one, $N_{re} = -(\varepsilon_0 + \chi e_{k,G})\widehat{EA}$ is applied at the center of stiffness k_G, and is the contribution related to the release of the restraints ($\varepsilon_0 \neq 0; \chi \neq 0$) that, in the case of member subjected to fire, can be seen as a "de-compression".

In this view, Equation 1 can be rewritten as follows:

$$\begin{cases} N = (\varepsilon_{0,in} + \chi_{in}e_{k,G})\widehat{EA} + (\Delta\varepsilon_0 + \Delta\chi e_{k,G})\widehat{EA} + (-\varepsilon_{th,0})\widehat{EA} \\ M = (\varepsilon_0 e_{k,G} + \chi e_{k,G}{}^2 - \varepsilon_{th,0}e_{th,G})\widehat{EA} + \chi\widetilde{EI} - \chi\widehat{EA}e_{k,G}{}^2 \end{cases} \Rightarrow \begin{cases} N = N_{in} - N_{re} + N_{th} \\ M = N_{in}e_{k,G} - N_{re}e_{k,G} + N_{th}e_{th,G} + \chi\widetilde{EI}_k \end{cases} \quad (2)$$

where it has been introduced the term $\widetilde{EI}_k = \widetilde{EI} - \widehat{EA}e_{k,G}{}^2 = \int E(y - e_{k,G})^2 dA$, which simply represents the sectional

251

stiffness with respect to the center of stiffness (and not with respect to the geometrical barycenter of the section).

In case of fire, $\varepsilon_{th,0}$ is a dilation as well as $\Delta\varepsilon_0$ (hence, negative strains), so making positive (thus a compression) the terms N_{th} and N_{re}. On the other hand, the initial axial deformation ε_0 is expected to be negative, since the lining is characterized by initial compression due to the static pressure of the surrounding soil.

As a last step, Equation 2 can be re-written recalling that $\chi = \chi_{in} + \Delta\chi$ and defining $M_{in} = \chi_{in}\widetilde{EI}_k$ and $M_{re} = \Delta\chi\widetilde{EI}_k$:

$$\begin{cases} N(t_{fire}) = N_{in} - N_{re}(t_{fire}) + N_{th}(t_{fire}) \\ M(t_{fire}) = N_{in} \cdot e_{k,G}(t_{fire}) - N_{re}(t_{fire}) \cdot e_{k,G}(t_{fire}) + N_{th}(t_{fire}) \cdot e_{th,G}(t_{fire}) + M_{in} + M_{re}(t_{fire}) \end{cases} \tag{3}$$

where all the quantities are functions of the fire duration t_{fire} excepted the initial system of actions N_{in} and M_{in}.

It is finally of interest, to analyze the case in which the total curvature in constantly zero (as it occurs in a circular ring exposed to fire at the inner face), and the two extreme situations, namely slab totally restrained to expands (hence, $\Delta\varepsilon_0 = 0$) and lining free to expand (hence, $\Delta N_{fire} = N_{th} - N_{re} = 0$). In such cases, it yields:

$$\Delta\varepsilon_0 = 0 \Rightarrow \begin{cases} N = N_{in} + N_{th} \\ M = N_{in}e_{k,G} + N_{th}e_{th,G} \end{cases} \qquad \Delta N_{fire} = 0 \Rightarrow \begin{cases} N_{th} = N_{re} \\ M = N_{in}e_{k,G} + N_{th}(e_{th,G} - e_{k,G}) \end{cases} \tag{4}$$

It can be noticed as the first situation ($\Delta\varepsilon_0 = 0$) leads to the development of compression during the exposure because of the restrained thermal expansion of the section, while the second situation ($\Delta N_{fire} = 0$) is characterized by nil variation of the axial force during the fire, but a higher bending moment (with respect to the case $\Delta\varepsilon_0 = 0$), since the "de-compression" force N_{re}, applied at a distance $e_{k,G}$ with respect to the geometrical barycentre, increases the applied bending moment.
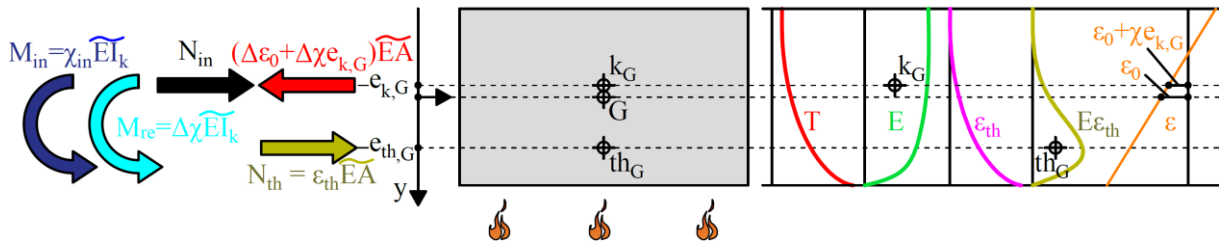

Figure 2: Temperature T, modulus E, thermal strain ε_{th} and total strain ε profiles in a slab heated at the bottom face and resultant of axial force and bending moment. (G, k_G, th_G, = barycenter of gross section, center of sectional stiffness and center of perfect-restrained thermal stress resultant, respectively).

3. SECTIONAL ANALYSIS FOR ASSESSING THE FIRE PERFORMANCE OF TUNNEL LININGS

As abovementioned, the expansion of the lining is partially restrained the surrounding soil which reacts with an overpressure. In order to take into account the evolution of such overpressure is important to observe that ε_0 not only represents the relative shortening/elongation of the sectional centroid, but also the relative shortening/elongation of the ring circumference, from which it follows that ε_0 also define the relative variation of the ring radius. The evaluation of the pressure exerted by the surrounding soil around the lining can be consequently calculated as indicated in Equation 5 via the product of the radial displacement, $\delta_r = \varepsilon_0 \cdot R$ (with R = radius of the tunnel lining), and of the elastic constant of the soil k_{soil} (which can be calibrated on the basis of the convergence law of the soil-tunnel system). Finally, the increase of the external axial compression applied to the lining because of the soil can be simply calculated on the base of the width b of the lining (Equation 6).

$$\Delta p_{th}(t_{fire}) = \varepsilon_0 \cdot R \cdot k_{soil} \tag{5}$$

$$N_{ext}(t_{fire}) = N_{in} + p_{th}(t_{fire}) \cdot b \cdot R \tag{6}$$

Enforcing translational and rotational equilibrium at the beginning of fire, since initial axial force and bending moment are both known, it is possible to evaluate ε_0 and χ. During the development of the fire, the curvature χ is considered to remain constant ($\chi = \chi_{in}$, this being on the safe side, since no structural redistribution of bending moment is allowed). This makes it possible to evaluate ε_0 by imposing the equilibrium in terms of axial force for any following time step, and then the bending moment acting on the section can be calculated via sectional stress integration.

The approach allows to easily consider the mechanical non-linearity of the materials by introducing the proper

constitutive laws σ-ε$_m$. For concrete in compression and for steel in tension/compression, EC2 [7] provides the equation describing the stress-strain relationships, also taking into account transient thermal strain. When a non-linear analysis is performed, thus using as input the realistic stress-strain laws of concrete and steel, properly taking into consideration the decay of mechanical properties, strength checks are not required, since collapse occurs just when the analysis does not converge, namely when at a given fire duration, no coupe of values ε$_0$, χ is able to satisfy the translational equilibrium equation. This aspect is rather emblematic, since it underlines as, under the assumption of axisymmetry, collapse can occur just due to compression (which is linked to equilibrium, since the external pressure of the soil must be equilibrated by the lining) and not by bending (since this latter action is just linked to compatibility as it occurs by definition in the case of indirect actions linked to impressed deformations).

Due to the non-linearity of the problem, the calculation procedure needs an iterative algorithm, which can be enforced at any fire duration as follows:
1. first attempt value for ε$_{0,1}$ (as for example 0 at time 0 or the final value of the previous time step);
2. evaluation of N$_{int}$ and of the error $\Delta N = N_{int} - N_{ext}(t) = N_{int} - (N_{20} + p_{th}(t) \cdot b \cdot R)$;
3. calculation of the corrected value of ε$_{0,2}$ as $\varepsilon_{0,2} = \varepsilon_{0,1} + \Delta\varepsilon_0$ (with $\Delta\varepsilon_0 = \Delta N / \widehat{EA}$).

The described algorithm has been implemented in a common programming language together with the algorithm for the evaluation of the temperature in the thickness via the typical finite element approach for a 1D system.

Figure 3a shows the variation with temperature of normalized compressive strenght f_c^T/f_c^{20}, tensile strength f_{ct}^T/f_{ct}^{20}, elastic modulus E_c^T/E_c^{20} and perfectly-restrained thermal stress $E_c^T/E_c^{20} \cdot \varepsilon_{th}$ according to EC2 [7] in the case of siliceous aggregate and the normalized decay of f_{R3}^T/ f_{R3}^{20} for Fibre-Reinforced Concrete according to [8,9]. Figure 3b reports ε_{c1}^T, ε_{cu}^T and ε_{th} with temperature. It is worth noting as the thermal strain for perfectly-restrained thermal expansion ($\varepsilon_0 = 0$, leading to $\sigma_{th} = \varepsilon_{th} \cdot E_c^T$) is almost negligible for temperature higher that 1000°C (since modulus E_c^T approaches the zero value for the high thermally-induced degradation), and also at 20°C (since ε_{th} is zero). Finally, Figure 4 shows the constitutive laws in compression [7] and in tension [8,9] for different temperatures.
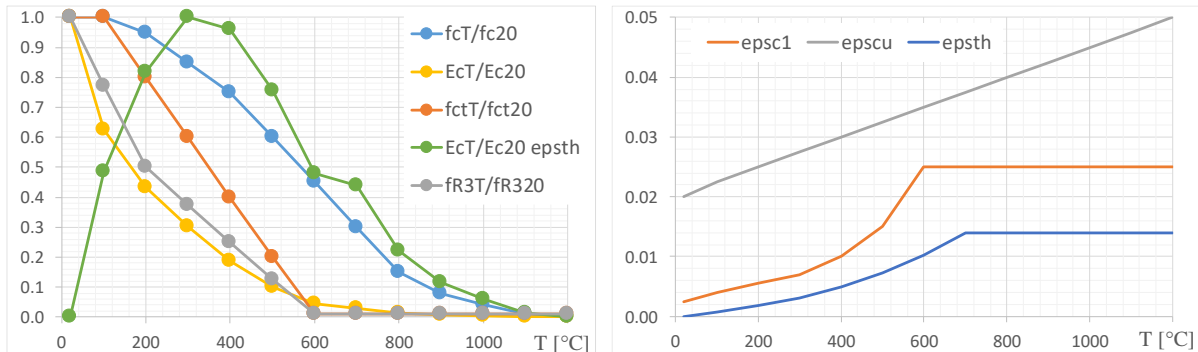

Figure 3: Variation with temperature of f_c^T/f_c^{20}, f_{ct}^T/f_{ct}^{20}, E_c^T/E_c^{20}, $E_c^T/E_c^{20} \cdot \varepsilon_{th}$ and f_{R3}^T/ f_{R3}^{20} (a) and of ε_{c1}^T, ε_{cu}^T and ε_{th} (b) according to EC2 [7] and fib [8,9].
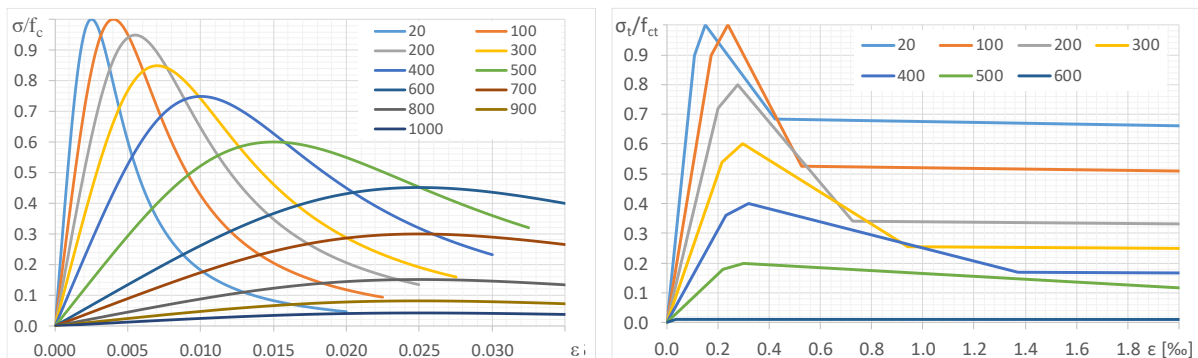

Figure 4: Constitutive laws for plain concrete in compression [7] and for fibre-reinforced concrete in tension [9] (in case of strain-softening response according to [8]).

3. NUMERICAL ANALYSES AND DISCUSSION

According to the methodology previously described (see also [10]), an ad hoc software code has been implemented which allowed to perform parametric analyses as reported in the following. In particular, it has been investigated the effect of lining thickness and initial compression to the overall flexural behavior of the tunnel lining during fire development. Furthermore, such parametric analyses have been performed via both an elastic approach (referred as ELA, in which for all the materials, an elastic behavior in both tension and compression has been adopted, obviously considering the decrease of the modulus with the temperature) and a non-linear approach (referred as NLA, in which the constitutive laws of Figure 4 have been introduced).

It is worth noting that an elastic approach is generally conservative, since it leads to larger values of indirect actions, but it needs strength checks at the end of the analysis, since such approach does not take into account the failure of the materials [6]. On the other hand, non-linear analyses lead to lower values of indirect actions, since, in addition to the degradation of the stiffness because of the temperature, it also introduces the mechanical degradation induced by stresses, this being linked to the decrease of the secant effective stiffness for increasing values of strain and due to cracking in tension. The mechanical degradation of the section can lead to a dramatic decrease of the flexural stiffness, drastically smoothing down the bending moment, since this latter action is not caused by external forces (thus equilibrium), but just by internal compatibility and thermal (self-)stresses. Non-linear approaches do not require any additional strength check at the end of the analyses as the possible failure is taken into account by the introduction of the effective constitutive laws. Collapse in non-linear analyses is observed if convergence is not obtained during the numerical iterations, this being ascribable to the impossibility of attaining equilibrium. It is worth noting that for sake of simplicity, all the following simulations are carried out in case of Fibre-Reinforced Concrete (thus with a non-negligible tensile strength) and without rebars.

In Figure 5, the variation with temperature of axial force N and bending moment M with time is shown in case of ISO 834 fire curve, for lining thicknesses of 0.4, 0.6 and 0.8 m. In all the cases, a ring width of 1 m and a ring external radium of 6 m have been considered, together with nil initial external compression $N_{ext}^{20} = 0$ kN, and very high (almost infinite) Winkler constant representing soil stiffness ($k_w = 10^3$ N/mm³). Only elastic analysis (ELA) is shown. It is also reported the normalized bending moment with respect to the one of the thinner lining (thickness of 0.4 m).
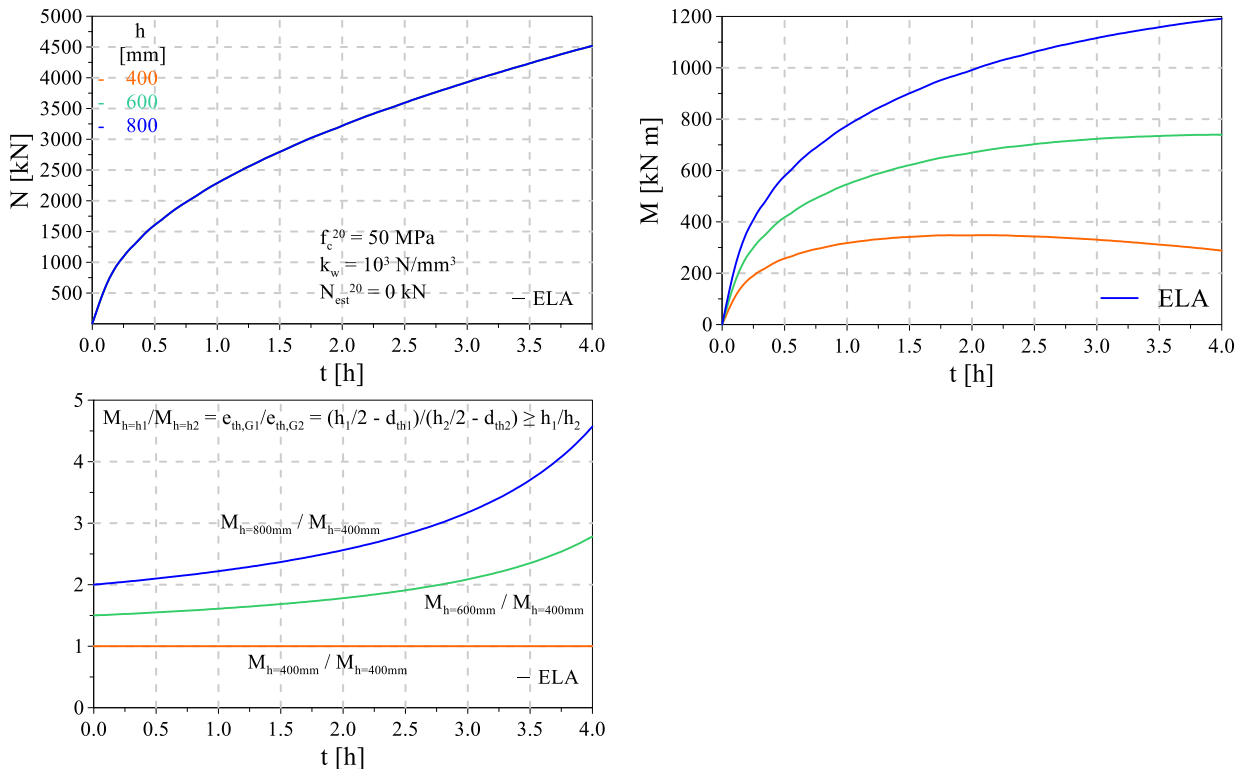

Figure 5: Variation with temperature of axial force N and bending moment M with time.

254

It is very interesting to observe as the development of the axial force is the same for the three lining thicknesses, since, thanks to the very high soil stiffness, the condition $\Delta\varepsilon_0 = 0$ of Equation 4 is attained.

On the other hand, during the development of the fire, bending moment is more than proportional to the thickness of the lining, since, in the special case of $\Delta\varepsilon_0 = 0$ (which makes the axial force in the lining independent from the lining thickness), the bending moment is proportional to the distance between the center of perfect restrained thermal stresses resultant and geometric center (barycenter) of the section ($e_{th,G}$ in Figure 2). In case of perfect restrained condition ($\Delta\varepsilon_0 = 0$), the distance between the center of perfect restrained thermal stress and the exposed face, d_{th} (= $h/2 - e_{th,G}$), does not depend on the lining thickness. This yields that bending moment is proportional to ($h/2 - d_{th}$), hence to $h \cdot (1/2 - d_{th}/h)$ thus with an increase with h more than linear.

In Figure 6, the variation with temperature of the strain at the center of the section ε_0, axial force N and bending moment M with time is shown in case of ISO 834 fire curve. On the left, the plots refer to a lining thickness of 0.5 m, while a thickness of 1 m is considered in the right side. In both cases, a ring width of 1 m and a ring external radius of 6 m have been considered, together with a moderate-low initial external compression N_{ext}^{20} = 500 kN, and a Winkler constant representing the soil stiffness k_w = 0.1 N/mm³. Thick solid lined refers to NLA, while thin lines refer to ELA.
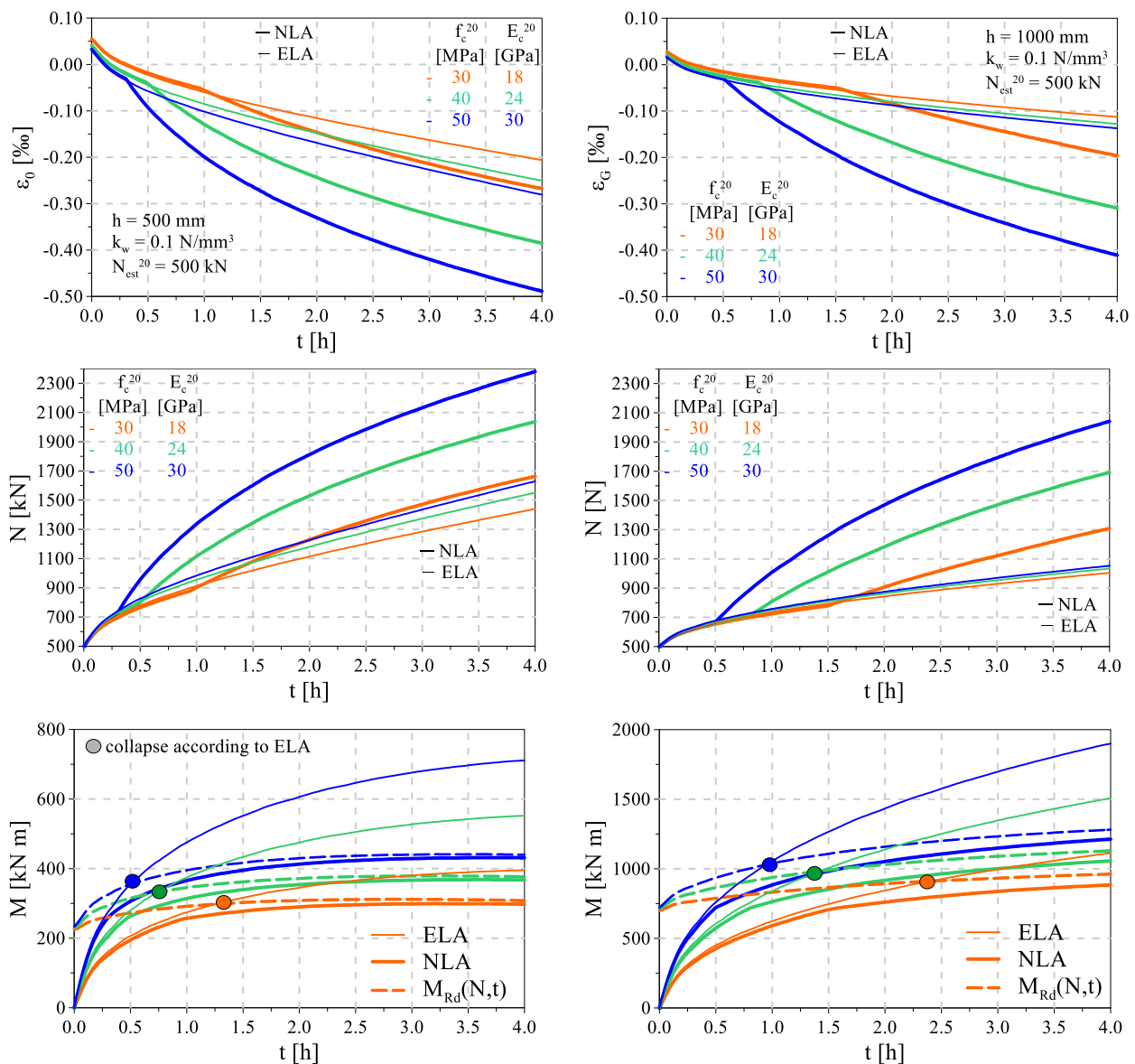

Figure 6: Variation with temperature of strain at the barycenter ε_0, axial force N and bending moment M with time. On the left, h = 0.5 m, while on the right, h = 1.0 m.

255

In the plots showing the bending moment evolution, it has been reported also the evolution of the resistant bending moment of the section according to the temperature profile and to the external axial force, evaluated by implementing the constitutive laws of Figure 4.

It is now interesting to focus on the development of the bending moment with time for the elastic analyses (ELA). First of all, it can be noticed as the thermal bending moment for the lining thickness of 1.0 m is more than twice (about 2.6 times) the one for the thickness of 0.5 m, as also highlighted for Figure 5. On the opposite, in the general case non corresponding to the perfect restrained condition ($\Delta \varepsilon_0 \neq 0$), thicker linings are characterized by lower values of axial force, since the average temperature in the thickness is lower and the expansion of the ring is more limited, thus activating a lower overpressure of the soil. Such decrease in the axial compression smooths down the increase of the bending moment with respect to the one highlighted for the case of Figure 5.

On the other hand, comparing the variation of bending moment obtained via ELA with the variation of M_{Rd}, it yields that failure occurs in the range 0.5-1.3h of heating for the lining thickness of 0.5 m and in the range 1.0-2.4 h for the lining thickness of 1.0 m, since the external moment equals the resisting one (namely, $M = M_{Rd}$). Failure, however, does not occurs for the same cases according to NLA, since the "virtual collapse" observed via ELA represents just the configuration in which section plasticization (due to crushing in compression or, more often, to cracking in tension) is obtained. As previously mentioned, when plasticization is attained, section stiffness starts reducing, thus bringing to a reduction of indirect actions, this being typical of all indirect actions such as those linked to concrete shrinkage, impressed distortions and so on.

This makes it important to define the condition in which collapse is attained. In case of indirect actions, failure occurs only when the bearing capacity of the structure is so degraded that it is no more possible to face the initial external forces, namely the gravitational actions due to the surrounding soil. In the case of a tunnel lining with initial axisymmetric loading (thus with an initial nil bending regime) this translates into the condition of an axial force decreasing with the fire duration, which means that the sectional shrinkage due to the compression is higher than the thermal dilation. Such configuration is not stable and thus not engineering allowable.

It is finally interesting to observe that when section plasticization takes place in non-linear analyses, the increase of axial compression and strain at the barycenter (ε_0) speeds up. This is caused by the fact that the cracking process taking place at the cold side during section plasticization reduces the internal restrain provided against to the thermal expansion of the hottest layers. The consequence is that thermal dilation increases and, therefore, the overpressure exerted by the surrounding soil.

In the following, the effect of the initial compression in the overall response of the lining during fire is investigated, proving as bending response results to be strongly affected.

In Figure 7, the variation with temperature of the strain at the barycenter of the section ε_0, axial force N and bending moment M with time is shown in case of ISO 834 fire curve. On the left, the plots refer to an initial compression $N_{ext}^{20} = 500$ kN, while an initial compression $N_{ext}^{20} = 2000$ kN is considered in the right side. In both cases, a ring width of 1 m and a ring external radius of 6 m have been considered, together with a lining thickness of 0.3 m, and a Winkler constant representing the soil stiffness $k_w = 0.1$ N/mm^3.

In the Figures, thick solid lines refer to NLA, while thin lines refer to ELA. In the plots showing the bending moment evolution, it has been reported also the evolution of the resistant bending moment of the section according to the temperature profile and to the external axial force, evaluated by implementing the constitutive laws of Figure 4.

The same comment previously highlighted holds for the present case regarding the configuration with low axial force (left side of Figure 7). On the other hand, it is worth noting as, significantly increasing the initial axial compression, the consequent increase of the bearing bending moment (M_{Rd}) makes it possible to not plasticize the section. This is clearly shown in the last plot of the right side of Figure 7, where the bending moment evaluated according to elastic analysis (ELA) remains always lower than the bearing capacity of the section (M_{Rd}). The consequence is that elastic and plastic analysis yield in this case rather similar results, since plasticization remain only latent without significantly affecting the overall sectional response.

Such considerations are corroborated by the evolution of the axial stiffness EA, of the distance between the center of perfect restrained thermal stress and geometric barycenter of the section ($e_{th,G}$ in Figure 2) and of the distance between the center of stiffness and geometric barycenter of the section ($e_{k,G}$ in Figure 2), all reported in Figure 8.
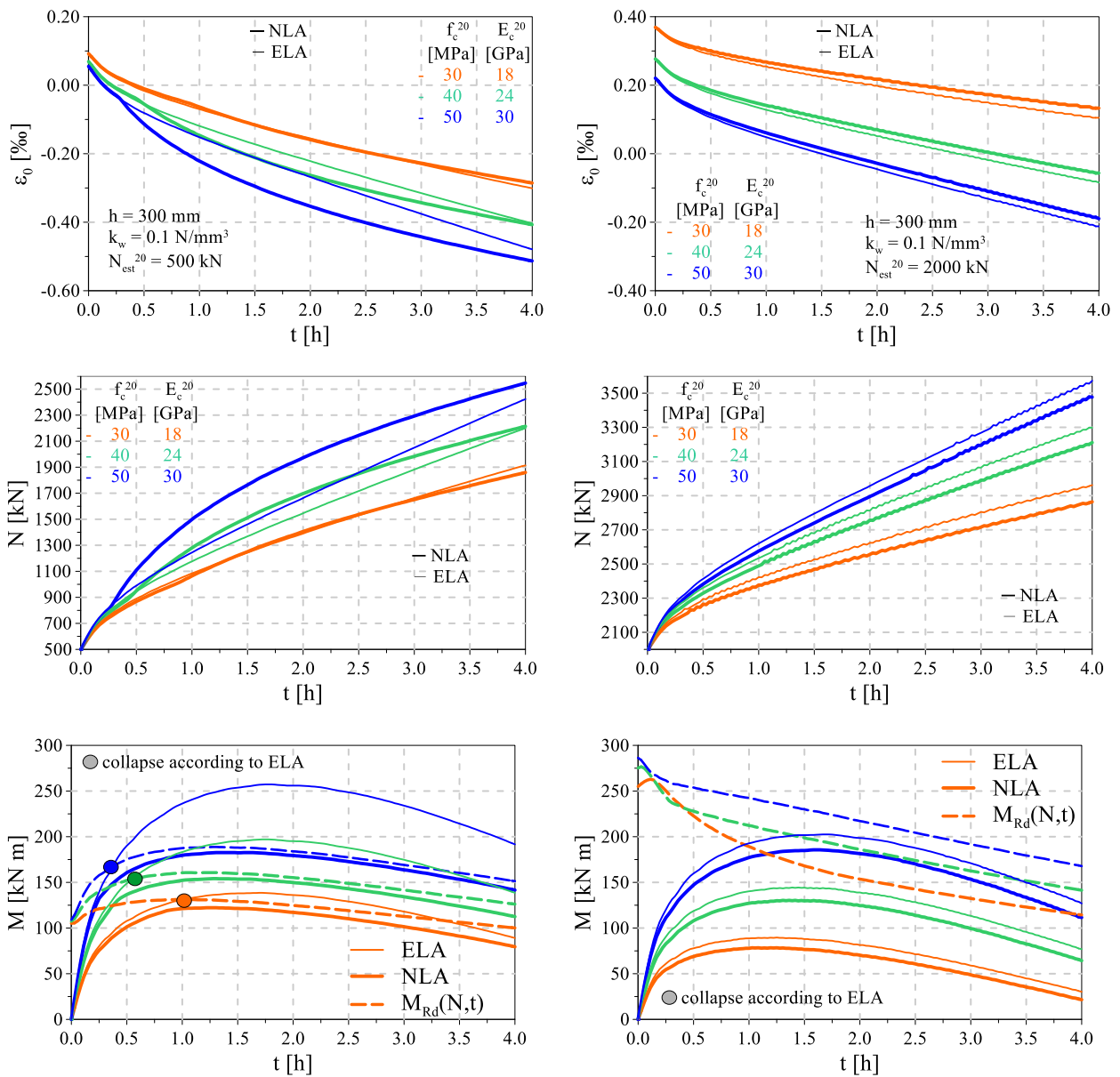
Figure 7: Variation with temperature of barycentre strain ε_0, axial force N and bending moment M with time. On the left, N_{ext}^{20} = 500 kN, while on the right, N_{ext}^{20} = 2000 kN.
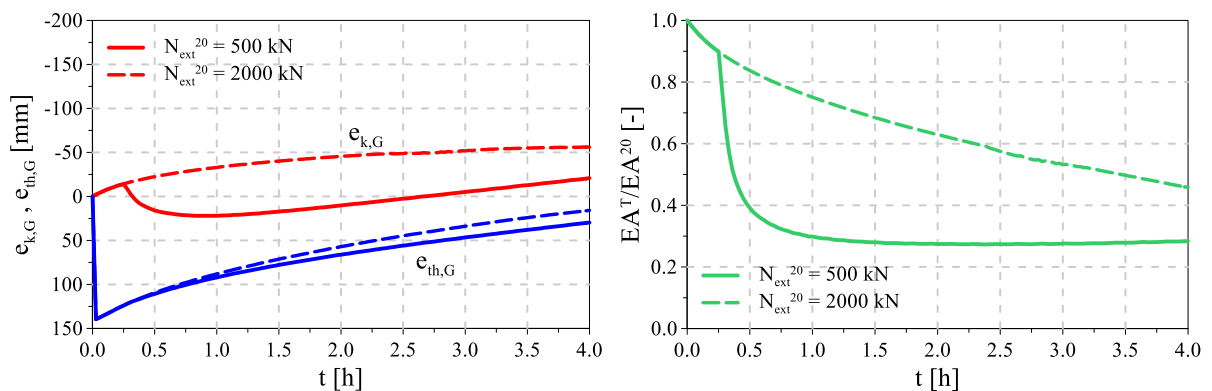

Figure 8: Variation with fire duration of center of stiffness, of perfectly restrained stress eccentricity and of sectional axial stiffness.

4. CONCLUDING REMARKS

In the present paper it is discussed the potential in the adoption of a simplified 1D beam approach to assess the structural performance of tunnel linings during fire. Such simplified approach lies in two main assumptions, namely axisymmetry of the lining (in terms of geometry and loading) and of plane sections according to the beam theory. In particular, axisymmetry allows to describe the overall structural behavior of the lining via a sectional approach, which, as generally maintained in both Service and Ultimate Limit States, keep the assumption of plane sections. Furthermore, since thermal and mechanical problems are not fully coupled, the method requires the sequential solution of the thermal problem to define the temperature distribution within the lining for any fire duration, and of the following linear or non-linear mechanical analysis.

The simplicity of the approach allows for the prompt and easy estimation of the structural performance of tunnel lining exposed to fire with very fast simulation characterized by very limited burden in modelling, with the possibility of monitoring all the main parameters involved, such as internal actions, stiffness, stresses, possibly highlighting the role played by single parameters such as lining thickness, soil stiffness, material characteristics, instrumental in understanding the sensitivity to different factors. The parametric analyses reported in the present paper confirm as a linear elastic analysis represents a conservative approach leading to more severe indirect actions and it requires strength checks. If checks are not satisfied, however, collapse does not necessarily occur, since sectional collapse (or better, plasticization) does not correspond to global failure. The role played by lining thickness appeared not so trivial, since its increase leads to a reduction of the compression, but to an increase of the bending moment because of the larger eccentricity of the compression in the hot layer. Finally, linings characterized by high initial pressure exerted by the soil to the lining tends to respond (almost) elastically during the fire thanks to the increased bearing capacity in bending.

Even though the described simplified approach appears powerful and effective, important aspects need to be better analyzed. In particular, the development of indirect actions evaluated according to such approach should be compared with those obtained by more advanced Finite Element analyses (such as, for example, by using Abaqus or Safir). Furthermore, it should be checked the possibility of adopting a 1D approach also for non-axisymmetric configuration, this latter being the most general condition for tunnel linings.

REFERENCES

[1] FIT. (2005). Technical Report – Part 1: Design Fire Scenarios. European Thematic Network FIT – Fire in Tunnels, Rapporteur A. Haack, supported by the European Community under the 5th Framework Programme 'Competitive and Sustainable Growth' Contract n° G1RT-CT-2001-05017.

[2] Maluk C., Tignard ., Ridout A., Clarke T., Winterberg R., (2021), "Experimental study on the fire behaviour of fibre reinforced concrete used in tunnel applications", Fire Safety Journal 120, art. n. 103173.

[3] Lo Monte, F., Felicetti, R., Meda, A., Bortolussi, A., "Assessment of concrete sensitivity to fire spalling: A multi-scale experimental approach", (2019) Construction and Building Materials, 212, pp. 476-485.

[4] Rossino C., Lo Monte F., Cangiano S., Felicetti R., Gambarova P.G., (2013), "Concrete spalling sensitivity versus microstructure: Preliminary results on the effect of polypropylene fibers", MATEC Web of Conferences, 6, art. no. 02002.

[5] Rossino C., Lo Monte F., Cangiano S., Felicetti R., Gambarova P.G., (2015), "HPC subjected to high temperature: A study on intrinsic and mechanical damage", Key Eng. Materials, 629-630, pp. 239 – 244.

[6] Lo Monte F., Bamonte P., Beltrami C., (2023), "Study on the effects of cooling phase and construction technology on the fire performance of R/C tunnels", Tunnelling and Underground Space Technology 132, art. no. 104838.

[7] EN 1992-1-2:2004. (2004). Eurocode 2 - Design of concrete structures - Part 1-2: General rules - Structural fire design. European Committee for Standardization (CEN), Brussels (Belgium).

[8] Bulletin 83. (2017). Precast tunnel segments in fibre-reinforced concrete. International Federation for Structural Concrete - fib.

[9] fib Model Code for Concrete Structures 2010, (2013) fédération internationale du béton/International Federation for Structural Concrete (fib).

[10] Lo Monte F. and Bamonte P., (2022), "Simplified Approach for the Evaluation of the Bearing Capacity of Deep R/C Tunnels Exposed to Fire", Proceedings of the 12th International Conference on Structures in Fire – SiF2022, November 30th – December 2nd, 2022, Hong Kong.

Fire Safety of Structures

OPTIMIZATION OF STEEL INDUSTRIAL BUILDINGS IN FIRE SITUATION

Filip Ljubinković[a]*; **Luís Laim**[b]; **Aldina Santiago**[c]; **Luís Simões da Silva**[d] and **Luís Cordeiro**[e]

ABSTRACT

Having an excellent strength-to-weight ratio, steel structures are the preferred solution for long-span industrial buildings. However, when compared to other construction materials, they possess relatively low fire resistance. To enhance their fire performance, adequate fire protection is required. An imprecise fire design, without considering the real influence of the main parameters on the development and propagation of natural fires, may lead to excessive amounts of already costly protective material. Moreover, the use of advanced software tools may be impractical, especially for time-consuming iterative computations when an optimal solution is sought. Hence, it is the goal of this work to present a simple and user-friendly calculation tool that allows users to define the sheds to be built, and based on a set of metrics, weights, and advanced algorithms, to find the most economical solution by reducing the steel and fire protection material consumption. To showcase the use of the tool and its possibilities, an example of a steel industrial shed is selected, for which different fire protection strategies are explored and discussed. The main conclusion is that the results obtained by the tool are comparable with the FEM results, and are obtained considerably faster than by expensive software tools.

Keywords: Steel industrial sheds; Fire design; Fire protection; Web application, Optimization.

1. INTRODUCTION

Owing to its excellent strength-to-weight ratio, steel structures are the preferred solution for long-span industrial buildings (see Fig. 1). However, when compared to other construction materials, they are vulnerable when subject to high temperatures (usually above 500ºC) [1].

High thermal conductivity and section factors lead to a rapid increase in temperature resulting in a rapid loss of structural stability. Hence, it is common practice to provide steel structures with protection to ensure the structural integrity of their elements for a minimum time, usually sufficient to allow the evacuation of the occupants and the intervention of firefighters to save human lives and reduce material damage.

---

[a]* ISISE, ARISE, Department of Civil Engineering, University of Coimbra, Portugal, (filj@uc.pt), corresponding author.

[b] ISISE, ARISE, Department of Civil Engineering, University of Coimbra, Portugal, (luislaim@uc.pt).

[c] ISISE, ARISE, Department of Civil Engineering, University of Coimbra, Portugal, (aldina@dec.uc.pt).

[d] ISISE, ARISE, Department of Civil Engineering, University of Coimbra, Portugal, (luisss@dec.uc.pt).

[e] OneSource, Consultoria Informática, Lda, Coimbra, Portugal, (cordeiro@onesource.pt).

Figure 1: Steel industrial sheds: a) @Pavilhoes Moreira; b) @Pinterest

Nowadays, there are multiple solutions for fire protection materials available on the market. Their main characteristics are low thermal conductivity, high heat capacity, physical heat absorption reactions (transpiration, evaporation, sublimation, ablation) as well as chemical reactions (endothermic decomposition, pyrolysis) and/or intumescence, i.e. formation of a thicker insulating foam after heating [2]. The solutions are not unique and each one provides different characteristics, from an economical, ecological, and sustainable standpoint. Among the fire protection materials, the most commonly used are gypsum-based coatings, cement-based materials, sprays, wools, and intumescent paints, among others.

A simplified fire design for steel buildings, i.e. without considering the real influence of the main parameters on the development and propagation of natural fires, such as the opening factor, the fire load density, the cladding materials, and the actual geometric configurations, can lead to solutions with protection that sometimes imply a high investment, which can compromise the competitiveness of steel structures. In this sense, the Switch2Steel project aimed to design and produce a computational platform to support architectural and engineering offices, manufacturers, and fabricants in the construction sector in calculating and optimizing the cost of industrial and commercial buildings made of steel, to increase their competitiveness in this type of construction and promote its advantages.

In the following sections, a realistic case of an industrial shed is first described, which is then calculated and verified using both the advanced FEM model and the developed calculation tool. To illustrate the adequate use of the developed tool and its main features, different fire protection strategies are considered, and the respective fire performance of the reference case study is evaluated.

2. CASE STUDY

2.1 Portal frame geometry

For this work, an example of a two-pitched steel industrial shed is selected as a reference case as shown in Fig. 2. The span of the main portal frame is L = 25m, with the column height equal to h = 7.5m, and a roof slope of 10%. The industrial shed has a total length of 100m, with the spacing between two successive portal frames of L/4 = 6.25m. The main frame is built of hot-rolled profiles – HEB260 for columns and IPE450 for rafters, both made in steel S355. Following the design practice recommendation, two haunches at two beam-to-column connections are 2.5m long (i.e. L/10), and approximately 0.714m high (i.e. L/35). The purlins over the rafters are placed at every 2.5m, including the one on the top of the column and one at the apex, whereas another intermediate purlin is placed at the middle of the haunches. The façade rail beams are placed over the exterior column face equidistantly at 1.875m. The portal frame is considered pinned at the column bases and horizontally braced. The required fire resistance for this portal frame is assumed to be R60.
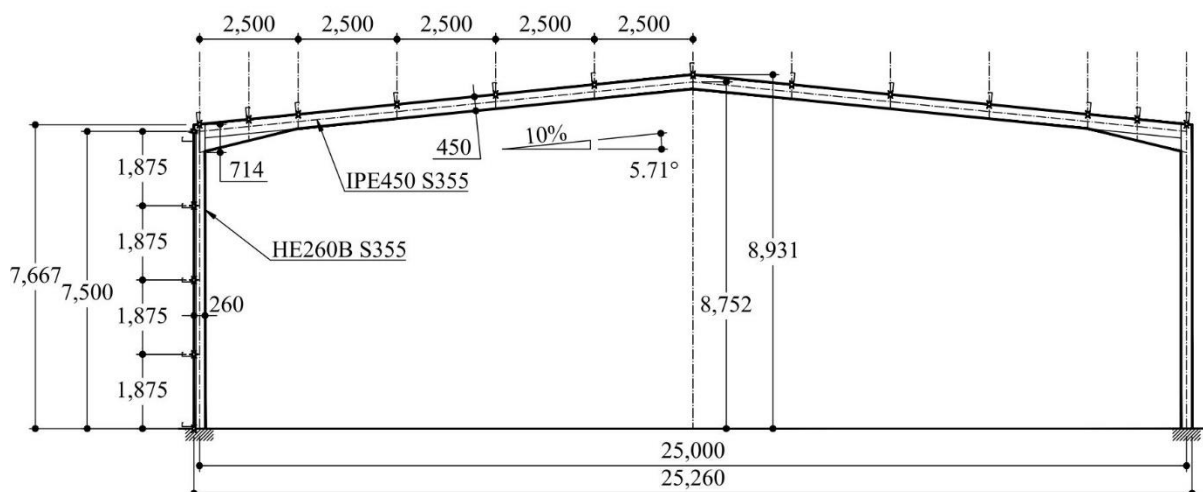
Figure 2: Two-pitched industrial shed – reference example (units in mm)

2.2 Load combinations

Regarding the loading, the building is of industrial use, with a light roof, located in Figueira da Foz (Portugal). Therefore, the following loads are considered:

- G_0: self-weight of the frame (evaluated according to dimensions).
- G_1: contributory self-weight of roof purlins (evaluated according to dimensions and spacing, but with a repercussion typically around 0.03–0.06kN/m^2). In this case, 0.05kN/m^2 is adopted.
- G_2: weight of roof panel (composite panel); the roof sandwich panel is manufactured with thicknesses between 30 and 100mm, with self-weight between 0.10 to 0.15kN/m^2.

For pre-design purposes, an approximate value of $G = 0.20$kN/m^2 is adopted.

- Q: variable imposed load (maintenance) on the roof (category H per EN 1991-1-1:2002 [3], $\psi_0 = 0$, $\psi_1 = 0$, $\psi_2 = 0$) of 0.40kN/m^2. The service load is conservatively added to the variable load, with a value of 0.15kN/m^2. In some cases, this service load is added to the dead load; however, due to the large effect of wind on the structure, this approach might be unconservative. Therefore, for pre-design purposes, a value of $Q = 0.55$kN/m^2 is considered.
- S: variable snow load calculated according to location (for $H < 1000$m a.s.l., $\psi_0 = 0.50$, $\psi_1 = 0.20$, $\psi_2 = 0$). For a building located at Figueira da Foz (Portugal), the snow load is $S = 0.20$kN/m^2.
- W: variable wind load calculated according to location ($\psi_0 = 0.60$, $\psi_1 = 0.20$, $\psi_2 = 0$). For a building located at Figueira da Foz (Portugal), the basic wind velocity is $v_w = 30$m/s whereas according to EN 1991-1-4 [4], Terrain Category II (area with low vegetation) is assumed. For the global analysis of the structure, this is equivalent to an approximate basic wind pressure value of 0.57kNm^2, which results in an overall lateral unit force (pressure + suction) of about 1.80kN/m^2, and a roof suction of about 0.36kN/m^2. For the individual analysis of the members, the inner pressure due to openings is considered, and for each wind direction (transverse and longitudinal), the most unfavorable situation is obtained by varying the internal coefficients between +0.2 and -0.3, leading to the three wind load distributions shown in Fig. 3.
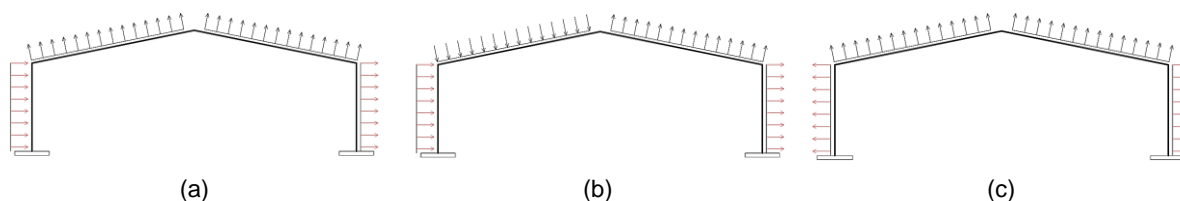

| (a) | (b) | (c) |

Figure 3: Wind load distribution on the walls and roofs: (a) wind in transverse direction ($\theta = 0°$) – suction, (b) wind in transverse direction ($\theta = 0°$) - pressure; (c) wind in longitudinal direction ($\theta = 90°$).

262

The pre-design of the portal frame is first carried out at the ambient temperature, considering ULS and SLS load combinations calculated according to EN 1990 [5]. The following 14 ULS and 14 SLS combinations are considered, as shown in Table 1 (ULS) and Table 2 (SLS). Finally, for the fire design of the portal frame, the accidental load combinations considered are summarized in Table 3. It should be noted that the imposed loads (Q_k) are not considered for the fire verification, since according to EN1990 (Annex A), the combination factors for the H category buildings (roofs of industrial buildings) are equal to 0 ($\psi_0 = 0$, $\psi_1 = 0$, $\psi_2 = 0$).

Table 1: Load combinations for the ULS verifications

Combination	G_k	Q_k	S_k	$W_{T\uparrow\uparrow}$	$W_{T\downarrow\uparrow}$	$W_{T\uparrow\downarrow}$	$W_{T\downarrow\downarrow}$	$W_{L\uparrow}$
1	1.35	1.50	0.75	-	-	-	-	-
2	1.0	-	-	1.50	-	-	-	-
3	1.0	-	-	-	1.50	-	-	-
4	1.0	-	-	-	-	1.50	-	-
5	1.0	-	-	-	-	-	1.50	-
6	1.35	-	0.75	1.50	-	-	-	-
7	1.35	-	0.75	-	1.50	-	-	-
8	1.35	-	0.75	-	-	1.50	-	-
9	1.35	-	0.75	-	-	-	1.50	-
10	1.35	-	1.50	0.9	-	-	-	-
11	1.35	-	1.50	-	0.9	-	-	-
12	1.35	-	1.50	-	-	0.9	-	-
13	1.35	-	1.50	-	-	-	0.9	-
14	1.0	-	-	-	-	-	-	1.50

Table 2: Load combinations for the SLS verifications

Combination	G_k	Q_k	S_k	$W_{T\uparrow\uparrow}$	$W_{T\downarrow\uparrow}$	$W_{T\uparrow\downarrow}$	$W_{T\downarrow\downarrow}$	$W_{L\uparrow}$
1	-	1.0	0.5	-	-	-	-	-
2	-	-	-	1.0	-	-	-	-
3	-	-	-	-	1.0	-	-	-
4	-	-	-	-	-	1.0	-	-
5	-	-	-	-	-	-	1.0	-
6	-	-	0.5	1.0	-	-	-	-
7	-	-	0.5	-	1.0	-	-	-
8	-	-	0.5	-	-	1.0	-	-
9	-	-	0.5	-	-	-	1.0	-
10	-	-	1.0	0.6	-	-	-	-
11	-	-	1.0	-	0.6	-	-	-
12	-	-	1.0	-	-	0.6	-	-
13	-	-	1.0	-	-	-	0.6	-
14	-	-	-	-	-	-	-	1.0

Table 3: Load combinations for the fire verifications

Combination	G_k	Q_k	S_k	$W_{T\uparrow\uparrow}$	$W_{T\downarrow\uparrow}$	$W_{T\uparrow\downarrow}$	$W_{T\downarrow\downarrow}$	$W_{L\uparrow}$
1	1.0	-	0.2	-	-	-	-	-
2	1.0	-	-	0.2	-	-	-	-
3	1.0	-	-	-	0.2	-	-	-
4	1.0	-	-	-	-	0.2	-	-
5	1.0	-	-	-	-	-	0.2	-
6	1.0	-	-	-	-	-	-	0.2

In these tables, W_T and W_L indicate the wind in the transverse and longitudinal direction, whereas the first arrow in the subscript indicates the orientation of the external wind coefficients (C_e) and the second arrow that of the internal (C_i) coefficient.

263

Since there are no normative deflection limits for SLS, a customary limit for the vertical deflections is $L/200$ for the characteristic combination but excluding the deflections due to dead load, generally counteracted by pre-camber. This limit is adopted hereby. The control point is the apex of the portal frame. Horizontal deflection is of no importance in these frames, as they are assumed to be braced in-plane with a suitable bracing system.

3. SWITCH2STEEL (S2S) APPLICATION

3.1 S2S Tool description

The S2S application is developed for the calculation and optimization of the cost of steel industrial sheds, customized for Android, iOS, macOS, Windows, and web applications. It is user-friendly, intuitive, and fast to access and use. The user interface allows for the manual configuration of different parameters in an intuitive step-wise manner, as shown in Fig. 4. The application combines several design techniques – depending on the requirements defined for the building and the legislation applicable to the place where it will be built. It also incorporates the legislation and technical regulations of several European countries, which will gradually be increased with the evolution and dissemination of the platform (see Fig. 4a).
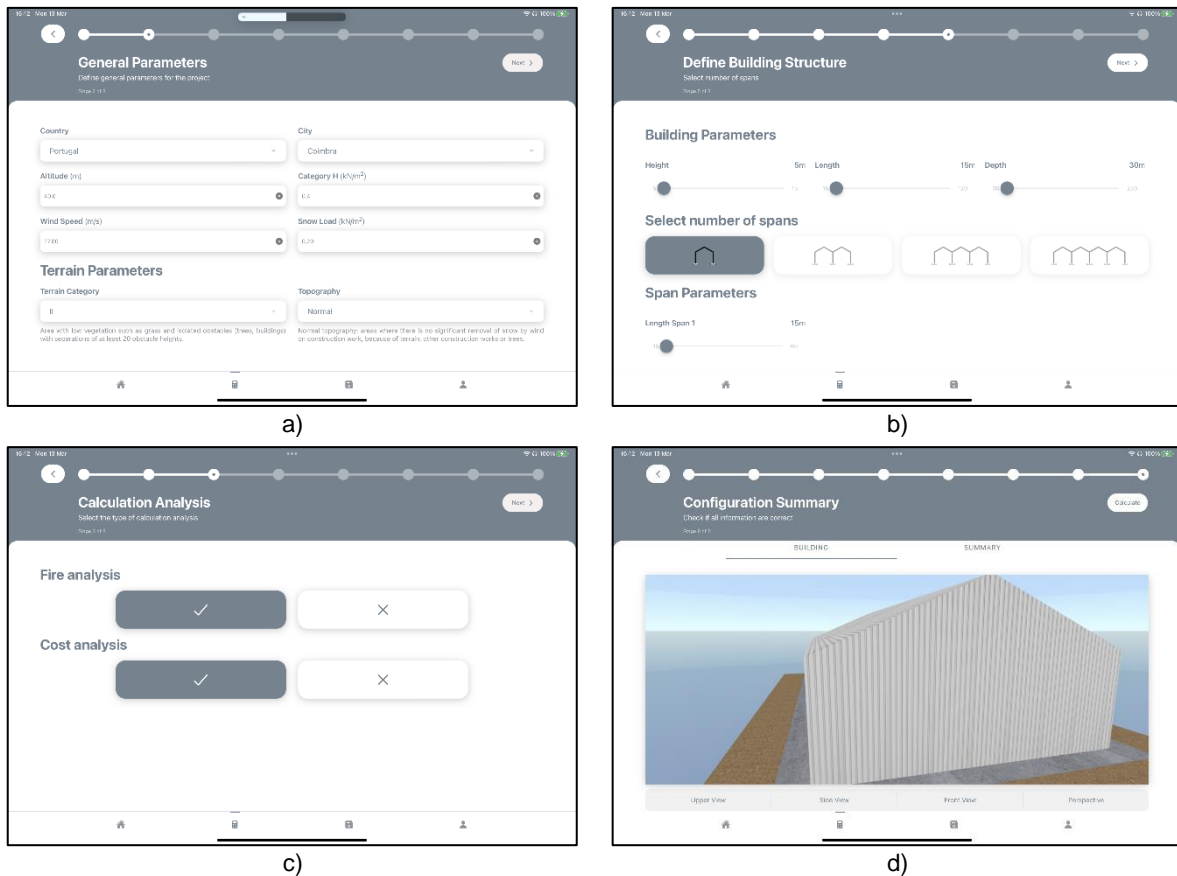

a)

b)

c)

d)

Figure 4: Switch2Steel computation tool interface

Regarding the computational algorithms, the tool has four main features: (i) structural analysis of steel portal frames at room and elevated temperatures, (ii) two-zone fire models, allowing for the performance-based design; (iii) automatic safety verifications according to respective design codes; and (iv) implementation of stochastic Genetic Algorithms (GAs), for structural optimization.

To obtain the effects of actions (internal forces and displacements), linear elastic analysis is carried out using a 2D structural solver developed in the high-level program language Python. The 2D solver is based on the displacement (stiffness) method [6] in which the structure is discretized by finite elements (FE). The second-order effects are also accounted for. Namely, according to cl. 5.2.1 of EN1993-1-1, the second-order effects for elastic analysis need to

be accounted for whenever $\alpha_{cr} = F_{cr}/F_{Ed} \leq 10$. Hence, the critical load factor (α_{cr}) is determined first for each load case using the modified stiffness matrix of the system to account for the presence of the axial force, composed of two parts (see Eq. 1): i) stiffness matrix obtained according to the first-order theory (K_0), and ii) so-called geometric stiffness matrix (K_G)

$$K_L = K_0 + K_G \tag{1}$$

Once the critical load factor (i.e. eigenvalue) is determined, the second-order effects are subsequently determined using the *amplified sway moments* method, implemented through the following steps:

- The first analysis is performed with restraints against horizontal translation (but not rotation) using ULS loads multiplied by $1/(\alpha_{cr} - 1)$.
- The horizontal restraint reactions are recorded.
- The second analysis is performed on the normal structure, using 1.0 x ULS loads plus horizontal loads recorded, equal in magnitude but opposite in direction to the reactions calculated from the first analysis.
- The design is performed using the output from the second analysis.

It should be highlighted that the S2S tool allows for the portal frames with the dimensions falling within the limits of common design practice, (i.e. one-span and multi-span frames with the spans not exceeding 50-55m each), hence avoiding highly slender structures with the critical load factor below $\alpha_{cr} = F_{cr}/F_{Ed} \leq 3.0$, where severe second order effects might occur.

Subsequently, the safety verification of steel structures, based on the Eurocodes methodologies (EN1993-1-1, EN1993-1-2, and EN1993-1-5 [7-9]), is incorporated in a software-as-a-service logic offering necessary functionalities to the target audience, with multi-channel support and parameterization.

In addition, the fire design is implemented in this tool (see Fig. 4c) and it is carried out for accidental loading, and localized fire scenarios. Whenever the configuration and characteristics of the building meet fire safety conditions less severe than the prescriptive methodologies, the platform enables performance-based fire design. For that purpose, to reduce the computation time, a two-zone model is integrated into the process of calculating the thermal actions from a localized fire using Consolidated Fire and Smoke Transport (CFAST_7.7.0) program [10], developed and maintained by the National Institute of Standards and Technology (NIST) in the United States of America. This approach has some important assumptions that must be understood and considered by the user [10].

Finally, the tool integrates calculation methodologies with evolutionary optimization techniques, namely genetic algorithms [11]. These algorithms are stochastic methods that allow the generation of possible solutions to the optimization problem within a domain, using an evolutionary way. They are search algorithms inspired by the concepts of natural and genetic selection, based on the strategy of survival of the fittest [11]. Although this type of technique requires a large number of evaluations of the objective function and constraints, with the evolution of computers, they have simplified the complexity of optimization problems with a large number of variables, namely to obtain the minimum amount of structural steel in industrial and commercial buildings.

3.2 Design of portal frame at ambient temperature

Switch2Steel platform allows for both manual and automatic generation of all relevant ULS and SLS load combinations, by varying the dominant variable load (imposed, snow and winds), and accounting for all possible combinations of wind pressure coefficients (internal and external) including both longitudinal and transversal wind directions. Subsequently, for each load combination, the structure is verified according to EC3, both on the cross-section level and on the global level (accounting for second-order effects and different member instability phenomena). In this study, the same 14 ULS and 14 SLS load combinations presented in Table 1 and Table 2 are considered. The envelope of utilization factors for 14 ULS load combinations is shown in Fig. 5.
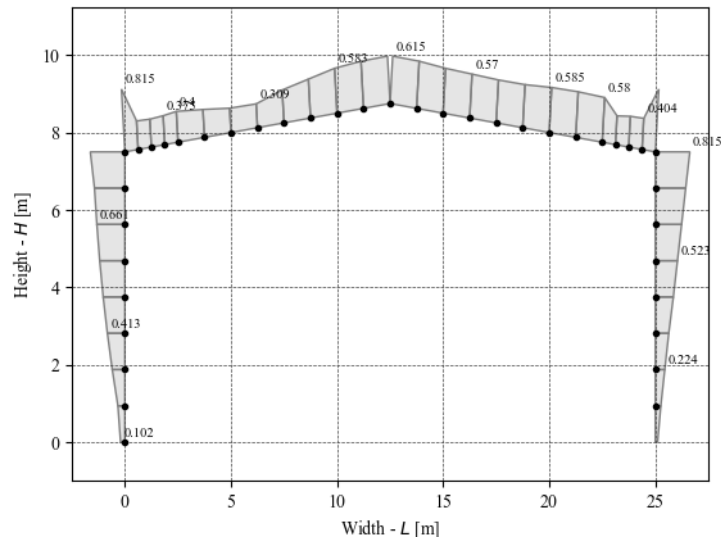
Figure 5: ULS utilization factor envelope

As it may be noticed, the maximum utilization factor of $UF_{ULS} = 0.815$ is reached in the cross-sections at the junction between the rafter and the column, obtained for the combination with the dominant vertical load (i.e. combination 1 in Table 1). As for the SLS verification, the maximum vertical displacement of 116mm is obtained in the middle of the span (at apex), which is less than the commonly accepted limit (L/200 = 125mm), resulting in an SLS utilization factor equal to $UF_{SLS} = 0.96$, obtained for the SLS combination with the dominant sucking longitudinal wind (i.e. combination 14 in Table 2).

3.3 Fire design of the portal frame

After the safety at the ambient temperature is verified for both ULS and SLS, the platform performs subsequently the fire safety verification. Namely, the corresponding accidental loads are automatically generated, and based on the desired fire resistance rating (R60 in this case), and selected fire protection material, the minimum required thickness is calculated. For this example, gypsum-based mortar with perlite is considered with the following thermal properties: thermal conductivity of 0.2309W/mK, specific heat of 861.79J/kgK, and mass density of 860.186kg/m^3. The minimum required material thickness is calculated considering columns exposed to fire on 3 sides, and rafters exposed to fire on all 4 sides, resulting in a minimum thickness of 6.5mm when the standard temperature-time curve ISO 834 [12] is considered.

4. FEM ANALYSIS

4.1 Model definition

In this section, the results obtained by the Switch2Steel tool are compared with more advanced calculation methodologies, namely, a three-dimensional shell finite element model developed in the finite element program Abaqus [13] (Fig. 6a). A linear four-node shell element with reduced integration (S4R) is used for the model discretization. The applied material (steel S355) is modeled as elastic-plastic without strain-hardening. The purlins and façade rail beams are not explicitly included in the model, but their presence is simulated by lateral restraints applied on the outer (exterior) flange of rafters/columns, as presented in (Fig. 6b).
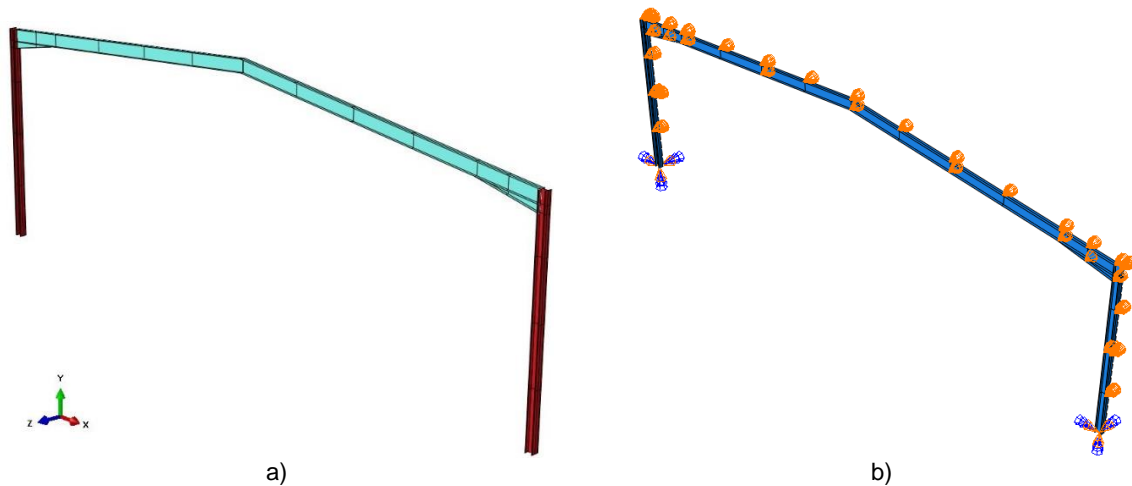
a)   b)

Figure 6: FEM model of a two-pitched industrial shed

4.2 Ambient temperature

For the design of the steel portal frame (at ambient temperature), in this study, two types of analyses are performed: i) Linear elastic bifurcation (or eigenvalue) analysis (LBA) and ii) Geometrically and materially nonlinear analysis with imperfections included (GMNIA). First, to generate the eigenmodes, the LBA is performed using the subspace algorithm available in ABAQUS. Subsequently, the extracted eigenmodes are used as the shapes of the initial geometrical imperfections in a GMNIA, in which the ultimate resistance of the frame is obtained and its elastic-plastic behavior examined. For that purpose, the General static method from the software's library is used, which gives non-linear static equilibrium solutions. The results presented in Fig. 8 and Fig. 9 are obtained for the ULS and SLS combination with the dominant vertical load, i.e., combination 1 in Table 1 and Table 2, respectively.

Due to significant computational time, not all 14 ULS and 14 SLS load combinations are assessed, but only those assessed as more critical. The linear buckling analysis (LBA) shows that the critical eigenmode is affine to the local torsional buckling of the bottom (compressed) flange between the two lateral restraints (Fig. 7a). This shape is adopted as the initial imperfection shape with an amplitude of $h_{beam}/200$. In addition, the initial imperfection of the columns is modeled based on the 4th eigenmode (Fig. 7b), with the corresponding amplitude of $h_{column}/200$.

Subsequently, the static analysis indicates that the applied load may be sustained without failure of the system, with the most critical cross-section being the one at the junction between the rafter and column (see Fig. 8), which coincides with results obtained using the S2S tool.
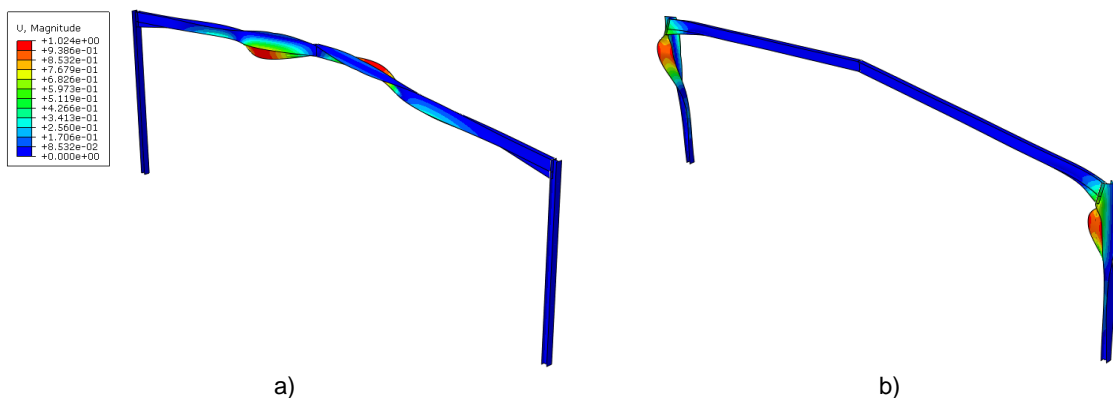

a)   b)

Figure 7: Linear buckling analysis: a) 1st eigenmode; b) 4th eigenmode
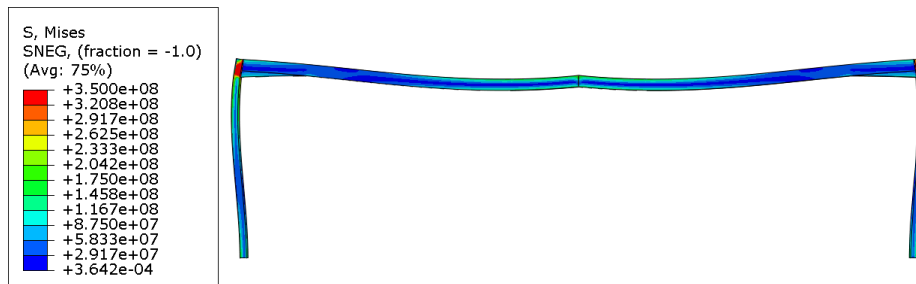
267

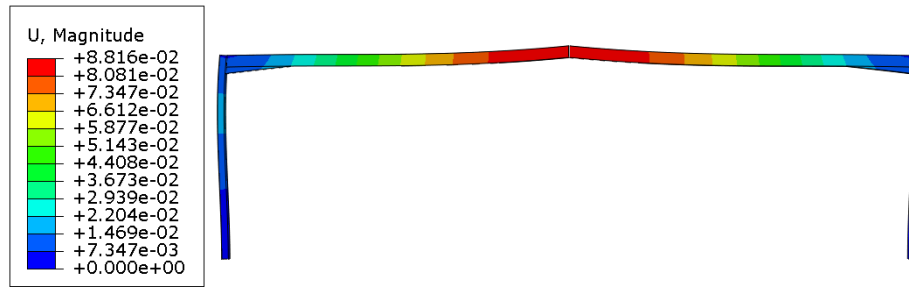Figure 8: Non-linear static analysis - ULS load combination 1

Figure 9: Non-linear static analysis - SLS load combination 1

For both limit states, the maximum utilization factors are derived and compared with the results obtained using the S2S tool at ambient temperature, as shown in Table 4.

Table 4: S2S tool vs FEM – ambient temperature

	S2S tool	FEM	Diff. (%)
ULS	0.815	0.743	9.7
SLS	0.957	0.874	9.5

The results show that a simplified 2D linear model, based on Eurocode design verifications and without initial imperfections, leads to a more conservative solution (in this case, around 9.6% for both ULS and SLS checks). However, one should not underestimate the amount of time and modeling experience required for a single analysis using a sophisticated 3D shell finite element model, which is particularly emphasized in the case of heat-transfer analysis, as indicated in the following sub-section.

4.3 Fire conditions

Subsequently, an additional finite-element analysis is carried out to investigate the fire resistance of the same steel portal frame protected with gypsum-based mortar with perlite (see section 3.3). Sequential analyses are performed in the following order: LBA, heat transfer analysis, and thermo-mechanical analysis with imperfections.

In the last analysis, the portal frame is subject to both accidental loading and a non-uniform heating rate according to the standard fire curve ISO 834 [12] up to failure. The structure collapses when either the magnitude of deflection or the rate of deflection exceeds the limits set by EN 1363–1 [14].

The thermal boundary conditions are defined according to the recommendations in EN 1991-1-2 [15], using two types of surfaces available in the software library, including 'film condition' for heat transfer by convection and 'radiation to ambient' for heat transfer by radiation to reproduce the net heat flux on the fire exposed surfaces. A coefficient of heat transfer by convection equal to $25W/(m^2K)$ and a resultant emissivity ($\varepsilon_m . \varepsilon_f$) to 0.63 are adopted. Thermal resistance to heat conduction at the mortar-steel interface is also adopted in the FEM, with a thermal contact conductance of $150W/(m^2K)$ up to 100^oC and of $80W/(m^2K)$ beyond that temperature [2, 16].

For the considered case study, i.e., under standard fire conditions, the results from the numerical simulations are similar to those obtained using the S2S platform in terms of both critical temperature and required fire protection,

as presented in Table 5. It is worth noting that a single simulation (i.e. for one load combination) in Abaqus lasts approximately two hours (with Intel® Core™ i7-6700 Processor, using 4 logical processors), while the same analysis in the S2S platform, with multiple load combinations, and with the complete optimization procedure, takes several minutes, in total.

Table 5: S2S tool vs FEM – fire conditions (R60)

	Critical temperature (ºC)	Protection thickness (mm)
S2S tool	742.6	6.5
FEM	740	6.2
Difference	0.4%	4.8%

5. ALTERNATIVE FIRE PROPERTIES USING S2S TOOL

In this section, different features from the S2S tool related to the fire performance of the industrial shed are presented. Once the user selects the module 'Fire analysis' (see Fig. 4c), a separate set of fire protection properties may be introduced, as shown in Fig. 10.
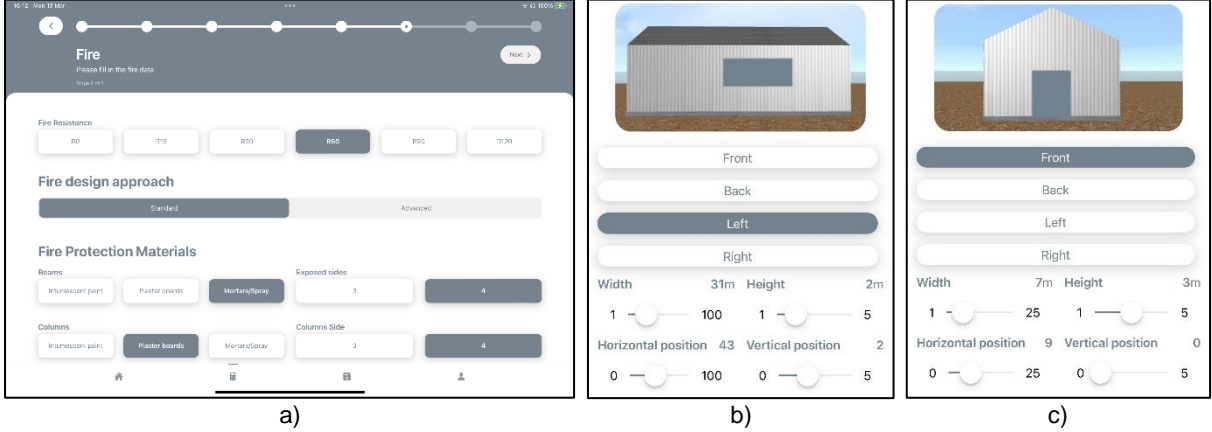

Figure 10: Switch2Steel computation tool interface – Fire design

Using the S2S tool, it is possible to select a series of parameters (Fig. 10a), such as the desired fire protection rate (R0 – R120), type of fire protection material (e.g. intumescent paints, plaster boards, mortars, sprays) for columns and rafters, separately, where the properties of protection material, as well as the number of sides exposed to fire, may be manually varied. In addition, the S2S tool allows for two fire design approaches: i) standard (with ISO 834 curve) and ii) advanced, in which a two-zone model is integrated into the process of calculating the thermal actions from a localized fire using CFAST software, whereas all the relevant parameters may be edited (e.g. fire load data, thermal properties of compartment walls, ceiling, floor, percentage of openings, etc.).

For this paper, to show the possibilities of the S2S tools, several parameters are varied, and their influence on the fire behavior of industrial sheds is illustrated. Namely, the standard approach (ISO) is compared with the natural fires, whereby different fire rate resistances are examined (from R15 to R90). The fire protection material is kept the same as in section 3.3 (i.e. gypsum-based mortar with perlite), however, two fire exposures of columns are considered (with 3 and 4 sides), and the roof openings of the industrial sheds are varied (i.e. 0%, 5%, 10% of the floor area) using the interface presented in Fig.10b and Fig.10c. All other dimensions of the industrial shed are kept constant as defined in 2.1., i.e., the dimensions of the large compartment are set to be 100m x 25m x 7.5m with two doorways of 3m x 3m (on the same longest facade). A 20cm concrete slab is assumed for the floor and 0.04m coverings with high thermal resistance are selected for the ceiling and walls. Their thermal properties are summarized in Table 6. Finally, the following fire load properties are considered: a fast fire growth rate, fire load density of 1500MJ/m^2, fire area of 25m^2, and heat combustion of 17500kJ/kg, whereas the maximum heat release rate is computed according to Eq. (E6) of EN1991-1-2.

Table 6: Thermal properties of compartment elements

Element	Thickness (mm)	Mass density (kg/m3)	Specific heat (kJ/kgK)	Thermal Conductivity (W/mK)	Emissivity
Ceiling	0.04	60	1.03	0.037	0.9
Walls	0.04	60	1.03	0.037	0.9
Floor	0.20	2300	1.00	1.6	0.9

The results for the studied set of parameters are presented in Fig.11. It may be noticed that the thickness of the fire protection varies considerably depending on the assumptions made and the case study. Namely, the major difference is noticed between the ISO fire curve and the natural fire for high fire resistance rates (beyond 45 minutes), since for the natural curves the specified time resistance represents the duration of the fire, including all phases (i.e. ignition, development, and decay). Since the selected fire scenario is fully developed for a short time (i.e. in less than 30-45min), the consideration of such localized natural fire would be conservative and uneconomical. Similarly, for resistances beyond 45 minutes, the consideration of the standard ISO curve would result in an overestimation of the protection thickness since this curve does not account for the decay phase.
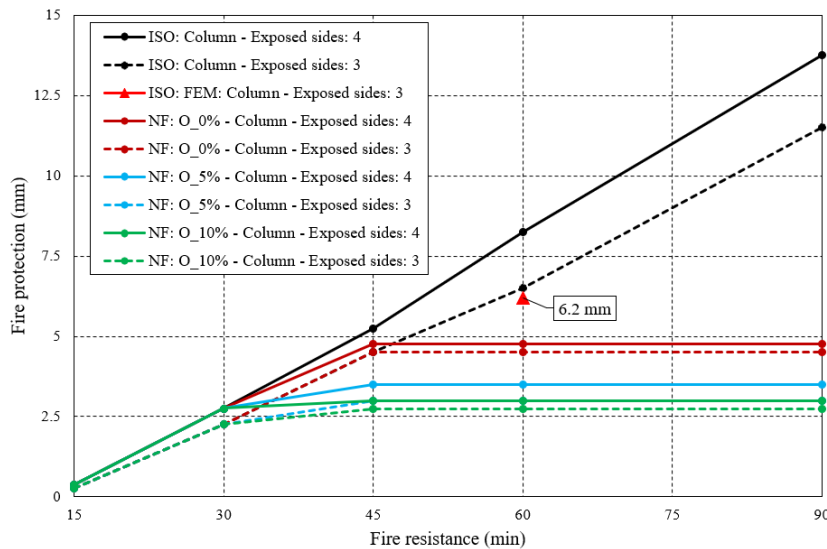

Figure 11: Fire protection thickness varying different parameters

Furthermore, when the ISO curve is considered, depending on the desired fire resistance, the thickness of the fire protection material varies almost linearly from zero for R15 up to almost 15mm for R90. The reason is that the thermal properties of all materials in this study are considered constant over time. The graph also shows the influence of the number of sides exposed to fire (3 or 4), whereby a more severe case (i.e. with all four sides exposed to fire) results in 21% higher thickness on average (c.o.v = 3.6%).

Finally, in the case of natural fires, the influence of the openings is studied, whereby it may be noticed that the consideration of roof openings is favorable for higher fire resistances (faster fire development), and in this case, for the resistances higher than 45 minutes, it results in considerable material savings of 43% and 60% on average, for the openings of 5% and 10%, respectively.

4. CONCLUSIONS

In this work, a web application is presented, developed within the research project Switch2Steel for the calculation and optimization of steel industrial sheds. Using a realistic example of an industrial shed, the results obtained using this tool are compared with results obtained using the more sophisticated finite element software Abaqus, both at ambient and elevated temperatures, and the results obtained are comparable, whereas significant modeling and computational time may be spared using the S2S tool. Finally, using the S2S tool, a small parametric study is carried

out, showing that an imprecise fire design, without considering the real influence of the main parameters on the development and propagation of natural fires, or considering idealized standard temperature-time curve, may lead to excessive amounts of costly protective material, decreasing the competitiveness of steel in this type of buildings.

REFERENCES

[1]   Wald, F.; Simões da Silva, L.; Moore, D.B.; Lennon, T.; Chladná, M.; Santiago, A.; Beneš, M.; Borges, L. (2006). *Experimental behaviour of a steel structure under natural fire*. Fire Safety Journal, vol. 41, no. 7, p. 509-522.

[2]   Laím, L.; Santiago, A.; Caetano, H.; Craveiro, H.D.; Shahbazian, A. (2022). *Numerical analysis and structural fire design of protected SHS steel columns with thermally enhanced gypsum-based mortars*. Journal of Building Engineering, vol. 54, p. 104629.

[3]   CEN, EN 1991-1-1 (2002). *Actions on structures - General actions — Densities, self-weight, imposed loads for buildings*. European Committee for Standardisation, Brussels, Belgium.

[4]   CEN, EN 1991-1-4 (2005). *Actions on structures - General actions — Wind actions*. European Committee for Standardisation, Brussels, Belgium.

[5]   CEN, EN 1990 (2002). *Basis of structural design*. European Committee for Standardisation, Brussels, Belgium.

[6]   McGuire, W.; Gallagher, R.H.; Ziemian, R.D. (2000) *Matrix structural analysis*. 2nd Edition, John Wiley & Sons, Inc.

[7]   CEN, EN 1993-1-1 (2005). *Design of Steel Structures. General Rules and Rules for Buildings*. European Committee for Standardization, Brussels, Belgium.

[8]   CEN, EN 1993-1-2 (2005). *Design of Steel Structures. General Rules. Structural Fire Design*. European Committee for Standardization, Brussels, Belgium.

[9]   CEN, EN 1993-1-5 (2006). *Design of Steel Structures. Plated Structural Elements*. European Committee for Standardisation, Brussels, Belgium.

[10] Peacock, R.D.; McGrattan, K.B.; Forney, G.P.; Reneke, P.A. (2015). *CFAST – Consolidated Fire and Smoke Transport (Version 7)*, Vol. 1: Technical Reference Guide, NIST Technical Note 1889v.

[11] Sourabh, K.; Sumit, S.C.; Vijay, K. (2021). *A review on genetic algorithm: past, present, and future*. Multimedia Tools and Applications, 80:8091–8126.

[12] ISO (1999), *ISO 834-1 Fire resistance tests -Elements of building construction, Part 1: General requirements*. International Organization for Standardization, Geneva, Switzerland.

[13] Abaqus/CAE. (2022) *Standard User's Manual Version*, Dassault systems, Simulia Corp., USA.

[14] CEN, EN 1363-1 (2012). *Fire Resistance Tests - Part 1: General Requirements*, European Committee for Standardization, Brussels, Belgium.

[15] CEN, EN 1991-1-2: 2002. *Eurocode 1: Actions on structures - Part 1-2: General actions - Actions on structures exposed to fire*. European Committee for Standardization. Brussels, Belgium.

[16] Aghabozorgi, P.; Santiago, A.; Laím, L.; Cândido, N. (2022) *A parametric study of tubular steel columns protected with gypsum-based mortars under fire load using finite element modeling*. 12th Int. Conf. on Structures in Fire (SiF 2022), Hong Kong.

THREE LARGE SCALE TRAVELLING FIRE EXPERIMENTS: INFLUENCE OF THE VENTILATION CONDITIONS ON THE FIRE DYNAMICS AND ON STEEL STRUCTURE

Ali. Nadjai [(a)*]   **Naveed Alam** [(b)]   **Marion. Charlier** [(c)]   **Olivier. Vassart** [(d)]

ABSTRACT

In the frame of the European RFCS-TRAFIR project, different natural fire tests in large compartment were conducted by Ulster University, involving steel structure, and aiming at understanding the conditions in which a travelling fire develops, how it behaves and impacts the surrounding structure. During these tests, the fire load was kept identical, but the opening layouts were modified (reduced from test to test). The two first tests highlighted a clear travelling nature while for the third one, a travelling fire leading to flashover occurred. This paper presents steel temperature measurements from steel columns and beam. It is shown that for the steel column, the heating profiles vary along the height, i.e., there is a vertical gradient of temperatures (effect more pronounced for test n°1 and n°2). For the steel beam, it was found that the recorded temperatures in the bottom flange, web and the top flange are non-uniform. The steel temperature profiles are not significantly affected by the change in ventilation from test n°1 to test n°2, conversely to test n°3. The results obtained during the tests and lessons learnt will help to understand the behaviour of the travelling fires and their influence on the structural members. This knowledge will help to reduce the travelling fire associated risks in future.

Keywords: Travelling fire tests; Steel Structure; Large-scale compartment; Natural fire tests.

---

[a]***** Ulster University (a.nadjai@ulster.ac.uk)**,** Corresponding author.

[b] Ulster University (n.alam@ulster.ac.uk)**.**

[c] Arcelor Mittal Luxembourg (marion.charlier@arcelormittal.com)**.**

[d] Arcelor Mittal Luxembourg (Olivier.vassart@arcelormittal.com)**.**

1. INTRODUCTION

It is well established that the response of a structure subjected to fire is dependent on the fire exposure conditions. Small compartment fires behave in a well understood manner defined as a post-flashover fire with uniform temperatures. Over time, the building designs have evolved and with modern architecture, there is an increase of open large-floor plan spaces, for which the assumption of post-flashover fire and uniform temperatures does not hold [1,2]. Instead, there is a smaller localised fire that moves across the floor starting in a certain area or a point. The current standard fire as well as the compartment fire exposure conditions have been developed by using data from small compartment tests. The existing test data is available from small compartment tests, the concept of a uniform distribution of gas temperatures fits well when dealing with similar scenarios. In case of large compartments, the assumption of uniform temperature distribution does not hold, and more research is needed to address such cases. During recent fires, the travelling fires have been observed and investigated, which include the destruction of the World Trade Centre Towers in New York City in 2001 [3], the Windsor Tower in Madrid in 2005 [4], and the Faculty of TU Delft Architecture building in Netherlands in 2008 [5]. The detailed investigations on the fire events in large compartments have revealed that such fires have a great deal of non-uniformity unlike the small compartment fires. They generally burn locally and move across floor which generates non-uniform temperatures and transient heating of the surrounding structure and are idealized as the travelling fires [1-6].

Although majority of the fire exposure scenarios provided in the design codes consider uniform temperatures within the compartment, there is also some guidance available related to non-uniform temperatures. In the EC2 (EN1991-1-2) [6], two models are provided which consider a non-uniform temperature distribution, the localised fire model, and the advanced fire models (zone models and computational fluid dynamic models). Although the localised fire is assumed to be static, it is possible to consider several localised fires, one localised fire spreading to other localised fires. Such effect covers a fire spread but does not directly allow to fully capture the science behind the travelling fires. For zone models, the situation starts as a two-zone model which assumes accumulation of combustion products in a layer beneath the ceiling, with a horizontal interface. Uniform characteristics of the gas may be assumed in each layer and the exchanges of mass, energy and chemical substance are calculated between these different zones [2]. Although this model considers a non- uniform temperature distribution within the compartment, it does not translate the travelling nature of a fire. The CFD (computational fluid dynamic) models enable to solve numerically the partial differential equations giving in all points of the compartment, the thermo-dynamic and aero-dynamic variables. These models are consequently complex and imply a high computational cost. Further, these modules need further refining through comparisons with experimental data. The recent years have seen growing interest in investigating travelling fires which underlined the inadequacy of uniform heating in large compartments [7-15]. Further research efforts are needed, especially to extend the experimental data related to such fire scenarios which is scarce, limited, and partial.

2. COMPARTMENT EXPERIMENTAL TESTS

Three large natural fire tests involving a continuous wood crib fuel bed in a steel-framed structure were conducted, aiming at performing large-scale tests with no artificial control over the fire dynamics with three specific objectives listed as:

- A fuel-controlled travelling fire, referred as test n°1 (more details given by Nadjai et al. [16]);
- Another travelling fire, with less ventilation than in test n°1, referred as test n°2 (more details given by Alam et al. [17]).
- A ventilation-controlled fire leading to a flashover, referred as test n°3 [18]:

The floor plan between the outer gridlines of the test structure was 15 m x 9 m while the level of the ceiling from the floor finish surface was 2.90 m as shown in Figure 1. The test compartment is a representative of a modern office building and represents a part of an open layout office building (see Figure 1a). The structure was made of hot rolled steel beams and columns as the main structural frame while hollow-core precast slabs were used for the construction of ceiling, see Figure 1. A solid concrete wall was built along one of the shorter sides while 1.0 m down-stands were provided along the longer dimensions of the test compartment as seen in Figure 1a.

The fuel load used for the travelling fire tests was determined to be a representative of an office building following the recommendations of the Eurocode 1 [6]. As the test compartment was representative of an office building, Eurocodes provide a medium fire growth rate (t_α = 300 seconds) and a fire load density of 511 MJ/m^2 for such occupancies. Gamba [11] performed a series of fire tests with uniformly distributed cellulosic fire loads, aiming at defining an arrangement representative of an office building according to Eurocode 1. This work led to devise a well-established methodology, used to define the fuel load for the experimental campaign described in this paper. To achieve a medium fire growth rate for the office building and reach a fire load density of 511 MJ/m^2, 9 layers of wooden sticks with an axis distance of 120 mm (90 mm intervals) were provided in three different directions. The wood sticks were 30 mm wide and 35 mm deep. The first layer of the wooden sticks was laid at 60° angle while the second layer was laid at an angle of 120°. The third layer was at 0° or 180° and the process was repeated in such a way the 6th layer of the sticks laid at 0° or 180° had a lateral offset of 60 mm with respect to the third layer
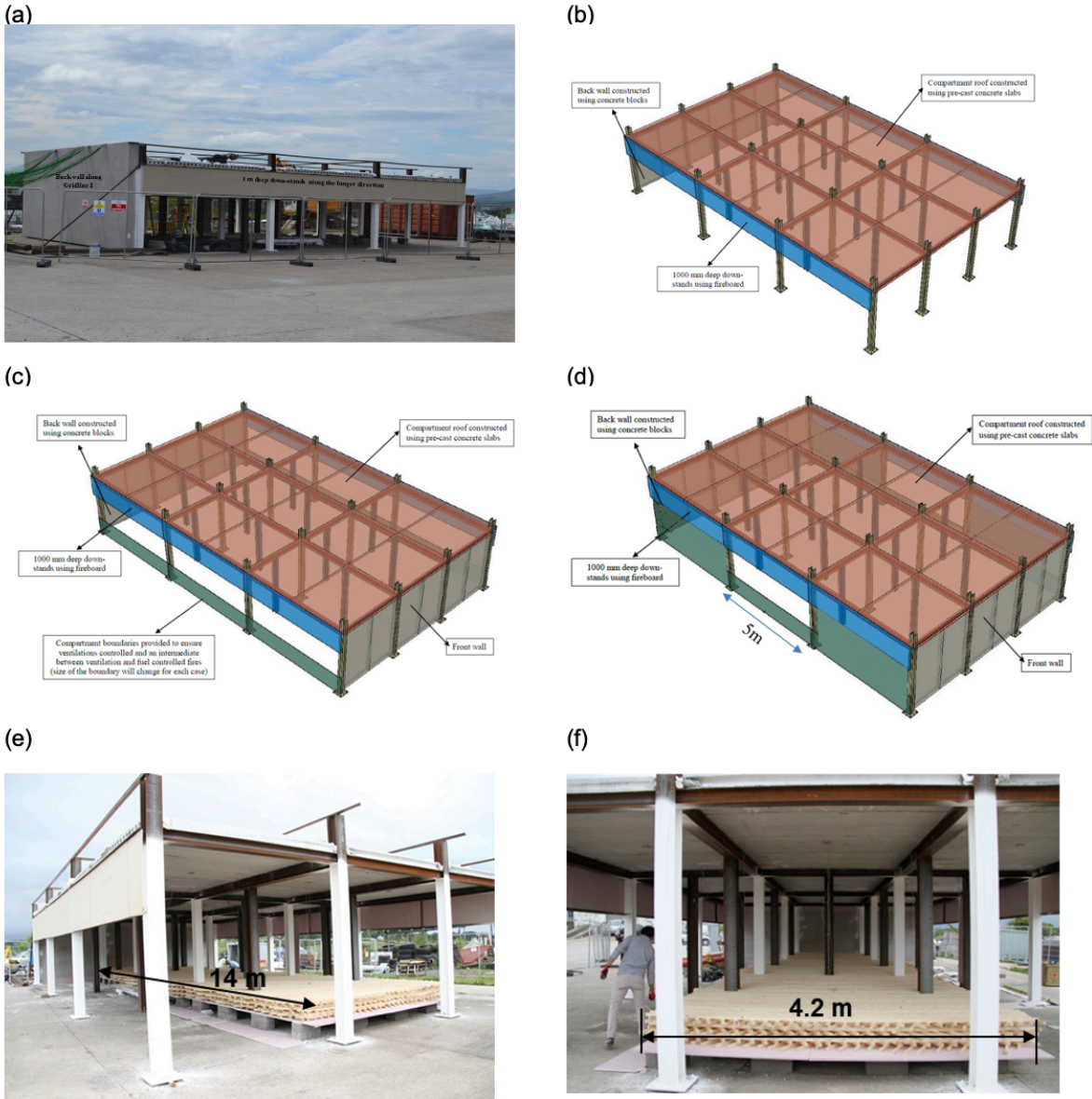

Figure 1: Layout of the three tests (highlighting the reduction in openings) and the fuel load arrangement.

as shown in Figure 1 (e) and (f). The final layer (the ninth layer) of the fuel wood was at 0° or 180°, such an arrangement helped to visually observe the travelling behaviour of fire from one stick to another. The fuel wood source consisted of the species "*Picea abies*" with an average density 470 kg/m^3 having a moisture content of

15.22%. The fuel wood was provided along the centre of the test compartment. The fire load was 14 m long stretching along the longer dimension of the test compartment. For convenience, a gap of 0.5 m was maintained between the walls and the edge of the fuel bed at both ends as seen in Figure 2 The width of the fuel bed was 4.2 m and was aligned with the centre line of the compartment. Such an arrangement of the fire load resulted in a distance of 2.4 m from the edge of the fuel bed to the centreline of the columns provided along in the longer dimension along gridline Ⓐ and Ⓓ.

For the purpose of ignition, a steel tray was positioned at 0.5 m from their edge close to gridline 1. This location generates a 1 m distance between the back wall and the centre of the steel tray. The fire load was kept identical (and representative of an office building following EN 1991-1-2 [6]; only the opening layouts were modified (reduced from test n°1 (total opening area of 85.2 m^2, see Figure 1b to test n°2 (total opening area of 30 m^2), see Figure 1c and from test n°2 to test n°3 (total opening area of 10 m^2, see Figure 1d.

Some dummy columns (which can be observed in Figure 1 (b,c,d)) provided for data acquisition purposes were erected between the concrete floor and the roof beams. The dummy columns were fixed to the floor and the bottom flange of the beams using two anchorage bolts. The steel used for the construction of the test compartment (including the dummy columns) was grade S355. Both the structural and dummy columns, as well as the beams provided along the longer direction of the test compartment, consisted of HEA 200 hot rolled steel sections (see Table 1). As the test compartment was intended to be used for multiple fire tests, the structural columns of the steel frame were protected using intumescent coating (R60) in order to maintain the structural integrity during the fire tests. It is seen in Figure 1(e) that only the structural columns were protected while the dummy columns are kept unprotected for data acquisition purposes. A summary of the steel frame used for the test is given in Table 1. It should be noted that the steel beams of the test compartment were not protected as these were restrained by the dummy columns in the middle of their span. They were also restrained by the precast slabs provided on top. As there were no additional loads applied on the beams, they were used for thermal data acquisition purposes.
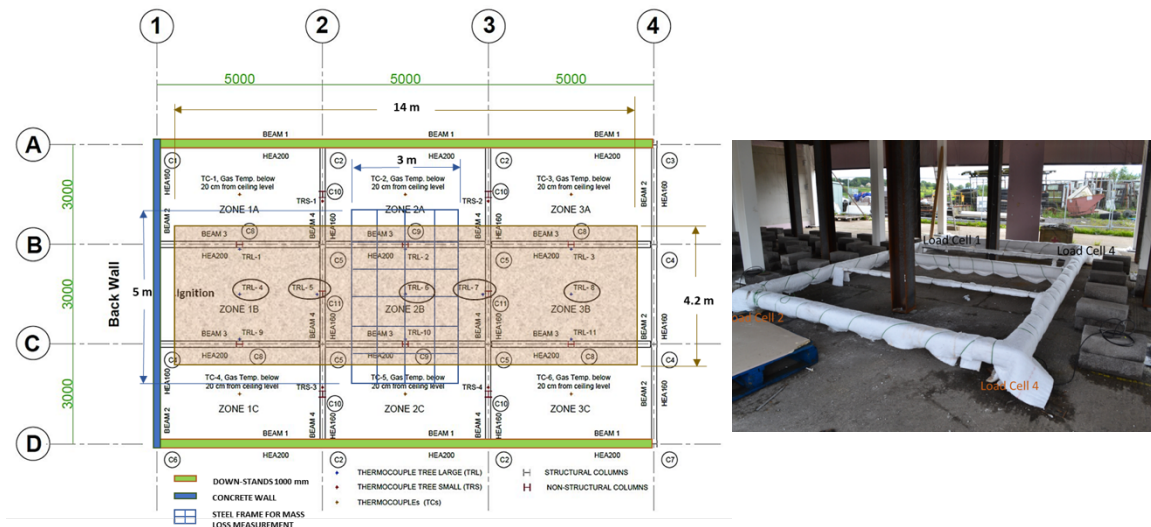

Figure 2: Fuel load arrangement and steel column provided in the test compartment.

Table 1: Summary of the steel frame and fire protection details

Description	Sections	Section Factor (m^{-1})	Length Height (m)	Protection Applied
Structural columns	HEA 200	211	3.5	Yes: R60
Dummy columns	HEA 200	211	2.7	No
Long beams	HEA 200	174	4.8	No
Short beams	HEA 160	192	3.0	No

One objective of this experimental work was to record the mass loss of the fuel wood during the travelling fire test. The mass loss of the fuel wood was monitored in the middle of the compartment between gridlines ② and ③ using a steel platform shown in Figure 2. The steel platform was 5 m long x 3 m wide and was supported on four load cells a shown in Figure 2. The load cells were connected to the data acquisition system to record the data. To avoid any damage to the steel platform during the fire tests, fire blanked was wrapped around each part. In addition to the steel platform, the load cells and the cables of the data acquisition system were also protected using the fire blanket as shown in Figure 2. On top of the steel platform, two layers of gypsum fire board were provided to support the fuel wood.

3. THE RECORDING OF TEMPERATURES

The gas temperatures in the compartment were recorded using thermocouples provided at different levels as an individual sensor and in groups as thermocouple trees. The details of the thermocouple trees positioning are shown in Figure 2. In this paper, recordings from some of the thermocouples provided along the centreline of the test compartment have been provided. The thermocouples along the centreline of the test compartment were provided using five thermocouple trees, TRL-4 through TRL-8. The first thermocouple tree, TRL-4, was positioned at 1.5 m from the back wall while the remaining thermocouple trees, TRL-5 through TRL-8 were positioned at 2.5 m intervals All five trees were equipped with six thermocouples at different levels. The positioning of the first thermocouple from the floor finish level was 0.5 m (L1). The thermocouples at levels 2, 3, 4 and 5 were at 1.0 m, 1.5 m, 2.0 m, and 2.5 m respectively (Figure 3(a)). The last thermocouple provided in each tree was at 2.7 m from the floor finish level (L6). Such arrangement of thermocouples allowed temperature recordings at different locations along the length as well at different heights and levels of the test compartment.
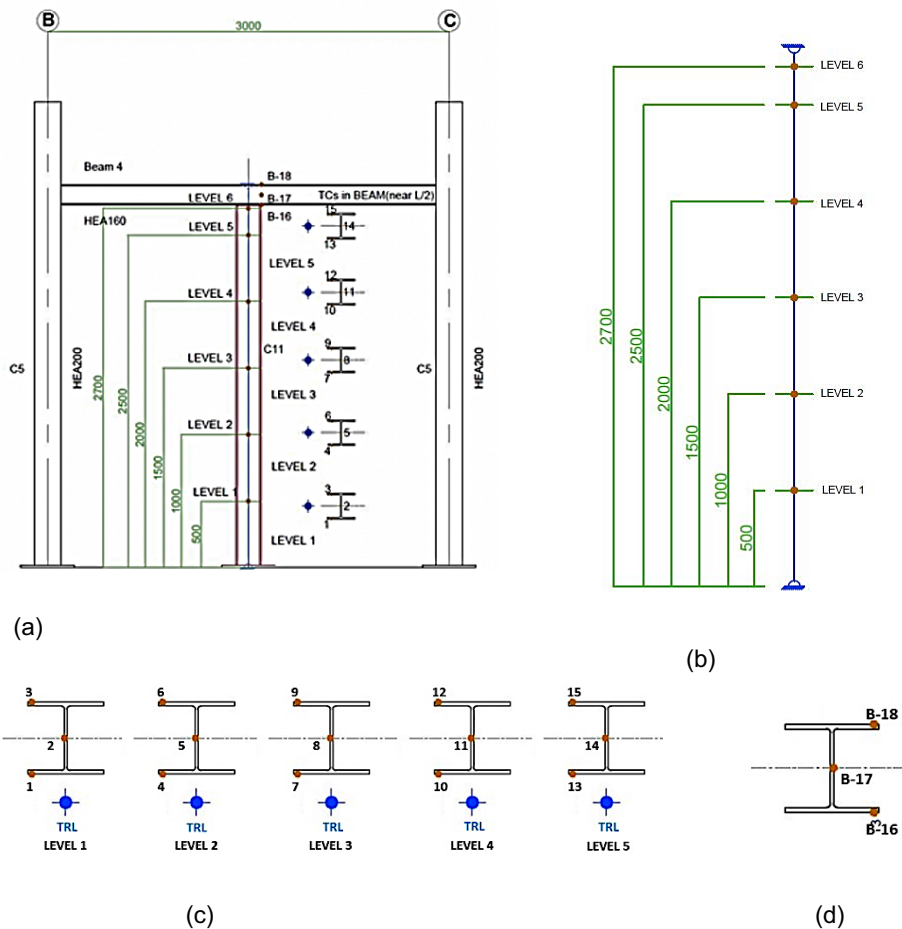

Figure 3: Details of thermocouples, (a) positioning of thermocouple trees (b) thermocouples in beams and columns, (c) thermocouples in large thermocouple trees; (d) thermocouples in columns, a closer view; (e) thermocouples in beams, a closer view

To analyse the influence of the travelling fire on the surrounding steel structure, intensive instrumentation was conducted to record the temperatures in the columns and the beams. Although temperatures were monitored in different columns, details of the instrumentation and recorded temperatures in the dummy columns located along the centreline of the travelling fire have been provided in this article. These columns are identified as C11 in Figure 2 which are adjacent to thermocouple trees TRL-5 and TRL-7. Temperatures in the columns (C11) were monitored at five levels: L1 to L5 as show in Figure 3(a). Temperatures in the columns at each level were recorded using three thermocouples. Two thermocouples were provided in the flanges while the third thermocouple was provided in the web as shown in Figure 3(b). In total, 15 thermocouples were employed to record the temperatures in each column positioned along the centreline of the test compartment within the fuel wood. These thermocouples have been identified as 1 through 15 in Figure 3(c).

Temperatures in the steel beams were monitored in the middle of the span adjacent to the thermocouple trees. In this paper, the discussion has been focused on the central beams between the gridlines Ⓑ and Ⓒ provided along the gridlines ② and ③. The selected beams are adjacent to thermocouple trees TRL-5 and TRL-7, Figure 2. Temperatures in each beam were monitored via three thermocouples. The first thermocouple was provided in the bottom flange (B-16) while the second thermocouple was provided in the web (B-17). The last thermocouple in the beams (B-18) was provided in the top flange as shown in Figure 3(d). It should be realised that the thermocouples in the structural steel elements were fixed by inserting them into the holes drilled at designated positions in selected beams and columns. The holes in the structural elements were 1.5 mm in diameter and were drilled using Bosch and DeWalt power drills.

4. THE FIRE DYNAMICS: COMPARISON

For the test n°1, the travelling behaviour (i.e. when both the fire front and the fire back progress) of the fire started at 28 minutes from ignition. This evolution suggests a fairly constant flame thickness of around 3.5 meters, with the lowest value occurring when the fire reached the central bay (quantifying the flame thickness with precision is not straightforward as the fire front presented an arch shape). For the test n°2 and n°3, the fire front also presented an arch (convex) shape and the travelling behaviour started at 27 and 29 minutes from ignition, respectively. For test n°2, the fire presented a travelling behaviour from the beginning until the end of the experiment, and the flame thickness evolved from around 3 meters to around 5 meters. For the test n°3, after 55 minutes from ignition, flames escaped through the openings of the compartment, confirming a ventilation-controlled fire. After 58 minutes, a small part of the fuel bed area near the fore-end of the compartment (isolated from the flames), ignited, phenomenon illustrating flashover. As for test n°2, the flame thickness increased with time.

5. GAS TEMPERATURES: COMPARISON BETWEEN THE THREE TESTS

Gas temperatures are recorded at different locations and levels using thermocouples. All thermocouples used for monitoring of temperatures in the compartment and in the structure are type K-310 with bead size measuring 1,5 mm. The length of all thermocouples was 3 m. Thermocouples trees are placed within the central zones along the fuel bed between gridlines B and C: they are equipped with thermocouples provided at six different levels. The first thermocouple was provided at 0,5 m from the floor finish level while the last one was provided at 2,7 m as shown in Figure 3.

The recoded data in the middle of the test compartment within the fuel bed using thermocouple tree TRL6, is shown in Figure 4. At level 3 (around mid-height), at 30 minutes: 40°C are measured for test n°1, 110°C for test n°2 and 200°C for test n°3. During test n°3 the maximum recorded gas temperature in TRL6 is approximately 1000ºC (versus 1000 C and 1100°C for tests n°1 and n°2, respectively) after around 58 minutes from ignition (measures from level 1 are not considered when finding this maximum, given the thermocouple deficiency for test n°3). During the peak of test n°3, contrarily to test n°2 where the higher temperatures are encountered for the lower levels, the temperatures are coinciding (around 1000°C). After the peak, the recorded temperatures reduce as the fire travels towards the end of the compartment. During the whole duration of the test, the higher temperatures are recorded at higher levels, and lower temperatures for lower levels.
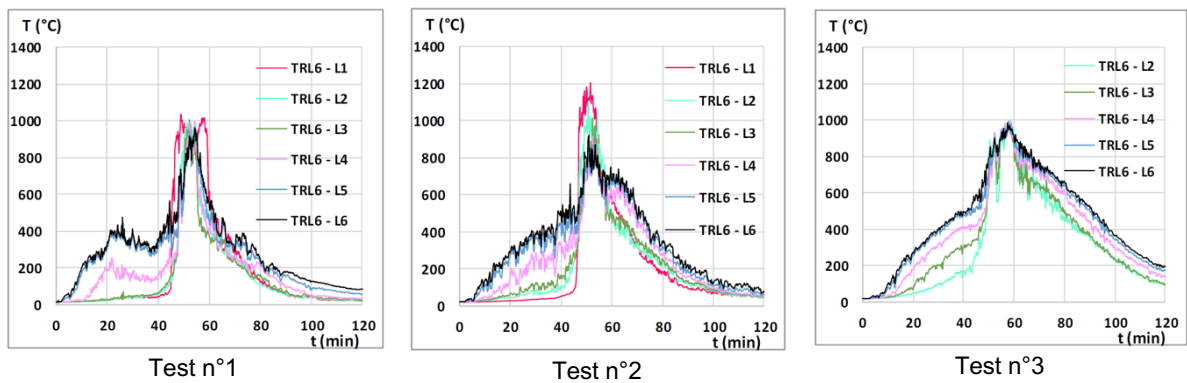
Figure 4: Gas temperatures in tests n°1,2 and 3, recorded in central TRL6.

6. STEEL TEMPERATURES: COMPARISON BETWEEN THE THREE TESTS

Temperatures were recorded in the unprotected dummy columns as shown in Figure 3. Figures 5,6 and 7 depicts in (a) the steel temperature measurements in column next to TRL7 (RHS-F); (b) Steel temperature measurements in column next to TRL5 (RHS-F). Tables 2,3 and 4 provides the maximum temperatures recorded in columns next to TRL5 and TRL7 at each level, the difference between these values (Δ(TRL7-TRL5)) and within each column, the maximum temperature gradient (Δ). The following observations can be made:

- The maximum steel temperature is 887°C at 68 minutes for the column next to TRL7 (versus 838°C at 63 minutes for test n°2 and 799°C at 63 minutes for test n°1) while it is 890°C at 56 minutes for the one next to TRL5 (versus 781°C at 49 minutes for test n°2 and 731°C at 46 minutes for test n°1). While there was no significant change while comparing tests n°1 and n°2, it appears the lower opening factor from test n°3 results in higher steel temperatures (around 100°C higher).

- For test n°2, the maximum temperature gradient within each column (Δ) was almost identical whereas for test n°1, a lower gradient was observed in column next to TRL7 than in column next to TRL5. For test n°3, the same tendency than for test n°1 is met. This could be explained by the flame thickness which is lower close to TRL5. For a same rate of heat released density, a thicker flame (and therefore a bigger diameter if the fire is represented as a localised fire) implies a higher flame length, implying a lower gradient in temperatures for the given heights.

- In previous tests, the gas temperatures from TRL5 were globally lower than the ones from other TRL's placed further away in the compartment, and this is also observed in the steel temperatures. This is not the case anymore for test n°3. When looking at the differences between maximum temperatures recorded in the two columns for each level (Δ(TRL7-TRL5)), one can see these values are very low, highlighting very similar steel temperatures in TRL5 and TRL7. Having less openings than in previous tests, more heat is contained within the compartment, blurring the differences in the different columns.

- When evaluating the period during which high temperatures (arbitrarily chosen above 600°C) are encountered, it can be observed that this period is quite similar for the column next to TRL7 (from ~60 to ~90 minutes, i.e. during approximatively 30 minutes) and for the one close to TRL5 (from ~45 to ~80 minutes, i.e. during approximatively 35 minutes). This period was ~20 minutes for test n°2, and ~15 minutes for test n°1, implying that the change in ventilation conditions (lowering the opening surfaces) elongates the heating time.

278

Table 2: Maximum steel temperatures measured during test n°1 in columns next to TRL7 and TRL5 (flanges)

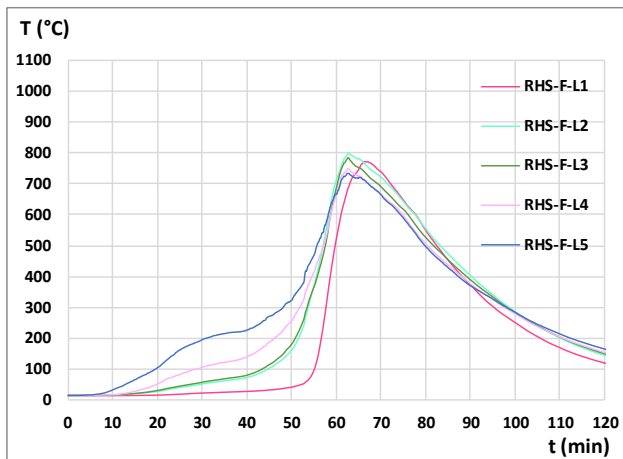|	Level 1	Level 2	Level 3	Level 4	Level 5	Δ
TRL5	731°C	663°C	652°C	640°C	654°C	91°C
TRL7	772°C	799°C	786°C	750°C	734°C	65°C
Δ(TRL7-TRL5)	41°C	136°C	134°C	110°C	80°C	
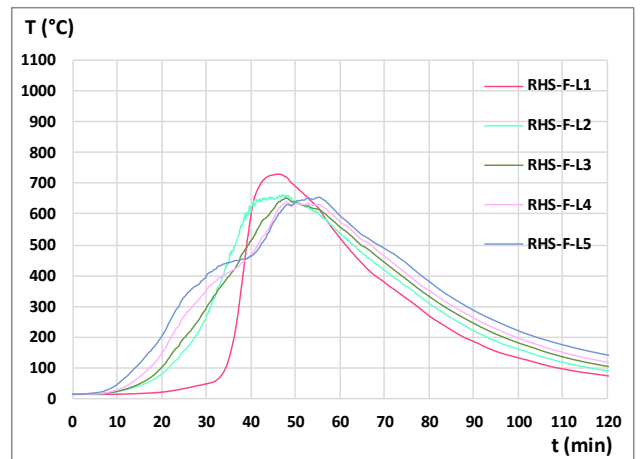
Figure 5: (a) Steel temperature measurements during test n°1 in column next to TRL7 (flange); (b) Steel temperature measurements during test n°1 in column next to TRL5 (flange)

Table 3: Maximum steel temperatures measured during test n°2 in columns next to TRL7 and TRL5 (flanges)

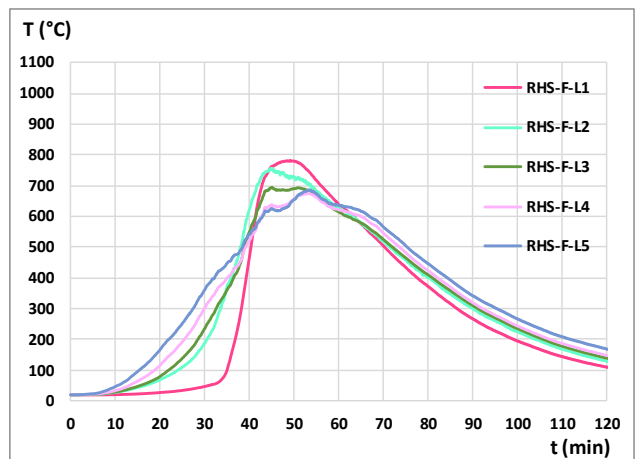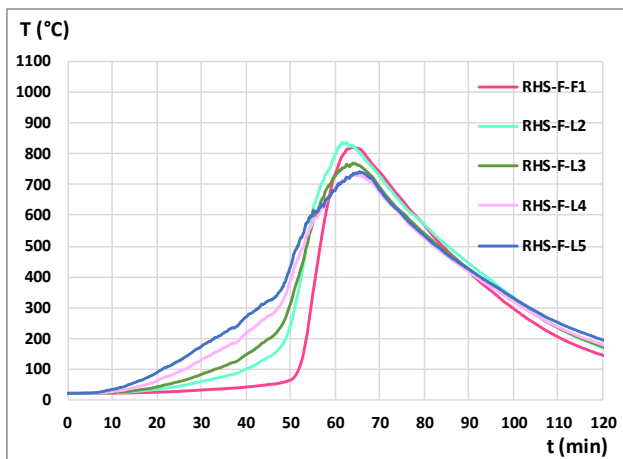|	Level 1	Level 2	Level 3	Level 4	Level 5	Δ
TRL5	781°C	757°C	694°C	675°C	686°C	106°C
TRL7	822°C	838°C	769°C	730°C	741°C	108°C
Δ(TRL7-TRL5)	41°C	81°C	75°C	55°C	55°C	

Figure 6: (a) Steel temperature measurements during test n°2 in column next to TRL7 (flange); (b) Steel temperature measurements during test n°2 in column next to TRL5 (flange)

Table 4: Maximum steel temperatures measured during test n°3 in columns next to TRL7 and TRL5 (flanges)

	Level 1	Level 2	Level 3	Level 4	Level 5	Δ
TRL5	806°C	890°C	882°C	852°C	850°C	84°C°
TRL7	824°C	887°C	853°C	846°C	859°C	63°C°
Δ(TRL7-TRL5)	18°C	3°C	29°C	6°C	9°C	

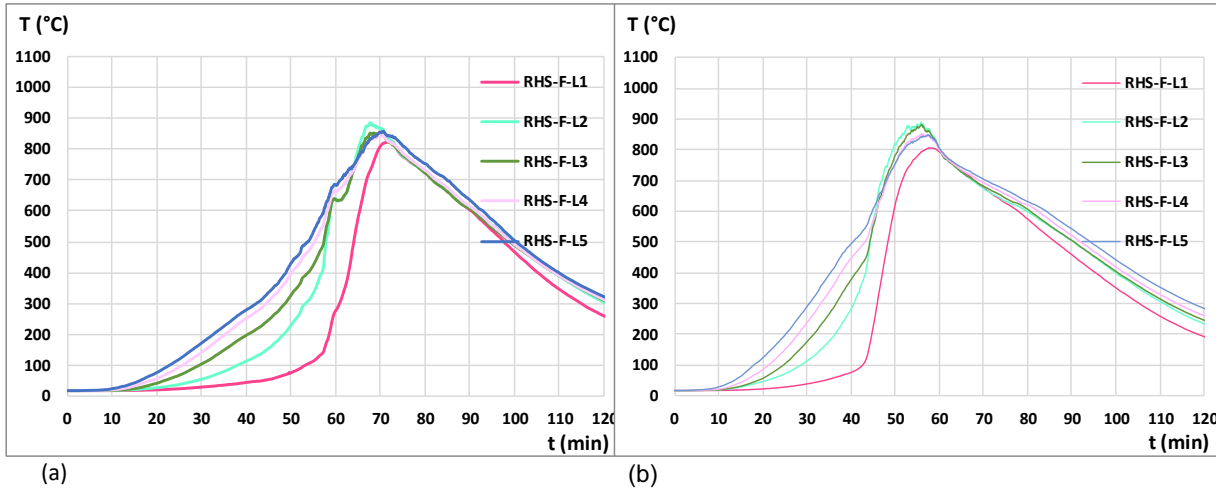(a)   (b)

Figure 7: Steel temperature measurements during test n°3 in column, a) next to TRL7 (flange); (b) next to TRL5 (flange)

Steel beams were instrumented with one set of three thermocouples, two on the flanges and one on the web, placed at mid-span. The beam considered for data presentation purpose is the hot rolled steel profile HE 200 A, placed along gridline B between gridlines 2 and 3. The thermocouple positioning is described in Figure 3 (c) (thermocouples in the bottom flange, the web and in the upper flange). The steel temperature measured in the beam are depicted in Figure 8. Three temperature evolutions are given: "BF" corresponds to the bottom flange temperature, "TF" to the top flange temperature and "Web" to the web temperature of the hot rolled profile. These are non-uniform: the temperatures in the top flange are lesser as compared to those recorded in the bottom flange (which can be explained by the protection brought by the concrete slab). As for the columns, the beam temperatures are higher in test n°3, for which less openings were present and therefore more heat containment. The Figure 9 depicts the averaged steel temperature measurements during test n°1, 2 and 3 in the considered beam. It can be observed that the curves broadly coincide for tests n°1 and n°2. Also, all three tests present a similar growing branch, but higher steel temperatures are met in test n°3, and these elevated temperatures are met for a longer period.

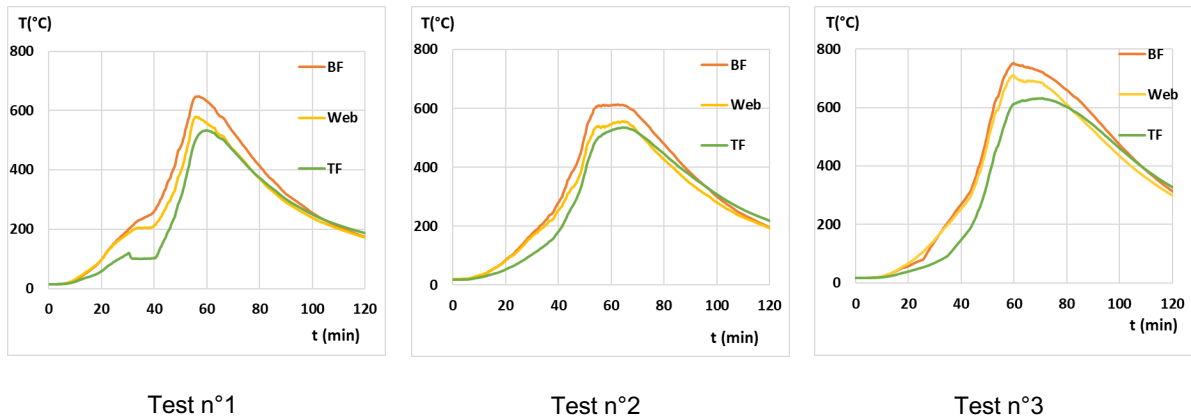Test n°1   Test n°2   Test n°3

Figure 8: Steel temperature measurements during test n°1, 2 and 3 in the beam placed along gridline B between gridlines 2 and 3
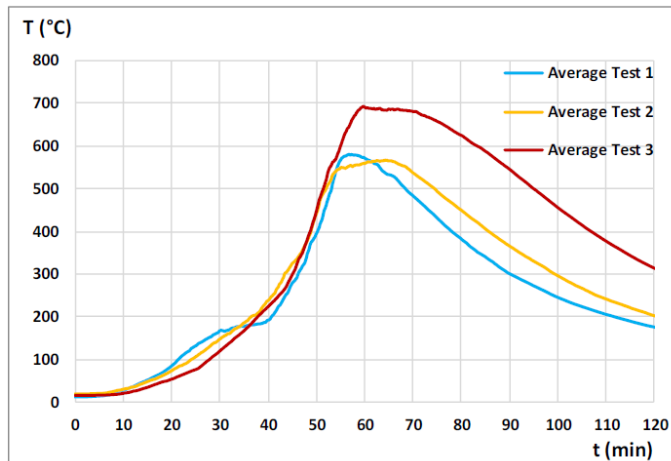
Figure 9: Averaged Steel temperature measurements during test n°1, 2 and 3 in beam placed along gridline B between gridlines 2 and 3.

7. CONCLUSIONS

Three large natural fire tests involving a continuous wood crib fuel bed in a steel-framed structure were conducted, aiming at performing large-scale tests with no artificial control over the fire dynamics. The fire load was kept identical (and representative of an office building following EN 1991-1-2); only the opening layouts were modified. The only change between these experiments was the total openings surface (reduced from test n°1 to test n°2 and from test n°2 to test n°3), which highlighted the influence of the ventilation conditions on the type of fire scenario. Indeed, a clear travelling fire was observed for test n°1 and test n°2 while a travelling fire leading to a flashover occurred for test n°3.

For the three tests, it can be observed that the gas temperatures evolutions present different profiles. For a given thermocouple tree, the temperatures measured at higher levels (levels 5 and 6) start to increase at earlier stages of the test as hot gases rise, resulting in a hot layer in the upper part of the compartment. This is followed by the rise in temperatures at the level 4, and then at lower levels (1-2-3) when flames reach the thermocouple tree. For the steel column temperatures, it can be observed that the heating profiles vary along the height of the column, i.e. there is a vertical gradient of temperatures (effect more pronounced for test n°1 and n°2). For the three experiments, the maximum steel temperatures in the columns were around 800°C, 850°C and 900°C, respectively. For the steel beam temperatures, it was found that the recorded temperatures in the bottom flange, web and the top flange are non-uniform, with temperatures in the top flange being the lowest. For the three experiments, the maximum steel temperatures in the beam were around 700°C, 700°C and 800°C, respectively. It can be observed that steel temperature profiles are not significantly affected by the change in ventilation from test n°1 to test n°2, conversely to test n°3.

ACKNOWLEDGEMENTS

REFERENCES

[1] J. Stern-Gottfried, G. Rein (2012). Travelling fires for structural design – Part I: Literature review. Fire Safety Journal 54. pp 74- 85.

[2] Dai X, Welch S and Usmani A (2017) A critical review of 'travelling fire' scenarios for performance-based structural engineering. Fire Safety Journal 91: 568–578.

[3] R. G. Gann, A. Hamins, K. McGrattan, H. E. Nelson, T. J. Ohlemiller, K. R. Prasad, and W. M. Pitts, (2013) Reconstruction of the fires and thermal environment in World Trade Center buildings 1, 2, and 7, Fire Technol., vol. 49, pp. 679–707.

[4] I. Fletcher, A. Borg, N. Hitchen, and S. Welch, (2005) Performance of concrete in fire: A review of the state of the art, with a case study of the Windsor Tower fire," in 4th International Work- shop in Structures in Fire, pp. 779–790.

[5] D. M. Zannoni, J. G. H. Bos, D. K. E. Engel, and P. dr. U. (2008) Rosenthal, Brand bij Bouwkunde.

[6] EN1991-1-2 (2002). Eurocode 1: Actions on structures – Part 1- 2: General Actions on structures exposed to fire. CEN, Brussels.

[7] G. Rein, X. Zhang, P. Williams, B. Hume, A. Heise, A. Jowsey, B. Lane, and J. L. Torero, (2007) Multi-storey fire analysis for high- rise buildings, in Proceedings of the 11th International Inter- flam Conference, London, UK, pp. 605–616.

[8] K. Horová, T. Jána, F. Wald (2013). Temperature heterogeneity during travelling fire on experimental building. Advances in En- gineering Software 62-63. pp 119-130.

[9] J.P. Hidalgo, A. Cowlard, C. Abecassis-Empis, C. Maluk, A.H. Maj- dalani, S. Kahrmann, R. Hilditch, M. Krajcovic, J.L. Torero (2017). An experimental study of full-scale open floor plan en- closure fires. Fire Safety Journal 89. pp 22-40.

[10] J. P. Hidalgo, T Goode, V. Gupta, A. Cowlard, C Abecassis-Empis, J. Maclean, A. Barlett, C. Maluk, J.M.

[11] Montalva, A. F. Osorio, J. L. Torero (2019). The Malveira fire test: Full-scale demonstration of fire modes in open-plan compartments. Fire Safety Jour- nal vol.108 No 102827.

[12] A. Gamba, M. Charlier, J.M. Franssen (2020). Propagation tests with uniformly distributed cellulosic fire load. Fire Safety Journal 117, 103213.

[13] J. Degler, A. Eliasson, A. Anderson, D. Lange, D. Rush (2015). A- priori modelling of the Tisova fire test as input to the experimental work. Proc. 1rst Int. Conf. on Struct. Safety under Fire & Blast, Glasgow, UK.

[14] M. Charlier, A. Gamba, X. Dai, S. Welch, O. Vassart, J.M. Franssen (2020). Modelling the influence of steel structure compartment geometry on travelling fires. Proceedings of the Institution of Civil Engineers – Structures and Buildings. https://doi.org/10.1680/jstbu.20.00073.

[15] A. Nadjai, N. Alam, M. Charlier, O. Vassart, S. Welch, A. Glorieux, J. Sjöström, Large scale fire test: The development of a travelling fire in open ventilation conditions and its influence on the surrounding steel structure, Fire Safety Journal, http://dx.doi.org/10.1016/j.firesaf.2022.103575, April 2022.

[16] A. Nadjai, N. Alam, M. Charlier, O. Vassart, S. Xu Dai, JM. Franssen, J. Sjöström, Travelling fire in full scale experimental building subjected to open ventilation conditions, Journal of Structural Fire Engineering, http://dx.doi.org/10.1108/JSFE-06-2021-0037, May 2022

[17] A. Naveed, A. Nadjai, M. Charlier, O. Vassart, S. Welch, J. Sjöström, X. Dai. Large-Scale travelling fire tests with open ventilation conditions and their effect on the surrounding steel structure – The second fire test. Journal of Constructional Steel Research, http://dx.doi.org/10.1016/j.jcsr.2021.107032, 2022.

[18] A. Nadjai, N. Alam, M. Charlier, O. Vassart, J.-M. Franssen and S. Welch. Large scale fire test: travelling fire leading to flashover under ventilation controlled conditions and its influence on the surrounding steel structure. Proceedings of the 12th International Conference on Structures in Fire, The Hong Kong Polytechnics University, December 2022.

OPTIMIZED DIMENSIONING OF RIBBED SLABS IN FIRE SITUATION, USING GENETIC ALGORITHM

Jessyca P. A. N. Fernandes 1

Tiago A. C. Pires 2,*

José J. R. Silva 3

ABSTRACT

The great development of technologies and numerical methods, has been providing increasingly better conditions for structural design, making the design of structures more productive and economical. The vast majority of concrete structures are not analyzed and designed in a fire situation. In this context, this work has as main objective to develop a computational interface to optimize the cross section of ribbed slabs in normal situation and in a fire situation, that meets the maximum functionality and safety with the minimum cost, following the normative prescriptions. The optimization algorithm and the computational interface were implemented using MATLAB. From the results, it was observed that the consumption of concrete and steel tends to be higher in the cases of slabs with cut fire function. In this way, it can be concluded that the use of optimization tools allows to obtain more economical solutions. The Genetic Algorithm method presented a good performance in the optimization and it can be highlighted as positive points: the ease of implementation and the flexibility in dealing with problems with several constraints, functioning as a tool that assists the engineer in its decision making.

Keywords: Optimization, Slabs, Fire Situation.

1. INTRODUCTION

The great development of the technologies and numerical methods in the field of Computational Mechanics, has been providing increasingly better conditions to analyze high complexity structures through numerical methods used for structural analysis and design. With the use of optimization techniques, it becomes possible to design structures or structural elements more rationalized, by reducing the material used for production and consequently of its final cost.

Several existing researches prove the efficiency of the optimization models applied to concrete. One of the optimization techniques, which has been gaining prominence, is the Genetic Algorithm (GA) technique, which was presented in the 1970s by researcher John Holland of the University of Michigan.

The majority of reinforced concrete structures are analyzed and projected based on the requirements of Brazilian Standard NBR 6118 (2014) Concrete Structures Project - Procedure, taking into account the requests arising from permanent and variable actions according to NBR 8681 (2004) Actions and safety in structures - Procedure. In general exceptional actions in the event of fires are rare are considered in the design of concrete structures. The current standard, NBR 15200 (2012) Design of concrete structures in a fire situation - Procedure, establishes the necessary criteria for the safety verification of

---

[1] UFPE (jessycanunes@ufpe.br)**.**

[2,] UFPE (tiago.anselmo@ufpe.br)

[3] UFPE (jjrs@ufpe.br)**.**

concrete structures in a fire situation, designed according to NBR 6118 (2014), demonstrating their compliance with the fire resistance requirements established in NBR 14432 (2001) Fire resistance requirements of building elements - Procedure.

In Brazil there is no disclosure of official data on fire cases, this framework makes it too impossible to discuss and elaborate efficient public policies to face this problem, with the aim of changing this scenario that the Sprinkler Brazil Institute - ISB since 2012 monitors related news to "structural fires" in Brazil, defined as those that can happen in several built-up places (hospitals, hotels, industrial and commercial installations, schools, warehouses, libraries, etc.) and that could be avoided or circumvented if an effective system of fires existed. fire safety. It is estimated, however, that the calculated numbers represent less than 3% of the actual number of occurrences.

In Brazil there is a great lack of studies that deal with fire in reinforced concrete structures. Studies indicate that when the thermal action from fire is used in structural design, the costs of fire projects are relatively lower when compared to possible restorations (ALBUQUERQUE, 2012). The fires that occurred in the 1970s in São Paulo, in the Andraus and Joelma buildings, generated a great impact, which until that moment was treated as something distant, became real and demanded immediate changes. In Brazilian legislation, this episode marked the beginning of a great debate to review construction methods and define standards for fire safety in buildings (SILVA, 2016).

Currently, there are several structural systems that employ reinforced concrete slabs, such as massive, ribbed, and prestressed slabs, among others. In Brazil, ribbed slabs are much used in civil construction, since their manufacture is simple and does not involve expensive or difficult maintenance equipment. Among the main advantages in its use, stand out the ease of handling and saving of materials.

The need for safety allied with saving materials is a goal sought by engineers. In this context, the present work aims to develop a computational interface for the optimized dimensioning of molded slabs in the site, which meets the normative constraints imposed by: NBR 6118 (2014) and NBR 15200 (2012). Also perform a comparison between the conventional sizing and the sizing with fire situation.

Among the first works that used optimization methods in civil engineering stand out: the work of Heyman (1951), which used linear programming to minimize material consumption in the design of beams and frames in the plastic regime. Since then, there has been considerable progress, noted by the number of books and articles published related to the topic.Among the researches that involved Genetic Algorithm and optimum sizing, stands out:

Castilho, Debs and Nicoletti (2007) studied the optimization of alveolar panels and prestressed beams, with the objective of minimizing the cost function through the use of Genetic Algorithms. The work identifies and describes the various costs involved in production, analyzing various selection strategies and various types of crossover and using real and binary representation. The results demonstrated that an AG-based method is a viable and effective approach to solving the cost problem, especially when there is little information on the solution space.

Freitas (2014) applied optimization techniques for the design of alveolar slabs and beams with precast and prestressed straight cable, considering the calculation of both immediate and dependent losses over time. The objective of the work was to obtain the optimum dimensions of the panel height, the number of cables, the diameters of the alveoli and the cables. In the study, the final limit state (ELU), service limit states (ELS) and constructive constraints were considered. The developed algorithm allowed to obtain the optimal dimensions of the structures in a short time, when compared to a conventional design analysis.

Serpik et al. (2016) created a procedure using genetic algorithm for the optimized design of reinforced concrete structures with flat frames manufactured without pre-tension reinforcement.

More recent studies, such as V. Albero et al (2018) proposed an ideal design model for prestressed concrete hollow core slabs, taking into account their fire resistance. Heuristic search algorithms, such as simulated annealing, were used to find the most economical slab design. The objective function considered was the economic cost of the hollow core slab. The obtained results showed that the ideal design of hollow core slab can be reached by the proposed model of optimization by algorithm of heuristic criteria. The ideal design achieved approximately 20% savings in cross-sectional area compared to common models on the market.

Shuna Ni et al. (2020) did a paper incorporating a probabilistic fire loss assessment method for reinforced concrete structures into a cost-benefit analysis to optimize a structural fire design.

The need for safety combined with the economy of materials is a goal pursued by engineers. In this context, this work has as main objective to develop a computational interface to optimize the cross section of ribbed slabs in normal situation and in a fire situation, that meets the maximum functionality and safety with the minimum cost, following the normative prescriptions. The optimization algorithm and the computational interface were implemented using MATLAB.

2 REINFORCED REINFORCED CONCRETE RIBBED SLABS IN FIRE SITUATION

According to NBR 6118(2014), ribbed slabs are slabs cast in place or with precast ribs, whose traction zone consists of ribs between which inert material can be placed. In Figure [1], an example of a bidirectional ribbed slab is shown.
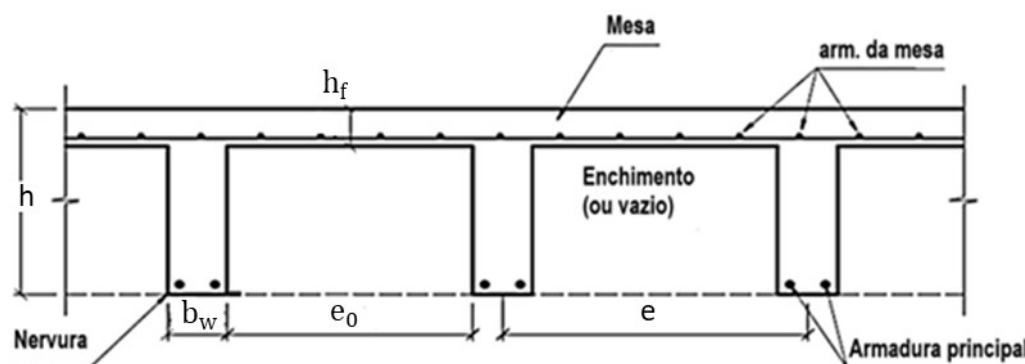

Figure 1. Cross section of a ribbed slab (author:2022)

The slabs are structural elements, in general, of small thickness and low coverings, increasing the risk of the concrete portion loosening, leaving the positive reinforcement exposed to the direct action of fire, causing excessive deformation of the steel, with consequent loss of adhesion with concrete, in addition to the sharp decrease in its strength. With that, it becomes of fundamental importance to verify the structural behavior of the slabs in fire situation.

Among the forms of disaggregation through which heated concrete passes, the spalling phenomenon stands out. According to the Merriam-Webster Online Dictionary, the verb "to spall" means "to break off chips, scales, or slabs – EXFOLIATE". Concrete spalling is exfoliation and disintegration of the surface layers of concrete elements, when exposed to high temperatures for long periods or to high thermal gradients characterized by very rapid heating.

The temperature that causes the collapse of a structural element in a fire situation is called the critical temperature, that is, the maximum temperature of the structure, from which its ruin is imminent. To ensure structural safety in a fire situation, the collapse temperature must be prevented from being reached. According to NBR 14432 (ABNT, 2000), required fire resistance time (TRRF) is the minimum fire resistance time of a constructive element subject to a standard fire. Obtaining its value depends on the type of occupation or use and the height of the building. The TRRF is standardized according to the risk of fire and its consequences at 30, 60, 90 and 120 minutes.

2.1 Tabular method for designing concrete structures in a fire situation

The Brazilian standard ABNT NBR 15200:2012 [7] uses tables for the design of concrete structures in fire situations. The tabular dimensioning method is the simplest method to be used for concrete structures to meet the verification requirements in a fire situation according to NBR 14432 (2000) – "Requirements of resistance to fire of constructive elements of buildings". The set of tables that associate the TRRF and the type of structural element to the minimum dimensions to be adopted in the project allows immediate application of the method in the structural design of the building.

In the consulted literature, the exact origin of these tables was not found. The American standard ACI 216R–89 presents the complete tabular method for the dimensioning of elements. For the pillars, a simple table containing the results of some tests is presented; for slabs, another simplified method of immediate application is indicated: determine the appropriate geometric characteristics in terms of the TRRF, by means of diagrams; beams by beams, the diagrams provided serve to assist another dimensioning method, known as the simplified method of verifying the load bearing capacity of the element.

Ocean standards AS-3600 (2001) and NZS 3101 Part 1 (1985) also present diagrams for dimensioning beams and columns. Both Brazilian standards NBR 5627 (1980) and Spanish Instrucción EH-80 (1980) apud CÁNOVAS (1988) were cancelled. The Spanish norm was replaced by regulation after the 1980s. The presentation of some old norms offers an overview of the evolution of normative recommendations in relation to more recent ones, particularly Eurocode 2 (prEN 1992-1-2 (2002)) and the Australian standard AS-3600 (2001), for the comparative study of this work.

In the tabular method, there is no need to check the resistance to flexion, shear, torsion and support conditions (anchoring in the structure). Verification of concrete disaggregation (spalling) is also not considered.
These tables are based on the principle that the further the geometric center of the reinforcement is from the concrete face exposed to heat, the lower its temperature and, consequently, the safer the structure will be in a fire situation. Temperatures tend to decrease in the center of the cross section of concrete due to its low capacity to conduct heat and, therefore, the greater the thickness of the pieces and the distance from the reinforcement axis to the face exposed to heat, the longer it will take for the element to structural failure under the acting load.

For the dimensioning of a slab in a fire situation, it must usually be considered that it fulfills, simultaneously, the function of fire protection and structural stability. ABNT NBR 15200:2012 provides minimum dimensions, through the tabular method, to ensure both functions. The fireproof function is guaranteed by the thickness of the cover, with or without coating. The structural function is guaranteed by the minimum width of the rib and the minimum distance between the CG of the reinforcement and the face exposed to fire. In the latter case, when the slabs have different dimensions, the fire resistance must be evaluated by means of more precise methods, either by experimental or numerical analyses.

3. OPTIMIZATION

According to Haftka and Gürdal (1991) optimization is interested in finding the best result of a particular operation, while satisfying certain constraints. Its structure is composed of an objective function that contains one or more design variables, and may or may not be subject to equality and / or inequality constraints by limiting the search space (viable region). Mathematically, an optimization problem can be defined as:

Be $f: \mathbb{R}, g: \mathbb{R}^m \longrightarrow \mathbb{R}^q, h: \mathbb{R}^m \longrightarrow \mathbb{R}^p$
Minimize / Maximize: $f(x_1, x_2, x_3, \ldots, x_n)$
Subject to:
$$h_k(x_1, x_2, x_3, \ldots, x_n) = 0 \quad k \in \{1, \ldots, p\}$$
$$g_j(x_1, x_2, x_3, \ldots, x_n) \leq 0 \quad j \in \{1, \ldots, q\}$$

Being, $x = [x_1, x_2, x_3, \ldots, x_n]$ the vector of design variables, $f(x)$ represents the objective function, being linear or non-linear, the functions $h_k(x)$ e $g_j(x)$ represent the equality and inequality constraint functions, respectively, that define the space of feasible solutions to the problem.

According to Bendsøe and Sigmund (2003), there are several ways to classify structural optimization, but the most general is divided into three types: parametric, shape and topological. The parametric optimization corresponds to the parameter optimization of the analyzed element. It aims to determine the optimal geometric characteristics of the structure: cross-sectional area of bars, moment of inertia of beams, thickness of plates or shells, etc.

The shape optimization aims to determine the optimal shape of the external and / or internal contour (hole) of a structure. The contours of the structure are parameterized (for example, spline curves) and the parameters of these curves constitute the design variables. This is a more general approach than parametric optimization. The topological optimization determines the optimal distribution of material in the design domain. The goal is to retrieve the material in an iterative and systematic way. The optimal distribution is related to a goal, which can be, for example, the minimization of the final volume of the structure, the maximization of stiffness, aiming material saving.

In this work, MATLAB implemented an optimization program for reinforced concrete slabs molded at the site in a fire situation using the Genetic Algorithm (GA) method. Aimed at developing a program to assist the design of ribbed slabs, in compliance with the regulatory constraints imposed by ABNT NBR 6118: 2014 and NBR 15200: 2012, in order to minimize the cost of materials (concrete and steel). The objective was to compare the consumption of concrete and steel in the dimensioning of the ribbed slabs when only the first standard was used or the two together.

3.1 Genetic Algorithms

The GA methods are analogous to Charles Darwin's theory of evolution, in which the less likely to survive and the fittest survive and bring offspring.

Briefly, the operation of the AG method can be given by the following steps: each individual represents a possible solution of a problem. A group of individuals forms a population. Each individual is assigned an aptitude value that corresponds to their degree of proximity to the optimal solution. Individuals who have a higher aptitude value, that is, are closer to the optimal solution (more adapted) are more likely to reproduce when compared to individuals with a lower aptitude value. To select the individuals that will reproduce, the algorithm uses methods that privilege the best adapted individuals. After the selection, a genetic recombination is made, in which individuals parents will combine to give rise to a new generation, theoretically better adapted than the previous generation. The algorithm follows in an iterative process until some stopping criterion is satisfied.

4. MATERIALS AND METHODS

In the MATLAB programming environment, there are already routines implemented to solve optimization problems using AG, in the toolbox called toolboxes. For validation of the implemented program, two numerical examples were used in order to evaluate the efficiency and the calibration of the program. To validate the implemented implementations for the dimensioning of unidirectional ribbed slabs, the numerical example 1.1 of Carvalho and Pinheiro (2009) was used. The example used for validation of implementations for dimensioning bidirectional ribbed slabs was obtained from Bocchi and Giongo (2007).

The first implementations are associated with the input of the data necessary for the execution of the program. In the second part of the implementations, the project variables used in the optimization (bw, hf, h, Asx and Asy) are defined, as well as the objective function and the constraint function calls. With the objective function implemented in this algorithm, the linear cost of two ribbed is minimized. In the process of minimizing the cost function, the set of restrictions imposed to the problem according to NBR 6118: 2014 and NBR 15200: 2012 must be respected for the dimensioning of reinforced concrete ribbed slabs.
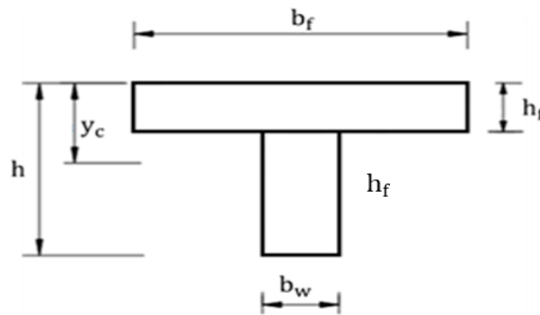

Figure 1 - Cross section of the ribbed slab (Author (2018)).

$$f = \text{Cost}_{\text{concrete}} + \text{Cost}_{\text{armor}} \tag{1}$$

$$\text{Cost}_{\text{concrete}} = (b_{fx} \, h_f + b_w \, h_w) \, l_{efx} \, C_c + (b_{fy} \, h_f + b_w \, h_w) \, l_{efy} \, C_c \tag{2}$$

$$\text{Cost}_{\text{armor}} = (l_{efx} \, A_{sx} \, \gamma_s \, C_{s50}) + (l_{efy} \, A_{sy} \, \gamma_s \, C_{s50}) \tag{3}$$

f: function objective (linear cost);

C_c: price of concrete per cubic meter (R\$/cm³);

C_{s50} : Price of steel CA 50 per kilogram (R\$/ kg);

l_{ef}: value of the effective length of the slab;

γ_s : specific weight of steel (kg/cm³);

A_s: total cross-sectional area of the steel bars;

b_w: thickness of the rib cross-section of the slab;

b_f: width of cross section table of ribbed slab;

h_f: Height of cross section table of ribbed slab;

h_w: Height of rib cross section of ribbed slab;

Finally, after the implementation of all the points mentioned above, one starts for the execution of the program and analysis of the results.

4. RESULTS

To validate the program developed in this research, examples exist in the literature. It is necessary to validate the implemented program in order to guarantee its functionality and the reliability of the results generated. As filler, in this analysis, 9x19x19 cm drilled ceramic bricks were considered, the other data are presented in Table 1.

Table 1 - Loads, mechanical and geometric properties considered in the example ribbed slabs (Author (2018)).

Description	Value / Unit
Resistances characteristic to concrete compression (f_{ck})	30 MPa
Resistances characteristic to the steel flow (f_{yk})	50 kN/cm²
Environmental aggressiveness class	2
Variable load	2 kN/m²
Overload	1 kN/m²
Price of CA50 steel	9,34 R$/Kg
Diameter of steel bar	12,5 mm
Required fire resistance time (TRRF)	60

4.1 Example of Unidirectional Vein Slab

This example (Figures 2) was extracted from the book by Carvalho and Pinheiro (2009). As the relationship between spans is greater than two, this ribbed slab was dimensioned as reinforced in one direction.
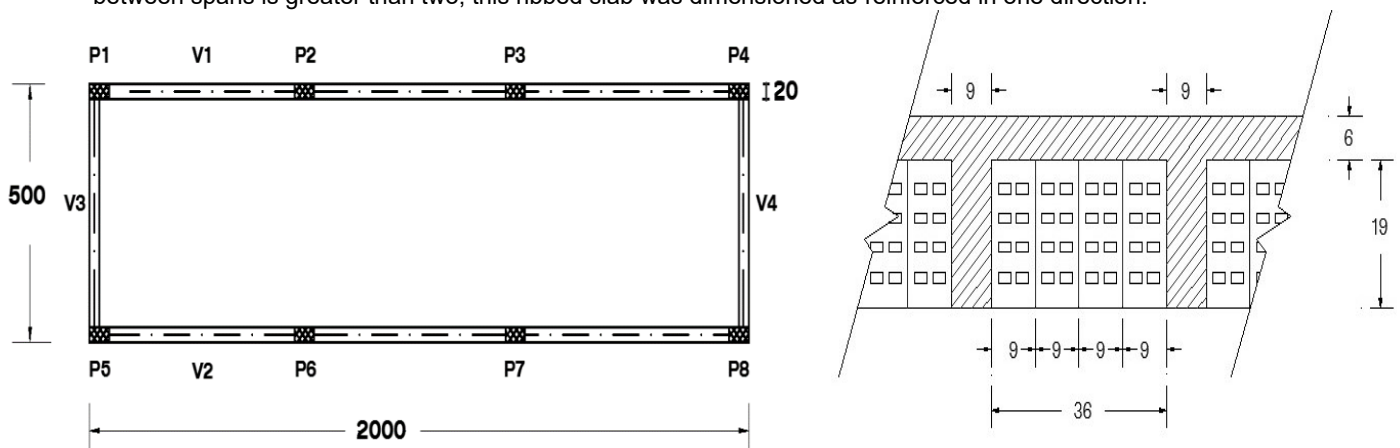

Figure 2– a) Example of unidirectional ribbed slab. b) cross section (dimensions in centimeters). (Author (2018)).

The Table 2 shows the results obtained by the program implemented in this research for the design in normal situation and in the fire situation of a unidirectional slab.

Table 2- Comparison between the unidirectional slab results obtained by the program implemented in this work (Author (2018)).

Parameter	NBR 6118 (2014)	NBR 6118 (2014) e NBR 15200(2012)	Difference
Width of the groove (b_w) (cm)	12	18	+50,0 %
Table height (h_f)(cm)	10	12	+20,0 %
Total height of slab (h) (cm)	40	31	-22,50 %
Coating (c) (cm)	2,5	5	+100,0 %
Steel area (A_{sx}) (cm²)	1,2	1,62	+35,22 %
Concrete cost (R$)	589,66	635,79	+7,82 %
Steel cost (R$)	216,10	244,46	+13,12 %
Total cost (R$)	805,76	880,25	+9,25 %

From the values presented in Table 2, it can be observed that the program implemented in this research obtained a T section in a fire situation with lower total height (h), but with greater width of the rib (b_w) and higher height of the table (h_f), increasing the area of this cross section of concrete. With these dimensions, an increase of approximately 7.82% in the cost of the concrete volume was obtained, compared to the sizing dimensions in normal situation.

It is observed that the variation of the height of the table and width of the rib have a significant importance in the cost of the concrete. Also, it can be affirmed with this that the decrease of the total height (h) of the cross section of the slab does not interfere significantly in the cost of the concrete. Since with the decrease of the height of the cross section, the area of reinforcement was larger, due to the decrease of the resistance contribution of the cross section of concrete. This leads to an increase in the cost of steel of 13.12%. Due to differences in sizing, a total cost of 9.25% was obtained.

4.2 Example of Bidirectional Nerve Slab

This example (Figures 3) was extracted from Bocchi and Giongo (2007). As the relationship between the spans is less than two, this ribbed slab was dimensioned as reinforced in two directions.
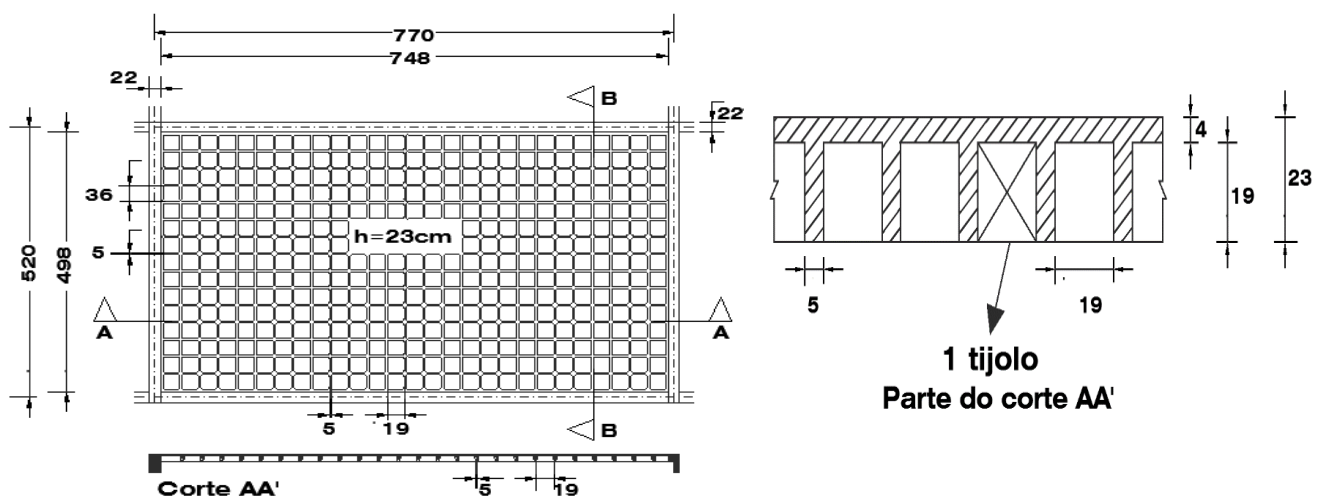

Figure 3 – a) Example of bidirectional ribbed slab: shape plant b) cross section (dimensions in centimeters). (Author (2018)).

Table 3 shows the results obtained by the program implemented in this research for the sizing in normal situation and in the fire situation of a bidirectional slab.

Table 3 - Comparison between the results of the bidirectional slab obtained by the program implemented in this work (Author (2018)).

Parameter	NBR 6118 (2014)	NBR 6118 (2014) e NBR 15200(2012)	Difference
Width of the groove (b_w) (cm)	13	18	+38,46%
Table height (h_f)(cm)	11	12	+9,09 %
Total height of slab (h) (cm)	41	36	-12,20 %
Coating (c) (cm)	2,5	5	+100,0 %
Steel area (A_{sx}) (cm²)	1,21	1,41	+16,32 %
Concrete cost (R$)	278,06	323,44	+16,32 %
Steel cost (R$)	105,12	122,29	+16,32 %
Total cost (R$)	383,18	445,73	+16,32 %

From the values presented in Table 3, it is observed that the values that program implemented in this research calculated for a bidirectional slab in fire situation, presented the same behavior already mentioned previously in the unidirectional slab. A section T with lower total height (h), but with greater rib width (b_w) and higher table height (h_f),increasing the area of this cross section of concrete. With these dimensions, an increase of approximately 16.32% in the cost of the concrete volume and the cost of the steel was obtained. This indicates that the parameter changes are not influenced by the size of the slab.

Through the results it can be stated that the implemented program was able to fulfill its objectives within the context of optimization, since all results are consistent. The Genetic Algorithms method presented a good performance in the optimization, working as a good tool that helps the user in his decision making.

5. CONCLUSIONS

Through the results it can be affirmed that the implemented program was able to fulfill its objectives within the context of the optimization, once all the results are shown coherent. The Genetic Algorithm method presented a good performance in the optimization, functioning as a good tool that assists the user in its decision making.

Based on the results of sizing according to NBR6118: 2014 and later to NBR15200: 2012, it was verified the consumption of concrete and steel tends to be higher in the cases of slabs with cut fire function. The parametron that increased the most was the width of the rib, which could already be expected since in NBR 15200: 2012 the structural function is guaranteed by the minimum width of the rib.

In this case, it is demonstrated that the tabular method for calculation of structures submitted to the action of temperature variation, although practical, is not economical, and therefore, the use of more precise methods is indicated.

ACKNOWLEDGEMENTS

REFERENCES

[1] ABNT -Associação Brasileira de Normas Técnicas. NBR 6118 - Projeto de estruturas de concreto – Procedimento, 221p., 2014.

[2] ABNT - Associação Brasileira de Normas Técnicas. NBR 8681 - Ações e segurança nas estruturas – Procedimento, p.18, 2003.

[3] ASSOCIAÇÃO BRASILEIRA DE NORMAS TÉCNICAS. NBR 14432:2001. Exigências de resistência ao fogo de elementos construtivos das edificações. Rio de Janeiro, 2001.

[4] ASSOCIAÇÃO BRASILEIRA DE NORMAS TÉCNICAS. NBR 15200:2012. Projeto de estruturas de concreto em situação de incêndio. Rio de Janeiro, 2012.

[5] ALBUQUERQUE, Gabriela Bandeira de Melo Lins de. Análise numérico-experimental de vigas de concreto armado com restrições axial e rotacional em situação de incêndio. 2018. 413 p. Tese. Doutorado em Engenharia de Estruturas – Escola Politécnica da Universidade de São Paulo, Brasil. Doutoramento em Engenharia de Segurança ao Incêndio – Universidade de Coimbra, Portugal.

[6] BENDSOE, M. P.; SIGMUND, O. Topology optimization : theory, methods and applications. Berlin ; Heidelberg ; New York ; Barcelona ; Hong Kong ; London ; Milan ; Paris ; Tokyo : Springer, 2003.

[7] BOCCHI, J; GIONGO. Concreto armado: Projeto e construção de lajes nervuradas – USP – EESC, 2007.

[8] CARVALHO, R. C.; PINHEIRO, L. M. Cálculo e detalhamento de estruturas usuais de concreto armado. v. 2. São Paulo, Pini, 2009.

[9] CASTILHO, V. C .; DEBS, M.K .; NICOLETTI, M. C. Optimization of prestressed concrete components using genetic algorithms. Cadernos de Engenharia de Estruturas, São Carlos - SP, v. 9, n. 38, p. 137-158, 2007.

[10] FREITAS, R. V. Optimization of Precast Concrete Elements: Alveolar Plates and Beams with Straight Cable. Dissertation (Master's) -Universidade Federal de Goiás - Goiânia - GO, 2014

[11] HAFTKA, R.T., E Z. GURDAL. Elements of Structural Optimization (Solid Mechanics and its applications). Kluwer Academic Publishers, Dordrecht, v.11, p. 504, 1991.

[12] HEYMAN, J. Plastic Design of Beam and Frames for Minimum Material Consumption. Q. Appl. Math, v. 8, p. 373-381, 1951.

[13] SERPIK, I.N.; MIRONENKO, I.V.; AVERCHENKOV, V.I. Algorithm for Evolutionary Optimization of Reinforced Concrete Frames Subject to Nonlinear Material Deformation. International Conference on Industrial Engineering, ICIE, 2016. Procedia Engineering, Vol. 150, p.1311 – 1316. 2016.

[14] SILVA, V. P. Projeto de estruturas de concreto em situação de incêndio: conforme ABNT NBR 15200:2012. São Paulo: Blucher, 2016.

[15] V. Albero, H. Saura, A. Hospitaler, J.M. Montalvà, Manuel L. Romero. Research paper Optimal design of prestressed concrete hollow core slabs taking into account its fire resistance. Instituto de Ciencia y Tecnología del Hormigón (ICITECH), Universitat Politècnica de València, Spain. Advances in Engineering Software 122 (2018) 81–92.

[16] Shuna Ni, Ruben Van Coile, Negar Elhami Khorasani, Danny Hopkin, Thomas Gernay. LIFETIME ECONOMICALLY OPTIMUM POSITION OF STEEL REINFORCEMENT IN A CONCRETE COLUMN EXPOSED TO NATURAL FIRE. SiF 2020 – The 11th International Conference on Structures in Fire The University of Queensland, Brisbane, November 30 - December 2, 2020.

ANALYSIS OF THE CATENARY ACTION OF RESTRAINED STEEL BEAMS IN FIRE SITUATION

**Igor Charlles
Siqueira Leite a***

**Valdir Pignatta
Silva b**

ABSTRACT

The main codes for the design of steel structures in fire situation are based on the criteria of critical temperature or strength limit state [2], [6]. The behavior of the beam is strongly influenced by the level of axial and rotational restriction. When the beam is inserted in frames, these restrictions are the columns and the connections. This behavior, in the expansion phase, induces compressive forces in the columns and tensile forces in the connections, at the catenary phase of the beam. This paper presents the results of a numerical study using the finite element computation software ABAQUS to study the behavior of steel beams in fire situation, with different levels of axial and rotational restraint on the supports. The focus of this study is the behavior of the beams in catenary action and the interaction that the tensile forces have with the adjacent elements, in this case the connections. A parametric analysis was performed by varying the fire coating, varying the span and different levels of axial and rotational restraint. It was found that tensile force in catenary action cannot be neglected in the design of fire situation beams. To facilitate structural engineers in the design of connections at high temperatures, the results of the parametric study were compared with the theoretical formulation proposed by authors to determine the value of the tensile force in the catenary action so that this formulation can be used in the future in the design codes of structures in fire situation.

Keywords: Catenary action; Steel beams; Fire engineering design; Finite element; Restrained steel beams

---

a* Dept. Structural and Geotechnical Engineering, Polytechnic School, University of Sao Paulo. Av. Prof. Almeida Prado, 83, Cidade Universitária, 05508-070 – São Paulo – SP – Brazil. (igorleite@usp.br), Corresponding author.

b* Dept. Structural and Geotechnical Engineering, Polytechnic School, University of Sao Paulo. Av. Prof. Almeida Prado, 83, Cidade Universitária, 05508-070 – São Paulo – SP – Brazil. (valpigs@usp.br).

2. INTRODUCTION

The evaluation of fire resistance in steel structures has been extensively researched and documented within the technical and scientific community, with a primary emphasis on analytical methods [1]. ABNT NBR 14323 [2] contains simplified calculation models that offer straightforward solutions for determining the behavior of beams in fire situation, both with and without fireproof protection. Calculations involve comparing the element's temperature at a specific time with the critical temperature, which causes the element to fail, or by determining the beam's load capacity at elevated temperatures.

In the case of beams integrated into a frame or supported by vertical elements such as columns, their support conditions will impose either axial or rotational constraints at their ends, and sometimes both can be present simultaneously. It is important to mention that beams typically have axial constraints in conventional design scenarios, with their stiffness value varying accordingly.

The presence of axial constraint at the support of a beam causes a distinct behavior compared to when it lacks such constraint. The thermal expansion of the beam is limited by the axial constraint, and this expansion converts into axial compressive force at the support. Under certain conditions of cantilever moment and compressive force, local buckling may arise close to the beam's ends, as Leite and Silva [3] demonstrated. As the temperature in the beam increases, the compressive forces reduce in value. The catenary phase ensues, with Usmani et al. [4] describing the development of tensile forces in the beam up to a maximum value, leading to the plastification of the section in the beam supports. Allam et al. [5] developed a formulation for the tensile force in catenary effect, which could affect safety considerations in connection design during a fire. Therefore, this study aims to analyze the behavior of coated beams with axial and rotational restraint in a fire situation. Furthermore, this work presents a method to determine the axial tensile force in catenary action to facilitate steel structure design in fire situation.

3. DESCRIPTION AND VALIDATION OF THE MODELS

The numerical modeling in this paper was segregated into two stages based on the thermostructural analyses performed in ABAQUS. The initial stage involved thermal analysis (heat transfer from ABAQUS), and the subsequent stage involved coupled thermostructural analysis. For the thermal analysis, the 8-node finite element DC3D8 was used for heat transfer. The C3D8R finite element was used to model the thermostructural analysis. This three-dimensional linear element features eight nodes and only one integration point. The ABAQUS/Explicit solver was used for all numerical modeling in this paper. The beams were subjected to a pre-determined load level and exposed to a uniform temperature increase, following the standard fire curve specified in Eurocode 3 - Part 1.2 [6]. To account for material non-linearity, the stress-strain diagram from Eurocode 3 Part 1-2 [6] was utilized. Geometric non-linearity was incorporated into the model by enabling the "NLGEOM" option in the ABAQUS Explicit solver. The thermal properties of steel were determined based on Eurocode 3 Part 1-2 [6], while those of concrete were based on Eurocode 2 Part 1-2 [7].

The boundary conditions used in the simulations considered the use of rigid plates that were affixed to the beam ends, and the plates were connected to the beam via the coupling constraint option in ABAQUS. To replicate the axial and rotational stiffness of the models, a CONN3D2 connection element that acts as a spring was used, with stiffness properties inserted in the connector section field. A wire-type element was connected between two points on the model: one point connected to the plate centroid and another at a farther position from the beam. At the first point, a boundary condition was imposed to release axial and rotational deformations. At the second point, a crimp-type boundary condition was applied to restrict all movements. This technique was necessary for the analysis to converge without stability issues. Note that it was assumed that the spring stiffness was not impacted by temperature. This scenario implies that the region where the beam connects (columns and connections) has been fire-protected.

To validate the results of this paper, considering the incorporation of springs for axial and rotational stiffness simulation, the experimental model by Liu et al. [8] was used. The study conducted a series of experiments to investigate the impacts of axial and rotational constraint on beams under high temperatures. To validate the models in their corresponding doctoral theses, Yin [9] and Najafi [10] utilized the study of Liu et al. [8]. Hence, this study will employ the outcomes of these authors to authenticate the results. The validation model comprises a UB178x102x19 profile made of S275 steel with a 2-meter span and two different concentrated axial load values, applied at rates of 0.5 and 0.7 of the ultimate loads at room temperature. The load values are 38.3 kN and 52.6 kN, respectively, as described in Najafi [10], and were applied within the width of the profile to prevent numerical errors. The model includes a spring with an axial stiffness of 8 kN/m and an estimated rotational stiffness of 14000

kN.m/rad, as the value was not presented in the original work by Liu et al. [8], according to Yin [9]. The model will be used for validation purposes. Figure 1 illustrates the setup of the model.
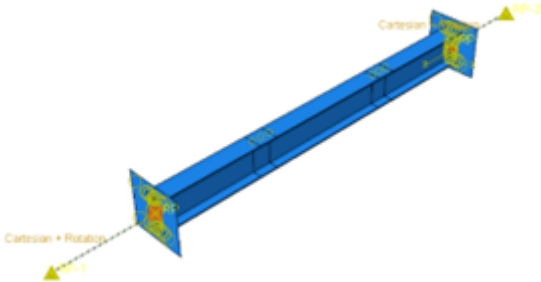

Figure 1: Representation of the numerical model used to validate the results of Liu et al. [8]

The results presented in Figure 2 indicate that the values obtained in this study are slightly more conservative than those reported by Yin [9], particularly about the critical temperature of the beam. However, both studies had the same initial stiffness, leading to similar displacements up to approximately 400°C. Despite some discrepancies, the experimental findings, as well as those of Najafi [10], demonstrated more conservative results, although with similar behavior. This variation may be attributed to the use of different values for the yield stress, as outlined in Yin [9] study. It is important to note that the disparity between our results and those of Najafi [10] can be attributed to distinct considerations made in ABAQUS, particularly concerning the coefficient of thermal expansion, which significantly affects the outcomes, depending on whether it is held constant or allowed to vary with temperature.
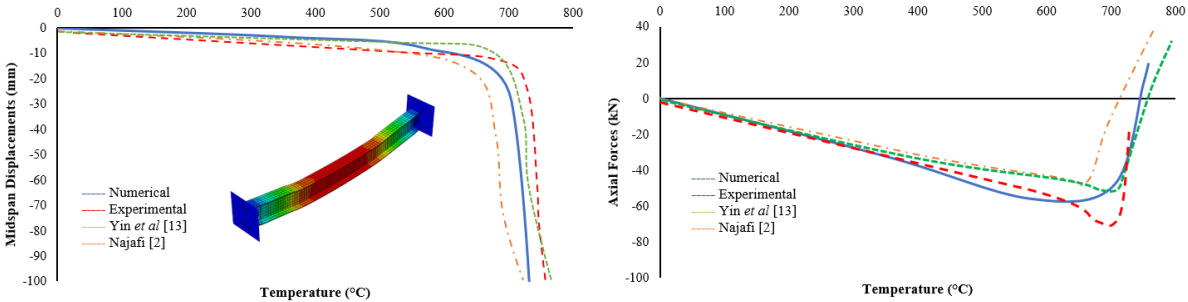

Figure 2: Comparison between works by Liu et al. [8], Yin [9] and Najafi [10] – K = 8 kN/mm and F = 38.3 kN (0.5 of the ultimate load) - Displacements and Axial Forces on Supports

4. PARAMETRIC STUDY OF STEEL BEAMS WITH AXIAL AND ROTATIONAL CONSTRAINTS WITH FIRE PROTECTION COATING

The parametric investigation of this paper examined spans of 5, 10, and 15 meters using welded Brazilian beams of VS 350 x 25, VS 500x73, and VS 700x154, respectively. The beam was subjected to a load of approximately 0.4 of the maximum loads at room temperature, assuming infinite axial and rotational constraints. The study aimed to simulate beam behavior in a substructure scenario, where the beam connects to a perimeter column on the right support and an intermediate column on the left support, as illustrated in Figure 3. S275 steel with a yield strength of 275 MPa was used, and the mechanical properties of steel at high temperatures were reduced using Eurocode 3 Part 1-2 [6] parameters. Heating of the beam was applied to the three lower faces to simulate a fire in a building. The fireproofing materials employed in this investigation included spray applied fire resistive material (SFRM) CACFO-300 and Carboline Type, intumescent paint, and square edge gypsum board. Numerical and experimental investigations were used to obtain the temperature-dependent thermal properties of fire protection materials, with references to Kodur and Shakya [11] (SFRM), Rigobello [12] (gypsum board) and Krishnamoorthy [13] (intumescent Paint).
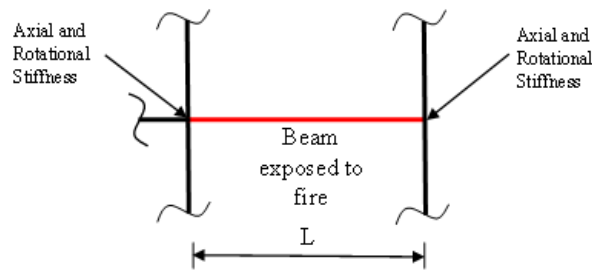
Figure 3: Representation of the structural model idealized for parametric analysis

Table 1 lists the fire protection materials employed in this parametric study, along with their respective nomenclature and thicknesses. The chosen thicknesses were based on the beam's mass factor, ensuring that after 120 minutes of thermal analysis via FEM, the steel beams reached a temperature close to that at the fire's end.

Table 1: Fire protection coating materials analyzed in the parametric study

Initials	Fire Coating	Thickness (mm)
APCa	CACFO 300	25.4
APCr	Carboline	25.4
PG	Gypsum Board	12.5
TI	Intumescent Paint	5

The parametric analysis will consider the following parameters: Beam length (L), Axial restraint level (Ka), Level of rotational constraint (Kr) and Fireproof coating materials. The axial restraint values used in this work were: Ka = 0.05KA, Ka = 0.1KA, Ka = 0.5KA and Ka = KA. The rotational restriction values used in this work were: Kr = 0.05KR, Kr = 0.1KR, Kr = 0.5KR, Kr = KR and Kr = KRI (infinite rotational restriction – crimp). With KA and KR taken respectively as (Eq. 1 and Eq. 2):

$$KA = \frac{EA}{L} \tag{1}$$

$$KR = \frac{2EI_x}{L} \tag{2}$$

Where "E" is the modulus of elasticity of the steel at room temperature (E = 200 GPa), "A" is the cross-sectional area of the profile, "I_x" is the moment of inertia of the profile around the largest bending axis and "L" the length of the beam. Table 2 shows the parameters of the cases investigated in this study for steel beams.

Table 2: Cases examined in the parametric analysis of steel beams

Model	Profile	Spans	Failure load at room Temperature	Failure load at fire situation	KA	KR
		m	kN/m	kN/m	kN/m	kN.m/rad
V1	VS350x26	5	37.1	14.9	130800	538,4
V2	VS500x73	10	56.4	22.5	184800	17107
V3	VS700x154	15	53.3	20.9	261067	48898

A parametric analysis was performed using ABAQUS to investigate the effect of finite element mesh refinement on the structural response of the models. Six different sizes of finite elements were studied to determine the optimal mesh size. The smallest mesh size, measuring 0.0075 m, required 197 minutes of analysis. The 0.01 m mesh size required 179 minutes of analysis, while the 0.015 m mesh size took a total of 25 minutes of analysis. Based on these results, a mesh size of 0.015 m was selected for this study.

The parametric analysis models will be presented according to the span, level of axial and rotational restriction, and respective fire protection material. For instance, the model V1-5-0.5KA-KR-TI represents a beam with a VS profile of 350x26, spanning 5 meters, having 50% of total axial restraint, full rotational restraint, and using intumescent paint as the fireproof coating material.

4.1. Parametric analysis results

According to the parameters already presented, the influence of the level of axial and rotational constraints, the span of the beam and the different fireproofing materials was analyzed. The aim was to compare the behavior of the beams in a fire situation and determine the influence of each parameterization. This paper presents results for beams with varying levels of axial and rotational stiffness, which are presented in the form of the follow curve: fire time versus axial reaction force. The results were evaluated individually for each fireproofing condition applied to steel beams. However, due to the page limitations of this paper, the most relevant results will be shown. The other results can be requested from the authors on demand. The study also investigated the influence of beam span and loading level, with varying levels of axial and rotational restraint. A total of 115 numerical models were created using the specified parameters. One of the models utilized in this paper, namely V1-5-KA-KRI-SP, is displayed in Figure 4.

Figure 4: Numerical modeling configuration of one of the models of this parametric study

4.1.1. Influence of axial and rotational restraint level for fire coated beams

Figure 5 demonstrates that decreasing the level of axial stiffness results in reduced compressive forces on the supports and consequently, reduced displacement of the beam at the center of the span. The reduction is due to the beam's increased horizontal displacement resulting from less axial constraint, which decreases vertical displacements and ultimately reduces axial support reactions. The temperature for maximum reaction values varies depending on the level of axial restraint, as shown in Figure 5, which is crucial information for designing surrounding elements. It is worth noting that tensile forces were not observed in models with SFRM Carboline-type fireproof coating. However, other models showed such forces during the catenary phase.
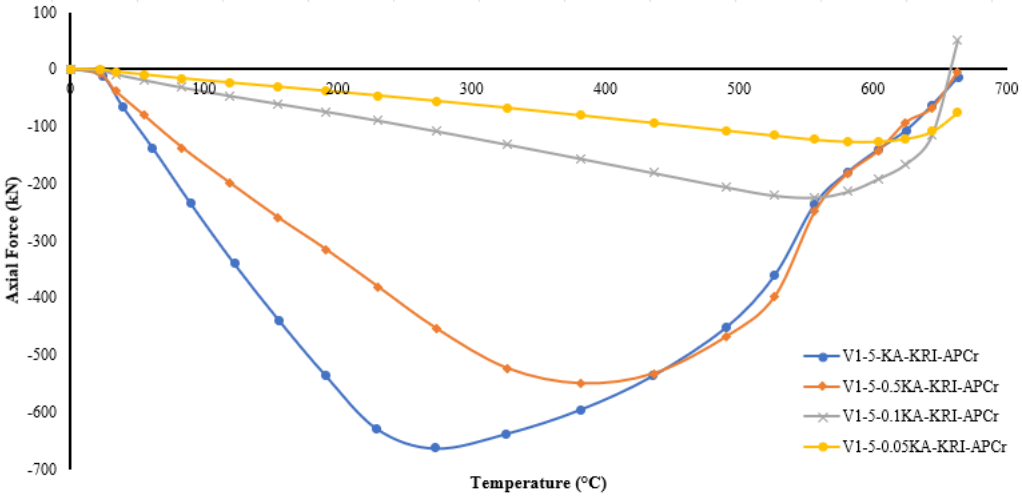

Figure 5: Results of axial forces on the supports of composite beams with Carboline type fireproof coating (VS 350x26 – 5 meter span) under different levels of axial restraint

Figure 6 shows that the variation in the rotational stiffness of beams coated with SFRM Carboline does not result in significant changes in axial forces or behavior. This indicates that the values of axial forces are mainly dependent on the level of axial constraint. Similar behavior is observed when using other fire-resistant coating materials.
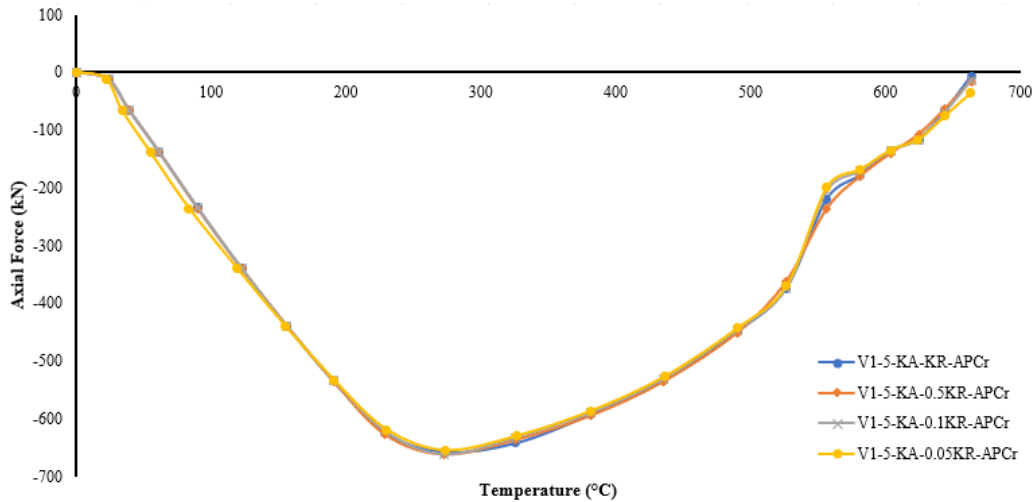

Figure 6: Results of axial forces on the supports of single beams with Carboline type fireproof coating (VS 350x26 – 5 meters span) under different levels of rotational restraint and total axial stiffness

4.1.2. Influence of the distinction of fire-proof coating materials

Figure 7 illustrates the behavior of various fire-resistant coatings used in the parametric analysis. It is observed that all fireproofing materials exhibit similar values for axial compressive force and, during the beam's catenary phase, for tensile force – except for the Carboline type, which, as previously discussed, does not display tensile forces after 120 minutes of fire exposure. Another noteworthy observation is that, with decreasing axial stiffness, the maximum axial compressive forces decrease, while the maximum tensile forces remain unchanged compared to beams with higher axial stiffnesses. Hence, it can be inferred that the reaction forces are determined by the equilibrium of the structural element, rather than temperature, when the beam is evaluated in isolation, as explained earlier.
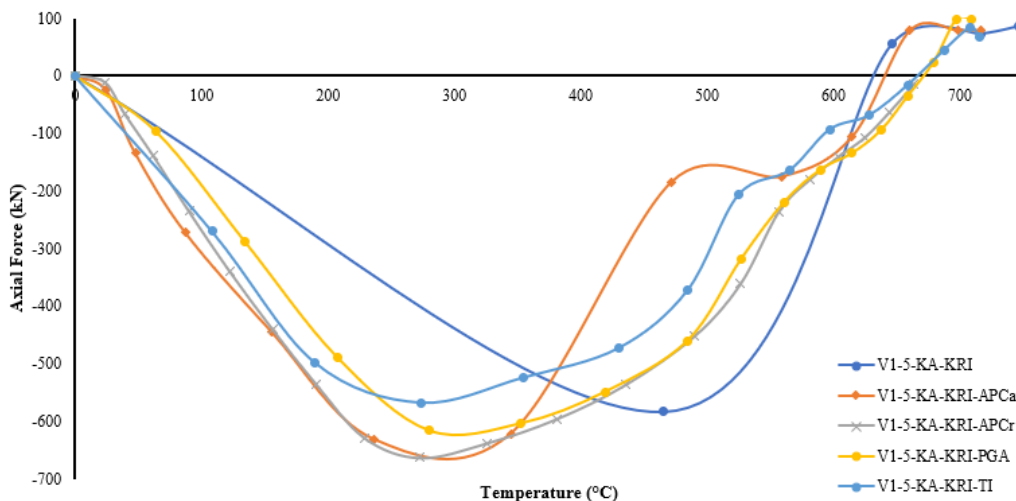

Figure 7: Results of axial forces on the supports of steel beams with variation in the fire coating with total axial stiffness and infinite rotational stiffness (VS 350x26 – 5 meters span)

4.1.3. Influence of span for fireproof coated beams

In relation to the effect of varying the beam span, it is evident from Figure 8 that the SFRM Carboline type fireproofing increases the maximum axial compressive forces of each beam as the span increases. It is also observed that the fire time in which the maximum compression force occurs also increases. This can be explained

297

by the decrease in the mass factor, since the larger the span, the greater the cross-sectional area of the beam, which delays the temperature distribution in the element. Only the beams coated with SFRM Carboline did not reach the catenary stage for spans of 5 and 10 m. However, for the span of 15 m, the Gypsum board coating also did not reach the catenary stage for certain levels of axial and rotational stiffness, leading to the conclusion that the occurrence of this effect depends on the temperature distribution in the beam.
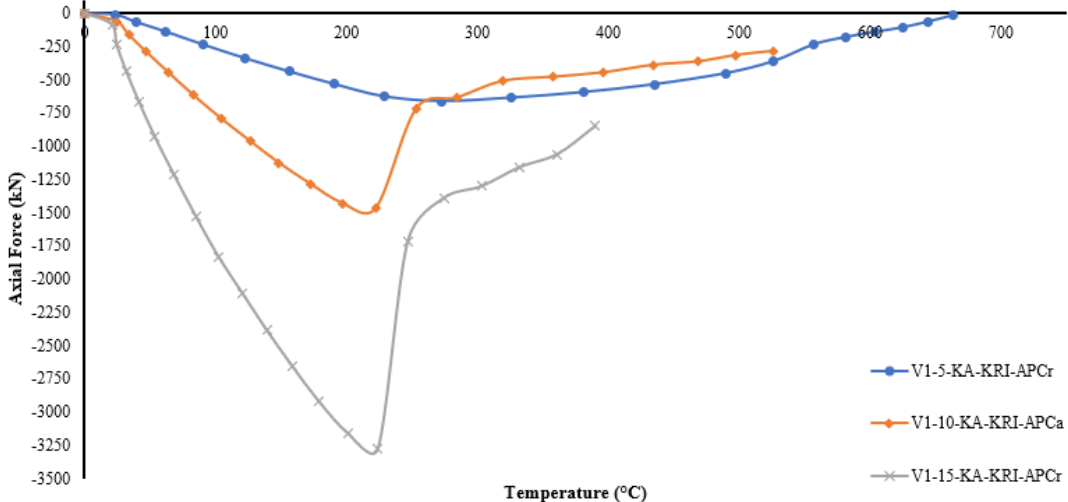

Figure 8: Results of axial forces on the supports of single beams with SFRM Carboline type fireproof coating (VS 350x26) for spans of 5, 10 and 15 meters, respectively.

The influence of the beam span variation was also observed in the variation of rotational stiffness (Figure 9). It was found that for the 5-meter span, the change in rotational stiffness had a negligible effect on the axial forces. However, for larger spans, decreasing rotational stiffness caused the axial forces to vary. This effect is due to the larger deformations of the beams with larger spans, as the beam moves more vertically before undergoing axial thermal expansion, which is responsible for the increase in axial forces. Therefore, it can be concluded that the rotation capacity of the connections has a direct impact on the axial forces generated in the elements surrounding the beams, especially the columns, in simple steel beams. Thus, the determination of the axial tensile forces in catenary action is crucial for the design of steel structures, particularly with regards to connections in fire situations.
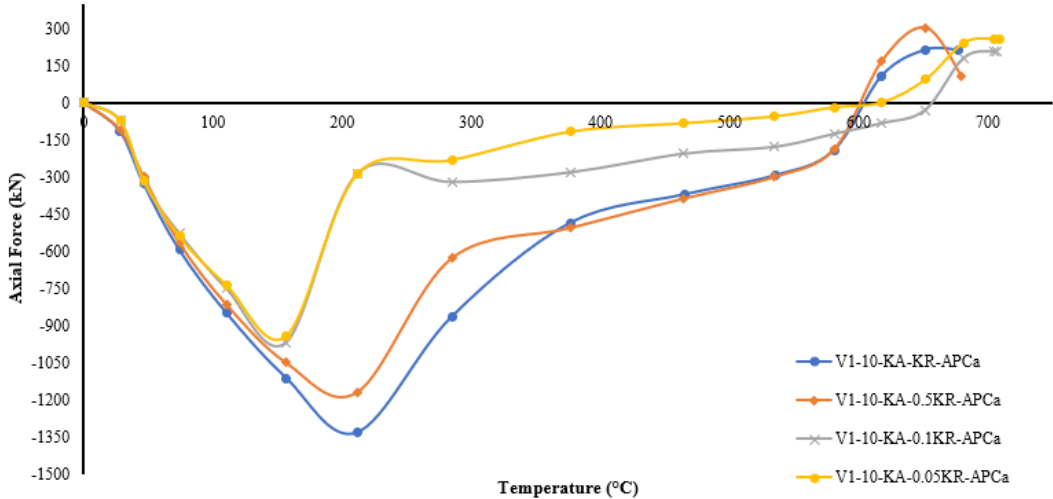

Figure 9: Results of the axial forces on the supports of the beams with variation in the rotational stiffness with fireproof coating SFRM CACFO-300 type (VS 500x73 – 10 meters span).

The following section of this paper will present an analytical solution for determining the tensile forces in catenary action, which can be applied in the design of steel structures under fire conditions.

4.2. Estimation of axial tensile forces in the catenary phase of the beam in a fire situation

The prediction of tensile forces in catenary action was based on the theory of cables stressed by uniformly distributed forces. To model the beam's behavior under fire, it was assumed that it can be likened to a cable suspended in a structure at normal temperature. The mathematical model developed aimed to determine the relationship between the deformation of the suspended cable and the axial tensile force, accounting for the high temperatures associated with the fire. The element's surrounding structure was considered to provide axial rigidity (K), and according to Sáles et al [14], the deformed cable can be approximated as a parabola. Figure 9 shows the mathematical model.
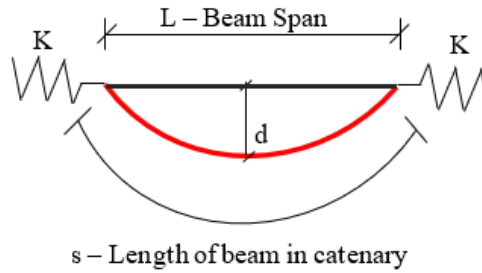

Figure 9: Mathematical model of the beam in catenary action

The theory of suspended cables predicts deformation, but in a fire scenario, three additional factors affecting the cable's length are considered: the impact of thermal expansion (δ_θ) (Eq. 3), elongation of the bar due to axial force (δ_A) (Eq. 5.4), and axial restraint of supports (δ_K) (Eq. 5).

$$\delta_K = \frac{P}{K} \tag{3}$$

$$\delta_\theta = \alpha\theta L \tag{4}$$

$$\delta_A = \frac{PL}{EA} \tag{5}$$

The equations include the coefficient of thermal expansion of steel denoted by "α" and the average temperature "θ" of the element. Other variables are the beam's span "L," axial compression force "P," and the horizontal stiffness "K" of the surrounding structure. The modulus of elasticity of steel at temperature "θ" is represented by "E" and the cross-sectional area is denoted by "A".

Integrating the general expression of the elementary parabola to determine the length of the cable as "s" yields the following equation (Eq. 6).

$$s = L\left[1 + \frac{8d^2}{3L^2}\right] \rightarrow s = L + \frac{8d^2}{3L} \tag{6}$$

where "d" is the vertical displacement of the beam and "L" is the total length of the beam.

Assuming that the final configuration of the cable must have a length of "s," the total impact of the factors affecting the cable's length is equivalent to the increase in length derived from equation 6. This can be expressed as (Eq. 7 and 8):

$$\delta_\theta + \delta_A + \delta_K = \frac{8d^2}{3L} \tag{7}$$

$$\alpha\theta L + \frac{PL}{EA} + \frac{P}{K} = \frac{8d^2}{3L} \tag{8}$$

Since the tension in a cable under a uniformly distributed load "p" can be represented by the equation P = pL²/8d, it is proposed that Equation 8 can be converted into the following equation through mathematical deductions (Eq. 9):

$$d^3 - \frac{3}{8}\alpha\theta L^2 d + \frac{3pL^3}{64}\left(\frac{1}{EA} + \frac{1}{K}\right) = 0 \qquad (8)$$

Equation 8 enables the calculation of the maximum displacement for the beam in catenary action, allowing for the determination of the required tensile force in designing connections under fire conditions. It's worth noting that the modulus of elasticity varies depending on the temperature being considered.

Although the cables can be considered inextensible, the longitudinal deformation caused by temperature variation can still be considered. One approach to account for this deformation is to use an expedited solution, as proposed by Sáles [14], which involves assuming the cable as a straight bar and calculating the length variation using Equation 9.

$$\Delta s = \frac{Ps_0}{EA} \qquad (9)$$

The symbol "P" represents the tensile force in the catenary action, "s_0" denotes the initial length of the beam, "E" represents the modulus of elasticity of the steel at the analyzed temperature, and "A" stands for the cross-sectional area of the element.

By utilizing equation 10, the final length of the bar can be determined. It should be noted that the final length "s_f" is equivalent to the initial length "s" plus the change in length "Δs". Therefore, it can express this relationship as follows:

$$s_f = L + \frac{8d_f^2}{3L} \qquad (10)$$

Through mathematical manipulation, it is possible to obtain the value of the final displacement, which is represented by Equation 11:

$$d_f = \sqrt{\frac{3L(s_f - L)}{8}} \qquad (11)$$

The axial force "P" is first calculated, followed by the determination of the initial displacement "s_0". The first variation in length, denoted by "Δs", is then calculated by adding it to the initial displacement to determine the final length. The resulting value is subsequently plugged into Equation 8 to determine the final displacement of the first equation. This procedure is repeated until the difference between the displacements in each interaction becomes negligible.

Table 3 compares the results obtained for the axial tensile forces in the catenary action of numerical models with shear connection (0.1KR and 0.05KR) of steel beams with those obtained using the analytical method of Equation 8 and the expedited incremental method presented in Equations 9 to 11. The table 3 presents the shear connection numerical models used in the analysis, the axial tensile value obtained in the numerical model (Tensile NM), the temperature (Temp) at which the maximum tensile force was found, the value of the tensile force obtained using the analytical method (AM), the value of the tensile force obtained using the expedited method (EM), the difference in values between the numerical model and the analytical model (Dif. 1), and the difference in values between the numerical model and the expedited model (Dif. 2).

Table 3: Comparison between tensile forces found in numerical models and in analytical and expedited models for steel beam with shear connection

Model	Tensile NM (kN)	Temp (°C)	AM (kN)	EM (kN)	Dif. 1	Dif. 2
V1-5-KA-0.1KR-SP	97.5	717	93.1	88.4	-5%	-9%
V1-5-KA-0.05KR-SP	88.1	717	93.1	88.4	6%	0%
V1-5-KA-0.1KR-APCa	125.6	699	93.75	89.4	-25%	-29%
V1-5-KA-0.05KR-APCa	81.3	699	93.75	89.4	15%	10%
V1-5-KA-0.1KR-PGA	100.3	698	93.8	89.5	-6%	-11%
V1-5-KA-0.05KR-PGA	97.5	697	93.8	89.5	-4%	-8%
V1-5-KA-0.1KR-TI	83.9	708	93.4	83.9	11%	0%
V1-5-KA-0.05KR-TI	83.9	708	82.3	79.5	-2%	-5%
V1-10-KA-0.1KR-SP	189.1	737	278.1	262	47%	39%

V1-10-KA-0.05KR-SP	221.4	737	278.1	262	26%	18%
V1-10-KA-0.1KR-APCa	206.9	706	281.3	266.9	36%	29%
V1-10-KA-0.05KR-APCa	255.7	706	281.3	266.9	10%	4%
V1-10-KA-0.1KR-PGA	262	715	280.4	265.6	7%	1%
V1-10-KA-0.05KR-PGA	195	716	280.4	265.6	44%	36%
V1-10-KA-0.1KR-TI	244	660	288.9	278.5	18%	14%
V1-10-KA-0.05KR-TI	237.7	660	288.9	278.5	22%	17%
V1-15-KA-0.1KR-SP	418	731	394	378.5	-6%	-9%

Table 3 shows that the expedited method values for the models of beams with shear connections that are more closely aligned with the numerical models, and some of the results are even exact matches. It was found that there is an average difference of 7% between the numerical models and analytical method. However, when comparing the results to the expedited method, this difference decreases to 2%. This suggests that the expedited method, which approximates the elongation of the beam during the catenary action, produces results that are more in line with the computational analysis.

To predict the temperature at which a structural element will reach its maximum tensile forces due to catenary action in fire situation, computational modeling may not always be feasible in design of steel structures in fire situation. Therefore, based on the findings from numerical models, the following method is suggested for determining this temperature in steel beams:

- Calculate the tensile strength of the beam at room temperature;
- Based on the average temperatures observed in numerical models, determine the maximum tensile force in catenary action. This occurs when the beam in a fire situation has 12.5% of its tensile resistant capacity at room temperature for uncoated elements, and 17.5% of its resistant capacity for elements with fire-resistant coating. Calculate this value;
- Determine the reduction factor for the yield strength ($k_{y,\theta}$), using the equation for tension members in a fire situation provided in Eurocode 3 Part 1-2 [6];
- Determine the temperature value of the steel based on the reduction factor for the yield strength ($k_{y,\theta}$).

Table 4 shows the axial tensile force in a fire situation according to the numerical models (NM), the corresponding temperature (Temp), the tensile values obtained from the proposed approximate method (AM), the difference between the force values obtained from the numerical model and the proposed approximate model (Dif. 1), the temperature in the proposed approximate method (Temp AM), and the difference between the temperatures obtained from the numerical model and the proposed method (Dif. 2).

Table 4: Comparison between tensile forces found in numerical models and proposed method for steel beam with shear connection

Model	Tensile NM (kN)	Temp (°C)	Tensile AM (kN)	Dif. 1	Temp AM (°C)	Dif. 2
V1-5-KA-0.1KR-SP	97.5	717	86.6	-11%	730	2%
V1-5-KA-0.05KR-SP	88.1	717	86.6	-2%	730	2%
V1-5-KA-0.1KR-APCa	125.6	699	91.6	-27%	685	-2%
V1-5-KA-0.05KR-APCa	81.3	699	91.6	13%	685	-2%
V1-5-KA-0.1KR-PGA	100.3	698	91.6	-9%	685	-2%
V1-5-KA-0.05KR-PGA	97.5	697	91.6	-6%	685	-2%
V1-5-KA-0.1KR-TI	83.9	708	91.6	9%	685	-3%
V1-5-KA-0.05KR-TI	83.9	708	91.6	9%	685	-3%
V1-10-KA-0.1KR-SP	189.1	737	259.9	37%	730	-1%
V1-10-KA-0.05KR-SP	221.4	737	259.9	17%	730	-1%
V1-10-KA-0.1KR-APCa	206.9	706	274.7	33%	685	-3%
V1-10-KA-0.05KR-APCa	255.7	706	274.7	7%	685	-3%
V1-10-KA-0.1KR-PGA	262	715	274.7	5%	685	-4%
V1-10-KA-0.05KR-PGA	195	716	274.7	41%	685	-4%
V1-10-KA-0.1KR-TI	244	660	274.7	13%	685	4%
V1-10-KA-0.05KR-TI	237.7	660	274.7	16%	685	4%
V1-15-KA-0.1KR-SP	418	731	378.8	-9%	730	0%

Table 4 shows that there is an average difference of only 1% between the temperatures obtained from the numerical models and those from the proposed model. The temperature variations are insignificant, except in some models

with a 10-meters of span. On the other hand, the average difference between the axial tensile forces is 16%, with some notable variations in values, especially in models with fire protection coating. Nonetheless, the main objective of this proposed method is to provide an easily obtainable reference for axial tensile forces in catenary action for design of connections in fire situation, and there are indications that this objective can be achieved. Furthermore, the proposed method can be used with reasonable precision in composite beams, especially for fire coated beams, provided that the load considered, and the cross-sectional area considers the contribution of the concrete slab.

5. CONCLUSIONS

This paper presents the results of a vast parametric study, which investigated the behavior of steel beams with axial and rotational constraints, in a total of 115 numerical models. The parametric study covered four distinct fireproofing materials, axial and rotational restraint levels, and beam span variation.

In conclusion, this study demonstrated that the behavior of steel beams in fire conditions varies based on the level of axial and rotational restraint at the supports. Beams with lower axial stiffness at the supports exhibit smaller vertical displacements and lower values of axial compression in fire. Additionally, the rotational restraint variation has little effect on beams with small spans but becomes more significant for longer spans, mainly in the axial compressive forces. The different types of fireproofing materials used in this study did not affect the values of axial compressive and tensile forces in catenary action, but the fire time for the appearance of each force varied. The span of the beam directly influenced the axial forces, and larger spans produced higher support reactions.

The study found that axial tensile forces in the catenary action of a beam only arise after its fire resistance time. This means that such forces would only appear if the fire lasted longer than the resistance time of the element. However, if the beams and connections are not coated, the decrease in connection resistance as a function of temperature is more rapid than for coated beams, so such a situation would not occur. To address the challenge of determining axial tensile forces on connections of steel beams in a fire situation, an expedited method based on the element's axial stiffness and the temperature at which catenary action starts to affect the beam's behavior was proposed. Comparison with numerical models showed the method to be valid. Given the difficulty in determining temperature in fire situations, an approximate method was proposed based on the tensile resistance capacity in a fire. Comparison with the expedited method showed that the proposed method can be useful for approximating axial tensile forces mainly for design of connections in fire situation.

ACKNOWLEDGEMENTS

REFERENCES

[1]   LUKOMSKI, M., TURKOWSKI, P., ROSZKOWSKI, P., PAPIS, B. Fire Resistance of Unprotected Steel Beams –Comparison between Fire Tests and Calculation Models. Modern Building Materials, Structures and Techniques, MBMST 2016.
[2]   Associação Brasileira de Normas Técnicas. "Steel Structures and Steel-Concrete Composite Structures Design of Buildings in Fire Situations", NBR 14323, 2013.
[3]   LEITE, I. C. S., SILVA, V. P. "Análise Termestrutural de Vigas de Aço com a Utilização da Ferramenta Computacional ABAQUS". In: XII Brazilian Congress of Bridges and Structures, 2021, Rio de Janeiro. XII Brazilian Congress of Bridges and Structures - Published Papers, 2021. p. 259-268.
[4]   USMANI, A. S. et al. Fundamental principles of structural behaviour under thermal effects. Fire Safety Journal, 36, 2001. 721-744.
[5]   ALLAM, A.; BURGESS, I.; PLANK, R. Performance-Based simplified model for a steel beam at large deflection in fire. 4th International Conference on Performance-Based Codes and Fire Safety Design Methods, Melbourne, 2002.
[6]   European Committee for Standardization. Eurocode 3: Design of steel structures - Part 1.2: General rules - Structural fire design. Brussels: CEN, 2005.
[7]   European Committee for Standardization. Eurocode 2: Design of concrete structures - Part 1.2: General rules - Structural fire design. Brussels: CEN, 2004.
[8]   LIU, T. C. H, FAHAD, M. K. DAVIES, J. M. Experimental investigation of behaviour of axially restrained steel beams in fire. Journal of Constructional Steel Research 58:1211-30. 2002

[9]   YIN, Y. Z. Advanced behaviour of steel beams under fire conditions. Doctor of Philosophy, University of Manchester, 2004.

[10]   NAJAFI, M. Behaviour of Axially Restrained Steel Beams with Web Openings at Elevated Temperatures. Doctor of Philosophy, University of Manchester, 2014.

[11]   Kodur, V. K. R., & Shakya, A. M. Effect of temperature on thermal properties of spray applied fire resistive materials. Fire Safety Journal, 61, 314-323. 2013

[12]   Rigobello, R. Desenvolvimento e aplicação de código computacional para análise de estruturas de aço aporticadas em situação de incêndio (Doctoral dissertation, Universidade de São Paulo). 2011.

[13]   Krishnamoorthy, R. R. The analysis of partial and damaged fire protection on structural steel at elevated temperature. The University of Manchester (United Kingdom). Doctoral Thesis. 2011.

[14]   Sáles, J. J. D., Munaiar Neto, J., Malite, M., Dias, A. A., & Gonçalves, R. M. Sistemas Estruturais: teoria e exemplos, 2015.

Experimental fire tests on steel-to-timber connections with 90 and 120 minutes fire resistance

Dhionis Dhima[a]; Maxime Audebert[b,*]; Abdelhamid Bouchaïr[c]; Nicolas Pinoteau[d]

ABSTRACT

This paper presents the results of twenty-one fire tests on unprotected steel-to-timber connections with dowel-type fasteners and one or two slotted-in steel plates. The experimental results of this type of connections available in existing studies have been mostly limited to a fire resistance duration of 60 minutes. The aim of this study is to provide connections specimens and experimental results for fire resistance up to 120 minutes. Two configurations of connections with one or two slotted-in steel plates, i.e., two or four shear planes, were tested. The temperatures were measured with thermocouples at different locations inside the wood members and along the steel plates. Two load levels for fire tests were determined on the basis of load bearing capacity of the connections obtained with tests at ambient temperature. The experimental results show that the specimens proposed for steel-to-timber connections with dowel-type fasteners are suitable for achieving fire resistance of 90 and 120 min. These results extend the scope of the analytical formulations proposed in the context of the revision of EN1995-1-2 for the determination of the fire resistance of timber connections.

Keywords: Timber connections; fire tests ISO834; high fire resistance

1. INTRODUCTION

The increasing use of wood in construction is driven by growing environmental concerns, by the suitability of timber constructions for prefabrication and also by the qualitative improvement of timber construction methods. In recent years, the emergence and widespread use of innovative and high-quality timber construction solutions (glued and cross laminated timber, high-performance connexion methods) has made it possible to expand the field of application of wood in construction. As a result, the construction of high-rise wooden buildings has considerably increased in few years. The fire resistance requirements for these new timber buildings are significantly more restrictive. Depending on the type and use of these buildings, fire resistance times of 90 to 120 minutes are required.

In flexible constructions such as timber ones, the resistance capacity depends on the mechanical behaviour of the connections, which represent the key points of the overall mechanical behaviour. Thus, in a fire situation, the fire resistance of the connections governs the fire performance of the structure. While the fire resistance of structural timber elements (beams, columns) is easily predicted by a "reduced section" calculation based on the charring

---

[a] CSTB, Centre Scientifique et Technique du bâtiment (dhionis.dhima@cstb.fr).

[b,*] Laboratoire de Tribologie et Dynamique des Systèmes (LTDS), Université de Lyon, Ecole Nationale d'Ingénieur de Saint-Etienne, 58 rue Jean Parot, 42100 Saint-Etienne (maxime.audebert@enise.fr) **Corresponding author**.

[c] Université Clermont Auvergne, Clermont Auvergne INP, CNRS, Institut Pascal, F-63000 9 Clermont-Ferrand, France, (abdelhamid.bouchair@uca.fr).

[d] CSTB, Centre Scientifique et Technique du bâtiment (nicolas.pinoteau@cstb.fr).

rate of wood, the thermomechanical behaviour of the connections is much more complex to predict, due in particular to the presence of steel fasteners. In this context, the current version of EN1995-1-2 [1] provides estimated fire resistance durations for timber connections, depending on the type of fasteners and the timber members thicknesses, as well as a simplified analytical method allowing a calculation of the fire resistance of the connections (t_{fi}). These provisions are of limited application, and provide too conservative fire resistance durations. For example, it is not possible to justify fire resistance greater than 60 minutes for protected timber connections and 40 minutes for unprotected connections. These limitations do not allow the validation of the fire performance required for new high-rise timber buildings. These design rules, defined almost 20 years ago, were formulated on the basis of limited experimental data [2].

To improve the knowledge of the thermo-mechanical behaviour of timber connections exposed to fire, and in the frame of the revision of EN1995-1-2, various research programs have been carried out since 1999. These works concern essentially experimental investigations on steel-to-timber connections subjected to a longitudinal tension and under a standard fire exposure, coupling to numerical modeling's of the tested connections. Some tests of timber connections subjected to other loads (tension perpendicular to grain and bending) were carried out. These tests identified tension parallel to grain as a predominant loading case in a fire situation [3].

These works have enabled a better understanding of the thermomechanical behaviour of timber connections assembled with dowel and bolt-type fasteners. In particular, it allowed the identification of the key parameters that govern the fire resistance of the connections: the thicknesses of the timber members, the type of the fasteners (bolts play a negative role on the fire resistance), the load ratio η_{fi} in fire situation. Based on these experimental results, numerical modelling works led to the proposal of a simplified analytical formula, allowing engineers to easily calculate the fire resistance duration of timber connections [4].

However, most of the tested specimens were designed for fire resistance durations of less than 1 hour, limiting the scope of the proposed analytical method to this duration. It should be noted, however, that some configurations were able to achieve fire resistances up to 70 or 80 minutes [3]. Recently, Brandon et al. conducted fire resistance tests of timber connections designed to achieve fire resistances of 90 minutes. Some configurations in this study achieved high fire resistances durations, between 100 and 122 minutes [5]. Although these results confirm that high fire resistance durations can be achieved with common timber connection configurations, they are insufficient to improve and extend the application of the analytical method to fire resistance durations greater than 1 hour. Further testing of high capacity connections is required.

This paper presents the results of a large experimental program on steel-to-timber connections subjected to fire exposure and designed to achieve high fire resistance. In the first section of this paper, the full experimental test program is explained. The geometries of the tested specimens are presented. The second section presents the experimental results obtained with tests at normal temperature and under ISO-fire exposure. In the last section these experimental results are analysed and commented. The version of the simplified analytical method improved with these tests results is presented. In order to check its validity, this analytical method is used to calculate the fire resistance of the tested configurations.

2. TEST SET-UP

2.1 Test program

The experimental program concerns two different configurations of steel-to-timber connections with dowel-type fasteners subjected to tension parallel to grain. This loading case was chosen because it was identified as predominant in a fire situation: a connection designed for a fire resistance time t_{fi} under tension parallel to grain will perform a fire resistance duration higher than that for another loading case [3]. The two configurations tested are:
- Configuration 1: steel-to-timber connection with one slotted-in steel plate (i.e., two shear planes) and connected with two raws of bolts and dowels of 16 mm diameter,
- Configuration 2: steel-to-timber connection with two slotted-in steel plate (i.e., four shear planes) and connected with four raws of dowels of 12 mm diameter.

Configuration 1 was chosen because it is directly comparable to configurations tested in previous experimental studies [3]. Compared to these earlier tests, the thickness of the timber side members is greater to increase the fire resistance duration. Configuration 2 is more realistic. In order to limit the lateral dimensions of the connections, a solution with 4 shear planes and 2 slotted-in steel plates is proposed.

For each configuration, different specimens are tested by varying the dimensions of the timber elements (thickness and height). For each specimen, three replicas were tested at ambient temperature to obtain the mean value of load-carrying capacity ($F_{u,mean}$). This mean value of the load-carrying capacity is necessary to define the applied mechanical load for tests under fire exposure (ISO 834). During the fire resistance tests, two load ratios were applied to each configuration: $0.10 * F_{u,mean}$ and $0.30 * F_{u,mean}$. In total, 21 specimens were tested at ambient temperature and 21 under ISO-fire exposure (10 tests for Configuration 1 et 11 tests for Configuration 2). The complete test program is presented on Table 1.

Table 1: Test program

Configurations	Number of tests at room temperature	Number of tests under fire exposure	
		Load ratio for fire test	
		$0,10*F_{u,mean}$	$0,30*F_{u,mean}$
1.1	3	2	2
1.2	3	2	2
1.3	3	1	1
2.1	3	2	1
2.2	3	2	2
2.3	3	1	1
2.4	3	1	1

All test specimens are made from the same materials (wood and steel elements). The timber members of test specimens consisted of glued laminated timber (spruce species) GL24h grade. For all connections tested at room temperature and under fire exposure, the moisture content of wood varies between 9.5 and 11.5%. The mechanical properties of the steel elements are presented on Table 2.

Table 2: Mechanical properties of steel elements of tested connections

Member	Grade	Yield strength (N/mm²)	Ultimate strength (N/mm²)
Dowels	S355	355	510
Bolts	6.8	480	600
Steel plates	S460	460	630

2.2 Test specimens

Figure 1 and Table 3 show respectively the types of connections and the dimensions of each tested configuration. The L_t dimensions, given in these figures and tables, represent the half-length of connections tested under standard fire conditions. As is show on Figures 1 and 2, the specimens tested in fire conditions are composed by two connections situated in both sides of a central joint. The joint dimensions and its tolerances are shown on the same figures.

The edge and end distances given in Table 3 are defined with respect to the minimum values specified in EN1995-1-1 [6]. For configurations 1.1 and 1.2 the minimum end distances a_3 and edge distances a_4 specified in EN1995-1-1 have been increased by $a_{fi} = 50$ mm. The configuration 1.3 is equivalent to configuration 1.1, but with the timber side-members thickness t_1 increased by $a_{fi} = 50$ mm. However, the length of fasteners of configuration 1.3 is equal to that of configuration 1.1, so the fasteners are shorter than the timber cross-section. The empty length of the holes was filled with wooden plugs with a length of 50 mm. This dimension a_{fi} is the additional timber thickness, specified by EN1995-1-2, to improve the fire resistance of timber connections. It was calculated taken $k_{flux} = 1$, $\beta_n = 0,7$ and $t_{req} = 90$ or 120 min. For configurations 2.1 to 2.4 with two slotted-in steel plates (i.e., four shear planes), the end and edge distances a_3 and a_4 were increased by the values of a_{fi} given in the Table 3.

The connection of configuration 2 is not using bolts but only dowels. In order to prevent the timber members from spreading apart during loading, side holding screws are used on the lateral sides of the connection. These screws should not be considered in the calculation of the carrying capacity of the connection. Their function is only to prevent the separation of the connected elements.
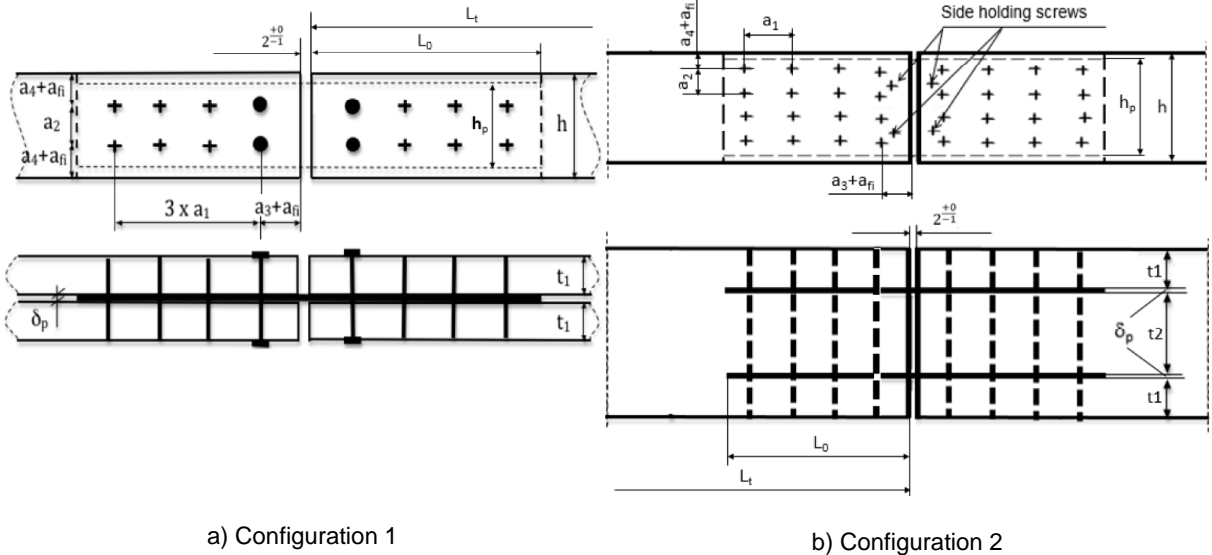

a) Configuration 1

b) Configuration 2

Figure 1: Geometry of the tested specimens

Table 3: Dimensions of tested specimens

Configuration		Geometric parameters												
		ϕ	t_1	t_2	a_1	a_2	a_3	a_4	a_{fi}	h	h_p	δ_p	L_0	L_t
1	1.1	16	150	-	112	64	112	48	50	260	114	10	523	1800
	1.2	16	200	-	112	64	112	48	70	300	114	10	543	1800
	1.3	16	200	-	112	64	112	48	50	260	114	10	523	1800
2	2.1	12	75	100	84	48	84	36	35	286	214	2x6	406	1800
	2.2	12	100	120	84	48	84	36	46	308	214	2x6	417	1800
	2.3	12	120	140	84	48	84	36	49	314	214	2x6	420	1800
	2.4	12	150	160	84	48	84	36	63	342	214	2x6	434	1800

2.3 Tests at room temperature

Each configuration is first tested under normal temperature conditions. These tests are used to determine the ultimate load carrying capacity ($F_{u,mean}$) of the specimens. This value of $F_{u,mean}$ is essential for determining the load F_{fi} to be applied in fire situation ($F_{fi} = \eta_{fi} \times F_{u,mean}$). In order to obtain a reliable average value of $F_{u,mean}$, 3 tests are carried out for each configuration.

Figures 2 and 3 show the dimensions and test arrangement of Configurations 1 and 2 tested at room temperature.
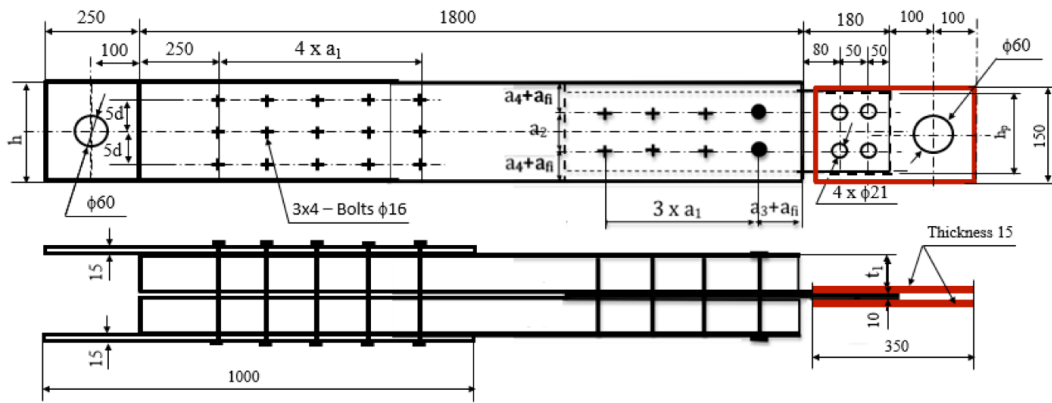
Figure 2: Configuration 1 tested at room temperature
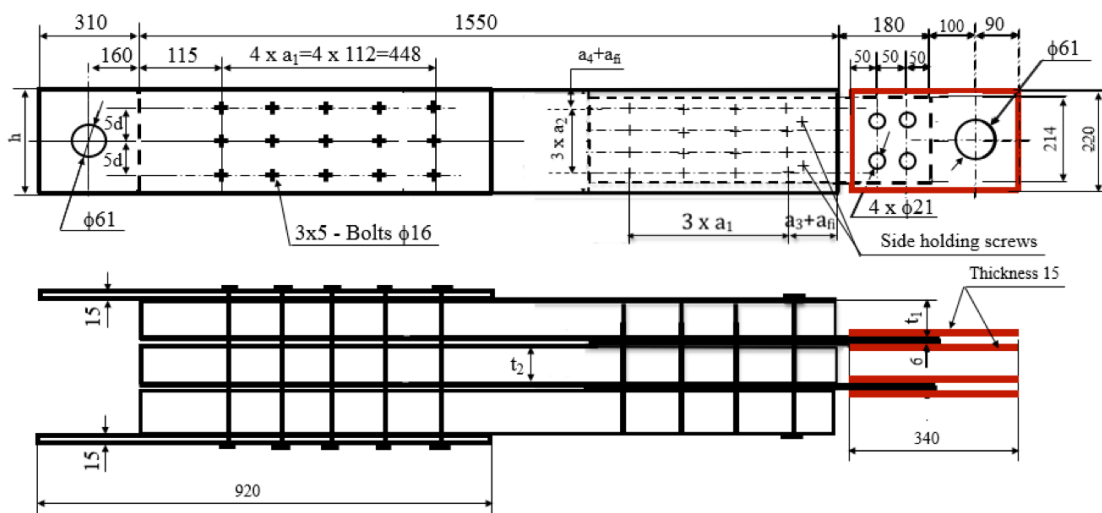
Figure 3: Configuration 2 tested at room temperature

2.4 Tests under fire exposure

The fire tests were carried out in horizontal furnace with dimensions 4x3 m. The tested connections were placed above the opening of the furnace, inside an additional compartment made with concrete walls and a horizontal Siporex. The test specimens extend beyond the additional compartment and are fixed to a steel frame, on one side, and to a hydraulic jack, on the other side. The test set-up for fire tests is presented in Figure 4.

Figure 4: Test set-up for fire tests

The mechanical loads applied during fire resistance tests were defined as a fraction (load ratio η_{fi}) of the mean experimental failure loads ($F_{u,mean}$) obtained with the tests at room temperature. The protocol used for the mechanical loading for fire tests was adapted from EN26891 standard [7] and is given in Figure 5. After pre-loading up to η_{fi} = 40% $F_{u,mean}$ and unloading to η_{fi} = 10% $F_{u,mean}$, the specimen is reloaded to a load ratio η_{fi} equal to 10% or 30% of $F_{u,mean}$. Then, the test specimen was exposed to the ISO 834 time–temperature curve. The load applied after this pre-loading protocol is named F_{fi} and was kept constant during the ISO-fire exposure until failure of the connection. After its failure, the test specimen is moved outside of the furnace and the combustion is stopped by projection of water. The time elapsed between the failure instant of the test specimen and its complete extinction of combustion was of the order of 4 to 5 minutes. This elapsed time is taken into account in the calculation of mean charring rate defined with the residual cross-section of test specimen. Figure 6 shows a test specimen during removal from the furnace.

Figure 5: Loading protocol for fire tests   Figure 6: Test specimen during removal from the furnace

During fire tests, the evolutions of temperatures of the furnace and those inside the connections have been recorded every 30 seconds with type K (nickel chromium/nickel aluminium) thermocouples. Furnace temperatures have been conducted with six plate thermometers positioned around the test specimen. The evolutions of temperatures within the timber members of connections have been recorded by sheathed thermocouples with a diameter of 1.5 mm.

For Configuration 1, eight thermocouples are positioned within the timber members at different depths from the exposed to fire surface. Three thermocouples are positioned on the steel plate, at the interface with the timber members, and six thermocouples are positioned on bolts and dowels at the midpoint of the timber members or 40 mm from the timber side exposed to fire. For Configuration 2, ten thermocouples are positioned within the timber members, four thermocouples are positioned on the steel plates and four other thermocouples are positioned on the dowels. Figure 7 shows an example of locations of the thermocouples for configuration 2.3.

Figure 7: Example of locations of the thermocouples (configuration 2.3)

Two sensors are used to record the displacements Δ_U of connected members (the slipping of connections). The sensor Δ_{Uj} recorded the slipping of two connections tested in fire only during the loading phase before that fire test started. The sensor Δ_{Us} recorded the slipping of the two connections tested in fire, as well as the slipping of the two connections that link the two ends of the tested specimen to the testing frame (hydraulic jack and reaction side), during the fire test including the pre-loading phase (see Figure 5). Failure time is reached when the displacement increases and the mechanical load can no longer be held (this corresponds to a displacement acceleration between 0.2 and 0.6 mm/s^2).

3. TEST RESULTS

3.1 Test results at room temperature

In Table 4 are given the experimental mean load-carrying capacities ($F_{u,mean}$) of connections obtained with tests at room temperature. This mean value $F_{u,mean}$ is obtained by averaging 3 tests. The coefficient of variation for each configuration shows very low variability. In this paper, the failure modes observed during these tests at room temperature are not commented. Here we focus on the fire behaviour of these connections. The load carrying capacities at room temperature are provided as they have been used to determine load ratio for fire tests.

Table 4: Load-carrying capacities of specimens tested at room temperature

Configuration	Experimental load-carrying capacity ($F_{u,mean}$)	Coefficient of variation (%)
1.1	484,0	2,51
1.2	457,6	1,97
1.3	473,0	1,79
2.1	876,2	0,39
2.2	877,3	0,37
2.3	877,0	0,43
2.4	870,6	0,37

3.2 Test results under fire exposure

In Table 5 are given the experimental failure resistances of tested specimens, and the failure modes associated. This table also indicates whether the steel plate is "protected" or not. This protection indicates whether the gap between the steel plates and the timber members, on the top and bottom sides of the connections, is filled or not. In order to reduce the heating of the steel plates, these gaps are filled with plywood for some configurations. Thus, the efficiency of this provision can be checked.

Table 5: Fire resistances and failure modes of the specimens under fire exposure

Configuration	Test number	Fire load F_{fi} (kN)	Experimental fire resistance t_{fi} (min)	Protection of the steel plate	Failure modes
1.1	1	$0,1*F_{u,mean} = 48,4$	96	yes	Row-shear failure without deformation of the fasteners
	2		91	no	
	3	$0,3*F_{u,mean} = 145,2$	74	yes	Row-shear failure with plastic hinge in the fasteners
	4		80	yes	
1.2	5	$0,1*F_{u,mean} = 47,8$	145	yes	Row-shear failure without deformation of the fasteners
	6		121	no	**Steel plate failure in tension**
	7		119	yes	
	8	$0,3*F_{u,mean} = 140,0$	117	yes	Row-shear failure with small deformation of the fasteners
1.3	9	$0,1*F_{u,mean} = 45,8$	142	yes	Row-shear failure without deformation of the fasteners
	10	$0,3*F_{u,mean} = 137,3$	89	no	**Steel plate failure in tension**
2.1	1'	$0,1*F_{u,mean} = 90,0$	81	no	Row-shear failure with small deformation of the fasteners
	2'		79	no	
	3'	$0,3*F_{u,mean} = 270,0$	64	no	Net cross-section failure with plastic hinge in the fasteners
2.2	4'	$0,1*F_{u,mean} = 90,0$	105	no	Row-shear failure with small deformation of the fasteners
	5'		104	no	Row-shear failure with small deformation of the fasteners
	6'	$0,3*F_{u,mean} = 270,0$	82	no	Net cross-section failure in tension with plastic hinges in the fasteners
	7'		85	no	
2.3	8'	$0,1*F_{u,mean} = 90,0$	118	no	Row-shear failure with plastic hinge in the fasteners
	9'		98	no	
2.4	10'	$0,3*F_{u,mean} = 270,0$	150	no	
	11'		134	no	Row-shear failure with plastic hinge in the fasteners, **failure of one steel plate**

Figures 8 shows an example of test results for configurations 1.2, loaded with a load ratio ηfi = 10% $F_{u,mean}$. The load-slip curve and temperature measurements on the steel plates are shown. These curves show that the failure of the connections is strongly linked to the temperature level inside the connection. All experimental results, measured temperatures and slips of tested specimens, are given in the public report reference [8].

a) Load-slip curve   b) Steel plate temperatures
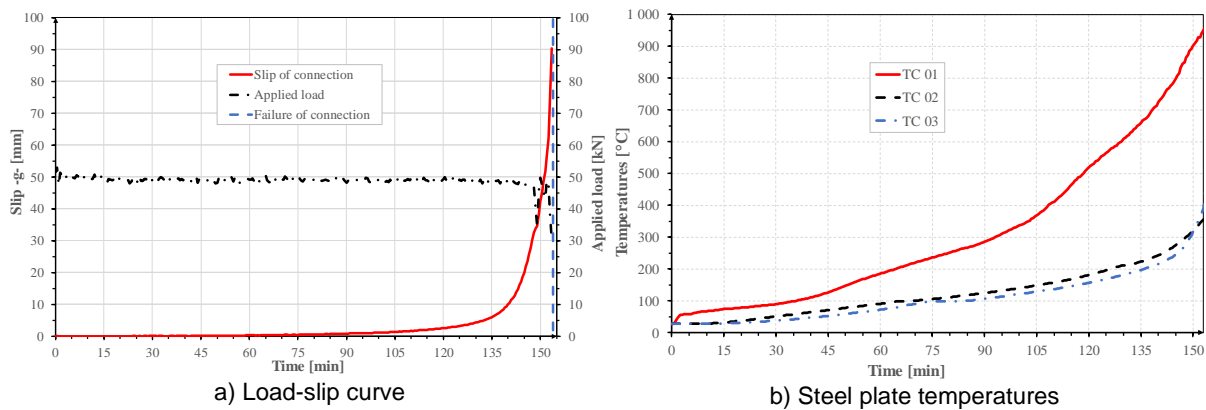
Figure 8: Experimental results for configuration 1.2 (test 5)

After the fire tests, all the test specimens were cut in order to measure the residual cross-section at the connection and beyond the area of the connection. For each type of connection, the mean charring rates have been calculated and varied between 0,55 and 0,76 mm/min, which is consistent with expected values.

4. DISCUSSION

4.1 Comments on the experimental results

For configuration 1 connections loaded at 10% of $F_{u,mean}$, the failure is governed by the embedment of the dowels in the timber members and ended by a shear-line failure. The load applied in fire situation is insufficient to bend the fasterners. For a load ratio equal to 0,3, the embedment of the dowels in the timber members is associated with a deformation of the dowels. These deformations are not equivalent for all the fasteners. Thus, it appears that the maximum deformations are measured for the bolt. Then, it is the "dowel 1", located opposite to the bolts, which present the greatest deformations (Figure 9). The two central dowels have approximately the same amount of deflection, although "dowel 3" has slightly higher deflection. These results confirm the numerical results obtained in previous numerical work [9].
Figures 10 shows the deformations of dowels 1 and 3 for connection number 3 (configuration 1.1).
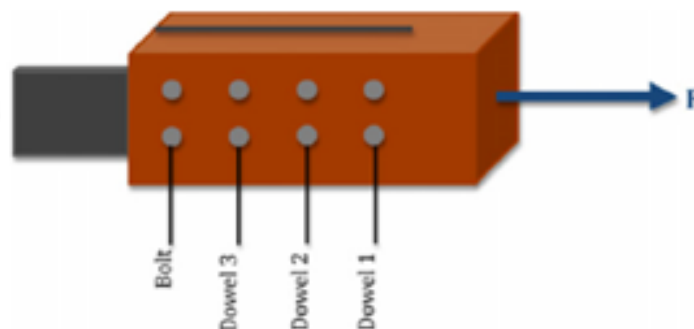
Figure 9: Numbering of the fasteners

a) Dowel 1
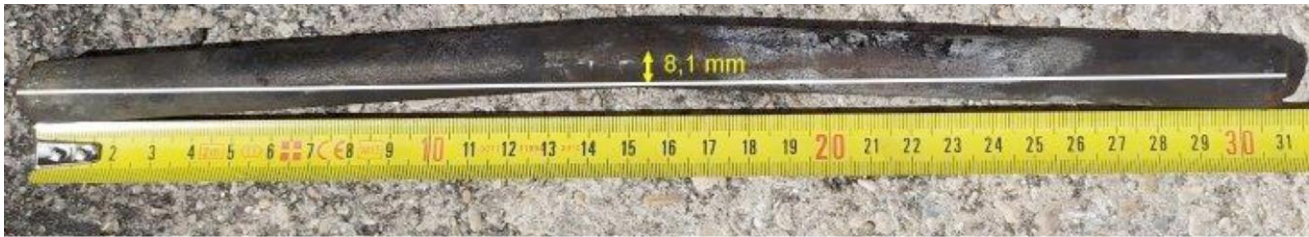
b) Dowel 3

Figure 10: Deformation of dowels for connection 3 (configuration 1.1)

Note that the dowel deflections are very small for connections 7 and 8. These results are counter-intuitive, since the dowels here have the same diameter as in tests 3 and 4 (16 mm), under an equivalent fire loading, but are more slender (higher t_1). For connection 10, failure occurs prematurely through tensile failure of the steel plate and no deformation of the dowels is observed. It should be noted that for this test, the steel plate was not protected.

Concerning the efficiency of the protection of the steel plates in the top and bottom sides of the specimen, it should be noted that the fire resistance duration was slightly lower for the specimens with unprotected steel plates than for those with protection on all sides (see specimen 1 vs specimen 2). The comparison between specimens 5 and 6 should not be taken as significant in view of the early failure of specimen 6 due to the failure of the steel plate (even if this early failure of the steel plate is related to its higher temperature and the absence of protection).

For configuration 2 connections loaded at 10% of $F_{u,mean}$, the failure was essentially generated by the embedment (pull-through) of the dowel in the timber members t_1 and ended by a shear line failure (timber embedment and splitting failure or shear line failure). For the same specimens loaded at 30% of $F_{u,mean}$, the plastic hinge of the dowels lead to their pull-through (embedment) in the timber members t_1 and generate a net cross-section failure in tension. A maximum deflection of 18,4 mm of the dowels has been measured (Figure 11).

Figure 11: Failure mode of connection n°11'

Figure 12: Failure mode of connection n°7'

If for configuration 1 connections, the deformations of the fasteners were identical on the 2 rows, it is important to note that for configuration 2 connections, the most deformed fasteners were those of the two central rows of dowels (2nd and 3rd row), as it can be clearly seen on Figure 12.

As noted in Table 5, for 4 tested specimens, their fire resistances have been defined by the failure time of steel plate. In the Table 6 are shown the design resistances of steel plates calculated in function of the measured temperature at the instant of their failure, as well as the values of the applied loads during the fire test. By the

comparison of these values it's easy to understand that rupture of the steel plates was inevitable. It is therefore advisable not to undersize the thickness of the steel plates, and to implement all possible protection device to delay the heating of these plates.

Table 6: Comparison of design fire resistances and applied loads of connection with steel plate failure

Connection type	Cross-section area (mm²)	Failure temperature of steel plate (°C)	$k_{y,\theta}$	f_y (MPa)	$N_{fi,\theta,Rd}$ (kN)	Applied load (kN)
1.2-test n°6	1140	1025	0.035	460	18.4	47.8
1.2-test n°7		741	0.1808		94.8	140
1.3-test n°10		772	0.1436		75.3	137.3
2.4-test n°11	1284	731	0.1928		113.9	135

4.2 Analytical approach

In 2020, a first analytical formulation, based both on experimental investigations carried out worldwide since 1999 and on numerical studies, was proposed in order to calculate with a simple formula the fire resistance of timber connections with bolts and dowels [4]. Although it significantly improved the accuracy of the calculation of the fire resistance of the connections compared to the current EN1995-1-1, this formulation remained limited to fire resistance durations of less than 90 minutes.

The experimental results presented here have made it possible to improve this analytical method in order to make it valid up to at least 120 minutes. This analytical method is now written as:

$$t_{fi} = \alpha_1 \cdot t_1 - \frac{1}{\alpha_2} \cdot \ln(\eta_{fi} \cdot 100) + \alpha_3 \tag{1}$$

Where:
- t_{fi} is the fire resistance time (in minutes);
- α_i are coefficients given in Table 7;
- η_{fi} is the load ratio for fire situation determined as:

$$\eta_{fi} = \frac{E_{d,fi}}{R_k} \tag{2}$$

- $E_{d,fi}$ is the design effect of actions for the fire situation, determined in accordance with EN 1991-1-2;
- R_k is the characteristic load-carrying capacity of the connection at normal temperature determined according to EN 1995-1-1 neglecting the effective number of fasteners and excluding brittle failure modes.

Table 7: Coefficients α_i for timber-to-timber and steel-to-timber connections with dowels

Connection type	Coefficients α_i			Maximum validity (min)
	α_1	α_2	α_3	
Timber-to-timber	0,88	0,048	50	90
Steel-to-timber with a single slotted-in steel plate	0,63	0,066	35	120
Steel-to-timber with two slotted-in steel plates	1,0	0,066	35	120
Steel-to-timber with three or more slotted-in steel plates	1,2	0,066	35	120

These coefficient values are proposed for dowelled connections, i.e. connections mainly using dowels and with eventually a few minor bolts that provide the connection holding function. For a connection composed exclusively of bolts, the values of these coefficients are more severe and the fire resistance of the connections has to be reduced by 25%.

In order to check the validity of the analytical method for connections with fire resistance durations greater than 90 minutes, the fire resistances obtained during the tests on configurations 1 and 2 presented above are compared with those calculated with the analytical formulation ($t_{fi,calc}$ – eq.(1)). For comparison, the fire resistance values $t_{fi,EC5}$ calculated with the current EN1995-1-2 method (the reduced load method - see EN1995-1-2 chapter 6.2.2) are also shown (Table 8). The relative gaps ε between calculated and experimental values are also provided. It can be noted that the relative gaps between the fire resistance durations calculated with the proposed analytical method and the experimental ones (ε_{calc}) are between 0.36 and 16% while the relative gaps for the current EN1995-1-2 method (ε_{EC5}) are between 61.9 and 86.5%.

Table 8: Experimental and calculated fire resistance durations

Connection configuration	Test Number	$t_{fi,exp}$ (min)	$t_{fi,calc}$ (min)	$t_{fi,EC5}$ (min)	ε_{calc} (%)	ε_{EC5} (%)
Configuration 1 (S-T-S)	1	96	90,2	28,5	6,04	70,3
	2	91	90,2	28,5	0,87	68,7
	3	74	73,5	15,6	0,68	78,9
	4	80	73,5	15,6	8,13	80,5
	5	145	122,6	29,2	15,4	79,9
	6	121	122,6	29,2	1,31	75,9
	7	119	105,9	16,2	11,0	86,4
	8	117	105,9	16,2	9,49	86,2
	9	142	122,6	29,2	13,7	79,4
	10	89	105,9	16,2	16,0	81,8
Configuration 2 (S-T-S-T-S)	1'	81	72,7	30,1	10,2	62,8
	2'	79	72,7	30,1	7,97	61,9
	3'	64	56,1	17,2	12,3	73,1
	4'	105	99	31	5,71	70,5
	5'	104	99	31	4,81	70,2
	6'	82	82,3	18,1	0,36	77,9
	7'	85	82,3	18,1	3,18	78,7
	8'	118	119	31	0,84	73,7
	9'	98	102,3	18,1	4,20	81,5
	10'	150	149	31	0,67	79,3
	11'	134	132,2	18,1	1,34	86,5

In order to visualize the improvement brought by the proposed simplified method in the prediction of the fire resistance of timber connections, compared to the current standard (EN 1995-1-2), Figure 13 shows the comparisons of the two methods with the experimental results. The coefficients of determination R^2 obtained by linear regression are calculated in each case. Figure 13 clearly shows that the method proposed by EN 1995-1-2 is not at all suitable for the calculation of the fire resistance of connections with a fire resistance of more than one hour, because this resistance is greatly underestimated. The EN 1995-1-2 method is therefore extremely limited for the use of timber solutions in construction. The proposed method presents a constant difference between calculated and measured fire resistances. The regression line obtained is collinear to the experimental one, with a satisfactory safety margin.
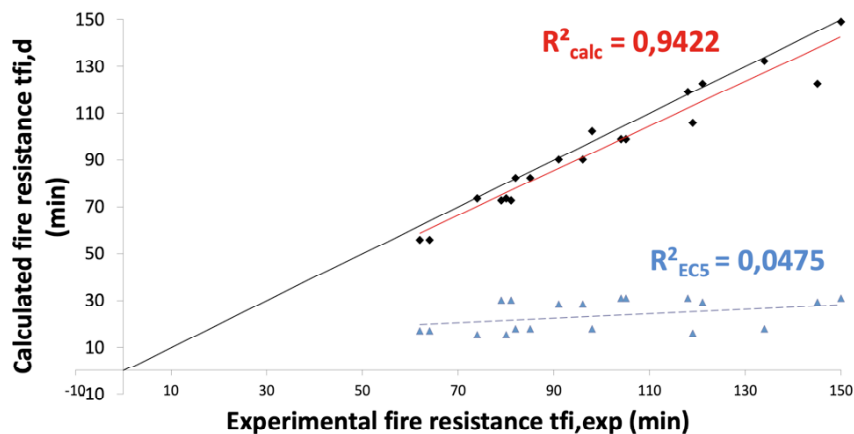
Figure 13: Fire resistance of connections calculated by the proposed simplified method and EN-1995-1-2 versus experimental results

5. CONCLUSION

The main objective of this experimental study was to bring experimental data in order to extend the field of design of steel-to-timber connections for fire resistance duration until two hours. This objective has been achieved. The experimental results presented in this paper were analysed and have improved the analytical simplified method that was proposed in 2020, extending its application to connections with fire resistance durations greater than 90 minutes.

The second objective of this study was to increase the understanding of the thermomechanical behaviour of timber connections. This experimental research allowed to highlight the role of thicknesses of lateral timber members and the load ratio in the fire resistance duration of timber connections. The role of the additional thickness (a_{fi}), added on the side edges (a_4) and the end distance (a_3) of steel-to timber connections, is an important parameter for increasing the fire resistance. The protection of steel plates on all sides, for thicknesses higher than 6 mm, is another necessary precaution for improvement of fire resistance of steel-to-timber connections. The steel-to-timber connections with four shear planes and dowels showed a high load carrying capacity and a higher ductile failure at room temperature with plastic deformation of the dowels, as well as a higher fire resistance compared with the connections with two shear planes. An important point highlighted by this experimental research is linked with the role of the gap between two connections. Especially, for connections with high fire resistance, the thicknesses of timber members are important, and during their drying, the shrink phenomenon is significant. Consequently, if the joint gap increases significantly, the failure of the connection due to the failure of steel plates represent a real risk. For that reason, it is interesting to have in mind this weak point of these connections and to look for a reliable solution.

The simplified proposed method related to timber connections and presented in the last chapter of this paper has been proposed in the frame of revision of EN 1995-1-2 and was retained in the latest proposed draft [10].

6. ACKNOWLEDGEMENTS

7. REFERENCES

[1]   EN 1995-1-2:2004, Eurocode 5: Design of timber structures, Part 1-2: General rules - Structural fire design, CEN, Brussel, November 2004.

[2]   König J., 2004. "Calculations vs fire testing—Limitations of Eurocode 5 and the need of fire testing." In Proc., Int. Symp. on Advanced Timber and Timber-Composite Elements for Building, 27–29. San Michele all'Adige, Italy: CNR-Ivalsa.

[3]   Audebert M., Dhima D., Bouchaïr A., Frangi A., 2019: Review of experimental data for timber connections with dowel-type fasteners under standard fire exposure; Fire Safety Journal 107 (2019) 217–234.

[4]   Audebert, M., Dhima D., Bouchaïr A., 2020. "Proposal for a new formula to predict the fire resistance of timber connections." Eng. Struct. 204 (Feb): 110041. https://doi.org/10.1016/j.engstruct.2019.110041.

[5]   Brandon D., Landel P., Ziethen R., Albrektsson J., Just A., 2019 : High-Fire-Resistance Glulam Connections for Tall Timber Buildings. RISE Report 2019:26, Smart Housing Smaland; 2019. ISBN 978-91-88907-52-3.

[6]   EN January 1, 1995: 2005, Eurocode 5. Design of timber structures. Part 1–1: General—Common rules and rules for buildings. CEN TC 250-SC5, Brussels, 2005.

[7]   EN 26891: timber structures. Joints made with mechanical fasteners. General Principles for the Determination of Strength and Deformation Characteristics. CEN; 1991.

[8]   Marie-Jeanne B-L., 2020: Rapport d'essais, Campagne expérimental relative au comportement au feu d'assemblage bois, 24 avril 2020, CSTB, France.

[9]   Audebert M., Dhima D., Taazount M., Bouchaïr A., 2011: Numerical investigations on the thermo-mechanical behaviour of steel-to-timber connections exposed to fire. Eng Struct. 2011;33:3257-3268.

[10] CEN-TC250-SC5-WG4_N0152_SC5T4_2ND_DOC_EN1995-1-2, Eurocode 5 – Design of timber structures, Part 1-2: General – Structural fire design, SC5.T4, 2nd Draft, May 3, 2020

NUMERICAL STUDY OF THE BEHAVIOR OF CONTINUOUS STEEL-CONCRETE COMPOSITE BEAMS UNDER NON-UNIFORM BENDING MOMENTS IN FIRE SITUATION

Bruno M. Siciliano
a,*

João Victor F. Dias
b

Rodrigo B. Caldas
c

ABSTRACT

Differently from simply supported beams, in a continuous composite beam, the lower portion of the cross section is under compression, therefore, local and global instabilities may occur, and they are potentiated due to the degradation of mechanical properties of the materials at elevated temperatures. The present work aims at performing a parametric study on continuous composite beams, submitted to non-uniform bending moments and under fire situation. In the study, influences of geometric variables of the composite beams, such as the length of their spans and the dimensions of their cross-section were evaluated. An increase in hogging moments at the central support region was observed due to the restriction of the thermal deformations, resulting in a local plastification at temperatures lower than 300 °C. With the local loss of stiffness, buckling become propitious to occur and the capacity of the beam to prevent them determines the temperature in which the hogging moments decrease, i.e., when the efforts redistribution to the mid span occurs. In general, the collapse of the evaluated beams occurred between 600 °C and 700 °C.

Keywords: Continuous Composite Beams; Fire; Numerical Study.

a,* Federal University of Minas Gerais, Av. Pres. Antônio Carlos, 6627 - Pampulha, Belo Horizonte - MG, Brazil, 31270-901, bruno.marani@ufmg.br, Corresponding author.
b Federal University of Espírito Santo, joao.v.dias@ufes.br.
c Federal University of Minas Gerais, caldas@dees.ufmg.br.

1. INTRODUCTION

Simply supported composite beams are more common in practical situations however, the continuity can provide a better distribution of bending moments along the length of the beams. According to [1], the height of the steel profile decreases, and the robustness of the cross-section increases in continuous composite beams, generating economy and better behavior in high temperatures.

In continuous composite beams, the lower part of the cross section (the lower flange and most part of the web) is compressed. Therefore, local instabilities such as FLB and WLB may occur and moreover, due to the tension in the concrete slab, its cracking may take place, significantly reducing the concrete influence in the cross-section resistance.

Due to the compressive efforts in the composite cross-section, the web may suffer warping, losing its planar shape. Moreover, the lower may displace transversally in a rigid body movement and the cracked slab still may prevent pure torsion deformations of the cross-section. The sum of these phenomena is a global instability called Lateral Distortional Buckling (LDB). The deformed shape of a two-span continuous composite beam is shown as it follows in Figure 1:
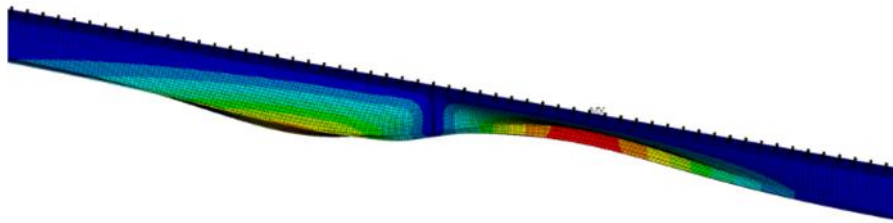
Figure 1: LDB deformed shape in a two-span continuous composite beam

At high temperatures, the degradation of mechanical properties of the materials occur and the restriction of thermal deformations may cause internal additional efforts in a beam. At approximately 550 °C, steel and concrete strengths and stiffness are reduced, in average, to 50%. In mid-span, when the beam is subject to an elevation of temperatures, a curvature towards the source of heat occurs and its restriction at the internal supports causes and elevation of the hogging moments and, thus, the increase of the compression stresses in the cross-section. Furthermore, the restriction of the beam longitudinal elongation may also cause the elevation of compressive stresses near the internal supports, therefore, these regions are more susceptible to instabilities.

The continuity of composite beams guarantees a reserve of security to them. Because of their hyperestaticity, in continuous beams, the formation of plastic hinge at the internal support does not mean their collapse. After the cross-section first plastification on the cracked concrete region, the bending moments are redistributed to mid-span. Only then, when the bending efforts cause the formation of another hinge in mid-span, the collapse of the beam may take place.

Yet, the behavior of continuous composite beams is not completely known. Only a few studies were established in this topic and the influences of geometric properties of the beams in their behavior at high temperatures must be studied, due to the complexity of the typical phenomena that occur in this type of element in such conditions.

2. LITERATURE REVIEW

2.1 Structural Behavior at Ambient Temperature

As mentioned before, at hogging moments regions, the concrete slab is tensioned and, thus, cracked. According to [3], for hogging moments about 30% to 40% of the ultimate resistant moment of the composite cross-section, the concrete may crack, and its resistance may be neglected in analytical calculations. Therefore, the slab rebar controls the location of neutral axis, and consequently, the part of the cross-section that is submitted to compressive efforts.

319

As the lower flange and most part of the web are under compression in bending, local instabilities may occur. The behavior of continuous composite beams relatively to local buckling is very similar to the one of a pure steel beam, as stated by [4]. Therefore, the classification of cross-section according to their slenderness found at [5] may be used to composite beams without any prejudice, according to [6].

Due to fact that most of the steel profile is compressed at hogging moments regions, the transversal displacement of the lower flange in buckling is only restricted by the flexural stiffness of the web, which may be insufficient to prevent such phenomenon. As stated by [2], the concrete slab, though cracked, can still restrict the pure torsional displacement of the cross-section, and as the web loses its planar shape and the lower flange displaces laterally, the Lateral Distortional Buckling (LDB) occurs. According to [1], the typical deformed shape of a continuous two-span composite beam under LDB is characterized by the formation of two opposite semi-waves around the central support, with non-sinusoidal characteristics.

It is important to state that local instabilities may influence the occurrence of global instabilities. In accordance with [7], FLB of the lower flange may instigate the occurrence of LDB, even though these two types of phenomena are treated separately in reference codes, such as [8] and [9]. As stated by these codes, the procedure for the assessment of the LDB resistance of a composite cross-section is similar to others on such a global instability has great importance on its final strength. First, all the influences caused by material and geometric imperfections, by residual stresses and by the instability itself are considered by a reduction factor of the plastification bending moment of the cross-section. This factor is related to a slenderness factor, which is dependent on the LDB buckling bending moment. The first approximation to the elastic buckling bending moment of composite continuous beams was stablished by [10], and it is called Roik's Equation.

In general, it is possible to say that the most critical sections of a continuous composite beam are located at hogging moments regions. In accordance with [11], the bending resistance in hogging moments is, in average, 70% of the one related to sagging moments, due to the local and global instabilities. Moreover, hogging moments are greater than sagging moments, considering a structural analysis in a continuous beam. In other words, in cracked concrete regions, there is greater solicitation and less resistance than in positive bending moments locations. Therefore, a design based only on a simple comparison between solicitation and resistance may be antieconomic and the possibility of moments redistribution may be used.

As the critical section lay on hogging moments regions, the formation of a first plastic hinge may occur in such locations. Nevertheless, due to the hyperestaticity of a continuous beam, this hinge does not mean the collapse of the structure, but only a change in support conditions. After the occurrence of the first hinge, the moments may be redistributed to the center of the spans, as long as the cross-section has enough plastic rotation capacity. Codes such as [8] allow the consideration of a redistribution of 40, 30, 20 e 10% for classes 1, 2, 3 and 4, respectively, according to the cross-section classification based on their capacity of plastification.

In continuous composite beams, there is another critical phenomenon that occur: the interaction between efforts. At hogging moments regions, there may be high bending moments and high shear efforts due to the central support. As stated by [12], these interactions may reduce the resistance of the beams in such regions, though the high contribution to the resistance of vertical shear provided by the concrete slab.

2.2 Fire Based on Codes

In a real fire situation, several variables may influence the heating rate, such as the type of fuel (hydrocarbons or cellulosic materials) and its amount, the geometry of the room subjected to fire and its openings and the presence of passive and active methods of fire combat. Therefore, normative standards have great importance in predicting the fire behavior, despite of their limitations due to the fact that, in the process of assessment, a lot of simplifications are made.

Prescriptions from [13] bring the Standard Fire curve to simulate the elevation of temperatures (T_{fi}) considering only the fire time (t, in minutes) and the ambient temperature (T_a) as entrance variables, as showed:

$$T_{fi} = T_a + 345\,log(\,8t + 1\,) \qquad\qquad (1)$$

Moreover, other codes such as [14] bring more precise equations to predict the fire behavior, dividing the phenomenon in two parts: the heating and the cooling phases. In this case, the type of fuel material, the area of the fire room and its openings are considered. The heating phase equation is presented as it follows:

$$T_{fi} = 20 + 1325(1 - 0{,}324e^{-0{,}2t^*} - 0{,}204e^{-1{,}7t^*} - 0{,}472e^{-19t^*}) \tag{2}$$

where t^* (in hours) is a modified time parameter given by:

$$t^* = t \times \Gamma \tag{3}$$

with Γ being a dimensionless parameter that considers the coating material of the room and its openings. A comparison between these two approximations (considering Γ as 1, 0,2 and 5) of the heating phase is showed in Figure 2:
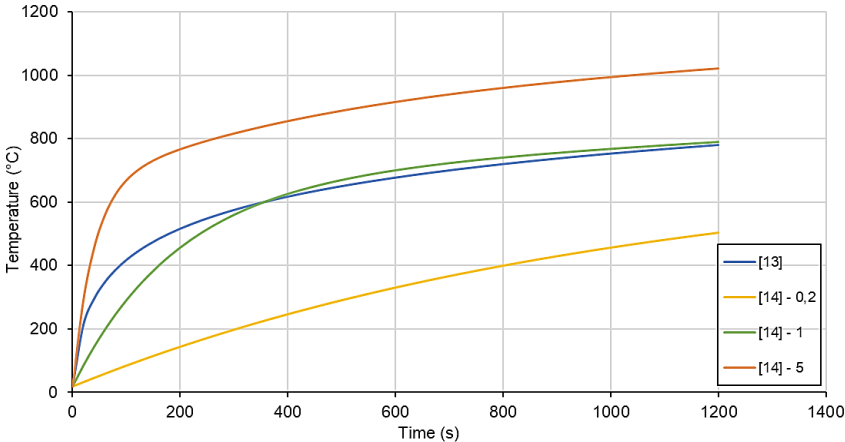
Figure 2: Comparison between heating phase curves

As it can be noticed, the Standard Fire approximates to the curve considering the dimensionless parameter as 1, for temperatures above 400 °C. The elevation of Γ results in higher heating rate.

2.3 Structural Behavior at High Temperatures

At high temperatures, the mechanical properties (strength and stiffness) of materials decay and thermal properties (specific heat, thermal conduction coefficient and thermal elongation) may vary. Reference codes, such as [15], brings prescriptions to determine theses variations of properties. In the case of mechanical properties, the reference code uses reductions factors for the strength and stiffness of profile steel ($k_{ya,\theta}$ and $k_{Ea,\theta}$) and rebar steel ($k_{ys,\theta}$ and $k_{Es,\theta}$), and also the strength of concrete ($k_{c,\theta}$), as it can be shown in Figure 3:
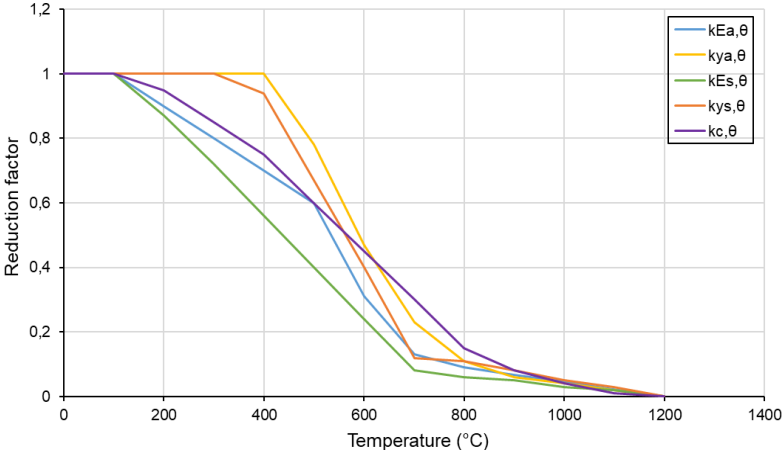
Figure 3: Reduction factors based on [15]

321

It can be noticed that both steel and concrete lose, approximately, 50% of their strength and stiffness at temperature near to 500 °C. The decay of concrete strength stars at 100 °C, while for steel, this occurs at temperatures above 300 °C.

When a continuous composite beam is subjected to fire along its spans, a formation of curvature towards the heat source occurs at mid-span. The restriction of this curvature provided by the central supports may generate an amplification of hogging moments, increases the compressive stresses in the steel profile and propitiating local and global instabilities. The same phenomenon occurs when the longitudinal thermal elongation of the beams is restricted by its supports. As instabilities occur, a loss of local stiffness may take place at central supports regions, elevating the vertical displacement at mid-span and resulting in a shortening tendency of the beam span. As the supports restrict this displacement, the beam is now subject to tension, that may resist bending efforts, in a phenomenon called catenary effect. At higher temperatures, the mechanical properties become very prejudiced, and the beam collapse may occur.

The first relevant study considering continuous composite beams under fire situation was proposed by [16]. In this study, the authors performed several in-scale tests, considering cantilever and continuous beams. The study observed very intense local buckling near the supports, at hogging moments region, but no LDB was verified. The last known study in the theme was developed by [2], in which four in-scale tests were conducted with continuous composite beams under uniform hogging moments. The author observed the interaction of local (FLB, WLB) and global (LDB) instabilities and this was the first time that a LDB test report were made. Moreover, the same study developed a finite element model, that was validated based on tests results. The model considered all elements on a composite cross-section: the steel profile, the concrete slab, stud-bolt connectors, and the slab rebars. Also, the geometric imperfections were considered based on the first buckling mode of the beams and the Standard Fire curve was used. Through a parametric study, the author proposed a calculus procedure of determining the resistance of continuous composite beams under fire situation.

3. METHODOLOGY

3.1 General Considerations

In this research, a numerical parametric study was developed based on the validated model proposed by [2]. Modifications were made in the model to adapt it to non-uniform moments and to consider different heating curves. The ANSYS Mechanical APDL v.2019 R3 was used for the analysis and further information about the functioning of it may be found in its manual.

All the beams had three hinged supports (allowing free longitudinal thermal elongation) and two spans. The profile and stud-bolts steel was ASTM A-572 Gr. 50, while for the rebars, a CA-50 steel (with yielding resistance of 500 MPa) was used. All profiles had a width of 200 mm and flange thickness of 16 mm. The concrete was from class C30, with characteristic compressive resistance of 30 MPa. The stud-bolts were designed based on [9] for hogging moments regions, and the spacing between them in these locations was extrapolated to sagging moments region. All the slabs were solid with thickness of 120 mm and width of 2000 mm. The consideration of their symmetry (it was considered a U mechanism, regarding other parallel beams to the one analyzed and joined by the slab) were established by imposing continuity restrictions of DOFs at their extremities.

In terms of mesh, a base maximum size was stablished considering the width of the flange divided by 4 ($b_f / 4$). This base size was used for the steel profile and for the concrete slab, along its longitudinal and transversal axes, the base size was multiplied by three and two, respectively, as it follows in Figure 4.

For structural analyses, the following types of elements were used:

- SOLID185: concrete slab
- SHELL181: steel profile
- BEAM188: stud-bolts
- REINF264: slab rebars
- CONTA173 and TARGE170: contact between the profile and slab

322

For thermal analyses, the element types were changed to the following:

- SOLID70: concrete slab
- SHELL131: steel profile
- LINK33: stud-bolts
- CONTA173 e TARGE170: contact between the slab and profile
- SURF152: heat flows of convection and radiation
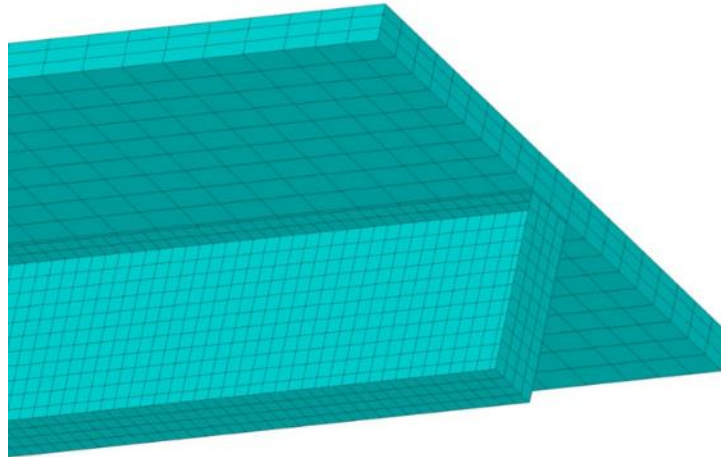
Figure 4: FEM mesh of the models

The procedure of the analyses began with the building of the beam geometry and the applying of the support conditions. Then, a pure thermal analysis was developed with the corresponding element types and considering a specified heating curve, based on [13] or [14]. The temperature field for each time step was stored and the corresponding reduction factors of mechanical properties and the thermal properties were determined based on [15].

Afterwards, a buckling analysis was developed, changing the types of elements (thermal to structural). The first buckling mode (shown in Figure 5) was then used to determine the geometric imperfections that were inserted in a non-linear analysis in ambient temperature.
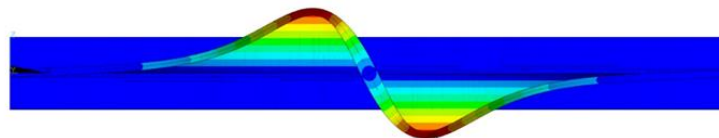
Figure 5: First buckling mode of the beams

The imperfections were considered as the length of one semi-wave divided by 1000. Then, the non-linear ambient analysis was performed and the ultimate resistant bending moment in hogging regions was determined. The corresponding distributed load to this bending moment was stored and later a fraction of it was used to determine the load level of the thermal-structural non-linear final analysis (which corresponds to 50% of the final load at ambient temperature).

Finally, the final transient analysis was developed, considering the geometric imperfections and the increase of temperature, based on the results from the first pure thermal analysis. The collapse temperatures and the evolution of negative and positive bending moments were stored.

323

3.1 Parametric Study

As stated before, a parametric study was proposed. In this case, the varying properties were the span length (L), the height (d) and thickness (t_w) of the profile web, the amount of negative rebars on the slab at hogging moments regions (A_s) and the rate of heating curves (HC). Most of these properties were chosen due to the high influences that they exert in ambient temperature. Therefore, the models analyzed are presented in Table 1:

Table 1: Parametric models analyzed

Model	L	d	t_w	A_s	HC
	(m)	(mm)	(mm)	-	-
M1	**10**	**600**	**12,5**	$30\phi8$	**[13]**
M2	**15**	600	12,5	$30\phi8$	[13]
M3	**7**	600	12,5	$30\phi8$	[13]
M4	10	**800**	12,5	$30\phi8$	[13]
M5	10	**400**	12,5	$30\phi8$	[13]
M6	10	600	**16,0**	$30\phi8$	[13]
M7	10	600	**10,0**	$30\phi8$	[13]
M8	10	600	12,5	$\mathbf{46\phi8}$	[13]
M9	10	600	12,5	$\mathbf{12\phi8}$	[13]
M10	10	600	12,5	$30\phi8$	**[14] – 0,2**
M11	10	600	12,5	$30\phi8$	**[14] – 5**

The properties shown in Table 1 are in accordance with Figure 6:
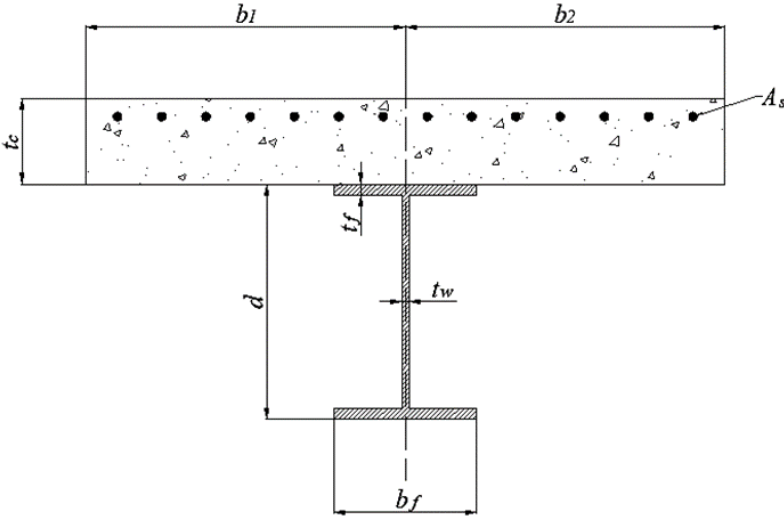
Figure 6: Properties of the composite cross-section

Thus, after the analyses of all models, several results at high temperatures were obtained and they are exposed as it follows.

4. RESULTS AND DISCUSSION

All the results presented were compared to the standard model (M1), as showed afterwards:
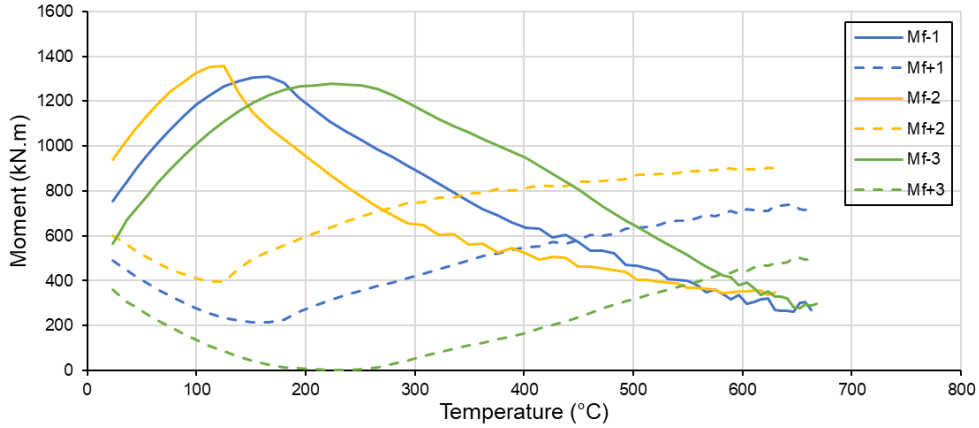
Figure 7: Comparison between M1, M2 and M3 (varying *L*)

In Figure 7, M_{f-} and M_{f+} are the hogging and sagging bending moments in modulus measured at the central support and at mid-span, respectively. With the start of transient analysis, both bending moments begin to rise, due to the elevation of thermal efforts. At low temperatures, the models achieve their maximum resistant hogging moment, which is corresponding to the plastification of great part of the cross-section, as shown in Figure 8 (red regions indicate the yield stress of steel):
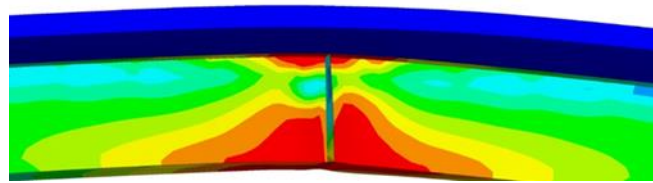
Figure 8: von Mises stress for M1 at hogging moments peak

After this peak, a local loss of stiffness at middle support regions occur and instabilities become more evident. The decay of hogging moments starts when an interaction between FLB, WLB and LDB takes place, as exposed in Figures 9 (a, b and c):

(a)

(b)

(c)
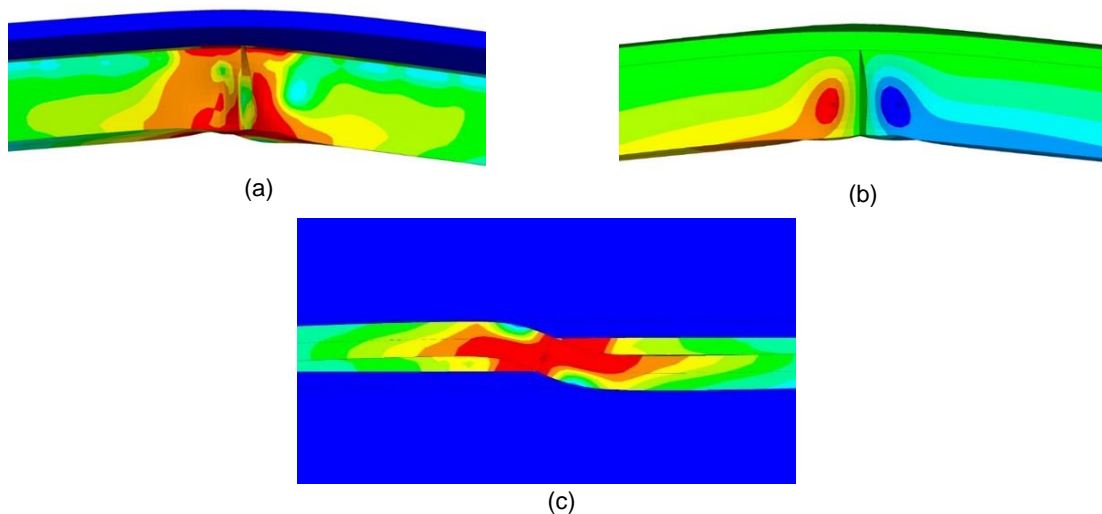
Figure 9: (a) FLB deformed shape in terms of von Mises stresses; (b) WLB in terms of transversal displacement; (c) LDB deformed shape in terms of von Mises stresses

Then, after the decay of hogging moments, redistribution occur to mid-span and at temperatures between 600 °C and 700 °C the beam collapse occurs, due to the high degradation of material mechanical properties and, consequently, due to the total plastification of mid-span cross-section.

It can be noticed by Figure 7, that for M3, the interval between the peak of hogging moments and the start of their decay in terms of temperatures is higher than the other models (here, this temperature interval will be called "threshold"). This can be explained due to the fact that with a lower beam span, both mechanical and thermal hogging moment at central supports are lower too, thus, the compressive stresses are lower, postponing instabilities to occur. Also, it is noticeable that the values of peaks of M1, M2 e M3 are very similar, due to the same plastification bending moments of the models, which have the same cross-section.

Observing Figure 10, it can be noticed that the peak of hogging moment for model M4 is higher than for the other models. This may be explained by the higher plastification bending moment of this model, as the height of the steel profile increases. Although, the threshold of this model is shorter than the others, which is explained by the greater slenderness of the web from model M4, causing earlier instabilities and, thus, the decay of hogging moments takes place ate lower temperatures.
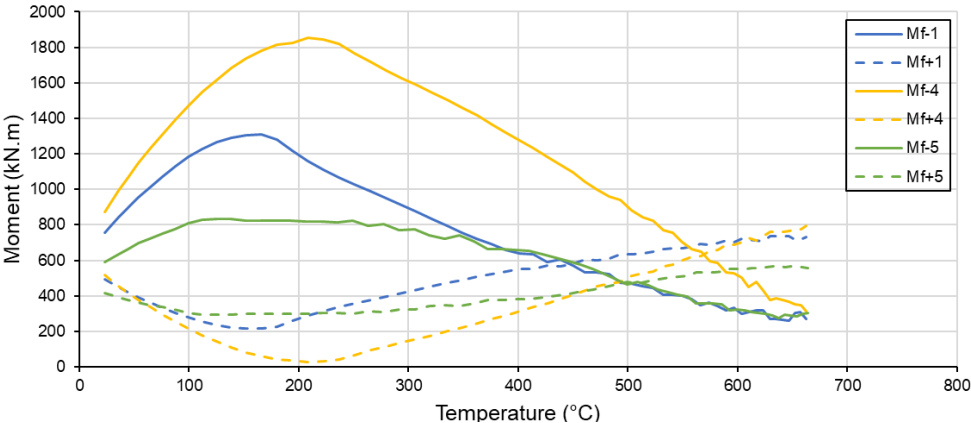
Figure 10: Comparison between M1, M4 and M5 (varying *d*)

As shown in Figure 11, both the peak of hogging moments and the temperature interval of the threshold of model M6 are greater than for the other models. In this case, by increasing the web thickness of the steel profile, the plastification bending moment increases and the web becomes less slender, postponing the instabilities to occur.
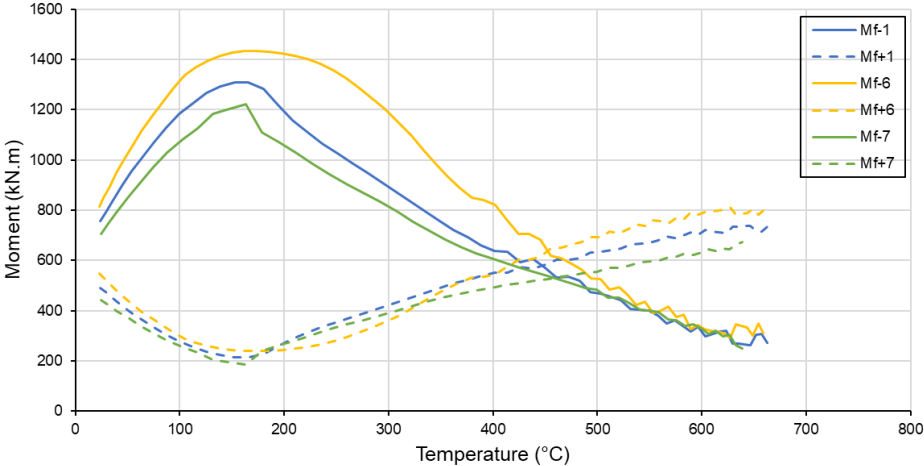
Figure 11: Comparison between M1, M6 and M7 (varying *t_w*)

As observed in Figure 12, the peak of hogging moments is greater for model M8 than for the others. The same statement may be done: the increase of negative rebar in cracked concrete regions increases the plstification bending moment of the cross-section. Also, it can be notices that the threshold of model M8 is shorter, which can be explained by the fact that with more rebar, the neutral axis is translated towards the concrete slab, increasing the compressed part of the steel profile, facilitating the instabilities to occur.
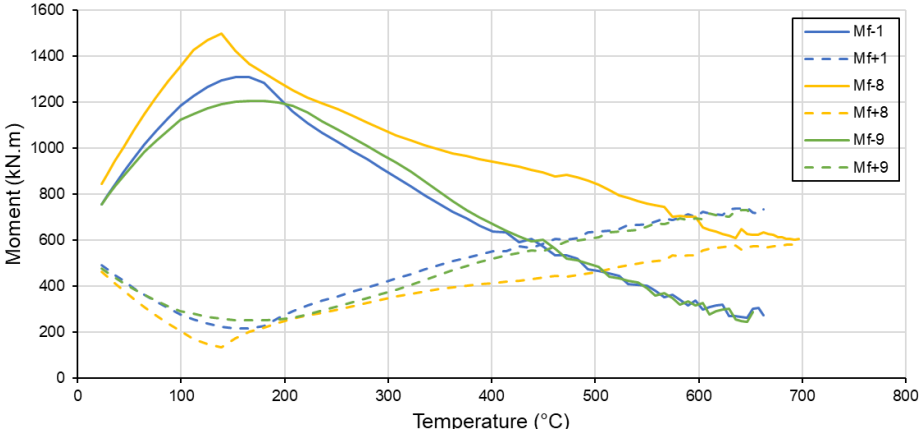
Figure 12: Comparison between M1, M8 and M9 (varying A_s)

By Figure 13, it can be noticed that the peak of hogging moments is very similar between M1, M10 and M11, because they have the same cross-section, and, consequently, the same plastification bending moment. Moreover, the critical collapse time of these models were 926,7 s, 2460,0 s and 447,0 s, respectively, indicating that higher heating rates may cause earlier collapse of the composite beams. Apparently, the threshold of model M11 is greater than for the others, nevertheless, due to the difference of heating rates, each temperature occur at different fire times between the models. When observing a time-domain analysis, instead of a temperature-domain one, it is noticed that the threshold of M10 is greater than the other. This may be explained by the fact that with lower heat rates, the hogging moments caused by the restriction of the thermal curvature are lower and, thus, the instabilities occur at higher fire times.
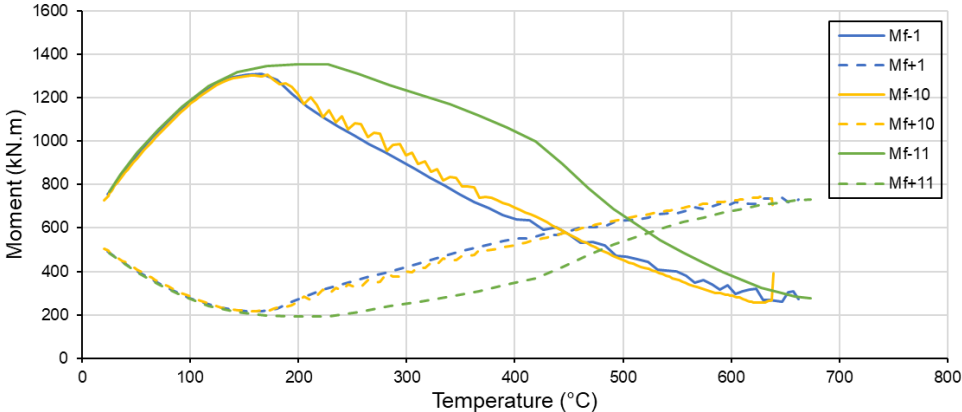
Figure 13: Comparison between M1, M10 and M11 (varying HC)

5. CONCLUSIONS

After the completion of the research, a pattern of behavior was observed for the continuous composite beams. First, the bending moments increase due to the increase of thermal deformations restrictions and, then, a peak is reached, which is related to the plastification bending moment of the cross-section. In other words, this peak is as higher as the amount of material in the cross-section. After the peak, a loss of local stiffness occur, facilitating local and global instabilities to take place. It was observed an interaction between FLB, WLB and LDB at lower temperatures (lower than 300 °C). The threshold between the peak and the start of hogging moments decay is as longer as the capacity of the cross-section to postpone instabilities. After the start of hogging moments decay, moment redistribution to the mid-span occur, and for temperatures between 600 °C and 700 °C, the collapse of the beam may occur, due to the formation of a another plastic hinge at this region, induced by material mechanical properties degradation.

The increase of the profile height increases the peak of hogging moments, although with the increase of web slenderness, the instabilities tend to occur earlier. The increase of web thickness showed to be one efficient way to increase the bending resistance of the cross-section and to avoid instabilities to occur. Increasing the amount of negative rebar in the slab, the peak also increases, nevertheless, with the rise of the neutral axis, instabilities may be hastened. Higher heating rates caused earlier collapse of beams, as the thermal efforts tend to be higher at lower fire times.

ACKNOWLEDGEMENTS

REFERENCES

[1] Johnson, R. P. (2004). *Composite Structures of Steel and Concrete - Beams, Slabs, Columns, and Frames for Buildings*, John Wiley & Sons Inc, 224 p.

[2] Dias, J. V. F. (2021). *Flambagem Lateral com Distorção de Vigas Mistas de Aço e Concreto em Situação de Incêndio: Análises Experimental e Numéricas e Proposta de Procedimento de Cálculo*. PhD Thesis, Federal University of Minas Gerais, 173 p.

[3] Dekker, N. W.; Kemp, A. R.; Trinchero, P. (1995). *Factors Influencing the Strength of Continuous Composite Beams in Negative Bending*, Journal of Constructional Steel Research, vol. 34, p. 161-185.

[4] Climenhaga, J. J.; Johnson, R. P. (1972). *Local Buckling in Continuous Composite Beams*, The Structural Engineer, vol. 50, no. 9, p. 367-374.

[5] European Committee for Standardization – EN 1993-1-1:2005. (2005). *Eurocode 3: Design of Steel Structures. Part 1-1: General Rules and Rules for Buildings*, 91 p.

[6] Johnson, R. P.; Fan, C. K. R. (1991). *Distortional Lateral Buckling of Continuous Composite Beams*, Proc. Instn. Civ. Engrs, vol. 91, p. 131-161.

[7] Fan, C. K. (1990). *Buckling in Continuous Composite Beams*. PhD Thesis, University of Warwick, 202 p.

[8] European Committee for Standardization – EN 1994-1-1:2004. (2004). *Eurocode 4: Design of Composite Steel and Concrete Structures. Part 1-1: General Rules and Rules for Buildings*, 118 p.

[9] Associação Brasileira de Normas Técnicas – ABNT. NBR 8800. (2008). *Projeto de Estruturas de Aço e de Estruturas Mistas de Aço e Concreto de Edifícios*, 237 p.

[10] Roik, K.; Hanswille, G.; Kina, J. (1990). *Solution for the Lateral Torsional Buckling Problem of Composite Beams*, Stahlbau, vol. 59, p. 327-332.

[11] Chen, S.; Jia, Y. (2008). *Required and Available Moment Redistribution of Continuous Steel-Concrete Composite Beams*, Journal of Constructional Steel Research, vol.64, p. 167-175.

[12] Liang, Q. Q.; UY, B.; Bradford, M. A.; Ronagh, H. R. (2004). *Ultimate Strength of Continuous Composite Beams in Combined Bending and Shear*, Journal of Constructional Steel Research, vol.60, p. 1109-1128.

[13] International Organization for Standardization – ISO 834-1:1999. (1999). *Fire Resistant Tests – Elements of Building Construction – Part 1: General Requirements*, 25 p.

[14] European Committee for Standardization – EN 1991-1-2:2002. (2002). *Eurocode 1: Actions on Structures. Part 1-2: General Actions – Actions on Structures Exposed to Fire*. Brussels, 59 p.

[15] European Committee for Standardization – EN 1994-1-2:2005. (2005). *Eurocode 4: Design of Composite Steel and Concrete Structures. Part 1-2: Structural Fire Design*, 109 p.

[16]   Zhao, B.; Kruppa, J. (1997). *Fire Resistance of Composite Slabs with Profiled Steen Sheet and of Composite Steel Concrete Beams – Part 2: Composite Beams*, ECCS, EUR 16822 EN, 77 p.

NUMERICAL SIMULATION OF CROSS-LAMINATED TIMBER-CONCRETE COMPOSITE FLOORS IN FIRE

Julie Liu [a],*; Erica C. Fischer [b]; Andre R. Barbosa [c] and Arijit Sinha [d]

ABSTRACT

Timber-concrete composite (TCC) floors exposed to fire experience charring and thermal degradation of timber, reducing load-carrying capacity. Finite element (FE) modeling supplements data from experimental fire testing and allows for fast and economical investigation of numerous design parameters. A two-dimensional FE modeling methodology is developed for cross-laminated timber (CLT)-concrete composite floors loaded with a uniformly distributed service-level live load and exposed to the ASTM E119 standard fire. The FE model is benchmarked against data from corresponding model tests. Results indicate that the load-carrying capacity of the floor is dependent on tensile stress redistribution to the uncharred parallel layers. The FE model is then used to conduct a parametric study investigating the behavior of the CLT-concrete floor with different percentages of composite efficiency. The failure time and deflection approach constant values at composite efficiencies higher than 40%. However, the percentage of composite efficiency improves fire performance more effectively for floors with shorter spans than for floors with longer spans. The results of this work provide insight into the efficient design of TCC floors for improved fire performance.

Keywords: Timber-concrete composite; cross-laminated timber; fire; structural fire engineering; numerical analysis

1. INTRODUCTION

The use of timber in multistory construction is motivated by sustainability, lightweight materials, reduced costs, and faster construction times [1]. Advanced performance of timber floor systems can be achieved by mechanically joining the timber floors with a concrete topping through shear connectors. This type of timber-concrete composite (TCC) construction has the potential for better structural and serviceability performance and improved vibration and acoustic properties [2]. Due to these benefits, TCC floors have been tested experimentally under a variety of serviceability and loading conditions (e.g., seismic, fire, and vibration).

During a fire scenario, charring of the timber and thermal degradation of the timber and concrete reduce the load-carrying capacity of TCC floors. When the TCC floor is constructed with timber panels (such as cross-laminated timber, or CLT), the insulating effect of the timber prevents the concrete topping from exceeding temperatures greater than 100°C [3]. Timber undergoes pyrolysis and combustion at elevated temperatures, leaving behind a char matrix with negligible strength and stiffness. Simultaneously, the strength and stiffness of the uncharred timber

---

[a],* Oregon State University, 220 Owen Hall, Corvallis, OR 97331, USA (liujuli@oregonstate.edu). Corresponding author.

[b] Oregon State University, Corvallis, OR, USA (erica.fischer@oregonstate.edu).

[c] Oregon State University, Corvallis, OR, USA (andre.barbosa@oregonstate.edu).

[d] Oregon State University, Corvallis, OR, USA (arijit.sinha@oregonstate.edu).

decrease due to the evaporation of moisture and thermal degradation [4,5]. Therefore, the load-carrying capacity of TCC floors during a fire exposure depends on the uncharred timber cross-section.

Analytical design methods for TCC floors in fire must consider both the reduction in the timber cross-section due to charring and the continually changing stress distribution throughout a fire scenario. Common analytical design methods are the elasto-plastic model [6] and the gamma-method [7], both of which can be utilized in conjunction with the reduced cross-section method [7] to calculate stress distributions through the TCC floor, deflections of the TCC floor, and flexural capacity of the TCC floor throughout a fire exposure. Limitations of these methods include the assumption that all shear connectors are either elastic or yielded, the timber and concrete materials behave elastically, and the timber section has constant stiffness through its depth in the span direction, as opposed to having laminations of varying stiffness as found in CLT panels.

Large-scale experimental fire testing provides data to evaluate the behavior of TCC floors in response to simultaneous mechanical loading and fire exposure. However, large-scale fire testing is costly and time-consuming. In addition, the harsh environment of fire testing places limitations on sensor placement, quantity, and type. Finite element (FE) modeling provides a fast and economically efficient methodology to supplement data collected from physical tests and explore additional parameters of TCC floors. FE modeling of TCC floors exposed to fire can be conducted through sequentially coupled thermal-structural analysis [8–10]. FE modeling methodologies can account for the reduction in strength and stiffness of the uncharred timber, the nonlinear behavior of timber and concrete materials, and internal stresses and connector forces that are difficult to obtain from experimental fire tests and empirical models. These data can identify anticipated failure mechanisms and improve analytical design methods.

Numerical parametric studies of TCC floors have focused on the relationship between the properties of the shear connectors and the ambient-temperature stiffness and capacity of the floor [11–13]. There have been very few numerical parametric studies of how varying the design parameters of a TCC floor affects its response to simultaneous fire exposure and mechanical loading [10,14]. Consequently, the objectives of this paper are to:

1. Benchmark FE modeling methodologies by comparing calculated deflections and failure times from FE models to corresponding experimental data.
2. Quantify the effect of composite efficiency on the fire performance of TCC floors, in terms of failure time and deflection.
3. Identify how FE models can provide insight into efficient fire safety design of TCC floors.

2. METHODS

2.1 Experimental tests

Experimental data from tests performed at the National Research Council of Canada were utilized to benchmark the FE methodology. Figure 1 shows the CLT-concrete composite floor, which was 4806 mm long by 1219 mm wide. The CLT was a V2M1.1 grade panel manufactured by StructurLam and assembled from five 35-mm thick laminations, resulting in a total depth of 175 mm. The CLT was topped with a layer of 57-mm thick, 35.7 MPa normal-weight concrete; W152 x W152 gauge 9/9 wire mesh was provided as shrinkage reinforcement in the concrete. The shear connectors joining the CLT to concrete were fully threaded ASSY VG CYL timber screws, 200 mm long and 9.5 mm in diameter. The screws were embedded in the CLT at a 45° angle with a 150 mm embedment length. Screws were spaced at 305 mm in the span and width directions, with an edge distance of 76 mm and 152 mm in the span and width direction, respectively.

The CLT-concrete floor was instrumented with Type K thermocouples embedded in the timber perpendicular to the isotherms via holes drilled from the unexposed side. The thermocouples embedded in the CLT were located at glue lines between laminations, corresponding to distances of 35, 70, and 140 mm from the exposed surface of the CLT. The vertical displacement of the floor was measured with string potentiometers located at mid- and quarter-points along the span. A distributed service live load of 3.83 kPa was applied to the floor with hydraulic rams. The floor was supported on roller supports above the test furnace, and the bottom surface of floor was exposed to the ASTM E119 standard fire curve [15].
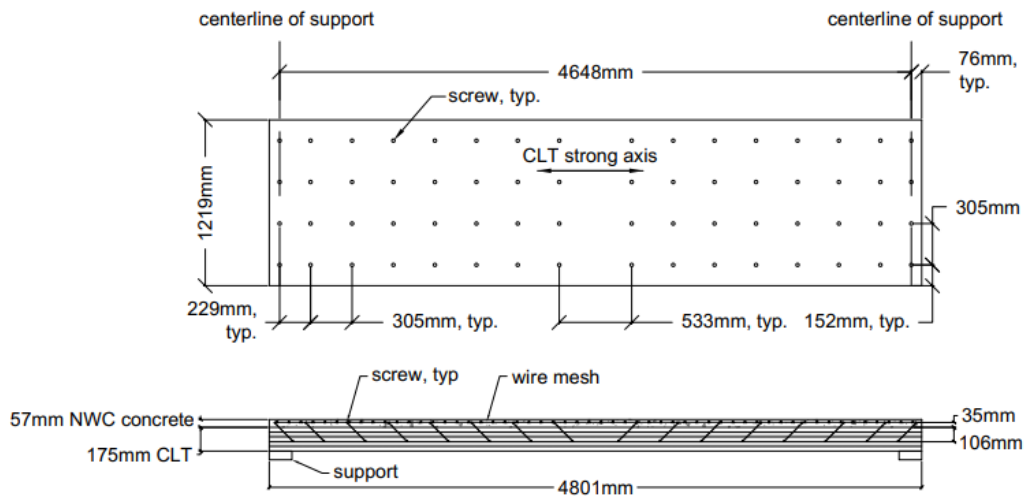
Figure 1: Plan and section views of CLT-concrete floor.

2.2 Numerical methods

A two-dimensional finite element modeling methodology was developed in ABAQUS [16], a commercially available software. ABAQUS was utilized for this study because it has the ability to incorporate nonlinear heat transfer analysis, temperature-dependent material models, sequentially coupled thermal-structural analyses, and implicit or explicit dynamic analysis of failure and behavior of structural components. ABAQUS utilizes the modified Riks arc-length solution algorithm [17,18]. A sequentially coupled thermal-structural analysis was performed where temperatures from the thermal analysis were utilized in the subsequent stress-based analysis to calculate temperature-dependent mechanical properties of the TCC floor at elevated temperatures. The sequential analysis assumes that the thermal analysis is independent of the stress-based analysis.

A two-dimensional thermal analysis was conducted in ABAQUS to calculate the internal temperatures in the TCC floors exposed to the ASTM E119 standard fire [15]. The thermal analysis results were previously validated against experimental tests of TCC floors in fire [19]. Timber and concrete were modeled with four-node linear quadrilateral elements (DC2D4) at approximately 5 mm x 5 mm mesh size. The shear connectors were not included in the thermal analysis because they have a negligible effect on heat transfer through the timber-concrete cross section [3]. The temperature-dependent density ratio, specific heat, and thermal conductivity of timber were referenced from EN 1995-1-2 [4], except that the peak in specific heat between 100°C and 120°C was replaced with latent heat equivalent to the energy absorbed by vaporization of moisture [20]. The moisture content of CLT was not measured prior to testing and was assumed to be 12% with a corresponding latent heat of 270 kJ/kg, in accordance with performance standards for moisture content [21]. The density of the CLT was provided by the manufacturer as 485 kg/m³. The temperature-dependent density ratio, specific heat, and thermal conductivity of concrete were referenced from EN 1992-1-2 [22]. Boundary conditions of convective and radiative heat transfer with gas temperatures following the ASTM E119 fire curve were applied to the exposed surface of the CLT and NLT. The convection coefficient was 25 W/m² [23], while the emissivity of timber was 0.8 [4]. The lateral sides of the specimen were defined as adiabatic, such that no heat transfer occurred through the lateral faces.

The stress-based analysis utilized the calculated temperatures from the thermal analysis, temperature-dependent mechanical properties of timber and concrete, and the force-slip behavior of the shear connectors to calculate the mechanical behavior of the TCC specimens under constant loading. The concrete and timber components of the TCC floors were modeled with 4-node bilinear plane stress elements (CPS4). The shear connectors were modeled as point-to-point wire connectors (CONN2D2). The mesh size of the model was 5 x 5 mm to ensure compatibility with the thermal model. Contact between the concrete and timber layers was defined as a frictionless hard contact interaction since the effect of frictional interaction between timber and concrete was included in the connector stiffness derived from experimental force-slip data [3]. The floor support conditions were defined as simply supported (pin and roller).

332

The elastic modulus of concrete was calculated as the secant value at $0.4f_c^{'}$, while the Poisson's ratio was set to 0.2 [24] (Table 1). The inelastic mechanical behavior of concrete was defined through the concrete damaged plasticity material model in ABAQUS [25,26]. The concrete damaged plasticity model allows for the definition of plasticity in compression and damaged elasticity under cyclic loading. The tensile behavior of concrete was defined as linear up to the tensile capacity, after which the material was defined as plastic. Plastic behavior of concrete in tension was adopted to improve model stability and prevent premature failure due to stress concentrations at the shear connector locations. The tensile capacity of concrete was calculated as the mean tensile strength, f_{ctm} [24]:

$$f_{ctm}= 0.3 \, (f'_c+8MPa)^{2/3} \tag{1}$$

where f'_c is the concrete compressive strength at 28 days. A temperature-dependent reduction factor was applied to the tensile capacity of concrete at elevated temperature [24]. The behavior of concrete after cracking was specified in terms of a stress-strain curve [27]. The temperature-dependent constitutive behavior of concrete in compression was calculated according to EN 1992-1-2 [22]. The stress-strain curve up to f'_c is given by:

$$\sigma(\varepsilon)=\frac{3f'_c\varepsilon}{\varepsilon_{c1}(2+(\varepsilon/\varepsilon_{c1})^3)} \tag{2}$$

where ε_{c1} is the strain at compressive strength. At strain greater than ε_{c1}, stress decreases linearly to zero at ultimate strain, ε_{cu}.

Base values of compressive strength, tensile strength, and elastic modulus of the parallel layers of the CLT were taken as the values for No. 2 SPF [28]. The tensile and compressive strength of the CLT cross-layers were the perpendicular-to-grain values [28,29]. The elastic modulus of the cross-layers of the CLT, E_{90}, was assumed to be 1/30 of the stiffness the parallel layers [21]. Base values of the mechanical properties of CLT utilized in the FE model are reported in Table 1. The concrete damaged plasticity type was utilized for the mechanical behavior of timber because this material type allows for the definition of different capacities in compression and tension. Timber was modeled as elastic-plastic in compression and tension. Elastic-plastic tensile behavior was adopted for stability of the shear connectors and to limit stresses within the timber to the tensile capacity of timber. Temperature-dependent reduction factors for strength and stiffness were applied to the timber material definition [4].

The shear connectors were modeled as point-to-point spring connectors located at the timber-concrete interface at the penetration point of the screws. The force-slip behavior of the shear connectors was based on direct shear tests [3] and was simplified as linear elastic-plastic, with stiffness defined by the secant slip modulus. The secant slip modulus was calculated as the peak force divided by the ultimate slip [3].

Table 1. Concrete and timber properties at ambient temperature.

	Compressive strength (MPa)	Tensile strength (MPa)	Elastic modulus (MPa)	Poisson's ratio
Concrete	35.7	2.76	21184	0.2
CLT parallel layers	7.93	3.10	9652	0.3
CLT cross-layers	2.93	0.40	322	0.3

2.3 Parametric study

Variables of the parametric study were selected based on design considerations for TCC floors and the properties of the physical test specimen. The demand-to-capacity ratio (d/c), f'_c, stiffness of the cross-layers within the CLT, and composite efficiency (λ) varied from their base values. The physical test specimen was loaded to 0.37 of the ambient-temperature capacity of the CLT-concrete floor. Consequently, d/c was increased to 0.5 and 0.7 in the parametric study. The concrete strength of the physical test specimens was 35.7 MPa. The parametric study investigated the impact of reducing the concrete by about 33% to 24.1 MPa. The stiffness of the cross-layers within the CLT is typically assumed to be 1/30 the stiffness of the parallel layers, or $E_0/30$ [21,29]. To determine the extent to which this assumption affected the fire behavior of the CLT-concrete floor, the stiffness of the cross-layers was increased to $E_0/10$ and $E_0/5$. The composite efficiency of the CLT-concrete floor was varied by changing the stiffness

of the shear connectors. The composite efficiency was defined as the difference between the theoretical deflection of a non-composite floor (δ_n) and the deflection of the partially composite floor (δ), divided by the difference between (δ_n) and the theoretical deflection of a fully composite floor (δ_c) [30,31]:

$$\lambda(\delta_i) = \frac{\delta_n - \delta_i}{\delta_n - \delta_c} \qquad (3)$$

The fire performance of the TCC floors was quantified in terms of the failure time of the floors and the midspan deflection at 90 min. The failure time was defined as the instant at which the analysis fails to converge due to model instability. Failure typically results from stresses at the top of the concrete exceeding the material capacity, leading to crushing.

3. RESULTS

3.1 Benchmarking of FE model

The deflection of the experimental specimen, the FE model, and the deflections calculated by the γ-method are plotted in Figure 2a. The CLT laminations have been numbered 1 through 5, where layer 5 is on the exposed surface, as annotated in Figure 2b. The vertical lines in Figure 2a indicate the times at which layers 5 and 4 charred through, defined as the times at which the 300°C isotherm reached the glue line between layers. The FE model showed a plateau in deflection when the char line progressed through layer 4, a cross-layer, between 54 min and 128 min. A similar plateau in deflection was also observed in the test data. When the char line was partway through layer 3, the middle parallel layer, the deflection rate increased until failure. The FE model estimated failure of the floor at 166 min, a difference of 1% compared to the experimental failure time at 165 min.

Figure 2b shows the stress profile calculated by the γ-method and FE models after 30 min of fire exposure. At 30 min, the char line was located partway through layer 5. The γ-method calculated a linear stress distribution through the depth of the CLT section because it did not account for the reduced strength and stiffness in the cross-layers. The reduced strength and stiffness in the cross-layers in the FE model resulted in higher stresses in layer 3, the middle parallel layer. The stress profile of the FE model confirmed that the load-bearing capacity of the CLT-concrete floor during fire was dependent on stress redistribution to the uncharred parallel layers, an effect that was not present in the internal stresses calculated by the γ-method.
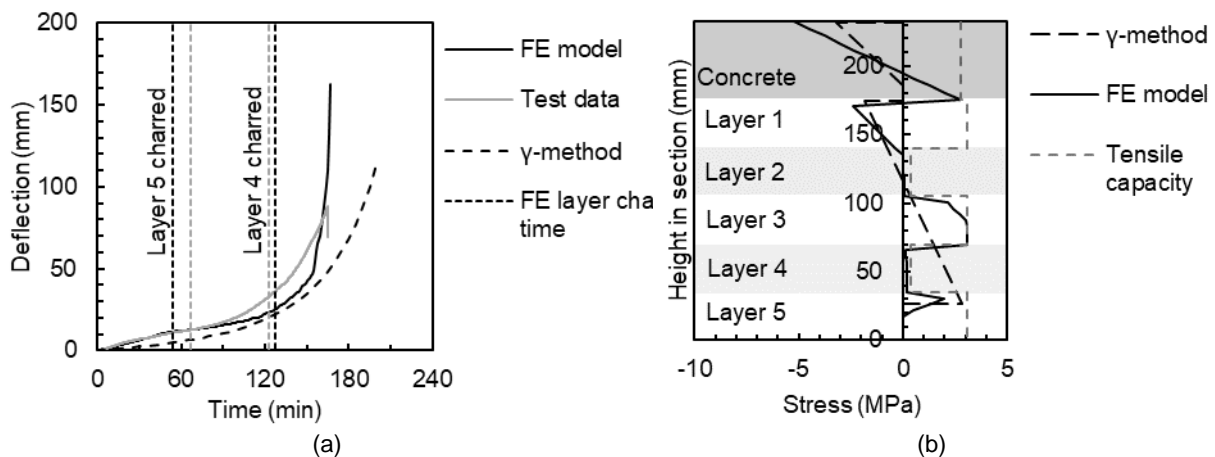
Figure 2. (a) Deflection history of CLT-concrete floor (b) Stress profile midspan of CLT-concrete floor after 30 min of fire exposure

3.2 Parametric study

The deflection history of the CLT-concrete FE models showed that the failure time of the floor was closely related to char-through times of the parallel layers (Figure 3). Increasing the demand-to-capacity ratio (d/c) of the CLT-

concrete floor from the base value of 0.37 to 0.5 (35% increase) led to a 21% earlier failure time. The vertical lines in Figure 3 denote the times at which layers 4 and 5 were completely charred. At 0.37*d/c*, the CLT-concrete floor was able to sustain load-carrying capacity until layer 3, the middle parallel layer, was partially charred. However, at 0.5*d/c*, the CLT-concrete floor failed as soon as the char line reached layer 3. At 0.7*d/c*, the CLT-concrete floor failed before layer 5, the parallel bottom layer, had completely charred.

As demand increased, each parallel layer became more critical to maintaining the load-carrying capacity of the floor. While the CLT-concrete floors with *d/c* of 0.3 and 0.5 could maintain load-carrying capacity despite the char-through of layer 5, the model with 0.7*d/c* could not. At high *d/c* ratios, the parallel layers were already highly stressed and further stress redistribution was not possible. Consequently, further charring of the parallel layers resulted in model failure. While CLT panels with a greater number of parallel layers would be expected to have better fire performance than CLT panels with fewer parallel layers, the improvement may be limited if the members are highly stressed.
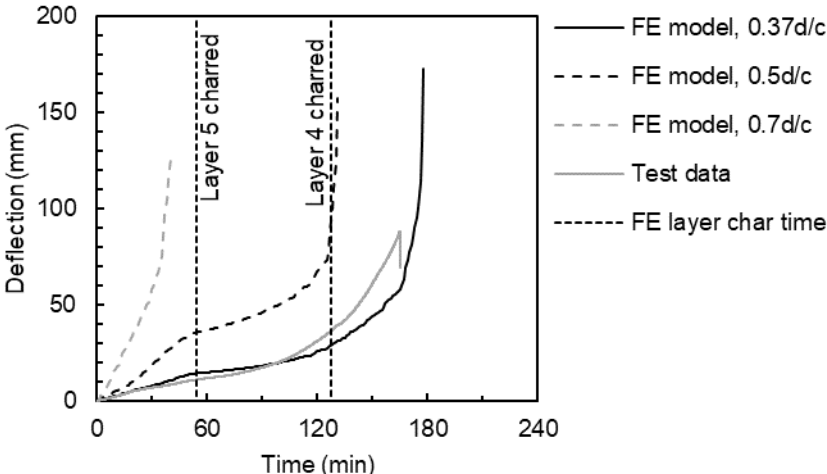
Figure 3. Deflection of CLT-concrete FE models with varied demand to capacity ratios

Reducing the concrete strength by 33% will led to an 82% increase in the deflection at 90 min, with only a 5% reduction in the failure time (Table 2). For most of the duration of the fire exposure, stresses within the concrete remained low compared to the concrete capacity, only to increase rapidly near the end of the analysis when the char line had reached the middle parallel layer. Consequently, the increased concrete strength had little effect on the failure time. However, the corresponding reduction in the stiffness of the concrete layer led to increased deflection. These results suggest that in a fire scenario, utilizing a higher strength concrete may reduce the deflection of the CLT-concrete floor, but will result in only a small increase in failure time. However, the concrete remained at ambient temperature throughout the analysis because it was insulated from fire exposure by the timber panel. The concrete properties seem to be more influential in beam-type TCC floors where the concrete slab is directly exposed to elevated temperatures.

Cross-layer stiffnesses between $E_0/10$ and $E_0/30$ resulted in similar fire behavior of the CLT-concrete FE models. When the cross-layer stiffness was increased to *1/10E*, failure time extended by 1% and deflection at 90 min was reduced by 7%. When the cross-layer stiffness was increased to $E_0/5$, the failure time of the model was extended by only 3%, but the deflection of the model at 90 min was reduced by 19%. Variation in the stiffness of the CLT cross-layers is unlikely to affect the fire performance of the CLT-concrete floor if E_{90} does not exceed $E_0/10$.

Table 2. Summary of CLT-concrete parametric study

Percent difference from base model						
Variable		*d/c*		*fc'*	E_{90}	
Reference value		0.34		35.7 MPa	$E_0/30$	
	Base model	0.5	0.7	~33% reduction	$E_0/5$	$E_0/10$
Failure time	166 min	-21%	-76%	-5%	+3%	-1%
Deflection at 90 min	15 mm	+199%	-	+82%	-19%	-7%

The composite efficiency of the CLT-concrete floors was varied from the base value of 70% by changing the stiffness of the shear connectors. The effects of varying composite efficiency were studied at two span lengths, the 4.8-m span of the base model and a longer span of 6 m. The lower bounds of shear connector stiffness were the smallest possible values that still maintained model stability at ambient temperature. These lower bounds were 0.5 kN/mm (17% composite efficiency) for the 4.8-m CLT-concrete floor, and 2.5 kN/mm (12% composite efficiency) for the 6-m CLT-concrete floor. For the purposes of comparison, the fire resistances of the non-composite CLT-concrete floors were calculated analytically. The non-composite 4.8-m floor was calculated to have a fire resistance time of 18 min, while the non-composite 6-m floor had insufficient flexural capacity to resist the applied loads at ambient temperature.

Figure 4 shows the failure time and normalized midspan deflection at 90 min, defined as the deflection Δ divided by span length L, F 90 min for varying composite efficiency. The failure time of the 4.8-m FE model increased with composite efficiency, but remained constant at composite deficiencies higher than 28%. Similarly, the deflection of the 4.8-m FE model at 90 min decreased with increasing composite efficiency, but approached a constant value at composite efficiencies greater than 36%. In contrast, the failure time of the 6-m FE model remained constant regardless of composite efficiency. The deflection of the 6-m FE model was also less affected by composite efficiency than the 4.8-m FE model. Whereas the deflection of the 4.8-m model at 90 min decreased by 92% when its composite efficiency was increased from 12% to 100%, the deflection of the 6-m model decreased by 54% when its composite efficiency was increased from 17% to 100%.

The failure time of the 4.8-m FE model leveled off at 28% composite efficiency due to a change in the failure mechanism. The FE model failed when concrete compressive stresses exceeded capacity, indicating crushing. Models with less than 28% composite efficiency developed stress concentrations near the shear connectors, which led to concrete failure at these locations. However, at composite efficiencies greater than 28%, the concrete failure occurred near midspan instead, i.e., the location of the greatest bending moment. Increasing the composite efficiency of the model changed the cause of failure from local stress concentrations in the concrete around the connectors, to concrete crushing resulting from the global bending moment.

Unlike the 4.8-m FE model, the failure mechanism of the 6-m FE model did not change with composite efficiency. The 6-m FE model failed due to concrete crushing at midspan over the entire range of composite efficiencies. As a result, although 6-m FE model showed improvement in deflection with increasing composite efficiency, its failure time remained constant, as shown in Figure 4. When an increasing composite efficiency corresponded to a change in the failure mechanism of the floor, dramatic improvements in failure time and deflection were observed. When increasing the composite efficiency did not change the failure mechanism, the floor deflection was reduced, but failure time remained constant.
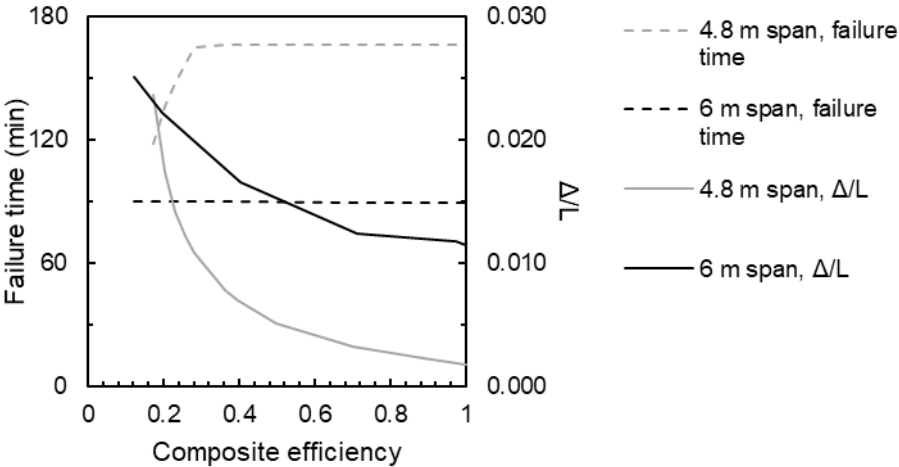
Figure 4. Failure time and normalized deflection of CLT-concrete floor model with varied composite efficiency and span length

4. CONCLUSIONS

This paper presents the development and application of an FE modeling methodology for CLT-concrete floors exposed to the ASTM E119 standard fire curve. The two-dimensional, sequential thermal-structural FE modeling methodology was developed in ABAQUS and benchmarked against corresponding experimental data from a large-scale furnace test of a CLT-concrete floor. The floor was constructed from a CLT panel joined to a normal-weight concrete slab with angled screws as shear connectors. The CLT-concrete floor was loaded with a distributed service live load and exposed to the ASTM E119 standard fire [15]. The FE modeling methodology was then applied to a parametric study that investigated the fire behavior of the CLT-concrete floor in response to varying the demand to capacity ratio, concrete strength, CLT cross-layer stiffness, and composite efficiency. The effect of these variations on the fire behavior of the TCC floors was quantified in terms of the failure time and deflection at 90 min.

The application of an FE modeling methodology to TCC floors has allowed for a detailed analysis of how changing the design parameters of TCC floors affects their fire behavior. Internal stresses from the FE model have allowed the fire behavior of TCC floors to be explained in terms of stress redistribution and failure mechanisms. The main conclusions from this work are as follows. These parametric study conclusions are only applicable to CLT-concrete floors with angled screws as shear connectors.

- Load-carrying capacity of a CLT-concrete floor was dependent on stress redistribution to the parallel layers. Demand to capacity ratios of 0.5 and greater, stress redistribution within the parallel layers of the CLT could no longer compensate for the loss of the timber cross-section to charring. As a result, the failure time of the CLT-concrete floor became closely related to the char-through times of the parallel layers.
- Reducing the concrete strength by 33% or increasing the stiffness of the CLT cross-layers to up to 1/10 of the stiffness of the parallel layers resulted in less than a 5% difference in failure time of the CLT-concrete floor.
- Although reducing the concrete strength had little effect on failure time, the corresponding reduction in concrete stiffness resulted in an 82% increase in deflection at 90 min.
- The failure time and deflection of the CLT-concrete floor improved with increasing composite efficiency, up to a composite efficiency of about 36%. The improvement resulted from the failure mode changing from local concrete crushing near the shear connectors to concrete crushing at midspan due to bending.
- Increasing the composite efficiency of the floor had more impact on the fire performance of shorter-span floors than longer-span floors because the failure mechanism of the 6-m floor remained concrete crushing at midspan due to bending over the entire range of modeled composite efficiencies.

Future studies could investigate how additional design parameters affect the fire behavior of TCC floors. Additional analysis of CLT-concrete floors with spans between 4.8 m and 6 m could identify the span at which the failure mode ceases to change with increasing composite efficiency. Although the connector model is more suitable for dowel connectors, floors with notched connections could also be modeled, with varied notch geometry. Incorporating brittle tensile and shear behavior of timber and concrete into the material models would be important for TCC floors with notched connections. Since the fire behavior of the CLT-concrete floor is strongly influenced by the presence of cross and parallel layers, other types of timber panels such as glulam and mass ply could also be investigated.

REFERENCES

[1]   Gosselin A; Blanchet P; Lehoux N & Cimon Y. (2016). *Main motivations and barriers for using wood in multi-story and non-residential construction projects*, BioResources, no. 12, p. 546–70.

[2]   Ceccotti, A. (1995). *Timber-Concrete Composite Structures, Timber Engineering, Step 2, 1st ed.* Centrum Hout. p. E13/1-E13/12.

[3]   Shephard, A; Fischer, EC; Barbosa, AR & Sinha, A. (2021). *Fundamental behavior of timber concrete composite floors in fire*, Journal of Structural Engineering, no. 147, p. 04020340.

[4]   European Committee for Standardization. (2004). *Eurocode 5: Design of timber structures - Part 1-2 - General - Structural Fire Design*, European Committee for Standardization, 69 p.

[5]   Kreschmann, D. (2010). *Mechanical Properties of Wood.* In: Ross RJ, editor. *Wood Handbook: Wood as an Engineering Material*, US Department of Agriculture, Forest Service, Forest Products Laboratory, 508 p.

[6]   Frangi, A & Fontana M. (2003). *Elasto-plastic model for timber-concrete composite beams with ductile connection.* Structural Engineering International, no. 13, p. 47–57.

[7]   European Committee for Standardization. (2004). *Eurocode 5: Design of timber structures - Part 1-1: General - Common rules and rules for buildings.* European Committee for Standardization, 121 p.

[8]   O'Neill, J; Abu, A; Carradine, D; Moss, P & Buchanan, A. (2014). *Modeling the fire performance of structural timber-concrete composite floors.* Journal of Structural Fire Engineering, no. 5, p. 113–24.

[9]   Caldová, E; Vymlátil, P; Wald, F & Kuklíková, A. (2014) *Timber Steel Fiber–Reinforced Concrete Floor Slabs in Fire: Experimental and Numerical Modeling.* Journal of Structural Engineering, no. 141, p. 04014214.

[10]   Du, H; Hu, X; Xie, Z & Meng Y. (2021). *Experimental and analytical investigation on fire resistance of glulam-concrete composite beams.* Journal of Building Engineering no. 44, p. 103244.

[11]   Khorsandnia, N; Valipour, H & Bradford, M. (2018). *Deconstructable timber-concrete composite beams with panelised slabs: Finite element analysis.* Construction and Building Materials, no. 163, p. 798–811.

[12]   Jiang, Y & Crocetti R. (2019). *CLT-concrete composite floors with notched shear connectors.* Construction and Building Materials, no. 195, p. 127–39.

[13]   Bedon, C & Fragiacomo, M. (2017). *Three-dimensional modelling of notched connections for timber-concrete composite beams.* Structural Engineering International, no. 2, p. 184–97.

[14]   Du, H; Hu, X; Zhang, B & Minli, Y. (2017). *Numerical simulation on behaviour of timber-concrete composite beams in fire.* IOP Conference Series: Earth and Environmental Science, Zhuhai, China, vol. 81, p. 012148.

[15]   ASTM International. (2020). *ASTM E119-20 Standard Test Methods for Fire Tests of Building Construction and Materials.* ASTM International, 36 p.

[16]   Dassault Systèmes Simulia Corp. (2018). *ABAQUS/CAE 2019.* Dassault Systèmes Simulia Corp.

[17]   Crisfield, MA. (1981). *A fast incremental/iterative solution procedure that handles "snap-through."* Computers and Structures, no. 13, p. 55–62.

[18]   Riks, E. (1979). *An incremental approach to the solution of snapping and buckling problems.* International Journal of Solids and Structures, no. 15, p. 529–51.

[19]   Liu, J & Fischer, EC. (2021). *Comparative study of thermal properties of timber.* World Conference on Timber Engineering, Santiago, Chile, p. 1-8.

[20]   Werther, N; O'Neill, J; Spellman, P; Abu, A; Moss, P; Buchanan, A & Winter, S. (2012). *Parametric study of modeling structural timber in fire with different software packages.* 7th International Conference on Structures in Fire, Zürich, Switzerland, p. 1-12.

[21]   ANSI. *ANSI/APA PRG 320-2019: Standard for Performance-Rated Cross-Laminated Timber.* Tacoma, WA, USA: APA - The Engineered Wood Association; 2019.

[22]   CEN. (2004). *Eurocode 2: Design of concrete structures - Part 1-2: General rules - Structural fire design.* European Committee for Standardization, 97 p.

[23]   CEN. (2002). *Eurocode 1: Actions on structures - Part 1-2: General actions - Actions on structures exposed to fire.* European Committee for Standardization, 59 p.

[24]   CEN. (2005). *Eurocode 2: Design of concrete structures - Part 1-1: General rules for buildings.* European Committee for Standardization, 225 p.

[25]   Lee, J & Fenves, GL. (1998). *Plastic-damage model for cyclic loading of concrete structures.* Journal of Engineering Mechanics, no. 124, p. 892–900.

[26]   Lubliner, J; Oliver, J; Oller, S & Oñate, E. (1989). *A plastic-damage model for concrete.* International Journal of Solids and Structures, no. 25, p. 299–326.

[27]   International Federation for Structural Concrete (fib). (2010). *Model Code 2010 - First complete draft - Volume 2.* International Federation for Structural Concrete, 292 p.

[28]   American Wood Council. (2018). *National Design Specification (NDS) Supplement: Design Values for Wood Construction.* American Wood Council, 192 p.

[29]   European Committee for Standardization. (2009). *EN 338: Structural timber - Strength classes.* European Committee for Standardization, 10 p.

[30] Gutkowski, R; Brown, K; Shigidi, A & Natterer, J. (2008). *Laboratory tests of composite wood–concrete beams.* Construction and Building Materials, no. 22, p. 1059–66.

[31] Zhang, L; Zhou, J; Chui, YH & Tomlinson, D. (2022). *Experimental Investigation on the Structural Performance of Mass Timber Panel-Concrete Composite Floors with Notched Connections.* Journal of Structural Engineering, no. 148, p. 04021249.

HYBRID FIRE FOLLOWING EARTHQUAKE TESTS ON FIRE PROTECTED STEEL COLUMNS

Patrick Covi[a],*

Nicola Tondini[b]

Manfred Korzen[c]

Marco Lamperti Tornaghi[d]

ABSTRACT

The paper reports on five Fire Following Earthquake (FFE) tests performed at the Federal Institute for Materials Research and Testing (BAM) by means of hybrid fire testing technique. In particular, an internal steel column of the ground floor belonging to a three-bay, four-storey concentrically braced steel building was tested, whilst the effect of the remainder of the structure was numerically simulated. Since the structure has a low degree of redundancy, the loss of a column can trigger global structural collapse. Two FFE tests were performed without any fire protection system and the other FFE tests were performed with three different fire protection solutions: conventional and seismic-resistant calcium silicate boards as well as vermiculite spray. Each column was firstly subjected to horizontal and vertical displacement histories resulting from seismic nonlinear time-history analysis performed on the numerical model of the case study; then, the furnace was switched on and the ISO 834 was followed with boundary conditions consisting in a constant axial stiffness representative of the surrounding structure.

Keywords: fire following earthquake; concentrically braced steel frames; fire protections.

1. INTRODUCTION

As it has happened in many historic occasions (e.g. the 1906 San Francisco, 1923 Tokyo, 1995 Kobe, 1999 Turkey, 2011 Tohoku and 2011 Christchurch earthquakes), after an earthquake, fire may be triggered by earthquake-induced rupture of gas piping, failure of electrical systems, etc. [1-3]. Fire following earthquake events are more difficult to tackle by the fire brigades because of their possible large number and extent as well as of possible disruptions within the infrastructural network that hinder their timely intervention and within the water supply system

---

[a],* University of Trento, Italy (patrick.covi@unitn.it), Corresponding author.

[b] University of Trento, Italy (nicola.tondini@unitn.it).

[c] Bundesanstalt für Materialforschung und -prüfung (BAM), Germany (manfred.korzen@t-online.de).

[d] European Commission, Joint Research Centre (JRC) – Ispra (IT) (Marco.LAMPERTI-TORNAGHI@ec.europa.eu).

[1]. The current engineering design methods still ignore many aspects of multi-hazard and in particular, fire following earthquake (FFE) analysis. In this context, developing a resilience plan is recommended to increase understanding of the impacts and the severe consequences of disruptions and failures to mitigate hazards, to contain the effects of disasters and to improve the strategic response to earthquakes/fires when they occur [4].

In a fire following earthquake scenario, the structural fire performance can deteriorate because the fire acts on a previously damaged structure. Moreover, fire protection elements may have been damaged by the earthquake and the fire can spread more rapidly if compartmentation walls have failed [4][5]. Thus, the seismic performance of the non-structural components may directly affect the fire performance of the structural members. As a consequence, the loss of fire protection is particularly dangerous for steel structures because the high thermal conductivity associated with small profile thicknesses entails quick temperature rise in the profiles with consequent fast loss of strength and stiffness.

Most of the literature involves numerical simulations on steel moment resisting frames [6][7][8][9] and only a few of them are dedicated to buckling-restrained and conventional brace systems [10][11]. Both developed a framework for evaluating the post-earthquake performance of steel structures in a multi-hazard context that incorporates probabilistic structural analyses under fire and seismic loads. Experimental studies have been performed on single elements [11] and full-scale reinforced concrete frames [12].

In this respect, the EQUFIRE project (Multi-hazard performance assessment of structural and non-structural components subjected to seismic action and fire following earthquake using hybrid simulation) [13] as part of the Transnational Access activities of the European SERA project was funded.
This project aims at experimentally and numerically studying the post-earthquake fire performance of concentrically braced steel buildings by also considering the damage to non-structural components such as the fire protection and the compartmentation elements. In particular, it consists of seismic full-scale tests based on hybrid simulation performed at the ELSA Reaction Wall at Joint Research Centre (JRC) and through FFE tests on single elements at the furnace of the Federal Institute for Materials Research and Testing (BAM).

2. DESCRIPTION OF THE CASE STUDY

A four-storey three-bay steel structure with concentric bracings in the central bay was selected as a case study for the experimental campaign, as shown in Figure 1. This frame is part of an office building with a square plan (12.5 m x 12.5 m) and the location of the building was assumed to be in the city of Lisbon (Portugal); thus, in an area of medium-high seismicity. The interstory height is 3.0 m, except for the height of the first floor, which is equal to 3.6 m. The lateral force-resisting system consists of concentrically braced frames (CBF).
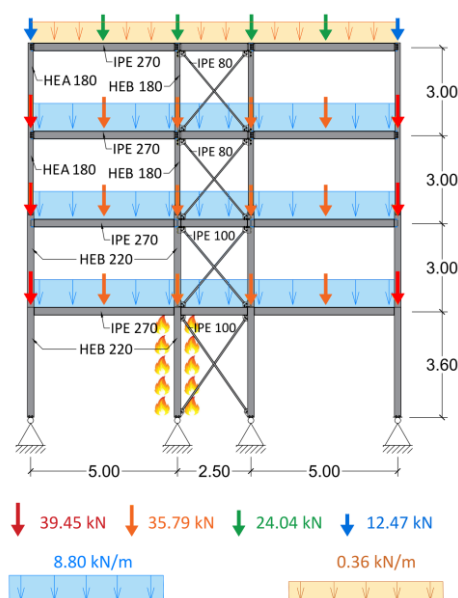
Figure 1 Configuration of the frame (Dimensions are in meters).

The steel grade S275 (EN 10025-2, 2019) was adopted for the bracing system (dissipative elements), while steel grade S355 was selected for all the other non-dissipative elements (beams and columns). It is worth pointing out that the yield strength for the bracings was taken as the mean value, i.e., 330 MPa, considering a coefficient of variation equal to 0.12 and using a lognormal distribution, whereas for the non-dissipative members was taken the experimental value obtained through material testing, i.e., 436 MPa [13].

In detail, IPE sections with the weak axis in the plane of the frame were used for the bracing elements to force in-plane buckling and, thus, to avoid possible damage to the walls where the bracing is inserted in.

The frame was designed according to the Eurocode standards and in particular the seismic designed was performed in accordance with Eurocode 8 [14]. In particular, linear dynamic analysis with response spectrum was carried out and the capacity design criterion was applied to design the structural members by considering a "High Ductility Class (DCH)". Then, nonlinear time-history analyses with natural accelerograms were employed to investigate the seismic response of the structure. The finite element software OpenSees [18] was used to the model the building. The general assumptions were the following:

- All connections were assumed as pinned.
- The columns were considered continuous along the height of the structure.
- The building was regular in plan and elevation.
- The building was located in Lisbon (Portugal) characterised by peak ground acceleration equal to 0.186 g and type B soil.

In order to perform non-linear time-history analyses, it was fundamental to model the seismic hazard through adequate selection and scaling of ground motion records. In this respect, a set of fifteen accelerograms for the significant damage limit state (SD) was selected considering the type of spectrum, magnitude range, distance range, style-of-faulting, local site conditions, period range, and ground motion components using the INGV/EPOS/ORFEUS European Strong motion Database [15]. The accelerograms were modified to match the target spectrum in the period range of 0.4÷0.9 s, that includes the fundamental period of the structure equal to 0.67 s. Among the fifteen accelerograms, the one shown in Figure 2, known as the Patras earthquake, was used in all EQUFIRE experimental tests, based on three main requirements:

- The selected accelerogram had to cause significant damage to the bracings.
- The horizontal displacement of the first floor had to be equal or lower than ± 30 mm to be compatible with the horizontal actuator stroke of the BAM furnace.
- The axial force of the internal columns at the beginning of the second floor had to be below 1000 kN in order to be compatible with the actuators used to impose the vertical loads on the specimen at the ELSA Reaction Wall.

The results of the non-linear time history analysis were used to estimate the displacement time-histories to apply to the specimens in the furnace before switching on the burners in the context of an FFE scenario.
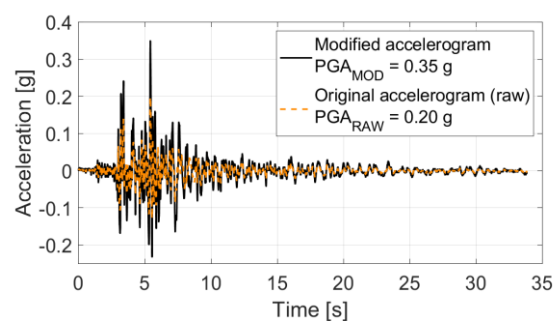
Figure 2: Comparison between the original and modified accelerogram for the FFE simulation

With respect to the design of the fire protection, the building was designed to withstand an exposure to the standard ISO 834 fire curve for 60 min. Since the unprotected structure was not capable of satisfying such requirement, two types of passive fire protection were envisaged, i.e. boards made of calcium silicate and mineral spray-based protection. The thickness of the protections was selected equal to 20 mm and this choice was also based on application purposes. Indeed, different applications were conceived: i) boards of calcium silicate with a standard application were employed; ii) moreover, the system to connect the boards of calcium silicate was also designed to achieve a better behaviour under seismic loading by adding a metallic substructure; iii) finally, a metallic mesh for a better adhesion in seismic regions of the spray-based protection was added.

3. EXPERIMENTAL PROGRAMME AND SETUP

For the EQUFIRE tests at BAM, the vertical furnace for testing columns was used as shown in Figure 3. It has a cylindrical shape with a diameter of 2.3 m. The movable bottom allows an adjustment of the combustion chamber height from 3.6 to 5.6 m. During the EQUFIRE tests, it was set to 3.6 m. Six oil burners arranged in two groups of three burners, orientated horizontally, are distributed almost regularly up the furnace's side. Two smoke vents lie above the highest pair of burners, and two lie above the lowest pair. From this furnace design, a strong vorticity of combustion gases, resulting in a rather constant gas temperature distribution in the axial direction, can be expected.
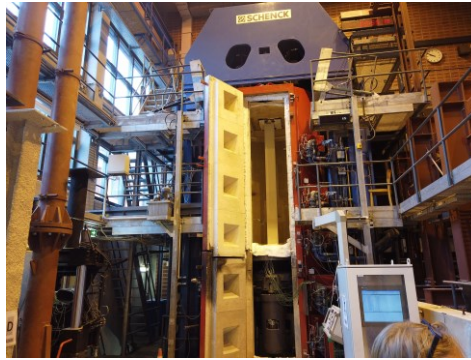
Figure 3: Vertical furnace for testing columns.

Five FFE tests were conducted at BAM:
- Test #0 Column E: column without fire protection system;
- Test #1 Column A: column without fire protection system;
- Test #2 Column B: column equipped with fire protection calcium silicate boards designed for seismic regions;
- Test #3 Column C: column equipped with fire protection calcium silicate boards not designed for seismic regions;
- Test #4 Column D: column equipped with sprayed vermiculite spayed coating, designed for applications in seismic region. A mechanical reinforcing mesh retains the sprayed coating. It is located in the middle of the overall coating thickness.

The experimental tests at BAM were performed using a sub-structuring technique [16] as shown in Figure 4, in which the physical column was heated by the standard ISO 834 curve [17] and a constant numerical axial stiffness representative of the surrounding structure was applied as boundary condition at the top of the physical column. During the FFE tests, the axial force of the column was measured and then used to obtain the effect of the rest of the structure in terms of displacement. Those displacements were imposed on the column to keep the two substructures in mechanical equilibrium.
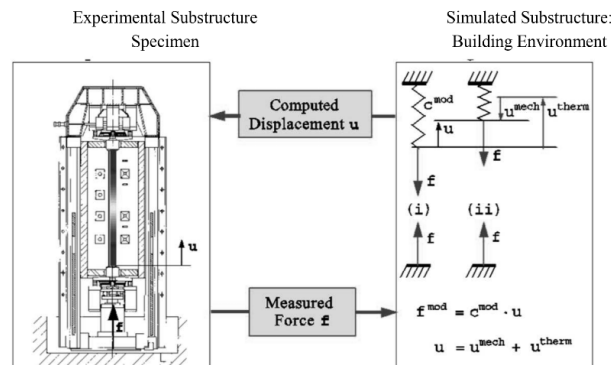
Figure 4: Sub-structuring method [16].

The axial stiffness of the upper part of the structure was numerically estimated by a static non-linear analysis in OpenSees [18]. In detail, the full structure was subjected to gravity loads and the selected accelerogram through non-linear time-history analysis. Then the physical column was removed and the frame was constrained at each floor to reproduce the boundary condition of the actual experimental setup at BAM. Finally, a monotonic displacement-controlled pattern, which continuously increases, was performed. The equivalent stiffness of the surrounding structure after the seismic event is neither constant nor linear. Due to this reason, it was not possible to exactly reproduce the same axial force condition in the column during the test. In order to determine the more appropriate equivalent axial stiffness constant value, a 3D model of the physical specimen was also modelled in OpenSees. Figure 5 shows the results in terms of the axial force and vertical displacement compared with the numerical analysis conducted on the whole structure. As it is possible to observe, a good value of the equivalent stiffness of the surrounding structure after the damage caused by the earthquake was equal to 5.3 kN/mm and this value was used in the tests. The value of K was chosen to reach a similar critical temperature and displacement.
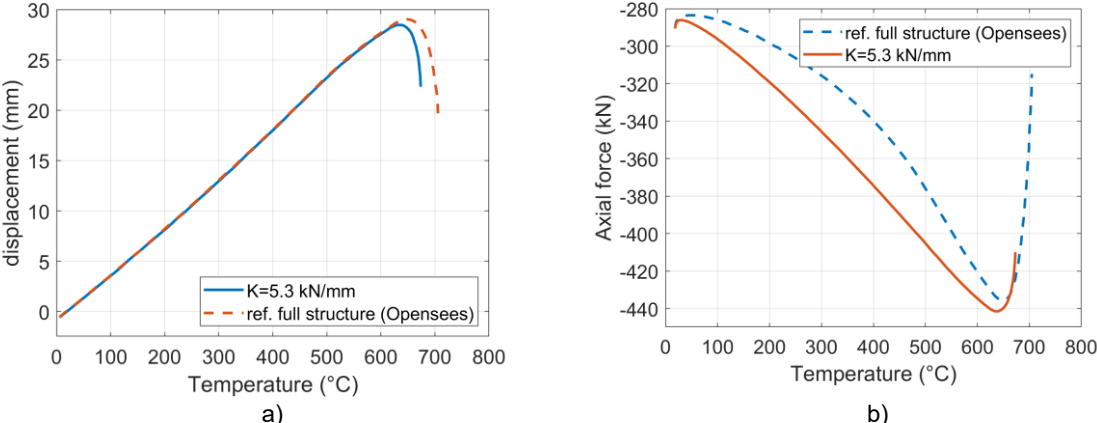
Figure 5: Comparison between the reference numerical solution and the single column with constant axial stiffness: a) axial displacements vs temperature curve; b) axial forces vs temperature curve.

The specimens were instrumented with thermocouples to measure the temperature at different positions of the cross-section and along the height, as illustrated in Figure 6. In detail, each specimen was equipped with 20 sheath thermocouples: six sensors in each section (two on the web and four on the flanges) at three different heights along the column and additionally one sensor at the top and the base of the column. According to EN 1363-1 [19], six plate thermometers measured the temperature inside the furnace. Additionally, two thermocouples measured the ambient temperature of the laboratory. An initial axial compression force of 315 kN was applied to the specimen.
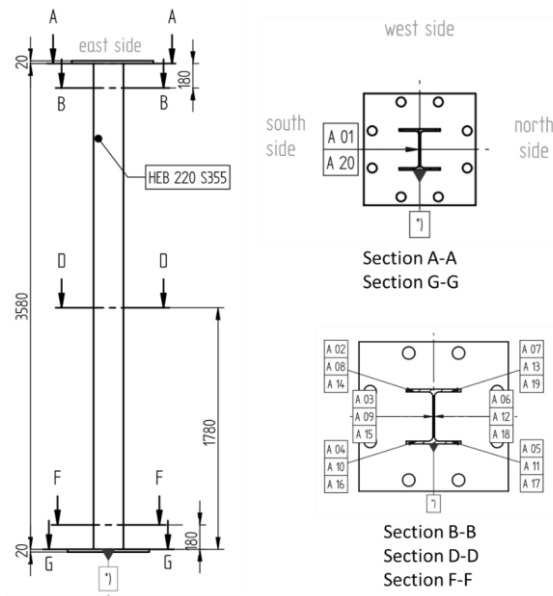
Figure 6: cross-section with the position of the thermocouples of the columns.

3. EXPERIMENTAL RESULTS

The results of the experimental tests at BAM are summarized in the following. The response history of the bare steel frame (without fire protection) computed with OpenSees was verified against the results of the experimental tests at BAM. Figure 7 compares the results of the seismic test and the numerical simulations in terms of horizontal displacement, axial displacement and axial force for all tested columns. The comparison demonstrates good agreement. There is a little difference in negative axial displacements, because the vertical actuator of the furnace could not apply tension forces to the specimen.

a)

b)
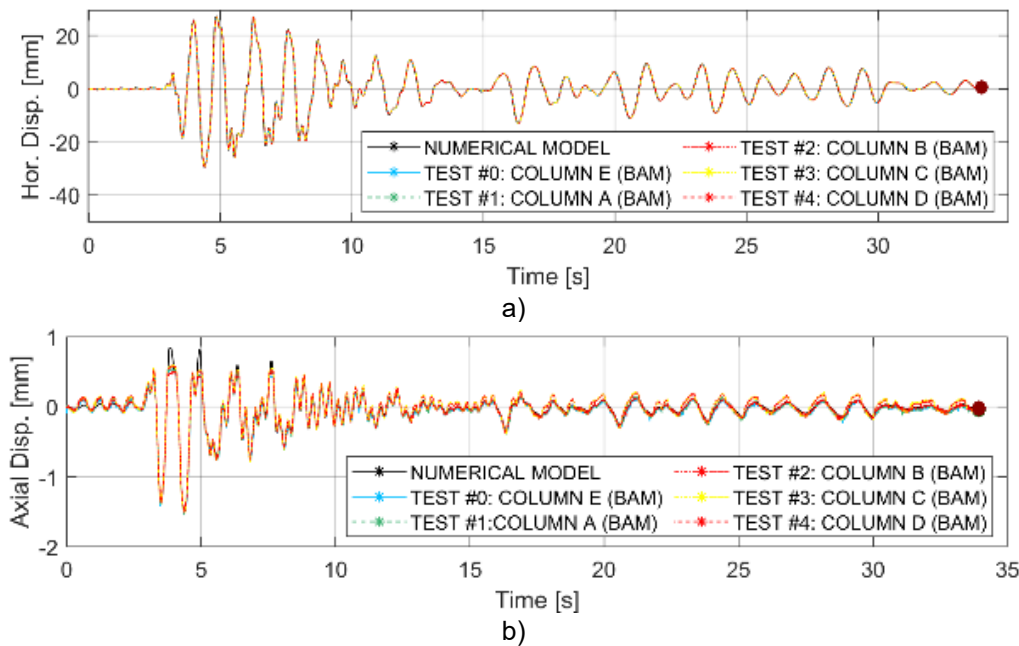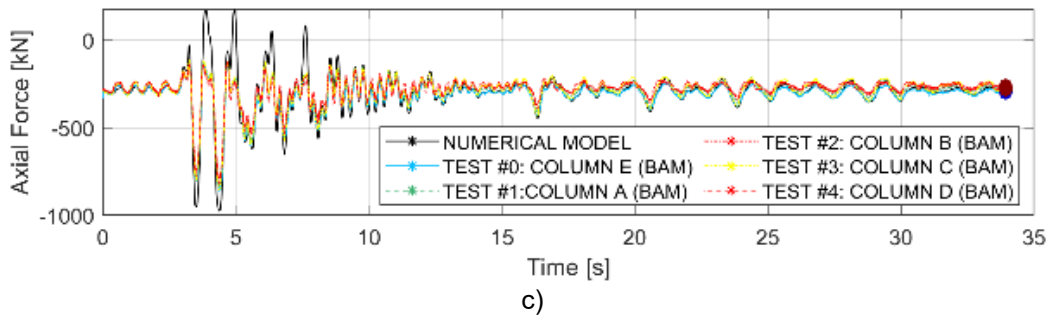
c)

Figure 7: Comparison between the numerical solution and the seismic
tests: a) axial displacement and b) axial force.

Figure 8 compares of the experimental results for the FFE tests on columns A and E without fire protection in terms of the evolution of the mean temperature, axial displacement and axial force. The comparison demonstrates the good repeatability of the FFE test procedures. Figure 8 also shows two snapshots of the columns under test in the furnace at BAM. The structural behaviour is typical of an axially restrained column, with an increase of axial force till a maximum value from which, owing to material property degradation, the axial force decreases.
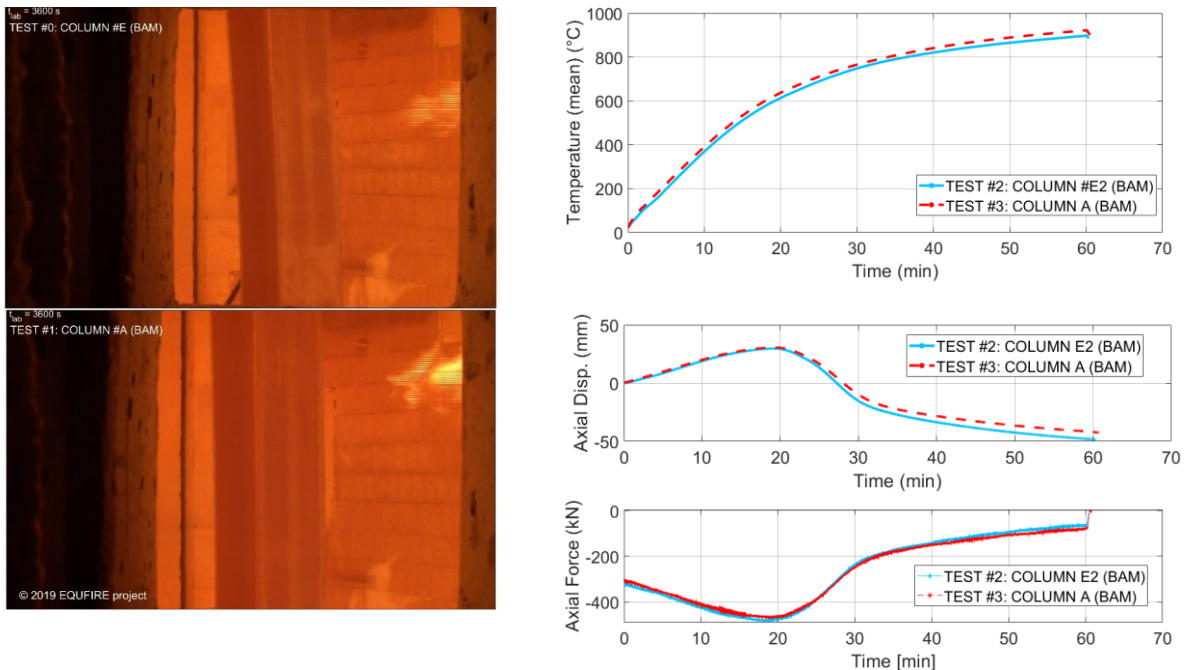
Figure 8: Comparison results of the FFE tests on the unprotected columns.

Figure 9 compares the evolution of the mean temperature, axial displacement and axial force of the FFE tests on the specimens with the three fire protection solutions (standard boards system, seismic-resistant boards system and vermiculite sprayed coating). Test #2 on column B was interrupted due to a component malfunction and then restarted. The specimens with the two types of fire protection board systems (columns B and C) showed similar performance. The gypsum-based wet mix spray-applied fire resistive material delayed the temperature development in column D with respect to columns B and C. Figure 9 shows again two snapshots of the columns under test at BAM. It is possible to observe that the fire resistance requirement was satisfied, even after undergoing a seismic event at the Significant Damage limit state. Indeed, this was mainly due to the fact that energy dissipation and damage are localised in the diagonals of the bracing system and not in the column and due to the limit of horizontal displacements that could be applied in the laboratory. As a result, Figure 10 shows the cracks on the fire protection elements developed due to the combination of seismic and fire actions. However, those cracks were not large enough to compromise the fire resistance of the columns. Moreover, the 60 min fire requirement was well

exceeded the fire protection thicknesses that could be thinner, but for application and comparison purposes had to be larger, as previously described.
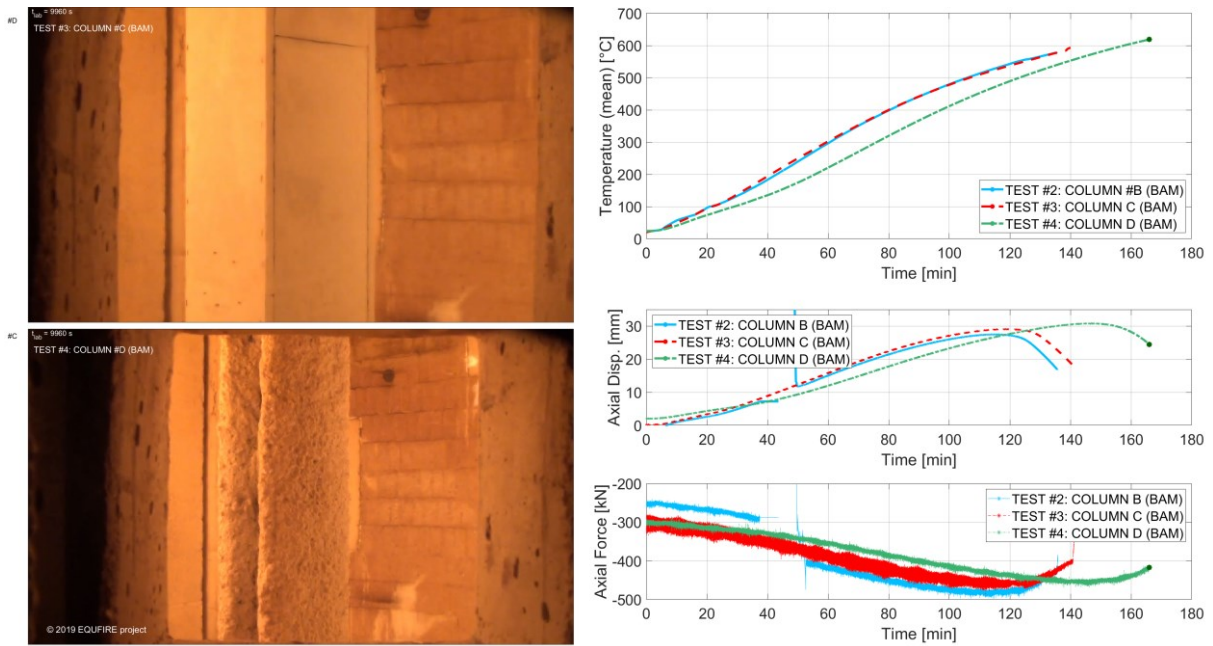
Figure 9: Comparison results of the FFE tests on the protected columns.

a) b) c)
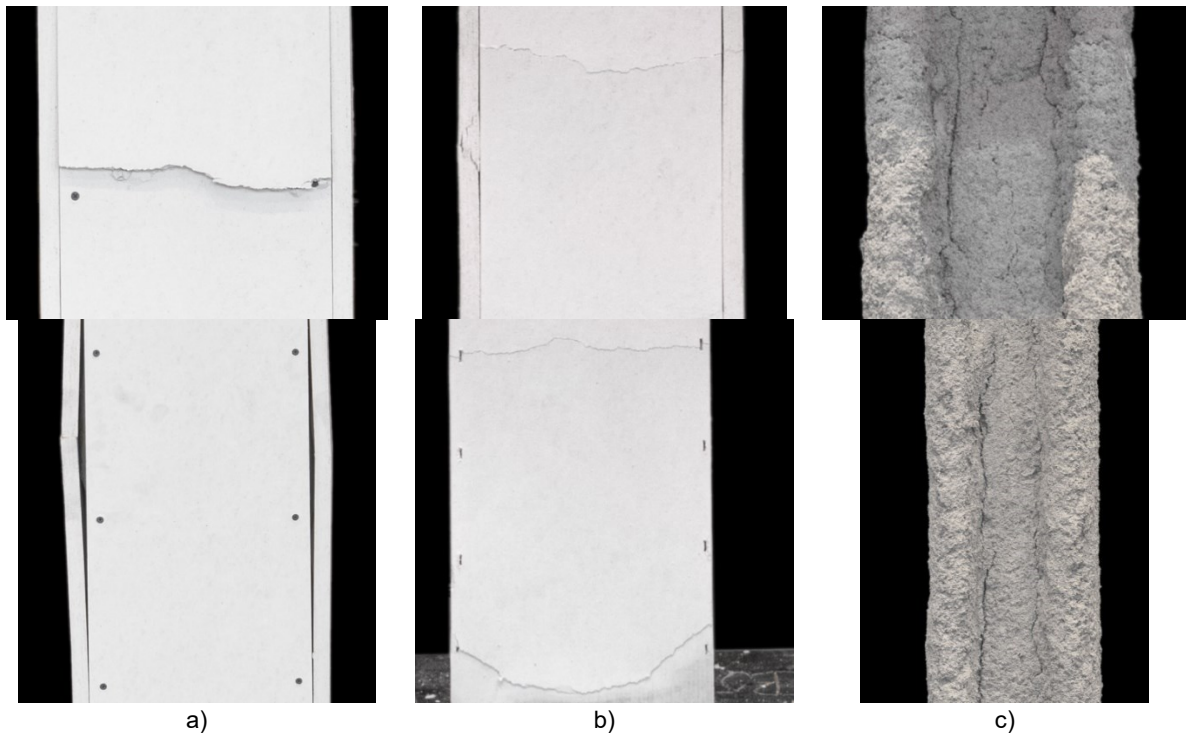
Figure 10: Damage of the fire protection elements due to the combination of seismic and fire actions: a) test #2 column B; b) test #3 column C; c) test#4 column D.

After each test, several photos of the specimen, in addition to the official ones, were taken in order to reconstruct a 3D model of the columns after the tests using the photogrammetry techniques. As an example, Figure 11 illustrates the 3D reconstruction of column D after the fire following earthquake.

| a) | b) |
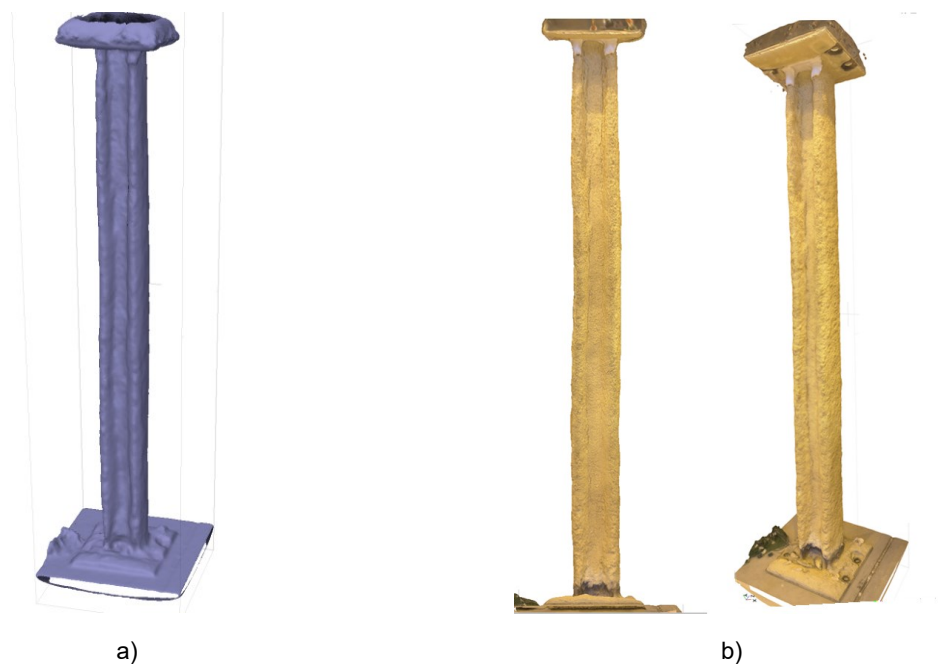
Figure 11: 3D model of column #D obtained using the photogrammetry methodology: a) wired model; b) Textured model

Photogrammetry allows to perform visual comparisons and also measurements in order to evaluate the evolution of damage before and after each test.

4. CONCLUSIONS

The paper presented the experimental study on a three-bay, four-storey steel frame with concentric bracing in the central span, subjected to fire following an earthquake, with the aim to study the performance of structural and non-structural components. Five preliminary FFE substructure tests were successfully carried out at the BAM laboratory in Berlin. FFE tests were carried out on two steel columns without fire protection and three columns with different fire protection solutions: conventional and earthquake-proof boards system and vermiculite-based wet mix spray-applied fire-resistive material. The specimens, being non-dissipative, remained in the elastic range after the seismic event. During the successive fire tests performed by considering the effects of the surrounding structure through a constant axial stiffness, no failure was detected after 60 min of exposure to the ISO 834 heating curve for unprotected columns and, respectively 138,141 and 165 min for the protected columns. The main reason was the low seismic damage undergone by the columns because are non-dissipative member and a larger thickness of the protections required to accommodate seismic-resistant solutions. In fact, in terms of fire protection, small cracks were observed on the fire protection boards and vermiculite-based spray-applied fire-resistive material. Nevertheless, no severe damage was observed that could undermine the fire resistance of the columns as they are non-dissipative members.

ACKNOWLEDGEMENTS

REFERENCES

[1] Scawthorn C, Eidinger JM, Schiff AJ. (2005) "Fire following earthquake". Technical Council on Lifeline Earthquake Engineering Monograph, No. 26. American Society of Civil Engineers

[2] N. E. Khorasani and M. E. Garlock, (2017), "Overview of fire following earthquake: Historical events and community responses," International Journal of Disaster Resilience in the Built Environment.

[3] Botting, R. (1998). "The Impact of Post-Earthquake Fire on the Built Urban Environment". Fire Engineering Research Report 98/1, University of Canterbury, New Zealand.

[4] Tsionis, G. (2014). Seismic resilience: concept, metrics and integration with other hazards. Joint Research Centre, Publications Office of the European Union, Luxembourg, doi, 10, 713724.

[5] Sharp, G. (2003). Earthquake damage to passive fire protection systems in tall buildings and its impact on fire safety.

[6] Della Corte G, Landolfo R, Mazzolani, FM. (2003) "Post earthquake fire resistance of moment resisting steel frames, Fire Safety Journal, Vol. 38, No. 7, pp. 593-612.

[7] Memari M, Mahmoud M, Ellingwood B. (2014), "Post-earthquake fire performance of moment resisting frames with reduced beam section connections", Journal of Constructional Steel Research, 103:215–229.

[8] Behnam B, Ronagh HR. (2015), "Post-Earthquake Fire Performance-based Behavior of Unprotected Moment Resisting 2D Steel Frames", KSCE Journal of Civil Engineering 19(1):274-284.

[9] Keller WJ, Pessiki SP (2012), "Effect of earthquake-induced damage to spray-applied fire-resistive insulation on the response of steel moment-frame beam-column connections during fire exposure". Journal of Fire Protection Engineering 22(4) 271–299.

[10] Khorasani NE, Garlock MEM, Quiel SE (2015), "Modeling steel structures in OpenSees: Enhancements for fire and multi-hazard probabilistic analyses", Computers and Structures, 157:218–231.

[11] Memari M, Xuguang W, Mahmoud H, Kwon OS (2020) Hybrid Simulation of Small-Scale Steel Braced Frame under Fire and Fire Following Earthquake, Journal of Structural Engineering, 146(1).

[12] Braxtan NL, Pessiki SP. Postearthquake (2011), "Fire Performance of Sprayed Fire-Resistive Material on Steel Moment Frames", Journal of Structural Engineering, 137(9): 946-953.

[13] Kamath P, Sharma UK, Kumar V, Bhargava P, Usmani A, Singh B, Singh Y, Torero J, Gillie M, Pankaj P. (2015), "Full-scale fire test on an earthquake-damaged reinforced concrete frame", Fire Safety Journal, 73:1–19.

[14] Covi, P. (2021). "Multi-hazard analysis of steel structures subjected to fire following earthquake", Doctoral dissertation, University of Trento. doi: 10.15168/11572_313383

[15] CEN (2005): EN 1993-1-2 "Eurocode 8: Design of structures for earthquake resistance - Part 1: General rules, seismic actions and rules for buildings".

[16] McKenna F., (2011) "OpenSees: A Framework for Earthquake Engineering Simulation", Computing in Science and Engineering.

[17] Luzi L, Puglia R, Russo E & ORFEUS WG5 (2016). "Engineering Strong Motion Database, version 1.0". Istituto Nazionale di Geofisica e Vulcanologia, Observatories & Research Facili-ties for European Seismology. doi: 10.13127/ESM.

[18] Korzen M., Magonette G., Buchet P., (1999). "Mechanical loading of columns in fire tests by means of the substructuring method" Zeitschrift für Angewandte Mathematik und Mechanik.

[19] ISO (1999): ISO834-1:1999, Fire-resistance tests -Elements of building construction- Part 1: General requirements.

[20] CEN (2012): EN 1363-1:1999 Fire Resistance Tests-Part 1: General Requirements. European Committee for Standardization.

NUMERICAL STUDY OF THE FIRE BEHAVIOUR OF A FUSIBLE LINK USING ALUMINIUM BOLTS FOR FIRE WALLS IN SINGLE-STOREY STEEL-FRAMED BUILDINGS

Thi Thuy MAI [a],∗, Sébastien DURIF[b], Abdelhamid BOUCHAIR [c], Christophe RENAUD[d], Bin ZHAO[e]

ABSTRACT

The aim of this paper is to present the results of numerical analyses devoted to the investigation of the fire behaviour of innovative fusible link solutions using aluminium bolts for fire walls in single-storey steel-framed buildings. Several 3D thermal and mechanical numerical models have been developed, allowing to better understand the fire behaviour of investigated fusible link solutions and to study in detail their failure modes under standard fire condition. Based on results, the link solutions that have been satisfactorily validated regarding fire resistance will be tested in the European FISHWALL research project.

Keywords: Fusible link, aluminium bolts, finite element model, fire wall, single-storey buildings, standard fire exposure

1. INTRODUCTION

The intrinsic fire resistance (without added protection) of single-storey steel-framed buildings is largely sufficient to guarantee the evacuation of occupants in the event of fire. Thus, for this type of building, the main concern of national fire regulations in Europe is how to prevent the spread of fire to the whole building. To achieve this objective, two requirements shall be satisfied, namely, the appropriateness of constructive systems to ensure that there is no progressive collapse between fire compartments, and the efficiency of fire walls to stop the fire inside the initial compartment regardless of the state of structures. In practice, many constructional solutions can be implemented in order to preserve the integrity of the fire walls, while accepting that the fire exposed part of the structure may collapse. One of the most common solutions is to place a non-load bearing wall between two independent structures and to connect it to them by means of "fusible" links. In a fire situation, these fusible links must allow the wall to be disconnected from the structure affected by fire without endangering the separating function of the wall, which must remain fixed to the steel structure on the other side of the wall and therefore not exposed to fire. It should be remembered that unprotected steel-framed structures exposed to fire conditions usually exhibit two successive steps of structural behaviour ([1], [2]). The first step is due to the thermal expansion of the heated members which results in pushing forces on the neighbouring structures. Then, as steel increases in temperature, it loses its resistance and stiffness and the heated steel structure starts to fall inwards, leading to tensile forces on the neighbouring structures. In case of a fire wall between adjacent steel structures, it is necessary to ensure that this fire wall does not fail with the steel structure submitted to fire. Thus, fusible links must be designed to resist the pushing phase and to fail for the tensile phase.

---

[a] Phd student, Research and Valorisation Dept., fire division, CTICM; Clermont Auvergne INP (ttmai@cticm.com)

[b] Dr., Université Clermont Auvergne, Clermont Auvergne INP, CNRS, Institut Pascal, Clermont-Ferrand (sebastien.durif@uca.fr)

[c] Pr., Université Clermont Auvergne, Clermont Auvergne INP, CNRS, Institut Pascal, Clermont-Ferrand (abdelhamid.bouchair@uca.fr)

[d] Dr., Research and Valorisation Dept., fire division, CTICM (crenaud@cticm.com)

[e] Dr., Research and Valorisation Dept., fire division, CTICM (bzhao@cticm.com)

Although such wall solutions are widely used in practice and have proven to be efficient from real fire cases, there is no known scientific investigation leading to the establishment of relevant construction details for adequate fire behaviour of "fusible" links when used in single-storey building with unprotected steel structures. In this context, the current paper aims at presenting a part of the work undertaken to evaluate the capacity of various configurations of fusible links to be used with fire walls made of lightweight sandwich panels to carry the loads due to the pushing phase. For this purpose, 3D thermo-mechanical models have been developed to study 3 different solutions of fusible links to steel portal frames in order to prepare future medium scale fire tests planned in the ongoing European FISHWALL research project [3].

2. INVESTIGATED FUSIBLE LINK SOLUTIONS

The investigated fusible links are based on common steel joints with aluminium bolts acting as the fusible component. They are intended to be used with fire walls made of lightweight sandwiche panels spanning horizontally between supporting steel columns. Considering the limited capacity of sandwich panels to resist out-of-plane horizontal forces, different fusible link solutions have been designed within the FISHWALL project. Figure 1 presents a schematic view of the three investigated solutions in order to present the different elements constituting the fusible links and the elements allowing the assembling with the columns of portal frames (HEA 320) and the fire wall column (HEA 140). The first system is composed of Z-shaped steel profiles and U-shaped steel profiles arranged back to back and assembled together with two M12 aluminium bolts. Each Z-profile is bolted to the column of portal frames while the U-profiles are bolted to the column supporting the sandwich panels (HEA 140), using four threaded steel rods passing through the fire wall on the wall side and four steel bolts on the other side. It should be mentioned that the steel rods must allow the transfer of pushing forces due to the thermal expansion of the steel portal frames exposed to fire to the structure on the unexposed side. The third solution is similar to the first one. However, the Z-profile is replaced by a gusset steel plate and a stiffener is attached to the U-shaped steel profile. Finally, the second link solution consists of an L-shaped steel profile assembled with aluminium bolts to a steel channel (UPN 240), spanning horizontally between the portal frame columns, each end of the UPN 240 being bolted with slotted holes to a steel stiffener welded between the flanges of the portal frames columns. These slotted holes should allow the free longitudinal thermal expansion of the UPN. The L-shaped profiles are attached to the wall steel column by means of four threaded steel rods passing through the fire wall on the wall side and four steel bolts on the other side.

a) 1st fusible link

c) 3rd fusible link
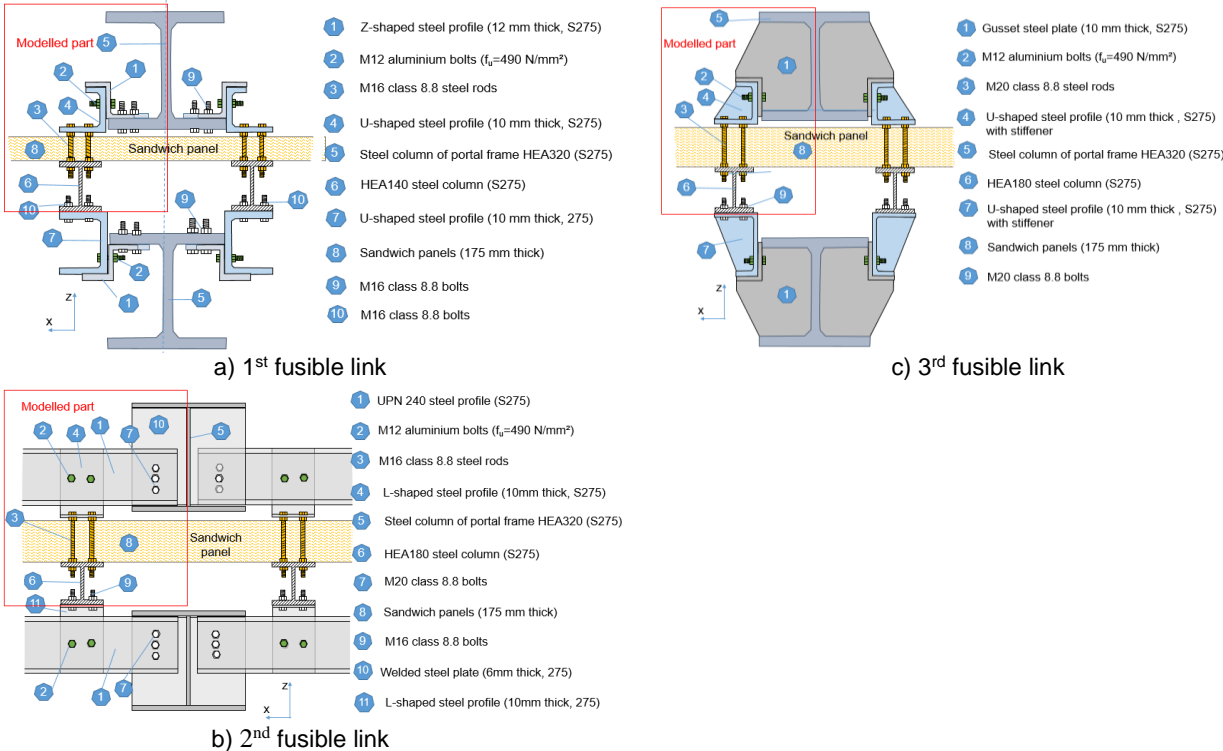
b) 2nd fusible link

Figure 1: Schematic top view of three studied fusible links

3. NUMERICAL MODELLING

Numerical modelling for the fusible links was conducted using the software ANSYS [3]. To simulate the fire behaviour of fusible links, a sequentially coupled 3D thermal-mechanical analysis procedure was adopted. It consists in conducting firstly a heat transfer analysis to obtain the temperature field and afterwards a mechanical analysis using the previously calculated temperature fields for calculating the structural response. Hence, for both thermal and mechanical models, the same meshing is adopted, but using adequate finite element formulations for each type of analysis. So, the nodal temperatures computed from the thermal analysis are stored as a function of time and then used as thermal loads in the mechanical analyses directly. Furthermore, a static-dynamic procedure developed at CTICM, which allows to pass through local instabilities (which would cause singularities in a full static analysis) and to simulate the global progressive collapse of steel structures under fire conditions generated by the local failure of steel members, was adopted to simulate the progressive failure mechanism of investigated "fusible" links exposed to fire.

| a) Thermal parameters | b) Mechanical boundary conditions |
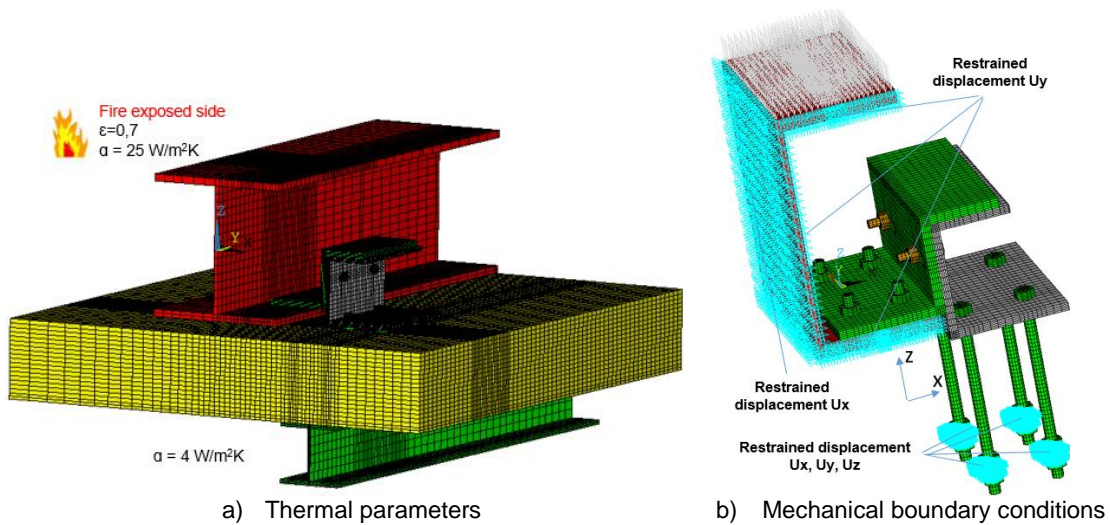
Figure 2: 3D FE models for thermal and mechanical analyses of the first fusible link [3].

| a) Thermal parameters | b) Mechanical boundary conditions |
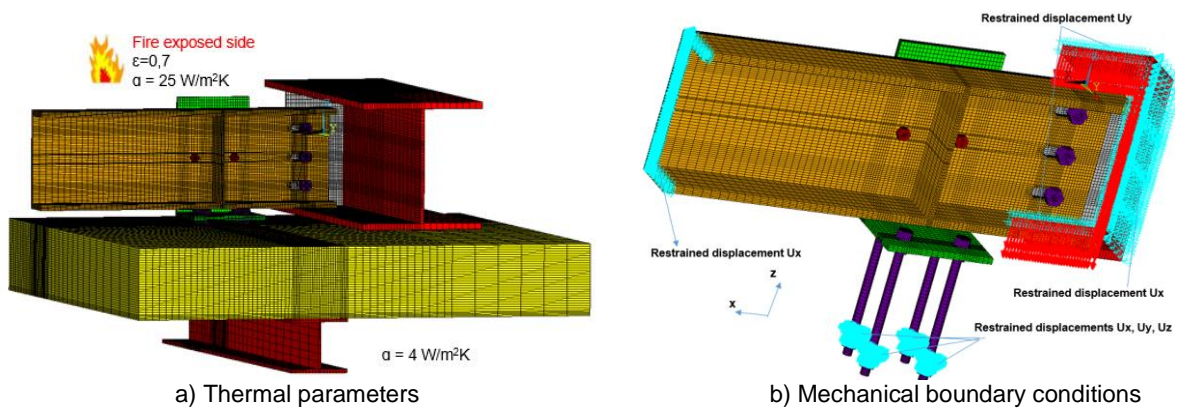
Figure 3: FE models for thermal and mechanical analyses of the second fusible link [3].

The 3D thermal-mechanical models developed for studied three link solutions are shown in Figure 2, Figure 3 and Figure 4 respectively. Several simplifications in the modelling were considered in order to reach an adequate compromise between the FE model accuracy and its computational cost. All the modelled components are meshed with 20-node brick FEs in order to have a suitable accuracy with a limited number of meshes (SOLID90 for the thermal models and SOLID186 for the mechanical models). Bolts and steel rods are modelled as detailed as possible. Nevertheless, some features of the geometry that are assumed to have insignificant effects on the response of the fusible links are ignored. First, threaded parts of the bolts, rods and nuts are omitted and the bolt–nut assembly is modelled as a simple component, assuming that relative motion between bolts and nuts, or loosening, does not take place during loading. Secondly, no washers are modelled and the bolt holes are slightly

larger than the bolt diameter. Further, thermal perfect contacts between all elements were assigned in the thermal models while automatic surface-to-surface contact was used, including frictional phenomenon in the mechanical models. This includes the contact between the steel profiles, between the bolts (heads and shanks) and the steel profiles (upper surface and holes) and between the threaded rods and the steel profiles. The friction coefficient was fixed to 0.25. For both developed models, the y-axis is related to the height of the wall.

a) Thermal parameters   b) Mechanical boundary conditions
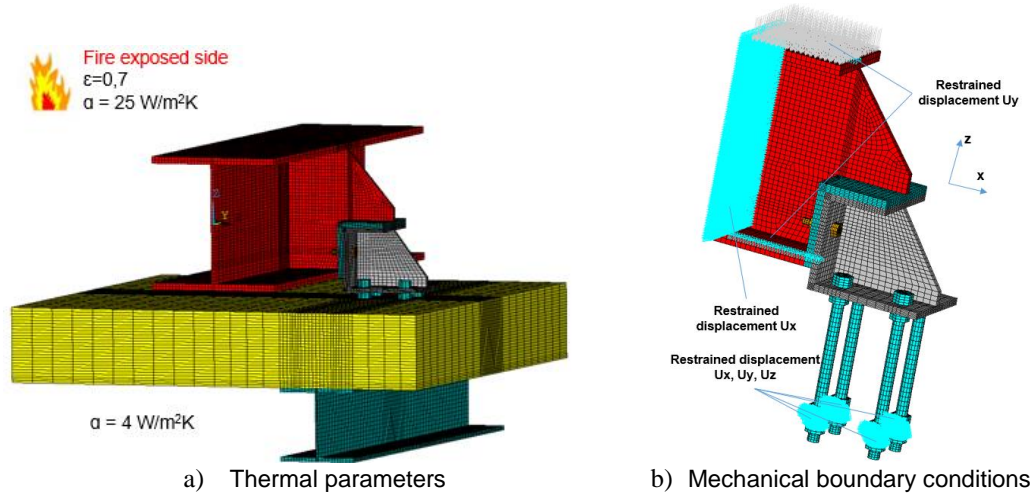
Figure 4: 3D FE models for thermal and mechanical analyses of the third fusible link [3].

The fusible links are exposed to standard temperature–time curve (ISO 834 standard fire curve). According to EN 1991-1-2 [5], the heat transfer modes of conduction, convection and radiation were considered in the form of appropriate boundary conditions and material property values. Thus, convective heat transfer coefficients of 25 and 4 W/m²/K were assigned to the fire-exposed and unexposed surfaces of the studied fusible link respectively. The fire emissivity was fixed to 1.0 and the surface emissivity of materials was taken equal to 0.7 for the studied materials. Moreover, thermal material properties of carbon steel and aluminium bolts such as specific heat, thermal conductivity and density are those given in EN 1993-1-2 [6] and EN 1999-1-2 [5] respectively, while the thermal properties of the mineral wool of sandwich panels (considered as independent of the temperature) were obtained from another analysis carried out in the scope of the FISHWALL project (density of 120 kg/m³, specific heat of 1000 J/kg.K and thermal conductivity of 0.045 W/m.K).

Regarding the mechanical models, only the fusible links exposed to fire, half of the portal frame columns near the fusible links and the steel threaded rods were modelled and meshed. The non-modelled parts were taken into account by appropriate boundary conditions. Thus, the four threaded rods are assumed to be fully restrained at the level of the steel column supporting the sandwich panels and their lateral restraints by the non-bearing wall were ignored. Besides, the lateral displacement Ux along the symmetry plane of the profile web as well as the displacement Uy at one end of the column portal frame are restrained. Moreover, for the third fusible link, as only a part of the UPN 240 length is meshed, its end is restrained against the longitudinal (X) displacement to take into account the effect of the unmodeled part. All these boundary conditions are reported in Figure 2 to Figure 4. Mechanical properties of steel profiles at elevated temperatures are taken from EN 1993-1-2, considering yielding plateau and strain hardening. Mechanical properties of aluminium bolts are defined from a tri-linear stress-strain relationship, adopting reduction factors at temperature given in EN 1999-1-2 [5]. The elevated temperature stress-strain curves of studied materials are shown in Figure 5. Further, it should be noted that, currently, the melting temperature of aluminium is about 500°C. In the pushing phase, the aluminium bolts are broken before the system's failure: either by shear failure due to the thermal expansion of the connected components or by their loss of resistance at the melting temperature. Consequently, the aluminium bolts are deactivated at the failure times determined during mechanical analyses. All investigated fusible link solutions are subjected to a constant pushing load of 25 kN. This applied load aims at representing the maximal pushing force which should be induced by the pushing phase of heated steel portal frames which will be tested in the FISHWALL project. It has been deduced from another thermo-mechanical analysis carried out modelling the test specimen with beam finite elements and spring elements. The pushing phase is planned to last 20 minutes (1200 seconds).
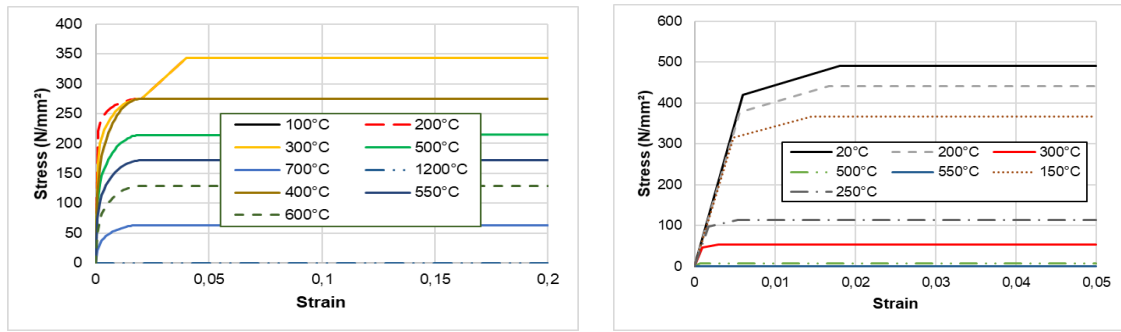
a) Steel profiles   b) Aluminium bolts

Figure 5: Stress-strain curves of studied materials at elevated temperature

4. RESULTS AND DISCUSSIONS

4.1 Heat transfer analysis

Figure 6 presents some thermal results for the first fusible link. It can be observed that the temperatures in the bolts are very similar to those of the connected steel profiles (column, Z-profile, U-profile). This result shows that there is a small temperature gradient in all the components represented (for example, at 500 seconds, there is a maximal difference of 200°, which is reduced thereafter). However, Figure 7 presents the temperature gradient in the steel rods. It can be observed that the upper mid part of the steel rod, in the side exposed to fire, has significantly higher temperatures compared to those on the other side of the fire wall, with temperatures at the vicinity of the heated steel profile very close to that of the U profile (Point 2 of Figure 6b). In fact, after 30 minutes of exposure to fire, the temperature of the parts of the rods directly exposed to fire is about 800°C, while the temperature of the section located at 1/4 of its length and in the middle (inside the wall) are about 570°C and 370°C respectively. This temperature gradient can be explained by the protection provided by the sandwich panels and by the fact that the rod is exposed to fire on a small part near its head. Same observations can be made for the other two configurations (Figure 8 to Figure 9).
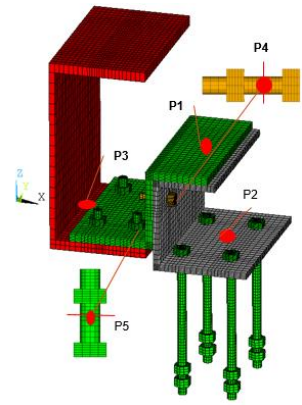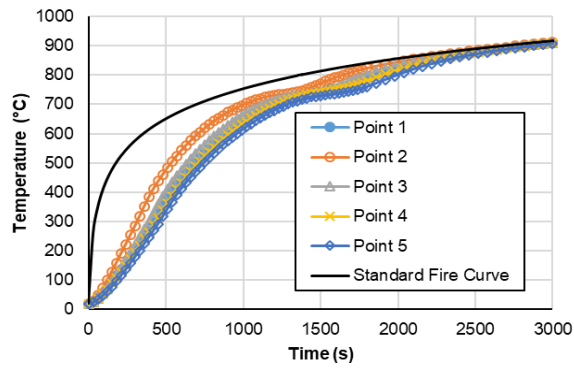
Figure 6: Time-temperature curves calculated in some points of the first fusible link
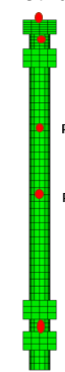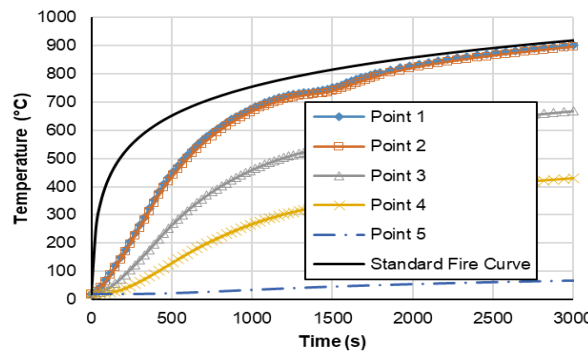
Figure 7: Time-temperature curves calculated in some points along the threaded rods of the first fusible link

354
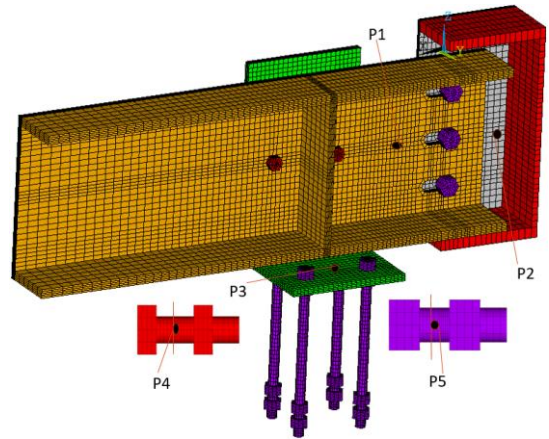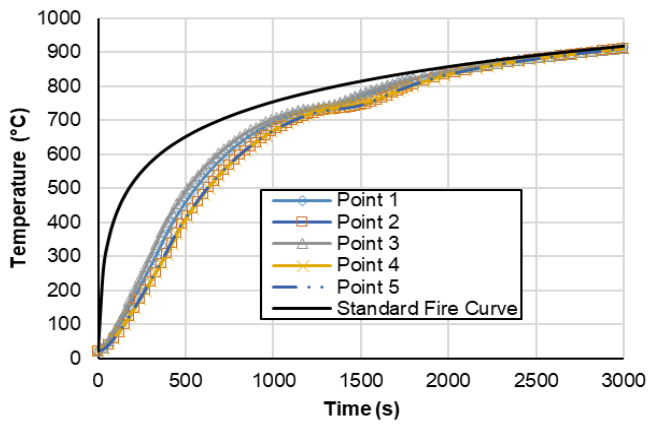
Figure 8: Time-temperature curves calculated in some points of the second fusible link
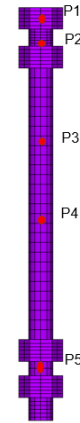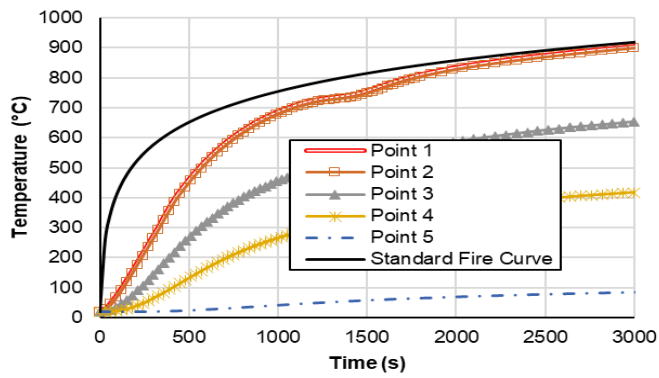
Figure 9: Time-temperature curves calculated in some points along the threaded rods of the second fusible link
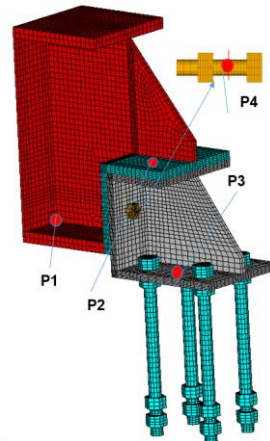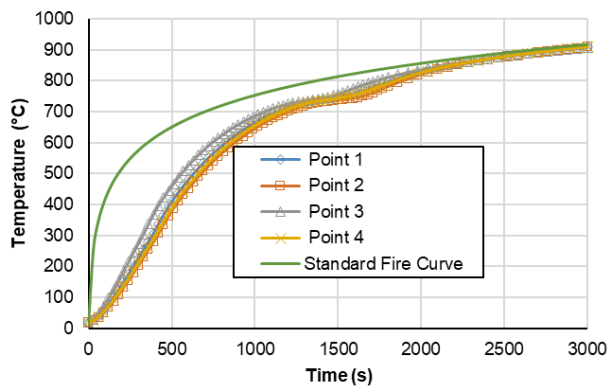
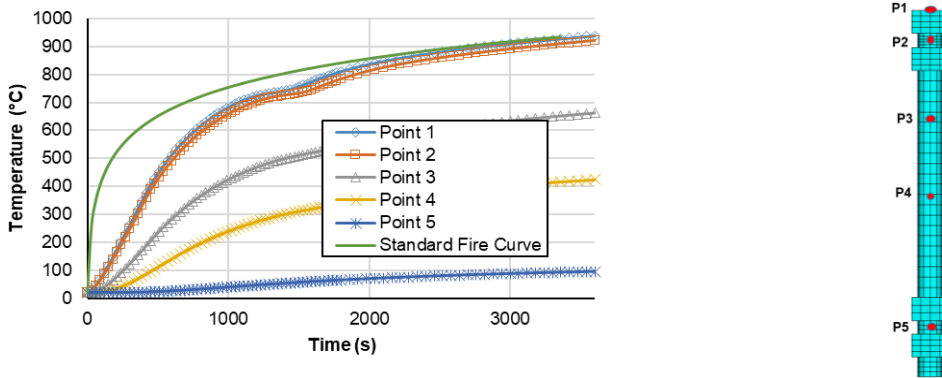Figure 10: Time-temperature curves calculated in some points in the third fusible link

355

Figure 11: Time-temperature curves calculated in some points along the threaded rods of the third fusible link

4.2 Mechanical analysis

4.2.1 - 1st fusible link

The results of the mechanical analysis for the 1st fusible link are shown in Figure 12 and Figure 13. Figure 12 presents an illustration of the von Mises equivalent plastic strain distribution with deformed shape and corresponding temperature field at failure time. Figure 13 gives the time-vertical (Uz) displacement curves ontained at different points. The Uz displacement is in the direction parallel to the rods length. The asymptotic shape of the curves reveals a failure of the system for a time of 713 seconds, which is significantly below the objective of 1200 seconds. The observation of the von Mises stresses shows that this failure is due to the local yielding of the column flange. This failure is obtained for a steel temperature of 500°C corresponding to a loss of 20% of its strength. Therefore, the 1st fusible link solution seems to have insufficient fire resistance for the planned fire test.

Nevertheless, regarding this failure mode, the partial modelling of the column and its applied load might not be able to represent the real interaction between this relatively flexible fusible link and the portal frame. Therefore, the design of the 1st fusible link needs to be improved through future research works considering various parameters (geometries, contacts).

a) Calculated von Mises equivalent plastic strain

b) Calculated temperature field
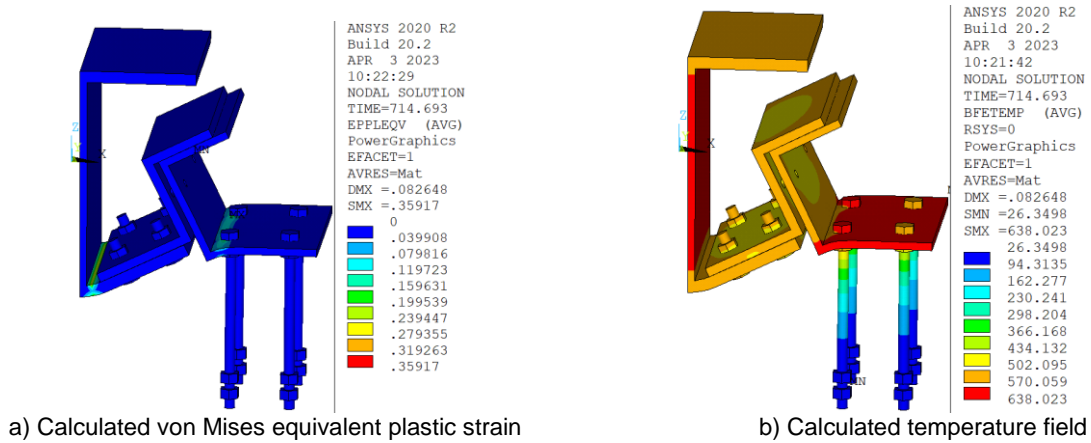
Figure 12: Von Mises plastic strain distribution with deformed shape and corresponding temperature field of the 1st fusible link at failure time (714.6 seconds)
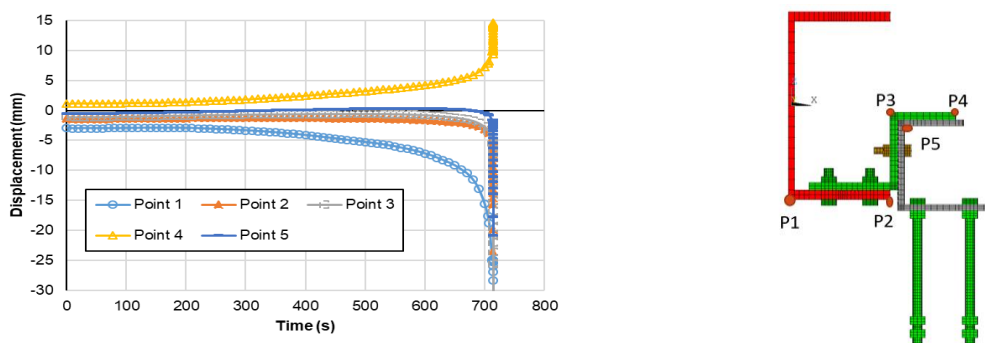
356

Figure 13: Time-vertical displacement (Uz) curves calculated for the 1st fusible link

4.2.2 - Second fusible link

The results of the mechanical analysis for the second fusible link are shown in Figure 14 to Figure 19. Figure 14 shows the location of the points where the displacements are observed. Figure 15 and Figure 16 present respectively the deformed shape of the fusible link and the temperature distribution at failure. Figure 17 gives an illustration of the von Mises equivalent plastic strain distribution in the three steel bolts, the four threaded rods, the L-profile, and the steel stiffener welded between the flanges of the portal frames columns. The results show that the failure mode of the fusible link is the local bending of the two bottom threaded rods in contact with the UPN after 1710 seconds of fire exposure (rods 1 and 2). At this time, it can be observed a flexural torsional buckling of the UPN associated with a significant local buckling of the stiffener welded between the flanges of the portal frame column as well as an important bending of the vertical wall of the L-profile.

In the direction of gravity (Y direction), the self-weight of the U-profile is supported by the thin stiffener (6 mm) welded between the flanges of the portal frame column and the vertical wall of the L-profile. The applied shear load is transmitted from the stiffener to the vertical web of U-profile by 3 steel bolts, and from the U-profile to the rods through the aluminium bolts and the L-profile. Thus, due to the unsymmetrical character of the connected steel elements, the existing eccentricity between the shear load applied to the stiffener plane and the support mobilizing mainly two threaded rods has a tendency to rotate the U-profile. This rotation is initially prevented by the stiffener welded to the column as well as the vertical wall of the L-profile. Moreover, it should be noted that the 6 mm thickness of stiffener is so weak compared to 10 mm of the L-profile. Therefore, the reduction in resistance of the thin stiffener with the increase in temperature makes it more deformable contrasting to the pushing/rotation of the U-profile. In addition, a considerable temperature gradient can be seen in the stiffener as well as the U-profile. In fact, Figure 16ª shows that the heating of the stiffener zones which are not in contact with the U-profile is faster than its part in contact. Consequently, the combination of these effects leads to the flexural torsional buckling of the UPN associated with a significant local bending of the stiffener at failure.

As seen in Figure 19, time-reaction curves calculated at the restrained end of the bottom threaded rods (1 and 2) indicate that the axial reactions on these rods are different. For this calculation, it should be noted that after 400s, the two fusible bolts were deactivated due to their shear failure because of the thermal expansion of the UPN profile and the significant strength loss of aluminium above 300°C. This explains the sharp drop observed at about 400s in the vertical reaction curve obtained for the first steel rod. The difference between the axial reactions of the threaded rods can be explained by the eccentricity of the load along x. In addition, it is obvious that from the beginning of exposure to fire to approximately 900°C, the axial reaction of the first rod increases from 14.5 kN to 17.5 kN and then it decreases to 14 kN at failure. However, an inverse evolution is observed for the second threaded rod. This is directly related to the progressive deformation due to the increase in temperature of the U-profile. Furthermore, due to the rotation towards y of the U-profile, it pushed to the vertical wall of the L-profile and the deformation of the L-profile causes the axial reaction on the 2 other rods which are not in contact with the UPN. In addition, with the increase in temperature, the L-shaped profile becomes more deformable, which leads to a redistribution of the axial reactions in the threaded rods and to the increase of the rotation of the UPN, resulting in the increase of horizontal reactions. Besides, there is a clear increase in the horizontal forces (along y) exerted on the head of the rods due to the eccentricity of load and the progressive deformation of the UPN-profile with the increase in temperature. Additionally, at 1710 seconds, as for the 1st fusible link, a significant temperature gradient was observed between the head of the threaded rod and its parts protected by the panels.
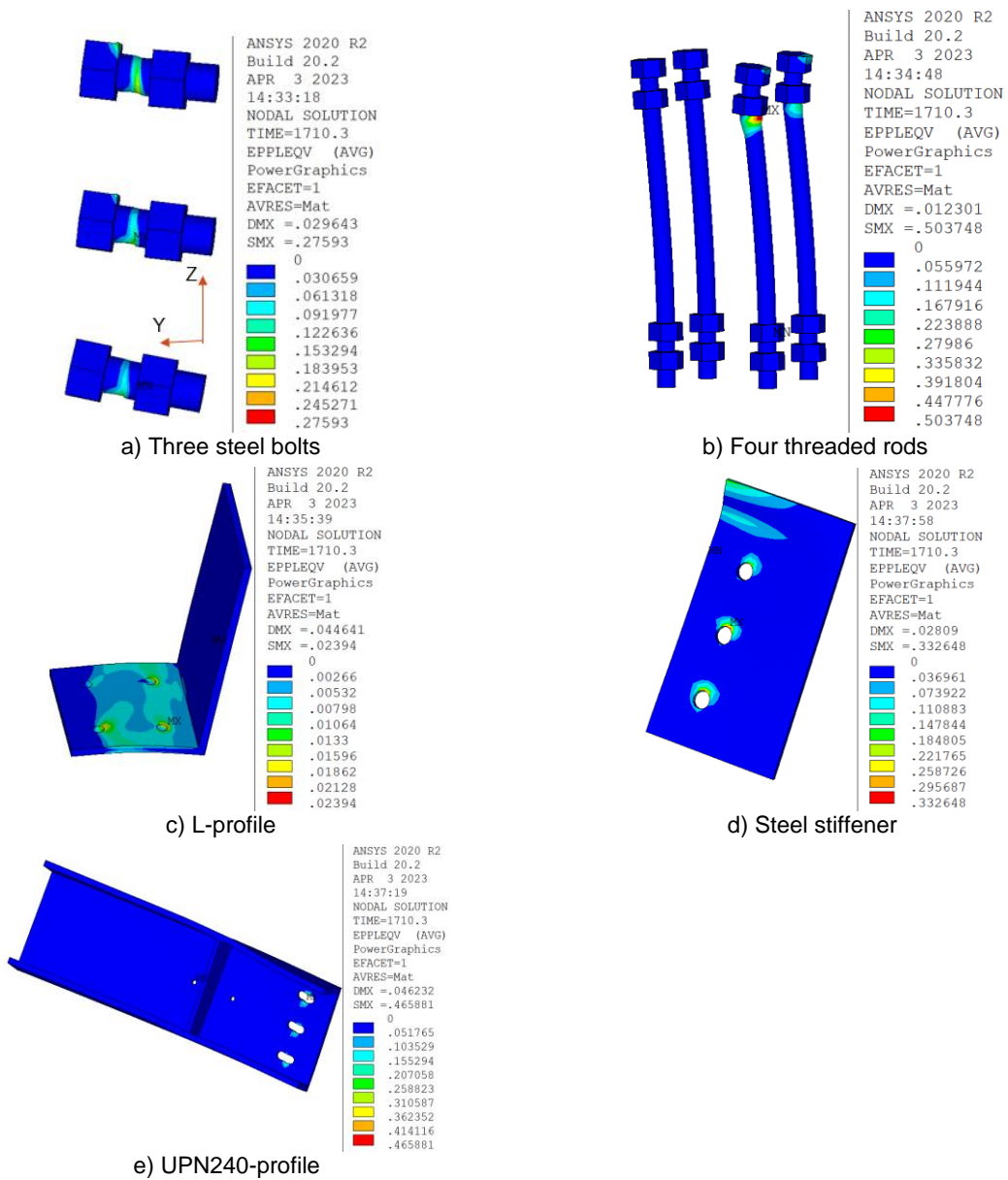
357

Indeed, at this time, the temperature of its head parts is about 750-780°C while the temperature of the sections located in the wall is in the range of 80-600°C. Therefore, under the combined effect of a significant compression force, the increase in the horizontal force exerted at the head of the threaded rod and especially the too-significant gradient temperature along the threaded rods as well as the reduction in their resistance with the increase in temperature, these lead to the local bending at the head parts of two thread rods in contact with the bottom flange of the U-profile resulting in the failure of the studied link fusible. In any case, the fusible link exhibits a failure time of 1710 seconds, which is much higher than the required time of 1200 seconds.

Figure 14: Location of points where displacements are observed for the second fusible link

a)   Side view   b) Oblique view

Figure 15: Deformed shape of the second fusible link at failure time

a)   Steels profiles   b)   Four threaded rods

Figure 16: Temperature field of the second fusible link at failure time

358

a) Three steel bolts

b) Four threaded rods

c) L-profile

d) Steel stiffener

e) UPN240-profile

Figure 17: Distribution of von Mises equivalent plastic strain in components in the second fusible link at failure time

a) Vertical displacement (Uz)

b) Horizontal displacement (Uy)
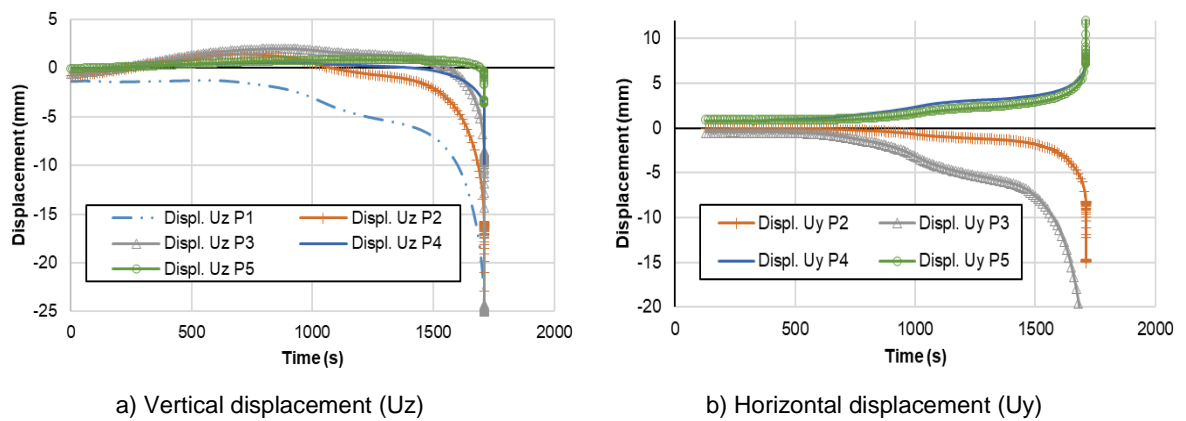
Figure 18: Time-displacement curves predicted for the 2nd fusible link

a) Horizontal reaction (Rx)

b) Horizontal reaction (Ry)

c) Axial reaction (Rz)
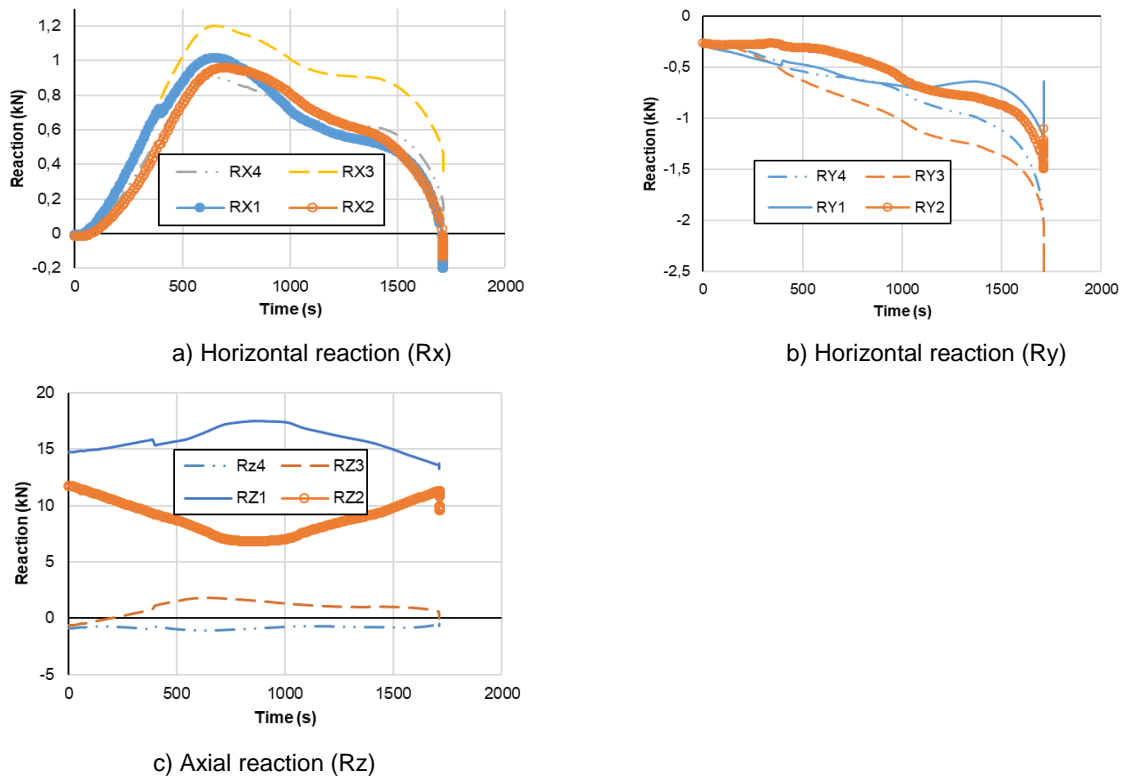
Figure 19: Time-reaction curves calculated at the restrained end of steel rods for the second fusible link

4.2.3 - Third fusible link

The results of the mechanical analysis for third fusible link are shown in Figure 20 to Figure 24. Figure 20 and Figure 21 present respectively the deformed shape and the temperature distribution at failure time. Figure 22 presents an illustration of the von Mises equivalent plastic strain distribution with deformed shape and corresponding temperature field at failure time. Figure 23 gives the time-displacement curves obtained at different points. The asymptotic shape of some curves reveals a failure of the link after 2170 seconds of standard fire exposure which is higher than the required time of 1200 seconds. The fusible link fails after the appearance of local buckling in the lower flange of the U-profile, followed by the local bending of the threaded rods at its head toward the stiffener of the U-profle. At this time, the temperature of the U-profile reaches about 850-860°C, corresponding to a loss of approximately 86% of the material strength. Besides, the temperature of the fire exposed side of the threaded rods is about 800-850°C while the temperature of the sections located in the wall is in the range of 70-750°C.

Figure 24 presents the time-reaction curves calculated at the restrained end of steel rods. The evolution of the axial reactions shows that the two threaded rods (1 and 2 on Figure 23d) are in compression with different values. It should be noted that after 550 seconds, the two fusible bolts were deactivated because their temperature was higher than the melting temperature. Before this time, the large difference between the axial reactions of two studied threaded rods (1 and 2) might be explained by the eccentricity of the applied load for which a part is transmitted to the vertical wall of the U-profile by two aluminium bolts. This eccentricity could be reduced when the two fusible bolts were deactivated, so that the load applied to the column transmits the full load to the U-profile through its upper flange. This could explain the convergence of axial reactions of two rods at about 500s. Afterwards, these axial reactions change corresponding to the progressive deformation of the lower flange of the U-profile influencing thus the resulting bending moment exerted in the U-profile and the threaded rods. Figure 24 also shows that there is a clear increase in the horizontal reaction (pushing force) exerted at the head's rods due to the progressive deformation of the U-profile, until the failure. It should be noted that at 2170 seconds, the strength of the steel profile material is reduced to 86%, in addition to the pushing of the thread rods, which leads to the local buckling of the lower flange of the U-profile. Besides, there is a clear increase in the horizontal reactions (Rx and Ry) exerted at the head of the steel rods due to the progressive deformation of the U-profile, until the failure. Hence, after the local buckling of the lower flange of the U-profile, due to the combined effect of the high compressive force, the increase of horizontal

360

force exerted at the head of the rods and the reduction of their strength with increasing temperatures and especially the high-temperature gradient along the length of the anchor rods, the threaded rods undergo local bending deformation. The third fusible link solution that fulfils the requirement of 1200 s needed for planned fire tests, performs the highest fire resistance in comparison with the two first links studied.
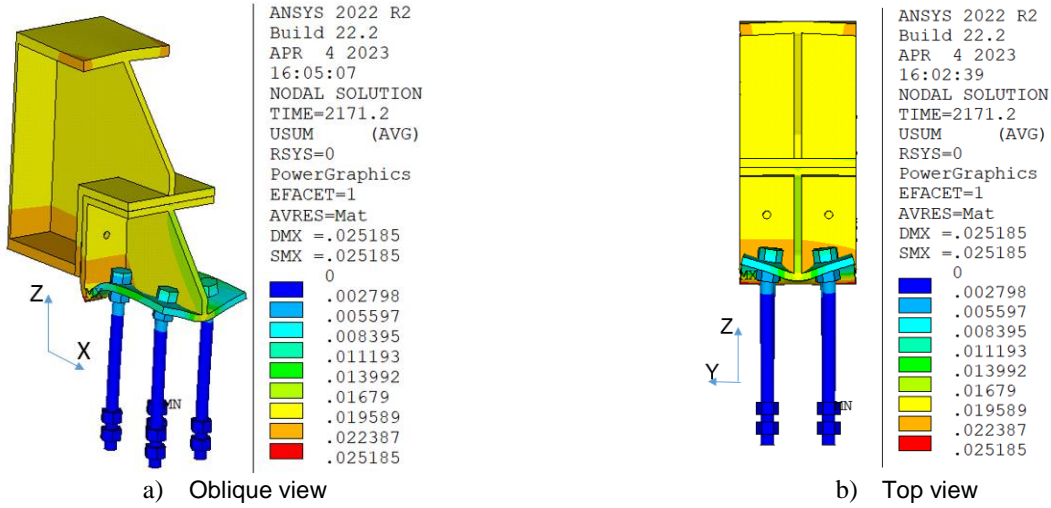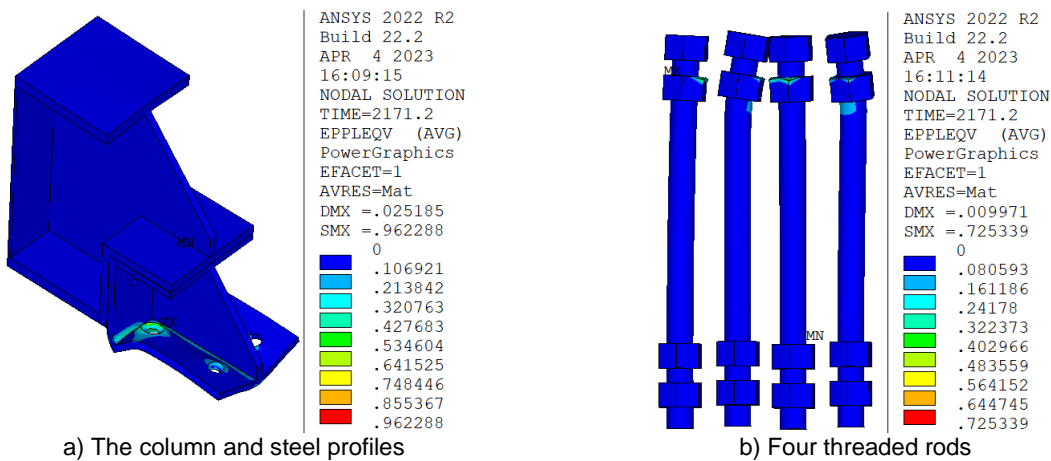

a) Oblique view

b) Top view

Figure 20: Deformed shape of the third fusible link at failure time

a) The steels profiles

b) The threaded rods
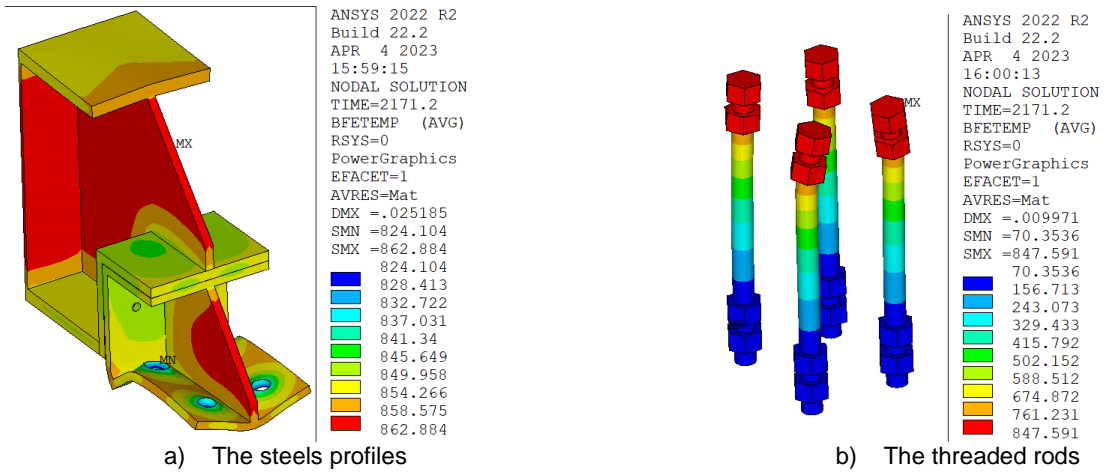
Figure 21: Temperature field of the third fusible link at failure time

a) The column and steel profiles

b) Four threaded rods

Figure 22: Von Mises equivalent plastic strain distribution in components of the third fusible link at failure time
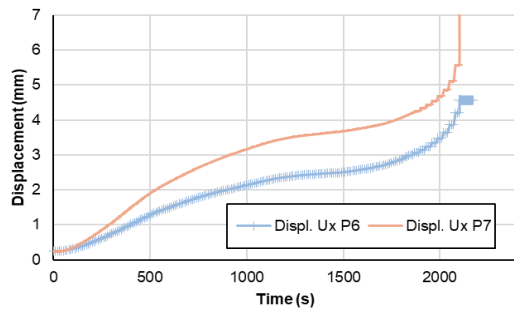
a) Time-Ux horizontal displacement curves
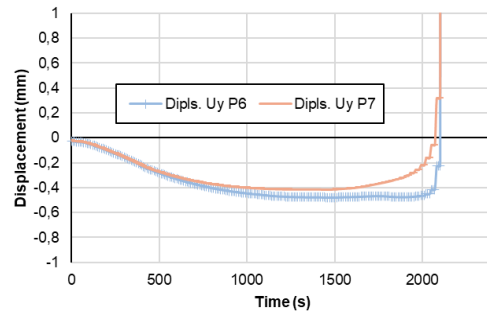
b) Time-Uy horizontal displacement curves
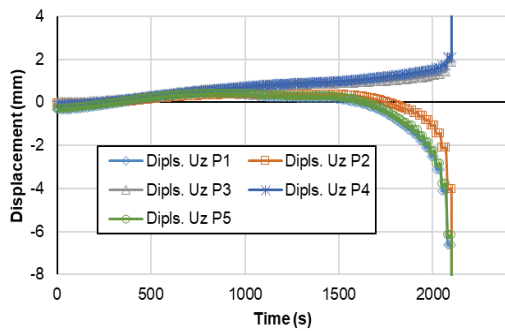
c) Time-Uz vertical displacement curves
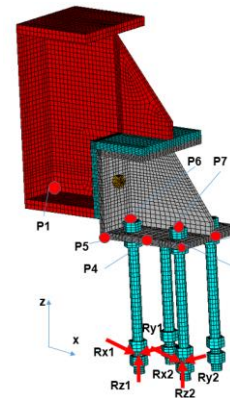
d) Location of points where displacements are saved

Figure 23: Time-displacement curves predicted for the third fusible link
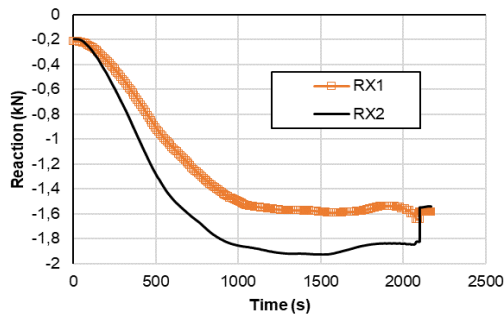
a) Horizontal reaction (Rx)
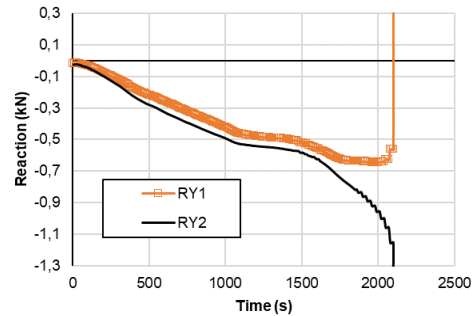
b) Horizontal reaction (Ry)
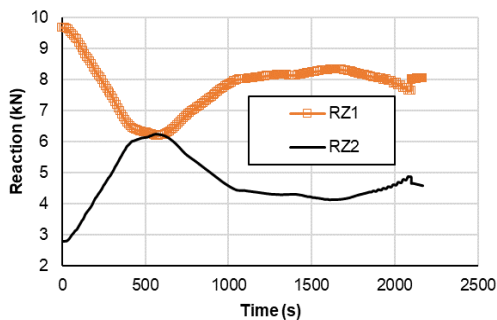
c) Axial reaction (Rz)

Figure 24: Time-reaction curves calculated at the restrained end of steel rods for the third fusible link

5. CONCLUSIONS

This paper has presented the details of finite element studies for three innovative fusible link solutions using aluminium bolts for fire walls in single-storey steel-framed buildings. The developed FE models can predict the

362

modes of failure of studied fusible links in fire situation. The following conclusions have been drawn from this study:

- Thermal finite element analysis allowed determining the distribution of temperature in different components of fusible links. The results obtained showed a small temperature gradient between the bolts and those of the connected steel profiles in all three studied fusible links. Nevertheless, it is noticeable that a significant gradient temperature along the length of the threaded rods by the protection provided by the sandwich panels makes the behaviour of the studied fusible links unpredictable by current analytical approaches.

- The fire resistance, as well as the failure modes of three studied links, have been successfully determined by the mechanical analysis. For the 1st fusible link, the failure is the local bending of the bottom flange of the column after 713 seconds, which is significantly below the required time of 1200 seconds. However, the second and third fusible links offer higher fire resistance. Indeed, the observed failure mode of the second fusible link is the local bending of the threaded rods in contact with the U-profile at about approximately 1710 seconds. At failure, a combination of other phenomena was also observed such as a flexural torsional buckling of the UPN, as well as a flexural buckling of the stiffener welded between the flanges of the portal frames columns. The failure mode of the third fusible link is the local buckling that appears in the lower flange of the U-profile, followed by the local bending of the threaded rods at about 2171 seconds. In a fire situation, this failure mode of the fusible links must be avoided in order to preserve the integrity of the fire wall and thus avoid the risk of collapse of the structure located at the unexposed fire side. With their high fire resistance, these two links will be tested in the series of experiments of the project. Further, it should be noted that one of the main reasons for these phenomena is the temperature gradient in the profiles, the threaded rods, etc. which could demonstrate the efficiency of the used coupled 3D thermal-mechanical analysis procedure in which the temperature fields of the studied links were calculated as detailed as possible.

- The second and third fusible link solutions that lead to the fire resistance higher than the required time of 1200 seconds will be prepared for future medium-scale fire tests planned in the ongoing European FISHWALL research project. In future research works, the design of the 1st fusible link will be investigated more in detail in order to evaluate the effect of certain parameters such as the boundary conditions of the modelled column and the continuity of contact between elements.

6. REFERENCES

[1] C. Renaud, «Guide de vérification du comportement au feu des bâtiments à simple rez-de-chaussée en charpente métallique,» 2017.

[2] O. Vassart, L-G. Cajot, B. Zhao, J. De Le Qunitana, J. Martinez deAaragon, A. Griffin, "Fire Safety of Industrial Halls and Low-rise Buildings: Realistic Fire Design, Active Safety Measures, Post-local failure simulation and Performance Based Requirements", ECSC Research 7210-PR-378, 2005.

[3] Deliverable D1.4: Design of tests, RFSC project FISHWALL, 2020.

[4] ANSYS, ANSYS User's Manual for Revision 8.0 – Volume IV – Theory, Swanson Analysis LINK, INC., Houston USA, 1992.

[5] EN 1999-1-2, Eurocode 9 - Design of aluminium structures - Part 1-2: Calculation of fire behaviour, Brussels, Belgium, CEN, 2007

[6] EN 1993-1-2: Eurocode 3: Design of steel structures – Part 1-2: General rules – Structural fire design, Brussels, Belgium, CEN, 2005.

NUMERICAL ANALYSIS OF SHEAR BUCKLING OF STEEL AND COMPOSITE PLATE GIRDERS UNDER FIRE EXPOSURE
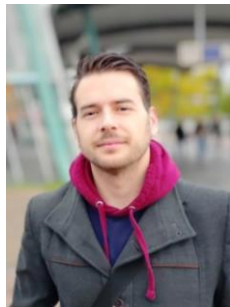
Mehmed Numanović a,*   **Markus Knobloch b**

ABSTRACT

Steel and steel-concrete composite plate girders represent structural elements often used in structural design of components carrying heavy loads or covering long spans. However, the designed slender webs of plate girders, although stiffened by lateral stiffeners, are highly susceptible to the out-of-plane shear buckling. Moreover, this failure mode becomes more pronounced when such girders are exposed to fire. However, the behavior of steel-concrete composite plate girders is still insufficiently researched when it comes to the phenomena of shear buckling both at ambient and at elevated temperatures.

This paper focuses on the development of a numerical model for the analysis of web shear buckling of plate girders at elevated temperatures using the ABAQUS software. Firstly, the model is validated with existing experimental results on steel and composite plate girders in shear conducted at ambient temperature and in fire. This modeling procedure is further implemented to develop benchmark steel and steel-concrete composite girders. In the end, a parameter study on most relevant parameters in web shear buckling is carried out, some of which include the study of the influence of: (a) web thickness (b) flange thickness (c) partial of shear connection (d) load ratio and (e) fire protection.

Keywords: Shear Buckling; Plate Girders; Composite Structures; Fire Design; Nonlinear Analysis.

---

a,** Ruhr-Universität Bochum, Universitätsstraße 150, 44801 Bochum, Germany, Mehmed.Numanovic@rub.de

b Ruhr-Universität Bochum, Markus.Knobloch@rub.de

1. INTRODUCTION

Steel plate girders represent structural elements that consist of narrow flanges and slender webs and are designed to carry high loads and cover long spans. These girders are essential for transfer beams, provide column-free floor space in buildings and represent major structural elements in small to medium span bridges. Designing these types of girders in a combination with a concrete slab, which is connected to the steel flange through shear studs, is a common practice. This newly assembled, more resistant system is referred to as steel-concrete composite plate girder. Nevertheless, the overall load carrying capacity of both steel and steel-concrete composite plate girders can be reduced through the shear out-of-plane buckling of the slender web plate. However, the buckling of the web plate, stiffened by the surrounding stiffeners and flanges, is not an automatic indication of the failure of the entire system. In reality, after the shear capacity of the web is reached, the buckled web plate begins anchoring in the surrounding flanges and, through the initialization of the membrane stresses in the tension field, the post-critical capacity of plate girders is activated. In this case, not only do the flanges start taking part in the load bearing capacity, but the tension field and plasticization expand in the web, thus engaging more surface area for load bearing. This means that higher loads can be applied before the failure of the entire system can be concluded. In most cases, the system failure is recognized in form of a sway frame mechanism in the connecting flanges, once their flexural capacity has been exhausted and plastic hinges have been formed.

This phenomenon found its breakthrough in Basler's work in 1960 [1, 2], in which he assumed that the flanges of steel plate girders do not possess the flexural rigidity to anchor the diagonal tension field of the web plate. In the years to follow, several alternative theories developed postulating otherwise [3-5]. This led to the development of different analytical models of shear buckling of plate girders. The resolution to these deviating theories was provided by the experimental study of Scandella [6], where a two-stage post-buckling behavior of steel plate girders in shear was recognized. The first stage is defined by plastic yielding of the web panel and its anchoring in the lateral stiffeners. This stage ends with a peak value referred to as girder's shear capacity. Beyond this point, the web panel loses stability through its primary buckling shapes and the girder loses stiffness. At one point, the web panel starts to stabilize through the secondary buckling shapes. The secondary buckling shapes enable the activation of the additional tension fields, through which the web anchors in the top and bottom flanges, and the post-buckling capacity is activated. The second stage concludes with the development of the second peak, the ultimate load. This value marks the onset of a failure mechanism with plastic hinges in the flanges.

As already mentioned, in case of the design of industrial buildings and bridges, plate steel girders are often seen in a combination with a concrete slab connected through shear studs to form steel-concrete composite girders. Nevertheless, many questions are still to be answered, like a) can the shear resistance of steel-concrete composite girders be calculated by adapting the existing formulations for steel girders to account for the composite action and to which extent and b) how the shear resistance of the concrete slab could be calculated. As a matter of fact, only a limited number of experiments have been conducted on steel-concrete composite plate girders in shear. Schanmugam and Basker [7] performed experiments on two bare steel and four steel-concrete composite plate girders and detected the development of a sway-frame collapse mechanism with plastic hinges in the flanges in composite girders, identical to the one observed in bare steel girders. Yet, it was observed that the tension field band was nonuniform with larger distances between plastic hinges in the flange attached to the concrete slab. Due to the composite action realized through shear studs, the attached concrete slab formed a highly rigid top flange with respect to the slender web panel. This caused an enlargement of the tension field in the web panel, enabling a larger web area to yield and strain-harden, and conclusively, generate higher shear capacity compared to bare steel plate girders. In [7] it was also established that the increase in shear capacity due to composite action was more pronounced in web panels with higher slenderness ratio. Within their research, Yatim et al. [8] analyzed the influence of shear studs and partial shear connection on the shear resistance and failure mechanism of the composite plate girders. As a result, a notable reduction in shear strength and a more ductile failure were observed when a lower number of shear studs was arranged. Regardless, the latest studies are insufficient to comprehensively understand the structural behavior of composite girders in shear. The main issue deals with quantifying the contribution of the concrete slab and shear connection in the overall shear resistance of composite girders. In the current structural Eurocode [9], the contribution of the concrete slab is neglected, and the shear strength of composite girders is computed based on the models for bare steel girders.

The phenomenon of shear buckling becomes much more challenging when plate girders are exposed to fire. Not only do steel and concrete materials deteriorate when exposed to higher temperatures, but thermal strains and

stresses arise in cross sections due to thermal gradients. In fact, most flexural buckling failure modes in plate girders at ambient temperatures are replaced by shear-dominated buckling of slender webs [10]. This is supported by the fact that due to exposure to high temperatures: (a) thermal restraint forces develop in the cross section owing to different temperatures generated in the web and flanges [10] and (b) material degradation at elevated temperatures could cause not only the loss of stiffness but also a reduction of the overall shear strength.

Only a few studies are available in the literature on the experiments conducted on plate girders at elevated temperatures. Vimonsatit et al. [11] and Tan et al. [12] carried out steady-state elevated temperature tests on steel plate girders and observed the tension field action and formation of plastic hinges in flanges, accompanied with the significant reduction in web shear strength at temperatures higher than 400°C. However, these tests were performed at constant elevated temperatures with a load increase until failure. A representative test of a realistic fire scenario would be a girder exposed to a constant load and a transient increasing temperature until failure. In the work by Scandella et al. [10], such a scenario has been modeled numerically. In this study, the researchers conclude the following: (a) thinner web panels heat a lot faster than the thicker flanges in a transient fire scenario and (b) failure mode of certain plate girders changed from flexural buckling of the flanges at ambient temperature to web shear failure in fire. The reason behind it is that the temperature gradients, which developed in a nonuniformly heated cross section, generate restraint stresses, which alter the failure mode to a shear-dominated loss of stability. Furthermore, in composite plate girders where the concrete slab is connected to the top flange, an asymmetrical temperature distribution and larger thermal gradients are to be expected. This further confirms the importance of the study of shear buckling of composite plate girders in fire.

Recently, Scandella [6] conducted an extensive experimental and numerical study on eight bare steel girders in shear exposed to transient increasing temperatures. His tests and subsequent numerical simulations confirmed that thermal strains and constraints bring about shear buckling, along with an early formation of the tension field during a fire exposure. Moreover, at the end of the test, a failure mechanism with larger distances between the plastic hinges formed in the flanges was recognized, when compared to that of the girders tested at ambient temperature. After evaluating the results of those tests, three phases in the behavior of steel girders in fire could be observed. During the first phase, no anchoring of the tension field in the flanges was observed, but thermal strains did influence the deformations. In the second phase of fire exposure, the tension field anchored in the cooler and stiffer flanges. Finally, the third phase became apparent when the tension field started to widen to account for the loss of stiffness and strength of the web panel and strain rates increased significantly. Aziz et al. [13] performed tests on bridge composite plate girders in transient fire and concluded a dominant influence of web slenderness and aspect ratio on the fire resistance. In their investigations, the authors also postulated a higher probability of web shear buckling in built-up plate girders than in rolled beams.

The phenomenon of shear buckling of composite plate girders in fire is to be investigated experimentally and numerically within the currently running German national research project carried out at Ruhr-Universität Bochum. In the scope of this paper, numerical models using the ABAQUS software will be developed to study the structural fire behavior of plate girders. After this model is validated with existing experimental results, it is further utilized to develop the benchmark steel-concrete composite girder, on which a parameter study is conducted.

2. METHODOLOGY

It is often strongly argued that, in order to truly comprehend the structural fire behavior of plate girders in shear, large-scale fire tests would be needed, which could in turn, generate unreasonably high costs. However, the modern finite element-based software has enabled the study of complex behavior in various engineering structures. Thus, these numerical models can complement large-scale fire tests and be used in the design of expensive fire tests to gain new and improved knowledge and develop prognosis models to predict the structural behavior, failure mechanisms, ultimate resistance etc. To ensure the development of a reliable numerical model with sound accuracy, results of the simulations need to be validated with physical tests on suitably sized girders. Once acceptable tolerances in results have been achieved, the numerical model is considered capable of replicating the tested behavior and can serve as a tool to investigate influential parameters through different parameter studies. In this paper, numerical models of steel- and steel-concrete composite plate girders exposed to fire have been developed with the help of the ABAQUS software. The most important parts of modeling, such as implemented finite element types, material models, analysis procedures etc., are discussed in detail.

2.1 Assembly of the numerical model

Many factors must be taken into account when creating a numerical model of the steel-concrete composite plate girder in ABAQUS. First off, there are various components to this kind of model: (1) steel girder with lateral stiffeners, (2) concrete slab, (3) shear studs, (4) lateral and longitudinal reinforcing bars, and (5) supports. These components are recognizable in the benchmark model used in this work, which is depicted in Figure 1.
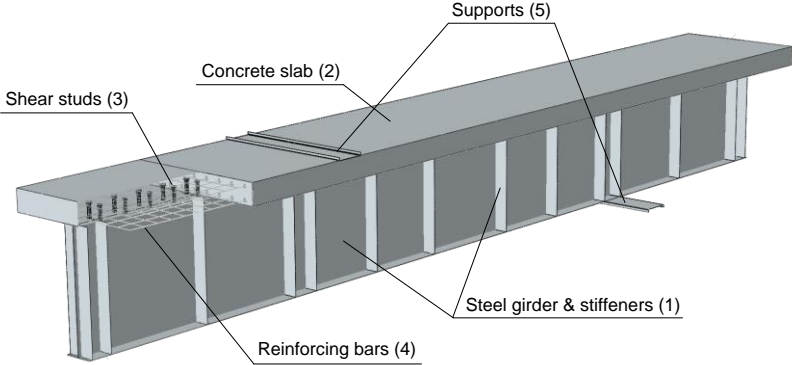

Figure 1: ABAQUS model of the benchmark composite plate girder

Each of the individual parts of the model are designated with a specific element type in ABAQUS, which serve to recreate tested or expected physical behavior of those parts. Furthermore, different element types are assigned in different analysis procedures. In this case, ABAQUS distinguishes between element types in eigenvalue analysis and stability analysis, and those necessary for the heat transfer analysis. Table 1 provides an overview of the implemented element types in the numerical models of this paper.

Table 1: Implemented element types of plate girder parts in ABAQUS

	Steel girder & lateral stiffeners	Concrete slab	Shear studs	Reinforcing bars	Supports
Eigenvalue & stability analysis	S4R	C3D8I	C3D8I	T3D2	Analytical rigid surface
Heat transfer analysis	DS4	DC3D8	DC3D8	DC1D2	

The most practical way of modelling a laterally stiffened steel girder whose web panel has a varying thickness in the longitudinal direction is to implement the four-node shell elements (S4R). Using solid elements for this kind of design not only necessitates more attention to detail in the assembly of the various steel plates, but it also results in uneven meshing and stress concentrations in the girder's connecting components. Moreover, the reduced integration option reduces computation time while producing more accurate findings [14]. Eight-node solid elements in incompatible mode (C3D8I) were assigned to the concrete slab and shear studs. The rationale is that the concrete damage is best represented with solid parts since these elements are both susceptible to bending and shearing. Moreover, the compatibility mode enables contact behavior and lessens the likelihood of volumetric and shear locking in those elements. Furthermore, since reinforcing bars only transfer axial forces throughout the system, they are represented by two-node truss elements (T3D2). Analytical rigid surfaces have also been utilized to simulate the supports in the system. The aforementioned element types have their equivalent in the heat transfer analysis and are, as such, listed in Table 1.

2.2 Material models

Accurately defining material models at elevated temperatures represents one of the most important aspects in the computational fire analysis of composite plate structures. Stiffness and strength degradations of individual girder parts in transient fire conditions not only influence the overall fire resistance, often defined through failure time and critical temperature, but also shape the outcome and failure mechanism of the heated girder. For this reason, when it comes to validation of fire tests conducted on steel and composite plate girders, material models provided

in respective references have been utilized. Subsequently, in case of fire analysis of the benchmark composite plate girder of this paper, material models defined in EN 1994-1-2 [15] have been implemented.

For the purposes of this study, temperature-dependent mechanical and physical material properties have been defined in ABAQUS for all girder parts. These include: (1) material elasticity (2) material plasticity (3) thermal expansion (4) density (5) conductivity and (6) specific heat. The concrete material model has been defined with the use of the Concrete Damaged Plasticity (CDP) material module provided in ABAQUS. This feature allows for (1) capturing brittle behavior in concrete in all types of structures (2) defining different tensile and compressive behavior in a material and (3) considering irreversible damage taking place in fracturing process [14].

2.3 Three-step fire analysis

Generally, the stability analysis of plate girders in fire consists of three main steps (1) Eigenvalue analysis, (2) Heat transfer analysis, and (3) Thermal Stress and Stability analysis. The eigenvalue analysis (*Buckle) is performed to extract (a) eigenvalues of the system in order to determine the elastic critical loads and (b) eigenmodes that would be scaled to apply initial imperfections in the system, necessary for the stability analysis. The second step includes the heat transfer analysis, in which the system is exposed to external temperature influences, and, through consideration of conduction, convection and radiation, temperature development and distribution are recorded in time. Finally, after introducing the initial imperfections, a constant load of magnitude lower than the limit load at ambient temperature is applied, and the girder is exposed to an increasing temperature until failure. This type of analysis is transient and is a representative scenario of real girders exposed to fire. When thermal stress and stability analysis is performed applying the Static, General step in ABAQUS, as it is the case in this paper, the previous two analysis (Buckle and Heat transfer) are completed separately and embedded as input in the Static analysis (uncoupled transient).

2.4 Output parameters

Depending on the analysis type, several output parameters should be considered. As already mentioned, the eigenvalue analysis mainly provides a shape of geometrical imperfections that are a perquisite of a stability-related problem. The relevant output of the heat transfer analysis includes computed nodal temperatures in time in different sections of the girder. Finally, to compute the fire resistance, displacement-time curves at points of load application and out-of-plane web displacement-time curves are extracted from the static analysis.

The overall fire resistance is defined by the girder's failure time, at point in time when the displacement-time curve approaches the vertical asymptote and corresponding displacement rates are large [6]. Additionally, the critical temperature is computed, which in this case, represents the maximum temperature achieved in the web panel at the time of failure. Often, it can also be of interest to compute out-of-plane web displacements and the corresponding displacement rate in time. These curves not only give an indication on the development of the out-of-plane deflections in a fire scenario, but also serve to observe primary and secondary buckling waves in the web panel and their anchoring in the surrounding supports (lateral stiffeners and flanges).

3. VALIDATION OF THE NUMERICAL MODEL WITH EXISTING EXPERIMENTAL RESULTS

Before the developed numerical model and the presented modeling procedure can be considered reliable, results of existing experiments conducted on steel and composite plate girders in fire are analyzed and recreated in this paper using the ABAQUS software. The generated results of the heat transfer and shear buckling are compared and validated. The first series involves fire tests on bare steel plate girders conducted by Scandella [6], whereas the second comprise of composite plate girders, investigated by Aziz et al. in [13].

3.1 Validation of the numerical model of steel plate girders

A thorough experimental investigation of steel plate girders in fire was conducted by Scandella in [6]. Within his research, Scandella conducted eight tests on steel plate girders in fire (Series II and III) and studied several different influences on their shear buckling behavior. These include: (a) web slenderness (b) aspect ratio (c) flange stiffness (d) load level and (e) thermal insulation. Dimensions of the tested girders are shown in Figure 2.
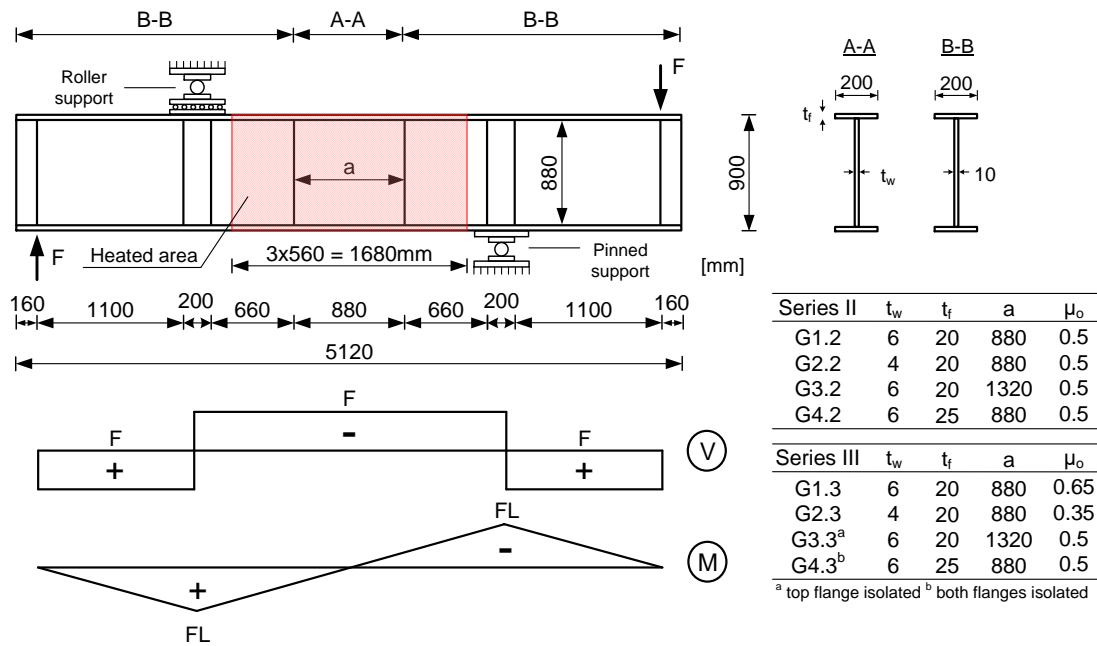
Figure 2: Dimensions of the tested steel plate girder in [6]

Series II	t_w	t_f	a	μ_o
G1.2	6	20	880	0.5
G2.2	4	20	880	0.5
G3.2	6	20	1320	0.5
G4.2	6	25	880	0.5

Series III	t_w	t_f	a	μ_o
G1.3	6	20	880	0.65
G2.3	4	20	880	0.35
G3.3[a]	6	20	1320	0.5
G4.3[b]	6	25	880	0.5

[a] top flange isolated [b] both flanges isolated

The analyzed web panel is located in the middle of the girder (Section A-A), with a reduced thickness compared to the rest of the girder (Section B-B), in order to ensure shear buckling failure mode in the middle web panel. Furthermore, to analyze the fire behavior of steel plate girders in shear, the static system with antisymmetric loading was selected. Compared to classical four-point bending tests, this static system reduces the influence of bending moments on the overall shear resistance of plate girders. The middle part of the girder was enclosed on all four sides with a furnace, set up to introduce high temperatures in the girder.

In [6], the fire tests were conducted in such a way that at first, two loads with equal amplitudes were introduced at girder ends (with defined load ratio μ_0 of the ultimate load at ambient temperature), before any heating had taken place. Afterwards, the loads were constant throughout the test. At the end, the furnace was activated, and heating of the girder was initiated. The heating of the girder was done according to the ISO 834 curve, with the exception of the initial phase, where a maximum heating capacity of the furnace (70°C/min) had to be used. In addition, Scandella conducted small-scale tests on steel plates of various thicknesses at different elevated temperatures. This, in turn, enabled a detailed definition of the material model, later implemented in the numerical model.

Integrating the provided geometry, loading, heating and boundary conditions, as well as the provided material model from [6], we have developed numerical models of these steel plate girders, following the modeling procedures described in the previous section. To validate the numerical model and prove its reliability and accuracy, the following output parameters are extracted and compared with experimentally obtained values, e.g.: (a) temperature in different girder plates and (b) lateral displacement at loading points.

At first, to recreate the temperature field in steel girders exposed to an increasing temperature, heat transfer analysis is initiated in the ABAQUS software. Aside from the standard physical properties defined in the material model (density, conductivity and specific heat), heating of the girder has to be introduced through the interaction of the girder's surfaces with the surrounding heated gas. This is done by providing convection interactions with film coefficients α_c on all heated surfaces of the plate girder. Although a standard value of this coefficient ($\alpha_c = 25$ W/(m²K)) has already been provided in [15], this uniform value is not suitable for girders that comprise of several plates of different thicknesses and existing temperature gradients in cross sections of plate girders. Therefore, for each of the eight tests performed in [6], a set of film coefficients has been calibrated, in order to achieve a temperature field closest to the one measured in tests. Based on these considerations, the temperature-time curves of heated gas, flanges and web have been extracted and put side-by-side with the temperatures measured in the experiments. The temperature-time curves of test Series II and Series III are shown in Figures 3a-d and Figures 4a-d, respectively.
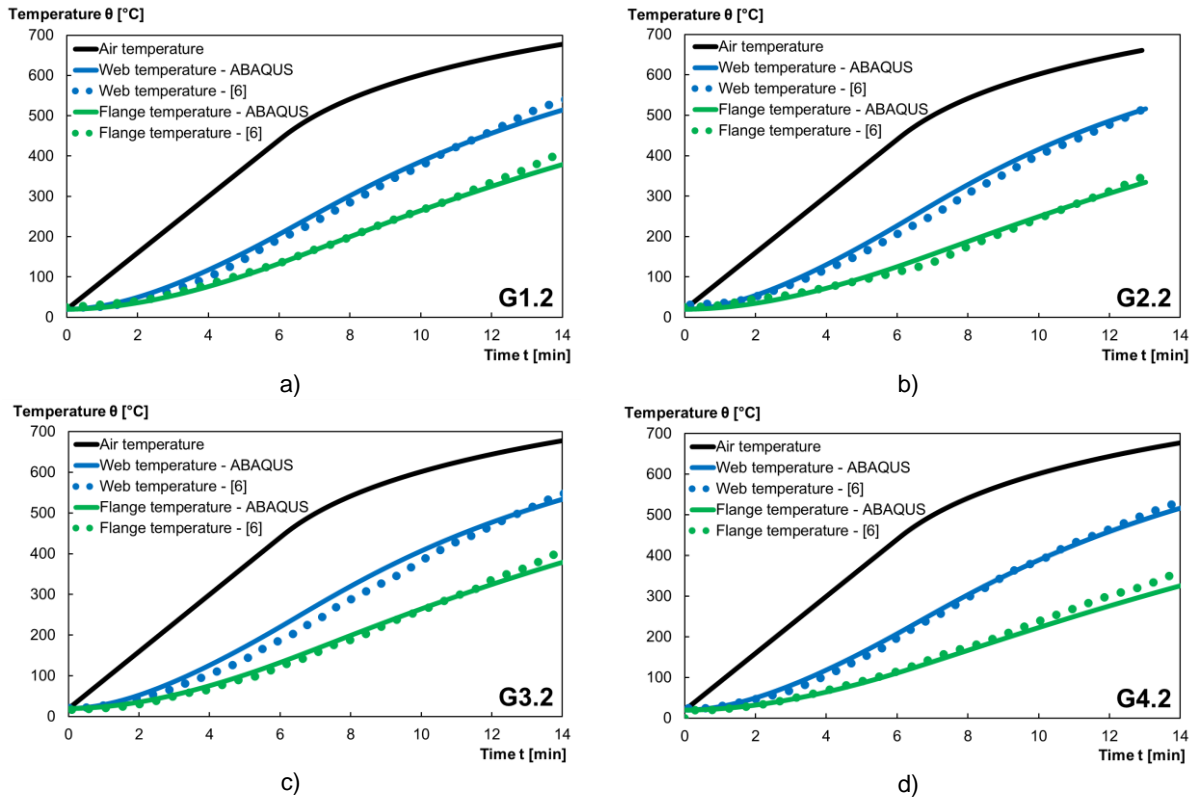
Figure 3: Comparison of temperatures of steel girders of Series II measured in [6] and computed with ABAQUS
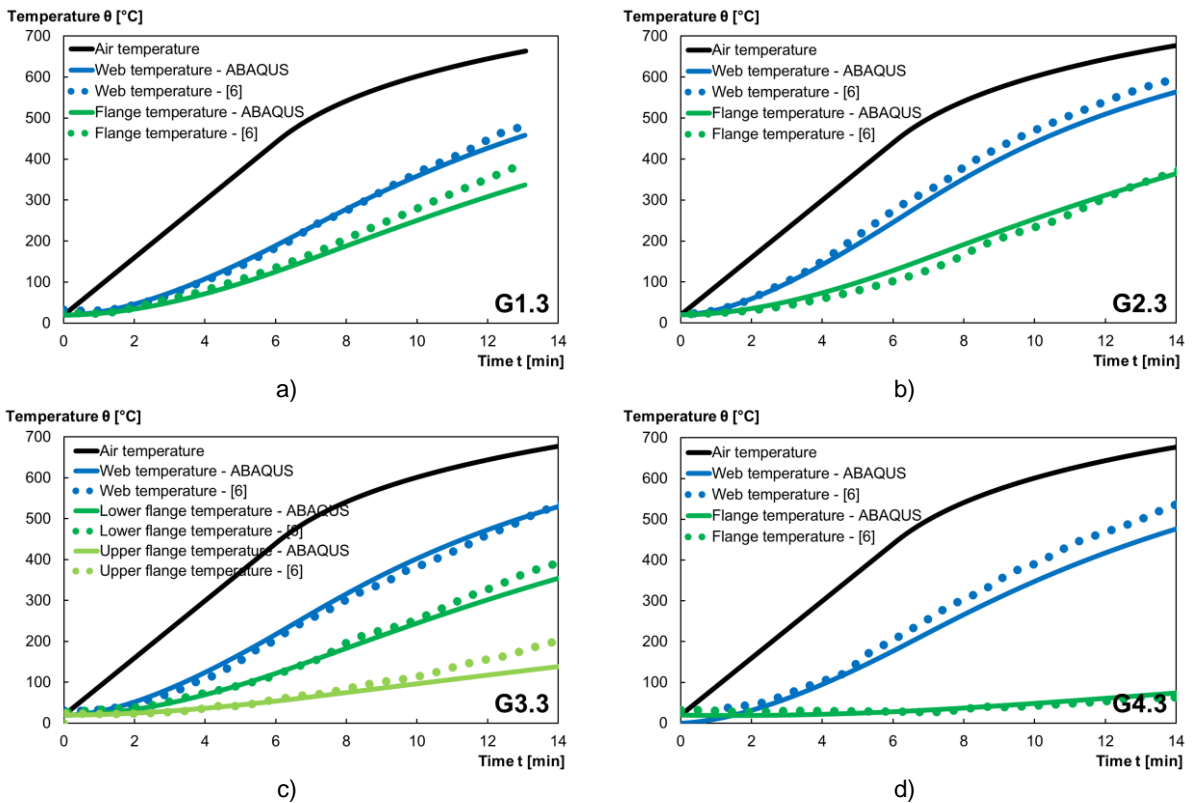

Figure 4: Comparison of temperatures of steel girders of Series III measured in [6] and computed with ABAQUS

As it is clear from the results above, our numerical model can recreate the temperature field of each of the tested steel girders, with minor deviations from the measured values. Thereupon, the corresponding mechanical loads

are introduced in the initially deformed girders, after the imperfections of the scaled eigenmode ($u_o = h_w/200$) have been applied. Afterwards, the girders are exposed to increasing temperatures until the sway-frame mechanism with plastic hinges is formed in the flanges and the entire system suffers due to loss of stability. The results of this analysis are presented with displacement-time and displacement-temperature curves at points of load application and compared to experimentally obtained values (where available) in Figures 5a-b and 6a-b, respectively.
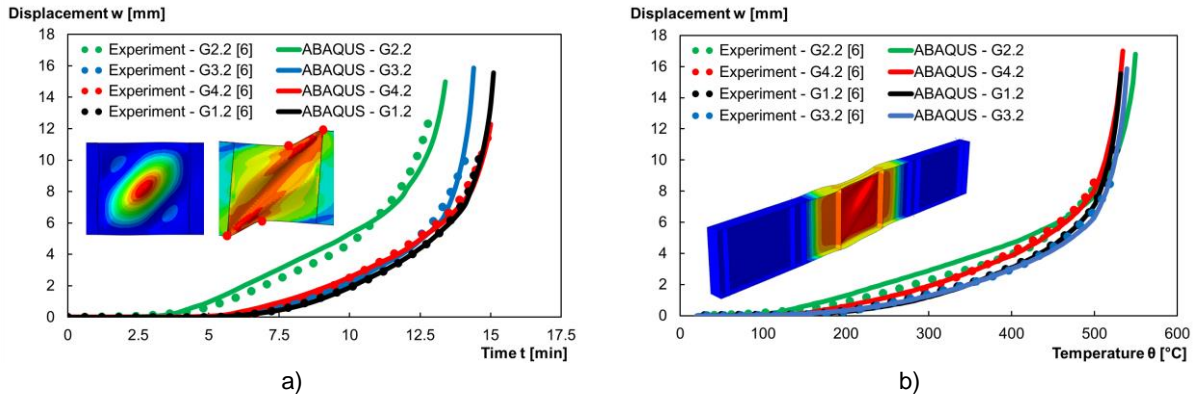
Figure 5: Comparison of a) displacement-time and b) displacement-temperature curves of steel girders of Series II at loading points measured in [6] and computed with ABAQUS
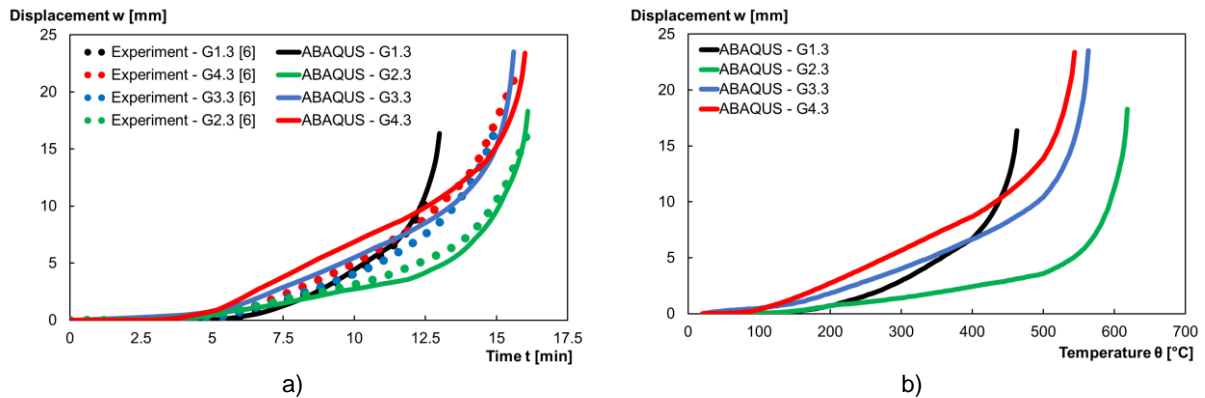
Figure 6: Comparison of a) displacement-time and b) displacement-temperature curves of steel girders of Series III at loading points measured in [6] and computed with ABAQUS

It is obvious that the developed numerical model can recreate the structural behavior of steel plate girders in fire in a satisfactory manner. The main advantage is the provided detailed material model of steel at elevated temperature. In fact, Scandella has shown a significant influence of the material definition on the overall capacity and fire resistance of steel plate girders. One should also point out that the experimental tests had to be terminated due to maximum deflections achieved in measuring instruments, while this is obviously not an issue in numerical simulations, which can be run until the displacement-time curves are almost asymptotical. The summary of the measured and computed failure times and critical temperatures is given in Table 2.

Table 2: Comparison of failure times and temperatures in web and flanges of steel girders from [6]

	G1.2	G2.2	G3.2	G4.2	G1.3	G2.3	G3.3	G4.3
Failure time t_R^{EX} [min]	14.7	12.9	14.1	15.0	12.7	16.1	14.9	15.7
Failure time t_R^{AB} [min]	15.1	13.5	14.4	15.3	13.0	16.1	15.6	16.0
Relative error [%]	2.72	4.65	2.12	2.00	2.36	0.00	4.70	1.91
$T_{web} = T_{critical}$ [°C]	533.6	515.9	538.7	576.5	483.3	598.1	555.6	525.8
T_{flange} [°C]	398.3	334.7	383.3	384.1	361.2	401.7	149.6[TF] 379.6[BF]	88.2

[TF] – temperature in the top flange; [BF] – temperature in the bottom flange

with t_R^{EX} – experimentally measured failure time, t_R^{AB} – numerically computed failure time, T_w – web temperature and T_f – flange temperature at the time of failure.

The computed temperature in the middle web panel is used as the representative value of the critical temperature. In case of Series II, it is clear that the fire resistance of steel plate girders with higher web slenderness (G2.2) and higher aspect ratio (G3.2) is reduced, with respect to the reference girder (G1.2). The slight increase in fire resistance in case of a higher flange stiffness (G4.2) is, generally, not to be neglected, but is in this case inferior to the other influences. In Series III, the load level has a significant influence on the fire behavior, with the higher load level (G1.3) producing a lower fire resistance with lower critical temperature; and vice-versa, the lower load level generating a higher fire resistance (G2.3) with higher critical temperature. In case of girders with insulated top flange (G3.3) and both flanges (G4.3), the failure time and critical temperature are similar; however, the temperature in the flanges is much lower in the latter case. This brings about higher temperature gradients in the web panel and higher initial deflections, as it is apparent from Figure 6a.

3.2 Validation of the numerical model of composite plate girders

Aziz et al. [13] carried out fire tests on three composite girders to observe the influence of web slenderness and aspect ratio on the overall fire resistance of typical bridge girders. In [13], girders G1, G2 und G3 were supported on their ends and loaded with a constant load in the middle of the span for 30 minutes, before being exposed to an increasing temperature. The loads introduced in the system prior to fire exposure were chosen as a percentage of the flexural capacity of these girders at ambient temperature, specifically 69%, 40% and 33% of the capacity of girders G1, G2 and G3, respectively. The dimensions of the tested girders are given in Figure 7.
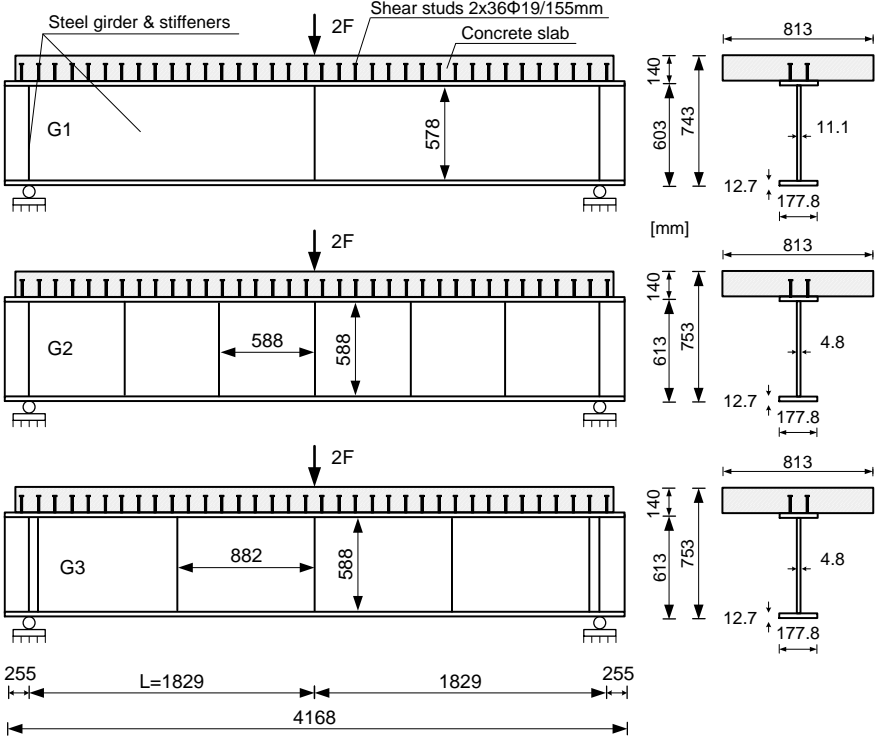
Figure 7: Dimensions and static system of the Aziz' girders in [13]

While Girder G1 was designed with no intermediate stiffeners and with web thickness t_w=11.1mm, girders G2 and G3 had intermediate stiffeners, positioned to produce panel aspect ratios of 1.0 and 1.5, respectively. In addition, to test the influence of web slenderness, a thinner web (t_w=4.8mm) was assigned to girders G2 and G3. The girders were heated on their sides and from the bottom with the fire test furnace. The temperature increase during the test followed the ASTM E119 temperature-time fire curve, until failure in girders was established.

Based on the given input parameters of the tested bridge girders in [13], a numerical model in ABAQUS software has been developed, by following the guidelines presented in the previous sections. In order to achieve a reliable and accurate numerical model, with the ability of reproducing experimental results on composite plate girders in [13], the following output parameters are extracted: (a) temperature in different cross section parts of the girders

and (b) lateral displacement at girder mid-span. Similar to the procedure described in the previous sub-section, eigenvalue analysis in ABAQUS is conducted to extract and scale the initial imperfections ($u_o = h_w/200$). Following that, heat transfer analysis is administered, with which the temperature field in every section of the girder is determined. Within this step, the effects of conduction, convection and radiation, which are dependent on multiple factors during the test, were considered and calibrated in an attempt to recreate the experimental results. The comparison of computed values achieved from the ABAQUS model and measured values from the tests on all three girders is shown in Figures 8a-c.
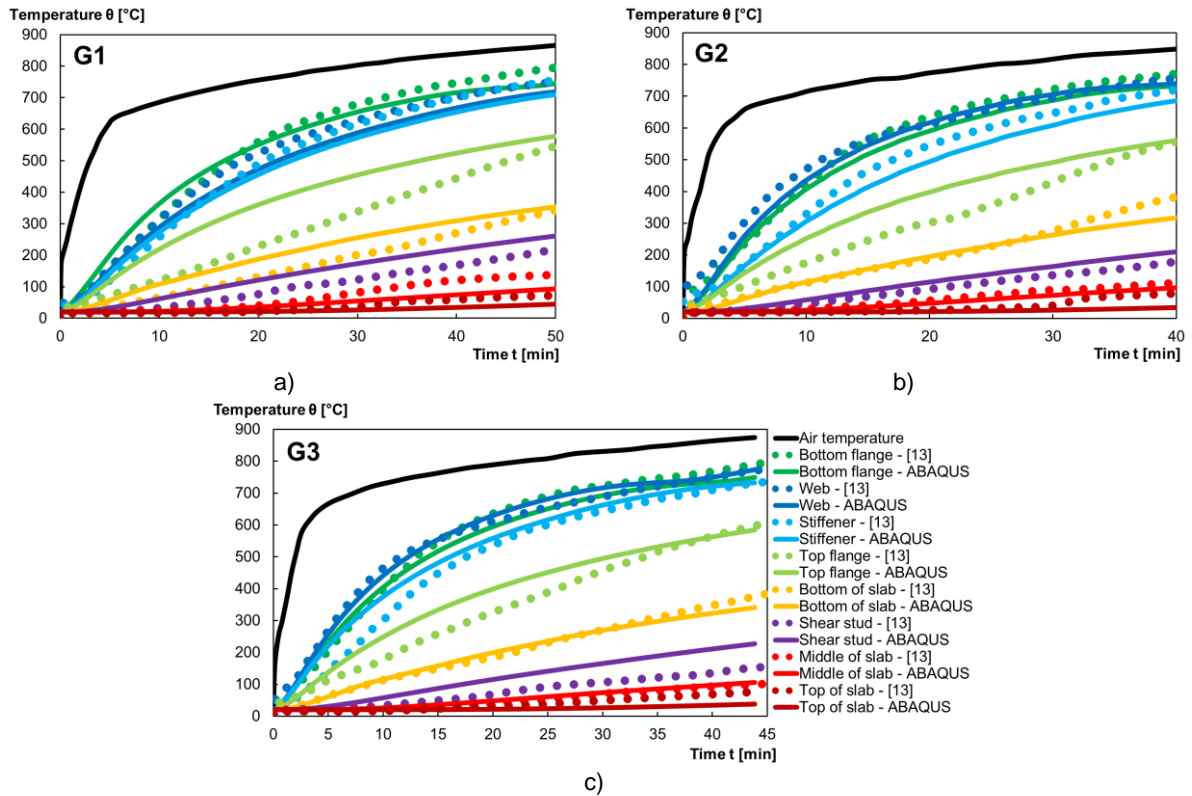
Figure 8: Comparison of temperatures of tested composite girders measured in [13] and computed with ABAQUS

With regard to Figures 8a-c, the temperatures in different parts of the girder are, for the most part, accurately reconstructed with the ABAQUS software. Keeping that in mind, there are not significant differences in the temperature distributions among the girders, aside from the faster heating of the thinner webs. The girders' bottom flange and web reach the maximum temperatures, between 700-800°C at the time of failure; the top flange, which is insulated by the concrete slab, did not attain temperatures higher than 600°C; and temperatures in the slab and studs did not surpass 400°C, with the minimum temperature recognized at the top of the slab.
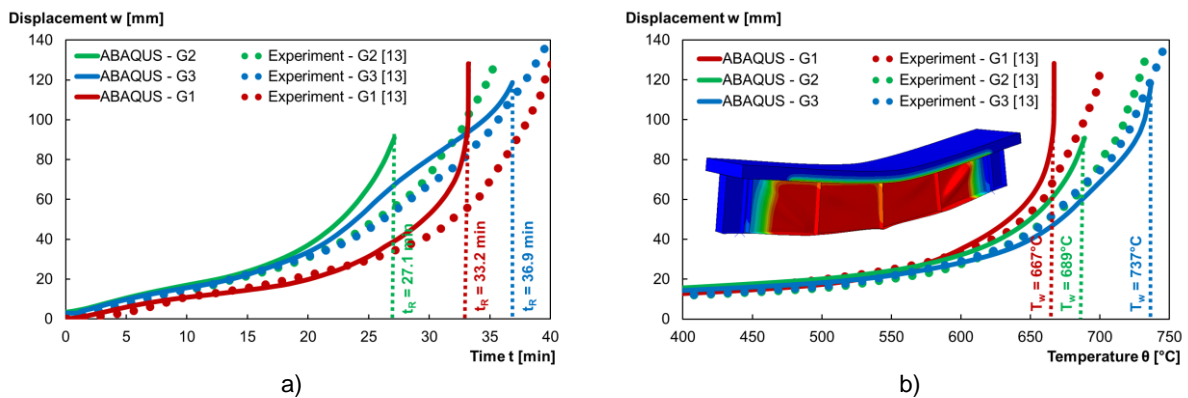
Figure 9: Comparison of a) displacement-time and b) displacement-temperature curves of composite plate girders G1, G2 and G3 at load application points measured in [13] and computed with ABAQUS

The calculated temperature field is adopted and used as an input value for the thermal stress and stability analysis. Meaning, by applying a constant load in the middle of the span, the computed temperature is increased until the girders reached their failure mode. To validate our numerical model, displacement-time curves at mid-span are computed and compared to the measured values in [13] and shown in Figure 9a. In addition, the mid-span displacement is plotted against web temperature and shown in Figure 9b. While girder G1 failed due to flexural buckling of the flange, with no notable out-of-plane deflections in the web, girders G2 and G3 failed due to shear buckling. Furthermore, girder G3 attained a lower fire resistance, which can be prescribed to the increased aspect ratio of 1.5. As it can be seen, the developed numerical model provides more conservative results, since it displays an earlier failure time than the girders from the experiment. The possible reasons could include: (a) the lack of the exact definition of the concrete material model at elevated temperatures in [13] and (b) the nonexistence of the steel model at elevated temperatures for different plate thicknesses in [13]. Nevertheless, this analysis provides a good insight into the phenomena of shear buckling of composite plate girders in fire and stresses the importance of a detailed definition of material models at elevated temperatures.

4. FIRE ANALYSIS OF THE BENCHMARK PLATE GIRDERS IN FIRE

Having validated the numerical model of steel and composite plate girders with the existing experimental tests, benchmark composite plate girder has been adopted, with which a parameter study of the most influential parameters on structural fire behavior of plate girders in shear is conducted. Following the example of [6], the static system with antisymmetric loading is chosen, in order to reduce the influence of bending moments on the shear capacity of the web panel. The previously described three-step procedure with eigenvalue, heat transfer and thermal stress and stability analysis has been applied analogously. The sketch of the chosen composite girder, which originates from the aforementioned currently running research project at Ruhr-Universität Bochum, is given in Figure 10.
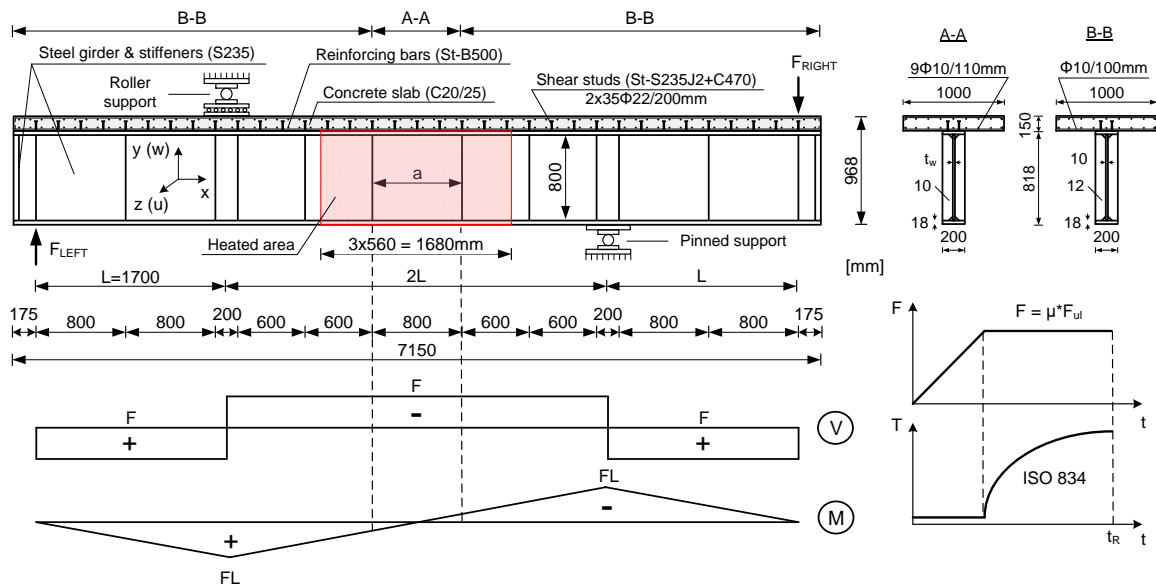

Figure 10: Dimensions and static system of the benchmark composite plate girder

The girder is exposed to fire on three sides (sideways and from the bottom), with the heating area corresponding to the length of three modules of modular electric furnace (3x560=1680mm). The fire simulations in ABAQUS are conducted in two phases. The first phase is the loading phase, where the loads are introduced at girder ends. At this point, imperfections are already considered. After the desired load level is reached, the girder is heated according to the ISO 834 fire curve until failure is established. The chosen load level for the reference girder is 500kN, which corresponds to 60% of its ultimate load at ambient temperature. The results of the numerical analysis of the benchmark composite girder are shown in Figures 11a-b. These include displacements and displacement rates at loading points and out-of-plane displacements in the middle of the web. Since the girder is not a doubly symmetric cross-section, displacements at the left and right loading point are not equal in magnitude, as it is the case of bare steel plate girders. Therefore, an average among the two is calculated and plotted below.
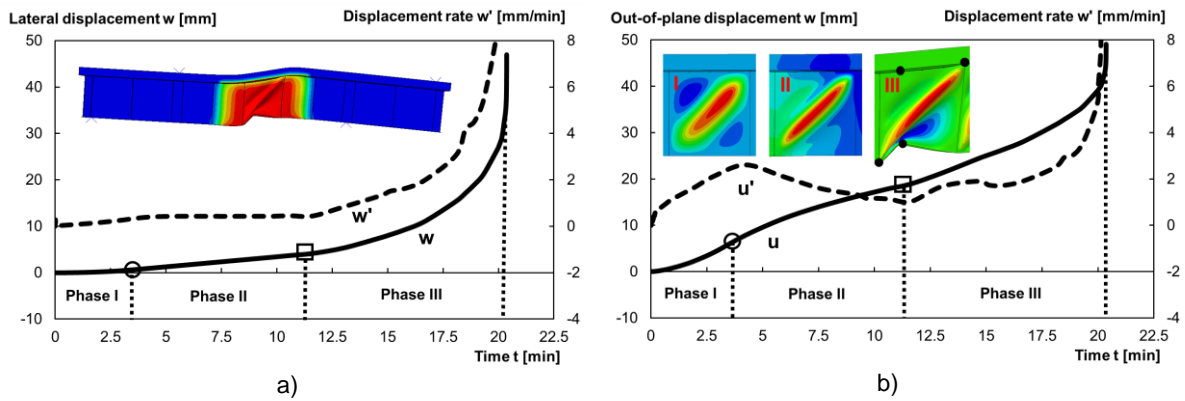
Figure 11: Displacement- and displacement rate vs. time in the: (a) loading points in the lateral y direction and (b) middle of the web panel in the out-of-plane z direction

Observing the obtained results from above, three different phases in structural fire behavior can be distinguished. During the first phase, no increase in global deflections w can be observed. However, the out-of-plane web deflections u and the corresponding rates u' are increasing i.e., the tension band forms in the web and anchors only in the surrounding stiffeners. Therefore, the increase in the out-of-plane deflection rate can only be attributed to the restraint forces caused by thermal expansion, since no material degradation occurs at low temperatures. By the end of the first phase, the out-of-plane deflections stabilize, which marks the beginning of the anchoring of web's tension band in the flanges. The second phase (3.5min) begins with the steady, almost linear increase in global deflections w and deflection rates w'. Yet, the out-of-plane web deflection rates u' slightly decrease until the end, with a quasi-linear increase in the web deflections u. The third and final phase (11.5min) is marked with an almost exponential increase in global deflections w and rates w'. Similarly, the rise in u' rates can be observed, followed by a nonlinear development in web's out-of-plane deflections. The reason is the pronounced material and stiffness degradation of the web panel and flanges due to exposure to high temperatures. With a reduced capacity to carry the loads, the tension band widens, integrating a larger web area to participate in the load carrying process and activating tensile stresses within the secondary buckling waves. This brings about the rise in the deformation of the surrounding flanges, until the deflection curves become almost asymptotical. At that point in time (20.4min), the girder has reached its fire resistance. Finally, the deformed shape of the girder indicates a pair of plastic hinges in each flange, which developed to produce a sway-frame mechanism and shear buckling failure of the plate girder. The maximum computed temperature in the web panel is 563°C. To investigate the temperature development, the temperature in the middle cross-section of the web panel is computed in time and displayed in Figures 12a-b.
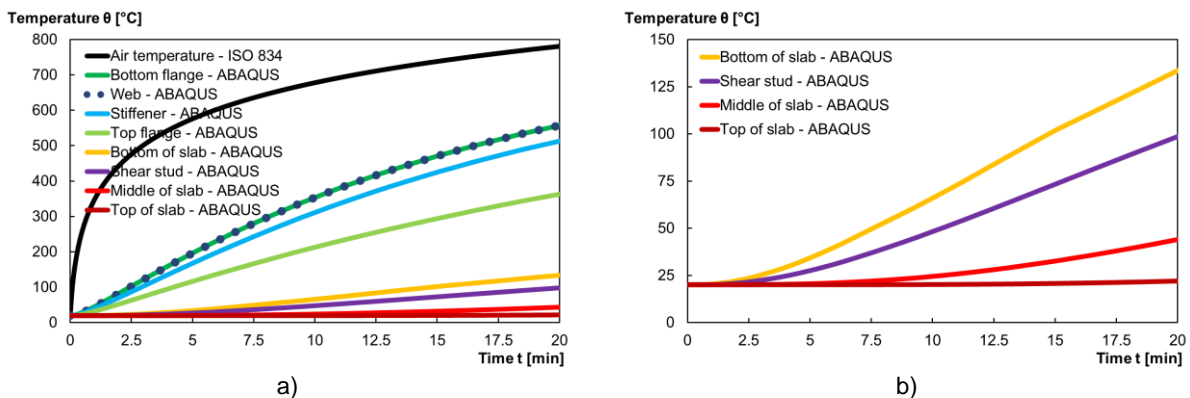

Figure 12: Temperatures in the middle cross-section of the composite plate girder

For the total heating time of 20.4 minutes, the highest temperatures are achieved in the web plate and bottom flange (563°C), while the top flange has notably lower temperatures (235°C), with slab and studs remaining relatively cold. Contrary to the composite girders from [13], the concrete slab did not attain larger temperatures, since it was not heated directly by the furnace from its sides and the heating time was only half as long.

375

In the following, the influence of several different parameters on the shear buckling behavior of composite plate girders is explored. At first, the load ratio μ was varied from 0.60 to 0.33. The displacement at loading points is plotted in time and given in Figure 13a. The failure time ranges from 20.4min to 35.4min, with a clear increase in fire resistance in case of lower load ratios. Analogously, the critical temperature in the web is highest for the lowest tested load ratio of 0.33 and equal to 714°C, compared to 563°C in case of the load ratio of 0.60. Subsequently, the influence of partial shear connection and fire protection is shown in Figure 13b. With regard to the reference girder, the number of shear studs was reduced from 70 to 21, by arranging only one row of studs at a distance of 340mm. This corresponds to the reduction of the degree of shear connection from 2.19 to 0.66. In a separate simulation, the bottom flange of the reference girder was insulated, providing for its slower heating, only possible through heat conduction. It is obvious that the fire resistance of composite girders with partial shear connection is decreased, with failure time of 18.9min and critical temperature of 474°C. On the other hand, with an insulated bottom flange, the overall fire resistance was increased to 22.0min, with 586°C in the web panel and a reduced temperature in the bottom flange of 175°C. Furthermore, the deflections are higher during the second phase of this simulation, compared to the other too, which can be attributed to the thermal stresses and strains that arise during temperature differences in the web and surrounding flanges.
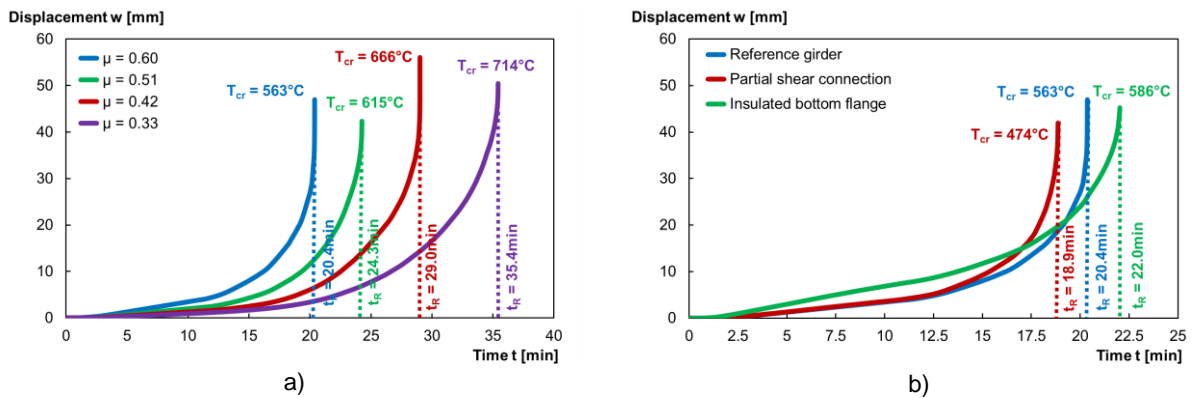
Figure 13: Displacement-time curves at loading points for: a) varying load ratio and b) partial shear connection and fire protection

In the end, the influence of the web and flange thickness on the fire resistance of plate girders in shear is investigated. At first, the thickness of the middle web panel was varied from 4mm to 8mm. In another set of simulations, the impact of the flange thickness of the entire girder was analyzed in the range from 15mm to 30mm. The results of these simulations are presented in Figures 14a-b.
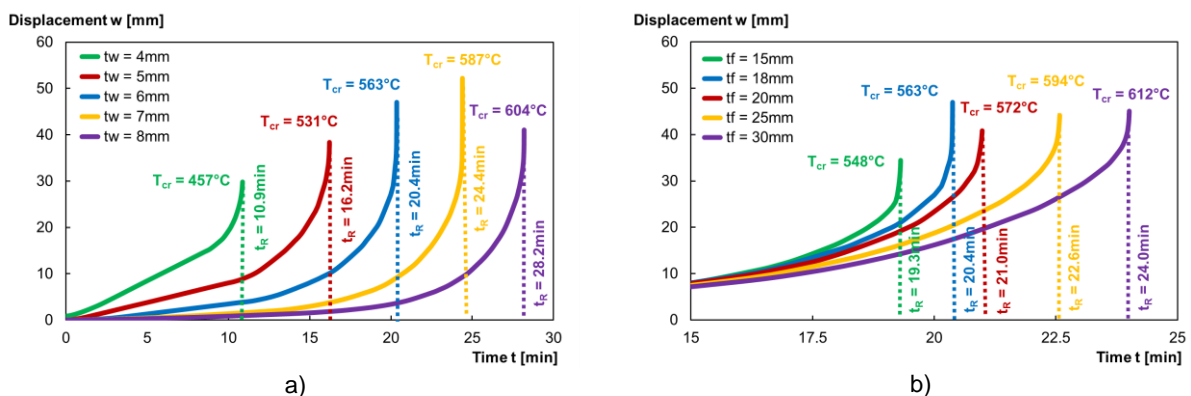

Figure 14: Displacement-time curves at loading points for varying: a) web thickness and b) flange thickness

As expected, Figure 14 shows that enlarging the thickness of the web panel or the flanges increases the overall fire resistance of the plate girder. Considering that the failure mode in all cases was web shear buckling, the influence on fire resistance is more significant in case of varying web panel thickness. In fact, by increasing the web thickness from 4mm to 8mm, the fire resistance rises from 10.9min to 28.2min. On the other hand, the fire resistance increased only slightly from 19.3min to 24.0min, when the flange was increased from 15mm to 30mm.

5. CONCLUSIONS

Within the scope of this paper, the fire resistance of steel and steel-concrete composite plate girders in shear has been investigated numerically with the implementation of the ABAQUS software. The developed models in heat transfer and stability analysis were, at first, validated with existing experimental results, before a parameter study on a chosen benchmark composite plate girder was conducted. With regard to the results achieved in this study, the following can be deduced:

- The developed numerical models are capable of reproducing the structural fire behavior of steel and steel-concrete composite plate girders in shear with satisfactory results.
- A comprehensive definition of steel and concrete material models at elevated temperatures is essential when recreating shear buckling behavior of plate girders in fire, since the lack of such may lead to deviations.
- The increase in web thickness and flange thickness as well as the consideration of fire protection provided a higher fire resistance in both steel and composite plate girders in shear. However, a higher aspect ratio, higher load ratio and partial shear connection reduced the overall fire resistance.
- The contribution of the concrete slab in plate girders exposed to fire is two-fold. It does not only stabilize the top flange and increase its stiffness, but it acts as an insulator to provide a slower heating of the top flange.

ACKNOWLEDGEMENTS

REFERENCES

[1] Basler, K.; Yen, B.T.; Mueller, J.A.; Thürlimann, B. (1960), *Web buckling tests on welded plate girders.* WRC Bull. No. 64. New York: Welding Research Council.

[2] Basler, K. (1961). *Strength of plate girders in shear,* J. Struct. Div. 87(7): 151-180.

[3] Rockey, K.C.; Skaloud, M. (1968). *Influence of flange stiffness upon the load carrying capacity of webs in shear*, Proc. 8th IABSE Congress, Final Report, 429-439. Zurich: IABSE.

[4] Rockey, K.C.; Evans, H.R.; Porter, D.M. (1978). *A design method for predicting the collapse behavior of plate girders*, Proc. Inst. Civ. Eng. 65(1): 85-112.

[5] Höglund, T. (1973). *Design of thin plate I girders in shear and bending with special reference to web buckling*, Stockholm: Royal Institute of Technology.

[6] Scandella, C. (2019). *Zum Schubtragverhalten von Blechträgern bei Raumtemperatur und im Brandfall.* Ph.D. thesis, ETH Zürich.

[7] Shanmugam, N.E.; Baskar, K. (2003). *Steel-Concrete Composite Plate Girders Subject to Shear Loading*, J. Struct. Eng. 129(9): 1230-1242.

[8] Yatim, M.Y.M.; Shanmugam, N.E.; Wan Badaruzzaman, W.H. (2015). *Tests of partially connected composite plate girders*, Thin-Walled Structures. Vol. 91: 13-28.

[9] CEN (European Committee for Standardization). (2010). *Eurocode 4: Design of composite steel and concrete structures – Part 1-1: General rules and rules for buildings*, EN 1994-1-1. Brussels: CEN.

[10] Scandella, C.; Knobloch, M.; Fontana, M.; (2014). *Numerical analysis on the fire behaviour of steel plate girders*, Structures in Fire, Proc. Eight Int. Conf., Shanghai, China, pp. 105-112.

[11] Vimonsatit, V.; Tan, K.H.; Qian, Z.H. (2007). *Testing plate girder web panel loaded in shear at elevated temperature*. J. Struct. Eng. 133(6): 815-824.

[12] Tan, K.H.; Qian, Z.H. (2008). *Experimental behaviour of a thermally restrained plate girder loaded in shear at elevated temperature*. J. Constr. Steel Res. 64: 596-606.

[13] Aziz, E.M.; Kodur, V.K.; Glassman, J.D.; Garlock, M. (2015). *Behavior of steel bridge girders under fire conditions.* J. Constr. Steel Res. 106: 11-22.

[14] ABAQUS 6.14-1 (2014). *ABAQUS/Standard user's manual*. Dassault Systèmes Simulia Coorporation. Providence, RI, USA.

[15] CEN (European Committee for Standardization). (2005). *Eurocode 4: Design of composite steel and concrete structures. Part 1-2: General rules – Structural fire design*, EN 1994-1-2. Brussels: CEN.

MATERIAL TESTS AND NUMERICAL INVESTIGATIONS ON COMPOSITE STEEL AND CEMENT-FREE CONCRETE SYSTEMS IN FIRE

Valentino Vigneri[a]*   **Fangxia Lu[b]**   **Ian Chamberlain[c]**   **Andreas Taras[d]**

ABSTRACT

An environmentally friendly composite construction system ("Stahlkammer") combining recycled steel profiles and a newly developed cement-free concrete (Cleancrete ©) and meant to be employed in residential buildings is being developed in a research project led by ZHAW and ETH and with the participation of industrial partners in Switzerland. This paper specifically described the behaviour of "Stahlkammer" columns, consisting of two steel C-profiles connected to an inner plate and partially filled with Cleancrete, with a special emphasis on the fire performance. Given the lack of knowledge of the thermal and mechanical behaviour of this new material, several material-level tests were carried out. From the material test results, it was found that Cleancrete shares similar thermal properties (heat capacity and thermal conductivity) with concrete-based materials. However, its modest strength and stiffness are seemingly less sensitive to the temperature increase, as for clay bricks. Based on the full characterization of the material, a non-linear finite element (FE) model of Stahlkammer column was developed, and heat transfer analyses and non-linear static analyses were conducted. The suitability of the models subjected to axial compression and elevated temperature was successfully validated against analytical models available in the European Standards for construction. The fire resistance of two different types of "Stahlkammer" columns was investigated by means of thermomechanical simulations in accordance with the fire design curve of the standard ISO 834-1. The results show that Cleancrete contributes indirectly to the enhancement of fire resistance by cooling down the temperature of the steel elements while the actual strength contribution is marginal. Considering a standard ground floor column, the fire resistance class R30 (i.e. at least 30 minutes in fire without failure) can be achieved providing that the vertical load does not exceed 160 kN. The addition of two embedded C-profiles UNP140 significantly increases the fire resistance class up to R60 with a design vertical load of 330 kN.

Keywords: Structural fire safety, Material test, Finite element modelling, Composite columns.

[a]*ETH Zürich (vigneri@ibk.baug.ethz.ch)**,** Corresponding author**.**

[b] ETH Zürich (lu@ibk.baug.ethz.ch).

[c] ETH Zürich (ian.chamberlain1996@gmail.com)**.**

[d] ETH Zürich (taras@ibk.baug.ethz.ch).

1. INTRODUCTION AND MOTIVATION

Avoiding unsustainable, man-caused climate change requires a rethink of most current practices in construction. Cement production alone accounts for nearly 8% of global CO_2 emissions [1]. The usage of new and sustainable building materials to replace conventional concrete can drastically reduce emissions and combat the increasing speed of climate change, which is threatening our world. One of these new building materials is called Cleancrete[©], produced by the ETH spin-off company Oxara. This novel eco-friendly material is meant to replace the role of conventional concrete for low-demand structures. Cleancrete is a cement-free concrete and has therefore a much smaller carbon footprint compared to conventional concrete, with an up to 90% reduction in greenhouse gas emissions [2]. Employing such a new material requires testing to ensure it behaves as intended in all conditions it could encounter. However, Cleancrete has never been tested with regard to its fire performance. Conventional concrete and composite structures behave well in the fire scenario. Concrete has a low thermal conductivity, high heat capacity and a lot of mass, which protects rebar and steel beams embedded in it from rapid heating. If Cleancrete behaves similarly to concrete, it would make an excellent insulation material.

Cleancrete needs to be tested with regard to its mechanical and thermal properties at elevated temperatures to see if this hypothesis holds true. The obtained mechanical properties need to be compared to other materials, mainly conventional and lightweight concrete, to determine if identical design approaches and codes are applicable when designing structures using Cleancrete.

As mentioned, Cleancrete is used in low-demand situations as it has a low compressive strength. To increase the usage, this new material is used in conjunction with steel to create the "Stahlkammer" system, as shown in Figure 1. A standard Stahlkammer column consists of two C-shaped cold-formed profiles made of recycled steel with a rectangular steel plate sandwiched in between them. The chambers are filled separately with Cleancrete and assembled together with the inner plate resulting in a partially embedded composite cross-section.

a)   b)

Figure 1: Production of "Stahlkammer" specimen and concept of a "Stahlkammer" column

In view of the lack of knowledge on the thermomechanical behaviour of this novel cement-free material, experimental tests were first conducted and presented in the following section. This enables a full characterization of Cleancrete in terms of both thermal and mechanical properties.

The experimental work is presented in Section 2 and the test results serve as inputs for the development of a reliable finite element model which is thoroughly described in Section 3. The aim of the numerical investigations is to evaluate the fire resistance performance of this newly conceived column by performing thermomechanical (fire) simulations and to check whether the system complies with the given fire safety requirements. However, the actual performance of the product will be assessed experimentally in the next months at room temperature as well as in fire by performing full-scale tests.

The workflow of the core activities presented in this paper is finally summarized in the flow chart below.
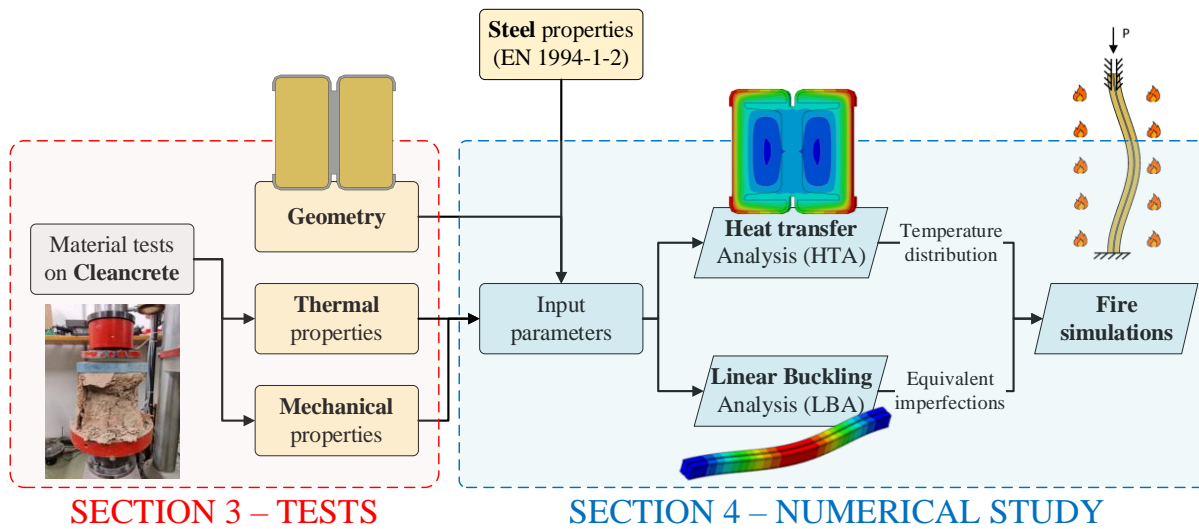
Figure 2: Outline of the presented study

2. MATERIAL TESTS ON CLEANCRETE

2.1. GENERAL

The material tests on Cleancrete were conducted to find mechanical, thermal and thermo-mechanical properties. The mechanical and thermo-mechanical properties consist of the compressive strength at room temperature, the residual compressive strength after exposure to elevated temperatures and the density. The thermal properties required are thermal conductivity and heat capacity.

Figure 3 shows the utilized workflow, which consisted of curing and drying the specimens before heating them to different temperature levels. After cooling down, the different properties were tested. The words "cup", "cuboid" and "cube" refer to different types of specimens, as different types of forms were needed for different experiments.
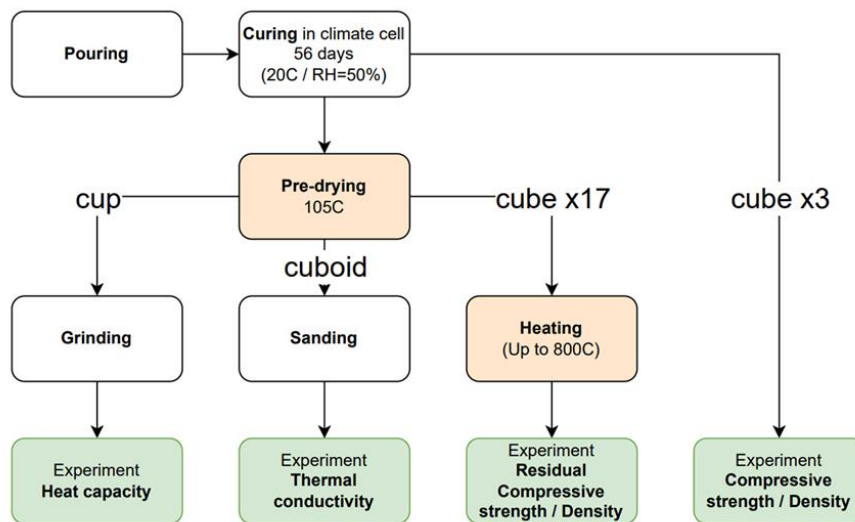
Figure 3: Workflow of the experimental study

2.2. PREPARATION OF THE SPECIMENS

The mixture was provided by Oxara, the company which produces Cleancrete. Cleancrete contains sludge, aggregates, fibres, water and an admixture called Oxacrete. Sludge acts as the cement in conventional concrete, binding the aggregates together. The fibres are flax, a natural fibre harvested from the identically called crop [3]. These are added to the mixture to increase the strength of Cleancrete, similar to steel-fibre reinforced concrete.

The admixture "Oxacrete" is a white powder produced by Oxara and acts as a superplasticizer, increasing the workability. The ingredients were added to the drum and mixed until a homogenous mass was obtained. The mixture was filled into the formwork to create various types of specimens, required to test the different properties. The specimens were placed in a climate chamber (20°C, 50% RH). The formwork was removed after 5 days and left to cure for an additional 51 days, resulting in 56 days of curing as specified by Oxara. Figure 4 shows the final mixture before filling of formwork and the specimens curing in the climate chamber.

a)   b)

Figure 4: Mixing and curing of Cleancrete specimens in the climate chamber.

After curing, the specimens were placed in an oven at 105°C for 3 days to remove any free moisture which could have negative effects on experiments, such as an increased thermal conductivity. Cleancrete was ground to a fine powder with a grain size similar to flour to test the heat capacity using the differential scanning calorimetry method. The produced cubes were heated up to 800°C, kept at the maximal temperature for 90 minutes to obtain steady state temperature conditions throughout the entire specimen and left to cool down at room temperature to test the density and compressive strength after heat exposure. 3 cubes were not heated to test the strength at room temperature. One specimen was placed inside a plastic bag to avoid moisture intake during the testing of the thermal conductivity.

2.3. THERMAL PROPERTIES

The ground Cleancrete was placed in the differential scanning calorimetry testing device and heated to the maximal possible temperature of 540°C while measuring the heat flow into the sample to determine the temperature-dependent heat capacity. 4 runs with different samples were conducted to check the variability of the results. 3 of the 4 runs showed similar results, while one showed drastically lower values. This run was neglected and the other 3 runs were averaged to obtain the results shown in Figure 5. The initial heat capacity at room temperature was approximately 800 J/kg*K and increased to 1'200 J/kg*K at 500°C. In addition to the obtained results, Figure 5 also shows values for different materials, namely (lightweight) concrete and clay units. This data was taken from the respective European norms for construction as a comparison, i.e. EN 1992-1-2 [4] for concrete and EN 1996-1-2 [5].
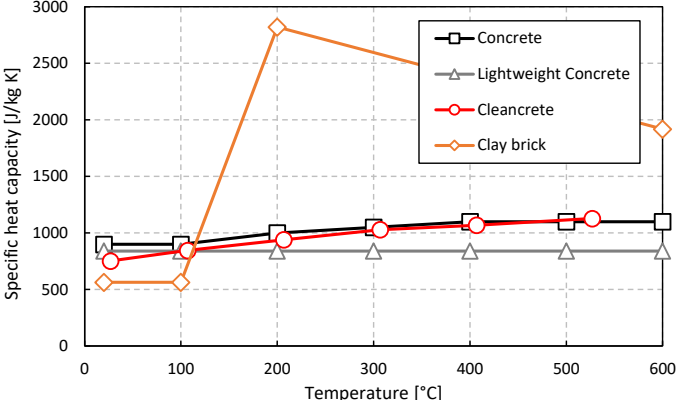

Figure 5: Heat capacity for different materials

Cleancrete behaves similarly to conventional concrete regarding the change in heat capacity. At higher temperatures, larger than 400°C, Cleancrete is an even better insulation material than concrete with values up to 1236 J/kg*K. While the initial value of lightweight concrete and Cleancrete matches very well, lightweight concrete does not show an increase in heat capacity at elevated temperatures according to Eurocode 2 [4]. The heat capacity of clay units is generally lower, between 500 and 700 J/kg*K, at room temperature [6, 7]. The behaviour at elevated temperatures is also different. Considering these values, Cleancrete can be classified as conventional concrete with regard to heat capacity.

The thermal conductivity was tested with a guarded hot plate device. The test runs failed to complete. The probable cause was most likely too high thermal conductivity of Cleancrete, as a device to test thermal insulation was used. The value of the thermal conductivity at room temperature is known as it was tested for a similar mixture in an earlier experiment. This value was taken and compared to values for concrete and clay bricks to determine which material is most similar to Cleancrete.

The known value of the thermal conductivity at room temperature is 1.2 W/m*K, which puts it in between lightweight and conventional concrete [4]. Clay bricks (fired and unfired ones) have a lower thermal conductivity, between 0.2 and 0.9 W/m*K, depending on the humidity content [8, 9, 10]. All these values are shown in Figure 6. Considering these values, Cleancrete can again be classified as (lightweight) concrete.

Finally, the thermal expansion coefficient was not measured but it was preliminarily assumed to be temperature-independent and equal to $8 \cdot 10^{-6}$/K as recommended for lightweight concrete in EN 1994-1-2 [11].
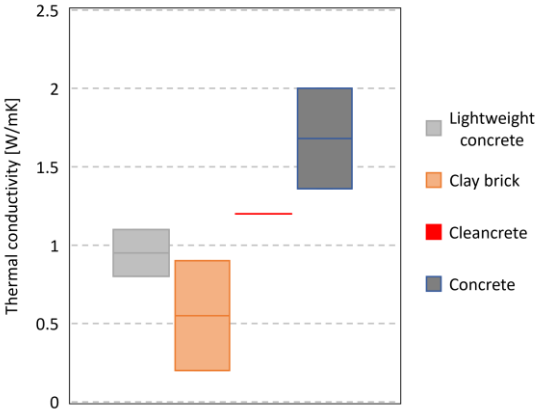

Figure 6: Comparison of thermal conductivities at room temperature for different materials

2.4. MECHANICAL PROPERTIES

The density of Cleancrete was tested with the cubes after heating in the oven and before compression strength testing. The initial density of 2502 kg/m^3 at room temperature was reduced to 1934 kg/m^3 after a heat exposure of 800°C, as shown in Figure 7.
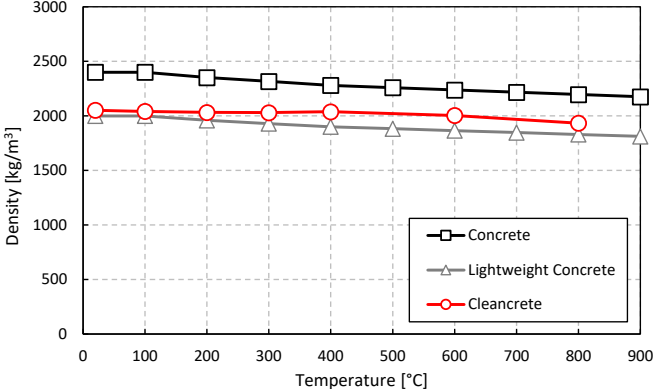

Figure 7: Density change of Cleancrete

These values lie between conventional concrete and lightweight concrete according to EN 1992-1-1 [4]. The density change of lightweight concrete was modelled identically to conventional concrete, with just a lower value at room

temperature. The density values for fired and unfired clay bricks are generally lower, at and below 1850 kg/m³ for various temperatures, as found by various studies [12, 13, 14, 15, 16]. Cleancrete can therefore be classified as lightweight concrete with regard to density values.The Cleancrete cubes were placed in the compression test device to test the residual compressive strength after heat exposure and cooling down. 3 cubes were tested for each temperature level, except for 100°C, for which only 2 cubes were tested. The compressive strengths of the unheated cubes were between 2 and 3 MPa, only a quarter of the strength of the lowest strength commercially available lightweight concrete, LC8/9. The compressive strength increased with heat exposure up to 3 to 4 MPa. The results from the residual compressive strength test are shown in Figure 8.
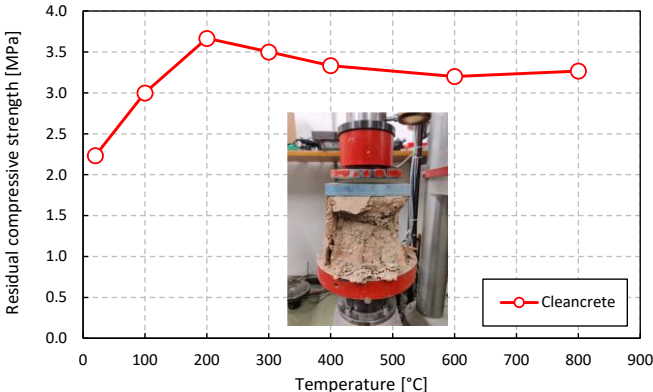
Figure 8: Residual compressive strength of Cleancrete

The normalized residual compressive strength was plotted against conventional concrete as well as clay bricks in Figure 9. Cleancrete behaves differently to conventional concrete, as the strength increased after heat exposure rather than decreased. In that sense, it acted more like clay bricks. A study conducted on fired clay bricks found, while not as drastic, a similar increase in residual compressive strength after heat exposure [17]. The thermo-mechanical behaviour is very much different than initially expected, as a decrease in strength was prognosed, similar to conventional concrete. Like how the burning of clay bricks increases the strength of the bricks, Cleancrete also showed an increase in strength with an increase in temperature.
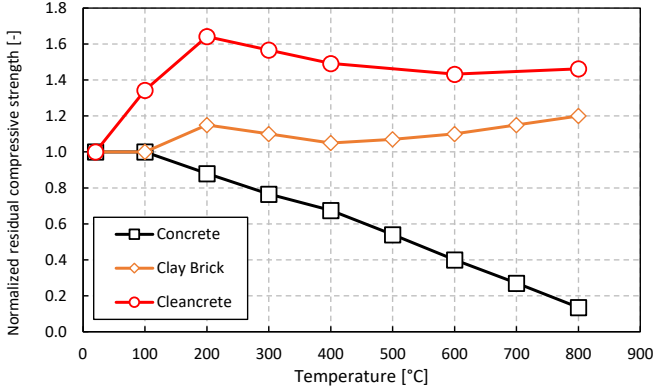
Figure 9: Normalized residual compressive strength for different materials

The residual compressive strength after heating represents an easy experimental approach to estimate the compressive strength at predefined temperature. However, it does not accurately depict the actual strength occurring during the fire scenario which would require more sophisticated instrumentation. This is also shown in EN 1994-1-2 annex C [4] for concrete where the compressive strength in fire is actually 1.11 times higher than after heating and cooling down considering the same reference temperature.

However, as can be seen in in Figure 9, the behaviour of Cleancrete after heating is closer to fired clay bricks with regards to its compressive strength at elevated temperatures. Unlike in standard and lightweight concrete, the strength of clay bricks in fire is smaller than the residual compressive strength of clay bricks by a factor of ca. 0.8 [17]. Finally, the mean value of the Young's modulus at room temperature (in MPa) was provided by the company Oxara where a mean value (in MPa) of approximately $800 f_c$ was found, with f_c in MPa. This yields to 1512 MPa which was finally taken in the current work. The relative reduction of the elastic modulus at different temperatures

has been finally extrapolated from the initial slope of the load-deformation curves of the compressive tests and the results are plotted in Figure 10.
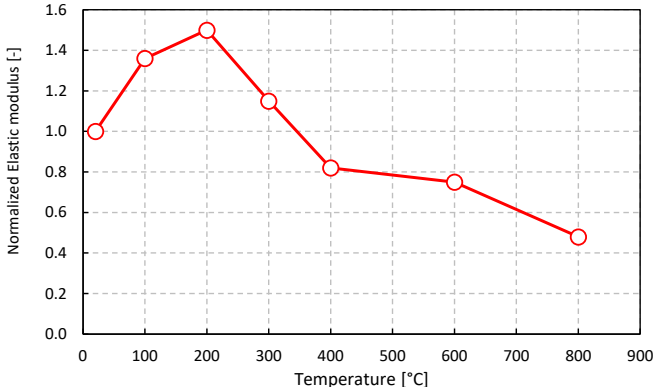

Figure 10: Normalized Elastic modulus for different materials

3. NUMERICAL MODELLING OF COLUMNS

3.1. OVERVIEW

The experimental characterization of the Cleancrete carried out in the previous section is used as input data for the development of a reliable finite element (FE) model, as can be seen in Figure 2. Although full-scale experimental tests of the structural members are necessary to assess the actual performance of the composite "Stahlkammer" system, a validated FE model can be helpful in supporting the design of the members in view of the static and fire safety requirements. The numerical study presented in this section focuses on two types of Stahlkammer columns which are currently under consideration: the "standard" and "modified" Stahlkammer columns shown in Figure 11 a) and b), respectively. All the configurations considered in this study refer to a length of 2.9 m. As most of the steel surface of the cross-sections is directly exposed, a special emphasis is laid on the fire performance of the columns.
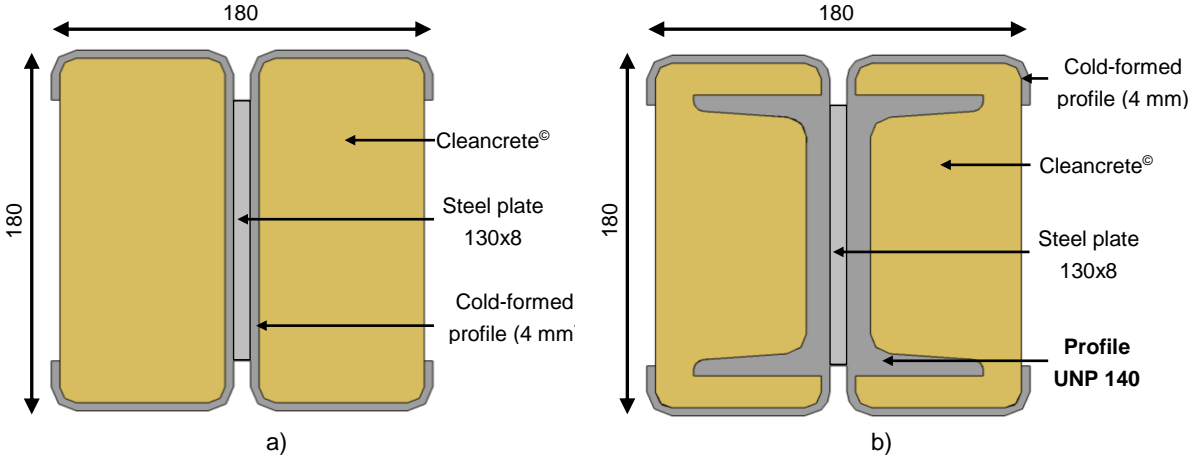

Figure 11: a) "Standard" and "modified" Stahlkammer cross-sections with dimensions (in mm).

The non-linear 3D finite element (FE) model is developed by using the software ABAQUS and all the relevant features are thoroughly described in the next sections. This includes all the input parameters used for modelling the materials for the thermal and mechanical simulations, i.e. heat transfer and static analysis, respectively.

The suitability of the presented FE model is checked by comparing the numerically-computed values of the resistance at room and at elevated temperatures with the current European Norms for construction.

Finally, thermomechanical simulations are carried out for simulating the design fire scenario according to the standards ISO 834-1 [18] and the results are discussed at the end of this section.

384

3.2. MESH MODELLING, CONTACT AND BOUNDARY CONDITIONS

Volumetric mesh elements C3D8R and DC3D8 mesh elements are used, for heat transfer analyses and companion mechanical simulations, respectively. An average mesh edge size of 10 mm was used with a finer mesh in proximity of the edges and geometrical discontinuities as can be seen in the Figure 12a) and b) for "standard" and "modified" Stahlkammer column, respectively.
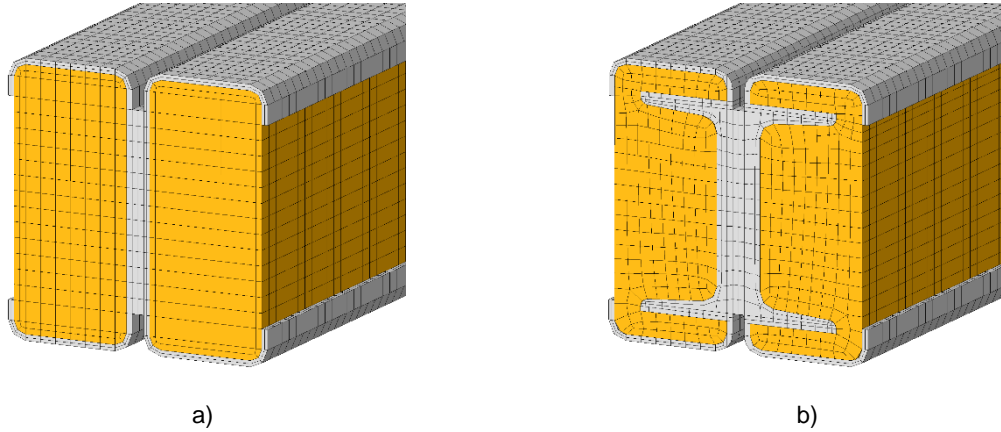

a)   b)

Figure 12: 3D mesh of the a) "Standard" and "modified" Stahlkammer.

For the sake of simplicity, the steel element, inner plate and C-profiled were separately generated and finally merged together as a single element. The constraint *TIE was applied to all the contact surfaces between steel parts and Cleancrete. This enables the full heat transfer in thermal analysis and it prevents any relative motion in the mechanical simulations (LBA and GMNIA). However, in the latter cases, only the inner plate was fixed to the Cleancrete where a series of bolted connectors is expected.

To reproduce the boundary conditions at the extremities of the columns, the end surfaces were coupled with a reference node and the kinematic and static conditions were applied accordingly. Based on the static system of the foreseen building, three typical boundary conditions were analysed in this study: fixed-fixed, fixed-pin and pin-pin resulting in a buckling length of 0.5L, 0.7L and 1.0L, where L indicates the real length of the column.

3.3. MATERIALS

The properties of Cleancrete measured in the material tests (specific heat capacity, thermal conductivity and density) and reported in Section 2.3 are implemented in the numerical modelling of the material, accordingly.

Given that no experimental full-scale test is currently available for validating the presented FE model and the scatter of the mechanical properties of Cleancrete is unknown, characteristic values of the strength were estimated based on the experimental measurements. This was done by taking the mean value of $f_{cm,\vartheta}$ which was further reduced by 10%. Whilst it could be argued that this approach might not be safe-sided, no information on the statistical variability is known and further tests are necessary to have a more reliable estimation of the characteristic values. Additionally, the mean value of the elastic modulus $E_{cm,\vartheta}$ was adopted based on the measurements provided in Figure 10. All these values are finally summarized below in Table 1.

Table 1: Measured residual compressive strength, mean and characteristic value of the strength, and elastic modulus at different temperatures for Cleancrete.

Temperature (°C)	20	100	200	300	400	600	800
$f_{cm,res}$ (MPa)	2.1	3	3.5	3.4	3.3	3	3.1
$f_{cm,\vartheta}$ =0.8 $f_{cm,res}$ (MPa)	2.1	3	2.8	2.7	2.6	2.4	2.5
$f_{ck,\vartheta}$ =0.9 $f_{cm,\vartheta}$ (MPa)	1.9	2.7	2.5	2.5	2.4	2.2	2.2
$E_{cm,\vartheta}$ (MPa)[*]	1512	2062	2268	1745	1237	1134	732

The stress-strain relationship of Cleancrete was introduced as the parabolic-rectangular stress-strain relationship for lightweight concrete, as given in [19, 4]. However, the relationship was adapted by adding an additional coefficient β to match the initial stiffness $E_{cm,\vartheta}$ in Table 1, and it is given by the following expression:

$$\sigma = \frac{3 f_{c,\theta} \left(\frac{\varepsilon}{\varepsilon_{c1,\theta}}\right)^{\beta}}{\varepsilon_{c1,\theta} \left(2 + \left(\frac{\varepsilon}{\varepsilon_{c1,\theta}}\right)^{1.8}\right)} \tag{1}$$

where the strain values $\varepsilon_{c1,\vartheta}$ and $\varepsilon_{cu1,\vartheta}$ are provided by EN 1992-1-2 [4] in tabular form.

Notwithstanding the lack of information about the failure criterion and yield surface of Cleancrete subjected to triaxial stress-strain fields, the Concrete Damaged Plasticity (CDP) model was assumed to be appropriate for modelling Cleancrete applications. Although future experimental investigations entailing more complex loading conditions may address these issues, it is thought that the failure criterion does not affect significantly the global response of the structural member in the application considered in this study.

For the characterization of the model in the software ABAQUS, the plasticity parameters given in Table 2 were adopted whereas the material damage was neglected.

Table 2: Assumed plasticity parameters of the "Concrete Damaged Plasticity" (CDP) model for Cleancrete.

Dilation angle (deg)	Biaxial-to-uniaxial Strength (MPa)	Eccentricity parameter (-)	Ratio of second stress invariants on tensile and compressive meridian (-)	Viscoplastic Parameter (-)
30	1.16	0.1	0.67	0.0001

The mechanical and thermal properties of carbon steel were simply chosen in accordance with the European Standards for steel structures (Eurocode 3), i.e. EN 1993-1-1 [20] and EN 1993-1-2 [21]. For the sake of consistency, nominal values of the S355 steel were employed in the model, i.e. the yielding strength was fixed to 355 MPa and no hardening was considered.

3.4. HEAT TRANSFER ANALYSES

The step type "Heat transfer" is selected to compute the temperature distribution over the column in fire. Tie constraints are considered between the materials enabling the full heat transfer at the contact interfaces.

The whole external surface was assumed to be directly exposed to fire via convection and radiation. The former is reproduced by means of the feature *SURFACE FILM CONDITION using a convection coefficient of 25 W/m^{2}K as suggested in EN 1991-1-2 [22]. Similarly, the heat transfer via radiation was implemented through the feature *SURFACE RADIATION with an emissivity coefficient ε=0.7 for both steel and Cleancrete surfaces, as recommended in EN 1994-1-2 [11].

Since no specific details about the fire scenario are currently available, the safe-sided ISO 834-1 [18] fire design curve in Figure 13 was considered to define the increase of the gas temperature in fire.
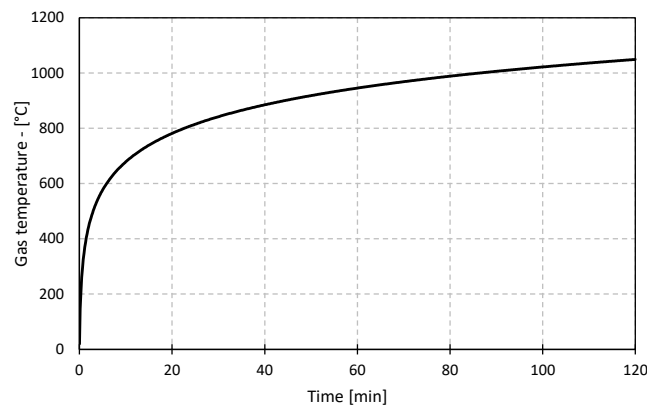

Figure 13: Fire design curve according to the standards ISO 834-1 [18]

3.5. STATIC ANALYSES AND COMPARISON WITH ANALYTICAL PREDICTIONS

The lack of full-scale experimental tests of the presented composite column precludes an appropriate validation of the numerical model. However, a comparison with analytical predictions at ambient and at given temperature

contours could be helpful for a preliminary evaluation of the suitability of the model. For the sake of simplicity, only the "standard" Stahlkammer column is taken into consideration in this section.

The static analyses carried out at this stage are geometrical and material non-linear analysis with imperfections (GMNIA) at ambient as well as at elevated temperatures.

First, a linear Buckling Analysis (LBA) was performed to extract the first buckling shape. This was used to extract the equivalent imperfections according to EN 1993-1-14 [23] which provides guidelines for FE-assisted design methods. The recommended maximum amplitude of the equivalent imperfections e_0 (i.e. accounting for geometrical and mechanical imperfection from residual stresses) is given by:

$$e_0 = \frac{\alpha L}{150} = 9.47 \ mm \qquad (2)$$

where an imperfection factor α=0.49 corresponds to the buckling curve "c", as recommended in EN 1994-1-1 [24] for partially encased composite columns.

The respective buckling shape was finally imported into the perfect geometry of the column amplified by the value e_0. After that, a reference temperature contour was assigned to the whole model before being vertically loaded. In this study, the temperature distribution refers to the ISO 834 fire design curve after 60 minutes. For the static analyses at ambient temperature, a constant value of 20°C was applied to the entire column.

Furthermore, three different boundary conditions (i.e. fixed-fixed, fixed-pin, and pin-pin) were considered for each 2.9 m long Stahlkammer columns leading to a total of 6 GMNIAs.

The numerically-computed resistance values of the columns were finally compared with the respective analytical predictions in accordance with the European Standards for composite structures in fire [11].

However, the analytical expressions for determining the buckling resistance requires the values of the temperature occurring in the different components. To overcome this issue, the temperature values of the single parts were directly extrapolated from the heat transfer analyses by means of the plug-in* VOLUME WEIGHTED AVERAGE TEMPERATURE available in the ABAQUS library. Owing to the high temperature gradient over the steel elements, flanges, web and inner plate were considered separately. Similar considerations applied to Cleancrete which was discretized in three elements.

Based on the degradation of the given temperature-dependent mechanical properties of the materials, all the key cross-sectional properties, such as the flexural stiffness EI_{eff} and the plastic resistance $N_{fi,pl,R}$ were derived. After that, the resulting normalized slenderness was calculated as follows:

$$\bar{\lambda}_\theta = \sqrt{\frac{N_{fi,pl,R}}{N_{fi,cr}}} \qquad (3)$$

where $N_{fi,cr}$ is the critical buckling load as a function of the effective flexural stiffness in fire $EI_{fi,eff}$.

Finally, the corresponding reduction factor accounting for the influence of the buckling is extracted from the buckling curve "c" shown in EN 1993-1-1 and the resulting design resistance in fire of the composite column subjected to axial compression is given by:

$$N_{fi,Rd} = \chi \cdot N_{fi,pl,Rd} \qquad (4)$$

Given the modest strength and stiffness of the Cleancrete, a second approach was undertaken in accordance with EN 1993-1-2, where only the steel section is considered for calculating the analytical value of the resistance. The companion numerically-derived values of the resistance remain unchanged. However, for the sake of consistency, the same temperature contour was imported in the model. Apart from the different cross-sectional properties, the reduction factor χ for determining the fire resistance in EN 1993-1-2 differs slightly from the one given in EN 1994-1-2 for composite columns.

Similarly, the resistance of the columns at room temperature was simply calculated according to EN 1994-1-1 (as composite column) and EN 1993-1-1 (as steel column).

As can be seen from results shown in Figure 14, both analytical approaches lead to similar outcomes as contribution of the Cleancrete in terms of buckling resistance is negligible.

The maximum deviation between analytical and numerical (GMNIA) values of the resistance does not exceed 8% at ambient temperature, see Figure 14a). A minor increase up to 12% can be observed in Figure 14b) for columns

subjected to elevated temperature. This discrepancy is mainly due to the simplified nature of the analytical equations while a finer discretization of the temperature may slightly increase the accuracy of the results. Also, the EN 1994-1-1 design procedure is calibrated on composite columns using normal strength concrete rather than low strength materials. Based on these considerations, it can be concluded that the presented numerical model is suitable for reproducing the non-linear static behaviour of the whole composite member at both ambient and at elevated temperatures.
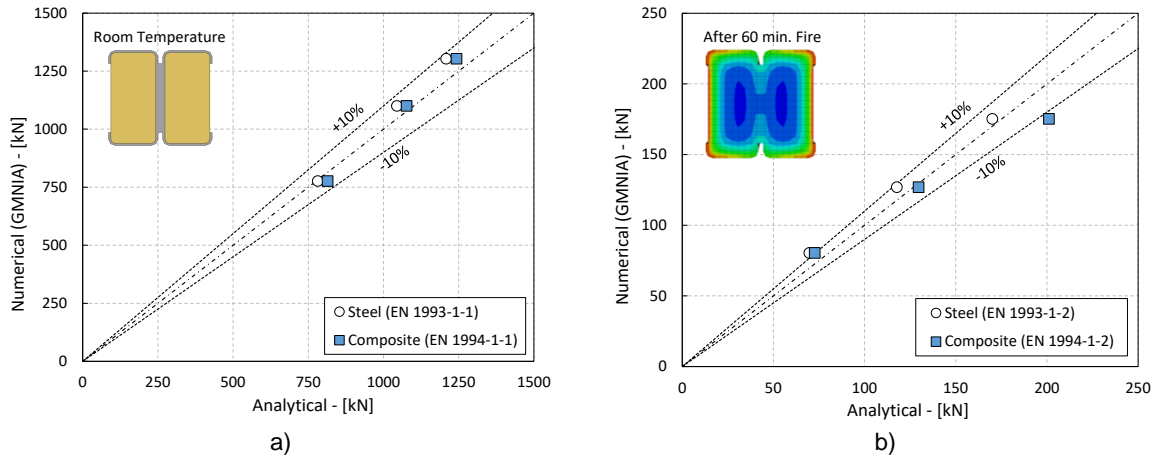
Figure 14: Buckling resistance values for Stahlkammer columns according to current norms and numerically-obtained value from GMNIA: a) at room temperature and b) after 60 minutes of fire.

It is worth noticing that Cleancrete enhances indirectly the buckling strength by thermally isolating and cooling down the steel elements, leading to lower temperature values in the steel elements, in particular within the inner steel plate. However, the actual fire resistance of the column can be quantified only by means of thermomechanical simulations which are presented in the following section.

3.6. FIRE SIMULATIONS AND DISCUSSION

In the frame of the ongoing STAHLKAMMER project, the expected scope of application of the structural members is a multi-storey residential building. Depending on the height and the number of storeys, different fire requirements are to be fulfilled. Considering a floor-to-floor height of ca. 3 m, a fire resistance class R30 may be sufficient for building up to 3 storeys while R60 class needs to be fulfilled for taller buildings.

Based on the predesign of the actions acting on the whole system, a vertical load of approximately 100 kN is estimated for each storey. However, given the uncertainties of this value, the fire simulations presented in this study aims to quantify the performance of this newly conceived product in order to support the further development of the "standard" and "modified" STAHLKAMMER columns.

As done in the GMNIA detailed in the previous section, the LBA-based imperfections are imported into the FE model accordingly. After that, a two steps solver procedure is defined in the software. The first step is dedicated to the application of the predefined vertical load keeping the temperature of the whole element at 20°C. In the second step, unlike in the static analyses, the temperature contour obtained from the companion heat transfer analysis is extrapolated over the entire duration of the fire. Therefore, the fire resistance of the column corresponds to the amount of time necessary to reach the failure conditions defined by given criteria. In this case, it is assumed that the structural integrity of the column in fire is limited by a maximum displacement and displacement rate, as recommended by EN 1363-1 [25]. These upper bounds are given by:

$$|u|_{max} = \frac{h}{100} = 29 \; mm \tag{5}$$

$$\left|\frac{du}{dt}\right|_{max} = \frac{3h}{100} = 8.7 \; mm/min \tag{6}$$

Where u is the vertical displacement in mm and h is the height of the column in mm. Positive values of u indicate the elongation of the column (as a result of the thermal expansion).

An example of vertical displacement and the displacement rate during fire is displayed in Figure 15a) and Figure 15b), respectively. Interestingly, it was found that the latter criterion was decisive in all the configurations analysed.
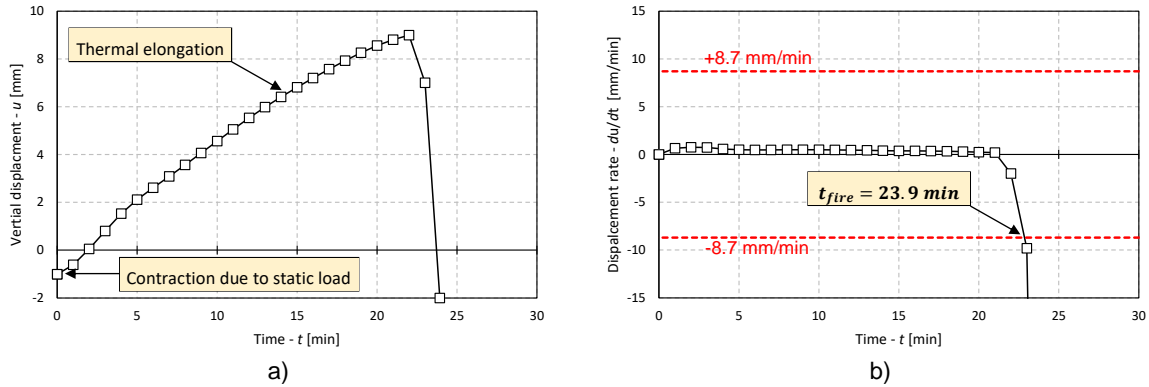

Figure 15: Example of a) vertical deformation and b) deformation rate under fire conditions.

The fire resistance values obtained from this parametric study are finally plotted in Figure 16 for fixed-fixed and fixed-pin configurations, separately. Whilst the fixed-fixed conditions (Figure 16a)) could be suitable for continuous inter-storey columns where the end rotation in fire is limited by the bending stiffness of the floor, the ground floor columns are simply hinged at the base. Thus, the fixed-pin boundary conditions are more representative of their actual behaviour in the building at elevated temperature.

Based on the results in Figure 16b), the proposed cross-section geometries are able to fulfil the R30 and R60 for standard and modified Stahlkammer geometries with a load of ca. 160 kN and 330 kN, respectively.

In view of the foreseen applications in multi-storey residential buildings, further enhancements may be needed to increase the fire resistance while further investigations are currently ongoing for a more accurate estimation of the design load.
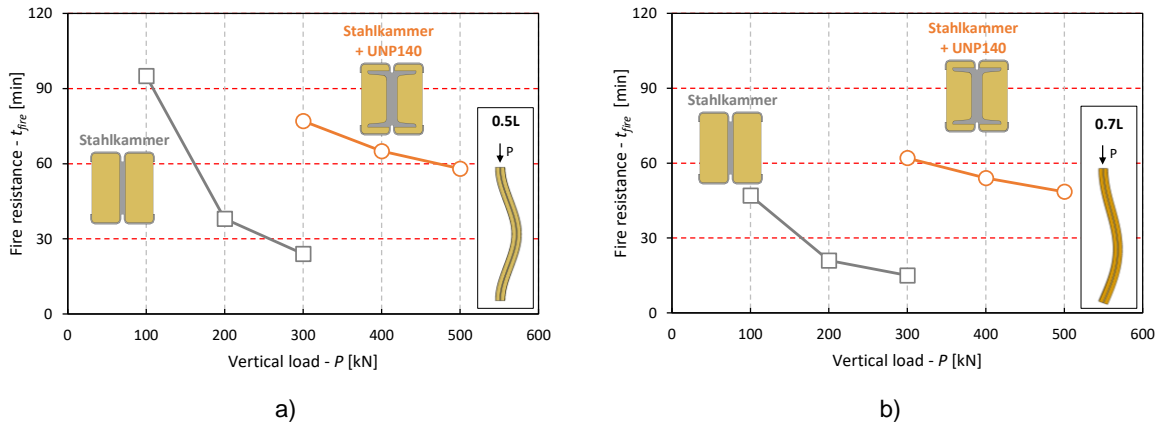

Figure 16: Numerically-computed values of the fire resistance t_{fire} as a function of the vertical load with a) fixed-fixed (0.5L) and b) fixed-pin (0.7L) boundary conditions.

4. SUMMARY AND OUTLOOK

The presented work focused on the fire performance of an innovative type of composite columns which combine cold-formed steel profiles with a new cement-free concrete named Cleancrete. An experimental campaign for characterizing this new material was carried out and the results were presented and discussed in this paper.

Based on the results of the material tests, a numerical model was developed and a parametric study was conducted to evaluate the fire performance of the system. The main conclusions can be summarized as follows:

- Cleancrete possess thermal properties (heat capacity and thermal conductivity) comparable with standard and lightweight concrete. Notwithstanding the modest compressive strength of ca. 3 MPa, the mechanical properties (strength and elastic stiffness) are seemingly less sensitive to the temperature increase, as is also known e.g. for clay bricks.
- Based on the thermomechanical characterization of the material, a non-linear numerical model of a "Stahlkammer" column was developed. This was used to perform heat transfer analyses (HTA) as well as geometrically and materially non-linear analyses with imperfections (GMNIA) at ambient and elevated temperatures.
- The suitability of the GMNIAs was ensured by comparing the numerically-obtained values of the resistance with the analytical predictions according to the current European Standards for 6 different configurations. A good agreement between the numerical and analytical results was achieved with a maximum deviation of 12%.
- The fire performance of Stahlkammer columns was finally investigated via thermomechanical simulations in accordance with the fire design curve of the standards ISO 834-1 [18]. The results show that the Cleancrete contributes indirectly to the enhancement of the fire resistance by reducing the temperature of the steel elements. The fire resistance class R30 (i.e. at least 30 minutes resistance) could be achieved by the column under a vertical load of ca. 160 kN. The addition of two embedded UNP140 steel profiles significantly increases the fire resistance class up to R60 while withstanding a design vertical load of 330 kN.

Despite the promising results, further enhancements are to be made in the near future in order to fulfil the given fire requirements while withstanding higher loads. Increasing the cross-sectional area of steel and adjusting the geometry of the cross-section could be a valid solution. Nevertheless, the local application of fire protection strips at the extremities of the inner plate is currently under consideration.

Another issue which has not been tackled in this study lies in the shrinkage arising in the Cleancrete which was observed in the fabrication of the specimens. This could worsen the thermal isolation of the steel elements as the heat may penetrate within the gap between the interfaces. Because of the uncertainties on the structural performance of this material at elevated temperature, full-scale tests are of key importance to ensure the reliability of the numerical predictions. Several beam tests at room temperature are currently ongoing but column tests at elevated temperature are foreseen in the next months.

REFERENCES

[1] IEA/WBCSD, "Energy Efficiency and CO2 Emission Reduction Potentials and Policies in the Cement Industry," in *Towards a Plan of Action, Workshop Proceedings,*, Paris, 2006.

[2] Oxara, "Sustainable Construction and Affordable Housing," 2023. [Online]. Available: https://oxara.earth/.

[3] C. Navin and F. Mohammed, Tribology of Natural Fiber Polymer Composites, Sawston: Woodhead Publishing, 2008, p. 10.

[4] British Standards Institution, EN 1992-1-2:2004 Eurocode 2 - Design of concrete structures Part 1-2: General rules - Stuctural fire design.

[5] British Standards Institution, EN 1996-1-2:2005 Eurocode 6 - Design of masonry structures Part 1-2: General rules - Stuctural fire design, 2005.

[6] F. El Fgaier, Z. Lafhaj, E. Antczak and C. Chapiseau, "Dynamic thermal performance of three types of unfired earth bricks," *Applied Thermal Engineering,* vol. 93, pp. 377-383, 2016.

[7] M. Charai, H. Sghiouri, A. Mezrhab, M. Karkri and K. El Hammouti, "Comparative study of a clay before and after fired brick-making process," *Materials Today: Proceedings,* vol. 31, pp. 103-108, 2020.

[8] J. E. Oti, J. M. Kinuthia and J. Bai, "Design thermal values for unfired clay bricks," *Materials & Design,* vol. 31, no. 1, pp. 104-112, 2010.

[9] M. Dondi, F. Mazzanti, P. Principi, M. Raimondo and G. Zanarini, "Thermal conductivity of clay bricks," *Journal of materials in civil engineering,* vol. 16, no. 1, pp. 8-14, 2004.

[10] F. El Fgaier, Z. Lafhaj, F. Brachelet, E. Antczak and C. Chapiseau, "Thermal performance of unfired clay bricks used in construction in the north of France: Case study," *Case studies in construction materials,* vol. 3, pp. 102-111, (2015)..

[11] British Standards Institution, EN 1994-1-2:2005 Eurocode 4 - Design of composite steel and concrete structures Part 1-2: General rules - Structural fire design, 2005.

[12] J. E. K. J. M. Oti and J. Bai, "Compressive strength and microstructural analysis of unfired clay masonry bricks," *Engineering Geology,* vol. 109, no. 3-4, pp. 230-240, 2009.

[13] A. Kumar, R. Kumar, V. Das, A. A. Jhatial and T. H. Ali, "Assessing the structural efficiency and durability of burnt clay bricks incorporating fly ash and silica fume as additives," *Construction and Building Materials,* vol. 310, p. 125233, 2021.

[14] K. Rashid, E. U. Haq, M. S. Kamran, N. Munir, A. Shahid and I. Hanif, "Experimental and finite element analysis on thermal conductivity of burnt clay bricks reinforced with fibers," *Construction and Building Materials,* vol. 221, pp. 190-199, 2019.

[15] N. B. Bohara, D. B. Ghale, Y. P. Chapagain, N. Duwal and J. Bhattarai, "Effect of firing temperature on physico-mechanical properties of contemporary clay brick productions in Lalitpur," *Bangladesh Journal of Scientific and Industrial Research,* vol. 55, no. 1, pp. 43-52, 2020.

[16] S. Karaman, S. Ersahin and H. Gunal, "Firing temperature and firing time influence on mechanical and physical properties of clay bricks," *Journal of Scientific and Industrial Research,* vol. 65, pp. 153-159, 2006.

[17] J. Bošnjak, S. Gambarelli, A. Sharma and A. Mešković, "Experimental and numerical studies on masonry after exposure to elevated temperatures," *Construction and Building Materials,* vol. 230, p. 116926, 2020.

[18] British Standards Intitution, ISO 834-1:1999/Amd 2:2021 - Fire-resistance tests - Elements of building construction. - Part 1: General requirements - Amendment 2., 2021.

[19] British Standards Institution, EN 1992-1-1:2004 Eurocode 2 - Design of concrete structures Part 1-1: General rules and rules for buildings, London, 2004.

[20] British Standards Institution, "EN 1993-1-1:2004 Eurocode 3 - Design of steel structures Part 1-1: General rules and rules for buildings," 2004.

[21] British Standards Institution, EN 1993-1-2:2005 Eurocode 3 - Design of steel structures Part 1-2: Structural fire design, 2005.

[22] British Standards Institution, EN 1991-1-2:2002 Eurocode 1 - Actions on structures Part 1-2: General actions - Actions on structures exposed to fire, 2002.

[23] CEN, prEN 1993-1-14:2021 Eurocode 3 - Design of steel structures Part 1-14: Design assisted by finite element analysis, 2021.

[24] British Standards Institution, EN 1994-1-1:2004 Eurocode 4 - Design of composite steel and concrete structures Part 1-1: General rules and rules for buildings, London, 2004.

[25] British Standards Institution, EN 1363-1: 2020 - Fire resistance tests. General requirements.

Thermomechanical behaviour of Steel-Timber Composite beams

Antoine Béreyziat[a,b],; Maxime Audebert[c,*]; Sébastien Durif[d]; Dhionis Dhima[e] and Abdelhamid Bouchaïr[f]

ABSTRACT

Full-size Steel Timber Composite (STC) beams, consisting of IPE steel profiles with timber beams embedded between their flanges are tested under four-point bending tests at room temperature and in standard fire conditions (ISO 834 heating curve). The length of the beams is 4.6 m with a load ratio in fire condition set at 43%. The first configuration (STC1) has its bottom flange exposed to fire, while the second (STC2) is fully encapsulated with wider lateral timber beams and a timber element protecting the bottom flange. In normal situation, STC1 and STC2 performed higher strengths than steel profile alone. STC1 and STC2 have a measured fire resistance reaching 29 and 81 min respectively. As a comparison, the estimated fire resistance of an unprotected steel profile is around 13 min. Some temperature measurements show that the deflection of timber and steel elements has an impact on the heat increase of the steel profile. A FEM numerical model is developed and validated on the basis of temperature and deflection measurements. It confirms that timber provides both fire protection and mechanical strengthening for steel in fire conditions.

Keywords: steel; timber; STC beams; fire tests; FEM model.

1. INTRODUCTION

Composite structures aim to get improved performances from complementarities that exists between various materials and components. In this study, it has been chosen to investigate complementarities between hot rolled steel profiles and glulam beams in bending. Previous studies have pointed out that a mutual strengthening can exist if steel and timber are combined in an appropriate way. First, loads are shared between steel and timber according to their respective stiffness when a device (fasteners, glue, contact, etc.) allows loads transfer [1]. Second, in most of existing applications, a steel profile is held laterally by timber members, which increases the buckling resistance [2]. Thus, it is possible to significantly reinforce timber beams using an inlaid steel profile [3] or to strengthen a H steel profile by inserting timber beams between its flanges [4]. Other studies showed that timber components can be used as fire protection for steel profiles. This protection can consist of a timber cladding [5] or a filling of the steel section with timber [6]. This fire protection is already used in Japan for several buildings [7].

[a] ENISE, 58 Rue Jean Parot, 42100 Saint-Étienne, France (antoine.bereyziat@enise.fr)

[b] ADEME, 20 Avenue du Grésillé, BP 90406, 49004 Angers Cedex 01, France

[c,*] ENISE, 58 Rue Jean Parot, 42100 Saint-Étienne, France (maxime.audebert@enise.fr)

[d] Université Clermont Auvergne, Clermont Auvergne INP, CNRS, Institut Pascal, F-63000 Clermont-Ferrand, France (sebastien.durif@uca.fr).

[e] CSTB, 84 Avenue Jean Jaurès, BP 02, 77447 Marne La Vallée Cedex 02, France (dhionis.dhima@cstb.fr).

[f] Université Clermont Auvergne, Clermont Auvergne INP, CNRS,, Institut Pascal, F-63000 Clermont-Ferrand, France (abdelhamid.bouchair@uca.fr).

The goal of this study is to evaluate the behaviour of Steel Timber Composite (STC) beams combining both mechanical and thermal complementarities of the two materials, as highlighted by previous studies. Thus, these hybrid beams could perform higher strength and better fire resistance than those made of a single material. The aim is to better understand the thermomechanical behaviour of such beams using fire tests and numerical simulations.

2. THERMOMECHANICAL TESTS

2.1 Tests description

Figure 1 presents the two configurations STC1 and STC2 that were tested under fire situation. Each configuration has been tested once. These beams consist in IPE 270 steel profiles associated with lateral pieces of glulam (GL24h) embedded between the flanges. The load is shared between timber and steel by contact, no structural shear connection (screws, bolt, etc.) is involved. Thin steel plates are fitted into assembly gaps, between the upper flange of the profile and the timber inner members, to ensure good contact. In the case of STC2 specimen, the timber elements between flanges are wider in order to increase the fire protection and to fix the wooden bottom cover, which is intended to protect the bottom flange of the steel profile from fire. Both configurations have the advantage of providing a mechanical reinforcement of the steel profile. Experimental tests led at room temperature showed an increase of strength, with an improvement of global section strength and also of lateral buckling strength. Indeed, configuration STC1 showed an increase of 38% and STC2 an increase of 68% in strength compared to a single steel profile. Moreover, timber parts protect the steel profile against fire. Configuration STC1 has steel partially exposed to fire, as the bottom flange is non-covered, whereas configuration STC2 offers a full protection against fire.
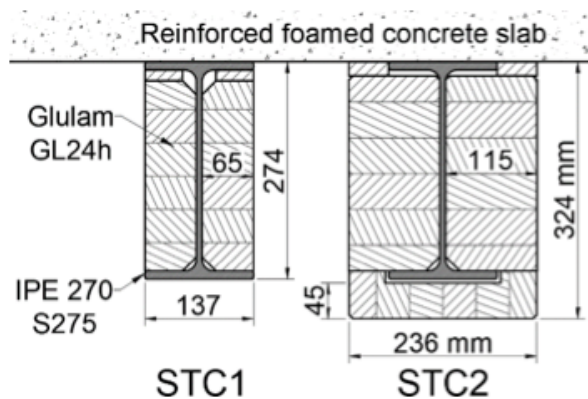

Figure 1: Tested configurations

For each test, a beam with a length of 4.6 m and a span of 4.4 m is exposed to a standard fire, considering the ISO 834 heating curve. The furnace temperature is controlled using 6 plate thermometers during both tests. These temperature measurements inside the furnace show that, after a slightly too high initial heating (between 2 and 3 minutes after the beginning of the test), the heating followed the ISO 834 reference curve with a good accuracy (Figure 4). Figure 2 presents the boundary and loading conditions of the beams, with a constant load in four-point bending test applied on the beams during the heating process. The applied load has been taken as 43% of the average ultimate load-carrying capacity of the beams measured during similar bending tests at room temperature. For each fire test, a 1.0 m long non-loaded beam, similar to the loaded one, is placed into the furnace to evaluate the impact of the loading on the efficiency of the fire protection provided by timber. The instrumentation consists in measuring both displacements and temperatures for the full-scaled beams, and only temperatures for the 1,0 meter non-loaded specimens. The displacements are measured at the mid-span of the beams, as presented in Figure 2.
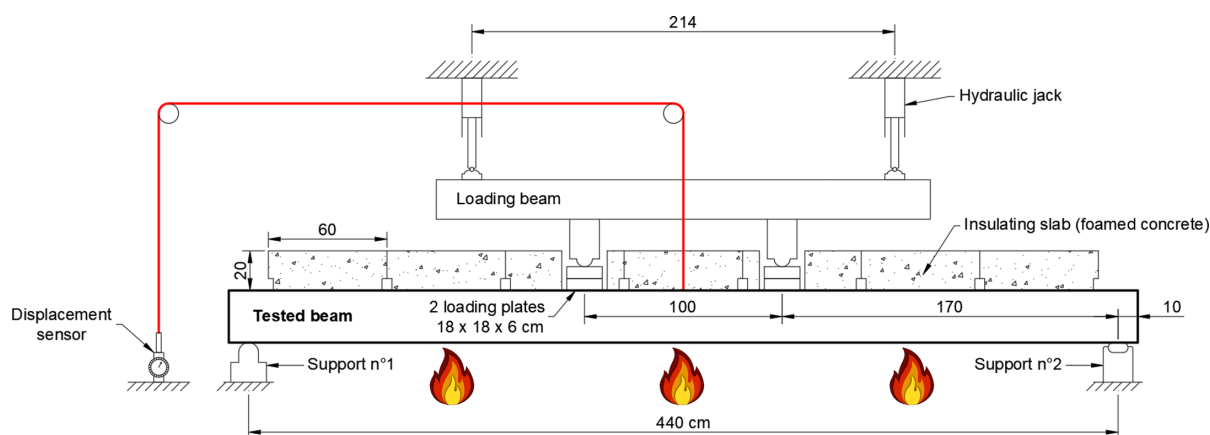
Figure 2: Experimental set-up

Various thermocouples were fitted in the beams in order to measure temperatures on steel and inside timber. In the case of steel temperature, type K thermocouples with a 12 mm diameter copper disc head have been used to measure temperatures along the section height (Figure 3-a). Regarding timber temperatures, type K thermocouples have also been used, with an insulation made of magnesium oxide and an inconel 600 shielding resisting up to 1150°C. Some notches have been made inside timber in order to allow the passage of thermocouples (Figure 3-b). Those thermocouples of 1.5 mm diameter have been inserted through boreholes of 80 mm deep having a 3 mm diameter. Those drilling were made transversally, in the direction parallel to the main exposed surface (lateral face), i.e. parallel to isotherms (Figure 3-c). Previous thermal studies showed that this disposition gives more reliable measurements [8-11].
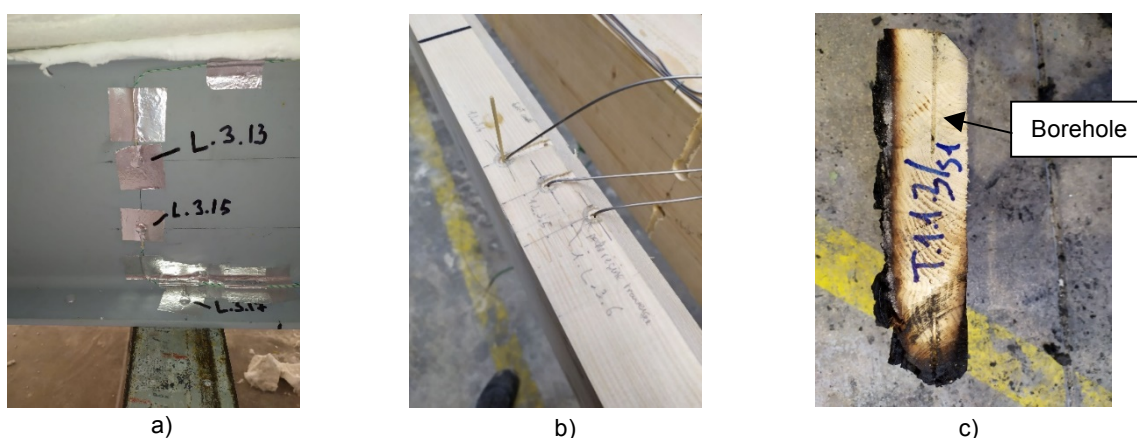

Figure 3: Installation of thermocouples on steel (a) and in timber (b), in boreholes parallel to isotherms (c)

2.2 Test Results

Figure 4 presents the evolution of the mid-span deflection in function of time for both configurations STC1 and STC2. The measured furnace temperatures are also given for both cases and compared to the ISO 834 heating curve. The failure of the beams is determined regarding the deflection value and its acceleration as proposed in EN 1363-1 [12] and EN 13501-2 [13]. For STC1, both criterion (limit deflection and limit deflection rate) are reached. For STC2, the limit deflection value is not reached as the test was stopped due to safety reason. In this case, failure is determined regarding the strain rate only. The load ratio for the test was 43% of the average load-carrying capacity of the beams determined with cold tests. Regarding such ratio, an unprotected steel beam (IPE270) should fail at around 13 min considering an applied calculated bending moment of 66 kN.m. However, it can be observed that the corresponding beam STC1 reaches a failure time of 29 min for an applied bending moment of 91 kN.m. Configuration STC2 reaches a failure time of 81 min for an applied bending moment of 111 kN.m. From those results, it can be said that timber, even only between flanges, provides significantly increased fire resistance.
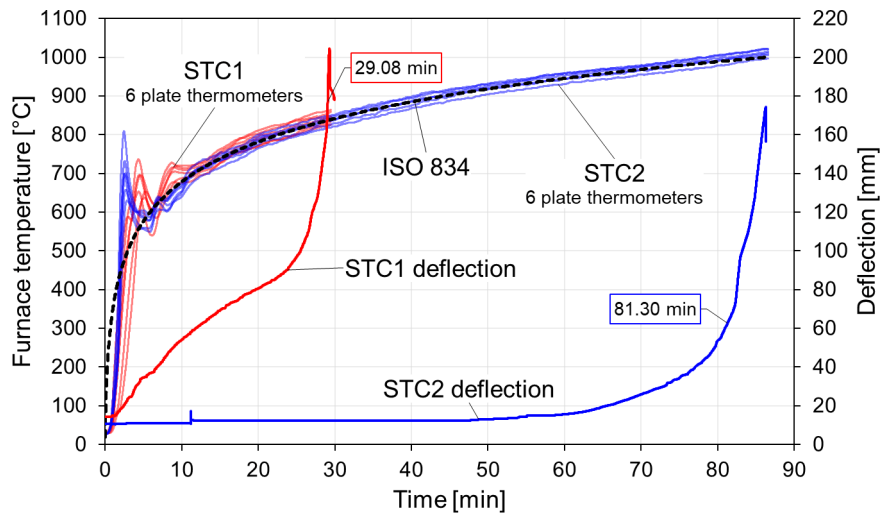
394

Figure 4: Furnace temperature and mid-span vertical displacement measured for STC1 and STC2

In both cases, timber played a significant role in the fire protection of steel. In the case of STC2, the progressive fall of burnt timber, constituting the protection of the bottom flange, is observed after 72 min of fire exposure. From this point onwards, as the bottom flange of the profile is directly exposed to the fire, the temperatures in the section increase rapidly, leading to the failure of the beam. Figure 5 shows the STC2 bema at the end of the fire test.

Figure 5: Picture of STC2 beam after being extracted from the furnace

The main first result of those test is the impact of the mechanical loading on the temperature increase in the section. Figure 6 compares the temperature of the bottom flange (measuring point n°18) of STC1 at 2 different sections, one located at approximately one fifth of the span and the other located at mid-span. This comparison shows that the exposed flange gets higher temperatures when it is affected by larger vertical displacement. This difference was not observed for the bottom flange when the comparison concerned measured values for non-loaded beam. So, the deflection level has an influence on the temperature of the bottom flange: the deflection induced by the loading tend to increase slightly the bottom flange temperature. In fact, the deflection of the beam induces some local openings of the joint between the bottom flange and the inner timber parts. This clearance is significant when the vertical displacement is important, i.e., at mid-span. We assume that the formation of this gap allows hot gases to heat a larger steel surface, causing the flange to heat up faster. However, in the case of STC1, the temperature difference remains around 50-80°C during the test. The same comparisons can be done for the web temperature (measuring point n°15) as illustrated in Figure 6.
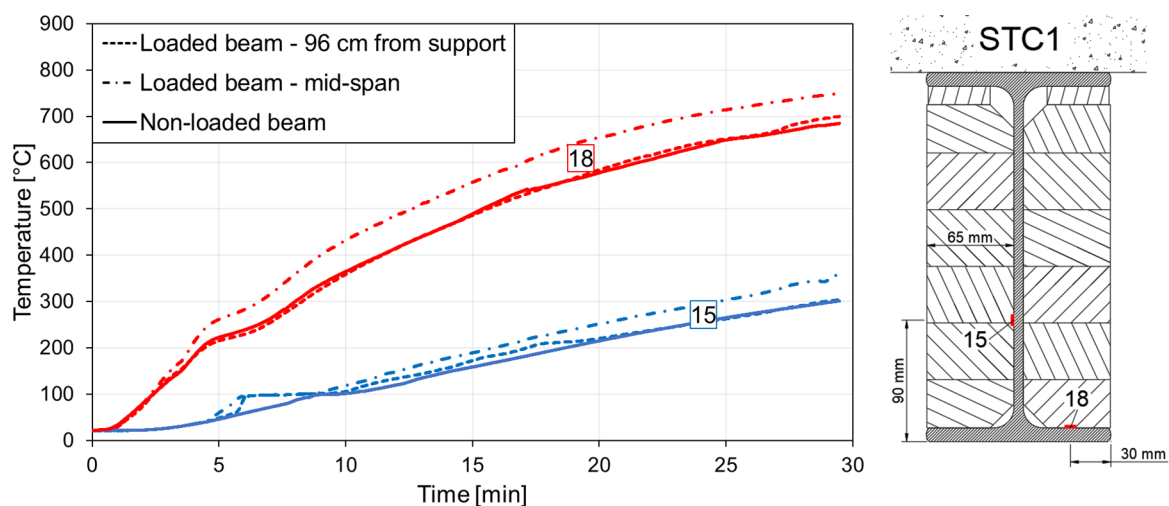
Figure 6: Temperature of the web and the bottom flange of STC1

3. NUMERICAL SIMULATION

3.1 Model Description

A finite element model is developed using the commercial software MSC Marc 2014.2.0 [14]. The thermo-mechanical model is based on an indirect coupling between a thermal model and a mechanical model. The two sub-models are three-dimensional and have strictly similar geometries. A thermal field "mapping" procedure, available in Marc 2014.2, allows considering different meshes for each sub-model. However, the interaction of the mechanical loading on the temperature fields in the materials is neglected: the impact of the beam deflection on the temperatures is not modelled. The mesh is built using hexahedrons-20 nodes elements (HEX20).

Two symmetry planes are considered to optimize the meshed geometry:
– The first one is the symmetry plan of the beam at mid span (figure 7-plane XY). Horizontal longitudinal displacements (along Z axis) are blocked as well as the rotations around X axis.
– The second one is parallel to the beam length (figure 7-plane YZ). It can be considered because geometric instabilities can be neglected. Indeed, the load is too low to induce buckling (43% of the ultimate load), the upper flange is partially connected to the reinforced foamed concrete slab, and the tensile part is the most exposed to fire. So no out-of-plane displacement is expected. Nodes in this plane are blocked from moving in the horizontal-transversal direction (along X axis).

As a result, the modelled geometries correspond to a quarter of the tested beams. Figure 7 gives an overview of the thermomechanical model produced. The load and the support reactions are applied through plates modelled as rigid solids. Contact interactions between solids (timber, steel and loading plates) are achieved by means of "rigid links YY" (Figure 7), i.e., springs that are infinitely rigid in the vertical direction and infinitely flexible in other directions. The fire situation is modelled considering radiative and convective heat flux and the temperature increase follows the average measured furnace temperatures (Figure 4). Radiative and convective parameters are chosen in accordance with Eurocodes [15-17].
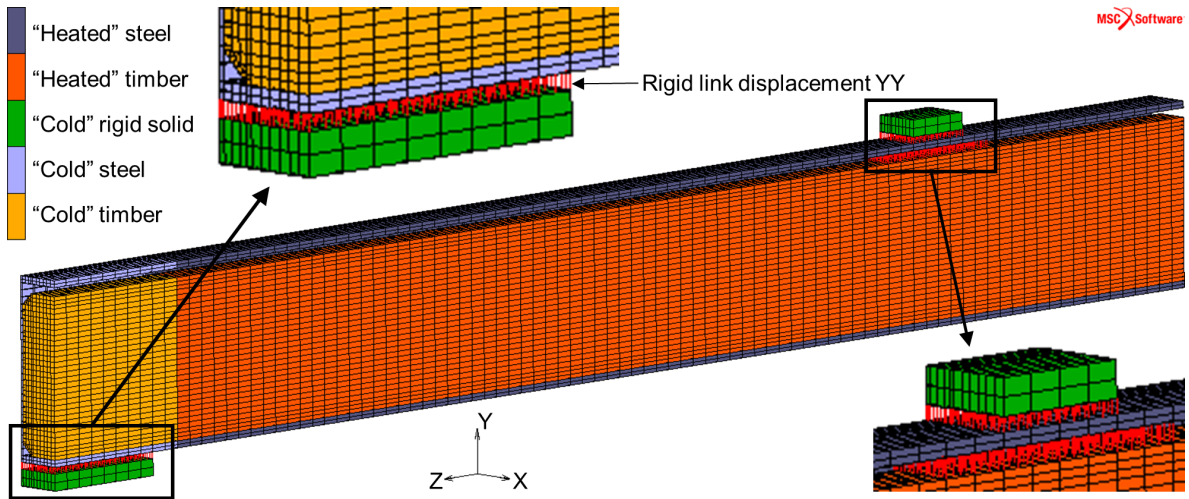
Figure 7: Thermomechanical model for STC1

The elastic limit of steel has been deduced from tensile tests performed on 7 samples [18]. The mean value of the obtained yield limit is 310 MPa. The elastic modulus and the Poisson's ratio are assumed to be 210 GPa and 0.3 respectively, as proposed in EN 1993-1-1 [19]. Steel is modelled as an elastic-perfectly plastic material (bilinear stress-strain curve without hardening).

Timber has been modelled as an anisotropic material, considering a "tetragonal" stiffness matrix [20,21] as described in equation (1). Both, longitudinal elastic modulus (E_L) and bending strength (f_m) have been deduced from bending tests made on 6 full-scale beams (4.6 m long). Three of these beams have dimensions similar to those of the STC1 timber elements, while the other three correspond to the STC2 timber elements (Figure 1). Transversal elastic modulus (E_T) has been deduced from 26 tests made as recommended in EN 408 [22]. The Poisson's ratios (ν_{LT} and ν_{TT}) and shear moduli (G_{LT} and G_{TT}) were deduced from values given by Guitard [23] and according the approach proposed by Davalos et al. [24]. All those values are given in Table 1. The limit of the elastic field is implemented as a Hill criterion and the failure criterion is based on Hoffman [14].

$$
\begin{Bmatrix} \epsilon_{11} \\ \epsilon_{22} \\ \epsilon_{33} \\ 2\epsilon_{23} \\ 2\epsilon_{31} \\ 2\epsilon_{12} \end{Bmatrix} =
\begin{bmatrix}
\frac{1}{E_T} & -\frac{\nu_{TT}}{E_T} & -\frac{\nu_{LT}}{E_T} & 0 & 0 & 0 \\
-\frac{\nu_{TT}}{E_T} & \frac{1}{E_T} & -\frac{\nu_{LT}}{E_T} & 0 & 0 & 0 \\
-\frac{\nu_{LT}}{E_T} & -\frac{\nu_{LT}}{E_T} & \frac{1}{E_L} & 0 & 0 & 0 \\
0 & 0 & 0 & \frac{1}{G_{LT}} & 0 & 0 \\
0 & 0 & 0 & 0 & \frac{1}{G_{LT}} & 0 \\
0 & 0 & 0 & 0 & 0 & \frac{1}{G_{TT}}
\end{bmatrix}
\begin{Bmatrix} \sigma_{11} \\ \sigma_{22} \\ \sigma_{33} \\ \sigma_{23} \\ \sigma_{31} \\ \sigma_{12} \end{Bmatrix}
\tag{1}
$$

Table 1: Mechanical properties considered for timber in numerical simulations

Property		STC1	STC2
E_L	[MPa]	9 500	11 047
E_T	[MPa]	400	400
G_{LT}	[MPa]	804	804
G_{TT}	[MPa]	84	84
ν_{LT}		0.41	0.41
ν_{TT}		0.41	0.41
f_m	[MPa]	29	36

The materials thermophysical and thermomechanical properties are chosen from Eurocodes [16,17] for both steel and timber. However, in the case of timber, some choices have been made by authors, especially regarding the bending strength and the elastic moduli at high temperatures. Indeed, the EN 1995-1-2 proposes reduction factors for either tension or compression [17]. In the current study, the simulated solids are subjected to both tensile and compressive stresses as they are loaded in bending. It has been chosen to manage this issue by using the mean value between tension and compression reduction factors given in EN 1995-1-2, as illustrated in Figure 8.
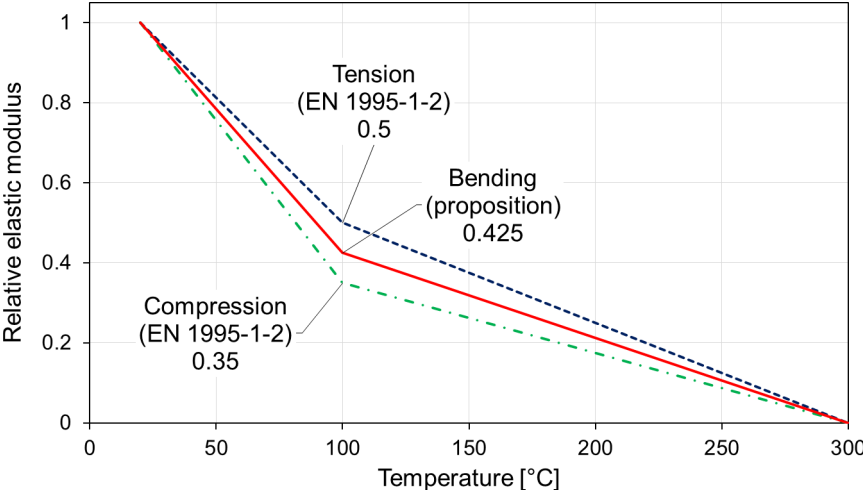
Figure 8: Reduction factors for the elastic moduli of timber.

3.1 Results and discussion

In this section, the results presented for illustration and discussion will be those obtained for the STC1 configuration. Figure 9 presents comparisons between measured and simulated steel temperatures for STC1, considering the unloaded beam. It can be observed that the model agrees well with the experimental results. Some temperature measurement on the web (e.g., measure 16) allow to record a "temperature dwell" around 100°C [25]. It reflects the consequences of the mass transfers that occurs in timber when it is exposed to fire: the accumulation of water against the inner steel parts [26, 27]. This temperature dwell is not reproduced by simulation curves because the dataset used for thermal properties of timber considers mass transfers implicitly [28]. Figure 9 also highlights the heterogeneity of the thermal field across the steel section despite the great thermal conductivity of steel. Even if the lower flange is severely affected by fire, a large part of the web remains at relatively low temperatures.
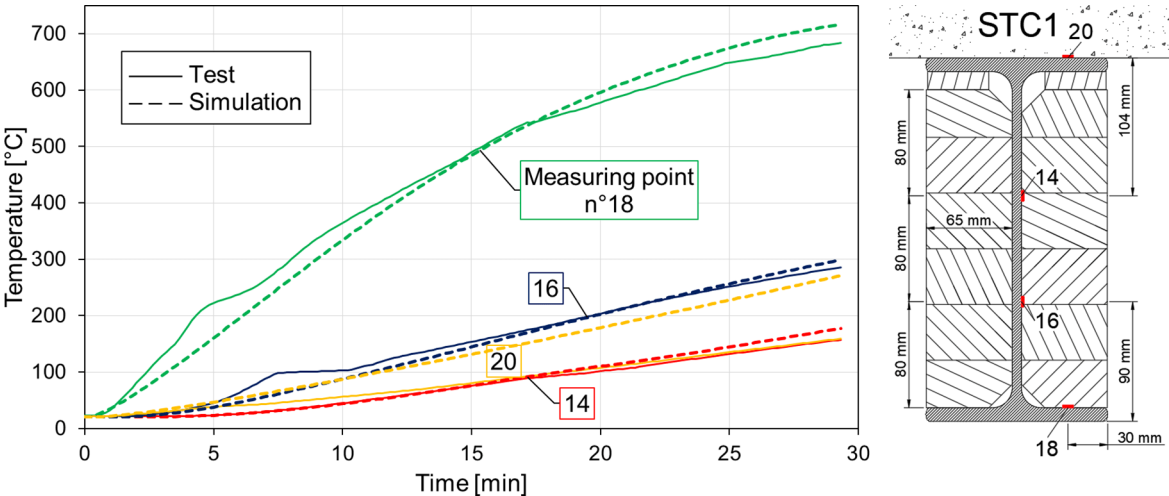

Figure 9: Temperatures on steel for STC1 specimen (non-loaded beam)

Figure 10 shows deflection versus time curves that allow comparison of numerical and experimental results. The numerical model allows to compare the behavior of the beam considering timber just as an insulation material or as a thermomechanical reinforcement, which means that its mechanical properties are also taken in account. It is observed that considering the mechanical strength of timber allows to improve the failure time by 4.7 min (19%). This observation demonstrates that timber contributes to the mechanical response of the beam. This mechanical aspect must be considered with caution as the test conditions, with insulated supports, allows a good transfer of force between steel and timber. It may be different in the case of a totally exposed beam and be more dependent on the connection device between steel and timber.
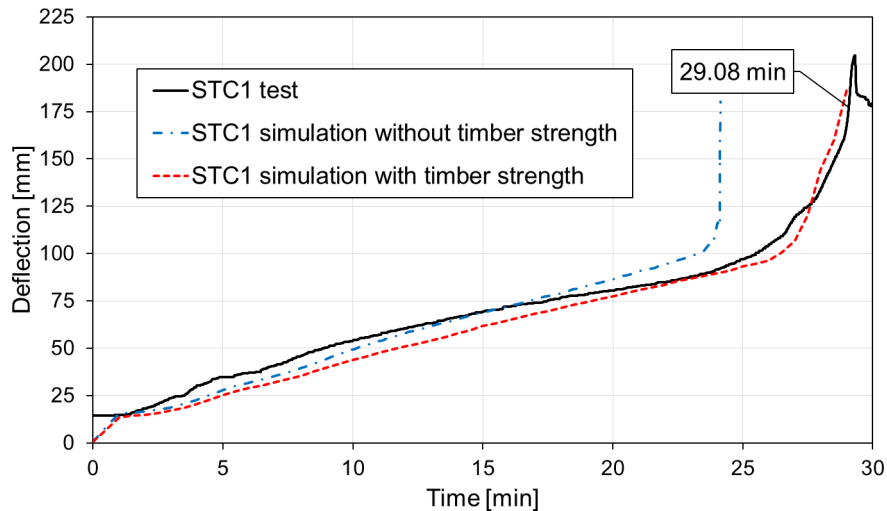
Figure 10: Mid-span vertical displacement of STC1 during fire exposure

4. CONCLUSIONS

The conducted fire tests showed that STC beams have a twofold benefit:
- There is a mutual reinforcement of steel and timber. This mutual strengthening allows configuration STC1 to bear a load 1.38 times greater than the one that an IPE270 steel profile can support. This ratio increases to 1.68 for STC2.
- Timber provides fire protection for steel and delays its collapse by taking up more load as the strength of steel decreases. An unprotected IPE270 steel profile has a fire resistance of 13 min when a 43% load ratio is considered, while STC1 and STC2 withstand fire conditions for 29 min and 81 min respectively under the same load level.

Some temperature measurement showed that the mechanical load impacts the thermal behaviour by deforming steel and timber in a different way, resulting in an opening of assembly joints. These clearances conduct timber to burn faster and steel to heat up more rapidly as it becomes more exposed to fire. Increasing the sinuosity of the assembly joints or keeping them closed (e.g., using glue) could result in better fire resistance.

Tests also allowed to point out that the char fall-off is of major importance in the case of fully protected configurations (like STC2). In this study, the solution chosen to protect the bottom flange is to fasten a machined timber protection on it using screws, but many other possibilities exist. The fire behaviour and the char fall-off may vary depending on the selected technical choice, so more experimental investigations may be needed.

The FEM simulation approach using the datasets proposed in Eurocodes [15-17] is found to give results in good agreement with temperature measurements in both timber and steel. The adjustment of reduction factors given in EN 1995-1-2 [17] to suit the case of a bending load is found to be satisfactory. Simulations based on the STC1 configuration showed that timber improve the fire resistance of steel profile by means of two mechanisms: it acts as a fire protective material, and it provides mechanical reinforcement by taking up the load that steel can no longer withstand as its mechanical properties decrease under the effect of heat. The simulation of the STC2 configuration is of less interest as the char fall-off is difficult to predict, resulting in less accurate results.

Therefore, simplified rules for fire-design, e.g., like the one proposed by Riola Parada [1], could be a suitable approach for this kind of STC beam.

5. ACKNOWLEDGEMENTS

6. REFERENCES

[1]   Riola Parada, F. (2016). *Timber-steel Hybrid beams for multi-storey buildings*, PhD Thesis, Technischen Universität Wien, 245 p.

[2]   Jurkiewiez, B.; Durif, S.; Bouchaïr, A. & Grazide, C. (2022). *Experimental and analytical study of hybrid steel-timber beams in bending*, Structures, vol. 39, p. 1231–1248. doi: 10.1016/j.istruc.2022.03.055.

[3]   Fujita, M. & Iwata, M. (2013*). Bending test of the composite steel-timber beam*, Appl. Mech. Mater., vol. 351–352, p. 415–421. doi: 10.4028/www.scientific.net/AMM.351-352.415.

[4]   Duan, S.; Zhou, W.; Liu, X.; Yuan, J. & Wang, Z. (2021). *Experimental Study on the Bending Behavior of Steel-Wood Composite Beams*, Adv. Civ. Eng., vol. 2021, p. 1315849. doi: 10.1155/2021/1315849.

[5]   Twilt, L. & Witteveen, J. (1974). *The fire resistance of wood-clad steel columns*, Fire Prev. Sci. Technol., vol. 11, p. 14–20.

[6]   Masuda, H.; Yusa, S.; Kawai, T. & Namiki, Y. (2004). *Fire resistance of hybrid wooden structure, Part 9: Loaded fire resistance test on heavy-timber beam structure*, Annual meeting of Architectural Institute of Japan, p. 139–140.

[7]   JR East Design Corporation (2016). *Kunimi Town Office Building, Steel construction Today & Tomorrow*, no. 49, p. 15–18.

[8]   Beck, J. V. (1962). *Thermocouple temperature disturbances in low conductivity materials, J. Heat Transfer*, vol. 84, no. 2, p. 124–131. doi: 10.1115/1.3684310.

[9]   Fahrni, R.; Schmid, J.; Klippel, M. & Frangi, A. (2018). *Correct temperature measurements in fire exposed wood,* World Conference on Timber Engineering, 10 p. doi: 10.3929/ethz-b-000289850.

[10]   Terrei, L.; Acem, Z.; Marchetti, V.; Lardet, P.; Boulet, P. & Parent, G. (2021). *In-depth wood temperature measurement using embedded thin wire thermocouples in cone calorimeter tests, Int. J. Therm. Sci.*, vol. 162, 11 p. doi: 10.1016/j.ijthermalsci.2020.106686.

[11]   Nguyen, M. H.; Ouldboukhitine, S. E.; Durif, S.; Saulnier, V. & Bouchaïr, A. (2023). *Method of measuring the temperature of wood exposed to fire with type K thermocouples, Fire Saf. J.*, vol. 137, p. 103752. doi: https://doi.org/10.1016/j.firesaf.2023.103752.

[12]   European Committee for Standardization (2020). *EN 1363-1 - Fire resistance tests - Part 1: general requirements*.

[13]   European Committee for Standardization (2016). *EN 13501-2 - Fire classification of construction products and building elements - Part 2: classification using data from fire resistance tests, excluding ventilation services*.

[14]   MSC Software Corporation (2015). *Marc 2014.2 - Volume A: Theory and User Information*.

[15]   European Committee for Standardization (2002). *EN 1991-1-2 - Eurocode 1 - Actions on structures – Part 1-2: General actions - Actions on structures exposed to fire*.

[16]   European Committee for Standardization (2005). *EN 1993-1-2 - Eurocode 3 - Design of steel structures - Part 1-2: General rules - Structural fire design*.

[17]   European Committee for Standardization (2004). *EN 1995-1-2 - Eurocode 5 - Design of timber structures - Part 1-2: General - Structural fire design*.

[18]   European Committee for Standardization (2019). *EN ISO 6892-1 - Metallic materials - Tensile testing - Part 1: method of test at room temperature*.

[19]   European Committee for Standardization (2005). *EN 1993-1-1 - Eurocode 3 - Design of steel structures - Part 1-1 : General rules and rules for buildings*.

[20]   Dieulesaint, E. & Royer, D. (1974). *Ondes élastiques dans les solides: application au traitement du signal,* Masson, 399 p.

[21]   Lemaitre, J. ; Chaboche, J. L.; Benallal, A. & Desmorat, R. (2020). *Mécanique des matériaux solides*,

Dunod, 596 p.

[22] European Committee for Standardization (2012). *EN 408+A1 - Structural timber and glued laminated timber - Determination of some physical and mechanical properties.*

[23] Guitard, D. (1987). *Mécanique du matériau bois et composites*, Cépaduès, 238 p.

[24] Davalos, J. F.; Loferski, J. R.; Holzer, S. M. & Yadama, V. (1991). *Transverse Isotropy Modeling of 3‑D Glulam Timber Beams, J. Mater. Civ. Eng.*, vol. 3, no. 2, p. 125–139. doi: 10.1061/(ASCE)0899-1561(1991)3:2(125).

[25] White, R. H. & Schaffer, E. L. (1981). *Transient Moisture Gradient in Fire-Exposed Wood Slab, Wood Fiber Sci.*, vol. 13, no. 1, p. 17–38.

[26] Audebert, M.; Dhima, D.; Taazount, M. & Bouchaïr, A. (2014). *Experimental and numerical analysis of timber connections in tension perpendicular to grain in fire, Fire Saf. J.*, vol. 63, p. 125–137. doi: 10.1016/j.firesaf.2013.11.011.

[27] Sedighi Gilani, M.; Hugi, E.; Carl, S.; Palma, P. & Vontobel, P. (2015). *Heat Induced Desorption of Moisture in Timber Joints with Fastener During Charring, Fire Technol.*, vol. 51, no. 6, p. 1433–1445. doi: 10.1007/s10694-014-0416-3.

[28] König, J. (2006). *Effective thermal actions and thermal properties of timber members in natural fires*, *Fire Mater.*, vol. 30, no. 1, p. 51–63. doi: 10.1002/fam.898.

SIMPLIFIED CALCULATION METHODS FOR FIRE RESISTANCE CHECK OF GALVANIZED STEEL MEMBERS

Margherita Autiero a*,   **Donatella de Silva b,**   **Antonio Bilotta c,**   **Emidio Nigro d,**

ABSTRACT

Fire resistance is a particularly important aspect for steel structures, for the temperature levels that are reached in these structures due to the high thermal conductivity of the steel and the reduced thickness of the metal profiles. Recent studies have shown that hot dip galvanizing, which is already effective to protect from corrosion, can also reduce the thermal field in steel elements exposed to fire thanks to a reduction in surface emissivity.

This paper shows the results of high-temperatures small-scale tests on square galvanized and ungalvanized steel plates, carried out in an electrical laboratory furnace. Based on the experimental temperatures and the application of the analytical method for the steel temperature development, the emissivity of the exposed surface of galvanized steel was calibrated. This emissivity was found to be dependent on the temperature of the steel, while it is not substantially affected by the section factor. The possibility of modeling the effect of galvanizing on the steel temperature, allows an easy implementation of the Eurocode design methods for assessing the structural fire resistance, without substantially changing the design process. Indeed, the second part of the paper describes the simplified "nomogram procedure" for galvanized steel elements, which allows to design and assess the fire resistance time in a very easy way. So it represents a practical tool useful to designers for estimating the fire resistance of hot galvanized steel elements, with different nominal fire curves.

Keywords: hot-dip galvanization, fire resistance, experimental tests, design tools.

1. INTRODUCTION

Galvanization is a surface coating process to protect steel members from corrosion, in which the steel is coated with zinc to prevent it from rusting. The most common galvanization method is hot-dip galvanizing, where the protective zinc coating is obtained by dipping the steel element into a bath of molten zinc usually at about 450°C. The zinc coating is formed by a metallurgic reaction during which several zinc-iron alloy layers are formed. Therefore, the coating is chemically bound to steel beneath, and it is not only laid on top of it. The formation of the zinc coating depends on several factors. On one hand, it depends on the galvanizing conditions such as melting temperature, dipping time and chemical composition of zinc bath. On the other hand, it is influenced by surface conditions and chemical composition of the steel (e.g. silicon and phosphorous content). Silicon concentration in

---

^a Department of Structures for Engineering and Architecture, University of Naples Federico II (Italy),

(margherita.autiero2@unina.it). Corresponding author.

^{b,} Department of Structures for Engineering and Architecture, University of Naples Federico II (Italy),

(donatella.desilva@unina.it).

^c Department of Structures for Engineering and Architecture, University of Naples Federico II (Italy),

(antonio.bilotta@unina.it)

^d Department of Structures for Engineering and Architecture, University of Naples Federico II (Italy),

(eminigro@unina.it).

quantities between 0.04% and 0.14% (Sandelin steel) or above 0.22% (hyper-Sandelin steels) can accelerate the iron-zinc reaction to form a thicker zinc coating with a different alloy layer structure [1]. Four steel categories (C_x), according to EN ISO 14713-2 [2] are defined based on the silicon concentration: C_A - Low silicon content steel (Si ≤ 0.04%), C_B: Non-Sandelin intermediate composition steels (14% < Si ≤ 0.22%), C_C: Sandelin steel (0.04% < Si ≤ 0.14%) and C_D: hyper-Sandelin steels (Si > 0.22 %).

The surface coating can modify the emissivity that is the ratio between the energy radiated from a surface of a material and the energy radiated from a black body, under same conditions, at same temperature and wavelength. Therefore, the emissivity ranges between zero and one. In particular, according to Eurocode [3] the radiative component of the net heat flux depends on the emissivity of flame ε_f, and on the member surface ε_m one.

The radiation of metal surfaces depends on atomic and molecular level. Sala [4] states that the radiation behavior depends on the chemical composition in a layer with a thickness of few microns. The radiation behavior of galvanized surfaces should hence be provided exclusively by the alloy layer (40 μm to 250 μm) or from the upper pure zinc layer alone, which is only a few micrometers thick [5]. Therefore, the emissivity of hot-dip galvanized steel elements is influenced by the alloy layer composition, by the oxidation of zinc, and by the melting of the outer zinc layer at a temperature of 419°C. As a result, the emissivity of galvanized surface is variable with temperature [5].

The Eurocode EN1993-1-2 [3] suggests a simplified surface-independent constant emissivity, $\varepsilon_m = 0.70$ for carbon steel, whereas recent studies [5] - [8], showed that galvanization can also reduce the surface emissivity with a beneficial effect on the temperature of steel members exposed to fire.

Jirku and Wald (2013) [6] performed a fire test in a real scale building and two fire tests in furnace on steel members with IPE200 and hollow tube cross-sections, obtaining a constant value of emissivity for galvanized steel equal to 0.32. While Bihina et al. [7] carried out three standard fire tests on hot-rolled steel structural members, finding an equivalent emissivity for hot-dip galvanized specimens, that increases with temperature.

Mensinger and Gaigl (2019) [5] assessed emissivity curves as a function of temperature for hot-dip galvanized steel elements by small-scale and full-scale tests. The temperature-dependent emissivity was determined for various hot-dip galvanized surfaces and steel categories C_A, C_B, and C_D were tested, combined with all possible surface conditions. The results showed an emissivity dependent not only on temperature, but also by the weathering, with the negative influence of outdoor storage. In fact, the authors pointed out that aging leads to an increase in surface emissivity. Moreover, the results highlighted that the zinc-iron alloy layers have a big influence on the emissivity value. In particular, only for steel of C_A and C_B, the emissivity value is lower than 0.7, for steel temperatures up to 530 °C. Due to chemical reactions, a new layer structure is formed with a higher roughness and a consequent increasing of surface emissivity. Therefore, while EN1993-1-2 [3] suggests a simplified surface independent constant emissivity for carbon steel $\varepsilon_m = 0.70$, the experimental results showed a temperature-dependent emissivity for hot-dip galvanized steel, with values lower than 0.7 for steel temperatures up to 500 °C. Since the studies conducted in literature showed a positive effect of galvanization on the steel temperature due to the variation of the emissivity, Mensinger and Gaigl [5] suggested an emissivity (ε_m) equal to 0.35 for steel temperature ($\theta_{a,t}$) lower than 500 °C and ε_m equal to 0.70 for $\theta_{a,t}$ greater than 500 °C. This equation, indeed, allows an easy implementation of the Eurocode design methods, without substantially changing the design process.

Starting from these considerations, this paper shows the results of high-temperature small-scale tests on square galvanized and ungalvanized steel plates, investigating and quantifying the effect of galvanization on the temperatures of steel elements, in order to calculate the emissivity of galvanized steel through small-scale tests in a common and economical electrical furnace. The first experimental phase of this research activity allowed defining of some practical tools to estimate the fire resistance for hot galvanized steel elements, with different nominal fire curves.

2. EXPERIMENTAL CAMPAIGN ON GALVANIZED STEEL ELEMENTS

2.1 Test specimens and setup

The experimental tests were performed on 44 steel plates, in an electrical laboratory furnace by exposing to heat only the upper surface of specimens, while the remaining parts were protected with an insulating material to reduce heat exchange. So, the steel samples consisted of plates, placed inside a box composed by a sequence of five calcium silicate boards 12.7 mm thick, to approximately obtain laterally adiabatic conditions (see Figure 1). The box was placed on a rockwool layer and finally on refractory bricks. Inside the box, a variable layer of rockwool was placed, to ensure that the sample and the box upper surfaces were aligned to each other (see Figure 1).
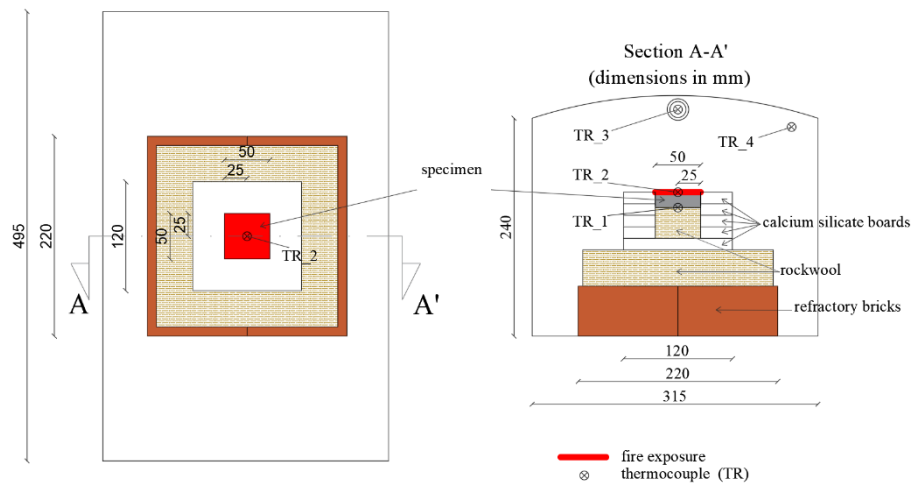
Figure 1: Test setup: top view, setup cross section A-A

The square samples had dimensions of 50x50mm, with a variable thickness, to obtain different section factors A_m/V (ratio between the surface area exposed to fire and the volume of the element) ranging between 20 and 200m^{-1}. For each section factor, one not-galvanized (NG) and three galvanized (G) specimens were tested to have a direct comparison between their temperatures.

The test samples were galvanized using a galvanizing bath according to UNI EN 1461:09. As a result, the galvanized specimens have a mean galvanizing thickness of about 120μm.

The ID of the specimen is defined in Table 1 as X-Y-Z: where X is the section factor of the specimen, Y indicates if the sample is galvanized (G) or not galvanized (NG) and Z indicates the number of the tested specimen.

Besides, the thickness of the specimens and their section factors are listed in Table 1.

Table 1 Test matrix

Not galvanized (NG)	Galvanized (G)			A_m/V [m^{-1}]	s [mm]
20_NG_1	20_G_1	20_G_2	20_G_3	20	50
30_NG_1	30_G_1	30_G_2	30_G_3	30	35
40_NG_1	40_G_1	40_G_2	40_G_3	40	25
50_NG_1	50_G_1	50_G_2	50_G_3	50	20
60_NG_1	60_G_1	60_G_2	60_G_3	60	17
70_NG_1	70_G_1	70_G_2	70_G_3	70	14
80_NG_1	80_G_1	80_G_2	80_G_3	80	12.5
90_NG_1	90_G_1	90_G_2	90_G_3	90	11
100_NG_1	100_G_1	100_G_2	100_G_3	100	10
125_NG_1	125_G_1	125_G_2	125_G_3	125	8
200_NG_1	200_G_1	200_G_2	200_G_3	200	5

Three Chromel/Alumel K thermocouples with a diameter of 2mm were inserted from the furnace inspection hole while the fourth one was assembled in the furnace (see Figure 2a). In particular, the thermocouple (TR_1) was used to measure the steel temperature in the directly exposed face, while the (TR_2) measured the temperature in the non-exposed face. To insert these two thermocouples each steel sample was previously drilled with a hole diameter of 2.5mm and a depth of 4mm. The (TR_3) was used to monitor the furnace temperature, as also the furnace thermocouple (TR_4); the scheme of these devices is shown in Figure 2a. An acquisition system allows to record all the temperatures detected by each thermocouple.

Since this type of electrical furnace doesn't allow to obtain a temperature development equal to the standard fire curve (ISO834), due to its limited electrical power, a different input curve was used. In particular, the thermal program was set with variable temperature development from 20°C to 800°C, with the maximum possible heating rate, but slower than the standard fire curve. Figure 2b shows the values of these temperatures recorded by TR_3, for some selected tests, demonstrating a very good agreement between all the input curves. Thus, having a stable input curve allows to make direct comparisons between the experimental results.
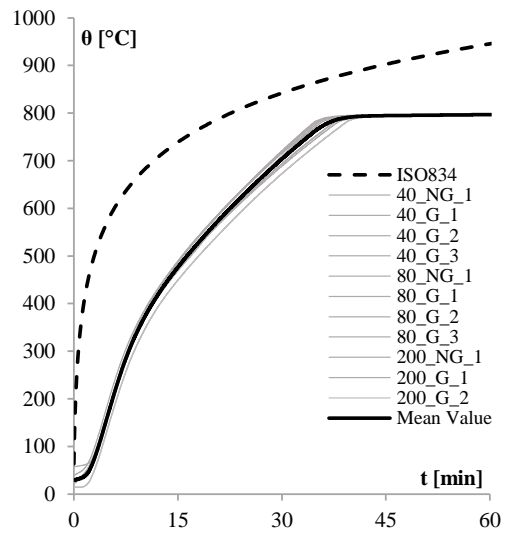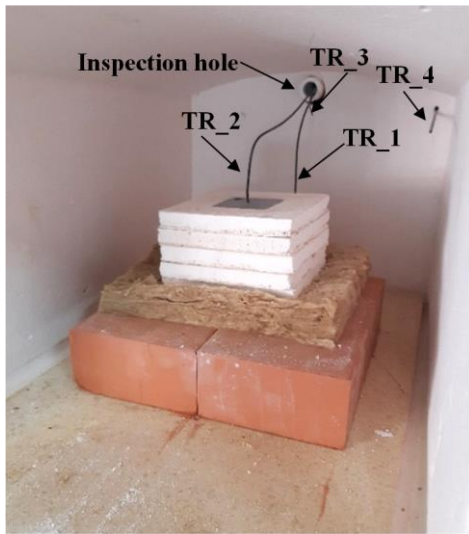
Figure 2: Setup in the furnace with position of the thermocouples (a), thermal input curves: temperatures recorded by TR_3 (b).

2.2 Experimental results

For sake of brevity, the results obtained for only three representative section factors (A_m/V= 40, 80, 200 m^{-1}) are discussed below. Figure 3 shows the temperature recorded by TR_1 for each galvanized sample and their mean value (black curve) for the three4 selected section factors. Furthermore, the graphs of Figure 3 also contain the input fire curve obtained as the mean of each test with same A_m/V (Mean_input_A_m/V).

In particular, for the section factors A_m/V= 40 and 80 m^{-1}, the results obtained for the three galvanized (G) and one not galvanized (NG) specimens are shown. While, for the section factor equal to 200 m^{-1} only the results obtained for two galvanized and one ungalvanized specimens are available, because one thermocouple didn't work during the test.
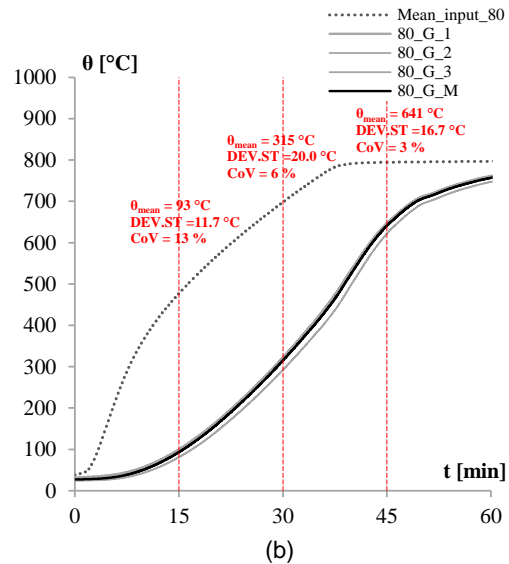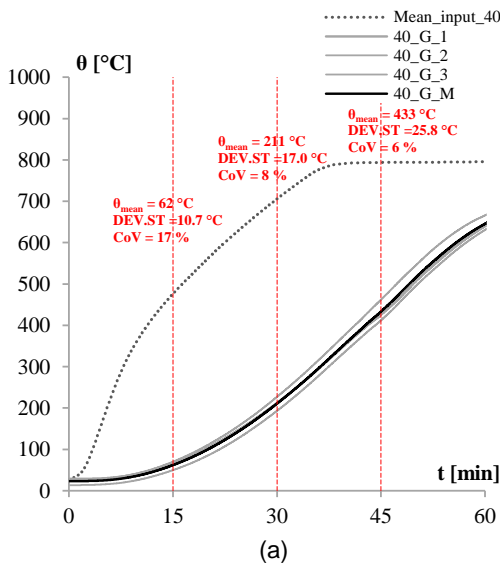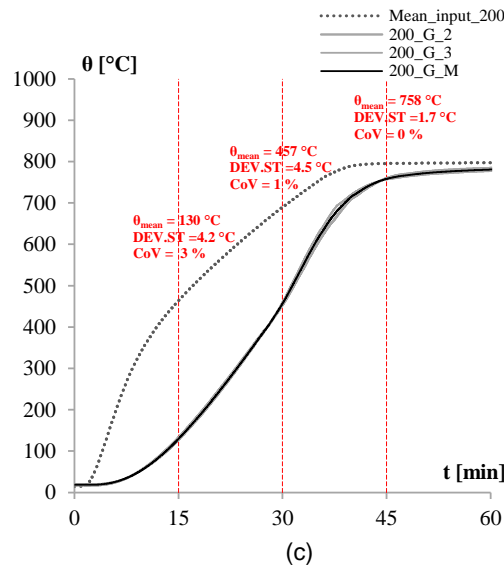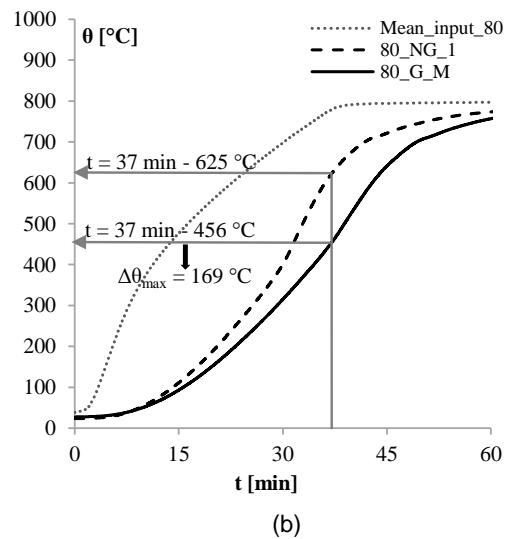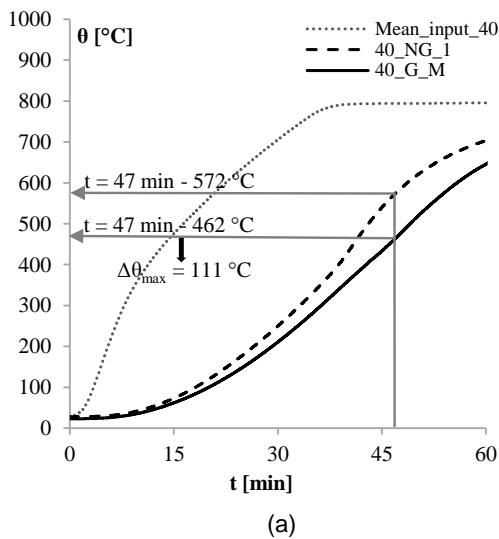
Figure 3: Comparison between temperatures of three galvanized specimens with same Am/V and their mean value (G_M); Am/V= 40 m-1 (a), Am/V= 80 m-1 (b) and Am/V= 200 m-1 (c).

In all the cases the steel temperatures recorded in the specimens during each test are very similar to each other, demonstrating not only the stability of the results, but also the reliability of the test setup. Since the stability of the results, the mean temperature value for each section factor is considered in the following comparisons; indicated as A_m/V_G_M for the galvanized elements and A_m/V_NG_M for the not galvanized ones.

Figure 4a shows the experimental results obtained for the not galvanized (40_NG) and galvanized (40_G_M) specimens with dashed and continuous curves respectively. These results show the effect of galvanizing in terms of lower temperatures of the hot dip galvanized specimens. For example, at 30 minutes of exposure time the temperature of blank specimen θ_{40_NG} reached 250 °C while the same galvanized specimens have a temperature θ_{40_G} of 211 °C. This difference of about 40°C changes during the heating with a maximum value ($\Delta\theta_{max}$) of 111 °C at 47 minutes, when the temperatures are 572 °C for the blank specimen and 462 °C for the galvanized ones.

In the Figure 4Figure 5b the results obtained for not galvanized (80_NG) and galvanized (80_G_M) specimens are represented. First of all, faster heating than the previous case (Figure 4a) is observed due to a lower thickness of the samples and a greater section factor ($A_m/V= 80$ m^{-1}), obtaining higher temperatures, both for galvanized and not-galvanized samples. Nevertheless, the effect of galvanizing on the steel heating is still appreciable, indeed the galvanized samples have lower temperatures than the corresponding not galvanized. For example, at 30 minutes in the not galvanized specimen θ_{80_NG} is 400 °C while in the same galvanized specimens θ_{80_G} is 315 °C. This difference of 86°C changes during the heating with a maximum value of 169 °C at 37 minutes, when the temperatures are $\theta_{80\_NG} = 625$ °C and $\theta_{80\_G} = 456$ °C respectively.

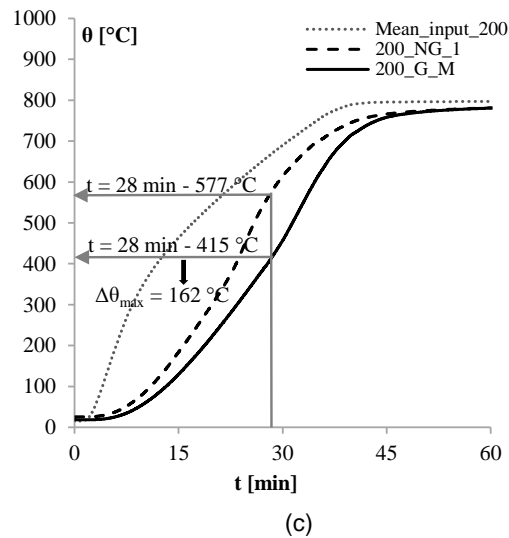(a)   (b)

(c)

Figure 4: Comparison between the recorded temperatures of the non-galvanized samples (NG_1) and the mean value of the galvanized ones (G_M) with the same A_m/V: (a) A_m/V= 40 m^{-1}, (b) A_m/V= 80 m^{-1}, and (c) A_m/V= 200 m^{-1}.

Passing from a section factor of 80 m^{-1} to 200 m^{-1} the specimens show faster heating (see Figure 4a,c), and the maximum beneficial effect of galvanizing on the steel temperatures appears already at 28 minutes; at this time $\Delta\theta_{max}$ is equal to 162 °C with θ_{200_NG} of 614 °C and θ_{200_G} of 457 °C. With the increase of exposure time, the beneficial effect of galvanizing is reduced due to the zinc layer melting at a temperature of 419°C, with a consequent loss of the beneficial effect of galvanizing. Figure 5 plots a direct comparison between the experimental results of galvanized and not-galvanized specimens obtained for the three A_m/V = 40, 80, 200 m^{-1}. Due to the different values of A_m/V, the steel temperature curves are clearly different, but for the same A_m/V, the maximum temperature difference between galvanized and blank samples is reached when the temperatures in galvanized specimens are about 450°C, i.e., a temperature close to the galvanization melting. This temperature is reached for the galvanized specimens at different heating times.
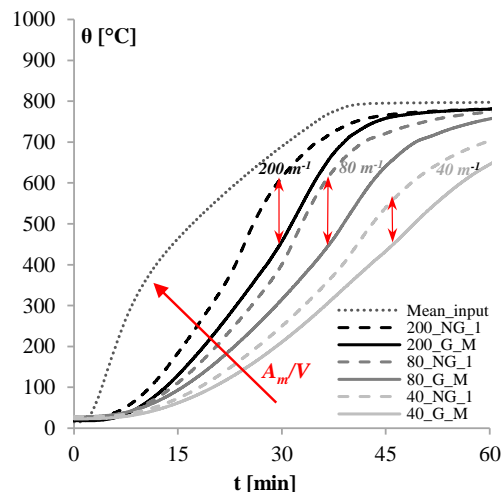

Figure 5: Comparison between experimental results of different galvanized (G) and blank (NG) specimens with A_m/V = 40, 80, 200 m^{-1}.

3. ANALYTICAL MODELLING OF GALVANIZED STEEL MEMBERS

Starting from the experimental results, a simulation of the tests on galvanized samples was carried out by implementing the analytical method for the steel temperature development, suggested also by Eurocode EN1993-1-2 [3], in which, an equivalent uniform temperature distribution in the cross-section is assumed.

A convection coefficient, α_c, lower than the one related to the standard fire curve was used to consider the convective thermal flux specific for these tests. This α_c value was calculated for non-galvanized specimens with three different section factors based on the mean of the temperatures recorded by the lower TC_1 and the upper TC_2 thermocouples. This α_c value was calculated by determining the Rayleigh and Nusselt numbers for natural convection problems defined in [9] and evaluating the thermophysical properties at the surface temperature. Correlations for either laminar or turbulent flow regimes depending on Ra_L values, with references to horizontal plates with upper surface hot plate, are then used [9]. Therefore, a mean value of α_c equal to 6.4 W/m^{2}K was calculated.

Moreover, some calibrations were conducted to obtain the surface emissivity variation with the steel temperatures. Starting from all the experimental results, the following analytical function was calibrated by comparing the galvanized specimens results with the analytical ones by varying the four parameters: ε_{max}, ε_{min}, β and γ:

$$\varepsilon = 0.5 \cdot (\varepsilon_{max} - \varepsilon_{min}) \cdot tanh\left[\left(\frac{1}{\beta}\right) \cdot (\theta_{a,t} - \gamma)\right] + 0.5 \cdot (\varepsilon_{max} + \varepsilon_{min}) \tag{1}$$

Two different calibrations were carried out; CAL_1, in which a single emissivity curve for each A_m/V was firstly calibrated; all these values were then averaged obtaining the dashed curve in Figure 7; CAL_2, in which the calibration was made by considering directly, all the A_m/V results together.

The Figure 6shows the development of the two curves obtained from equation (1) for CAL_1 and CAL_2 and a comparison with the two-stages emissivity relationship (NEW_EN_G).

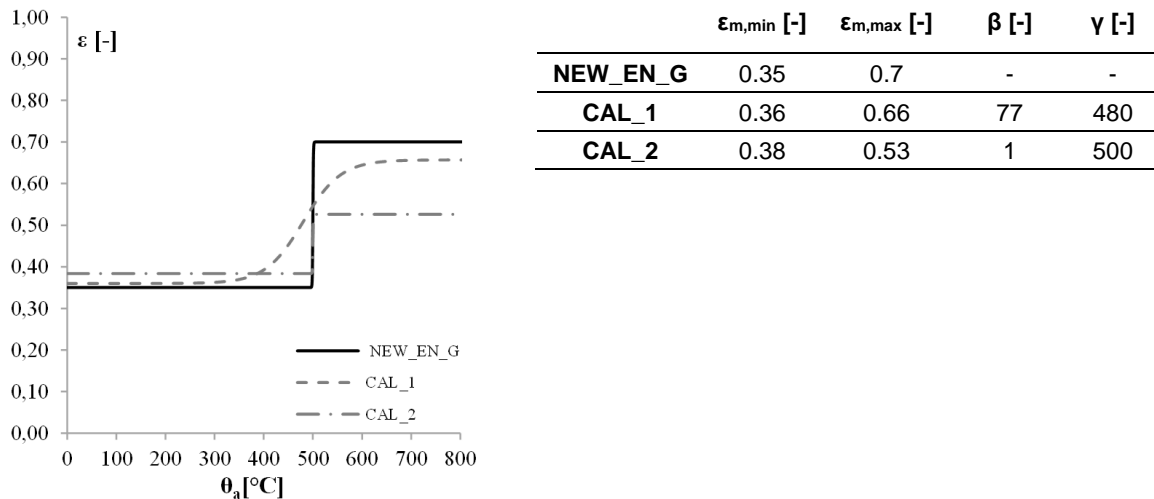|	$\varepsilon_{m,min}$ [-]	$\varepsilon_{m,max}$ [-]	β [-]	γ [-]
NEW_EN_G	0.35	0.7	-	-
CAL_1	0.36	0.66	77	480
CAL_2	0.38	0.53	1	500

Figure 6: Comparison between emissivity curves obtained for the two different calibrations, (CAL_1, CAL_2) and the NEW_EN_G.

Even though these two curves are based on results of small-scale tests performed in a common and cheap electrical furnace, they confirmed that the development of galvanized steel emissivity depends on the steel temperature.

Figure 7 compares the experimental temperatures and the analytical ones calculated using the emissivity values of CAL_1, CAL_2 and NEW_EN_G: a very good agreement with the experimental curves can be observed for A_m/V= 80 m^{-1}, while a small difference is found in the case of A_m/V= 40 m^{-1} and A_m/V= 200 m^{-1}.

Furthermore, the analytical curves are very similar to each other using emissivity values according to CAL_1, CAL_2 and NEW_EN_G. Therefore, considering that CAL_1, CAL_2 were calibrated using an input curve slower than the standard ISO834 fire curve, the comparison results of Figure 7 show that the several applied emissivity formulations may be used also for fire curves different from the standard one, as they are able to provide emissivity values for properly modelling the behavior of galvanized steel elements with good accuracy.
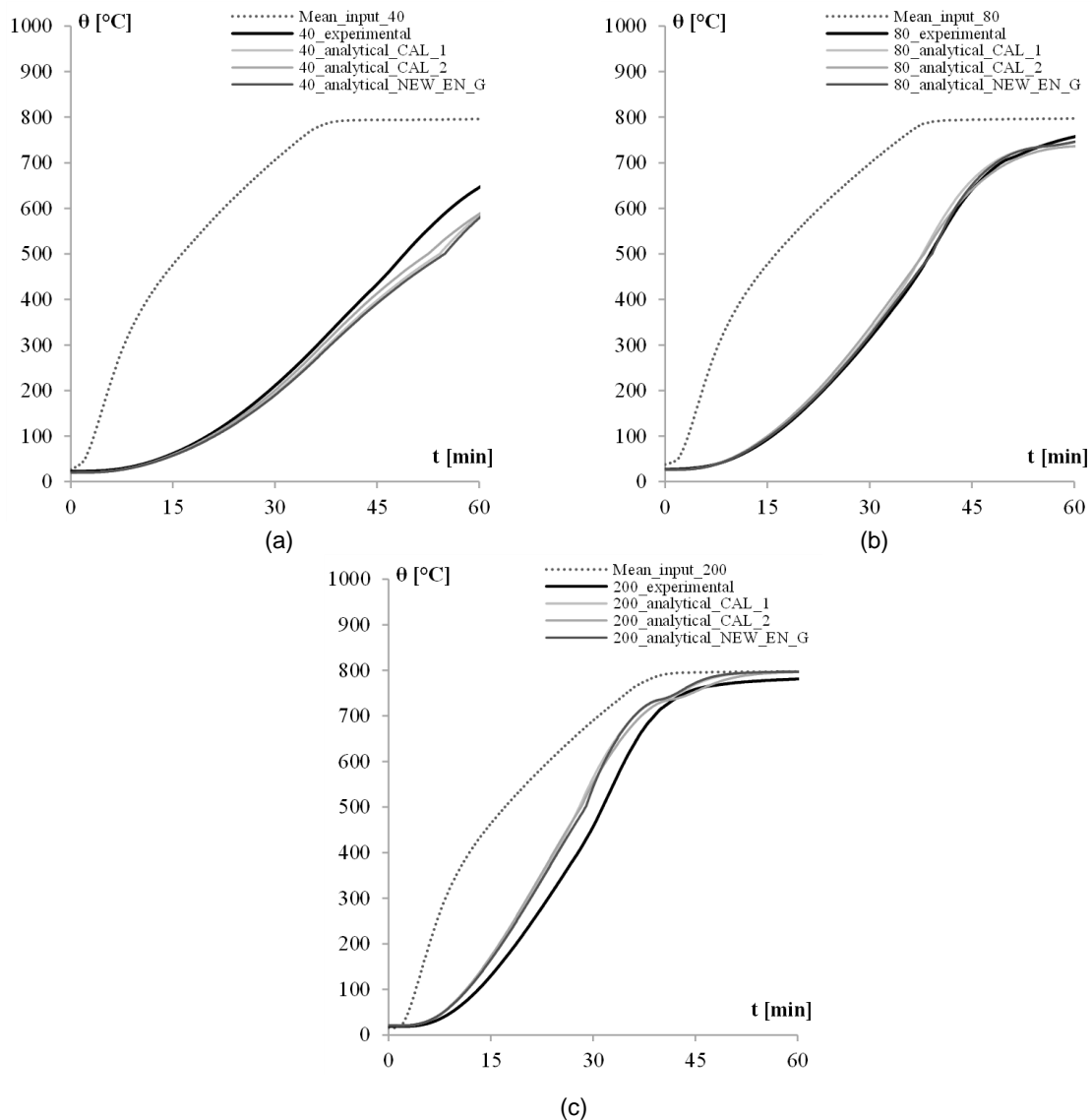
Figure 7: Comparison between experimental and analytical results for (a) A_m/V= 40 m^{-1}, (b) A_m/V= 80 m^{-1}, and (c) A_m/V= 200 m^{-1}.

4. PRACTICAL TOOLS FOR ASSESSING THE EFFECT OF GALVANIZATION

On the base of experimental results, the second part of the paper presents an analytical assessment of the galvanizing effect by varying both the fire curves and the section factors. The possibility of modeling the effect of galvanizing on the steel temperature according to the previously described two-stage emissivity relationship, indeed, allows an easy implementation of the Eurocode design methods for assessing the structural fire resistance, without substantially changing the design process.

For structural fire assessment and verification, the Italian code [9], according to the European ones, defines five performance levels (PL), depending on the importance of the building; for example, in the case of industrial ones, PLI and PLII can be chosen. In particular, in PLI the absence of external consequences due to structural collapse has to be demonstrated, whereas according to the PLII the structure has also to maintain its fire resistance capacity for a period of time sufficient for the evacuation of occupants to a safe area outside of the building. In order to comply with the performance level, different design solutions can be chosen, based on prescriptive or performance-based approaches. The main difference between the prescriptive (PA) and the performance based (PBA) approaches is that the first one is based on standard fire resistance tests or empirical calculation methods, using nominal fire curves. In particular, the code provides three types of conventional fire curves (standard ISO834, hydrocarbon, and external nominal curve), selected according to the nature of the combustible materials in the compartment. Among the simplified methods for fire verification and design of steel elements, one of the most used

409

is the Nomogram [13], which in this work was created for galvanized steel elements, by using the three nominal fire curves.

### 4.1 The Nomogram for galvanized steel sections

The "Nomogram" is a simple operational tool, provided form the Eurocode EN1993-1-2 in Annex A [3], that the designer can use for the estimation of the fire resistance of unprotected steel members. The main assumptions for the application of the Nomogram are: uniform temperature distribution, indirect actions due to prevented thermal expansion are neglected, for the ductility class 4 sections the critical temperature is equal to 350 ⁰C. The procedure is valid for all steel grades indicated in EN10025. As Figure 8 shows, the nomogram has two quarter placed side by side along the axis of temperatures, which allows to relate the degree of utilization μ_0, defined as the ratio between the action in the fire condition and the resistance at time t=0; the time of fire resistance and the section factor (A_m/V) defined by considering the *shadow effect*:

- in the quarter on the left the critical temperature development as a function of the degree of utilization μ_0 at time t=0 and by varying adaption factors k=k1·k2 is reported;
- in the quarter on the right the temperature curves as a function of the exposure time of the nominal fire curves; obtained for different values of the section factors and for the galvanized steel elements are represented.

Considering the introduced simplified assumptions, it is generally possible to use the nomogram for the design or the preliminary fire resistance verification of steel beams and columns, both galvanized and not galvanized. However, the procedure does not replace the complete procedure of EN 1993-1-2 [3], which should be considered when the main assumptions and use limitations are not verified.

Figure 8 shows the nomogram calculated for galvanized a not galvanized member by using the three standard nominal curves described above. By analyzing the diagrams in Figure 8 it is possible to observe how the galvanization effect on the verification of the fire resistance of galvanized steel elements is strongly dependent on different variables such as the fire curve considered, on the section factor, on the exposure time and utilization factor. Therefore, this effect, in the case of the ISO834 curve (Figure 8a), is more significant for low cross-sections ($A_m/V < 100$ m^{-1}) and exposure times to the standard fire curve of 15-30 minutes. Whereas the hydrocarbon fire curve (Figure 8b) has a more heavy development than the other two nominal ones (higher temperatures reached more quickly), the effect of galvanization is less appreciable, even in the case of lower sectional factors. So, this effect is only significant for very low cross-sections ($A_m/V=50$ m^{-1}).

Finally, since the development of the external fire curve (Figure 8c) is the less heavy, the effect of galvanization can also be observed in the case of higher values of the section factor (see Figure 8c).
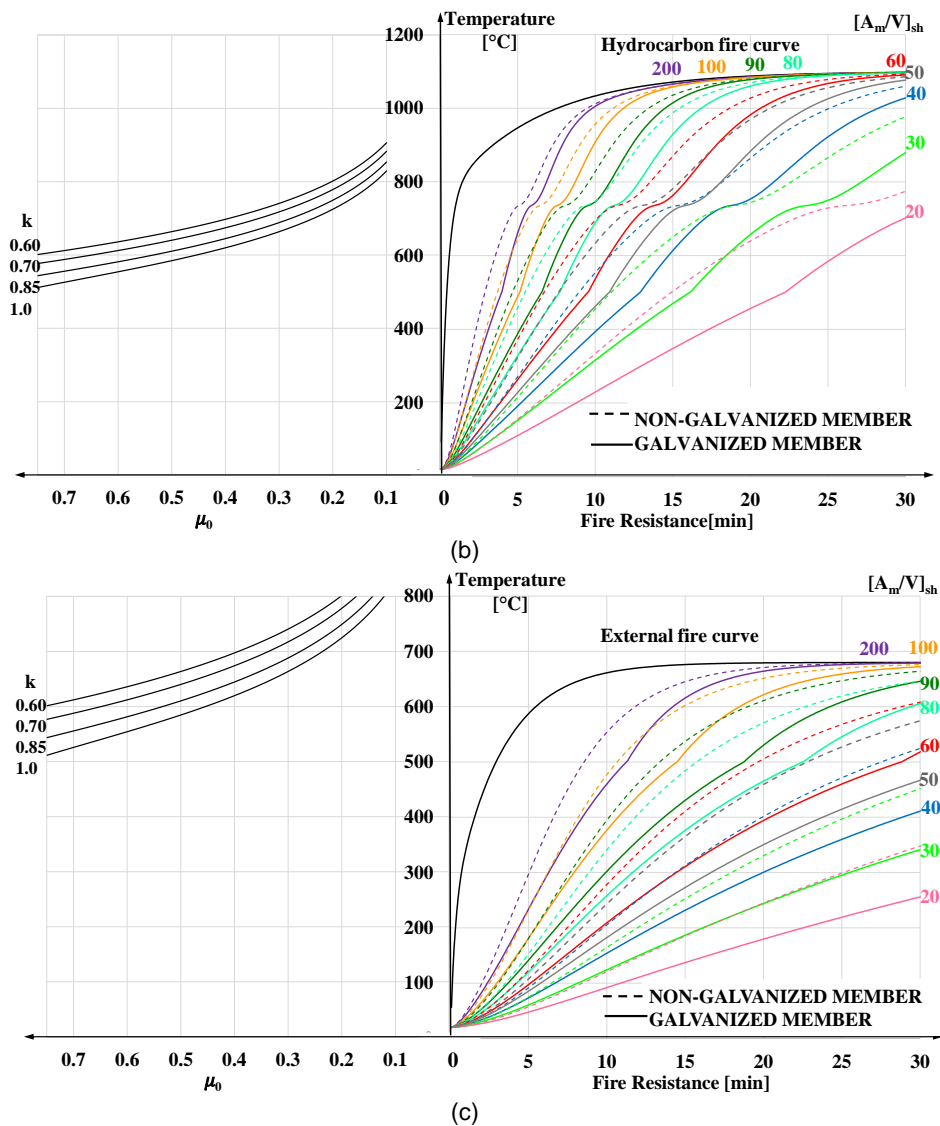

(a)
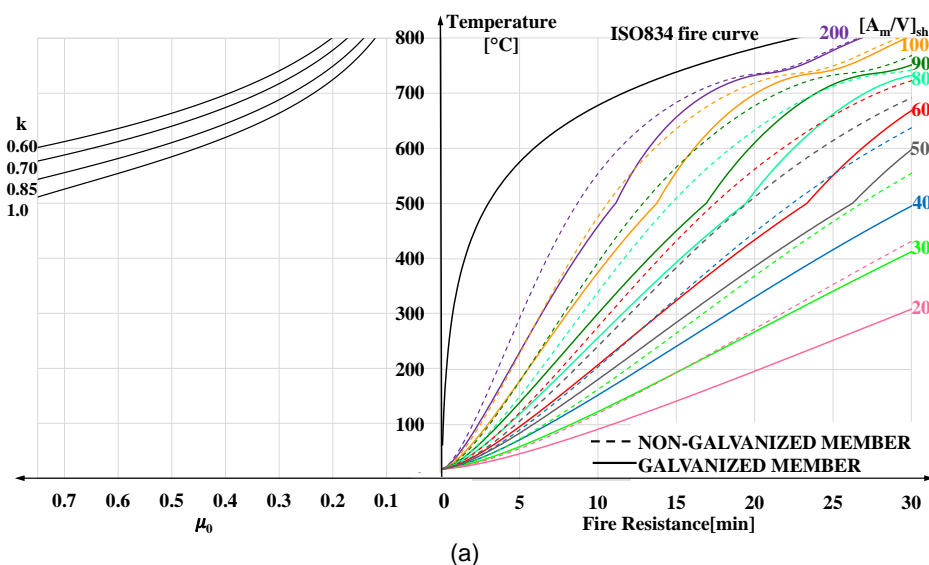
Figure 8: Nomograms for galvanized elements with (a) ISO 834 fire curve; (b) hydrocarbon fire curve; (c) external fire curve.

4.2 Calculation example

Knowing the required fire resistance, it is possible to obtain the temperature at a certain time by using the nomogram, and then verifying if it is lower than the critical one. This simplified calculation procedure can be applied to elements subjected to pure tension, pure bending, or pure compression. The method is not applicable to elements subject to combined stresses and buckling phenomena. In the following, an application example of the galvanizing effect evaluated experimentally in the previous paragraphs on a full-scale element is reported. However, the results of this example would have to be validated with a full-scale experimental campaign which is planned as future development. The example is related to HEM240 beam made of S275 (f_y) steel, subjected to a bending moment equal to 130kNm ($M_{fi,d}$). The beam is connected to a concrete slab, therefore the buckling can be neglected also in fire condition. The required fire resistance is R30.
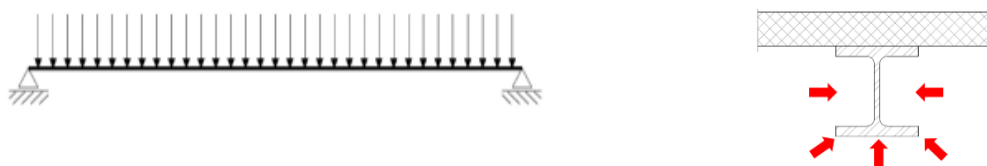

Figure 9: beam under fire condition.

411

The degree of utilization, μ_0 for a beam cross section of class 1 subjected to pure bending can be calculated as function of the plastic resistance modulus W_{pl}:

$$\mu_0 = \frac{M_{fi,d}}{W_{pl} \cdot f_y} \frac{130 \cdot 10^5}{1006 \cdot 10^3 \cdot 275} = 0.47 \tag{2}$$

The beam is not protected and exposed on three sides; therefore, the coefficient k is $k_1 \cdot k_2 = 0.7$, therefore, by using the nomogram of Figure 8 it is possible to obtain the critical temperature: $\theta_{cr} = 650$ °C, while the section factor $[A_m/V]_{sh}$ is equal to 55 m^{-1}. The application of the Nomogram in Figure 8a shows that the critical temperature is reached with a time of fire exposure equal to 26 min and 31 min in the case of not galvanized and galvanized element respectively. So, the same steel element could be classified with a fire resistance R30 thanks to galvanization effect.
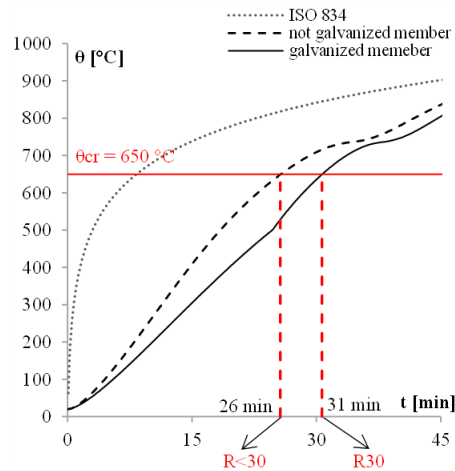

Figure 10: Comparison between temperatures of the not galvanized element and galvanized one ($A_m/V=55m^{-1}$)

5. CONCLUSIONS

The results of an experimental program aimed at the investigation of the behavior of galvanized steel members confirmed that the temperatures in the hot dip galvanized specimens are lower than those recorded in the not galvanized ones. Therefore, based on the experimental temperatures and the application of the analytical method for the steel temperature development, the emissivity of the exposed surface of galvanized steel was calibrated. This emissivity was found to be dependent on the temperature of the steel, while it is not substantially affected by the section factor. The possibility of modeling the effect of galvanizing on the steel temperature according to the previously described two-stage emissivity relationship, allows an easy implementation of the Eurocode design methods for assessing the structural fire resistance, without substantially changing the design process. In this framework, the simplified "nomogram procedure" approach, typically used for steel members, has been adjusted by authors for galvanized steel elements. This procedure provides a practical tool useful to designers for estimating the fire resistance of hot galvanized steel elements, with different nominal fire curves.

ACKNOWLEDGEMENTS

REFERENCES

[1] Pernice L. (2021). *Zincatura a caldo*. Mirapromotion Srl. 174p, (In Italian)
[2] ISO 14713-2:2009, Zinc coatings — Guidelines and recommendations for the protection against corrosion of iron and steel in structures — Part 2: Hot dip galvanizing
[3] EN 1993-1-2, Eurocode 3: Design of steel structures - Part 1-2: General rules -Structural fire design, 2005.
[4] Sala A. (1986). *Radiant properties of materials: Tables of radiant values for black bodies and real materials*, Elsevier Science Ltd.

[5] Gaigl C., (2019). *Fire resistance of hot-dip galvanized steel structures*, PhD Thesis, Technical University of Munich.

[6] Jirku J., Wald F., (2013). *Influence of zinc coating to a temperature of steel members in fire, in ASFE'13 - Application of Structural Fire Engineering*, 19-20 April 2013, Prague, Czech Republic.

[7] Bihina G., Zhao B. (2021). *Hot dip galvanizing of steel structural members: an alternative to passive fire insulation?* Ce/papers 4, Proceedings of Eurosteel 2021: 1–3 September 2021, Sheffield, England.

[8] Autiero M., Bilotta A., de Silva D., Nigro E., Pernice L. (2021). *Temperature of galvanized steel specimens heated in electrical furnace*, ASFE 2021 - Applications of Structural Fire Engineering, 10-11 June 2021, Lubiana, Slovenia. Paper Id. 62, p. 211-216.

[9] J. R. Lloyd and W. R. Moran (1974), Natural Convection Adjacent to Horizontal Surface of Various Planforms, ASME Paper 74-WA/HT-66.

[10] EN 1991-1-2, Eurocode 1: Actions on structures - Part 1-2: General actions - Actions on structures exposed to fire, 2002.

[11] Elich, J. and Hamerlinck, A. (1990). *Thermal radiation properties of galvanized steel and its importance in enclosure fire scenario*s, Fire Safety Journal, vol. 16, pp. 469-482.

[12] D.M. 3 agosto 2015 "Approvazione di norme tecniche di prevenzione incendi, ai sensi dell'articolo 15 del decreto legislativo 8 marzo 2006, n. 139", GU n. 192 del 20/8/2015 – S.O. n. 51. (In italian)

[13] Nomogramma - Metodo grafico di valutazione della resistenza al fuoco di strutture in acciaio (based on EN 1993-1-2 luglio 2005 Commissione per la Sicurezza delle Costruzioni in Acciaio in caso di Incendio. (in Italian)

STRUCTURAL PERFORMANCE OF A LARGE-SPAN BI-DIRECTIONAL PARTIALLY PRECAST WAFFLE SLAB SYSTEM UNDER FIRE EXPOSURE

Bruno Dal Lago a,*   **Francesco Lo Monte b**

ABSTRACT

This paper describes the evaluation of the structural performance under fire exposure of a partially precast waffle slab system employed in the 1970s for the construction of residences in high-mountain skying stations in the Italian Alpine arch. Full information is available about this structural arrangement, including geometry and reinforcement shop drawings, and material properties, adjuvated by on-site non-destructive detection tests. The bi-directional waffle slab system at study was not designed according to any specific rule or calculation concerning fire resistance. The performance of the slab system under fire exposure is investigated through numerical analysis employing non-linear equivalent beam elements under the standard ISO 834 temperature-time exposure, where sectional non-linear temperature distribution and moment-curvature diagrams are evaluated separately and attributed to the numerical model. The modelling is aimed at evaluating the structural performance of the waffle slab under fire exposure with an advanced method taking into account of indirect actions caused by the temperature rise in this highly-statically-undetermined structural arrangement, cheking the actual safety as well as stress and deformation profiles of the slab members under different time exposures. The simulation also aims at assessing the benefits brought in by structural redundancy and stress/force redistribution capacity, this being of primary importance for structures not designed to withstand the recent provisions in case of fire.

Keywords: Fire; Reinforced Concrete; Precast Structures; Indirect Actions; Waffle Slab.

ᵃ,* Department of Theoretical and Applied Sciences, Università degli Studi dell'Insubria, via Dunant 3, 21100 Varese, Italy (bruno.dallago@uninsubria.it), Corresponding Author.

ᵇ Department of Civil and Environmental Engineering, Politecnico di Milano, Milan, Italy (francesco.lo@polimi.it).

1. INTRODUCTION

In the last decades, the fire performance of structures and infrastructures attracted increasing attention among scientists and practitioners due to the occurrence of a few severe accidents which led dramatic losses of lives and huge economical/social consequences [1-4]. Such events proved as, despite the rather good fire resistance of concrete at the material level (this being possible thanks to some its inherent characteristics such as incombustibility and low thermal diffusivity), the fire performance of R/C structure need to be properly assessed, since local/global failure collapse can occur also involving brittle failure mechanisms such as punching/shear in slabs or buckling in columns [3,4]. Moreover, recent field observations inspired research devoted to the characterisation of the complex fire performance of thin-walled open-section precast concrete elements, where the thermal actions and the second order geometrical non-linearities can impose distortions of the cross-sections [5].

As it is well-known, reinforced-concrete and prestressed-concrete two-way slabs are structural arrangements allowing medium/large covers of floors and foundation mats to efficiently spread the loads on rather soft soils (slabs-on-grade). Thanks to their reduced thickness (with span over thickness ratio usually in the range 22-35 and even approaching 40 in the case of pre-stressed systems) and architectural adaptability, two-way slabs represent a powerful solution for designers and a valid alternative to more traditional structures such as beams coupled with unidirectional slabs. In case of large-span slabs, however, in order to increase the stiffness while keeping as limited as possible the weight, pre-stressing or bi-directional beams/ribs (namely, waffle slab systems) have been introduced. In the present study, a bi-directional waffle slab system for large-span flooring, as several can be found in structures realised since the 60s in many parts of the world, including Italy, is investigated.

Concerning the code framing of two-way slabs, fib Model Code 2010 [6], Eurocode 2 [7,8] and ACI 318M-14 [9] allow a proper design at both the Service and Ultimate Limit State. Also the Italian Standards NTC2018 [10] provides indications regarding the design of slabs, these being aligned with the European provisions [7]. It is finally worth recalling that the structure under scrutiny was designed according to obsolete Italian Standards of the early 1970s.

Waffle slab systems, in particular, can be considered as the anticipation of more recent voided bi-directional slabs as in the case of Cobiax® or U-boot® systems, which allow to reduce the weight of 30-40% (with respect to constant-thickness slabs), while almost maintaining the stiffness of solid slabs (with a decrease of about 10-15%). Fascinating and emblematic applications of similar systems of ribbed slabs in 60s and 70s can be found in [11-12]. In the case at issue, the regular distribution of columns and the resultant repeatability of the floor module allowed for a partially pre-fabrication of the elements, this shortening the time of construction and leading to a better control of the result in terms of quality of concrete and positioning of reinforcements.

Despite the great benefits in terms of overall weight and material saving allowed by the optimisation of the cross-section of bi-directional waffle slab systems, however, their structural performance in case of fire deserves to be deepened, since its particular shape leads to a faster increase of the temperature within the element with respect to constant-thickness slabs, due to the larger specific exposed face. In particular, this favors a faster increase of the temperature in the reinforcing bars and a more severe decrease of the overall bearing capacity during the exposure to a fire event.

Furthermore, for continuous slabs, indirect actions also play a major role due to the partially restrained thermal curvature, with the consequent increase of negative moments at the support. On the other hand, the possible increase of membrane compression due to the restrained thermal dilation of the slab is expected to be marginal for both the limited displacement involved and the limited restrain provide by the lateral flexural stiffness of columns. On the other hand, it is worth noting that the structural redundancy of continuous slabs provides important benefits to the fire performance thanks to the increased role played by negative bending moments at the supports, where the reinforcing bars under tension are at the cold side, thus experiencing a far lower decrease of the bearing capacity with respect to mid-span sections.

In the following, the numerical evaluation of the fire performance of a partially precast waffle slab system is described. Calculations are based on the information available about the structural layout, including geometry and reinforcement distribution, and material properties. The performance of the slab system under exposure to ISO834 fire curve is investigated through numerical analysis employing non-linear equivalent beam elements, where sectional non-linear temperature distribution and moment-curvature diagrams are evaluated a-priori and later

introduced in the numerical model. The investigation is aimed at evaluating the indirect actions caused by the temperature rise in such highly-statically-undetermined structural layout, and the actual safety as well as stress and deformation profiles of the slab members under different time exposures.

2. WAFFLE SLAB SYSTEM AT STUDY

The waffle slab system at study is inspired by a large residential/commercial complex designed and realised since the early 1970s in the Alpine region of Northern Italy. This complex was progressively built up to the late 1980s up to the current remarkable size with around 20 multi-storey blocks employing the same partially precast construction system. The complex, located in high mountain at an altitude of about 1400 m^2, found inspiration from the high-quote urbanistic nuclei devoted to the development of the ski sport market realised in that period in the alpine regions of Italy, France, and Switzerland, building touristic premises destinated to be occupied only in holiday time directly close to the ski lift facilities, so far destressing the urbanistic development of the historical valley villages.

The structure is made with a brutalist architectural style, with exposed reinforced concrete and large windows. All complexes are made with a multi-storey frame system coupled with wall cores, conceived to easily adapt to the steep level variation of the mountain. Each block is made by several parallel sub-blocks separated by an expansion joint and having elongated rectangular plan, strictly being it 15 m wide and with variable length up to 96 m, eventually even longer but jointed with an orthogonal further expansion joint. Columns have square cross-section with side of either 50 or 60 cm rotated by 45° with respect to the main directions of the building, and they are strictly distanced by an interaxis of 9 m in both directions. At each storey, a large square solid capital with side of 210 cm, itself oriented inclined by 45°, is placed to transfer the slab load to the column avoiding punching shear. The waffle slab is cast in continuity with the capitals with a strict modular square rib grid having 3 m of side. Hence, the slab ribs are strictly distanced by an interaxis of 3 m in both directions. Fig. 1 shows pictures of typical views of the buildings at study. A partially precast concrete system was used for the construction of these buildings, consisting in the prefabrication of the square slab plates 8cm thick before lifting them, positioning them over the modular mould, and completing the casting of the slab by pouring the 37cm deep trapezoidal ribs up to the top level of the slab plates, which were conglobated with special reinforcement welded to steel plates inserted during the production of the slab plates. A schematic drawing of the slab cross-section is shown in Fig. 2. To be noted that the slab is drawn with an assumed effective collaborative width of slab plate equal to 120 cm, whilst the modulus is always 3 m.

The original calculation report and shop drawings of the structural system were found in the archives of the province of Trento, containing full information about the conception of the structure and all structural details. An example of excerpt of the shop drawings is shown in Fig. 3, specifically describing the waffle slab reinforcement. Is it outstanding to note that the designer, Eng. Perini, employed in 1972 the Method of Limit States to proportion the structure, employing pioneering computational analysis to obtain the actions in the complex bi-directional structure, even accounting for the stress hardening of steel in the structural checks.

Concrete class C28/35 (cubic nominal characteristic strength of 35 MPa) and pioneering high-strength steel delivered in octagonal ribbed rebars equivalent to what will be later classified as class FeB44k steel (nominal characteristic yield strength of 440 MPa) was employed for the reinforcement. Traditional non-invasive testing techniques were employed to check the strength of concrete with rebound-hammer and the position of rebars with pacometre. The 160 rebound-hammer measurements carried out gave all results associated to at least one concrete class higher than what prescribed, with mean cubic strength evaluated to be 52.0 MPa. On the safe side, also in absence of destructive tests, the nominal strength is considered in the further analyses. Moreover, pacometric measurements allowed to confirm the position and the diameter of the designed rebars, although the concrete cover was measured to have variations larger than what typically allowed in modern construction. The design position of rebars was considered in the further analysis.

According to the specifications found in the calculation report of the original design, the concrete cover of rebars type A, B, and E is 30 mm from the bottom (and from the side for type A) concrete surface to the rebar centre; the cover of rebars type C, and D is 40 mm from the top concrete surface to the rebar centre, being these relatively small concrete covers representative of the typical praxis of the time. Correspondence between the letter code and the specific rebars is shown in Fig. 2. Moreover, the specific rebar diameter for each waffle slab grid element is attributed in Table 1. For the sake of brevity, the position of the 12 cross-sections analysed with different reinforcement arrangement (section S1 to section S12) is shown later when the numerical model is presented.
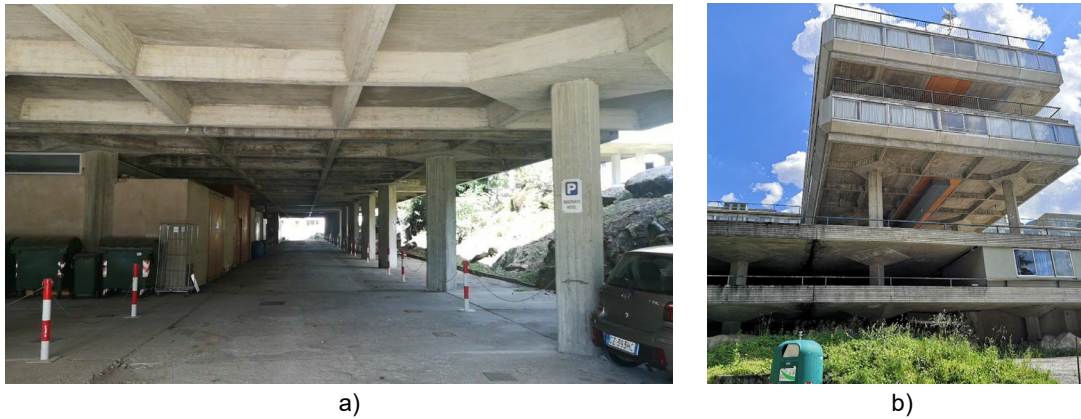
Figure 1: Structural system at study based on waffle slabs supported on square columns - a) view of a typical slab; b) view of a typical building
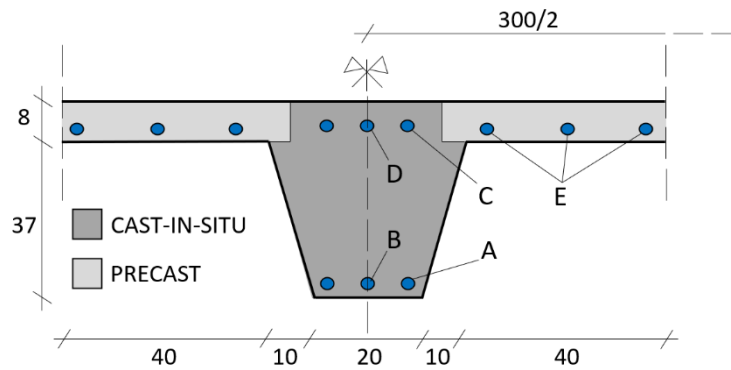

Figure 2: Cross-section of a slab rib with typical position of rebars
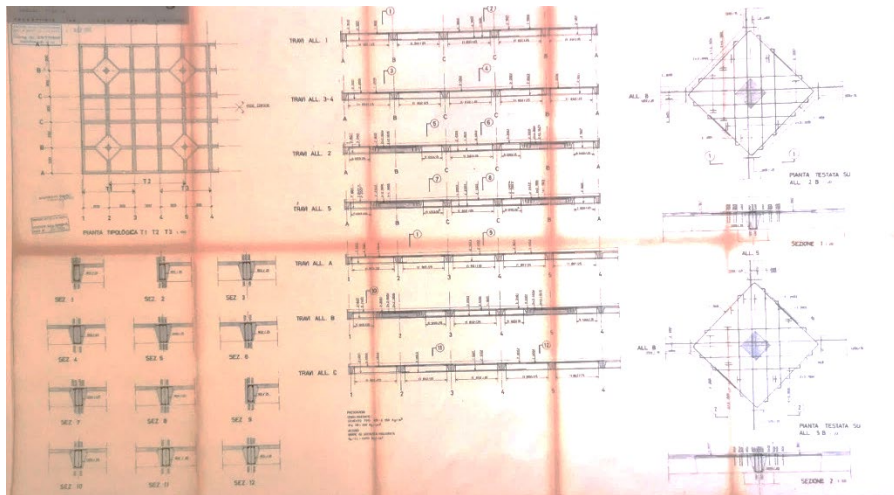
Figure 3: Excerpt from the original shop drawings dated 1972

Table 1: Reinforcement layout per each cross-section

POS	S1	S2	S3	S4	S5	S6	S7	S8	S9	S10	S11	S12
A	1Φ12	1Φ20	1Φ12	1Φ20	1Φ20	1Φ20	1Φ20	1Φ20	1Φ16	1Φ12	1Φ20	1Φ16
B	-	-	-	-	1Φ16	1Φ16	1Φ20	1Φ20	-	-	-	-
C	1Φ16	1Φ12	1Φ20	1Φ12	1Φ24	1Φ12	1Φ24+1Φ20	1Φ12	1Φ12	1Φ24	1Φ20	1Φ20
D	1Φ16	1Φ12	1Φ20	-	1Φ24	-	-	-	1Φ12	1Φ24	-	1Φ20
E	3Φ8	3Φ8	3Φ8	3Φ8	3Φ8	3Φ8	3Φ8	3Φ8	3Φ8	3Φ8	3Φ8	3Φ8

3. THERMAL MAPPING

To map the temperature distribution in the slab elements, a transient thermal analysis was carried out with the finite element software Straus7 [14] employing the nominal standard ISO834 temperature time history.

Following the instructions provided in Eurocode 2 [8], both convection and radiation thermal flues were considered in the surfaces of the elements, either exposed to fire (right) or to eternal temperature of 20 °C (left). The conductivity flux was evaluated by the finite element solver based on the non-linear thermal properties of concrete again described in [8], considering density, conductivity (curve 2), and specific heat (calcareous aggregates – 1.5% of base moisture). Possible spalling phenomena have not been taken into account.

It is to be noted that thermal modelling included not only the 370 mm thick structural depth, but also further 80 mm non-structural screed allowing for the installation of MEP systems in the apartments, due to its unsafe effect with regards to the increase of temperature in the structural concrete element. On the safe side from the thermal point of view, the physical properties of this non-structural sand-cementitious layer were set similar to those of the structural concrete. Moreover, not the whole slab modulus was modelled, but only half of it, thanks to the geometry around the vertical ais, and an upper slab portion limited to 600 mm since it was not relevant to do more due to the distance from the rib, and this mirrored cross-section was actually considered to be the structurally-collaborating slab part.

The thermal maps are shown in Fig. 4 for growing exposure times. As expected, the temperature rises rapidly in the exposed perimeter, concentrating the higher temperature in correspondence of the sharp corners, exposed from two sides. In the meantime, most of the top of the cross-section where the upper main reinforcement layer is placed remains at relatively low temperature.
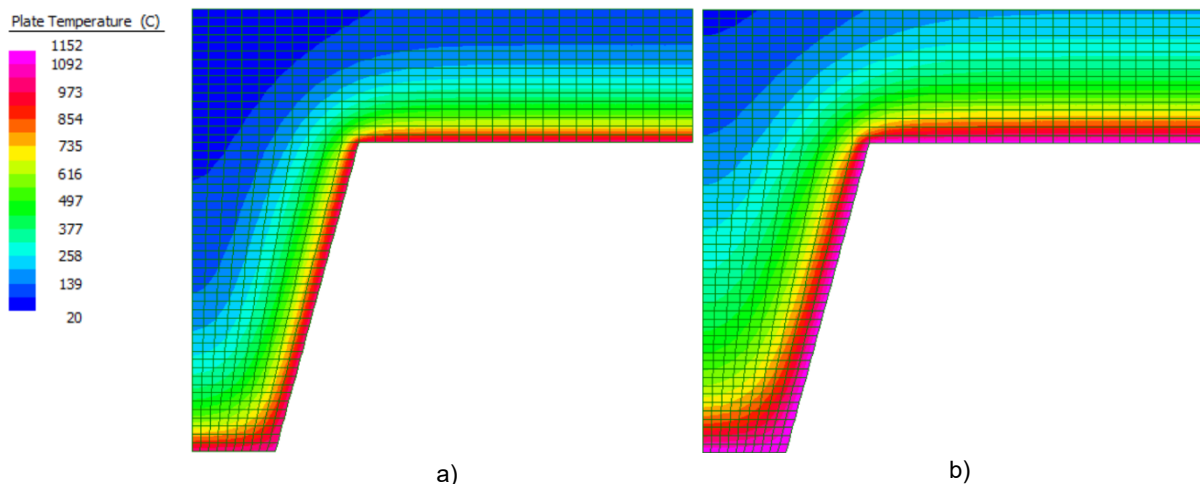

a)
b)

Figure 4: Thermal mapping of a slab modulus for exposure to ISO834 curve of a) 120 minutes, b) 240 minutes

4. THERMO-MECHANICAL CROSS-SECTIONAL ANALYSIS

The thermo-mechanical performance of the slab rib members was evaluated on the basis of a cross-sectional analysis [5,15-18] with the aim to check the demand over capacity ratio of the slab when exposed to fire. The material constitutive laws variable with temperature described in Eurocode 2 [8] were implemented in a self-written code in Mathcad 15 [19] following the nominal characteristic material strengths described above. It is reminded that the Eurocode 2 [8] constitutive law formulations consider implicitly the effect of transient thermal creep [20].

After having introduced the geometry of the elements, the algorithm solves the sectional equilibrium equations of translation and rotation, as shown in Eq. 1 and 2, respectively, under the assumption of plane sectional deformation. To be noted that the temperature in the slab evolves in a 2D plane, both along the bottom-top and the transverse directions. Formally, the problem should be solved by adopting a resolution algorithm considering a bi-dimensional problem. However, a simplified assumption was made, resulting in a much easier solution algorithm, where the slab cross-section was ideally divided into n = 11 stripes having same width along the outer-inner direction. The temperature distribution was then derived based on output adjusting and interpolating operations for each stripe, as shown in Fig. 5 for the single time exposure of 240 minutes. Finally, the problem was solved in pure bending following Eq. 1 and Eq. 2 by considering the n cross-sections in parallel. It is pointed out that this simplified

procedure allows to fully account for the self-equilibrated stress generated by the thermal strain in the direction of the procedure, as well as the resulting global sectional curvature and mean elongation, whilst it neglects this contribution in the transverse direction, which however is deemed not to mine the affordability of the results.

The problem is defined by four variables, two of which are defined by the eternal loads (N,M) and the remaining two of which by the strain diagram (ε_{ctop},χ). By imposing null the eternal axial load N (thus neglecting possible axial load distribution induced by the lateral stiffness of the columns) and by setting specific progressive values of the curvature χ, the system of two equilibrium equations can be solved finding out the two remaining variables, both associated to the strain diagram per each imposed curvature. This operation is carried out through the numerical solution techniques implemented into the software.

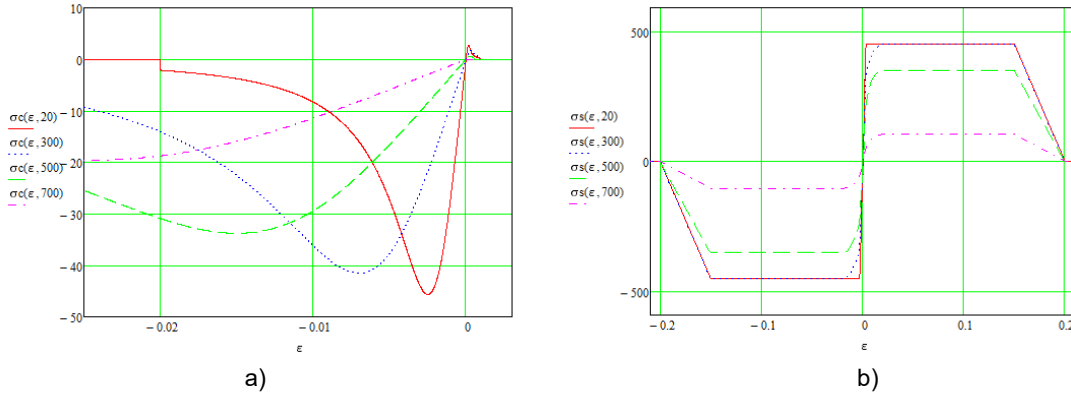a)   b)

Figure 5: Material constitutive laws in tension (+) and compression (-) as a function of the temperature following Eurocode 2 [8]: (a) concrete C28/35; (b) steel FeB44k (Stress in MPa)

$$N(\varepsilon_{ctop},\chi) = \sum_{i=1}^{n}\left(\int_0^H \sigma_c\left(\varepsilon(y,\varepsilon_{ctop},\chi) - \varepsilon_{c\theta}(\Delta\theta_n(y)),\Delta\theta_n(y)\right)\frac{b(y)}{n}dy\right) \\ + \sum_{i=0}^{n_s}\sigma_s\left(\varepsilon(y_i,\varepsilon_{ctop},\chi) - \varepsilon_{s\theta}(\Delta\theta(y_i)),\Delta\theta(y_i)\right)A(y_i)$$ (1)

$$M(\varepsilon_{ctop},\chi) = \sum_{i=1}^{n}\left(\int_0^H \sigma_c\left(\varepsilon(y,\varepsilon_{ctop},\chi) - \varepsilon_{c\theta}(\Delta\theta_n(y)),\Delta\theta_n(y)\right)\frac{b(y)}{n}(y - y_g)dy\right) \\ + \sum_{i=0}^{n_s}\sigma_s\left(\varepsilon(y_i,\varepsilon_{ctop},\chi) - \varepsilon_{s\theta}(\Delta\theta(y_i)),\Delta\theta(y_i)\right)A(y_i)(y_i - y_g)$$ (2)

where:
N is the external axial load;
M is the external bending moment;
ε is the total longitudinal strain as a function of y;
ε_{ctop} is the longitudinal strain of the top concrete chord;
χ is the sectional curvature;
σ_c is the concrete longitudinal stress;
σ_s is the steel longitudinal stress;
$\Delta\theta$ is the temperature gradient;
n_s is the number of steel rebar levels;
H is the total depth of the concrete cross-section;
y is the coordinate through the thickness of the element starting from the eternal side;
n is the number of stripes in which the cross-section is divided;
$\varepsilon_{c\theta}$ is the thermal strain of concrete as defined by EC2 law;
$\varepsilon_{s\theta}$ is the thermal strain of steel as defined by EC2 law;
b is the chord width of the concrete cross-section;
y_g is the centre of gravity of the idealised cross-section;
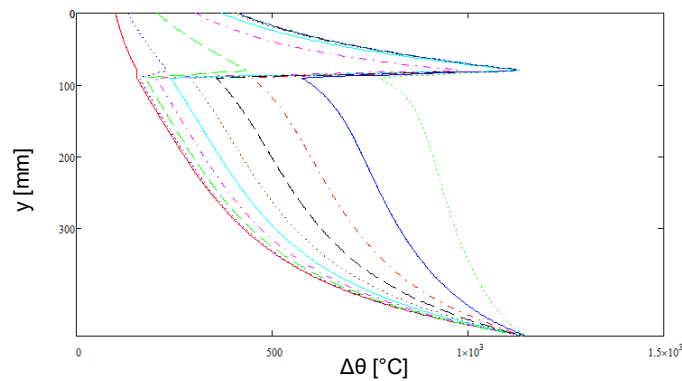A is the area of the steel rebars for a specific level.

Figure 6: Temperature functions for each of the *n* stripes in which the cross-section is discretised for the single exposure of 240 minutes

The resulting non-linear moment-curvature diagrams are collected in Fig. 7 for the three considered exposure time windows. It can be clearly observed that there is a generalised reduction of strength with the exposure time, as well as a stretch in the strain ais due to the increased deformability of the cross-section. Nevertheless, the temperature effect over the strength reduction is not symmetric: it can be clearly observed that the strength reduction for hogging moment (sign "+" in Fig. 7), mainly depending upon the degradation of the bottom concrete layer in compression, is much less severe than the one for sagging moment (sign "-" in Fig. 7), which depends upon the degradation of the bottom steel rebars highly exposed to the temperature gradient. Indeed, the resistance for sagging moment becomes practically negligible for an exposure of 240 minutes. Moreover, it can be observed that, whilst the moment-curvature diagrams for cold condition all pass through the axes at their origin, an increasing sagging curvature is imposed to the cross-section for null moment, induced by the thermal curvature generated by the temperature gradient differential between exposed and unexposed sides.
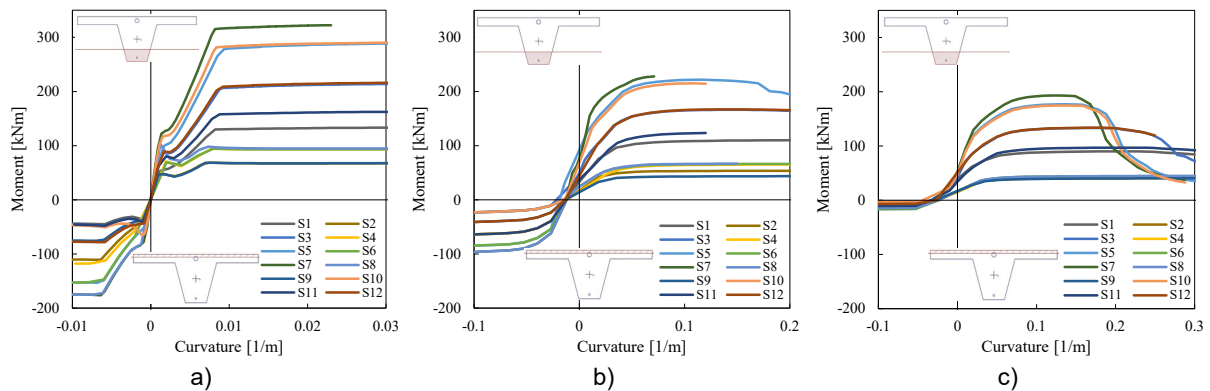

Figure 7: Non-linear moment-curvature diagrams calculated for the different reinforcement arrangements of the considered cross-sections under exposure time of a) 0 minutes, b) 120 minutes, c) 240 minutes (strain axes not on same scale)

4. NUMERICAL FINITE ELEMENT ANALYSIS

Numerical models were set to analyse the effect of fire to the waffle slab system. To this aim, it is recalled that the slab is strictly 15m wide (3 moduli between the columns and 1 cantilevering modulus per each side), but having variable number of moduli in length, from a minimum of 5 (square configuration) to a maximum of up to 32 (see also the general structural model in Fig. 8a, used for global structural check purposes). In order to encompass all the critical configurations, two models were developed, one consisting of a square arrangement (5 moduli x 5 moduli) shown in Fig. 8b, and one consisting of a rectangular arrangement (5 moduli x 8 moduli). The square and compact rectangular configurations maximise the sagging (positive) and hogging (negative) bending moment, respectively, and are therefore deemed to represent extreme conditions for all slabs.
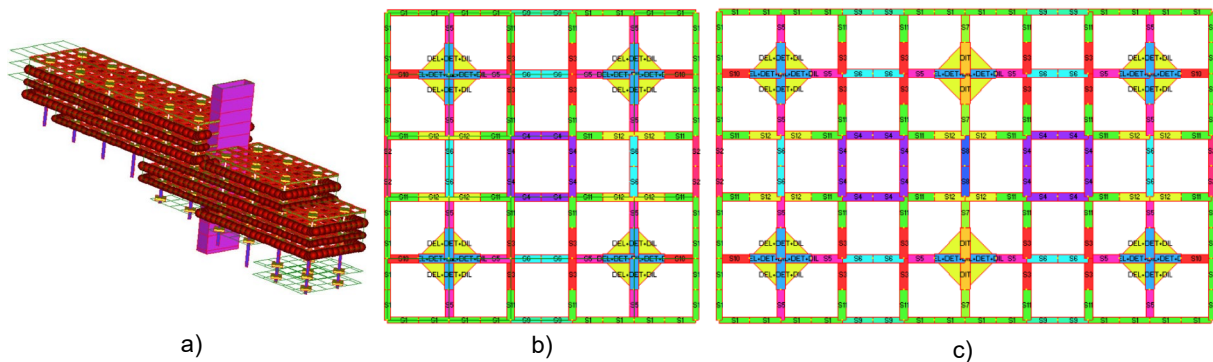
Figure 8: Numerical models – a) general model of a typical building unit, b) single bay model, c) double bay model

Figs. 8b and 8c also contain the denomination and the map of the different cross-sections attributed to the different grid members, all modelled with beam elements. Perfect vertical support was considered for all the nodes associated to the column centres of mass. Moreover, to a single one of these nodes was attributed lateral restraint in both horizontal directions and torsional rotation restraint. Thus, the stiffening contribution of the column deformation is neglected in the models, simulating an external simple-support static scheme and the absence of indirect axial compression actions caused by partial restraint of beam elongation. The non-linear moment-curvature diagrams previously evaluated were attributed to the structural model developed again in Straus7 environment [14]. To be noted that the square capitals were also modelled with equivalent beam elements, to which non-linear moment-curvature diagrams were also attributed based on the actual reinforcement layout located at the interface with the column. Since this reinforcement is fully located in the top part of the solid thick capital, which is assumed to be only slightly affected by the exposure to the fire, their moment-curvature diagrams were not modified in the analysis considering fire exposure. The solver automatically distributes plasticity along the beam elements during the analysis through embedded discrete Gauss-Lobatto integration points. The effect of the thermally-induced curvature is taken into account automatically, and hence the flexural indirect actions are accounted for. The loads are included diffusely in the structural models. In particular, the structural self-weight of the waffle ribs is attributed to the beam elements; the non-structural dead weight induced by windows and bow windows (270 kg/m) is attributed on the peripheral beam elements as a distributed load; the structural dead weight due to waffle precast solid plates, as well as the non-structural distributed dead loads (200 kg/m^2) and live load (60 kg/m^2 in the pertinent exceptional combination), are modelled through load patches plate elements supported on all sides.

Non-linear static analysis including mechanical non-linearity was carried out by attributing an increasing value of distributed live loads up to failure (non-convergency). Analyses at cold condition (exposure to 0 minute), 120 minutes, and 240 minutes of exposure to the nominal standard ISO834 curve were carried out. Fig. 9 and Fig. 10 show the state of bending action and deformation of the square and rectangular slab, respectively, in the load condition associated with exceptional load combination following Eurocode approach and for both cold condition and 120 minutes of exposure to fire. The analysis on both models assuming 240 minutes of fire exposure did not converge even at the first load step, meaning the slabs are not able to sustain even only their dead weight.

It can be observed that the exposure to fire causes the slab to deform remarkably towards the fire compartment below, passing from a maximum displacement of 40 mm in cold condition to 247 mm at 120 minutes of exposure for the square model, and from 34 mm in cold condition to 197 mm at 120 minutes of exposure for the rectangular model. It is recalled that the deformed shape of the single bay square slab model is not symmetric despite the geometry due to asymmetry in the reinforcement layout of the rib members. Both models present for 120 minutes of fire exposure an overstrength factor of around 1.9 with respect to the live load (failure is expected at around 115 kg/m^2 of live load), much lower than that associated to the cold condition. This trend is also depicted in Fig. 11 resuming the capacity over demand ratii from the non-linear static analyses.

Regarding the bending moment distribution, it can be observed that the exposure to fire tends to reduce the maximum sagging (positive) bending moment in the centre of the slab, as a result of the redistributive effect induced by the non-linear combination of damage distribution and indirect actions caused by the thermal curvature. This redistribution is however thresholded by the attainment of rebar plasticisation in the rib members conveying in the capitals, subjected to strong hogging (negative bending moment).

Figure 9: Results of non-linear static analysis on single bay model in terms of displacement profile and bending moment distribution under fire load combination at different exposures – a) 0 minutes, b) 120 minutes
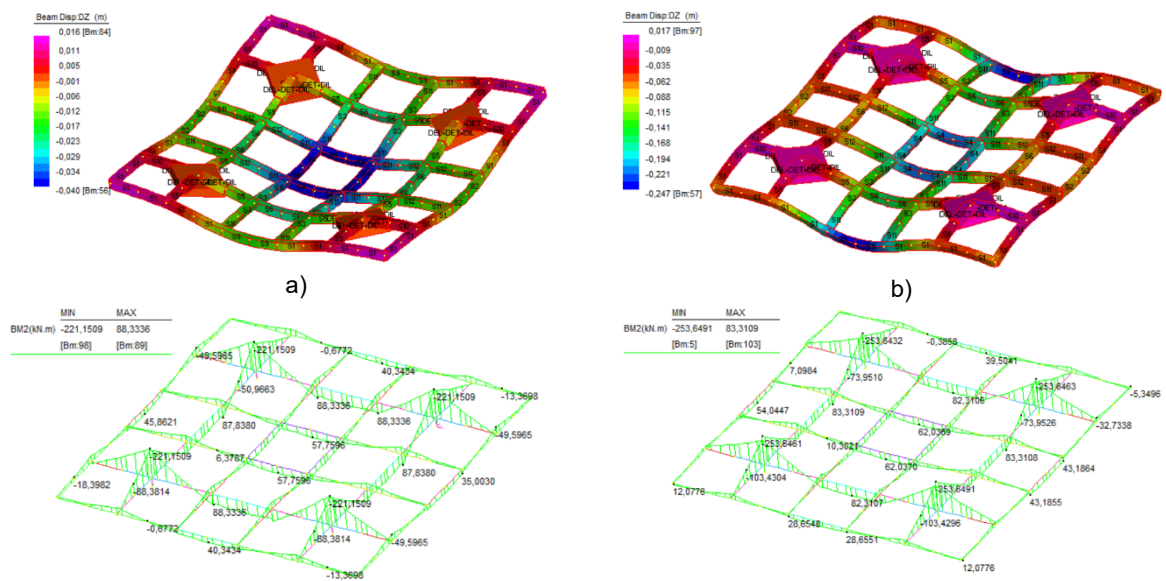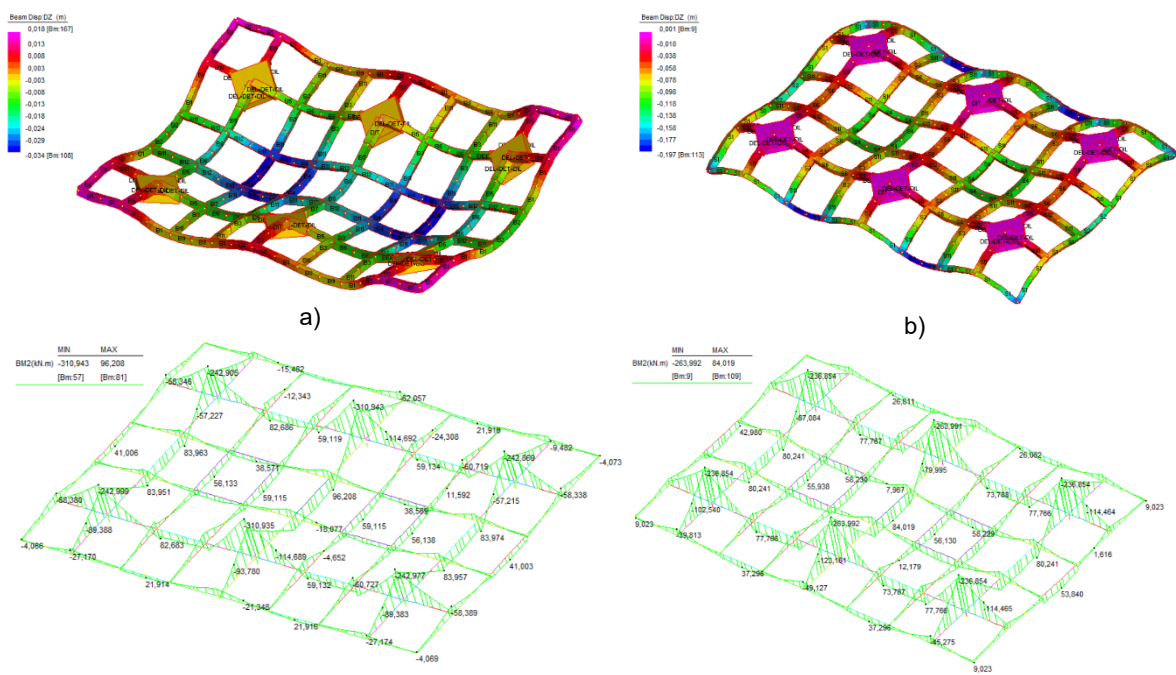

Figure 10: Results of non-linear static analysis on double bay model in terms of displacement profile and bending moment distribution under fire load combination at different exposures – a) 0 minutes, b) 120 minutes
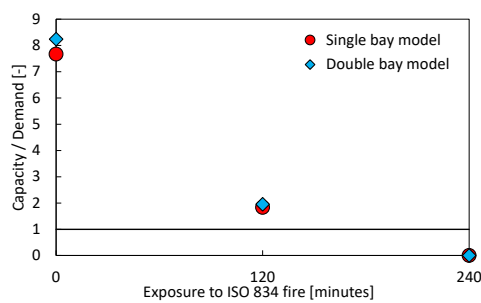

Figure 11: Capacity over Demand multiplier of the live load for different fire exposure time

422

5. CONCLUSIONS

The advanced calculation method employed to investigate the waffle system at study allowed to characterise its structural behaviour, identifying its performance under exceptional load combination for different fire exposure times, as well as failure modes and overstrength factors. A classical simplified calculation method based on the actions coming from elastic modelling would have attributed to the slab a resistance class R60, mainly due to the strong damaging of the bottom rebars acting in sagging (positive) moment, whilst the non-linear static analysis allowed to account for the coupled effects of mechanical non-linearities, thermal curvature, and moment redistribution effects, thus characterising a resistance class R120, also showing that however these effects are way far from attributing to the structure the ability to get to R240. Further advances of this work are planned to be carried out by analysing further intermediate fire exposure time steps, by implementing in the model the effect of the columns and of the partial axial restraint component, and by proposing an engineering interpretation of the results based on the plastic hinge method.

REFERENCES

[1] Usmani, A. S.; Chung, Y. C. & Torero, J. L. (2003). *How did the WTC towers collapse: a new theory*, Fire Safety Journal, vol. 38, no. 6, p. 501-533.

[2] McKenna, S. T.; Jones, N.; Peck, G.; Dickens, K.; Pawelec, W.; Oradei, S.; Harris, S.; Stec, A. A. & Hull, T. R. (2019). *Fire behaviour of modern façade materials – Understanding the Grenfell Tower fire*, Journal of Hazardous Materials, vol. 368, p.115-123.

[3] Mlakar, P. F.; Dusenberry, D. O.; Harris, J. R.; Haynes, G.; Phan, L. T. & Sozen, M. A. (2005). *Description of structural damage caused by the terrorist attack on the pentagon*, Journal of Performance of Constructed Facilities, vol. 19, no. 3, p. 197-205.

[4] Annerel, E.; Taerwe, L.; Merci, B.; Jansen, D.; Bamonte, P. & Felicetti, R. (2013). *Thermo-mechanical analysis of an underground car park structure exposed to fire*, Fire Safety Journal, vol. 57, p. 93-106.

[5] Dal Lago, B. & Tucci, P. (2023). *Causes of local collapse of a precast concrete industrial roof after a fire event*, Computers & Concrete, vol. 31. no. 5.

[6] fib (2013). *Model Code 2010*. fib Bulletin No. 66, Ernst & Sohn.

[7] EN 1992-1-1 (2004). Eurocode 2 - Design of Concrete Structures - Part 1-1: General Rules and Rules for Buildings, European Committee for Standardization.

[8] EN 1992-1-2 (2005). Eurocode 2 - Design of Concrete Structures - Part 1-2: General Rules - Structural Fire Design, European Committee for Standardization.

[9] ACI 318M-14 and ACI 318RM (2015). *Building Code Requirements for Structural Concrete and Commentary on Building Code Requirements for Structural Concrete*. Report by ACI Committee 318, ACI-American Concrete Institute (Farmington Hills, MI-USA).

[10] NTC2018 - *Italian Technical Provisions for Constructions* - Ministerial Decree January 17, 2018, Italian Ministry of Infrastructures and Transportation (in Italian).

[11] Sorace, S. & Terenzi, G. (2013). *Structural assessment of a modern heritage building*, Engineering Structures, vol. 49, p.743-755.

[12] Halpern, A. B.; Billington, D. P. & Adriaenssens, S. (2013). *The ribbed floor slab systems of Pier Luigi Nervi*, Journal of the International Association for Shell and Spatial Structures, vol. 54, no. 176-177, p. 127-136.

[13] Buchanan, A. H.; Abu A. K. (2017). *Structural Fire Design for Fire Safety*. Edition 2. Wiley, 440 p.

[14] G+D Computing (2010). *Using Strand7 (Straus7) - Introduction to the Strand7 finite element analysis system system*, Ed. 3, Strand7 Pty Limited, Sidney, Australia.

[15] Riva, P. & Franssen, J. M. (2008). *Non-linear and plastic analysis of RC beams subject to fire*. Structural Concrete, vol. 9, no. 1, p. 31-43.

[16] Bamonte, P.; Kalaba, N. & Felicetti, R. (2018). *Computational study on prestressed concrete members exposed to natural fires*. Fire Safety Journal, vol. 97, p. 54-65.

[17] Felicetti, R.; Gambarova, P. G. & Meda, A. (2009). *Residual behaviour of steel bars and R/C sections after a fire*. Construction and Building Materials, vol. 23, p. 3546-3555.

[18] Dal Lago, B.; Nicora, A.; Tucci, P. & Panico, A. (2023). *Precast concrete industrial portal frames subjected to simulated fire*, Building for the Future: Durable, Sustainable, Resilient, Ed. A. Ilki, 2. doi:10.1007/978-3-031-32511-3_2.

[19] Parametric Technology Corporation (2010). Mathcad release 15.0, Needham, MA, USA.

[20] Franssen, J.M. & Gernay, T. (2012). *A formulation of the Eurocode 2 concrete model at elevated temperature that includes an explicit term for transient creep*. Fire Safety Journal, vol. 51, p. 1-9.

A SOFTWARE APP FOR ASSESSING THE FIRE RESISTANCE
OF REINFORCED CONCRETE BEAMS

Gabriela B. M. L. Albuquerque a,*; Valdir P. Silva b; Alio E. Kimura c; Johnny A. B. Fontana d

ABSTRACT

The structural elements must be checked according to a fire resistance rating (R) established in regulations. Based on the European fire standard, Brazil's standard presents tabulated data for checking reinforced concrete (RC) beams. Although simple to use, the tabular method offers only four solutions for each pre-set R, with demands to raise this ceiling. Moreover, the Brazilian tables do not follow the Eurocode strictly, with the maximum temperature for longitudinal reinforcements being 500°C. The purpose of this research project was thus to find an alternative design method offering more solutions, which was also safe and easy to use. More than 2300 RC beams were studied, through a finite element software. The findings of these thermo-structural analyses underpinned the development of the TRFVIG application (app). Just as practical as the tabular method, this software allows more accurate design for beams in fire. The goal of this paper is to present details of the study proving the accuracy of the app. As noted in some examples, the TRFVIG app may indicate more economical fire resistances, compared to the tables. Thermal analyses and fire-specific software are not necessary for using the app, making it a feasible alternative for most engineers.

Keywords: fire; reinforced concrete; beam; design; app.

---

a,* Post-doctoral Researcher, University of São Paulo, Brazil. Departamento de Engenharia de Estruturas e Geotécnica da Escola Politécnica da USP. Avenida Professor Almeida Prado, travessa 2, n 271. Cidade Universitária, Edifício da Engenharia Civil. 05508-900 São Paulo – SP. BRASIL. +55 11 3091 5367 (gabriela.lins@usp.br) – Corresponding author.

b Professor, University of São Paulo, Brazil (valpigss@usp.br).

c Managing Partner, TQS Informática, Brazil (alio@tqs.com.br).

d Civil Engineer, TQS Informática, Brazil (johnny@tqs.com.br).

1. INTRODUCTION

The behavior of structural elements at high temperatures must be verified for a fire resistance rating (R), which is established by standards and codes. Developed on the basis of European Standard EN 1992-1-2 [1], Brazil's ABNT NBR 15200 Standard [2] presents tabulated data for checking reinforced concrete beams. If the tabular method is used, designing beams for exposure to high temperatures is quite simple. However, this method is very restrictive for use in project, as it offers only four solution options for each pre-set standard fire resistance level, imposing limits on the activities of engineers. There was a demand for this figure to be increased. Moreover, although the ABNT NBR 15200 [2] tables are based on EN 1992-1-2 [1], they do not follow its recommendations strictly, with the maximum temperature for longitudinal reinforcements being 500 °C.

The purpose of this research was thus to find an alternative design method offering more solutions, which was also safe and easy to use. Consequently, more than 2300 reinforced concrete beam cross-section models were studied, with different widths, heights, covers and reinforcement arrangements (with varying diameters, number of layers and moment positions, both positive and negative) through a software based on the finite element method. Presented in full in Albuquerque [3-4] and Silva [5], the findings of these thermo-structural numerical analyses underpinned the development of the TRFVIG application (app). This was made available to members of the Brazilian Concrete Institute (IBRACON) and the Brazilian Structural Engineering and Consulting Association (ABECE), as a technical and scientific contribution to the fire prevention field. Just as practical as the tabular method, this software allows more accurate design of beams in fire situation. The goal of this paper is to present details of the study proving the accuracy of the TRFVIG app.

2. METHOD

The fire resistance results provided by the TRFVIG app come from an alternative method for designing reinforced concrete beams in a fire situation, called the Graphical Method (Albuquerque; Silva and Rodrigues [6]). This method was developed on the basis of numerical analyses performed by the Swedish Temperature Calculation and Design v. 5 – TCD software [7]. The TCD software performs transient bi-dimensional thermo-structural analyses using the finite element method. This section of the paper presents the graphical method, starting with the approach used in the $M_{Rd,fi}$ parameter validation study, which represents the design resistance to bending moment of the cross-section of a reinforced concrete beam exposed to high temperatures. The $M_{Rd,fi}$ parameter consists of the main graphical method variable.

2.1 Resistance to bending moments analysis

Since the fire resistance to bending moment ($M_{Rd,fi}$) obtained by the TCD is the main variable used for conceiving the graphical method and consequently the TRFVIG app, its validation was very important. For this, some reinforced concrete beam cross-sections were adopted so that their respective resistances to bending moments were determined based on different methods and then compared to the TCD values. In Albuquerque; Silva and Rodrigues [6], several procedures were analyzed to calculate the resistant bending moments of these beams subjected to high temperatures and it was found that all procedures lead to very close results. Table 1 summarizes the findings for some cross-sections selected as representative.

For the thermal analysis of the four section models (a – d) and the five procedures, the TCD [7] software was used. The heating rate compliant with ISO 834 Standard fire [8] was applied on three faces (sides and bottom). For safety reasons, the face not exposed to fire was considered adiabatic (Figure 1). The physical and thermal parameters of the concrete variable with the temperature – thermal conductivity ($\lambda_{c,\theta}$), specific heat ($c_{p,\theta}$) for moisture content at 1.5%, and density ($\rho_{c,\theta}$) with ρ = 2400 kg/m^3 at ambient temperature, compliant with ABNT NBR 6118 [9] – were determined by the equations shown in [1] and [2]. A coefficient of heat transfer by convection (α_c) was adopted equal to 25 W/(m^2 °C), and the resultant emissivity (ε_r) on faces exposed to fire is equal to 0.7, the values recommended in [1] and [2]. The domain was discretized with a mesh of four-node rectangular elements with sides measuring 0.005 m. A time step was assumed equal to 0.002 h. From these input data, the Super Tempcalc thermal module of the TCD determines the results: temperature field and isotherms, both as a function of the time of exposure to fire (Figures 2 and 3). The design resistant moments ($M_{Rd,fi}$) were determined from the thermal field.

Table 1 – Results of resistances to bending moments in fire, calculated using different methods, for the cross-sections of reinforced concrete beams a – d.

Representation of analyzed cross-sections [*]

a	b	c	d
40 cm c = 2.5 cm A_s = 2ϕ20 mm 19 cm	40 cm c = 2.5 cm A_s = 3ϕ10 mm 14 cm	60 cm c = 3.0 cm A_s = 2ϕ12.5 mm 35 cm	50 cm c = 4.0 cm A_s = 2ϕ25 mm 30 cm

Design resistance to bending moment in fire ($M_{Rd,fi}$) [kN m]

Section	Fire exposure time [min]	1 Direct result of TCD	2 Calculation based on mean strength	3 Calculation based on mean temperature	4 500 °C isotherm method	5 Advanced method
a	90	45.24	45.25	45.38	45.26	44.12
b	60	37.42	38.44	38.65	35.40	37.38
c	120	57.47	58.39	58.14	53.58	56.87
d	120	138.26	138.29	138.89	138.23	135.88

[*] Stirrups with diameter of 5 mm, f_{ck} = 25 MPa and f_{yk} = 500 MPa.
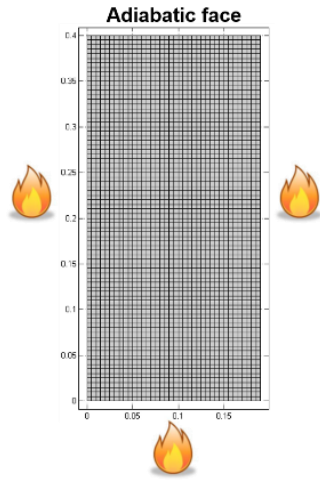

Figure 1: Beam model adopted for thermal analysis in TCD.
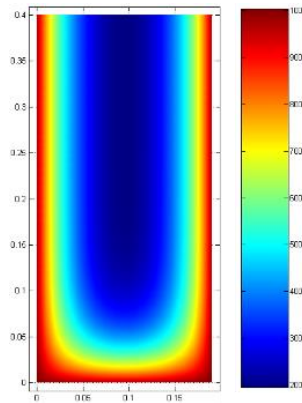

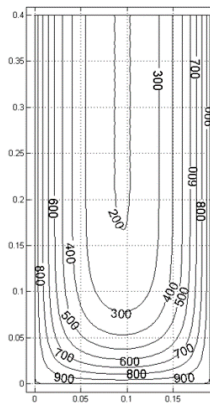Figure 2: Temperature fields for the 90 min interval of exposure to fire.

Figure 3: Isotherms for the 90 min interval of exposure to fire.

Column 1 of Table 1 presents the results obtained through the CBeam tool of the structural module of the TCD (called Fire Design), which calculates the resistance to bending moment in fire of the section discretized with finite element mesh, based solely on the equilibrium of forces, as shown in Figures 4 and 5. The software considers the full plastic strain of both concrete and steel, and does not impose limit strains for the materials. For the calculation of the resultant force in the reinforcement (Equation 1), the TCD determines the temperature on the axis of each bar and, depending on this, the respective steel strength reduction coefficient.

$$F_{sd,fi} = \frac{f_{yk}}{\gamma_{s,fi}} \sum_{i=1}^{n} k_{s,\theta i} A_{si}$$

(1)

where A_{si} is the cross-sectional area of reinforcing bar i [cm²]; $F_{sd,fi}$ is the design resultant force in the reinforcement in fire [kN]; f_{yk} is the characteristic tensile strength of reinforcing steel at ambient temperature [kN/cm²]; $k_{s,\theta i}$ is the reduction coefficient of the strength at temperature θ of steel bar i [non-dimensional] and $\gamma_{s,fi}$ is the partial safety factor for steel strength in fire [non-dimensional].

For the resultant force in the compressed concrete block (Equation 2), the axis temperature is determined for each finite element and then the respective material strength reduction coefficient, as a function thereof.

$$F_{cd,fi} = \alpha_{fi} \frac{f_{ck}}{\gamma_{c,fi}} \sum_{j=1}^{m_{fi}} k_{c,\theta j} \, A_{cj} \tag{2}$$

where A_{cj} is the area of compressed concrete finite element j [cm²], $F_{cd,fi}$ is the design resultant force in the compressed concrete area of the cross-section in fire [kN], f_{ck} is the characteristic compressive strength of concrete at ambient temperature [kN/cm²], $k_{c,\theta j}$ is the reduction coefficient of the strength at temperature θ of compressed concrete finite element j [non-dimensional], $\gamma_{c,fi}$ is the partial safety factor for concrete strength in fire [non-dimensional] and α_{fi} is the reducer of design compressive strength of concrete in fire [non-dimensional].
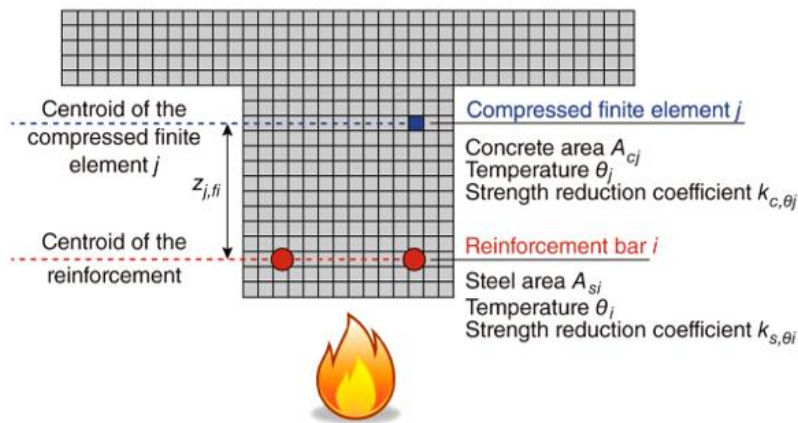
Figure 4: Reinforced concrete section discretized by a finite element mesh.
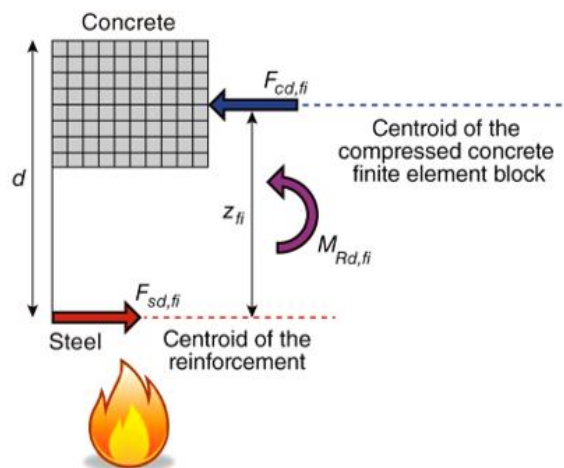
Figure 5: Equilibrium of resultant forces in the section.

When the resultant force in the compressed concrete block is equal to the resultant force in the reinforcement, i.e., when equilibrium is reached (Equation 3), the TCD determines the resistance to bending moment of the section exposed to fire (Equation 4), multiplying the resultant force in each compressed finite element by its respective lever arm.

427

$$F_{cd,fi} = F_{sd,fi} \qquad (3)$$

$$M_{Rd,fi} = \alpha_{fi} \, \frac{f_{ck}}{\gamma_{c,fi}} \sum_{j=1}^{m_{fi}} k_{c,\theta j} \; A_{cj} \; z_{j,fi} \qquad (4)$$

where $M_{Rd,fi}$ is the design value of resistance to the bending moment of the section in fire [kN cm] and $z_{j,fi}$ is the distance of the centroid of compressed finite element j from the horizontal line that goes through the centroid of the reinforcement in fire [cm].

It is noteworthy that the TCD software [7] performs these calculations on input data. The following factors are adopted in this paper: the characteristic compressive strength of the concrete (f_{ck}) is 25 MPa and 500 MPa for tensile steel (f_{yk}); strength partial safety factors ($\gamma_{c,fi}$ and $\gamma_{s,fi}$) at 1.0 for both materials in a fire situation and the reducer of the design value of the compressive strength of the concrete in fire (α_{fi}) is 1.0, by [1] and [2]; the reduction coefficients of the strengths due to high temperatures ($k_{c,\theta}$ and $k_{s,\theta}$) accepted are also compliant with [1] and [2].

In column 2 of Table 1, the moments were found using the recommendations in the Brazilian ABNT NBR 15200 Standard [2]. In one of the hypotheses of its simplified method, this standard states that resistant internal forces and moments in fire may be calculated by adopting for the materials the "high temperatures mean mechanical strength" and that this average can be obtained by evenly distributing the total loss of mechanical strength by the heating of the materials throughout the compressed part of the concrete section and the total reinforcement. Comparing the method proposed by the TCD [7] to that in the Brazilian Standard [2] leads to the conclusion that the software adopts a more refined calculation procedure, once it applies point-to-point strengths values instead of mean strengths.

For column 3 of Table 1, a simplification of the recommendations in ABNT NBR 15200 [2] was adopted. The authors [6] felt that it would be easier to work with mean temperatures instead of mean mechanical strengths. In other words, mean temperatures are determined by strips, then the respective reduction coefficients of the mechanical strengths of concrete due to fire exposure and, finally, the mean strengths of the section compressed area would be found. As seen in the results, when starting from either the mean temperature (simplified calculation hypothesis) or the point-to-point strength (TCD [7]), similar values are found. Therefore, the recommendation in the Brazilian Standard may possibly be replaced by that of the mean temperature, or indicate it as an alternative.

In column 4, the 500°C isotherm method was used, indicated in the EN 1992-1-2 [1]. The method simulates the heated concrete strength decrease from the reduction of its resistant area. The discarded region is where the temperature in the concrete is higher than 500 °C. The reduced section is surrounded by the 500°C isotherm and, according to the hypothesis adopted in the method, the characteristic compressive strength of concrete in this region is the same as at ambient temperature, i.e., in the calculations, the reduction coefficient of the strength of this material due to high temperatures is disregarded.

According to the European standard, the fire resistance to bending moment may be determined from the conventional calculation methods, that is, by the balance of forces in the section, applying the reduction coefficients of the steel strength. To do so, the temperature on the axes of the bars must be determined. Although strength reduction is considered only in steel, when calculating the resultant forces in both materials, both the strength partial safety factors and the reducer of the design value of the compressive strength of the concrete should be applied to the fire situation.

Finally, in column 5, an advanced analysis method was used. In order to evaluate the resistance to bending moment values calculated by simplified methods, additional analyses were performed using the FNC-FIRE computational procedure developed by Klein Júnior [10], based on the guidelines in Annex B.3 of EN 1992-1-2 [1]. In this method, the beam section is discretized in a fiber matrix, subjected only to uniaxial tensile or compressive stresses. From previously calculated temperature fields, the temperature in the center of each fiber is determined using two-dimensional linear interpolation. The thermomechanical properties of each fiber, as a function of its temperature, are calculated according to the guidelines of [1].

The next step is the calculation of resistant internal forces and moments of the section ($N_{Rd,fi}$ – design value of the axial force in fire and $M_{Rd,fi}$ – resistance to bending moment in fire) for a given axial strain pair ε_0 in the center of the stresses and $1/r$ curvature. Bernoulli's hypothesis is assumed for the total specific linear strain (ε_{tot}), in which the section remains plane after thermal and mechanical strains. For the determination of the specific mechanical strains (ε), the thermal strains (ε_{th}) are deducted from the total specific linear strain ε_{tot}. Several $N_{Rd,fi}$ and $M_{Rd,fi}$ pairs may be calculated by varying the ε_0 and $1/r$ parameters. Joining the points of the same curvature $1/r$ gives the $N_{Rd,fi}$-$M_{Rd,fi}$ diagram. Interpolating a given applied axial force in fire $N_{Sd,fi}$ for each curvature $1/r$, gives the moment-curvature graph. For simple beam bending, $N_{Sd,fi}$ is considered as 0. The FNC-FIRE does not limit values for section deformations. The moment-curvature graph shows the maximum value of the resistance to bending moment of the section and the drop in its value as the curvature increases. This decrease is due to the depletion of the strength of materials to large deformations, represented by the descending branch of the stress-strain curves for steel and concrete given by [1].

For design purposes, the results using both the simplified methods and a more advanced method were very close (see Table 1). Thus, the determination of the resistance to bending moment in fire ($M_{Rd,fi}$) with the aid of TCD [7] is justified for the continuation of this research project, as carrying out these calculations manually for so many cases of beams adopted for the construction of the alternative design method would be impracticable.

2.2 Results

The software TCD [7] provides the design resistance to the bending moment of a given heated section through graphs, which relate these values to the fire exposure time. Another graph provided by the software has two curves, shown in Figure 6. The solid line indicates the relationship between the design resistance to bending moment in fire and the design resistance to bending moment in fire determined for the initial temperature (ambient, at 20°C), respecting the fire exposure time. The dotted line shows the relationship between the design resistance to bending moment in fire and the design resistance to bending moment at ambient temperature, calculated without imposing limit strains on either material, as a function of the fire exposure time.
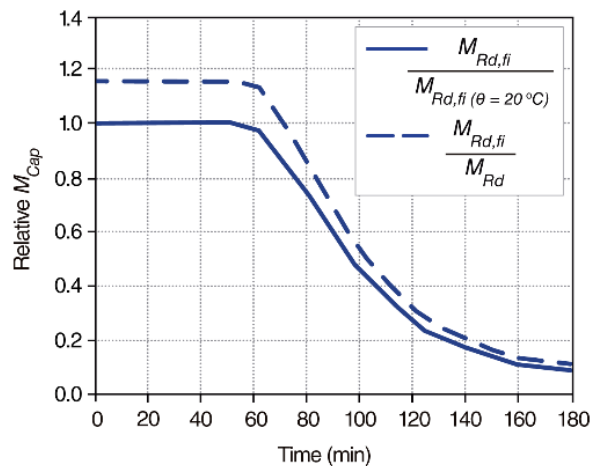
Figure 6: Curves of relative resistances to bending moments, as a function of the fire exposure time, provided by the TCD.

This research project used the dotted line curve, which provides the μ parameter, as shown in Equation 5, for constructing the alternative design method. Safety is assured when $M_{Ed,fi} \leq M_{Rd,fi}$. Consequently, by admitting $M_{Ed,fi} = M_{Rd,fi}$ into *parameter μ*, it is possible to find the maximum time for fire resistance (TRF) of the structural element. Equation 5 thus becomes Equation 6.

$$\mu = \frac{M_{Rd,fi}}{M_{Rd}} \tag{5}$$

$$\mu = \frac{M_{Ed,fi}}{M_{Rd}} \tag{6}$$

where M_{Rd} is the design resistance to the bending moment of the section at ambient temperature [kN cm]; $M_{Ed,fi}$ is the design applied bending moment of the section in fire [kN cm] and μ is the relative moment [non-dimensional].

With an extremely short duration and a low probability of occurring during the useful life of a construction, thermal action may be treated as an accidental action. Consequently, calculation of applied actions for fire situations may encompass an accidental combination of actions. In other words, the applied actions in an exceptional fire condition are reduced, in relation to the values normally used at ambient temperature. Brazil's ABNT NBR 8681 Standard [11] recommends Equation 7 for the accidental ultimate combination of actions, with the ψ_2 value reduced to $0.7\psi_2$ in a fire situation.

$$F_{d,fi} = \sum_{i=1}^{m} \gamma_{g,fi} \, F_{Gi,k} + \gamma_{q,fi} \, F_{Q,fi} + \gamma_{q,fi} \sum_{j=1}^{n} \psi_2 \, F_{Qj,k} \tag{7}$$

where $F_{d,fi}$ is the design value of accidental combination action [kN] (equivalent to $E_{d,fi}$); $F_{Gi,k}$ is the characteristic value of permanent action i [kN]; $F_{Q,fi}$ is the representative value of the thermal action (accidental action) [kN]; $F_{Qj,k}$ is the characteristic value of variable action j [kN]; $\gamma_{g,fi}$ is the partial factor for permanent actions in fire, according to ABNT NBR 15200 [2] [non-dimensional]; $\gamma_{q,fi}$ is the partial factor for variable actions in fire according to [2] [non-dimensional] and ψ_2 is the combination factor used to determine the reduced values of the variable actions according to [2] [non-dimensional].

Equation 7 is similar to the expression for the accidental combination of actions proposed by EN 1990 [12]. Although both are recommended by the Brazilian ABNT NBR 8681 [11] and European EN 1990 [12] Standards, respectively, to determine the design effect of actions in fire situation, they have different combination factors. This does not prevent them from being applied to use the alternative method for design presented here. Since the $M_{Ed,fi}$ consists of an input data for the graphs (and for the app, as explained ahead), the engineer decides the most appropriate expression for it to be determined, with this choice depending on the country and the respective standards that must be followed.

After the thermo-structural analyses and the validation of the main variable provided by TCD [7], $M_{Rd,fi}$, more than two thousand and three hundred curves that provide the ratio between the resistance to bending moments in fire and at ambient temperature, depending on the fire exposure time, were generated. These curves, illustrated earlier by the dotted line in Figure 6, are representative of the beam sections with different geometries and reinforcement configurations, which were adopted when preparing the alternative method for design.

Rectangular cross-section beams were assumed, with widths of 14, 19, 25, 30 and 35 cm and heights of 40, 50, 60 and 70 cm, all overlaid by a slab 5 cms thick and 60 cms wide. Reinforcement bars with diameters of 10, 12.5, 16, 20 and 25 mm diameter, arranged in one and two layers, positive and negative, with covers of 25, 30 and 40 mm were considered. 5 mm diameter stirrups were adopted, which is the minimum value allowed by the ABNT NBR 6118 Standard [9]. The amount of steel, as much as possible, was inserted in the sections for each width complying with the values of free minimum spacing between the faces of the longitudinal bars, proposed in [9].

For the thermal analysis of these T-shaped sections, the same parameters were adopted as presented previously for the beam models used for the $M_{Rd,fi}$ study (see the second paragraph of section 2.1 Resistance to bending moments analysis). On the boundary conditions, ISO 834 Standard fire scenario [8] was considered on the side and bottom faces of the beam and under the slab. The non-exposed faces (side and upper faces of the slab), for safety purposes, were set as adiabatic. The parameters adopted for the structural analysis were also the same: f_{ck} equal to 25 MPa, f_{yk} equal to 500 MPa, etc. For more information, see section 2.1 again.

Thus, the height, width, layers of reinforcements (1 or 2), position of reinforcements (positive or negative) and cover varied for each cross-section. Extracting the values of the relation of moments found for each case by the TCD software [7] from the graphs, 204 tables were constructed, similar to Table 2. Based on all the data present in the tables, an application was devised for determining the fire resistance of reinforced concrete beams.

Table 2 – μ parameter as a function of the characteristics of the cross-section of a beam and fire resistance time.

1 positive layer					Beam 14x40 (cover = 2.5 cm / $\phi_{stirrups}$ = 5 mm)									
						μ								
ϕ [mm]	t[min]/ϕ	0	15	30	45	60	75	90	105	120	135	150	165	180
10	2ϕ10	1.0000	1.0000	1.0000	1.0000	0.7228	0.4479	0.2605	0.1804	0.1203	0.0955	0.0738	0.0634	0.0566
	3ϕ10	1.0000	1.0000	1.0000	1.0000	0.8188	0.5458	0.3370	0.2236	0.1505	0.1114	0.0857	0.0714	0.0607
12.5	2ϕ12.5	1.0000	1.0000	1.0000	1.0000	0.7714	0.4857	0.2907	0.1966	0.1314	0.1014	0.0793	0.0656	0.0585
	3ϕ12.5	1.0000	1.0000	1.0000	1.0000	0.8580	0.5804	0.3642	0.2418	0.1617	0.1187	0.0908	0.0741	0.0627
16	2ϕ16	1.0000	1.0000	1.0000	1.0000	0.8343	0.5449	0.3398	0.2199	0.1491	0.1100	0.0872	0.0690	0.0614
20	2ϕ20	1.0000	1.0000	1.0000	1.0000	0.9062	0.6168	0.3985	0.2509	0.1727	0.1201	0.0965	0.0758	0.0647

3. TRFVIG APP

3.1 Inserting the database into the App

The results of an alternative method for the design of reinforced concrete beams in a fire situation, the graphical method [6], enabled the development of software, more specifically an application (app) called TRFVIG. The acronym TRFVIG comes from the Portuguese phrase for *Fire Resistance Time of Reinforced Concrete Beams (Tempo de Resistência ao Fogo de VIGas de Concreto Armado)*. TRF refers to *Fire Resistance Time* (in Portuguese: *Tempo de Resistência ao Fogo*). TRF is equivalent to "design fire resistance". VIG refers to *Beams* (in Portuguese: *VIGas*).

The database was fed into the app for calculating the fire resistance of reinforced concrete beams as follows: input data were previously stored in the Excel v.2007 software [13], illustrated as an example in Table 2, and the first step was thus to reorganize and transfer this data to text files in table format.

In order to be readable by the app, each table was reconfigured as follows (see Figure 7): the top line shows the characteristics of its data, namely the width (b_w) and height (h) of the cross-section of the beam in question, the cover (c) of the reinforcements, the number of layers into which these reinforcements are distributed (one or two) and the position of the bending moment (whether positive or negative), with the dimensions of this line indicated in centimeters. The second line presents the fire resistance values established as a basis for obtaining the results from the thermo-structural analysis performed using the TCD software [7], with these times indicated in minutes. The subsequent rows show the μ parameter values from the TCD for each of the pre-established fire resistances. The first column of these rows indicates the corresponding reinforcement, i.e., 2f10 indicates that this line refers to the μ values for a 2ϕ10 reinforcement, meaning two 10 mm steel bars; the μ values have no dimensions, as they represent relative bending moments.

```
bw=14.0;h=40.0;c=2.5;layers=1;M=+
TRF    0      15     30     45     60     75     90     105    120    135    150    165    180
2f10   1.0000 1.0000 1.0000 1.0000 0.7228 0.4479 0.2605 0.1804 0.1203 0.0955 0.0738 0.0634 0.0566
3f10   1.0000 1.0000 1.0000 1.0000 0.8188 0.5458 0.3370 0.2236 0.1505 0.1114 0.0857 0.0714 0.0607
2f12.5 1.0000 1.0000 1.0000 1.0000 0.7714 0.4857 0.2907 0.1966 0.1314 0.1014 0.0793 0.0656 0.0585
3f12.5 1.0000 1.0000 1.0000 1.0000 0.8580 0.5804 0.3642 0.2418 0.1617 0.1187 0.0908 0.0741 0.0627
2f16   1.0000 1.0000 1.0000 1.0000 0.8343 0.5449 0.3398 0.2199 0.1491 0.1100 0.0872 0.0690 0.0614
2f20   1.0000 1.0000 1.0000 1.0000 0.9062 0.6168 0.3985 0.2509 0.1727 0.1201 0.0965 0.0758 0.0647
```

Figure 7: Example of the layout configuration of one of the tables in the text file with the app database, for calculating the fire resistance time of reinforced concrete beams.

It is important to mention that an order was established for uploading these tables into the database. Furthermore, they were uploaded little by little, in order to run app operating tests at various data input stages. For example, each set of nine or twelve tables saved in the text file were confirmed for the number of new tables and new data characteristics, together with multiple checks of the fire resistance results produced by the app.

The tables were uploaded in the following order: (1) beams with positive reinforcements distributed in one layer; (2) beams with positive reinforcements distributed in two layers; (3) beams with negative reinforcements distributed in one layer and (4) beams with negative reinforcements distributed in two layers. Figure 8 presents an outline showing the relationship among the existing tables for these four cases, indicating the characteristics of their data, as defined in the first line of each of them, shown in Figure 7 and explained in a previous paragraph. Figure 8 also presents the total number of tables (204) in the database, in addition to the number of solutions for design. This is reflected in the number of rows represented by the rebar arrangements (number of bars/bar diameters) with the respective μ parameter values (the rows are also explained above).

3.2 Implementation of the TRFVIG App

The entire implementation of the TRFVIG app was handled in the C# language under the Microsoft. NET® Framework platform. The graphical interface was built on Windows Presentation Foundation® (WPF). It is thus expected that the app is compatible with the recent versions of the Windows operating system (version 7 or later), provided that the Framework platform is properly installed on the computer. The app installer was written on *Inno Setup®*. The main challenge for implementing this app was defining how the massive results dataset (with more than 2300 beam models) would be uploaded into its database. After some initial analyses, it was decided to convert these values into spreadsheet format (tables), in a formatted text file, which was later converted into a binary file. Initially, only a few tables were converted and tested. It was only after confirming the efficiency of the methodology for adapting the results of the work for use in the application that all the tables were gradually converted.

During the app development stage, designing a simple, logical and intuitive user interface was also a matter for close attention. All the input data and results are gathered in a single window. For *the* μ values, a linear interpolation is adopted when the user-defined value differs from the values that were originally available. No extrapolation was considered. Figure 9 shows the main app window, with input data on the left. An initial message with warnings, credits, etc. is displayed in the right panel as soon as the app loads. Optionally, μ may be calculated by entering the $M_{Ed,fi}$ and M_{Rd} bending moments value. A query methodology was defined for the app database, optimizing calculation times. Once the data is entered, processing is started by a single *Calculate Fire Resistance* button, with the results displayed instantly in the right panel. In addition to these fire resistance time values, the μ vs fire resistance graph is also presented, as shown in Figure 10. Although countless tests have been run, the authors accept no liability for results obtained through the app. Users must thus run their own validation checks.

The TRFVIG app is available for free to members of the Brazilian Concrete Institute (IBRACON – *Instituto Brasileiro do Concreto*) and the Brazilian Association of Structural Engineering and Consulting (ABECE – *Associação Brasileira de Engenharia e Consultoria Estrutural*). It may be downloaded from the following websites: https://site.ibracon.org.br/ or https://site.abece.com.br/, after logging in to the Members areas. At the time of the submission of this paper, the development of the English version of the TRFVIG app is concluded and it is expected to be released in the near future. Figures 9 and 10 present a look-up of the English version (the currently available version is in Portuguese).
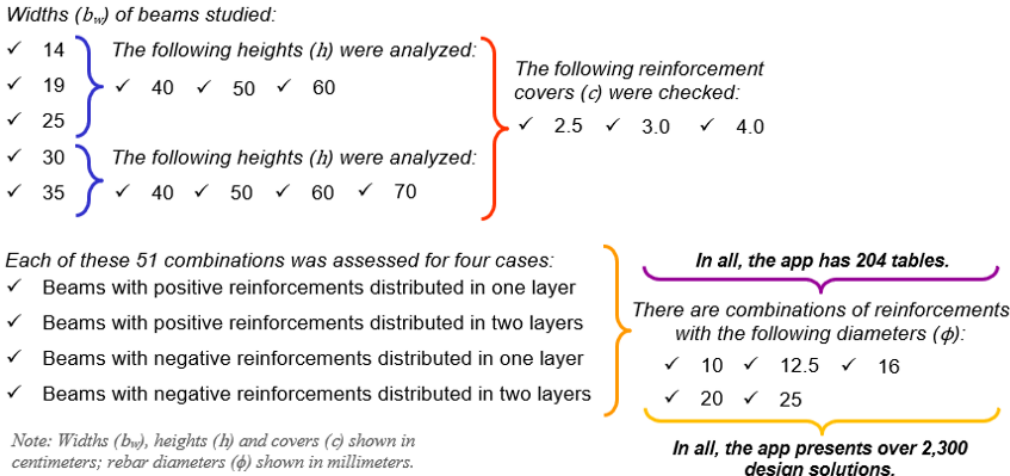

Figure 8: Schematic with characteristics of the concrete beams, quantities of tables and design solutions in the TRFVIG app database.
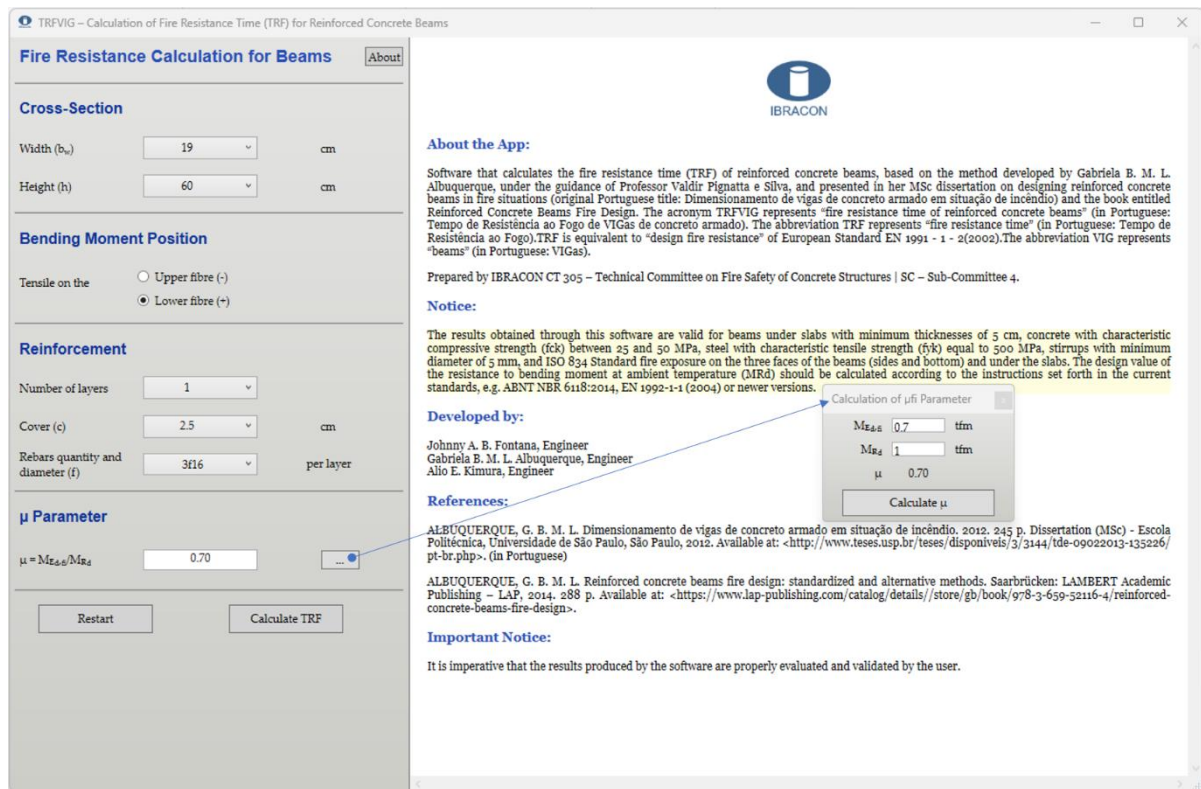
Figure 9: Main window of the TRFVIG app.

4. CONCLUSIONS

Based on isotherm distribution shapes in rectangular beams, fire resistances to bending moments ($M_{Rd,fi}$) do not change much, when shifting between simplified procedures for defining them. The TRFVIG app may be used for around 2300 cross-section/reinforcement alternatives for each standard fire resistance rating (R). This paper presents the hypotheses that guided the development of this app for determining the fire resistance time (TRF). This encompasses the inclusion of the cross-section and reinforcement characteristics of a reinforced concrete beam, and the relationship between applied and resistant bending moments. The fire resistance time (TRF), which is equivalent to "design fire resistance", must be greater than or equal to the standard fire resistance rating *(R)*, which is equivalent to "required fire resistance time" (TRRF, in Brazil).

When determining fire resistance time, the app does not establish a temperature limit on reinforcements, but rather an equilibrium of resistant forces on reinforcements and the compressed concrete block, in order to lead to more accurate results than the tabular method. This is why the app may occasionally indicate more economical fire resistance values, compared to figures from the tables, as noted in certain application examples that were analyzed [3-4, 6].

Although not as streamlined as the tabular method, the use of this app is also relatively simple. This is because it needs only six cross-section characteristics of the beam under analysis, defined in the design at ambient temperature. The only input datum that really needs to be calculated by the engineer is the μ parameter. In turn, this μ parameter is defined from $M_{Ed,fi}$ and M_{Rd}, which are also easy to determine. Thermal analyses and specific fire area software are not required when using the TRFVIG app, thus making it a feasible alternative for most structure design professionals.

The TRFVIG app may be applied to design beams overlaid by slabs (T cross-sectional shapes), concrete with compressive strength (f_{ck}) between 25 MPa and 50 MPa, reinforcing steel with tensile strength (f_{yk}) equal to 500 MPa, ISO 834 Standard fire scenario and heat exposure on the three faces of the beams (sides and bottom) and under the slabs. The other parameters and properties of the materials used in the thermal and structural analyses

drawn up to develop the app, might also need to be analyzed in order to ascertain its applicability, in terms of the design standards in effect in each country.
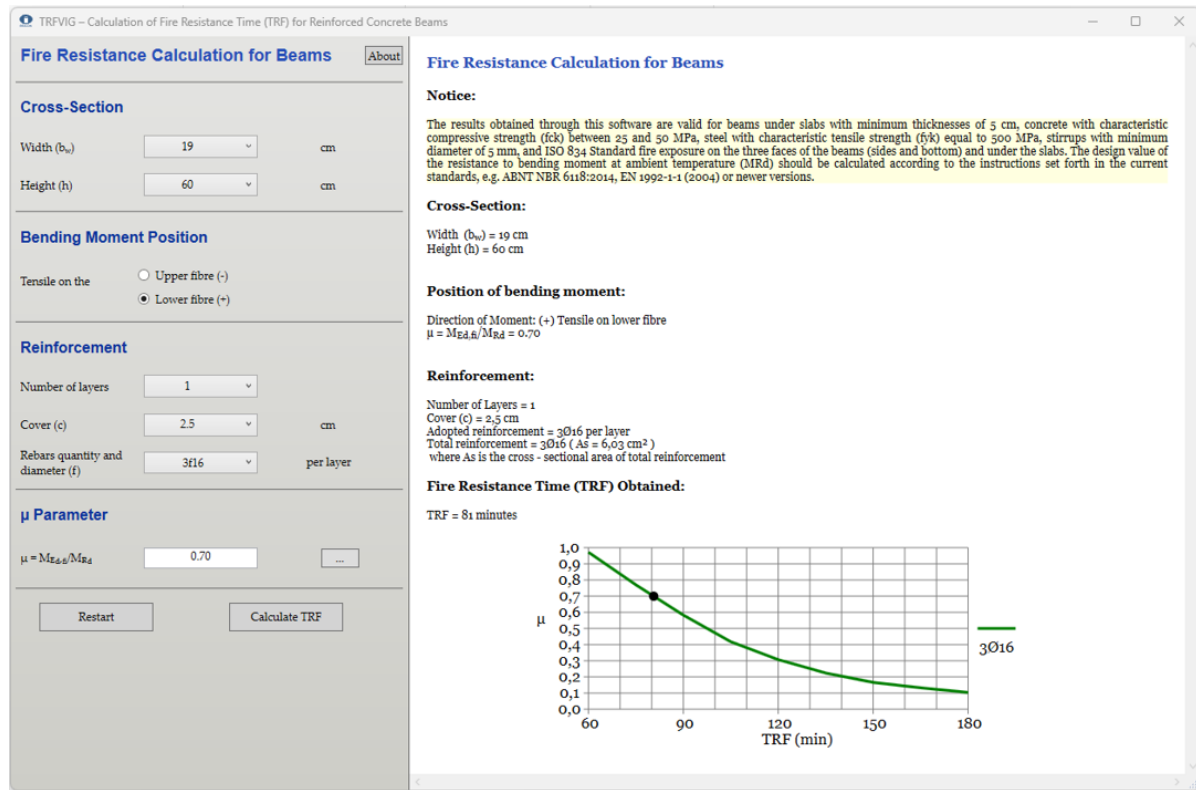

Figure 10: Graph showing μ vs fire resistance presented in the TRFVIG app.

ACKNOWLEDGEMENTS

REFERENCES

[1]   European Committee for Standardization. (2004). *EN 1992-1-2: Eurocode 2: Design of Concrete Structures - Part 1.2: General Rules - Structural Fire Design*, Brussels, 97 p.

[2]   Associação Brasileira de Normas Técnicas. (2012). *NBR 15200: Projeto de Estruturas de Concreto em Situação de Incêndio*, Rio de Janeiro, 52 p. [in Portuguese]

[3]   Albuquerque, G. B. M. L. (2012). *Dimensionamento de Vigas de Concreto Armado em Situação de Incêndio*, Master's thesis, University of São Paulo, 245 p. [in Portuguese]

[4]   Albuquerque, G. B. M. L. (2014). *Reinforced Concrete Beams Fire Design: Standardized and Alternative Methods.* LAMBERT Academic Publishing – LAP, 262 p.

[5]   Silva, V. P. (2012). *Projeto de Estruturas de Concreto em Situação de Incêndio: Conforme ABNT NBR 15200:2012*. Edgard Blücher, 237 p. [in Portuguese]

[6]   Albuquerque, G. B. M. L.; Silva, V. P. & Rodrigues, J. P. C. (2022). *A Graphical Method for Fire Design of Reinforced Concrete Beams*, Fire Technology, vol. 58, no. 2, p. 737- 775.

[7]   Fire Safety Design – FSD. (2007). *TCD 5.0 User's Manual*, Fire Safety Design AB, Lund, 129 p.

[8] International Organization for Standardization. (1999). *ISO 834: Fire-Resistance Tests: Elements of Building Construction - Part 1: General Requirements for Fire Resistance Testing*, Geneva, 25 p. (Revision of first edition ISO 834:1975).

[9] Associação Brasileira de Normas Técnicas. (2014). *NBR 6118: Projeto de Estruturas de Concreto: Procedimento,* Rio de Janeiro, 238 p. [in Portuguese]

[10] Klein Júnior, O. (2011). *Pilares de Concreto Armado em Situação de Incêndio Submetidos à Flexão Normal Composta*, Master's thesis, University of São Paulo, 208 p. [in Portuguese]

[11] Associação Brasileira de Normas Técnicas. (2004). *NBR 8681: Ações e Segurança nas Estruturas*, Rio de Janeiro, 18 p. [in Portuguese]

[12] European Committee for Standardization. (2002). *EN 1990: Eurocode 0: Basis of Structural Design*, Brussels, 116 p.

[13] Microsoft® Office. (2006). *Microsoft Office Excel 2007 Manual*, [S.l.], 37 p.

FIRE BEHAVIOUR OF LIMESTONE MASONRY DURING AND AFTER FIRE

Pierre Pimienta a,*   **Armita Obaie b**   **Elodie Donval c**   **Duc Toan Pham d**

Albert Noumowe e   **Javad Eslami f**   **Dashnor Hoxha g**

ABSTRACT

The work presented in this paper is part of a larger French project, POSTFIRE, developed following the Notre-Dame Cathedral fire. Six fire resistance tests were performed on 3 m x 3 m x 20 cm thick masonry walls. The tests were performed on 3 stones: Saint Leu (soft stone), Tervoux (firm stone) and Massangis (hard stone). The nature and compressive strength of the mortars were adapted to each stone. The walls were exposed to the standard 834-1 temperature curve for two hours followed by a 24-hour cooling phase. For each stone, one wall was tested without mechanical loading and one with mechanical loading. The applied mechanical loads during the fire test correspond to 50% of the allowable loads calculated according to Eurocode 6. The tests were very extensively instrumented: thermocouples, displacement sensors, digital image correlation, thermal camera and endoscopes. The recordings were made during the heating and cooling phase. At the end of the cooling phase, the walls were loaded again until failure to determine their residual wall bearing capacity. The walls were stored for at least 2 weeks for further observations. The results of the test campaign on the 6 walls made with the 3 stones will be presented.

Keywords: Masonry; Limestone; Fire resistance; Cooling phase; Residual bearing capacity.

[a,*] CSTB (pierre.pimienta@cstb.fr), Corresponding author.

[b] L2MGC CY Cergy-Paris Université, Université d'Orléans, CSTB (armita.obaei@cyu.fr).

[c] CSTB (elodie.donval@cstb.fr).

[d] CSTB (ductoaan.pham@cstb.fr).

[e] L2MGC CY Cergy-Paris (albert.noumowe@cyu.fr).

[f] L2MGC CY Cergy-Paris (javad.eslami@cyu.fr).

[g] Université d'Orléans (dashnor.hoxha@univ-orleans.fr).

1. INTRODUCTION

Masonry construction has been used for centuries due to its durability and resistance to the elements. However, when exposed to fire, masonry structures can experience significant damage. The recent, devastating fire of Notre Dame de Paris has enlightened once more the vulnerability of historic architectural heritage and the general concern for the residual stability of the monument. As a fact, many ancient buildings and monuments have withstood violent fires during their history; structural masonry often survives fires. This can be explained by the generally high thickness of these structures and the tendency of the stones to show lower temperature degradation compared to other building materials. On the other hand, the residual structural capacity of masonry walls, pillars, columns and vaults is difficult to quantify [1]. Generally, only destructive tests (DT) can provide quantitative assessment of mechanical properties; but the need for heritage preservation generally forces post-fire surveyors to rely mainly upon non-destructive tests (NDT) [2]. On the other hand, even performance-based codes for the fire resistance assessment of masonry structures – like Eurocode [3] and the USA code NFPA 914 [4]– do not contain specific strength calculation methods for post-fire situation.

In the field of civil engineering, the high temperature behaviour of stones is much less known and investigated than that of steel or concrete. At high temperatures, microscopic physical and chemical transforms trigger macroscopic changes in the physical, thermal and mechanical properties of masonry units and mortars [5]. In carbonate rocks, e.g. limestone, decarbonisation is the cause for material contraction beyond 800°C, while the formation of Portlandite brings on a volume increase during the cooling phases [6] [7]. Damage increase can show up even days after the fire event [8],[9], having major consequences on the safety of buildings after fire.

Additionally, the composite nature of masonry brings on the problem of interface cohesion deterioration, which is a crucial parameter especially in the shear response [10]. Among the exposure characteristics, the maximum temperature is the most relevant parameter for the property decay [11]. As well, the cooling regime can also be crucial [12]. Finally, high heating rates (which are typical of real fires) can also be linked to damage increase and, depending on the stone nature, spalling [13].

Despite the importance of understanding how masonry behaves in fire situations and after the fire, the available research on these topics is limited and the very heterogeneous results claim for increasing scientific contributions. However, we can mention the work carried out at the CSTB (Centre Scientifique et Technique du Bâtiment) over the last few years, including the performance of fire resistance tests on masonry walls [14][15]. The tests were performed on Saint-Vaast limestone which is very close to the soft stone Saint Leu studied in the present paper. This work is currently being continued and includes detailed work on the modelling of the failure behavior under fire.

In this context, the French POSTFIRE project – *Safety and Preservation of cultural heritage stone masonry buildings after fire events* – aims at understanding and examine the multi-scale mechanical behaviour of traditional stonework, during the fire and, with a particular focus, after the fire. This project includes the carrying out of a fire resistance test campaign on the 6 walls in CSTB. This work also completes the ongoing research on Saint Vaast stones [14][15] which focuses mainly on the masonry behavior under fire and little on the behavior after cooling. The tests were very extensively instrumented: thermocouples, displacement sensors, digital image correlation, thermal camera and endoscopes. This paper presents the program, equipment, test procedures and the main tests results and analysis.

2. EXPERIMENTAL PROGRAM

In order to investigate the behavior of Limestone in fire situations, six masonry wall tests were conducted (Table 1). Tests were carried out on 3 m x 3 m x 20 cm thick masonry walls and performed on 3 three types of limestone from the French Rocamat company: Saint Leu (soft stone), Tervoux (firm stone) and Massangis (hard stone). Mean values of the stones compressive strengths achieved by testing 10 cubic 10 cm-side samples according to NF EN 772-1 are given in the table.

Table 1: Experimental program

Wall	Stone	Stone compressive strength (MPa)	Mortar	Mortar compressive strength (MPa)	Curing time (months)	Applied compressive load on the walls
LEU NL	Saint-Leu	7.3 ± 1	350 kg NHL2	Hor. : 0.67 Vert. : 0.65	4	Lightly loaded – 14 tonnes (0.23 MPa)
LEU L	Saint-Leu				4	Loaded – 36.3 tonnes (0.61 MPa)
TER NL	Tervoux	37.3 ± 1	250 kg NHL3.5 + 100 kg cement	Hor. : 1.5 Vert.: 1.75	2	Lightly Loaded– 30 tonnes (0.5 MPa)
TER L	Tervoux				2	Loaded – 141 tonnes (2.35 MPa)
MAS NL	Massangis	102.4 ± 6	200 kg NHL3.5 + 150 kg cement	6.7	3	Lightly Loaded – 26 tonnes (0.43 MPa)
MAS L	Massangis				3	Loaded – 375 tonnes (6.25 MPa)

The nature and compressive strength of the mortars were adapted to each stone. In order to reproduce site practices, the fluidity of the mortars, and therefore their water content, was adapted for the filling of horizontal and vertical joints. The water content of the mortars for vertical joints was higher (Table 1). Then, Saint-Leu stone was bonded with mortar made of sand and natural hydraulic lime NHL 2 with a compressive strength of 0.65 – 0.67 MPa. Mortars used for Tervoux and Massangis stones were made of sand, cement, and natural hydraulic lime NHL 3.5. Their compressive strengths was respectively 1.5 – 1.75 MPa and 6.7 MPa. The curing time was adapted to the strength kinetics of the mortars. A longer curing time (4 months) was applied for the Saint-Leu limestone walls bonded with the mortar made with natural hydraulic lime NHL 2.

The walls were exposed to the standard 834-1 temperature curve for two hours followed by a 24-hour cooling phase. For each stone, one wall was tested unloaded (in practice with a very low mechanical loading in order to ensure a good fit of the wall in the concrete frame) and one with mechanical loading. The applied mechanical vertical loads during the fire test correspond to 50% of the bearing capacity at ambient temperature calculated according to Eurocode 6. In the table and the rest of the paper, the stones from Saint Leu, Tervoux and Massangis are referred to as LEU, TER and MAS respectively. The unloaded and loaded tests are denoted by NL and L.

The recordings were made during the heating and cooling phase. At the end of the cooling phase, the walls were loaded again until failure in order to determine their residual bearing capacity. The walls were stored for at least 2 weeks for further observations.

3. TEST PROCEDURE

The walls were erected by Rocamat company within a reinforced concrete frame. The blocks sizes were: 72 cm x 36 cm x 20 cm (length x height x thickness). The mortar layer thickness was: 10 mm. A layer of mortar was applied between the wall and the top and bottom beams. Their thickness was respectively of 55 mm and 20 mm. A 60 mm-wide rock wool strip was positioned between each lateral side of the wall and the RC frame in order to ensure thermal insulation and prevent any mechanical action on the lateral sides of the walls (free edges).

To accurately characterize the behavior of masonry walls in fire situations, we employed a comprehensive instrumentation and measurement protocol that enabled us to monitor the temperatures, displacements and visual changes: thermocouples, displacement sensors, digital image correlation (DIC), thermal camera and endoscopes (Figure 1).

The structure was placed in front of a furnace and exposed to a conventional ISO 834-1 fire (EN 1991-1-2) on one side for 120 minutes according to NF EN 1365-1. The temperature was uniformly increased on the surface of the wall until it reached 1050°C after 120 minutes (Figure 2). The wall was held against the furnace during the cooling phase. During this phase, the exhaust fans were kept running at high speed and openings were made in the sealing of the furnace to accelerate the cooling rate. During both phases, the temperatures in the furnace were measured using 9 plate thermometers positioned 10 cm from the walls. An example of the results is given in Figure 2.
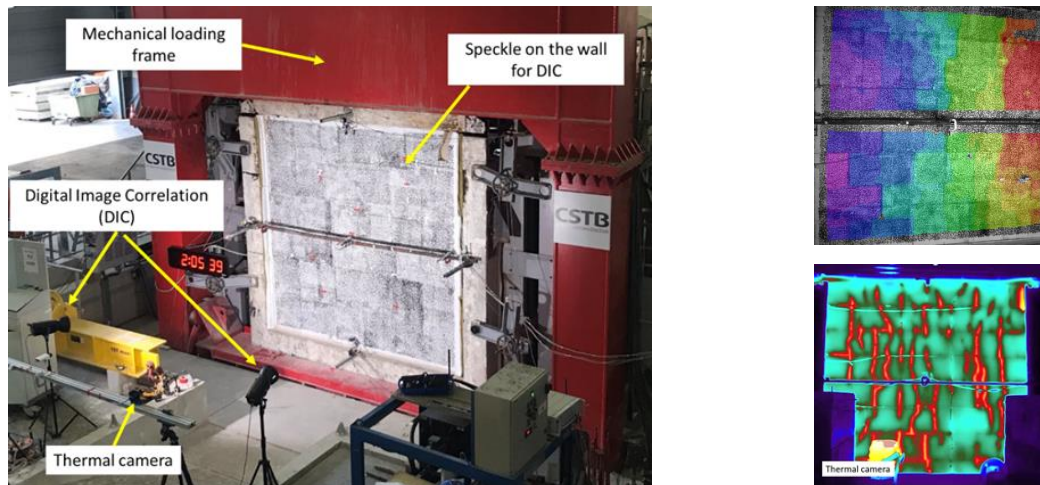
Figure 1: Fire resistance test on the Massangis stone block wall with the cameras of the digital image correlation, the thermal camera, the speckles applied on the wall, the mechanical loading frame (left). Example of contours of horizontal displacement in the non-exposed side after 120 minutes of heating (right top). Example of image captured with the thermal camera. The higher temperature at the cracks are visible (rigth bottom).

Vertical compressive load was applied through hydraulic jacks placed under a reinforced concrete frame. A mechanical loading test was carried out the next day to determine the residual capacity of the wall.

In each wall, 3 stones were instrumented with 6 thermocouples positioned at different depths from the face exposed to the fire: 1, 2, 5, 8, 12 and 17 cm. The evolution of temperature fields of the unexposed side was recorded by using 5 thermocouples and a thermal camera.

Three different techniques were employed to accurately measure the masonry wall displacement during the test. Seven Linear Variable Differential Transformers (LVDTs) were placed at different heights and locations on the non-exposed side of the wall to measure the out-of-plane displacement. Additionally, the vertical displacement of the wall at the top of both the right and left sides were recorded using two sensors. Furthermore, the Digital Image Correlation (DIC) technique was used to obtain displacement fields in three directions of the wall using two cameras, without any contact. To achieve this, a painted speckle pattern was applied to the unexposed surface of the wall, which enabled the system to determine the displacement of a set of points by comparing pictures taken at two different times. The position of the two cameras was calibrated before the test to calculate the displacements in the three directions by triangulation. The measurements obtained using these techniques facilitated the wall determination of the deflection, displacement, cracks and other relevant data.

In addition to all these measurements, the endoscopic cameras were placed inside the furnace to film the changes that occurred to the exposed surface during the heating.
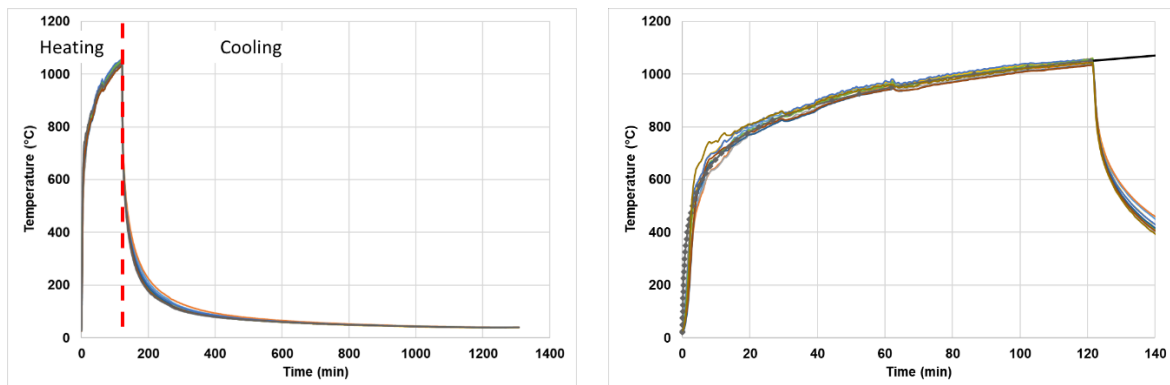

Figure 2: The measured temperature in the furnace during the heating and cooling phase in comparison to the ISO 843-1 curve for the test 3, Unloaded Tervoux
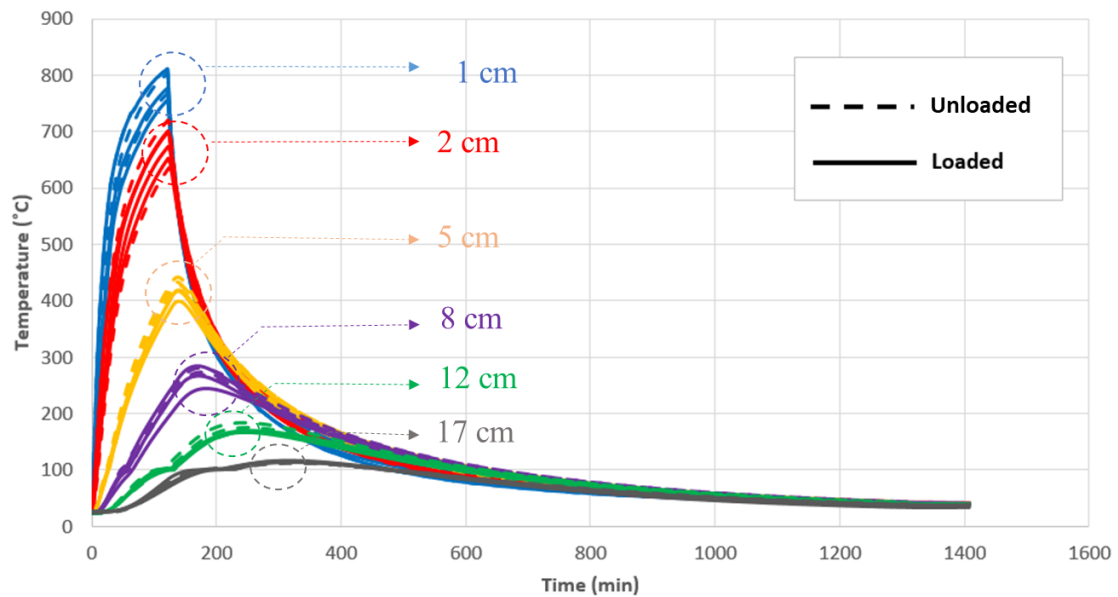
Figure 3: Measured temperature in the wall versus the time and the distance to the exposed side (example of the 2 Tervoux walls)

4. TEST RESULTS AND DISCUSSION

4.1 Temperature distribution

The measured temperature in the wall versus the time and the distance to the exposed side are illustrated in Figure 3. This graph shows the temperatures in both unloaded and loaded Tervoux limestone walls. This graph is representative of the results obtained on the other two walls.

For depths greater than or equal to 8 cm, we can observe the appearance of a vaporization plateau. This type of plateau is frequently observed during fire tests on concrete specimens. The length of the plateaus is less than that observed during tests on Saint-Vaast walls [14]. This can be explained by the longer drying time and the lower water content in the stone in the walls tested in this project. These plateaus result from the energy consumed by the water from the exposed surface to the depth of the measurement. Therefore, the presence of the plateaus, and their length increases with depth.
We can observe that the curves show a greater dispersion of results at shallower depths. This is due to the positioning errors of the thermocouples. Indeed, near the surface, the temperature measurements are more sensitive to positional deviations.

The Figure 4 represents the profiles of temperatures versus the distance to the exposed side determined on the 6 walls at 2 different times: 15 min et 120 min. The actual depths (not the theoretical depths) are plotted on the x-axis. This representation allows the effect of the thermocouple position error to be eliminated and the profiles obtained for the three stones under the 2 mechanical loadings to be compared.
The analysis shows that, for each of the 3 stones, and as expected, mechanical loading has no influence on the temperature profiles.
Although in this representation, the temperatures of the 3 stones are very close at both test times we can observe a trend. The measured temperatures are generally ordered as follows: Saint-Leu, Tervoux and Massangis from the lowest to the highest temperatures.
This agrees with the thermal conductivity measurements determined on the 3 stones [16]. This is also consistent with the compactness and compressive strengths of the limestones (Table 1).

4.2 Out-of-plane displacement distribution

Masonry walls out-of-plane displacement and deflection can fluctuate significantly in response to high temperatures. In the situation of high temperatures, the limestones experience thermal expansion. Because of the temperature gradient, this thermal expansion varies through the thickness of the wall, which leads to an increase in their overall deflection. Such a deflection, also known as thermal bowing, tends to add additional bending moments to the initial compressive stresses borne by the wall, which might trigger its collapse.
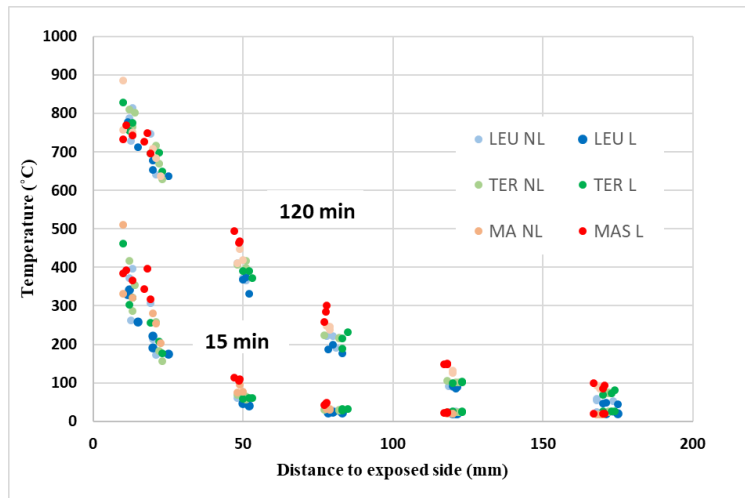
Figure 4: Profile of temperatures versus de depths determined on the 6 walls after 15 and 120 minutes.

The deflection values of the walls during heating and cooling were determined by using five LVDTs and DIC techniques. Positions of the LVDTs are shown in Figure 5-left. Out-of-plane displacement in the middle of the wall versus the time during the heating phase and the beginning of the cooling phase are displayed in the Figure 5-right. Among all the LVDTs, the ones placed in the middle of the wall recorded the maximum out-of-plane displacement in all cases.

Moreover, the results indicated that the unloaded walls had higher out-of-plane displacement compared to the loaded walls, except for the Saint-Leu limestone walls. Thus, the maximum value of out-of-plane displacement was observed for the unloaded Tervoux wall (39 mm). The deflections of the unloaded walls from largest to smallest are as follows: Tervoux (39 mm), Massangis (33 mm) and Saint-Leu (24 mm). The ones of the loaded walls are: Saint-Leu (27 mm), Tervoux (22 mm) and Massangis (6 mm). The 2 Saint-Leu walls out-of-plane displacement values were very close. This small variation can be attributed to the low difference in load between the "unloaded" and the loaded tests (Table 1). On the contrary, the loaded Massangis wall shows a very low deflection compared to the unloaded wall. This is consistent with the very high load applied to the loaded wall (375 tonnes). The rate of increase of out-of-plane displacement was highest during the first 30 minutes and gradually decreased thereafter (Figure 5).

The DIC method is a versatile tool that can offer important information regarding the out-of-plane displacement of the walls. The contours of out-of-plane displacements in the non-exposed side after 120 minutes of heating in 5 of the walls are displayed in Figure 6. Values from the unloaded Saint wall test are not available due a technical problem. From these figures, it can be observed that the maximal deflection occurs very generally near mid-height or a bit above for all walls. For both Tervoux walls, the maximal deflection did not occur at mid-width but was a bit off-center. This is attributed to the asymmetric development of the major vertical cracks (see below).
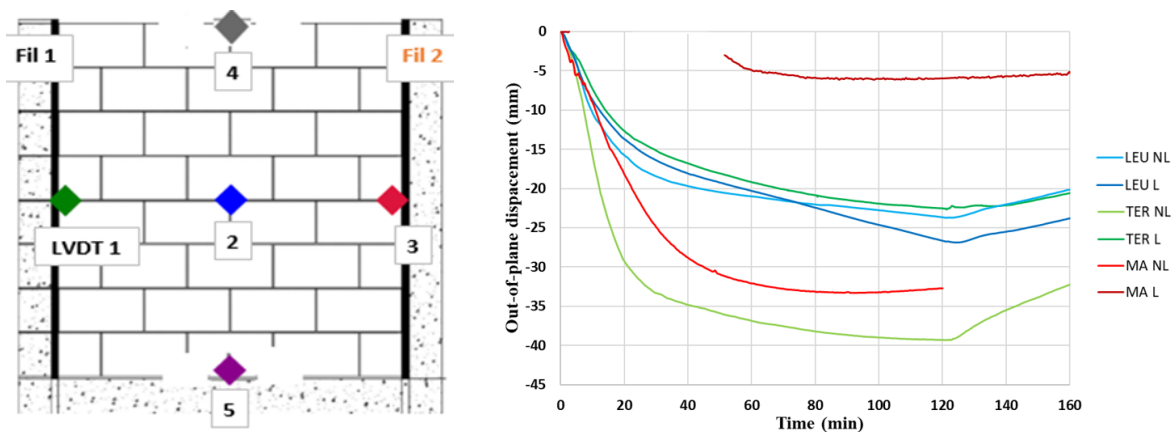

Figure 5: Positions of the LVDTs on the non-exposed side (left); Out-of-plane displacement in the middle of the wall versus the time during the heating phase and the beginning of the cooling phase (right).
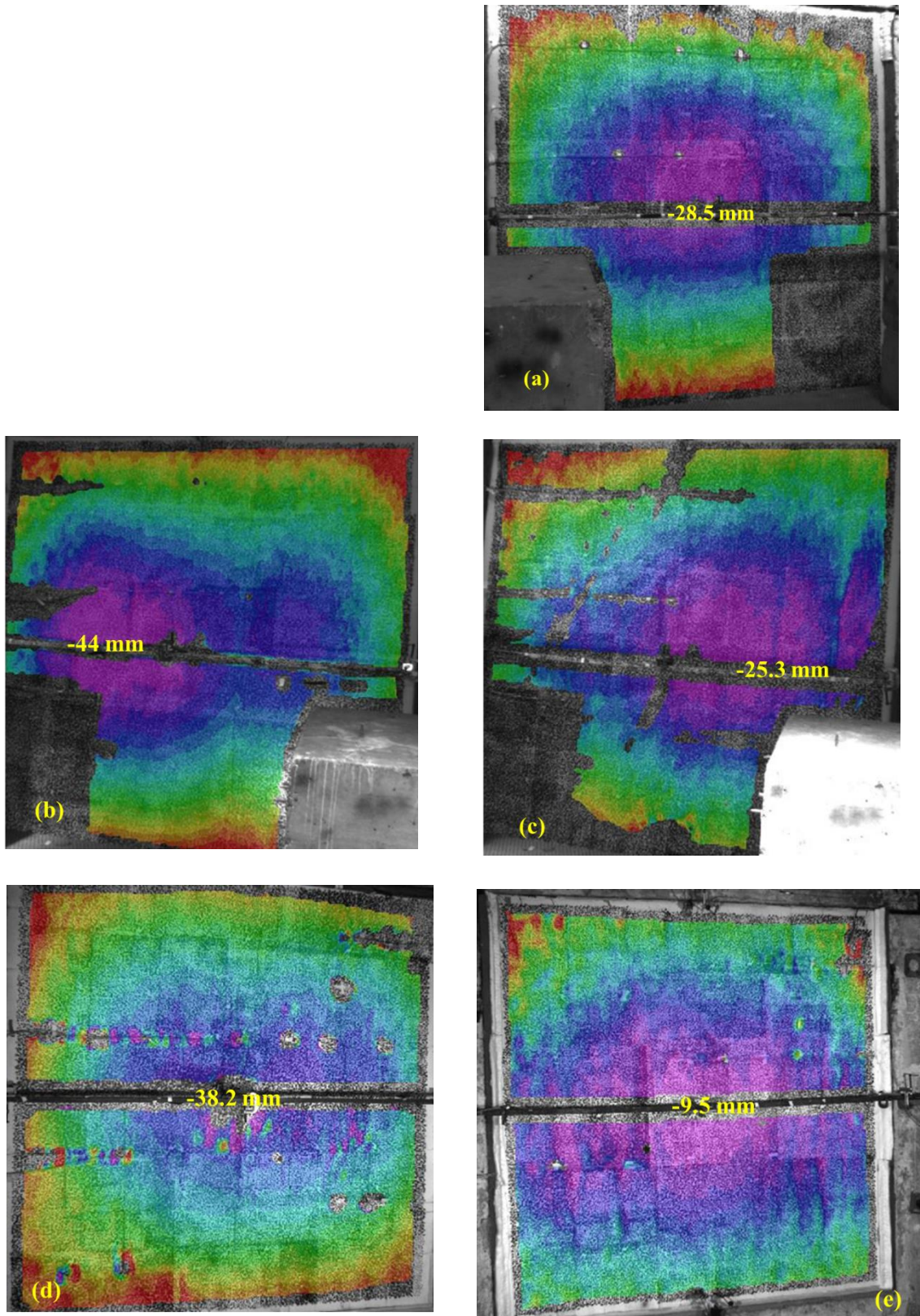
441

Figure 6: Contours of out-of-plane displacements in the non-exposed side after 120 minutes of heating in Loaded Saint Leu (a); Unloaded Tervoux (b); Loaded Tervoux (c); Unloaded Massangis; Loaded Massangis (e)

In Figure 7, as an illustration, deflection profiles determined from the DIC recorded data on the unloaded Tervoux wall at different times during the heating phase are displayed. Profiles are given along the width at the mid-height (top) and along the height at mid-width (bottom). Curves are compared with the values determined by the 5 LVDTs and represented by colored dots. The results show a relatively good correlation between these two measurement methods. These 2 figures picture well the increase in deflection on both sides during the heating phase. These curves can be usefully compared with those obtained on the Saint-Vaast walls studied by Pham et al [14]. The maximum deflection thus determined after 120 minutes on the unloaded wall was 39 mm.

Figure 8 shows the deflection of the central vertical and horizontal lines of all the walls at the end of the heating phase (120 minutes). These figures also illustrate well the creation of a circular bulge toward the fire.

At the beginning of the cooling phase, the value of out-of-plane displacement started to decrease for all walls. Figure 9 shows a comparison between the values at the end of the heating phase (120 minutes) and the end of the cooling phase (1 day). The ratios between the 2 values are given above in % in the figure. The values are between 6 and 54 %. We can then observe that the deflection is partially reversible. It is almost completely reversible in the case of the unloaded Massangis wall.
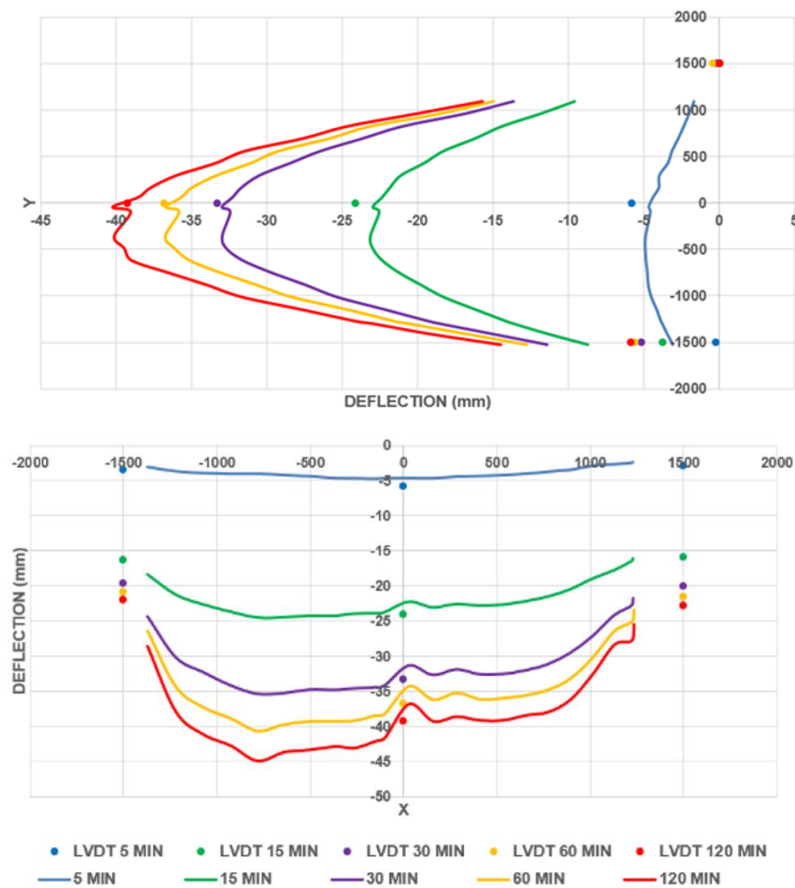

Figure 7: Deflection profiles determined on the unloaded Tervoux wall at different times during the heating phase. Profiles are given along the width at the mid-height (top) and along the height at mid-width (bottom).
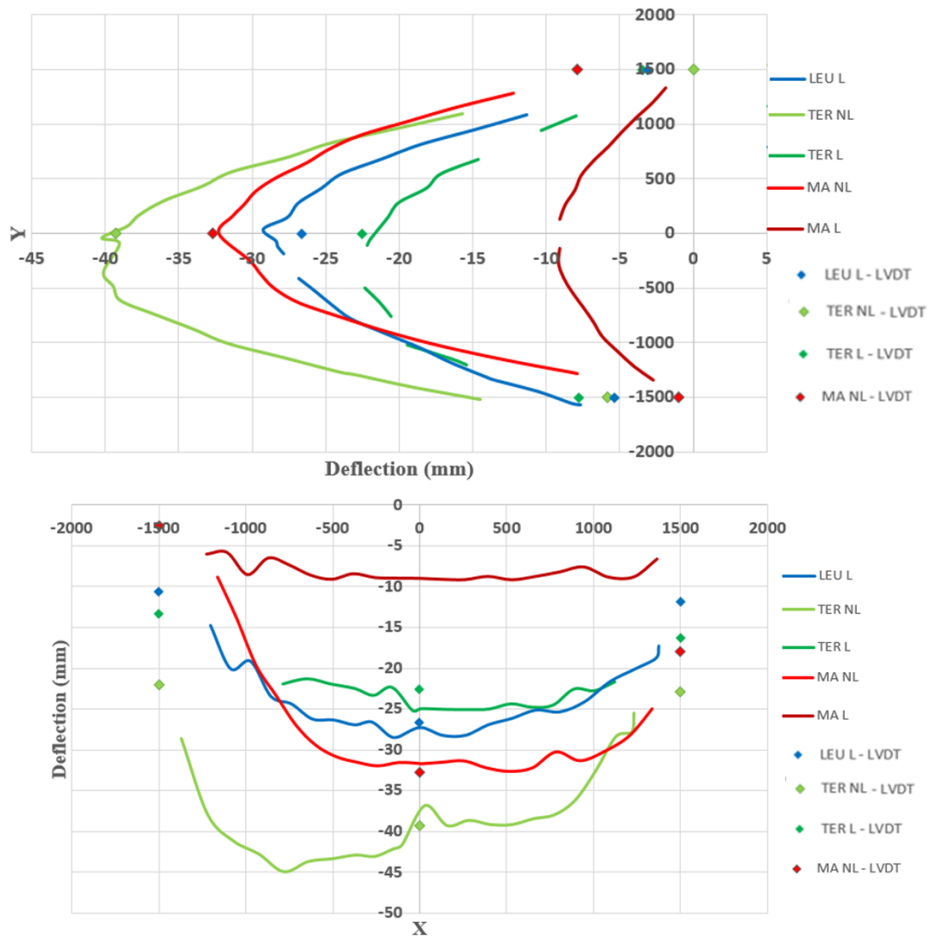
Figure 8: Comparative deflection profiles determined on the walls at the end of the heating phase (120 minutes). Profiles are given along the width at the mid-height (top) and along the height at mid-width (bottom).
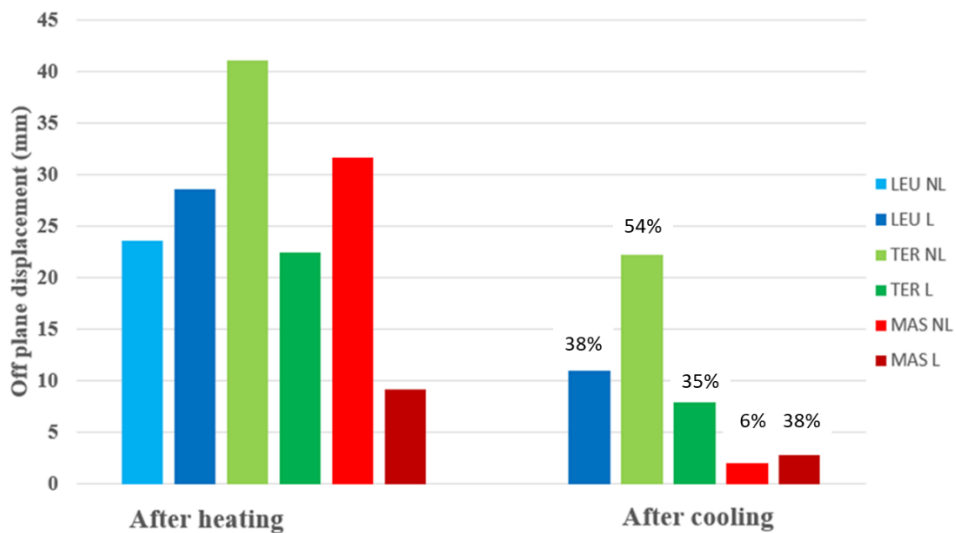

Figure 9: Out-of-plane displacements at the end of the heating phase and at the end of the cooling in all six walls. The ratios between the 2 values are given above in %. All the values have been determined from the DIC measurements except the one determined on the unloaded Saint-Leu wall. This value was determined by LVDT

4.3 Residual load capacity

All six walls, after being subjected to 120 minutes of fire in both unloaded and loaded tests, remained intact and did not fail. To assess their residual mechanical behavior, the day after the heating test, when the temperature in all thicknesses of the walls had stabilized, the walls were loaded again until failure to determine their residual bearing capacity. The compressive vertical load was applied at a gentle speed over ten minutes and increased the load until the walls failed. Values of the calculated load capacity according to Eurocode 6, the applied load during the fire tests and the determined residual capacity are given in the Figure 10. The upward pointing arrows indicate that the applied loads allowed by the equipment used for each test were not high enough to break the walls. Both Saint-Leu walls failed at a load of 100 tonnes. For the Tervoux walls, the wall which was loaded during the fire test wall failed at 200 tones. The unloaded wall was able to withstand a load greater than 200 tonnes. The Massangis walls (unloaded and loaded walls), with the highest compressive strength among the three types of limestone, had a residual capacity exceeding 375 tonnes and did not fail (Figure 10).

These results are among the most important findings of this work. They show that even after fire exposure, the limestones masonry walls can retained a significant amount of their load-carrying capacity.
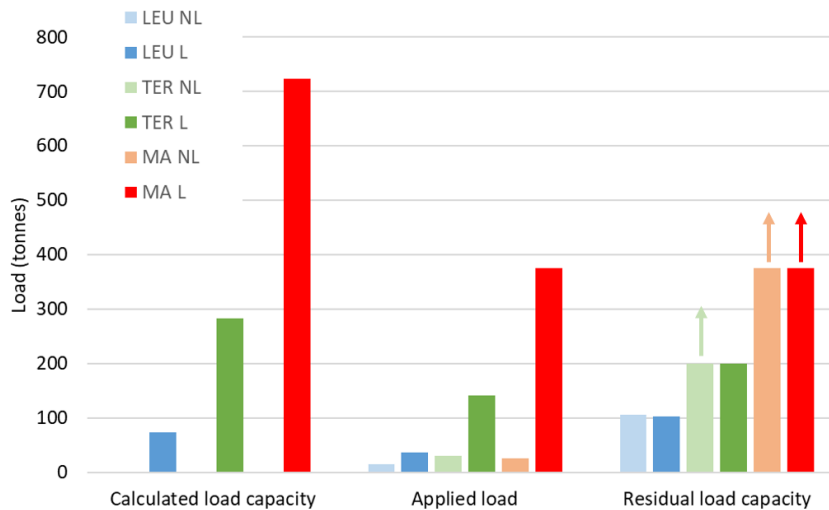

Figure 10: Calculated theoretical load capacity, applied load during heating and residual load capacity after cooling. Arrows are displayed when failure have not been reached when the load was applied after cooling

4.4 Visual changes and cracks during the heating and cooling phases

The evolution of the face exposed to fire was observed and recorded by means of endoscopes. Few changes were observed. In some tests we observed small delamination. None of the three stones exhibited any spalling phenomena.

Cracks development on the unexposed side

The observed cracking patterns on the non-exposed side of the masonry walls after 120 minutes of heating are displayed in Figure 11. It is noteworthy that vertical cracks were prevalent in comparison to horizontal cracks and indeed, in all cases, the cracks emerged from the vertical joints and propagated vertically through the stones, originating from the center of the wall. The first cracks appeared within the first ten minutes of heating in all six tests. The depth of the cracks varied from 5 mm to 17 mm across the length of the wall, and transverse cracks were present in all walls. In loaded walls, the presence of cracks in the top angles and lateral sides was more pronounced compared to not-loaded walls. In some cases, a large horizontal crack was observed at the bottom of the wall, between the blocks and the mortar bed (Figure 11).

The number of vertical cracks was similar in all cases. In most of the cases the number was between 7 and 9. However, we can note that the number of cracks in the case of the Massangis walls was lower (about 6 for the unloaded case) and higher (about 14 for the loaded wall case). Interestingly, these observations can be compared with the horizontal displacement measurements determined by means of the DIC. An example of contours of

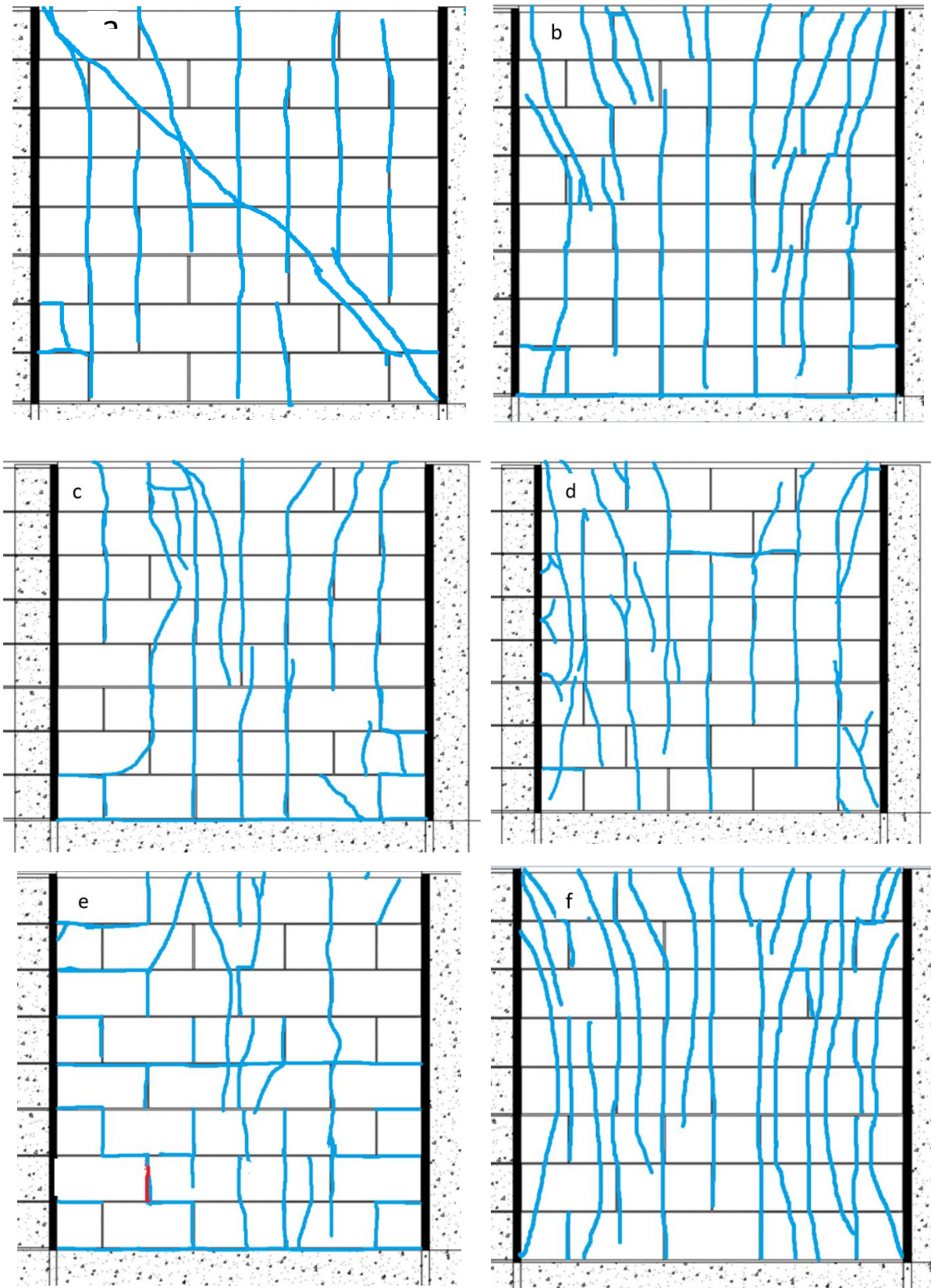Figure 11: crack patterns on the exposed side of wall after 14 days in Not-loaded Saint-Leu (a); Loaded Saint-Leu (b); Not-Loaded Tervoux (c); Loaded Tervoux (d); Not-Loaded Massangis (e); Loaded Massangis (f)
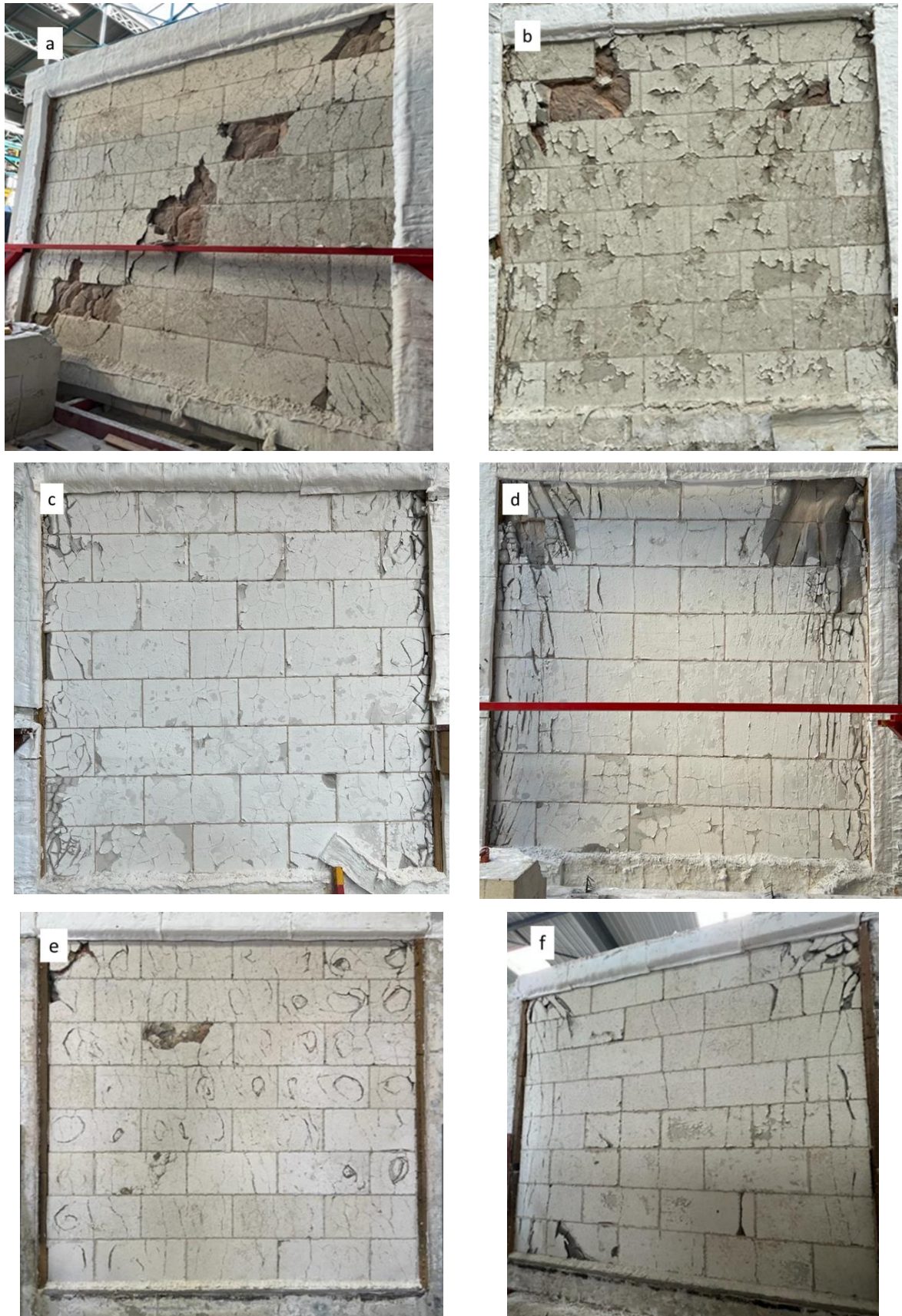
Figure 12: Pictures of the exposed sides of the walls after 14 days in unloaded Saint-Leu (a); Loaded Saint-Leu (b); Unloaded Tervoux (c); Loaded Tervoux (d); Unloaded Massangis (e); Loaded Massangis (f)

horizontal displacement is given in Figure 1. The measurements showed that the total horizontal elongations for all the walls after 120 minutes of heating were all between 20 and 24 mm. Therefore, the width of the cracks was in the majority of cases of the order of 2.5 mm. In the case of the two unloaded and loaded Massangis walls, they were respectively of the order of 3.5 and 1.7 mm. The images recorded with the thermal camera also allow the visualization of cracks. The cracks show locally higher temperatures during the heating phase (Figure 1). The detailed analyze of the data from the DIC system and the thermal camera which have not been presented in this paper will be presented in a future article.

4.5 Observations after the tests

After one day of cooling and mechanical load assessment, the reinforced concrete frame containing the wall was removed from the furnace to inspect the exposed side of the wall. Figure 12 illustrates the condition of the exposed side of all six walls after 14 days. Notably, the walls that failed due to the applied mechanical load exhibited a more severe cracking pattern. The observations also showed that some stones showed cracking parallel to the plane of the wall. This was particularly noticeable in the Saint-Leu stones. It was relatively easy to detach large blocks of about 3 cm thickness by tapping the surface with a hammer. In addition to the cracks, a visible change in the color of the limestone blocks was observed. Indeed, limestones exposed to high temperatures experienced a color change at different temperatures [7]. For temperatures greater than 730 degrees of Celsius, decarbonization of the calcite in these stones occurs, and upon exposure to the humidity in the air, it transforms into lime and eventually falls apart. Based on the evaluation of temperature distribution across the wall, it is estimated that approximately 1 cm of the thickness of the wall failed during this time.

CONCLUSIONS

In conclusion, this study investigated the behavior of masonry walls made of three different types of limestone with different compressive strengths subjected to fire exposure for 120 minutes, followed by the assessment of their residual capacity. In this paper, we mostly present the study of the out-of-plane displacements, residual mechanical behavior, and cracking patterns of the walls.

The results indicate that the unloaded walls experienced more significant out-of-plane displacement toward the fire – in comparison to the loaded ones - during heating, with the highest displacement occurring in the center of the walls and decreasing along the boundaries. The DIC analyses showed that the out-of-plane displacements for the majority of the tests had relatively high symmetry. However, we have noted that for both Tervoux walls, the maximal deflection did not occur at mid-width but was a bit off-center.

After heating, all six walls remained intact and did not fail. The walls with the higher value of compressive strength, retained a significant amount of their load-carrying capacity, as demonstrated by the residual mechanical behavior tests. The compressive strength of the limestone and the amount of load during heating differed, resulting in varying residual loads for each case. The Massangis walls demonstrating the highest residual capacity exceeding 375 tonnes.

Cracking patterns on the non-exposed side of the masonry walls after 120 minutes of heating showed that vertical cracks were prevalent, originating from the vertical joints and propagating vertically through the stones, more specifically in the center of the walls. Transverse cracks were present in all walls, and in loaded walls, the presence of cracks in the top angles and lateral sides was more pronounced compared to unloaded walls.

In addition, the study found that the exposed side of the walls shows a visible color change of the limestone blocks after exposure to high temperatures. The study estimated that approximately 1 cm of the thickness of the wall failed during heating due to the decarbonization of the calcite in the limestone blocks.

This work highlights the importance of considering the behavior of masonry walls under fire exposure and the potential impact on their load-carrying capacity and structural integrity. Results show that, even after fire exposure, the limestones masonry walls can retain a significant amount of their load-carrying capacity. which can inform the development of more resilient and fire-safe building designs.

Supplementary analysis of the experimental data (DIC system, thermal camera …) which have not been presented in this paper and numerical simulations of the effect of high temperature on the behavior of limestone masonry walls are under way and will be presented in future articles.

REFERENCES

[1] Gomez-Heras M, Mc Cabe, S. et al. (2009). Impacts of fire on stone-built heritage – An overview. Journal of Architectural Conservation 15(2):47-58

[2] Mertz, J. D., Colas, E., Ben Yahmed, A., Lenormand R (2016). Assessment of a non-destructive and portable mini permeameter based on a pulse decay flow applied to historic surfaces of porous materials. In: Proc. of the 13th International Congress on the deterioration and conservation of stone, 6-10th September 2016, Paisley, Scotland.

[3] Comité Européen de Normalisation (2007). EN 1996-1-2: 2007 – Design of masonry structures – Part 1-2: General rules – Structural fire design.

[4] National fire Protection Association (2019). NFPA® 914 Code for the Protection of Historic Structures, 2019 Edition. Available at https://www.nfpa.org/codes-and-standards

[5] Ingham, J. P. (2009). Application of petrographic examination techniques to the assessment of fire-damaged concrete and masonry structures. Materials Characterization 60:700-709.

[6] Sippel, J., Siegesmund. S., Weiss, T., Nitsch, K. H., Korzen, M. (2007). Decay of natural stones caused by fire damage. In: Přikryl R and Smith BJ (eds.), Building stone decay: from diagnosis to conservation. Geological society of London, Special Publications, 271:139-151

[7] Vigroux, M. (2020) Influence de la microstructure et de la minéralogie sur l'endommagement mécanique des pierres de construction utilisées dans le patrimoine bâti sous l'effet de conditions environnementales sévères, PhD Thesis, Université de Cergy Pontoise, 399 p.

[8] Koca, MY, Ozden, G, Yavuz, A. B. et al. (2006). Changes in the engineering properties of marble in fire-exposed columns. International Journal of Rock Mechanics & Mining Sciences, 43:520-530

[9] McCabe, S, Smith, B. J., Warke, P. A. (2010). Exploitation of inherited weakness in fire-damaged building sandstone: the 'fatiguing' of 'shocked' stone. Engineering Geology, 115:217–225

[10] Russo, S, Sciarretta F (2012). Experimental and theoretical investigation on masonry after high temperature exposure. Experimental Mechanics, 52:341-359

[11] Russo, S, Sciarretta F (2013). Masonry exposed to high temperatures: Mechanical behaviour and properties – An overview. Fire Safety Journal, 55:69-86

[12] Wu, Q., Weng L et al. (2019). On the tensile mechanical characteristics of fine-grained granite after heating/cooling treatments with different cooling rates. Engineering Geology 253:94-110

[13] Ghobadi, M. H., Babazadeh, R. (2015). Experimental studies on the effects of cyclic freezing–thawing, salt crystallization, and thermal shock on the physical and mechanical characteristics of selected sandstones. Rock Mechanics and Rock Engineering, 48:1001-1016

[14] Pham, D. T., Donval, E., Pinoteau, N., Pimienta, P., Pallix, D. (2022). Test of loaded and unloaded natural stone masonry walls exposed to fire, Materials and Structures/Materiaux et Constructions, 55/9, November 2022, art. 229

[15] Donval, E., Pham, D.T., Hassen, G., de Buhan, P., Pallix, D. (2022) Essai de résistance au feu d'un mur en maçonnerie en pierre naturelle. Academic Journal of Civil Engineering : Proceedings of the 40th meeting of universities in civil engineering (RUGC) - Lille.10.26168/AJCE.40.1.50

[16] Daoudi, A., Sciarretta, F., Eslami, J., Beaucour, A. L., Noumowé, A., Experimental characterization of physical, thermal, transport and mechanical properties of 13 french limestones, Construction and Building Materials (under review).

EFFECT OF Mo ADDITION ON THE STRUCTURAL PERFORMANCE OF STRUCTURAL STEEL COLUMNS AT ELEVATED TEMPERATURES

Waibhaw Kumar a,*   **Umesh K. Sharma b**

ABSTRACT

The present research focuses on comparing the structural performance of cold-formed fire-resistant structural steel with that of cold-formed plain carbon structural steel at elevated temperatures. The present fire-resistant steels (YSt-355-FR (0.1% Mo) and YSt-355-FR (0.126% Mo)) used in this study have 0.1% and 0.126% Mo content by weight, respectively; whereas, the plain carbon steel (YSt-355) have no presence of Mo in its metallurgical composition. The finite element analysis was performed using Abaqus tool to estimate the buckling strength of the YSt-355-FR (0.1% Mo), YSt-355-FR (0.126% Mo), and YSt-355 structural steel columns at elevated temperatures, and the results obtained were compared to buckling strength obtained using the provision of EC3 and AS 4100 to judge their competence pertaining to newly developed fire-resistant steel. The finite element analysis has confirmed the superior performance of fire-resistant steel columns at the structural level as compared to that of plain carbon steel columns at elevated temperatures, driving the designers, architects, and structural engineers to use fire-resistant steel in lieu of plain carbon steel.

Keywords: Finite element analysis; Structural performance; Fire-resistant steel; Plain carbon steel.

---

a,* Research Scholar, Department of Civil Engineering, Indian Institute of Technology Roorkee, 247667, India (wkumar@ce.iitr.ac.in), Corresponding author.

b Professor, Department of Civil Engineering, Indian Institute of Technology Roorkee, 247667, India (umesh.sharma@ce.iitr.ac.in).

1. INTRODUCTION

In the present time, structural steels are the main structural material used in the construction industry that offers high strength, strength to dead weight ratio, and ductility to the structures compared to other structural materials. In addition to its capabilities to mould in any shape with fast erection of structural members at constructional site, the structural steels are widely used in the prefabricated structures and providing aesthetic pleasing steel structures. Commercially, structural steels are available in the market depending on the rolling, forming, grade (strength), alloying elements, heat treatment; moreover, majority of the fire standards [1–5] categorizes the structural steel based upon the grade and rolling of the structural steels. Therefore, recommendations in these fire-design standards of structural steels are based on the grade and rolling process. The detailed discussion were made by the researchers [6–9] regarding the characterization of steel based on the grade and rolling.

In order to achieve higher performance of structural steel at elevated temperatures, several elements like carbon, silicon, manganese, chromium, molybdenum, niobium, etc., were micro-alloyed with plain carbon steel to produce super-alloy fire-resistant structural steel [10–15]. The fire-resistant structural steel is the steel that retains 67 percent of the specified room-temperature yield strength at 600°C. The purpose of adding microalloying elements in the plain carbon steel was enumerated in Table 1. Most of the previous researchers [8,10–16] micro-alloyed the plain carbon steel with Mo and Nb to achieve high strength and retention factor at room- and elevated-temperatures. Further, the heat-treatment and cooling condition also influence the mechanical properties of the structural steels. The present fire-design standards [1–5] did not categorize the structural steels based on presence of the key alloying elements and their percentage composition that influences the mechanical properties drastically. Authors [17] compared the mechanical properties of various grade of structural steels in terms of reduction factors.

In terms of performance at the material level, these structural steels [8,15,16] have proven higher performance in terms of strength properties; and yield- and ultimate- strength reduction factors at elevated temperatures compared to plain carbon structural steel. Further, the researchers [12,15,16] have compared the mechanical properties of fire-resistant steel and plain carbon steel; however, both the structural steels used by the researchers belong to different grades that resulted in a vague comparison of both the steels having different grades. However, the researchers [8,9,18] compared the mechanical properties of fire-resistant steel and plain carbon steel having same grade and reported a significant improvement in the mechanical properties of fire-resistant steel over the plain carbon steel. Coming to comparison of structural performance of plain carbon steel and fire-resistant steel, a few authors [12,13,16,19] conducted experimental and numerical investigation to report the performance of both the steels at elevated temperatures. The authors reported that the performance of fire-resistant structural steel members is superior to plain carbon structural steel members, however, both the structural steel members have different grade of structural steels, that makes comparison of structural performance of both the structural steels insignificant. Therefore, a huge void is left in the literature regarding the structural performance of fire-resistant steel and plain carbon steel at elevated temperatures, that makes the motivation of the present study.

Table 1: Alloying element used in Fire-resistant steel

Element	Description
Carbon	Alloying the steel with carbon increases the yield strength and hardness; however, reduces ductility and weldability of the steel.
Silicon	Increasing the percentage of silicon in the steel increases the strength at high temperatures.
Manganese	Manganese is used as a deoxidant in the steel and its presence contribute to temperature embrittlement.
Chromium	Presence of chromium makes the steel corrosion-, oxidation-, and heat- resistant.
Molybdenum	Molybdenum is the key alloying element in fire-resistant steel that enhances the high-temperature strength, creep, and corrosion resistance of steel. Further, it reduces temper brittleness in steel.
Niobium	Presence of Niobium in the steel enhances the strength at room- and elevated-temperature with marginally affecting weldability. Further, it also improves the creep strength.

2. RESEARCH SIGNIFICANCE

The present study is constituted to show the effect of Mo addition on the structural performance of the structural steels at elevated temperatures. Toward this end, the compression tests were conducted on the structural steel tubes to validate the finite element model, and the buckling strength of fire-resistant and plain carbon steel columns at elevated temperatures is estimated by using a finite element tool. The fire-resistant steels reported in the literature have Mo content greater than 0.2% by weight; however, the newly developed fire-resistant steels (YSt-355-FR (0.126% Mo) and YSt-355-FR (0.1% Mo)) have Mo content less than 0.126% by weight. Further, the plain carbon steel (YSt-355) and fire-resistant steel (YSt-355-FR (0.126% Mo) and YSt-355-FR (0.1% Mo)) of same grade (355 MPa) used in this study.

3. CHEMICAL COMPOSITION

The chemical composition of the structural steels under consideration (YSt-355, YSt-355-FR (0.126% Mo), and YSt-355-FR (0.1% Mo)) have been listed in Table 2. It is clear from Table 2 that Mo is the principal alloying element present in the fire-resistant steel (YSt-355 (0.126% Mo) and YSt-355 (0.1% Mo)), while the amount of Mo content in the conventional steel (YSt-355) is negligible.

Table 2: Metallurgical composition (% wt.) of structural steels.

Alloying element	YSt-355	YSt-355-FR (0.1% Mo)	YSt-355-FR (0.126% Mo)
C	0.056	0.055	0.053
Mn	0.920	1.051	1.042
P	0.023	0.022	0.020
Si	0.290	0.189	0.202
Al	0.035	0.045	0.049
V	0.017	0.051	0.064
Ti	0.056	0.002	0.002
Nb	0.044	0.004	0.001
Mo	0.001	0.100	0.126
Cr	0.025	0.029	0.028
Ni	0.018	0.020	0.020

4. METHODOLOGY

4.1 Structural steel tube dimension

The cross-sectional dimensions and length of structural steel tubes taken for the present study are 180 x 180 x 8 mm and 3.0 m, respectively.

4.2 Geometric Imperfection

The geometric imperfection of the YSt-355, YSt-355-FR (0.126% Mo), and YSt-355-FR (0.1% Mo) structural steel tubes were measured using the testing arrangement built of LVDTs and levelled surface. The maximum geometric imperfection reported for the YSt-355, YSt-355-FR (0.126% Mo), and YSt-355-FR (0.1% Mo) structural steel tubes were L/1691, L/1734, and L/1808, respectively.

4.3 Numerical validation

The finite element validation is carried out using ABAQUS, a finite element tool. The finite element model is verified through the ref. [9,18,20]. The estimation of the buckling strength of the structural steel tube column was

452

carried out by performing two types of finite element analysis. The *BUCKLE and non-linear load-deformation procedure was performed from the ABAQUS library to find the different buckling shapes and buckling strength of the structural steel tube column, respectively. The *BUCKLE procedure is first performed to estimate the probable buckling shape of the structural steel tube column. The *BUCKLE procedure incorporates elastic modulus of structural steel, and the buckling shapes of the column depend on the cross-section, elastic modulus, and end boundary conditions. The non-linear load-deformation analysis is the next analysis which utilizes the first (lowest mode) buckling shape from the previous analysis (*BUCKLE) to evaluate the buckling strength of the structural steel tube column. The first buckling shape of the column is the lowest buckling mode. Initial data like initial geometric imperfection and material non-linearity (true stress-strain data points) were fed to the model. The engineering stress-strain data points presented in ref. [8,9,18] were converted to true stress-strain data points using calibration module from the ABAQUS library. The non-linear geometry parameter was incorporated in the column model using *NLGEOM module from the ABAQUS library. The end boundary conditions taken for this study were fixed-fixed with vertical deformation allowed at top. The rate of deformation of 0.0167 mm per second is applied at the top of the finite element model as compressive load.

4.4 Mesh optimization

Optimization of mesh was carried out to obtain good results comparable to experimental test. The mesh sizes of 10 mm, 15 mm, and 20 mm were taken for this study. It is observed that the finite element models with mesh size of 10 mm have a good match with the results of the experimental test. The results of the mesh optimization analysis are matched with the experimental test conducted in ref. [18]. Therefore, the C3D8R mesh with size of 10 mm is chosen for highly efficient and low-cost analysis.
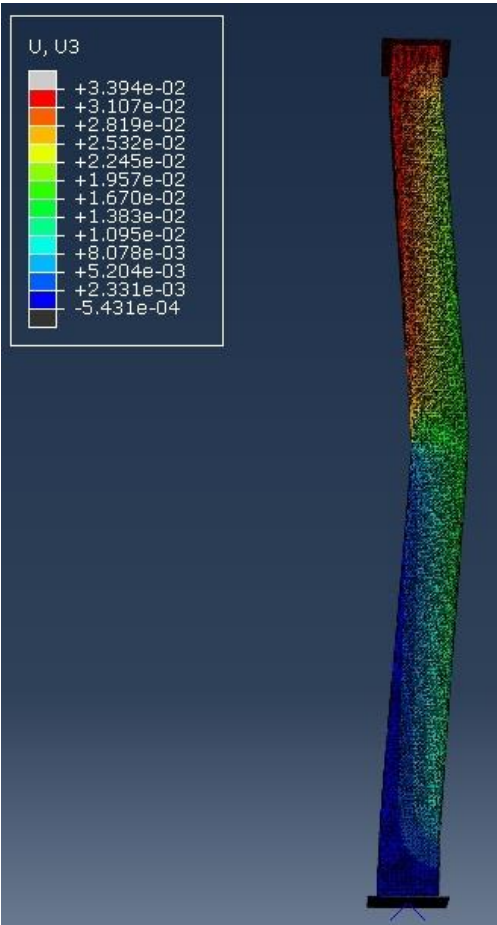

Figure 1: Buckling shape of the finite element model (Structural steel tube column).

5. RESULTS AND DISCUSSION

The buckling strength-deformation curve of the YSt-355, YSt-355-FR (0.126% Mo), and YSt-355-FR (0.1% Mo) structural steel tube columns at 20°C,100°C, 200°C, 300°C, 400°C, 500°C, 600°C, 700°C, and 800°C is presented in Figures 2, 3, 4, 5, 6, 7, 8, 9, and 10, respectively. The buckling strength is defined at the maximum axial load carrying capacity of the column. The buckling strength of the structural steel tube columns were noted from Figure 2 – 10 and presented in Table 3.

From Figure 2, it can be observed that the buckling strength of YSt-355-FR (0.1% Mo) structural steel tube column is highest, followed by YSt-355-FR (0.126% Mo) and YSt-355 structural steel tube columns. Despite of being same grade of structural steel, the fire-resistant steels (YSt-355-FR (0.126% Mo) [9] and YSt-355-FR (0.1% Mo) [18]) have higher nominal yield strength compared to plain carbon steel (YSt-355 [8]), and this can be attributed to the higher buckling strength of fire-resistant steels compared to plain carbon steel at 20°C. Further, the presence of Mo in the chemical composition of fire-resistant steels resulted in higher nominal yield strength compared to plain carbon steel, which is ultimately reflected in increased buckling strength. It can be observed from Table 4 that the buckling strength of YSt-355-FR (0.126% Mo) and YSt-355-FR (0.1% Mo) columns is 10.44% and 14.32% higher than that of YSt-355 column, respectively. Moreover, from Figure 2, the buckling strength of YSt-355-FR (0.1% Mo) is higher than that of YSt-355-FR (0.126% Mo) despite of being less amount of Mo content. This can be reasoned to higher amount of cold-forming in the YSt-355-FR (0.1% Mo) steel leading to increased nominal yield strength compared to YSt-355-FR (0.1% Mo). In Table 4, the buckling strength of YSt-355-FR (0.1% Mo) is 3.51% higher than that of the YSt-355-FR (0.126% Mo) column. Similar observations are made for the structural performance of fire-resistant steels and plain carbon steel columns up to 400°C (Figures 3, 4, 5, and 6). The buckling strength of fire-resistant steel columns is almost 6-14 percent higher than that of plain carbon steel columns up to 400°C (Table 4). Further, the buckling strength of YSt-355-FR (0.126% Mo) is higher than that of the YSt-355-FR (0.1% Mo) column beyond 200°C as the effect of higher cold-forming diminishes up to 200°C in YSt-355-FR (0.1% Mo).
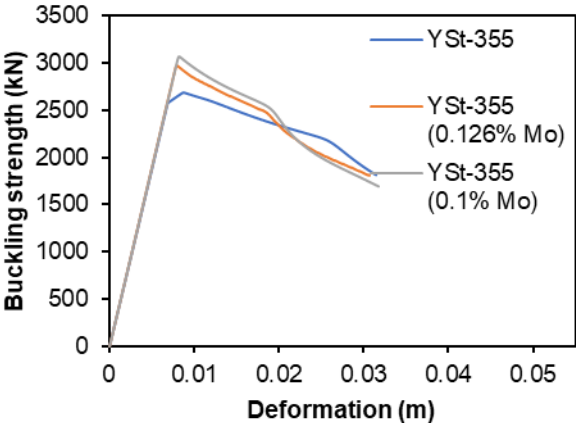

Figure 2: Comparison of buckling strength – deformation curve of YSt-355, YSt-355-FR (0.126% Mo), and YSt-355-FR (0.1% Mo) structural steel tube columns at 20°C

Figure 3: Comparison of buckling strength – deformation curve of YSt-355, YSt-355-FR (0.126% Mo), and YSt-355-FR (0.1% Mo) structural steel tube columns at 100°C

Figure 4: Comparison of buckling strength – deformation curve of YSt-355, YSt-355-FR (0.126% Mo), and YSt-355-FR (0.1% Mo) structural steel tube columns at 200°C

Figure 5: Comparison of buckling strength – deformation curve of YSt-355, YSt-355-FR (0.126% Mo), and YSt-355-FR (0.1% Mo) structural steel tube columns at 300°C
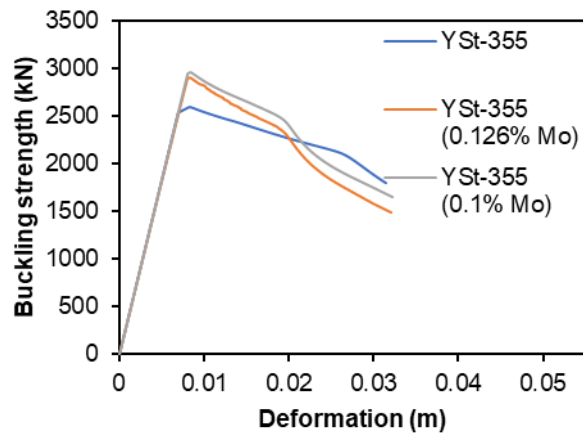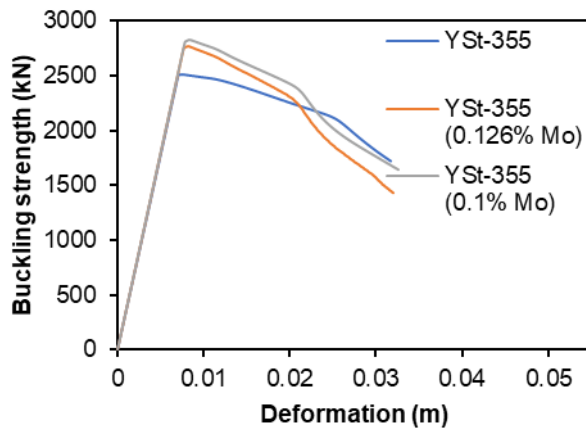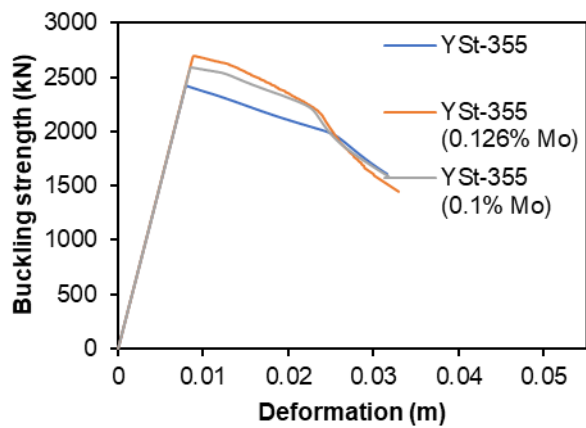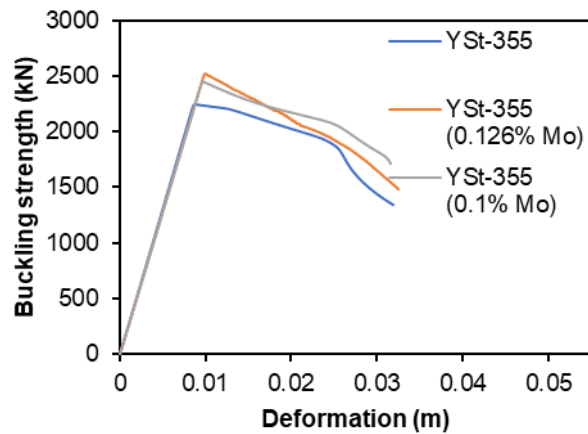
Figure 6: Comparison of buckling strength – deformation curve of YSt-355, YSt-355-FR (0.126% Mo), and YSt-355-FR (0.1% Mo) structural steel tube columns at 400°C

Table 3: Buckling strength of structural steel tube columns at elevated temperatures estimated by finite element analysis

T (˚C)	Buckling strength (kN)		
	YSt-355	YSt-355 (0.126% Mo)	YSt-355 (0.1% Mo)
20	2689.16	2969.51	3074.38
100	2592.69	2903.70	2950.75
200	2515.73	2768.06	2824.66
300	2429.43	2692.62	2588.33
400	2243.05	2522.11	2451.76
500	1665.00	2170.09	2125.83
600	1056.09	1617.67	1601.60
700	602.49	1025.11	899.02
800	299.50	450.19	429.58

Table 4: Percent increase in the buckling strength of structural steel tube columns at elevated temperatures estimated by finite element analysis

T (˚C)	Percent increase in buckling strength		
	YSt-355 (0.126% Mo) vs. YSt-355	YSt-355 (0.1% Mo) vs. YSt-355	YSt-355 (0.1% Mo) vs. YSt-355 (0.126% Mo)
20	+10.44	+14.32	+3.51
100	+12.00	+13.83	+1.63
200	+10.15	+12.38	+2.03
300	+10.80	+6.54	-3.85
400	+12.42	+9.26	-2.81
500	+30.30	+27.61	-2.06
600	+53.07	+51.57	-0.97
700	+69.76	+49.21	-14.02
800	+50.33	+43.43	-4.79

From Figures 7-10, it can be observed that the buckling strength of YSt-355 structural steel tube column drastically reduced compared to YSt-355-FR (0.126% Mo) and YSt-355-FR (0.1% Mo) structural steel tube columns beyond 400°C. Higher yield strength and strength retention factor of fire-resistant steels compared to plain carbon steel at material level enhance the structural performance of fire-resistant steel columns beyond 400°C. Enhanced yield strength and retention factor of fire-resistant steels compared to plain carbon steel at elevated temperatures can be contributed to the presence of Mo in its chemical composition. At 500°C, the buckling strength of YSt-355-FR (0.126% Mo) and YSt-355-FR (0.1% Mo) columns is 30.30% and 27.61% higher than that of YSt-355 column, respectively. Further, the buckling strength of the fire-resistant steel columns is fifty percent greater compared to YSt-355 column at 600°C. At 700°C, the buckling strength of YSt-355-FR (0.126% Mo) and YSt-355-FR (0.1% Mo) columns is 69.76% and 49.21% higher in comparison with YSt-355 column, respectively. Moreover, the buckling strength of YSt-355-FR (0.126% Mo) and YSt-355-FR (0.1% Mo) columns is 50.03% and 43.43% higher in comparison with YSt-355 column, respectively, at 800°C. Therefore, it is clearly observed that the presence of Mo in the chemical composition of structural steels drastically improves the buckling strength of steel columns at elevated temperatures.

The fire-design parameters recommended in standards [1–5] are for plain carbon steel and cannot be applicable for super-alloyed fire-resistant steels. The use of fire-design parameters recommended in these standards for the evaluation of the structural capacities of the fire-resistant structural members will give very conservative and uneconomical design strength values. Therefore, the new design parameters will be incorporated in the present fire standards for safe and economical design of the super-alloyed fire-resistant structural steel members.

Figure 7: Comparison of buckling strength – deformation curve of YSt-355, YSt-355-FR (0.126% Mo), and YSt-355-FR (0.1% Mo) structural steel tube columns at 500°C

Figure 8: Comparison of buckling strength – deformation curve of YSt-355, YSt-355-FR (0.126% Mo), and YSt-355-FR (0.1% Mo) structural steel tube columns at 600°C
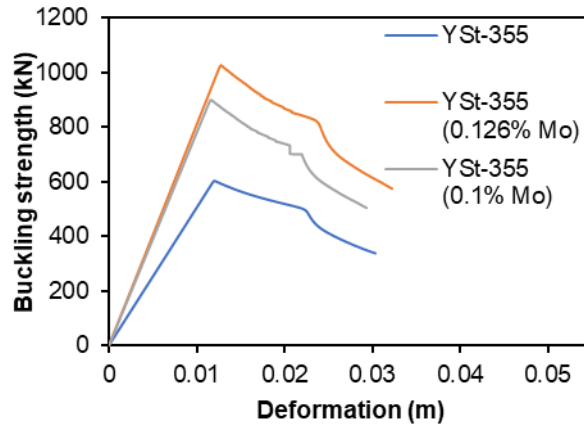
Figure 9: Comparison of buckling strength – deformation curve of YSt-355, YSt-355-FR (0.126% Mo), and YSt-355-FR (0.1% Mo) structural steel tube columns at 700°C
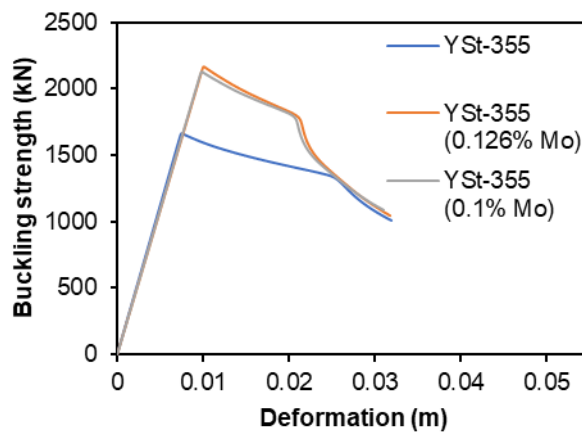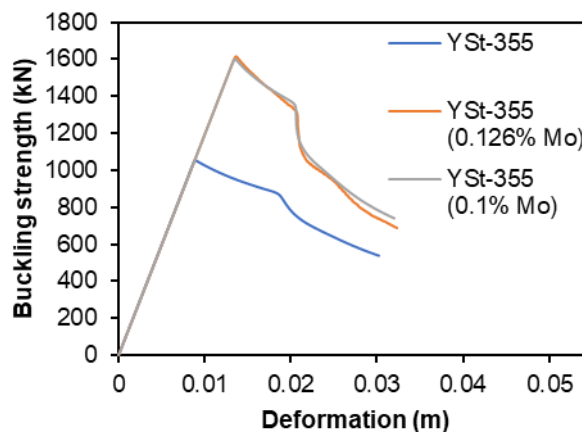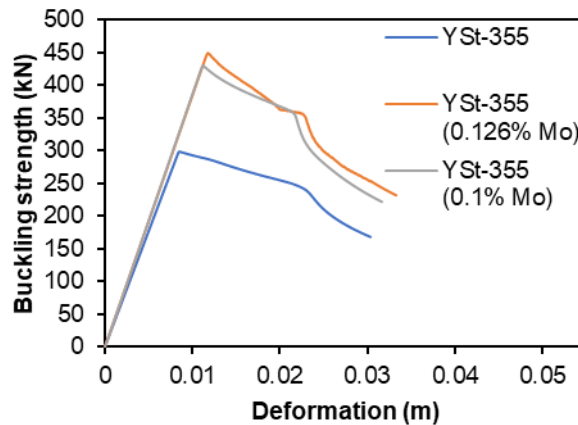

Figure 10: Comparison of buckling strength – deformation curve of YSt-355, YSt-355-FR (0.126% Mo), and YSt-355-FR (0.1% Mo) structural steel tube columns at 800°C

6. CONCLUSION

At material level study, it earlier was marked that the fire-resistant steel has higher strength properties and strength retention ability compared to plain carbon steel at room- and elevated- temperatures due to the presence of Mo in their chemical composition. The present study extended the limits and incorporated the influence of addition of Mo on the structural performance of structural steels. Up to 400°C, the structural performance of fire-resistant steels is 10 percent higher compared to plain carbon steel. However, a drastic improvement in the structural performance of fire-resistant steels (greater than 50 percent) is observed in comparison with plain carbon steel beyond 500°C. Therefore, it can be observed that the presence of Mo in the structural steels enhances their structural performance at room- and elevated- temperatures. Further, the present fire design standards cannot be used for designing the super-alloyed fire-resistant structural steel members.

ACKNOWLEDGEMENTS

REFERENCES

[1]   European Committee for Standardization, EN1993-1-1. (2009). *Eurocode 3 - Design of Steel Structures — Part 1-1: General Rules and Rules for Buildings*, CEN, Brussels.

[2]   American Institution of Steel Construction (AISC). (2016). S*pecification for Structural Steel Buildings*, ANSI/AISC 360-16, Chicago.

[3]   Bureau of Indian Standards (BIS). (2007). *General Constructions in Steel - Code of Practice*, IS 800, New Delhi.

[4]   Standards Australia (AS). (1998). *Steel Structures*, AS 4100, Sydney, Australia.

[5]   British Standard Institute (BSI). (2003). S*tructural Use of Steelwork in Buildings Part 8: Code of Practice for Fire Resistant Design*, BS 5950-8, London.

[6]   Wang, W.; Liu, B.; Kodur, V.; (2013). *Effect of Temperature on Strength and Elastic Modulus of High-Strength Steel*, Journal of Material in Civil Engineering, vol. 25, p. 174–182. https://doi.org/10.1061/(ASCE)MT.1943-5533.0000600.

[7]   Kankanamge, N. D.; Mahendran, M.; (2021). *Mechanical properties of cold-formed steels at elevated temperatures*, Thin-Walled Structures, vol. 49, p. 26–44. https://doi.org/10.1016/j.tws.2010.08.004.

[8]   Kumar, W.; Kumar, U. K.; Shome, M.; (2021). *Mechanical properties of conventional structural steel and fire-resistant steel at elevated temperatures*, Journal of Constructional Steel Research, vol. 181, p. 106615. https://doi.org/10.1016/j.jcsr.2021.106615.

[9]   Kumar, W.; Sharma, U. K.; Pathak, P.; (2022). *Mechanical properties of low-alloyed YSt-355-FR (0.126%Mo) cold-formed steel tube at elevated temperatures*, Journal of Constructional Steel Research, vol. 192, p. 107198. https://doi.org/10.1016/j.jcsr.2022.107198.

[10]   Wan, R.; Sun, F.; Zhang, L.; Shan, A.; (2012). *Development and study of high-strength low-Mo fire-resistant steel*, Materials & Design, vol. 36, p. 227–232.

[11]   Wan, R.; Sun, F.; Zhang, L.; Shan, A.; (2012). *Effects of Mo on high-temperature strength of fire-resistant steel*, Materials and Design, vol. 35, p. 335–341. https://doi.org/10.1016/j.matdes.2011.09.009.

[12]   Sakumoto, Y.; Yamaguchi, T.; Ohashi, M.; Saito, H.; (1992). *High-temperature properties of fire-resistant steel for buildings*, Journal of Structural Engineering (United States); vol. 118 (1992), p. 392–407. https://doi.org/10.1061/(ASCE)0733-9445(1992)118:2(392).

[13]   Fushimi, M.; Chikaraishi, H.; Keira, K.; (1995). *Development of fire-resistant steel frame building structures*, Nippon Steel Technical Report.

[14]   Mizutani, Y.; Ishibashi, K.; Yoshii, K.; Watanabe, Y.; Chijiiwa, R.; Yoshida, Y.; (2004). 5*90MPa class fire-resistant steel for building structural use*, Nippon Steel Technical Report., p. 45–52.

[15]   Sha, W.; Chan, T. M.; (2002). *High temperature transient tensile properties of fire resistant steels*, Advances in Steel Structures (ICASS '02), vol. II, p. 1095–1102. https://doi.org/10.1016/b978-008044017-0/50128-1.

[16]   Kelly, F. S.; Sha, W.; (1999). *A comparison of the mechanical properties of fire-resistant and S275 structural steels*, Journal of Constructional Steel Research, vol. 50, p. 223–233. https://doi.org/10.1016/S0143-974X(98)00252-1.

[17]   Kumar, W.; Sharma, U. K.; (2022). *Incompetence of current fire standard to predict design reduction factors for cold-formed steels*, in: Cold-Formed Steel Research Consortium (CFSRC) Colloquium. http://jhir.library.jhu.edu/handle/1774.2/67716.

[18]   Kumar, W.; Sharma, U. K.; Pathak, P.; (2023). *Comparison of mechanical and structural performance of fire-resistant steels at elevated temperatures*, Structures, vol. 48, p. 478–491. https://doi.org/10.1016/j.istruc.2022.12.103.

[19]   Ding, J.; Li, G. Q.; Sakumoto, Y.; (2004). *Parametric studies on fire resistance of fire-resistant steel members*, Journal of Constructional Steel Research, vol. 60, p. 1007–1027.

[20]   To, E. C. Y.; Young, B.; (2008). *Performance of cold-formed stainless steel tubular columns at elevated temperatures*, Engineering Structures, vol. 30, p. 2012–2021. https://doi.org/10.1016/j.engstruct.2007.12.015.

BEHAVIOUR OF MINIMALLY FIRE PROTECTED WOOD-STEEL-WOOD BOLTED CONNECTIONS REINFORCED WITH SELF-TAPPING SCREWS

Oluwamuyiwa A. Okunrounmu [a]

Osama (Sam) Salem [b,*]

George V. Hadjisophocleous [c]

ABSTRACT

One of the challenges encountered in timber construction is the safe design of timber connections in fire conditions as their fire behaviour depends on many factors. This paper investigates the effect of load ratios and bolt patterns on the failure time of minimally fire-protected wood-steel-wood (WSW) bolted connections reinforced with self-tapping screws (STS). Four full-size fire experiments were conducted on glulam beam end connections loaded perpendicular-to-wood grain to develop shear and bending moment on the connections. Two connection configurations were studied, each utilizing six bolts arranged in two different patterns. The glulam beam end connections were reinforced perpendicular to wood grain with eight STS and exposed to elevated temperatures that followed the CAN/ULC S101-19 [1] standard fire time-temperature curve, while subjected to load ratios of 100% and 130% of the maximum moment designed capacity of the weakest unreinforced connection configuration. The test results showed that the connections' failure time exceeded 50 minutes, which surpassed the 45-minute minimum fire resistance rating recommended in applicable building codes. However, increasing the load ratio from 100% to 130% reduced the failure time of the connections. Importantly, reinforcing the connections with STS prevented splitting or row shear failures, which are frequently encountered in unreinforced WSW connections.

Keywords: Failure time; load ratio; wood-steel-wood connections; standard fire; self-tapping screws.

---

[a] Carleton University (oluwamuyiwaokunrounm@cmail.carleton.ca).

[b,*] Dept. of Civil Engineering, Lakehead University, 955 Oliver Road, Thunder Bay, ON P7B 5E1, Canada, (sam.salem@lakeheadu.ca), **Corresponding author**.

[c] Carleton University (george.hadjisophocleous@carleton.ca).

1. INTRODUCTION

In North America, the use of timber as a construction material has been on the rise over the past few decades owing to its abundance in the region, renewability, sustainability, and availability of innovative high-quality engineered products such as glued-laminated timber (Glulam) and Cross-Laminated Timber (CLT). Among many other benefits of using wood as a construction material is its distinctive high strength-to-mass ratio over other construction materials (i.e., concrete and steel) and good fire-endurance performance due to the formation of char. In high-rise buildings, mass timber members such as glulam are used as structural members (i.e., columns and beams) to transfer loads among the members of the structure. These members are linked together using connections that comprise fasteners (i.e., steel bolts or dowels) and steel plate sections. Timber structures are susceptible to fire because of the combustible nature of wood material. In the event of a fire, connections are the most vulnerable structural components due to the presence of metal connecting elements, which aids the transfer of heat to the inner core of the wooden component of the connection. As a result, the wood chars with an increased charring rate around the metal connecting components in the connections [2]. Thus, the connections are the weakest link and most critical structural component of any timber structure under fire exposure.

Bolted wood-steel-wood (WSW) connections are used in high-rise buildings by designers due to their good aesthetic appearance and their ability to transfer shear forces since wood is well recognized to be weak in longitudinal shear and tension perpendicular-to-grain [3]. Beam-to-column WSW connections are widely used in tall buildings to provide rigidity to the structure where they can sustain bending moments that can be developed due to lateral loads [4]. Also, moment-resisting beam-to-column connections with high capacity are vital in portal frame structures susceptible to earthquake excitations [5]. Previous studies had shown that the predominant failure modes of moment-resisting bolted wood-steel-wood connections loaded perpendicular to wood grain at ambient temperatures are parallel-to-grain row shear and perpendicular-to-grain tensile splitting. In the past few decades, various reinforcing techniques have been employed to improve the capacity of wood connections and strengthen them against brittle and ductile failures. One of the solutions to strengthen connections against brittle failures as well as to retrofit existing wood structures is to employ fully threaded self-tapping screws (STS) as perpendicular-to-grain reinforcement. This technique of reinforcing connections is widely used due to its simple installation and economic benefit over other traditional reinforcement methods [6].

Extensive studies have shown that self-tapping screws can be effectively used to prevent or fully control brittle and ductile failure modes frequently encountered in connections. Bejtka and Blaß [7] strengthened dowel-type connections with self-tapping screws to enhance their load-carrying capacity. It was reported that placing the screws in contact with dowel fasteners increased the stiffness and the load-carrying capacity of the connections by up to 120% when compared to the unreinforced connections [7]. Zhang et al. [8] used partially threaded self-tapping screws to improve the mechanical performance of dowel-type WSW connections in timber portal frames. Test results showed that the screws effectively controlled splits propagation and increased the moment-resisting capacity of the connections as well as their ultimate rotation by 31% and 51%, respectively. In another study, Petrycki and Salem [5] investigated the behaviour of beam-to-column bolted wood-steel-wood connections reinforced with self-tapping screws, while subjected to monotonic loading in a column removal scenario. It was reported that the screws increased the moment-carrying capacity of the reinforced connections by a factor ranging between 1.3 and 2.4.

Studies reported in [3] and [4] demonstrated that ductile and high-capacity moment-resisting bolted WSW connections can be achieved by employing self-tapping screws. The test results showed that the capacity of moment-resisting beam-to-column connections subjected to reverse cyclic loading increased by a factor of 1.7. In another study, Lam et al. [9] studied the influence of self-tapping screws in the performance of bolted glulam connections with slotted-in steel plates, subjected to monotonic and reverse cyclic loadings. In that study, failed unreinforced connections were also retrofitted with self-tapping screws. It was reported that the capacity of the reinforced connections increased by a factor of 2 and 1.7 under monotonic and reverse cyclic loading, respectively; while an increase by a factor of 1.87 and 1.53 was observed in the capacity of the retrofitted connections when subjected to monotonic and reverse cyclic loading, respectively.

Despite the extensive studies to understand the behaviour of self-tapping screws as reinforcement in connections experimentally tested at ambient temperatures, limited experimental studies have been conducted at elevated temperatures to investigate the fire performance of such reinforced connections. Thus, further research is needed

at elevated temperatures to better understand the influence of self-tapping screws on the fire performance of beam-to-column WSW connections in order for such connections to comply with the prescribed fire-resistance rating in applicable codes for combustible buildings, and also promote high-rise timber construction.

In the past decade, extensive studies have been conducted both experimentally and numerically to investigate the behaviour of various connection configurations at elevated temperatures. A number of papers have been published on connections subjected to perpendicular-to-grain [10] and parallel-to-grain [11] tensile loading; however, limited studies exist on the fire performance of beam-to-column WSW connections loaded to develop shear and bending moment on the connections. Recent studies [12–14] had shown that perpendicular-to-grain tensile splitting and parallel-to-grain row shear are the major failure modes of connections tested at elevated temperatures. Other failure modes reported on WSW connections are hole elongation (ductile failure) and edge shear out [15], with splitting being the most frequently encountered failure mode. In an effort to control or prevent such brittle failure modes at elevated temperatures, Petrycki and Salem [16] and Palma et al. [17] strengthened wood-steel-wood connections in a perpendicular direction with self-tapping screws. Petrycki and Salem [16] reported that the screws enhanced the failure time of the connections, while Palma et al. [17] observed a reduction in the fire resistance of some connections due to the premature exposure of the screws to fire, which caused an increase in the charring rate of the connections. Both authors reported that the tensile splitting failure frequently experienced in the unreinforced connections was prevented and the failure time of the connections reported was below the minimum fire-resistance rating of 45 minutes recommended in the current National Building Code of Canada (NBCC) [18] for combustible construction.

Other studies by Peng et al. [15] and Akotuah et al. [19] investigated the effect of load ratio on hybrid steel-timber connections. Both authors reported that increasing the load ratio reduced the time to failure of the connections. To further improve the fire resistance of WSW connections, Owusu et al. [12] and Peng et al. [15] investigated the effect of metal protection on the fire performance of WSW connections. Owusu et al. [12] protected the metal connecting components (i.e., bolt heads and nuts, and steel plate edges) using the same glulam material and reported a failure time of 23 minutes more than that of the unprotected connections. Peng et al. [15] employed a single layer of 15.9 mm Type X gypsum board and a double layer of 12.7 mm plywood to protect the connecting metal components of the connections. Test results reveal that the Type X gypsum board improved the failure time by about 30 minutes, while the double-layer of 12.7 mm plywood increased the failure time of the connections by 15 minutes.

To further improve the fire performance of WSW connections, the research reported herein focuses on the evaluation of the behaviour of bolted WSW connections reinforced perpendicular-to-grain with STS and exposed to CAN/ULC-S101-19 [1] Standard time-temperature curve. Variables that affect the fire performance of connections, such as the applied load ratios, bolt patterns and influence of STS, were experimentally examined. The test results provide a better understanding of the rotational behaviour of the connections in standard fire conditions.

2. EXPERIMENTAL PROGRAM

2.1 Materials

In all tests, a Canadian black spruce pine (SP) with a stress grade of 24f-EX and an architectural grade was used for the wooden members of the connections. The glulam beam sections had rectangular cross-sectional dimensions of 184 mm wide x 362 mm depth x 1600 mm long. The beams were conditioned indoors at 20℃ and 60% relative humidity (RH). Some of the beams experienced shrinkage of about 2 mm in depth due to the reduction of moisture content. The test assemblies were supported on one beam end by a W200 steel column of grade 300 W, having a flange and web thickness of 8 mm and 6 mm, respectively. The steel column was fire-protected with ceramic fibre blankets before the start of the fire test. The mechanical properties of the glulam sections were obtained from the Canadian Construction Materials Centre (CCMC) Evaluation Report 13216-R [20].

In this study, the two steel T-stub connectors considered were manufactured from a 12.7 mm (1/2") thick steel plate of grade 300W. Both T-stub connectors' flanges had a height of 302 mm in order to accommodate the

protection of a 30 mm rectangular glued-in wood strip at both the top and bottom side of the steel T-stub connector. The dimensions and bolt pattern of the individual T-stub connector depend on the test connection configuration. The steel bolts used were made of 19.1 mm (3/4") diameter A325M high-strength structural steel bolts and thus, all the bolt holes on the T-stub connectors were sized to be 1 to 2 mm (1/16 inch) larger than the bolts' diameter as per CAN/CSA O86-19 [21]. Therefore, all the steel connector holes were 20.6 mm (13/16 inch) in diameter and a weld size of 6 mm was used to join the connector's knife plate to its flange that was flushed with the cross-section of the glulam beam. SWG ASSY VG plus CSK self-tapping screws (STS) were employed to reinforce the connection specimens from top to bottom in a perpendicular-to-grain direction. The fully threaded self-tapping screws were produced from carbon steel and had a bending yield strength of 1,015 MPa and an unfactored shear strength of 641 MPa. The screws were 300 mm long and 8 mm in outer thread diameter.

2.2 Test Specimens

2.2.1 Connection configuration types and test matrix

To investigate the effect of applied load and bolt patterns on the performance of minimally fire-protected glulam WSW connections reinforced with self-tapping screws, two different connection configurations were tested, with one similar specimen per configuration but under different load ratios. A monotonic transverse load was applied on the beam-to-column connections at the beam-free end to develop shear and bending moment on the connection. The first connection configuration (bolt pattern P1) had two of its bolt rows symmetrically positioned near the top and bottom sides of the beam cross-section, while the second connection configuration (bolt pattern P2) had the bottom row shifted upward to the mid-height of the beam to be in the tension side and as a result, further contribute to the moment-resisting capacity of the connection. Consequently, the unloaded edge distance of the connections with bolt pattern P1 was 91 mm, and for those with bolt pattern P2 was 181 mm. All the metal connecting components of the connections, that is, bolt heads and nuts, and steel plate edges were fire protected with glued-in wood plugs and strips, respectively. The WSW connection configurations were designed to satisfy the Canadian Engineering design in wood standard CSA O86-19 [21]. The dimension and details of the bolt and self-tapping screws layout of the tested beam-to-column WSW connections are presented in Figures 1 and 2. Table 1 summarizes the test matrix of the fire tests presented in this paper.
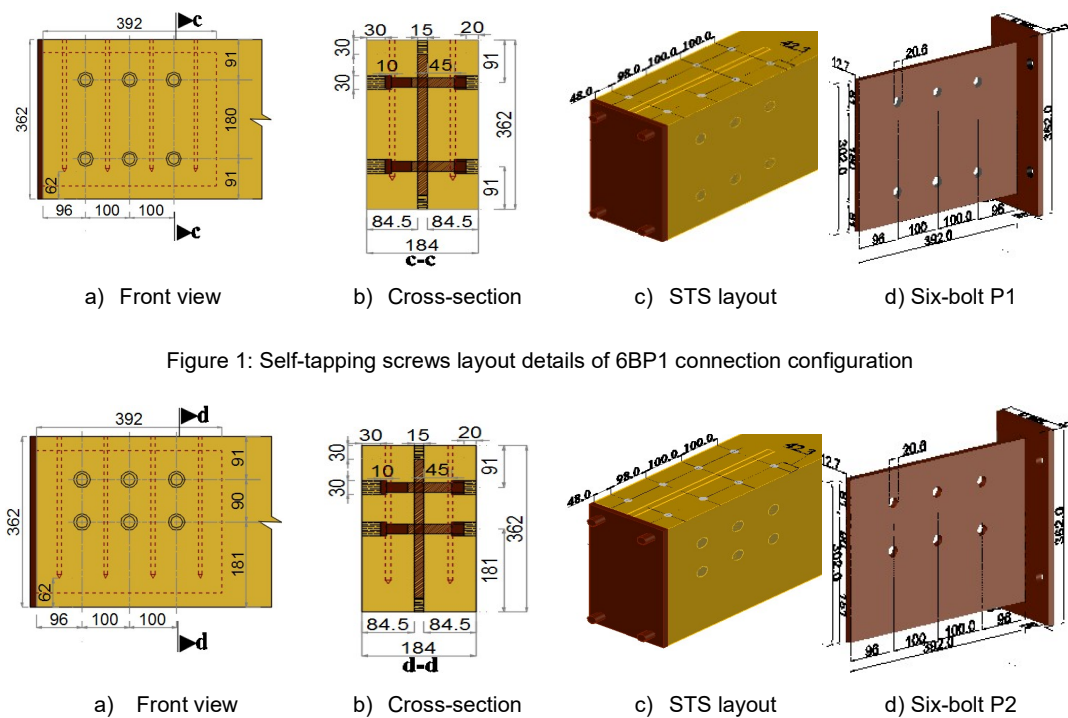

a) Front view　　b) Cross-section　　c) STS layout　　d) Six-bolt P1

Figure 1: Self-tapping screws layout details of 6BP1 connection configuration

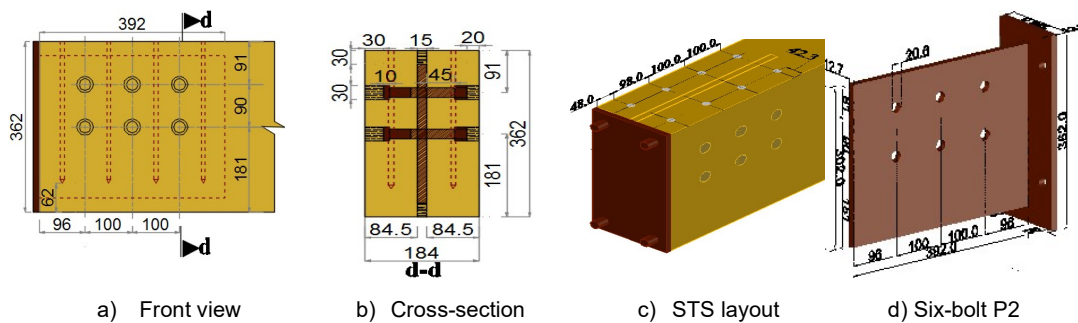a) Front view　　b) Cross-section　　c) STS layout　　d) Six-bolt P2

Figure 2: Self-tapping screws layout details of 6BP2 connection configuration

Table 1: Test matrix of all fire tests

Connection configuration ID.	Bolt pattern	Applied moment (kN.m)	Number of bolts	Number of Self-tapping screws	Initial wood cover underneath the bottom row of bolts (mm)
6BP1-LR100	P1	14.8	6	8	91
6BP2-LR100	P2	14.8	6	8	181
6BP1-LR130	P1	19.3	6	8	91
6BP2-LR130	P2	19.3	6	8	181

Note(s): 6B for six bolts; P1 and P2 for the first and second bolt pattern, respectively; LR for load ratio.

2.2.2 Test assembly details and fabrication process

Each of the four full-size test assemblies consisted of a 1600-mm long glulam beam that was structurally connected via a steel T-stub connector at one end to a sturdy supporting steel column. In each glulam beam, a vertical slot was made using a portable bandsaw in order to sandwich the T-stub connector between the wood side members. The slot for the 12.7 mm (1/2") T-stub plate was cut to a width of 15 mm in order to allow for a fabrication tolerance of 1 to 2 mm as required in the Canadian Engineering design in wood standard CAN/CSA O86-19 [21]. Circular holes were drilled into the glulam beam faces with the use of a 30 mm diameter spade bit to embed the bolt heads and nuts, as well as to accommodate the wood plug protection. After, the inner 19.1 mm bolt holes were milled using a 20 mm drill bit to allow for a minimum 1 mm fabrication tolerance as specified in CAN/CSA O86-19 [21]. The T-stub plate was slotted into the 184 mm x 362 mm beam cross-section, thereby sandwiched between two wood members with side thickness of 84.5 mm each and fastened together with 19.1 mm (3/4") diameter A325M high-strength structural steel bolts. Subsequently, the metal components of the connections were protected with glued-in wood plugs and strips. Thereafter, the STS were installed from the top to bottom of the glulam beam section in a perpendicular-to-grain direction. The test specimen was connected to the supporting steel column via the T-stub connector using 19.1 mm (3/4") diameter structural steel bolts and tightened with nuts. The spacing of the fasteners was designed in accordance with CAN/CSA O86-19 [21].

2.2.3 Tests setup and procedure

A hydraulic cylinder supported by a steel frame mounted around the furnace was used to apply a monotonic transverse load on the specimen at the free end of the beam at 1400 mm away from the beam support. Figure 3 shows one of the specimens installed inside the fire testing furnace located at Lakehead University Fire Testing and Research Laboratory (LUFTRL). Each specimen was gradually pre-loaded to the targeted load level in four increments, each of 25%, to allow for the stabilization of deflections after each increment in accordance with CAN/ULC S101-19 [1]. The test commenced 30 minutes after the full transverse load was applied. During the fire test, the load level on the specimen was measured and maintained constant until the failure criterion was reached. An LVDT installed outside the furnace was used to continuously measure the beam's vertical displacement throughout the fire test.
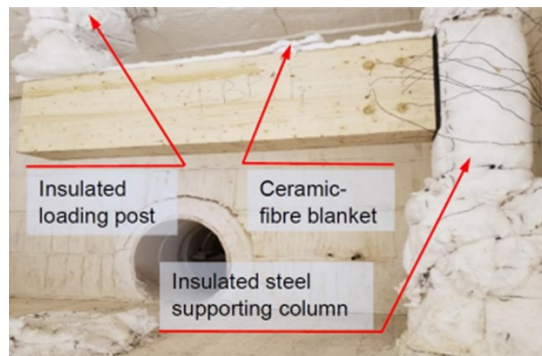

Figure 3: A test specimen installed inside the fire testing furnace at LUFTRL

The test specimens were exposed to elevated temperatures that followed the CAN/ULC S101-19 [1] standard time-temperature curve on all sides except the top one simulating the existence of a slab on top of the beam. The

top of the beam and the supporting steel column was protected from fire using a 1.0-inch thick ceramic-fibre blanket. The failure criterion for the connections occurred when the beam-end deflection corresponds to the rotational limit of magnitude 0.1 radians. However, the tests continued beyond this point until the test assembly could not sustain the applied load, and a significant load drop with no recovery was observed, at which the test was terminated, and the cooling phase of the furnace commenced. The time to failure and the thermal measurements of each test specimen were recorded and the temperatures measured by the different thermocouples installed at different depths inside the wood were used to determine the average charring rates of the wood at the connection location since there was a complete burnout of the remaining beam section when it was possible to open the furnace door after it was completely cooled down.

3. EXPERIMENTAL RESULTS

The experimental results presented in this paper describe the effects of applied load and bolt patterns on the rotational behaviour, failure modes and time to failure of the four minimally fire-protected WSW connections reinforced with self-tapping screws. Furthermore, time-temperature curves were developed and analyzed from the thermal measurements recorded from the thermocouples, and the charring rate was determined for each connection configuration.

3.1 Load and connection rotational limit

Figure 4 shows the applied load, failure criterion and connection rotation with respect to time curves for the first bolt pattern (P1) connection with a 130% load ratio applied. The failure criterion for the connections was determined when the beam-end deflection corresponds with the maximum connection's rotational limit of 0.1 radians. However, the tests continued beyond this point for a few more minutes and until the test assembly could not sustain the applied load, and a significant load drop with no recovery was observed. This is represented on the time-load curve by a significant fall in the load magnitude with no recovery.
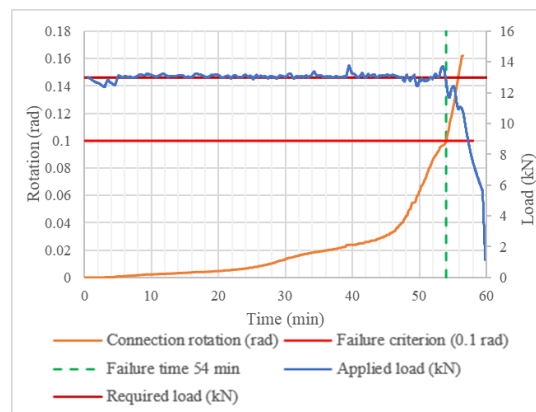
Figure 4: Applied load and connection rotation vs. time relationships for the six-bolt connection configuration with the first bolt pattern (6BP1-LR130)

3.2 Time-temperature curves

Figure 5 illustrates the time-temperature curves for the connection configuration of 6BP1-LR100. The time-temperature curves were plotted from the thermal measurements recorded from twelve (12) metal-shielded Type K thermocouples installed at different locations within the beam end connection. As shown in Figure 5, at the early stage of all fire tests, thermocouples TC9 and TC10 inserted at 20 mm depths from the fire-exposed face of the beam recorded a temperature of 100°C after about 5 minutes. As the temperature continues to increase above 100°C, the moisture in the wood started to evaporate and as a result, at around 180°C to 200°C the wood starts to decompose and subsequently char at 300°C at about 20 minutes into the fire test. In all tests, it was observed that the temperature of the steel plate recorded by TC2 and TC6, as well as that of thermocouples TC4

and TC5 installed at a depth of 60 mm into the wood were all below 300ºC. This indicates that the char layer thickness of the beam section did not reach the 60 mm depth from the fire-exposed surface, and the steel plate did not contribute to the charring of the wood due to the 30-mm thick glued-in wood plugs and strips which protected the metal connecting components within each connection. However, it was observed that the bolt head temperature had risen above 300ºC at approximately 35 minutes, which assisted in accelerating the charring around the bolt holes later in the fire test. This also led to noticeable elongation of the holes that further increased the rotation of the connection. Thermocouples TC3 and TC7 installed at 40 mm inside the wood recorded temperatures that correspond with the wood's charring temperature (i.e., 300 ºC) at approximately 47 minutes, at which the char layer progressed to the location of the STS embedded inside the glulam section. At the failure time of the connection, thermocouples TC9 and TC10 installed at a depth of 20 mm measured temperatures as high as the furnace temperature, whereas thermocouples TC2 and TC6 installed at the face of the steel plate measured temperatures below 300ºC.
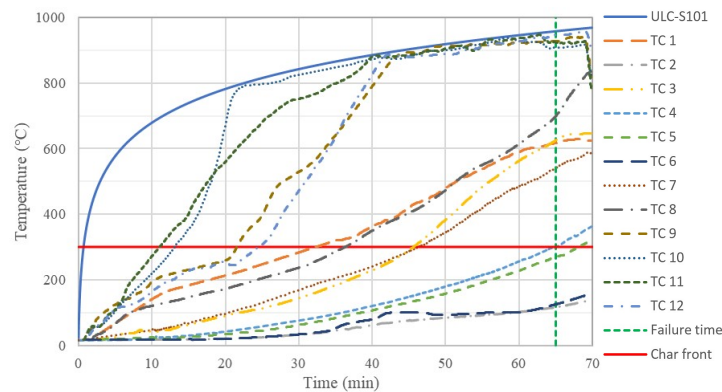

Figure 5: Time-temperature curves for the six-bolt connection configuration with bolt pattern P1 at 100% load ratio

3.3 Charring rates

Charring rate can be defined as the rate at which wood turns to char (or the rate of advance of char into the wood). It is also referred to as the dimensional rate, i.e., the ratio of charred depth to exposure time (mm/min). Charring rate is an important factor in structural fire safety design for timber structures since the strength and stiffness of the structural components under fire exposure depend largely on the uncharred cross-sections (residual sections). The thermal measurements recorded during the fire tests presented in this paper were used to calculate the charring rate of the connection configurations. The charring rate was determined from the position of the 300ºC isotherm, which implies that the charring rates of the connections were calculated from the times at which the temperatures measured by thermocouples TC3 and TC7 (installed at 40 mm depth), and TC9 and TC10 (installed at 20 mm depth) reached 300ºC, using Equation (1). This was the only method that could be used to determine the average charring rate of the connections since the glulam beam sections were burnt out completely before it was possible to open the furnace door after it was cooled down.

$$\beta = C / t \qquad (1)$$

Where, β is the rate of charring (mm/min)

 C is the depth difference for the char front to reach depths of 40 and 20 mm

 t is the time difference for the thermocouples at depths 20 mm and 40 mm to reach 300ºC which is the wood charring temperature.

The time to reach 300ºC at the two selected depths inside the wood (i.e., 20 and 40 mm) from the fire-exposed surface of the beam section was analyzed to calculate the actual charring rates of the connections as summarized in Table 2. Based on the temperatures measured by the thermocouples installed at different depths, it was found that the protection applied to the metal components (i.e., bolt heads and nuts, and steel plate edges) significantly slowed down the transfer of heat into the wood core section and thus, reduced the charring rates.

Table 2: Charring rates estimated for the four connection configurations (mm/min)

Connection configuration ID.	TC3 and TC9	20-40 mm	TC7 and TC10
6BP1-LR100	0.79	0.71 (Avg.)	0.62
6BP2-LR100	0.73	0.64 (Avg.)	0.55
6BP1-LR130	0.59	0.67 (Avg.)	0.74
6BP2-LR130	0.73	0.79 (Avg.)	0.85

Note(s): 6B for six bolts; P1 and P2 for the first and second bolt pattern, respectively; LR for load ratio.

3.4 Failure time

The main results of the fire tests for the four reinforced WSW connections are summarized in Table 3. In this study, the time to failure is described as the time from the start of the fire test to the time the failure criterion was reached, which is when the deflection of the beam's free end corresponds with the rotational limits of 0.1 radians. Overall, the failure times of all four connection configurations exceeded 50 mins, which is more than the minimum fire-resistance rating of 45 minutes prescribed in the current National Building Code of Canada (NBCC) [18] for combustible construction.

From Table 3, it is observed that increasing the load ratio from 100% to 130% in the first and second bolt patterns (P1 and P2), decreased the failure time by 11 mins (approximately 17% decrease) and 9 mins (approximately 15% decrease), respectively. Therefore, the effect of load ratio significantly influences the time to failure of the connections. This confirms the test results reported by Peng et al. [15, 22], Ali [23] and Akotuah et al. [19]. In addition, it is noticed that connections with bolt pattern P1 performed better in failure time than bolt pattern P2. For the effect of bolt patterns, bolt pattern P1 with a failure time of 65 minutes performed better than bolt pattern P2 by 4 minutes (about a 6.6% increase) at a 100% load ratio. Similarly, at 130% load ratio, the failure time of the six-bolt pattern P1 was slightly higher than that of the six-bolt pattern P2 by only two minutes. The effect of load ratios on the failure time of the connections was more pronounced than the effect of bolt patterns which is almost insignificant.

It is worth mentioning that none of the four reinforced connection configurations exhibited brittle failure such as wood splitting or row shear. The STS was effective in increasing the failure time of the connections when compared with the failure times reported by Owusu [24] on identical, but unreinforced connections subjected to the same applied load in standard fire conditions. In that prior study [24], lesser failure times were reported due to an earlier splitting failure that occurred at the glue line of the glulam beams at the connection location.

Table 3: Summary of test results

Connection configuration ID.	Applied moment (kN.m)	Time to failure (min)	Failure mode
6BP1-LR100	14.8	65	Excessive rotation due to deflection
6BP2-LR100	14.8	61	Excessive rotation due to deflection
6BP1-LR130	19.3	54	Excessive rotation due to deflection
6BP2-LR130	19.3	52	Excessive rotation due to deflection

Note(s): 6B for six bolts; P1 and P2 for the first and second bolt pattern, respectively; LR for load ratio.

3.5 Connection rotations

The measured vertical displacements of the beam's free end were used to calculate the rotations of the connections and thus plot their time-rotation curves, shown in Figure 6. The time-rotation curves show similar trends of increased rotation with time for all four tested connection configurations. At the early stage of the fire tests, all the connections' rotation curves remained constant for the first few minutes (about 5 minutes) before exhibiting a linear increase in rotation values with time. Subsequently, the curves rose significantly and rapidly until structural failure occurred. The gradual decomposition of the wood material caused the glulam beam to lose cross section and strength due to charring, which as a result increased the rotations of the beam-end connection.

During the fire tests, the applied load was kept constant until failure, after which the load dropped with no recovery. This is reflected on the time-rotation curves by a plateau at the end of the tests. All four connection configurations experienced a gradual failure.

3.5.1 Effect of load ratio on the connection rotations

The effect of increasing the load ratio from 100% to 130% on the connections' rotation was pronounced, which resulted in an increase in the rate of the connection rotations. Figure 6a depicts the time-rotation curves for the six-bolt pattern P1 connection subjected to 100% and 130% load ratios. At both load ratios, it is observed that the connections exhibited a similar trend of increased rotations with time, whereas the connection subjected to a load ratio of 130% underwent a faster-increased rotation than that of the connection loaded to 100% load ratio. For the connection loaded to 100% load ratio, it is observed that the connection's rotations linearly increased for about 32 minutes, after which the rotational values increased gradually for about 23 minutes before rapidly increasing at 55 minutes to failure. A similar increased rotation trend is observed for the connection loaded to 130%, but with lesser time intervals. The connection exhibited a faster rate of rotation and rapidly increased at 45 minutes to failure. This resulted in an 11-minute difference in the failure time of the connections with the connection subjected to a 100% load ratio performing better than the connection loaded to a 130% load ratio.

Like the six-bolt pattern P1 connection, increasing the load ratio from 100% to 130% for the six-bolt pattern P2 connection had a considerable effect on the connection's rotational behaviour. Figure 6b shows the time-rotation curves for the six-bolt pattern P2 connection subjected to 100% and 130% load ratios. Both connections experienced a similar trend of increased rotations for about 17 minutes, after which the connection subjected to a load ratio of 130% exhibited a significant increase in its rotation values than those of the connection subjected to a 100% load ratio. This results in a reduction in the time to failure by 9 minutes. Figure 7 illustrates how the six-bolt connection with the first bolt pattern (P1) at a 100% load ratio exhibited different rotations during the fire test.
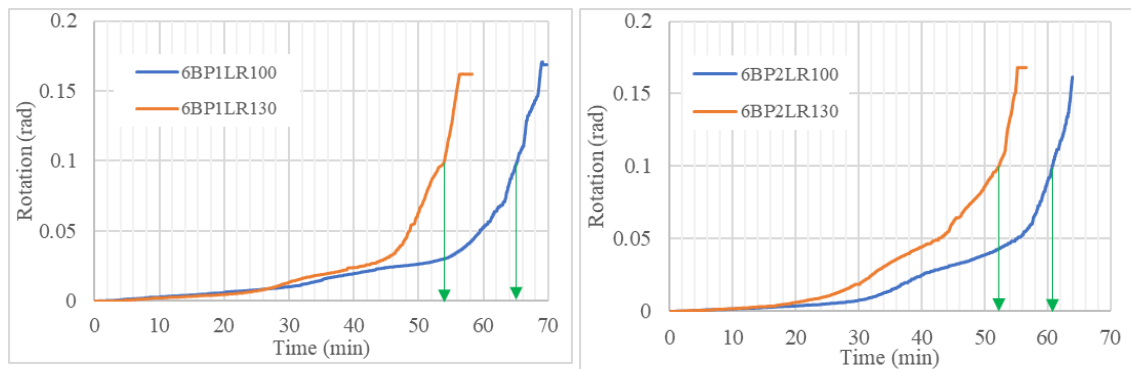
a) Effect of bolt pattern on six-bolt patterns P1

b) Effect of bolt pattern on six-bolt patterns P2

Figure 6: Time-rotation curves illustrating the effect of load ratios on the six-bolt pattern P1 and P2 connections.
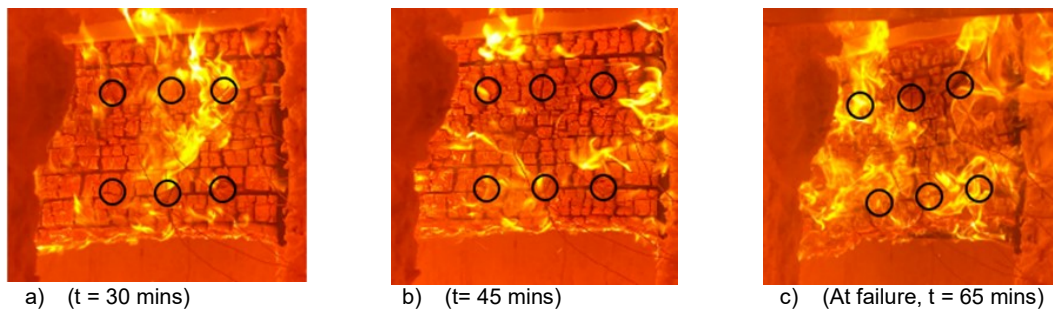

a) (t = 30 mins) b) (t= 45 mins) c) (At failure, t = 65 mins)

Figure 7: Six-bolt connection with the first bolt pattern (6BP1-LR100) undergoing standard fire testing.

3.5.2 Effect of bolt pattern on the six-bolt connection rotations at 100% and 130% load ratios

Figure 8 shows the effect of the bolt patterns on the connection rotations for the six-bolt connection configurations subjected to 100% and 130% load ratios. For the six-bolt connections subjected to a 100% load ratio, the rotations of the connection configurations 6BP1 and 6BP2 stayed unchanged for the first few minutes (about 5 minutes) before increasing linearly. The rotations of the connection configurations that employed bolt pattern P1 increased linearly for about 27 minutes, and then significantly rises for about 23 minutes, while the rotations of the configuration with bolt pattern P2 gradually increased for about 29 minutes and subsequently increased significantly for about 13 minutes until failure. The rotations of the configurations that employed bolt patterns P1 and P2 increased rapidly at 55 minutes and 50 minutes into the fire tests, respectively. Thus, the connection configurations with bolt pattern P1 performed better in terms of their failure time compared to those that employed bolt Pattern P2.

While at 130% load ratio, the effect of the bolt pattern for the six-bolt connection configurations was almost negligible as the difference in time to failure of the connections with six-bolt patterns P1 and P2 was only 2 minutes. As shown in Figure 8b, the time-rotation curve for the bolt pattern P2 connection had a greater slope than that of the bolt pattern P1 connection. Similarly, the rotations of the two connections were constant for the first 5 minutes, after which the connection with bolt pattern P2 rotated faster than that with bolt pattern P1. Thereafter, it is observed that the rotations of the connection with bolt pattern P1 gradually increased for about 33 minutes, and after that significantly increased for about 7 minutes before it rapidly increased to failure. The six-bolt pattern P2 connection experienced a similar trend but with lesser time intervals. This led to a reduction in time to failure for the 6BP2 connection, which is only 2 minutes lesser than that of the 6BP1 connection. No significant difference in failure time was observed between the two connection configurations. Figure 9 illustrates how the six-bolt connection with the second pattern at a 100% load ratio exhibited different rotations during the fire test.
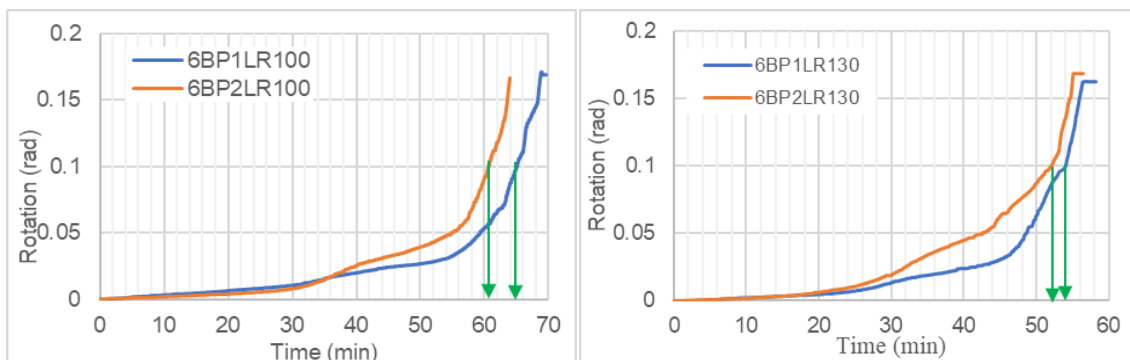
a) Effect of bolt pattern on the six-bolt connections subjected to 100% load ratio

b) Effect of bolt pattern on the six-bolt connections subjected to 130% load ratio

Figure 8: Time-rotation curves illustrating the effect of bolt patterns on the six-bolt connections with different load ratios.
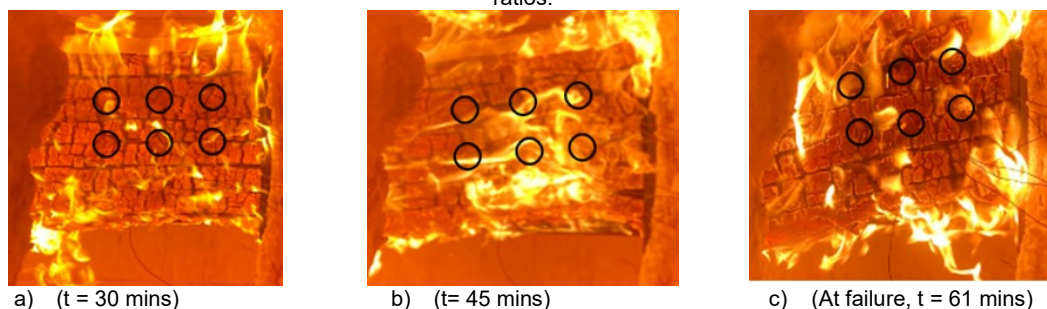

a) (t = 30 mins)   b) (t= 45 mins)   c) (At failure, t = 61 mins)

Figure 9: Six-bolt connection with the second bolt pattern (6BP2-LR100) undergoing standard fire testing.

469

Overall, at both load ratios, it is observed that the bolt pattern P1 connection exhibited lower rotations than that of bolt pattern P2 connections and thus, had higher failure times.

4. CONCLUSIONS

This paper presents the results of an experimental study to investigate the effects of applied load ratios and bolt patterns on the fire behaviour of minimally fire-protected WSW connections reinforced with STS. Four full-size beam-to-column glulam connections, involving two different connection configurations were tested in the large-size fire testing furnace under exposure to the effects of elevated temperatures that followed the CAN/ULC S101-19 [1] standard time-temperature curve on three sides of the beams' cross-section. Based on the experimental results, the following conclusions can be drawn on the fire performance of beam-to-column WSW connections reinforced with STS:

- The experimental results show that the failure time of the four connection configurations surpassed 50 minutes, which exceeded the minimum fire-resistance rating of 45 minutes recommended in the NBCC [18] for combustible constructions.
- The tendency of brittle failures, such as wood splitting and row shear, frequently encountered in unreinforced timber connections were prevented by the application of self-tapping screws as a mean of perpendicular-to-wood grain reinforcement, and thus, all four STS-reinforced connection configurations had increased strength and stiffness and enhanced failure time compared to the respective connection configurations without reinforcement.
- With the increase of the load ratio of the connections from 100% to 130%, the failure time of the connections significantly decreased. Thus, the behaviour of the connections in fire is largely influenced by the applied load ratio.
- The connection configurations that employed the first bolt pattern (P1) exhibited greater failure time at both applied load ratios. It can be concluded that the connections which had two rows of bolts symmetrically positioned near the top and bottom sides of the beam cross-section (bolt pattern P1) performed better than those with their bottom row raised to the mid-height of the beam section (bolt pattern P2).
- Although the new results are based on only four fire experiments due to budget and time constraints, it can be recommended that utilizing self-tapping screws for perpendicular-to-wood grain reinforcement in the connection configuration with the first bolt pattern (P1) can achieve a one-hour fire resistance rating.

5. ACKNOWLEDGEMENTS

6. REFERENCES

[1]   CAN/ULC S101, (2019). *Standard methods of fire endurance tests of building construction and materials*. Underwriters Laboratories of Canada, Fifth edition, Ottawa, Canada.
[2]   Peng, L.; Hadjisophocleous, G.; Mehaffey, J & Mohammad, M. (2010). *Fire resistance performance of unprotected wood–wood–wood and wood–steel–wood connections: a literature review and new data correlations*, Fire Safety Journal, vol. 45, no.6-8, p. 392–399.
[3]   Gehloff, M.; Closen, M. & Lam, F. (2010). *Reduced edge distances in bolted timber moment connections with perpendicular-to-grain reinforcements*. Word Conference on Timber Engineering, p. 1–8.
[4]   Lam, F.; Gehloff, M. & Closen, M. (2010). *Moment-resisting bolted timber connections. Proceedings of the Institution of Civil Engineers - Structures and Buildings*, no. 163, p. 267–274.
[5]   Petrycki, A. R. & Salem, O. S. (2020). *Structural Integrity of Bolted Glulam Frame Connections Reinforced with Self-Tapping Screws in a Column Removal Scenario. J. Struct. Eng.*, vol. 146, no.10, p. 04020213.

[6] Dietsch, P. & Brandner, R. (2015). *Self-tapping screws and threaded rods as reinforcement for structural timber elements – A state-of-the-art report. Construction and Building Materials*, Report 97, p. 78–89.

[7] Bejtka, I. & Blaß, H. J. (2005). *Self-tapping screws as reinforcements in connections with dowel-type fasteners, in: Proceedings of the CIB-W18 Meeting*, vol. 38.

[8] Zhang, C.; Guo, H.; Jung, K.; Harris, R. & Chang, W. S. (2019). *Using self-tapping screw to reinforce dowel-type connection in a timber portal frame. Engineering Structures*, vol. 178, p. 656–664.

[9] Lam, F.; Schulte-Wrede, M.; Yao, C. C. & Gu, J. J. (2008). *Moment resistance of bolted timber connections with perpendicular to grain reinforcements, in: Proceedings of the 10th World Conference of Timber Engineering (WCTE)*, vol. 2, p. 978-985.

[10] Audebert, M.; Dhima, D.; Taazount, M. & Bouchaïr, A. (2014). *Experimental and numerical analysis of timber connections in tension perpendicular to grain in fire. Fire Safety Journal*, vol 63, p. 125–137.

[11] Audebert, M.; Dhima, D.; Taazount, M. & Bouchaïr, A. (2012). *Behaviour of dowelled and bolted steel-to-timber connections exposed to fire. Engineering Structures*, vol 39, p. 116–125.

[12] Owusu, A.; Salem, O. S. & Hadjisophocleous, G. (2019). *Fire performance of protected and unprotected concealed timber connections, in: Proceedings of the 3rd International Fire Safety Symposium (IFireSS)*, p. 370–378.

[13] Palma, P.; Frangi, A.; Hugi, E.; Cachim, P. & Cruz, H. (2016). *Fire resistance tests on timber beam-to-column shear connections. Journal of Structural Fire Engineering*, vol. 7, no. 1, p. 41–57.

[14] Hubbard, C. & Salem, O. S. (2019). *Fire resistance testing of glulam beam end connections utilizing threaded steel rods in a pilot connection configuration, in: Proceedings of the 3rd International Fire Safety Symposium (IFireSS)*, p. 355–363.

[15] Peng, L.; Hadjisophocleous, G.; Mehaffey, J. & Mohammad, M. (2012). *Fire Performance of Timber Connections, Part 1: Fire Resistance Tests on Bolted Wood-Steel-Wood and Steel-Wood-Steel Connections. Journal of Structural Fire Engineering*, vol. 3, p. 107–132.

[16] Petrycki, A. R. & Salem, O. S. (2019) *Structural fire performance of wood-steel-wood bolted connections with and without perpendicular-to-wood grain reinforcement. Journal of Structural Fire Engineering*, Emerald Publishing, UK.

[17] Palma, P.; Frangi, A.; Hugi, E.; Cachim, P. & Cruz, H. (2013). F*ire resistance tests on steel-to-timber dowelled connections reinforced with self-drilling screws, in: 2nd CILASCI-Ibero-Latin-Amerian Congresso n Fire Safety Engineering*, Eidgenösische Technische Hochschule Zürich.

[18] NBCC (2020) *The National Building Code of Canada. Commission on Building and Fire Codes*, National Research Council of Canada, Ottawa, Canada.

[19] Akotuah, A. O.; Ali, S. G.; Erochko, J.; Zhang, X. & Hadjisophocleous, G. V. (2015). *Study of the Fire Performance of Hybrid Steel-Timber Connections with Full-Scale Tests and Finite Element Modelling, in: Applications of Structural Fire Engineering*.

[20] CCMC (2018). *Evaluation Report: Nordic Lam. Canadian Construction Materials Centre*, Report No. CCMC 13216-R.

[21] CAN/CSA O86 (2019). *Engineering design in wood*, Canadian Standards Association, Rexdale, ON, Canada.

[22] Peng, L., (2010). *Performance of heavy timber connections in fire,* Ph.D. Thesis, Carleton University, Ottawa, Ontario, Canada.

[23] Ali, S. G. (2016). *Fire Performance of Hybrid Timber Connections*, Ph.D. Thesis, Carleton University, Ottawa, Ontario, Canada.

[24] Owusu, A. (2019). *Structural Performance of Hybrid Timber Connections with Varying Bolt Patterns at Ambient and Elevated Temperatures*, M.A.Sc Thesis, Carleton University, Canada.

NONLINEAR THERMAL ANALYSIS ON TIMBER CROSS-SECTIONS VIA CS-ASA/FA ENHANCED BY GID GRAPHICS PRE- AND POST-PROCESSORS

Jackson S. Rocha Segundo[(a)], Caroline A. Ferreira[(b)], Ricardo A. M. Silveira[(c)], Thiago C. Assis[(d)], Lavínia L. M. Damasceno[(e)], Dalilah Pires[(f)], Rafael C. Barros[(g)], Ígor J. M. Lemes[(h)]

ABSTRACT

As timber is an anisotropic material, with irregular fibers, presence of knots, and flammable, and used in civil construction, it becomes a target for the study of realistic structural behavior in fire conditions. The main aim of this study is to perform a nonlinear analysis of timber cross-sections used in civil constructions, using a computational thermal module called CS-ASA/FA (Computational System – Advanced Structural Analysis/Fire Analysis), enhanced by GiD. Such analyses are essential for evaluating the performance of structures (beams, columns, trusses, and frames) during fire conditions, as the physical strength and properties of timber tend to deteriorate with increasing temperature. This promotes considerable losses in the bearing capacity and stiffness of the structural member or system. Considering the complexity of the timber sectional thermal problem and the nonlinear analysis to be performed, the input data flow and the visualization of the results can demand some time and effort from the analyst. Therefore, to increase the efficiency of the nonlinear sectional thermal analysis, a graphics pre- and post-processor via GiD was developed and coupled to the CS-ASA/FA. The pre-processor will guarantee a friendly graphical interface for the modeling of the timber cross-section and for its subsequent thermal analysis via the Finite Element Method (FEM); the post-processor will allow the analyst to evaluate the results by determining the temperature at any point in the timber cross-section for any instant of time during the analysis. Therefore, it will be possible to investigate whether the CS-ASA/FA module can yield the necessary information for a thermo-structural analysis, considering the evaluation of strength and stiffness loss in the structural material when exposed to fire.

Keywords: Thermal analysis, timber cross-section, pre- and post-processors, CS-ASA/FA, GiD.

1. INTRODUCTION

Timber is a material that is widely used in civil construction due to its good mechanical properties and good resistance in relation to its weight. It is also a thermal insulator that is easily machinable, renewable, and economically viable. However, it also has unfavorable characteristics, such as anisotropy, irregular knots and fibers, and flammability. When flammable materials such as timber are used, the concern of fire becomes quite relevant.

[a] Federal University of Ouro Preto (jackson.segundo@aluno.ufop.edu.br)

[b] Federal University of Ouro Preto (caroline.af@aluno.ufop.edu.br)

[c] Federal University of Ouro Preto (ricardo@ufop.edu.br)

[d] Federal University of São João del-Rei (thiagoclaudinoassis@gmail.com)

[e] Federal University of São João del-Rei (lavinialuisa@aluno.ufsj.edu.br)

[f] Federal University of São João del-Rei (dalilah@ufsj.edu.br)

[g] Concremat Engenharia e Tecnologia (rafaelcesario@hotmail.com)

[h] Federal University of Lavras (igor.lemes@ufla.br)

When wood is exposed to high temperatures, its resistance capacity and support of the structural elements or system get compromised because its physical and mechanical properties deteriorate with the increase in temperature. Therefore, it is essential to evaluate its structural behavior in a fire situation.

Structural element thermal analysis involves determining the variation in the temperature field when they exposed to fire, as a function of the fire elapsed time. The main goal of this work is to test the performance of timber cross-sections used in civil construction, through nonlinear analysis using the computational thermal module called CS-ASA/FA (Computational System – Advanced Structural Analysis/Fire Analysis) [1] enhanced by GiD [2].

The thermal numerical analysis process can be divided into three main phases: the creation of the cross-section model, calculating the temperature of the model, and visualizing the results. The analysis process begins with defining the material used, the cross-sectional geometry and properties of the material, the applied thermal load and boundary conditions, and other such details. Subsequently, the numerical solution is determined and in the last phase, the results are presented in such a way that the user can verify the cross-section temperature response with all the necessary details.

The use of a graphical pre-processor tool helps to reduce the efforts required to define a model, provides the necessary data for the analysis, and ensures greater accuracy and quality of the data that is to be used to describe the structural problem. The use of a graphical post-processor allows the user to evaluate the results quickly. Therefore, to ensure more efficiency in the nonlinear sectional thermal analysis, a graphical pre- and post-processor via GiD were developed and coupled to the CS-ASA/FA.

A commercial software called SAFIR [11] was used to validate the transient thermal analysis implementations of the timber cross-sections in the CS-ASA/FA module. It was possible to verify that the answers of this computational module were very satisfactory and consistent.

2. INTEGRATED SYSTEM GID/CS-ASA

The computer program called GiD [2] is widely used in computational mechanics as a pre- and post-processor, as it meets the needs of numerical solutions in the phases of data creation and results visualization. This tool provides a simple and intuitive interface for the elaboration of customized input files. The interaction between GiD and CS-ASA/FA for pre-processing was made possible through computational implementations in the GiD Problem Type (Figure 1), which include a set of text files that were used to customize the modeling. In the case of timber cross-section thermal analysis, a file containing information related to the materials used, boundary conditions (exposed faces), cross-section geometry, and other parameters necessary for the thermal analysis was generated. During the integration of the CS-ASA/FA module with GiD for post-processing, implementations were also made to create a new results file that was compatible with the reading and graphical presentation of GiD.

Next, the three phases of the numerical simulation (pre-processing, analysis, and post-processing) were exemplified according to the computational interventions that were performed to make the CS-ASA compatible with the GiD. A timber cross-section was used to elucidate each step of the transient thermal analysis.

2.1 Graphical Pre-processor

Graphical pre-processor is a tool that assists and speeds up the representation of a structure model (geometry and material properties, loads applied, boundary conditions, and other such characteristics). It also allows the user to make direct and simplified changes in the data parameters that are necessary to perform a structural analysis. This computational tool is important and indispensable to structural analysis programs that are based on the Finite Element Method (FEM) or any other numerical method. It provides a user-friendly and intuitive interface that assists the analysts in editing and visualizing the structural model and conducting the analysis with greater efficiency.

Figure 1 illustrates the operation of the GiD graphic-interactive interface that allows the proper creation of the input file for the CS-ASA/FA module.
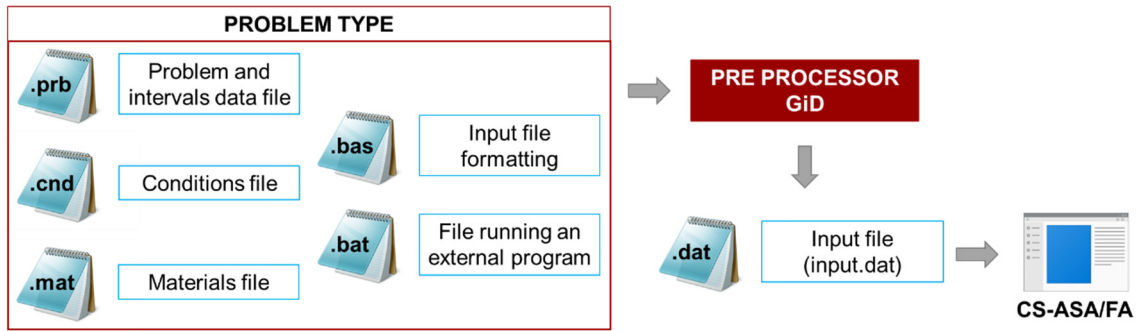
Figure 1: GiD and CS-ASA/FA interaction flowchart

The GiD pre-processor begins its work with the creation of the cross-section geometry and finite element mesh. Next, one must apply the model parameters using the *CND*, *MAT*, and *PRB* files (see Figure 2). The *CND* file (Figure 2a) is responsible for informing the boundary conditions imposed on the thermal problem (the faces that will be exposed to fire are assigned the value 1). The *MAT* file (Figure 2b) shows the thermal properties of timber (cross-sectional material that is analyzed) with respect to exposure to standard fire as presented by Eurocode [5]. The *PRB* file (Figure 2c) lists all the other essential parameters that the analyst must provide to use the CS-ASA/FA. Based on the assignments specified by the user, the *BAS* file organizes the *DAT* input file according to the format accepted by the CS-ASA/FA computational module. Using this integration between GiD and CS-ASA/FA, it was possible to transform two data input files into just one [1]. Finally, with the *BAT* file is possible to run CS-ASA/FA.
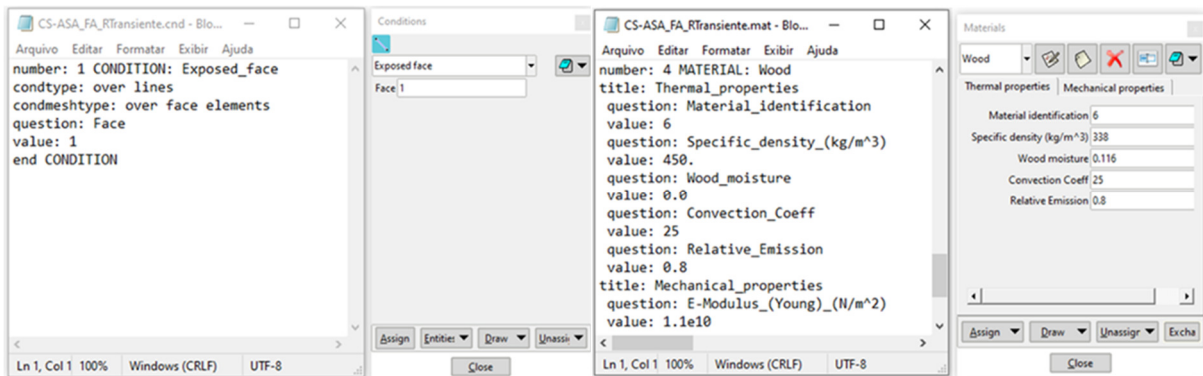
a) Conditions file (*CND* file) b) Materials file (*MAT* file)
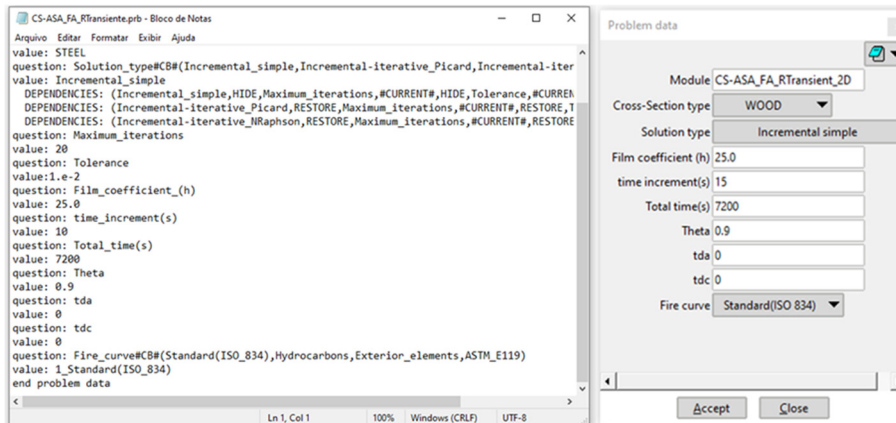
c) Control parameters file (*PRB* file)

Figure 2: CS-ASA/FA pre-processor text file formats

474

To understand the operation of this pre-processor, the cross-section of a glued laminated timber beam previously studied by Dârmon and Lalu [4] was analyzed. The temperature was evaluated on the cross-section external surface (point P1), as shown in Figure 3, and two finite element meshes were used to simulate this thermal problem using the CS-ASA/FA module: the first with 396 quadrilateral (Q4) finite elements, which is the same amount used by [4]; the second, more refined, with 792 Q4 finite elements.
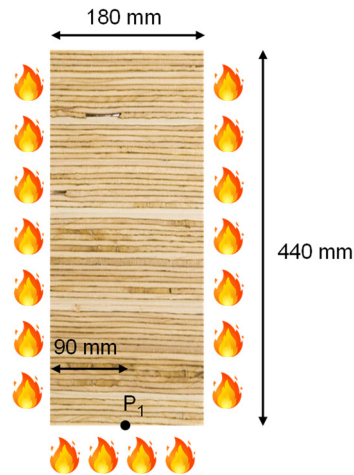

Figure 3: Laminated timber cross-section under fire situation

Figure 4a illustrates the geometric characteristics (180 mm wide and 440 mm high) of the timber cross-section and the 396 Q4 finite element mesh. Figure 4b presents the properties of the timber material: dry density equal to 338 kg/m³ and moisture content of 11.6%, as presented by [4]; convection coefficient of 25 W/(°Cm²) and emissivity coefficient of 0.8, taken from Eurocode [5]. Figure 4c indicates the faces of the timber that were exposed to fire in red color. Figure 4d presents the type of solution that was used: incremental simple, film coefficient of 25 W/m°C, time increment equal toof 15 seconds, fire time exposure of 7200 seconds, and the ISO 834-1 [6] standard fire curve.

2.2 Processor CS-ASA/FA

The computational program CS-ASA was designed such that new formulations and new types of finite elements could be developed and adapted easily and quickly to the system [3]. This computer system runs static and dynamic analyses of structures and considers nonlinear effects. To perform nonlinear timber thermal analysis in a transient regime, the CS-ASA/FA (Fire Analysis) module was adapted. This module is a part of the CS-ASA system and was developed based on the FEM. It performs the thermal analysis of the timber cross-section in a transient and steady state. When coupled with the CS-ASA/FSA (Fire Structural Analysis) module, it allows the thermo-structural analysis of the structures.

In the FEM context, the equilibrium equation that governs the transient heat transfer problem is described below in matrix form:

$$C\dot{T} + KT = R \tag{1}$$

where C and K are the capacitance matrix (thermal capacity) and the thermal conductivity matrix, respectively; R and T are, respectively, the nodal heat flux vector and the nodal temperature vector to be calculated; $\dot{T}$ is the partial derivative of temperature with respect to time. To obtain the solution for Eq. (1), an integration numerical model based on the Finite Difference Method was adopted. This model was previously presented and used by Lewis *et al.* [7], Rigobello [8], and Nunes [9]. Due to the material properties' dependence on the temperature, the transient heat transfer problem presents a nonlinear character.

The CS-ASA/FA module has two procedures for solving the discrete equation system: simple incremental strategy and incremental-iterative strategy. In the second option, the iteration process can be performed using the classical Newton-Raphson method or the Picard algorithm (Successive Approximation Method).

In this study, the simple incremental strategy proved to be quite adequate, even considering the nonlinear aspect of the problem. The solution algorithm based on this numerical procedure is shown in Table 1. The parameter θ, which appears in Table 1 defines, within each time interval, the instant at which Eq. (1) will be satisfied. By varying the parameter θ, different time integration schemes can be obtained. In CS-ASA/FA, the parameter θ is defined by the user, and in general, the value of 0.9 is adopted just as given in the SAFIR software [11].

a) Geometry and mesh

b) Definitions of materials

c) Exposed faces

d) General problem data
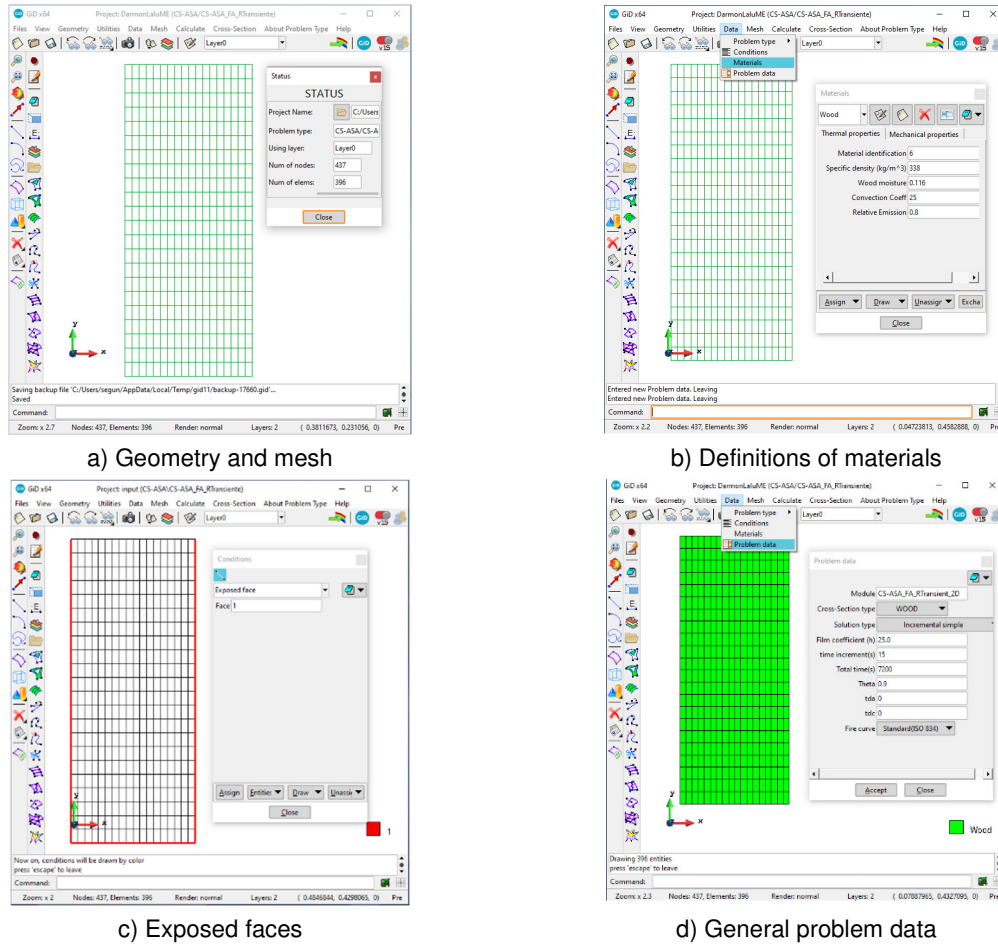
Figure 4: GiD and CS-ASA/FA integration (graphical pre-processor)

Table 1: Simple incremental strategy algorithm

1.	Set input data, initial conditions, and boundary conditions
2.	Do: $T_n = T_{n+1} = T_0 = 20\,°C$
3.	**INCREMENTAL PROCESS**: *inc =* 1, 2, 3..., *nmax*
4.	Calculate the capacitance matrix: $\boldsymbol{C}_{n+\theta}$
5.	Calculate the thermal conductivity matrix: $\boldsymbol{K}_{n+\theta}$
6.	Calculate the heat flux vector: $\boldsymbol{R}_{n+\theta}$
7.	Get: $\hat{\boldsymbol{K}}_{n+\theta} = \boldsymbol{C}_{n+\theta} + \theta\Delta t\,\boldsymbol{K}_{n+\theta}$
8.	Get: $\hat{\boldsymbol{R}}_{n+\theta} = \left[\boldsymbol{C}_{n+\theta} - (1-\theta)\Delta t \boldsymbol{K}_{n+\theta}\right]\boldsymbol{T}_n + \boldsymbol{R}_{n+\theta}$
9.	Solve the equation system: $\boldsymbol{T}_{n+1} = \left(\hat{\boldsymbol{K}}_{n+\theta}\right)^{-1}\hat{\boldsymbol{R}}_{n+\theta}$
10.	**GIVE A NEW TIME INCREMENT AND GO TO STEP 3**

For the example adopted in Subsection 2.1, after the pre-processing step (model creation), an input file (*INPUT. DAT*) is created and used by the CS-ASA/FA thermal module for solving the transient heat transfer problem. In sequence, an output file (*POST.RES*) is generated with the results obtained.

2.3 Graphical Post-processor

A graphical post-processor is a tool that is used for verifying and visualizing the results obtained by a processor. This tool helps to reduce the effort and time required by the analyst to visualize the results, thus facilitating the interpretation of the data generated by the analysis program.

Figure 5 illustrates the GiD interactive interface operation that allows the visualization of the results obtained by the CS-ASA/FA module. An output file is created with the temperature values of each nodal point of the cross-section over time, in text format, according to the GiD post-processor compatibility.
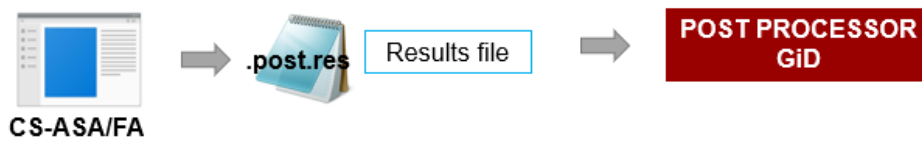

Figure 5: CS-ASA/FA and GiD interaction flowchart

Figure 6 presents the results obtained from the transient thermal analysis of the laminated timber cross-section presented in Subsection 2.1. This illustrates the operation of the post-processor. It is possible to visualize the temperature elevation as a function of time at a specific nodal point (in this case, point P1) using the Temperature *versus* Time curve provided by the post-processor (Figure 6a). In addition, the temperature field variation can be studied at each instant of time, by observing the color gradient variation (blue color for lower temperatures to red color for higher temperatures; Figure 6b).

a) Temperature *versus* Time: P1   b) Temperature variation in 30 minutes
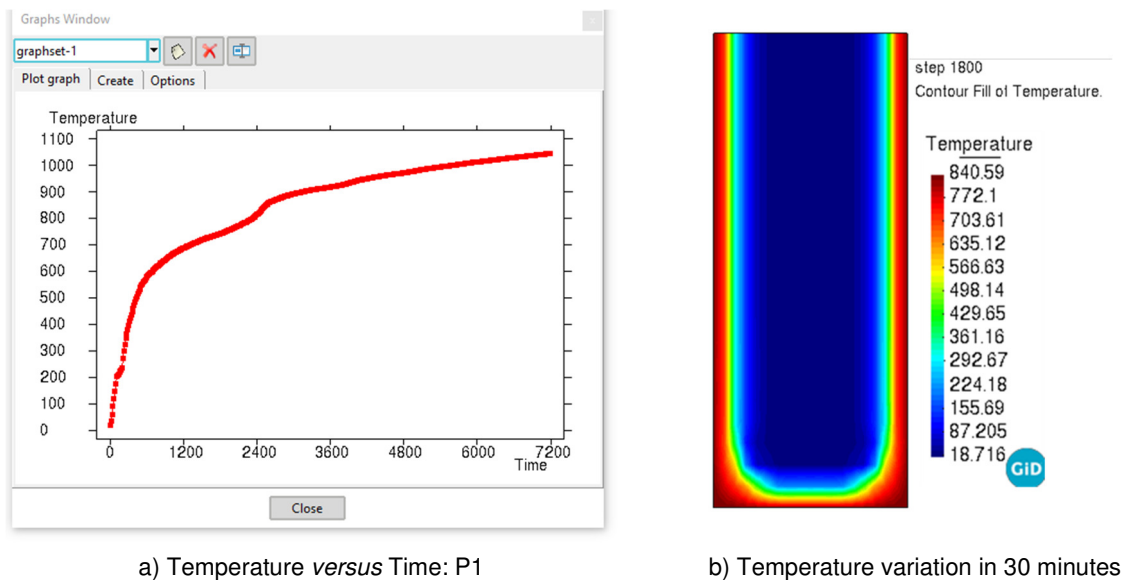
Figure 6: Visualization of results obtained through CS-ASA/FA-GiD integration: post-processor

Figure 7 shows the similar behavior of the Temperature *versus* Time curves for the two finite element meshes that were adopted, namely, the 396 and 792 Q4 elements. The curves show good conformity with the behavior of the timber properties as described by EN 1995-1-2:2004 [5], presenting the same ranges of behavior change. In addition, good agreement was observed between the results obtained using the SAFIR software [11] and those given by the CS-ASA/FA module.

477
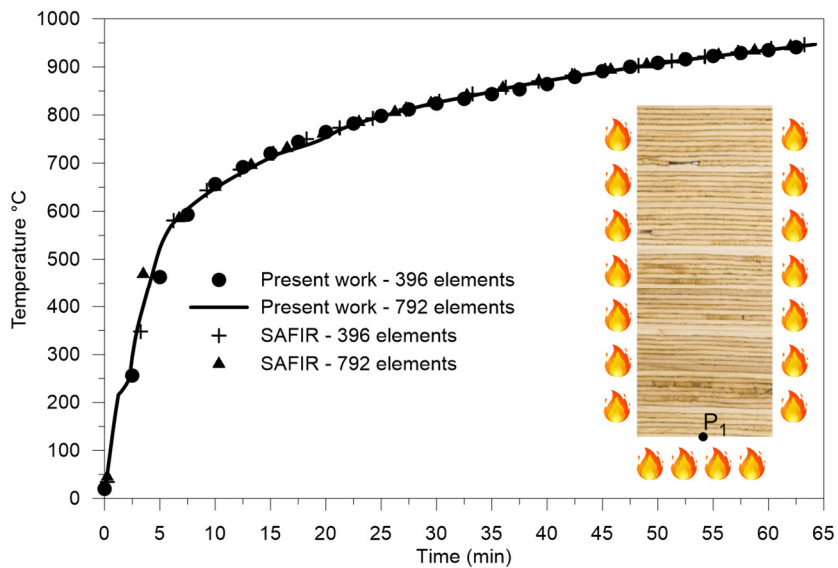
Figure 7: Thermal analysis for laminated veneer lumber cross-section (CS-ASA *versus* SAFIR)

3. ADDITIONAL EXAMPLE

As an additional example, this research analyzed a laminated veneer lumber panel. Thi *et al*. [10] studied the behavior of this timber cross-section experimentally and numerically (using finite element tests) under standard fire situations.

The experimental configuration was set up using a cross-section measuring 146mm wide and 60mm thick, with a length equal to 1000 mm and all sides exposed to fire. For the finite element, model symmetry was used to model a quarter of the total cross-sectional area (73mm wide and 30mm thick). Figure 8 illustrates this model. Temperatures were calculated for depths of 5 mm and 15 mm vertically (P1 and P2, respectively) and horizontally (P3 and P4, respectively) on the faces that were not exposed to fire.
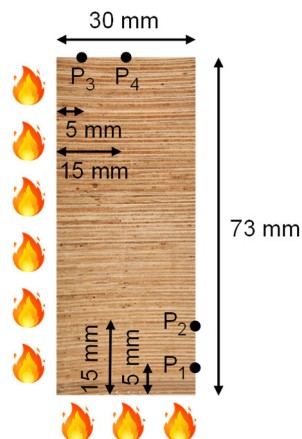
Figure 8: Laminated veneer lumber cross-section

The moisture content of the timer used for this experiment was equal to 12% and the dry density was equal to 570 kg/m³. The results of the thermal analyses are shown in Figures 9a, 9b, 9c, and 9d, in the form of Temperature *versus* Time graphs. Two meshes were used to numerically simulate this problem using the CS-ASA/FA module: the first one with 348 Q4 elements and the second, more refined, with 876 Q4 elements. The time increment for the analysis was 15 seconds. In addition, the SAFIR software numerical solution was used to validate the implementations made in the CS-ASA/FA module.

478

By observing Figures 9 and 10, it is possible to perceive a good agreement between the results found (CS-ASA/FA *versus* SAFIR). Another positive indication is the fact that the Temperature *versus* Time curves present similar behavior for the different points when their locations in the cross-section are placed in perspective. It can also be noticed that the curves present well-defined levels in the initial heating phase and similar behavior for the two meshes. This fact may be related to the behavior change in the thermal properties of the timber as described in the previous sections, which evidences the model's conformity with the expected behavior.

a) Temperature *versus* Time: P1

b) Temperature *versus* Time: P2

c) Temperature *versus* Time: P3

d) Temperature *versus* Time: P4

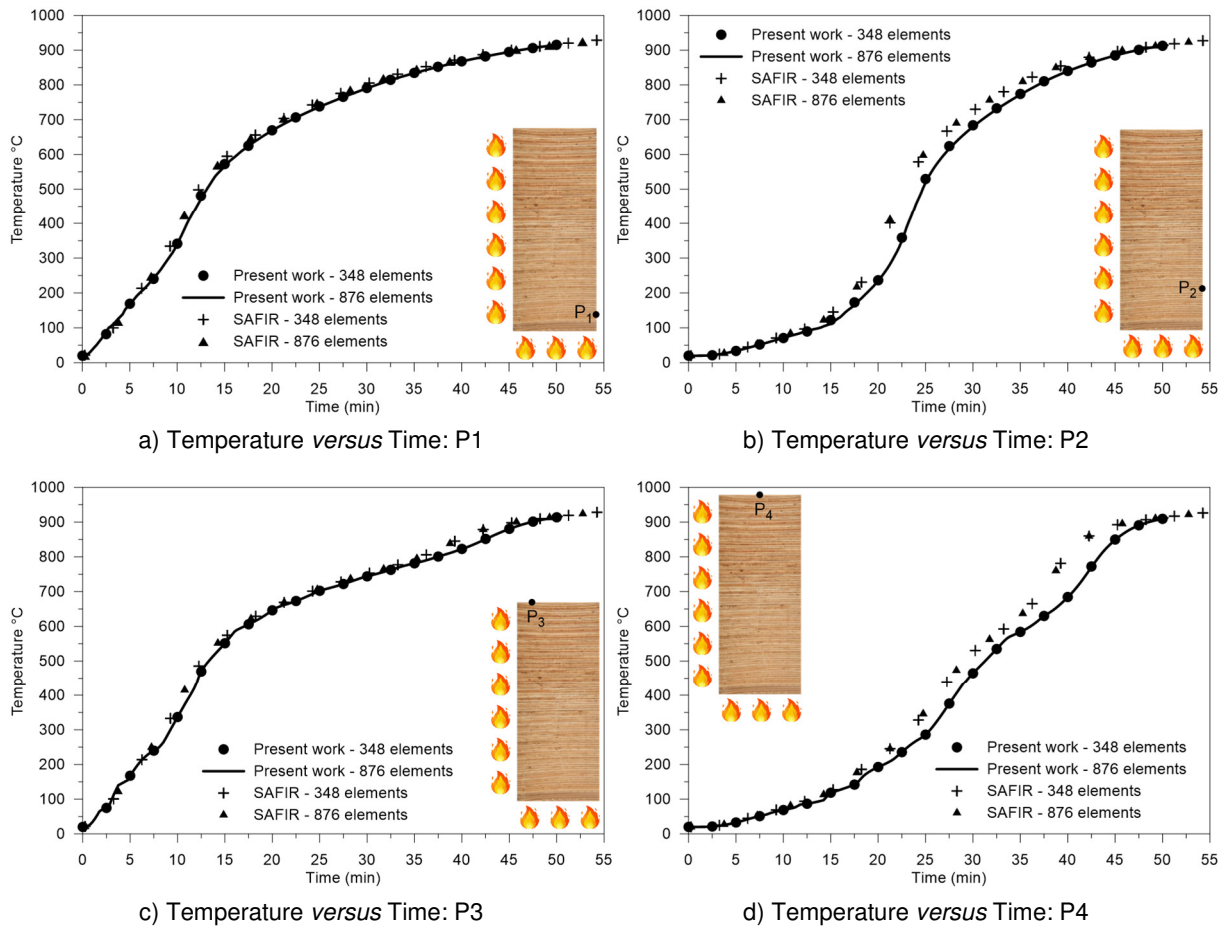Figure 9: Thermal analysis for laminated veneer lumber cross-section

4. FINAL COMMENTS

The integration between the CS-ASA/FA module and the GiD graphical capabilities indicate that the implementations of this study were successful. These numerical procedures reduced the effort required for the modeling and visualization of the CS-ASA/FA results to a great extent. This allowing the program user to make direct and simplified changes in the parameters necessary for the thermal analysis and facilitating the interpretation of the data generated.

Two timber cross-sections were considered under fire situation through the expansion made in the CS-ASA/FA module. The examples were determined considering their practical applications. With this, it was possible to perceive the difference in behavior between timber species under high temperatures and different fire scenarios. The results obtained were compared with those from SAFIR, and the answers were found to be satisfactory and consistent. This shows the program's ability to perform nonlinear transient thermal analysis of timber cross-sections.

This research will continue with the thermomechanical analysis of timber structural members and their systems. Therefore, future research should concentrate on the following: (1) determining the behavior of the stiffness and resistance of timber materials at high temperatures (2) considering more complex thermal effects (such as carbonization), and (3) assembling the material degradation that is compatible with the finite element formulations.
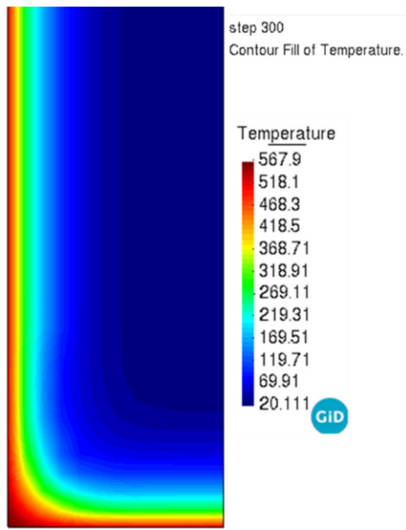
a) 5 minutes: GiD/CS-ASA
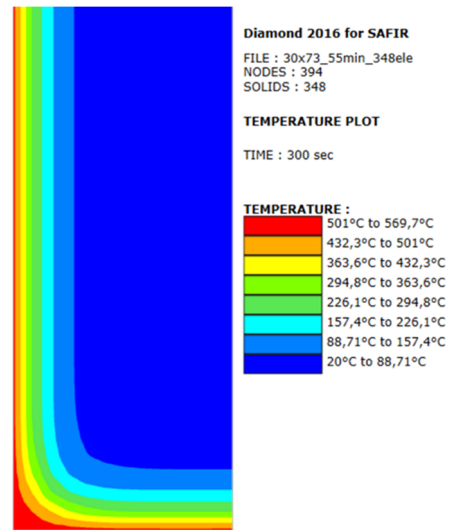
b) 5 minutes: Diamond/SAFIR
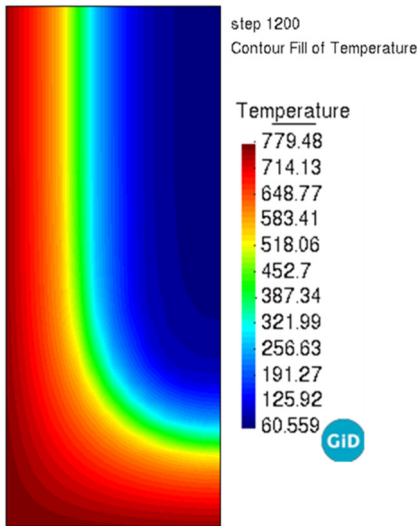
c) 20 minutes: GiD/CS-ASA
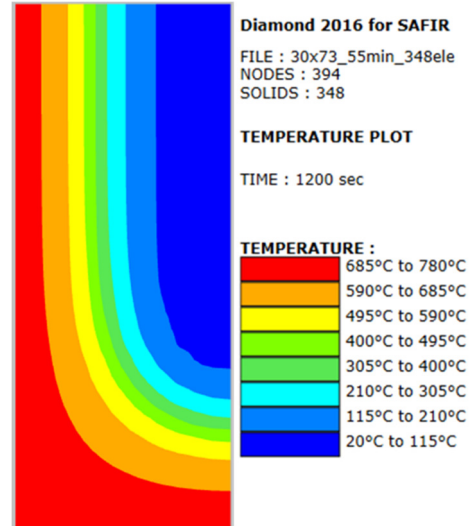
d) 20 minutes: Diamond/SAFIR
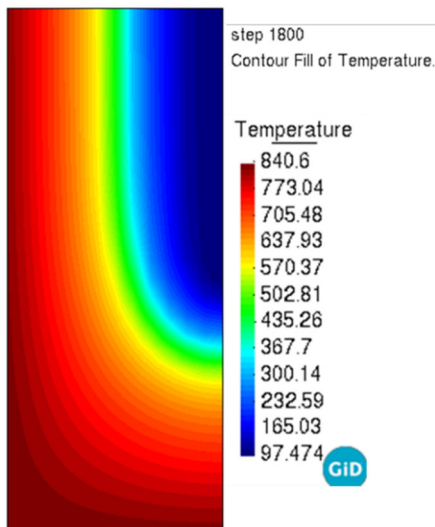
e) 30 minutes: GiD/CS-ASA
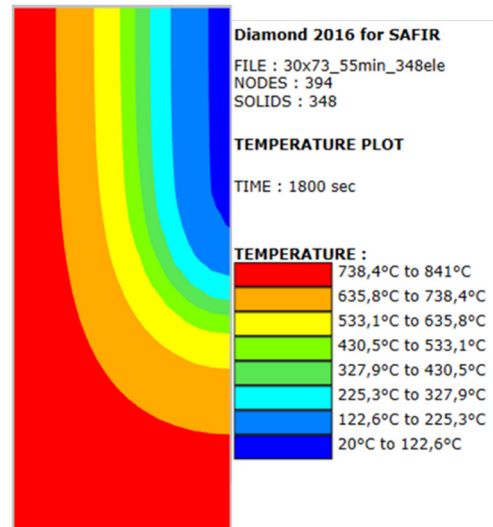
f) 30 minutes: Diamond/SAFIR

Figure 10: Temperature variation over the timber cross-section (CS-ASA/FA *versus* SAFIR)

480

REFERENCES

[1] Pires, D. (2018). *Análise numérica avançada de estruturas de aço e de concreto armado em situação de incêndio*, Tese de Doutorado, PROPEC/Deciv/EM/UFOP, Ouro Preto, MG, Brasil, 197 p.

[2] GiD – The personal pre and post processor. c2023. Barcelona (Spain): CIMNE; [accessed 2023 January 25]. www.gidsimulation.com.

[3] Prado, I. M. *CS-ASA Preprocessor: Sistema Gráfico Interativo de Pré-processamento para Análise Avançada de Estruturas*, Dissertação de Mestrado, PROPEC/Deciv/EM/UFOP, Ouro Preto, MG, Brasil, 163 p., 2012.

[4] Dârmon, R.; Lalu, O. *The fire performance of Cross Laminated Timber beams*. Procedia Manufacturing, 32, 121-128, 2019.

[5] European Committee for Standardization – EN 1994-1-2:2005. Eurocode 4*: Design of composite steel and concrete structures, Part 1-2: General rules, Structural Fire Design*, Bruxelas, 2005.

[6] ISO 834-1, *Fire resistance tests - elements of buildings construction, Part 1: General requirements. ISO - International Organization for Standardization*. Geneva, 1999.

[7] Lewis, R.W.; Nithiarasu, P.; Seetharamu, K.N., *Fundamentals of the Finite Element Method for Heat and Fluid Flow*. John Wiley & Sons, Chichester, 2004.

[8] Rigobello R. *Desenvolvimento e aplicação de código computacional para análise de estruturas de aço aporticadas em situação de incêndio*. Tese de Doutorado, Programa de Pós-Graduação em Engenharia de Estruturas, Escola de Engenharia de São Carlos da Universidade de São Paulo. São Carlos, SP, Brasil, 2011.

[9] Nunes, N. E. M. *Código computacional para análise térmica tridimensional de estruturas em situação de incêndio*. Dissertação de Mestrado, Programa de Pós-Graduação em Engenharia de Estruturas, Escola de Engenharia de São Carlos da Universidade de São Paulo. São Carlos, SP, Brasil, 2014.

[10] Thi, V. D.; Khelifa, M.; Oudjene, M.; Ganaoui, M. E.; Rogaume, Y. *Finite element analysis of heat transfer through timber elements exposed to fire*. Engineering Structures, 143, 11-21, 2017.

[11] Franssen, J. M., 2005. *SAFIR - A thermal/structural program modelling structures under fire*. Engineering Journal AISC, vol. 42(3), pp. 143-158.

A NUMERICAL PARAMETRIC STUDY OF THE MEMBRANE ACTION OF CONTINUOUS COMPOSITE STEEL-DECK AND CONCRETE SLAB

Matheus V. R. de Castro [a]

Carla N. Costa [b*]

João Paulo. C. Rodrigues [c]

ABSTRACT

Composite steel-concrete slabs are commonly used in steelwork construction, particularly in tall commercial and retail buildings as well as industrial and warehouse buildings, due to their rapid construction and high structural performance. However, the interaction between the concrete and the steel-deck profile in fire conditions is not yet fully understood.

Several studies [1-11] have highlighted that the fire calculation methods of the European standard EN 1994-1-2:2011 [6] and the Brazilian standard ABNT NBR 14323:2013 are overly conservative as they fail to consider the realistic behaviour of composite steel-concrete slabs at high temperatures.

This paper presents a parametric numerical study of the structural behaviour of composite steel and concrete slabs using the Abaqus/Explicit software package. The results of thermal and mechanical numerical modelling are compared with experimental results [1,2]. The parameters analysed in the numerical analysis include the hogging bending moment and the anti-crack mesh steel reinforcements on the upper surface of the continuous composite slab. The reinforcement ratio can influence the development of tensile membrane action, and therefore must be evaluated, along with the behaviour of the composite steel-deck concrete floor system.

Keywords: steel and concrete composite slab; membrane action; fire resistance; structural performance.

State University of Campinas, Brazil (matheus_vrc@hotmail.com)**.**

[b,*] State University of Campinas (carlac@fec.unicamp.br)**,** Corresponding author.

[c] University of Coimbra, Portugal; Federal University of Minas Gerais, Brazil (jpaulocr@dec.uc.pt)**.**

1. INTRODUCTION

Composite steel-concrete slabs consist of a concrete layer cast on top of a cold-formed steel formwork, commonly referred to as steel decking. Once the concrete has hardened, the resulting composite system exhibits a high load-bearing capacity at ambient temperatures, behaving as a unified material. During the casting process, the steel decking serves as a formwork, and upon hardening, it functions as continuous positive reinforcement. The use of this system not only provides high load-bearing capacity but also reduces waste and construction time by eliminating the need for wooden formwork [1].

Fire represents one of the most severe events that a structure can encounter during its use, and it can be considered an exceptional action that modifies the material behavior by reducing their mechanical properties, decreasing their compressive and tensile resistance, and reducing their ductility. When a fire occurs, the heat affects the steel decking beneath the concrete layer, causing a rapid degradation of its mechanical properties. Consequently, the steel decking loses its ability to function as continuous positive reinforcement, resulting in the behavior of the slab being similar to that of non-reinforced concrete [2,3].

Traditionally, the design of structures for fire situations has followed a prescriptive-based approach, which provides simple rules based on the assessment of isolated elements of the building such as columns, beams, or slabs. These elements are typically evaluated under standard fire curves and at a reduced scale, which makes it difficult to assess the actual level of safety of a real structure. This is because a building does not perform as an isolated small-scale element, and a fire does not necessarily follow a time-temperature relationship that is similar to those used during tests [4, 5, 6].

Current design codes predict that structural collapse will occur at approximately 680°C, which is significantly lower than temperatures measured during real-scale tests such as those conducted at Cardington [6]. In these tests, some elements experienced temperatures exceeding 1000°C without experiencing imminent structural collapse. Therefore, the current composite slab design codes do not accurately predict the behavior of buildings under fire situations [7, 8].

During a fire, slabs can undergo significant vertical displacements, which can result in in-plane forces that generate membrane action within the depth of the concrete slabs. Tensile membrane action can occur in floor slabs that are vertically and horizontally restrained or in two-way floor slabs that are vertically supported but horizontally free, leading to the formation of a compression ring in the perimeter of the slab (as shown in Figure 1). This compression ring anchors the tensile membrane action that occurs in the middle of the slab [4, 5, 9, 10].
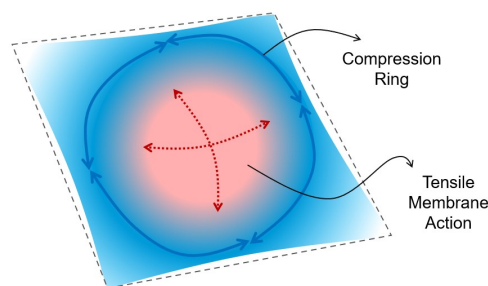
Figure 1: Membrane action and compression ring formation in a floor slab with no horizontal restraint (Author).

Under large displacements, the loading-carrying capacity of the floor slab significantly increases, which is dependent on the deflected geometry of the slab. However, in normal use of the building, there is no practical use for this phenomenon as the deflections are limited by the serviceable limit-states. In fire situations, the focus is on maintaining the structure stable for a sufficient period to save lives. Therefore, the mobilization of tensile membrane action is only possible if properly designed and the deflections are not limited by the serviceability criteria.

Several experimental studies [1-11] have been conducted to fully understand the behavior of composite steel-concrete structures under high temperatures, motivated by the results of the Cardington Test [6]. Bailey, White,

and Moore [7] tested a composite steel-concrete slab measuring 10.5 m in length, 7.45 m in width, and 150 mm in average depth. The concrete slab was composed of Grade C35 lightweight concrete cast onto a "PMF F60" steel profile shuttering, and an A12 anti-cracking mesh was placed on the upper surface of the slab with a 15 mm cover. After the concrete had hardened, the steel formwork was removed to simulate the loss of steel strength due to heating, and then, a uniformly distributed load was applied until the slab failed at 4.81 kN/m², slightly higher than double the load-carrying capacity of 2.3 kN/m² calculated using the classic yield line analysis.

Huang et al. [5] conducted a parametric study using the computer program Vulcan to analyze a 36 m x 36 m composite steel-concrete floor slab under a uniform fire load, considering different fire protection regimes and slab reinforcement details. The study used A142 and A393 anti-cracking mesh and tested three different fire protection regimes: (i) all primary beams protected (with a span of 9 m between each one) and secondary beams left unprotected; (ii) primary beams protection in each 18 m and all secondary beams unprotected; and (iii) all internal beams left unprotected. For the protection regime 'i', the tensile membrane action was mobilized, and the floor slab maintained its structural stability even for displacements of L/15, which is much greater than the L/30 typically proposed in the design codes. These results support the findings of the Cardington test [6].

Bednár et al. [8] studied the membrane action of composite floors with steel fiber-reinforced concrete slab exposed to high temperatures. They tested six simple-span composite floor slabs of 4.5 m x 3 m, with four of them at ambient temperatures and the remaining two under high temperatures. The slabs tested under the fire situation exhibited cracking patterns typical of those in which the compression ring is formed during the mobilization of tensile membrane action to simple-span floor slabs that are vertically supported.

NGUYEN et al. [10] conducted an experimental study to investigate the impact of slab continuity and secondary beams on the performance of composite steel-concrete slabs under fire conditions. Three one-quarter scale specimens were tested, where the concrete slab, four columns, and steel beams were enclosed in an electric furnace. The specimens were categorized into three groups: (i) no secondary beams and corners beams with freely rotations, (ii) two unprotected secondary beams and corners beams restrained, and (iii) no secondary beams with corners beams restrained. The tests were terminated upon the occurrence of "failure," and all three specimens exhibited diagonal cracks near the beam-to-column joints at the four corners, followed by additional cracks along the protected beams. The compression ring formation was observed in all specimens, and the reinforcement near the protected edge beams fractured due to the increase in hogging moment, caused by the stiffness losses occurring at the bottom of the slab under high temperatures, as proposed by Bailey [4].

Bolina et al. [1,2] conducted a parametric study, validating a numerical model developed in ABAQUS software with the experimental results of eight composite steel-concrete floor slabs under high temperature and different reinforcement details. The specimens with high upper reinforcement ratio (hogging moment) exhibited lower vertical displacement values and higher load-carrying capacity, indicating that the behavior of composite steel-concrete floor slabs is more sensitive to upper reinforcement (hogging moment) than to bottom reinforcement (sagging moment). This could be attributed to the lower temperatures measured in the upper reinforcement, provided by the thermal barrier offered by the concrete.

2. PLASTIC DAMAGE MODEL

It is well established that the concrete surrounding cracks in reinforced concrete elements still has residual strength and is capable of carrying tensile stresses due to the bond between the reinforcing bars and the concrete matrix [11].

Modeling reinforced concrete within the finite element theory is a complex task, as the material exhibits heterogeneity and non-linear behavior beyond its plastic peak stress. A finite element model must accurately represent the compressive and tensile behavior of the material in both its elastic and plastic phases [12]. A variety of constitutive models have been proposed to represent the tension and compression behavior of concrete, ranging from simple to highly sophisticated models of great complexity [13-18].

The Concrete Damaged Plasticity (CDP) model, implemented in ABAQUS software, is a constitutive model based on the models proposed by Lubliner et al. [18], with modifications proposed by Lee and Fenves [19]. This model is

suitable for quasi-brittle materials and has the potential to represent the inelastic behavior of the material during compression and the cracking behavior of the material during tension, including its damage characteristics.

The CDP model assumes that the reduction of the elastic modulus is given by equation 1, where 'E_0' represents the undamaged modulus of the material and 'd' represents the damage factor, which ranges from zero for undamaged material to 1 for fully damaged material.

$$E = (1 - d) E_0 \tag{1}$$

The stress-strain relations for the general three-dimensional multiaxial condition are described by equation 2, in which 'D_0^{el}' denotes the undamaged elasticity matrix, 'ε' represents the total strain (both elastic and plastic), and 'ε^{pl}' represents the plastic strains.

$$\sigma = (1 - d) D_0^{el} : (\varepsilon - \varepsilon^{pl}) \tag{2}$$

The Figure 2 illustrates the concrete response to uniaxial loading in tension (a) and compression (b).

a) Tensile response; b) Compressive response.
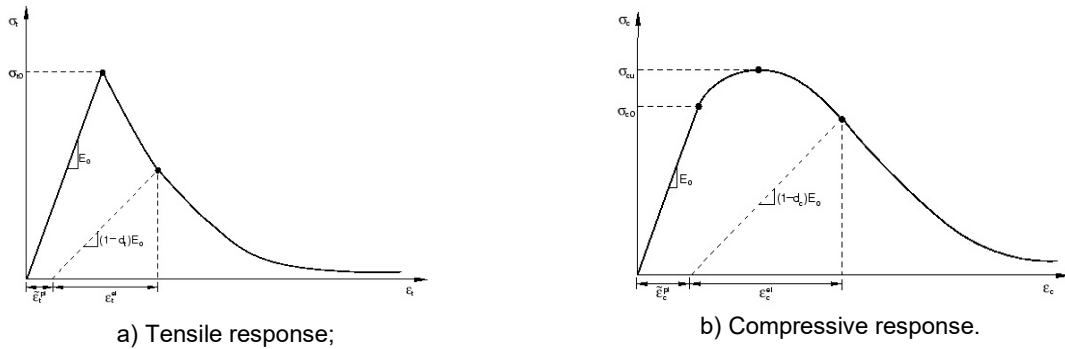
Figure 2: Response of concrete in the CDP model (Abaqus manual).

The compression damage 'd_c' and the tension damage 'd_t' can be computed using the equation 3 [20]:

$$d_c = 1 - (\sigma_c / f_c)$$
$$d_t = 1 - (\sigma_t / f_t) \tag{3}$$

Where 'σ_c' is the compressive stress considered, 'f_c' is the concrete compressive strength, 'σ_t' is the tensile stress considered and 'f_t' is the concrete tensile strength.

In order to define the elastic behavior of the material, the user must input the Young's modulus (E_0) and a constant value for Poisson's ratio (v), even for cracked concrete. To define the stress-strain relation of the concrete under compression, the compressive stresses (σ_c), inelastic strains (ε^{in}) corresponding to a compressive stress value, and damage properties corresponding to inelastic strains (d_c) must be provided in a tabular format. For the concrete under tension, the inputs should be the tensile stresses (σ_t), cracking strain (ε^{cr}) corresponding to a tensile stress value, and damage properties corresponding to a cracking strain (d_t). To complete the plastic damage model, the dilation angle (Ψ) in the p-q plane, flow potential eccentricity (ξ), the ratio of biaxial compressive strength/uniaxial compressive strength (f_{b0}/f_{co}), and the ratio of tensile/compressive meridian (K_c) must also be inputted. As ABAQUS/Explicit was used, the viscosity parameter 'μ' is ignored by the software.

3. NUMERICAL SIMULATIONS

A parametric study was conducted using the ABAQUS/Explicit software to analyze the behavior of composite steel-concrete floor slabs, considering the contribution of the anti-cracking mesh typically used but not considered structurally significant in design approaches at ambient temperatures.

The model was validated using the results of the experimental research [1, 2], and subsequently, a parametric study was conducted. The material properties of concrete, reinforcing bars, steel decking, and anti-cracking mesh are detailed in the following sections.

3.1 Concrete Damage Plasticity

The dilation angle 'Ψ' in p-q plane, flow potential eccentricity 'ξ', 'f_{b0}/f_{c0}' relation, 'K_c' ratio and viscosity parameter 'μ' used in the model are informed in Table 1.

Table 1: CDP model Inputs

Ψ	ξ	f_{b0}/f_{c0}	K_c	μ
30°	0.1	1.16	0.667	0

Based on the material tests conducted by Bolina [1,2], the characteristic compressive and tensile strength of the concrete were assumed to be 42 MPa and 4 MPa, respectively. The Young's modulus (E_0) was determined to be 36.292 GPa and the Poisson's ratio (v) was 0.2. The plastic behavior of the concrete under compression and tensile stress was modeled using the approach proposed in EN 1992-1-2 [14], which is illustrated in Figure 3.
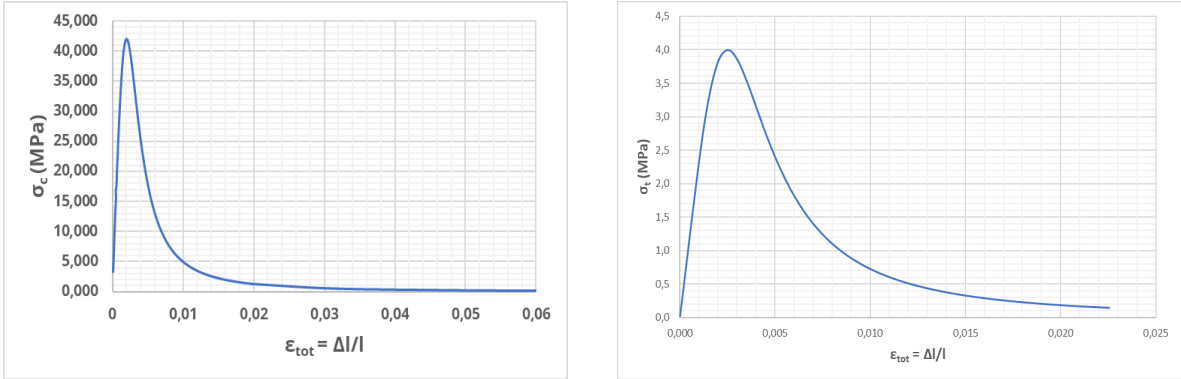
a) Compressive behavior;   b) Tensile behavior.
Figure 3: Concrete compressive and tensile behavior (Author).

The concrete compressive damage parameter is illustrated in the following figure.
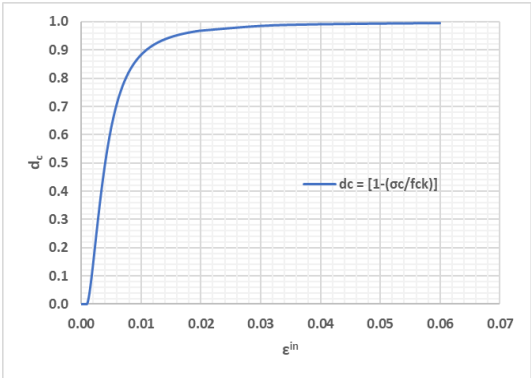
Figure 4: Compressive damage parameters (Author).

3.3 Plastic Model

The steel formwork considered was Polydeck 59S, produced by *AcelorMittal*, with a characteristic yield stress 'f_{py}' of 280 MPa. The rebars were classified as C-class according to EN 1992 1-1 [21] and had a tensile strength 'f_y' of 500 MPa. The plastic parameters used for both materials considered the strain-hardening behavior as proposed in EN 1993-1-2 [22] and are illustrated in Figure 5 bellow.

a)   Steel formwork Polydeck 59S;   b)   Rebars.
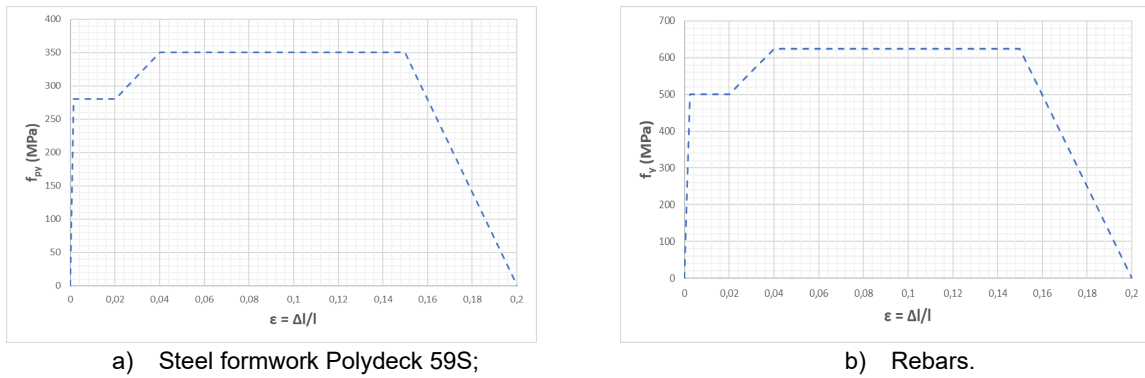
Figure 5: Plastic parameters (Author).

3.3 Thermal Simulation

The thermal simulation was performed using the heat transfer package of ABAQUS/Standard, with input parameters governing thermal diffusion such as specific heat, thermal conductivity, and density. These parameters were obtained from EN 1992 1-2 [14] for concrete and from EN 1993 1-2 [22] for rebars and steel formwork. The specific heat of concrete was obtained with consideration of 3% moisture content. The thermophysical properties of the concrete adopted in this study are shown in Figure 6.

Specific Heat;   Thermal Conductivity;   Density (specific mass).
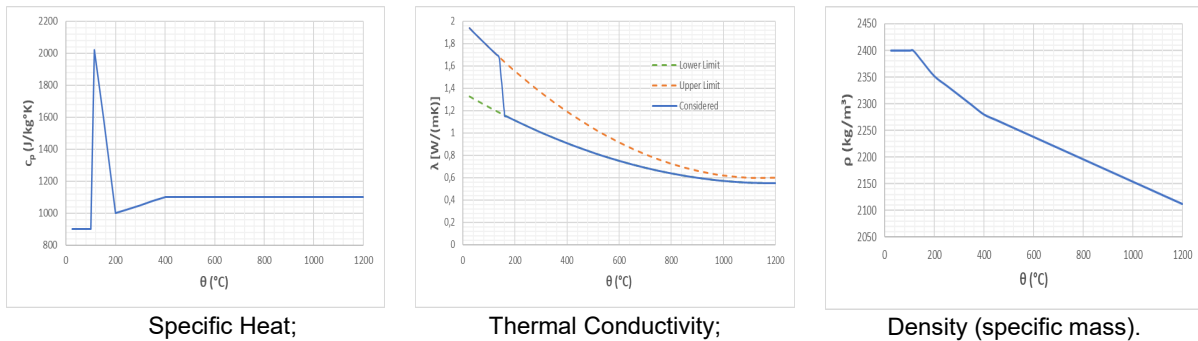
Figure 6: Concrete thermal parameters (Author).

Steel formwork and rebars were assumed to have a constant density of 7850 kg/m³ across all temperatures. The specific heat for both steel formwork and rebars were also assumed to be the same, with variations depending on temperature (Figure 7).

Specific heat for rebars and steel formwork;   Thermal conductivity.
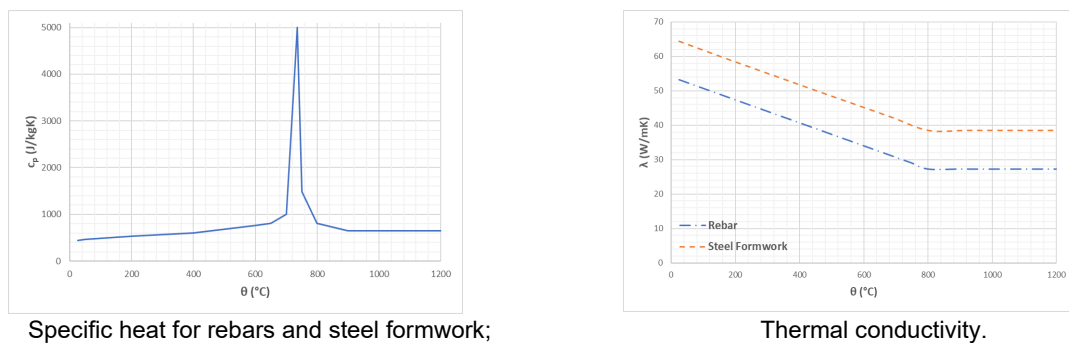
Figure 7: Thermal parameter for rebars and steel formwork (Author).

During the experimental tests conducted by Bolina [1,2], it was observed that the steel formwork detached from the concrete during the initial stages of the fire exposure. This phenomenon created an air layer, which acted as an insulating material, affecting the isotherms in the slab cross-section. The numerical model considered this effect by incorporating a 1 mm-thick air layer. The thermal properties of air were obtained from Çengel and Ghajar [23] and are presented in Table 2.

487

Temperature (°C)	C_p [J/(kg.K)]	λ [W/(m.K)]	ρ_{ar} (kg/m³)
20	1007	0,02514	1,2040
30	1007	0,02588	1,1640
60	1007	0,02808	1,059
100	1009	0,03095	0,9458
200	1023	0,03779	0,7459
300	1044	0,04418	0,6158
400	1069	0,05015	0,5243
500	1093	0,05572	0,4565
600	1115	0,06093	0,4042
700	1135	0,06581	0,3627
800	1153	0,07037	0,3289
900	1169	0,07465	0,3008
1000	1184	0,07868	0,2772
1500	1234	0,09599	0,199

The absolute zero considered was –273.15 °C, and the Stefan-Boltzmann constant was 5.67×10^{-8} W/(m².K⁴). The initial temperature was set to 25°C, and the emissivity of the steel element was assumed to be 0.4. The heat transfer coefficients for convection for the exposed and unexposed faces were 25 W/(m².K) and 9 W/(m².K), respectively. The heating curve was based on the ISO 834 standard.

3.4 Thermomechanical Simulation

The thermomechanical analysis was conducted using an uncoupled procedure, in which a thermal model was executed to obtain the nodal temperature distribution through time across the cross section. Subsequently, the obtained data were incorporated into a new model, which accounted for the mechanical properties of the material as a function of temperature. A constant distributed load of 1.5 kN/m² was applied to the model.

The compressive strength of the concrete at increasing temperatures (Figure 8-a) was obtained from the experimental results of Bolina [1,2] and was used to calculate the stress-strain relationship of the concrete under compressive and tensile stresses (Figure 8-b,c) [14]. The thermal elongation and coefficient of thermal expansion of the concrete were determined based on EN 1992-1-2 [14] and are presented in Figure 8-e,f.
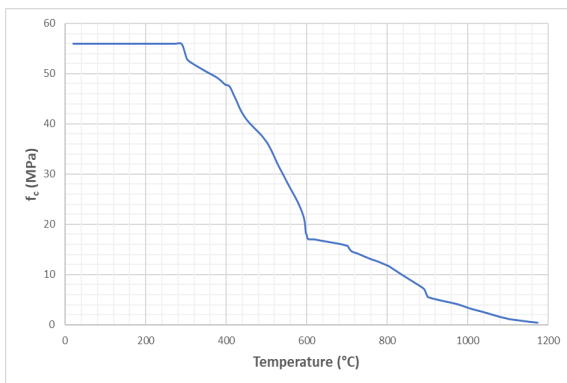
a) Compressive concrete strength;
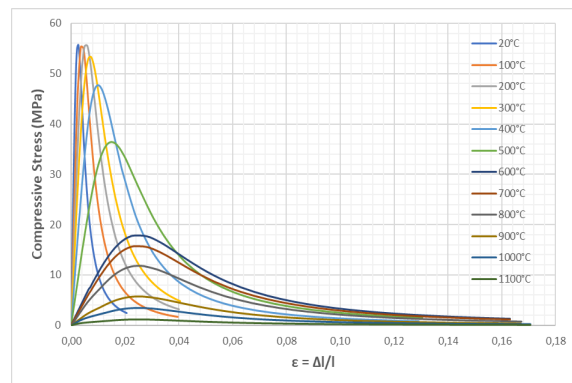
b) Compressive stress-strain behavior;
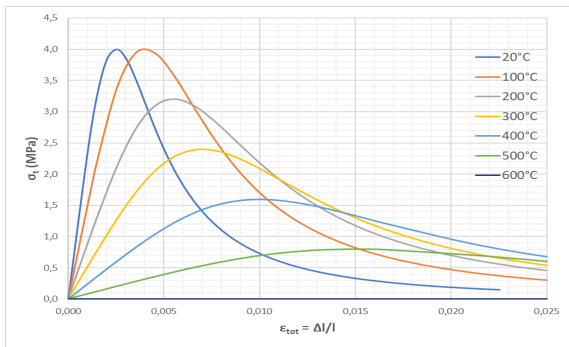
c) Tensile stress-strain behavior;
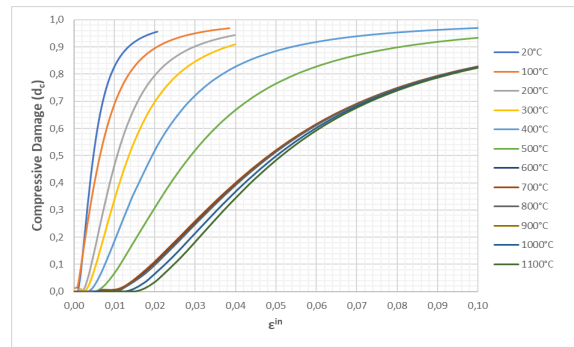
d) Damage compressive parameter.
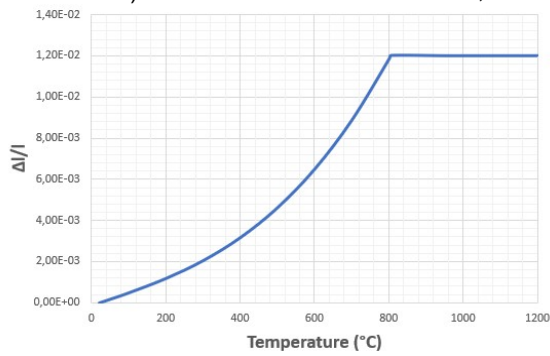
e) Thermal elongation;
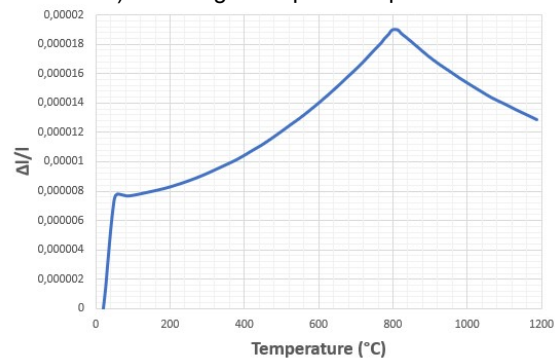
f) Coefficient of thermal expansion.

Figure 8: Thermomechanical concrete properties (Author).

The thermomechanical properties of rebar (Figure 9-a) and steel formwork (Figure 9-b) were obtained from EN 1992-1-2 [14] and EN 1994-1-2 [24], respectively.
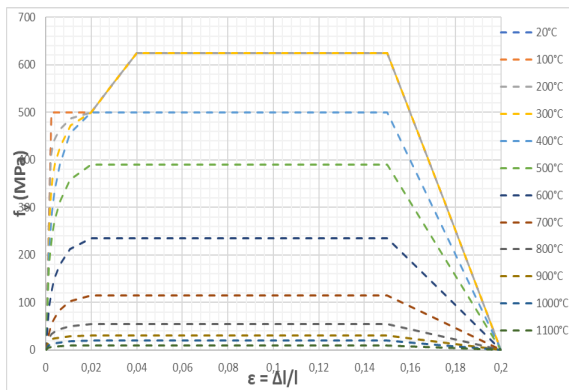
a) Rebar stress-strain behavior;
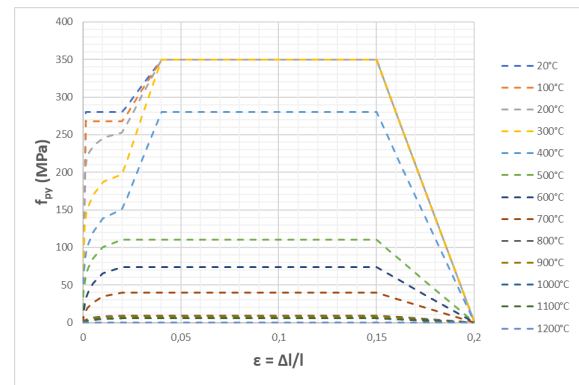
b) Steel formwork stress-strain behavior.
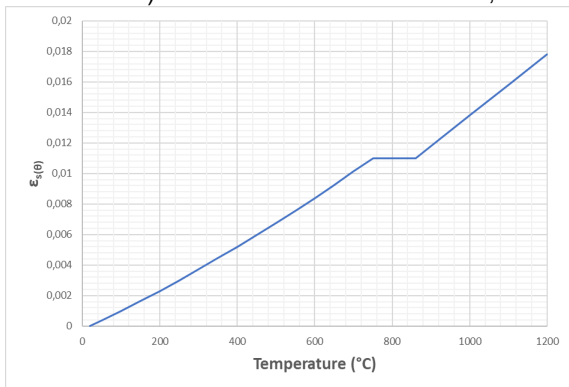
c) Thermal elongation;
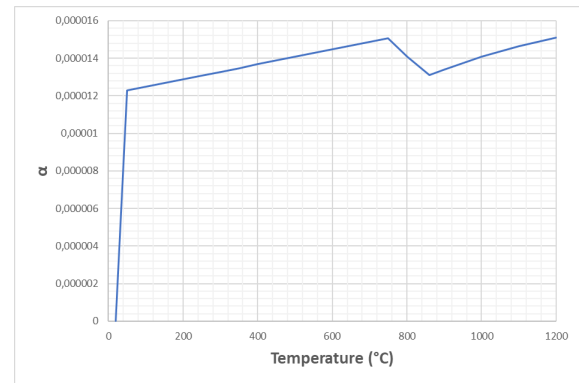
d) Coefficient of thermal expansion.

Figure 9: Thermomechanical steel properties (Author).

489

3.5 Elements and Geometry

The concrete was modeled using a solid element C3D8R available in the ABAQUS library, which is an eight-node brick element with reduced integration. A shell element S4R suitable for large-strain analysis was used for the steel formwork, while beam element B31 was used for the mechanical approach and truss element was used for the thermal approach to model the rebars and the cracking mesh.

The optimal mesh size for the cross-section was determined through a mesh sensitivity analysis, and the resultant mesh is presented in Figure 10. The mesh spacing along the slab was set at 25 mm.
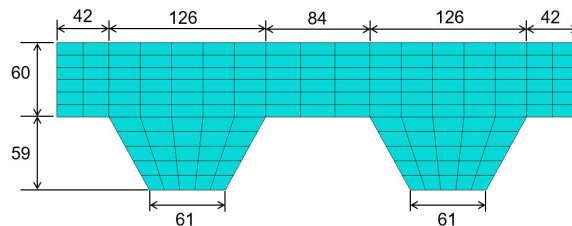
Figure 10: Mesh used in the numerical model (Author).

4 NUMERICAL VALIDATIONS

The numerical results obtained from ABAQUS was compared with the experimental results obtained by Bolina [1,2] to validate the numerical simulation.

4.1 Mechanical Simulation

Six numerical models were simulated in ABAQUS and then compared with the experimental results to validate the accuracy of the simulation. The simulations were conducted to replicate the five-point bending test with two 2.3 m spans exactly as carried out in the experiment.

The primary discrepancy between the numerical and experimental results was observed in the first model (Figure 11-a), which can be attributed to the highly nonlinear behavior of unreinforced concrete. However, in models with rebars, this nonlinearity was better controlled, and the results were found to be in close agreement with the experimental data. All the comparisons are presented in Figure 11 (a-c) and 'LA' refers to the experimental tests and 'NM' refer to the numerical analysis.
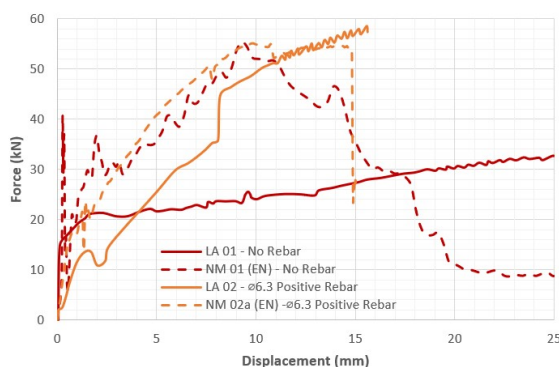
a) No rebar and 6.3 mm positive rebar diameter;
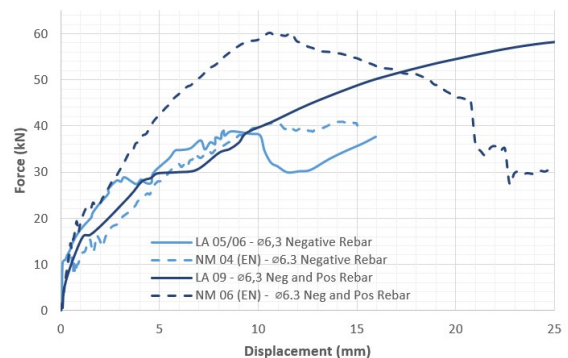
b) 6.3 mm negative rebar diameter and 6.3 mm positive and negative rebar.
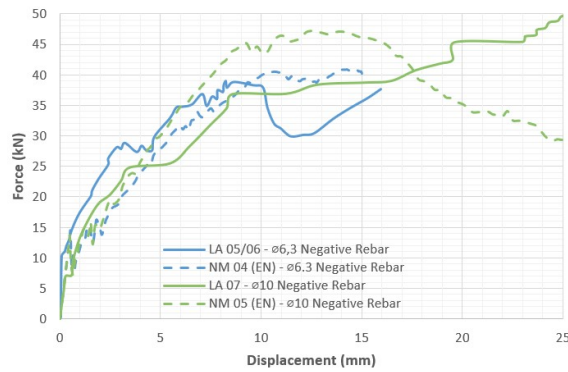
c) 10 mm positive rebar diameter and 10 mm negative rebar diameter.

Figure 11: Numerical and experimental mechanical results (Author).

4.2 Thermal Simulation

The numerical thermal results used for comparison with the experimental results were those obtained during the experimental research, as shown in Figure 12 (a-d). The results obtained from the numerical simulations showed good agreement with the experimental results, except for the temperatures of the rebars, which showed a significant difference.

This difference can be explained by the placement of thermocouples on the bars, which are placed on the surface of the rebars while in numerical analysis, the value collected refers to the center of the bar. This positional difference can affect the temperature and could result in significant temperature differences.
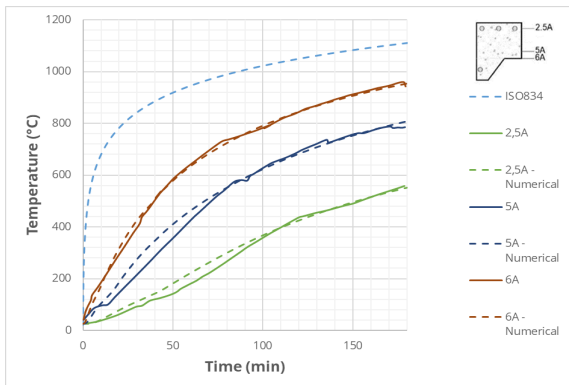
a) Temperature in the upper slab flange;
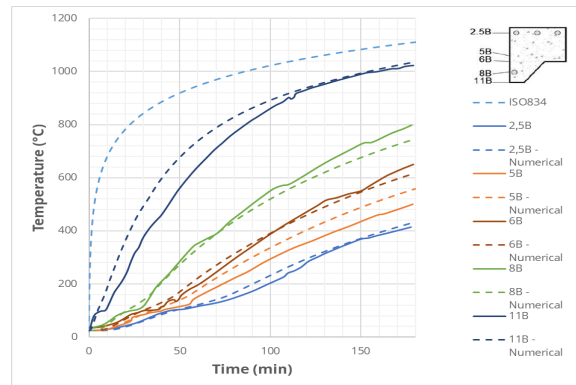
b) Temperature in the ribs;
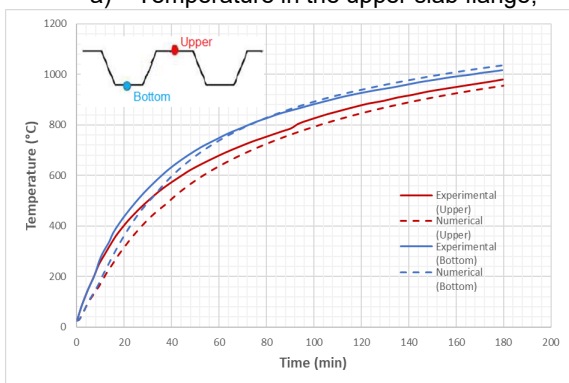
c) Polydeck 59S;
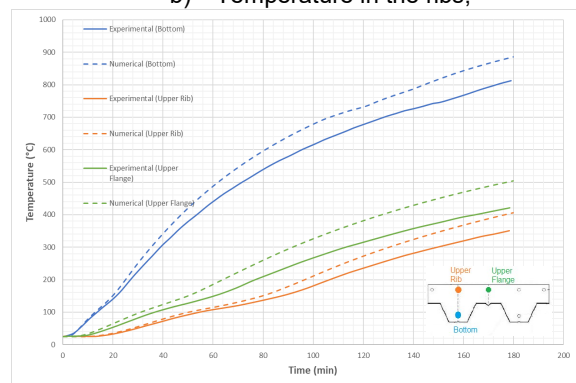
d) Rebars.

Figure 12: Experimental and numerical thermal results (Author).

4.2 Thermomechanical Simulation

The thermomechanical modelling results were similar to those obtained in the experimental program up to 100 minutes of heating. However, beyond this time, the numerical results were more conservative, with lower displacement values than those measured during the experimental tests. The results are presented in the following figures.
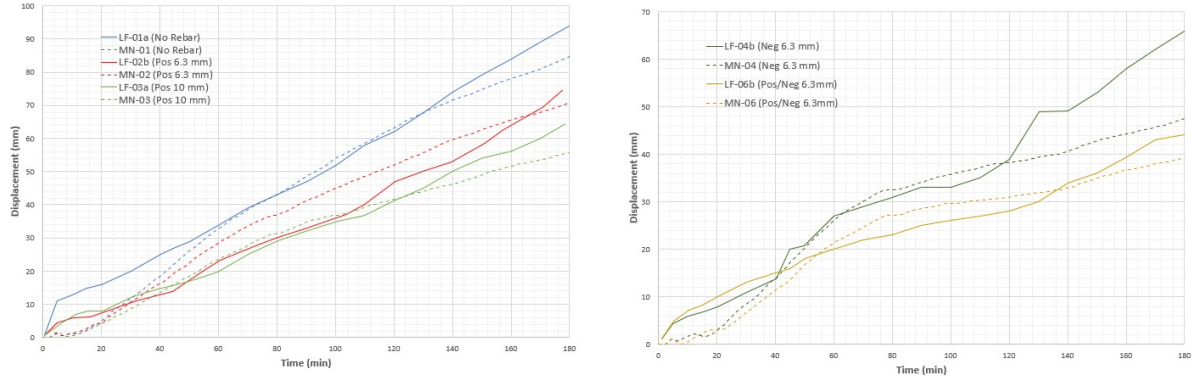
a) Experimental Tests *vs.* Numerical Modelling (No rebar and only positive rebars);

b) Only negative rebars and both positive and negative rebars.
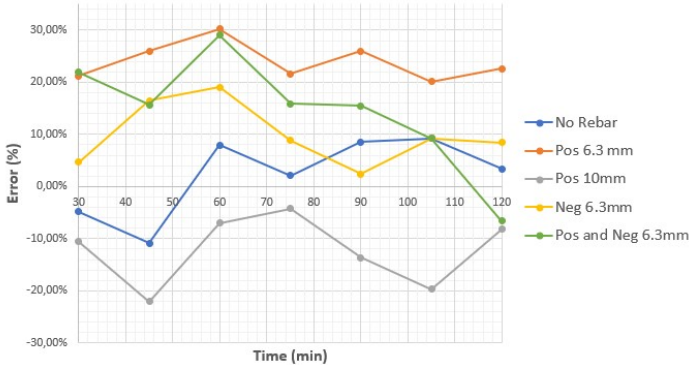
c) Error comparing numerical and experimental results.

Figure 13: Thermomechanical modelling results (Author).

As seen in Figure 13, the numerical approach showed significant differences during the first 30 minutes of heating. Afterward, the results indicated a difference of less than 10% in approximately 120 minutes. Subsequently, the difference started to increase again, reaching around 20% until 140 minutes and exceeding 30% at 180 minutes of heating. Therefore, the numerical model can be considered suitable for structures requiring fire resistance times of up to 120 minutes.

5. PARAMETRIC ANALYSIS

An analysis was conducted to investigate the influence of the anti-cracking mesh commonly used in Brazil, specifically the EQ45, EQ61, and EQ138, on the behavior of composite slabs with only positive reinforcement and those with both positive and negative reinforcement (as depicted in Figure 14). The geometric properties of the anti-cracking mesh are presented in Figure 15 and Table 3.

492
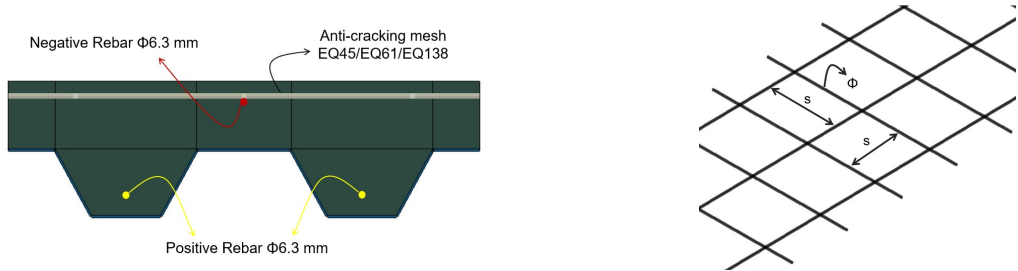
Figure 14 – Slab transversal section (Author).   Figure 15 – Anti-cracking mesh (Author).

Table 3: Anti-cracking geometric properties (Author).

Anti-cracking mesh	Space (s)	Diameter (Φ)
EQ45	20 cm X 20 cm	3.4 mm
EQ61	15 cm x 15 cm	3.4 mm
EQ138	10 cm x 10 cm	4.2 mm

5.1 Results

The inclusion of anti-cracking mesh in the composite slab resulted in a 14% reduction in displacement for EQ61 and a 22% reduction for EQ45 and EQ138, in cases where no negative rebar was used (Figure 16-a). To minimize computational demands during analysis, only two ribs (half of the specimen - Figure 10) were modeled, resulting in no difference in the transversal area between EQ45 and EQ61 in the model, as both mesh specifications have the same diameter. Therefore, the different behavior observed in the two models can be attributed to the position of the longitudinal wires within the anti-cracking mesh, which led to varying temperatures.

For models which included negative rebar, an increase in displacement at mid-span was observed (Figure 16-b). This can be explained by the increase in temperature experienced by the negative rebar due to the presence of the anti-cracking mesh. Since steel is a better conductor of temperature than concrete, it allowed heat to be transmitted through the concrete to the negative rebar, which resulted in decreased performance.

a) Only positive rebar and anti-cracking mesh;   b) Positive and negative rebar and anti-cracking mesh.
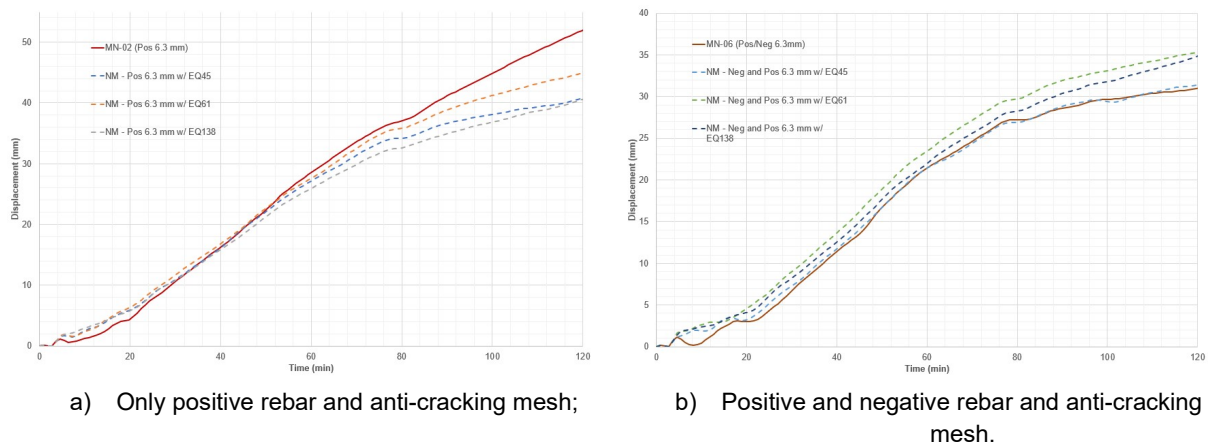
Figure 16 – Parametric analysis results (Author).

6. CONCLUSIONS

The use of anti-cracking mesh has the potential to enhance the performance of concrete-steel composite slabs in situations where negative reinforcement bars are not present. However, in cases where negative reinforcement bars are included, the position of the anti-cracking mesh becomes crucial. This is because the position of the longitudinal wires within the concrete can significantly impact the insulation of the negative reinforcement bars, as the mesh can function as a temperature conductor and elevate the temperature of the negative rebar. As a result, the higher temperatures experienced by the reinforcement bars can lead to decreased mechanical properties of the steel, ultimately affecting the behavior of the entire composite slab.

Further research is needed to explore the influence of the positioning of the longitudinal wires within the anti-cracking mesh on the performance of concrete-steel composite slabs. The objective of such studies would be to identify an optimal position that can maximize the performance of the composite slab when utilized as a structural material. These investigations should focus on the thermal behavior of the composite slab and take into account various factors such as the dimensions and properties of the reinforcement bars and the position of the longitudinal wires of the anti-cracking mesh.

REFERENCES

[1] Bolina, F. L.; Tutikian, B & Rodrigues, J. P. C. (2021). *Experimental analysis on the structural continuity effect in steel decking concrete slabs subjected to fire*, Engineering Structures, vol. 240, 16 p. https://doi.org/10.1016/j.engstruct.2021.112299

[2] Bolina, F. L.; Tutikian, B & Rodrigues, J. P. C. (2021). *Thermal analysis of steel decking concrete slabs in case of fire,* Fire Safety Journal, vol. 121, 14 p. https://doi.org/10.1016/j.firesaf.2021.103295

[3] Wang, Y. C. (2002). *Steel and Composite structures*. Spon Press, 331 p.

[4] Bailey, C. G. (2004). *Membrane action of slab/beam composite floor systems in fire,* Engineering Structures, vol. 26, p. 1691-1703. https://doi.org/10.1016/j.engstruct.2004.06.006

[5] Huang, Z.; Burgess, I. W. & Plank, R. J. (2004). *Fire resistance of composite floors subject to compartment fires,* Journal of Constructional Steel Research, vol. 60, p. 339-360. https://doi.org/10.1016/j.jcsr.2003.08.012

[6] A European Joint Research Programme (1999). *The behaviour of multi-storey steel framed buildings in fire*, British Steel, Swinden Technology Centre, Building Research Establishment, London, 73 p.

[7] Bailey, C. G.; White, D. S. & Moore, D. B. (2000). *The tensile membrane action of unrestrained composite slabs simulated under fire conditions,* Engineering Structures, vol. 22, p. 1583-1595. https://doi.org/10.1016/S0141-0296(99)00110-8

[8] Bernár, J *et al.* (2013). *Experiments on membrane action of composite floors with steel fibre reinforced concrete slab exposed to fire,* Fire Safety Journal, vol. 59, p. 111-121. https://doi.org/10.1016/j.firesaf.2013.04.008

[9] Cordeiro, L. C. S. (2014). *Sobre as lajes mistas de aço e concreto em situação de incêndio*. Master Thesis, University of São Paulo, 262 p. https://doi:10.11606/D.3.2014.tde-29042015-163950

[10] Nguyen, T. -T.; Tan, K. -H. & Burgess, I. W. (2015). *Behaviour of composite slab-beam systems at elevated temperatures: Experimental and numerical investigation,* Engineering Structures, vol. 82, p. 199-213. https://doi.org/10.1016/j.engstruct.2014.10.044

[11] Stramandinoli, R. S. B. & La Rovere, H. L. (2008). *An efficient tension-stiffening model for nonlinear analysis of reinforced concrete members,* Engineering Structures, vol. 30, no. 7, p. 2069-2080. 10.1016/j.engstruct.2007.12.022

[12] Wahalathantri, B. L. *et al.* (2011). *A material model for flexural crack simulation in reinforced concrete elements using ABAQUS,* eddBE2011 Proceedings, p. 260-264.

[13] Massicote, B.; Elwi, A. E. & MacGregor, J. G. (1990). *Tension-stiffening model for planar reinforced concrete members,* Journal of Structural Engineering, vol. 116, no. 11, p. 3039-3058. https://doi.org/10.1061/(ASCE)0733-9445(1990)116:11(3039)

[14] EN 1992-1-2 (2004). *Design of concrete structures – Part 1-2: General rules – Structural fire design,* Brussels: European Committee for Standardization.

[15] Genikomsou, A. S. & Polak, M. A. (2015). *Finite element analysis of punching shear of concrete slabs using damaged plasticity model in ABAQUS,* Engineering Structures, vol. 98, p. 38-48. https://doi.org/10.1016/j.engstruct.2015.04.016

[16] Demin, W. & Fukang, W. (2017). *Investigation for plastic damage constitutive models of the concrete material,* Procedia Engineering, vol. 210, p. 71-78. https://doi.org/10.1016/j.proeng.2017.11.050

[17] Chen, S. & Shi, X. (2011). *Shear bond mechanism of composite slabs – A universal FE approach,* Journal of Constructional Research, vol. 67, p. 1475-1484. https://doi.org/10.1016/j.jcsr.2011.03.021

[18] Lubliner, J. *et al.* (1989). *A plastic-damage model for concrete*, International Journal of Solids and Structures, vol. 25. no. 3, p. 299-326. https://doi.org/10.1016/0020-7683(89)90050-4

[19] Lee, J. & Fenves, G. L. (1998). *Plastic-damage model for cyclic loading of concrete structures,* Journal of Engineering Mechanics, vol. 124, no. 8, p. 892-900. https://doi.org/10.1061/(ASCE)0733-9399(1998)124:8(892)

[20] Dinh, P. T. *et al.* (2022). *Numerical modelling techniques and investigation into the flexural behaviour of two-way posttensioned concrete slabs with profiled steel sheeting,* Structural Concrete fib, p. 1-25. https://doi.org/10.1002/suco.202200180

[21] EN 1992-1-1 (2004). *Design of concrete structures – Part 1-2: General rules and rules for buildings,* Brussels: European Committee for Standardization.

[22] EN 1993-1-2 (2005). *Design of steel structures – Part 1-2: General rules – Structural fire design,* Brussels: European Committee for Standardization.

[23] Çengel, Y. A.; Ghajar, A. J. (2014). *Heat and Mass Transfer: Fundamentals and Applications.* McGraw Hill, 992 p.

[24] EN 1994-1-2 (2005). *Design of composite steel and concrete structures – Part 1-2: General rules – Structural fire design,* Brussels: European Committee for Standardization.

EXPERIMENTAL BEHAVIOUR OF INTUMESCENT PAINTING PROTECTED STEEL BEAMS SUBJECTED TO A NATURAL FIRE
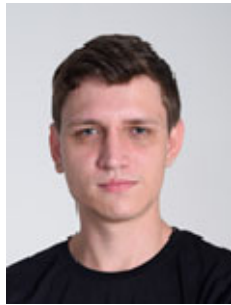
Marcus César Q. Araújo [a,*]

João P. C. Rodrigues [b]

ABSTRACT

The aim of this study is to determine several aspects on the performance of steel load-bearing beams protected with intumescent coatings subjected to a natutal cellulosic fire. Thus, fire resistance tests were carried out at the training field of the Military Academy of the Fire Departament of Minas Gerais to test steel beams, with three different cross-sections, protected with dry thickness of intumescent film for the required fire resistance time of 60 minutes. The materials used in the tests had their properties characterized. Then, this test aided in understanding the expansive behavior of the intumescent paint when exposed to a natural fire similar to those that occur in residential occupancies. The temperature of the protected surface and the fire were measured, as well as the displacements throughout the entire beam section.

Keywords: Intumescent painting, fire, steel beam, natural fire.

1. INTRODUCTION

The use of intumescent coatings for passive fire protection has been increasingly used in recent years. Features such as good quality surface after application and good performance as a thermal barrier have led researchers to develop studies to characterize this type of material for protecting steel elements in case of fire [1]. The fire resistance mechanism of intumescent paint is closely tied to the dry thickness of the applied coating and the temperature exposure. This process relies on the foaming effect, where the low thermal conductivity material undergoes volumetric expansion due to the presence of a polymer matrix during the fire event. As the burning process concludes, a carbonaceous layer remains. This layer is inert to fire resistance. During this heating curve, the paint can generate a carbonaceous foam up to 200 times its original volume [1].

[a,*] Master Science Student – UFMG, Belo Horizonte, Brazil (marcuscquintao@ufmg.br), **Corresponding author**.

[b] Professor – UFMG, Belo Horizonte, Brazil (jpcrod@ufmg.br).

As characterized by Lucherini [2], the chemical composition of intumescent coatings is designated by an acidic source called a catalyst, a carbonaceous compound, and a foaming agent. The functions of each active component are well defined and act in different phases of the intumescence process, as it can be observed in thermogravimetry (TG) and differential scanning calorimetry (DSC) tests. During heating, the first reaction that occurs is the decomposition of the catalyst at temperatures around 150 and 250 [ºC]. Above 200 [ºC], the acid reacts with the carbonaceous compound, releasing pure water (H_2O) and forming a carbonaceous residue. Simultaneously, the foaming agent is consumed, producing gases that expand the carbonaceous residue generated in the previous reaction. These actions are endothermic, thus promoting the cooling of the generated heat, which in turn limits the heating of the protected surface. In summary, the combination of the chemical compounds forms a polymeric matrix that plays a fundamental role in reducing the heating rate of a steel profile exposed to a fire condition.

For beams subjected to bending and protected with intumescent coatings, fire resistance tests provide parameters that describe the behavior of the tested materials. In these tests, it is possible to analyze the development of the intumescent layer, the influence of edge effects, and establish a relationship between the profile's massiveness factor and the thickness of the applied paint layer. Additionally, critical temperature and fire resistance time for the metal element, as well as critical displacements, can be determined. As the compartment temperature rises, the steel undergoes a significant loss of mechanical strength, and the temperature measured at the moment of collapse is known as the critical temperature.

2. EXPERIMENTAL PROCEDURES

Initially, it should be noted that the main objective of the adopted methodology is to extract data for validating and calibrating a numerical model for testing fire protected steel beams with intumescent painting. In order to determine the fire load acting in a natural fire situation, based on ABNT NBR 14432:2001 [3], the typical occupation of residential units was considered, with a fire load equal to 300 MJ/m². In order to obtain such fire load, pine wood pallets were used to ignite the fire. Per test, 160 kg of wood was used.

Due to the test conditions, the heating of the steel beam was done all over its bending moment region, since the external loading applied was carried out by point loads at the ends, as represented below in Figure 1. The maximum bending moment that the beam can withstand corresponds to 30% of its load-bearing capacity at ambient temperature.
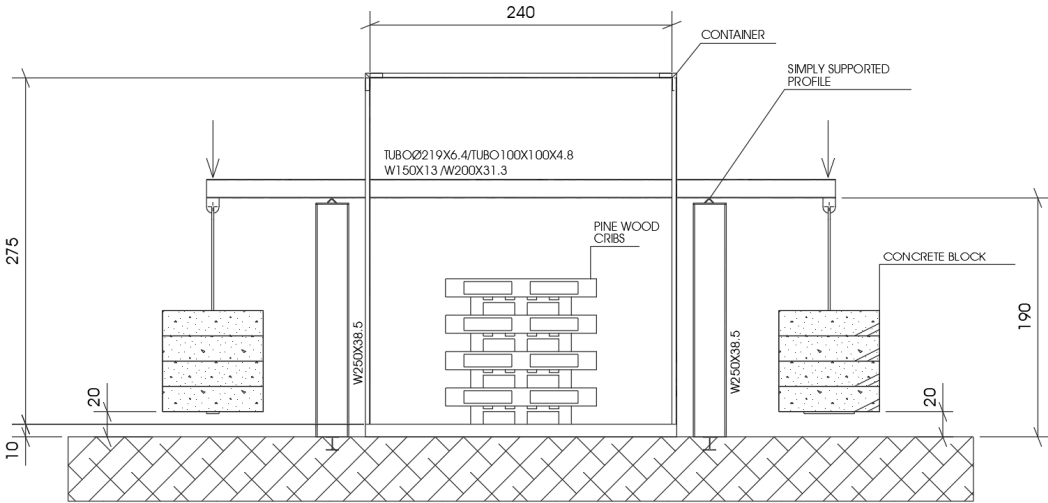
Figure 1. Squemathic design of the experimental test.

In order to adapt the test to real conditions, openings of 50cm x 30cm will be made in the side wall of the maritime container to allow for the positioning of the beams in the desired configuration. During the execution of the test, the opening will be closed with a ceramic wool blanket to concentrate the heat inside the test environment. The

beam profiles will be simply supported on steel columns fixed on the floor. The support should allow for longitudinal displacement of the profile during the test. Therefore, a circular plate bracket will be positioned on top of the column to create the labeled support, as this allows for the longitudinal displacement of the profile.

2.1 Characterization of the intumescent painting

Initially, for the characterization of the steel profiles (ASTM A572-Gr.50 and ASTM A36), four samples of each steel type were subjected to tensile testing at room temperature. The procedures described in ASTM E8/E8M-21 [4] were followed to extract the test specimens from the existing profiles. The obtained values for yield stress and Young modulus from each test are described in Tables 1 and 2, respectively. It can be observed that the obtained values are higher than the values specified by the steel manufacturer.

Table 1: Results of samples of ASTM A572-Gr.50 submitted to tensile test at room temperature

Sample	Yield Stress (MPa)	Young Modulus (MPa)
V1	424,97	181,31
V2	415,98	183,19
V3	398,18	179,20
V4	413,32	183,98

Table 2: Results of samples of ASTM A36 submitted to tensile test at room temperature

Sample	Yield Stress (MPa)	Young Modulus (MPa)
V5	380,17	197,37
V6	383,78	199,13
V7	377,23	194,65
V8	375,14	192,00

To characterize the intumescent paint used, the thermogravimetry and differential scanning calorimetry tests were conducted. This test involves determining the mass loss and temperature variation of a sample exposed to different programmed heat flows. The sample mass is approximately 10 [mg], and for this test, heat flows of 5, 10, 15, and 25 [ºC/min] were used in both air and nitrogen atmospheres for comparison purposes. The results are exposed in Figures 2 and 3.
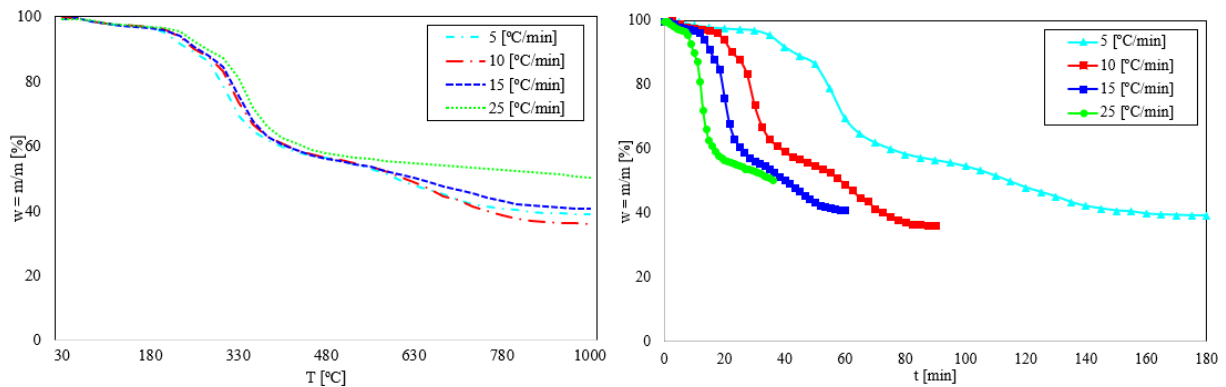
Figure 2: TG curves for differentes heating rates.
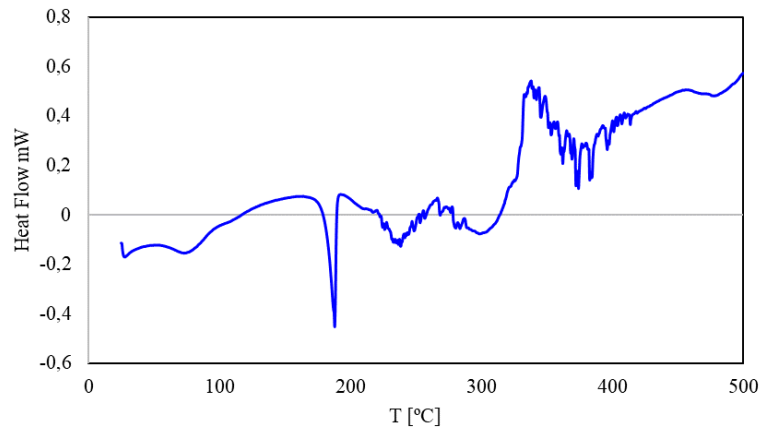
Figure 3: DSC analysis of intumescent paint.

Based on these results, it can be observed that the deterioration of the paint begins in the temperature range of 150-250 [ºC], which is where the foaming reaction initiates. From the DSC test, it is noticeable that the degradation of intumescent paints starts around 170 [ºC].

2.2 Preparation of test samples

The tested beams and their characteristics are described in Table 3. To prepare the metallic surface, a primer epoxy was initially applied, with 75 [μm] dry thickness. Then, StopTherm 600 intumescent paint was applied. Made in Brazil, this paint is water based and require eight hours to dry. Once the paint had fully cured, a synthetic enamel was meticulously applied to provide a final touch to the surface. This procedures are similar to the conventional process application of intumescent coatings in constructions.

Table 3: Tested steel profiles and their characteristics

Steel Profiles	Squemathic Representation of Profiles	Section Factor (cm/cm²)	Dry Thickness of Intumescent Film (μm)
W150X13		404	500
W200X31,3		231	300
TB100X100X4,75		219	275

To ensure the application of the correct thickness of intumescent paint, a wet thickness gauge was used, as shown in Figure 4.

Figure 4: Measurement of applied intumescent paint thickness.

2.3 Test instrumentation

As instrumentation, 10 probe thermocouples were used to measure the gas temperatures in the container, with similar positioning to Figure 5. Thermocouples were strategically positioned at a quarter of the span on one side of the container, while on the other side, they were placed at half of the span to ensure comprehensive temperature monitoring. This was adopted to verify the internal temperature uniformity.
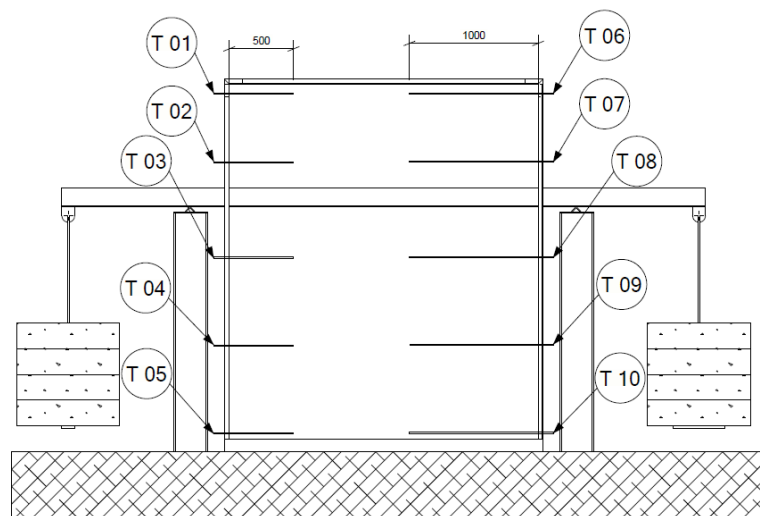
Figure 5: Position of thermocouples to measure the container temperature

To measure the temperature of fire protected profiles, 6 type K thermocouples were welded to the metallic substrate. In addition, 2 LVDT's (Linear Variable Differential Transducer) were placed, 1 at each cantilevered end of the beams. The thermocouple and displacement meters placement configuration are illustrated in Figure 6.
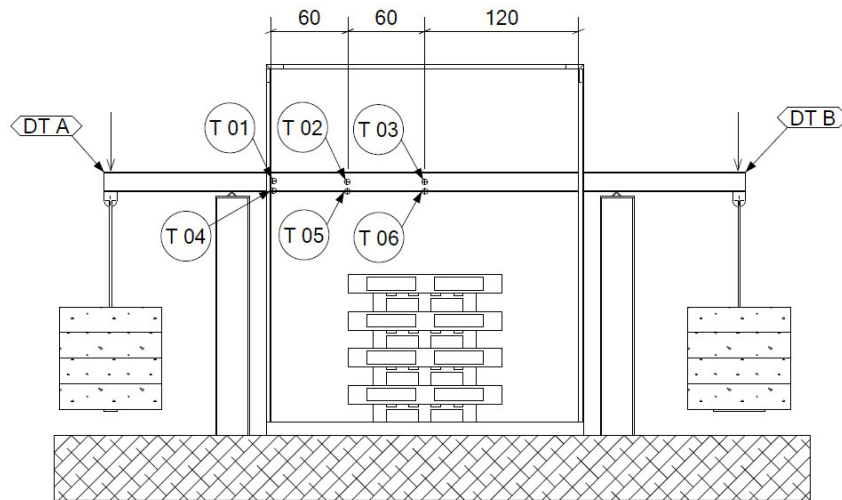
Figure 6: Position of welded thermocouples on beams and displacement gauges for instrumentation.

3. RESULTS AND DISCUSSION

From conducting the tests, the following notable points can be highlighted for the analysis of the results:

a) The average temperatures of the ambient and beam thermocouples were taken to construct the graphs;
b) Measurement of displacements required the adaptation of a metal rod to prevent overheating of the LVDT's, highly sensitive measurement equipment (Figure 7);
c) The fire load was evenly distributed in the internal compartment area of the container to avoid localized flames acting on the beam (Figure 8);
d) Wooden pallets were disassembled to standardize the fire load;
e) The test duration was 90 minutes, with results displayed for 60 minutes;
f) The overall behavior of the structure met initial expectations, and the results were satisfactory.

Figure 7: Internal view of the container before the test.

Figure 8: Adaptation for measuring displacements.

3.1 Temperatures

Given the above, graphs were constructed that relate the temperature of the internal environment of the container, the temperature of the protected metal substrate, and an estimate of the temperature of the beam. The beam temperature was subjected to the same fire curve as the test, but without fire protection. This estimate was made based on the equation described in item 8.5 of the ABNT NBR 14323:2013 standard.

For the test of the square tubular beam, TB100X100X4.75, the graph in Figure 9 was obtained.
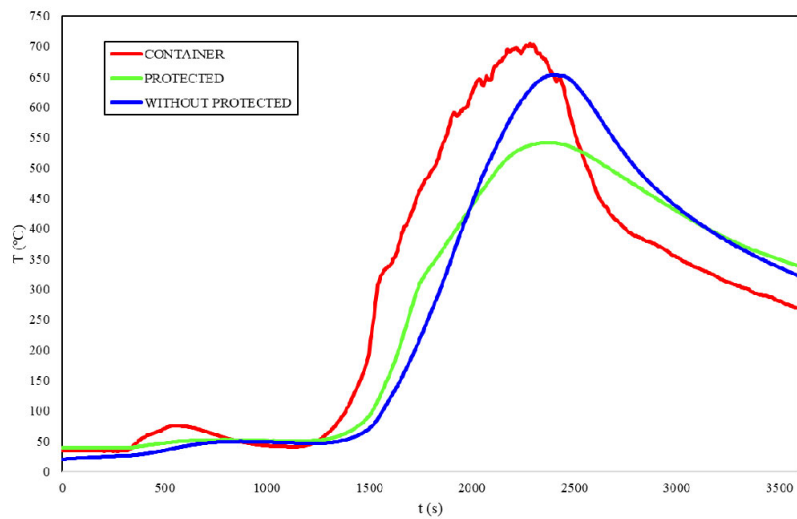
Figure 9: Temperature profiles for TB100X100X4.75 test.

For the test of W150x13, the graph in Figure 10 was obtained.
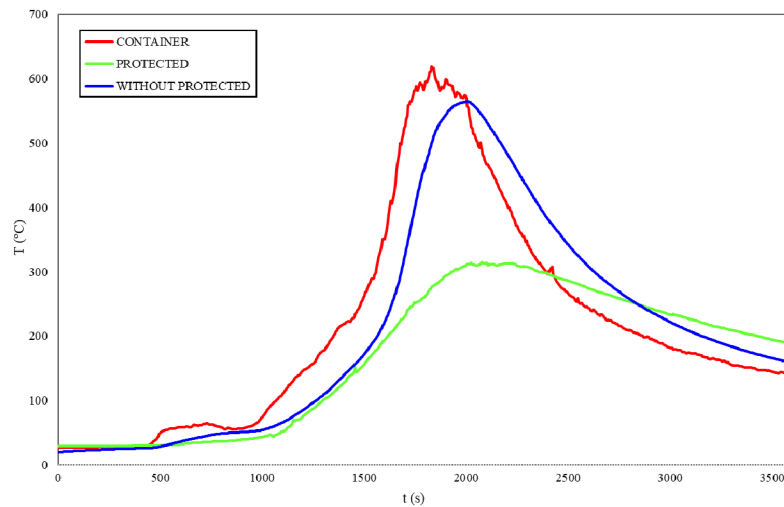
Figure 10: Temperature profiles for W150X13 test.

For the test of W200x31.3, the graph in Figure 11 was obtained.
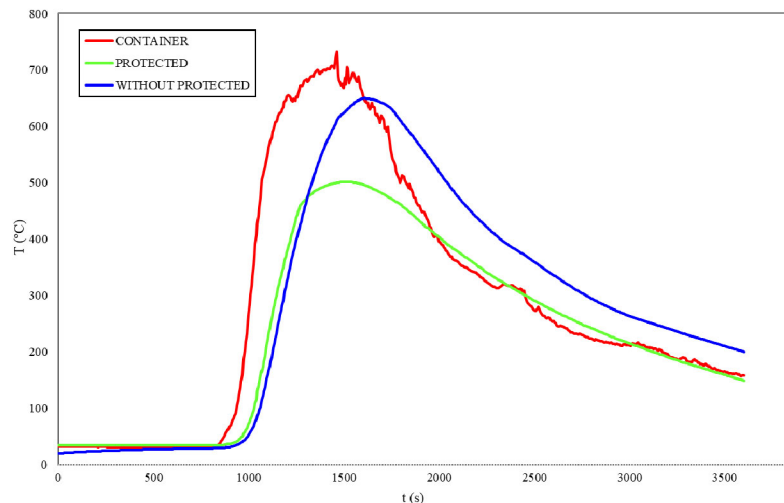
Figure 11: Temperature profiles for W200X31.3 test.

From the illustrated graphs above, it can be observed that the temperature of the protected metal substrate remains below approximately 150 to 200 ºC compared to the fire temperature and the estimated temperature of the unprotected beam. This confirms the effectiveness of the intumescent paint in the different phases of the fire, preventing temperature escalation.

3.2 Displacements

Displacements were measured during the test using an LVDT (Linear Variable Differential Transformer) equipment. After the cooling of the beam, final displacement measurements were manually taken using a tape measure at the designated points indicated in Figure 12. The values obtained for each test are displayed in Table 4.

During the measurements throughout the tests, inconsistencies were observed in the data for the W150X13 and W200X31.3 beams, and the results were disregarded. For the TB100x100x4.75 beam, it was possible to determine the vertical displacement of the deflected end, as illustrated in Figure 13.
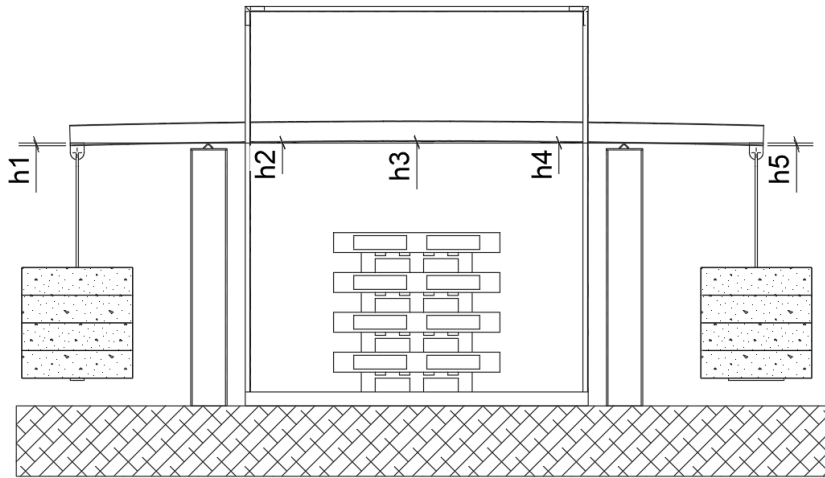
Figure 12: Manual measurement points of displacements after testing.
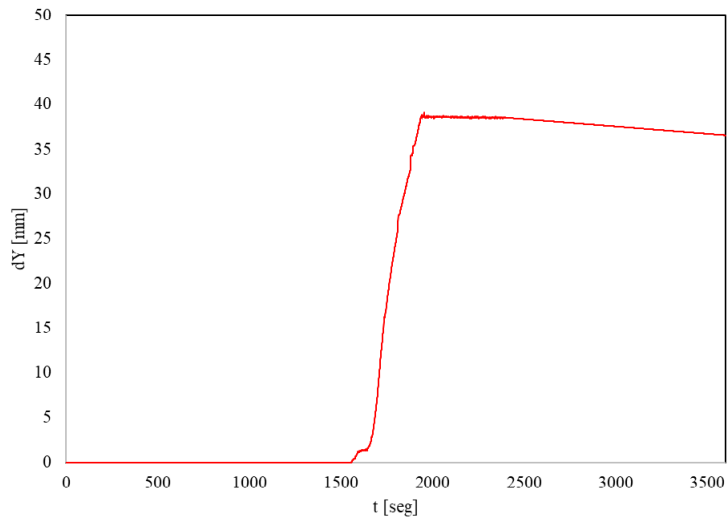
Figure 13: Displacement measured via LVDT after test – TB100x100x4,75.

Table 4: Displacements of beams tested.

	h1 (mm)	h2 (mm)	h3 (mm)	h4 (mm)	h5 (mm)	LVDT (mm)
TB100X100X4,75	27	11	33	10	24	38
W150X13	3	4	5	3	2	N/A
W200X31,3	2	5	7	5	3	N/A

3.3 Expansion of intumescent paint

After the test, it is possible to analyze the volumetric expansion process of the intumescent paint for different geometric sections. The following figures show the final result after heating and cooling of the tested beam.

<center>(a)</center>

<center>(b)</center>

Figure 14: Expansion of intumescent paint on TQ100X100X4.8

<center>(a)</center>

<center>(b)</center>

Figure 15: Expansion of intumescent paint on W150x13

<center>(a)</center>

<center>(b)</center>

Figure 16: Expansion of intumescent paint on W200x31.3

4. CONCLUSIONS

In these tests, it was possible to evaluate the aspects of the behavior of the intumescent painting on steel beams with different cross-sections, the influence of the localized fire on the volumetric expansion process of the carbonaceous layer, as well as the action of the paint under more rigorous fire curve conditions, such as natural fires.

Regarding the temperature profile obtained in each of the tests, it can be concluded that the behavior of the intumescent paint was similar in all tests, remaining between 150 to 200 [ºC] below the fire temperature. This demonstrates the effectiveness of the paint in protecting the steel profile, as seen in comparisons with the unprotected steel profile. As for displacements, considering the maximum allowable deflection for beams equal to L/350, only the TB100x100x4.75 beam exceeded the permissible limits in terms of the maximum deflection observed after the test.

Regarding the formation of paint expansion, it can be observed that the paint did not perform adequately at the edges of the TB100x100x4.75 profile, which is a critical region for absorbing heat from the profile. It is recommended, therefore, to exercise greater technological control over the application processes in these areas to ensure that the recommended dry thickness is achieved. For the W150x13 profile, which has a higher massiveness factor, a thicker layer of intumescent paint was applied, and in this case, an excellent expansion behavior of the paint process was observed. In the case of the W200x31.3 profile, the volumetric expansion process was unsatisfactory. The faster heating rate (as seen in the slope of the curves in Figure 11) compared to the other tests was one of the contributing factors to this outcome.

Therefore, it can be concluded that the results of the experiments were satisfactory for the intended purpose, allowing for result analysis and obtaining parameters that will be crucial for the creation of a numerical model to simulate the behavior of intumescent paints in steel structures.

5. ACKNOWLEDGEMENTS

6. REFERENCES

[1]   Mesquita L. M. R. *Estudo experimental e numérico do comportamento de um material intumescente na proteção passiva de elementos estruturais submetidos a incêndio.* Tese (Doutorado). Universidade do Porto – Portugal. Jun, 2015. 342p.

[2]   Lucherini A., Maluk C. *Intumescent coatings used for the fire-safe design of steel structures: A review.* Journal of Construction Steel Research, 2019, vol 162. 12p.

[3]   ASSOCIAÇÃO BRASILEIRA DE NORMAS TÉCNICAS – ABNT. *NBR 14432 – Exigências de resistência ao fogo de elementos construtivos de edificações – Procedimento.* Rio de Janeiro, 2001.

[4]   AMERICAN SOCIETY FOR TESTING AND MATERIALS – ASTM. *ASTM E8 / E8M – 21. Standard Test Methods for Tension Testing of Metallic Materials.* Pennsylvania, Estados Unidos, 2021.

[3]   ASSOCIAÇÃO BRASILEIRA DE NORMAS TÉCNICAS – ABNT. *NBR 14323:2013 – Projeto de estruturas de aço e de estruturas mistas de aço e concreto de edifícios em situações de incêndio.* Rio de Janeiro, 2013.

TEMPERATURE INCREASE THROUGHOUT HOT-DIP GALVANIZED STEEL SECTIONS AND CONNECTIONS OF COMPOSITE BEAMS IN THE FIRE SITUATION

AUTHORS: JUSTUS FRENZ A*; JOCHEN ZEHFUß B; MARIA-MIRABELA FIRAN C; MARTIN MENSINGER D

Justus Frenz a*   **Jochen Zehfuß b**   **Maria-Mirabela Firan c**   **Martin Mensinger d**

ABSTRACT

Hot-dip galvanization (HDG) reduces the emissivity of component surfaces, thereby slowing down the temperature increase of structural components in a fire situation. However, it is unclear, how HDG secondary structural components impact conventionally protected main beams. Therefore, the temperature increase and distribution through steel connection details was investigated for a variation of main beams, secondary beams and connection types in the test fire situation according to ISO 834. The secondary beams were all hot-dip galvanized, while the main beams were either hot-dip galvanized or protected with an intumescent coating. The shading between the adjacent structural components at the connection point as well as the additional mass of material from plates and angles appear to retard the temperature increase. These effects intensify for more bulky connection types with thicker material dimensions. The temperature insertion into the main beams depends on the connection type. It is small for long or mass-loaded connection details, but cannot be neglected for short connection types.

Keywords: Composite beams; hot-dip galvanizing; section temperature profile; ISO 834, steel connections

---

a***** TU Braunschweig, iBMB, Division of Fire Safety (J.Frenz@ibmb.tu-bs)**,** Corresponding author**.**

b, TU Braunschweig, iBMB, Division of Fire Safety (J.Zehfuss@ibmb.tu-bs.de).

c TU Munich, TUM School of Engineering and Design, Chair of Metal Structures (m.firan@tum.de)

d TU Munich, TUM School of Engineering and Design, Chair of Metal Structures (mensinger@tum.de)**.**

1. Introduction

At small scale, hot-dip galvanizing according to [6] has shown to reduce the emissivity of steel both in a test furnace [9, 10] and in the fire situation in the research project IGF 18887 N at the Technical University of Munich [1]. Instead of the current global emissivity specification of ε = 0.70, as in [3] and [4], those results led to a proposal of a temperature-dependent definition of the emissivity ε [2] in two steps: ε = 0.35 for a component temperature up to 500 °C and ε = 0.7 for a component temperature above 500 °C. The proposal has since been included in German regulation of steel construction and is adopted in the current revision of [3] and [4].

In an ongoing research project, the effect of hot-dip galvanization in fire is investigated at real scale in order to verify the transferability of the small-scale results to full-size structural elements (research project IGF 21536 N, 2021-2023 [12]). In this project, the global structural behavior of mechanically loaded composite beams in the fire situation was investigated. Beams were also fitted with numerous thermoelements to measure the heating of all elements of the composite section. In addition, each beam had a secondary beam allocated at mid-span, transverse to the longitudinal direction, connected to the main beam with different connection details. This paper presents the result data of the temperature increase through the connection detail in the test fire situation.

Current design guidelines state that in a system of similarly protected main and secondary beams, the temperature increase throughout the connection detail is slower than in the general span situation because of shading and additional material mass located around the connection point. [3] specifies temperature reduction parameters that may be assumed for connections. However, if an unprotected secondary beam is connected to a main beam that is protected with capsulation or intumescent paint, [11] requires a 300 – 600 mm continuation of the protection onto the unprotected component in order to control the temperature insertion through this gap of the protective measure. In a second test series of this project, HDG secondary beams are connected to intumescent coat protected main beams. In the test fire situation, the temperature development of the secondary beams, various connection details and the main beams was monitored to investigate if those connections require additional protection on the secondary beam or if the temperature insertion through the connection is acceptable, so that no further protection measures has to be required.

2. LARGE SCALE FIRE TESTS

2.1 Hot-dip galvanized beam tests

A series of six composite beams with hot-dip galvanized steel sections, subjected to the ISO 834 standard fire curve, were tested with mechanical load in the slab testing furnace (dimensions 9.0 m x 4.0 m) at the iBMB of the Technical University of Braunschweig. Each beam was 9.0 m long, designed with a trapezoidal sheet (Holorib HR51) on the bottom face of the concrete deck and had a secondary beam connected at mid-span. The concrete deck (class C35/45) and steel beam were connected with stud shear connectors (SD 1, d=22 mm, l=125 mm) welded through the pre-punched trapezoidal sheets directly onto the flange of the steel profile. Between the beams, the steel section dimensions and construction method varied from hot-rolled standard sections (HEB300 and HEB 450), welded I-sections (approximate "HEA300" and "HEA450") to optimized sections (halved standard IPE500 section welded to a 30 mm lamella as the bottom flange). The secondary beams were standard hot-rolled sections (IPE200 and IPE330) connected with flag-sheets or equal length angle profiles (L80x8 and L100x10). The steel grade was chosen as S460M and S690QL as well as S355 for connection elements and secondary beams. For the evaluation in this paper, four connection details (Table 1) with similar beam height were selected whose results could be compared to the unloaded test series (see description below).

Table 1: Connection details to the composite beams

Connection Detail	Main beam	Secondary beam	Connection description	Sketch
C-1	HEB300	IPE200	Long flag-sheet, t = 10 mm	
C-2	Welded "HEA300"	IPE200	Equal length angle profile L80x8 (both sides)	
C-3	Optimized profile ½ IPE500 with bottom flange	IPE200	Short flag-sheet t = 10 mm	1/2 IPE 500, S460M
C-4	Optimized profile ½ IPE500 with bottom flange	IPE200	Short flag-sheet t = 20 mm	1/2 IPE 500, S460M

During the fire tests, the temperature measurement in the furnace was conducted by surface plate thermocouples, which were arranged uniformly in the furnace directly underneath the steel sections. Type K thermocouples recorded the temperatures throughout the composite beam sections. For the hot-dip galvanized beams, thermocouples were placed in small boreholes (3 mm diameter) at a depth of half of the thickness of the respective section element. In the concrete, temperatures were measured with thermocouple-ladders, so that temperature development over the deck height can be recorded. Thermocouple ladders were placed in both the high and low rib locations for concrete decks with trapezoidal sheets. The measurement was carried out on several sections over the beam length. The arrangement of the thermocouples on the steel profile was staggered over the length of the beam in order to compensate possible temperature differences due to shadowing effects. Some stud shear connectors were modified with a borehole so that the temperature could be recorded near the connection point to the beam inside of the connector (connector height: 125 mm, borehole depth from the top: 100 mm). An additional amount of thermocouples was placed throughout the connection details. The positioning of thermoelements on the secondary beam (both flanges and web), flag-sheet, main beam web and bolts for connection detail C-1 is shown in figure 1. The analysis of the results considered only the temperature in the web for main and secondary beam. Beam deformation, end rotation and slip between concrete deck and steel section were recorded but will not be discussed in this paper.
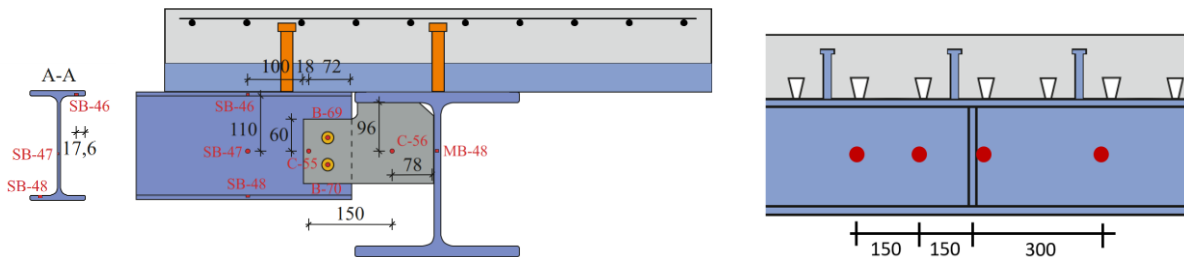
Figure1: Exemplary beam geometry and positioning of the temperature measurements at connection detail C-1 (TU Munich)

The beams were supported on hinges on both ends above the furnace wall (Fig. 2). Gas concrete elements were placed on the upper side of the concrete beams to close the top side of the furnace, as two beams were tested in every experiment. The beams were mechanically loaded with three presses aligned in the longitudinal centerline and placed at mid-span and both quarter-span points. All beams were loaded before the start of the fire. After 20 min of mechanical loading, the ISO 834 fire was introduced for all beams. The target duration was 30 min of ISO fire. The results of the load bearing behavior of the construction method will be published in future.

a)   b)

Figure 2: Large-scale fire test setup: furnace and composite beams (a) and temperature measurement at connection detail (b) (TU Braunschweig)

In order to avoid excessive deformation, leading to uncontrolled heat leakage and subsequently damage to the furnace and the load application devices, sand-lime bricks were placed centrally under the beams, limiting the maximum deformation of the beams for the case of total failure. Fig. 2 illustrates the test setup.

2.2 Fire tests on connection details between hot-dip galvanizing beams and with intumescent paint protected beams

Another series of two real-scale fire tests was conducted at the TU Munich. Here, two main beams were connected to two secondary beams, so that in each test setup four connection details could be investigated in the fire situation (Fig. 3). The structure was not loaded mechanically, as temperature spread and distribution was the main focus of the investigation. HEB, HEA and IPE profiles (steel grade S235JR) were used in different dimensions for the main and secondary beams for the two experimental setups. The secondary beams were connected to the main beams by different connection details consisting of double angles or plates of different thicknesses and lengths. The length of the main beams was 3.50 m whilst the secondary beams were approximately 1.50 m long. The connections were positioned at 1.30 m from each other and 1.10 m from each end of the main girder. All main beams were protected with intumescent paint R30, while the secondary beams were hot-dip galvanized. Connecting details that were part of the main beam, such as flag-plates, were coated with the beam itself. All other components (angle profiles, bolts, etc.) were hot-dip galvanized.
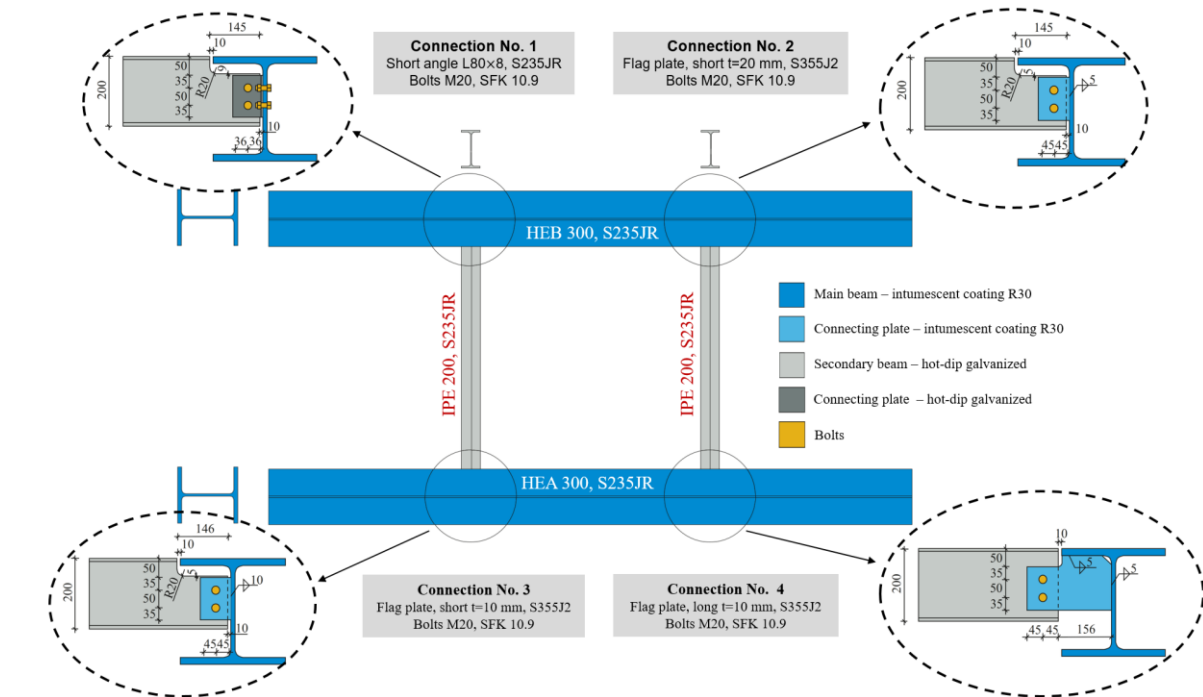
Figure3: Experimental setup unloaded beam tests (TU Munich)

The furnace produced the test fire according to ISO 834 for 60 minutes so that temperatures could be recorded. In the following evaluation the temperatures after 30 minutes of standard fire are considered. All temperature measurements were obtained with thermocouples type K, located in small boreholes distributed evenly throughout the beams and connection elements, so that the requirement in [11] can be investigated for this type of connections. The measuring points in the secondary beam were placed on the web and both flanges at 100 mm from the edge of the connection plate. The measuring point in the connection plate was positioned centrally between the edge and the axis of the bolts. On the main beams, five measuring points of the web were defined in the area of the connections as one measuring point directly behind the connection part and four measuring points at 200 mm between the points.

3. TEMPERATURE DEVELOPMENT IN CONNECTION DETAILS

3.1 HDG beam experiments

The connection details were fitted with thermocouples (type K) on the secondary beam, flag sheets or angle profiles, bolts and with several distances on the main beam. The oil-burners in the furnace produced the ISO 834 standard fire until the load bearing capacity of the beams (constant mechanical load throughout the experiment) was reached and the test had to be terminated. The test duration for beams with connections C-1 & C-2 was 24 minutes and 31

minutes for C-3 & C-4. The temperature profile plot shows the maximum temperature value recorded directly before the end of the fire test. The temperature profile plot shows both the longitudinal and transverse directions from the connection point of the beam (Fig. 5 & 6). One sided connection details therefore have a single temperature profile extending outwards from the center-point in the transverse direction, while two-sided connections as well as the main beam have two profile trajectories. In the longitudinal direction, two trajectories are plotted as temperatures were recorded on the main beam on both sides of the connection point (Fig. 4).
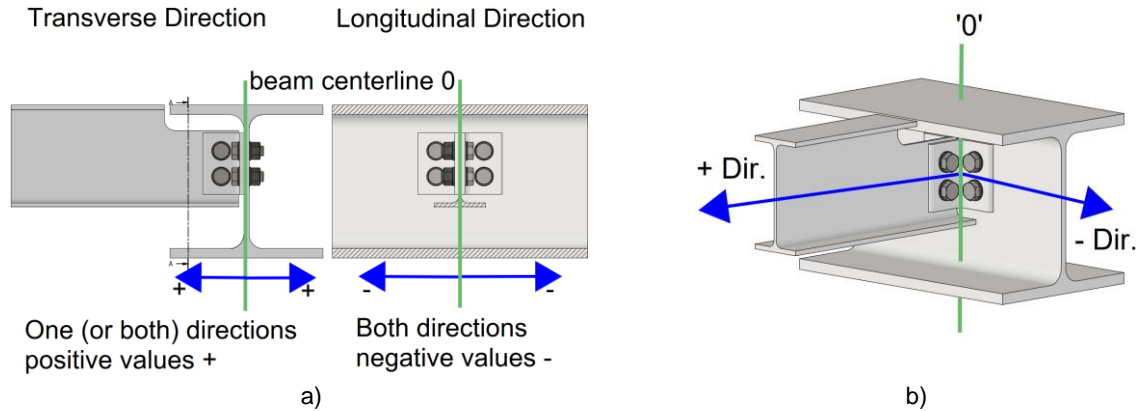
Figure 4: Trajectory orientation in temperature plots (TU Braunschweig)
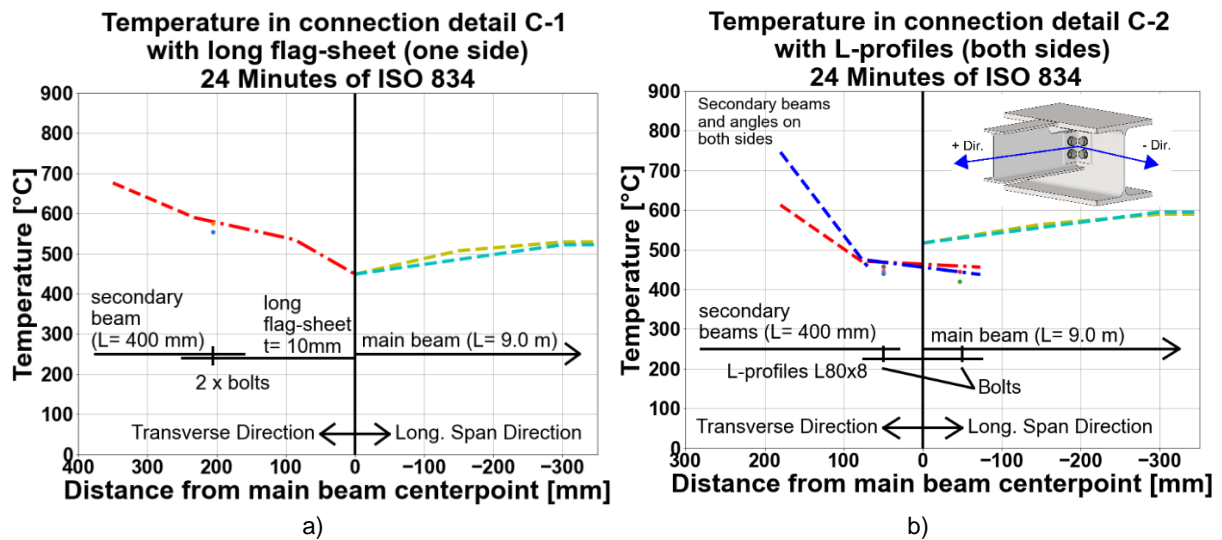
Figure 5: Temperature development in connection details C-1 and C-2 (TU Braunschweig)

512
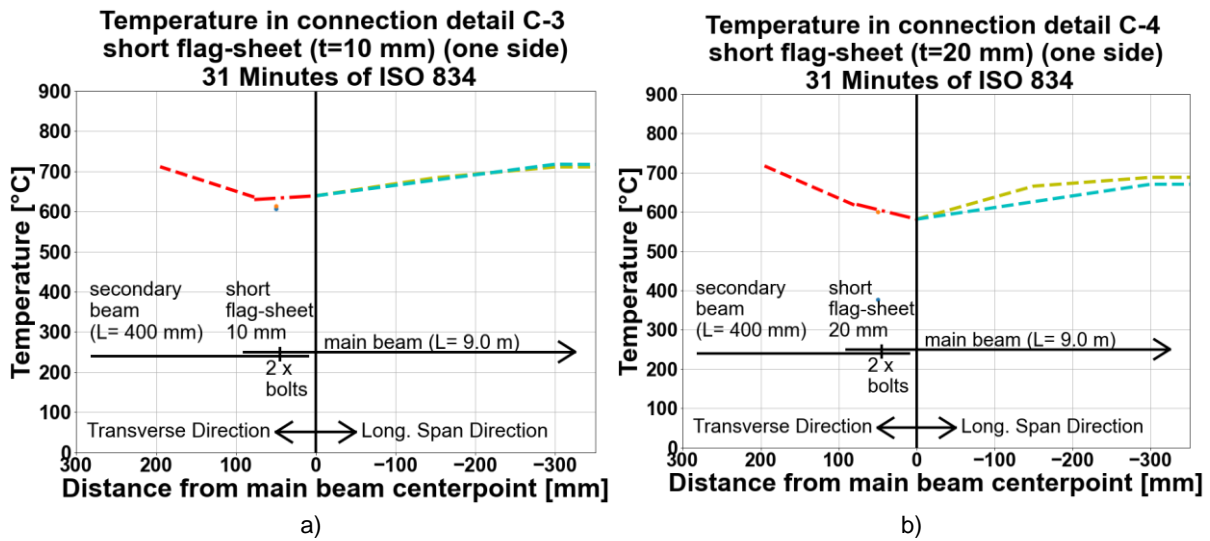
Figure 6: Temperature development in connection details C-3 and C-4 (TU Braunschweig)

For all tested connection details, the temperature increase in the area of the contact points of the two beams is slower than for the other temperature measuring points along the main beam. The deformation limitation (longitudinal length under the beam of 800 mm) may lead some shading, but any influence is assumed to be similar for the main beam length from -300 mm to +300 mm around mid-span, so that the relative temperature distribution is evaluated. Because of the difference in test duration, the comparison is drawn after 24 minutes of ISO 834 fire in Fig. 7.
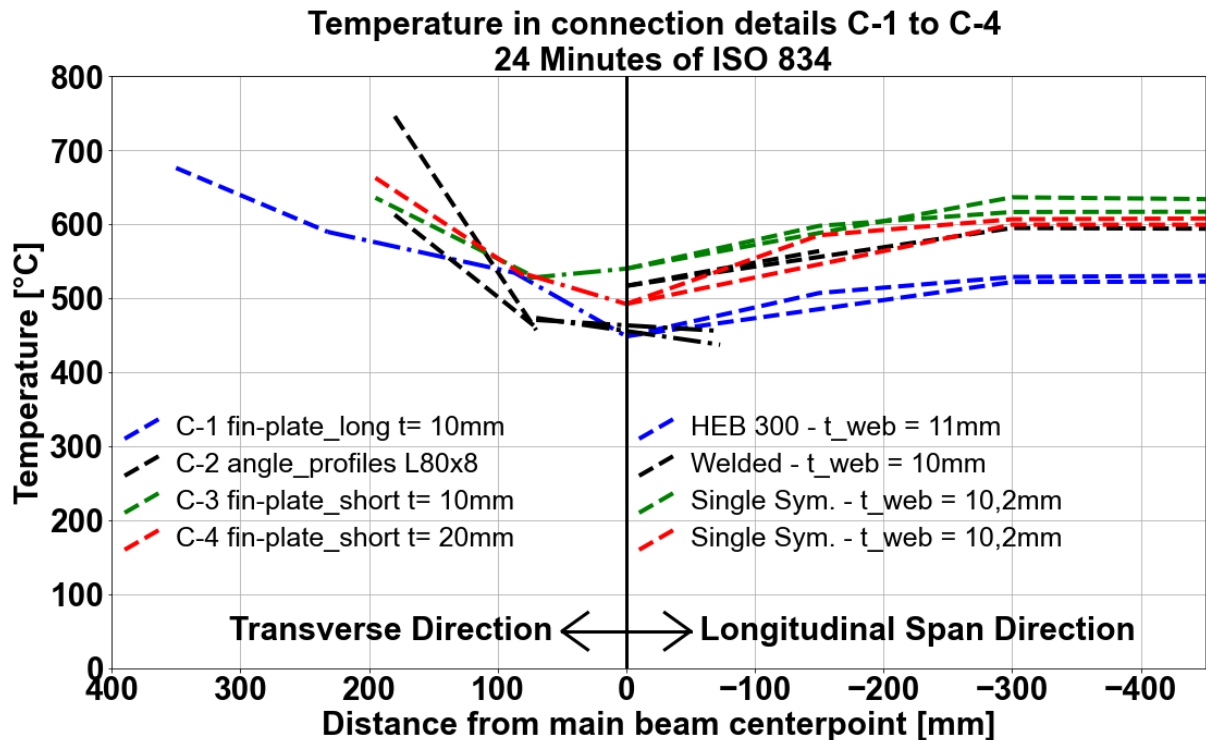
Figure 7: Temperature development in connection details C-1 to C-4 after 24 minutes (TU Braunschweig)

The web temperature of the main beam of connection C-1 (HEB300) remains slightly cooler than the beams of C-2 to C-4, but for all beams the connection point temperature is lower than in the surrounding beam elements. It can also be seen, that the temperature in the short, thin flag-sheet is the highest, while the temperature in the short,

513

thick flag-sheet and the long flag-sheet are around 50 K and 100 K lower respectively. The temperatures in the angle profiles are also relatively low, as they are only bolted to the other components. There is no direct heat transfer, so there is a small temperature difference between the angles and the beam. Especially for more bulky connection types with thicker flag-sheets or angle profiles, the temperature difference at the connection point increases compared to the beam temperature at a regular span and the heating occurs slower.

3.2 HDG and protected beams experiments

Similar connection details were examined in the tests with the protected main beam. Connections C-1, C-2, C-3 and C-4 (all elements HDG) correspond respectively to connections No.1, 2, 3 and 4 (secondary beam HDG, main beam protected with intumescent paint). The following diagram shows the temperature after 30 min in connection details 1, 3 and 4.
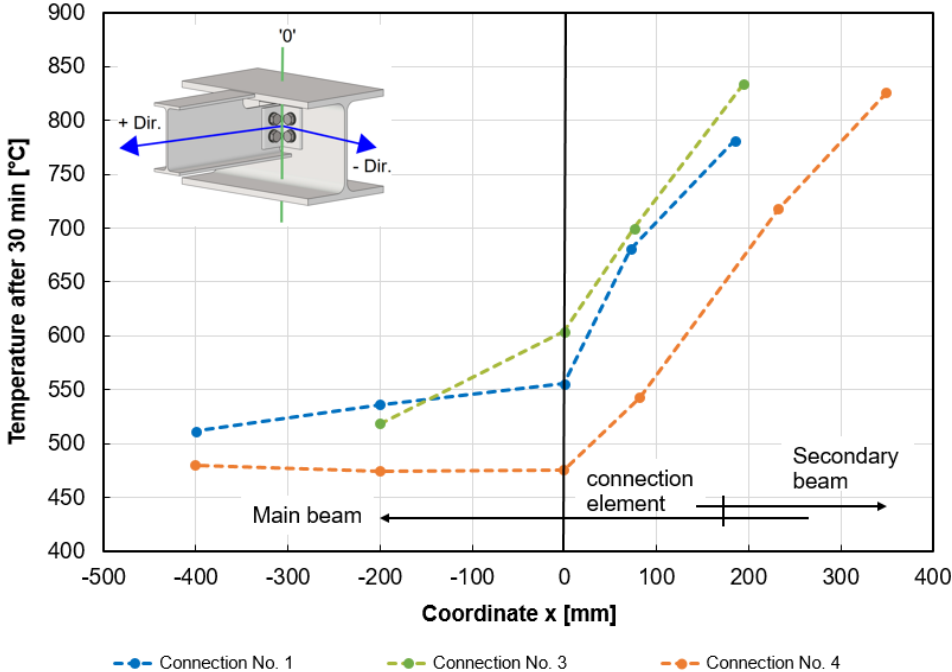
Figure 8: Temperature development in connection details No.1, 3 and 4 after 30 minutes

In the connections details of this experimental series, a greater difference can be identified between the temperature of the main beam and that of the secondary beam, as the intumescent paint retards the temperature increase significantly more intensely than the hot-dip galvanization. Looking at the temperature transfer through the connection from the uncoated elements, the increase for the long flag-sheet (Connection No. 4) appears to be small as the temperature in connection point of the main beam does not significantly deviate from the temperature of the span in the vicinity of the connection point. For the short angle profile (Connection No. 1) and the short thick flag-plate (Connection No. 2, not shown), a small increase in temperature can be identified compared to the neighboring measurement points. However, for the short flag-sheet (Connection No. 3), a significant temperature gradient from the connection point was recorded in the main beam.

The experimental results of connection investigation (Fig 8) show, that through the connection, especially for more bulky connection types with longer, thicker flag-sheets or angle profiles, rather small amounts of heat are transferred to the main beam. However, small connections with relatively low material mass (short, thin flag-plate) act as a weak point in the fire protection and heat can be transferred to the main beam. For these connection details, additional protection measures for the main beam extending to the secondary beam should not be omitted.

3.3 Numerical study and simplified temperature distribution estimation formula

With the original experimental data presented in this paper, a numerical model of the thermal behavior of the connection details is currently being established and validated, which includes a variation of connection types, geometry of the beams and hot-dip galvanization of the main and secondary beams. Subsequently, numerical investigations with a wide range of connection detail configurations are intended in the research project so that a general conclusion for connections with hot-dip galvanized structural elements can be established.

Based on the experimental results and regression analysis, a formula is currently being developed to estimate the temperature distribution throughout the connection detail at the Technical University of Munich. The aim is to include different connection types, dimensions and materials in the formulation so that it can be easily applied in design practice.

4. CONCLUSIONS

The temperature distribution through steel connection details was studied for a variation of main beams, secondary beams and connection types in the test fire situation according to ISO 834. The shading between the adjacent structural elements in this point as well as the additional mass of material from plates and angles appear to retard the temperature increase. These effects intensify for more bulky connection types with thicker material dimensions. The corresponding guideline, which assumes lower temperatures at the connection compared to the free span, can be confirmed.

In the connection situation, where HDG secondary beams are connected to an intumescent paint protected main beam, the amount of temperature transferred to the main beam is dependent on the connection detailing. For long and bulky flag-sheets or angles, the temperature transfer is low. For connections with short elements and low mass, the heat transfer to the main beam cannot be neglected and further protective measurements should be taken to ensure structural reliability in a fire situation.

REFERENCES

[1] Mensinger, M.; Gaigl, C. (2018) Schlussbericht zu IGF-Vorhaben Nr. 18887 N - Feuerwiderstand von feuerverzinkten, tragenden Stahlkonstruktionen im Brandfall.

[2] Gaigl, C.: Fire resistance of hot-dip galvanized steel structures. München, Technische Universität München, Dissertation, 2019.

[3] DIN EN 1993-1-2:2010-12, Eurocode 3 (2010) Design of steel structures - Part 1-2: General rules - Structural fire design; German version.

[4] DIN EN 1994-1-2:2010-12, Eurocode 4 (2010) Design of composite steel and concrete structures - Part 1-2: General rules - Structural fire design; German version.

[5] DIN EN ISO 14713-2 (2020), Zinc coatings - Guidelines and recommendations for the protection against corrosion of iron and steel in structures - Part 2: Hot dip galvanizing; German version.

[6] DIN EN ISO 1461 (2009) Hot dip galvanized coatings on fabricated iron and steel articles - Specifications and test methods (ISO 1461:2009); German version.

[7] DIN EN 1363-1:2020-05 Fire resistance tests - Part 1: General requirements; German version.

[8] Mensinger, M.;Gaigl, C.:"Feuerwiderstand verzinkter Stahlkonstruktionen", Stahlbau 88, 1, 3–10, 2019.

[9] Jirku, J.; Wald,F.: "Influence of Zinc Coating to a Temperature of Steel Members in Fire", Journal of Structural Fire Engineering 6, 2, 141–146, 2015.

[10] Bihina, G.; Zhao, B.: "Hot-dip galvanizing of steel structural members: an alterna-tive to passive fire insulation?", Proceedings 9. European Conference on Steel and Composite Structures (Eurosteel 2021), 1.-3. September 2021, Sheffield, Großbritannien. https://doi.org/10.1002/cepa.1427.

[11] DIN 4102-4:2016-05: Fire behaviour of building materials and building components – Synopsis and application of classified building materials, components and special components. German standard.

[12] Mensinger, M.; Zehfuß, J.; Firan, M.; Frenz, J.: Feuerwiderstand von feuerverzinkten Verbundträgern aus höher- und hochfesten Baustählen. Research Project IGF 21536 N from the GAV - Gemeinschaftsausschuss Verzinken e.V., Düsseldorf, FOSTA - e. V., Düsseldorf and DASt Deutscher Ausschuss für Stahlbau e.V., Düsseldorf.

DEEP LEARNING-DRIVEN REAL-TIME PREDICTION OF KEY PHYSICAL PARAMETERS' EVOLUTION FOR EARLY-WARNING FIRE-INDUCED COLLAPSE OF STEEL TRUSSES

Jinyu LI [a]   **Guo-Qiang LI [b]**   **Shaojun ZHU [c*]**

ABSTRACT

Steel trusses are widely used in public and industrial buildings. Fire-induced collapses of steel trusses result in significant property loss and pose a great threat to the lives of firefighters and trapped people. This paper proposes a real-time method to predict the evolution of key physical parameters for early-warning collapse of steel trusses in fire based on the deep learning (DL) model. The easily measured parameters, rotations and temperatures, which can reflect uncertain structural parameters and fire scenarios are set as inputs. The displacements that are hard to measure but of great importance to early warn fire-induced collapse of steel trusses are set as the physical parameters of outputs. The long short-term memory network is used in the DL model, which can be trained offline in a large numerical database. Results indicate that predicted displacement-time curves are highly closed to the real curves. A numerical case study is presented to illustrate the application process of the proposed method for the early-warning collapse of steel trusses exposed to fire. Combined with the early-warning theory, the predicted and actual remaining time to collapse of the steel truss case agree with each other satisfactorily, which indicates the effectiveness of the proposed method.

Keywords: early warning; intelligent firefighting; deep learning; fire-induced collapse; steel truss

1. INTRODUCTION

Steel trusses are widely used as roof structures in public and industrial buildings. However, fire-induced collapse cases of steel trusses are frequently reported worldwide since the low redundancy and the significant loss of

---

[a] College of Civil Engineering, Tongji University, Shanghai 200092, China (lijinyu98@tongji.edu.cn)**.**

[b] College of Civil Engineering, Tongji University, Shanghai 200092, China (gqli@tongji.edu.cn)**.**

[c*] College of Civil Engineering, Tongji University, Shanghai 200092, China (zhushaojun@tongji.edu.cn)**,** Corresponding author.

strength and stiffness of steel at high temperatures [1]. Unexpected fire-induced collapses of buildings pose a great threat to the firefighters and people trapped inside. Therefore, it is urgent to develop early-warning methods for the fire-induced collapse of buildings. Song *et al.* [2] defined the refined critical temperature of the concrete-filled steel tubular columns and used refined critical temperatures to prewarn against the fire-induced failure of the columns. Jiang *et al.* [3] monitored the collapse state of the steel truss structures based on the critical temperatures of the truss members. However, real critical temperatures, closely related to the real loads and material properties, differ from the values calculated by design loads and material properties. Besides, these parameters, i.e., real loads and material properties, which can be called uncertain structural parameters, are hard to be determined rapidly in real fire scenes. Therefore, it is insufficient to prewarn the collapse of structures in fire based on temperatures only.

Recently, Li *et al.* [4-6] proposed early-warning methods for fire-induced building collapses based on real-time measurement of displacements and velocities, as these parameters can reflect uncertain structural parameters. However, displacements are hard to be measured directly at real fire scenes because of the dense smoke, which limits the application of the proposed method. Though microwave radar can be used in real fire scenes to monitor displacements [7, 8], finding a suitable place to set up the radar stably and quickly is challenging. Besides, the radar has limited vision and cannot detect the displacements of the top or interior joints of the buildings.

With the development of computer science, deep learning (DL) is widely used in structural fire engineering for fire detection [9,10] and reducing the computational cost of thermal-structural analysis [11,12]. Besides, Ye *et al.* [13] trained a long short-term memory (LSTM) network to predict structural fire responses in the immediate future based on the coupled computational fluid dynamics (CFD)–finite element (FE) framework. Xiao *et al.* [14] proposed a new approach to predict the post-fire load-displacement curves of high-strength steel plate girders based on LSTM networks. Ji *et al.* [15] obtained the hard-to-measure parameters of steel portal frames by the easily measured parameters based on the DL model to prewarn the collapse state of steel portal frames in the fire. However, the displacements at the eaves of the steel portal frames still need to be measured by radar directly.

Inclinometers, which can be easily pre-embedded in the key positions of the structure, can easily measure the rotations. They have been widely used in monitoring bridge deflection [16] and building deformation[17, 18]. This paper tackles the problem of real-time prediction of key physical parameters for early warning of the fire-induced collapse of steel truss structures based on easily measured rotations and temperatures. Rotations and temperatures can reflect the uncertain structural parameters and fire scenarios. The paper starts by presenting a FE model of the steel trusses, presenting the process of the dataset for training, discussing the development of the DL model for predicting the displacements at key joints, and then presenting a numerical case study to demonstrate the application process.

2. FE MODEL AND DATA GENERATION

2.1 FE model

A planar steel trapezoid truss designed according to the Chinese code [19] is shown in Figure 1. The truss roof is fully pinned to the reinforced concrete columns on both sides without fire protection. This truss structure consists of 8 planar trusses with an interval of 6 m. The span of each planar truss is 24 m. All of the truss members are made of Q235 steel, and the cross-sectional information of the members is tabulated in Table 1.
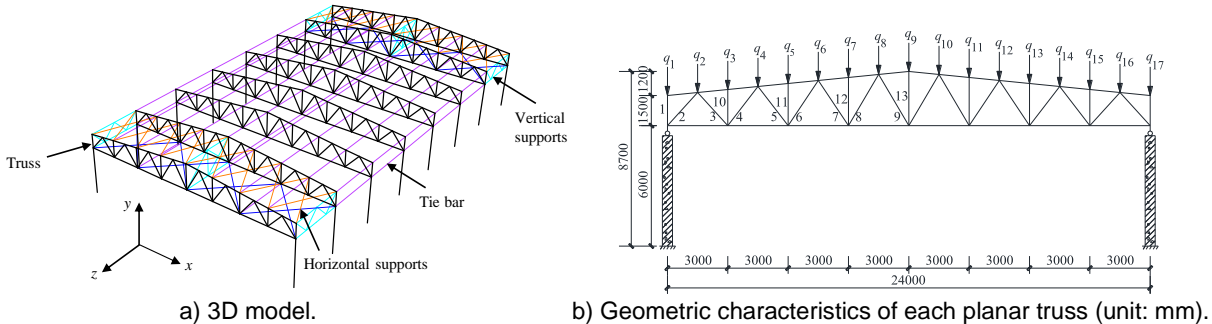
a) 3D model.   b) Geometric characteristics of each planar truss (unit: mm).
Figure 1: Geometric model of the planar steel trapezoid truss.

The datasets used for training the DL model are generated based on thermal-structural analysis in the general FE software ABAQUS utilizing the explicit module. The Timoshenko beam element B31 is adopted to simulate the steel members. An element mesh size of 0.05 m is used for truss members through careful mesh sensitivity analysis. The FE analysis includes two load steps: apply random loads, which will be explained in Section 2.2, at ambient temperature, then heat the truss members at the same loads. The detailed validation of the FE model can be referred to in literature [4].

Table 1: Cross-sectional information of the members.

Member type or number	Section dimensions (unit: mm)
Top chord	Φ159×4.5
Bottom chord	Φ140×4.5
Tie bar	Φ89×3
Supports	Φ83×2.5
1, 10-13 (and symmetric members)	Φ70×2
2 (and symmetric member)	Φ121×3.5
3, 4 (and symmetric members)	Φ102×2.5
5-9 (and symmetric members)	Φ83×2

2.2 Uncertain structural parameters and fire scenarios

Since the quality of steel for all truss members is Q235, the quality of Q235 will meet the requirements when the yield strength f_y is no less than 235 MPa, and the ultimate strength f_u is between 370-500 MPa at ambient temperature according to the Chinese code GB/T 700-2006 [20]. Therefore, the real values of f_y and f_u are assumed to obey uniform distribution. The scope of the probability distribution of f_y and f_u is determined as 235-350 MPa and 370-500 MPa, respectively. The surface loads of the truss structure are considered by concentrate loads applied at each joint of the top chords according to their tributary areas. The loads at different joints of the top chords are set as different random values since the loads may vary during the service stage of the structure. The intensity of concentrate load at the ith joint q_i, as shown in Figure 1, is assumed to obey uniform distribution $U(0.3q_{u,i}, 0.6q_{u,i})$, where $q_{u,i}$ is the ultimate concentrate load of the ith joint under uniform load distribution at ambient temperature.

The gas temperature field is obtained by the simplified parametric curve. Since the steel trusses are often used in large spaces where the temperature field is non-uniform, the temperature-rise curve of large-space building fires proposed in literature [21] is used to simulate the gas temperature field:

$$T(x,z,t) - T_{g,0} = T_{g,max}(z)\left(1 - 0.8e^{-\beta t} - 0.2e^{-0.1\beta t}\right)\left[\eta + (1-\eta)e^{-\frac{x-b}{\mu}}\right] \tag{1}$$

where $T_{g,0}$ is the ambient temperature, which can be taken as 20°C; $T_{g,max}(z)$ is the maximum temperature at height z; η and μ are the factors dependent on the floor area and ceiling height; b is the distance from the edge of the fire surface to the central axis of the fire; x is the horizontal distance from the central axis of the target point to the central axis of the fire; β is a constant related to the fire growth types. Once the temperature field can be obtained, the temperature of steel members can be calculated according to Chinese code GB 51249-2017 [22].

For simplicity, the fire is assumed to be ignited at the fourth bay of the truss, as shown in Figure 1. A total of 10 fire development conditions (denoted as F1-F10), which are the random combinations of five heating conditions along the span (S1-S5) and two heating conditions along the bays, are considered as shown in Figure 2. The red members in the red dotted line box are heated while the others remain at ambient temperature. The non-uniform temperature field along the span is calculated by Eq. (1), and the β is assumed to obey uniform distribution $U(0.0004, 0.002)$, i.e., the fire growth rate is between slow fire and ultra-fast fire [21]. In this way, 500 fire scenarios are generated to establish the dataset.

a) Five heating conditions along the span.

b) Two heating conditions along the bays.
Figure 2: Fire development conditions.
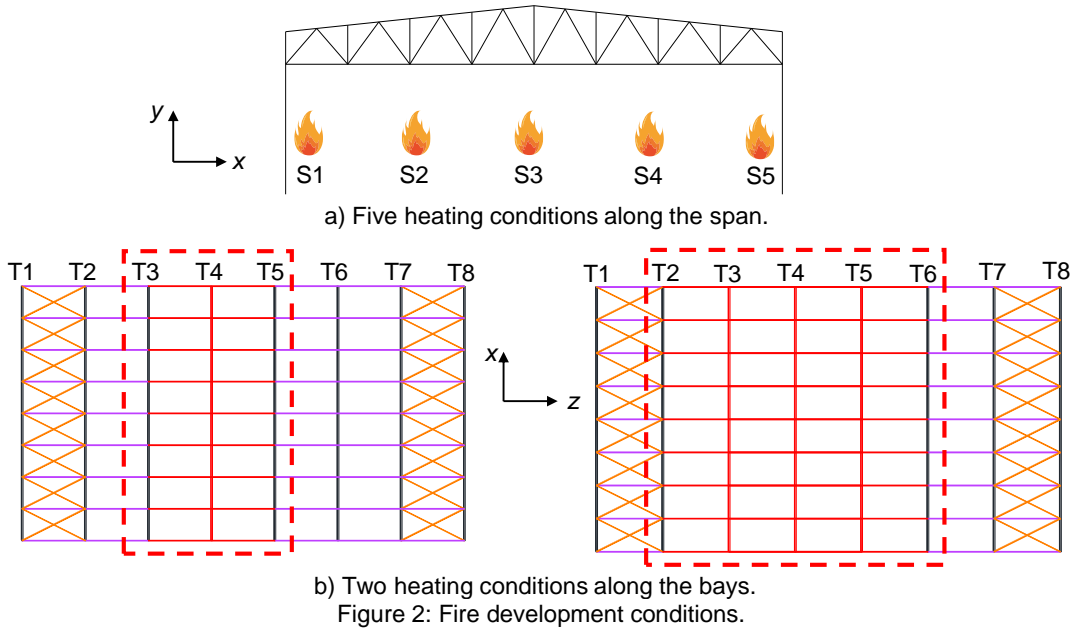
2.3 Key data involved in the DL model

Note that the paper aims to obtain hard-to-measure displacements of steel trusses in fire based on the easily measured parameters, i.e., key rotations and temperatures. Therefore, the inputs of the DL model are rotations and temperatures in key positions, while the outputs are displacements used for early warning. The steel truss structure shown in Figure 1 comprises 8 relatively independent trusses. Therefore, the rotations and temperatures reflect the structural states and fire scenarios of the corresponding truss, respectively. In this way, the different trusses shown in Figure 1 should share the same DL model since they have the same geometric characteristics and boundary conditions. To obtain the structural data as much as possible, inclinometers are symmetrically placed at key joints of top chords, as shown in Figure 3. Gas temperatures can reflect the fire development and non-uniform temperature field. Therefore, the other inputs are the gas temperatures at different parts, including G1-G5, as shown in Figure 3.

Figure 3: Arrangements of inclinometers and thermocouples.
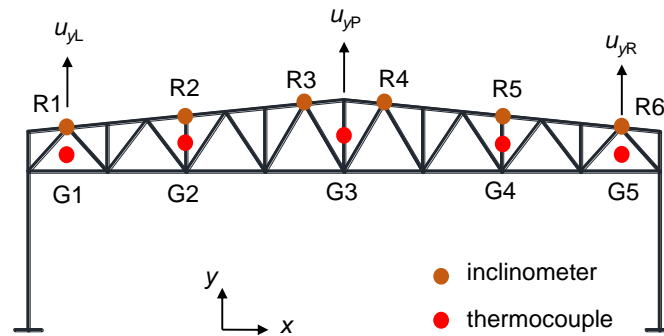
According to the early-warning method for the fire-induced collapse of planar steel trapezoid trusses proposed by Li *et al.* [4], the displacements u_{yP}, u_{yL}, and u_{yR} which are of great importance to early warning are set as outputs of the DL model. Since the fire is assumed to be ignited from the truss T4, the data for training the DL model are extracted from the truss T4. Five hundred samples are established by thermal-structural analysis in ABAQUS. Figure 4 shows the detailed procedure of the dataset generation. Note that the random parameter matrix **A** stores f_y, f_u, fire development conditions, and β in Eq. (1), respectively. Random load matrix **B** stores the load at each joint of the trusses. Matrixes **R**, **G**, and **D** store rotations, gas temperatures, and displacements at key positions of the truss T4, respectively.
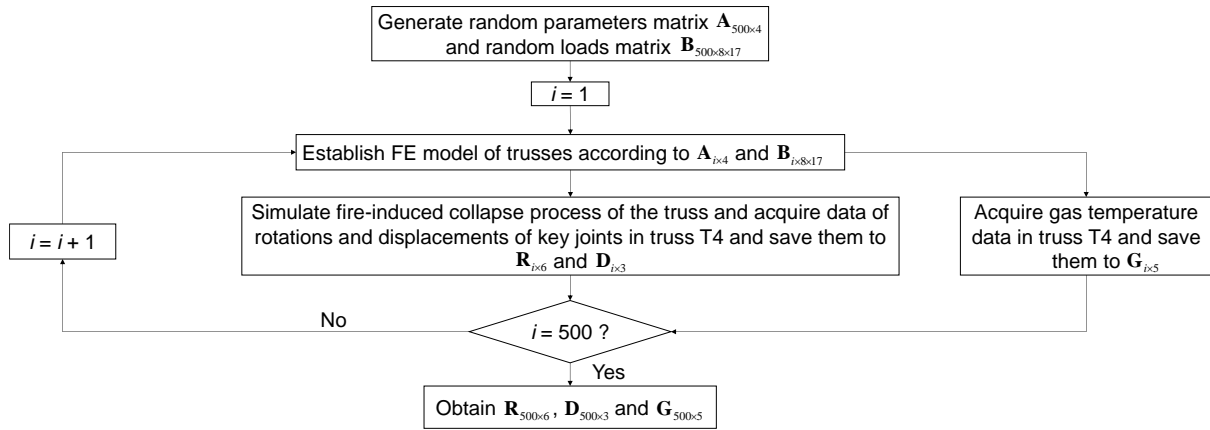
Figure 4: Flow chart of the dataset generation.

3. DEVELOPMENT OF THE DL MODEL

3.1 Network architecture and training

The DL model aims to learn the complex non-linear temporal relationship between rotations, temperatures, and displacements. The LSTM network, which consists of a chain of repeated cells with various gates, is adopted in this study since it can not only handle the problem of long-term dependencies well but also resolve the gradients vanishing and exploding problems [23]. The LSTM layers are incorporated with fully connected (FC) layers and different activation functions to form the network in this study, as shown in Figure 5. 'ReLU' is the activation function for strengthening the non-linear ability. 'Dropout' indicates that a certain percentage of neurons within the network will be omitted during the current training step to avoid overfitting, which is adopted as 0.2 in this study.
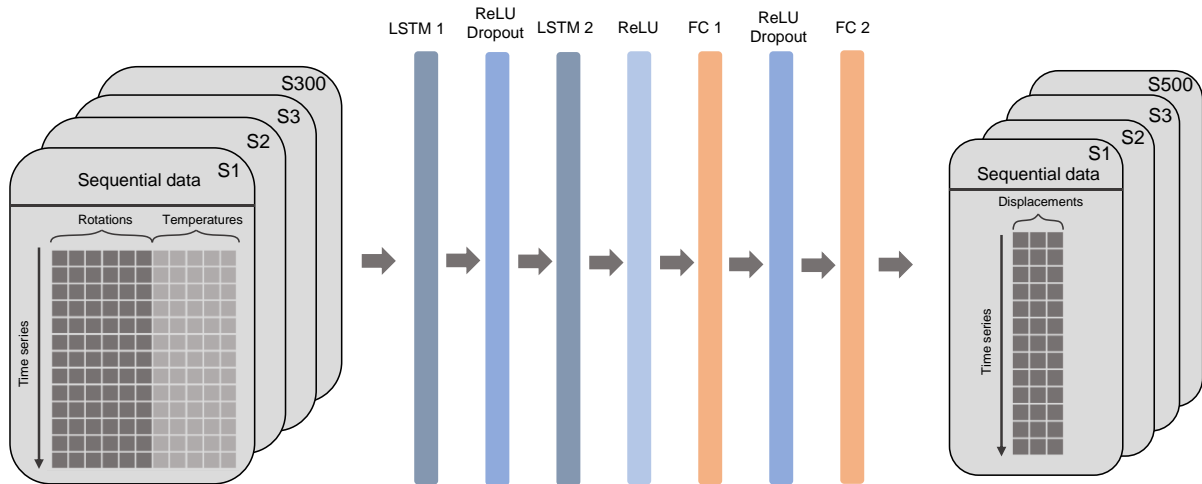
Figure 5: Network architecture

The 500 samples are randomly divided into three subsets, including the training dataset with 300 samples, the validation dataset with 100 samples, and the test dataset with 100 samples. Only the training and validation datasets will be involved in updating the learnable parameters. The test dataset can be regarded as a completely unknown dataset for the evaluation of the trained agent. The DL model is developed in Python by Pytorch [24]. Before training the model, the inputs and outputs are all scaled within the range of [-1, 1] to avoid numerical problems. The mean squared error is adopted as the loss function. The training phase consists of 50,000 epochs with a batch size of 128. The adaptive moment estimation optimizer Adam is used to train the DL model because of its robustness on complex optimization problems, fewer requirements of memory, and ease of implementation [25]. The history of the losses is shown in Figure 6 on a logarithmic scale. It can be observed that the value of loss converges at a low value after 20000 epochs.

521
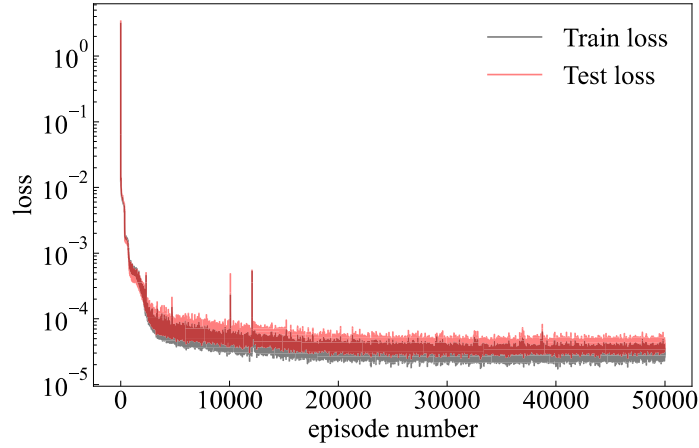
Figure 6: Training history.

3.2 Performance of the DL model

This section will evaluate the model performance by comparing the actual and predicted displacement–time curves of the test dataset. Here we note again the test dataset has not participated in the training process and can be regarded as a completely unknown dataset. To quantitatively evaluate the performance of the trained agent, the following indices are introduced:

1)   Root mean squared error *RMSE*

$$RMSE_j = \sqrt{\frac{\sum_{t=1}^{t_{max}}\left[y_{j,pred}^{(t)} - y_{j,true}^{(t)}\right]^2}{t_{j,max}}}$$ (2)

2)   Coefficient of determination R^2

$$R_j^2 = 1 - \frac{\sum_{t=1}^{t_{max}}\left[y_{j,pred}^{(t)} - y_{j,true}^{(t)}\right]^2}{\sum_{t=1}^{t_{max}}\left[y_{j,true}^{(t)} - \bar{y}_{j,true}\right]^2}$$ (3)

where subscript *j* represents the *j*th evaluated sample, superscript '(*t*)' denotes the *t*th element of the time series, and subscript 'true' and 'pred' indicate the actual and predicted time series, respectively. $\bar{y}$ is the average value of the time series data, and t_{max} is the length of the time-series data. When the values of *RMSE* and R^2 are close to 0 and 1, a satisfactory prediction can be concluded.

The test samples are fed into the DL model to predict the u_{yP}, u_{yR}, and u_{yL}, as shown in Figure 3. The distribution histograms of *RMSE* and R^2 are shown in Figure 7. It can be observed that the R^2 and *RMSE* of most test samples are larger than 0.9 and less than 5 mm, respectively. Note that u_{yP} has a larger *RMSE* than u_{yR} and u_{yL} for most test samples, while the R^2 of u_{yP} performs well. Further analysis shows that the value of u_{yP} reaches a considerable value when the truss collapses. Therefore, even a little error will cause a large *RMSE* at the collapse time of the truss. But this large error has little influence on the R^2. As opposed to u_{yP}, the value of u_{yL} is relatively small when the truss collapses. Therefore, the *RMSE* of u_{yL} is small for most test samples, while the R^2 performs not as well as u_{yP}. Figure 8 shows 4 typical cases of the actual and predicted displacement–time curves. Results show a satisfactory agreement between the predicted and true curves.

522
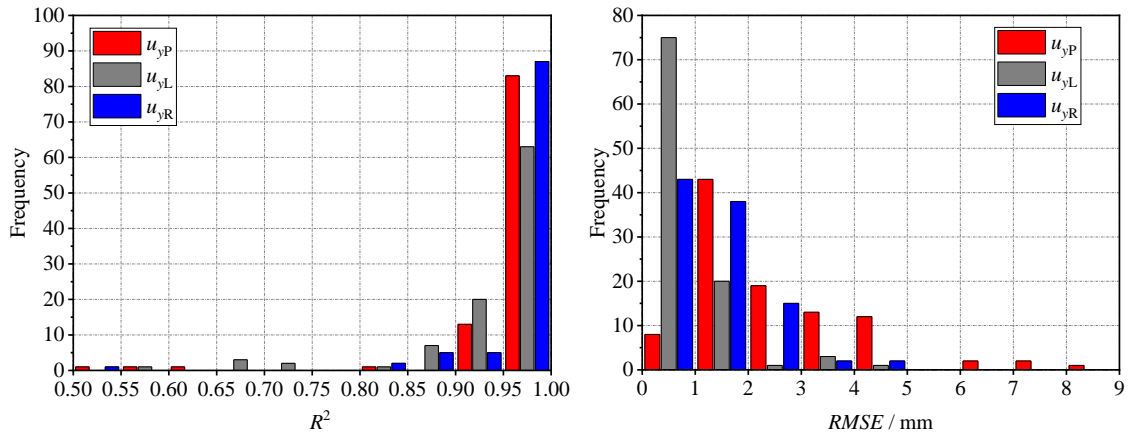
Figure 7: Distribution histograms of *RMSE* and R^2.

a) Case 1

b) Case 2

c) Case 3

d) Case 4
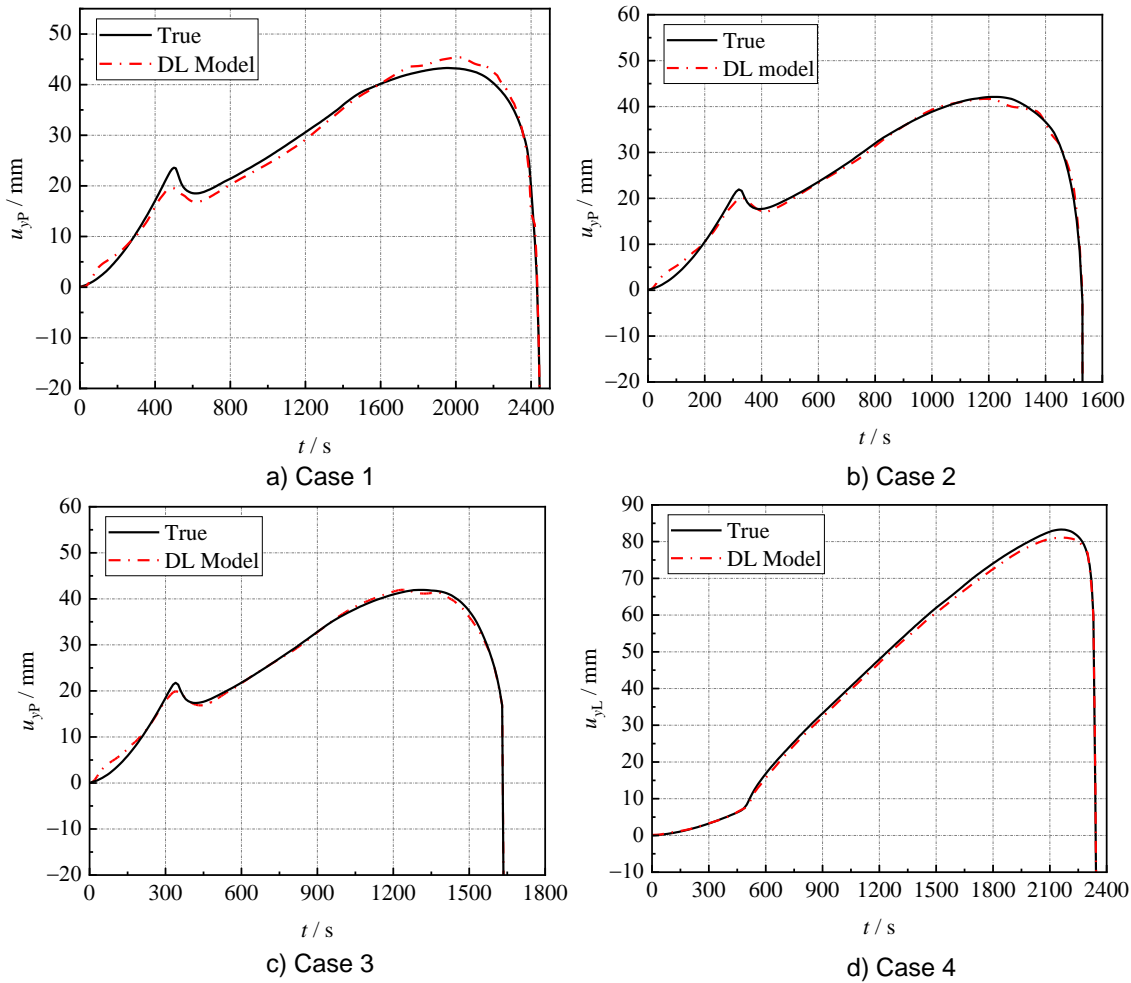
Figure 8: Typical comparison cases between actual and predicted displacement–time curves.

4. CASE STUDY

To illustrate the application process of the proposed method, a numerical case study is presented in this section. In this example, the fire is still ignited at truss T4. Assume that the inclinometers and thermocouples are all pre-embedded in the truss structure, as shown in Figure 3 in practice. In this way, the rotations and temperatures can be real-time obtained, as shown in Figure 9. Figure 10 shows the vertical displacements of the key joints predicted by the DL model synchronously based on the real-time measured rotations and temperatures.

523

a) Rotations   b) Temperatures
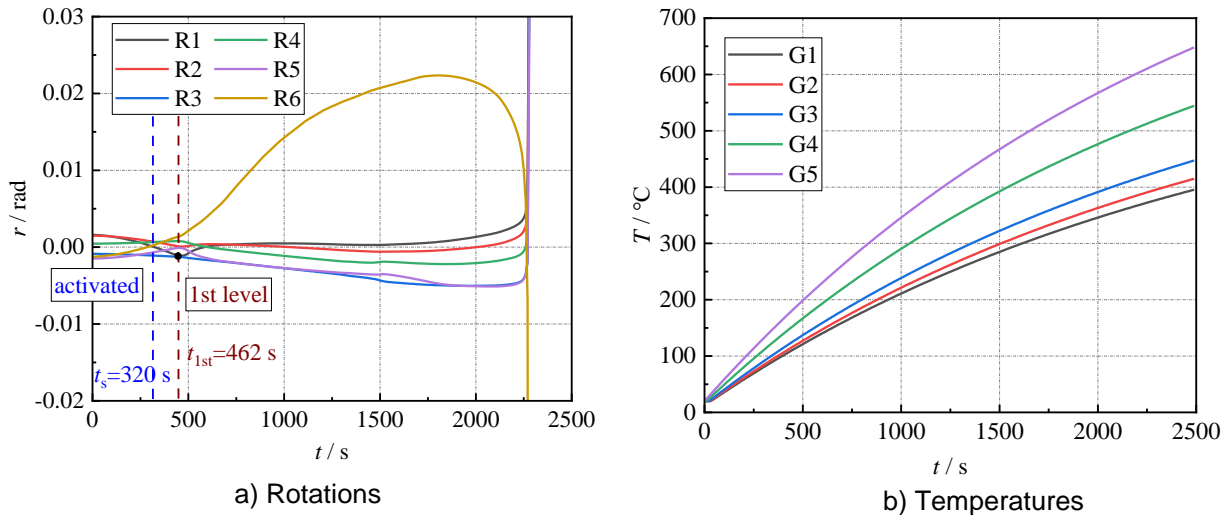
Figure 9: Real-time monitored rotations and temperatures.

After fire ignition, the air temperature rises, and the steel members are heated. According to the early-warning method proposed by Li *et al.* [4], when the maximum temperature of the bottom chord reaches 50 °C at 320 s, the early-warning system is activated. At about 462 s, the rotations in some nodes vary suddenly, and u_{yP} develops downwards at the same time. Therefore, the post-buckling collapse mode (collapse mode B) can be identified [4], and the 1st early-warning level is given. At this time, the truss has been influenced by the fire, and the risk of collapse is increasing, while there is still a relatively long time before the truss collapses, so the firefighters can continue to rescue trapped people. When the u_{yP} reaches the peak value at 1735 s, the 1st warning state is converted into the 2nd warning state. In this case, the firefighters should speed up their rescue process and prepare for evacuation. When the u_{yR} reaches the peak value at 2098 s, the 3rd early-warning level is given. At this time, the truss is very dangerous, and firefighters must evacuate as soon as possible to avoid second causalities. At about 2290 s, the truss collapses.
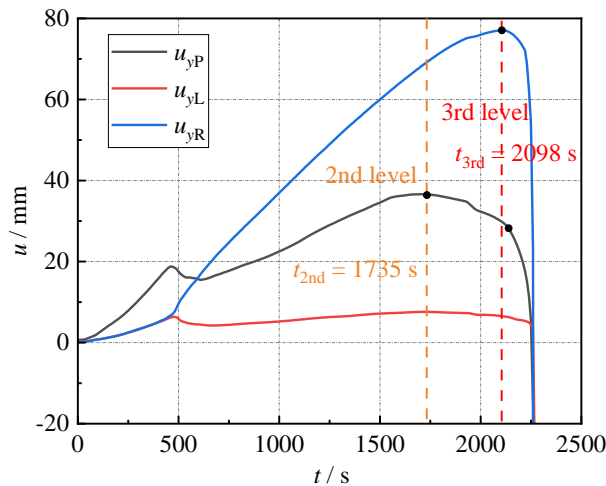
Figure 10: Predicted vertical displacements of key joints in real-time.

The comparison of the predicted and real remaining time to collapse according to the method in literature [4] is shown in Table 2. It can be observed that the predicted time is more and more closer to the actual one as the early-warning level is higher, which is identical to the previous conclusions [4], since the collapse state is more apparent as the temperature rises. The remaining time to collapse will be updated once a new early-warning level appears. In this case, when the 3rd early-warning level is given, there is a satisfactory agreement between the real and predicted values, whose error is only 2%. Therefore, the proposed framework can be successfully used for early warning of fire-induced truss collapse.

Table 2 Comparison of predicted and actual remaining time to collapse.

Warning level	t_i^E	Predicted t_i^R	Actual t_i^R
Activated	320 s	/	/
1st	462 s	450 s	1828 s
2nd	1735 s	382 s	555 s
3rd	2098 s	196 s	192 s

5. CONCLUSIONS

This paper proposes a real-time prediction method to obtain key physical parameters for early-warning collapse of steel trusses in fire based on the deep learning (DL) model. The random FE models with uncertain structural parameters and unlimited fire scenarios are considered to generate the numerical dataset for training the DL model. The LSTM network is adopted in the DL model to fit the complex relationships between the easily-measured rotations and temperatures and hardly-measured displacements at key locations of the truss in fire. The good performance of the DL model is illustrated in this paper. A case study is presented to demonstrate the effectiveness of the method for early warning the fire-induced collapse of planar steel trapezoid trusses. The conclusions of the study can be summarized in the following points:

1   The displacements at key joints of steel trusses can be real-time obtained by the well-trained DL model based on easily-measured rotations and temperatures at key positions of steel trusses. Rotations and temperatures can reflect the effects of uncertain structural parameters and fire scenarios, respectively.
2   Combined with the approach for early-warning fire-induced collapse of planar steel trusses, the proposed method can be employed to predict the real remaining time to collapse of steel trusses. A case study demonstrated that the predicted remaining time to collapse agrees with the actual one satisfactorily.
3   So long as the inclinometers and thermocouples are pre-embedded at the key positions of trusses, the collapse process can be monitored, and the real remaining time to collapse can be predicted. The proposed method can increase the practicability of the available early-warning method for steel trusses in real fire conditions.

ACKNOWLEDGEMENTS

REFERENCES

[1]   Li, G.Q.; Jiang, S.C.; Yin, Y.Z.; Chen, K. & Li, M.F. (2003). *Experimental studies on the properties of constructional steel at elevated temperatures*, Journal of Structural Engineering, vol. 129, no. 12, p. 1717-1721.
[2]   Song, T.Y.; Yu, W.C.; Xiang, K; & Zhou, H.Y. (2022). *Critical temperatures of concrete-filled steel tubular columns for early-warning of fire-induced failure*, Journal of Constructional Steel Research, vol. 191, p. 107190.
[3]   Jiang, S.; Zhu, S.; Guo, X.; Chen, C. & Li, Z. (2020). *Safety monitoring system of steel truss structures in fire*. Journal of Constructional Steel Research, vol. 172, p. 106216.
[4]   Li, G. Q.; Li, J. & Zhu, S. (2023). *An Approach for Early-warning Collapse of Planar Steel Trapezoid Trusses Exposed to Fire*, Fire Safety Journal, vol. 137, p. 103778.
[5]   Ji, W.; Li, G.Q; & Lou, G.B. (2022). *Early-warning methods for fire-induced collapse of single span steel portal frames*. Journal of Constructional Steel Research, vol. 190, p. 107154.
[6]   Ji, W.; Zhu, S.; Li, G.Q.; Lou, G. & Jiang, S. (2022). *Approach for early-warning collapse of double-span steel portal frames induced by fire*, Fire Safety Journal, vol. 131, p. 103628.

[7] Li, G.; Ji, W.; Feng, C.; Wang, Y.; Li, X.; Liang, T.; Shi, X. & Liu, X. (2021). *Collapse test of steel portal frame under fire and effective analysis of radar-based displacement measuring system*, China Civil Engineering Journal, vol. 54, no. 9, p. 56-65 (in Chinese).

[8] Yin, L.; Kan, Q.; Fan, F. & Ye, Ji. (2020). *Discussion on early warning means of building structure collapse under fire and application of interference radar*, Fire Science and Technology, vol. 39, no. 12, p. 1668-1671 (in Chinese).

[9] Wang, Z.; Zhang, T.; Wu, X. & Huang, X. (2022). *Predicting transient building fire based on external smoke images and deep learning*, Journal of Building Engineering, vol. 47, p.103823.

[10] Namozov, A. & Im Cho, Y. (2018). *An efficient deep learning algorithm for fire and smoke detection with limited data*, Advances in Electrical and Computer Engineering, vol. 18, no. 4, p. 121-128.

[11] Moradi, M.J.; Daneshvar, K.; Ghazi-Nader, D. & Hajiloo, H. (2021). *The prediction of fire performance of concrete-filled steel tubes (CFST) using artificial neural network*, Thin-Walled Structures, vol. 161, p.107499.

[12] Xu, J.; Zhao, J.; Wang, W. & Liu, M. (2013). *Prediction of temperature of tubular truss under fire using artificial neural networks*, Fire Safety Journal, vol. 56, p. 74-80.

[13] Ye, Z. & Hsu, S.C. (2022). P*redicting real-time deformation of structure in fire using machine learning with CFD and FEM*, Automation in Construction, vol.143, p.104574.

[14] Xiao, L.; Hua, J.; Li, H.; Xue, X.; Wang, N. & Wang, F. (2022). *Quantitative analysis on post–fire–resistant performance of high–strength steel plate girders using LSTM*, Journal of Constructional Steel Research, vol. 199, p. 107588.

[15] Ji, W.; Li, G. Q. & Zhu, S. (2022). *Real-time prediction of key monitoring physical parameters for early warning of fire-induced building collapse*, Computers & Structures, vol. 272, p.106875.

[16] Hou, X., Yang, X. & Huang Q. (2005). Using inclinometers to measure bridge deflection, Journal of Bridge Engineering, vol. 10, no. 5, p. 564-569.

[17] Hou, S., Zeng, C., Zhang, H.,& Ou, J. (2018) Monitoring interstory drift in buildings under seismic loading using MEMS inclinometers, Construction and Building Materials,vol. 185, p. 453-467.

[18] Ji, W., Zhu, S., Li, G. Q. & Chen, B. (2023) Synchronous displacement acquisition approach for early warning of fire-induced collapse of steel portal frames. Fire Technology, doi: 10.1007/s10694-023-01395-7.

[19] National building standard design atlas (circular steel tube, square steel tube) (06SG515-1), China Planning Press, Beijing, 2006 (in Chinese).

[20] Carbon structural steels (GB/T 700-2006), China Standards Press, Beijing, 2007 (in Chinese).

[21] Du, Y. & Li, G. Q. (2012). *A new temperature–time curve for fire-resistance analysis of structures*, Fire safety journal, vol. 54, p.113-120.

[22] Code for fire safety of steel structures in buildings (GB51249-2017), China planning Press, Beijing, 2017 (in Chinese).

[23] Yu, Y.; Si, X. ; Hu, C. & Zhang, J. (2019). *A review of recurrent neural networks: LSTM cells and network architectures*, Neural computation, vol. 31, no. 7, p. 1235-1270.

[24] Paszke, A.; Gross, S.; Massa, F.; Lerer, A.; Bradbury, J.; Chanan, G.; Killeen, T.; Lin, Z.; Gimelshein, N.; Antiga, L. & Desmaison, A. (2019). *Pytorch: An imperative style, high-performance deep learning library*, 33rd Conference on Neural Information Processing Systems (NeurIPS 2019), Vancouver, Canada, p. 32.

[25] Kingma, D.P. & Ba, J. (2014). *Adam: A method for stochastic optimization*. arXiv preprint arXiv:1412.6980.

EVALUATION OF THE BEHAVIOR OF COMPOSITE DOUBLE WEB-ANGLE CONNECTIONS AT AMBIENT TEMPERATURE AND IN A FIRE SITUATION

Renato S. Nicoletti
a, *

Alex S. C. Souza[b]

Saulo J. C. Almeida[c]

ABSTRACT

Steel-concrete composite connections are those in which the transfer of efforts between the structural elements are guaranteed, simultaneously, by components and elements in steel and concrete. In addition to the importance of connections, it is worth mentioning that the safety of structures in fire situations is becoming an increasingly recent concern worldwide. This paper aims to research, through numerical analysis, the behavior of composite double web-angle connections at ambient temperature and in a fire situation. Once the numerical models were adjusted, a parametric analysis was performed. From the results, it was verified that the composite double web-angle connections at ambient temperature were classified as semi-rigid. In addition, it was found that the fire caused a change in the failure mechanism of the connections. From the parametric analysis, it is noteworthy that the negative reinforcement rate equal to 0.75% resulted in the highest stiffness value at room temperature and in the greatest variation in rotational capacity, in a fire situation. Such values were up to 4.1% and 160% higher, respectively. Furthermore, the slab type, the degree of interaction of steel-concrete, the direction of the bending moment, and the resistance of steel and concrete exerted a significant influence on the connection behavior.

Keywords: steel-concrete composite structures; composite connections; fire situation; numerical analyses; design.

1. INTRODUCTION

Structures, in general, must be designed to resist all active actions during their useful life, simultaneously ensuring adequate levels of safety, performance, and durability with compatible construction and maintenance costs. In this context, the connections are essential to achieve these objectives, being responsible for promoting the union

---

a,* Universidade Federal de São Carlos, São Carlos/SP (renato_nicoletti@hotmail.com)**,** Corresponding author.

b Universidade Federal de São Carlos, São Carlos/SP (alex@ufscar.br).

c Universidade Estadual de Campinas, Campinas/SP (saulojca@unicamp.br).

between the parts of the structure or a part of it with an external element. In other words, connections are devices responsible for transferring efforts between the elements that make up the structure and/or between its supports. Thus, the correct design, fabrication, and assembly of the connections have an essential importance in the structural behavior, since, in addition to transferring the efforts, they ensure that the design hypotheses are valid.

In this context, steel and concrete composite connections are those in which the transfer of efforts between structural elements, as well as stiffness and resistance are guaranteed, simultaneously, by steel and concrete components and elements. Such connections can be used in beam-column and beam-beam connections. The main advantage provided by composite connections is the increase in strength and stiffness compared to the purely metallic connection.

In addition to the importance of connections per se, it is worth mentioning that the safety of structures in fire situations is becoming an increasingly recent concern worldwide. The analysis of the safety of structures in a fire situation has two main objectives: to protect the lives of building users and to minimize property losses. Fire safety is highly dependent on knowledge of fire dynamics, while the proper interpretation of scenarios enables the designer to develop systems that result in better risk management.

The fire dynamics, as well as the analysis of the behavior and safety of structures subjected to high temperatures, have been heavily studied, culminating in important results that confirm and complement the main normative codes and technical documents that are references on the subject in Brazil and the world.

Given this and the importance of the connections for the behavior of the structure as a whole, knowing their behavior when they are subjected to a fire situation is very important, as temperature variation causes significant changes in the distribution of resistance and stiffness of the connections and the structural elements linked to them, and may even change the failure mechanisms concerning the behavior of the connection at room temperature.

In short, even at room temperature, composite connections have complex behavior. However, especially in fire situations, the behavior of connections and their effects on the structure still needs to be better studied and understood. In this context, a widely used connection is the composite double web-angle connection, whose scheme is shown in Figure 1.
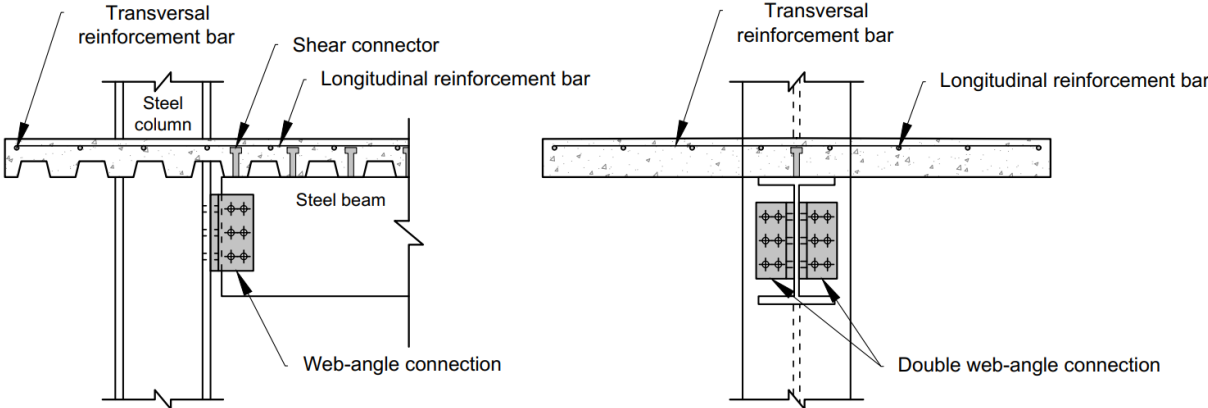
Figure 1: Composite double web-angle connections.

In composite double web-angle connections, it is the longitudinal steel reinforcement, the shear connectors, and the couple of forces in the angle that contribute to the strength and stiffness [1]. Figure 2 schematizes the transfer of efforts between the elements of the composite beam-column connection with a double web angle. In Figure 2, the stresses in blue are shear; compression stresses in red; and the tensile stresses in yellow.
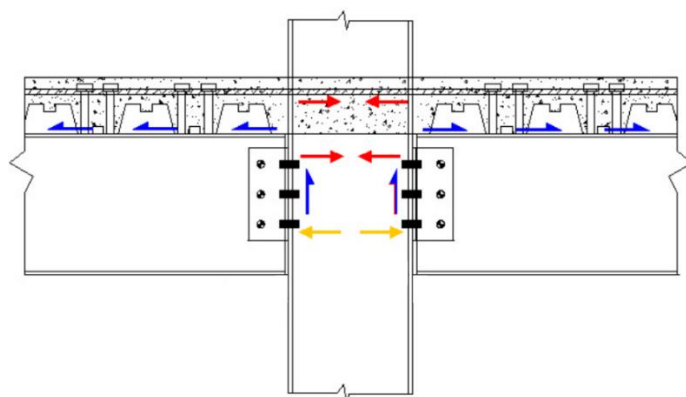
Figure 2: Internal efforts in a composite double web-angle connections. Source: Adapted from Pires (2003).

In this type of connection, they are considered double web-angle in the beam web, bolted to the support element, and can be welded or bolted to the beam to be supported. In this conception, the double web-angle is responsible for resisting all shear stresses and contributing to flexural strength along with the other components [1]. Furthermore, in the design of the connection, it is idealized that the plastic and elastic neutral lines of the composite connection are located in the double web-angle, so that the resulting effort in the pair of angles is only a bending moment, with tension above the neutral line, and compression below. If this situation does not occur, the region of the lower table becomes subject to high efforts, which may cause instabilities in the beam [2-3]. The design of this connection also results in high compressive forces in the reinforcement as well as high cracking in the concrete in the region of the connection. For this reason, Leon *et al.* [4] and SCI [5] recommend the use of reinforcing steel bars with a minimum diameter of 12.5 mm to avoid the occurrence of an effect called "tension stiffening", which is characterized by the occurrence of cracks that reduce the load on the reinforcement bars and consequently reduces their axial deformations, causing the reinforcing steel bars to yield.

The web angles, due to their great deformation capacity, do not reduce the rotation capacity of the composite connection, only accompanying the rotation imposed by the other components. In the steel-concrete composite beam-column connection with double web-angle, at room temperature, Pires [1] and Campelo [6] verified that the contribution of the web angles in the resistance of the composite connection to bending moment is not significant (less than 10% in the example studied). Tristão [7] found that, in connections with a column web stiffener, the application of compression force on the column reduced the initial stiffness by 11%, showing that the influence of the compression force on the initial stiffness was much greater for the connections without stiffener than with web stiffener. Bessa [8] observed that the increase in the secondary reinforcement rate of the composite beam (from 0.2% to 1%) proved to be efficient in restricting the opening of cracks in the slab in the region close to the connection. However, no significant variations were noted in the stiffness and strength of the connections.

In addition, no research was found dealing with steel-concrete composite beam-column connections with only the double web angle. All similar papers found also consider the presence of seat angles. In a fire situation, there is a lack of research for both configurations.

Given this, this paper aims to research, through numerical analysis, the behavior of steel-concrete composite beam-column connection with double web-angle at ambient temperature and in a fire situation. For that, a parametric analysis was carried out whose analyzed variables were: a combination of beam-column cross sections, the negative reinforcement rate of the composite connection, the steel-concrete interaction degree, the slab type, the orientation of the bending moment, steel strength, and concrete strength.

2. METHODOLOGY

The methodology section of this paper is divided into two sections. The first deals with the construction and validation of the numerical model of the composite double web-angle beam-columns connection. In turn, the second section details the parametric analysis performed.

2.1 Construction of the numerical model

For the analysis of the models in a fire situation, it is initially necessary to process thermal models, whose main input data were, in addition to the geometry of the model, the behavior over time of the specific heat, thermal conductivity, and density of the materials present in the model.

In addition, at this stage, it must also be informed which regions of the model are exposed to fire. To simulate these phenomena, the standard fire curve of ISO 834 [9] was used. To model the fire action, the recommendations of EN 1991-1-2 [10] were considered and, more specifically:

- Convection heat transfer coefficient equal to 25 W/m²K on exposed faces;
- Convection heat transfer coefficient equal to 9 W/m²K on unexposed faces;
- Emissivity factor equal to 0.70 to consider heat transfer by radiation on exposed faces;
- Zero emissivity factor on unexposed faces.

It is worth noting that the thermal properties of concrete, structural steel, and reinforcement steel were considered based on the recommendations of EN 1992-1-2 [11]. In this regard, it is worth noting that:

- EN 1994-1-2 [12] presents lower and upper limit values for thermal conductivity. In numerical modeling, average values between the two were adopted;
- The thermal elongation values proposed for concrete with calcareous aggregate were used;
- A moisture content of 3.0% of the weight of the concrete was considered for the consideration of the specific heat;
- The Stefan-Boltzmann constant was assumed to equal to $5.67 \cdot 10^{-8}$ W/m²·°C4 and the temperature corresponding to absolute zero was equal to -273 °C.

Then, thermostructural models were designed. In this step, in addition to geometry, the main input data were binding, loading, material properties (density, modulus of elasticity, constitutive model, and thermal elongation), and, finally, the thermal analysis results file. Thus, when processing the thermostructural model, the effects of temperature are considered simultaneously with the actions acting on the model.

It is worth mentioning that, for the analyzes at room temperature, an analysis similar to that of the thermostructural models was carried out, however, without the association with the thermal analysis results file.

In short, the thermal models consist of a single processing step in which the structure is heated based on the standard fire curve. The thermostructural models are submitted to two processing steps. The first, is when the external load is applied, and the second, is when the temperature effects are applied.

In the thermal models, the "Heat Transfer" type analysis was used, with a total time of 3,600, initial increment of 1 s, minimum and maximum increments of 0.0001 s and 60 s, respectively, and maximum temperature variation per increment of 500 °C.

In turn, in the thermostructural models, the external loading processing step was modeled with "Static, General" analysis, using an initial increment of 0.01, minimum and maximum increments respectively equal to 0.00001 and 0.1. Finally, the structure heating step was performed using "Mistletoe" analysis. The processing step size and increments were adopted equal to those of the thermal models, to maintain consistency with the temperature input. In both steps of the thermostructural models, the "Dissipated Energy" stabilization method was used with a coefficient equal to 0.002; effects of geometric nonlinearities were included. The Newton-Raphson resolution method was adopted and the processing error due to the loss of resistance of the structural element was the stopping criterion.

In all processes, initially, it is necessary to model the geometry of the parts that constitute the numerical model and define the type of finite element. In the thermal analyses, DCD20R diffusive heat transfer elements were used for the discretization of beams, columns, slabs and connection elements. These are prismatic, three-dimensional, with 20 nodes each and reduced integration. As for the steel reinforcement bars and connectors, the DC1D2 element was used, which is a heat transfer element with 2 nodes, I recommend it for linear objects. As for the

thermostructural and structural analyzes at room temperature, to form the mesh of the beams, columns, slabs and connecting elements, the solid element C3D8R was used, which has 8 nodes with 3 degrees of freedom per node (translations in the x, y and z), as this element supports plastic analysis with high deformations and displacements, in addition to being possible to insert reinforcement bars inside it. For longitudinal and transverse reinforcement, T3D2 truss elements were used, which have 2 nodes with 3 degrees of freedom per node (translations in the x, y and z directions), which is a great element to represent the behavior of bars, trusses and cables subjected to axial forces. Finally, for the stud bolt shear connectors, B31 beam elements were used, characterized by having 2 nodes with 6 degrees of freedom per node (translations in the x, y and z directions and rotations around such exist), due to the cost of calculation of such an element when compared to solids.

Steel elements could be discretized using shell element, requiring less processing time. However, the use of shell elements does not match the degrees of freedom properly. Thus, knowing that the best finite element to discretize the concrete is the hexahedral element and this element achieves better results for the steel member, the finite element C3D8R was chosen to discretize the steel and concrete components. Furthermore, in all models, clearances of 2 mm were considered in the holes of the connecting elements in relation to the diameter of the body of the bolt.

The steel cross sections, reinforcements and shear connectors were described by a constitutive stress-strain relationship with perfect elastoplastic behavior and Von Mises plasticity criterion. Specifically, the Earls model (1999a, 1999b) was used.

For concrete, the constitutive model of Concrete Damaged Plasticity (CDP) by Carreira and Chu [13-14] was adopted, as this model predicts with great precision the behavior of concrete and other brittle materials such as rock and mortar, in addition to considering the cracking effects.

The reinforcement and the slab were linked using the "embedded constraint" tool of Abaqus®. Thus, the degrees of freedom of the reinforcement nodes were restricted to translation. The connectors, in turn, had their base nodes coupled to the steel cross section using the "tie constraint" tool, which restricts all degrees of freedom between the elements. Finally, the interaction between the connectors and the concrete slab was also modeled using the "embedded constraint" command, to efficiently simulate the action of the connector against shear forces inside the concrete. As for the region of contact between the concrete slab and the upper tables in steel beam, tangential contact of the "Hard contact – Penalty" type was considered, which uses the classic Lagrange multiplier method to impose the restrictions and normal contact with a coefficient of friction equal to 0.4 between steel and concrete materials [15].

Figure 3 shows the application position and the typical boundary conditions of the models. In turn, Figure 4 presents the numerical model interactions.
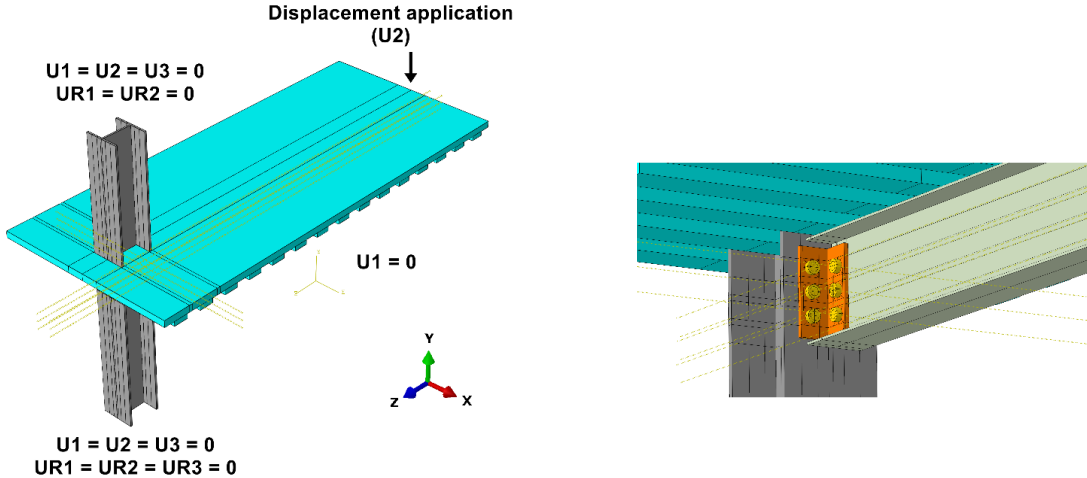
Figure 3: Boundary conditions typical of numerical models.
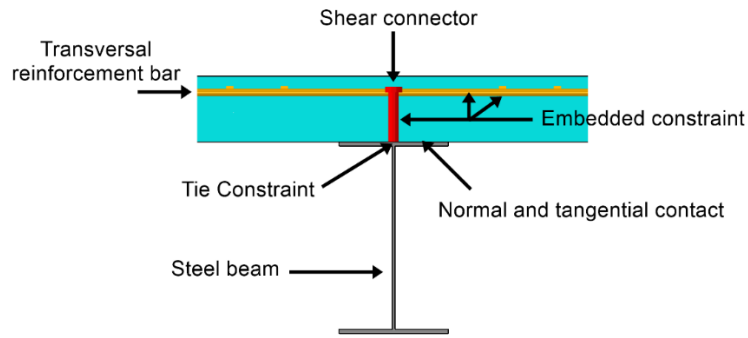
Figure 4: Numeric model interactions.

Furthermore, Figure 5 illustrates the regions of the model where the temperature variation was imposed.
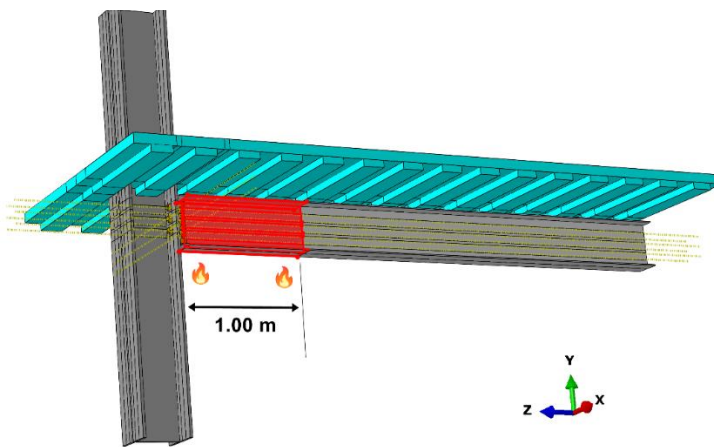
Figure 5: Faces exposed to fire in thermal numerical models.

For the construction of the numerical model steel-concrete composite beam-column connection with double web-angle, experimental tests from the literature with increasing complexity were modeled and verified.

Initially, the tests by Ostrander [16] and Figueiredo [17] of beam-column steel connections at room temperature were modeled. Next, the tests by Figueiredo [17] and Haremza *et al.* [18] of steel-concrete composite beam-column connections at room temperature. Finally, the experimental test by Haremza *et al.* [18] in steel-concrete composite beam-column connection. Table 1 presents the order of the tests reproduced and verified, as well as their characteristics.

Table 1: Experimental tests used to verify the behavior of the built numerical model.

Order	Author	Description	Situation
1º	Ostrander [16]	Steel beam-column connection	Room temperature
2º	Figueiredo [17]	Steel beam-column connection	Room temperature
3º	Figueiredo [17]	Steel-concrete composite beam-column connection	Room temperature
4º	Haremza *et al.* [18]	Steel-concrete composite beam-column connection	Room temperature
5º	Haremza *et al.* [18]	Steel-concrete composite beam-column connection	Fire situation

2.2 Parametric analysis

To investigate the influence of the position of the column on building floor and the influence of the level of loads, six combinations of beam-column cross sections were defined. For the composite beams, the VS 350 x 38 cross section was pre-dimensioned, which is coherent for spans of 8 m, which are usual in steel structures. In turn, for the columns, representative connections of the corner, lateral and central columns were sought. In addition, to verify the influence of the loading level, loads are consistent with buildings with 10 and 3 floors. Thus, considering a

532

distance between columns of 8 m, steel with the yield strength of 25 kN/cm², and a distributed load on the slabs of 10 kN/m², six sections of columns were designed, which are shown in Table 2.

Table 2: Pre-dimensioned steel column sections.

n_{floors}	Column position	Influence area [m²]	Cross-sectional area [cm²]	Profile
10	Corner	0,25	128	CS 350 x 144
10	Lateral	0,50	256	CS 450 x 280
10	Central	1,00	512	CS 600 x 546
3	Corner	0,25	38,4	CS 250 x 49
3	Lateral	0,50	76,8	CS 300 x 92
3	Central	1,00	153,6	CS 400 x 155

Table 3 presents the sets of beam-column profiles studied.

Table 3: Combinations of beam-column cross sections used in parametric analysis.

#	Beam	Column
C1	VS 350 x 38	CS 350 x 144
C2	VS 350 x 38	CS 450 x 280
C3	VS 350 x 38	CS 600 x 546
C4	VS 350 x 38	CS 250 x 49
C5	VS 350 x 38	CS 300 x 92
C6	VS 350 x 38	CS 400 x 155

In addition to the combination of beam-column cross sections, the parametric analysis variables were the negative reinforcement rate of the composite connection, the degree of steel-concrete interaction between the composite beam and the slab, the slab type, the orientation of the bending moment, steel strength and concrete strength. For that, 17 models were needed for each combination of cross sections. Table 4 illustrates the characteristics of these models, exposing the parameterized variables and their values.

Table 4: Models analyzed for each combination of profiles.

#	Negative reinforcement steel rate	Degree of interaction	Slab type	Bending moment orientation	Steel strength [MPa]	Compressive strength of concrete [MPa]
1	0.50%	100.00%	Steel deck	Positive	$f_y = 250$ and $f_u = 400$	30
2	0.75%	100.00%	Steel deck	Positive	$f_y = 250$ and $f_u = 400$	30
3	1.00%	100.00%	Steel deck	Positive	$f_y = 250$ and $f_u = 400$	30
4	1.25%	100.00%	Steel deck	Positive	$f_y = 250$ and $f_u = 400$	30
5	0.75%	50.00%	Steel deck	Positive	$f_y = 250$ and $f_u = 400$	30
6	0.75%	75.00%	Steel deck	Positive	$f_y = 250$ and $f_u = 400$	30
7	0.75%	100.00%	Steel deck	Positive	$f_y = 250$ and $f_u = 400$	30
8	0.75%	100.00%	Solid	Positive	$f_y = 250$ and $f_u = 400$	30
9	0.75%	100.00%	Steel deck	Positive	$f_y = 250$ and $f_u = 400$	30
10	0.75%	100.00%	Steel deck	Positive	$f_y = 250$ and $f_u = 400$	30
11	0.75%	100.00%	Steel deck	Negative	$f_y = 250$ and $f_u = 400$	30
12	0.75%	100.00%	Steel deck	Positive	$f_y = 250$ and $f_u = 400$	30
13	0.75%	100.00%	Steel deck	Positive	$f_y = 345$ and $f_u = 450$	30
14	0.75%	100.00%	Steel deck	Positive	$f_y = 600$ and $f_u = 800$	30
15	0.75%	100.00%	Steel deck	Positive	$f_y = 250$ and $f_u = 400$	30
16	0.75%	100.00%	Steel deck	Positive	$f_y = 250$ and $f_u = 400$	50
17	0.75%	100.00%	Steel deck	Positive	$f_y = 250$ and $f_u = 400$	70
			Default variable			

In Table 4, f_y is the yield strength of the steel and f_u is the ultimate tensile strength of the steel.

3. RESULTS AND DISCUSSION

Figure 6 presents the initial stiffness of the 102 models analyzed at room temperature. In Figure 6, it is observed that only 15 of the 102 connection models were classified as rigid connections according to the criteria of NBR 8800

(ABNT, 2008). Of these 15, 13 are from set 6, and the other 2 are from set 2. Both are characterized by having columns with CS cross sections with heights equal to or greater than 450 mm. Most of the models in set 2 presented a failure mechanism with the local buckling of the beam web in the connection region and the local buckling of the beam flange in the middle of the span. In turn, most of the models in set 6 failed due to reinforcement yielding any excessive damage to the slab.
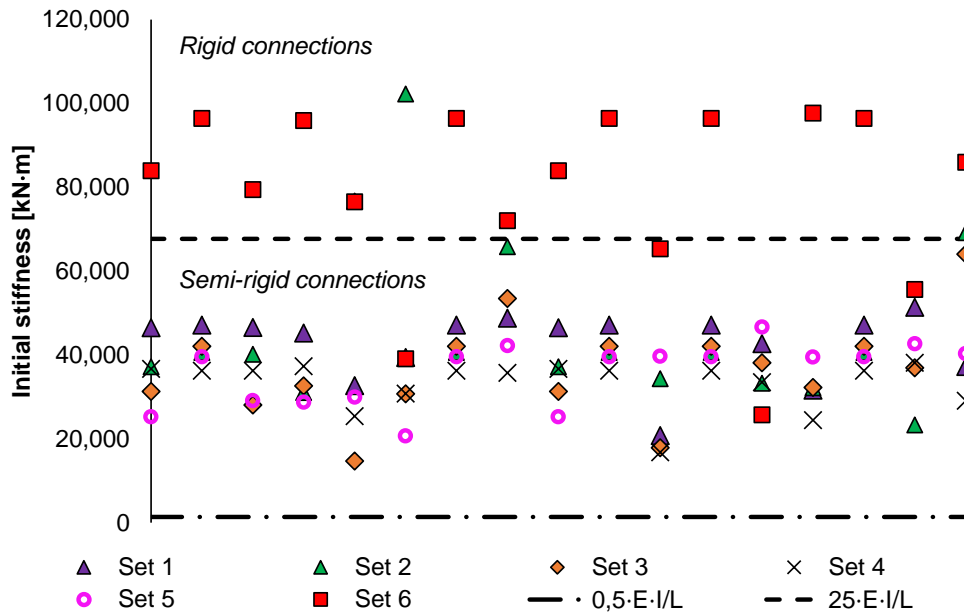
Figure 6: Distribution of initial stiffness of all numerical models of connections at room temperature.

Figure 7 presents the distribution of the resistant moment of the numerical models of connections.
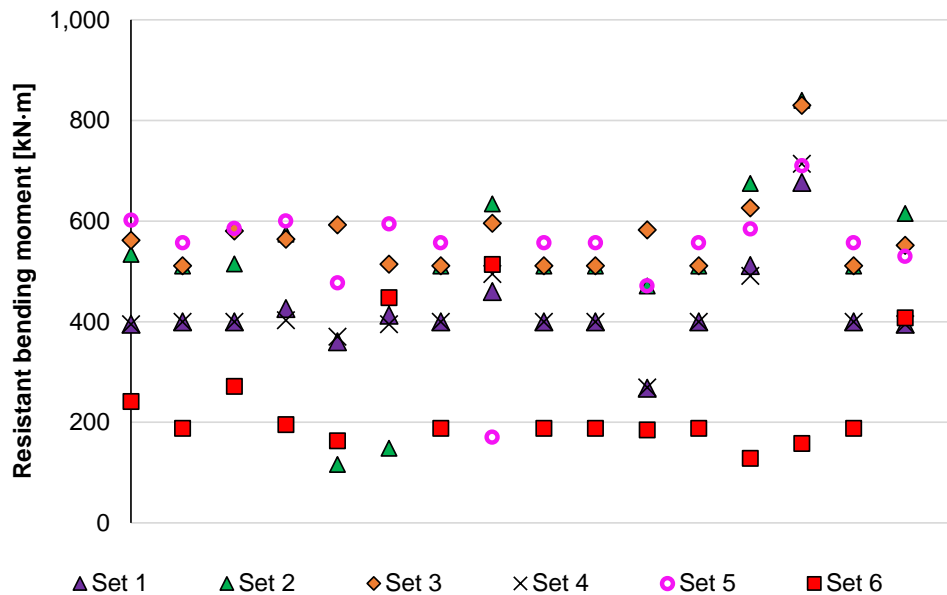
Figure 7: Resistant bending moment distribution of all numerical models of connections at room temperature.

From Figure 7, of the analyzed sets, the ones that presented the highest average of resistant bending moment were sets 3 and 5, in that order. These sets are lateral and/or central columns, which receive efforts from two directions. In the analysis of isolated connections, it was also noted that 31 of the 34 models analyzed (91%) presented lateral buckling of the beam web in mid-span as a failure mechanism. In the other assemblies, the main failure mechanisms

were, in that order, local buckling of the flange in the middle of the span, local buckling of the web in the connection region, and reinforcement yielding excessive damage to the slab in the connection region.

As for the stiffness analysis, it was noted that the position and cross-section of the column exert great influence. The set of models that presented the highest maximum rotation and, consequently, the lowest stiffness, was the C4 set. This set is characterized by having a column with a slender section and by being a corner column. Thus, the bending moment that the beam induces in the column occurs on only one side of the column, which favors the rotation of the beam since the column also rotates. Figure 8 shows the influence of parametric variables on the resistance moment and connection stiffness of the models from set 1, at room temperature.
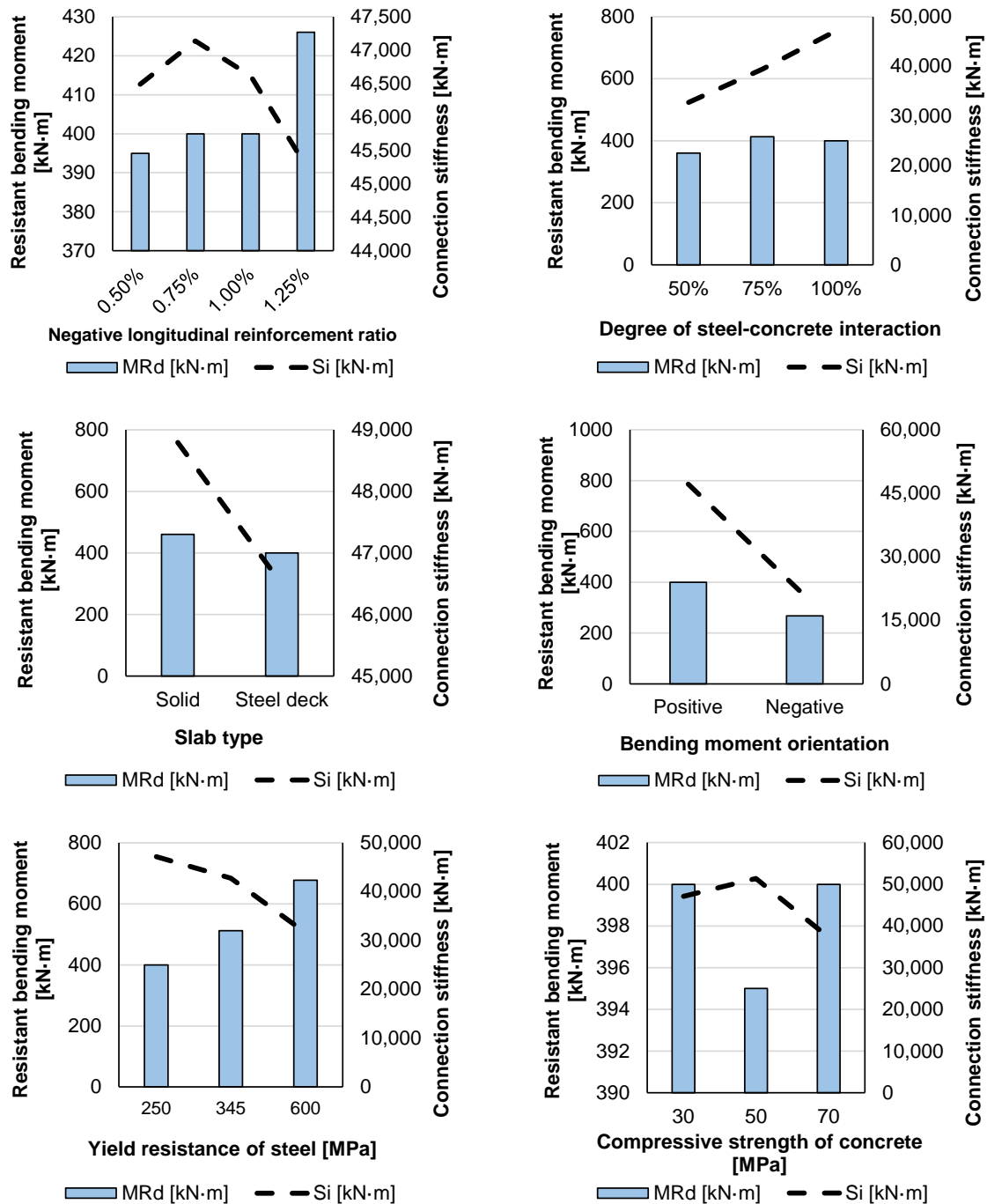
Figure 8: Influence of parametric variables on the resistant moment and connection stiffness of numerical models of connections from set 1, at room temperature.

In the analyzes of set 1, 14 of the 17 models presented local buckling of the flange in mid-span as a failure mechanism. The models that disagreed were the one with a negative bending moment, which failed due to excessive damage to the slab in the middle of the span; and models with a concrete compressive strength greater than 30 MPa, which fail due to local web buckling in the connection region, possibly due to a change in the position of the neutral axis. In addition, from Figure 8, it is observed that:

- The negative steel reinforcement ratio was directly related to the resistant bending moment of the composite connection. However, the negative steel reinforcement rate equal to 0.75% resulted in the highest stiffness value, however, the greatest variation was 4.1%, concerning the model with a negative reinforcement rate equal to 1.25%. In addition, it is worth mentioning that the model that presented the highest rotation capacity until failure was the one with the highest negative reinforcement rate, with a rotation value of 49.24 mrad. The models with a negative reinforcement rate equal to 0.50%, 0.75%, and 1.00% presented a maximum rotation capacity of, respectively, 40.95 mrad, 39.80 mrad, and 40.88 mrad. Therefore, the average variation concerning the model with a 1.25% negative steel rate was approximately 21%;
- The connection stiffness was directly influenced by the degree of steel-concrete interaction. The model with total interaction (degree of steel-concrete interaction of 100%) presented a stiffness value of 44.1% and 19.5% higher than the models with interaction degrees of 50% and 75%, respectively. Regarding the resistant moment, the model with a degree of interaction of 75% was the one that presented the highest moment. Its value was 3.3% higher than that of the model with total interaction and 14.7% higher than that of the model with a degree of interaction of 50%;
- The model with solid concrete slab showed higher stiffness and bending moment values than the model with steel deck slab (variation of 4.9% and 15.0%, respectively). Furthermore, it is worth mentioning that the rotation capacity of the model with solid slab was 25.0 mrad, while that of the model with steel deck slab was 39.8 mrad – a difference of 59.2%;
- The direction of the bending moment in the connection exerted a significant influence on both the stiffness and the resistant bending moment. The model whose connection was subject to a positive moment presented better behavior, resulting in values of the resistant moment and stiffness higher by 126.7% and 49.3% in relation to the model with a negative moment in the connection. Such results can be explained by the fact that concrete has a low tensile strength, mainly. This caused the model to fail earlier, due to excessive damage to the slab in the connection region. It is also worth mentioning that the maximum rotation capacity of the model subject to a negative bending moment was 53.91 mrad, a value 35.4% higher than that of the model subject to a positive bending moment, whose maximum rotation capacity was 39.80 mrad;
- As for the parameterization of steel resistance, it was observed that the greater the resistance, the greater the resistant bending moment, but the lower the stiffness. The model with $f_y = 600$ MPa presented moment resistance with values 69.3% and 33.2% higher than the models with yield strengths of 250 MPa and 345 MPa. Furthermore, in relation to the same models, the stiffness was 33.0% and 26.0% lower. Finally, it is worth noting that the maximum rotation capacity increases with the increase in flow resistance from 250 MPa to 345 MPa (direct variation of 27.6%). However, there was practically no difference between the models with $f_y = 345$ MPa and $f_y = 600$ MPa (indirect variation less than 3%);
- Finally, there was no clear behavior of the influence of the strength of concrete on the behavior of the connection. The model with C30 concrete presented local buckling of the flange in mid-span as a failure mechanism. In addition, this model, compared to those that used C50 and C70 concrete, was the one that presented the highest rotation capacity and bending moment. In turn, the model with C50 concrete had the highest stiffness and the lowest moment resistance. Both this last model and the one with C70 concrete failed due to local buckling of the beam web in the connection region. A possible justification for the change in the failure mechanism is the increase in the height of the neutral line, which became closer to the position of the concrete slab in the cross-section.

As for numerical analyzes in fire situations, in all models, the fire resistance time was approximately 26 min, with variations of less than two minutes between models. During this time, due to the expansion of the materials, the main phenomenon observed is the development of compressive stresses in the lower region of the beam and tensile stresses in the upper region, causing a rotation in the opposite direction to that previously caused by the loading of service (considered as 30% of the load that caused the failure in the structural model. Table 5 shows the rotation variation of the connection of the models of set 1, in a fire situation.

Table 5: Variation of connection rotation of models from set 1, in fire situation.

Model	θ_i [mrad]	θ_f [mrad]	$\Delta\theta$ [mrad]
1	-2.52	-2.83	0.31
2	-2.52	-1.65	0.86
3	-2.51	-2.84	0.33
4	-2.51	-2.84	0.33
5	-2.52	-3.22	0.70
6	-3.26	-3.80	0.54
7	-2.52	-1.65	0.86
8	-2.51	-2.84	0.33
9	-2.52	-1.65	0.86
10	-2.52	-1.65	0.86
11	-2.51	-2.84	0.33
12	-2.52	-1.65	0.86
13	-2.53	-2.07	0.46
14	-2.53	-2.66	0.13
15	-2.52	-1.65	0.86
16	-2.19	-1.64	0.55
17	-1.97	-2.42	0.45

From the parametric analysis of the models of set 1 in a fire situation, it was verified that:

- The model with a negative steel reinforcement rate of 0.75% resulted in the greatest variation in rotational capacity (and consequently, better redistribution of efforts). The percentage difference was approximately 160% in relation to the other models;
- The model with solid slab presents a variation in rotation capacity around 160% lower than the model with steel deck slab;
- The greater the strength of the steel and the strength of the concrete, the smaller the variations in rotation capacities. For the models with higher resistances, the failure also happened more prematurely. In such models, the resistance capacity at room temperature is higher. However, at high temperatures, the reduction of the beam's bearing capacity due to the degradation of the materials will also be greater. The model that used steel with a yield strength of 600 MPa showed a rotation variation 84.6% lower than the model that used steel with a yield strength of 84.6%. In turn, the model with class C70 concrete showed a rotation capacity 47.9% lower than that of the model with class C30 concrete;
- From the analysis of the degree of steel-concrete interaction, the simulated models did not allow for obtaining any clear behavior.

Figure 9 illustrates the variation of connection deflection as a function of temperature for model 2 of connection set 1. The temperature was measured at the end of the beam, at the geometric center of the cross section.
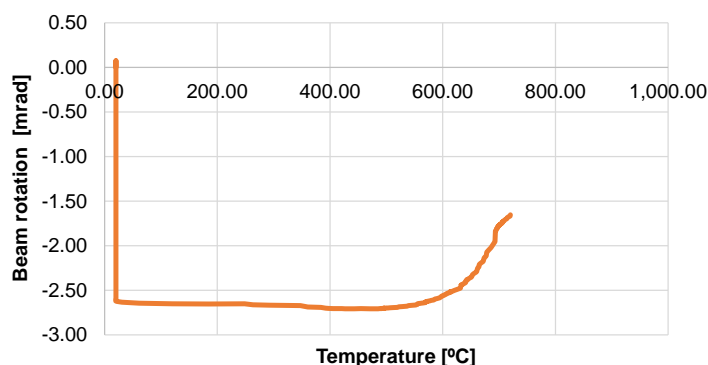
Figure 9: Deflection behavior as a function of temperature of model 2 of set 1 of connections.

Figure 10 presents the axial displacement of the beam for different loading situations, corroborating and illustrating the phenomenon described above.

Composite connection without loading

Composite connection with failure loading

Composite connection with service load (equal to 30% of failure load)

Composite connection with service load after failure by fire
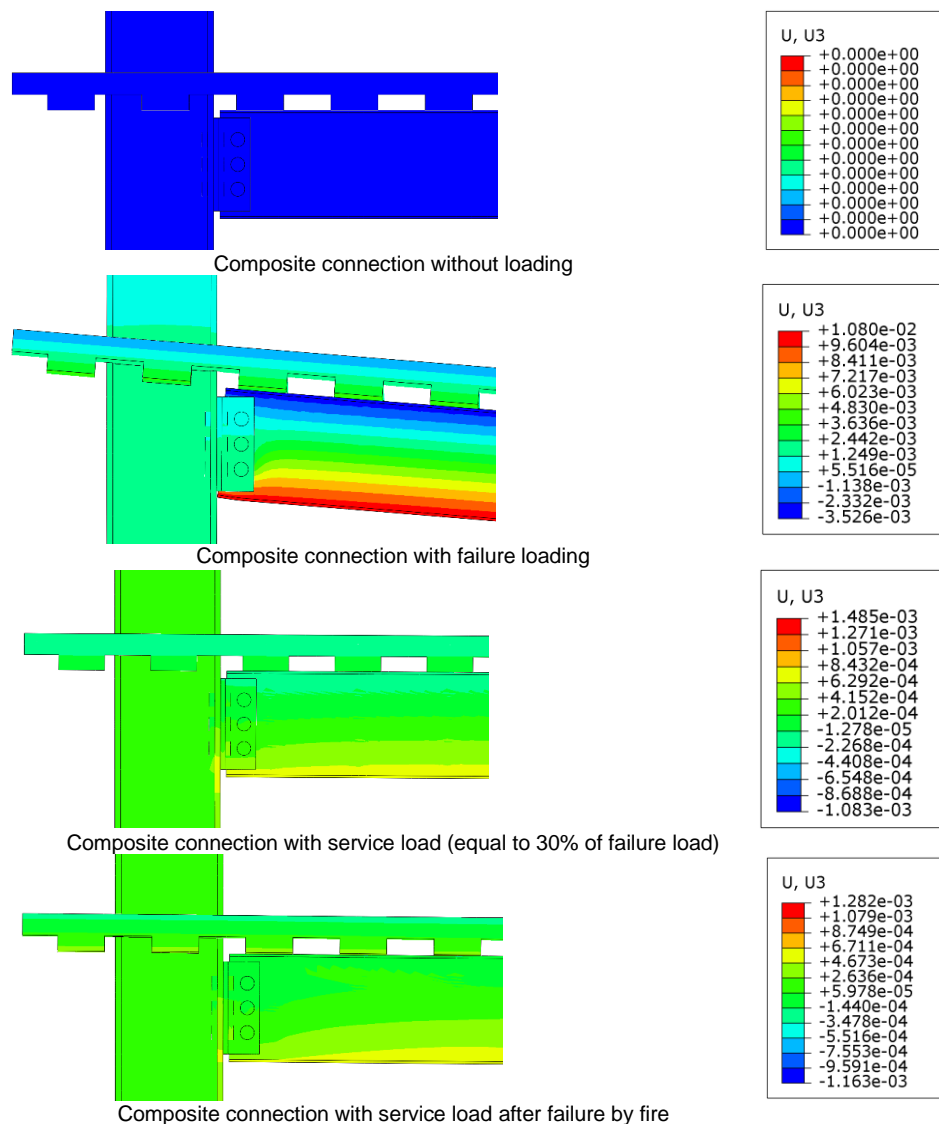
Figure 10: Axial displacement of the connection beam for various loading situations.

In addition, Figure 11 shows the connection elements with axial tensile stresses before the start of the fire and after its occurrence. From Figure 11, a change in the direction of stresses can be observed. Before the fire, the tensile stresses were mostly located in the beam, with greater magnitudes in the middle of the span. However, after the fire, tensile stress values occurred in the concrete slab, especially in the connection region. This phenomenon explains the variation in connection rotation as well as the change in failure mechanisms.

(a)   Before the fire
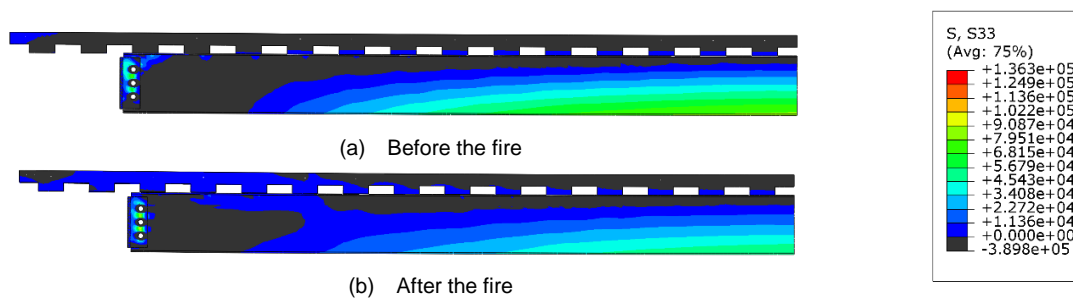
(b)   After the fire

Figure 11: Axial tensile stresses in the connection (a) before the fire and (b) after the fire. Units in kN/m².

Due to the expansion of materials and the change in the resistant capacity of materials as a function of temperature, the mechanism of failure of connections also changed. Set 1, at room temperature, failed predominantly due to local buckling of the beam flange mid-span. However, in a fire situation, all models had the processing interrupted due to the failure of the bolts that held the double web-angle in the beam web. In some cases, in addition to the failure of the bolts, there was also the tearing of the holes in the beam.

In particular, the bolts' failure can be explained by the fact that they were previously stressed by a prestress equal to 70% of their strength. Thus, with the reduction of resistance due to temperature, the bolts closest to the fire constitute a critical point in the efficiency of the composite connection.

4. CONCLUSIONS

Based on the moment-rotation curve of the numerical models and the criteria of NBR 8800 [1], the composite double web-angle connections at ambient temperature were classified as semi-rigid. Through parametric analysis of model set 1 at room temperature, it was found that:

- The negative steel reinforcement ratio was directly related to the resistant bending moment of the composite connection. However, the negative reinforcement rate equal to 0.75% resulted in the highest stiffness value;
- The stiffness of the connection was directly influenced by the degree of steel-concrete interaction;
- The model with solid slab presented higher values of stiffness and bending moment in relation to the model with steel deck slab;
- The direction of the bending moment in the connection exerted a significant influence on both the stiffness and the resisting moment. The model whose connection was subject to a positive moment performed better;
- As for the parameterization of steel resistance, it was observed that the greater the resistance, the greater the resistant bending moment, but the lower the stiffness;
- Finally, there was no clear behavior of the influence of the strength of concrete on the behavior of the connection. Including, the variation of the concrete resistance had an impact on the change of the connection failure mechanism.

At room temperature, most of the models in set 1 presented local buckling of the beam flange in mid-span as a failure mechanism. In turn, in a fire situation, it is worth mentioning that the models of set 1 presented as prevailing failure mechanisms were the failure of the bolts located in the beam's web and/or the tear of the hole in this region.

In a fire situation, all analyzed models failed due to the rupture of the bolts that held the double web-angle in the beam web. In some cases, in addition to the failure of the bolts, there was also the tearing of the holes in the beam. This can be explained by the fact that the bolts, before the fire, already had a pretension of 70% of their resistant capacity. With the reduction of its resistance due to the increase in temperature, the bolts closest to the fire constituted a critical point composite connection efficiency. Moreover, due to the expansion of the materials, the main phenomenon observed is the development of compressive stresses on the lower edge of the beam and tensile stresses on the upper edge, causing a rotation in the opposite direction to that previously caused by the service load (considered as 30% of the load that caused the structural model to fail.

Furthermore, from the analysis in a fire situation, it was noticed that the model with a negative steel reinforcement rate of 0.75% resulted in the greatest variation in rotational capacity concerning steel rates of 0.5%, 1.0%, and 1.25%. In addition, the use of a solid slab also resulted in a rotation capacity variation of around 160% less than that of the model with a steel deck slab. Furthermore, it is worth noting that the greater the strength of the steel and the strength of the concrete, the smaller the variations in rotation capacities.

Finally, in the context of structural analysis, knowing the behavior of connections subjected to fire is very important, since temperature variation leads to changes in the distribution of strength and stiffness of connections and structural elements attached to them, and may even change failure mechanisms concerning connection at room temperature.

REFERENCES

[1]   Pires, V. H. S. (2003) *Automação do cálculo de vigas mistas semi-contínuas incluindo ligações mistas*. 198 f. Dissertação (Mestrado em Engenharia de Estruturas) – Universidade Federal de Minas Gerais, Belo Horizonte/MG.

[2]   Queiroz, G., Mata, L. A. C. (2001). *Análise do comportamento de ligações mistas aço-concreto em pórticos deslocáveis sujeitos a carregamentos de vento e de gravidade*. IV Seminário Internacional, I CICOM, O Uso de Estruturas Metálicas na Construção Civil, São Paulo, SP, Brasil.

[3]   Chen, W. F., Lui, E. M. (1991). *Stability Design of Steel Frames*. CRC Press, USA.

[4]   Leon, R. T., Hoffman, J. J., Teager, T. (1996). *Partially Restrained Composite Connections*. AISC Design Guide Nº.8. Chicago, USA: American Institute of Steel Construction.

[5]   SCI-213. The Steel Construction Institute (1998). *Joints in Steel Construction, Composite Connections*. The Steel Construction Institute, SCI & BSCA, Ascot.

[6]   Campelo, P. C. (2018). *Estudo numérico de ligações mistas de aço e concreto em vigas semicontínuas*. 124 f. Dissertação (Mestrado em Engenharia de Estruturas) – Universidade Federal de Ouro Preto, Ouro Preto/MG.

[7]   Tristão, G. A. (2006) *Análise teórica e experimental de ligações viga mista-pilar de extremidade com cantoneiras de assento e alma*. 282 f. Tese (Doutorado em Engenharia de Estruturas) – Universidade de São Paulo, São Carlos/SP.

[8]   Bessa, W. O. (2009). *Análise experimental e numérica de ligações viga mista-pilar com cantoneiras de alma e assento - pavimento tipo e ligações isoladas*. 278 f. Tese (Doutorado em Engenharia de Estruturas) – Universidade de São Paulo, São Carlos/SP.

[9]   International Organization for Standardization (ISO) (1999). *ISO 834-1: Fire-resistance tests — Elements of building construction — Part 1: General requirements*. Genebra.

[10] European Committee for Standardization (CEN) (2002). *EN 1991–1–2: Actions on structures - Part 1-2: General actions - Actions on structures exposed to fire*. Brussels.

[11] European Committee for Standardization (CEN) (2004). *EN 1992–1–2: Design of concrete structures - Part 1-2: General rules - Structural fire design*. Brussels.

[12] European Committee for Standardization (CEN) (2004). *EN 1994–1–2: Design of composite steel and concrete structures - Part 1-2: General rules - Structural fire design*. Brussels.

[13] Carreira, D. J.; Chu, K. (1985). *Stress-strain relationship for plain concrete in compression*. Journal Proceedings. p. 797-804.

[14] Carreira, D. J.; Chu, K. (1986) *Stress-strain relationship for reinforced concrete in tension*. Journal Proceedings. 1986. p. 21-28.

[15] Pathirana, S. W.; UY, B.; Mirza, O.; Wijesiri. (2016). *Flexural behaviour of composite steel–concrete beams utilising blind bolt shear connectors*. Engineering Structures, v. 114, p. 181-194.

[16] Ostrander, J. R. (1970). *An experimental investigation of end plate connections*. Tese de Doutorado. University of Saskatchewan.

[17] Figueiredo, L. M. B. (2004). *Ligações mistas viga-pilar - análise teórica e experimental*. 215 f. Tese (Doutorado em Engenharia de Estruturas) – Universidade de São Paulo, São Carlos/SP.

[18] Haremza, C.; Santiago, A.; Silva, L. S. (2013). *Experimental behaviour of heated composite steel–concrete joints subject to variable bending moments and axial forces*. Engineering Structures, v. 51, p. 150–165.

[19] Associação Brasileira de Normas Técnicas (ABNT) (2008). *NBR 8800: Projeto de Estruturas de Aço e de Estruturas Mistas de Aço e Concreto de Edifícios*. Brazil.

STATE OF ART STUDY: ULTRASOUND TESTING ON STRUCTURAL CONCRETE BLOCKS SUBMITTED TO HIGH TEMPERATURES

Rafaela O. Amaral a*; Everton F. C. Souza b; Armando L. Moreno Jr. c; Gisleiva C. S. Ferreirad

ABSTRACT

Currently in Brazil, there are no performance and fire safety standards for structural masonry. Internationally, there are EUROCODE 6 Part1.2:2005, ACI/TMS 216.1-14:2014, and AS 3700:2011. Adopting the ultrasound test for characterization of concrete blocks is an excellent alternative, as it improves both the representativeness of results in relation to the batch, and also "in loco" measurements to determine their residual resistance. However, there is a shortage of studies on the subject, which requires adaptations of concrete standards (ABNT NBR8802:2019, ASTM C597:2016, BS EN12504 Part4:2021, RILEM NDT1:1972, ABNT NBR 15630:2008, BS 1881 Part203:1986) for concrete blocks, reducing the accuracy of the results. Present literature has a lack of information to define a methodology for ultrasound tests on concrete blocks. Therefore, this study intends to propose a first version of test procedures, considering the main factors that interfere both in the blocks and in the ultrasound tests. This can enable the first step towards a future standard and an experimental basis for studies on the subject, which are being developed by the MATS Research Group (Sustainable Materials and Technologies), linked to the Graduate Program in Civil Engineering at UNICAMP.

Keywords: Structural concrete block; Nondestructive test; Ultrasonic tests; Fire; Standardization.

ᵃ * University of Campinas (rafaela.amaral@engenharia.ufjf.br)**.** 224 Saturnino de Brito St. Cidade Universitária Zeferino Vaz. Campinas, São Paulo, Brazil. Corresponding author.

ᵇˑ University of Campinas (e233480@dac.unicamp.br).

ᶜ University of Campinas (armoreno@unicamp.br).

ᵈ University of Campinas (gisleiva@unicamp.br).

1. INTRODUCTION

To ensure the safety of people in a burning building, the mechanical strength of the concrete has to be enough to prevent the structure from collapsing, in addition to preventing the passage of gases and guaranteeing thermal insulation. Resistance and compartmentalization projects must meet the Required Fire Resistance Time (RFRT), established by the fire department, according to Technical Instruction No. 08/2015 [1] and NBR 14432 - Annex A [2]. The RFRT corresponds to the shortest time between the time limit for rupture to occur (mechanical resistance), the passage of gases (tightness) and the face not exposed to fire to reach between 140 °C to 180 °C (thermal insulation). The main Brazilian standards (NBR 5628 and NBR 10636 [3] [4]) and international standards (ASTM E119 and ISO 834 [5] [6]) establish the test conditions for the RFRT determination.

However, some construction techniques, for example, structural masonry, still require studies to establish the specific RFFT, in addition to other parameters related to mechanical properties. At the international level, the requirements on the design of structures in fire situations, built in structural masonry, are specified in EUROCODE 6 [7], where the RFRT is determined from the type of block, component materials and types of coating. The American standard ACI:TMS 216.1 [8] specifies minimum values for the effective thickness of the walls, and thus guarantees safety in fire situations, taking into account the type of block (configuration of the voids) and the finish used.

When considering the scarcity of national standards to obtain parameters related to structural concrete masonry building elements, under fire conditions, it shows a gap to be studied. However, tests and analyzes still need to be developed, considering the complexity and variety of factors that can interfere with the residual properties of this type of structural element. To reduce such difficulties, non-destructive tests can be indicated, with emphasis on the ultrasound technique, already consolidated for other cementitious materials such as concrete and mortar. Through Ultrasonic Pulse Velocity (UPV) it is possible to obtain the mechanical properties (resistance to compression, dynamic modulus of elasticity), considering national and international standards (ABNT NBR 8802:2019, ASTM C597:2016, BS EN 12504-Part 4 :2021, RILEM NDT 1:1972, ABNT NBR 15630:2008 [9] [10] [11] [12] [13]). As these parameters are essential to define the residual strength of structural concrete masonry, after being subjected to high temperatures, the hypothesis of using ultrasound for this purpose is valid. However, there are no specific standards or procedures (technical bulletins) for this purpose, the closest being a recent standard for monitoring and inspection of solid masonry panels (ABNT NBR 16805:2020) [14]. Therefore, studies on test methodologies are needed to characterize the structural concrete blocks and, additionally, consider the specificities of those exposed to high temperatures.

Some studies available in the literature indicate that ultrasound tests on concrete blocks need their own methodology, considering the geometry (holes), molding process (homogeneity), and moisture content. Regarding the test method, the frequency and type of transducers and ultrasonic pulse transmission method should be considered (direct, indirect or semi-direct) [15] [16] [17] [18] [19]. Nevertheless, only Santos [9] carried out ultrasound tests on concrete blocks subjected to high temperatures. In this scenario, there is a lack that needs to be studied and thus obtain necessary parameters to validate the use of this non-destructive method in estimating the residual mechanical properties of concrete blocks.

Therefore, the main objective of this work is to gather information available in the literature on ultrasound testing in structural masonry blocks, which can help in proposed methodologies for the same test and material, however, after exposure to high temperatures.

2. ULTRASOUND TESTS ON CONCRETE BLOCKS

Santos [15], Sombra and Haach [16] and Gondim [17] studied the mechanical behavior of structural masonry with ultrasound at room temperature. Rodrigues et al [18] and [19] evaluated with ultrasound the mechanical behavior of non-structural concrete blocks at room temperature and at elevated temperatures, respectively.

Santos [15] carried out a study to correlate the characteristic compressive strength (f_{bk}) with the Ultrasonic Pulse Velocity (UPV) in hollow structural concrete blocks, with nominal strengths ranging from 3 to 8 MPa and in 3 types of blocks (150x200x400 mm; 150x200x540 mm and 150x200x300 mm), considering 6 samples for each type. The

tests were carried out at the factory and on construction elements, following the procedures adapted from NBR 8802 [9], using TICO and PUNDIT equipment and flat 54 KHz transducers. Ultrasound tests were performed by indirect transmission, with a distance between transducers of 200 mm (Figure 1), considering the longest side (400 mm; 540 mm; 300 mm). The mean correlation factor (ratio between axial compressive strength and UPV: K1=fbk/v) obtained for the PUNDIT device was 2.90 and for the TICO device it was 3.82. According to the results obtained for K1, the author noted that the type of device used influences the ultrasound tests performed on concrete blocks, requiring the adoption of a correlation factor for each type of device. He points out that this fact was also observed by Gomes [20] in the tests carried out on the reinforced concrete material. Santos [15] also observed that the correlation factors (K1=fbk/v) provide finer and closer adjustments to the compressive strength when the blocks are isolated and obtained from the same production, batch, class, type and origin. The author did not statistically evaluate the UPV results, but he provides the UPV obtained for each type of block in his dissertation. Table 1 shows some of these results. Using the Origin 2018 software, through the Tukey test (ANOVA) for a confidence interval equal to 5%, it is possible to verify that there are no significant differences in the UPV values between the 3 readings (Figure 1), which were taken in different positions at the along the height of the longitudinal face of the block.

Table 1: UPV results (Km/s) of tests performed in the Laboratory via TICO and PUNDIT equipment [15].

	f_{bk} (MPa)	Measurement	Samples						Mean	Significant Measurement differences
			1	2	3	4	5	6		
Pundit	8.0	1	2.98	3.21	3.00	3.73	2.92	2.98	3.01 ± 0.33	1-2: nonexistent
		2	3.05	3.04	3.03	3.01	2.73	2.74		1-3: nonexistent
		3	2.92	2.91	2.91	2.48	2.74	3.87		2-3: nonexistent
	6.0	1	2.53	2.38	2.08	2.48	1.81	1.94	2.25 ± 0.36	1-2: nonexistent
		2	2.75	2.30	2.51	2.38	1.83	1.50		1-3 nonexistent
		3	2.76	2.48	2.46	1.81	2.46	2.02		2-3: nonexistent
	4.0	1	3.97	3.80	2.61	2.36	3.50	2.50	3.13 ± 0.64	1-2: nonexistent
		2	3.85	3.57	2.54	2.47	3.73	2.70		1-3: nonexistent
		3	3.80	3.60	2.41	3.81	2.59	2.48		2-3: nonexistent
	10.0	1	2.97	2.75	2.42	2.41	2.76	2.33	2.71 ± 0.24	1-2: nonexistent
		2	2.78	2.78	2.81	3.00	2.99	2.86		1-3: nonexistent
		3	3.00	2.79	2.82	2.30	2.42	2.57		2-3: nonexistent
TICO	4.5	1	1.64	1.91	1.93	2.03	1.69	1.70	1.79 ± 0.14	1-2: nonexistent
		2	1.61	1.90	1.73	1.80	1.69	1.69		1-3: nonexistent
		3	1.86	2.12	1.70	1.70	1.80	1.93		2-3 nonexistent
	6.0	1	1.99	2.46	1.97	1.97	1.70	1.72	1.92 ± 0.20	1-2: nonexistent
		2	1.80	2.34	1.81	1.78	1.76	1.81		1-3: nonexistent
		3	1.93	1.99	1.96	1.81	1.84	1.86		2-3: nonexistent
	4.0	1	1.90	2.10	2.03	2.19	2.34	1.83	1.97 ± 0.14	1-2 nonexistent
		2	1.88	1.78	1.94	2.14	1.92	1.91		1-3: nonexistent
		3	1.86	1.85	1.97	1.98	1.93	1.98		2-3: nonexistent
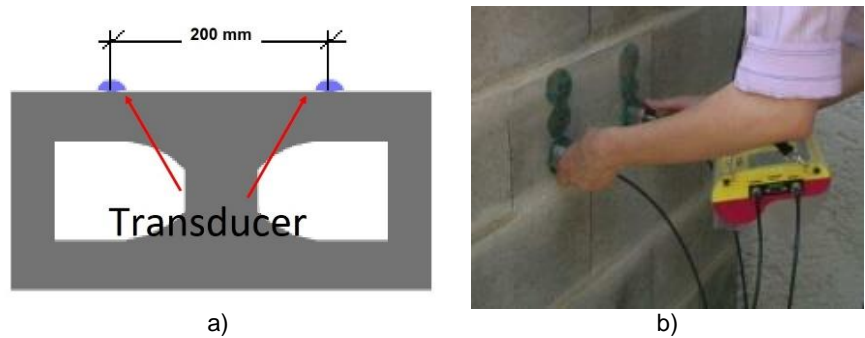
Figure 1: (a) Used position of the transducers on the concrete block (b) Test being performed on the blocks directly on the wall [15].

Sombra and Haach [16] estimated the elastic properties (Ed; Gd and μ) of concrete blocks (f_{bk} 14 MPa), with ultrasound tests, adapting the procedures of the NBR 8802 (ABNT, 2019) and ASTM C597 (2016) standards, and also obtained correlations between UPV and uniaxial compressive strength. The ultrasound tests were performed with 54 kHz (longitudinal wave) and 250 kHz (transverse wave) transducers, using direct transmission, as shown in Figure 2. Table 2 shows the results of the mechanical properties (f_{bk}; E; Ed; Gd, μ and UPV), in addition to statistical analysis, using the Tukey test (ANOVA), with the aid of the Origin software (2018). Statistically, no significant variations were noted for UPV values. However, both 2 types of blocks showed UPV variations in the height direction, suggesting a non-homogeneity associated with the molding process. The estimated value for Poisson's coefficient (using the average velocities of primary and secondary waves), both for full-block and half-block samples, was close to 0.20, a value normally adopted for concrete of different classes. Even though the nominal resistance of the entire block and half-block were the same, the static modulus of elasticity (E) differed from each other, (15.35±1.13 GPa and 21.26±3.73 GPa, respectively). Ed was also different for the two types of samples, which confirm this behavior. Comparing the static and Ed, there is a big difference between the values for each type of sample. To calculate the Ed through the UPV, it is necessary to know the value of the Poisson coefficient. The Poisson coefficient was calculated using the average velocities of longitudinal and transverse waves, in this case this parameter is subject to two sources of error. In addition, E is influenced by the geometry, the type of capping or its absence, the form of instrumentation for the acquisition of deformations (without standardization), among other factors. For concrete, Mehta and Monteiro (apud [16]) predict an increase of up to 40% for the Ed in relation to the static one, depending on the resistance class.
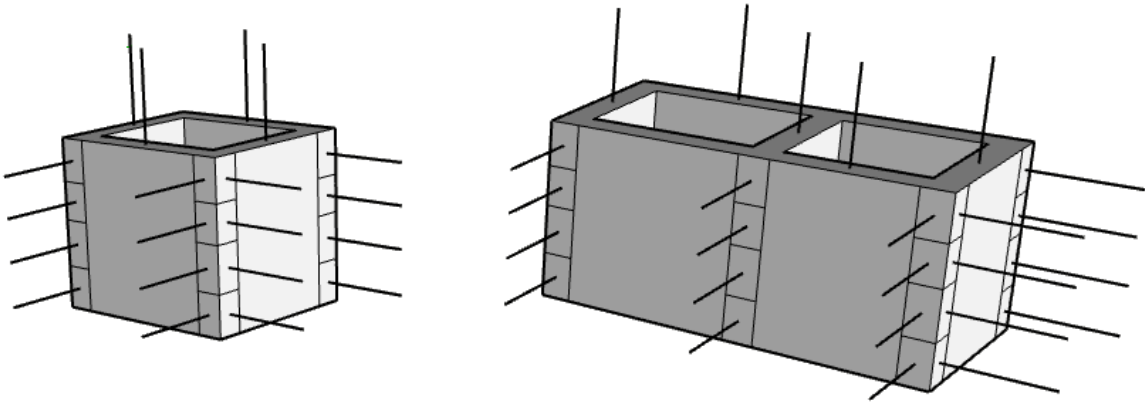
Figure 2: Position of the transducers in the ultrasound test for the whole block and half-block, respectively, evaluated by [16].

Table 2: Results obtained for characteristic compressive strength (f_bk), static modulus of elasticity (E) (according to ACI 530-05), dynamic modulus of elasticity (Ed), dynamic shear modulus (Gd), Poisson coefficient (µ) and UPV for longitudinal and transverse wave in transverse (T), longitudinal (L) and axial (A) directions [16].

f_{bk} (MPa)	E (MPa)	E_d (GPa)	Gd (GPa)	µ	UPV – longitudinal wave (m/s)			UPV – transverse wave (m/s)		
					T	L	A	T	L	A
Whole block										
14.22	15.35 ± 1.13	38.24	15.53	0.23	4,430.3 ±34.3	4,306.9 ±45.3	4,356.6 ±44.9	2,606,1 ±16.7	2,552.0 ±29.8	2,601.1 ±43.6
Significant differences between measures. Homogeneous groups - P-value <0.05					a	b	a	c	c	c
Half-block										
15.39	21.26 ± 3.73	47.05	18.91	0.24	4,830.0 ±33.2	4,806.5 ±24.5	4,708.2 ±133.7	2,792.3 ±27.9	2,793.6 ±22.2	2,783.3 ±15.3
Significant differences between measures. Homogeneous groups - P-value <0.05					d	d	e	f	f	f

In order to evaluate the acoustoelastic effect, Gondim [17] carried out ultrasound tests, following the recommendations of NBR 8802 (ABNT, 2019), in blocks with 10 MPa of nominal resistance, 3 filled with grout and 3 unfilled. The author used shear wave (S) transducers with a frequency of 250 KHz, which also emit longitudinal waves. The points analyzed, by direct arrangement of the transducers only in the transverse direction of the block, are indicated in Figure 3. Through the characterization tests, the average axial compression strength of the hollow blocks (unfilled) was 17.45±2.21 MPa and of the filled blocks 24.42±4.04 Mpa. The average E of the hollow blocks was 15.17±1.97 GPa and of the for the filled blocks was 26.11±7.12 GPa. Table 3 and 4 show the obtained results for blocks without and with grout, respectively. The author noted that when positioning the transducers on the block in the grouted region, it is possible for the wave to deviate from the grout, passing only through the concrete region. Therefore, even in filled elements, it is preferable that the transducers are positioned only in the septa regions of the blocks (not in the voids region).
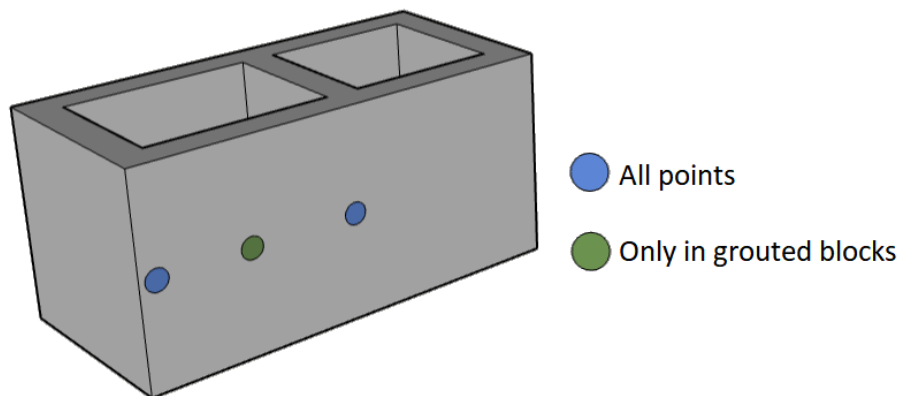
Figure 3: Points measured with ultrasound [7].

Table 3: UPV and wavelength in unfilled blocks [17].

Block	UPV transverse wave (m/s)		UPV longitudinal wave (m/s)		Wavelength λ (mm)	
	Ext. septum	Int. septum	Ext. septum	Int. septum	Ext. septum	Int. septum
1	4,215.6	4,055.6	2,578.7	2,542.2	16.9	16.2
2	4,448.7	4,387.3	2,674.8	2,662.1	17.8	17.5
3	4,423.4	4,477.1	2,670.7	2,714.8	17.7	17.9
Mean	4,334.6±164.9		2,640.6±65.7		17.33±0.7	

Table 4: UPV and wavelength in filled blocks [17].

Block	UPV transverse wave (m/s)			UPV longitudinal wave (m/s)		
	Ext. septum	Int. septum	Grout	Ext. septum	Int. septum	Grout
1	2,710.5	2,719.5	2,574.9	4,492.9	4,485.7	4,086.4
2	2,652.5	2,714.8	2,552.4	4,402.5	4,490.1	4,392.8
3	2,675.8	2,787.2	2,568.3	4,455.8	4,662.0	3,834.6
Mean	2,710.1±45.9		2,565.2±11.6	4,498.2±87.2		4,104.6±279.5

Rodrigues et al [18] evaluated the mechanical properties of concrete blocks (140X190X390 mm) using ultrasound tests, with an average characteristic strength (f_{bk}) of 3.5 MPa after 28 days of curing. The UPV was obtained with Steinkamp ultrasound equipment (BP7 model) and 45 KHz exponential transducers. Measurements by direct transmission were taken at 7, 14, 21 and 28 days after manufacture, considering the three directions (axial, longitudinal and transverse). In each direction, 6 measurement points were considered, as shown in Figure 4. Table 5 shows the results obtained. Statistical analysis showed that, for the longitudinal and axial directions, the UPV presents a statistically significant difference, while for the transverse and longitudinal directions, the UPV does not present a statistically significant difference. The authors point out that for the length and width directions, there is a wall mold confinement effect, which does not happen with the height direction.

Table 3: UPV, in Km/s, measured after 7, 14, 21 and 28 days of concreting [18].

	7 days	14 days	21 days	28 days
Transverse	2.06	2.09	2.15	2.08
Longitudinal	2.14	2.10	2.19	2.15
Axial	2.02	2.12	2.09	2.05
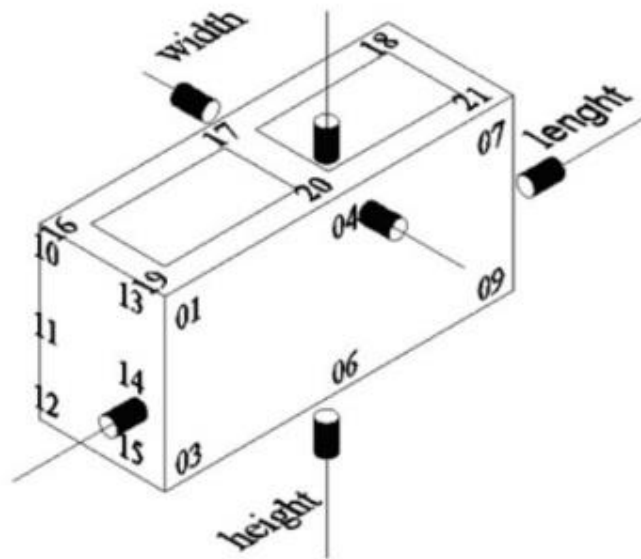
Figure 4: Direction and points measured with ultrasound [18].

Santos [19] used ultrasound, following the recommendations of NBR 8802, to identify changes in the mechanical strength of non-structural hollow concrete blocks, with 5.4 MPa of characteristic strength, after being heated to 500 °C, with a heating rate of 1°C/min. The author produced 14 blocks, 7 of which were subjected to high temperatures and 7 used to control, reference and enable the methodology used. The mix, by mass, was 0.935 Kg of Portland cement (type V ARI), 1.495 Kg of sand, 3.738 Kg of stone dust, 2.243 Kg of stone gravel (type 0), 1.639 Kg of water and 4.2075 g of additive. He used the USLab ultrasound machine and transducers with metallic encapsulation, exponential and flat, with a frequency of 45 KHz. For the readings, the transducers were positioned in relation to the height, width and length of the blocks. Table 6 shows the average UPV obtained using a flat and exponential transducer for room temperature and 500°C. For the author, the flat transducer is more suitable than the exponential one, because the it is more stable during the test and has greater contact with the surface of the faces of the blocks.

Transducer type	Temperature	Transverse	Longitudinal	Axial
Plan	Room	3.46 ± 0.13	3.47 ± 0.17	3.18 ± 0.14
	500°C	2.43 ± 0.26	2.44 ± 0.18	2.31 ± 0.23
Exponential	Room	3.64 ± 0.16	4.18 ± 0.57	3.97 ± 0.65
	500°C	2.66 ± 0.26	3.43 ± 0.33	2.94 ± 0.25

Table 6: Mean UPV values (Km/s) in blocks [19].

3. NORMATIVE RECOMMENDATIONS FOR RESIDUAL STRENGTH OF CONCRETE BLOCKS USING ULTRASOUND

Structural masonry will have its fire resistance depending on how each of the materials that constitute it behaves at high temperatures [21]. This type of resistance is related to its mechanical strength, tightness and thermal insulation. The main national standards (NBR 5628 and NBR 10636 [3] [4]) and international standards (ASTM E119 and ISO 834 [5] [6]) that establish the test conditions for determining this parameter, guide that the sample of the element to be tested is placed in an oven with the programmed temperature variation, observing the conditions of these three properties.

Specifically regarding to the evaluation of the mechanical properties of structural masonry components, blocks and laying mortars, under high temperatures, it is necessary to emphasize the need for standardization of the methodology used. It is necessary to evaluate the national structural masonry components according to only one standard, so that the results can be compared to other similar national and international studies. Standardizing sample size, rate of rise in temperature over time, time for heating samples to that maximum temperature, and rate of cooling is necessary. As for concrete blocks, there is no international or national methodology for assessing residual mechanical strength. What can be done, in the same way as Medeiros et al. [22], is an adaptation of the cited international standard of RILEM-200 HTC [23]. To obtain the residual mechanical strength of the concrete, this standard establishes that the cylindrical concrete specimens are heated in an oven at a rate of 0.5 °C/min, 1 °C/min, 2 °C/min and 4 °C C/min for specimens with 150 mm, 100 mm, 80 mm and 60 mm in diameter, respectively, until reaching the temperature of interest, remaining at the maximum temperature for 60±5 minutes and then cooling at the same rate. The concrete blocks evaluated by Santos (2017) were heated at a rate of 1°C/min, one of the rates recommended by RILEM-200 HTC [23].

Medeiros et al. [12] evaluated the effect of temperature on the mechanical properties of hollow structural concrete blocks with gneiss aggregate, 14 cm wide, 19 cm high and 39 cm long. The adopted test method was adapted from the RILEM TC 200-HTC [23] by the group of researchers in structural masonry in fire situation at the University of Campinas and Federal University of São Carlos. The blocks were heated at a rate of 1°C/min until reaching maximum temperatures of 100, 200, 300, 400, 500, 600, 700 and 800°C. Each maximum temperature of interest was maintained for 60 minutes before slow cooling and evaluation of the residual mechanical strength of the blocks. Figures 5 and 6, below, present the results of residual compressive strength and modulus of deformation, as a function of the maximum temperature of interest evaluated by Medeiros et al. [22]. The researchers report a loss of mechanical strength with increasing temperature and that, in the case of residual compressive strength, only after 400 °C does this loss become significant. For the authors, the aggregate and cementitious materials chosen for the block can help to reduce these negative effects; emphasizing that the geometry of the blocks and the porosity of the concrete used in the execution of the units can be taken as parameters of relative influence on the evaluated residual mechanical properties.
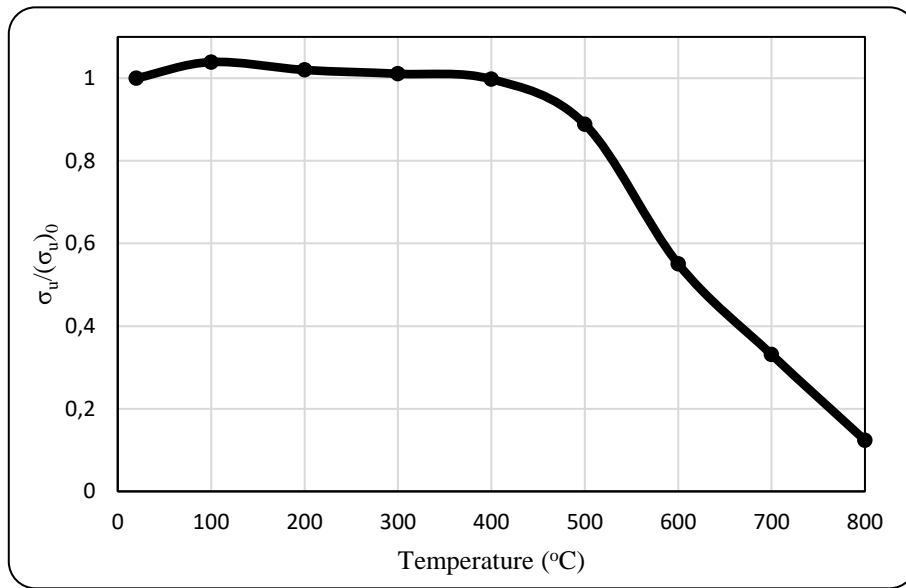
Figure 3: Residual compressive strength X temperature [22].
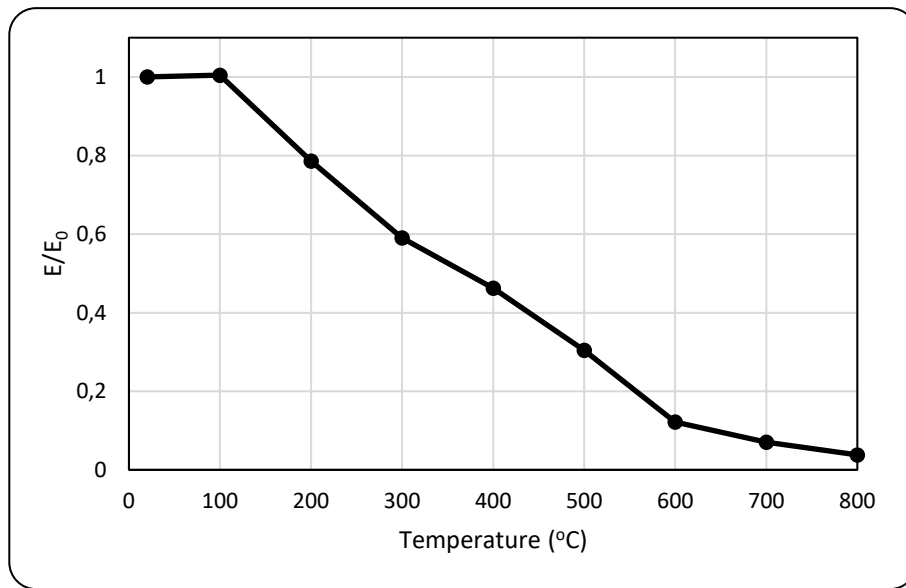
Figure 4: Residual elastic modulus X temperature [22]

To evaluate the post-fire mechanical behavior, a good alternative is to use the ultrasonic wave propagation test, as it is a non-destructive test (NDT) that is easy to perform. However, as already mentioned, studies to evaluate the residual resistance with ultrasound in structural concrete blocks are rare and there is no specific standard for this purpose. Also, there is no norm or standardized ultrasound test methodology for the characterization of concrete blocks, but there are normatives about ultrasound in concrete. The main standards are: NBR 8802:2019, ASTM C597:2016, BS EN 12504-Part 4:2021, RILEM NDT 1:1972 and NBR 16805:202016805. Table 7 compares some guidelines established by these standards [10] [14] [15] [16]. The frequency of transducers ranging from 20 to 100 KHz satisfies all of them at the same time. RILEM NDT 1:1972 explains that transducers with higher frequencies, around 200 kHz, can be used especially in path lengths shorter than 500 mm to obtain a clearer pulse onset, as long as the provided device is designed for this use. In accordance with BS EN 12504-Part 4:2021 high frequency pulses (200 KHz) have a definite start but as they pass through concrete they become attenuated more quickly than lower frequency pulses (10 KHz). Therefore, it is preferable to use high frequency transducers (60 kHz to 200 kHz) for short path lengths (up to 50 mm) and low frequency transducers (10 kHz to 40 kHz) for long paths (up to a

maximum of 15 m). Transducers with a frequency of 40 kHz to 60 kHz are useful for most applications. These standards require the surface to be air-dried, clean and flat. As per BS EN 12504 Part 4: 2021, when the concrete surface is very rough and uneven, the surface area must be smoothed and leveled by grinding, or by using an epoxy resin. Regarding the number of samples, BS EN 12504-Part 4:2021 establishes that it is equal to 3, in addition, for each sample there must be at least three measurements of the UPV, spaced by the length of the specimen. Another important issue is that the wave propagation time through the concrete material must be within ± 1% of the mean value of these three measurements, otherwise the sample must be rejected or the tests redo. Other standards specify UPV measurement accuracy in ± 1% (NBR 8802:2019) and 0.5% (ASTM C597:2016). For all standards, it is necessary to calibrate the ultrasound device using reference bars and use a couplant material to position the transducers in the solid to be tested. The minimum distance between the transducers placed in the concrete must be 100 mm for aggregates up to 20 mm and 150 mm for aggregates between 20 and 40 mm, according to BS EN 12504-Part 4:2021, and 100 mm for aggregates up to 30 mm and 150 mm for aggregates up to 45 mm, in accordance with RILEM NDT 1:1972. In Brazil, the most common approach has been to adapt NBR 8802 to concrete blocks, a solution adopted by the aforementioned authors [15] [16] [17] [18] [19].

Table 7: Main standards for ultrasound testing on concrete

Procedure	NBR 8802/2019	ASTM C597/2016	BS EN 12504 Part 4: 2021	RILEM NDT/1972
Generator-receiver circuit	Ultrasonic low-frequency electrical pulse apparatus, with high stability and reading resolution of at least 0.1 µs	3 pulses per second	-	-
Transducer	20 to 150 kHz	20 to 100 kHz	20 to 150 KHz	20 to 200 KHz
Time meter circuit	-	Measurement resolution of at least 0.1 µs	-	-
Preparation of test specimens	Air dried, clean and flat	Air dried, clean and flat	Air dried, clean and flat	Flat
Number of samples	-	-	3	-
Calibration	Calibrate the instrument using the reference bar or equivalent device.	Reset time; apply coupling agent to the transducer faces and press the faces together; use reference bar.	It should be able to measure transit times on the calibration bar with a limit deviation of ± 0.1 µs and an accuracy of 2%.	External reliable electronic calibration, or by using stable standard prisms with known pulse travel time.
Coupling	Apply a thin layer of couplant. For shear wave transducers, the couplant material cannot be water-based	Viscous material (such as oil, petroleum jelly, water-soluble petroleum jelly, moldable rubber or grease)	Typical couplants are petroleum jelly, grease, mild soap, and kaolin/glycerol paste	-
Distance between transducers	Accuracy ± 1%	Accuracy 0,5%	Accuracy ± 1%	Accuracy ± 1%
Velocity measurements	Accuracy ± 1%	Accuracy = 0,5%	Accuracy ± 1%	-
Wave type	Longitudinal and transverse	Longitudinal	Longitudinal and transverse	Longitudinal
Length of paths	-	50mm to 15m	-	150mm for direct and 400mm for indirect.

4. CONCLUSIONS

To write this work, references were sought that evaluated the mechanical behavior of structural concrete blocks with post-heating ultrasound. No studies were found that fully covered all the factors of this search, so the references used refer to parts of this theme, in different ways. Selected works include Santos [15], Sombra and Haach [16] and Gondim [17] who studied the mechanical behavior of structural masonry with ultrasound at room temperature, but without analysis at high temperatures. The works by Rodrigues et al [18] and Santos [19] were also part of this research. They evaluated, respectively, the mechanical behavior of non-structural concrete blocks at room temperature and at elevated temperatures using ultrasound, although none of them analyzed structural blocks. The research carried out by Rodrigues et al. [18] did not evaluate specimens at elevated temperatures, as well. In addition to these, it was mentioned the work by Medeiros et al. [22], which evaluated the effect of temperature on the mechanical properties of hollow structural concrete blocks through destructive tests, differing by not approaching ultrasound analysis (NDT).

For ultrasound tests on concrete blocks, practically all references followed the recommendations of NBR 8802, except by Sombra and Haach [16], who also followed ASTM C597 instructions. Only Santos [15] positioned the transducers indirectly, while the other authors performed the tests with a direct arrangement. Virtually all used longitudinal waves. The frequencies used by these authors are in accordance with the recommendations of standards NBR 8802:2019 [9], ASTM C597:2016 [10], BS EN 12504-Part 4:2021 [11] and RILEM NDT 1:1972 [12]. Gondim [17] used a much higher frequency than the other authors. This variance was due to the differetnt objective of this study, where the author used the ultrasound test to determine the acoustoelastic effect in blocks.

Santos [15] was the only reference that evaluated 6 samples for each type of block. The other studies evaluated 3 samples for each type of block, demonstrating that this amount is sufficient to obtain reliable results. The tested blocks have thickness varying along the height and, also, there is a suggestion of non-homogeneity in the units along the height due to the compression process in the manufacture of the blocks, that is why the authors Santos [15], Sombra and Haach [16] and Rodrigues et al [17] measured the UPV in the longitudinal and transverse directions considering different layers in the height of the block. Statistically, the results of UPV with indirect transmission from Santos [15] do not show significant differences for the 3 measurements along the height of the longitudinal face of the block. However, for the test with direct transmission, Sombra and Haach [16] noticed that both the entire block and the half-block had UPV variation along the height. It is noteworthy that Gondim [17] considered only one layer at half the height (this layer was probably chosen to minimize and compensate for differences in readings that could occur in different layers along the height).

Only Sombra and Haach [16] and Rodrigues et al [18] evaluated the UPV in the three directions (transverse, longitudinal and axial). Through Sombra and Haach [16] results for the whole block, there are significant differences only between the results for the longitudinal and transverse directions. Whereas Rodrigues et al [18] research identified differences for the results between the longitudinal and axial directions. Rodrigues et al [18] point out that there is a confinement effect of the wall mold for the length and width directions, which does not happen with the height direction.

Still, Santos [15] noted that the type of ultrasound device influences the results, so he recommends that the correlation between the UPV and the axial resistance of concrete blocks be established for each type of device. For Gondin [17] it is preferable that the transducers are positioned only in the regions of the septa of the blocks (not in the region of the voids). Santos [19] recommends that the flat transducer is more suitable than the exponential one, because the flat transducer is more stable during the test and has greater contact with the surface of the faces of the blocks.

As for Santos [19] results, it is noted a reduction in the UPV as the heating temperature increased, which can be explained by the progressive deterioration of the cementitious matrix and also the concrete aggregates of the blocks. These physical-chemical changes of the materials result in density reduction of the concrete, also reducing the UPV.

It is noted the need for a standardization of the ultrasound test method in concrete blocks to favor the analysis of the results obtained by different authors and to guarantee the preparation and use of correlation tables of the UPV and static mechanical properties.

REFERENCES

[1] Military Police of São Paulo State, Fire Department. (2015). *Technical instruction no. 08/2015: Fire resistance of building elements*. São Paulo: Secretary of State for Public Security Affairs.12 p.

[2] Brazilian Association of Technical Standards. (2001). *NBR 14432: Fire resistance requirements of building construction elements - Procedure*. Rio de Janeiro. 14 p.

[3] Brazilian Association of Technical Standards. (2002). *NBR 5628:2022: Structural building components - Fire resistance test*. ABNT: Rio de Janeiro. 65 p.

[4] Brazilian Association of Technical Standards. (2022). *NBR 10636: Non-structural building components — Fire resistance test Part 1: Walls and subdivision partitions*. ABNT: Rio de Janeiro. 46 p.

[5] American Society for Testing and Materials. (2020). *E119-20: Standard Test Methods for Fire Tests of Building Construction and Materials*. 36 p.

[6] International Organization for Standardization. (1999). *ISO 834: Fire-resistance tests: elements of building construction -part 1.1: general requirements for fire resistance testing*. Geneva, 25 p. (Revision of first edition ISO 834:1975). 14 p.

[7] European Committee for Standardization. (2005). *Eurocode 6: EN 2005-1.2: design of masonry structures: part 1-2: general rules: structural fire design*. Brussels. 123 p.

[8] American Concrete Institute. (2014). *ACI/TMS 216.1: code requirements for determining fire resistance of concrete and masonry construction assemblies*. Michigan. 28 p.

[9] Brazilian Association of Technical Standards. (2019) *NBR 8802: Hardened concrete – determination of ultrasonic wave propagation velocity*. ABNT: Rio de Janeiro. 11 p.

[10] American Society for Testing and Materials. (2016). *ASTM: C597-16: Standard Test Method for Pulse Velocity Through Concrete*. West Conshohocken. 4 p.

[11] European Standards. (2021). *BS EN 12504. Testing concrete in structures. Part 4 – Testing concrete in structures Determination of ultrasonic pulse velocity*. BSI, London. 19 p.

[12] The International Union of Laboratories and Experts in Construction Materials, Systems and Structures (1972). *Rilem NDT 1 Testing of concrete by the ultrasonic pulse method*. P. 73-82.

[13] Brazilian Association of Technical Standards. (2009). *NBR 15630 Mortar for laying and covering walls and ceilings - Determination of the dynamic modulus of elasticity through ultrasonic wave propagation*. ABNT: Rio de Janeiro. 4 p.

[14] Brazilian Association of Technical Standards. (2020). *NBR 16805: Non-destructive testing — Ultrasound — Characterization of panels by ultrasonic wave propagation velocity*. ABNT: Rio de Janeiro. 7 p.

[15] Santos, C. E. O. (2011). *Analysis of structural concrete blocks using the ultrasound technique*. Masters dissertation. Graduate Program in Civil Construction at the Federal University of Minas Gerais. Belo Horizonte, MG. 85 p.

[16] Sombra, T. N. & Haach V. G. (2022). *Application of Acoustic Tests for the Mechanical Characterization of Hollow Masonry Units*. Journal of Materials in Civil Engineering, vol. 34, n. 6, p. 04022079, 2022.

[17] Gondim, R. M. L. (2022) *Investigation of the acoustoelastic effect in masonry elements of concrete blocks*. Doctoral thesis. Department of Structural Engineering at the School of Engineering of São Carlos (USP), São Carlos, São Paulo. 185 p.

[18] Rodrigues, M. S.; Ferreira, G. C. S.; Shiroma, L.; & Beraldo, A. L. (2013). *Nonconventional concrete hollow blocks evaluation by destructive and non-destructive testing*. Revista IBRACON de Estruturas e Materiais, 6, p. 392-398.

[19] Santos, V. C. (2017). *Evaluation of hollow concrete blocks after exposure to high temperature using ultrasound tests*. Completion of course work, University of Campinas. 49 p.

[20] Gomes, A. M. (2009). *Technical inspection report on reinforced concrete parts*. Belo Horizonte.

[21] Leite, H. A. L.; Moreno Júnior, A. L.; & Torres, D. L. (2016*). Design of masonry walls in situations of fire: a contribution for a future Brazilian standard*. Ambiente Construído, 16, p. 89-107.

[22] Medeiros, W. A.; Parsekian, G. A.; & Moreno Jr., A. L. *The effect of high temperatures on the mechanical performance of concrete blocks made with gneiss aggregates*. Brick and Block Masonry - From Historical to

Sustainable Masonry. Proceedings of the 17th International Brick/Block Masonry Conference (17thIB2MaC 2020), July 5-8, 2020, Kraków, Poland.

[23] The International Union of Laboratories and Experts in Construction Materials. (2007). *RILEM Technical Committee. Recommendation of RILEM TC 200-HTC: mechanical concrete properties at high temperatures— modelling and applications. Part 2: Stress–strain relation*. Materials and Structures, vol 40, p. 855-864.

Fire Safety Regulations, Standardization and Construction Trends

RECENT ADVANCES IN BRAZILIAN PASSIVE FIRE PROTECTION STANDARDIZATION
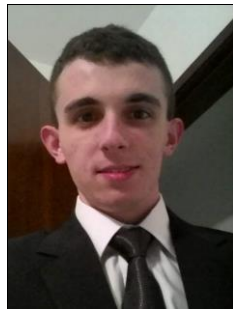
**Marcos V. M.
Sylverio** [a, *]

Antonio F. Berto [b]

ABSTRACT

Fire protection is crucial for saving lives and preserving properties and requires multiple systems working together. Passive fire protection is one of the main aspects of fire protection and is associated to architectural and constructive features of a building, including its components, and elements. Testing and specifications are necessary to ensure the efficiency of passive fire protection and are strongly associated to Standards worldwide. However, the body of Brazilian Standards related to passive fire protection was narrow and lacked several Standards which were existent worldwide. This started to change in the last decade with the review and publication of several Standards compatible with international documents and Standards. This paper presents an overview of the Brazilian Standards that were issued recently, aiming to publicize the work that has been done, and discusses the benefits brought to the fire safety and the next steps for the passive fire protection standardization in Brazil along with the importance of incorporating these Standards into the official Fire Departments' Regulations.

Keywords: Standardization; Fire Safety; Fire tests, Passive fire protection.

1. INTRODUCTION

Saving lives and preserving property are important goals for fire protection, which are better accomplished through several fire protection systems working together. Each system must be designed, tested, and constructed according to requirements of specific standards. However, several fire protection existing systems in Brazilian buildings are malfunctioning or completely inoperable [1–4], which is a result of one or more of the following problems: poor designs, inadequate installation and maintenance, lack of inspection and testing.

[a, *] Institute for Technological Research – IPT (marcosvms@ipt.br), Corresponding author.

[b] Institute for Technological Research – IPT (afberto@ipt.br).

Within the fire protection systems, the materials applied in claddings, finishing, ceilings, etc. must present a fire behavior consistent with minimum performance levels related to its usage in the building. Unfortunately, several materials applied in these building elements nowadays are still the same that promoted tragedies in other buildings like the Kiss nightclub and the Grenfell Tower [4]. This represents a great risk for building occupants, which increases due to existing problems in emergency exits [3]. Figure 1 presents the Kiss Nightclub (a) and Grenfell Tower (b) after the fire incidents in which several people died.

<center>a)   b)</center>

Figure 1: Kiss Nightclub (a) and Grenfell Tower (b) after the fire incidents (source: Reuters)

Until recently, the body of Brazilian Standards related to passive fire protection was narrow and lacked several Standards which were existent worldwide. Aiming to elevate the importance of passive fire protection in Brazil, an effort has been made in the last decade to review and issue several Standards compatible with international documents.

This paper presents an overview of these Standards, aiming to publicize the work that has been done, and discusses the benefits brought to the fire safety, the next steps for the fire protection standardization in Brazil and the importance of incorporating these advances into the official Fire Departments' Regulations.

2. BRAZILIAN STANDARDIZATION

Standardization in Brazil is managed by the Brazilian Association for Standardization (ABNT), which is a non-profit entity founded in 1940. The ABNT is divided in Committees for each field in which standardization is present. Each Committee is also divided in Study Commissions which cover specific topics within the Committee field.

Fire Safety is covered by the Committee nº 24 of ABNT (CB-024), which contains Study Commissions concerning active fire protection systems: fire extinguishers, hydrants, sprinklers, detection, and alarm, etc.; and passive fire protection systems: testing and classification of the fire behavior of finishing and coating products, testing and classification of fire resistance of building elements, etc. In general, CB-024 has been producing several important Standards concerning fire protection.

Passive fire protection systems are incorporated to the building and react passively during a fire limiting the spread of fire, facilitating evacuation, preventing structural collapse, etc. [5]. The two main topics relevant to passive fire protection in buildings are reaction to fire of materials and fire resistance of building elements. Reaction to fire determines the behavior that the building materials will present during a fire, facilitating the occurrence of fire, developing smoke, and contributing or not to the development and spread of fire. Fire resistance determines how long the building elements can maintain their function supporting the building loads and preserving the compartmentation to prevent the spread of the fire to the whole building. Both concepts have great impact in the speed in which the building occupants will be affected by the fire and how much of the building

will suffer the deleterious effects of the high temperatures. Therefore, both concepts have great importance for preserving lives and property.

CB-024 has one Commission concerning reaction to fire: "Reaction to fire of materials" and another Commission concerning fire resistance: "Fire resistance of building elements". The Standards presented in this paper were developed in these two Commissions.

CB-024 is not the only Committee concerned with fire safety. The Committee nº 02 of ABNT (CB-02): "Civil Construction" also discusses some themes related to passive fire protection like the design of building structures for loadbearing capacity during a fire and of emergency exists of buildings for evacuation, which are important passive fire protection measures.

It is important to highlight that the design of building structures for fire incidents is intrinsically related to the design in normal conditions, therefore CB-02 is an appropriate Committee for this theme. However, the design of emergency exits and evacuation of buildings is more related and dependent on other fire safety systems.

3. OVERVIEW OF THE DEVELOPMENT

A Standard to classify the reaction to fire of building materials was developed. Reaction to fire is the first thing that should be considered when analyzing combustible materials incorporated to building elements. The classification implemented in the Standard classifies the reaction to fire of a material based on the speed at which fire spreads through the material and on the optical density of the smoke that the burning of that material produces. A new classification was also provided for when a material generates flaming droplets, which is a dangerous behavior during a fire [6].

Standards to classify the fire resistance of building elements were developed. The classification consists in separating the fire resistance of a building element into several criteria, the main ones being: R for loadbearing capacity, E for integrity, I for thermal insulation and W for radiation reduction. Additional criteria for mechanical actions, self-closing devices and smoke control are also presented to complement the main classification [7]. Each criterion is determined through fire resistance tests in which the time that each criterion was attended is registered through different methods employed during the test. The full fire resistance classification of a building element is a result of the combination of these criteria into one expression: for example, an element that attends the R, E and I criteria for 90 minutes is classified as REI 90.

The loadbearing capacity (R) is defined as the ability of a loaded element to maintain structural stability under fire. This criterion is verified through observation of the deformation of the specimen during the test. The time in which this criterion is attended is defined as when the deformation surpasses a limit that is defined according to each type and dimensions of the building element [7].

The integrity (E) is defined as the ability of a separating element to prevent the passage of flames or hot gases from the side exposed to fire to the other side that is not exposed to fire. This criterion is verified if any of the following events occur: appearance of cracks of certain dimensions in the specimen; appearance of flames in the unexposed side; or ignition of a cotton pad in the unexposed side [7].

The thermal insulation (I) criterion is defined as the ability of a separating element to limit the transmission of temperature from the side exposed to fire to the other side that is not exposed to fire. This criterion is verified through positioning of thermocouples that measure the temperature on several location in the side that is not exposed to fire. The increase in temperatures should not surpass 180°C in any position or 140°C in the average values measured by all thermocouples [7].

The radiation reduction (W) criterion is defined as the ability of a separating element to limit the transmission of heat radiation from the side exposed to fire to the other side that is not exposed to fire. This criterion is verified by measuring the radiation levels on the unexposed side. The time in which this criterion is attended is defined when the radiation level surpasses 15 kW/m² [7].

The application of the test methods also requires several equipment and knowledge of procedures that are common to each method. To avoid repetitions, another Standard was created as a general guidance that would complement each test method, giving the basis for their procedures. This Standard is also important because it specifies the general equipment that is used for the conduction of fire resistance tests, which may contribute to the creation and development of laboratories across the country.

Testing is one of the approaches for the evaluation of passive fire protection systems. The test methods must reproduce typical or critical fire conditions and test specimens that reproduce an end use application.

Another important type of Standards are requirement standards, which guide manufacturers and consumers to produce, install, use, do maintenance and verify the performance of building elements to achieve minimum standards for that product.

The scope of each Standard that was recently created is present briefly in the following sections along with a small description of the respective test or application of the Standard.

3.1 Newly developed Standards in CB-024

3.1.1 ABNT NBR 16626 – Fire reaction classification of building products

Defines the reaction to fire classification for building elements: finishing, cladding, coatings, etc. [6].

3.1.2 ABNT NBR 16945 – Fire resistance classification for building elements

Defines the fire resistance classification for several building elements: non-loadbearing elements, loadbearing elements, coating products for structural building elements and elements for compartmentation with or without glass portions [7].

3.1.3 ABNT NBR 16965: Fire resistance tests for elements of building construction — General guidance

General guidance on the equipment and procedures required to conduct fire resistance tests. This Standard is a basis for all the test methods that are specific for testing each type of building element [8].

3.1.4 ABNT NBR 16841 – Fire performance of roof coverings subjected to an external source of ignition

Test method for determining the fire behavior of roofs to an external ignition source. The specimen simulates a roof in which a flaming wooden straw is positioned. Several criteria must be attended to obtain a positive classification [9].

3.1.5 ABNT NBR 16944-1 - Requirements and fire resistance tests for linear and penetration seals – Requirements

This Standard establishes the requirements for classification, application, performance, specification, responsibilities, testing, maintenance, and commissioning fire resistance seals that should be used in electrical, plumbing, mechanical, air-conditioning, communications (telephone, data) and all passages that allow communication between compartmentalized areas, including perimeter joints and construction joints.

This Standard also offers some resources to verify supplementary information related to the environmental, mechanical, and physical properties of the sealing system; longevity; durability; and sealing system performance, as these characteristics can affect the installation and performance of the sealing system [10].

3.1.6 ABNT NBR 16944-2 - Requirements and fire resistance tests for linear and penetration seals – Fire resistance test for seals systems of service installations

This Standard specifies a test method and criteria for the evaluation (including field of application rules) of the ability of a penetration seal to maintain the fire resistance of a separating element at the position at which it has been penetrated by a service.

Penetration seals used to seal gaps around chimneys, air ventilation systems, fire rated ventilation ducts, fire rated service ducts, shafts and smoke extraction ducts are excluded from this Standard except for mixed penetration seals, i.e. penetration seals installed in fire dampers. The fire resistance of those services itself cannot be assessed with the methods described in this Standard [11].

3.1.7 ABNT NBR 16944-3 - Requirements and fire resistance tests for linear and penetration seals – Fire resistance test for linear joints seals

This Standard presents a test method for determining the fire resistance of linear seals, which are used to seal joints in construction [12].

3.1.8 ABNT NBR 16951 - Fire performance of external cladding systems for façades — Test method, classification and application of the results of fire spread in façade surfaces

This Standard provides a test method for determining the fire performance characteristics of non-loadbearing external cladding systems, rainscreen overcladding systems, external wall insulation systems, curtain walling, glazed elements, in fill panels and insulated composite panels when applied to the face of a building and exposed to an external fire under controlled conditions.

The fire exposure is representative of an external fire source or a fully-developed (post-flashover) fire in a room, venting through an opening such as a window aperture that exposes the cladding to the effects of external flames, or from an external fire source.

This Standard also specifies procedures and rules used to evaluate variations and changes to products and some systems which have been tested and, where appropriate, defines options and limits for preparing reports based on the direct and extended application criteria provided. This Standard does not cover exposure to radiant heat from a fire in an adjacent building.

This Standard is relevant because small scale common tests for determining the fire behavior of some materials may not represent well the behavior that would be seem in real conditions [13].

3.1.9 ABNT NBR 10636-2: Non-loadbearing building elements — Fire resistance test - Part 2: Ceilings

Test method for determining the fire resistance of suspended or self-supporting ceilings. Includes fire exposure both from below and above, to simulate a fire in the cavity within the ceiling [14]. This Standard is not applicable to the determination of the contribution of protective horizontal membranes to the fire resistance of horizontal load-bearing elements.

3.2 Standards reviewed in CB-024

3.2.1 ABNT NBR 14925: Fire resistant glazed building elements for compartmentation

Fire resistance classification for glazed elements, considering the new approach based on R, E, I, W criteria [15].

3.2.2 ABNT NBR 5628: Structural building components — Fire resistance test

Test method for determining the fire resistance of walls, slabs, beams, and columns. Includes fire exposure on one side for walls, from the underside for slabs, three sides for beams and full exposure for columns [16].

3.2.3 ABNT NBR 6479: Doors and shutters – Fire resistance test

Test method for determining the fire resistance of hinged, pivoted, sliding, sectional, folding, tilting, rolling doors and shutters, openable windows, removable shutters, and operable curtains. General guidelines for mechanical pre-evaluation of the element before the conduct of the fire-resistance test are also part of this Standard [17].

3.2.4 ABNT NBR 10636-1: Non-loadbearing building elements — Fire resistance test - Part 1: Walls and partitions for compartmentation

Test method for determining the fire resistance of non-loadbearing internal or external walls with or without glazing portions. Includes fire exposure from one side. In the case of external walls, the exposure may be simulated with external fire curve which is less severe than the standard fire curve [18]. This Standard was originally a unique part, but was divided in three parts after the revision, contemplating not only walls, but also ceilings and curtain walling.

3.2.5 ABNT NBR 15281: Entrance fire door for units entrances and specific compartments in buildings

Requirements for manufacture, installation, functioning, performance, maintenance, and tests for fire doors for units entrances and specific compartments in buildings [19].

3.2.6 ABNT NBR 11711: Fire resistant doors and shutters with wood core for compartmentation in warehouses and industries - Requirements

Requirements for manufacture, installation, functioning, performance, maintenance, and tests for fire doors for warehouses and industries. Several types of doors are covered: hinged, sliding, drill doors with vertical and horizontal displacement and fixed shutters.

These doors are intended for opening protection of commercial and industrial environments. The separating elements in which these doors are inserted may have up to 240 min of fire resistance

3.3 Standards currently being developed

3.3.1 ABNT NBR 10636-3 – Non-loadbearing building elements – Fire resistance test – Part 3: Curtain-walling – Full or partial configuration systems and perimeter seals

Test method for determining the fire resistance of curtain walls and perimeter seals. The curtain walls may be tested in full configuration or in isolated parts. The fire resistance of curtain walling may be determined under internal or external exposure conditions. In the latter case the external fire exposure curve given in ABNT NBR 16965 may be used.

This Standard does not cover double skin façades, over-cladding systems and ventilated façade systems on external walls, neither deals with the reaction to fire behavior of curtain walling.

3.3.2 Fire resistance test for fire dampers

This Standard specifies the test method for determining the fire resistance of dampers installed in ventilation ducts that penetrate compartments and close under specific conditions, in order to maintain compartmentalization between environments. The damper may be installed in the separating element, on the separating element or adjacent to the separating element.

This Standard is not suitable for testing dampers on suspended ceilings. This standard is not suitable for testing non-mechanical dampers, like intumescent grids that seal the opening of the duct during a fire.

3.3.3 Fire resistance tests for membranes and coatings for protection of structural elements - Eight Parts covering steel, wood, concrete and mixed elements

Test method for determining the contribution of a membrane or coating to the fire resistance of structural building elements. The building elements may be walls, slabs, beams, or columns and made of steel, wood, concrete or

mixed materials. The protective coatings may include paints, blankets, and boards in one or more layers. The protective coating can be partially or completely fixed to the elements.

The Standards will evaluate the ability of the coating to delay the temperature rise in the structural element and the ability of the coating to remain adhered or fixed to the structural element during the test.

It is important to highlight that the results provided from the tests with these Standards do not directly provide the fire resistance classification of the tested construction. The results are used to provide data that can be used to calculate the fire resistance of structural building elements according to the specific design Standards according to each type of construction.

3.4 Standards currently being revised in CB-024

3.4.1 ABNT NBR 11742: Fire-resistant door for emergency exit

Requirements for manufacture, installation, functioning, performance, maintenance, and tests for fire doors for emergency exit in buildings.

The revision of this Standard is associated to three important points: incorporate another Standard that covers doors' hardware to ABNT NBR 11742; To adequate the requirements presented in the current Standard to the fire resistance classification; Divide the doors for emergency exit in two distinct types of fire-resistant doors;

The new version of this Standard will divide doors that are used for enclosure of stairways and for compartmentation in refugee areas, which are an important requirement for the adoption of a progressive horizontal evacuation strategy. This strategy is a new implementation from the revision of ABNT NBR 9077, which is a currently being developed in CB-02.

3.4.2 ABNT NBR 14432: Requirements for the fire resistance of structure and compartmentation in buildings

Requirements for the fire resistance of building elements for the structure and compartmentation in buildings concerning the new classification proposed by ABNT NBR 16945. This Standard will be divided into two parts covering respectively the structure and the compartmentation.

4. BENEFITS OF STANDARDIZATION AND THE NEW STANDARDS

The standardization process is broadly democratic: any person from any group may participate with equal rights in the decision-making process. While this prevents the prevalence of interests of a singular group, the many interests of several people and groups can make the discussions difficult and lengthily, even halting the development of the documents, because achieving consensus among the specialists can be hard. This slow process may also result in uncertain conditions in the construction sector because changes in the industry and technological advancements usually happen at a faster pace.

Standardization gives the basis for product manufacture or performance analysis. In general, this procedure brings several advantages. Specialists from several fields may contribute to standardization, which ensures that a Standard receives inputs from distinct perspectives and addresses the needs of various sectors. Moreover, the diverse field of specialists aid the development by providing information related to the latest research and best practices available. This means that Standards will promote more safety, quality, and innovation and will be better suited to the needs of end-users.

Standardization also promotes innovation and healthy competition, because minimum requirements defined by the Standards must be attended by the whole market. Moreover, the Standardization allows comparison of different solutions available in the market, which ultimately benefits both producers and consumers alike.

The new fire testing and requirements Standards in Brazil mostly follow the already well stablished European Standards that are employed along with the Eurocode [20]. This harmonizes the sector not only internationally, but also in Brazil because most of its code design Standards were already based on the Eurocode. Internationally, this favors the producers which can import their products from abroad and favors consumers, as the products are manufactured to achieve international levels of performance. This is also one of the reasons for maintaining for each criterion the same letters that were already used abroad.

A big contribution that the new Standards brought is certainly the possibility of providing results for a wider range of elements than that was tested, by means of the "direct field of application of results". Each new testing Standard provides rules for the definition of the critical condition for the test concerning several parameters. If the test is executed in the critical condition, the results will be valid for elements within the range of variability the rules allow. This is done in succession to the test without the need of carrying out further tests.

This means that the same classification that was obtained in the test with the critical condition may be applied to the same element with a range of variabilities. This wider application favors the producers and test sponsors, because it can reduce the number of tests required to launch a product or for it to be applied in the market.

Additionally, the Standards permit the employment of the "extended application of results". In this case there is the need to do additional tests and/or simulations and/or analysis to apply the results to an even wider scope or generate new classification for an element with other variabilities or in a range that is not covered by the rules of the direct field of application of results.

The positive aspects of the new Standards certainly represent an improvement for the whole fire safety construction sector: laboratories may provide more detailed and better analyzes for the test sponsors and obtain better data from the tests; Test sponsors and producers may get more precise results for their products with fewer tests, and a wider scope of application; And the consumers get access to increased diversity and better products.

5. ROLE OF THE STANDARDS IN BRAZIL

One of the biggest obstacles for the improvement of the fire safety and its Standards is the absence of reliable statistics concerning the occurrence of fires in Brazil [21]. As a result, it becomes harder to justify increases in requirements, which would require an increase in investments in fire safety. Adequate statistics would lead to a better understanding of the major problems, which in turn, could lead to more directive and efficient measures to improve fire safety. Adequate statistics would also confirm in a broader aspect the existent problems in buildings, that, as already demonstrate by [1–4], are grave.

A great issue still prevents a bigger advance of the fire safety and impact of the Standards in Brazil. In Brazil the Standards are not mandatory and mandatory guidelines are only given in Government's decrees and Fire Departments' Regulations. The guidelines of the current regulations do not fully adopt the Standards' recommendations and do not produce an adequate safety level for the buildings [22].

A better path for the Regulations would be to fully adopt the Standards' recommendations, since the Standards are documents approved by the whole society. Moreover, Standards are applicable across the country, while the Fire Departments and its Regulations are divided by state, which complicates the process of designing buildings in multiple states, since each state may require different obligations. Fully adopting the Standards would not only improve the current Regulations but also allow the Fire Department's to focus on inspection and enforcement, which are also fragile in Brazil [22].

It is important to highlight that the implementation of performance-based design and fire safety engineering codes has several prerequisites [23,24] and are more effective in countries where the fire safety with a prescriptive approach is already in good condition [22]. Fire safety in Brazil still suffers from several problems, and, therefore, is not ready for the upgrade to a performance-based approach [22]. Nevertheless, the new Standards stablish the basis for the implementation of this approach in the Fire Department's Regulations and, in the future, achieve the required level for the full implementation of a performance-based approach.

6. CONCLUSIONS

The standardization process is often slow due to lengthy discussions, the distinct points of view and resistance to changes. Lack of reliable statistics on fire occurrences in Brazil makes it harder to justify new Standards for passive fire protection. Adequate statistics would also lead to a better understanding of the major problems and efficient measures to improve this field.

The advancements made in Brazilian passive fire protection standardization represent a significant improvement and bring several benefits for producers and consumers alike. While the passive fire protection standardization in Brazil has been improving in recent years, they are not currently mandatory. Fire Department's Regulations are the official mandatory documents, which are slow to incorporate the advancements that standardization presents. The full adoption of Standards in the Regulations would not only improve them, but also allow the Fire Department to focus on inspection and enforcement. It would also promote a better condition for the adoption of performance-based approach in the future. Only when the Fire Department's Regulations fully adopt the Standards their importance will be entirely recognized by the construction sector.

7. REFERENCES

[1]   Berto, A.F.; de Paula, D.J.; & Böttger, I.F. (2018) *Segurança contra incêndio? - Parte 1.* Revista Emergência. (117), p. 46–55.
[2]   Berto, A.F.; de Paula, D.J.; & Böttger, I.F. (2019) *Segurança contra incêndio? - Parte 2.* Revista Emergência. (118), p. 34–41.
[3]   Berto, A.F.; de Paula, D.J.; & Böttger, I.F. (2019) *Segurança contra incêndio? - Parte 3.* Revista Emergência. (119), p. 30–38.
[4]   Berto, A.F.; de Paula, D.J.; & Böttger, I.F. (2019) *Segurança contra incêndio? - Parte 4.* Revista Emergência. (120), p. 42–51.
[5]   Berto, A.F. (1991) *Medidas de proteção contra incêndio: Aspectos fundamentais a serem considerados no projeto arquitetônico dos edifícios*, Master's dissertation, Universidade de São Paulo, 1991.
[6]   Brazilian Association for Standardization - ABNT (2017) *ABNT NBR 16626 - Classificação da reação ao fogo de produtos de construção.*
[7]   Brazilian Association for Standardization - ABNT (2021) *ABNT NBR 16945 - Classificação da resistência ao fogo de elementos construtivos de edificações.*
[8]   Brazilian Association for Standardization - ABNT (2021) *ABNT NBR 16965 - Ensaio de resistência ao fogo de elementos construtivos — Diretrizes gerais.*
[9]   Brazilian Association for Standardization - ABNT (2020) *ABNT NBR 16841 - Comportamento ao fogo de telhados e revestimentos de cobertura submetidos a uma fonte de ignição externa.*
[10]   Brazilian Association for Standardization - ABNT (2022) *ABNT NBR 16944-1 - Selagens resistentes ao fogo em elementos de compartimentação - Parte 1 - Requisitos.*
[11]   Brazilian Association for Standardization - ABNT (2021) *ABNT NBR 16944-2 - Selagens resistentes ao fogo em elementos de compartimentação - Parte 2 - Ensaio de resistência ao fogo em selagens de aberturas de passagem de instalações de serviço.*
[12]   Brazilian Association for Standardization - ABNT (2022) *ABNT NBR 16944-3 - Selagens resistentes ao fogo em elementos de compartimentação - Parte 3 - Ensaio de resistência ao fogo em selagens de juntas de construção.*
[13]   Brazilian Association for Standardization - ABNT (2021) *ABNT NBR 16951 - Reação ao fogo de sistemas e revestimentos externos de fachadas — Método de ensaio, classificação e aplicação dos resultados de propagação do fogo nas superfícies das fachadas.*
[14]   Brazilian Association for Standardization - ABNT (2023) *ABNT NBR 10636-2 - Componentes construtivos não estruturais — Ensaio de resistência ao fogo - Parte 2 - Forros.*
[15]   Brazilian Association for Standardization - ABNT (2019) *ABNT NBR 14925 - Elementos construtivos envidraçados resistentes ao fogo para compartimentação.*
[16]   Brazilian Association for Standardization - ABNT (2022*) ABNT NBR 5628 - Componentes construtivos estruturais — Ensaio de resistência ao fogo.*

[17]   Brazilian Association for Standardization - ABNT (2022) *ABNT NBR 6479 - Portas e vedadores - Ensaio de resistência ao fogo*.

[18]   Brazilian Association for Standardization - ABNT (2022) *ABNT NBR 10636-1 - Componentes construtivos não estruturais — Ensaio de resistência ao fogo - Parte 1 - Paredes e divisórias de compartimentação*.

[19]   Brazilian Association for Standardization - ABNT (2021) *ABNT NBR 15281 - Porta resistente ao fogo para entrada de unidades autônomas e compartimentos específicos de edificações*.

[20]   European Committee for Standardization (2005) *EN 1990, Eurocode - Basis of structural design*.

[21]   Corrêa, C.; Duarte, D.; & Braga, G. (2021) *Fragilidade das estatísticas de incêndios estruturais no Brasil*. in: p. 32–38.

[22]   Tavares, R.M. (2009) *An analysis of the fire safety codes in Brazil: Is the performance-based approach the best practice?* Fire Safety Journal. 44 (5), p. 749–755.

[23]   Spinardi, G. (2016) *Fire safety regulation: Prescription, performance, and professionalism*. Fire Safety Journal. 80, p. 83–88.

[24]   Maluk, C.; Woodrow, M.; & Torero, J.L. (2017) *The potential of integrating fire safety in modern building design*. Fire Safety Journal. 88, p. 104–112.

THE ULTIMATE TEST: COMPARING FIRE RESISTANCE TEST STANDARDS FOR NON-LOADBEARING WALL CONSTRUCTION

Chris D. McDonald a

Alex P. Duffy b,*

Angela Solarte c

ABSTRACT

Governments around the world mandate Fire Safety through legislated standards and regulations. These standards and regulations reference a fire testing method to a specified test standard. Adherence to the fire test standard provides evidence that a product achieves a certain accepted fire performance for passive fire protection – and therefore complies with the legislated fire safety regulations. This paper previews and compares key characteristics of the British, Australian, European and American test standards for non-loadbearing walls. The key characteristics compared include furnace set-up, heating regime, pressure regime, instrumentation, failure criteria and reporting requirements. This comparison is intended to initiate an exploration into the equivalency of the test standards, and in turn the potential equivalency of the fire ratings applied to products that are tested to them. Demonstrated equivalency between test standards would facilitate expansion of the tested fire rated product market. It is generally concluded that the European and Australian fire test standards are very similar to one another, the British fire test standard is similar but with more differences, and the American fire test standards are the most different.

Keywords: fire resistance, fire testing, test standards, compliance

1. INTRODUCTION

Fire resistance is an essential feature of modern building design. Within a building, fire resistance is required of elements of construction to provide a level of protection to the building, its occupants, and attending fire brigade. For loadbearing structures, fire resistance is primarily concerned with maintaining structural stability. For non-

ᵃ Arup (Chris.McDonald@arup.com).

ᵇ,* Arup, 5/151 Clarence St. Sydney NSW 2000 Australia, alexpduffy@gmail.com (Alex.Duffy@arup.com), Corresponding author.

ᶜ Arup (Angela.Solarte@arup.com).

loadbearing structure (e.g. non-loadbearing fire-resisting walls), it is concerned with reducing the potential for fire spread from one side of the element of construction to the other i.e. maintaining its integrity and insulation.

A building is generally required to achieve some prescribed level of fire resistance under the legislation, regulation and/or design codes and practices enforced in its location. The fire resistance of a building (or more specifically, the fire resistance of its constituent structural elements) is effectively implemented in the construction process via a three-pronged approach for demonstrating compliance to the accepted standard:

1. Product compliance – fire testing to validate a product's performance to the accepted standard;
2. Design compliance – designing the product to be used in accordance with the certified fire performance, as evidenced through fire testing; and
3. Installation compliance – installing the product in accordance with its designed arrangement.

Testing, to a specified fire resistance test standard, is used as the means of demonstrating and evidencing that a building product achieves the fire resistance required. For a non-loadbearing fire resisting wall, fire testing involves the construction of the wall in a test furnace. The wall is then subjected to a heating regime and specific measurements are taken. The wall is evaluated continuously throughout the test against a set of specified failure criteria which, upon being exceeded, the wall is considered to have failed the test. The outcome of the test is then documented in a test report with the tested arrangement being given a performance classification specified as a duration in minutes e.g. 60 minutes fire resistance level (FRL). At this point, the specimen tested has achieved product compliance, in that its performance has been validated against a fire test standard.

There are many fire resistance test standards consistently used around the world, all of which fundamentally aim to provide a quantified measure of fire resisting performance. However, products used within a building may only be deemed compliant if they have achieved the required fire rating when tested to the fire test standard or standards specified under the local/specific legislation. This restricts the available fire rated products that may be (compliantly) used in construction to those that have been tested strictly to the legislated fire resistance test, despite other fire rated products that may be available but that have been tested to other fire test standards.

During the COVID pandemic, supply chain issues forced developers, designers and builders to widely source fire rated products tested to various standards. This led to challenges in demonstrating compliance with the relevant legislation. If the details between fire resistance test standards could be comprehensively compared to determine if any test standards could be deemed "equivalent", or if any single standard could be considered as the most severe, there would be technical grounds for legislative bodies to consider endorsement of one or more test standards. Doing so would instantly expand the available market of fire rated products for the local construction industry. An expanded passive fire protection market would be more resilient to supply chain pressures, give suppliers more customers for their products and builders more products to use in construction. This would be especially helpful where designers and builders may be pursuing more sustainable products, but where roadblocks to compliance may currently inhibit their use more widely.

To this end, this paper intends to initiate a broad discussion on the comparability of fire resistance test standards by comparing a selection of international fire resistance test standards. A focus has been drawn specifically to certain specific characteristics of the fire resistance testing for non-loadbearing fire-resisting walls.

2. FIRE RESISTANCE TEST STANDARDS

The fire resistance test standards from the European, British, Australian, and American standards have been considered. These standards have been selected for inclusion in this study based on the authors' observation that these standards appear to be most consistently ratified under English-speaking national legislations. This list is not exhaustive; while many countries are known to adopt these standards by way of their relevant Legislation and Regulations, many countries either do not rely on these standards, employ their own locally-written standards, or it has not been confirmed what standard is adopted (see Figure 1). A more detailed study would benefit from expanding the investigation to consider more test standards.
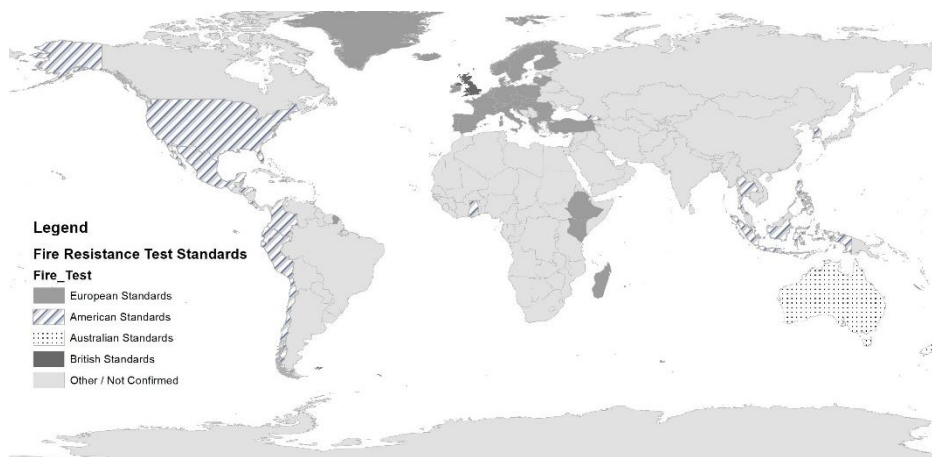
Figure 1: A global overview of where the European, American, Australian and British Standards are adopted. Countries where other standards are used on the standard(s) used has not been confirmed are also indicated.

2.1 European test standards

The European test standards are prepared by the European Committee for Standardisation (CEN) under a mandate by the European Commission and European Free Trade Association. The content relevant to the fire resistance testing of non-loadbearing walls within the European standards appears in EN 1363-1 *Fire resistance tests Part 1: General Requirements* [1] and EN 1364-1 *Fire resistance tests for non-loadbearing elements Part 1: Walls* [2]. The current versions at the time of writing, are EN 1363-1 (2020) and EN 1364-1 (2015).

The International Standards Organisation (ISO) is a separate organisation that generates standards for use across the globe. The ISO 834 *Fire resistance test* series was first published in 1965 and pertains to fire resistance testing. In 1991, the Vienna Accord between CEN and ISO was reached to ensure technical harmonization between their respective test standards [3]. Accordingly, while the details of ISO 834 have not been analysed as part of this study, ISO 834 is generally understood to closely align with the testing criteria outlined in the European fire test standards developed by CEN.

2.2 British test standards

One of the relevant fire resistance test standards for non-loadbearing walls in the United Kingdom (the European Standards are also accepted in the UK) is the British Standard (BS) 476-20 *Fire tests on building materials and structures Part 20: Methods for determination of the fire resistance of elements of construction (general principles)* [4] & 476-22 *Fire tests on building materials and structures Part 22: Methods for determination of the fire resistance of non-loadbearing elements of construction* [5]. At the time of writing, the current versions of these standards are BS 476-20 (1987) and BS 476-22 (1987).

The British test standards noted are developed by the British Standards Institute (BSI), who represent the UK interests in the International Organisation for Standardisation (ISO) and the European Standards Organisation (CEN, CENELEC and ETC). The first edition of BS 476 was published in 1932 [6]. The BS series of standards are published by the BSI standards limited under licenses from the British Standards Institute and are enacted through the relevant building codes within the United Kingdom. It is understood that the BS series are, or have been, also applied in other countries outside of the UK.

2.3 Australian test standard

In Australia, the relevant fire resistance test standard for non-loadbearing walls is Australian Standard (AS) 1530.4 *Methods for fire tests on building materials, components, and structures. Part 4: fire-resistance tests for elements of construction* [7]. The current version at the time of writing is the 2014 issue.

AS 1530.4 is published by Standards Australia and is enacted through the Building Code of Australia. Standards Australia are Australia's member of the International Organisation of Standardisation (ISO). The earliest revision of

566

the Australian Standard (AS A30-1935) directly adopted the British test at the time (BS 476-1932). Future revisions, starting from 1958, formed their own separate documents and, while still corresponding in many respects to the British test, included additional provisions and differences in detail [8].

2.4 American test standards

In the United States, the relevant fire resistance test standards for non-loadbearing walls are either ASTM E119 *Standard test methods for fire tests of Building Construction Materials* [9] or UL 263: *Standard for safety: Fire tests of building construction and materials* [10]. Both test standards are enacted through the NFPA 101: Life Safety Code [11] and the International Building Code (IBC) [12]. The current versions at the time of writing is ASTM E119 (2022) and UL 263 (2011). Originally published by the American Society for Testing and Materials (ASTM) in 1917, ASTM E119 has its origins in the earliest days of fire resistance testing. UL 263 is published by Underwriters Laboratories and its history runs parallel to that of ASTM E119, with the ASTM time-temperature curve first being published by UL in 1916 [13].

3. KEY CHARACTERISTICS FOR COMPARISON

The following characteristics from each fire resistance test standards have been considered as related to non-loadbearing fire-resisting walls:

1. Furnace set up: the configuration of the furnace and the materials which it is made from. This relates to the size of the specimen being tested and the potential contribution of the test furnace to the conditions within the furnace [14] [15].
2. Heating regime: the heat applied within the furnace over a specified time period. This relates to the heat to which the test specimen is exposed to over the duration of the test.
3. Pressure regime: the pressure conditions inside the furnace. This dictates the pressure that is applied to the test specimen across its area.
4. Instrumentation: the measurement instruments used to monitor the failure criteria of the specimen. This equipment and its location provide the data used for analysing the performance of the test specimen.
5. Failure criteria: the criteria which determines when a specimen has failed the test and therefore determines its fire resistance performance. This is the fundamental criteria for determining fire resistance performance.
6. Reporting requirements: the required information to be presented in a test report. This information is what is presented as a record of the test and the means of evidencing the fire resisting performance of the specimen. The test report is the means of demonstrating product compliance and outlining the limitations of the test outcomes.

3.1 Furnace setup

The furnace setup is the arrangement and conditions in which the specimen is tested.
Table 11 presents the requirements for the furnace's size, geometry and furnace linings as outlined by the British, European, Australian and American Standards.

Table 11: Summary of the furnace setup conditions required across the subject standards [1][4][7][9][10]

Standard	Size and geometry	Furnace linings
European Standard BS EN 1363-1	• No details on the furnace size or geometry requirements.	• Furnace linings ρ <1000 kg/m^3 • Minimum thickness =50mm • Constitute at least 70% of the internally exposed surface of the furnace.
British Standard BS 476-20	• Furnace to be able to accommodate the full-size element. • Any space between the specimen and the furnace is to be filled by means of an associated construction or a furnace closure. • Vertical furnaces to have a chamber depth of not less than 600mm and not more than	• Furnace lining thickness of at least 50mm, • Materials with low thermal inertia where $\kappa\rho C < 500$ Ws$^{1/2}$/(m^{2}K) at 500°C.

567

	1300mm, excluding any areas where flues or other openings enter the furnace chamber. • Total area of flues and other openings to not exceed 25% of the surface area of the wall. • Furnace for testing columns to have a minimum horizontal dimension of 1.4m.	
Australian Standard AS 1530.4	No details provided on the furnace size or geometry requirements.	• Furnace linings ρ <1000 kg/m³ • Minimum thickness =50mm • Constitute at least 70% of the internally exposed surface of the furnace.
American Standard ASTM E119	Does not provide specific construction detail (size, geometry nor furnace lining) of the furnace. Readers are urged to consult reference documents for a more comprehensive review of furnace design and performance [16].	
American Standard UL 263	No details on the furnace size, geometry or furnace lining requirements.	

Across the five different standards, only the British Standard provides requirements for the dimensions of the furnace. Regarding furnace lining requirements, the British standard requires the furnace lining to have a minimum thickness of 50 mm and its thermal inertia, which is the ability of a material to conduct or store heat, to be less than 500 Ws$^{1/2}$/(m^{2}K) at 500°C. The European and Australian standards also require the furnace lining material to have a minimum thickness of 50 mm, and both require a maximum density of 1000 kg/m³ The American Standards (ASTM E119 and UL 263) do not include any requirements for the furnace lining's thickness, density, or thermal inertia.

It is the authors' understanding that at present the design of test furnaces, beyond what is nominated in the test standards, has not been formally standardised. It is understood that for non-loadbearing walls, a furnace that can accommodate a 3 m by 3 m specimen is generally used in fire resistance testing, but other characteristics of the furnace are less controlled. With no specification provided, the principles of a fire resistance test standard can still be met using furnaces that may differ in specific characteristics. Accordingly, variability in the potential test outcome may not be as result of variations within the test standards, but rather variations in the furnace set up. In other words, the same wall subjected to the same test standard may perform differently based upon the furnace in which it is being tested in [17].

3.2 Heating regime

Heating regime refers to the temperature of the furnace as varied over the duration of the test. Generally speaking, the heating regime is intended to mimic an intense fire exposure that a building element may face. It is widely acknowledged that the standard fire resistance test heating regime i.e. the time-temperature fire curve is not reflective of a real fire [6] [13]. However, its consistent application has enabled a standardised approach for comparison. Table **2** presents the heating regime criteria as outlined in the British, European, Australian and American Standards.

Table 2: Summary of the heating regime criteria required across the subject standards [1][4][7][9][10]

Standard	Heating Regime
European Standards BS EN 1363-1	The average temperature of the furnace is derived from the thermocouples specified in 4.5.1.1 shall be monitored and controlled such that it follows the relationship: $T = 345 \log_{10}(8t + 1) + 20$ Where, T is the average furnace temperature, in degrees Celsius. t is the time, in minutes.
British Standards BS 476-20	The temperature/time conditions shall be given by the equation $T = 345 \log_{10}(8t + 1) + 20$ Where,

	T is the mean furnace temperature in (°C)
	t is the time (in min) up to a maximum of 360 min.
Australian Standards AS 1530.4	The temperature of the furnace shall be controlled to vary with time, as closely as possible, in accordance with the following relationship:
	T = 345 $\log_{10}$(8t + 1) +20
	Where,
	T = furnace temperature at time (t), in degrees centigrade
	t = time into the test, measured from the ignition of the furnace, in minutes
American Standards ASTM E119	The furnace temperatures shall be controlled to follow the standard time-temperature curve…the points on the curve that determine it's character are:
	• 1000 deg F (538 °C) at 5 min
	• 1300 deg F (704 °C) at 10 min
	• 1550 deg F (843 °C) at 30 min
	• 1700 deg F (927 °C) at 1 hr
	• 1850 deg F (1010 °C) at 2 hr
	• 2000 deg F (1093 °C) at 4 hr
	• 2300 deg F (1260 °C) at 8 hr or over
American Standards UL 263	The conduct of fire tests of materials and construction is to be controlled by the standard time-temperature curve…the points on the curve that determine its character are:
	a) 1000 deg F (538°C) at 5 min
	b) 1300 deg F (704°C) at 10 min
	c) 1550 deg F (843°C) at 30 min
	d) 1700 deg F (927°C) at 1 hr
	e) 1850 deg F (1010°C) at 2 hr
	f) 2000 deg F (1093°C) at 4 hr
	g) 2300 deg F (1260°C) at 8 hr or over

The European, British and Australian Standards utilize the Standardized Fire Curve, which is defined as:

$$T = 345 \log_{10}(8t + 1) + 20 \tag{1}$$

This equation-based definition of the fire curve appears in the ISO 834 standard and is thus more generally known as the ISO 834 curve [18].

By comparison, the time temperature curve employed by the American Standards (ASTM E119 and UL 263) is defined by specific defined points on the curve, rather than by an equation. This curve shall heretofore be referred to as the ASTM curve. Figure 2 presents both curves on the same plot:
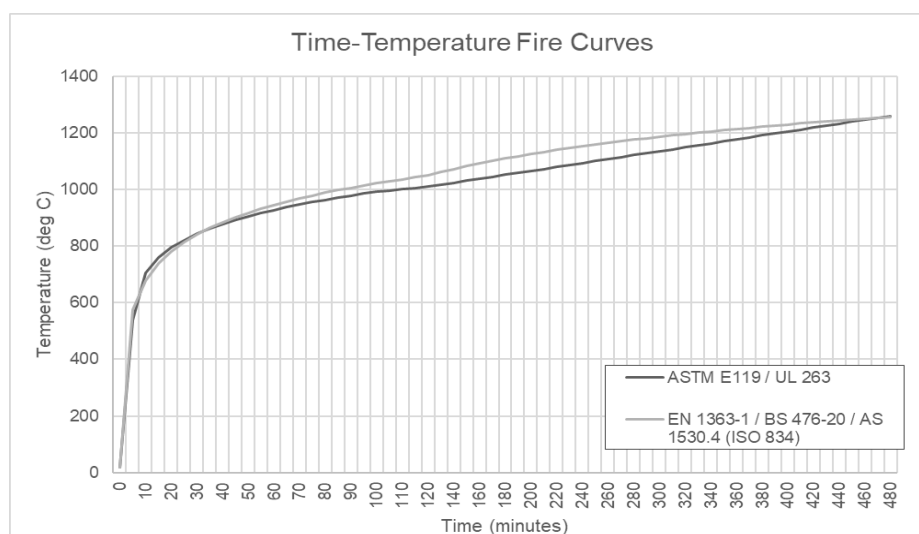
Figure 2: The Time-Temperature Fire Curves used within the subject standards.

569

While the two curves are generally similar, there are noteworthy differences. At the 5-minute mark, the ISO 834 curve reaches 576 °C, whereas the ASTM curve only reaches 538 °C (a difference of 38°C). Subsequently, between 10-minutes and 30-minutes, the temperature under the ASTM curve exceeds that of the ISO 834 curve. Subsequently, the ISO 834 curve is consistently a higher temperature than the ASTM curve through the end of the heating regime. The maximum difference between the curves occurs at the 210-minute mark, when the ISO 834 curve is 61 °C higher than the ASTM curve (1962 °C compared to 1072 °C). Between the 90-minute and 120-minute mark (1½ hr to 2hrs), the temperature of the ASTM curve lags behind the temperature of the ISO 834 curve by approximately half an hour. Between the 120-minute and 360-minute mark (2hrs to 6hrs), the temperature of the ASTM curve lags behind the temperature of the ISO 834 curve by approximately one hour.

Accordingly, specimens tested to the British, Australian, and European Standards heating regime (the ISO 834 curve) are exposed to higher temperatures earlier than specimens tested to the American heating regime (the ASTM curve) after 30 minutes. This may result in a greater chance of failure, particularly between 90 min and 360 min - an important window of the test where specimens qualify for many fire resistance levels e.g. 90 min. 120 min. 180 min and 240 min.

3.3 Pressure regime

The Pressure regime refers to the pressure conditions inside the furnace during testing. Table 33 provides an overview of the differences between the pressure condition requirements in the furnace between the British, European, American and Australian Standards. Vertical test conditions apply to wall construction.

Table 33: Summary of the pressure conditions required across the subject standards [1][4][7][9][10]

Standard	General	Vertical Test Conditions
European Standards BS EN 1363-1	• Pressure gradient 8.5 Pa per meter height of the furnace. • Pressure to be monitored and controlled after 5 min into the test. • Measurement variations for sensors within the range shall be limited to: 5<t<10 $\pm$ 5Pa t>10 $\pm$ 3Pa of the nominal pressure specified for the particular element under test. • The methodology for processing the data shall be clearly explained in the test report If it is presented as fixed or floating average values.	• The pressure at the top of a vertical test construction shall not exceed 20 Pa at any time.
British Standards BS 476-20	• Pressure gradient 8.5 Pa per meter height of the furnace. • After the 5 min heating period, a positive pressure shall be achieved throughout the test. • The pressure condition shall be controlled to within $\pm$2Pa.	• The pressure at the top of a vertical test construction shall not exceed at any time 20 Pa. • Vertical test to be determined with respect to the element's positional height relative to notional floor level.
Australian Standards AS 1530.4	• Pressure gradient 8.0 Pa per meter height of the furnace. • Measurements to be taken after 5 min start of test • Measurement variations for sensors within the range of: 5<t<10 $\pm$ 5Pa t>10 $\pm$ 3Pa	Furnace to operate zero pressure at the height of 500 mm above the notional floor level.
American Standards ASTME119	• Requirements for furnace's pressure is not specified, it notes that it can generally be slightly negative, and acknowledges that the pressure may have an effect on the test results, and the test conditions should always be carefully controlled.	

Standard		
American Standards UL 263	Requirements for furnace's pressure is not specified. However, pressure is to be recorded once per min and data included in test report.	

The European, British and Australian indicate that the pressure should be recorded after 5 mins of the start of the test. The European and British standard both indicate a pressure gradient within the furnace of no more than 8.5 Pa per meter height, while the Australian standard requires a pressure gradient of 8.0 Pa per meter height of the furnace. The European and Australian standards indicate that the pressure measured should not deviate more than $\pm$ 5Pa between 5 and 10 min and $\pm$ 3Pa after 10 mins. Both American standards do not indicate any maximum pressure gradient in the furnace.

For vertical test conditions, the European and British standards require the pressure at the top of the furnace to not exceed 20 Pa at any time. The Australian Standard requires the furnace to have a pressure of zero at 500mm above the specimen's notional floor level. American Standard ASTM E119 does not include any requirements regarding pressure in a vertical test. UL 263 does not either, however it does require the pressure to be recorded once per minute, and to be documented in the test report.

In summary, the European, British and Australian standards provide very similar pressure requirements. Although some minor differences can be found, they are likely to be of negligible impact. Regarding the furnace vertical tests, the European and British standards have an equal approach for pressure conditions, which differ from those required under the Australian standards. The American standards do not provide explicit pressure requirements for furnace testing; however, the UL 263 test does include strict requirements for ensuring that pressure is recorded once per minute throughout the test.

3.4 Instrumentation

Each testing standard outlines the required instrumentation to measure key variables experienced by the test specimen, including temperature across the product, pressure across the furnace enclosure and, in most cases, the deflection of the product within the furnace enclosure because of thermal expansion. Table **4** provides an overview of the instrumentation requirements across the subject standards.

Table 4: Summary of the instrumentation criteria required across the subject standards [1][5][7][9][10]

Standard	Temperature	Pressure	Deflection
European Standards BS EN 1363-1	Average temperature measured via five thermocouples, one located at centre of specimen and one close to the centre of each quarter section. For specimens with discrete areas, at least two thermocouples for each discrete area to monitor average temperature rise. Additional thermocouples to measure maximum temperature rise at specific locations that are considered to have higher heat transfer.	Pressure in the furnace measured via a specified sensor, to a precision of +/- 2 Pa. Measuring system to have the capacity to disregard rapid fluctuations.	All significant deflection (i.e. > 5 mm) to be measured. One deflection measurement at the centre of the specimen. If height or width >3m, additional measurement, at ¼ and ¾.
British Standards BS 476-22	Position five surface temperature measuring thermocouples with one placed approximately in the centre of the specimen and one in the centre of each quarter section. At least one thermocouple on each component material (when comprises of more than one material) Additional surface temperature measuring thermocouples at positions…where the temperature rise is likely to be higher than	At least one pressure sensing head in the furnace such that the pressure conditions in the furnace are measured…and so that the sensing heads do not interfere with the deflection of the specimen.	Locate the deflection measuring equipment at the anticipated point of maximum deflection. Where this position cannot be predetermined, take more than one deflection measurement and

	elsewhere…which may be required for evaluation of the maximum temperature rise.		report maximum deflection measured.
Australian Standards AS 1530.4	Five thermocouples – one thermocouple placed closed to the centre and the rest placed close to the centre of each quarter section. For specimens with discrete areas, at least two thermocouples for each discrete area to monitor average temperature rise. Additional thermocouples to measure maximum temperature rise at specific locations that are considered to have higher heat transfer. Roving thermocouple to measure maximum temperature at any point on the surface of the specimen during the test.	Pressure in the furnace measured via a T sensor or Tube sensor, to a precision of +/- 2 Pa.	Measurements made at mid-height at the centre of the specimen and 50 mm from the free edge.
American Standards ASTM E119	Temperatures recorded at not fewer than nine points on the surface: Five symmetrically disposed, one to be approximately at the centre of the test specimen, and four at the centre of its quarter sections. Other four shall be located to obtain information on the performance of the test specimen.	Furnace pressure not specified and is generally slightly negative. The pressure may influence the test results, and the test conditions should always be carefully controlled.	Not required
American Standards UL 263	Temperatures recorded at not fewer than nine points on the surface: Five symmetrically disposed, one to be approximately at the centre of the test specimen, and four at the centre of its quarter sections. Other four shall be located to obtain information on the performance of the test specimen.	≥ two pressure sensors, to not be subject to direct impingement of convection currents from flames or path of exhaust gases. Reading pressure to be within accuracy of 0.01 in of water (2.5 Pa) increments.	Not required

For the measurement of temperature, an array of thermocouples is arranged on the unexposed face to specifically measure the temperature across the specimen. Across the subject standards, five thermocouples are generally required: one placed close to the centre of the specimen and four others placed at the centre of each quarter section. Beyond this five-thermocouple array, additional thermocouples are also recommended. The American Standards recommend at least four additional thermocouples to be placed at the discretion of the testing authority to "obtain representative information on the performance of the test specimen". These thermocouples are to be used along with the five-thermocouple array to determine an average temperature measurement across the specimen (unless a 30% rise over the specified limit of the test is measured at a single location).

In the British Standard, the application of additional thermocouples beyond the five-thermocouple array is such worded that these be applied "at points on the surface where the temperature rise is likely to be higher than elsewhere due to lower levels of insulation & which may be required for evaluation of maximum temperature rise".

Most specifically, the European and Australian Standards specify that the five-thermocouple array are to specifically measure the *average* temperature across the specimen. Additional thermocouples are then to be attached to measure the *maximum* temperature rise at locations that are considered to have a higher heat transfer. The only difference in wording between the Australian and European standards regarding the location of these maximum temperature rise thermocouples relates to the thermocouple placed at the free edge. The Australian standard

specifies 100mm from the edge, whereas the European standard specifies 150mm from the edge. This 50mm discrepancy regarding the permitted placement of the free edge thermocouple is not expected to have a significant impact.

For pressure, each standard identifies the placement of pressure sensors to confirm the pressures within the furnace. The British standards specifies one pressure sensing head in the furnace positioned so as not to interfere with the deflection of the specimen. The US standards require a minimum of two pressure sensors, located where they will not be subject to direct impingement of convection currents from flames or in the path of the exhaust gases. Similar to the location of thermocouples, the Australian and European Standards use near identical wording, stating that Pressure in the furnace is to be measured via a sensor as outlined in elsewhere in the standard, to a precision of +/- 2 Pa.

For deflection, the British, European and Australian Standards advise that deflection measuring equipment is to be applied to the specimen. The US standards have no such requirement. With regards to where to take deflection measurements, the British Standard advises that measurement should be taken at the anticipated point of maximum deflection, or where this position cannot be determined, more than one deflection measurement report each maximum deflection measured. The European Standard advises one (1) deflection measurement be taken at the centre of the test specimen (and more if larger than 3m in width and/or height). The Australian Standard simply advises that measurement be taken at mid-height at the centre of the specimen and 50mm from the free edge.

3.5 Failure criteria

The determination of a non-loadbearing wall's fire resistance is based upon set failure criteria being surpassed. The following failure criteria are relevant for non-loadbearing fire resisting walls:
- Integrity: the ability of the specimen to restrict the passage of flames and hot gases and prevent occurrence of flames on the unexposed side.
- Insulation: the ability of the specimen to restrict the temperature rise on the unexposed face.

Table 5 below provides a comparison of the respective failure criteria across the subject standards.

Table 5: Summary of the failure criteria required across the subject standards [2][3][7][9][10]

Standard	Integrity	Insulation
European Standards EN 1364-1	• Flaming (for 10 seconds or longer) • Cotton pad test (where cotton pad is caused to glow or flame. Pad shall be applied for 30s if failure not reached). • 6mm gap gauge extends into furnace and can be moved for 150mm. • 25mm gap gauge can penetrate into the furnace.	• Average unexposed face temperature increases by more than 140k above initial average temperature. • Temperature at any location on unexposed face exceeds 180k above initial average unexposed face temperature.
British Standards BS 476-20	• Specimen collapse. • Sustained flaming on the unexposed face (for 10s or longer) • Cotton pad test (where cotton pad is caused to glow or flame. Pad shall be applied for between 10 and 15 seconds) • 6mm gap gauge extends into furnace and can be moved for 150mm. • 25mm gap gauge can penetrate into the furnace.	• Mean unexposed face temperature increases by more than 140°c above initial value. • Temperature on unexposed face exceeds 180°c above initial mean unexposed face temperature. • If integrity failure occurs
Australian Standards AS 1530.4	• Sustained flaming on the unexposed face (for 10 seconds or longer) • Cotton pad test (where cotton pad is caused to glow or flame. Pad shall be applied for 30+or-2seconds) • 6mm gap gauge extends into furnace and can be moved for 150mm.	• Average unexposed face temperature increases by more than 140k above initial value. • Temperature on unexposed face exceeds 180k above initial mean unexposed face temperature.

Standard		Reaction to fire test
American Standards ASTM E119	• Cotton pad test (where cotton pad is caused to glow, flame or smoulder. Pad shall be applied for 30+or-1 second) • Hose stream test (where hose stream applied immediately after test for duration of half the fire resistance period. Hose stream not required for fire resistance level of less than 1 hour)	Average unexposed face temperature increases by more than 139°C. Temperature at any location on unexposed face exceeds 30% of 139°C (i.e. 180°C).
American Standards UL 263	• Cotton pad test (where cotton pad is caused to glow, flame or smoulder. Pad shall be applied for 30+or-1 second) • Hose stream test (where hose stream applied immediately after test for duration of half the fire resistance period. Hose stream not required for fire resistance level of less than 1 hour). Failure if opening that permits projection of water from steam beyond unexposed face.	Average unexposed face temperature increases by more than 139°C Temperature at any location on unexposed face exceeds 30% of 139°C (i.e. 180°C).

(note: first visible row top shows "25mm gap gauge can penetrate into the furnace.")

For integrity, the sustained flaming criteria is the same for the British, Australian and European standards. The American Standard does not include criteria on sustained flaming. The cotton pad test is similar for each standard. The British Standard however does not require the pad to be applied for as long (approximately only half the time period) as the other test standards. This would suggest that there is potential that the cotton pad may ignite earlier in the European, Australian and American standards. The gap gauge criterion is the same for the British, Australian and European standards. The American Standard does not include any criteria using gap gauges. The American Standard appears to be the only standard that applies the hose stream test as a failure criterion.

The insulation criteria is the same for all standards i.e. average temperature rise of 140°C or a single point rise of 180°C. The British standard makes reference to failure of integrity also resulting in failure of insulation. It is considered that this would be an implied failure irrespective of being explicitly listed in the other standards.

Accordingly, with respect to the failure criteria, the British, European, Australian and American standards are broadly equivalent. The British standard may be considered marginally less onerous as a result of its reduced required time for application of the cotton pad. The American test standard may be considered marginally less onerous in that it does not apply the gap gauges required by the other standards, however it does require a hose stream test to be administered which is not required by the other standards.

Whilst deflection is not stated as a failure criterion, significant deflection of a non-loadbearing wall would impact on its fire resistance performance. It is assumed that deflection is not stated as a failure criterion on the basis that if the wall deflects sufficiently, the specimen will fail the sustained flaming, cotton pad, or in the case of European, British and Australian standards, the gap gauge criteria. In the British, European and Australian standards, deflection is noted as a criterion that may be measured. The purpose of this is for extending the potential application of the test results as this information is useful for evaluating increases in wall height for example. The American Standards do not appear to allude to measurement of deflection for non-loadbearing tests.

3.6 Reporting requirements

Understanding the test reports is important for assessing the specimens achieved fire resistance level, as this information is what is presented as a record of the test and the means of evidencing the fire resisting performance of the specimen, and is the information that will be used to determine if elements are compliant for use in a design.Table 6 **6**shows the main items required in the testing reporting of each of the standards.

Table 6 6: Summary of the main reporting requirements across the subject standards [1][2][4][7][9][10]

Standard	British Standards BS 476-20	Australian Standards AS 1530.4	European Standards EN 1364-1:2015 (follows EN 1363-1)	American Standards ASTM E119	American Standards UL 263

Name, Date address of testing laboratory, accreditation	Yes	Yes	Yes	Yes	Yes
Name of manufacturer of specimen	Yes	Yes	Yes	Yes	Not specified
Description of the test specimen	Yes	Yes	Yes	Yes	Yes
Loadbearing elements and load applied to the test specimen	Yes	Yes	Yes	Yes	Yes
Support and restraint conditions employed and the rationale	Yes	Yes	Yes	Yes	Yes
Location of the location of the thermocouples	Not specified	Yes	Yes	Yes	Yes
Pressure measurements and deflection measurement devices	Yes	Yes	Yes	Yes	Yes
Laboratory Ambient conditions	Yes	Yes	Yes	Yes	Not specified
Pressure conditions within the furnace	Yes	Yes	Yes	Not specified	Yes
Temperature and time curves of the furnace hearing conditions	Yes	Yes	Yes	Yes	Yes
Description of any significant behaviour	Yes	Yes	Yes	Yes	Yes
Deflections	Yes	Yes	Yes	Yes	Yes
Disclaimer	The results only relate to the behaviour of the specimen of the element of construction under the particular conditions of test; they are not intended to be the sole criteria for assessing the potential fire performance of the element in use or do they reflect the actual behaviour in fires		Because of the nature of fire resistance testing and the consequent difficulty in quantifying the uncertainty of measurement of fire resistance, it is not possible to provide a stated degree of accuracy of the result.		

All five standards consider the same information in their test reports, with minor discrepancies. The European and Australian report exactly the same information, while the British standard, although is very similar, does not explicitly require the location of where the thermocouples were installed during the test to be reported. The American Standards are similar, except that ASTM E119 does not require pressure conditions within the furnace to be documented, and the UL 263 testing report does not require the name of manufacturer nor ambient pressure conditions of the tests, to be indicated.

4. CONCLUSION

The key findings from the review of key criteria from the subject tests standards are as follows:

Furnace geometry: The British Standard provides the strictest requirements regarding the furnace build-up. The rest of the standards do not specify any requirements at all, which allows for a big variability between different furnace build-ups. The European and Australian standards require the same conditions for the material lining, while the British standard appear to be closely aligned, providing same material thickness but characterising the material in terms of the thermal inertia, rather than a density. The American standards do not prescribe any requirements in terms of the material lining, allowing for any material to be installed as the furnace lining, which could potentially affect the final outcomes of the tests. The lack of consistency between the requirements of furnace size, geometry and lining materials within the same standard may lead to a poor level of repeatable testing conditions among different furnaces. This variability can lead to changes to the heat transfer conditions that depend on the geometry and size of the furnace as well as the material wall linings, burner design, and fuel among other variables.

Heating regime: Specimens tested against the ISO 834 time-temperature curve (used in the British, Australian, and European Standards) will be exposed to higher temperatures earlier in the test than specimens tested against the ASTM curve used in the American standards. This may result in a greater chance of failure, particularly between 90 min and 360 min when specimens qualify for many fire resistance levels.

Pressure regime: The European, British and Australian standards generally provide similar pressure requirements. Although some minor differences are identifiable their impacts are expected to be negligible. The American standards do not prescribe explicit pressure requirements for furnace testing. The pressure received by a specimen tested against the European, British and Australian standards could be considered equivalent, as it can be assumed that similar conditions would be applied to any non-loadbearing wall fire resistance test. On the other hand, as no pressure criteria is provided for the fire resistance tests under the American standards, the specimen tested could be subjected to variable pressure conditions that could influence its performance. This variability could affect and compromise the failure criteria of the specimen tested.

Instrumentation: A five-thermocouple array is required across all the standards to take an average temperature across the specimen. The American standards recommend at least four additional thermocouples to be placed at the discretion of the testing authority to help determine an average temperature measurement across the specimen, whereas the British, European and Australian Standards require additional thermocouples to measure the maximum temperature rise. The European and Australian Standards specify explicit locations in near identical terms, whereas the British Standard leaves it to the discretion of the testing authority. Regarding pressure readings, the Australian and European Standards again use near identical wording, the British standards deviates somewhat, UL 263 provides detailed guidance and whereas ASTM E119 provides none. For deflection, the British, European and Australian Standards advise that deflection measuring equipment be applied to the specimen, with varying degrees of specificity but with the implied aim of measuring the maximum deflection experienced by the specimen. The US standards include no such requirement.

Failure Criteria: The British, European, Australian and American standards all utilise similar failure criteria. The European and Australian standards are most closely aligned (utilising the same failure criteria) and both deviate in minor ways from the British standard, which does not require the cotton pad to be applied for as long a duration (10-15 in seconds instead of 30 seconds in European, American and Australian tests). The American standards do not include the use of gap gauges as a means of demonstrating failure of integrity, which the European, British and Australian standards do. The American standards require a hose stream test to be applied. The relevance of this is unclear. It is assumed that the application of the hose stream test is relevant for when fire brigade intervention occurs, at which point it is likely that occupants will have evacuated the compartment of fire origin. The hose stream test therefore offers additional information on the continued performance of the compartment wall that may relate to fire-fighting operations within a fire compartment, rather than for containment of a fire for occupant safety.

Reporting requirements: The European and Australian standards require identical information in their test reports. The British standard, while very similar, does not explicitly require the report to document the location of where thermocouples were installed during the test. The American Standards are similar, however ASTM E119 does not require pressure conditions within the furnace to be indicated, and UL 263 does not require the name of the manufacturer, or the ambient pressure conditions of the test, to be recorded.

In sum, the European and Australian Standards are highly consistent with one another. This is suspected to be a result of their close respective relationships with the International Standards Organization and accordingly with the ISO 834 standard. A direct comparison to the ISO 834 standard would be required to confirm this hypothesis. The British Standard is also very similar to the European and Australian Standards but deviates more consistently in subtle ways from the other two. The American Standards differ the most relative to the other standards. While they correlate very closely with one another, the requirements under these tests are generally more discretionary when compared with the requirements outlined in the European, Australian and British tests for the test criteria investigated for non-loadbearing walls.

This comparative review intends to launch a broader discussion on the comparability of the subject test standards, in order that the equivalency of the standards may be explored, which could open and avenue for jurisdictions to permit more than one test standard as a means demonstrating product compliance. To fully realise this objective, further research is needed to comprehensively expand upon this study's conclusions. Other elements of

construction that are subjected to fire resistance testing should be compared, including loadbearing elements, floors, ceilings, windows, doors and service penetrations. Other potential variables within the testing regimes that could have an impact of the severity of the test should be scrutinized e.g. heat source and control e.g .fuel types, ventilation requirements, and specimen setup e.g. curing times. Other fire resistance testing standards could be included; for example, a focused comparison between the European and Australian Standards to ISO 834 (which is understood to be adopted in many countries) would be illuminating and would help to frame the global influence of ISO 834. It is expected that there are many nationally specific standards, akin to the Australian Standard explored in this study, that would have their roots in one of the standards investigated in this study.

REFERENCES

[1]   European Committee for Standardization. (2020). *EN 1363-1: 2020 Fire resistance tests Part 1: General Requirements.* CEN-CENELEC.

[2]   European Committee for Standardization. (2015). *EN 1364-1: 2015 Fire resistance tests for non-loadbearing elements – Part 1: Walls.* CEN-CENELEC.

[3]   British Standards Institution. (2014). *BS 476-10:2009 Fire tests on building materials and structures – Part 20: Guide to the principles, selection, role and application of fire testing and their outputs.* BSI Standards Limited.

[4]   British Standards Institution. (2014). *BS 476-20:1987 Fire tests on building materials and structures – Part 20: Method for determination of the fire resistance of elements of construction (general principles).* BSI Standards Limited.

[5]   British Standards Institution. (2014). *BS 476-22:1987 Fire tests on building materials and structures – Part 22: Method for determination of the fire resistance of non-loadbearing elements of construction.* BSI Standards Limited.

[6]   Law, Angus & Bisby, Luke. (2020). *The rise and rise of fire resistance.* Fire Safety Journal. 116. 103188. 10.1016/j.firesaf.2020.103188.

[7]   Standards Australia. (2014). *AS 1530.4:2014 Methods for fire tests on building materials, components and structures, Part 4: Fire-resistance tests for elements of construction.* Standards Australia.

[8]   Standards Association of Australia. (1958). *AS No. A30-1958 Fire Tests of Building Materials and Structures.* Standards Association of Australia.

[9]   ASTM International. (2022). *ASTM E119 – Standard Test Methods for Fire Tests of Building Construction and Materials.* ASTM – ASTM International.

[10]   Underwriters Laboratories Inc. (2022). *UL 263 Standard for Fire Tests of Building Construction and Materials.* Underwriters Laboratories Inc.

[11]   National Fire Protection Association. (2021). *NFPA 101: Life Safety Code 2021.* National Fire Protection Association.

[12]   International Code Council, Inc. (2020). *2021 International Building Code.* International Code Council, Inc.

[13]   Gales, J., Chorlton, B. & Jeanneret, C. (2021). *The Historical Narrative of the Standard Temperature–Time Heating Curve for Structures.* Fire Technology. vol. 57, pg. 529–558.

[14]   Keough J.J. (1976). *Design of Furnaces for Testing Fire Resistance of Structures.* Experimental Building Station, Australia, 6pp.

[15]   Harmathy, T. & Sultan, M & MacLaurin, J. (1987). *Comparison of severity of exposure in ASTM E 119 and ISO 834 fire resistance tests.* Journal of Testing and Evaluation. 15. 10.1520/JTE11036J.

[16]   Harmathy, T.Z. (1969). *Design of fire test furnaces.* Fire Technology. vol. 5, pg. 140-150.

[17]   Maluk, Christian & Bisby, Luke. (2012). *120 years of structural fire testing: Moving away from the status quo.* 2nd Fire Engineering Conference, Valencia, Spain.

[18]   International Organization of Standardization. (1999). *ISO 834-1 Fire Resistance Tests – Elements of Building Construction – Part 1 General Requirements.* International Organization of Standardization.

HORIZONTAL SEPARATION REQUIREMENTS TOWARDS FIRE SPREAD REDUCTION BETWEEN ADJACENT DWELLINGS: A NUMERICAL ASSESSMENT

Felipe R. Centeno[a]*
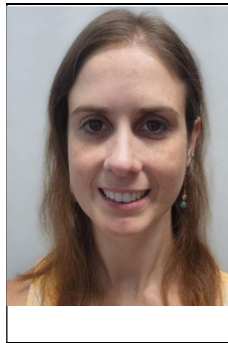
Liuá Hauser[b]

Rodolfo P. Helfenstein[c]

ABSTRACT

The present work aims to establish a comparative analysis between different horizontal separation requirements provided in Technical Resolution 04 of CBMRS [1] to evaluate their effectiveness to reduce or, ideally, prevent the fire spread between adjacent neighboring dwellings (horizontal fire spread) using numerical modeling. To carry out the numerical study the Fire Dynamics Simulator (FDS) software was used, going through a rigorous validation process, using experimental data to verify its ability to simulate the studied scenarios. The results showed that the case with the safest conditions was represented by Case 05, which introduces a wall of 0.9 m width between the adjacent doors acting as a passive fire spread barrier. For aligned doors, the increase from 1.2 m (Case 01) to 2 m (Case 02) between the doors did not seem to be effective to maintain the fire safety level as fire loads increased from medium to high. Parallel/facing doors (Case 03), even distanced 5 m as required in RT-04 of CBMRS, proved to be the most dangerous scenario, with the highest heat fluxes on the adjacent door. A performance-based design would be recommended for high risk buildings (e.g. buildings with high fuel and/or people densities, buildings difficult to evacuate, etc.).

Keywords: Fire spread; Fire regulations; Building fires; FDS.

---

[a]* Federal University of Rio Grande do Sul (UFRGS), Professor at the Mechanical Engineering Department and at the Fire Safety Engineering Graduate Program (frcenteno@mecanica.ufrgs.br), corresponding author

[b] Federal University of Rio Grande do Sul (UFRGS), Graduated in Fire Safety Engineering Graduate Program (liuahauser@gmail.com)

[c] Federal University of Rio Grande do Sul (UFRGS), PhD Student at the Mechanical Engineering Department (rodolfo.helfenstein@ufrgs.br)

1. INTRODUCTION

The increase in world population brings as one consequence higher densities of people living in cities. It turn, this reveals a challenge for urban planners in terms of housing due to building agglomeration and higher fire risk. Fire Departments have been figuring out how to deal with such danger and in many cases, they provide regulations and technical instructions to guide engineers and architects to design safer buildings. One of these technical regulations [1] focuses on separation distances between buildings and specification of materials types and fire loads in order to avoid or minimize fire spread between adjacent buildings.

The present paper aims to assess the effectiveness of the requirements specified by [1] to reduce or, ideally to avoid, fire spread between adjacent neighboring buildings (horizontal fire spread). This is performed using the software FDS [2] by means of numerical simulations and thermal engineering analysis based on fire spread mechanisms.

2. METHODOLOGY

Initially, the experimental study of [3] was numerically modeled as a validation step, to demonstrate the ability of the software to reproduce this kind of scenario and that the results provided are reliable by comparing experimental data to numerical results. A fire model software known as Fire Dynamics Simulator (FDS) was used, which is widely used by fire safety engineers worldwide to carry out numerical studies. After that, six different cases were considered, following the specification of [1], with the aim of evaluating the effectiveness between different requirements of horizontal separation used to reduce or, ideally, prevent the spread of fire between adjacent neighboring buildings (horizontal fire spread), through the analysis of temperature, heat flux and flame length measurements obtained numerically using FDS.

FDS is a widely used and well established software for fire engineering applications. It is an open source CFD (computational fluid dynamics) software developed by the NIST/USA and VTT/Finland. FDS solves numerically a form of the Navier-Stokes equations for low Mach numbers (Ma < 0.3), using Large Eddy Simulation (LES) methodology as a turbulence modeling approach. A more detailed description of the software, equations and models can be found in [2].

2.1 Problem statement and numerical modeling

To carry out the FDS numerical model validation step, part of the experimental study performed by [3] was used. The experiment had three different compartments, made of fiberboard walls, with a front face of 0.5 m x 0.5 m with depths of 0.5 m, 1.0 m and 1.5 m, in modules of 0.5 m x 0.5 m x 0.5 m. The openings, positioned in the middle of the front wall (façade), had four different sizes (width x height): 7.5 cm x 20 cm, 10 cm x 25 cm, 20 cm x 20 cm and 30 cm x 10 cm. Propane and methane rectangular burners were the heat source with heat release rate (HRR) of 30 kW, 40 kW, 50 kW and 60 kW. Flame height was measured using a CCD camera facing the façade.

As the purpose of the validation step is to verify the software ability to predict the studied parameters, which will be used to carry out the tests with the modeling described by [1], only one module was submitted to the validation process. The module was rectangular of size 0.5 m x 0.5 m x 0.5 m. The opening at the front wall (façade) was considered with three different sizes (width x height): 0.1 m x 0.25 m, 0.2 m x 0.2 m and 0.075 m x 0.2 m. All characteristics of the experimental setup of [3] were reproduced in FDS. The obstructions (walls and ceiling) were defined as "EXPOSED" in FDS, so that the model could calculate heat fluxes and temperatures. Thermal properties of the material are shown in Table 1.

Table 1: Wall and ceiling thermal properties

Material	Density (kg/m³)	Conductivity (W/m.K)	Specific heat (kJ/kg.K)
Fiberboard	200	0.1	1.0

Temperatures and heat fluxes were obtained from FDS as outputs, while the numerical size of the venting flames (emerging from the door opening) was obtained from Smokeview, defining the temperature at 550 °C and opacity at 0.01 m.

2.2 Domain, Mesh resolution and Numerical model validation

The influence of the computational domain extension in fire modeling has been studied by [4] and [5]. The studies showed that the domain extension produces a better agreement with the experimental data, recommending the extension in the value of one hydraulic diameter of the opening, in the perpendicular direction. Thus, the domain size for the validation cases was defined as 1.0 m x 0.7 m x 1.7 m, using a higher domain extension than recommended.

The fire community uses a widely known method to estimate the mesh control volume size, called the characteristic fire diameter, $D*$ [2]. According to [6], the ratio between the characteristic fire diameter and the mesh size, $D*/\delta x$, with values ranging between 4 and 16 provides an adequate mesh resolution.

$$D^* = \left(HRR/\rho_\infty T_\infty c_p \sqrt{g}\right)^{\wedge}(2/5) \tag{1}$$

where HRR is the heat release rate, ρ_∞ is the density of the ambient fluid, T_∞ is the ambient fluid temperature, c_p is the fluid specific heat and g is the acceleration of gravity.

Table 2 presents the values of $D*$ and $D*/\delta x$ for the two evaluated meshes (δx = 5 cm and δx = 2.5 cm), considering four HRR's (30 kW, 40 kW, 50 kW and 60 kW), which were used in the numerical experiment, and Figure 1 represents the numerical model submitted to the validation process, using an opening of 0.1 m x 0.25 m and HRR of 50 kW, for a mesh of 2.5 cm.

Table 2: Mesh analysis for the validation cases

HRR (kW)	$D*$ (m)	$D*/\delta x$	
		δx = 5 cm	δx = 2.5 cm
30	0.24	4.7	9.4
40	0.26	5.3	10.6
50	0.29	5.8	11.5
60	0.31	6.2	12.4
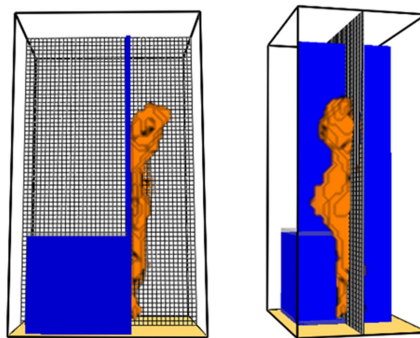
Figure 1: Numerical model for a 0.1 m x 0.25 m opening and HRR of 50 kW, using a mesh of 2.5 cm

As can be seen in Table 2, all tested meshes were adequate according to [6] criteria. As both meshes are within the suggested range of values, a sensitivity analysis of the meshes was performed, in which the numerical results of the flame heights were compared to the experimental data. The comparison between them is shown in Figure 2.

Analyzing the results presented in Figure 2, it is noted that both meshes (δx = 5 cm and 2.5 cm) provided similar results when compared to the experimental values, with deviations of less than 5% for scenarios with HRR 30 kW, 40 kW and 50 kW, and of about 20% for the case with HRR = 60 kW. Thus, it can be considered that the numerical model represents the fire phenomenon with good precision with an acceptable computational effort, being suitable for carrying out the remaining of this numerical study.
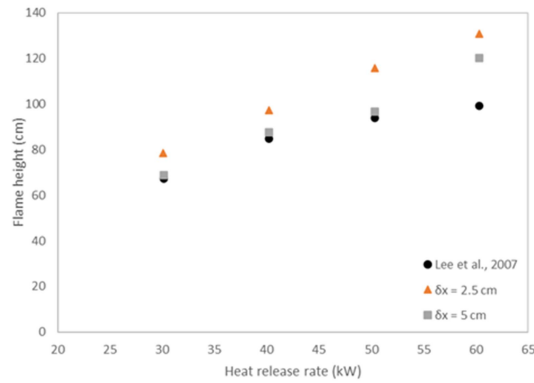
Figure 2: Mesh sensitivity analysis of the flame height for a validation case

2.3 Case study of RT-04 of CBMRS

The case study of Technical Resolution 04 (RT-04) of CBMRS (*Corpo de Bombeiros Militar do Rio Grande do Sul*) [1] encompass numerical simulations to analyze the horizontal separation criteria between dwellings.

Buildings geometries and fire loads are based on specifications provided in [1] regarding horizontal fire spread. Two adjacent dwellings are considered, each one with 25 m² of floor area and 3 m high; there is one wall that is shared between the dwellings. They have a door measuring 1.3 m x 2.2 m each. The room in which the fire load is placed will be called the *fire room* and the room next to it will be called the *adjacent room*. The problem was modeled considering brick walls and the ceiling and floor of concrete, thermal properties of the materials are presented in Table 3. In all cases, the fire was modeled as a square burner with dimensions of 3 m x 3 m (represented in red in the figures of Table 4), using propane as fuel with a heat of combustion of 46.46 MJ/kg.

Table 3: Thermal properties applied to the numerical model to study RT-04

Material	Density (kg/m³)	Conductivity (W/m.K)	Specific heat (kJ/kg.K)
Concrete	525	0.125	1.05
Brick	1600	0.69	0.84

For each fire scenario, fire loads are considered as 300 MJ/m² (low risk), 750 MJ/m² (medium risk), 1200 MJ/m² (high risk); thus, the HRRPUA (heat release rate per unit area) was calculated according to the fire loads: 231.481 kW/m² (low), 578.703 kW/m² (medium), 925.93 kW/m² (high). The time used to calculate the HRRPUA was one hour. Table 4(a)-(f) illustrates six cases that will be studied in this paper, for each fire load, totalizing 18 scenarios. These 6 cases represents the 6 cases mentioned in Paragraphs 5.3.5 and 5.3.6 of RT-04 [1], as the 3 fire loads were also selected to encompass the full range of dwellings configurations and fire loads as mentioned in Paragraphs 5.3.5 and 5.3.6 of RT-04 [1].

Table 4: Dwellings' geometries and plan view of each case to study RT-04

Case ID	Numerical domain / Buildings geometries in FDS	Plan view
Case 01		

Case 02
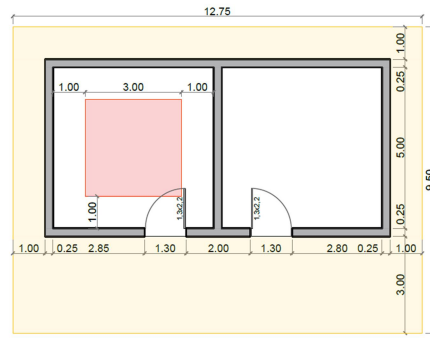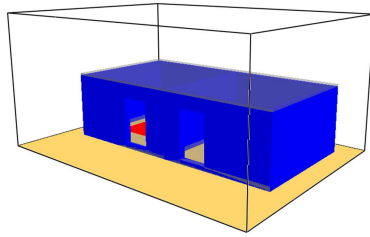
Case 03

Case 04

Case 05

582
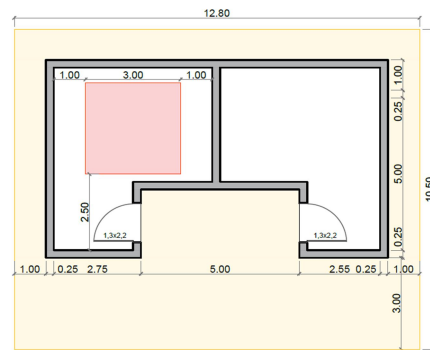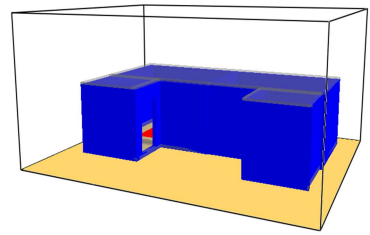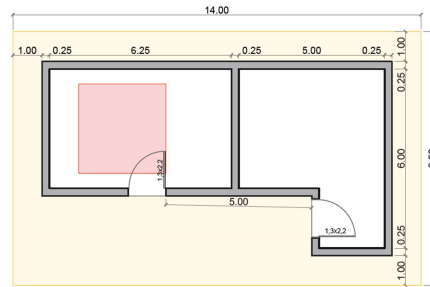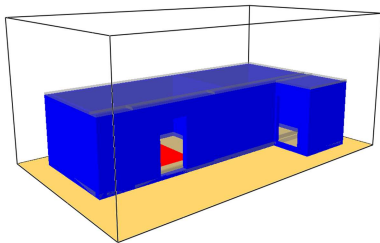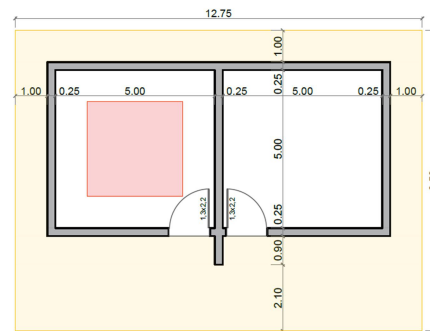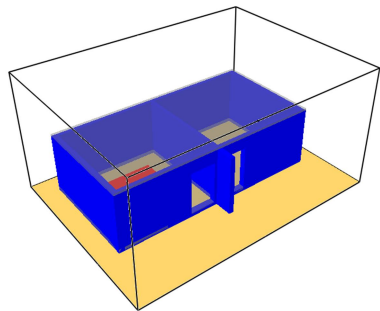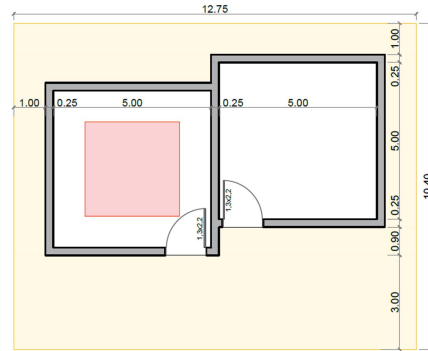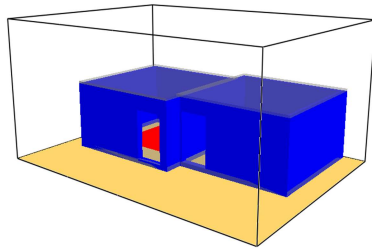
The temperature values were obtained through analysis/verification of slices. Heat flux was measured at the center of the adjacent room door. Measurements were performed at 900 s for low risk and 600 s for medium and high risks. The simulations were run until 1000 s for low risk cases and 700 s for medium and high risk cases. Since FDS computes all parameters temporally (transient model), all results shown and analyzed in this paper were time-averaged for a time-interval of 100 s after the parameter stabilized in time (after a quasi-steady state condition was reached).

The mesh used in the studies of RT-04 was composed of two control volume sizes: 5 cm in front the fire room opening (door), and a coarser mesh, 10 cm, in the other regions of the domain, as shown in Figure 3. The most refined mesh in front of the door opening was chosen for more accurate results, as the objective was to analyze the venting flames through the door opening, its behavior and influence on the environment. This allowed the use of a coarser mesh in the rest of the domain, reducing the computational effort needed to run the simulations. Domain size was defined as 12.75 m x 9.5 m x 6.1 m, using domain extensions longer than that recommended by [4] and [5] in the direction in front of the door opening due to the venting flames.
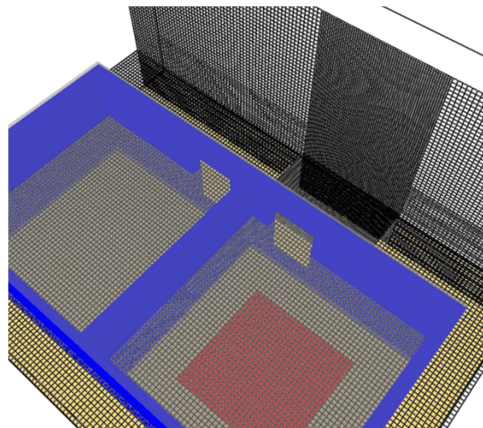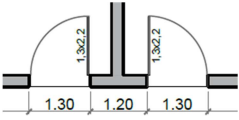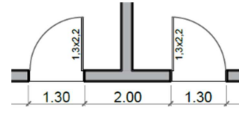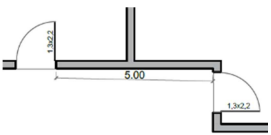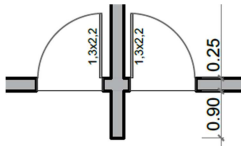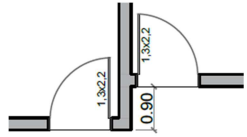
Figure 3: Numerical domain showing the two mesh refinements employed to study RT-04 (mesh is finer in front of the door opening and it is coarser in the remaining of the domain)

3. RESULTS AND DISCUSSIONS

For this study, the heat flux at the adjacent room door (H_{fa}), the distance from the flame tip (emerging from the fire room door opening) to the adjacent room door (L_a), and the temperature in the fire (T_f) and adjacent (T_a) room doors, were evaluated for each of the 18 scenarios mentioned (6 cases as mentioned in Table 4 x 3 fire loads = 18 scenarios). It is important to emphasize that Case 01 (see Table 4) configuration is valid for low and medium fire loads according to RT-04 CBMRS [1], not being applied for high fire loads; however, this condition was also simulated for comparison purposes. Table 5 presents the results obtained for each one of the 18 scenarios studied in this work.

583

Cases 1 and 2 have almost the same layout, the difference between them is the distance between doors on the same wall plane, the distance for Case 01 is 1.2 m and for Case 02 is 2 m. Analyzing the obtained results for these cases in Table 5, it can be noted that with the fire load increase there is a heat flux increase at the adjacent room door, for both cases, the measured values in Case 02 being smaller due to the larger separation distance between the doors. An illustration of the emerging flames for these cases is shown in Figure 4. Since RT-04 CBMRS [1] specifies a distance of 1.2 m for low and medium fire loads, which is represented here by Case 01, and it specifies a distance of 2 m for high fire loads, which is represented here by Case 02, it is implied that [1] intends to keep the same level of safety in terms of fire spread by increasing the distance between the doors as the fire load increases. Comparing the heat flux of Case 01 for the medium fire load, 0.44 kW/m², and Case 02 for a high fire load, 0.92 kW/m², it can be seen that increasing the distance between the doors would not be enough to compensate the fire load increase as suggested in [1], although those relatively low heat fluxes would not be enough to ignite nearby materials.

Table 5: Numerical data obtained for each case studied

Case ID		Fire load	T_f (°C) *	T_a (°C)	L_a (m)	H_{fa} (kW/m²)
Case 01		Low	400	-	1.20	0.11
		Medium	700	-	0.96	0.44
		High	800	-	0.96	1.26
Case 02		Low	400	-	2.00	0.06
		Medium	750	-	1.01	0.25
		High	900	-	1.01	0.92
Case 03		Low	450	21.3	5.00	0.17
		Medium	800	25.9	2.68	1.29
		High	900	33.7	2.29	3.70
Case 04		Low	500	20.4	5.00	0.05
		Medium	700	21.7	4.66	0.31
		High	850	23.7	4.69	0.85
Case 05		Low	500	20.3	0.90	0.03
		Medium	750	21.1	0.90	0.11
		High	850	23.3	0.90	0.33
Case 06		Low	400	20.7	0.90	0.09
		Medium	750	22.7	0.90	0.39
		High	850	26.5	0.90	0.99

(a) Case 01, medium fire load   (b) Case 02, high fire load
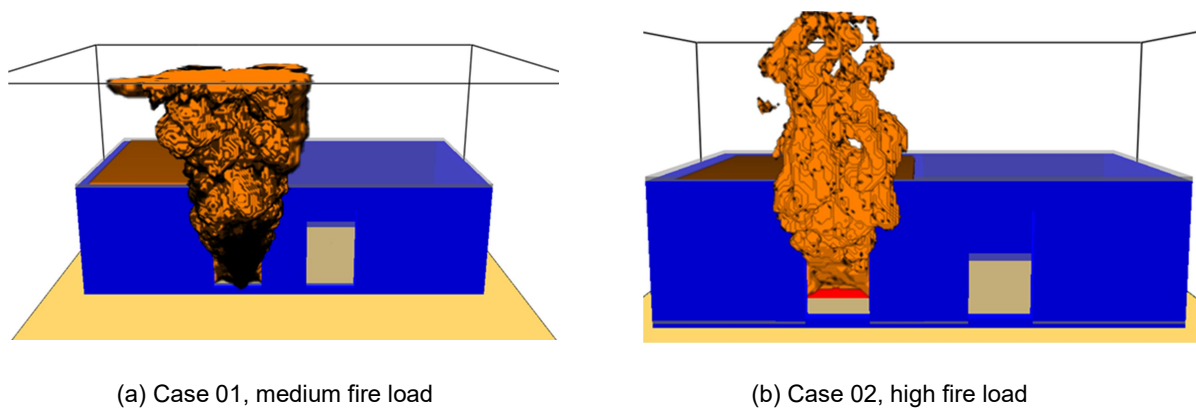
Figure 4: Comparison between Case 01 (medium fire load) and Case 02 (high fire load)

Evaluating the results for Case 03, doors on parallel-facing walls, distanced 5 m, it can be noted that the fire load increase leads to an increase in the temperature and heat flux at the adjacent room door. It is assumed that this behavior occurred due to the architectural configuration and the fire position in relation to the opening of the fire and adjacent room, since, with the fire load increase, the flame moves closer to the adjacent room, as illustrated in Figure 5, increasing the temperature and heat flux of the region. Considering a high fire load, the heat flux measured at the door in front of the fire room (adjacent room door) reached 3.70 kW/m² (the highest measured value in this work) and for a medium fire load 1.29 kW/m² was obtained. Comparing the heat flux results, for a medium fire load, between Case 01 (0.44 kW/m²), Case 02 (0.25 kW/m²) and Case 03 (3.7 kW/m²), it is evident that for Case 03 (doors on facing walls) the distance should be even greater than 5 m due to the high heat flux measured at the adjacent room door, which is almost fifteen times greater than that obtained in Case 02.

(a) Low fire load   (b) High fire load
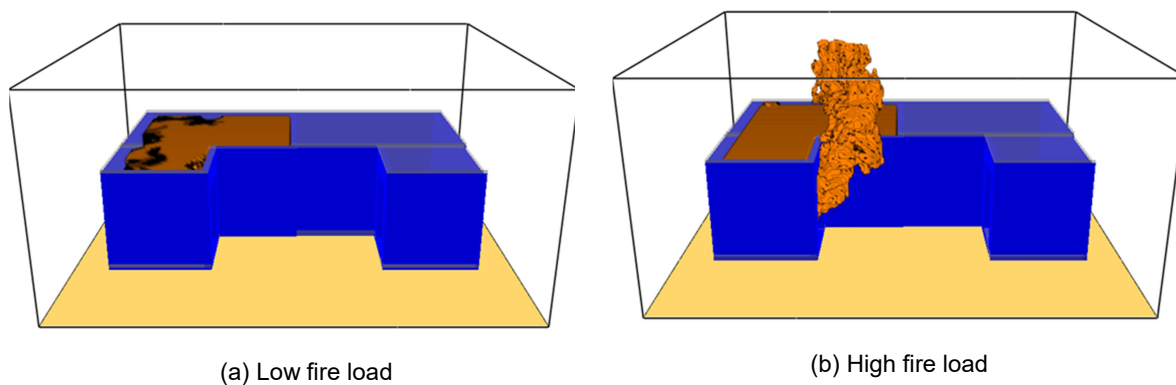
Figure 5: Behavior of the fire load increase in Case 03

The results obtained for Case 04, doors on perpendicular walls, distanced 5.0 m, presents the same trends as the other cases (heat fluxes, temperatures and flame lengths are increased as fire loads increase). Comparing heat fluxes between cases with high fire load, Case 01 (1.26 kW/m²), Case 02 (0.92 kW/m²), Case 03 (3.7 kW/m²) and Case 04 (0.85 kW/m²), it can be noted that, while the distance between doors for Case 03 should be greater than 5 m, the distance between doors for Case 04 is adequate when compared to Case 01 and Case 02, because, even with the adjacent room door facing the flame, it is not facing the neighboring fire room door, so the distance between them compensated the fire load increase, as can be seen in Figure 6.

(a) Case 02   (b) Case 04
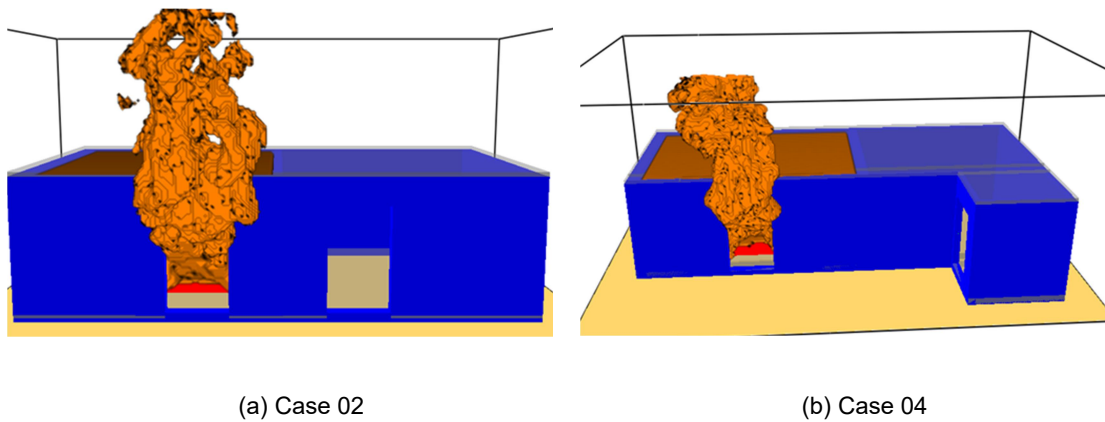
Figure 6: Comparison between Case 02 and Case 04, with high fire load

Case 05 is similar to Cases 01 or 02, but it includes a wall extension of 0.9 m width between the doors (which in turn are located in aligned walls). This case obtained the best results among those presented in Table 5 in terms of fire spread parameters. For instance, considering the heat flux for a medium fire load, Case 01 achieved 0.44 kW/m² compared to Case 05 which obtained 0.11 kW/m². For a high fire load, Case 02 reached 0.92 kW/m² compared to 0.33 kW/m² in Case 05. This occurred because the extended wall separating the compartments acts as a passive fire spread barrier, preventing the direct heat exchange between the flame and the adjacent room. Figure 7 illustrates this behavior by depicting Case 02 and Case 05 for a high fire load. Therefore, the application of this configuration is considered effective.

(a) Case 02   (b) Case 05
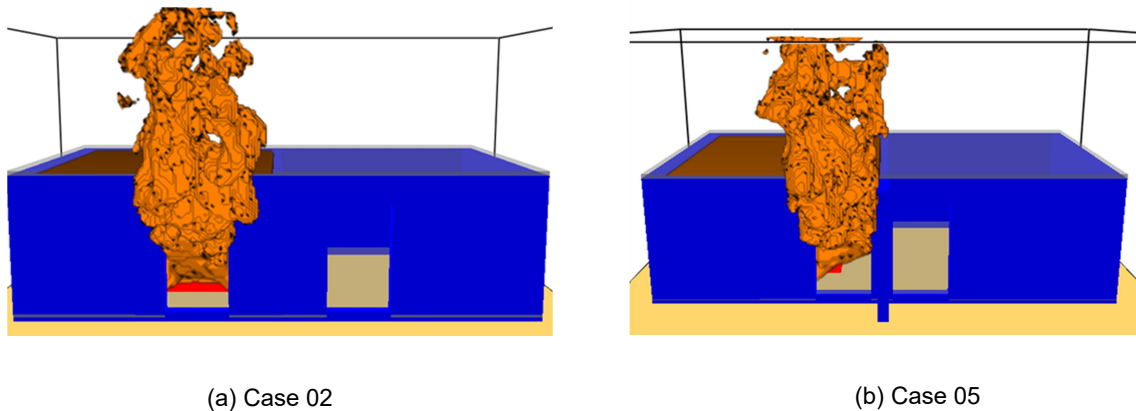
Figure 7: Comparison between Case 02 and Case 05, with high fire load

Finally, results of Case 06 are discussed, in which doors are on parallel walls, but walls are shifted 0.9 m. The fire room, compartment on the left, had its façade moved forward, thus, there was no contact of the flames with the door of the adjacent room, as illustrated in Figure 8. However, the temperature increase measured at the adjacent room door was higher than in previous cases. The heat flux measured at the adjacent room door was 0.39 kW/m² for a medium fire load. Comparing these results with Case 01 (0.44 kW/m²) and Case 02 (0.25 kW/m²), it can be concluded that, for this scenario in which the fire is positioned in the compartment with the facade shifted 0.9 m forward, the configuration presents satisfactory results. However, if the fire was in the other room, the flame would be closer to the adjacent room door, which would significantly increase the temperature and heat flux measured, therefore, a wall shift greater than 0.9 m would be suggested (such scenario was not tested in the present work).
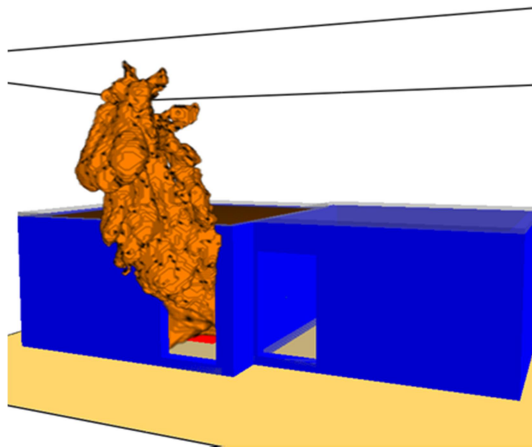
Figure 8: Case 06 flaming behavior for a high fire load

4. CONCLUSIONS

The Fire Dynamics Simulator (FDS) software was used to simulate different horizontal separation requirements of RT-04 CBMRS [1] to evaluate their effectiveness to reduce or prevent the fire spread between adjacent neighboring dwellings. It was found that the case with the safest conditions was represented by Case 05, which introduces a wall of 0.9 m width between the adjacent doors acting as a passive fire spread barrier. When comparing Case 01 (doors distanced 1.2 m, located in aligned walls) and Case 02 (doors distanced 2 m, located in aligned walls), it was shown that the increase from 1.2 m to 2.0 m would not be enough to maintain the fire safety in the adjacent room, so for high fire loads the distance should be greater. Case 03 (doors on parallel walls, distanced 5 m) was the most dangerous scenario, so attention should be paid when designing buildings with this topology; a fire barrier-like wall would be a recommended passive measure to protect neighboring rooms from fire. Despite these results are not final since other rooms/dwellings/fire configurations could be simulated, the presented results show that precaution should be taken when designing buildings based on requirements of RT-04 CBMRS; a performance-based design would be recommended for designing high risk buildings (e.g. buildings with high fuel densities and/or high people densities, buildings difficult to evacuate, etc.).

ACKNOWLEDGEMENTS

REFERENCES

[1] Soares Júnior, L. C., N. (2022). *Resolução Técnica CBMRS N.° 04 – Isolamento de Riscos*, Corpo de Bombeiros Militar do Rio Grande do Sul, 2022, p. 1-35.

[2] McGrattan, K.; Hostikka, S.; Floyd, J.; McDermott, R.; Vanella, M. (2022). *Fire Dynamics Simulator User's Guide*, Sixth Edition, NIST Special Publication, Gaithersburg, MD.

[3] Lee, Y.P., Delichatsios, M. A., & Silcock, G. W. H. (2007). *Heat fluxes and flame heights in façades from fires in enclosures of varying geometry, Proc of the Combustion Institute*, vol. 31, 2007, p. 2521-2528.

[4] He Y., Jamieson C., Jeary A., Wang J. (2008). *Effect of Computation Domain on Simulation of Small Compartment Fires*. Fire Safety Science – Proceedings of the International Symposium 9:1365-1376.

[5] Zhang X., Yang M., Wang J. (2010). *Effect of Computational Domain on Numerical Simulation of Building Fires*. Journal of Fire Protection Engineering 20: 225-251.

[6] Salley, M.H., Kassawara, R.P. (2007). *Verification and Validation of Selected Fire Models for Nuclear Power Plant Applications*, Volume 7: Fire Dynamics Simulator (FDS), U.S. Nuclear Regulatory Commission, Office of Nuclear Regulatory Research (RES), Rockville, MD.

REVIEW OF TEST METHODS FOR EVALUATING THE BEHAVIOUR OF BUILDING ROOF SYSTEMS SUBJECTED TO EXTERNAL FIRES

Deives J. de Paula[(a)a]; João Paulo C. Rodrigues[(b)]; Aline L. Camargo[(c)]; Rúben F. R. Lopes[(d)]

ABSTRACT

Mediterranean regions are characterised by areas where wildland vegetation intermingles with human settlements and industrial facilities, called wildland-urban interfaces (WUI) and wildland industrial interfaces (WII), respectively. Moreover, their climate conditions are prone to fire ignition and propagation in very flammable vegetation during specific periods of the year. In the current climate change and demographic expansion context, there is increasing attention on the WUI and WII, often considered one of the main drivers of fire risk to human lives and property. Therefore, improve fire safety measures in buildings in these areas are essential. After the 2017 forest fires in Portugal, one of the most critical aspects verified in studies post-fire relates to the type and location of structural ignition. More than 60% of the structures have been ignited due to incandescent particles (firebrands) depositions in different weak points, and more than 60% of these ignitions occurred on roofs. This occurs mainly because of the fire behaviour associated with the supporting structures and materials. This paper provides a comprehensive review of some studies and fire test methods to evaluate the fire performance in roof covering systems used in the US and EU standards for better understanding the test scenarios and their approaches. In addition, the underlying fire scenario, the test conditions, their criteria and application in local building regulations are discussed.

Keywords: roof systems, roof coverings, fire spread, external fires, fire reaction.

1.   INTRODUCTION

Mediterranean regions are characterised by areas where wildland vegetation intermingles with human settlements and industrial facilities, called wildland-urban interfaces (WUI) and wildland industrial interfaces (WII), respectively. Moreover, their climate conditions are prone to fire ignition and propagation in very flammable vegetation during specific periods of the year. In the current climate change and demographic expansion context, there is an increasing attention to the WUI and WII, often considered one of the main drivers of fire risk to human lives and property. Therefore, the improvement of fire safety measures in buildings in these areas is essential [1].

WUI fires have also revealed severe consequences. The acceptable roofing systems' behaviour towards fire to reduce the onset of fire in the building and avoid fire spread is a relevant topic. These fires have caused significant destruction to communities in Australia, Greece, Portugal, Spain, and US [2]. There have been relevant fire events

(a) University of Coimbra, CERIS, Itecons, Portugal, e-mail: deives.paula@itecons.uc.pt – Corrresponding author

(b) University of Coimbra, CERIS, Dep. of Civil Eng. and Itecons, Portugal, and Federal University of Minas Gerais, Brazil, e-mail:jpaulocr@dec.uc.pt

(c) University of Coimbra, CERIS, Itecons, Portugal, e-mail:aline.camargo@itecons.uc.pt

(d) University of Coimbra, CERIS, Itecons, Portugal, , e-mail: ruben.lopes@itecons.uc.pt

in California from 2003 to 2013 for example, the 2013 Cedar Fire. This fire resulted in 2 B$ in insured losses and destroyed over 3,000 homes [2]. The 2007 Southern California Fire displaced more than 300,000 people, destroyed over 1,000 structures, and resulted in 1 B$ paid by insurance companies [2].

The 2017 Greatest Forest Fires in Portugal affected wildland industrial interface areas, with more than 500 affected companies and estimated damage and loss of revenue value of 275 M€ [3]. One of the most critical aspects verified after these fires was that more than 60% of the structures had been ignited due to incandescent particles (firebrands) depositions in different weak points. More than 60% of these occurred on roofs [3]. These occur mainly because of the vulnerability associated with the supporting structures and materials. The building envelope structures are the first parts affected by external fires (Fig. 1).

a   b

Fig.1 – Damages in the building envelope in industrial sites affected by 2017' Greatest Forest Fires in Portugal [3]

This paper summarises the fire exposure scenarios for standards that evaluate external fire exposure in roof systems and roof covering in Europe and North America. In addition, their main parameters and factors influencing the testing methods are reviewed and discussed. They will be also presented the current status of the most used external fire testing methods to classify roof systems and contribute for a better understanding and a practical application of these requirements in buildings located in WUI areas.

2. EXTERNAL FIRE EXPOSURE SCENARIOS

The spread of an external fire to a roof system can cause damage to both the interior and exterior of a building. Combustible roof covering materials may generate burning droplets, which can penetrate the roof system, propagate to exterior facades, or even ignite other exposed combustibles inside the building, causing new fires. Even during construction or rehabilitation, some roof components with combustible properties are particularly vulnerable to fire. Therefore, contractors using torch welding or any hot work during installation should be aware of the fire risks associated with handling or assembling these materials.

Depending on where the roof system is installed, assessing external fire risks should consider the most likely fire exposure scenario. For example, in some standard test methods, roof decking and their underlying insulation are exposed to radiation heat or a small fire load consisting of an open flame and an airflow across the surface or combined. Also, these roofing systems are qualified and limited by the maximum slope in which it was tested.

The existing test methods in Europe and North America have different parameters and characteristics, each intending to simulate specific exposure conditions [4]. These parameters are the fire scenario, fuel source, the radiant heat flux on the tested surface, the airflow across the specimen, specimen dimensions and the roof system slope conditions, as presented in Table 1.

CEN/TS 1187 [5] fire tests have four different approaches, as following: Test 1 - burning brands only (Fig. 2.a); Test 2 - burning brands with wind (Fig 2.b) ; Test 3 - burning brands, wind and supplementary radiant heat (Fig 2.c [6]); and Test 4 - Two stage method with burning brands, wind and supplementary radiant heat (Fig 2.d).

ASTM E108 [7] is the primary test method used in North America to evaluate external fire exposure in roofing systems. The technical basis of UL790 [8], NFPA 256 [9] and CAN/ULC-S107 [10] standards are similar. There are four different fire exposure conditions in ASTM E108 test method to address the behaviour of roof coverings:

intermittent flame, the flame spread, burning brand and flying brand tests. The flame spread test consists in applying a luminous gas flame burner at the edge of the specimen (1.0 m side), and the specimen is installed inclined with an airflow of 5.3 m/s. The burning brand test simulates various sizes ranging from 9.25 g to 2000 g (depending on which class is intended to evaluate) of burning embers landing on the surface of the roof covering. The intermittent flame test is a series of on/off flame exposures over a specified period. The propensity of the roof covering burn-through occurrence under the combustible deck is assessed with these two tests.

Table 1 - External fire exposure to roofs: test details

| | ASTM E-108 | CEN / TS 1187 | | | |
		Test 1	Test 2	Test 3	Test 4
Fire Scenario	Four fire exposure conditions: intermittent flame, spread of flame, burning brand and flying brand.	Burning brand only and with no imposed airflow over the roof.	Burning brand only and with an imposed airflow over the roof of either 2.0m/s or 4.0m/s.	Burning brand as well as radiation and with an imposed airflow over the roof of 3.0 m/s.	Burning brand (Stage 1) and then a penetration test with burning brand, radiant heat and wind (Stage 2).
Fuel Source	Spread of flame and intermittent flame test: Gas Burner Burning Brand test: Class A: 1 brand 2kg. Class B: 2 brands 0.5kg. Class C: 20 brands 9.25g	650+50g of wood wool in a steel mesh basket suspended 10mm from surface	Wood crib consists of eight pieces 10x10x100mm nailed together. Total weight 40g	Four fiberboard brands with 250 kg/m^3, with 55x16x25mm soaked in heptane. Wood crib weight: 82g. Radiant panel is positioned 500mm away parallel to the specimen.	The burning brand (Stage 1) is a gas flame 230mm long. Radiant panel positioned in a plane parallel to the surface. (Stage 2) with 915mm^2.
Radiant Heat Flux	-	-	-	12,5±0,5 kW/m^2	12±1,5 kW/m^2
Length and width of specimen	Intermittent flame/burning brand: 1.0m x 1.3m Spread of flame: A = 1.0m x 2.4m B = 1.0m x 2.7m C = 1.0m x 4.0m	1.8m x 0.8 m	1.0m x 0.4 m	3.0m x1.2 m	0.84m x 0.84 m
Roof slope	Max slope specified by manufacturer: 416mm/m	15º apply for a slope between 0 – 20º. 45º apply to a slope higher than 20º	30º	15º apply for a slope between 0 – 10º. 30º apply for a slope higher than 10º.	0º apply for a slope between 0 – 10º. 45º apply for a slope higher than 10º.

The dimensions of the specimens and their assembling characteristics have a relevant influence on bench-scale methods and are different between them. For example, in ASTM E-108 tests, the specimen length can vary from 2.4 m to 4.0 m according to the intended classification (A, B or C Class) and the width is 1.0 m. Otherwise, specimens need to be assembled in CEN TS 1187 Test 1 with a minimum of 0.8 m in width and 1.8 m in length and have a possibility to test roof lights with specific requirements. They shall be representative of all practical application details. In the Tests 3 and 4 apparatus the test specimen's dimensions are limited to test setup, and some situations could be impractical to evaluate (*e.g.* roof lights in real scale).
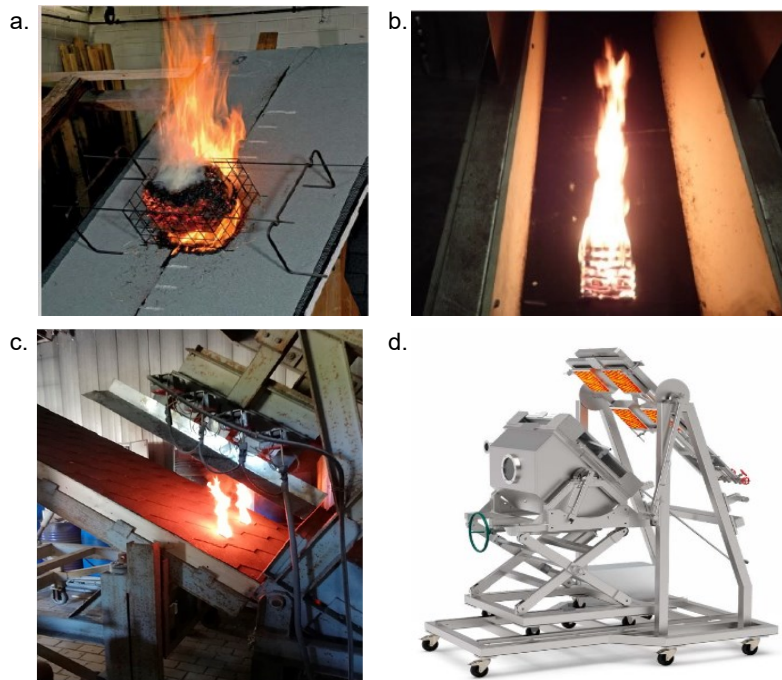
Fig. 2 – CEN TS 1187 test apparatus:
a. Test 1 [11]; b. Test 2 [12]; c. Test 3 [6]; d. Test 4 [13]

In the WUI areas, three types of forest fire attack must be considered when trying to prevent buildings against them: firebrand attack, radiant heat and/or direct flame contact from the forest fire. Firebrand attack is maybe the most important mechanism of fire propagation because it can occur even if the forest fire front is hundreds of meters away, and could severely affect the buildings' roofs. Post-fire studies in forest fire events have observed building ignition mechanisms where tiny firebrands penetrate under the non-combustible tile roof covering. These studies show the firebrands accumulated under ceramic tiles/gaps during a period in a dynamic process [2], different from the wood crib's ignition mechanism in the existing bench scale test methods described in Table 1. Despite this, firebrands generated by the wood crib could be blown off the roof during testing.

Therefore, they could not represent a realistic simulation of a firebrand attack because they may not accumulate. Bench-scale experimental tests conducted by Manzello and Suzuki evaluated a firebrand attack in an ignition-resistant roof system. These tests confirm the firebrand ignition mechanism (Fig. 4). ASTM E2726 [14] standard was developed based on this experimental system. However, this method only applies to determine the fire response of deck structures attached to or near primary structures.

Fig. 3 – ASTM E 108 test [x]

Fig. 4 – NIST/BRI Experimental tests [2]

3. ROOF SYSTEMS EXTERNAL FIRE CLASSIFICATION AND LOCAL REGULATIONS

3.1 Europe

CEN/TS 1187 [5] technical specification is used in the European Union to conduct the external fire exposure in roof coverings and roof assemblies and consists of four different tests. Unfortunately, these are not harmonised or equivalent, so finding one test that could satisfy European regulators' requirements was not possible. However,

each member state can determine in their regulation which test should be conducted to classify the roofing systems. These four tests were based on standards DIN 4102-7 [15]; NT FIRE 006/32 [16]; French test [17], and BS 476-3 [18] and are identified as Test 1, Test 2, Test 3 and Test 4 in CEN/TS 1187, respectively. The classification criteria for each test method are given in EN 13501-5 [19] and shown in Table 2.

Table 2 – European classification for roofs and roof coverings according to CEN TS1187 tests

Test	Class	Classification criteria
1	$B_{ROOF}(t_1)$	All of the following conditions shall be satisfied for any one test: - external and internal fire spread upwards < 0.7 m; - external and internal fire spread downwards < 0.7 m; - maximum burned length external and internal < 0.8 m; - no burning material (droplets or debris) falling from exposed side; - no burning/glowing particles penetrating the roof construction; - no single through opening > 25 mm^2; - sum of all through openings < 4,500 mm^2; - lateral fire spread does not reach the edges of fire measuring zone; - no internal glowing combustion; - maximum radius of fire spread on 'horizontal' roofs, external and internal < 0.2 m.
	$F_{ROOF}(t_1)$	No performance determined.
2	$B_{ROOF}(t_2)$	For both test series at 2 m/s and 4 m/s wind speed: - mean damaged length of the roof covering and substrate ≤ 0,550 m; - max. damaged length of the roof covering and substrate ≤ 0,800 m.
	$F_{ROOF}(t_2)$	No performance determined
3	$B_{ROOF}(t_3)$	T_E ≥ 30 min and Tp ≥ 30 min
	$C_{ROOF}(t_3)$	T_E ≥ 10 min and Tp ≥ 15 min
	$D_{ROOF}(t_3)$	Tp ≥ 5 min
	$F_{ROOF}(t_3)$	No performance determined.
4	$B_{ROOF}(t_4)$	- No penetration of roof system within 1 hour. - In preliminary test, specimens burn for < 5 min after the test flame's withdrawal. - In preliminary test, flame spread < 0,38 m across region of burning.
	$C_{ROOF}(t_4)$	- No penetration of roof system within 30 min. - In preliminary test, specimens burn for < 5 min after the test flame's withdrawal. - In preliminary test, flame spread < 0.38 m across region of burning.
	$D_{ROOF}(t_4)$	- Roof system is penetrated within 30 min. but is not penetrated in the preliminary test. - In preliminary test, specimens burn for < 5 min after the test flame's withdrawal. - In preliminary test, flame spread < 0.38 m across region of burning.
	$E_{ROOF}(t_4)$	- Roof system is penetrated within 30 min but not in the preliminary test. - Flame spread is not controlled
	$F_{ROOF}(t_4)$	No performance determined.

T_E = Time for external fire spread to the edge of the measuring zone; Tp = Time to fire penetration.

In UK Regulation [20], roof systems' performance against external fire exposure is measured by fire penetration through the roof and flame spread over its surface. Roof constructions are classified within the European system using Test 4 results and EN 13501-5 classification criteria. B_{ROOF} (t$_4$) indicates the highest performance, and F_{ROOF} (t$_4$) is the lowest. However, some products may be lawfully on the market using the classification system set out in previous editions. A transposition from EN 13501-5 classification to BS-476-3 classification in Section B18 of Annex B addressed this issue. Nordic Countries [21] use Test 2 results and EN 13501-5 [19] classification criteria, and their regulations nowadays are harmonised.

Portugal only considers external fire exposure to roofs in the forest fire safety requirements for buildings near the WUI, made by National Authority for Emergency and Civil Defense (ANEPC) [22]. The Portuguese Fire Safety Regulation [23], which every building in Portugal must comply with, in the external fire exposure only mentions fire reaction classification accordingly to EN 13501-1 [24] and fire resistance classification from EN 13501-2 [25]. These forest fire safety requirements only apply to buildings implemented on land use classified as rural under articles 60º and 61º of Decree-Law N.º 82/2021 [26]. In this regulation, when the building is under 300 m from grassland and inside the Prevention and Protection Priority Areas classified according the Portuguese Agency for Integrated Management of Rural Fires (AGIF) [26], the external fire exposure performance need to be B_{ROOF} (t$_1$), B_{ROOF} (t$_2$), B_{ROOF} (t$_3$) or B_{ROOF} (t$_4$), the highest classification for each test method in EN 13501-5 [19].

3.2 North America

The classification of a roof system or roof covering is established in function of fire exposure, using the ASTM E108 [6] standard. The classification could be A, B or C Class, and their severity is defined by the type of fire load required by the test method. Class A roof coverings are effective against severe fire test exposures, and Class B and C are effective against moderate and light fire test exposures, respectively. These can be conducted on a combustible wood deck (sheathing boards or plywood) or a non-combustible deck made of metal, concrete, or poured gypsum.

One of the performance criteria to assess the roof system classification is the flame spread on the roof's exposed surface. The flaming cannot spread beyond 1.8 m for Class A, 2.4 m for Class B and 4.0 m for Class C during the test. In addition, significant lateral spread of flame from the area directly exposed to the test flame is not permitted. For all three classes of fire exposure (A, B and C) at no time during intermittent flame, flame spread or burning brand tests can: any portion of the roof blow off in the form of flaming or glowing brands that continue to glow after reaching floor; the roof deck become exposed (except for non-combustible decks) and; portions of roof deck fall away that continue to glow when reaching the floor. Also, at no time during intermittent flame or burning brand test can there be sustained flaming under the deck.

In International Wildland Urban Interface Code [27] proposed by International Code Council, are presented specific requirements for roof or roof coverings in forest fire-prone areas, using the ASTM E-108 [6] in the function of fire hazard severity, defensible space and water supply for fire-fighting availability. According to this code, these parameters will assess the Ignition Resistant Construction Type (IRC 1, IRC 2 or IRC 3) the building must comply with. IRC 1 is more restrictive, and roofs shall have a Class A roof covering or assembly. For IRC 2 type, roofs shall have at least a Class B roof covering or assembly or an approved non-combustible roof covering. IRC 3 is less restrictive, and roofs shall have at least a Class C roof covering or assembly or an approved non-combustible roof covering. For roof coverings where the profile allows a space between the roof covering and roof decking, the space at the eave ends shall be fire-stopped to preclude the entry of flames or embers.

California Building Code [28], after relevant fire events in WUI areas over the years, included a specific topic for materials and construction methods for exterior wildfire exposure in Section 705A of Chapter 7A. This section presents the requirements for external fire exposure in roof assemblies and roof coverings and requires compliance according to Class A, B or C using the ASTM E108 [7] or UL 790 [8] test methods. In addition, fire-retardant-treated wood roof coverings shall be tested under ASTM D2898 [29] to evaluate the accelerated ageing effect in these constructive solutions. The minimum classification on this code the building roof coverings shall comply are based on the type of construction of the building. The roof covering shall be a fire-retardant Class A when the building is within Very High Fire Hazard Severity Zones, according to the following situations: the entire roof covering of every existing structure, where more than 50 % of the total roof area was replaced within one-year period; or the entire roof covering of every new structure; any roof covering applied in the alteration/repair or replacement of the roof of every existing structure.

3.3 Other countries

In Japan, it was adopted to evaluate the external fire exposure to roofs by ISO 12468-1:2013 [30], and this standard basically establishes the same test setup of CEN/TS 1187 Test 3 method. In Brazil, the ABNT Fire Safety Committee developed the ABNT NBR 16841:2020 [31] standard, based on CEN/TS 1187 Test 1 method.

4. FINAL CONSIDERATIONS

Construction requirements in codes and standards for building roof coverings systems are essential in building fire protection. When these buildings are inside forest fire-prone areas, they are relevant for building protection and resilience against external fires. The roof materials must be selected according to the fire severity that the building could be exposed. This issue must be addressed within the codes and regulations, supported by test methods that reproduce the most critical conditions for building protection against external fire action. The North American approach for the classification of roof systems is harmonised and currently required in codes and regulations for urban and WUI areas using the test method ASTM E 108. Since the test methods are not harmonised in EU countries, each country needs to establish their fire safety level for roof systems and identify which of the four testing methodologies inside the CEN/TS 1187 standard should be adopted.

CEN TS 1187 Test 1 have the most simplified test apparatus of the four methods, proposing a qualitative approach to measure the fire propagation and penetration of the exterior fire in the specimen. This test method assesses in a feasible and realistic way the damages on the test specimen. Also, with this test method is possible to evaluate the damage on joints and layers in the roofing system and change specimens' dimensions when needed. However, this test does not assess the exposure of the specimen to radiant heat, only the attack of direct flames on the roof

with the placement of the fire load, and this will be conducted in a draft-free area (without wind effect). The uncertainty sources assessment needs to be carefully verified. For example, the wood species used to make the wood wool and the expected burning time, assessed in a calibration test; the technician's knowledge of test criteria to verify the parameters and not missing any relevant information during the tests.

ASTM E 108 and CEN/TS 1187 Tests 2, 3 and 4 test apparatus have ventilators to apply a wind flow effect on test specimen' surface, a relevant issue to address the external fire spread in roofing systems. In addition, the radiant heat exposure by external fires could be simulated by CEN/TS 1187 Tests 3 and 4 test apparatus. The ignition mechanisms by the flame attack and radiant heat exposure combined with the wind effect in CEN/TS 1187's Tests 3 and 4 reflect a broader approach to evaluate the roofing systems' behaviour against external fires.

The test results could not be available for the same roof assembly for different reasons (*e.g.* testing costs, product availability in the market, particular fire safety regulation requirements for external fires in each country, and others). This situation reflects an absence of testing data to engineers and architects select the appropriate roofing system for the building. Furthermore, different roof fire safety requirements in every country represent some trade barriers within EU countries today. However, the development of a single harmonised roof test method for EU market, suggested in RISE Report 2008:29 [18], combined with an experimental campaign to evaluate the most common roofing systems in European market is a way to break the technical barriers between countries and an opportunity to establish a reasonable fire safety level for roof systems in EU.

ACKNOWLEDGMENTS

REFERENCES

[1] Ganteaume, A.; Barbero, R.; Jappiot, M.; Maillé, E., Understanding future changes to fires in southern Europe and their impacts on the wildland-urban interface, Journal of Safety Science and Resilience, Vol. 2, Issue 1, 2021, pp 20-29, ISSN 2666-4496, https://doi.org/10.1016/j.jnlssr.2021.01.001.

[2] Manzello, S. L.; Suzuki, S., Experimentally Simulating Wind Driven Firebrand Showers in Wildland-urban Interface (WUI) Fires: Overview of the NIST Firebrand Generator (NIST Dragon) Technology, Procedia Engineering, Vol. 62, 2013, pp 91-102, ISSN 1877-7058, https://doi.org/10.1016/j.proeng.2013.08.047

[3] Comissão Técnica Independente; Guerreiro, J.; Fonseca, C.; Salgueiro, A.; Fernandes, P.; Lopez Iglésias, E.; de Neufville, R.; Mateus, F.; Castellnou Ribau, M.; Sande Silva, J.; Moura, J. M.; Castro Rego, F.; Caldeira, D. N.; - Coords. 2018. "Avaliação dos incêndios ocorridos entre 14 e 16 deoutubro de 2017 em Portugal Continental". Relatório Final. Comissão Técnica Independente. Assembleia da República. Lisboa. 274 pp

[4] Messerschmidt, B.; Scott, J. Fire testing of low slope roof assemblies - An international review, 13th Fire and Materials international conference and exhibition, http://www.intersciencecomms.co.uk/html/conferences/conferencearchive.htm, 2013.

[5] CEN/TS 1187:2012 - Test methods for external fire exposure to roofs, European Committee for Standardization (CEN), Brussels, 2012.

[6] Gravit, M; Polishchuk, E; Dmitriev, I; Shakhova, M. Flame spread on the pitched roof covering from a single ignition source, E3S Web Conf., 2020, DOI: https://doi.org/10.1051/e3sconf/202015706030

[7] ASTM E108. Standard Test Methods for Fire Tests of Roof Coverings. West Conshohocken, PA: American Society for Testing and Materials, American Society for Testing Materials (ASTM), US, 2020. DOI: 10.1520/E0108-20A.

[8] UL 790. Standard Test Methods for Fire Tests of Roof Coverings, Underwritter Laboratories (UL), US, 2022

[9] NFPA 256. Standard Methods of Fire Tests of Roof Coverings. National Fire Prot Ass., Quincy, MA, US, 2003.

[10] CAN/ULC-S107-10. Methods of Fire Tests Of Roof Coverings. Underwriter Laboratories of Canada, Ottawa, CA. 2019.

[11] University of Stuttgart. Description of Fire Safety Department Materials Testing Institute activities. https://www.mpa.uni-stuttgart.de/en/institute/publications/departments_flyer/fire_safety_51300.pdf. Accessed in 05/06/2023.

[12] Middag, W.J.B., Hameete, A.R. Test report 0422-L-20/1, Test on external fire exposure to roofs according to CEN/TS 1187 test 2, Kiwa N.V., 12/11/2020, https://www.takcentrum.se/wp-content/uploads/2021/01/0422L20.1-Brooft2-Resitrix-SK-W-external-fire-exposure-TS1187-2-Test-report.pdf. Accessed in 05/06/2023.

[13] NETZSCH-Gerätebau GmbH, Determining the Performance of Roofs against External Fire Exposure TD4 Equipment, https://analyzing-testing.netzsch.com/pt-BR/products/fire-testing/tdp-t4. Accessed in 05/06/2023.

[14] ASTM E2726. Standard Test Method for Evaluating the Fire-Test-Response of Deck Structures to Burning Brands. American Society for Testing and Materials (ASTM), West Conshohocken, PA, US, 2012. DOI:10.1520/E2726_E2726M–12A.

[15] DIN 4102-7. Fire behaviour of building materials and elements – Part 7: Roofing – Concepts, requirements and testing. German Institute for Standardisation, Berlin, Germany. 1998.

[16] NORTEST, NT FIRE 006: Roofings: Fire spread. NORDTEST, edition 2, Esbo, FL. 1985.

[17] Ministere de L´interieur, Arrêté du 10 septembre 1970 relatif à la classification des covertures en matériaux combustibles par rapport au danger d'incendie résultant d´un feu exterior, Journal Officiel de La République Française, Paris, FR,1970.

[18] BS 476-3:2004. Fire tests on building materials and structures – Part 3: Classification and method of test for external exposure to roofs, British Standards, UK, 2004.

[19] EN 13501-5. Fire classification of construction products and building elements - Part 5: Classification using data from external fire exposure to roofs tests, European Committee of Standardization (CEN), Brussels, 2018.

[20] Approved B document, Fire Safety – Vol. 2: Buildings other than dwellings, Department for Levelling Up, Housing and Communities, Ministry of Housing, Communities & Local Government, UK, 2022.

[21] Thureson, P., Sundström, B, Mikkola, E., Bluhme, D, Steen-Hansen, A., & Karlsson, B. RISE Report 2008:29 -The use of fire classification in the Nordic countries - Proposals for harmonisation, Technical Research Institute of Sweden, 2008.

[22] Autoridade Nacional de Emergência e Proteção Civil, 2022. "Despacho n.º 8591/2022 - Requisitos para adoção de medidas de proteção relativas à resistência do edifício à passagem do fogo, a constar em ficha de segurança ou projeto de especialidade no âmbito do Regime Jurídico de Segurança contra Incêndio em Edifícios." DR n.º 134/2022, Série II de 2022-07-13, 67 – 72, Portugal.

[23] Secretaria de Estado da Administração Interna, 2020. "Portaria n.º 135/2020 de 2 de junho - Alteração ao Regulamento Técnico de Segurança contra Incêndio em Edifícios (SCIE), aprovado pela Portaria n.º 1532/2008, de 29 de dezembro", Diário da República n.º 107/2020, Série I de 2020-06-02, 2 – 214, Portugal.

[24] EN 13501-1. Fire classification of construction products and building elements - Part 2: Classification using data from fire resistance tests, excluding ventilation services, European Committee of Standardization (CEN), Brussels, 2016.

[25] EN 13501-2. Fire classification of construction products and building elements - Part 2: Classification using data from reaction to fire tests, European Committee of Standardization (CEN), Brussels, 2018.

[26] Presidência do Conselho de Ministros, 2021. "Decreto-Lei n.º 82/2021: Estabelece o Sistema de Gestão Integrada de Fogos Rurais no território continental e define as suas regras de funcionamento", Diário da República n.º 199/2021, Série I de 2021-10-13, 2 – 47, Portugal.

[27] International Code Council. 2021 International Wildland-Urban Interface Code, ISBN 978-60983-974-1, 2020.

[28] International Code Council. 2019 California Building Code, ISBN: 978-1-60983-891-1, 2019.

[29] ASTM E2898. Standard Practice for Accelerated Weathering of Fire-Retardant-Treated Wood for Fire Testing. American Soc. Testing Materials (ASTM), West Conshohocken, PA, US, 2017. DOI: 10.1520/D2898-10R17.

[30] ISO 12468-1:2013. External exposure of roofs to fire — Part 1: Test method, International Organization for Standardization, Switzerland, 2013.

[31] ABNT NBR 16841. Comportamento ao fogo de telhados e revestimentos de cobertura submetidos a uma fonte de ignição externa, Associação Brasileira de Normas Técnicas, Rio de Janeiro, 2020.

IMPLEMENTATION OF FIRE SAFETY ENGINEERING APPROACH IN THE REGULATORY FRAMEWORK AND DESIGN PRACTICE IN EUROPE

Adamantia Athanasopoulou a; Francesca Sciarretta b,*; Maria Luisa Sousa c; Silvia Dimova d

ABSTRACT

Approaching fire safety design with a performance-based method addressing the entire building, requires the necessary assessments to be made using Fire Safety Engineering (FSE) tools. An enquiry on the FSE implementation status details was carried by the Joint Research Centre of the European Commission addressed to the principal fire regulators of the EU/EFTA countries, United Kingdom and Serbia. The enquiry has revealed that the FSE approach is not yet fully implemented in the national regulatory framework of the responding countries, even in cases of recently issued or updated national regulations. Moreover, when addressing the technical details within the FSE approach, prescriptive methods are largely prevalent in practice throughout the European countries, even if FSE approach is allowed. The lack of implementation tools, education and experience in FSE-related issues were noted as reasons for not incorporating the FSE approach in the regulatory system. The absence of an explicitly defined qualification framework for professionals involved in FSE practice or regulatory reviewers of the FSE approach in projects was noted in many European countries. The fire regulators commented on the need for FSE implementation supported by research for standardisation, especially for the benefit of professionals who are involved in fire safety design practice.

Keywords: fire safety engineering; regulatory framework; standardization; education; training.

1. INTRODUCTION

1.1 Fire safety in the built environment – the EU policy and standardisation context

Traditionally, most designs for the fire safety of structures have been based on prescriptive requirements set by building regulations, building codes and associated standards. Approaching fire safety design with a performance-based method addressing the entire building, requires the necessary assessments to be made using Fire Safety Engineering (FSE) tools. The adoption of Fire Safety Engineering in fire safety design practices offers several benefits, including building-scale approach, a wider range of potential cost-effective fire safety measures, and innovative solutions not allowed by traditional prescriptive regulations. In the European Union (EU), fire safety in the built environment is a national competence and thus, regulated by the EU Member States (MS). Significant

---

ᵃ Hellenic Open University, Greece; formerly at European Commission, Joint Research Centre, Ispra, Italy (adamantia.athanasopoulou@gmail.com)**.**

ᵇ,***** European Commission, Joint Research Centre, Ispra, Italy (Francesca.SCIARRETTA@ec.europa.eu), Via E. Fermi 2749 21027 Ispra (VA), Italy, Corresponding author.

ᶜ National Laboratory for Civil Engineering, Lisbon, Portugal; formerly at European Commission, Joint Research Centre, Ispra, Italy (luisa.sousa@lnec.pt)**.**

ᵈ European Commission, Joint Research Centre, Ispra, Italy (Silvia.DIMOVA@ec.europa.eu)**.**

improvements have been achieved in the implementation of fire safety strategies over the past decades in the European countries. Fire safety in the built environment is embedded in several EU initiatives and plans for action related to the construction ecosystem – the European Green Deal [1], the Renovation Wave for Europe [2] and the New European Bauhaus initiative [3]. Moreover, technological developments and the need for improved energy-performing and climate-resilient buildings have changed significantly the built environment, bringing a new challenge for the European policy makers and regulators.

The EU level regulation on fire safety of the built environment is exercised mainly through the Construction Product Regulation [4] and the related harmonised technical specifications. The review [5] of the Construction Products Regulation further ensures that the design of new and renovated buildings, at all stages, is in line with the needs of the circular economy, leading to increased digitalisation and climate-proofing of the building stock. The Commission proposal for revision of the Energy Performance of Buildings Directive [6] also brings attention to fire safety in the built environment requesting Member States to address fire and seismic safety for new buildings and existing buildings undergoing major renovations. In addition, the new EU strategy on adaptation to climate change [7] sets out how the EU can adapt to the unavoidable impacts of climate change and become climate resilient by 2050, as well as to improve protection from natural and human-made disasters (floods, heatwaves, fires, earthquakes, landslides). Following the updated EU Industrial Strategy, the Transition Pathway for Construction [8] was published in March 2023 and delineates a vision for a swift green and digital transition of the construction ecosystem. This means the use of new materials, products, and technologies, for which the experience and knowledge base are still limited – and which bring along also new types of risks.

The European Commission also initiates and coordinates complementary activities to regulatory fire safety at the EU level. The most prominent of those in the construction sector was the establishment of the Fire Information Exchange Platform (FIEP) in 2017 with the aim to enhance cooperation among Member States, as well as to facilitate the exchange of knowledge, information and best practices, and cross-learning from fire safety activities. Five priority areas have been identified within FIEP´s scope: statistics, fire prevention, innovation in products and applications including high-rise buildings, experience from fire accidents and fire safety engineering.

Complementary to the EU policies in support of improvements in the construction ecosystem, European standards are fundamental for reaching such objectives. This is recognized in the new Standardisation Strategy [9] that enables global leadership of EU standards in promoting values and a resilient, green and digital Single Market. Within the standardisation framework for the construction sector, the Eurocodes have a prominent role as a series of 10 European Standards, EN 1990 to EN 1999, providing common technical rules for the design of buildings and other civil engineering works. The Eurocodes contain specific parts – the "fire parts" – dealing with the fire resistance of structures. The application of fire safety engineering approach is possible in the general framework of the Eurocodes. In particular, EN 1991-1-2 "Eurocode 1: Actions on structures - Part 1-2: General actions - Actions on structures exposed to fire" - Annex E "Fire Load Densities" introduces the fire safety engineering approach, which is based on design fire scenarios. It establishes links between active and passive fire protection measures and determines a procedure for the calculation of the design fire load density to be used in natural fire models.

1.2 Activity at the EC Joint Research Centre to map the implementation of FSE in Europe

Appreciating and acknowledging the advances in fire safety engineering approach and the opportunities this design approach may bring to cope with the societal challenges, the Joint Research Centre (JRC) of the European Commission explores the needs and options for further harmonisation of the FSE approach in the EU/EFTA Member States, having direct link to FIEP's scope and activities. The activity also contributes to define the needs for guidance and training of professionals on FSE, as well as the standardisation needs, to be explored and discussed with relevant stakeholders.

In the period November 2020-October 2021, JRC conducted an enquiry to map the implementation status of the FSE approach in the regulatory framework and design practice in Europe. The enquiry aims to support JRC's work towards a proposal for the harmonisation of FSE application on European level, defining the needs for guidance and training of professionals, promote the acceptance and/or incorporation of the approach in the national regulatory frameworks and facilitate an increased awareness of the status across Europe. The enquiry focused on the built environment (housing, offices, theatres, shopping malls, hotels, airports, etc.;) and it did not deal with industrial buildings or plants. This paper presents the most important results and conclusions yielded by the JRC from the results of the enquiry, and elaborates the next steps of the activity focusing in particular on the education, training and standardisation needs towards a full implementation of the FSE approach in Europe. The full description of the results is available in a JRC Technical Report by Athanasopoulou et al. (2023) [10].

2. STATUS OF IMPLEMENTATION OF FSE APPROACH IN EUROPE

2.1 Methodology of enquiry

A questionnaire was developed by the JRC, inspired by previous work carried on by ISO/TC92 "Fire Safety" (survey on the performance-based fire safety design practices in different countries by its Sub-Committee 4 [11]), and CEN/TC127 "Fire Safety in buildings" (*The Benefits of Fire Safety Engineering within the European Union* – BeneFEU programme [12]). Principal national fire regulators from 32 countries provided responses to the enquiry for each country, namely: the 27 EU Member States, 3 EFTA Member States (Iceland, Norway and Switzerland) and 2 countries with National Standardisation Bodies members of the European Standardisation Committee (CEN), i.e., Serbia and United Kingdom. As far as the replies were collected in the period November 2020 – September 2021, the analysis reflects the state of Fire Safety Engineering approach implementation in 2020-2021.

Two countries (Belgium and Germany) provided one reply for the country and one for a specific region. This paper does not account for the results related to such regions, which were useful to propose comparisons between national and regional status, included in the report [10]. Thus, 32 responses (one per country) are accounted for in this paper. The questionnaire consisted of 24 questions divided into six parts, namely

1) Responder's general information;
2) General information on the existing fire regulation(s) at national level;
3) Allowance of Fire Safety Engineering approach (yes/no);
4) [if relevant based on previous reply] Status of implementation of Fire Safety Engineering approach / [if relevant] Reasons for not applying Fire Safety Engineering approach;
5) Fire Safety Engineering training, education and research;
6) Comments and recommendations.

As the questionnaire part 4 aimed to provide a detailed description on the status of Fire Safety Engineering implementation in each country,12 main Technical Areas (TAs) or technical details were selected, in general agreement with the technical areas already used in the previous surveys by ISO, BeneFEU and CEN/TC127/WG8 but providing more details. The selected 12 TAs are listed in Table 1, which also provides the abbreviations to be used in the following section of the paper and related figures. The TAs selected are used to describe the nature and extent of technical detail through the different countries or regions, obtaining a detailed mapping of the level of integration for the FSE approach in fire design regulations of the countries.

Table 1: The 12 Technical Areas (TAs) referred in the JRC enquiry on the FSE implementation status.

Definition	Abbreviation
Fire detection	FireDete
Early suppression / suppression systems	EarlySup
Evacuation routes	EvacRout
Smoke control systems	SmokCoSy
Structural fire safety	StructFS
Fire compartmentation	FireComp
Smoke compartmentation	SmokComp
Prevention of fire spread to neighbouring buildings	PrFiSpre
Material / system selection for facades	MaSelFac
Material / system selection for all other relevant areas (e. g. interior finishing, cables, internal insulation, furniture, etc.)	MaSelOth
Firefighting (fire brigade access and intervention	FireFigh
Building installation	BuilInst

2.2 Implementation of FSE approach through technical areas, assessment methods and coverage of construction types

JRC published the results of the enquiry, with the support of its Fire Safety Engineering expert network, in January 2023 [10]. Generally, the enquiry has revealed that the FSE approach is not yet fully implemented in the national regulatory frameworks of the responding countries, even in case of recently issued or updated national regulations. However, only four countries (Portugal, Greece, Bulgaria and Slovakia) have responded that FSE approach is not allowed in fire safety design (Figure 1). Rather than related to any legal restriction, this fact seems due to the practical lack of tools, education and experience in FSE-related issues, also resulting in the insufficiency of

infrastructure components – legal, insurance, professional certification, education, etc. – that was indicated by all the four countries as a reason for not implementing the FSE approach. On the other hand, the reasons why the FSE approach is implemented are mostly related to innovation in technology, architecture and construction, and to structures or elements not covered by prescriptive fire design provisions.
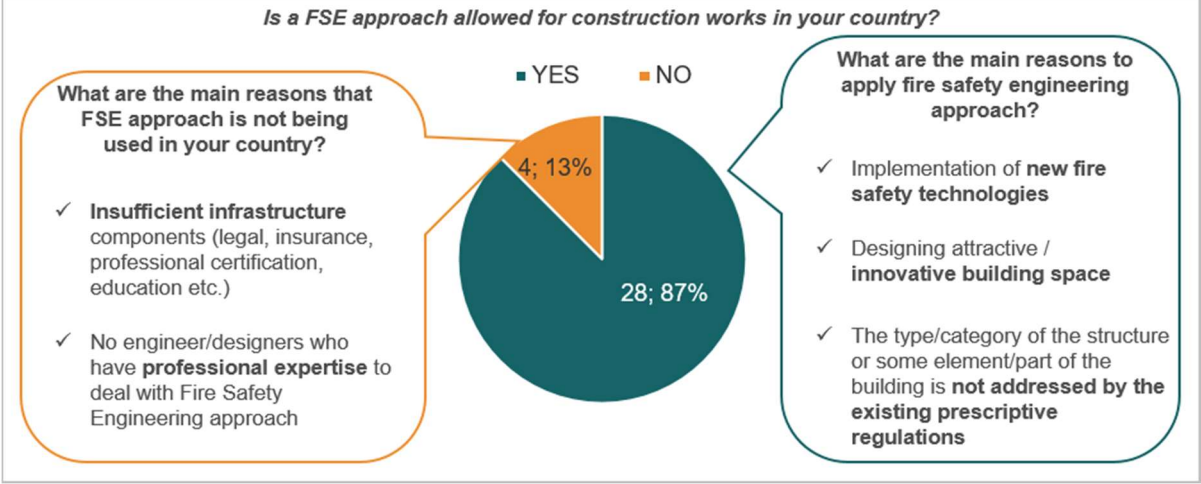
Figure 1: Reasons for allowance / non-allowance of FSE approach in fire safety design

The questionnaire assumed the following underlying concepts of fire design solutions:
1) Prescriptive solutions: application of minimum requirements to single building members, according to tabulated data, to comply with fire safety and performance standards; no further demonstration is requested to the designer;
2) Deemed-to-satisfy solutions: application of methods that are deemed to meet the performance requirements; this type of solution is similar to prescriptive;
3) Performance-based solutions: fire design deviating from prescriptive rules, performed with analytical methods, on single members, assemblies or whole buildings; the compliance of these solutions with fire safety and performance standards must be demonstrated with Fire Safety Engineering methods.
To address the technical details, prescriptive methods are largely prevalent in practice throughout the countries responding to the enquiry, even if FSE approach is allowed. Through the different technical areas (Table 1), the shares of applicability of the different available approaches are almost the same. About 50% of the available fire safety solutions are prescriptive, 20-25% deemed-to-satisfy and 25-30% performance-based (Figure 2). The technical areas that performance-based design method apply the most are Structural fire safety (StructFS), Evacuation routes (EvacRout), Smoke control systems (SmokCoSy) and Smoke compartmentation (SmokComp).
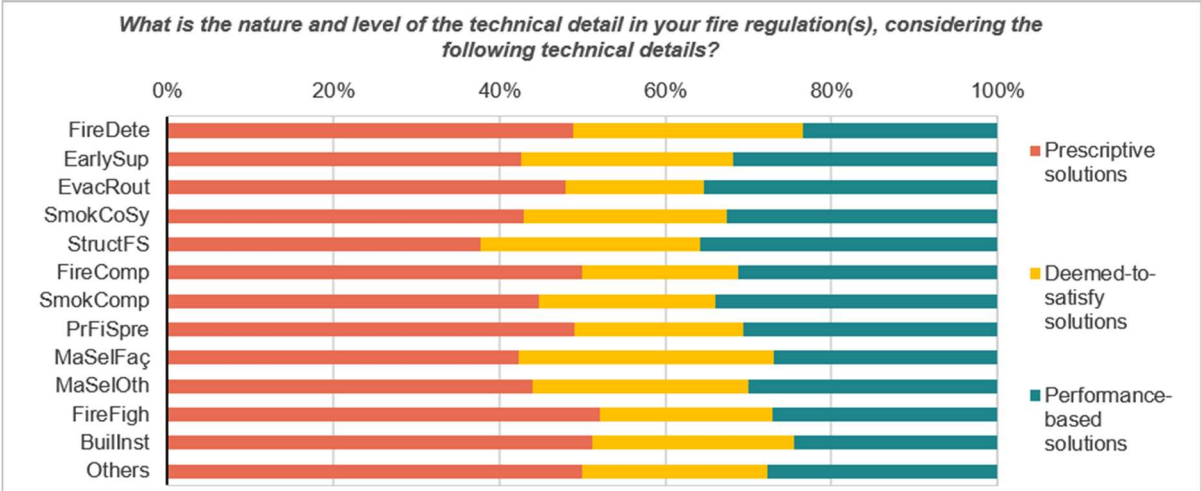
Figure 2: Shares of the different approaches to fire safety design through the selected 12 TAs for FSE approach
(replies from countries allowing the application of FSE approach)

In FSE-allowing countries (i.e. 28 countries), performance-based design solutions are mainly available for all or most of the 12 TAs; only in 6 of these countries the use of performance-based design solutions is limited to certain technical areas. This point reveals a potentially wide implementation of FSE approach for the majority of countries. However, in 22 countries (65%), mainly only one approach is available per technical area, indicating a restricted choice for fire designers; about 30% of the countries allow, at least, for choice between two approaches (Figure 3). As far as it concerns the assessment methods in FSE-allowing countries, the enquiry has underlined the importance of building / fire regulations and international standards referenced in such regulations. Finally, the application of FSE-based assessment and design methods virtually covers any type of construction in most countries. Exceptions are mostly due to the availability of code-established prescriptive solutions – which often indirectly prevent the application of FSE approach to residential buildings – and any threshold of construction size or capacity (Figure 4).
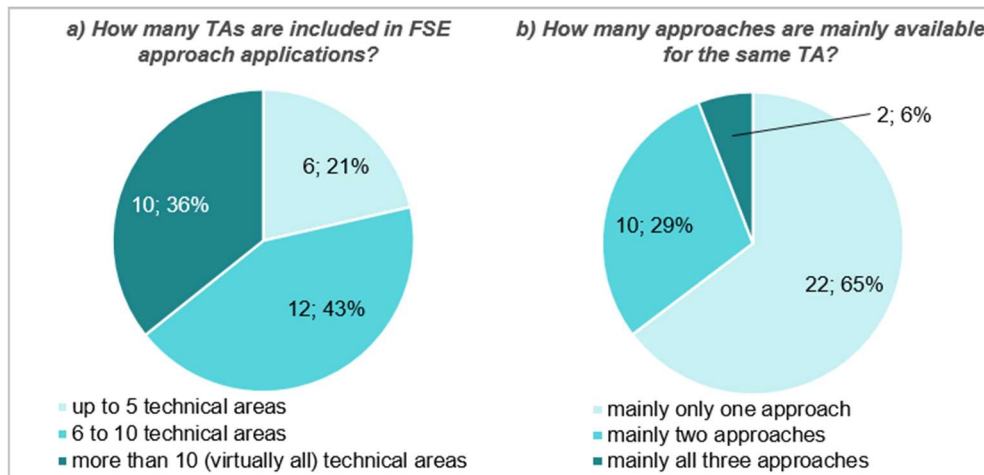
Figure 3: Number of TAs included in FSE approach and number of approaches available per TA
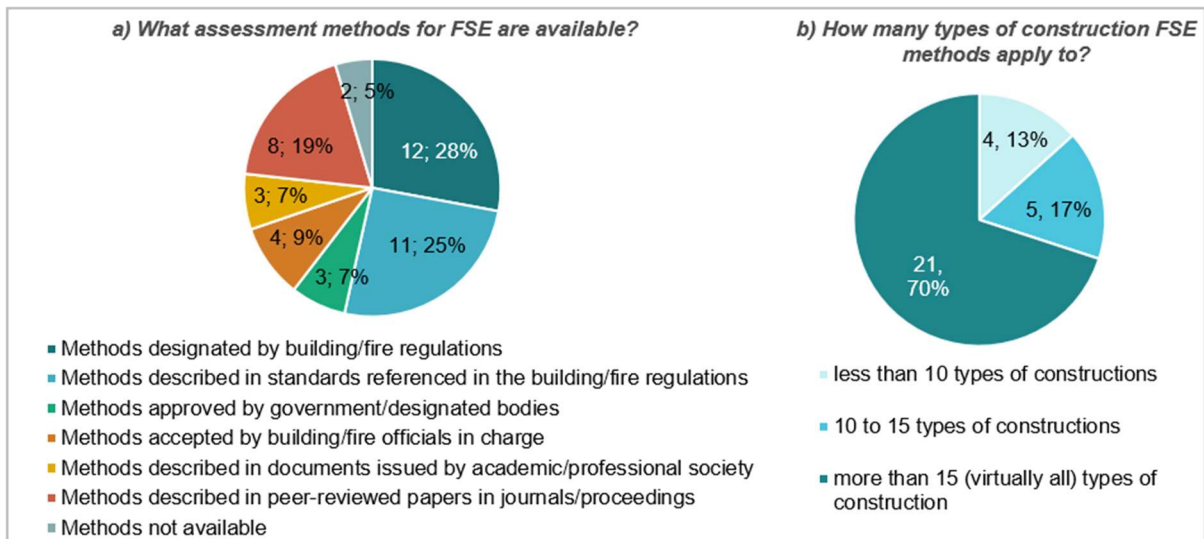
Figure 4: Number of TAs included in FSE approach and number of approaches available per TA

2.3 Liability for fire safety design

Through all the responding countries, the liability for fire safety design – applying FSE approach or not – and compliance of the design to regulations shows significant differences. The 32 responding fire regulators indicate, as possible liable subject(s), the architect (23 responses), the fire safety engineer (21 responses) and the civil/structural engineer (21 responses). Other liable subjects are also very frequently indicated (13 responses).

Two main groups can be identified based on the provided information, as follows (Figure 5):

1) In 22 countries, the fire safety engineer can be liable for fire safety design; other subject(s) – architect, structural designer or others – can also be liable depending on different criteria, i.e. the complexity and/or size of the

600

building, the design competency and the occupancy. However, in many cases, the responders have not specified any criterion.

2) In 10 countries, the fire safety engineer cannot be liable for fire safety design. A further distinction is recognizable between the cases where the liability for fire design remains on a designer figure and those where it transfers to the responsible for the construction or the service life of the building (builder, contractor or owner).
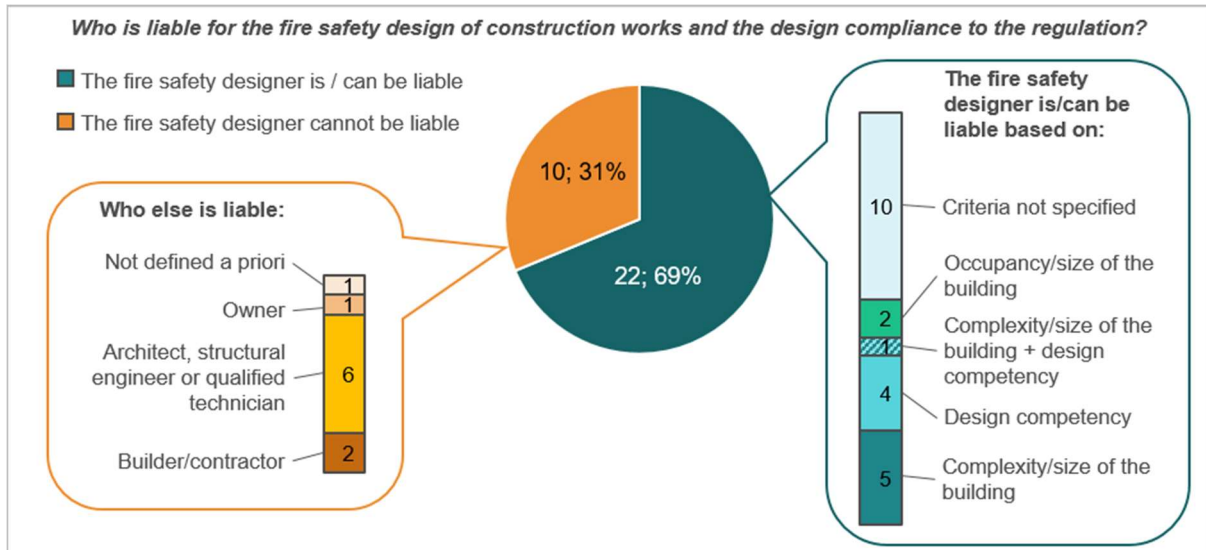
Figure 5: Liable subjects for fire safety design for the construction in the responding countries

2.3 Process of approval of a fire safety project

The approval process of a fire safety project relies on three main actors, namely the local building authority (20 cases), the fire brigade (13 cases) and the national building authority (7 cases). The approval mechanisms in place in the 32 responding countries can be grouped, as follows, by the roles of these authorities (Figure 6):
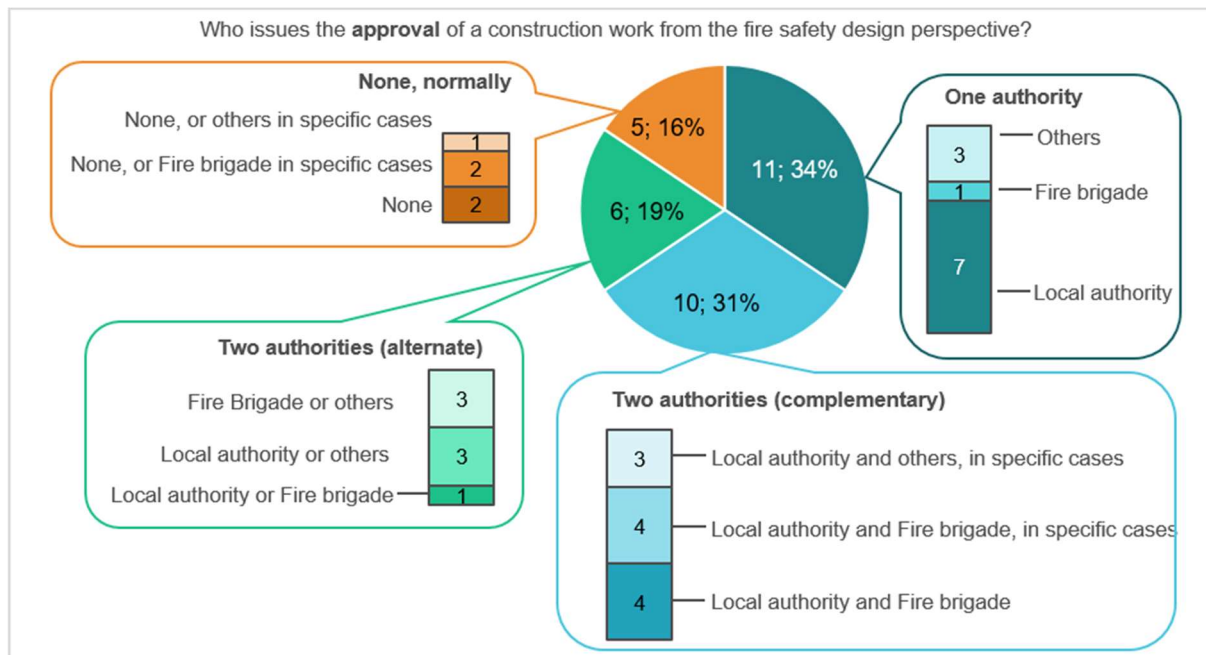
Figure 6: Actors approving the fire safety design of buildings in the responding countries

1) In 11 countries, only a certain authority approves the project.
2) In 10 countries, two authorities acting in a complementary way are involved in the approval process.

3) In 6 countries, two authorities act in an alternate way, depending on the building occupancy, the entity of fire risk of the project, or sometimes on local regulations.
4) In 5 countries, no approval is normally required (it involves an authority approval only in specific cases).

Finally, in 5 cases, third bodies – private companies, a FSE expert, a technical commission or an independent controller – are also involved in the approval process, generally under specific circumstances like the size of the project, the fire risk or clauses in local regulations. Figure 7 shows the interacting involvement of all the bodies in the process of fire design approval. The interactions are very diverse throughout the responding countries.
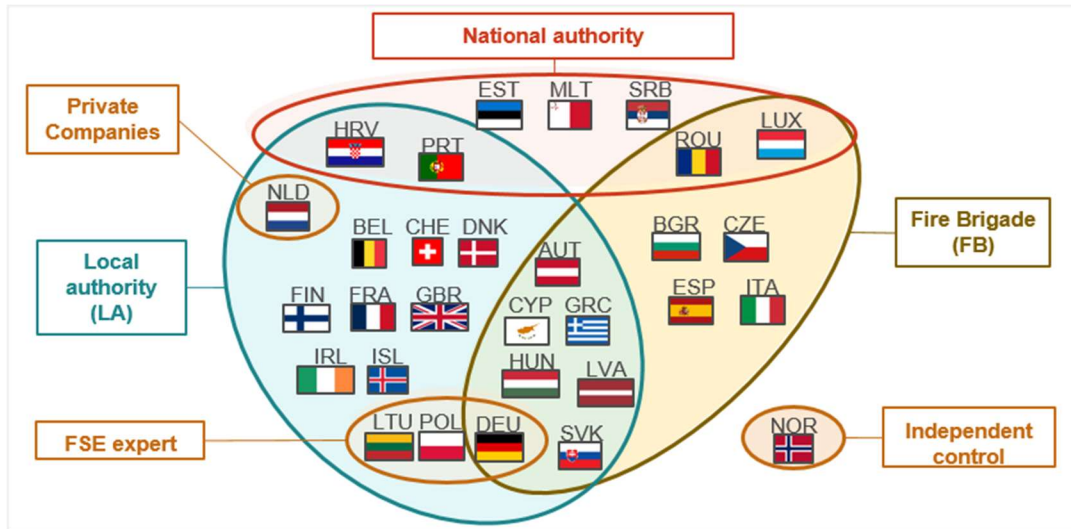
Figure 7: Bodies involved in the approval process of fire safety design of buildings

2.4 Qualifications framework for practitioners and reviewers

The FSE-allowing countries have indicated the qualification requirements for professionals and reviewers to be officially qualified to engage in FSE projects and review FSE-based projects, respectively (Figure 8).
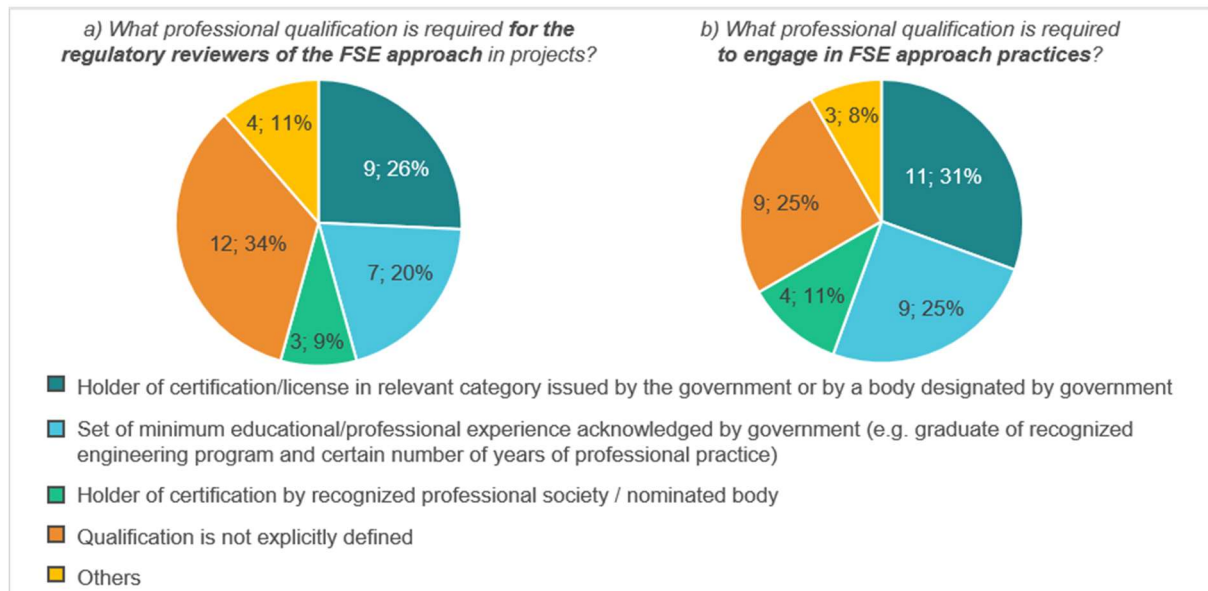
Figure 8: Qualifications framework for FSE-allowing countries

The same types of requirements were considered for both categories, namely:
1) certification or license released by the government,
2) certification or license released by recognized professional society or nominated body, and
3) minimum educational or professional experience acknowledged by the government.

602

Finally, the responders could also indicate

4) the possibility that qualification is not explicitly defined, as well as,

5) other types of requirements.

As Figure 8 demonstrates, qualification issued or acknowledged by the government (certification / license or educational / professional experience) is the most frequent requirement for both categories, especially for professionals. However, the qualification remains not explicitly defined in 34% of cases for reviewers and in 25% of cases for professionals. Figure 9 compares the qualification framework for the two categories –design practitioners and reviewers for the FSE approach – accounting that the responding fire regulators could indicate more than one type of requirement. The majority (18 out of 28) of FSE-allowing countries sets symmetrical requirements; the largest group (10 countries) establishes that the qualification of both reviewers and practitioners dealing with FSE must be issued or acknowledged by the government. Contrary, in a group of 5 countries, the qualification framework is not explicitly defined for both categories.
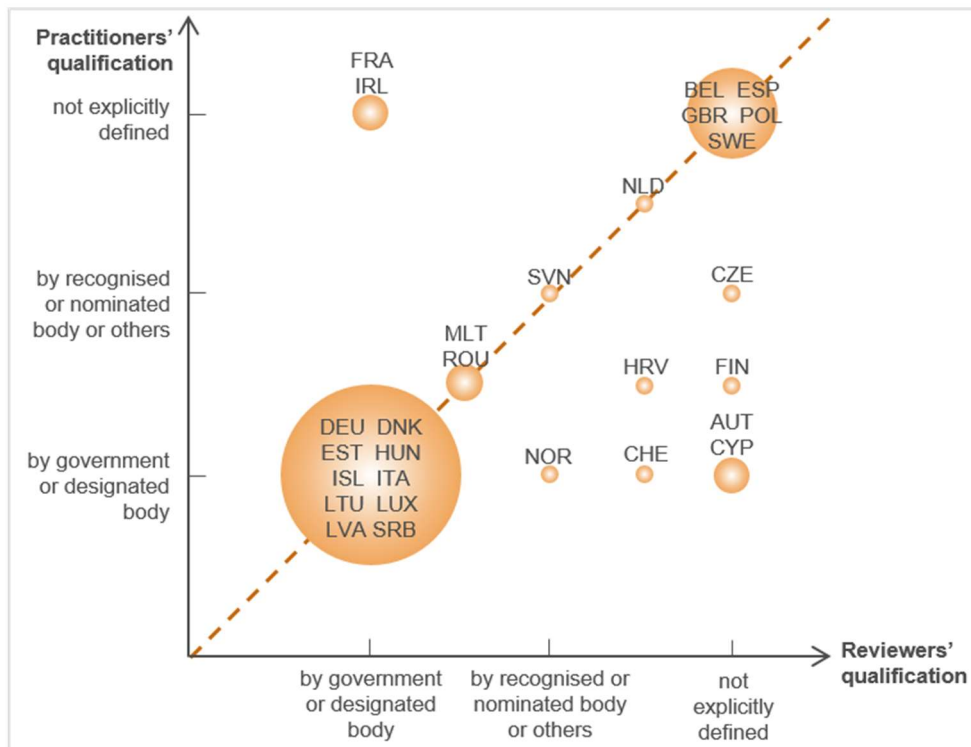
Figure 9: Comparison of required qualifications for practitioners and reviewers in FSE-allowing countries

2.5 The role of the fire consultant / engineer in the fire design process

In the large majority of FSE-applying countries, the engineer with fire design expertise has a key role in the most relevant tasks of fire design.

In detail, the specification of fire scenarios relies mostly on the fire consultant, as indicated by 26 out of 43 responses (multiple choice was allowed in this case), as shown in Figure 10. Even when the responders have indicated the option "Other", the fire consultant is nonetheless involved in this basic step of the building fire design, according to the information provided in the additional explanations.

As well, the engineer – whose choice of method or calculation is subjected to the approval of competent authority – is the specifier of both design fires and safety criteria in the majority of cases (Figure 11). The engineer can rely on its own expert judgement or on the guidance of internationally recognized documents. Comparing the specification of design fire safety criteria shown in Figure 11, the different options have similar relevance; more than half of the responders indicate the engineer, with higher prevalence (64%) in the case of design fires, while the role of regulations and national guidelines / recommendations appears secondary but more relevant in the specification of safety criteria. Generally, the selection / determination / proposal of these fundamental parameters of the building fire design is a task of the designer rather than of the approving officers or building authorities.
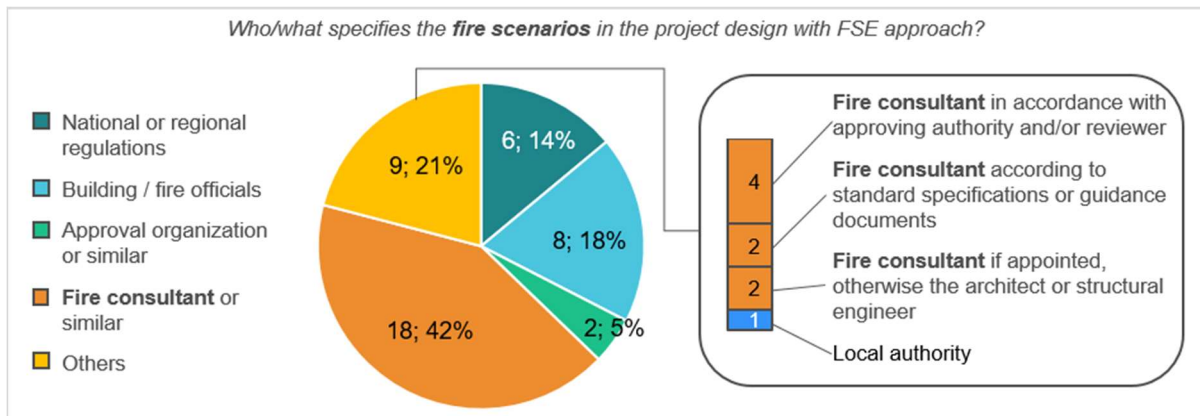
Figure 10: Sources and actors for thespecification of fire scenario
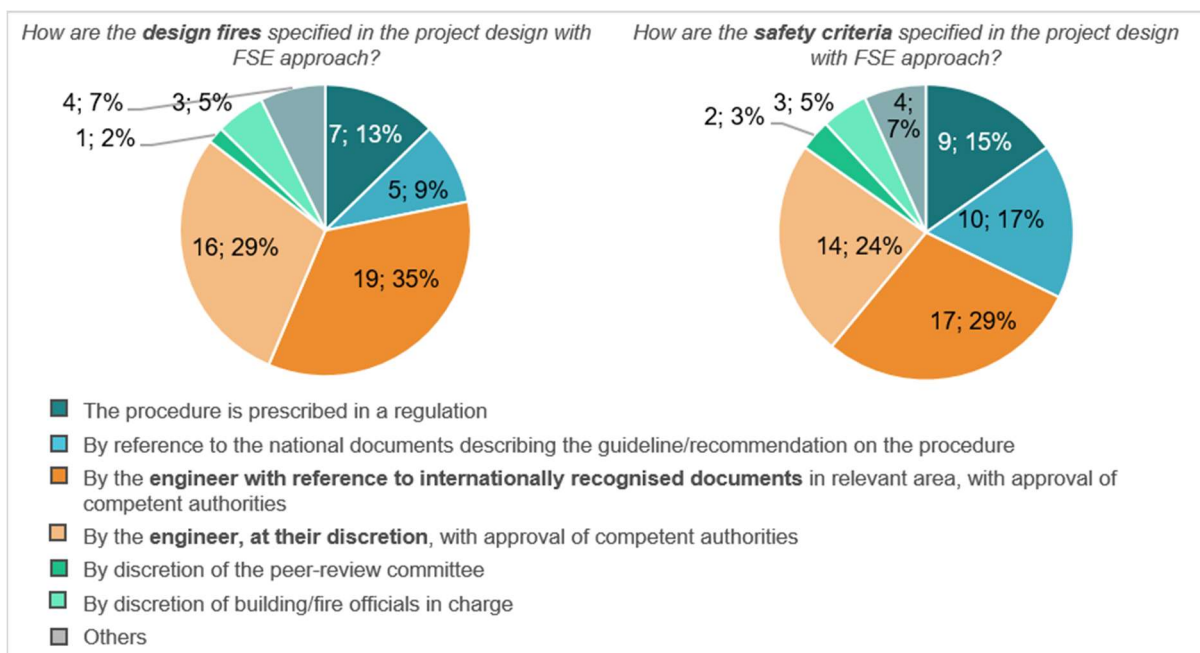
Figure 11: Specification of design fire and safety criteria

3. DISCUSSION OF OPEN ISSUES

3.1 The role of education and training

Education and training for professionals and officers engaged in FSE design practice and review are mainly provided by governmental bodies. In particular, universities are the main FSE education providers, especially at postgraduate level [10].Secondary education institutions as well as other bodies (nominated or recognized by governmental bodies) can be also FSE-related training providers, as the qualification framework seems to indicate (see Figure 8 above). Generally, all the responding fire regulators have expressed the need for increasing and improving the education and training offered on FSE in their countries [10].

The results of the enquiry enlighten various paths connecting FSE-oriented education and training to the effective implementation of the FSE approach in the responding countries, and vice versa. This is supported by the finding through the survey that the lack of specific education for subjects involved at every step of fire safety projects for buildings is the main reason for not implementing FSE. These connections the enquiry has allowed to assess in a general way, should be clarified and elaborated in the next steps of the JRC activity.

Education and training form the basis for the necessary qualifications of the different categories of subjects involved in building design, approval, construction and assessment process, namely:

604

- all the professionals who can legally design or certify the building fire safety (fire engineer / consultant, architect, civil / structural engineer, other professionals and technicians);
- local authority officers and firefighters whose duties cover the review and approval of fire safety design projects, as well as private consultants who can be nominated as third reviewers.

Throughout the countries, the liability profiles of the different actors within the fire design process, as well as the qualification framework, should be assessed in parallel to the FSE-related education and training offered. This comparison will allow to assess the extent of fire safety competency, as well as awareness and understanding on FSE that liable subjects achieve, especially focusing on the following cases:

- where the liability for the fire safety of a constructed building lies on other subject(s) than the fire safety designer;
- where the fire engineer or fire consultant is appointed to make the main fire design choices, i.e. specification of fire scenario(s), design fire and safety criteria;
- where the qualification framework for professionals and reviewers is not explicitly defined or asymmetrical.

Finally, the education-related reasons for the practical inapplicability of the FSE approach in construction projects – even in countries that allow for its application at the national regulations level – should be assessed within the mechanisms of fire design approval throughout the countries. The impaired implementation of FSE might be due to the lack of specific education of the approving officers or non-specialist designers (architects, engineers or other professionals) who are legally allowed to design a building project from the fire safety point of view.

3.2 Standardization needs

According to the views of the fire regulators of the countries that allow for the use of FSE approach in construction projects, the most important topics for standardisation to be further developed are, namely: the fire safety performance and acceptance criteria, and the selection of design fires and design fire scenarios (Figure 10). Standardised FSE assessment methods, definition of limits in simulation models, and objectives and functional requirements of fire safety designs are also identified as important topics.
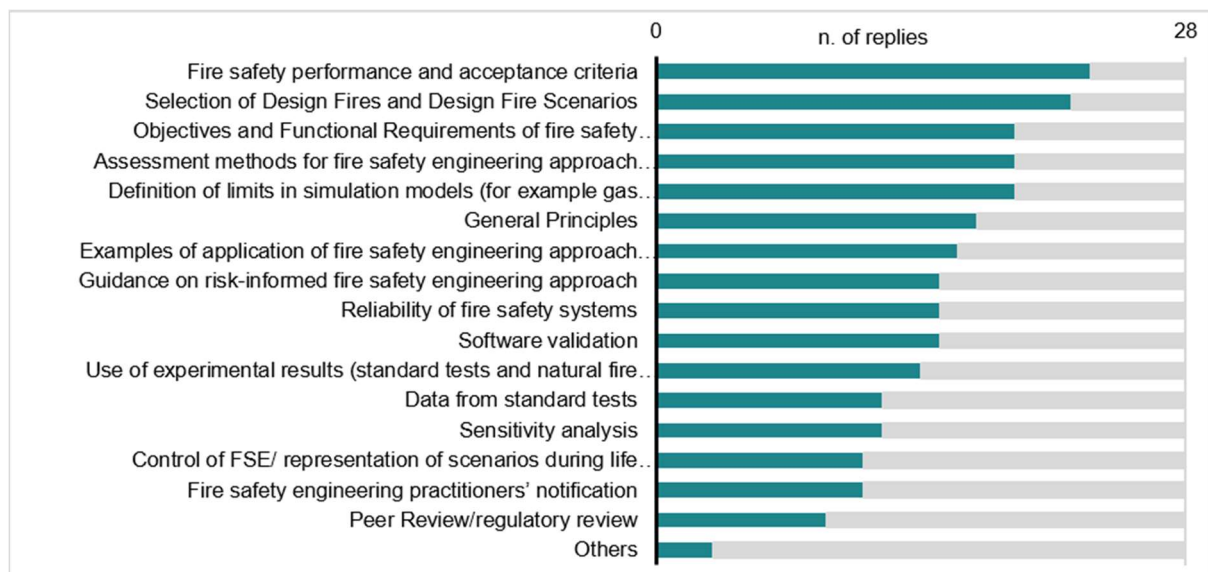
Figure 10: Topics in need of development by standardization organisations, according to the responders of FSE-allowing countries

In the countries that apply FSE approach in building fire design, the need for standardisation is particularly high in the selection of design fires and fire scenarios, as well as in the fire safety performance and acceptance criteria. In fact, such responsibilities currently rely on expert judgement, as shown by the responses about the specifiers of fire scenarios, design fires and fire safety criteria. The development of standards in such fields would increase the uniformity and objectivity in the processes of design and evaluation of FSE projects.

The research needs identified by all responding countries / regions (FSE-allowing and not) are illustrated in Figure 11. It is noted that according to the responders' opinions, there are many areas of research in need of development to improve the implementation of FSE approach.

It seems that the fire safety design in innovative buildings might be the ideal target for the use of FSE based design methods (new materials and innovative solutions). Moreover, it is evident that the design procedures should be based on scientifically obtained data and models (i.e., fire science, such as fire spread, flame spread, smoke spread, smoke developments, smoke toxicity, other) and further focus on the users' communities (Human behaviour and/or evacuation).

Moreover, the objectives and functional requirements of fire safety design, the assessment methods for FSE approach (such as evacuation safety design, structural fire safety design, and smoke control) and the definition of limits in simulation models (e.g. gas concentration, visibility, shoot yield, walking pace) are indicated by the responders as topics of interest for standardisation. This indeed confirms the need of support, especially for designers in the use of advanced calculation methods.

Finally, there is agreement about the importance of research for the future development of FSE-based approach. As the responses of all countries / regions indicate, research should deepen the knowledge in fire science and material behaviour in fire as well as human behaviour and/or evacuation and fulfil the need for innovative materials and solutions for fire design. This points out that the fire safety design of innovative buildings – especially featuring innovative materials or technological solutions – is seen as the main task of FSE; it must rely on scientifically obtained data and models from physics (of fire, materials etc.) as well as from human sciences.
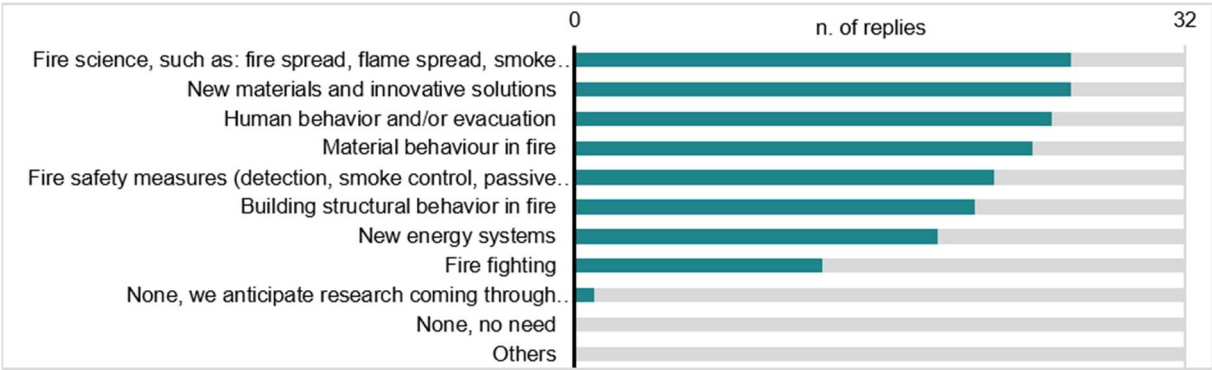
Figure 11: Research needs for FSE implementation, according to all the responders

4. CONCLUSIONS

The results here presented and elaborated will be useful to plan the next steps of the JRC's activity in support of the incorporation of a FSE approach in Europe. The information collected through the JRC enquiry enlightened the main aspects of the fire design practice in building construction (excluding industrial buildings and plants) process. The JRC enquiry was carried by means of a questionnaire addressed to selected recipients (fire regulators of the EU/EFTA countries, United Kingdom and Serbia). Generally, it enlightened that the implementation of FSE in building fire design is not yet fully achieved, being the availability of performance-based solutions generally lesser than prescriptive ones throughout the considered FSE technical details or areas.

The prospects for FSE implementation in the building fire regulations of the European countries appear positive, because FSE is virtually applicable in all or many FSE related technical areas, and to all or many types of constructions. However, mainly only one assessment approach for technical solutions per technical area is available, and the availability of assessment methods mainly depends on the availability of national regulations and standards.

In most cases (22 countries), the liability for fire safety design can be undertaken by a subject with specific expertise in fire safety. Generally, this figure is seen as a specialist to be involved in the design of a building based on certain criteria – mainly related to the physical and functional characteristics of the project and to the principle that designers are responsible for what they design. However, further insight is necessary on such criteria (10 countries have not specified any of them). In the ten countries where the fire safety designer cannot be liable, there is the need for clarifying the level of specific fire safety expertise of the liable subjects – especially, the education and training of designers like the architect or the structural engineer. In the limited cases where other subjects are liable, further insight is needed to clarify how fire safety competency is granted in the whole process of project design, review and approval.

A significant fact emerging from the enquiry result is the frequent absence of an explicitly defined qualification framework for professionals involved in FSE practice (4 countries) or regulatory reviewers of the FSE approach in projects (2 countries), or both (5 countries). On the other hand, in 10 countries the qualification of both actors of the

building fire safety process depends on acknowledgement by the government in different ways. These strong differences in approach deserve further study to explore their relationship with the level of FSE implementation in the different countries.

Fire engineers / consultants generally undertake the basic tasks of fire safety design in construction projects. To perform their tasks, they need to be aware of internationally recognised documents as well as of the availability of data, tools and methods for applying FSE design. The construction of an effective dialogue between professionals and approving authorities, when it comes to FSE application – especially local authorities and fire brigade – is also very important to support implementation of FSE approach in practice.

The effective implementation of a FSE approach in building fire design largely depends on the availability of FSE-oriented education and training – particularly for design professionals and officers (including firefighters) called to review and approve fire design projects. The responders also agree on the need for FSE implementation supported by research for standardisation, especially for the benefit of professionals who are involved in fire safety design practice.

ACKNOWLEDGEMENTS

REFERENCES

[1] European Union: European Commission, Communication from the Commission to the European Parliament, the Council and the European Economic and Social Committee and the Committee of the Regions: The European Green Deal, 11 December 2019, COM(2019) 640 final.

[2] European Union: European Commission, Communication from the Commission to the European Parliament, the Council and the European Economic and Social Committee and the Committee of the Regions: A Renovation Wave for Europe – greening our buildings, creating jobs, improving lives, 14 October 2020, COM (2020) 662 final.

[3] European Union: European Commission, Communication from the Commission to the European Parliament, the Council and the European Economic and Social Committee and the Committee of the Regions: New European Bauhaus Beautiful, Sustainable, Together, 15 September 2021, COM (2021) 573 final.

[4] Regulation (EU) No 305/2011

[5] European Union: Proposal for a Regulation of the European Parliament and of the Council laying down harmonized condition for the marketing of construction products, amending Regulation (EU) 2019/1020 and repealing Regulation (EU) 305/2011, 30 March 2022: COM(2022) 144.

[6] European Union: Proposal for a Directive of the European Parliament and of the Council on the energy performance of buildings (recast), 15 December 2021: COM (2021) 802 final.

[7] European Union: European Commission, Communication from the Commission to the European Parliament, the Council and the European Economic and Social Committee and the Committee of the Regions: Forging a climate-resilient Europe – the new EU Strategy on Adaptation to Climate Change, 24 February 2021, COM (2021) 82 final.

[8] Papadaki, I.; Moseley, P.; Staelens, R.H.; Nieto Sanz, O.; Lipari, M.; Gutierrez Velayos, P.; Vaananen, H.; Transition Pathway for Construction, European Commission, 2023.

[9] European Union: European Commission, Communication from the Commission to the European Parliament, the Council and the European Economic and Social Committee and the Committee of the Regions: An EU Strategy on Standardisation Setting global standards in support of a resilient, green and digital EU single market, 2 February 2022, COM(2022) 31 final.

[10] Athanasopoulou, A.; Sciarretta, F., Sousa, M.L.; Dimova, S., The status and needs for implementation of Fire Safety Engineering approach in Europe, EUR 31383 EN, Publications Office of the European Union, Luxembourg, 2023, doi:10.2760/031591, JRC131689

[11] International Standard Organisation, Fire safety engineering – Survey of performance-based fire safety design practices in different countries, SC4 N1290 ISODTR 20413, 2019.

[12] Joyeux, D., BeneFEU - Benefits of fire Safety Engineering in the EU, The potential benefits of Fire Safety Engineering in the European Union, Final Report to DG Enterprise, 19 July 2002.

NUMERICAL ANALYSIS OF VERTICAL COMPARTMENTATION IN MULTI-STORY BUILDINGS UNDER FIRE SITUATIONS

Jaete C. Junior a

Macksuel S. Azevedo* b

João V. F. Dias c

ABSTRACT

Fires cause great disruption and damage, and it is necessary to adopt control measures to minimize their spread. For this reason, experimental and numerical research plays a fundamental role in advancing scientific knowledge on this topic. Experimental tests have high added value, and with the improvement of computer processing, computational numerical analyses are increasingly used for this type of research. The Fire Dynamics Simulator (FDS) is a computer program capable of performing computational numerical analyses of fluid dynamics, widely used by researchers worldwide. Thus, this research aims to numerically analyze with the aid of FDS, whether the control requirements (horizontal projection and projections summation), disposed in IT (technical instruction) 09/2019 are effective in combating the external vertical fire propagation, by means of temperature measurements on the facade, comparing with ignition values of materials present in upper floors of buildings. The obtained results show that the models by projections summation do not present the same efficacy among themselves, and with the temperatures extracted from this study, it is concluded that for the models analyzed in this work, the fire propagation would not occur to the upper floors of the building under study.

Keywords: Fire Dynamics Simulator; computational fluid dynamics; numerical analysis; vertical compartmentation; passive protection.

ᵃ Jaete Corrêa Junior (jaetejunior@hotmail.com).

ᵇ, * Macksuel Soares de Azevedo, Corresponding Author – Graduate Program in Civil Engineering at the Federal University of Espírito Santo. Address: Avenida Fernando Ferrari, 514, Goiabeiras Campus, Vitória, ES, Postal Code: 29.075-910, email: macksuel.azevedo@ufes.br.

ᶜ João Victor Fragoso Dias (joao.v.dias@ufes.br).

1. INTRODUCTION

The increasing demand for different arrangements of openings in facades has left buildings susceptible to the risk of external flame propagation that emerges between floors. Therefore, countries have adopted specific standards that deal with horizontal and vertical compartmentation, presenting parameters to prevent the spread of fire to other environments. The study of vertical fire propagation on the facade aims to technically evaluate the requirements contained in current fire safety standards, in order to enable the verification of the effectiveness of these control requirements (spandrel, horizontal projection and summation of both).

The Fire Dynamics Simulator (FDS) is a computer program that uses the finite volume method in computational fluid dynamics (CFD) and is viable for computational numerical analysis of fire propagation, being used by researchers worldwide. According to Zhang, Zhu, and Zhao (2016), there are financial and experimental limitations for fire safety research due to its high added value. However, with the rapid improvement in computer processing capacity, the use of computational numerical analyses is becoming increasingly viable.

There are no ABNT (Brazilian Association of Technical Standards) standards on the topic of vertical compartmentation, leaving it up to each state to develop its own technical instructions (IT). Technical Instruction No. 09/2019 of the São Paulo State Fire Department deals with horizontal and vertical compartmentation and is the main reference for the development of technical instructions in other states.

Technical Instruction No. 09/2019 of the São Paulo State Fire Department specifies that spandrel must offer a minimum separation of 1.20m between the openings of subsequent floors. In the case of the use of horizontal projections, this separation by extending the floors must have, at least, 0.90m beyond the facade alignment (CBMESP, 2019). The use of a combination of vertical and horizontal projections is also allowed, as long as the occupations of these buildings are low-risk, with a fire load of up to 300MJ/m², and have a minimum sum of horizontal and vertical dimensions of 1.20m.

The main objective of this analysis is to numerically evaluate the requirements for containing external vertical fire propagation contained in IT 09/2019 in force, in order to enable the verification of the effectiveness of these control requirements (spandrel, horizontal projections, and summation of both), through the comparison between temperatures on the upper floor facade with auto ignition temperatures of typical materials on facades of buildings. Other models similar to those contained in IT 09/2019 were also analyzed for greater research coverage.

2. REGULATORY STANDARDS FOR VERTICAL COMPARTMENTATION IN BUILDINGS

In this research, safety regulations against fire were used, which deal with the sizing of vertical compartmentation in buildings, for the containment of vertical fire propagation to other environments, from four countries: Brazil, Portugal, the United States of America, and England.

2.1 Brazil

In Brazil, each state has its own regulatory safety standards against fire, called Technical Instructions (or Technical Standards), which are different from the Brazilian Standards (NBR) that regulate the entire national territory. The Technical Instructions of the Military Police Fire Brigade of the State of São Paulo are known for their quality, and because other states in the federation adopt their text. Therefore, in this work, Technical Instruction No. 09/2019 from São Paulo is considered, which deals with the horizontal compartmentation and vertical compartmentation of buildings.

Spandrel must offer a minimum separation of 1.20 m between the openings of subsequent floors (Figure 9). In the case of the use of horizontal projections, this separation must be made by prolonging the mezzanine floors, at least 0.90 m beyond the facade alignment (CBMESP, 2019). Technical Instruction No. 09/2019 (CBMESP, 2019) also allows the use of a combination of spandrel and horizontal projections, provided that the occupations of these buildings are of low risk (up to 300MJ/m²), meet a minimum of 1.20 m in combined dimensions, and are exposed to the external environment.
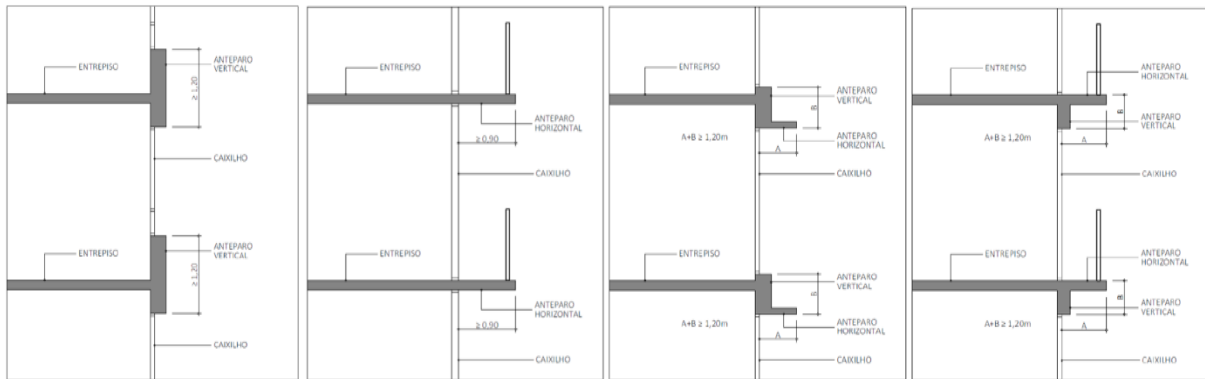
Figure 1: Models of projections contained in IT 09/2019

2.2 Portugal

In Portugal, fire safety regulations are specified in Portaria N° 1532/2008. In Portuguese regulations, facade elements with the same alignment and located on successive floors must have a height greater than 1.10 m. The use of protruding elements such as canopies, balconies or terraces is also allowed, provided that they extend more than 1.00 m to each side of the facade openings. In addition, a value of 1.10 m must be considered as the distance between overlapping openings added to the projection of the protruding elements, provided that these elements can guarantee the EI 60 fire resistance class (fire-cutting element with airtightness to flames for 60 minutes).

2.3 United States of America

In the United States of America, fire safety regulations are specified by the standards of the National Fire Protection Association (NFPA). The Building Construction and Safety Code, NFPA 5000 (2021), deals with the necessary requirements for the vertical separation of external openings in buildings.

According to NFPA 5000 (2021), buildings with four or more floors that are not protected by a sprinkler system, according to NFPA 13 or NFPA 13R, must be separated or protected by at least one of the following:

1) The exterior walls between the openings must provide a minimum fire resistance of 60 minutes;
2) Vertical protection (spandrel) must not be less than 0.915 meters in height and must be located between the openings;
3) Horizontal protection must not be less than 0.760 meters in length and must be located between the openings.

2.4 England

In England, fire safety regulations are specified in the Building Regulations 2010 (2020). This document deals with construction techniques, including fire safety. According to the regulation, in case of fire spread through the facade, external walls of buildings must adequately resist vertical fire spread and spread from one building to another, taking into account the height, use, and position of the building.

Regarding vertical projections (spandrel) for vertical fire containment, the value considered is 1.00 m, while for horizontal projections, no specific value was found.

3. METHODS

The method used for this study is computational numerical analysis, where numerical simulations are carried out to evaluate the possibility of vertical external fire propagation in multi-story buildings. The numerical simulations of the study will be processed through the computational numerical analysis program Fire Dynamics Simulator (FDS), developed by the Institute of Standards and Technology (NIST) and the VTT Technical Research Centre of Finland (MCGRATTAN et al., 2021).

The experimental design of this research consists of conducting twelve numerical simulations, to perform comparative analyses between horizontal projections and sum of projections, considering the minimum values prescribed in the regulations, in order to evaluate the effectiveness of the different projections models contained in the IT 09/2019 of the Fire Department of São Paulo. Table 1 shows the list of analyzed numerical simulation models.

Table 1: Simulation models

ACRONYM	PROJECTIONS	LEVELS	DIMENSIONS	FIRE LOAD (MJ/m²)
M-V0,0-H0,4	Horizontal projections	Level 1	0,40m	300
M-V0,0-H0,6		Level 2	0,60m	300
M-V0,0-H0,8		Level 3	0,80m	300
M1-V0,6-H0,6	Sum of spandrel and horizontal projections - Model 1	Level 1	0,60m + 0,60m	300
M1-V0,4-H0,8		Level 2	0,40m + 0,80m	300
M1-V0,8-H0,4		Level 3	0,80m + 0,40m	300
M2-V0,6-H0,6	Sum of spandrel and horizontal projections - Model 2	Level 1	0,60m + 0,60m	300
M2-V0,4-H0,8		Level 2	0,40m + 0,80m	300
M2-V0,8-H0,4		Level 3	0,80m + 0,40m	300
M3-V0,6-H0,6	Sum of spandrel and horizontal projections - Model 3	Level 1	0,60m + 0,60m	300
M3-V0,4-H0,8		Level 2	0,40m + 0,80m	300
M3-V0,8-H0,4		Level 3	0,80m + 0,40m	300

3.1 Building Geometry

The proposed building geometry in this work aims to reproduce a typical room of a multi-story building, with internal dimensions of 3.00m x 3.00m and a height of 2.60m. All walls and slabs of the building were considered to have a thickness of 0.20m. Thus, a standard model was created, to which independent variables were subsequently added one at a time, enabling the evaluation of their respective efficacies. It is important to note that no type of closure was provided on the front facade, only the projections were present on it.

3.2 Models of projections analyzed

The models of projections analyzed in this study were those prescribed in IT 09/2019, with variations in their dimensions. Other models similar to those contained in IT 09/2019 were also analyzed for greater research coverage. Table 1 shows the acronyms, models, and dimensions of the projections used.

In the models with horizontal projections, slab extensions of 0.80 m, 0.60 m, and 0.40 m were inserted. It is worth noting that the dimensions of these horizontal projections are not adequate for IT 09/2019, but were simulated to enable a comparison between these dimensions of horizontal projections with models by sum of projections with a horizontal projections component equal to the dimensions presented above, as shown in Figure 2.
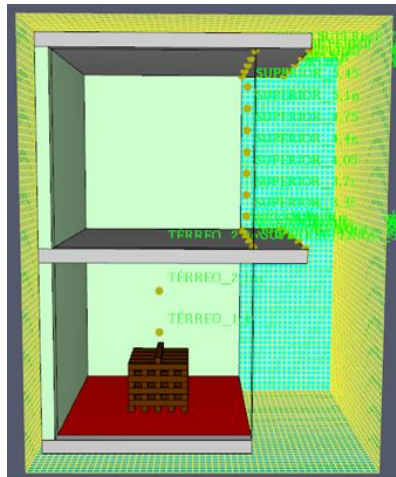
Figure 2: Model with horizontal projections

The models for the sum of spandrel and horizontal projections were evaluated according to the two models contained in IT 09/2019, and a third model proposed by the author. For all the analyzed models, normative prescriptions were respected which established that the sum of the spandrel and the horizontal projections should be greater than or equal to 1.20 m. As the Technical Instruction does not specify limits for the measurements of the projections, this work used measures defined by the authors and displayed in Table 1, always respecting the minimum limit defined by IT 09/2019. In Figure 3, models 1, 2, and 3 of vertical compartmentation by sum of spandrel and horizontal projections are presented.
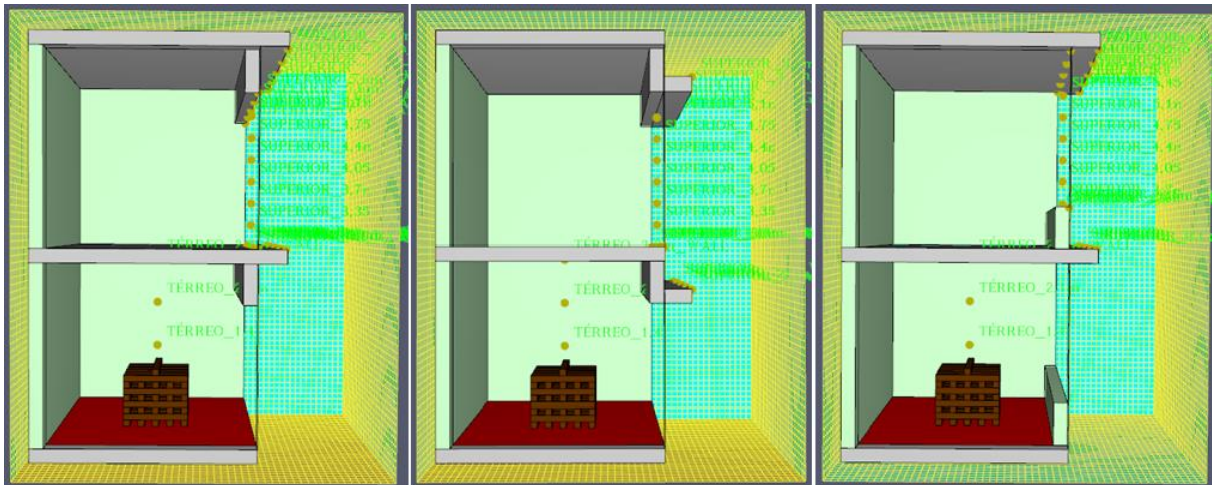
Figure 3: Models 1, 2, and 3 of vertical compartmentation by summing of spandrel and horizontal projections.

3.3 Fire load

To reproduce the fire load in this study, the methodology known as "wood equivalent" was used, in which wood is used to reproduce the necessary fire load in a given environment. For this study, a quantity of wood was arranged to simulate a fire load of 300 MJ/m².

To compose the fire load of 300 MJ/m², wooden elements were arranged in the dimensions of 0.10m x 1.00m x 0.10m (width x length x thickness) in the quantity of 41 wooden units divided into 8 layers of 5 units and 1 layer of 1 unit, forming an element similar to a pallet. Table 2 shows the characteristics of the woods used for the composition of the fire load.

Table 2 - Wooden elements for the composition of the fire load of 300 MJ/m²

Description		Units	Properties of the wood
Characteristics of the wood	Density	kg/m³	369,60
	Calorific Potential	MJ/kg	17,90
Geometry of wooden pieces	Width	m	0,10
	Length	m	1,00
	Thickness	m	0,10
	Volume	m³	0,01
Overall	Compartment Area	m²	9,00
	Total Fire Load	MJ	2712,51
	Specific Fire Load	MJ/m²	301,39
	Quantity of elements	un.	41,00

3.4 Temperature measurement devices

The temperature measurement devices used in this study included gas temperature measurement devices inside the fire compartment, as well as on the facade of the upper floor. Surface temperature measurement devices were also placed on the underside of the floor slab of the fire compartment and at the ends of the spandrel and horizontal fire projections, to enable the analysis of temperature on the underside of the slab and the fire containment elements. Flat temperature measurement devices, called "slices", were placed longitudinally in the central part of the building and transversely in the central and facade parts of the building (Figure 4).
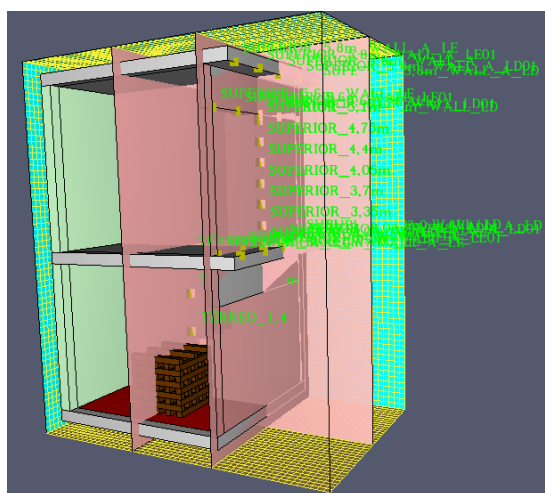
Figure 4: Measurement devices

The devices are named according to their positions in the building. For example, the gas measurement device named "SUPERIOR_4,4 m" is located on the upper floor of the building at a height of 4.40 meters above ground level. The surface temperature measurement device named "TÉRREO_2,8 m_WALL" is located on the lower floor of the building at a height of 2.80 meters above ground level.

4. RESULTS

The results of the models presented in this study have their names and characteristics presented in Table 1. Therefore, a comparison of the effectiveness of the models with horizontal projections and the three models with sum of spandrel and horizontal projections will be presented.

4.1 Comparative of models by sum of spandrel and horizontal projections

For the execution of this comparative study, numerical simulations were carried out using FDS, which made it possible to evaluate the behavior of the fire in the models by sum of spandrel and horizontal projections. Three fire scenarios were carried out, keeping the same dimensions for models 1, 2, and 3, in addition to the insertion of a model with only a horizontal projections in the same dimension as the horizontal part of the aforementioned models. It is worth mentioning that the models by sum of spandrel and horizontal projections analyzed have a horizontal sum of a minimum dimension of 1.20 m, to comply with the instruction contained in IT 09/2019. Table 3 shows the characteristics of each comparison.

Table 3: Characteristics of fire scenarios

MODELO	SCENARIO 1		SCENARIO 2		SCENARIO 3	
	ACRONYM	DIMENSIONS	ACRONYM	DIMENSIONS	ACRONYM	DIMENSIONS
Horizontal projections	M-V0,0-H0,4	0,40m	M-V0,0-H0,6	0,60m	M-V0,0-H0,8	0,80m
Sum of spandrel and horizontal projections - Model 1	M1-V0,8-H0,4	0,80m + 0,40m	M1-V0,6-H0,6	0,60m + 0,60m	M1-V0,4-H0,8	0,40m + 0,80m
Sum of spandrel and horizontal projections - Model 2	M2-V0,8-H0,4	0,80m + 0,40m	M2-V0,6-H0,6	0,60m + 0,60m	M2-V0,4-H0,8	0,40m + 0,80m
Sum of spandrel and horizontal projections - Model 3	M3-V0,8-H0,4	0,80m + 0,40m	M3-V0,6-H0,6	0,60m + 0,60m	M3-V0,4-H0,8	0,40m + 0,80m

Figures 5 and 6 show the values of temperatures on the building facade measured by the "SUPERIOR_5.1 m" device for scenario 1 and the behavior of the fire, respectively.

614

Figure 6: Behavior of the fire in scenario 1. In the grids, each division represents 50 cm

The fire reached its maximum temperature at this point on the facade of 28.49 °C at 952.80 seconds for model M-V0.0-H0.4, 112.99 °C at 849.61 seconds for model M1-V0.8-H0.4, 159.85 °C at 900.01 seconds for model M2-V0.8-H0.4, and 34.23 °C at 2359.21 seconds for model M3-V0.8-H0.4. Note that the data extracted from figures 5 and 6 indicate that the horizontal firebreak acting alone was more effective in containing the vertical fire propagation, as shown in figure 6, the fire had a tendency to move away from the building for this firebreak model. However, the sum of spandrel and horizontal projections models showed lower efficiency than the horizontal projections model, even though the horizontal measure (0.4 m) of all models is the same. It is worth highlighting that all analyzed models have the same fire load of 300 MJ/m².

Figures 7 and 8 show the values of temperatures on the building facade measured by the "SUPERIOR_5.1 m" device for comparison 2 and the behavior of the fire, respectively.

Figure 7: Scenario 2

Figure 8: Behavior of the fire in scenario 2. In the grids, each division represents 50 cm

The fire reached its maximum temperature at this point on the facade at 24.32 °C at 1219.21 seconds for model M-V0.0-H0.6, 59.45 °C at 708.00 seconds for model M1-V0.6-H0.6, 110.07 °C at 775.20 seconds for model M2-V0.6-H0.6, and 25.11 °C at 2179.20 seconds for model M3-V0.6-H0.6. Note that the data extracted from figures 7 and 8 also indicate that the horizontal projections acting alone was able to more effectively contain the vertical fire propagation, as shown in figure 7, where the fire tended to move away from the building for this projection model. The models with sum of spandrel and horizontal projections presented inferior effectiveness compared to the model with only the horizontal projections, even though the horizontal measure (0.6 m) of all models was equal. It is important to note that, compared to scenario 1, the temperatures on the facade presented in the models of scenario 2 were lower, since the horizontal projections in this scenario is larger than in the first.

Figures 9 and 10 show the values of the temperatures on the building facade measured at the "SUPERIOR_5.1 m" device for the comparison 3 and the fire behavior, respectively.
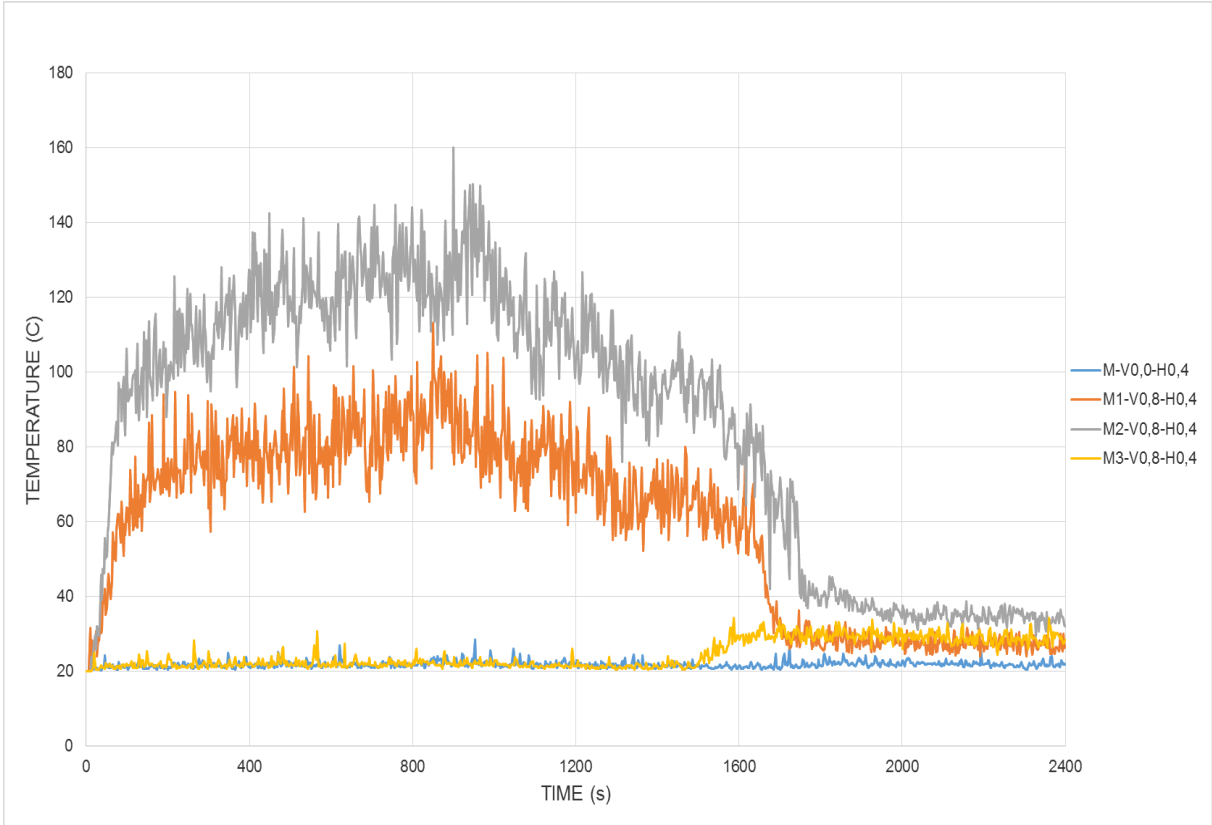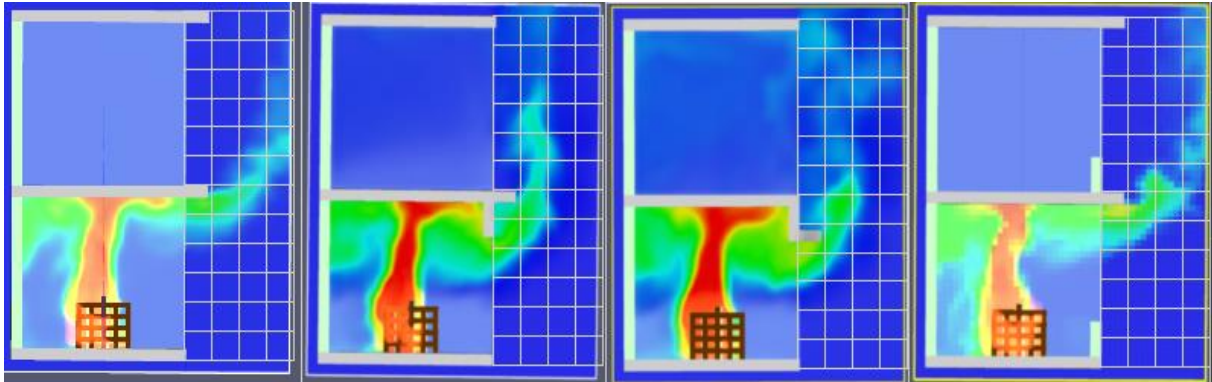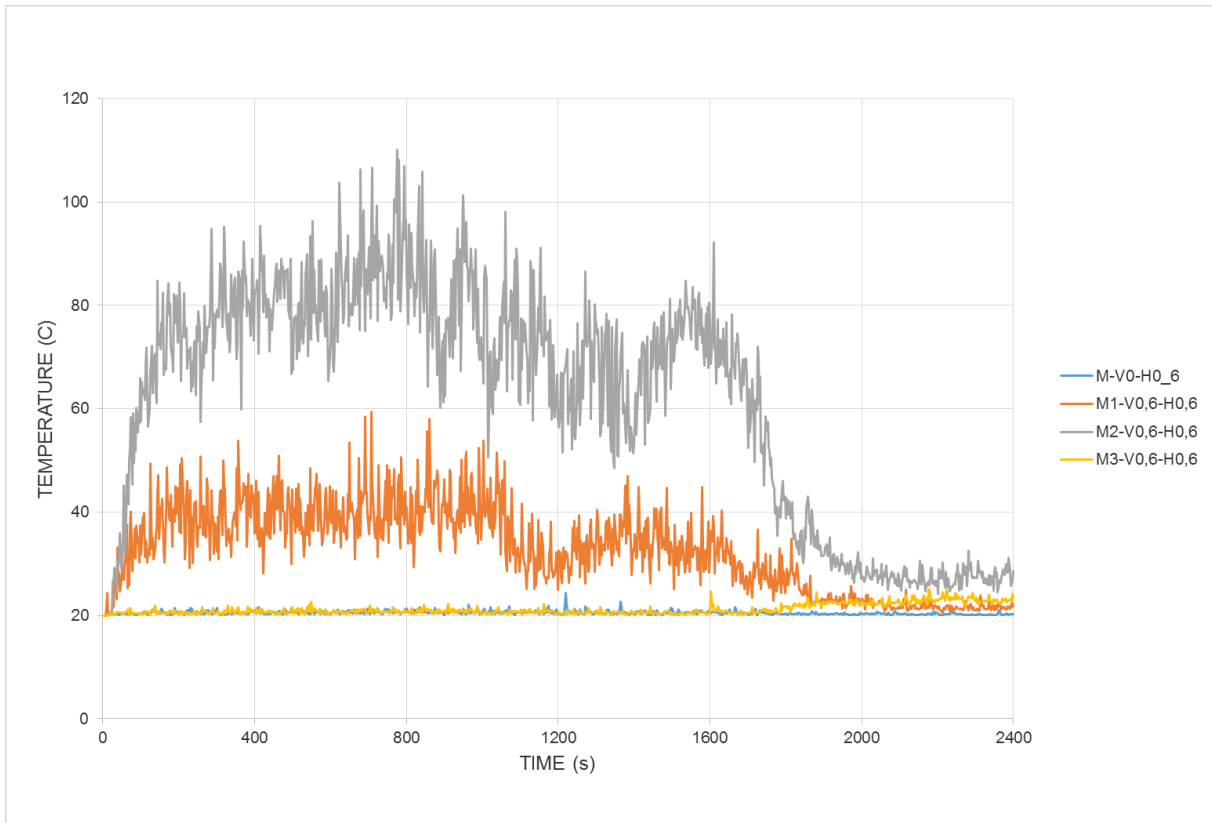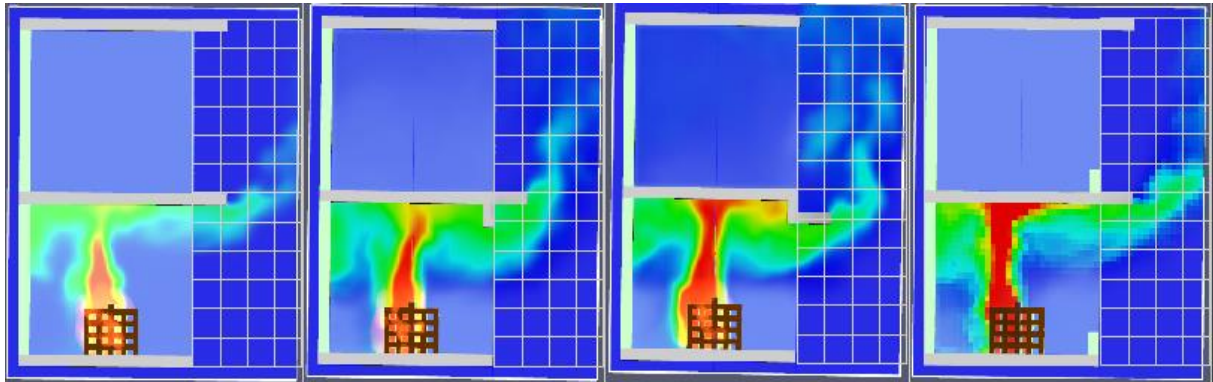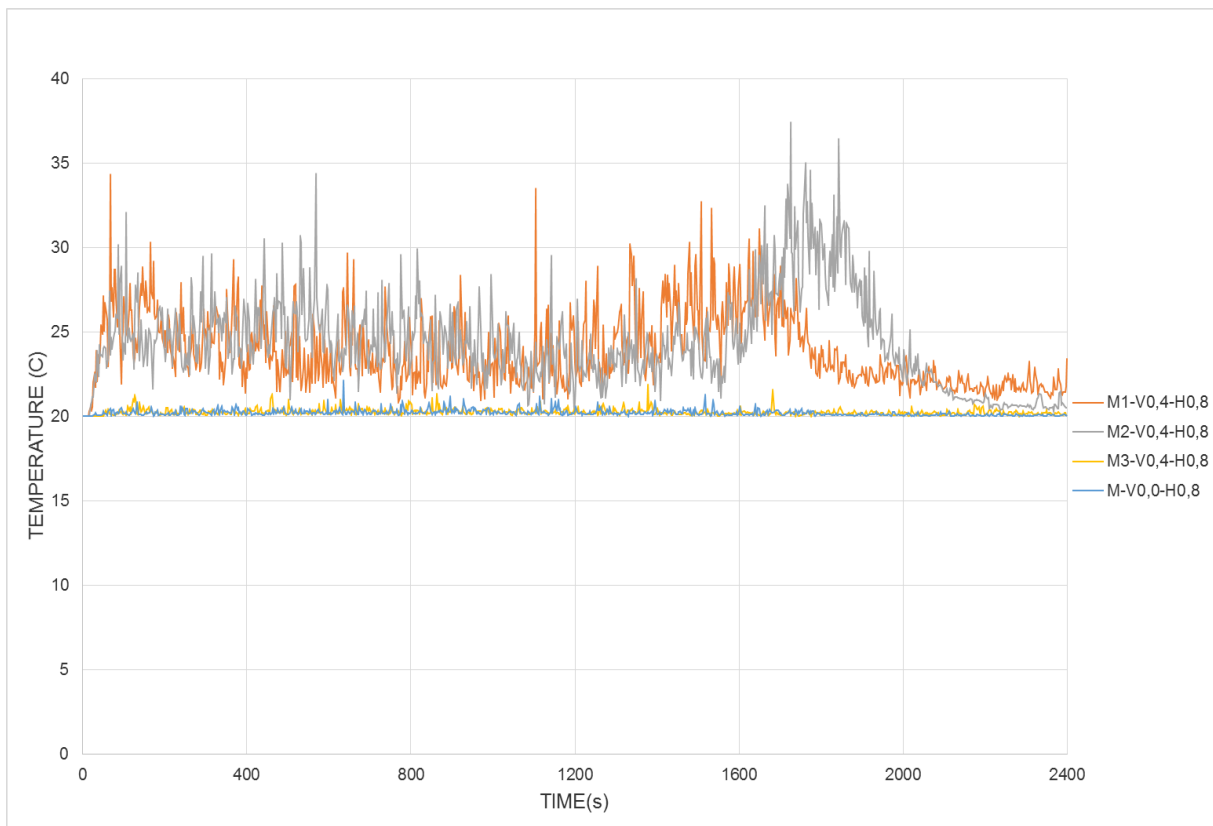

Figure 9: Scenario 3
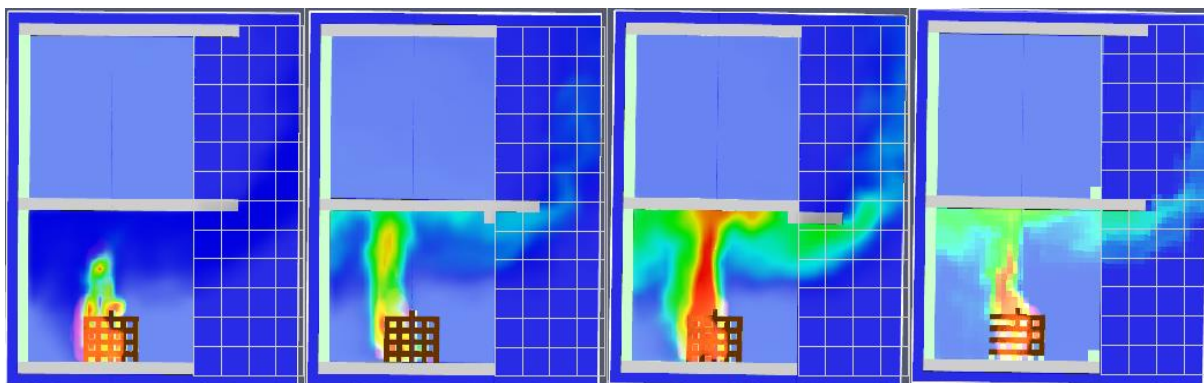
Figure 10: Fire behavior in scenario 3. In the grids, each division represents 50 cm

The fire reached its maximum temperature at this point on the facade at 22.06 °C at 636.01 seconds for model M-V0.0-H0.8, 34.30 °C at 67.21 seconds for model M1-V0.4-H0.8, 37.36 °C at 1725.60 seconds for model M2-V0.4-H0.8, and 21.85 °C at 1377.61 seconds for model M3-V0.8-H0.8. Note that the data extracted from figures 9 and 10 also indicate that the horizontal projections acting alone was able to more effectively contain the vertical fire propagation, except for model M3-V0.8-H0.8, which had slightly better performance, but which can be considered equivalent to model M-V0.0-H0.8 due to the small percentage difference in the maximum temperature. The fire had a tendency to move away from the building for these projections models. The models M1-V0.4-H0.8 and M2-V0.4-H0.8 with sum of spandrel and horizontal projections presented inferior effectiveness compared to the model with only the horizontal projection, even though the horizontal measure (0.8 m) of all models was equal. It is important to note that, compared to scenarios 1 and 2, the temperatures on the facade of the model in scenario 3 were lower, which occurred due to the larger portion of the horizontal projection in this scenario.

The behaviors of fires and the temperatures presented previously in scenarios 1, 2, and 3 can be explained by the fact that when there is a wall above the opening of the burning floor, the tendency of hot gas is to rise close to the building wall, thus increasing the temperature in the upper floor (YOKOI, 1960). It is also important to mention that the rates of openings in the burning floor influence the temperature in the upper floor. It is possible to observe that higher rates of openings on the facade of a building lead to lower temperatures, while lower rates of openings lead to higher temperatures. Therefore, the larger the free openings on a facade, the tendency is for the temperatures in the upper floor to be lower (GUIMARÃES, 2022). Thus, it is possible to verify that the models by summation of spandrel and horizontal projections contained in IT 09/2019 (scenarios 1 and 2) and the model proposed by the author (scenario 3) are not equivalent because they do not present the same efficacy in containing the fire in the burning floor. This occurs because when a designer chooses to use a greater spandrel in the model by summation of spandrel and horizontal projections, the temperature in the upper floor tends to rise, making it necessary to establish normative criteria (limits) for the best use of these measures.

5. CONCLUSIONS

In this work, the effectiveness of 1 horizontal projection model and 3 models using a sum of spandrel and horizontal projections was analyzed using the FDS computational numerical analysis program. The dimensions defined for the horizontal projection models were established considering the value of the horizontal measurement of the model by the sum of the spandrel and horizontal projections, therefore, in the configurations adopted, all have values lower than 0.9m, thus being a measurement lower than that proposed in the IT 09/2019. For models 1, 2, and 3 using a sum of spandrel and horizontal projections, dimensions were defined that were summed up to at least 1.20 m, as prescribed in technical instruction IT 09/2019. It is important to note that models 1 and 2 are contained in the IT, while model 3 was defined by the author in order to increase the scope of the work.

In comparing the temperatures of the aforementioned models, it is noted that they do not have the same effectiveness, since projections with larger horizontal dimensions will always tend to obtain better results. This occurs due to the horizontal projection being more effective than other measures for controlling the propagation of external fire. It is also noted that when choosing to use a larger spandrel portion in the sum of spandrel and horizontal projections models, the temperature in the upper floor tends to rise, since the presence of a wall above

the opening of the burning floor causes a tendency for the hot gas to rise closer to the building facade, thus increasing the temperature in the upper floor.

On the facades of models with larger portions of spandrel, it was noticed that the temperatures in the upper floor were higher, since in these cases, it is possible to associate this with a lower availability of oxygen entry into the interior of the burning floor, as oxygen acts as an oxidizer in the propagation of fire, where a lower portion of oxygen in this case delays the burning of the fuel (wood) a little more, making the fire longer-lasting and consequently raising the temperatures on the building facade. In the opposite case where the openings on the facade are larger, the supply of oxidizer will be abundant, causing a rapid burning of the fuel, making the fire faster and with lower temperatures on the building facade.

In the numerical modeling of this research, a maximum temperature of 159.85 °C was found at 900.01 seconds for model M2-V0.8-H0.4, a relatively low temperature for the propagation of fire to the upper floors of a building. According to Lawson (2009), temperatures up to 100 °C can cause discomfort and severe burns on human skin, but when it comes to the auto ignition of constituent materials around a facade, such as cotton and fabrics, this temperature is not capable of initiating the carbonization process of these materials, since temperatures between 250 to 399 °C would be necessary for that to happen. Therefore, it is possible to affirm that for the models simulated in this work with a fire load of 300 MJ/m², there would be no propagation of fire to the upper floors of the building under study.

6. ACKNOWLEDGMENTS

7. REFERÊNCIAS

[1] BRAGA, G. C. B. (2016). *Temperature and heat flux in a fire situation and its consequences for firefighters*, Flammae, vol. 2, no. 4, 2016, p. 09-28.

[2] CORPO DE BOMBEIROS DA POLÍCIA MILITAR DO ESTADO DE SÃO PAULO - CBPMESP. (2019). *Technical Instruction No. 09/2019: Horizontal compartmentation and vertical compartmentation,* São Paulo: Secretaria de estado dos Negócios da Segurança Pública, 20 p.

[3] CORPO DE BOMBEIROS DA POLÍCIA MILITAR DO ESTADO DE SÃO PAULO - CBPMESP. (2019). *Technical Instruction No. 014/2019: Fire load in buildings and risk areas,* São Paulo: Secretaria de estado dos Negócios da Segurança Pública, 12 p.

[4] GUIMARÃES, S.A. (2021). Numerical analysis of fire porpagation between confrontes buildings, Masters dissertation, Federal University of Espírito Santo, 174 p.

[5] HM GOVERNMENT. (2020). *The Building Regulations 2010: The Merged Approved Documents,* England, 1274 p.

[6] McGRATTAN, K., et al. (2021). *Fire Dynamics Simulator User's Guide: Sixth Edition,* NIST Special Publication 1019: National Institute of Standards and Technology – NIST, Maryland (USA), 314 p.

[7] NATIONAL FIRE PROTECTION ASSOCIATION - NFPA. (2021). *NFPA 5000: Building Construction and Safety Code, USA*, 683 p.

[8] LAWSON, J. R. (2009). *Fire Facts, NIST Special Publication 1102, National Institute of Standards and Technology*, Gaithersbusg, MD, 7 p.

[9] NILSSON, M.; HUSTED, B.; MOSSBERG, A.; ANDERSON, J.; MCNAMEE, R. J. (2018). *A numerical comparison of protective measures against external fire spread*, Fire and Materials, vol. 42, Edição 5, 2018, p. 493-507.

[10] PORTUGAL - PAÍS. (2008). *Portaria n° 1532/2008: Technical Regulation for Fire Safety in Buildings, PORTUGAL*, 78 p.

[11] TABACZENSKI, R.; CORRÊA, C.; ANCELMO, T.; RÊGO SILVA, J. J. (2019). *Numerical simulation and fire experiment in residential dormitory,* Alconpat, vol. 9, Edição 1, 2019, p. 15-29.

[12] YOKOI, S. (1960). *Study on the Prevention of Fire-spread Caused by Hot Upward Current*, Report No. 34, Japanese Building Research Institute, Tokyo, 137 p.

[13] ZHANG, G.; ZHU, G.; ZHAO, G. (2016). *Analysis of the Influence of Construction Insulation Systems on Public Safety in China,* International Journal of Environmental Research and Public Health, v. 13, Edição 9, 2016, Article 861.

Mechanical and Thermal Properties of Materials at High Temperatures

INFLUENCE OF THE DURATION OF FIRE INCIDENTS ON THE POST-FIRE IMPACT STRENGTH OF SELECTED STEEL GRADES USED IN CONSTRUCTION

Mariusz Maslak [1,*]
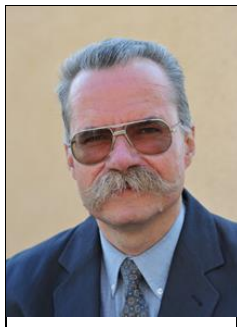
Michal Pazdanowski [1]

Marek Stankiewicz [1]

Paulina Zajdel [1]

ABSTRACT

The results of experimental research dealing with the influence the duration of exposure of selected steel grades to fire exerts on their post-fire brittleness are presented and substantively discussed. The detailed analysis pertains to steels of varied microstructure, in particular: *S355J2+N* steel – representative for conventional ferritic-pearlitic structural steel grades, and a few stainless steel grades, such as: *X6CrNiTi18-10* steel – characterized by austenitic structure, as well as *X2CrNiMoN22-5-3* and *X2CrMnNiN21-5-1* steels – both of mixed austenitic-ferritic structure, however, the first of these is of standard duplex type while the second one – of lean duplex type. The considered scenarios of simulated fire exposure have been selected so, as to follow the rules of steady state heating regime. The first series of experiments, associated with the "short" fire scenario, consisted of fast heating the samples to the assigned temperature and then keeping them in that temperature for one hour. In the second series of experiments, associated with the "long" fire scenario, the effective heating time has been extended to 10 hours. Two different levels of heating temperature have been applied, namely 600°C and 800°C. The cooling mode of the test samples has been varied as well. Slow cooling in the open air has been opposed to rapid cooling in water mist, simulating the results of extinguishing action conducted by fire brigade.

Keywords: fire exposure; fire duration; steel microstructure; impact strength; instrumented Charpy test.

1. INTRODUCTION

It is widely known, that the mechanical properties of steel cooled down after prior more or less prolonged action of fire temperature would substantially differ from analogous properties exhibited by the same steel, but evaluated a

---

[1] Cracow University of Technology, Warszawska 24, 31-155 Cracow, Poland, (e-mails: mmaslak@pk.edu.pl, michal.pazdanowski@pk.edu.pl, marek.stankiewicz@pk.edu.pl, paulina.zajdel@pk.edu.pl).

* Corresponding author.

priori, i.e. before initiation of fire action. Under such scenario these properties would be influenced not only by the intensity and heating method [1] realized in practice as well as the temperature reached during heating and the duration of the heating process itself, but also and perhaps even above all by the rate and speed of the cooling process affecting the steel during fire extinguishing phase, often associated with the firefighting operation. The permanent thermally induced changes in the microstructure of the material, including in particular changes in the shape, size, and arrangement of grains in the metallic matrix weakening the cohesion of grain embedding in this matrix, harmful secondary precipitates, micro-notches and micro-cracks growing uncontrollably, local hardening of the material, etc. [2] will determine the post-fire behavior of the evaluated steel after application of the external loads to structural components made of it, and thus the suitability of given steel grade for possible extended service after undergoing a fire incident. The allotropic transformation, especially the austenitic one, occurring at sufficiently high temperature level seems to be the key here.

The research conducted so far in this field had been in general limited to taking the inventory of quantitative changes induced by fire in the basic mechanical properties of the considered material, and in particular changes in the yield limit, ultimate bearing capacity or the modulus of the longitudinal elasticity. Detailed analyses have been made at first for conventional structural unalloyed steels [3], and subsequently for the steels of the same kind, but exhibiting increased strength [4, 5]. A difference in post-fire behavior of cold formed steel and hot rolled steel had been noted and analyzed [6, 7]. Another group of authors dealt with high strength steels (HSS) [8-16]. A significant difference in properties of these steel grades, exhibited after exposure to fire episodes, when compared against the properties of traditional unalloyed steel grades subjected to the same conditions has been found out. In addition, a significant influence of the way the fire extinguishing action has been conducted on the post-fire mechanical properties of such steels has been emphasized. In the context of analyses reported in this paper readers' attention should be turned to the works dealing with post-fire mechanical properties of stainless steels, in particular those exhibiting ferritic [19] structure as well as duplex steels [20, 21]. The papers [22-24] dealing with permanent changes in mechanical properties of various structural steel grades observed after a fire incident may be of special interest as well, as the traditional formal analysis is accompanied in these papers by statistical analysis, undoubtedly facilitating and validating the conclusions drawn.

The considerations presented in this paper are concentrated on a different aspect of such analyses. Here we analyze in detail the experimentally determined post fire impact strength exhibited by several, intentionally selected, steel grades. We recognize, that this material property may be treated as a reliable indicator of the forecast a posteriori resistance to brittle fracture. The results presented here represent a supplement to the results presented previously in [25-27]. We intend to show, in a somewhat expanded scope, how the behavior of steel, identified after finished fire incident followed by cooling, changes depending on the duration of the fire exposure.

2. STEEL GRADES SELECTED FOR ANALYSIS

The following steel grades have been selected for analysis:
- *S355J2+N* steel – a grade representative for conventional structural steels exhibiting two phase ferritic – pearlitic structure. This is a normalized steel, well weldable, with increased manganese content, with banded pearlite. Up to 350ºC it is relatively insensitive to short term thermal action. In the commercial nomenclature it is denoted by the symbol (Werkstoffnummer) 1.0577. Properties of this steel are listed in the code EN 10025-2 [28].
- *X6CrNiTi18-10* steel – a grade typical for stainless, acid resistant steels of single phase austenitic structure. This is a high alloy, chromium – nickel steel, sometimes with low amount of ferrite and carbon stabilized with addition of titanium. It is supersaturated from the temperature of 1100ºC. Is characterized by very good weldability. Exhibits good resistance to corrosion in natural environment, provided that low concentration of chlorine, salt, nitrogen acid and organic acids is ensured. This steel is applied in particular when high resistance to intercrystalline corrosion is required. Represents a group of special steel grades recommended for application in the temperature below 600ºC (due to the risk of harmful sigma phase precipitating in the temperature range of 650ºC-800ºC). In the commercial nomenclature it is denoted by the symbol (Werkstoffnummer) 1.4541. Properties of this steel are listed in the code EN 10088-1 [29].
- *X2CrNiMoN22-5-3* steel – as a grade typical for the stainless steels exhibiting a two phase austenitic-ferritic structure of standard duplex type (SDSS). This is a high alloy steel, chromium – nickel – molybdenum, supersaturated from the temperature of 1050ºC in water. Exhibits very good resistance to pitting and surface corrosion. Represents a group of duplex steels recommended for application in the

temperature up to 300ºC (due to the occurrence of harmful 475ºC brittleness phenomenon). In the commercial nomenclature it is denoted by the symbol (Werkstoffnummer) 1.4462. Properties of this steel are listed in the code EN 10088-1 [29].

- *X2CrMnNiN21-5-1* steel – a grade representative for the group of low alloy stainless steels, exhibiting two phase austenitic-ferritic structure of the lean duplex type (LDSS). The steels of this type, if compared against the traditional standard duplex steels, exhibit decreased chromium, molybdenum and nitrogen content. The chemical composition of these steels has been balanced as to obtain good resistance to localized and uniform corrosion. The microstructure of the duplex type, similarly to the SDSS steels, contributes to their high resistance to brittle fracture, in particular when dealing with advanced stress induced, intercrystalline and pitting corrosion. In the as delivered state this steel grade is characterized by high fatigue strength. Due to the risk of brittle fracture this steel should not be applied in the temperature higher than 250ºC. In the commercial nomenclature it is denoted by the symbol LDX 2101 (Werkstoffnummer 1.4162). Properties of this steel are listed in the code EN 10088-1 [29].

These steels differ in the scope of application in construction industry. Their varied microstructure, conditioned by the properly balanced chemical composition directed us in the selection of these steel grades for detailed analysis, as we intend to show, that the differences in chemical composition to a high extent determine the properties of these steels observed a posteriori, in the cooled state, after surviving fire incidents differing in the duration and scenarios intentionally programmed by us.

3. THE SIMULATED FIRE SCENARIOS

Prior to the impact strength tests, the samples made of each steel grade tested by us and having the dimensions and shape typical of the Charpy test with V type notch have been subjected to thermal treatment simulating a short term (for the samples belonging to the first group) or long term (for the samples belonging to the second group) action of fire temperature. During the first phase o this process the samples have been heated with a constant heating speed of 100ºC/min to the temperature of 600ºC (series 1.1 and 2.1) or 800ºC (series 1.2 and 2.2), respectively. Following the heating period, the samples have been kept at the constant temperature for 60 minutes – following the "short" fire scenario (series 1.1 and 2.1), or for 600 minutes – following the "long" fire scenario (series 1.2 and 2.2), conforming to the conventional procedure of steady state heating regime. After heating the samples have been cooled to the ambient temperature. For comparison, during each series of tests, two alternative cooling modes have been applied, namely: slow cooling in the open air, simulating self extinguishing of the fire, and rapid cooling in water mist, simulating the action of a fire brigade. The preliminary thermal treatment scenarios described above and applied to the tested samples are depicted in Fig. 1.
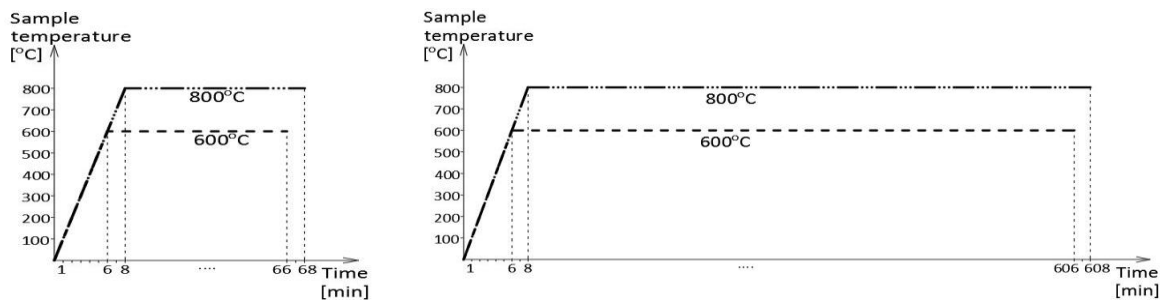
Figure 1: Simulated fire development scenarios followed during the experiment, namely: "short" fire (at left) and "long" fire (at right).

The heating and keeping of the samples at constant temperature in each of the considered testing scenarios have been conducted in the KJ-M1200-64L-IC muffle furnace made by Kejia Furnace Co. Ltd. (Fig. 2). The sample heating temperature values, namely the lower one – equal to 600ºC (series 1.1 and 2.1) and the higher one – equal to 800ºC (series 1.2 and 2.2) have been selected intentionally. These temperature values are to be related to the temperature of the allotropic change occurring in the structure of the steel, and in particular transformation of the δ-ferrite into γ-austenite (in the δ→γ relation or possibly in inverse relation γ→δ). The first of these two levels is to low, while the second one is sufficiently high to allow for the expected structural changes of permanent character to occur in the tested steel samples.

Figure 2: Equipment used to conduct the tests: muffle furnace KJ-M1200-64L-IC (at left and in the center), instrumented Charpy hammer JB-W450E-L (at right).

4. IMPACT STRENGTH TESTING METHODOLOGY

The impact strength tests of cooled samples have been conducted on instrumented Charpy hammer JB-W450E-L (Fig. 2), with a potential energy of 450J, following the recommendations of the codes [30-33]. The R8 hammer (of American type) has been used during the tests, following the assumption that in construction industry an impact by an object of flatter surface (with respect to the classical R2 hammer of European type) is more probable. The hammer had been equipped with a transducer used to measure the force hitting the sample, while the accompanying displacement of the force application point had been recorded with an encoder. The impulses generated by both devices were processed by a data logger of high sampling frequency. The results of each test have been depicted on automatically generated graphs, expressing the relation of force, breaking energy and the displacement of force application point as functions of time or force and breaking energy as a function of the displacement. The location of characteristic limit points had been automatically indicated on the graphs by the software.

The samples have been tested at the temperature of +20ºC, to simulate the potential post-fire service of the structure in summer and at the temperature of –20ºC, to simulate the potential post-fire service of the structure in winter.

Thus 72 qualitatively different test cases have been considered. For each of the considered four steel grades and two impact strength test temperature values eight independent tests related to the steel cooled after prior simulated fire incident have been considered (two heating temperature levels multiplied by two different cooling scenarios and multiplied by two different heating periods) accompanied by one so called reference case, pertaining to the sample in the virgin state (unaffected by fire action preceding the impact strength test). Each test was repeated on a set of six statistically independent samples to satisfy the requirements of adequately reliable final estimation. As a result 432 separate impact strength tests have been performed. Therefore the *F-s* curves presented below are to be interpreted each time as the relations averaged over a six element statistical sample

The obtained results have been archived, using a four digit description code, with every digit of the description interpreted as shown in the Table 1. The cases denoted with single digit, i.e. 1, 2, 3 and 4 refer in this code to the six element set of the so called reference cases obtained on the samples made of steel remaining in the virgin state (i.e. made of material unaffected by the simulated fire action preceding the actual impact strength test).

Table 1 Coding system applied to encode the results obtained on sample sets subjected to impact strength tests.

1st digit of the description – steel grade	2nd digit of the description – heating temperature	3rd digit of the description – cooling mode	4th digit of the description – heating time
1 – S355J2+N **2** – X6CrNiTi18-10 **3** – X2CrNiMoN22-5-3 **4** – X2CrMnNiN21-5-1	**6** – 600ºC **8** – 800ºC	**0** – slow cooling in the open air **1** – cooling in the water mist	**No mark** – "short" fire **X** – "long" fire

5. DESCRIPTION OF THE RESULTS OBTAINED AND THEIR INTERPRETATION

5.1 Steel *S355J2+N*

The *F-s* curves obtained by us on the samples made of this stele grade, depicting the relation between the force applied to the sample and the displacement of the force application point are depicted in Fig. 3, for the tests conducted at +20ºC and in Fig. 4 for the analogous tests conducted at –20ºC.

Figure 3: *F-s* curves obtained in post-fire impact strength tests of the *S355J2+N* steel. Testing temperature +20ºC. Top graph – samples cooled slowly in the open air, bottom graph – samples cooled in water mist.

Analysis of the scenario related to the samples cooled in the open air leads to the general conclusion, that the "short fire" incident (samples 160 and 180) lowered the impact strength of the material when compared against the impact strength of the virgin metal (sample 1). However, long term action of the fire (samples 160X and 180X) proved to be beneficial to the material, as its impact strength increased as a result. The higher heating temperature proved to have significant influence on the final results of the test. On one hand the reduction in the impact strength observed on the sample 180 proved to be significantly smaller than the analogous reduction observed on the sample 160. On the other hand, however, the increase in impact strength observed on the sample 180X proved to be significantly higher than the analogous result observed on the sample 160X.

Cooling of the hot samples in water mist, if preceded by heating at the temperature of 600ºC yielded results qualitatively similar to the results described above referring to the samples cooled in the open air. The reduction in the impact strength observed on the sample 161 was quantitatively similar to the reduction observed previously during the tests on the sample 160. The increase in this property, measured on the sample 161X, in this testing scenario proved to be substantially higher than the one found earlier on the sample 160X, cooled slowly in the open air. However, when comparing both groups of pictures (Fig.3), the qualitatively different behavior of the sample 181X when compared against the behavior of sample 180X seems to be the most interesting here. A rapid cooling in water mist preceded by heating at the temperature of 800ºC, in the case of this steel grade led to the *F-s* curve typical for samples exhibiting unstable generation of microcracks in the material, and thus susceptible to brittle fracture.

625

Figure 4: *F-s* curves obtained in post-fire impact strength tests of the *S355J2+N* steel. Testing temperature –20ºC. Top graph – samples cooled slowly in the open air, bottom graph – samples cooled in water mist.

Analysis of the graphs juxtaposed in Fig. 4 leads to the conclusion that the impact strength exhibited by this material on the samples tested at –20ºC proved to be significantly lower than the impact strength exhibited on samples made of the same material but tested at +20ºC. However, there exists one very significant qualitative difference. Regardless of the sample cooling mode enforced in this test, all the tested simulated fire episodes affecting this material proved to be beneficiary to the post-fire mechanical properties of this steel grade. The *F-s* curves obtained on the samples denoted with the digit 1 in the Fig. 4 in both presented cases encircled the smallest area, and this translates into the lowest possible external energy required to break the tested sample. In all the tested fire scenarios "long" fires increased the post-fire impact strength to a significantly larger extent than the "short" fires. A beneficiary influence of the higher heating temperature on the impact strength exhibited post-fire may be observed on the samples cooled slowly in the open air. However, this phenomenon does not affect the samples heated at the temperature of 800ºC and subsequently cooled in water mist (sample 181X). Under such circumstances a material very prone to brittle fracture has been obtained.

The results obtained during testing of post-fire impact strength of this steel grade seem to confirm the following conclusions:
- the higher heating or cooling speeds generate higher internal stress levels and this decreases impact strength,
- with increasing material temperature, in the range of 600-800ºC, a gradual coagulation of the cementite plates occurs in the pearlite up to the globular forms, resulting in increased impact strength,
- analogous effect is observed when the heating time at this temperature range is extended,
- the temperature of 800ºC is located on the *Fe-C* phase equilibrium graph between the A_1 and A_3 critical temperature values, therefore under those conditions pearlite → austenite (or alternatively austenite → pearlite) phase change may occur, and thus:
  o slow cooling from this temperature level leads to fragmentation of crystallographic matrix grains in the areas of pearlite, thus increasing impact strength of the steel,
  o fast cooling from this temperature level initiates local transformation of austenite created from former pearlite grains into hard and brittle martensite, which hardens the material but also induces an unstable propagation phenomenon of microcracks generated in it, thus increasing susceptibility to brittle fracture and decreasing the impact strength.

626

A short term fire episode in the 600ºC/1h scenario does not induce visible changes in the microstructure of the tested steel grade [27]. Under those circumstances the increase in the thermally generated stresses seems to dominate the picture. Finally, this results in that the *F-s* curves related to the samples 160 and 161, during the tests conducted at +20ºC indicated reduced breaking energy (when compared against the energy obtained on the sample 1). However, when the "short" fire simulation is related to the 800ºC/1h scenario and slow cooling in the open air (sample 180), the consequences are somewhat less deleterious when compared against the consequences of simulations conducted on the sample 160. The difference here may be attributed to partial fragmentation of the crystallographic matrix grains in the pearlite zones. The curves described here conform to the type A according to the recommendations of the code [31], that is correspond to the fully plastic fractures. Fast cooling in water mist after simulated short time fire incident (sample 181), did not result in properties typical for unstable material fracture and thus does not indicate the presence of martensite in its microstructure.

A fire episode of long duration, in the 600ºC/10h scenario induced coagulation of cementite plates in the pearlite, thus positively affecting the post-fire impact strength of the tested steel grade, regardless of the cooling speed applied in the test or the temperature at which the test has been conducted. The *F-s* curves pertaining to this scenario, and obtained on the samples 160X and 161X may be assigned to the category E and F according to the classification [31]. The simulation of the "long" fire in the 800ºC/10h scenario, associated with slow cooling of the samples in the open air (sample 180X), regardless of the testing temperature, resulted in significant fragmentation of the crystallographic matrix grains, and this in turn resulted in significant improvement in the impact strength exhibited by the samples (a curve of the type A according to the classification [31]). However, when the sample heated at the temperature of 800ºC had been rapidly cooled in the water mist, the local transformation of austenite into hard and brittle martensite occurred in the structure of the steel. As a result, regardless of the testing temperature a post-fire brittleness has been observed, and thus accompanying zones of unstable fracture have been found. This conclusion is supported by the shape of *F-s* curves observed on the sample 181X (a D type curve according to the classification [31]). One may expect that in the case of testing temperature decreased by a few or a dozen grades Centigrade, the F-s curve related to this sample would evolve to the shape typical for the category A (according to [31]), and this in turn means an imminent danger of the structural failure.

5.2 Steel *X6CrNiTi18-10*

The *F-s* curves obtained on the samples made of this steel grade are depicted in Fig. 5 – in the case of tests conducted at +20ºC, and in Fig. 6 – in the case of analogous tests conducted at –20ºC.

The graphs juxtaposed in Fig. 5 indicate a qualitative difference when compared against corresponding graphs depicted above in Fig. 3. In the case of *X6CrNiTi18-10* steel grade for most of the analyzed testing scenarios (only the scenarios related to the samples denoted as 260 and 261 proved to be an exception here) the simulated fire episode acting on the sample proved to negatively affect the post-fire impact strength of the tested material, regardless of the heating time and the cooling mode applied. During the simulation of a "short" fire the higher heating temperature (samples 280 and 281) resulted in higher reduction in the impact strength (when compared against analogous reduction observed on the samples 260 and 261). However, when the samples have been affected by the simulated "long" fire, the opposite proved to be true. The reduction in the post-fire impact strength observed on the samples 280X and 281X happened to be significantly smaller than the reduction observed independently on the samples 260X and 261X. In the case of this steel grade the cooling mode applied only slightly differentiates the results obtained.

The curves depicted in Fig. 6 lead to analogous statement. The specified impact strength based on the tests conducted at –20ºC is quantitatively lower than the one determined at +20ºC. Regardless of the applied sample cooling mode, the "short" fire episode in the 600ºC/1h scenario (samples 260 and 261) does not result in significant differences in impact strength when compared against the impact strength exhibited by the sample in virgin state (sample 2). However, the "long" fire episode in the 600ºC/10h scenario results in a very significant reduction in the breaking energy (samples 260X and 261X). The heating temperature increased from 600ºC to 800ºC at a fire episode of long duration slightly improves the indicated impact strength. This phenomenon is not observed after one hour long heating of the samples, as in a so short time the action of increased temperature could not induce appropriate transformations in the microstructure of tested steel grade and thus could not create the conditions required for it to appear.
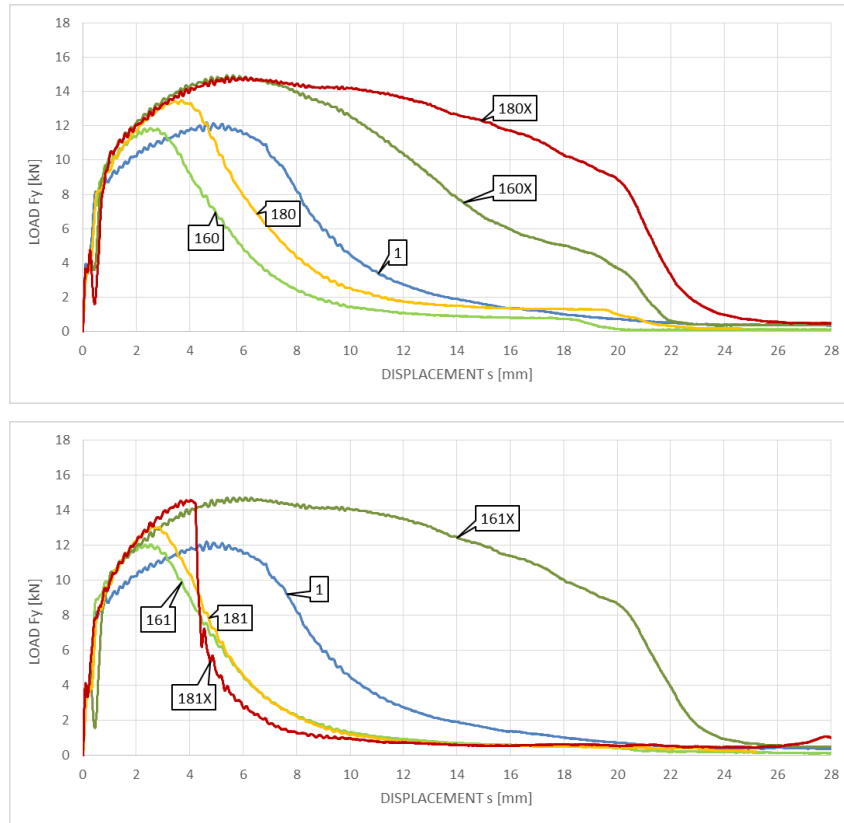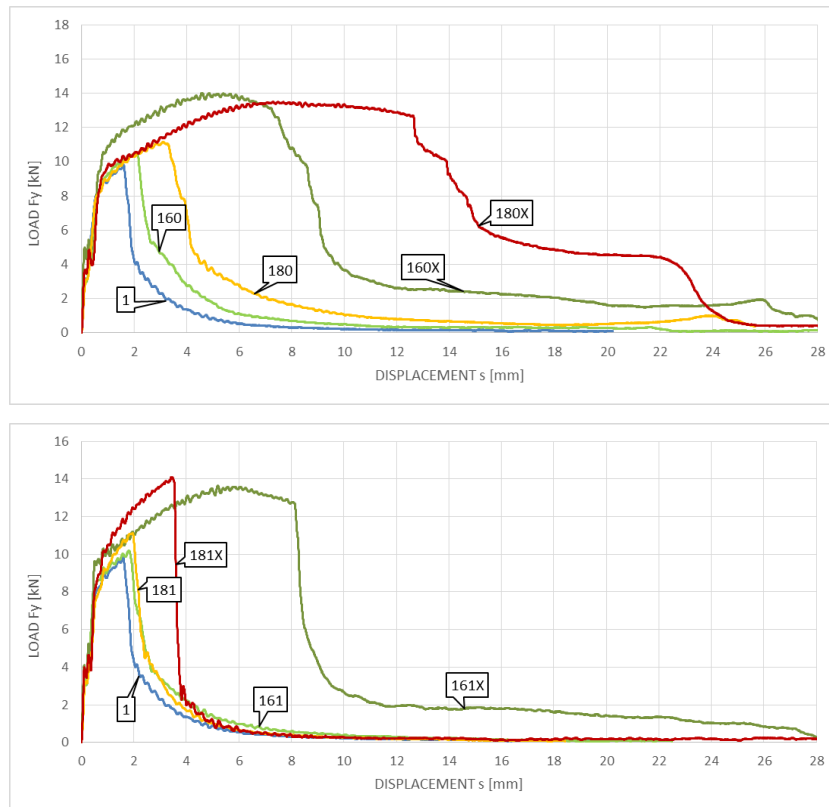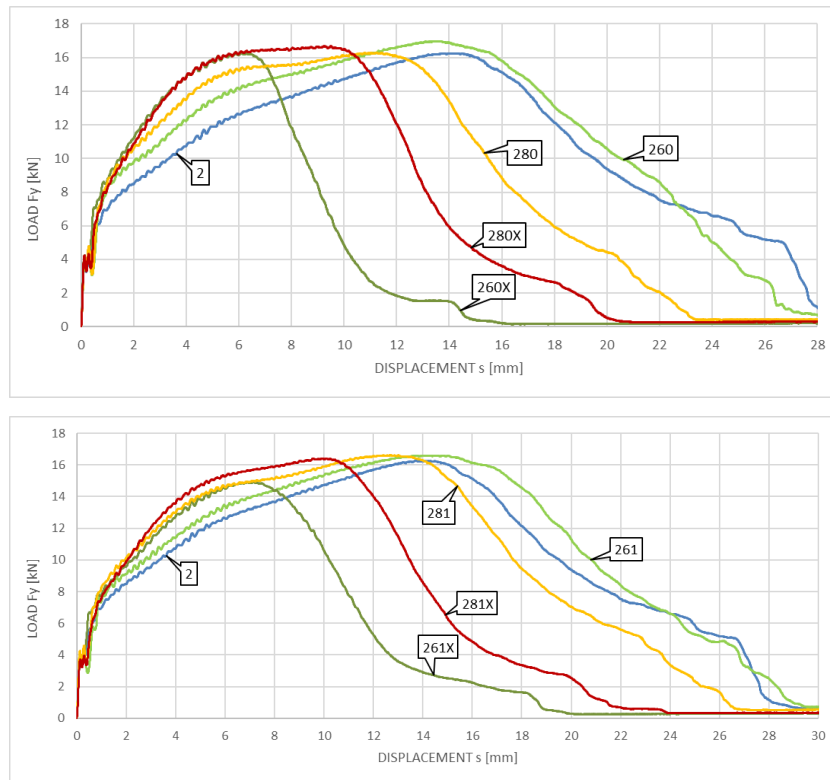
Figure 5: *F-s* curves obtained in post-fire impact strength tests of the *X6CrNiTi18-10* steel. Testing temperature +20ºC. Top graph – samples cooled slowly in the open air, bottom graph – samples cooled in water mist.

The graphs depicted in Figs 5 and 6 confirm the substantial influence of fire duration on the level of impact strength reduction observed a posteriori. The temperature of 600ºC is located on the *TTT* (time – temperature – transformation) graphs referring to this steel grade at the bottom limit of its sensibility to intercrystalline corrosion, and thus on precipitation of $Cr_{23}C_6$ carbide and intermetallic phase σ on grain boundaries. Both these precipitates, due to their brittleness, exhibit a very deleterious influence on the energy required to fracture the sample. However, due to the thermodynamics of such precipitate development, in a steel exhibiting austenitic structure the negative consequences of this phenomenon have not been observed (sample 260). Nevertheless, the simulated fire lasting 10 hours proved to be sufficiently long to intensify creation of those precipitates (sample 260X). It seems that precipitation of $Cr_{23}C_6$ dominated the picture here, as the increased content of the σ phase would render the tested steel completely brittle.

The temperature of 800ºC is located on the *TTT* graph corresponding to this steel grade in the coexistence zone of local precipitation of the $Cr_{23}C_6$ carbide and σ phase and solution of these precipitates in the crystallographic matrix. As the activation of the diffusion processes at the temperature of 800ºC is easier than at 600ºC, the reduction in impact strength after a fire episode of short duration is significantly higher when the higher temperature had been applied (samples 280 and 281). However, in the case of long lasting episode, following the 800ºC/10h scenario, regardless of the sample cooling mode applied, those heated at 800ºC (samples 380X and 381X) yield a posteriori higher values of fracture energy when compared against analogous values obtained on samples 360X and 361X, as at this temperature the dynamics of secondary precipitate dissolution surpasses the dynamics of new precipitate development.
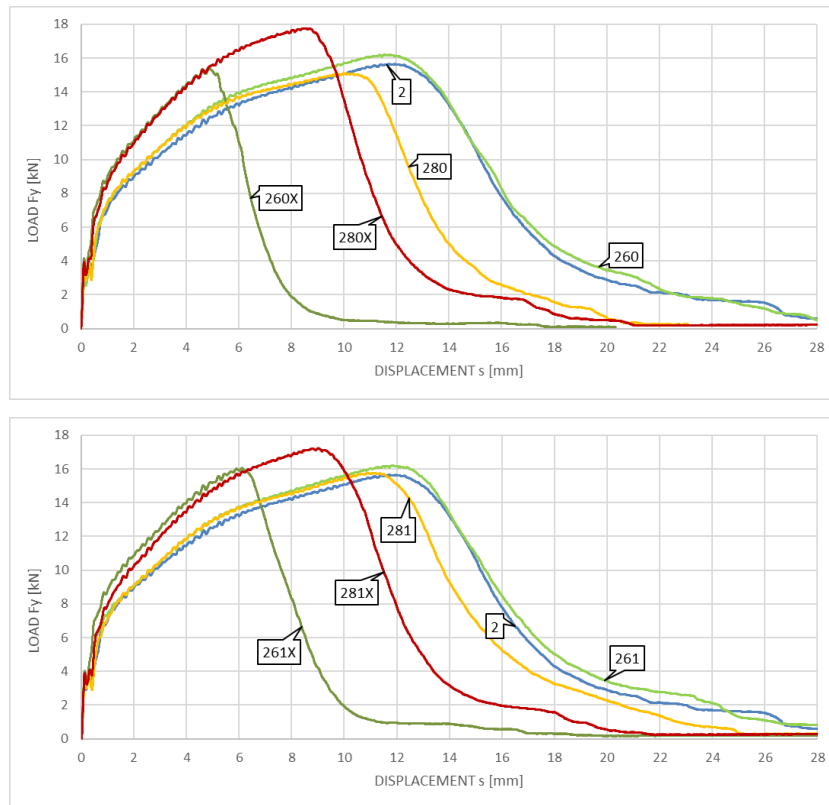
Figure 6: *F-s* curves obtained in post-fire impact strength tests of the *X6CrNiTi18-10* steel. Testing temperature –20ºC. Top graph – samples cooled slowly in the open air, bottom graph – samples cooled in water mist.

In all the fire scenarios tested on this steel the obtained *F-s* curves indicate the capability to self arrest an initiated process of fracture. In this context these curves may be assigned to the type E (ductile fracture) or alternatively to the type F (plastic fracture) in the sense of classification listed in the code [38]. The observed tendencies lead to the conclusion, that due to the potential post-fire brittleness, the extremely long lasting fires with heating temperature exceeding 600ºC may present a danger here.

5.3 Steel *X2CrNiMoN22-5-3*, of the SDSS type

The duplex steels of two phase, austenitic – pearlitic internal structure are characterized on the appropriate *TTT* graphs by two basic temperature zones where deleterious phase transitions may be initiated. These are as follows:
- the 475ºC brittle zone – related to the partial transition of the δ-ferrite to the coniferous secondary α'-ferrite, and precipitation of brittle π, ε and G phases (occurring at the temperature between 300ºC and 550ºC),
- the 800ºC brittle zone – caused by the precipitation of carbides Me_7C_3 and $Me_{23}C_6$, nitrides Cr_2N and secondary σ, χ, R, $γ_2$ phases from the constant solution (mostly δ-ferrite) (occurring at the temperature between 600ºC and 1050ºC).

The difference in the chemical composition between the SDSS and LDSS steel grades tested by us mainly comes down to the absence of molybdenum Mo and decreased nitrogen N content in the LDSS steel grade resulting in (with respect to the analogous threshold values typical for SDSS steel grades):
- increased top threshold initiation temperature of the 475ºC brittleness phenomenon,
- decreased bottom threshold initiation temperature of the 800ºC brittleness phenomenon.

The *F-s* curves obtained during the tests conducted on samples made of *X2CrNiMoN22-5-3* steel grade (of the SDSS type) are presented in Fig. 7 – with respect to the impact strength tests conducted at +20ºC and in Fig. 8 – with respect to analogous tests conducted at –20ºC. One may easily notice, that in the case of SDSS steel fire episodes negatively affect the impact strength of the samples observed after fire.

Figure 7: *F-s* curves obtained in post-fire impact strength tests of the *X2CrNiMoN22-5-3* steel (of SDSS type). Testing temperature +20ºC. Top graph – samples cooled slowly in the open air, bottom graph – samples cooled in water mist.
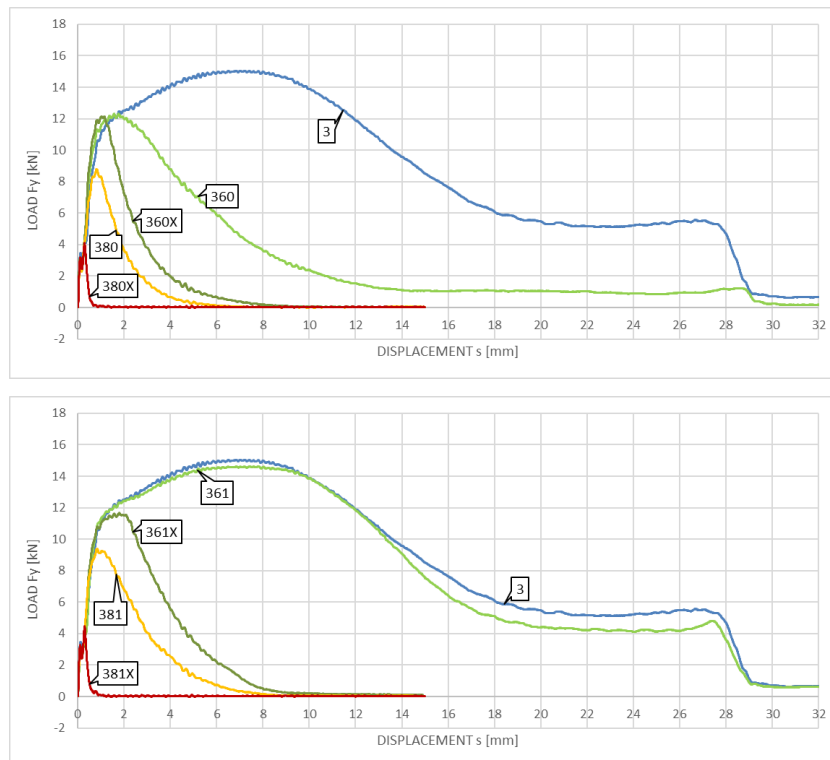
Figure 8: *F-s* curves obtained in post-fire impact strength tests of the *X2CrNiMoN22-5-3* steel (of SDSS type). Testing temperature –20ºC. Top graph – samples cooled slowly in the open air, bottom graph – samples cooled in water mist.

630

A short term fire episode following the 600ºC/1h scenario is located between the 475ºC and 800ºC brittle zones. Slow cooling in the open air extends the sample transition time through the 475ºC brittle zone (sample 360). This results in significant decrease in the breaking energy when compared against the sample kept in the virgin state (sample 3). However, when the sample is rapidly cooled in water mist this transition time through the 475ºC brittle zone is substantially shortened (sample 361). Under such circumstances the reduction in post-fire impact strength would not be observed.

Prolongation of the sample heating time, following the 600ºC/10h scenario, locates the tested steel within the zone of the *TTT* curve related with both partial 475ºC brittleness and partial 800ºC brittleness (samples 360X and 361X). Keeping a sample at this temperature for prolonged period of time results in substantial decrease in the impact strength exhibited post fire. This reduction is smaller when the sample is cooled in water mist (sample 361X) as then the sample is subjected to the temperature remaining within the 475ºC brittle zone for a much shorter period of time.

A long term fire episode following the 800ºC/10h scenario proved to be the most deleterious in the case of the SDSS steel. Under those circumstances, regardless of the sample cooling mode applied and impact strength testing temperature, due to the 800ºC brittleness phenomenon occurring at full magnitude, the samples were characterized by complete brittleness, and thus exhibited breaking energy close to zero.

The SDSS steel tested in the as manufactured state (sample 3) as well as tested after a short term fire episode following the 600ºC/1h scenario (samples 360 and 361), was characterized by the *F-s* curves conforming to the F type according to the recommendations [31]. In the case of partial impact strength reduction (samples 380, 381, 360X, 361X) one deals with the curves which may be assigned to the types D and E. The samples exhibiting complete absence of impact strength (samples 380X and 381X), with completely unstable fracture development are assigned to the type A according to these recommendations.

5.4 Steel *X2CrMnNiN21-5-1*, of the LDSS type

The *F-s* curves obtained during the tests of post-fire impact strength exhibited by *X2CrMnNiN21-5-1* steel (of the LDSS type) are depicted in Fig. 9 – with respect to the impact strength tests conducted at +20ºC and in Fig. 10 – with respect to analogous tests conducted at –20ºC.

In the case of this steel one may easily notice, that in all the testing scenarios considered the simulated fire episodes affecting the samples definitely worsen the impact strength observed post fire. The values of impact strength obtained at the testing temperature of –20ºC are substantially lower than the corresponding values obtained at the testing temperature of +20ºC. The influence of sample cooling mode is hardly visible. Nevertheless, rapid cooling in water mist, in the case of this steel grade as well, shortens the transition time through the 475ºC brittle zone. This results in lower reduction of the impact strength when compared against the samples made of the same steel grade but slowly cooled in the open air.

The fire episodes of long duration, following both 600ºC/10h scenario and 800ºC/10h scenario, under those circumstances result in only slight decrease in impact strength. This is in general true regardless of the testing temperature applied. The *F-s* curve corresponding to the sample 461X represents a kind of an exception here, as the highest reduction in the impact strength has been observed on this sample. A comparison of the shapes of *F-s* curves obtained on the samples 460X and 461X leads to the conclusion, that under those circumstances faster transition through the 475ºC brittle zone seems to be irrelevant. The long term (10 hours long) holding of the sample at high temperature related to this phenomenon seems to decide. However, the differences may be noted when the 800ºC/10h scenario is followed accompanied by impact strength testing at the temperature of +20ºC. Then rapid cooling of the sample in water mist to a high extent negates the influences described above (sample 481X). Nevertheless, one has to note that in this test the long heating of the sample occurred at the temperature of 800ºC, not related to the 475ºC brittleness phenomenon.
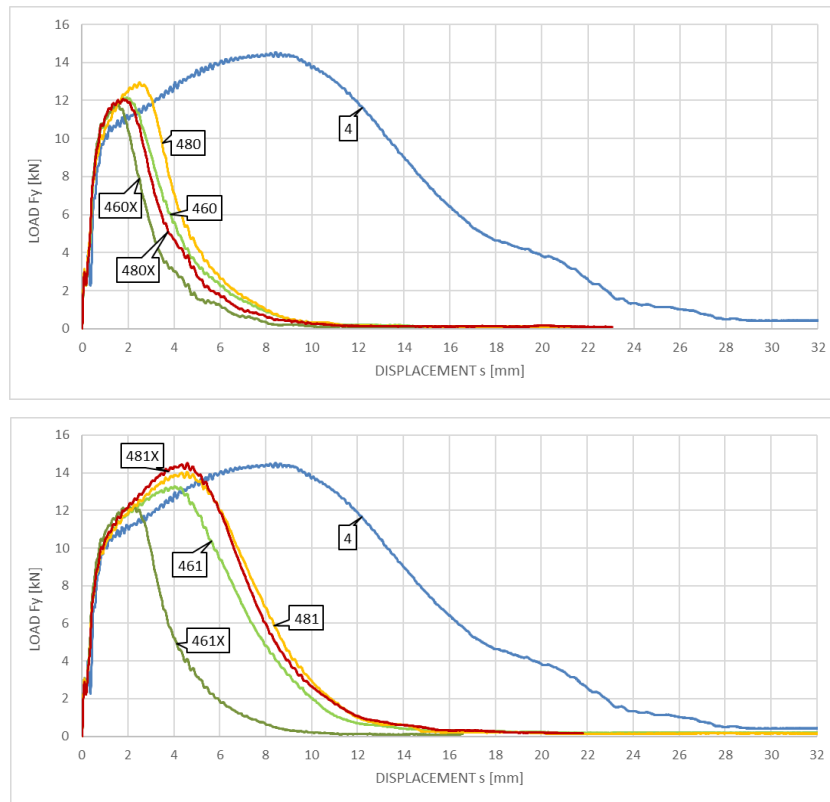
Figure 9: *F-s* curves obtained in post-fire impact strength tests of the *X2CrMnNiN21-5-1* steel (of LDSS type). Testing temperature +20ºC. Top graph – samples cooled slowly in the open air, bottom graph – samples cooled in water mist.
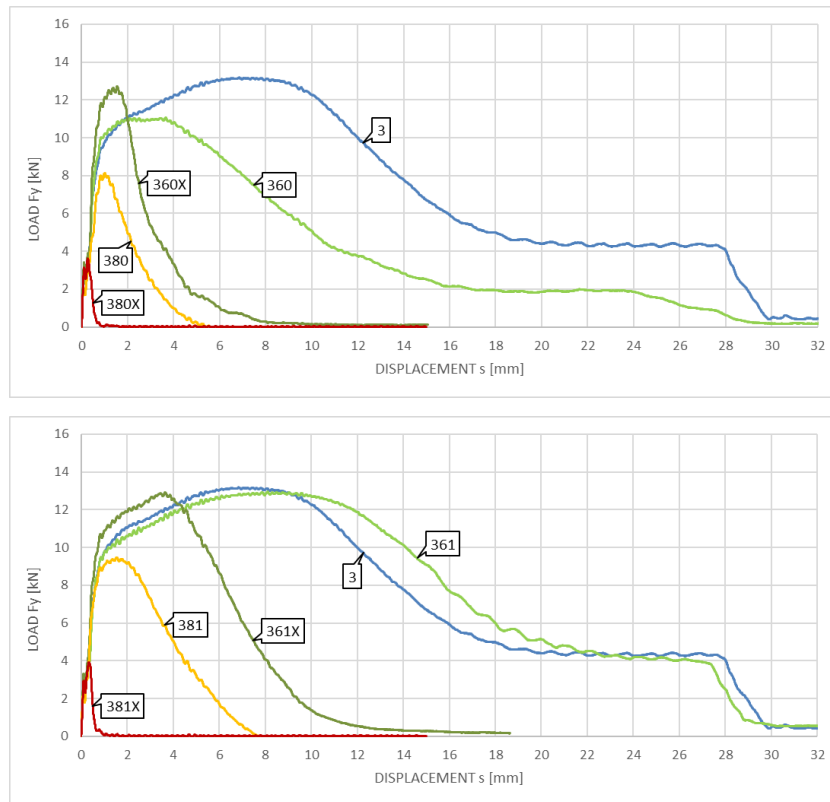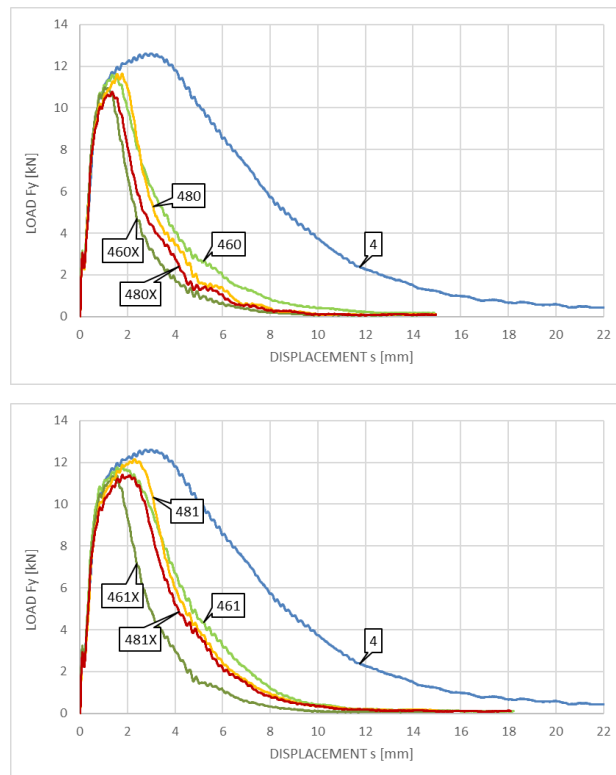

Figure 10: *F-s* curves obtained in post-fire impact strength tests of the *X2CrMnNiN21-5-1* steel (of LDSS type). Testing temperature –20ºC. Top graph – samples cooled slowly in the open air, bottom graph – samples cooled in water mist.

The low influence of the duration of a simulated fire incident on the impact strength exhibited post fire by the tested sample clearly distinguishes the steel of the LDSS type from the steel of the SDSS type. This is a consequence of a shift to the right on the *TTT* graph of the temperature zone correlated with the 800ºC brittleness phenomenon. The *F-s* curves obtained for the LDSS steels represent fully plastic mode of fracture corresponding to the category F following the classification set in [31]. From the practical point of view an application of the LDSS steels seems to be safer when compared against the SDSS steels, should one take into account only the potential risk of fire exposure.

6. CONCLUDING REMARKS

The results presented in this paper confirm the opinion, that post-fire impact strength of considered steel grade, affecting its possible service in the future, may turn out to be very different, not only in the quantitative but also in the qualitative sense. The results of a posteriori evaluation of samples cooled down following the fire exposure depend on many factors of a random character appearing a priori. One deals here not only with the fire development scenario, which occurred in practice and in particular the level of temperature to which the considered steel had been heated in fire conditions, the effective heating time or the cooling mode and speed, but also with the internal structure of the steel and its susceptibility to phase transitions which seems to be no less important. We have shown, that the fire episodes do not have to result in permanent worsening of the mechanical properties exhibited by considered steel grade. In many cases, following appropriate testing scenarios, the final impact strength significantly improved when compared against the same property exhibited by virgin material unaffected by fire action. We have shown as well that the duplex steels of a two phase austenitic – pearlitic structure are particularly resistant to the detrimental thermal actions related to the accidental design situation of a fully developed fire. This property may prove to be very useful in many applications in construction industry, especially when LDSS steels are considered.

However, the most important conclusion of our tests seems to be that for each of the considered steel grades a critical scenario may be indicated, that is a scenario which, if followed, would generate in given material cooled down after a fire episode a risk of brittle failure, disqualifying it from prolonged service.

7. REFERENCES

[1]   Bednarek Z.; Kamocka R. (2006). *The heating rate impact on parameters characteristic of steel behaviour under fire conditions*, Journal of Civil Engineering and Management, XII, 4, p. 269-275.
[2]   Maslak M.; Zwirski G. (2017). *Changes in structural steel microstructures following heating and cooling episodes in fires, Safety & Fire Technique*, 48, p. 34-52.
[3]   Chong Ren; Liusi Dai; Yuner Huang; Wenfu He (2020). *Experimental investigation of post-fire mechanical properties of Q235 cold-formed steel, Thin–Walled Structures*, 150, 106651.
[4]   Gang Shi; Shihao Wang; Chengxiao Rong (2022). *Experimental investigation into mechanical properties of Q345 steel after fire, Journal of Constructional Steel Research*, 199, 107582.
[5]   Chuntao Zhang; Bin Jia; Junjie Wang (2020). *Influence of artificial cooling methods on post-fire mechanical properties of Q355 structural steel, Construction and Building Materials*, *252*, 119092.
[6]   Jie Lu; Hongbo Liu; Zhihua Chen; Xiangwei Liao (2016). *Experimental investigation into the post-fire mechanical properties of hot-rolled and cold-formed steels, Journal of Constructional Steel Research*, 121, p. 291–310.
[7]   Shanmuganathan Gunalan; Mahen Mahendran (2014). *Experimental investigation of post-fire mechanical properties of cold-formed steels, Thin-Walled Structures*, 84, p. 241–254.
[8]   Xuhong Qiang; Bijlaard F.S.K.; Kolstein H. (2012) *Post-fire mechanical properties of high strength structural steels S460 and S690, Engineering Structures,* 35, p. 1–10.
[9]   Chuntao Zhang; Ruheng Wang; Gangbing Song (2020). *Post-fire mechanical properties of Q460 and Q690 high strength steels after fire-fighting foam cooling, Thin–Walled Structures*, 156, 106983.
[10] Xuhong Zhou; Xuanyi Xue; Yu Shi; Jinyong Xu (2021). *Post-fire mechanical properties of Q620 high-strength steel with different cooling methods, Journal of Constructional Steel Research*, 180, 106608.
[11] Guo-Qiang Li; Huibao Lyu; Chao Zhang (2017). *Post-fire mechanical properties of high strength Q690 structural steel, Journal of Constructional Steel Research*, 132, p. 108–116.

[12] Dan Huang; Linbo Zhang; Weiyong Wang; Hailiang Mu (2022). Test on post-fire residual mechanical properties of high strength Q690 steel considering tensile stress in fire, *Journal of Constructional Steel Research*, 194, 107340.

[13] Chiew S.P.; Zhao M.S.; Lee C.K. (2014*). Mechanical properties of heat-treated high strength steel under fire / post-fire conditions*, *Journal of Constructional Steel Research*, 98, p. 12–19.

[14] Li H.T.; Young B. (2018) *Post-fire mechanical properties of high strength steels*, 12th International Conference on Advances in Steel-Concrete Composite Structures (ASCCS 2018)*, València, Spain, June 27-29, 2018, p. 83-90.

[15] Xia Yan; Yu Xia; Blum H.B.; Gernay T. (2021). *Post-fire mechanical properties of advanced high-strength cold-formed steel alloys*, *Thin–Walled Structures*, 159, 107293.

[16] Lou Guo-Biao; Fei Chu-Ni; Wang Yan-Bo; Chen Lin-Heng (2022). *Experimental study on post-fire mechanical properties of high-strength fire-resistant steel*, *Engineering Mechanics*, 39, 9, p. 153-159.

[17] Maraveas C.; Fasoulakis Z.; Tsavdaridis K.D. (2017). *Post-fire assessment and reinstatement of steel structures*, *Journal of Structural Fire Engineering*, 8, 2, p. 181-201.

[18] Lin-Xin Song; Guo-Qiang Li (2021). *Processing and cooling effects on post-fire mechanical properties of high strength structural steels*, *Fire Safety Journal*, 122, 103346.

[19] Li-An Xie; Xing-Qiang Wang; Zhi-Jiang Han; Xin Yu; Alim M.A.; Manninen T.; Zhong Tao (2022). *Post-fire stress-strain response of structural ferritic stainless steels*, *Journal of Constructional Steel Research*, 196, 107389.

[20] Xiang Li; Lo K.H.; Kwok C.T.; Sun Y.F.; Lai K.K. (2018). *Post-fire mechanical and corrosion properties of duplex stainless steel. Comparison with ordinary reinforcing-bar steel*, *Construction and Building Materials*, 174, p. 150–158.

[21] Huang Y.; Young B. (2018). *Mechanical properties of lean duplex stainless steel at post-fire condition*, *Thin-Walled Structures*, 130, p. 564–576.

[22] Molkens T.; Cashell K.A.; Rossi B. (2021). *Post-fire mechanical properties of carbon steel and safety factors for the reinstatement of steel structures*, *Engineering Structures*, 234, 111975.

[23] Molkens T.; Cashell K.A.; Malaska M.; Alanen M.; Rossi B. (2020). *Post-fire behaviour of structural stainless steel*, *ce/papers* 4, 2-4, p. 1411-1420.

[24] Molkens T.; Cashell K.A.; Malaska M.; Alanen M., Rossi B. (2021). *Performance of structural stainless steel following a fire*, *Engineering Structures*, 235, 112001.

[25] Maslak M.; Pazdanowski M.; Stankiewicz M.; Zajdel P. (2021). *The impact strength of selected steel types after fire. Experimental tests related to simulated fire conditions*. 7th International Conference "Applications of Structural Fire Engineering" (ASFE), June 9-11, 2021, Ljubljana, Slovenia, p. 55-60.

[26] Maslak M.; Pazdanowski M.; Stankiewicz M., Zajdel P. (2021). *Post-fire susceptibility to brittle fracture of selected steel grades used in construction industry – assessment based on the instrumented impact test*, *Materials,* 14, 3922.

[27] Pancikiewicz K.; Maślak M.; Pazdanowski M.; Stankiewicz M.; Zajdel P. (2023). *Changes in the microstructure of selected structural alloy steel grades identified after their simulated exposure to fire temperature*, *Case Studies in Construction Materials*, 18, e01923.

[28] EN 10025-2 (2019). *Hot rolled products of structural steels, Part 2: Technical delivery conditions for non-alloy structural steels*.

[29] EN 10088-1 (2014). *Stainless steels, Part 1: List of stainless steels*.

[30] EN-ISO 148-1 (2006). *Metallic materials – Charpy pendulum impact test. Part 1: Test method*.

[31] EN-ISO 14556 (2015). *Metallic materials – Charpy V-notch pendulum impact test. Instrumented test method.*

[32] ASTM E 23-92 (2016). *Standard test methods for notched bar impact testing of metallic materials*.

[33] ASTM E 2298-18 (2018). *Standard test method for instrumented impact testing of metallic materials*.

FIRE ON AN INDUSTRIAL SHED: MORTAR, STEEL, COATING AND THERMAL INSULATING MATERIALS BEHAVIOUR

Christian Paglia a

Cristina Mosca b

ABSTRACT

A train wagon located along a railway line used for the download of paper material caused a fire, which exposed for a brief period of time an industrial shed. The flames developed outside the structure and reached several roofing elements. The structure consisted of coated steel beams and a roofing system, which contained thermal insulation materials. Aside from the train wagon, a building coated with a mortar was present. The heat produced during the fire induced a pink coloring of the facade. Microcracks developed on the surface. SEM investigation indicated the cracks to occur within the cementitious paste and along the cement-stone aggregate interface. On the contrary, the facade more distant from the high temperature exhibited no significant cracks. The temperature in this region reached at least 300 ºC. The flames locally reached the steels and the roofing beams. The steel coating was completely absent close to the fire zone, while within a distance up to 10 meters from the fire, detachments and bubbles were observed. The roofing thermal insulation showed a carbonization of the first 30 mm, more in depth, 20 mm indicated a dark coloring. The panels were composed of a polyurethanic foam and were coated with 80 μ thick metal sheets. These latters showed cracking due to the high temperature, that likely reached a temperature between 370-400 ºC. The steel beams tensile strength decreased right above the fire region. This correlated with a decrease in the Vicker's hardness. The polyethylene pipes were deformed, thus indicating a temperature range between 110 ºC and 140 ºC.

Keywords: fire, industry, mortar, steel, coating, insulating material

^a *Institute of Materials and Construction, Supsi, V. Flora Ruchat 15, CH-6850 Mendrisio, Switzerland.*
Email: christian.paglia @supsi.ch, corresponding author
Researchgate: https://www.researchgate.net/profile/C-Paglia

^{b,} *Institute of Materials and Construction, Supsi, V. Flora Ruchat 15, CH-6850 Mendrisio, Switzerland.*

1. INTRODUCTION

Fires are among the most deleterious events taking place on structures. Climatic changes, inadequate safety precautions, wrong choice of materials and construction systems and wrong emergency escape ways all contribute to dramatic consequences. In some cases, the type of building materials significantly influence the development, the propagation and the duration of fires. The materials behaviour at high temperature largely affects the safety of people. Form this point of view the planning of buildings still scarcely consider the reaction of materials under fire. A modified planning of new materials, in particular thermal insulation systems needs to be implemented. In addition, fire suppression systems, new system design and the development of performance-based codes have to be discussed [1]. Reinforced concrete, low-carbon steels and thermal insulation are the most common construction materials widely used in building structures and civil engineering infrastructure. Environmental factors such as, the rate of heating and cooling [2-5], the fire duration and the maximum temperature [6] influence the extent of the damage. Furthermore, the loading condition also affect the durability [7] and the residual strength of concrete [8]. The behaviour of sustainable concrete and recycled materials is a major concern that needs to be further investigated [9]. Steel rebars may also be significantly affected by the temperature, although they are protected by the low thermal conductivity of concrete. They start to loose the mechanical strength between 300-400 °C [10]. Thermal insulating cladding materials are a major concern in case of fire. Their general high level of flammability contribute to the fast spreading of the flames outside the buildings. This particularly occurs along the external facades and limiting their combustibility may a relevant feature to implement the general safety [11].

The aim of this work is to analyze a case of fire in an industrial shed caused by a railway wagon. The flames and the high temperature differently affected the properties of the building materials of the structure. Cementitious mortars, coated steel beams, polymeric water distribution pipes and roofing thermal insulating elements reacted differently. The degradation took place in a variable extent and the temperature distribution could be estimated depending on the material type and behaviour.

2. EXPERIMENTAL PROCEDURE

The industrial shed was built in 1970. It is mainly composed of low-carbon structural steel beams and concrete. The roofing thermal insulating panels consist of wood and aluminum thin sheets (80 μ) that contain a polymeric materials with a thickness of 140 mm. A polyethylene pipe is placed outside the building. An overview of the fire affected region is depicted in Figure 1. The fire initiated and propagated outside the industrial shed, although the influencing area remained in the vicinity of a train wagon, which set the fire. A visual inspection and sampling of the materials were done. Specimens were taken from the steel beams, the mortar and the thermal insulting material from the fire affected area and the unaffected regions. The hardness measurements of the steel elements were taken with the ultrasonic contact impedance method, by using a Equotip 550, soda UCI instrument. The measurements were done for the middle and lower parts of the beams (10 measures in four zones) and in the lower part for the strut (10 measures for three zones). For the shelves, 20 measurements were done. All the Vicker's HV5 measurements were taken on site. The tensile strength of the steels were determined [12] and the sampling was carefully kept under control [13]. The samples had a length from 90 mm to 100 mm. The shelves samples were shorter, i. e. 50 mm normalized length, because of the reduced thickness. The microstructure was investigated by means of an optical and a scanning electron microscope.

Figure 1. Fire affected zone of the industrial shed. A view of the outdoor roofing elements where the fire initiated.

3. RESULTS AND DISCUSSION

3.1 Visual inspection

The fire caused a variable extent and type of deterioration depending on the material and exposure. The outdoor rain water drain 200 mm diameter PE pipe exhibits a significant deformation in the fire affected zones (Fig. 2 left). The PE is a thermoplastic material with a melting point ranging from 110 to 140 °C. The reached temperatures caused a permanent deformation of the pipeline. The outdoor pipeline insulating material of the heating plant also shows relevant blackened and darkened surfaces as well as cracking, deformation and detachment from the pipe substrate (Fig. 2 centre). Metal installations in the fire area indicate a clear bending (Fig. 2 right).

Fig. 2. Deterioration of the installations outside the building in the fire region.

The wood panels along the external roofing edge exhibit a charred surface (Fig. 3 left). Approximately 20 meters away from the fire region, the panels do not indicate any sign of degradation. The wood ignition temperature approaches 250 °C. The roofing panels are composed of rigid thermal insulating polyurethanic foams and they exhibit a microcracked pattern due to exposition to high temperature (Fig. 3 right). For these elements the deterioration and the carbonization phase starts at 370-400 °C.
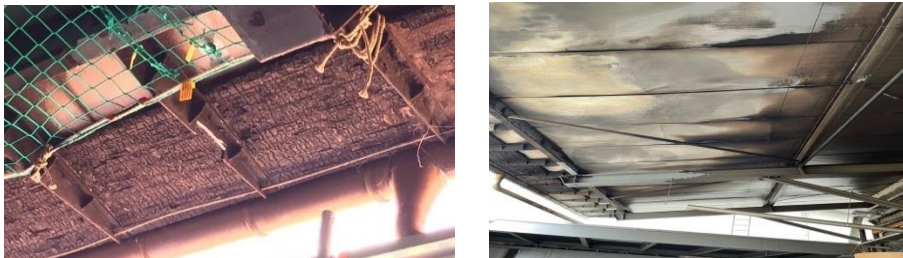
Fig. 3 Degradation of the thermal insulating panels of the roofing elements.
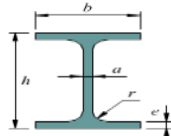
The steel beams are protected with an organic coating. In the fire region, bubbles with variables dimensions and with a diameter up to 100 mm are seen (Fig. 4 left). In the area where the fire initiated, the coating is completely absent from the steel substrate for distances up to 150 cm (Fig. 4 centre). Local coating detachments are not preceded by microcracking (Fig. 4 right). These phenomena are present in a distance range of 7 meters from the fire initiation point.

Fig. 4. Organic coating damage with bubble formation and detachments.

The dimensions and geometry of the steel elements are indicated in Table 1.

Table1. Steel elements of the industrial sheds affected by fire.

Element	Dimensions	b [mm]	h [mm]	e [mm]	a [mm]
beam type 1		300	340	13.0	not measured
beam type 2		150	300	10.8	not measured
strut		140	135	8.6	not measured

The concrete façade of the industrial building does not exhibit visible signs of deterioration due to high temperature. On the other hand, a small building close to the train wagon exhibits a clear coloration difference between the façade in more direct contact with the fire (Fig. 5 left). This latter shows a pink coloration typically observed in cementitious materials that are exposed to temperature of at least 300 ºC. Numerous visible cracks are seen of the façade surface (Fig. 5 right). On a very short distance, the facade not directly exposed to the fire, indicates a typical grey coloration, thus showing a very limited influence and temperature increase caused by the fire.

Fig. 5. Coloration of a cementitious façade of the building in the fire area. The crack width reaches1.5 mm (right).

3.2 Physical and mechanical properties of the steel elements

The steel type for the beams and the struts were assumed to be the same. The hardness values between these two type of elements generally do not exhibit significant differences between the fire affected and the unaffected zones. The lower parts of the beams indicate lower hardness as compared to the central parts. The beam placed close to the fire zone indicates similar values (Table 2).

Table 2. Hardness values for the steel elements.

Id. specimen		Number of measurements	Hardness Vickers HV5			
			min	max	mean	Std. dev.
Beam type 1 (fire zone)	Central part	40	105	186	144	± 17.2
	Lower part	10	93	166	143	± 19.1
Beam type 2	Central part	30	128	189	157	± 14.5
	Lower part	10	119	145	132	± 8.9
Beam type 2	Central part	30	142	336	185	± 47.4
	Lower part	10	102	160	126	± 18.6
Beam type 2	Central part	30	109	171	146	± 17.5
	Lower part	10	118	140	130	± 6.9
Strut 1 (fire zone)	Lower part	30	89	170	130	± 25.0
Strut 2	Lower part	20	84	155	120	± 24.6
Strut 2	Lower part	20	100	217	142	± 28.5
Shelf (fire zone)		20	102	175	132	± 16.5
Shelf		20	124	201	166	± 17.6

On the contrary, a clear hardness difference is detected for the mean values between a shelf placed in the fire region and the shelf away from the fire affected region (Fig. 6).
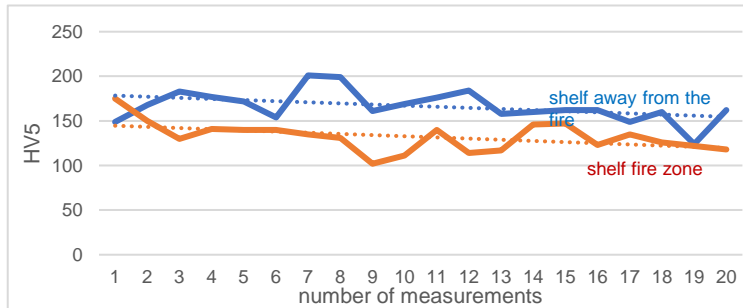
Fig. 6. Hardness difference of the shelves influenced by the high temperature.

The steel beams show similar yield and ultimate tensile strength as well as elongation to rupture, regardless of the position with respect to fire. This may also be due to the massive dimension of such elements and the relative distance of the beams, that very likely came in direct contact with the flames for a relatively short period of time. The values are similar to a S235 steel type [13] and exhibit a conventional ductile fracture mode. On the other hand, the shelf in the fire zone exhibits significantly lower yield and ultimate strength values as compared to the shelf away from the fire zone. It can be stated that in these regions the temperature may have reached at least 300-400 ºC [10]. The elongation is not a clear discriminating factor of the fire influence and an induced thermal treatment of the microstructure. Generally, it can be stated that the tensile strength correlates with the hardness trend.

Table 3. Mechanical properties of the steel elements.

Id. specimen	Yield strength R_e [N/mm^2]	Tensile strength R_m [N/mm^2]	Elongation to rupture A [%]
Beam type 1 (fire zone)	274	405	37
Beam type 2	286	397	34
Shelf	417	554	30
Shelf (fire zone)	321	415	36

3.3 Thermal insulation panels

A surface typing with a hammer allows to determine the areas of the roofing element where the metals sheets are no longer bond with the polyurethanic foam. The sampling in a detachment zone exhibits a damage depth of the insulating panels down to 50-60 mm. The first 30-40 mm are charred, the rest 20-30 mm are darkened (Fig. 7 left). Away from the fire and on the roof upper part along to the perimetral concrete façade, the sampling indicates an undamaged insulation (Fig 7. centre and right).
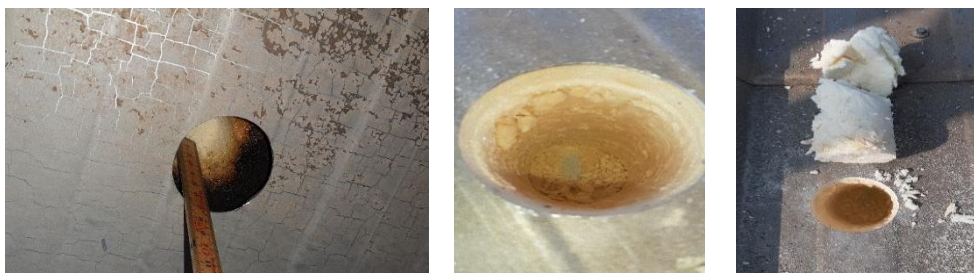
Fig. 7. Insulating roofing panels.

3.4 Cementitious mortar microstructure

The mortar of the building adjacent to the railway lines is composed of a surface layer with a thickness 1-1.5 mm with a maximum aggregate size of 500 μm. The base layer exhibits a thickness up to 10 mm and the aggregates reach a maximum diameter of 1.5 mm. The façade placed toward the fire was in direct contact with the flames and exhibits branched microcracks within the cement-based hydrated paste and along the aggregate interfaces (Fig. 8 left).
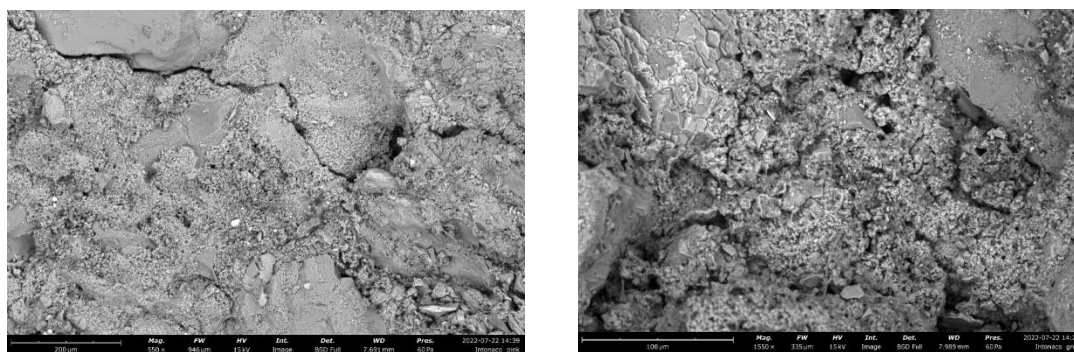
Fig. 8. Scanning electron microscope images of the cementitious mortar directly in contact with the fire (left-scale 200 μm) and from the fire unaffected zone (right- scale 100 μm).

The façade not directly exposed to the high temperature, just placed perpendicular to the former fire affected façade, does not exhibit significant microstructural features related to damage. These observations well correlate with the macroscopic fracture pattern seen on the mortar surface and the different coloring of both facades.

4. CONCLUSIONS

The fire damage of the different material types is limited to the fire region along a distance of maximum 20 meters. This limitation is partially due to the outdoor fire circumstances. The steel shelves close to the fire exhibit a relevant decrease in the tensile strength as well as in the Vicker's hardness. Within the 20 meters, the thermal insulating material shows a deterioration of the first 40 mm in depth. Outside this distance range, the panels are not affected by damage. The façade mortar facing the fire exhibits microcracks and a red coloration of the surface. The perpendicular adjacent facade of the building does not indicate damage or surface features related to high temperature changes.

ACKNOWLEDGEMENTS

REFERENCES

[1] V. Kodur and P. Kumar, Fire hazard in buildings: review, assessment and strategies for improving
fire safety, Fire hazards in buildings, PSU Research Review: An International Journal, 2019.
[2] C. S. Poon, S. Azhar, M. Anson, Y.-L. Wong, Strength and durability recovery of fire-damaged concrete after post-fire-curing, Cem. Concr. Res. 31, pp. 1307–1318, 2001.
[3] C.S. Poon, S. Azhar, M. Anson, Y. L. Wong, Comparison of the strength and durability performance of normal- and high-strength pozzolanic concretes at elevated temperatures, Cem. Concr. Res. 31, pp. 1291–1300, 2001.
[4] C. S. Poon, S. Azhar, M. Anson, Y.L. Wong, Performance of metakaolin concrete at elevated temperatures, Cem. Concr. Compos. 25, 83–89 pp., 2003.
[5] Mohamedbhai, Effect of Exposure Time and Rate of Heating and Cooling on Residual Strength of Heated Concrete, pp. 151–158, 1986.

[6] Cheng, Fu-Ping, Kodur V.K.R., Wang, Tien-Chih, Stress-strain curves for high strength concrete at elevated temperatures, Journal of Materials in Civil Engineering, Volume 16, Issue 1, Pages 84 – 90, 2004.

[7] I. Lillamand, J.F. Chaix, M.A. Ploix, V. Garnier, Acoustoelastic effect in concrete material under uni-axial compressive loading, NDT E Int. 43, pp. 655–660, 2010.

[8] C. Paglia, S. Antonetti, C. Mosca, The fire interaction with the main mechanical properties of concrete and rebar: case studies, FireCORR Virtual conference, AMPP Association for materials protection and performance, 2021.

[9] S. Ali Memon, S. Farasat Ali Shah, R. A. Khushnood, W. L. Baloch, Durability of sustainable concrete subjected to elevated temperature – A Review, Construction and Building Materials 199. pp., 435–455, 2019.

[10] U. Schneider, Properties of materials at high temperatures, Concrete, Rilem report 44-PHT, 2. Edition, Universität Kassel Juni, 1986.

[11] L. Peng, Z. Ni, X. Huang, Review on the fire safety of exterior wall claddings in high-rise buildings in China, The 9th Asia-Oceania Symposium on Fire Science and Technology, Procedia Engineering 62, pp. 663 – 670, (2013).

[12] Standard EN ISO 6892-1, Metallic materials, tensile testing, Part 1 Method of test at room temperature, 2020.

[13] Standard EN 10025 Structural wrought steels, 2019.

THERMAL ANALYSIS COUPLED WITH MICROSCOPY FOR IN-SITU INVESTIGATION OF INTUMESCENT FIRE PROTECTIVE COATINGS

Hafeez Ahmadi[a], Aixiao Fu[a], Hao Wu[a], Kim Dam-Johansen[a], [1]

(a) The Hempel Foundation Coatings Science and Technology Centre (CoaST), Department of Chemical and Biochemical Engineering, Technical University of Denmark (hahm@kt.dtu.dk)

Keywords: In-situ, microscopy, thermal analysis, hot stage, intumescent coatings

Abstract:

The research on intumescent coatings as passive fire protection of substrates has increased rapidly in recent years. Herein, improvement of existing intumescent systems and exploring new systems are closely related to the drawbacks of existing commercial intumescent coatings. These include incorporation of toxic species, exothermic decomposition, release of toxic gas, and low mechanical strength [1]. To make a breakthrough in the market of intumescent coatings, the aforementioned challenges must be solved. However, the temperature-activated working mechanism of intumescent coatings is complex to map. Currently, a large variety of technical methods exist to characterize, and ultimately understand, the thermal induced interactions. However, those are mainly based on post-mortem analyses. Hot stage microscopy (HSM), shown in Figure 1, is one of few techniques allowing in-situ characterization of dynamic changes at high temperatures, which has been a long-lasting challenge within intumescent coatings research.
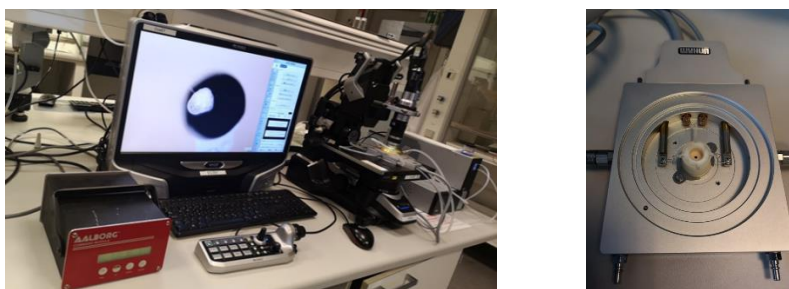
Figure 1: left) Hot Stage Microscopy (HSM) setup, right) heating stage.

[1] Professor and Head of Department Kim Dam-Johansen, Department of Chemical and Biochemical Engineering, Technical University of Denmark (kdj@kt.dtu.dk)

Complete understandings of physical and chemical material properties require characterization at their natural states. HSM combines the best of microscopy and thermal analysis to reveal dynamic changes as they take place. Combined with TGA and rheometer, the technique can detect and clarify working mechanisms of various materials [2], [3]. The present study investigates the use of hot stage microscopy to perform controlled heating to 1100℃, while observing structural changes of an intumescent coating through digital and scanning electron microscopes.The chemical interactions are mapped and related to known literature, herein, important physical and chemical characteristics such as softening, melting, char formation, gas release, expansion, solidification, and more are identified. In addition, relative expansions are quantified using in-built area and height features within the microscope. The area is determined by binarization or free-hand drawing, while the height is approximated by applying the focus feature to create 3D compositions. Furthermore, the work reports the influence of various parameters such as air flow (between 10 and 50 cc min^{-1}) and heating rate (between 10 and 200℃ min^{-1}). This provides a much needed understanding of the impact of test conditions [4]. Ultimately, the use of hot stage microscopy for intumescent coating is evaluated and suggestions made. The latter emphasizes on its use within alternative intumescent systems such as silicate- or silicone based coatings, and other fire retardant materials that influence the timely softening and gas release mechanisms [5], [6].

Conclusions

The work provides a methodology for characterization of intumescent coatings using hot stage microscopy. Herein, the observed changes of a known commercial hydrocarbon coating revealed unseen insights to its degradation mechanisms. The results are to be correlated with other techniques to improve the understanding of intumescent coatings.

References

[1]   Puri, R. G.; Khanna, A. S. (2017). *J. Coat. Technol. Res*, vol. 14, no. 1, pp. 1–20.

[2]   Podor, R.; Bouala, G. I. N.; Ravaux, J.; Lautru, J.; Clavier, N. (2019). *Materials Characterization*, vol. 151. Elsevier Inc., pp. 15–26, May 01.

[3]   Kumar, A.; Singh, P.; Nanda, A. (2020). *Applied Microscopy*, vol. 50, no. 1. Springer.

[4]   Dreyer J. A. H.; Weinell, C. E.; Dam-Johansen, K.; Kiil, S. (2021). *Fire Safety Journal*, vol. 121. Elsevier Ltd.

[5]   Ulusoy, B.; Fu, A.; Ahmadi, H.; Dam-Johansen, K.; Wu, H. (2022). *J. Coat. Technol. Res.*

[6]   Gardelle, B.; Duquesne, S.; Rerat, V.; Bourbigot, S. (2012). *Polym. Adv. Technol., 23: p. 62-69.*

FIRE RETARDANT PROPERTIES OF GLASS FIBER REINFORCED POLYMERS WITH TRI-HYDRATED ALUMINUM

Priscila T.T. Araujo a,*

Alexandre Landesmann b

Simone P. da S. Ribeiro c

ABSTRACT

The potential of glass fiber reinforced polymer (GFRP) as structural materials has made them increasingly attractive for use in building industry. However, due to the polymeric matrix properties, GFRP is susceptible to fire damage and is potentially flammable. Accordingly, the ATH (tri-hydrated aluminum) has been used as a fire retardant additive, through the formation of Al_2O_3 (aluminum oxide) that acts as a protective layer on the composite's surface. However, there are some aspects of ATH such as particle size and concentration that influence its fire-retardant efficiency. This paper aims to evaluate the concentration´s influence of small ATH particle size on combustibility in the isophthalic polyester matrix in GFRP materials. These evaluations were compared to a typical industrial loading (37phr) between the following concentrations: 40 phr, 47.5 phr, 50 phr, and 55 phr, to determine the best ATH concentration to improve the flame retardant properties. The fire retardant properties were evaluated by calorimetry cone, limiting oxygen index, and glow wire tests. Simultaneous thermogravimetric analysis and differential scanning calorimetry was performed to evaluate the thermal stability and enthalpy. Moreover, ATH was characterized by its chemical composition, particle size, crystalline phases and superficial area. The composites with 40 phr and P47.5 phr of ATH reduced the PHRR by 27% compared to sample P37. Moreover, the composite with 40 phr is noteworthy because obtained promising MLCC, glow wire and thermal analysis results.

Keywords: GFRP; fire retardancy; reaction to fire; polyester composites; Alumina trihydrate.

a,* Civil Engineering Program, Federal University of Rio de Janeiro (priscila.araujo@coc.ufrj.br), Corresponding author.

b, Civil Engineering Program, Federal University of Rio de Janeiro (alandes@coc.ufrj.br).

c Polo de Xistoquimica, Federal University of Rio de Janeiro (spsilva@iq.ufrj.br).

1. INTRODUCTION

GFRP combines high efficiency (higher strength and lower weight), low production costs, low electrical conductivity, manufacturing versatility, corrosion resistance, reduced maintenance, and increased durability [1]. Due to the properties of the polymeric matrix, GFRP is susceptible to fire damage and is potentially flammable, causing risk to human lives when used in habitable construction. The fibers used as reinforcement are typically composed of inert materials, such as type E-glass. However, the polymeric matrices generally used are highly combustible [2]. Currently, high levels of flame retardation are achieved with organohalogenated compounds. However, the future of these compounds is uncertain due to environmental problems, toxicological concerns, and the risks of emitting corrosive substances [3].

ATH has been used as a flame retardant due to its low cost, good flame retardant properties, and reduced release of non-toxic smoke [4]. Still, ATH is applied at high loads (concentrations), usually more than 60% [5], to obtain a favorable result, motivating studies to improve its use. ATH contributes to the decrease in the temperature of the material, thus attenuating heat exchange, and the formation of Al_2O_3 (aluminum oxide) as a protective layer on the product's surface reduces the diffusion of oxygen to the reactive medium and hindering heat exchange [6]. The composite with flame retardant characteristics and low toxicity and smoke emission, complying with the ABNT NBR 15708 standard, can be used in products for offshore industry.

This paper aims to evaluate the concentration´s influence of small ATH particle size on combustibility in isophthalic polyester matrix GFRP materials. These evaluations are compared to a typical industrial loading (37%) as a baseline to determine the best ATH concentration to improve the flame retardant properties. Combustibility was evaluated using mass loss cone calorimetry (MLCC), glow-wire and limiting oxygen index (LOI). Thermal analysis of the composites was performed by simultaneous thermogravimetric analysis and differential scanning calorimetry (TGA/DSC). ATH was characterized by its chemical composition, surface area, crystalline phases and particle size.

2. MATERIALS AND METHODS

2.1 Materials

All composites (Figure 1) used in this experimental investigation were prepared with low viscosity isophthalic polyester thermoset polymeric resins and using Cristalan 869 - Novapol reinforced with 51% low-conductivity E-glass. They were supplied by *Cogumelo Indústria e Comércio LTDA* (RJ, Brazil) and produced through pultrusion processing. The fiberglass layer is positioned in the longitudinal direction of the pultrusion.

The ATH, MoldX P18, manufactured by J.M. Huber Corporation, was used as a flame retardant mixed with the other resin components. This retardant costs around 35% more than usual, but presents promising results. Several ATH loads were tested, starting with 37 phr (parts per hundred rubber) content used commercially as a filler element in the material, then 40 phr, 47.5 phr, 50 phr, 55 phr. All percentages of ATH are respect to the resin. The samples codes are presented in table 1.
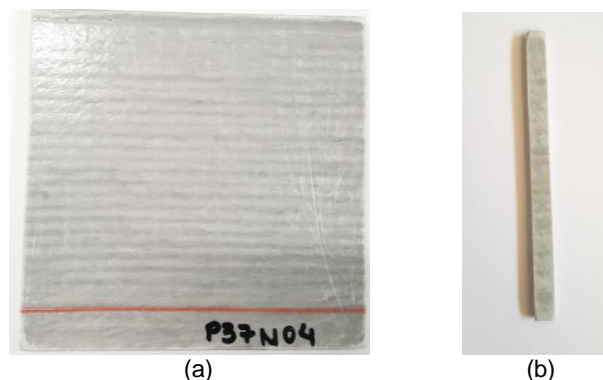
Figure 1: Specimens of GRFP polyester resin a) MLCC b) LOI

Table 1: Specimens codes according to ATH concentration

Material	GFRP polyester isophthalic matrix				
ATH quantity	37 phr	40 phr	47.5 phr	50 phr	55phr
Specimens code	P37	P40	P47.5	P50	P55

2.2 ATH characterization

The alumina trihydrate's chemical composition was determined by energy-dispersive X-ray fluorescence (XRF), using the EDX-720 spectrometer from Shimadzu. The energy-dispersive detector measures the signals and qualitatively determines which elements are present in the material.

The granulometric analyzes provide particle size distributions by laser diffraction, and they were conducted by a Malvern Instruments Mastersizer 2000 particle analyzer.

The surface area was analyzed by the Quantachrome 1200e NOVA instrument, this analysis measures the specific area through the adsorption and desorption isotherms of gaseous nitrogen molecules by the BET (Brunauer - Emmet - Teller) method. The ATH sample was prepared by a thermal pre-treatment at a temperature of 350 °C at a rate of 10 °Cmin^{-1} to remove water molecules and other substances absorbed and adsorbed on the powder surface.

The X-ray diffractometry (XRD) test was performed using the D8 Focus Bruker AXS equipment to identify the crystalline phases (structures) and the semi-qualitative identification of ATH constituents. The results were compared to data published by the Joint Committee on Powder Diffraction Standards - JCPDS (International Centre of Diffraction Data, Swarthmore, Pennsylvania, USA) for the diffraction spectra characteristics of crystalline phases in terms of interatomic spacing, relative intensities, diffraction peaks, and Miller indices.

2.3 Fire-Retardant Properties

The MLCC is a more elaborate (medium-sized bench-scale) method due to its ability to simultaneously determine several fire properties of a material including the heat release rate (HRR), peak heat release rate (PHRR), total heat released (THR), and time-to-ignition (TTI). It is described by ISO 17554 [7] and ISO 13927 [8]. The test is complete 2 minutes after the end of combustion or in cases where there is no ignition, 10 minutes after the start of the test. Three samples of each composite specimen, measuring 100 × 100 × 3 mm, were tested horizontally, with a heat flux of 50 kW/m². For evaluation purposes, the specimens with the highest PHRR results were chosen.

The LOI test determines the minimum oxygen content necessary for ignition and maintenance of combustion for at least 3 minutes or a 5 cm specimen burn. A propane pilot flame is inserted through the top of a glass cylinder containing a mixture of nitrogen and oxygen to promote the ignition of a specimen measuring 100 mm x 7 mm x 5 mm. The contact between the flame and the specimen occurs three times, for 5 seconds each. The test was performed on a Fire Testing Technology (FTT) device, standardized by ISO 4589-2 [9].

The incandescent wire method determines if a material can ignite and propagate a flame through two tests: (i) the glow-wire flammability index (GWFI); and (ii) the glow-wire ignition temperature (GWIT). The GWIT corresponds to a temperature 25 ºC above the highest temperature tested in which the specimen does not ignite in three consecutive tests. The GWFI corresponds to the highest temperature where the flame or incandescence is extinguished within 30 seconds after removing the glowing tip in three consecutive trials, and there is no ignition via dripping onto paper positioned below the specimen. It is standardized by IEC 60695-2-10 [10], IEC 60695-2-12 [11], and IEC 60695-2-13 [12].

2.4 Thermal Analysis

Simultaneous thermogravimetric analysis (TGA) and differential scanning calorimetry (DSC) of the composites was carried out in a TA Instruments SDT-Q600 analyzer. In these tests, sample masses ranging from 70 to 80 mg (Figure 2) were heated from 25 to 850 ºC at a 10 ºCmin^{-1} heating rate at atmospheric pressure.
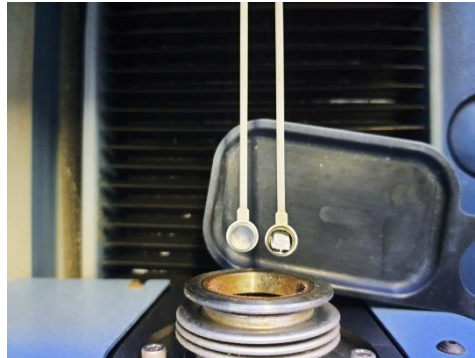
Figure 2: Specimen of GRFP polyester resin in TA Instruments SDT-Q600 analyzer

3. RESULTS

3.1 ATH characterization

The X-ray fluorescence (XRF) determined the chemical composition and verified the purity. The ATH consists of 97.72% Al_2O_3, demonstrating a high level of purity. The small percentage of impurities can be from the Bayer process used to obtain alumina from bauxite [13]. Moreover, from the granulometric analyzes, ATH is within the smallest micrometric size range, D50 is 6.425 µm and D90 is 15.096 µm. And ATH sample had a surface area equivalent to 148 m²g^{-1}.

The XRD revealed the presence of alumina (Al_2O_3), gibbsite ($Al(OH)_3$), sillimanite (Al_2SiO_5) and quartz (SiO_2). The XRD peaks and the θ values were related to standard spectra from the Joint Committee on Powder Diffraction Standards (JCPDS) and confirmed the presence of crystalline alumina in the α phase (JCPDS no. 10.173) and gibbsite extracted from bauxite (JCPDS no. 033.018). Other crystalline elements were also identified, such as quartz; however, as measured by XRF, the amount of quartz and sillimanite is very low.

3.2 Fire-Retardant Properties

This burning ATH composites process (Figure 3 (a-b)) in MLCC includes the following steps: heating, pyrolysis, ignition, combustion and propagation, and extinction. The surface of the specimen is heated over a load cell, the sample darkens and releases gaseous products, forming a mixture with flammable oxygen and begins to release smoke due to the different combinations of the substances released. Then, ignition occurs, and the peak heat release rate is reached as pyrolysis products experience ideal levels of oxygen, temperature and combustible gas concentration. In propagation, there is an intense combustion and release of smoke while there is combustible material available, before the flames decrease and extinguished [14].

A darker layer on the specimen (Figure 3(c)) corresponds to lower polymer matrix degradation [1], as the ATH load increases and the residue on the sample surface. This aluminum oxide surface layer formed during combustion increased the sample's protection against external radiation.
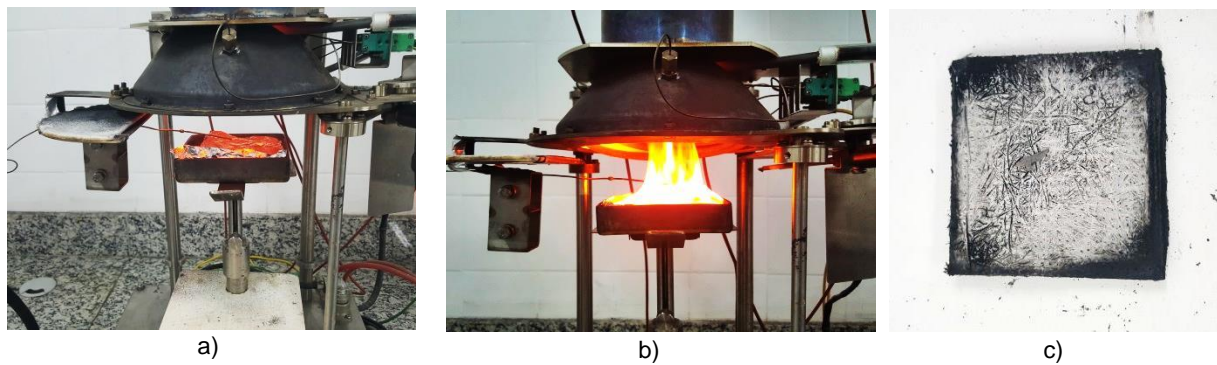
Figure 3: a) Pyrolyses b) Combustion c) Degraded specimen

Table 2 summarizes the specimens' peak heat release rate (PHRR), total heat released (THR) and time-to-ignition (TTI) from the MLCC test. The specimens included in this table were chosen according to the highest PHRR parameter.

Table 2: Results of MLCC with different ATH concentrations

Specimens	ATH (phr)	Mass (g)	PHRR (kW/m²)	THR (MJ/m²)	TTI (s)
P37	37	85.4	162.77	37.4	116
P40	40	82.6	119.71	34.4	140
P47.5	47.5	84.8	116.58	34.6	97
P50	50	83.7	94.57	32.9	152
P55	55	85.1	102.78	34.0	136

Compared to P37 (162.8 kW/m²), all specimens showed a significant decrease in PHRR (table 2). The good performance of ATH in reducing the PHRR is due to the water released during the endothermic reaction, which dilutes the effect of gases during pyrolysis and reduces the heat of the sample [15]. The PHRR of the GFRP polyester resin without any retardant is around 317 kW/m² [1]. Although P50 presented the lowest PHRR, P40 and P47.5, in particular, are notable since they have a lower amount of ATH and similar results to P50 and P55. The P40 composite showed a significant reduction in PHRR, with a value 27% below that for P37.

In THR analyzes the GFRP polyester resin without any retardant had a value of 92.4 MJ/m² [1]. Therefore, all specimens reduced the THR, improving the properties for this parameter. P50 had the lowest total heat released, achieving the best result. Sample P40 showed a favorable reduction compared to P37 and obtained a similar result as the other specimens.

The ignition time (TTI)—the time required to start the flame—characterizes the ease of igniting the material. A higher TTI value leads to a better performance of the composite. The GFRP polyester resin without any retardant ignites in 134 seconds [1]. Therefore, P50 shows the best result, resisting ignition for the longest time, 152 seconds due to the ATH endothermic reaction, which increases its ignition time by reducing the heat of the sample [15].

In MLCC tests conclusion, the P40 sample significantly reduced the HRR and THR compared to P37, while also increasing the TTI.

The LOI results for all specimens were nearly identical at 23% or 24% since the error of this analysis is ±1 unit of LOI. Although, the increase in the ATH load used in this research did not significantly change the LOI, all specimens with ATH increased the oxygen content of the pure matrix. According to previous work [1], the LOI of a GFRP isophthalic polyester resin without retardant is equivalent to 21%. The Figure 4(a) presents de LOI

equipment. The samples P50 (Figure 4(b)) and P55 (Figure 4(c)) reached 24% of oxygen self-extinguishing the flame before 180 s.

(a)   (b)   (c)
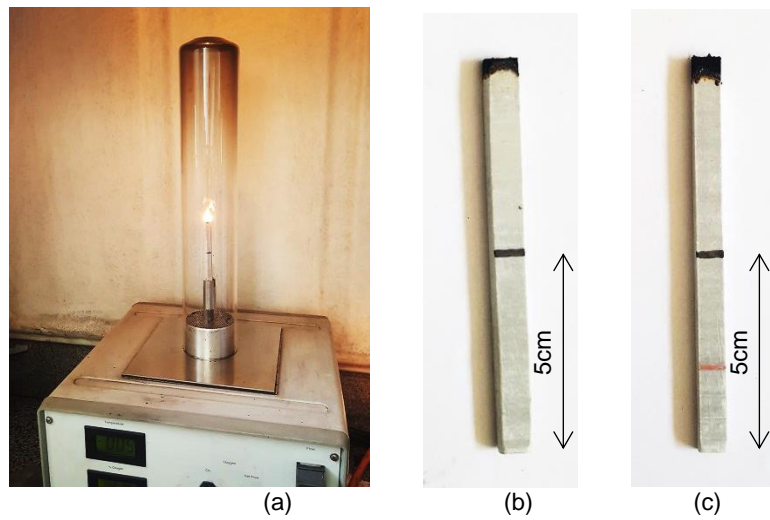
Figure 4: a) LOI equipment b) sample P50 at 24% of LOI c) sample P55 at 24% of LOI

In Glow Wire tests, specimens P37, P40, P47.5 and P50 had similar results: 960 ºC in GWFI and 900 ºC in GWIT (Figure 5). Therefore, P37 had the best performance: 960ºC for GWFI and 900 ºC for GWIT, because it has the lowest ATH load, a desired commercial result for wires and cables, and the 960 ºC GWFI temperature is the maximum stipulated by the standard [16]. The GFRP polyester resin without retardant has 800 ºC for GWFI and 850 ºC for GWIT [1]. Therefore, ATH raised the GWFI and GWIT temperatures of all samples. The composites studied in this paper could be used in the electricity sector, as the parameters obtained were superior to what is required by the standard.
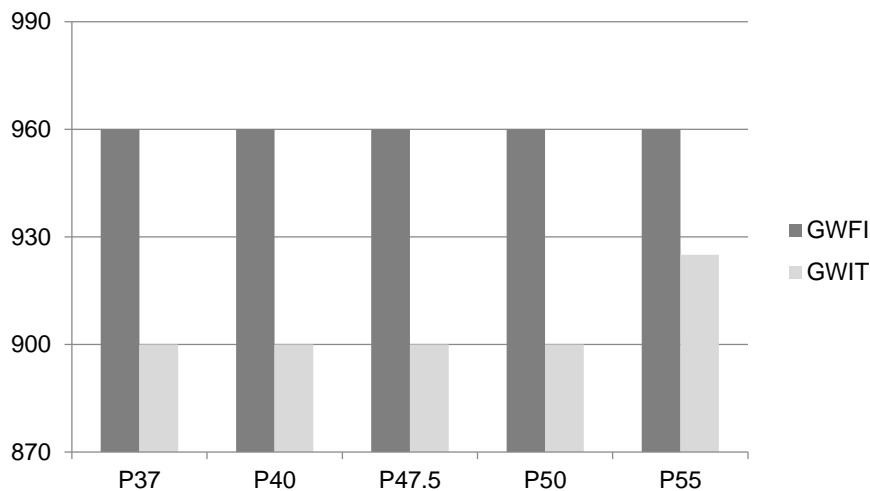
Figure 5: GWFI (ºC) and GWIT (ºC) results

3.3 Thermal Analysis

The thermal analysis results are presented in Table 3, for GFRP polyester resin. All the specimens showed two stages of degradation corresponding to the decomposition of the ATH polymeric matrix around 320ºC and 400ºC. Some of the mass loss observed in the first stage degradation around is related to water loss from ATH [1]. The sample P37 had the highest percentage of residue, about 65%, at 800 °C. The GFRP polyester resin without

retardant also showed two degradation and mass loss stages, the first being 32% and the second 3.9%, leaving 64.1% of residue at 800°C [1], therefore, ATH tested in this research did not increase the amount of residue.

In DSC analyze (Table 3) the specimens showed an endothermic peak around 320°C related to water loss from ATH, which absorbs heat [4], and two exothermic peaks associated with the heat released during combustion, with the first peak around 400°C and the second and larger exothermic peak around 515°C. Sample P55 had the lowest exothermic enthalpy value of the two energy release peaks, demonstrating that the enthalpy value decreases as the ATH load increases. However, sample P40 had the highest endothermic enthalpy and also obtained promising MLCC results with lower ATH than P55.

Table 3: TGA and DSC results of different ATH concentrations

Speci mens	TGA					DSC				
	Stages´Onset temperatures (°C)		Weight loss (%)		Residue at 800 °C (%)	Peak temperatures (°C)			Enthalpy (J/g)	
	T1	T2	(25 – 450 °C)	(450 – 800 °C)		Endoth ermic	Exother mic (1)	Exother mic (2)	E1 (endo)	E2 (exo)
P37	320	400	28.38	6.46	65.09	303	402	518	35	-1926
P40	326	404	30.54	6.67	62.74	322	402	513	73	-1919
P47.5	320	400	31.10	6.19	62.70	317	398	512	47	-1815
P50	321	405	30.53	6.78	62.62	319	404	517	52	-1864
P55	323	405	30.84	6.45	62.66	321	402	517	51	-1740

4. CONCLUSIONS

Several tests were used to characterize ATH, and different ATH concentrations were evaluated (37 phr, 40 phr, 47.5 phr, 50 phr, 55 phr) to find the ideal load for improved flame retardant properties. Although all specimens with different ATH concentrations have combusted in the MLCC, the P40 and P47.5 samples reduced the PHRR by 27% compared to sample P37. For the LOI, all specimens with ATH increased the oxygen content compared to the pure matrix values. Moreover, analyzing the glow wire results, all composites achieved the desired flame retardant commercial properties for wires and cables applications. It was concluded from the thermal stability analysis that the increase in the ATH concentration decreased the combustion enthalpy of the composites. Finally, the composite with 40 phr is noteworthy because obtained promising MLCC, glow wire and thermal analysis results and contain an ATH concentration closer to a typical industrial loading which is 37 phr. Therefore, the use of ATH with particle size around 10 µm can be a good approach in GFRP based on polyester resin with flame retardancy properties, decreasing costs and facilitating processing.

REFERENCES

[1] Nascimento, M. A. F. R. (2018). *Enhancement of fire retardancy properties of glass fibre–reinforced polyesters composites*, D.Sc. Thesis, Federal University of Rio de Janeiro, 162 p. In Portuguese.

[2] Ribeiro, L. M.; Ladchumananandasivam, R. & Galvão, A. O. (2013*). Flammability and flame retardancy of the composite: pineapple fiber reinforced unsaturated polyester (palf)*, Holos, vol. 29(1), p 115-126. In Portuguese.

[3]   Tibiletti, L.; Longuet, C. & Ferry, L. (2011). *Thermal degradation and fire behaviour of unsaturated polyesters filled with metallic oxides*, Polymer Degradation and Stability, vol 96 (1), p 67-75.

[4]   Elbasuney, S. (2017)*. Novel multi-component flame retardant system based on nanoscopic aluminium-trihydroxide (ATH)*, Powder Technology, vol. 305, p 538-545.

[5]   Kiliaris, P. & Papaspyrides, C. D. (2014). *Polymer Green Flame Retardants*, Elsevier, 942 p .

[6]   Silva, V. L. D. (2006). *Mechanical and flammability behavior of recycled polypropylene composite with coconut fiber and aluminum hydroxide*, M.Sc. Dissertation, Federal University of Pará, 115 p. In Portuguese.

[7]   ISO 17554 (2014). *Reaction to fire tests - Mass loss measurement*, International Organization for Standardization.

[8]   ISO 13927 (2015). *Plastics - Simple heat release test using a conical radiant heater and a thermopile detector*, International Organization for Standardization.

[9]   ISO 4589-2 (2017). *Plastics- Determination of burning behaviour by oxygen index- Part 2: Ambient-temperature test*, International Organization for Standardization.

[10] IEC 60695-2-10 (2013). *Fire hazard testing- Part 2-10: Glowing/hot-wire based test methods - Glow-wire apparatus and common test procedures*, International Electrotechnical Commission.

[11] IEC 60695-2-12 (2010). *Fire hazard testing - Part 2-12: Glowing/hot-wire based test methods- Glow-wire flammability index (GWFI) test method for materials*, INTERNATIONAL ELECTROTECHNICAL COMMISSION.

[12] IEC 60695-2-13 (2010). *Fire hazard testing - Part 2-13: Glowing/hot-wire based test methods- Glow-wire ignition temperature (GWIT) test method for materials*, International Electrotechnical Commission.

[13] Abreu, S. L. (2011). *Characterization and dispersion of α-Alumina with submicron and nanometer particle size in aqueous suspension*, M.Sc. Dissertation, Federal University of Ouro Preto, 80 p. In Portuguese.

[14] Gallo, J. B. & Agnelli, J. A. M. (1998). *Aspects of Polymer Behavior in Fire Conditions*, Polymers: Science and Technology, vol 8, p 23-37. In Portuguese.

[15] Hapuarachchi, T. D. & Peijis, T. (2009). *Aluminium trihydroxide in combination with ammonium polyphosphate as flame retardants for unsaturated polyester resin*, Express polymer letters, vol. 3, p 743–751.

[16] Ribeiro, S. P. S.; Estevão, L. R. M. & Nascimento, R. S. V. (2017). *Glow-wire evaluation of polymeric materials for the electric sector: Effect of the interlayer spacing of montmorillonite*, Applied Clay Science, vol. 143, p 399-407.

MATERIAL CHARACTERISATION OF ULTRA-HIGH-STRENGTH STEEL S960QL AT ELEVATED TEMPERATURES UNDER STEADY-STATE AND TRANSIENT-STATE TEMPERATURE CONDITIONS

Sara Uszball[a,*]   **Markus Knobloch[b]**

ABSTRACT

For state-of-the-art buildings, the use of high- and ultra-high-strength steels has increased in recent years, since the good strength-to-weight ratio can contribute to resource and energy efficiency of steel structures. For a thorough understanding and a realistic modeling of the structural behavior of steel structures, in particular in case of fire, comprehensive knowledge of the material behavior is the basis. Experimentally validated results regarding the mechanical behavior of ultra-high-strength steels in case of fire are yet very rare. Therefore, the paper provides results of an extensive tensile test program regarding the material behavior of ultra-high-strength quenched and tempered steel of grade S960QL including elevated temperature tests under steady-state and transient-state temperature conditions considering different strain- and heating-rates.

The test results show that the constitutive behavior of ultra-high-strength steel S960QL becomes nonlinear at elevated temperatures and high temperatures lead to significantly reduced strengths and stiffness values. Further, the mechanical material behavior is strain-rate-sensitive for temperatures exceeding 550°C. Additionally, it is shown that for an accurate prediction of the behavior of ultra-high-strength steel S960QL, high-temperature-creep effects need to be considered within the framework of fire design of steel structures, since slow heating- or strain-rates lead to significantly higher total strains at elevated temperatures.

Keywords: Ultra-high-strength steel; Mechanical material behavior; Elevated temperature tests; High-temperature creep.

---

[a],* Ruhr-Universität Bochum (sara.uszball@rub.de), Tel.: +49 234 32-22390, Corresponding author**.**

[b] Ruhr-Universität Bochum (markus.knobloch@rub.de).

1. INTRODUCTION

High- and ultra-high-strength structural steels are increasingly used in modern multi-storey buildings and industrial structures in the form of plates, tubes and sections. They can contribute to the resource and energy efficiency of steel structures. For structures with fire protection requirements, the use of high-strength structural steels is yet still inhibited by a lack of knowledge about the temperature- and rate-dependent material behavior in case of fire. Fire incidents can have a significant economic impact on both the owners of buildings and society in general, and represent one of the most serious hazards to the built environment [1]. Accurate predictions of the load-bearing behavior of steel structures in case of fire are therefore necessary and ensure the fire safety of structures in a cost-effective manner [2]. Comprehensive knowledge of the material behavior in case of fire is the basis for a general understanding as well as a realistic modeling of the load-bearing behavior.

The temperature-dependent material behavior of high-strength structural steels has been investigated in various research projects in the past. In particular, the focus was on investigations regarding the behavior of steels of grade S460 [3-5], since those are already established in the construction industry. Experimental results are also available on the material behavior of high-strength structural steels of grade S690 [6-12].

Tests under steady-state and transient-state temperature conditions indicate for high-strength structural steels that the temperature-dependent reductions of the material stiffness and strength are generally higher in transient-state tests than in steady-state tests. However, systematic studies on the influence of the strain rate in steady-state tests or the heating rate in transient tests are yet not available, so that a conclusive evaluation cannot be made. In addition, it was found that the temperature-dependent reductions of the material properties of high-strength steels were similar to those of mild steels. The reduction factors according to EN 1993-1-2 [13] are therefore able to represent the material behavior of high-strength steels sufficiently accurate. Therefore, within the scope of the revision of the Eurocodes, the application range of the constitutive model according to EN 1993-1-2 has already been extended to structural steels up to and including S700 [14] for fire scenarios with steadily increasing temperatures.

For an analogous extension of the application range of part 1-2 of EN 1993 to ultra-high-strength steels with nominal yield strengths $f_y > 700$ N/mm^2 or the development of supplementary regulations within the framework of a new part 1-12 of EN 1993 for ultra-high-strength steels [15], experimentally verified knowledge of the temperature- and rate-dependent material behavior is essential. Currently, the results regarding the behavior of ultra-high-strength steels are very rare. Qiang et al. investigated the behavior of quenched and tempered structural steel S960QL under steady-state temperature conditions in [16] and the residual properties after fire exposure in [17]. In [6], the behavior of S960QL was also investigated under steady-state temperature conditions. These investigations were supplemented in [18] by extensive studies of the structural material behavior of S960QL during the cooling phase of natural fire scenarios.

The present study provides an extensive tensile test program on ultra-high-strength steel S960QL to characterise the material behavior in case of fire. Test results of steady-state tests are presented and evaluated. Subsequently, results of tensile tests under transient temperature conditions are presented and compared to the results of the steady-state tests.

2. ELEVATED TEMPERATURE TESTS

2.1 Test program

Table 1 shows the parameters of the steady-state and the transient-state tests of the tensile test program on ultra-high-strength steel (UHSS) of grade S960QL to characterise the temperature- and rate-dependent material behavior in case of fire.

According to the nomenclature of Anderberg [19] there are two main test procedures for the material characterisation in fire. In steady-state tests, the test specimen is heated mechanically unloaded to the target temperature, this temperature is kept constant during the subsequent mechanical loading, and a tensile test is performed strain-controlled until the fracture of the specimen. Stress-strain relationships for a defined state of temperature and strain rate are obtained directly from the tests. In case of the steady-state tests of the present study, two different strain rates of 0.2 %/min and 1.0 %/min were predefined for the strain-rate-controlled tests to investigate the effects of the strain rate, in particular on the measured strength values during the test.

Tensile tests under transient temperature conditions are more related to the thermo-mechanical situation of a real structural component in case of fire. The test specimens are firstly exposed to a constant load level and

subsequently heated with a defined heating rate. In the present study, transient tests were carried out with three different heating rates, so that effects on the constitutive material behavior from slow, medium-fast and fast heating could be determined. Heating rates of 3 K/min, 10 K/min and 50 K/min were applied. In case of slow heating with 3 K/min, it was assumed that distinct creep effects could be observed. The heating rate of 50 K/min represents the limit heating rate of common test furnaces and it can be assumed that it is sufficiently fast to avoid high temperature creep. The heating rate of 10 K/min was chosen because it corresponds to an average heating rate of protected steel structures in common fire scenarios. The selected heating rates of the transient tests also comply with the application range of the constitutive material model according to EN 1993-1-2 [13] with heating rates from 2 to 50 K/min.

Table 1: Test program

Steady state tests		Transient tests	
Temperature T [°C]	Strain rate $\dot{\varepsilon}$ [%/min]	stress level σ [% of $f_{2.0,20°C}$]	Heating rate $\dot{T}$ [K/min]
20		10	
400	0.2	30	3
550	1.0	50	10
700		65	50
900		80	

The tests were performed on small-scale specimens made of plate material with an initial thickness of t_0= 12 mm of ultra-high-strength quenched and tempered steel of grade S960QL. The geometry of the specimens is shown in Figure 1 and corresponds to the constraints of the existing test setup. The dog-bone-shaped specimens had a total length of L= 170 mm and a constant thickness of t= 6 mm. The initial gauge length in the center of the specimens was L_0= 45 mm. Further, a specimen geometry with two fillet radii was selected. The first fillet radius R_1= 15 mm served the form-fitted installation in the specimen holder and the second fillet radius R_2= 10 mm ensured that necking and fracture of the specimens occurred in the range of the gauge length.
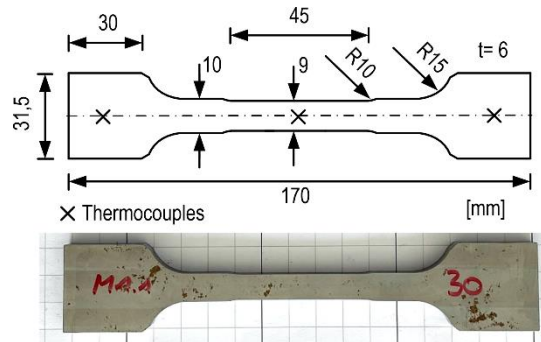
Figure 1: Test Specimens.

2.2 Test setup

For the material characterisation tests, a combined test setup consisting of a universal testing machine (manufacturer Schenck) with a maximum load capacity of 250 kN and an electric furnace (manufacturer Koenn) was used. The test setup is shown schematically in Figure 2(a). Figure 2(b) shows photographs of the test equipment.

The furnace has three vertically arranged independently controllable heating zones. The air temperature was measured with three mantle thermocouples type N (D_1= 3 mm). In the current study, the heating was controlled by three additional mantle thermocouples type N (D_2= 1.5 mm), which were placed directly on the specimen surface. For the strain measurement during the tensile tests, a high-temperature extensometer (manufacturer Maytec) was used. The ceramic rods of the extensometer were placed directly on the specimen surface through a vertical opening at the front of the furnace. The measured strain also served as a feedback variable for a closed-loop-feedback control during the strain-rate-controlled steady-state tests.
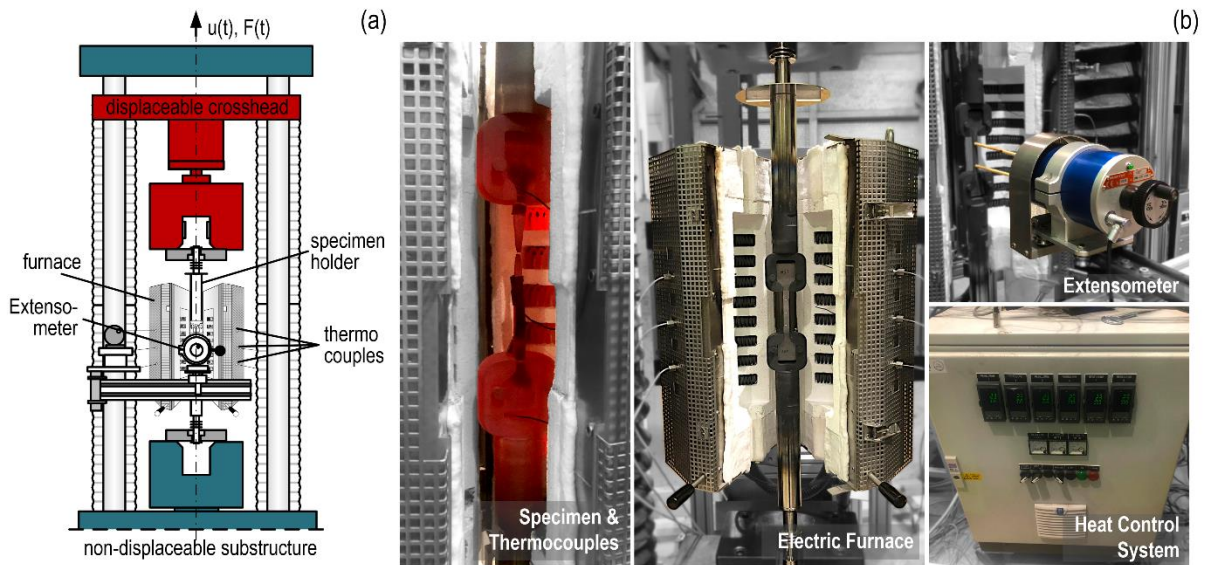
Figure 2: (a) Schematic illustration and (b) photographs of the test setup.

2.3 Test procedure

Figure 3 shows the time-force (top) and time-temperature (bottom) relationships of the test procedures for (a) the steady-state tests and (b) the transient-state tests.

In case of both test procedures, firstly five loading and unloading cycles in the linear-elastic strain range were performed at ambient temperature to determine the Young's modulus at ambient temperature and to ensure the centric alignment of the specimens in the test setup.
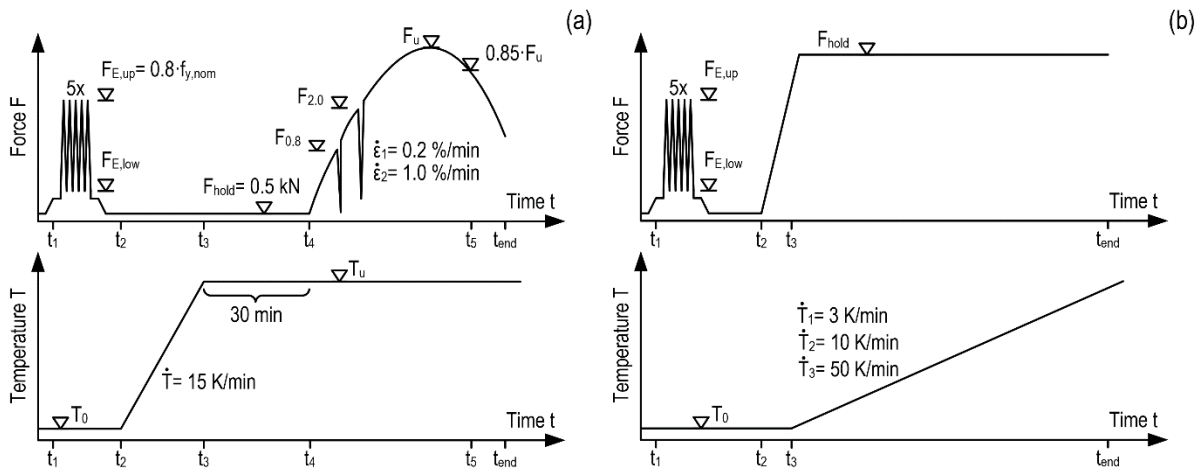
Figure 3: Time-force and time-temperature relationships of (a) steady-state tests and (b) transient-state tests at elevated temperatures.

In case of the steady-state tests (Figure 3(a)), the specimens were subsequently heated with a constant heating rate. When the target temperature T_t was reached, this temperature was kept constant for 30 min to ensure that the entire cross-section of the specimen had a uniform temperature and thermal expansion during the tensile test could be excluded. The tensile test was then performed strain-rate-controlled using a closed-loop-feedback control with the high-temperature extensometer. At a force reduction of 15 % based on the maximum force of the test, the extensometer was removed to avoid damage of the equipment by the sudden fracture of the specimen. The test was then continued using a displacement-control via the crosshead displacement of the testing machine until the fracture of the specimen.

In case of the transient-state tests (Figure 3(b)), after determining the Young's modulus at ambient temperature, the specimen was subjected to a force-controlled loading with a predefined load, which was kept constant during

the test. Once the target load level was reached, the heating device of the furnace was switched on and the specimen was heated with a constant heating rate. At the beginning of the test, the strain was measured with the high-temperature extensometer. However, the extensometer was removed when the deflections of the ceramic rods reached a specified limit in order to avoid damage due to large deformation. From this point, the elongation of the specimen was measured by means of the crosshead displacement of the testing machine.

3. TEST RESULTS

3.1 Material behavior of S960QL under steady-state temperature conditions

Figure 4 shows the stress-strain curves from steady-state tests with a strain rate of $\dot{\varepsilon}= 0.2$ %/min (dashed lines) and $\dot{\varepsilon}= 1.0$ %/min (solid lines) at various elevated temperatures. In addition to the stress-strain curves at 400°C (blue), 550°C (green), 700°C (grey) and 900°C (orange), the curves at ambient temperature (black) are shown for comparative purposes.

The stress-strain curves at ambient temperature show a linear-elastic increase at the beginning of the tests and a distinct proportional limit. The different strain rates during the tests apparently do not affect the results of the tensile tests at ambient temperature. Almost identical strengths and stiffnesses are achieved.

At elevated test temperatures (here from 400°C), the material behavior is nonlinear. There is no distinct change from linear-elastic to plastic material behavior. In addition, the strengths decrease significantly compared to tests at ambient temperature.
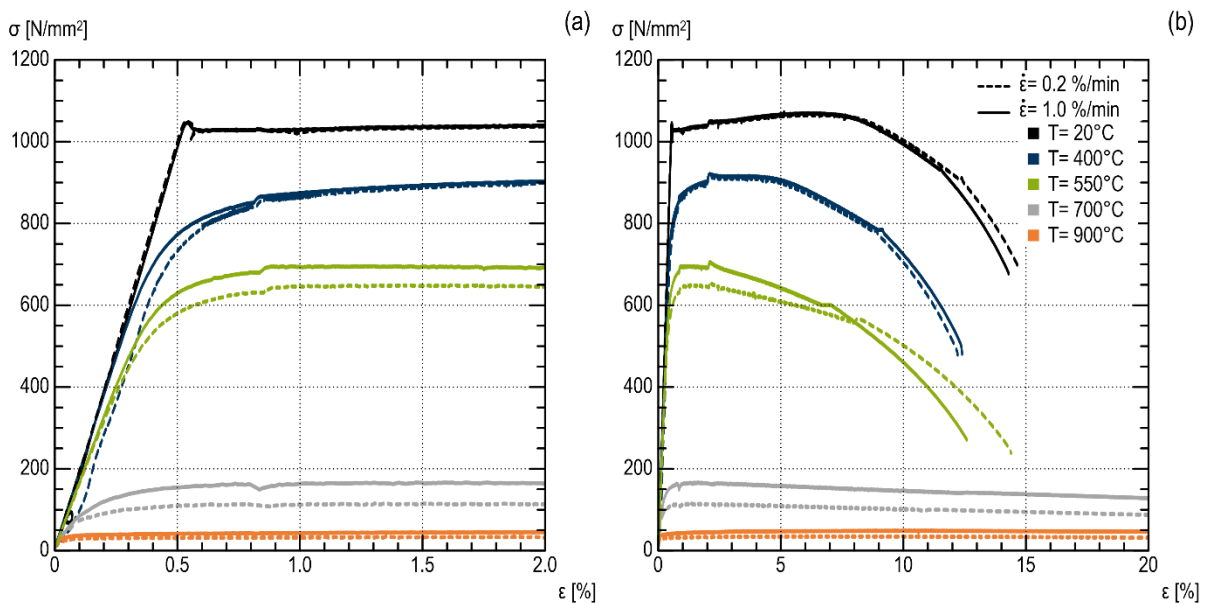
Figure 4: Stress-strain curves from steady-state tests on S960QL for the strain range up to (a) 2 % and (b) 20 %.

In tests with temperatures of T≥ 550°C, the strain rate has a significant influence on the material strengths. A higher strain rate leads to higher strength values in the tests. This behavior is already known from normal strength structural steels [20] and it can be assumed that this results from a greater influence of high-temperature creep at longer test durations due to the slow mechanical loading.

From the stress-strain curves, material properties, i.e. macroscopic strength and stiffness values, can be determined. The material properties derived from the curves in Figure 4 are summarised in Table 2. The table contains the temperature-dependent values for the Young's modulus E_θ, the proportional limit $f_{p,\theta}$, the 0.2 % proof stress $f_{y,0.2,\theta}$, the stresses at 2.0 % total strain ($f_{y,2.0,\theta}$), the tensile strength $f_{t,\theta}$, and the elastic fracture strain $\varepsilon_{u,\theta}$.

Table 2: Material properties of S960QL from steady-state tests

T [°C]	$\dot{\varepsilon}= 0.2$ %/min						$\dot{\varepsilon}= 1.0$ %/min					
	E_θ $\left[\frac{N}{mm^2}\right]$	$f_{p,\theta}$ $\left[\frac{N}{mm^2}\right]$	$f_{y,0.2,\theta}$ $\left[\frac{N}{mm^2}\right]$	$f_{y,2.0,\theta}$ $\left[\frac{N}{mm^2}\right]$	$f_{t,\theta}$ $\left[\frac{N}{mm^2}\right]$	$\varepsilon_{u,\theta}$ [%]	E_θ $\left[\frac{N}{mm^2}\right]$	$f_{p,\theta}$ $\left[\frac{N}{mm^2}\right]$	$f_{y,0.2,\theta}$ $\left[\frac{N}{mm^2}\right]$	$f_{y,2.0,\theta}$ $\left[\frac{N}{mm^2}\right]$	$f_{t,\theta}$ $\left[\frac{N}{mm^2}\right]$	$\varepsilon_{u,\theta}$ [%]
20	190855	1041.4	1029.9	1038.5	1067.8	14.4	202052	1048.1	1030.5	1041	1071.3	14
400	184873	632.4	804.4	900.6	918.3	12	186570	640.1	823.1	903.6	916	12.2
550	155366	408.8	603.2	645	656.5	14.3	161122	466.6	658.3	692.1	696.1	12.5
700	91357	51.2	99.5	112.5	114.4	-*	86766	82.1	144.4	162.9	164.3	-*
900	86046	19.2	28.2	30.1	41.4	-*	84076	28.3	37.6	43.4	47.6	-*

*Value of $\varepsilon_{u,\theta}$ could not be determined as there was no distinct fracture point due to the large deformation capacity of the material.

3.2 Material behavior of S960QL under transient temperature conditions

From transient-state tests, total strain-temperature curves for defined mechanical stress levels are obtained. These are shown in Figure 5 for heating rates of Ṫ= 3 K/min (dotted lines), Ṫ= 10 K/min (solid lines) and Ṫ= 50 K/min (dashed lines) in the strain range (a) up to 2 % and (b) up to 30 % total strain. The curves represent the test results for defined stress levels of 10 % (orange), 30 % (grey), 50 % (green), 65 % (yellow) and 80 % (blue) of the effective yield stress at 2 % total strain at ambient temperature $f_{y,2.0,20°C}$. The measured strains include, in addition to mechanical strains from load application, thermal strains and implicitly creep strains.

The heating rate significantly influences the results of the transient-state tests. The failure temperatures (temperatures at fracture of the test specimens) are highest for the fastest heating rate at all stress levels. The lowest failure temperatures are obtained for slow heating of 3 K/min. As a result of the larger creep strains, the total strains are larger for slow heating and failure occurs at an earlier time than in the case of fast heating. The differences between the curves of different heating rates are increasing for higher stress levels.
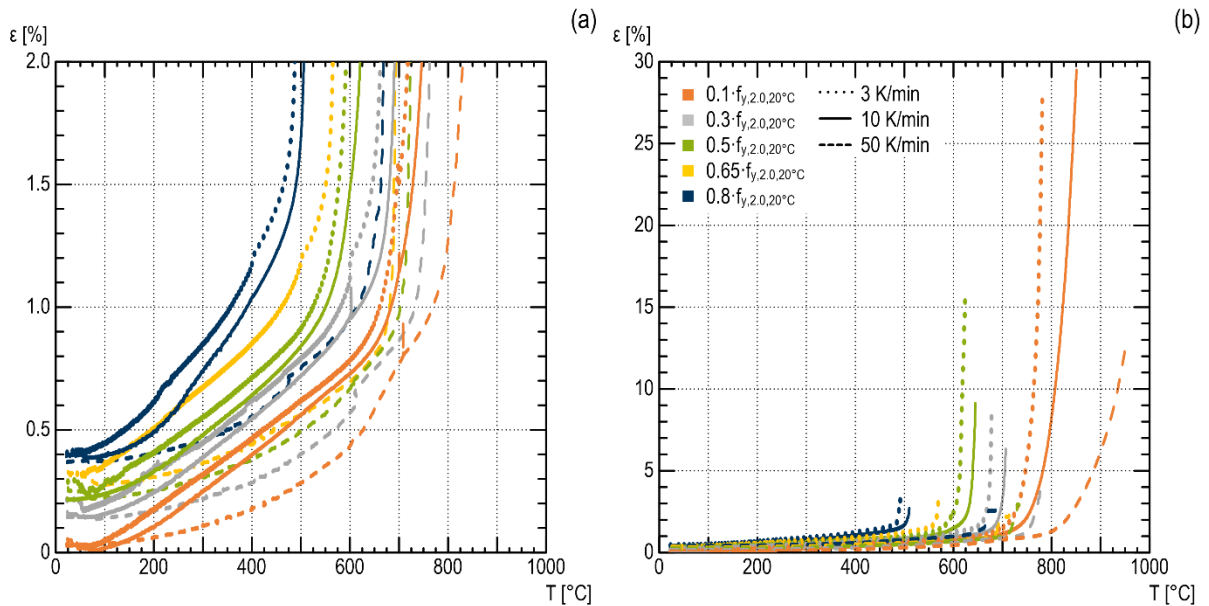
Figure 5: Total strain-temperature curves from transient-state tests for the strain range up to (a) 2 % and (b) 30 %.

Thermal strains were determined in reference tests in order to extract them from the total strain-temperature curves of the transient tests. For that purpose, specimens were heated according to the test procedure of the heating phase of the steady-state tests (see Figure 4(a)) but with the selected heating rates of the transient tests of 3 K/min, 10 K/min and 50 K/min, and the deformations of the specimens were measured during the heating.

The experimentally determined thermal strains are shown in Figure 6 for the investigated steel of grade S960QL and, moreover, the thermal strains according to EN 1993-1-2 [13] as well as experimental data for high-strength steel of grade S690QL and a mild steel S355 J2+N from [18] and for high-strength steel of grade S690M from [8] are shown.
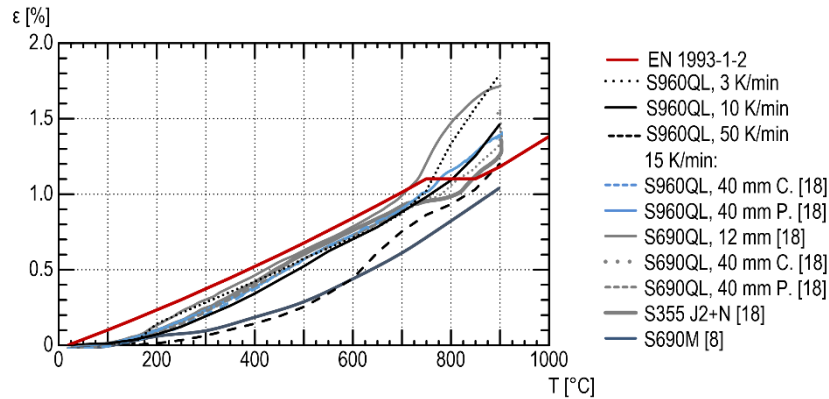
Figure 6: Thermal strains of high-strength steels from tests with various heating rates and according to EN 1993-1-2.

The thermal strains of steel S960QL from Figure 6 were subtracted from the measured total strains from transient tests (Figure 5).
The calculated mechanical strains and the defined stress levels then lead to data points for deriving stress-strain relationships. These are shown for temperatures of T= 400, 550, 700°C in Figure 7.
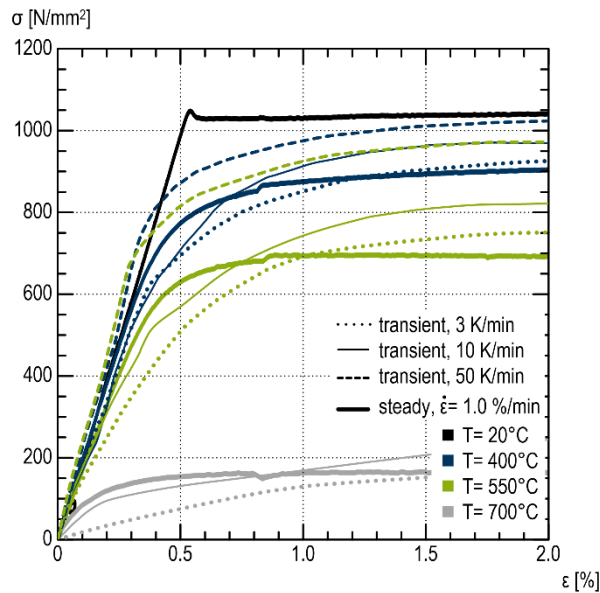
Figure 7: Stress-strain curves from tensile tests on S960QL under transient and steady-state temperature conditions.

The stress-strain curves prove that the heating rate affects the test results from transient tests. The stress-strain curves from tests with a heating rate of 50 K/min are in all cases above the curves resulting from tests with lower heating rates. The results of transient tests with medium fast and slow heating rates are qualitatively similar to each other and reflect the material behavior from steady-state tests with a temperature-dependent reduction in stiffness and strength. In case of the stress-strain relationships from tests with a heating rate of 50 K/min, however, deviations from the other results are apparent. It is assumed that the cross-sections of the specimens were not completely heated (in thickness direction, t= 6 mm) as a result of the high heating rates and short test durations, since the furnace control was by measuring the surface temperature of the 6 mm thick specimens and no measurements of the core temperature are available. Lower temperatures inside the specimens could positively affect the test results and lead to the higher values of the measured strengths and stiffnesses. The assumption is

also supported by the significantly lower thermal strains of the reference tests with a heating rate of 50 K/min compared to tests with lower heating rates in Figure 6. In order to exclude non-uniform heating of the specimens at fast heating rates, a specimen geometry with a smaller thickness could be used. Due to consistency and for better comparability of the results of the different test series, such an adaptation was not made in the present study. In the following evaluations, the results from tests with a heating rate of 50 K/min are therefore not considered.

The comparison of the stress-strain curves from transient tests with heating rates of 3 K/min and 10 K/min to the curves from steady-state tests with a strain rate of $\dot{\varepsilon}$ = 1.0 %/min for identical test temperatures in Figure 7 shows that the degradation of the strength at elevated temperatures from steady-state and transient tests is similar for both test methods. However, the curves from transient tests are always below the curves from steady-state tests for small strains. This proves that high temperature creep effects influence the constitutive material behavior at long test durations due to low heating or strain rates.

The material properties derived from the stress-strain curves of the transient tests are listed in Table 3.

Table 3: Material properties of S960QL from transient tests

$\dot{T}$ [K/min]	T [°C]	E_θ [N/mm^2]	$f_{p,\theta}$ [N/mm^2]	$f_{y,0.2,\theta}$ [N/mm^2]	$f_{y,2.0,\theta}$ [N/mm^2]
3	100	189411	880.5	936.2	1017.5
	300	185950	661.2	849.7	888.1
	400	171526	621.9	779.9	925.5
	500	168702	509.9	657.6	736.1
	550	139734	237.7	581.8	751.1
	600	111215	197.1	343.4	534
	700	15199	76.1	139.1	162.4
10	100	192308	971.6	1016.1	1047.2
	300	195660	772.1	853.5	978
	400	173748	551.3	861.2	969.5
	500	166056	515.8	688.9	851.9
	550	162925	274.9	613.4	821.8
	600	142848	256.5	422.3	610.7
	700	52324	87.9	125.4	243.8

4. COMPARATIVE STUDY

Reduction factor-temperature relationships were derived for the determined material properties from Tables 2 and 3 by relating the temperature-dependent values to the respective initial values at ambient temperature. Figure 8 shows the reduction factor-temperature relationships for (a) the Young's modulus E_θ, (b) the effective yield strength $f_{y,2.0,\theta}$, and (c) the proportional limit $f_{p,\theta}$. In addition to the results of the conducted tensile tests on S960QL of the present study, data points from literature on specimens of mild steels with $f_{y,nom} \leq 460$ N/mm^2 (grey) [3-5, 20-23] as well as high-strength steels with $460 < f_{y,nom} \leq 700$ N/mm^2 (blue) [6-12] and ultra-high-strength steels with $f_{y,nom} > 700$ N/mm^2 (green) [16, 24] are shown in Figure 8. The dark red lines in the graphs correspond to the reduction factors according to EN 1993-1-2 [13]. A distinction is made between steady-state and transient temperature conditions during the tests for the test data of the present tests as well as for results from literature, in order to investigate the influence of different test methods.

In the case of the measured strengths in Figure 8(b), the test results of the present study and literature data on ultra-high-strength steels agree well and the scatter is comparatively small. Overall, the reduction factor-temperature relationships show a decrease in material strengths at high temperatures. The degradation of the strengths of high- and ultra-high-strength steels at elevated temperatures is not significantly higher than for mild steels.

Based on the results of the steady-state tests on S960QL, it is also evident that the strain rate during the test has a small influence on the measured strength values. The relative reductions of the strength from tests with lower strain rates are slightly higher at high test temperatures than the corresponding values of tests with higher strain rates.
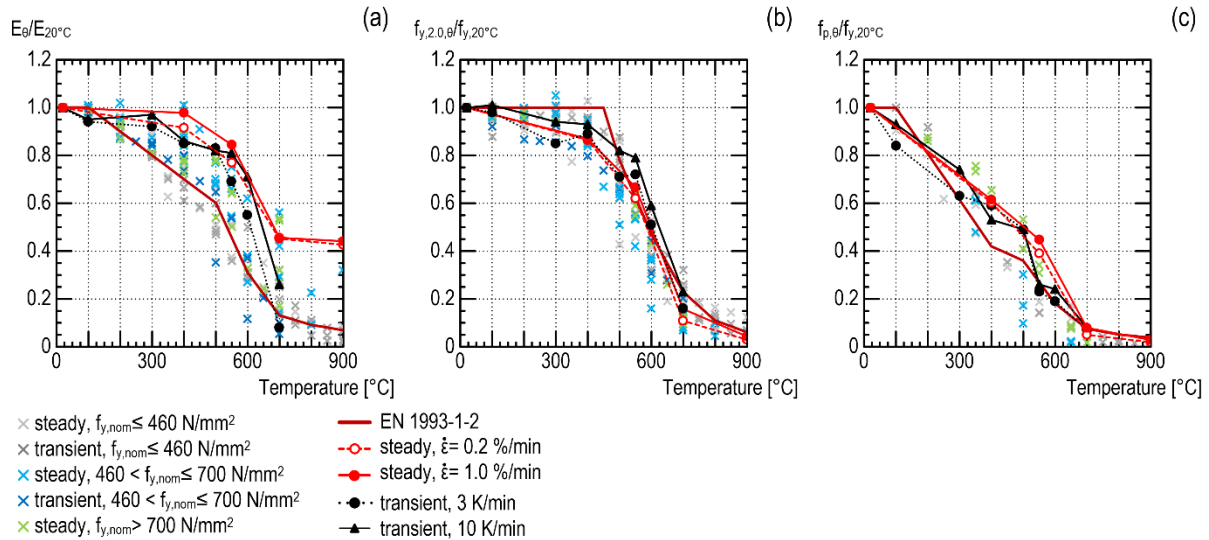
Figure 8: Reduction factor-temperature relationships from transient and steady-state tests on S960QL for (a) the Young's modulus E_θ, (b) the effective yield strength $f_{y,2.0,\theta}$, and (c) the proportional limit $f_{p,\theta}$.

Regarding the decrease in stiffness, a greater scatter can be seen between the individual test series of ultra-high-strength steels of the present study and from literature. However, this is apparently due to the high sensitivity of the Young's modulus to the test procedure and, in particular, the measurement accuracy in the small strain range.

The comparison of the test results to the reduction factors according to EN 1993-1-2 shows that the reduction factors $k_{E,\theta}$ for the Young's modulus (Figure 8(a)) and the proportional limit (Figure 8(c)) are mostly conservative for mild steel as well as for high- and ultra-high-strength steels. In case of the effective yield strength (Figure 8(b)), the experimentally determined strengths are partly overestimated by the normative values, in particular at temperatures up to 400°C. However, it can be seen that the deviations between reduction factors from tests and the values according to EN 1993-1-2 for mild steel as well as high- and ultra-high-strength steels are of the same order of magnitude.

From the reduction factors of elevated temperature tests on mild steels, high- and ultra-high-strength steels average values for the tests under steady-state and transient temperature conditions were determined.

Figure 9 shows the relative deviations between the average values of reduction factors from transient and steady-state tests of the present study (red) and of test data of mild steels (grey) and high-strength steels (blue) from literature for (a) the Young's modulus and (b) the effective yield strength.

The relative deviations between transient and steady-state tests increase in case of the high-strength steels from literature and the steel S960QL from the present study at high temperatures ≥ 500°C for both the Young's modulus (Figure 9(a)) and the effective yield strength (Figure 9(b)). However, the test method has a higher impact on the temperature-dependent development of the stiffness than on the strength, as the maximum deviation between steady-state and transient tests is about 80 % for the Young's modulus (Figure 9(c)) and about 40-50 % for the effective yield strength (Figure 9(d)) at 700°C. The degradations of the Young's modulus of high-strength steels from steady-state tests are remarkably lower compared to transient tests and in case of the yield strength there are higher temperature-dependent degradations for tests under steady-state conditions, as the deviations between reduction factors from steady-state and transient tests are positive in case of the Young's modulus and negative in case of the effective yield strength. In case of mild steels, the temperature-dependent reduction of the Young's modulus is also higher in steady state tests, but the relative deviations between steady-state and transient tests are remarkably smaller compared to high-strength materials with a maximum deviation of about 35 % at 900°C. The reduction of the effective yield strength is lower in transient tests on mild steels than in steady-state tests.

The reduction factor-temperature relationships determined from the results of tests under transient or steady-state temperature conditions overall agree well for mild steels as well as high-strength steels in the temperature range up to 500°C and the higher relative deviations at higher test temperatures result mostly from the small absolute values of the reduction factors.

*s= steady-state tests, t= transient tests
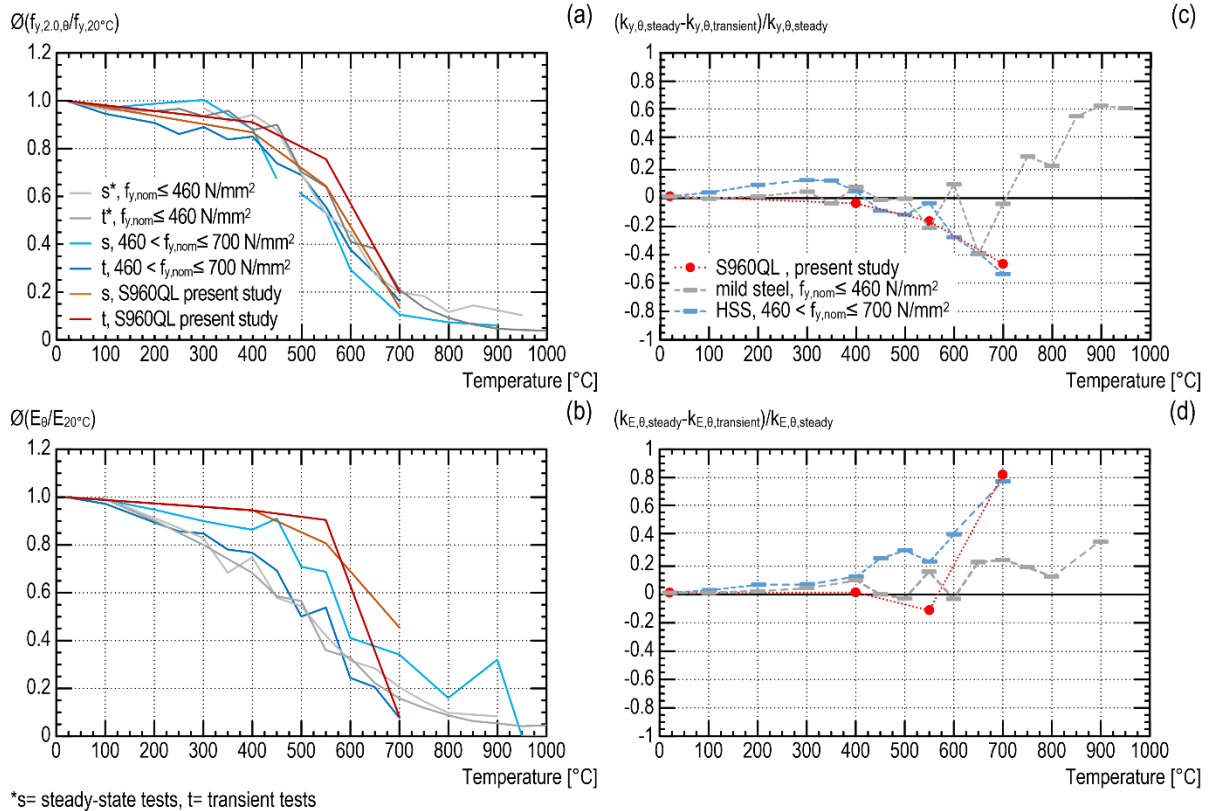
Figure 9: Average reduction factors for (a) the effective yield strength $f_{y,2.0,\theta}$ and (b) the Young's modulus E_θ from steady-state and transient tests and relative deviations between reduction factors from transient and steady-state tests for (c) the effective yield strength $f_{y,2.0,\theta}$ and (d) the Young's modulus E_θ.

5. CONCLUSIONS

The material behavior of quenched and tempered ultra-high-strength structural steel S960QL in fire has been systematically investigated within an extensive tensile test program comprising elevated temperature tests under steady-state and transient-state temperature conditions.

The test results have shown that the constitutive material behavior of the investigated structural steel at elevated temperatures is nonlinear and the strength and stiffness of the material are significantly reduced compared to ambient temperature. The comparison of results from steady-state tests with different strain rates has shown that high-temperature creep effects affect the measured material behavior above a temperature of 550°C and lead to a noticeable increase in the measured total strain at long test durations. This is supported by the results of transient tests with different heating rates. Here, slow heating rates also resulted in higher strains compared to values of tests with fast heating at the same stress levels.

The comparison of reduction factors for material properties from steady-state and transient-state tests with the reduction factors of tests on various mild and high-strength steels has proven, that the overall development of material properties of ultra-high-strength quenched and tempered steels is similar to mild steels and high-strength steels. In addition, applying the reduction factors according to EN 1993-1-2 results mostly in a conservative fire design for the investigated ultra-high-strength steel of grade S960QL. In case of the material strength, the reduction factors also provide a sufficiently accurate representation of the experimentally measured material behavior.

Further, the analysis of the differences between results from elevated temperature tests under steady-state and transient temperature conditions has shown that the test method predominantly affects the measured material behaviour at high test temperatures. However, the test results of both test methods agree well in general and the

661

combination of test results from transient-state and steady-state tests enables an accurate description of the material behavior in fire of the investigated steel of grade S960QL.

REFERENCES

[1] Faber, M. H.; Kübler, O.; Fontana, M.; Knobloch, M. (2004) *Failure Consequences and Reliability Acceptance Criteria for Exceptional Building Structures.* IBK Report No. 285, ETH Zürich.

[2] Fontana, M. (2016) *Darf eine Gesellschaft den vorbeugenden Brandschutz unter rein wirtschaftlichen Gesichtspunkten optimieren?* Der Prüfingenieur 48, S. 66-68.

[3] Lange, J.; Wohlfeil, N. (2007) *Untersuchungen zum Werkstoffverhalten des Feinkornbaustahls S 460 unter erhöhten Temperaturen.* Bautechnik 84, S. 711–720.

[4] Qiang, X.; Bijlaard, F. S. K.; Kolstein, H. (2012) *Deterioration of mechanical properties of high strength structural steel S460N under steady state fire condition.* Materials & Design 36, S. 438–442.

[5] Qiang, X.; Bijlaard, F. S. K.; Kolstein, H. (2012*) Deterioration of mechanical properties of high strength structural steel S460N under transient state fire condition.* Materials & Design 40, S. 521–527.

[6] Neuenschwander, M.; Scandella, C.; Knobloch, M.; Fontana, M. (2017) *Modeling elevated-temperature mechanical behavior of high and ultra-high strength steels in structural fire design.* Materials & Design 136, S. 81–102.

[7] Qiang, X.; Bijlaard, F. S. K.; Kolstein, H. (2012) *Dependence of mechanical properties of high strength steel S690 on elevated temperatures.* Construction and Building Materials 30, S. 73-79.

[8] Chen, J.; Young, B.; Uy, B. (2006) *Behavior of High Strength Structural Steel at Elevated Temperatures.* Journal of Structural Engineering 132, S. 1948–1954.

[9] Xiong, M.; Liew, J. R. Y. (2016) *Mechanical properties of heat-treated high tensile structural steel at elevated temperatures.* Thin-Walled Structures 98, S. 169–176.

[10] Chiew, S. P.; Zhao, M. S.; Lee, C. K. (2014) *Mechanical properties of heat-treated high strength steel under fire/post-fire conditions.* Journal of Constructional Steel Research 98, S. 12–19.

[11] Choi, I.; Chung, K.; Kim, D. (2014) *Thermal and mechanical properties of high-strength structural steel HSA800 at elevated temperatures.* Materials & Design 63, S. 544–551.

[12] Li, G.-Q. et al. (2003) *Experimental Studies on the Properties of Constructional Steel at Elevated Temperatures.* Journal of Structural Engineering, S. 1717–1721.

[13] DIN EN 1993-1-2:2010-12 (2010) Eurocode 3: Design of steel structures- Part 1-2: General rules – Structural fire design.

[14] CEN/TC250/SC3/WG2 (2021) N119: prEN 1993-1-2:2021-Eurocode 3: Design of steel structures- Part 1-2: General rules – Structural fire design.

[15] CEN/TC 250/SC 3/WG 12 (Feb. 2022) prEN 1993-1-12: Eurocode 3-Design of steel structures-Part 1-12: Additional rules for steel grades up to S960, N 126, Working draft.

[16] Qiang, X.; Jiang, X.; Bijlaard, F. S. K.; Kolstein, H. (2016) *Mechanical properties and design recommendations of very high strength steel S960 in fire.* Engineering Structures 112, S. 60–70.

[17] Qiang, X.; Bijlaard, F. S. K.; Kolstein, H. (2013) *Post-fire performance of very high strength steel S960.* Journal of Constructional Steel Research 80, S. 235–242.

[18] Knobloch, M.; Uszball, S. (2019-2021) *CoolFire - Mechanische Materialeigenschaften für die Abklingphase von Naturbrandszenarien.* AiF/DASt Forschungsvorhaben, IGF No.:20915 N.

[19] Anderberg, Y. (1988) *Modelling steel behaviour.* Fire Safety Journal 13, S. 17-26.

[20] Knobloch, M.; Pauli, J.; Fontana, M. (2013) *Influence of the strain-rate on the mechanical properties of mild carbon steel at elevated temperatures.* Materials & Design 49, S. 553-565.

[21] Outinen, J.; Mäkeläinen, P. (2004) *Mechanical properties of structural steel at elevated temperatures and after cooling down.* Fire and Materials 28, S. 237–251.

[22] Mäkeläinen, P.; Outinen, J.; Kesti, J. (1998) *Fire design model for structural steel S420M based upon transient-state tensile test results.* Journal of Constructional Steel Research 48, S. 47–57.

[23] Ranawaka, T.; Mahendran, M. (2009) *Experimental study of the mechanical properties of light gauge cold-formed steels at elevated temperatures.* Fire Safety Journal 44, S. 219–229.

[24] Schurgacz, P.; Knobloch, M. *Betongefüllte Hohlprofil-Verbundstützen für Geschossbauten – Innovation und Bemessung*, FOSTA Forschungsvorhaben P 1287/37/2017; AiF/IGF Projekt 19677 N.

663

EFFECT OF AUTOGENOUS SELF-HEALING ON HIGH TEMPERATURE EXPOSED ULTRA HIGH-PERFORMANCE CONCRETE

Niranjan Prabhu Kannikachalam[1],*; *Ahmed M. E. M.* Alhadad[2]; *Francesco* Lo Monte[3]; *Enrico Maria* Gastaldo Brac[4]; *Roberto* Rosignoli[5]; Nele De Belie[6] and *Liberato* Ferrara[7]

ABSTRACT

Mechanical properties of Ultra High-Performance Concrete (UHPC) degrade when exposed to elevated temperatures, even more than ordinary concretes due to its dense microstructure. Concerning, in particular, the special application of nuclear power plants, in which UHPC can find a promising use, concrete can be subjected to moderately high temperature (usually lower than 400 °C) along the working life, this making of interest the study on the influence and persistence of UHPC's innate self-healing capabilities over the thermal degradation. In this context, the paper focuses on an experimental study of UHPC recovery ability by autogenous self-healing after being exposed to high temperatures. The UHPC specimens have been made with hybrid fibers, that is, polypropylene and steel fibers, and have been pre-cracked up to a cumulative crack width of 0.3 mm under 4-point flexural test. The pre-cracked specimens have been exposed to a temperature of 200 °C or 400 °C, with a heating rate of 1 °C / minute from room temperature and kept at the target temperature for two hours, with a following slow cooling at a rate of <1 °C / minute. The specimens have been kept in the lab environment for 24 hours after reaching room temperature. Then they have been tested for residual flexural capacity or allowed to self-heal under water immersion for six months. The damage and healing evolution have been monitored periodically using ultra-sonic pulse velocity survey and digital microscope inspection. In spite of the thermal degradation, during the healing period UHPC showed a significant recovery in terms of strength assessed by ultrasonic pulse velocity tests.

Keywords: Self-healing; High Temperature; Ultra High-Performance Concrete; UHPC; Nuclear Power Plant.

1. INTRODUCTION

Ultra-High-Performance Concrete (UHPC) has emerged as a promising material for a variety of infrastructure applications due to its exceptional mechanical properties and durability. It is typically composed of a combination of cement, fine aggregate, silica fume, and steel fibers, which are mixed together in precise proportions to produce a dense and compact matrix. Precisely this dense and compact matrix, which sets it apart from conventional concrete, makes UHPC more susceptible to spalling when exposed to high temperatures [1]. This can threaten its

---

1,* Department of Civil and Environmental Engineering, Politecnico di Milano, Italy
and Department of Structural Engineering and Building Materials; Magnel-Vandepitte Laboratory, Ghent University, Belgium (niranjanprabhu.kannikachalam@polimi.it), **Corresponding author**.

2 Department of Civil and Environmental Engineering, Politecnico di Milano, Italy (ahmed.alhadad@mail.polimi.it).

3 Department of Civil and Environmental Engineering, Politecnico di Milano, Italy (francesco.lo@polimi.it).

4 Penetron Italia, Italy (direzione.tecnica@penetron.it).

5 Azichem, Italy (tecnologia@azichem.com).

6 Department of Structural Engineering and Building Materials; Magnel-Vandepitte Laboratory, Ghent University, Belgium (nele.debelie@ugent.be).

7 Department of Civil and Environmental Engineering, Politecnico di Milano, Italy (liberato.ferrara@polimi.it).

structural integrity and restrict its practical use in extreme environments. Spalling refers to the breaking, chipping, or flaking of concrete that occurs due to the expansion of moisture inside the material. This water vapor can build up pressure inside the UHPC, higher than in conventional concrete, and cause the surface layers of the material to break off. This often occurs when the concrete is exposed to high temperatures, such as during a fire. Spalling can result in a reduction in the concrete cover and overall cross-sectional area, which in turn can decrease the fire resistance of concrete members. The extent of spalling in a fire-exposed concrete member is determined by properties such as permeability, porosity, and tensile strength. To reduce spalling, steel and polypropylene (PP) fibers are commonly incorporated into the concrete mixture [2].

Polypropylene fibers are synthetic fibers that are added to concrete to improve its toughness, durability, and resistance to cracking. When exposed to high temperatures, polypropylene fibers can melt at 165 °C and create voids in the concrete, which can relieve the internal stresses and prevent the material from undergoing further damage. Several studies have demonstrated the advantages of using polypropylene fibers in UHPC exposed to high temperatures. For instance, Du et. al.[3] found that adding 0.15% by volume of polypropylene fibers prevented explosive spalling in a 115-135 MPa concrete. Xu et. al.[4] conducted tests on a UHPC with a hybrid fibers, steel and polypropylene fibers, where granulated steel slags were used as aggregates to enhance the thermal performance. This UHPC maintained around 60% of its initial compressive strength even after being exposed to a temperature of 800 °C.

However, despite its many advantages, UHPC requires extensive repair or complete demolition of the structures post-fire. To address this issue, researchers have been exploring different approaches to enhance the performance of UHPC after high-temperature exposure. In recent years, there has been growing interest in a promising approach to enhance the durability of concrete, which involves the development of self-healing concrete. The term "self-healing" refers to the capacity of a substance to heal itself using its innate chemical and physical characteristics or through autonomous self-healing methods such as micro/macro capsules, vascular network, or bacteria-based techniques, without requiring any external intervention [5]–[7]. Numerous studies demonstrated the autonomous self-healing potential of UHPC under extreme scenarios [8]–[13]. The chemical process of autogenous self-healing is primarily driven by three mechanisms: the hydration of unreacted cement particles, pozzolanic/latent hydraulic activity of supplementary cementitious materials, and the diffusion of calcium and silicates leading to the precipitation of calcium carbonate [5]. During post-fire curing, 30-50% [14] of UHPC's unhydrated cement particles, along with the anhydrous C_2S [15]–[17] resulting from high-temperature exposure, are expected to hydrate and help restore the mechanical and durability properties of the material. However, unlike conventional concrete, there have been relatively few studies on post-fire curing of UHPC. In conventional concrete, post-fire-curing has been found to enable the healing of the mechanical properties and pore structure of the damaged concrete. This recovery process involves the rehydration of dehydrated components that were exposed to high temperatures, allowing the resulting products to fill cracks and repair the microstructure of the cement matrix. Although the porosity can return to pre-fire levels, the rehydration products have been observed to be less dense and compact than the original structure, resulting in an inability to restore the mechanical properties and durability to their pre-fire levels [18]. The current study aims to investigate the post-fire curing/autogenous self-healing potential of thermally damaged UHPC specimens using a novel spalling-resistant UHPC containing a blend of steel fiber and polypropylene fiber.

2. MATERIALS AND METHODS

This study has focused on a UHPC, which incorporated steel and polypropylene fibers to prevent explosive spalling under high temperatures. The necessary material for the experiment, consisting of six slabs measuring 500 x 500 x 30 mm^3 each, was provided by Azichem under the patented name Rinfor Grout Col ®. After 28 days of lab curing at 20±2 °C and ≥95% relative humidity, each slab was cut into thin beams of 500 x 100 x 30 mm^3. The mix composition is listed in Table 1.

Four-point flexural tests were conducted to characterize the one-month-old specimens' mechanical performance. The specimens were mounted on supports with a span length of 450 mm and a distance of 150 mm between the point loads and their supports, as shown in Figure 1. The load was applied under position control at a rate of 15 μm/s using an Instron machine, while the cumulative displacement was measured by LVDTs attached to the specimen's tension fiber on both sides, covering the middle 150 mm where the maximum/constant bending moment

occurs and leading to the appearance of multiple cracking. A total of 30 specimens were used for the study. Out of these, five were utilized as reference specimens to characterize the flexural strength and were denoted as REF.

Table 1: Mix composition of the investigated Rinfor Grout Col ® UHPC

Constituent	Dosage (kg/m^3)
Cement (CEM I + CEM II)	700
Siliceous sand 0-5 mm	1210
Microsilica and reactive filler	130
Polypropylene fibers (l_f = 6 mm)	0.6
Steel fibers (l_f = 20 mm)	100
Superplasticizer	30
Crystalline admixture Penetron Admix ®	0.9% by weight of cement
Water/cement ratio	0.29
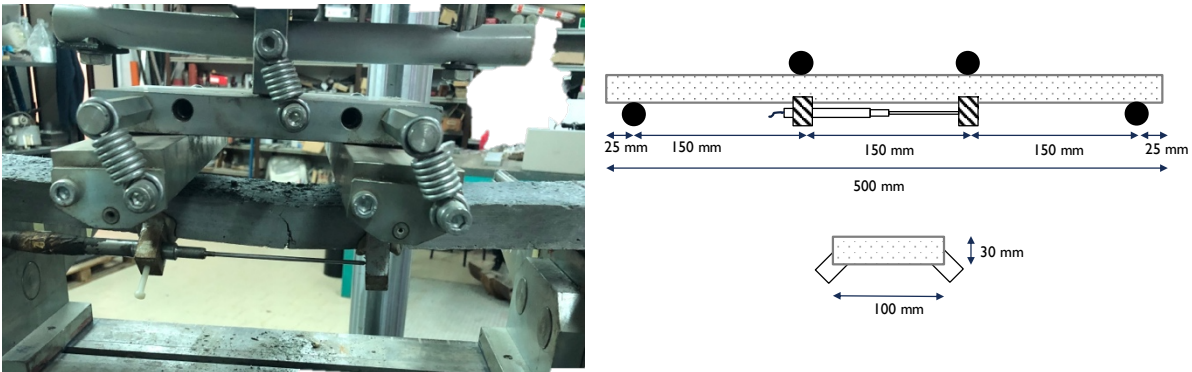
Figure 1: Four-point bending setup.

Two temperature exposures were examined, 200 °C and 400 °C, as at higher temperatures concrete structures will require extensive restoration work. To ensure safety measures against explosive spalling, three specimens at a time were exposed to the target temperature by placing them in the oven encased into two steel cages (Figure 2a) to protect the oven interior walls from eventual explosive spalling. One cage contained two specimens, and the other contained one specimen. The temperature of the furnace was regulated by thermocouples located on the top two corners. An additional thermocouple was placed between the specimens, with the tip of the thermocouple touching the surface of a specimen to measure its temperature, as also shown in Figure 2a. An auxiliary thermocouple was placed on the surface of the furnace. The temperature was raised by 1 °C per minute until it reached the target temperature, and then it was held constant for two hours. Afterwards, the temperature was slowly reduced at a rate of less than 1 °C per minute until it reached 100 °C, as shown in Figure 2b. Finally, the furnace was opened completely to bring the specimen temperature down to room temperature.

The specimens utilized for high-temperature mechanical property testing are shown in Table 2. For each exposure temperature of 200 °C and 400 °C, three uncracked specimens were tested for residual flexural stress after 24 hours and were labelled as T200 and T400, respectively. Fifteen specimens were pre-cracked to a cumulative crack opening displacement (COD) of 0.3 mm, out of which three specimens were allowed to heal for six months in tap water under submerged conditions without any temperature exposure and were denoted as REF″. Six pre-cracked specimens were exposed to 200 °C, out of which three specimens were tested for residual flexural strength after 24 hours from the exposure and were labelled as T200′. The remaining three specimens were allowed to heal in submerged conditions for six months and were labelled T200″. Similarly, another six pre-cracked specimens were exposed to 400 °C. Three specimens were tested for residual flexural strength and were designated as T400′. The remaining three specimens were allowed to self-heal and were designated as T400″. Two specimens were kept in the lab environment for six months to evaluate the gain in flexural strength due to long-term hydration (REF-6mo.). The remaining two specimens were used for the preliminary work to set the experimental campaign.
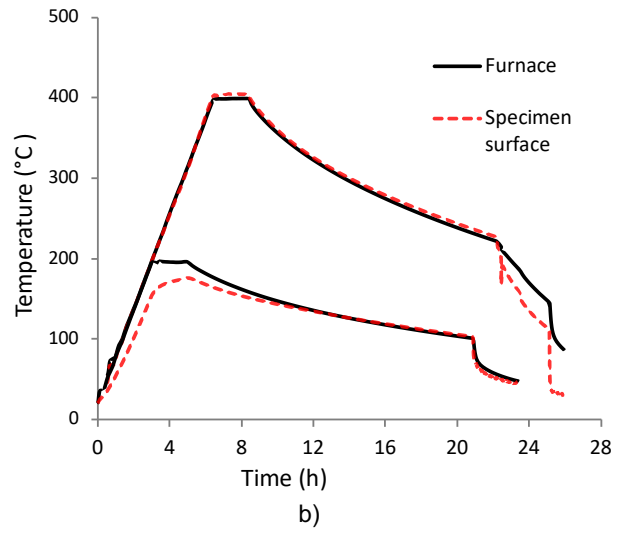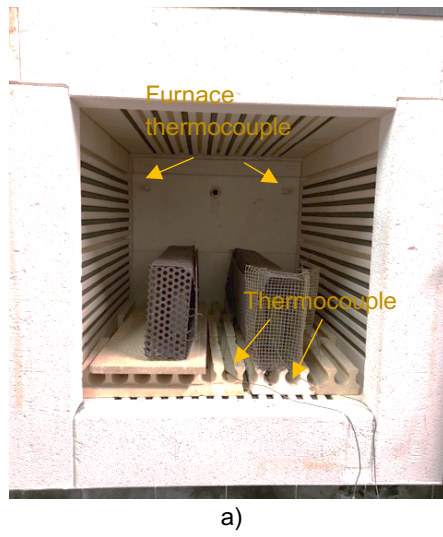
Figure 2: Furnace and heating profile

Table 2: Specimens utilized for high-temperature mechanical property tests

Series	Specimens	Specimen condition	High-temperature exposure	After exposure
REF	5	Uncracked	-	Flexural test
REF″	3	Pre-cracked	-	Self-healing
REF-6mo.	2	Uncracked	-	Flexural test after 6 months
T200	3	Uncracked	200 °C	Flexural test
T200′	3	Pre-cracked	200 °C	Flexural test
T200″	3	Pre-cracked	200 °C	Self-healing
T400	3	Uncracked	400 °C	Flexural test
T400′	3	Pre-cracked	400 °C	Flexural test
T400″	3	Pre-cracked	400 °C	Self-healing

To monitor the degradation and recovery of UHPC, ultrasonic pulse velocity testing (UPV) and microscopic imaging of surface cracks were employed. UPV measurements were taken at various stages, including uncracked, pre-cracked, after thermal exposure, and during the healing stage at 1, 2, 3, and 6 months. UPV readings were taken after cooling the thermally exposed specimens at room temperature for 24 hours. During the healing stage, the specimens were dried in the lab environment for three days before taking the UPV readings. Microscopic images were captured at the same location after pre-cracking and thermal exposure and after the 1, 2, 3, and 6-month healing stages.

3. Results and discussion

3.1 Four-point flexural test

After the specimens were exposed to 200 °C and 400 °C, the uncracked specimens (T200 and T400) and pre-cracked specimens (T200′ and T400′) were tested to failure by four-point flexural test after 24 hours during which they were kept at room temperature. Figure 3 shows nominal flexural stress vs COD curves for reference and pre-cracked specimens and for specimens tested for residual flexural stress after the exposure. The damage index was evaluated using the equation (1).

$$\text{Damage index from the flexural stress} = \frac{f_{REF} - f_T}{f_{REF}} \times 100 \qquad (1)$$

where, f_{REF} is the average peak flexural strength of the tested reference specimens (REF) and f_T is the flexural strength of thermally exposed specimens.

667
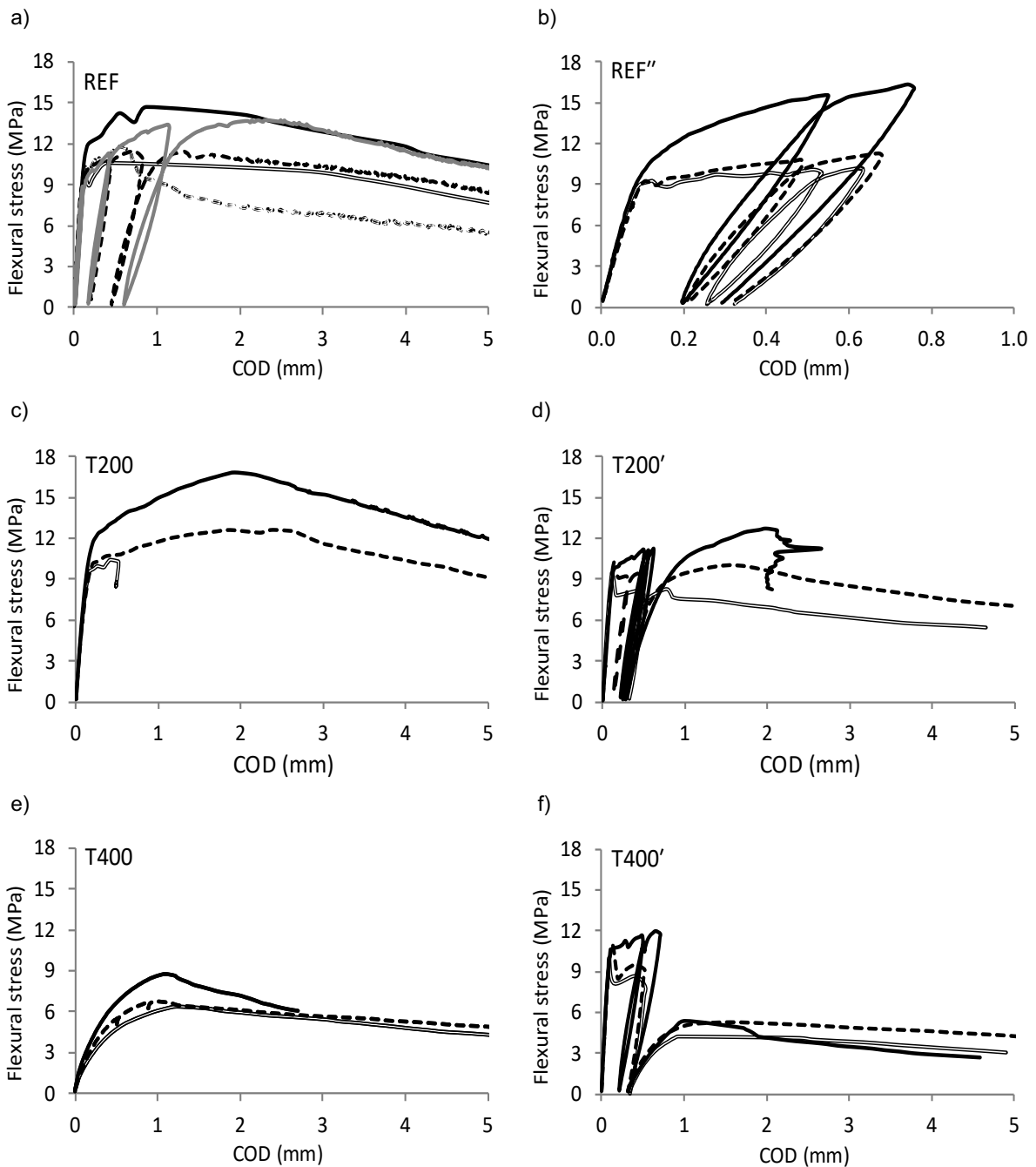
Figure 3: Flexural stress vs COD, a) reference, b) pre-cracked, c) uncracked specimens exposed at 200 °C, d) pre-cracked specimens exposed at 200 °C, e) uncracked specimens exposed at 400 °C, f) pre-cracked specimens exposed at 400 °C. Results of three replicates are presented.

The average flexural strength of the mix (REF) was about 12.5 MPa, as shown in Figure 4, and the uncracked specimens, T200, showed the material did not lose any of its strength after being exposed to 200 °C. However, the pre-cracked specimens, T200′ showed a significant decrease in the flexural strength of about 17%; this could be because the fibers bridging the multiple cracks were exposed directly to the atmosphere and high-temperature results in oxidation of the bridging steel fibers. It has also been noted that there weren't any additional visible cracks after being exposed to 200 °C. The uncracked specimens, T400, exposed to 400 °C showed a significant decrease in the flexural strength, equal to about 40%. Other studies also showed UHPC material tends to deteriorate around 40% of its strength when exposed to 400 °C [1].

Series	No. of Specimens	Flexural stress (MPa)
REF	5	12.5 ±1.7
REF″	3	Ongoing
REF-6mo.	2	Ongoing
T200	3	13.3 ±3.3
T200′	3	10.3 ±2.2
T200″	3	Ongoing
T400	3	7.3 ±1.3
T400′	3	5 ±0.6
T400″	3	Ongoing

′ → pre-crack

″ → pre-crack + self-healing
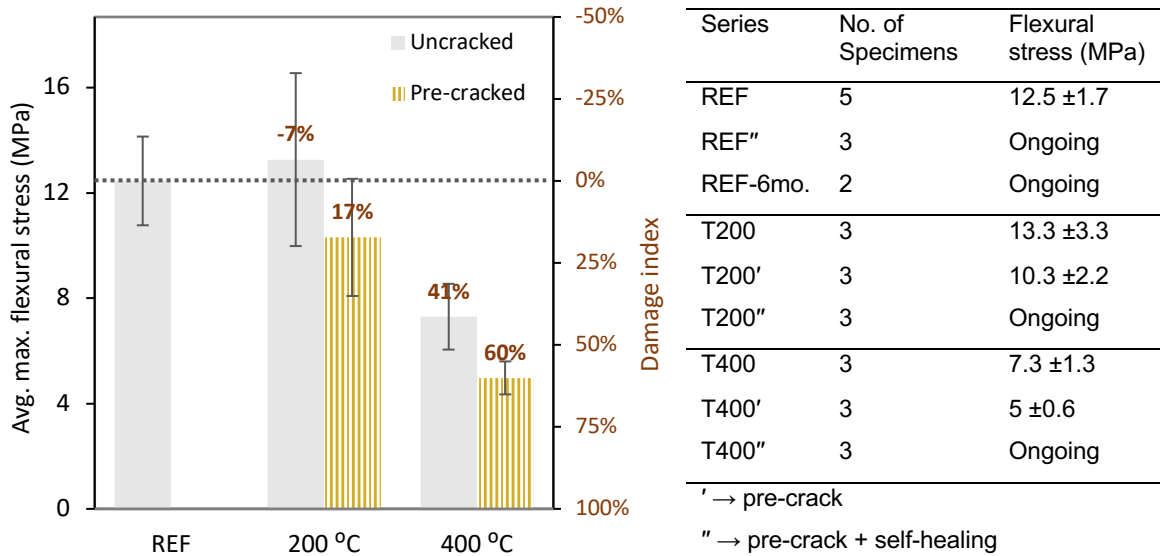
Figure 4: Average maximum flexural stress and their damage index

The nominal flexural stress vs COD curves were used to measure the stiffness of the UHPC, which is demonstrated in Figure 5. The stiffness of the reference specimens and of the uncracked specimens T200 and T400 was measured from the loading curve (Figure 5a) As for the pre-cracked specimens, two stiffnesses were measured. The first one is the unloading stiffness ($K_{unloading}$), measured from the unloading curve at the desired crack width, which was approximately 0.3 mm. The second one is the reloading stiffness ($K_{reloading}$) which was measured from the reloading curve of the flexural test after thermal exposure (Figure 5b). The slope line for reloading stiffness was drawn from the starting point of reloading to just before the reloading curve started to show the sign of displacement hardening.
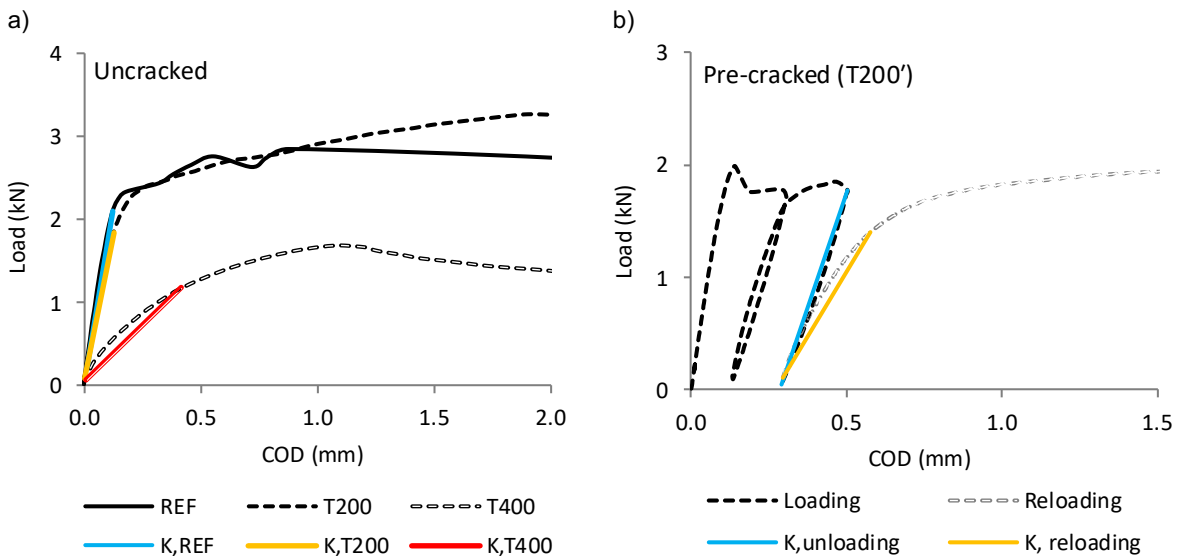
Figure 5: Evaluation of loading stiffness (a), and unloading and reloading stiffness for T200' (b)

The reference specimens, denoted as REF, had a stiffness (K_{REF}) of approximately 17 kN/mm, whereas the stiffness values for T200 and T400 were around 13.6 and 2.4 kN/mm, respectively, (Figure 6a). Using the equation (2), the damage index DI_{SU} was determined from the stiffness measurements of the uncracked specimens. Where, K_T is the stiffness of T200 or T400. The T200 specimen had a damage index of about 20%, but its flexural stress did not indicate any decrease in strength. On the other hand, the T400 specimen showed a damage index of about 86% (Figure 6b), with the reduction in flexural capacity being nearly half of this value. Using the equation (3), the damage index DI_{SP} was determined from the stiffness measurements of the pre-cracked specimens. T200′ lost around 45%

of its stiffness after the exposure compared to the unloading stiffness, while T400′ lost around 80% of its stiffness. In both cases, flexural strength, and stiffness, T200′ showed higher degree of damage than T200. While T400 and T400′ showed damage indices for stiffness that were quite close; it could be that the deterioration in stiffness of the material reached the saturation point.

$$DI_{SU} = \frac{K_{REF} - K_T}{K_{REF}} \times 100 \tag{2}$$

$$DI_{SP} = \frac{K_{unloading} - K_{reloading}}{K_{unloading}} \times 100 \tag{3}$$
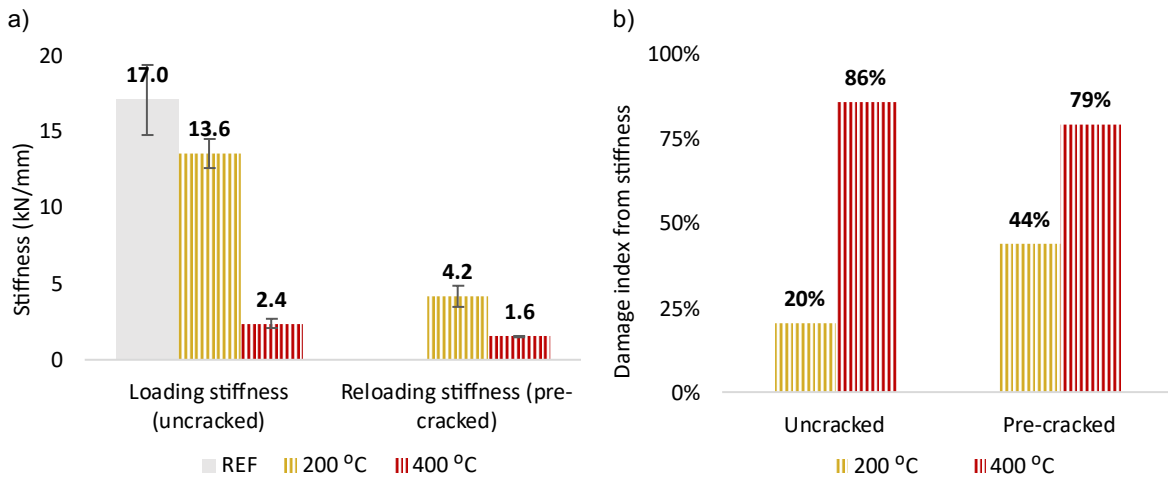
Figure 6: Stiffness of the specimens (a) and damage index (b)

3.2 Non-destructive tests

To assess the degradation caused by thermal exposure and the recovery of mechanical and durability properties, both ultrasonic pulse velocity (UPV) test and microscopic image were utilized. UPV measurements were conducted at various stages, including the uncracked stage, after pre-cracking, after thermal exposure, and at 1, 2, 3, and 6 months of healing. Indirect UPV measurements were taken at the mid-section of the specimens by placing the transmitter and receiver 150 mm apart. The damage index for UPV was computed using equation (4), and Figure 7 shows the damage index for all specimen groups. The pre-cracked reference specimens (REF″) had a damage index of approximately 16%, whereas the T200 had a damage index of 5%, indicating that this particular mixture is resilient to 200 °C. However, it appears that this resilience only applies to uncracked specimens, as T200' and T200″ exhibited a total damage index of roughly 11% and 21%, respectively; their average value was similar to the reduction in flexural strength of T200'. The total damage index of T400, T400' and T400″ was about 43%, 47% and 49%, respectively. The specimens REF″, T200″, and T400″ underwent a healing process of up to 6 months, and the Figure 8 illustrates the UPV values for the initial three months. It indicates that the damage resulting from mechanical and/or thermal exposure was restored during the first month of healing. The UPV values have a correlation with the recuperation of strength and durability. Therefore, the flexural test, which is set to be conducted at the conclusion of six months, is expected to show recovery of most of the strength that was lost due to mechanical and thermal damages.

$$\text{Damage index from UPV} = \frac{UPV_{uncracked} - UPV_t}{UPV_{uncracked}} \times 100 \tag{4}$$

where the subscript t refers to the time of mechanical or thermal damage at which the UPV has been taken.

The Figure 9 showcases the microscopic image of REF", T200", and T400" specimens following pre-cracking, at one-month healing/after thermal exposure, and at the end of three months healing. The initial crack size in the specimens ranged from a few micrometers to 100 μm. The reference specimen exhibited nearly complete closure of the crack after three months of healing while submerged in tap water. However, the specimens exposed to 200 °C and 400 °C experienced an increase in crack width of up to 50% and beyond 100%, respectively, and at the end of three months, the surface crack width was partially closed. In addition to the increase in crack width, new microcracks appeared on the concrete surfaces following exposure to high temperatures, and it was observed that the specimens exposed to 400 °C had significantly more microcracks than those exposed to 200 °C.
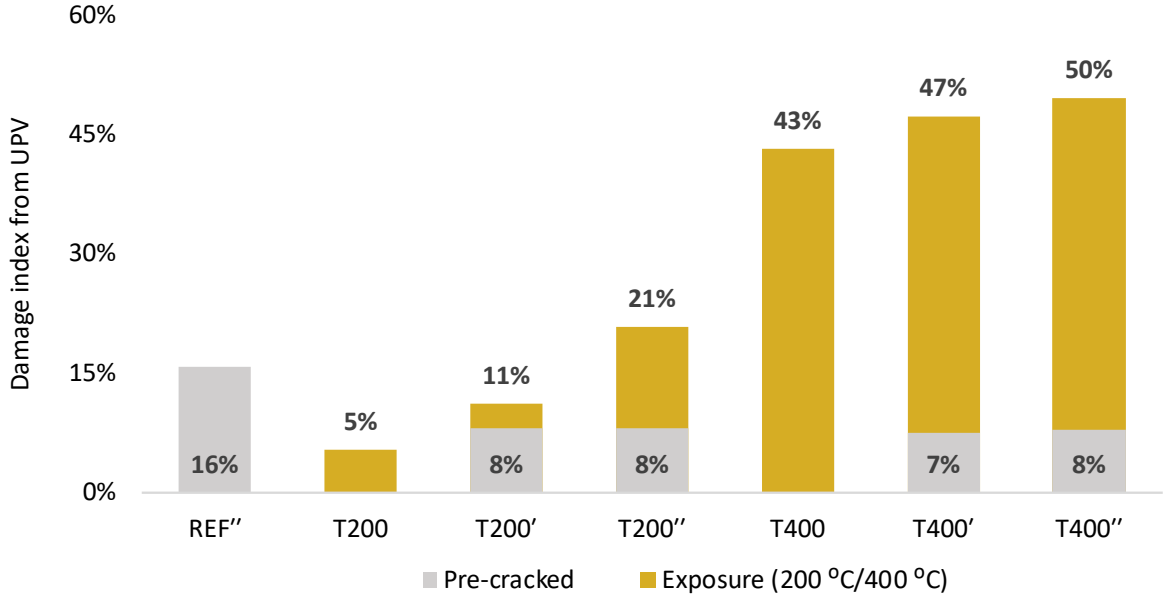
Figure 7: Damage index from UPV measurements
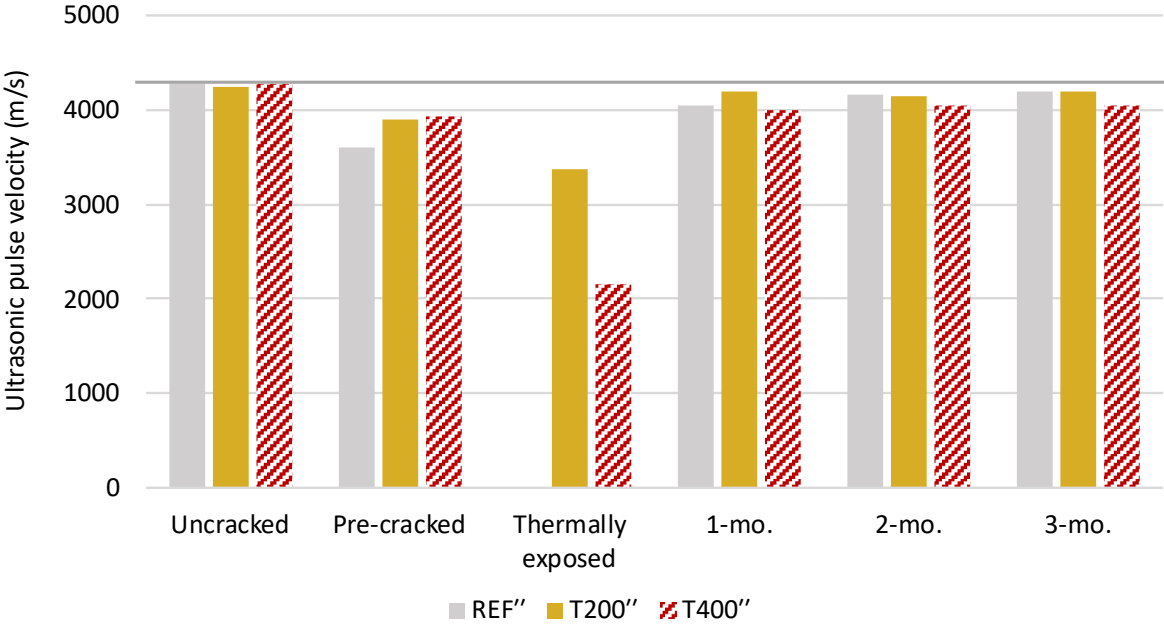
Figure 8: Ultrasonic pulse velocity measurement results

671

REF″ pre-cracked.	REF″ 1-month	REF″ 3-months
T200″ pre-cracked.	T200″ thermally exposed.	T200″ 3-months
T400″ pre-cracked.	T400″ thermally exposed.	T400″ 3-months
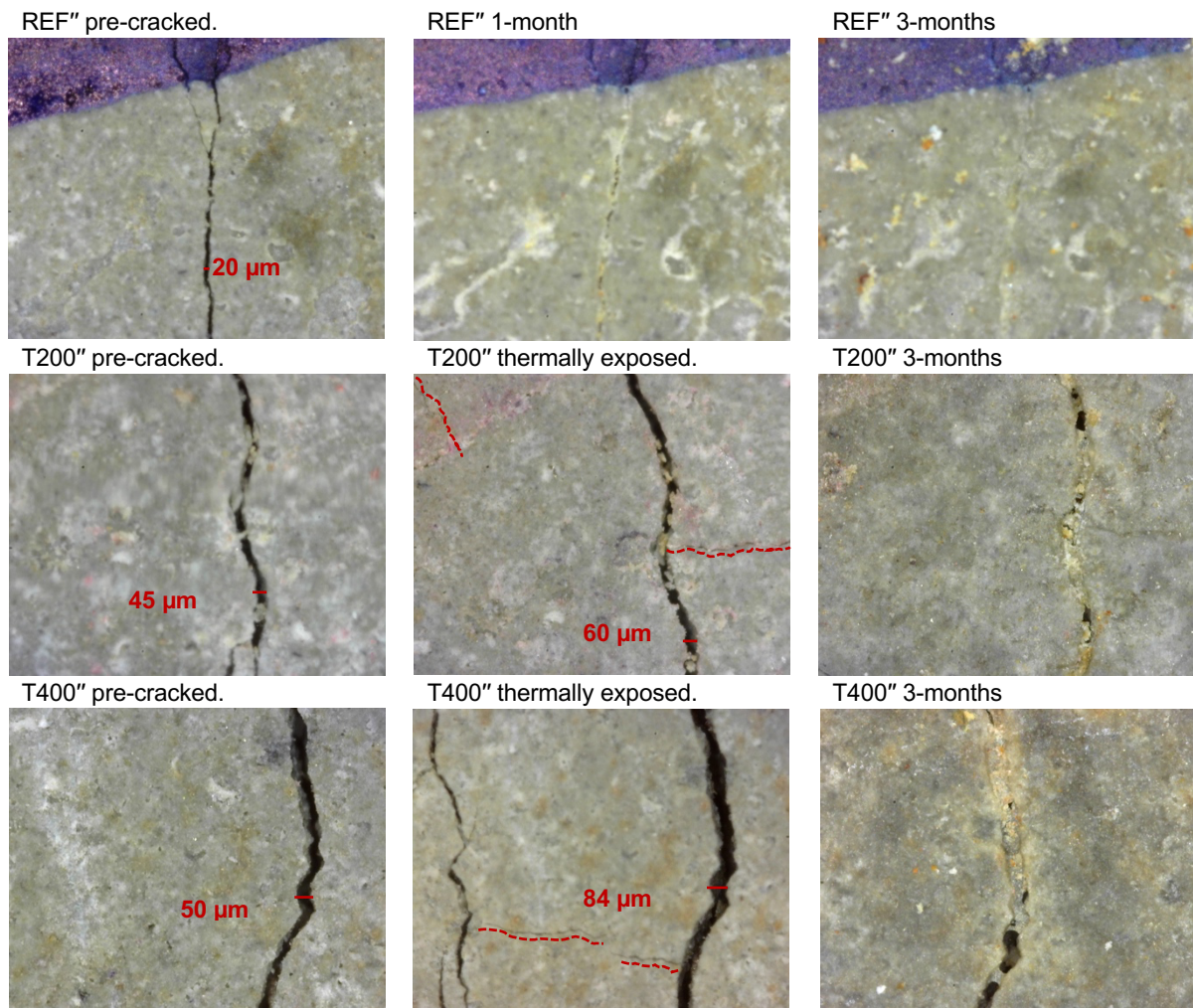
Figure 9: Microscopic images of REF″, T200″ and T400″

4. CONCLUSIONS

This research study aimed to explore the persistence of autogenous self-healing potential of UHPC specimens that were thermally damaged and the possibility of exploiting this for damage recovery through post curing, utilizing a novel fire-resistant UHPC material incorporating a combination of steel fiber and polypropylene fiber.

The preliminary findings of this study can be summarized as follows:

- For the uncracked specimens exposed to 400 °C, the damage index for flexural strength was 41%, and for pre-cracked specimens, it was 60%. The uncracked specimens exposed to 200 °C did not exhibit any reduction in flexural strength, while the pre-cracked specimens lost 17% in strength. Higher damage in pre-cracked specimens could be due to the oxidation of the fibers bridging the cracks.
- The damage index for UPV in uncracked specimens exposed to 400 °C was 43%, and for pre-cracked specimens (T400′), it was 47%. In contrast, the damage index for uncracked specimens exposed to 200 °C was only 5%, which was much lower than the damage resulting from pre-cracking induced mechanical loading, with a damage index of 16% for reference specimens (REF″). Additionally, pre-cracked specimens (T200′) exposed to 200 °C experienced an 11% loss in ultrasonic pulse velocity. However, the specimens that were allowed to heal showed that the majority of the damage was healed within one month.
- The crack width for the specimens ranged from a few micrometers to 100 μm following pre-cracking. The specimens exposed to 200 °C and 400 °C experienced an increase in crack width immediately after the thermal exposure. However, at the end of three months healing, the surface crack width was partially closed.

672

5. ACKNOWLEDGEMENTS

6. REFERENCES

[1]   Banerji, S.; Kodur, V., *Effect of temperature on mechanical properties of ultra-high performance concrete*, Fire Mater., vol. 46, no. 1, pp. 287–301, Jan. 2022, doi: 10.1002/FAM.2979.

[2]   Varona, F. B.; Baeza, F. J.; Bru, D.; Ivorra, S., *Influence of high temperature on the mechanical properties of hybrid fibre reinforced normal and high strength concrete*, Constr. Build. Mater., vol. 159, pp. 73–82, Jan. 2018, doi: 10.1016/J.CONBUILDMAT.2017.10.129.

[3]   Du, Y.; Qi, H. H.; Huang, S. S.; Richard Liew, J. Y., *Experimental study on the spalling behaviour of ultra-high strength concrete in fire*, Constr. Build. Mater., vol. 258, p. 120334, Oct. 2020.

[4]   Xu, Z.; Li, J.; Wu, P.; Wu, C., *Experimental investigation of triaxial strength of ultra-high performance concrete after exposure to elevated temperature*, Constr. Build. Mater., vol. 295, p. 123689, Aug. 2021.

[5]   De Belie, N. *et al.*, *A Review of Self-Healing Concrete for Damage Management of Structures*, Adv. Mater. Interfaces, vol. 5, no. 17, pp. 1–28, 2018, doi: 10.1002/admi.201800074.

[6]   Ferrara, L. *et al.*, *Experimental characterization of the self-healing capacity of cement based materials and its effects on the material performance: A state of the art report by COST Action SARCOS WG2*, Constr. Build. Mater., vol. 167, pp. 115–142, 2018, doi: 10.1016/j.conbuildmat.2018.01.143.

[7]   Cappellesso, V. *et al.*, *A review of the efficiency of self-healing concrete technologies for durable and sustainable concrete under realistic conditions*, Int. Mater. Rev., 2023, doi: 10.1080/09506608.2022.2145747.

[8]   Kannikachalam, N. P.; Asensio, E. C.; Brac, E. M. G.; Rosignoli, R.; De Belie, N.; Ferrara, L., *An experimental methodology to assess effects of healing on freeze-thaw damaged ultra high-performance concrete*, in *6th fib International Congress on Concrete Innovation for Sustainability*, 2022, pp. 280–287.

[9]   Kannikachalam, N. P.; Clerque Vela, D. A.; Ocampo Pacheco, Y. G.; Lo Monte, F.; de Belie, N.; Ferrara, L., *Fatigue behavior and effect of stimulated autogenous self-healing in Ultra High-Performance Concrete*, in *14th fib PhD Symposium in Civil Engineering*, Sep. 2022, vol. 7, no. 1, pp. 297–304. doi: 10.2/JQUERY.MIN.JS.

[10]   Kannikachalam, N. P. *et al.*, *Assessment of Sustainability and Self-Healing Performances of Recycled Ultra-High-Performance Concrete*, ACI Mater. J., vol. 120, pp. 117–132, 2023, doi: 10.14359/51737336.

[11]   Kannikachalam, N. P.; Marin Peralta, P. S.; Snoeck, D.; De Belie, N.; Ferrara, L., *Effects of stimulated autogenous self-healing of Ultra High-Performance Concrete slabs under repeated impact loading*, Cem. Concr. Compos., 2023.

[12]   Al-Obaidi, S. *et al.*, *Structural validation of geothermal water basins constructed with durability enhanced ultra high performance fiber reinforced concrete (Ultra High Durability Concrete)*, Case Stud. Constr. Mater., vol. 17, p. e01202, Dec. 2022, doi: 10.1016/J.CSCM.2022.E01202.

[13]   Davolio, M.; Al-Obaidi, S.; Altomare, M. Y.; Lo Monte, F.; Ferrara, L., *A methodology to assess the evolution of mechanical performance of UHPC as affected by autogenous healing under sustained loadings and aggressive exposure conditions*, Cem. Concr. Compos., vol. 139, p. 105058, May 2023.

[14]   Wu, X.; Yaoling Luo, #; Yang, W.; Gao, Y.; Bi, Y.; Xie, Y., *EFFECT OF REHYDRATION OF UNHYDRATED CEMENT ON ULTRA-HIGH PERFORMANCE CONCRETE AFTER HEAT CURING*, Ceramics-Silikáty, vol. 65, no. 3, pp. 305–315, 2021, doi: 10.13168/cs.2021.0032.

[15]   Piasta, J.; Sawicz, Z.; Rudzinski, L., *Changes in the structure of hardened cement paste due to high temperature*, Matériaux Constr., vol. 17, no. 4, pp. 291–296, Jul. 1984.

[16]   Alonso, C.; Fernandez, L., *Dehydration and rehydration processes of cement paste exposed to high temperature environments*.

[17]   Castellote, M.; Alonso, C.; Andrade, C.; Turrillas, X.; Campo, J., *Composition and microstructural changes of cement pastes upon heating, as studied by neutron diffraction*, Cem. Concr. Res., vol. 34, no. 9, pp. 1633–1644, Sep. 2004, doi: 10.1016/S0008-8846(03)00229-1.

[18]   Li, L. *et al.*, *A review on the recovery of fire-damaged concrete with post-fire-curing*, Constr. Build. Mater., vol. 237, p. 117564, Mar. 2020, doi: 10.1016/J.CONBUILDMAT.2019.117564.

INFLUENCE OF THE COMPRESSIVE STRENGTH IN THE OCCURRENCE OF SPALLING IN HIGH RESISTANCE CONCRETES SUBJECTED TO HIGH TEMPERATURES

photo
Author 1

30 mm
×
40 mm
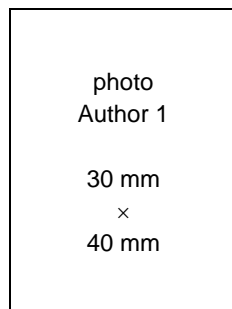
Paulo I. B. Perin a

Ângela G. Graeff b,*

ABSTRACT

This paper presents the results from an experimental program about the influence of concrete compressive strength in the occurrence of explosive spalling and residual compressive strength. Results of compressive strength, ultrasonic pulse velocity and mass loss were obtained for concrete specimens of three different initial strengths (50, 80 and 100 MPa), cured by two different methods, exposed to room temperature, 300°C and 600°C. The main results indicated that 100 MPa test specimens are more susceptible to explosive spalling failure, as opposed to 50 MPa. Moist-cured test specimens are significantly more affected by explosive spalling then the air-cured specimens. Results also showed that the test specimens with compressive strength of about 80 MPa presents the best results in terms of strength loss and UPV results.

Keywords: High resistance concrete; High temperatures; Compressive strength; Spalling; Fire.

1. INTRODUCTION

The development of improved dosage techniques, together with the development of the materials technology, made the use of High Resistance Concrete (HRC) more economic and more accessible, especially when higher resistance is required (especially for the elements subjected to compressive loads such as columns). In comparison with conventional concrete (CC), HRC presents many advantages, such as: improved durability and abrasion resistance and reduced permeability and deformability [1, 2 e 3]. However, considering the behaviour when subjected to high temperatures, HRC have shown a considerable disadvantage when compared to CC [5], especially because it is more susceptible to explosive spalling. This phenomenon is characterised by sudden

ᵃ Federal University of Rio Grande do Sul (paulo.iuri@hotmail.com)**.**

ᵇ,* Federal University of Rio Grande do Sul, Av. Bento Gonçalves, 9500 – Setor 4, Laboratório LEME, Porto Alegre/RS, Brazil (angela.graeff@ufrgs.br)**,** Corresponding author.

detachments of concrete pieces, exposing the reinforcement bars directly to fire, which may lead to differential deformations between the steel and the surrounding concrete, leading to bond loss between concrete and steel, with potential damages to the structure [4, 5, 6 e 7].

Two main hypotheses are used to explain spalling occurrence: first, due to water evaporation from the concrete pores, and consequently vapour confinement for low permeable concretes, pore pressures are originated inside the pores, which develop transversal tension stresses that can be as high as 8 MPa and are in general higher than the tensile strength of concrete [6]. Second, also for the fact that concrete has low thermal conductivity, when it is exposed to heat in the external faces, an intense thermal gradient occurs towards its interior, generating restrained strains of thermal origin, which develop compression stresses parallel to the exposed face [7]. Spalling is, notoriously, a complex phenomenon and difficult to predict, as it is dependant of many factors, such as: the internal humidity of concrete, porosity, load conditions, aggregate type, cross sectional [4] and heat rate [6].

This work aims to determine the influence of initial compressive strength and curing conditions on the occurrence of spalling and on the residual compressive strength when subjected to high temperatures, taking into account only high resistance concretes.

2. RESEARCH METHOD

An experimental program was developed to identify the influence of the compressive strength on the explosive spalling for three different classes of HRC, aiming to identify if spalling could be reduced (due to the higher strength to resist the tensile stresses caused by vapour confinement) or influenced as the compressive strength increases. Three different concrete mixes were used in the study (named as M1, M2 and M3), based on the work developed by [8]. The target average compressive strength for the three mixes were 50 MPa, 70 MPa and 100 MPa. The other research variables included two curing conditions (one in ambient laboratory conditions – air-cured specimens - and the other in fully saturated condition – water-cured specimens -, both for 56 days) and two exposure temperatures (300ºC and 600ºC), aiming to simulate temperatures that may occur during a fire. Table 1 shows a compilation of the research variables adopted in this study.

Table 1: Research variables of the study

Concrete average compressive strength	Curing condition	Temperature
50 MPa	Ambient laboratory conditions	300 ºC
70 MPa	Fully saturated	600 ºC
100 MPa	-	-

2.1 Materials

The materials used to cast specimens were the ones as follow: Portland High Initial Strength cement; TEC-FLOW 8000 superplasticiser; basalt coarse aggregate with specific mass of 2.9 g/cm³, maximum diameter of 38 mm and fineness modulus of 7.06; gravel with specific mass of 2.63 g/cm³, maximum diameter of 2.4 mm and fineness modulus of 2.14; and non-densified silica fume, produced by ELKEM. The gradation results for both aggregates are shown in Tables 2 and 3, respectively.

Table 2: Coarse aggregate gradation results

Mesh (mm)	% retained	% total retained
38	0	0
19	7.41	7.41
9.5	91.28	98.69
4.8	13.31	100
< 4.8	0	100

Mesh (mm)	% retained	% total retained
2.4	4.51	4.51
1.2	13.72	18.22
0.6	4.47	22.69
0.3	54.43	77.11
0.15	14.42	91.53
< 0.15	8.47	100

2.2 Mix proportions and casting of specimens

The three mixes M1, M2 and M3 were cast with the same materials. Silica fume was used as a binder addition aiming to obtain the desired high compressive strengths. The slump test was carried out according to the Brazilian Standard NBR NM 67 [9]. Superplasticizer was needed to allow good workability for the concretes, especially because of the low water/binder ratios used to obtain the target strengths. The amount of each material used to produce the three mixes proportions, for each cubic meter of concrete, the water/binder (w/b) ratios and the slump measured for each mix are shown in Table 4. The mixes were based on the work developed by [8]. The 50 MPa mix, named as M1 in this study, was adjusted in order to get a strength closer to the one aimed in this study.

Table 4: Amount of material, target average compressive strength, slump test and w/b ratios for each mix proportion.

Mix Proportion	M1	M2	M3
Target average compressive strength (MPa)	50	70	100
Water/binder ratio	0.44	0.26	0.19
Slump test (mm)	85	90	180
Cement (kg/m³)	484.9	487.4	587.8
Silica fume (kg/m³)	38.6	42.3	46.6
Fine aggregate (kg/m³)	760.7	662.0	613.4
Coarse aggregate (kg/m³)	1221.2	1191.7	1165.1
Superplasticizer (kg/m³)	-	3.0	8.9
Water (kg/m³)	230.2	135.9	120.0

2.3 Exposure to high temperatures

Aiming to create a favourable situation for spalling, specimens were exposed to a constant heating rate of 27.4ºC/min, which gives initial values close to the ISO 834 standard heating curve. An electric furnace was used to heat the specimens up. In total, four heating procedures were performed, each one with 9 specimens: the first with specimens cured in air, subjected to 300 ºC; the second with the same temperature, but with specimens cured in water; the third with specimens cured in air subjected to 600 ºC, and the last with specimens cured in water subjected to 600 ºC.

Specimens were placed randomly inside the furnace, and a special attention was given so they were not too close to the furnace resistances. After reaching the target temperatures, the specimens were maintained inside the furnace within the maximum temperature (300ºC or 600ºC) for 120 minutes aiming to uniformly distribute the temperature throughout the specimens. After this period the furnace was turned off and the door open for the specimens to cool down until the next day, when the tests were performed.

2.4 Visual evaluation of spalling

Cylinder specimens measuring 20 cm in height and 10 cm in diameter were used to perform the visual analysis in terms of spalling occurrence, cracking and any other damage that may had occurred with the specimens after being exposed to high temperatures. The specimens had their mass recorded before and after exposure to high temperatures as another way to quantify (even if empirically) spalling. Compressive strength and ultrasonic pulse velocity (UPV) were also performed after exposure to high temperatures for the specimens that were not affected

or destroyed by spalling. As for comparison in terms of compressive strength and UPV, extra specimens were cast and tested in ambient temperature. Eighteen specimens were cast for each mix, leading to a total of 54 specimens.

2.5 Compressive strength

The compressive strength was measured using a SHIMADZU equipment with 2000 kN of capacity. The loading speed used was 0.45 MPa/s, following the procedures of Brazilian Standard NBR 5739 [10].

2.6 Ultrasonic pulse velocity

The ultrasonic pulse velocity tests were performed according to the Brazilian Standard NBR 8802 [11], by the direct method, using a PUNDIT (Portable Ultrasonic Nondestructive Digital Indicating Tester) equipment, with a 0,1 µs resolution. The measurements were made before the compressive strength tests, for both reference specimens and the ones subjected to high temperatures.

2.7 Mass measurement

The mass measurements were made before subjecting the specimens to high temperatures and at the day after exposing them, immediately before the UPV and compressive strength tests, by using an electronic scale with a 0,1 g resolution.

3. RESULTS AND DISCUSSION

This section presents the main results obtained from the tests and a discussion about the main outputs of the research.

3.1 Visual evaluation of spalling

Table 5 presents a general view of the visible damage caused by the high temperatures, which can also be seen in Figures 1 and 2.

Table 5: General view of damages in the specimens through visual evaluation

Curing	Mix	300°C			600°C			
Water curing	M1	black	black	black	black	black	black	yellow
	M2	yellow	black	black	yellow	red	yellow	
	M3	yellow	yellow	red	black	black	yellow	
Air curing	M1	black	black	yellow	black	black		
	M2	black	black	yellow	black	yellow		
	M3	black	yellow	black	black	red	red	

Color code		
black	No signs of visible detachments	
red	Total failure by spalling	
yellow	Superficial detachment, with no total failure	
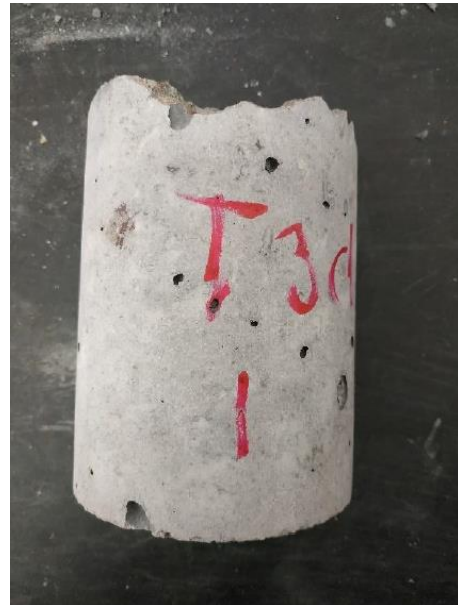
Figure 1: Images from the inside of the furnace with detachments of specimens due to spalling, after (a) being exposed to 600ºC (cured in air) and (b) being exposed to 600ºC (cured in water). Cracking and detachment of air-cured M3 specimen after being exposed to 300ºC (c). Cracking of moist-cured M3 specimen after being exposed to 600ºC (d).

<div align="center">a)</div>
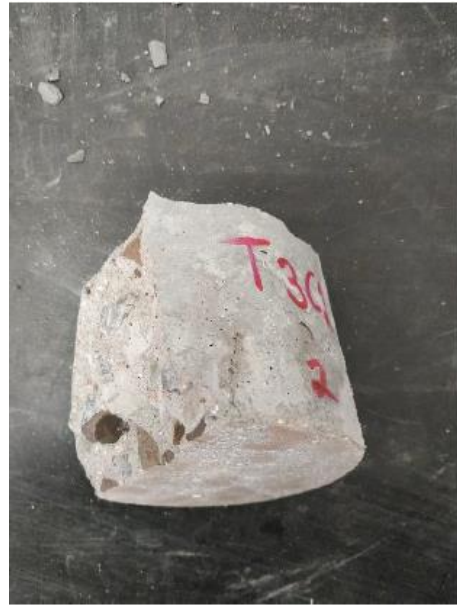
<div align="center">b)</div>

<div align="center">c)</div>

<div align="center">d)</div>

Figure 2: Detachment of moist-cured M1 specimen, after being exposed to 600ºC (a). Detachments of air-cured M3 specimen after being exposed to 600ºC (b). Moist-cured M1 and M2 specimens after being exposed to 300ºC (c and d).

Considering the results presented in Table 5 and Figures 1 and 2, it is evident that the M3 specimens were the ones more affected to high temperatures, with more damage in all situations. For the specimens exposed to 600ºC, half of them failed due to spalling. Similar results were also observed in other studies [4 5, 6 and 7]. It can also be seen that specimens cured in water presented more detachments, even though the number of total failures by spalling was the same for both curing procedures. This result is in line with the ones obtained from [4].

The visual inspection show that M1 specimens were the ones that were less affected. This is also an expected result, since concretes with higher w/c ratio usually have higher permeability [3], thus reducing the development of pore pression which is caused by the confinement of water vapour [5, 6 and 7] inside concrete when it is heated up to high temperatures.

3.2 Compressive strength

Table 6 presents the average values and the standard deviation (when its calculation was possible) of the compressive strength results for all variables analysed in this research. Due to the higher variability compared to the initial average strength, the compressive strength of specimen 1 from mix M1 cured in air was discarded and the average value was recalculated, resulting in the values presented in the last column of the table. The table shows that the target compressive strength of mix M1 was very close to the results obtained from the tests, for both curing conditions. Mix M3 showed consistent results for specimens cured in air and water, however, slightly higher than the target strength. Mix M2, however, showed results close to the target of 70 MPa only for specimens cured in air. M2 specimens moist-cured showed results considerable higher than the target strength.

Table 6: Results of compressive strength

Curing condition	Mix	Temperature	Compressive strength (MPa)					
			Spec 1	Spec 2	Spec 3	Average	Standard deviation	Recalculated average
Water curing	M1	Ambient	46.88	53.99	49.78	50.22	2.92	50.22
		300ºC	41.21	38.05	45.22	41.49	2.93	41.49
		600ºC	33.08	32.43	33.03	32.85	0.30	32.85
	M2	Ambient	78.53	75.52	73.18	75.81	2.19	75.81
		300ºC	64.88	72.38	78.65	71.97	5.63	71.97
		600ºC	61.10	**	58.91	60.01	1.10	60.01
	M3	Ambient	105.91	111.92	98.12	105.32	5.65	105.32
		300ºC	92.55	97.54	94.06	94.72	2.09	94.72
		600ºC	**	76.63	77.03	76.83	0.20	76.83
Air curing	M1	Ambient	33.18*	48.67	46.24	42.70	6.80	47.46
		300ºC	40.31	44.10	44.61	43.01	1.92	43.01
		600ºC	25.93	28.28	23.97	26.06	1.76	26.06
	M2	Ambient	98.30	91.02	100.57	96.63	4.07	96.63
		300ºC	93.90	92.39	89.94	92.08	1.63	92.08
		600ºC	57.12	62.94	48.13	56.06	6.09	56.06
	M3	Ambient	109.81	118.72	97.31	108.61	8.78	108.61
		300ºC	93.59	98.85	112.49	101.64	7.96	101.64
		600ºC	74.88	**	**	74.88	-	74.88

* result was discarded
** failure by spalling

Figures 3 and 4 show the results of the average compressive strength for each mix, as a function of the temperature, for specimens cured in air and water, respectively. Both figures show the results in terms of absolute values. Figure 5 shows the relative loss of compressive strength (%) in relation to the reference strength (ambient temperature) for each mix, for both curing procedures.
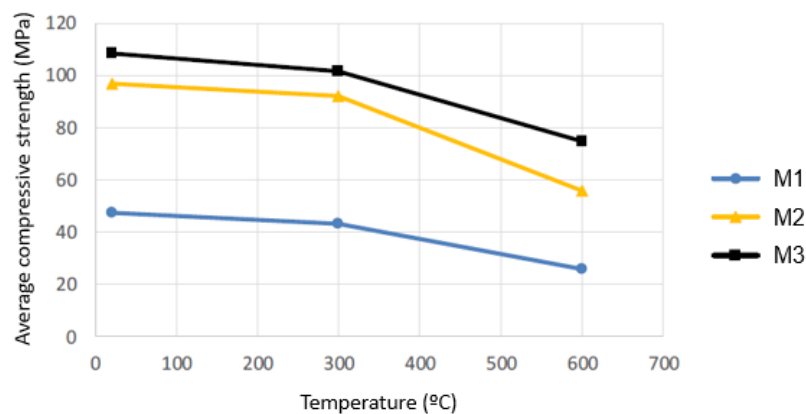
Figure 3. Average compressive strength as a function of temperature for specimens cured in air.
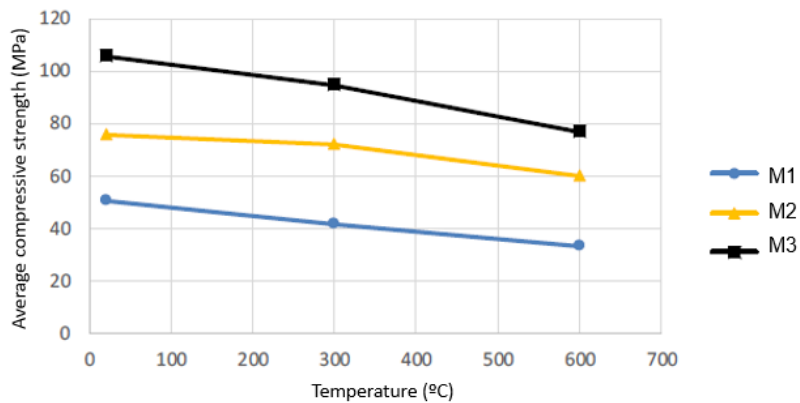
Figure 4. Average compressive strength as a function of temperature for specimens cured in water.
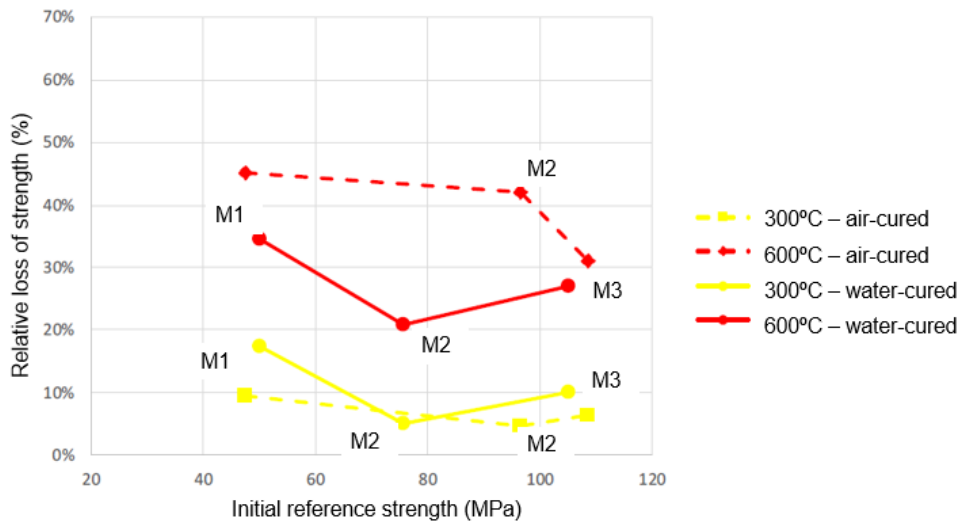
Figure 5. Loss of compressive strength (%) in relation to the reference compressive strength for each mix, for both curing procedures.

The analysis of Figure 5 shows that M2 specimens presented the best behavior in terms of the loss of compressive strength for all cases, except for the ones cured in air and exposed to 600ºC. It is important to emphasize, however, that the residual compressive strength was calculated only for specimens that did not fail by spalling. It is also important to note that there is a different behavior when comparing the curing *versus* the exposure temperature, that is, for the lower exposure temperature of 300ºC, the specimens cured in air had the lower loss of relative strength, whilst for the temperature of 600ºC, specimens cured in water had the lower loss of relative strength. These results are in accordance with [3].

3.3 Ultrasonic pulse velocity (UPV)

Table 7 presents the results of UPV for all specimens, including the average UPV results and standard deviation. Figure 8 shows the average UPV results as a function of the average relative compressive strength (in relation to the reference specimens – ambient temperature).

Table 7: Results for UPV tests.

Curing condition	Mix	Temperature	UPV (m/s)				
			Spec 1	Spec 2	Spec 3	Average	Standard deviation
Water curing	M1	Ambient	4952	4888	4924	4922	26
		300ºC	4301	4230	4414	4315	76
		600ºC	2174	2156	2316	2215	72
	M2	Ambient	5218	5205	5318	5247	50
		300ºC	4844	4878	4925	4882	33
		600ºC	2770	**	2946	2858	88
	M3	Ambient	5205	5273	5108	5195	68
		300ºC	4916	4923	4850	4896	33
		600ºC	**	2638	2924	2781	143
Air curing	M1	Ambient	4871	4879	4919	4890	21
		300ºC	4264	4277	4262	4268	7
		600ºC	2012	1822	1899	1911	78
	M2	Ambient	5229	5144	5200	5191	35
		300ºC	4869	4935	4870	4892	31
		600ºC	2595	2564	2489	2550	45
	M3	Ambient	5224	5198	5256	5226	24
		300ºC	5003	5020	4911	4978	48
		600ºC	2591	**	**	2591	-
** failure by spalling							
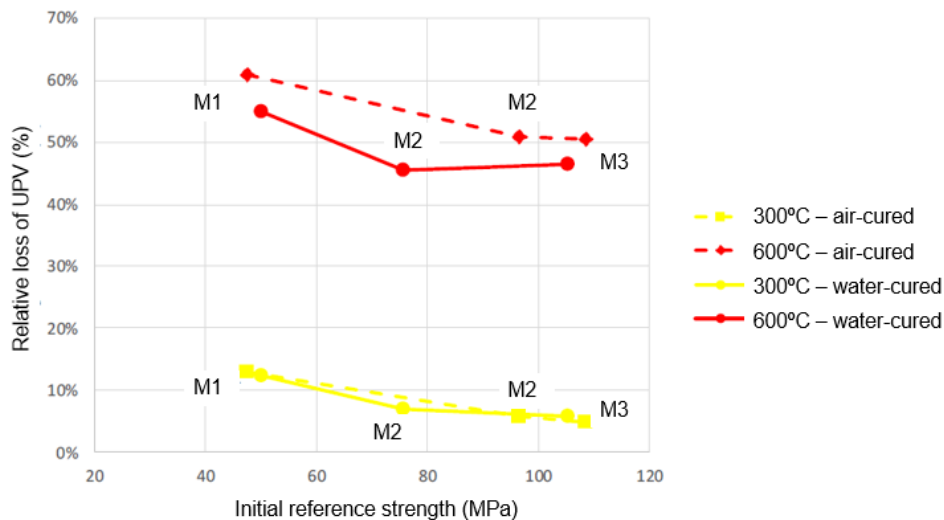
Figure 8: Results for average UPV for each mix as a function of the initial reference compressive strength

From Figure 8 it is possible to observe that, for both curing procedures, the UPV decreased between 50 to 60% for all mixes, for the temperature of 600ºC. However, for the 300ºC temperature, the difference was about 10%. In comparison with mix M1, mix M2 presented approximately 50% reduction of the UPV at 300ºC, and 80% reduction of the UPV at 600ºC.

This figure also shows that specimens from mix M2 had similar damage to mix M3 at the temperature of 600ºC. However, at 300ºC mix M3 showed the best results. The results presented in Figure 8 are in accordance with the results presented in section 3.2 of this paper, and also with the conclusions presented by Almeida [12], which indicate that the micro cracks of the concrete measured by UPV are perceived with more confidence at lower temperatures than the differences in the compressive strength, being more accentuated at 600ºC.

3.4 Mass loss

Table 8 shows the results in terms of initial (before being exposed to high temperatures) and residual (one day after being exposed to high temperatures) mass for all specimens.

Table 8: Results for initial and residual mass

Curing condition	Mix	Temp (ºC)	Mass (g)							
			Spec1 Initial	Spec1 Resid	Spec2 Initial	Spec2 Resid	Spec3 Initial	Spec3 Resid	Aver Initial	Aver Resid
Water curing	M1	300ºC	3797.0	3670.3	3814.0	3675.7	3816.5	3693.5	3809.2	3679.8
		600ºC	3782.3	3481.0	3840.8	3548.5	3825.2	3533.9	3816.1	3521.1
	M2	300ºC	3961.5	3901.1	3965.5	3900.7	3969.0	3906.7	3965.3	3902.8
		600ºC	3914.4	3693.0	3914.7	**	3970.4	3742.0	3933.2	3717.5
	M3	300ºC	3915.5	3858.5	3945.0	3877.3	4003.0	3945.7	3954.5	3893.8
		600ºC	3936.9	**	4029.0	3813.5	3964.2	3759.0	3976.7	3786.3
Air curing	M1	300ºC	3762.4	3603.7	3811.8	3665.0	3827.0	3676.0	3800.4	3648.2
		600ºC	3793.1	3527.5	3890.5	3621.5	3774.3	3507.6	3819.3	3552.2
	M2	300ºC	3887.3	3817.7	3931.6	3862.4	3908.0	3837.2	3909.0	3839.1
		600ºC	3893.2	3683.3	3880.7	3677.3	3929.6	3699.5	3901.2	3686.7
	M3	300ºC	3995.8	3931.7	3963.7	3906.6	3930.6	3858.5	3963.4	3897.9
		600ºC	3970.5	3760.0	3966.0	**	3946.4	**	3961.2	3760.0
			** failure by spalling							

Figure 9 shows the relative mass losses, for both curing procedures, as a function of concrete strength, for each specimen. The specimens that failed due to spalling were not considered in this analysis.
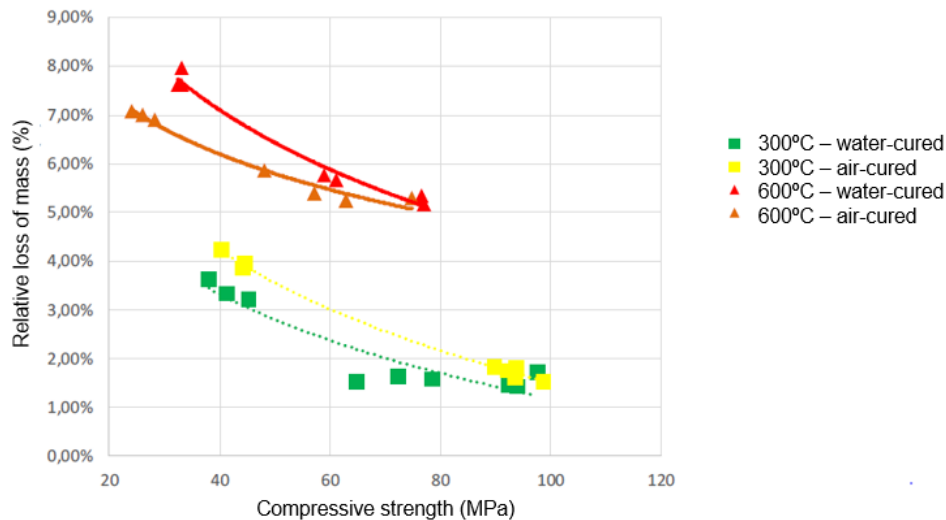
Figure 9. Relative mass loss (%) as a function of the compressive strength for each specimen, for both curing procedures.

It is important to note that, in the majority of the cases, these results are mainly due to water evaporation of the concrete, and they cannot be used alone as a way to measure spalling. However, if they are analysed together with the results from the visual investigation, shown in section 3.1, they can contribute to the analysis of spalling.

Specimens subjected to 300ºC showed more detachments for the ones cured in water, as shown in Table 4. In this case the difference in the loss of mass for both curing procedures is more due to the loss of solid material. For specimens subjected to 600ºC the amount of detachments were similar for both curing conditions. In this case the loss of mass is probably due to water evaporation.

3.5 Comparison of compressive strength results with code standards

NBR 15200 [13] and the EUROCODE 2 Part. 1-2 [14] present curves with the compressive strength reduction factor (kc,θ) as a function of the temperature to which concrete was exposed, valid for concretes with silicon aggregates, and compressive strength between 20 and 50 MPa and specific mass ranging from 2000 to 2800 kg/m³. EUROCODE 2 Parte 1-2 presents compressive strength reduction factors for high resistance concretes, for classes I (C55 and C60), II (C70 and C80) and III (C90). Figure 10 shows these curves and the results obtained from this research.
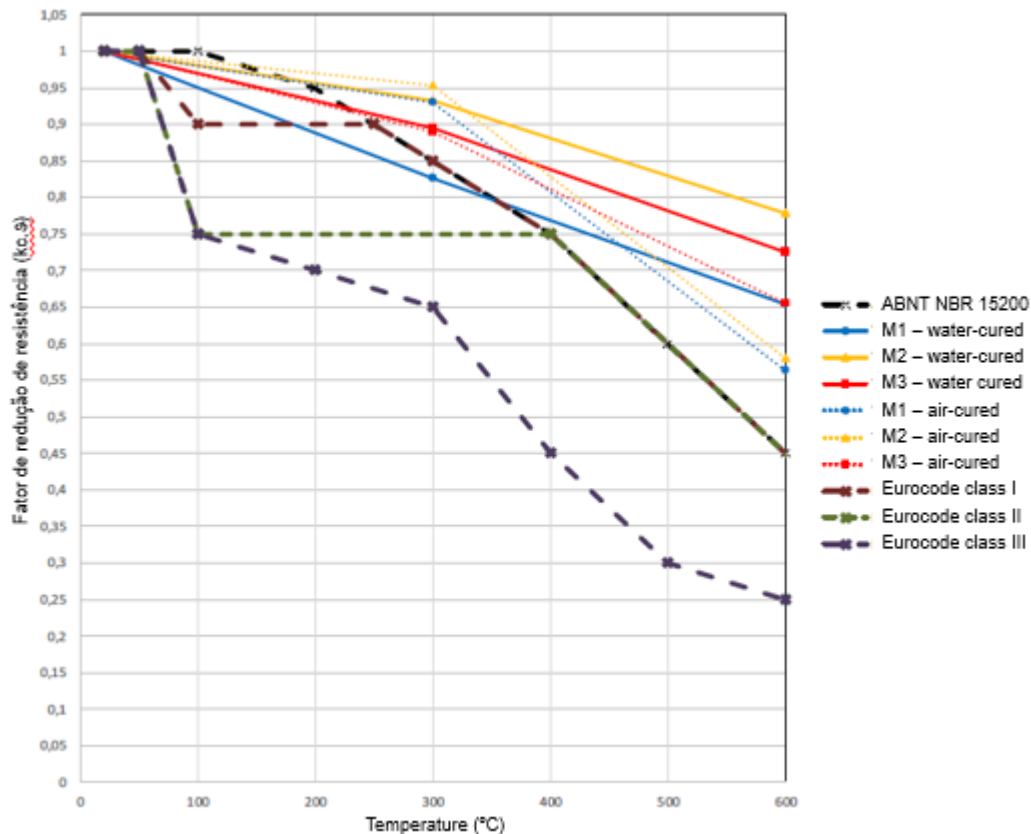
Figure 10. Compressive strength reduction factors (kc,θ) obtained from the results of the research in comparison with the data from NBR 15200 [13] and EUROCODE 2: Part 1-2 [14].

It can be noted that the factors given by the codes [13 and 14] are more conservative in comparison with the ones obtained from the tests. For the mix M3 the value given by [13] was about one third of the one obtained from this research. Exception applies for mix M1 cured in water, which was very close to the factor recommended for its strength class. One possible cause for such variation is the use of different heating rate curves, the curing conditions, mix proportions and other characteristics of test procedures used in the codes and in this research, as well as different periods of time at which each specimen is maintained after the maximum temperature has been reached.

It is important to emphasize that NBR 15200 [13] does not consider the probability of spalling occurrence. As shown in Table 4. For the 600ºC temperature, many specimens failed due to spalling (even for the ones cured in air).

4 Conclusions

The following conclusions can be driven from the research:

- High resistance concretes, with resistance about 100 MPa, seem to be more susceptible to spalling;
- For concretes with lower resistances, around 50 MPa, the probability for spalling to occur is low for the temperatures used in this research;

684

- Concretes with intermediate strength considering the ones tested in this research (around 75 MPa), cured in air, presented, in general, the best behavior in terms of relative compressive strength loss and spalling analysis.
- Concretes cured in water are more susceptible to spalling;
- In a general way, temperatures of 300ºC caused small damages;
- Concretes that lost more water during the mass loss test, in general, had lower superficial detachments, indicating that less permeable concretes develop more pore pression in high temperatures, causing spalling;
- NBR 15200 [13] and EUROCODE 2 PART 1-2 [14] show more conservative values in terms of compressive strength reduction factors in comparison with the ones shown in this research.

Due to the limitations of this research, which comprises the limited number of specimens, the conclusions presented cannot be generalized unless more work is carried out.

Acknowledgements

REFERENCES

[1] Aïtcin, P. C. (1998). *High-performance concrete.* Routlege, Londres.

[2] Neville, A. M.; Brooks, J. J. (2013). *Tecnologia do concreto.* Bookman.

[3] Neville, A. M. (1976). *Properties of concrete.* Pitman Publishing, Londres.

[4] Purkiss, John A. (1996). *Fire safety engineering design of structures.* Butterworth Heinemann, Oxford.

[5] Phan, L. T. (w. d.). *High-Strength Concrete at High Temperature − An Overview.* p. 15.

[6] Phan, L. T. (2008). *Pore pressure and explosive spalling in concrete.* Materials and Structures, vol. 41, no. 10, p. 1623–1632.

[7] Kodur, V.; Mcgrath, R. (2003). *Fire Endurance of High Strength Concrete Columns.* p. 15.

[8] Dal Molin, D. C. C. et al. Desenvolvimento de um Método de Dosagem de Concretos de Alta Resistência com Baixo Consumo de Cimento. [s.l: s.n.].

[9] Associação Brasileira de Normas Técnicas. (1998). *NBR NM 67: Concreto - Determinação da consistência pelo abatimento do tronco de cone.* Rio de Janeiro.

[10] Associação Brasileira de Normas Técnicas. (2018). *NBR 5739: Concreto - Ensaio de compressão de corpos-de-prova cilíndricos.* Rio de Janeiro.

[11] Associação Brasileira de Normas Técnicas. (2019). *NBR 8802: Concreto Endurecido – Determinação da velocidade de propagação de onda ultrassônica.* Rio de Janeiro.

[12] Almeida, J. M. A. (2017). *Comportamento em altas temperaturas e na reidratação de concretos convencional e com cinza de casca de arroz,* PhD Thesis, Universidade Federal do Rio Grande do Sul.

[13] Associação Brasileira de Normas Técnicas. (2012). *NBR 15200: Projeto de estruturas de concreto em situação de incêndio.* Rio de Janeiro.

[14] European Committe for Standardization (2004). *EUROCODE 2 Part 1-2 – Design of Concrete Structures. General rules – Structural fire design.*

THERMAL-PROPERTIES OF ULTRA HIGH-PERFORMANCE CONCRETE (UHPC)

F. Bolina a[*]   **G. Poleto b**

ABSTRACT

Ultra-high-performance concrete (UHPC) has exceptional mechanical properties at room temperature. However, its fire performance is not well known. There are no standardized procedures for characterizing UHPC at high temperatures. This is justified by the lack of research on the subject, leaving gaps for experimental and numerical investigations. This study raised a set of parametric data of UHPC at high temperatures. Thermal diffusivity, thermal conductivity and specific heat as thermal parameters; compressive strength and modulus of elasticity as mechanical; and thermal elongation and density as physical were defined for different temperature ranges. The results were compared with other structural concrete (NSC, HSC and UHSC) proposed by the literature. The UHPC had a particular fire behavior. In relation to NSC, HSC and UHSC, the thermal extension and mechanical parameters of UHPC are less affected in fire, but its thermal conductivity and mass loss is higher. UHPC also showed the highest specific heat compared to other concretes. The thermal field of UHPC tends to be higher in relation to the others.

Keywords: UHPC. Thermal properties. Mechanical properties. Physical properties.

Notation:

CA	Coarse aggregate
FA	Fly ash
HSC	Hight-strength concrete
NSC	Normal-strength concrete
PVA	Polyvinyl acetate
SF	Silica fume
UHPC	Ultra-High-Performance Concrete

[a] ***** Unisinos University (fabriciobolina@gmail.com)**,** Corresponding author.

[b,*] Unisinos University (giovanapoleto@hotmail.com).

UHSC	Ultra-High Strength Concrete
w/b	Water-binder ratio
C_p	Specific heat
E_c	Elastic modulus of concrete at room temperature
$E_{c,\theta}$	Elastic modulus of concrete in fire
$f_{c,k}$	Compression strength of concrete at room temperature
$f_{c,\theta}$	Compression strength of concrete in fire
k	Thermal conductivity
$k_{c,\theta}$	Partial factor for concrete (compression strength) in fire
$k_{cE,\theta}$	Partial factor for concrete (modulus of elasticity) in fire
$k_{\rho,\theta}$	Partial factor for concrete (mass loss) in fire
ρ	Density

1. INTRODUCTION

Ultra-High-Performance Concrete (UHPC) is a cementitious concrete with exceptional mechanical properties at room temperature. According to ASTM C1856 (2017) [1], the specified compressive strength must be at last 120 MPa. UHPC is characterized by low w/b ratio, high cement content, aggregates, fibers (steel, PVA, glass), superplasticizer. Their matrix is very dense and has a minimal structure of disconnected pores, making it an interesting solution in chemically aggressive environments. UHPC can also be used in the precast concrete, being an ideal solution for structures with high loading and high span with the minimum cross-section.

Buildings are subject to fire. According to Zhu et al. (2021) [2], there are few studies on the UHPC at elevated temperatures. However, for application as a structural material, UHPC must have fire performance. Research such as Xiong and Liew (2016) [3], Kodur and Khaliq (2011) [4], Li, Qian and Sun (2004) [5], Poon, Shui and Lam (2004) [6], Kodur and Sultan (2003) [7] and Shin et al. (2002) [8] already show that high strength concrete (HCC) does not have the same fire performance as normal strength concrete (NSC), due to concrete spalling, as also explain Ullah et al. (2022) [9] and Akca and Zihnioglu (2013) [10]. According to Liang et al. (2013) [11], UHPCs usually spalling more than NSCs due to their dense structure and low permeability. In fact, research that sought a parametric evaluation of UHPC was dedicated to concrete spalling analysis [3, 10, 11, 12, 13, 14, 15, 16, 17].

There are no standard criteria for the fire design of UHPC structures. Standards such as EN 1992-1.2 (2004) [18], ACI-216 (2014) [19], AS 3600 (2018) [20], NZS 3101-1 (2006) [21] and NBR 15200 (2012) [22] do not provide thermomechanical parameters for fire-design concrete structures with f_(c,k)>100 MPa. There are few researches on this subject and the fire behavior of UHPC is not well known. Few researches sought to define the thermal properties of UHPC to fire. In this sense, authors such as Ullah et al. (2022) [9] does not recommend UHPC in case of fire, suggesting further research.

There is a contradiction. Authors such as Du et al. (2021) [23], Willie, Naaman and Parra-Montessinos (2011) [24] and Habel et al. (2006) [25] believe that UHPC is one of the most promising building materials for the future, but others such as Zhu et al. (2021) [2] and Ullah et al. (2022) [9] discuss the sensitivity of UHPC to fire. On the other hand, the most recent researches on UHPC do not evaluate its fire behavior. Research as Zhang et al. (2022) [26] evaluated the mechanical behavior of RC column with UHPC jacket at room temperature; Tian and al. (2022) [27] and Zhou et al. (2023) [28] studied the UHPC performance under cyclic load; Zhang et al. (2022) [29] the flexural behavior of UHPC beams; Zhang et al. (2023) [30] using UHPC with recycled concrete fines; Li et al. (2023) [31] the UHPC mechanical properties with different cement type, Cui et al. (2023) [32] with expansion agent in the concrete mix, among others.

Research on UHPC in fire needs to be improved. According to SFPE (2008) [33], the fire behavior of the structures depends on the high temperature properties of their materials. According to Kodur and Khaliq (2011) [4] and Abid et al. (2019) [14] these parameters are of physical, thermal and mechanical origin. Thermal and physical properties include conductivity, specific heat, thermal diffusivity, expansion and mass loss. As mechanical properties include strength, thermal deformation and modulus of elasticity. All of these properties change with temperature and are also influenced by concrete mix proportions, permeability, aggregate and cement type, fiber presence, chemical additives.

The mechanical deterioration of UHPC in fire also needs to be discussed. Temperatures between 100-300°C cause an increase in compressive strength, as shown by Park et al. (2019) [34] and Kahanji et al. (2018) [35]. This is due to the rehydration of non-hydrated cementitious compounds in the cement paste, as described by Banerji and Kodur (2021) [12] and Xuan and Shui (2011) [36]. It is activated by temperatures due to the SF that did not react with the cement paste and by the water vapor produced, as shown by Zhu et al. (2021) [2]. After 800 °C, UHPCs may suffer a strength loss of up to 80%, as Liang et al. (2018) [11] describes. According to Ullah et al. (2022) [9] and Choe et al. (2015) [13], in the range of 1000-1200 °C, intense physical and chemical changes occurred in its concrete matrix, resulting in a severe decrease in mechanical properties.

Kodur et al. (2020) [37] studied thermal parameters of UHPC. Conductivity, specific heat, mass loss and expansion were investigated. The literature review proposed by Zhu et al. (2021) [2] proved to be the only research that proposed thermal parameters for UHPC in different temperature ranges. The UHPC studied by Kodur et al. (2020) has SF, silica sand, PP and steel fibers, slag and coarse aggregate (CA), with f_c between 164 to 178 MPa. However, the use of UHPC without CA occurs in some cases. Yang and others. (2019) [38] already show that CA reduces the UHPC thermal field, i.e., UHPC without CA has a much greater temperature gradient than UHPC with CA. The UHPC in this research does not have CA, but has PVA fibers and 750 days of concrete curing, making this study unprecedented. UHPC without CA has not yet been evaluated by the literature.

Parametric data are essential for numerical investigations, mainly in FEA (Finite Element Analysis). However, there is a lack of data to support FEA analysis of UHPC structures in fire. Researchers who intend to develop numerical studies with UHPC structures will not find enough data to calibrate numerical models. The lack of standard data (such as EN 1992-1.2 [18] and others [19-22]) also motivated this research.

This research defined the thermal and mechanical parameters of UHPC. As thermal parameters, conductivity, diffusivity and specific heat have been defined. As mechanical parameters, modulus of elasticity and nominal compressive strength. They have been set for different temperature ranges. In addition, physical parameters such as density and thermal extension in fire were also evaluated.

2. METHODS

2.1 Materials

The cement used was a high-initial resistance type that contained fewer chemical cement additions. It is a Portland cement used in Brazil classified as CP-V ARI by NBR 16697 [39]. Silica fume (88.5% silicon contained) and fly ash (50.0% of silicon content) were used with, respectively, specific gravity of 350 kg/m³ and 210 kg/m³. Silica fume acts as a microfiller. It also reacts with calcium hydroxide, thus increasing the final strength.

A natural quartz sand with 260 kg/m³ was incorporated. It is a river sand that received a washing process to eliminate impurities. The steel fiber had a length of 25 mm and a diameter of 0.75 mm, with a tensile strength of 1100 MPa and a modulus of elasticity of 210 GPa. The PVA (polyvinyl acetate) fiber had a length of 12 mm and 0.04 mm in diameter, tensile strength of 1600 MPa and modulus of elasticity of 41 GPa. Superplasticizing additive based on polycarboxylates was incorporated to improve the workability of the concrete. The UHPC production and mix was made according to Christ et al. (2022) [40] method.

The average compression strength of the concrete at 28, 150 and 750 days were 108.0, 146.4 and 162.4 MPa, respectively. The elastic modulus was 41.4, 44.0 and 46.1 GPa at, respectively, 28, 150 and 750 days. These results were obtained by testing a concrete cylinder with a dimension of 150x300 mm (diameter x length) made according to ASTM C470 [41]. The concrete compressive strength testing was obtained according to ASTM C39

[42] and the elastic modulus in accordance to ASTM C469 (2014) [43] procedures. The concrete specimens are produced in accordance to ASTM C31 [44] and ASTM C192 [45].

The concrete mix is presented in Table 1.

Table 1 – Concrete mix

Material	Unit content (kg/m³)	Ratios of concrete mix
Cement	488	1.00
Silica fume	268	0.55
Fly ash	235	0.48
Natural sand (fine aggregate)	1025	2.10
Steel fiber	120	0.25
PVA fiber	6	0.02
Chemical additive	17.6	0.03
Water	178	0.36

2.2 Thermal properties definition

The thermal diffusivity, specific heat and conductivity parameters were determined as shown below.

2.2.1 Diffusivity

The thermal diffusivity of UHPC was obtained according to the Flash Method proposed by ASTM E1461 [39]. The method is used to measure values of thermal diffusivity of a wide range of solid materials. The results were obtained by testing a concrete cylinder with a dimension of 12.7x2.5 mm (diameter x thickness) in accordance to ASTM E1461-13 [46] prescriptions. The UHPC specimens were heating to 100, 200, 300, 400, 500 and 600°C. The test equipment used was a thermal diffusivity analyzer (TDA) with a temperature range from -125°C to 500°C, a thermal diffusivity measurement ranges from 0.01mm²/s to 1000mm²/s and a thermal conductivity range from 0.1W/mK to 2000W/mK. The TDA setup is shown in Figure 1.

Figure 1 – TDA setup

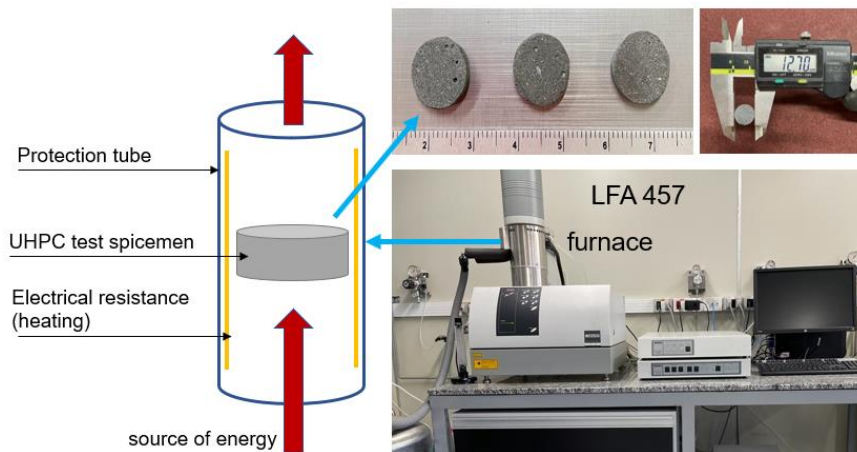According to the thermal diffusivity (α) results and with the density in fire (ρ) it is possible to obtain the specific heat (Cp) and thermal conductivity (k) according to Equation (1).

$$\alpha = k/\rho . C_p \qquad (1)$$

2.2.2 Specific heat

According to the thermal diffusivity results and according to Equation 1, the specific heat values were defined for the same temperature ranges as in section 2.2.1.

689

2.2.3 Conductivity
According to the results of thermal diffusivity and Equation 1, the thermal conductivity values were defined for the same temperature ranges as in section 2.2.1.

2.3 Physical and mechanical properties definition

The heating of the UHPC samples was made according to RILEM TC 129 [47, 48]. The samples were put in an electrical small-scale furnace with a constant heating rate of 0.25 °C/min to the required test temperature. The furnace dimensions are 600x450x450 mm. After reaching the temperature required, it was maintained for a period of 360 min. After previous analyzes and tests carried out by the authors, this was the time required for the UHPC samples to reach a uniform and constant temperature. This preliminary test was done with a sacrifice specimen, where a thermocouple was installed at its centroid.

To avoid the concrete spalling, the fire test was carried out after 750 days of construction of the UHPC spicemen. In order to avoid rehydration of the concrete with the humidity of the air, the samples of UHPC were tested immediately after removal from the furnace. These results were obtained by testing a concrete cylinder with a dimension of 150x300 mm (diameter x length) made according to ASTM C470 [41].

2.3.1 Compression strength
Axial compression strength was made according to RILEM TC 129-3 [47]. Temperatures of 100, 200, 300, 400, 500 and 700 °C were assumed. This test was carried out 750 days after the production of the specimen. Comparing with the values at room temperature, the UHPC compression strength reduction factor for each temperature range was then measured.

2.3.2 Elastic modulus
Compression strength was made according to RILEM TC 129-5 [48]. Temperatures of 100, 200, 300, 400, 500 and 700 °C were assumed for the concrete aged 750 days. The UHPC modulus of elasticity reduction factor for each temperature was then measured when compared to the values at room temperature.

2.3.3 Expansion
The linear expansion of UHPC was obtained according to ASTM E228 [49] procedures, using horizontal dilatometers. The measurement of expansion involves two parameters: change of length and change of temperature. The results were obtained by testing a rectangular concrete cube with a dimension of 10x50x10 mm (width x length x thickness). The sample is placed on the holder and then a cylindrical oven is moved to envelop the sample evenly on all sides. The UHPC specimen is subjected to a pre-programmed heating rate (i.e., 5°C/min) and the linear expansion corresponding to the temperature rise is measured. The UHPC specimens were heating to 100, 200, 300, 400, 500 and 600 °C.

2.3.4 Density (mass loss)
The density was obtained with the same samples used to define the compressive strength. Before submission in the furnace, the weight (kN) and volume (m³) of the UHPC specimen was measured. The same was done after its removal from the furnace. Comparing with the values at room temperature, the UHPC density reduction factor for each temperature range was then measured.

2.4 Correlation with the standard procedures and references
The results (data available in this research) were compared with those proposed by the references. When possible, the data were compared with normal-strength (NSC), high-strength (HSC), ultra-high-strength (UHSC) and, when available, ultra-high-performance (UHPC) concrete similar to this research.

3. RESULTS AND DISCUSSION

3.1   Physical and mechanical properties in fire

3.1.1   Compressive strength and modulus of elasticity

Table 1 and Fig.2a and b show the compressive strength and modulus of elasticity of UHPC for different temperature ranges.

According to Fig. 2a, in terms of compression strength, the fire performance of UHPC can be separated into three stages. Stage 1 shows that up to 100°C UHPC decreases its compression strength. Stage 2 between 100-300°C, UHPC increases its strength. Stage 3 shows that after 300°C the UHPC has a gradual reduction in its compressive strength. The increase in strength (between 100-300°C) is explained by the rehydration of non-hydrated cementitious compounds in the cement paste. Banerji and Kodur (2021) [12] and Xuan and Shui (2011) [36] explain that it is activated by temperatures, because the hydration process is not complete at room temperature according to Zhu et al. (2021) [2]. After heating, the SF produced new C–S–H (secondary hydration). In addition, xonotlite and tobermorite form through the transformation of the C–S–H gel, which increases the compactness of the internal structures. Xiong and Liew (2016) [3] shown another reason for the increase of strength at 200-300 °C: the increases in the forces between the gel particles (van der Waals forces) due to the water removal and the shrinkage.

Table 1 – UHPC mechanical properties in fire

Temperature (°C)							
Ref	100	200	300	400	500	600	700
Elastic modulus (GPa)							
46.1	46.8	36.8	28.7	16.8	16.1	14.0	2.9
Compression strength (MPa)							
162.4	151.4	165.9	181.7	173.0	134.6	134.6	75.6
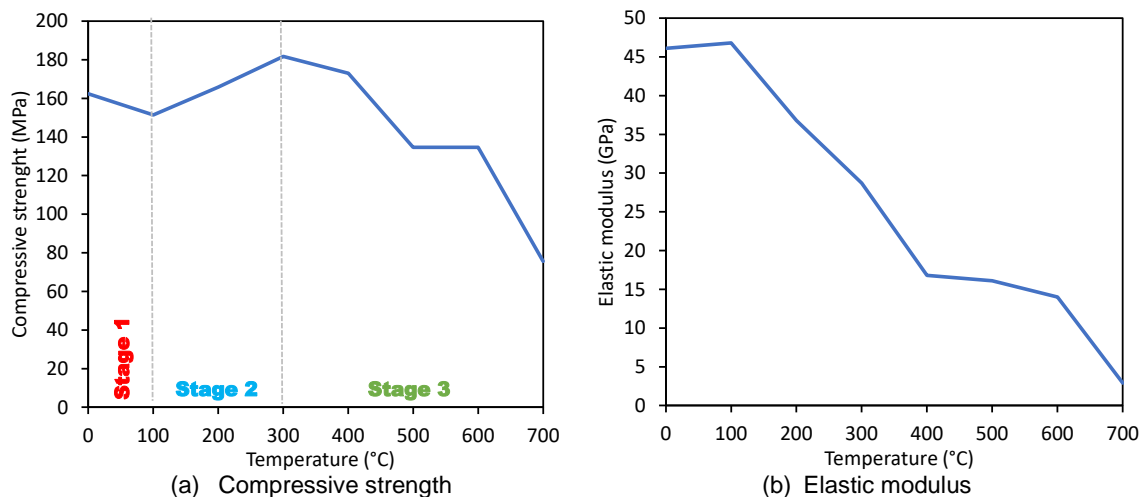
(a) Compressive strength (b) Elastic modulus
Figure 2 – Mechanical properties for different temperatures

According to Zhu et al. (2021) [2] and Zang, Liu and Tan (2021) [51], in the temperature range up to 400°C, decrease in compressive strength is mainly due to concrete dehydration, shrinkage, aggressive expansion, phase changes (C–S–H or C–H decomposition and fibers transformation), crack development in the concrete matrix, and thermal incompatibility between matrix and aggregate.

In the 400-700°C range, the paste-aggregate interface is also affected due to thermal incompatibility between the materials. The disintegration of $Ca(OH)_2$ and C-S-H also occurs in these temperatures. It is important to emphasize the influence of PVA fibers. Its deterioration increases the porosity of concrete, affecting its mechanical properties. Xiong and Liew (2016) [3], Banerji and Kodur (2021) [12] and Sanchayan and Foster (2016) [15], and have already evaluated the influence of PVA fibers on the reduction of these properties of concrete.

The modulus of elasticity at high temperatures (Fig. 2b) decreases as the temperature increases. The temperature of 100°C is an exception, showing a slight increase (1.5%) in relation to the room temperature values. Xiong and Liew [3] also found reduction and then recovery on the modulus of elasticity in the temperature range of 100–200 ºC. This phenomenon is also identified for residual compressive strength according to Fig. 2a. The researchers justify it by the increase in internal pressure due to the evaporation of free water.

691

In terms of compressive strength, the partial factor k(c,θ) for the UHPC studied is shown in Table 2a. To fire design of UHPC structures, the suggestion of the authors is to neglect the increase in compressive strength shown in Fig. 2a (stage 2). This seems to be the most rational criterion, as it is influenced by the concrete mix, w/c ratio, heating rate of the structure, aggregate. However, the strength loss up to 100°C (stage 1) cannot be neglected. Table 2 shows the proposition of partial factor k(c,θ) coefficients of UHPC in fire assuming strength loss up to 100°C (stage 1) but neglecting the strength increase up to 300°C (stage 2). The same k(c,θ) was assumed up to 400°C (equal to 0.93). After 400°C, k(c,θ) decreases above that identified until 100°C (stage 1).

In terms of elasticity modulus, the partial factors of the UHPC used in this research are shown in Table 3a. These values are compared to (i) normal-strength concrete (NSC) in Table 3b and c to, respectively, siliceous (Sili) and limestone (Lime) aggregate; (ii) to high-strength concrete (HSC) in Table 3d (class 1, C1), e (class 2, C2) and f (class 3, C3, according to EN 1992 classification in terms of concrete strength); (iii) ultra-high-strength concrete (UHSC) in Table 3g; and (iii) ultra-high-performance (UHPC) in Table 3d proposed by the references. To NSC, a f_ck of 40 MPa and the thermal extension (Δl/l) proposed by EN 1992-1.2 [11] was assumed. To HSC proposition, a f_ck of 70, 85 and 100 MPa were used to, respectively, C1, C2 and C3 (with their respective k_(c,θ) shown in Table 2). In accordance to EN 1992-1.2 [11], the same Δl/l for NSC was used to HSC definitions, also considering siliceous aggregate (Sili).

Table 2 – Partial factor: correlation between UHPC and references (compressive strength)

Temp. (°C)	Partial factor ($k_{c,\theta} = f_{c,\theta}/f_{ck}$) – compressive strength						
	UHPC Test Data	EN 1992 NSC (Sili) (C20/50)	EN 1992 NSC (Lime) (C20/50)	EN 1992 HSC-C1 (C55/75)	EN 1992 HSC-C2 (C70/95)	EN 1992 HSC-C3 (C90/105)	UHSC (Xiong and Liew,2016)
	(a)	(b)	(c)	(d)	(e)	(f)	(g)
25	1.00	1.00	1.00	1.00	1.00	1.00	1.00
100	0.93	1.00	1.00	0.90	0.75	0.75	0.77
200	0.93	0.95	0.97	0.90	0.75	0.70	0.89
300	0.93	0.85	0.91	0.85	0.75	0.65	0.94
400	0.93	0.75	0.85	0.75	0.75	0.45	0.84
500	0.83	0.60	0.74	0.60	0.60	0.30	0.71
600	0.65	0.45	0.60	0.45	0.45	0.25	0.61
700	0.47	0.30	0.43	0.30	0.30	0.20	0.50

Table 3 – Partial factor: correlation between UHPC and references (modulus of elasticity)

Temp. (°C)	Partial factor ($k_{cE,\theta} = E_{c,\theta}/E_c$) – modulus of elasticity							
	UHPC Test Data	EN 1992 NSC (Sili) (C20/50)	EN 1992 NSC (Lime) (C20/50)	EN 1992 HSC-C1 (C55/75)	EN 1992 HSC-C2 (C70/95)	EN 1992 HSC-C3 (C90/105)	UHSC (Xiong and Liew,2016)	UHPC (Banerij and Kodur,2021)
	(a)	(b)	(c)	(d)	(e)	(f)	(g)	(h)
25	1.00	1.00	1.00	1.00	1.00	1.00	1.00	1.00
100	1.00	0.60	0.32	0.56	0.47	0.47	0.83	0.83
200	0.80	0.39	0.12	0.41	0.34	0.32	0.90	0.60
300	0.62	0.27	0.07	0.30	0.27	0.23	0.75	0.35
400	0.36	0.18	0.05	0.18	0.19	0.11	0.55	0.33
500	0.35	0.08	0.02	0.10	0.10	0.05	0.46	0.20
600	0.21	0.04	0.01	0.04	0.04	0.03	0.31	0.10
700	0.06	0.03	0.00	0.03	0.03	0.02	0.26	0.08

The comparison between the partial factors of elastic modulus and compressive strength is shown in Fig. 3a and b, respectively.

Fig. 3a shows that the UHPC of this research has k(c,Eθ) convergent to those proposed by Xiong and Liew (2016) [3] and Banerij and Kodur (2021) [22]. This indicates that there is a consensus: the thermal extension (Δl/l) of UHPC is lower in relation to the NSC and HSC values proposed by the EN 1992-1.2 [11] and also its f(ck,θ) is less affected by high temperatures. This is validated by the Figure 4b, where the values of k(c,θ) are shown. In fire, the UHPC studied (Table 1a) showed the smallest reduction in compressive strength (k(c,θ) parameter) compared to NSC (Table 1b and c), HSC (Table 1d, e and f), and UHPC (Table 1g) according to standard and references.
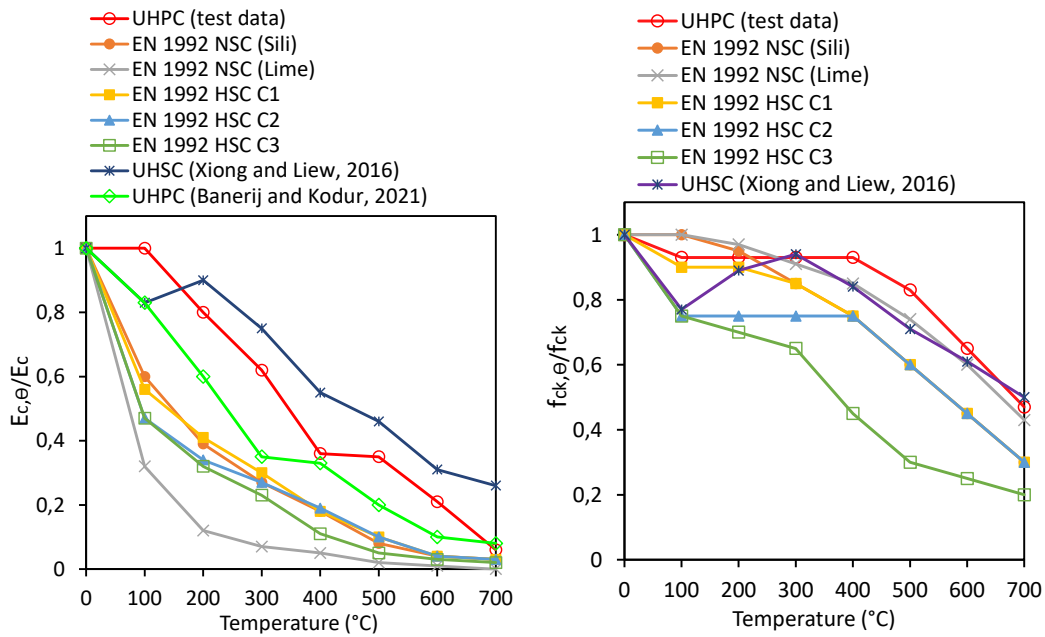
(a) $k_{c,E\theta} = E_{c,\theta}/E_c$ (b) $k_{c,\theta} = f_{c,\theta}/f_{ck}$

Figure 3 – Partial factor: comparison between the UHPC with other references

3.1.2 Thermal elongation

Table 4 and Fig. 4a show the thermal elongation ($\Delta L/L_o$) results of UHPC for different temperature ranges. Fig. 4b shows the comparison of these results with references.

UHPC (test data)   UHPC (test data) and references
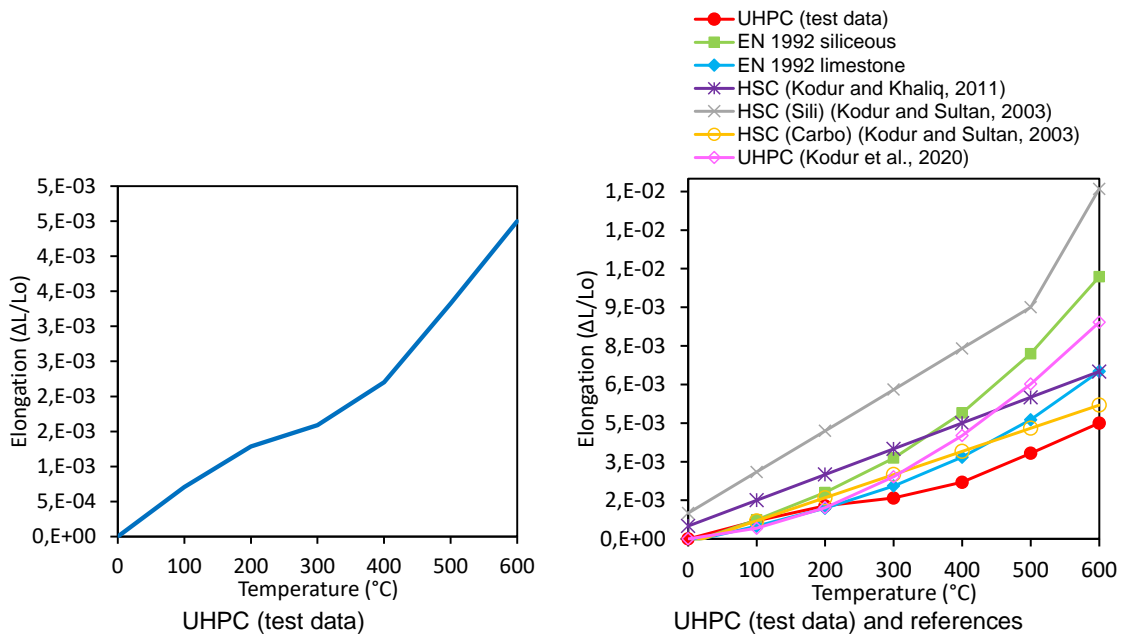
Figure 4 – Thermal elongation at high temperatures

UHPC (Table 4a) has positive thermal elongation when exposed to high temperatures, as with other concretes (Table 4b-g). The UHPC of this research had the lowest $\Delta L/L_o$ value in relation to the others. Up to 100°C thermal elongation can be related to the loss of humidity (free water) in the concrete. Between 200 and 300°C, it can be related to the loss of adsorbed water from hydrated cement compounds and aggregates. Between 300 and 500°C, values may be associated with $Ca(OH)_2$ and CaO dehydration, as reported by Laneyrie et al. (2016) [16]. The lower expansion of UHPC (Table 4a) in relation to the other concretes (Table 4b to f) shows the influence of the coarse

aggregate in this aspect. In relation to the UHPC tested by Kodur et al. (2020) [37], in addition to the aggregate, also the experimental procedure (see section 2).

Table 4 – Thermal elongation: correlation between UHPC and references

Temp. (°C)	Thermal elongation $\Delta L/L_o$ (x10^{-3})						
	UHPC Test Data	EN 1992 NSC (Sili) (C20/50)	EN 1992 NSC (Lime) (C20/50)	HSC (Kodur and Khaliq,2011)	HSC - Sili (Kodur and Sultan,2003)	HSC - Carbo (Kodur and Sultan,2003)	UHPC (Kodur et al., 2020)
	(a)	(b)	(c)	(d)	(e)	(f)	(g)
25	0.00	0.00	0.00	0.00	0.00	0.00	0.00
100	0.71	0.74	0.50	1.50	2.60	0.70	0.41
200	1.28	1.80	1.19	2.50	4.20	1.60	1.21
300	1.59	3.14	2.06	3.50	5.80	2.50	2.41
400	2.20	4.89	3.18	4.50	7.40	3.40	4.01
500	3.33	7.20	4.63	5.50	9.00	4.30	6.01
600	4.50	10.2	6.50	6.50	13.6	5.20	8.41

3.1.3   Density (mass loss)

The variation in the density of UHPC at high temperatures is shown in Table 5 and Figure 5. Figure 5 also shows the partial factors and comparatives with other references.

Table 5 – UHPC density variation in fire

Temperature (°C)							
Ref	100	200	300	400	500	600	700
Density (kN/m³)							
22.4	22.5	22.0	20.7	20.6	20.8	20.5	20.5

(a) UHPC (test data)   (b) $k_{\rho,\theta} = \rho_\theta/\rho$
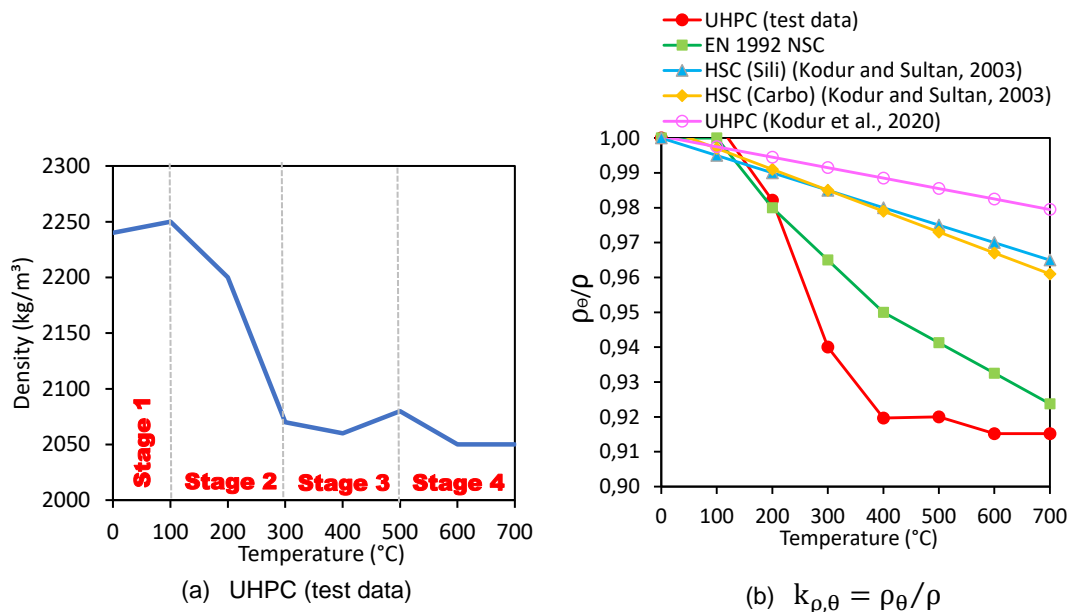
Figure 5 – Density and mass loss at high temperatures

The UHPC density variation can be separated into four phases, named stages, as shown in Figure 5a. In stage 1 (between 25-100°C), the density variation is negligible in relation to the measurement at room temperature. The increase in readings is related to the process of evaporation of free water. Considering the curing age of the UHPC specimens (750 days), added to the low w/c ratio, the free water can be assumed low. Therefore, the density variation due to the phase change of free water (liquid to gas) are low can be neglected as described by Abid et al. (2017) [14]. The small increase in density can be attributed to some degree of dehydration of the cementitious compounds or humidity adsorbed by the aggregates. Research by Kodur and Sultan (2003) [7] also showed an increase in density – but in HSC specimens – according to the aggregated nature. Between 100-300°C (stage 2),

the reduction in density may be related to humidity loss and phase change of the PVA fibers volatilization, similar to the results of Liang et al. (2016) [11]. According these authors, before 200°C a small mass loss is observed in UHPC specimens due to the high compactness of UHPC.

Between 300-500°C mainly to Ca(OH)2 decomposition, as Laneyrie et al. (2016) [16] explain. In the temperature range of 500-700°C, the variation of mass is due to the complete dehydration of the cementitious compounds.

According to Kodur, Banerji and Solhmirzaei (2020) [52], the amount of fibers in concrete is not enough to justify significant changes in its mass loss. At around 200-700°C, these authors also explain that the mass loss does not exceed 8.0%. In this research, in the same temperature range proposed by Kodur, Banerji and Solhmirzaei (2020), the mass loss was around 7.9%.

In terms of mass loss, Table 6a shows the $k(\rho,\theta)$ values for the UHPC of this research. For structural fire design purposes, the increase in density at 100 and 500°C was neglected. This is a rational decision as it depend on the amount of hydrated compounds and free water in the concrete. The partial values $k(\rho,\theta)$ of the UHPC were compared with the values proposed by EN 1992-1.2 for normal strength (NSC), and also for high strength concrete (HSC) by Kodur and Sultan (2003) for siliceous (Sili) and carbonate (Carbo) aggregates.

Table 6 – Partial factor: correlation between UHPC and references (mass loss)

Temp. (°C)	Partial factor ($k_{\rho,\theta} = \rho_\theta/\rho$) – Mass loss				
	UHPC Test Data	NSC EN 1992	HSC - Sili (Kodur and Sultan,2003)	HSC - Carbo (Kodur and Sultan,2003)	UHPC (Kodur et al., 2020)
	(a)	(b)	(c)	(d)	(e)
25	1.00	1.00	1.00	1.00	1,00
100	1.00	1.00	1.00	1.00	0,99
200	0.98	0.98	0.99	0.99	0,99
300	0.94	0.97	0.99	0.98	0,99
400	0.92	0.95	0.98	0.98	0,99
500	0.92	0.94	0.98	0.97	0,98
600	0.91	0.93	0.97	0.97	0,98
700	0.91	0.92	0.97	0.96	0,98

It is important to highlight that the UHPC of this research showed the highest mass loss compared to the other concretes shown in Figure 5 and Table 6. This is a variable that influences the thermal diffusivity of concrete, and therefore its thermal field, according to Equation 1.

3.2   Thermal properties in fire

3.2.1   Specific heat
Figure 6a and Table 7 show the specific heat results of UHPC in different temperature ranges. Figure 6b shows the comparison of these results with references.
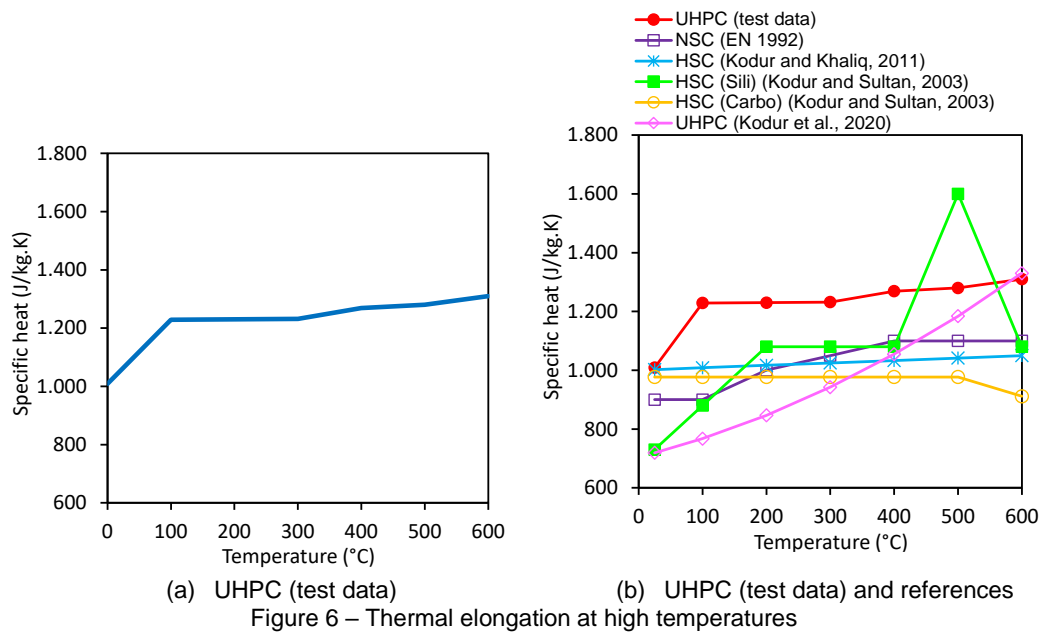
(a) UHPC (test data) (b) UHPC (test data) and references

Figure 6 – Thermal elongation at high temperatures

Table 7 – Thermal elongation: correlation between UHPC and references

Temp. (°C)	Specific heat (J/kg.K)						
	UHPC Test Data	NSC EN 1992 (C20/50)	NSC (Shin et al., 2002)	HSC (Kodur and Khaliq, 2011)	UHPC (Kodur et al., 2020)	HSC - Sili (Kodur and Sultan,2003)	HSC - Carbo (Kodur and Sultan,2003)
	(a)	(b)	(c)	(d)	(e)	(f)	(g)
25	1009	900	1104	1000	720	730	977
100	1229	900	-	1008	767	880	977
200	1230	1000	-	1016	846	1080	977
300	1232	1050	-	1025	942	1080	977
400	1269	1100	-	1033	1055	1080	977
500	1280	1100	1354	1041	1184	1600	977
600	1310	1100	-	1050	1330	1080	911

Specific heat is the amount of heat (i.e., energy) required to raise the temperature of a unity mass (i.e., weight) of any material by one degree (i.e., per unit temperature rise). Specific heat changes with temperature due to chemical and physical changes that occur in cement past and aggregates when in heating. According to fib Bulletin 38 (2007) [55] and Kodur et al. (2020) [37], specific heat around 100°C increases because of evaporation of moisture present in the form of free water (Figure 6). Between 100°C–300°C, specific heat increases further due to the evaporation of moisture present in the remaining free water, in addition to the adsorbed and bonded water. In 300-500°C range, the Cp value remains almost constant because of the counteracting effects of decrease in moisture due to complete evaporation of free water and the increase in humidity due to Ca(OH)2 decomposition. There is a small increase in Cp after this temperature due to the release of moisture from the decomposition of the C–S–H gel and significant deterioration of the microstructure within the concrete.

In the case of the UHPC, Figure 6a and Table 7a show that at 25°C its specific heat is 1009 J/kg.k. This means that the amount of energy required to increase the temperature of 1 kg of UHPC by 1K is 1009 J. At the same temperature, these values are similar to those presented by Shin et al. (2002) [8] for NSC, by Kodur and Khaliq (2011) [4] for HSC and Kodur and Sultan (2003) [7] by HSC with carbonate aggregate. however, the UHPC value at 25°C (Table 7a) was lower than those reported by EN 1992 for the NSC (Table 7b), for the UHPC evaluated by
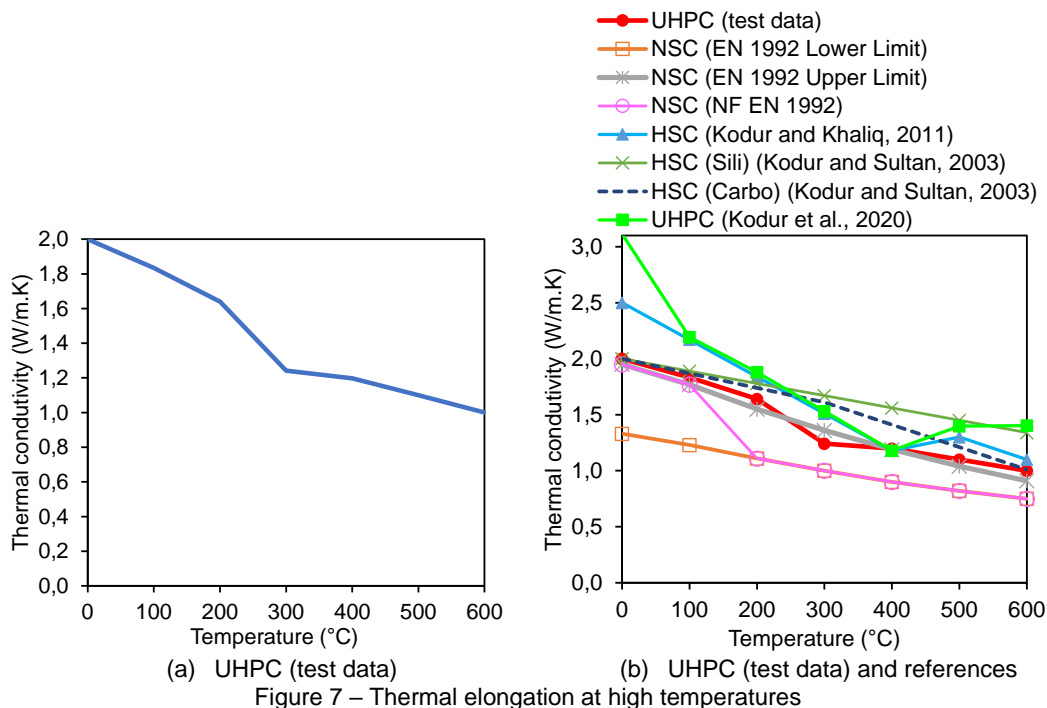
Kodur et al. (2020) [27] (Table 7e), and also for HSC with siliceous aggregates proposed by Kodur and Sultan (2003) [7] (Table 7f).

According to Figure 6a and Table 7a, at 100°C, the Cp of the UHPC tested increased to 1229 J/kg.K. At the end of the tests (600°C) the value was 1310 J/kg.K. For the equations proposed in section 5, the value of the specific heat in the range from 100 to 600°C was defined as the average of the C_p readings in this temperature range (i.e., 1270 J/kg.K). This is a practical simplification of fire design since there is variability between the results, according to Table 7.

In the temperature range 100-600°C, the same interpretation and comparison made at 25°C between researches is preserved (Table 7a-g). However, the research of Kodur et al. (2020) [37] for UHPC (Table 7e) and Kodur and Sultan (2003) [7] (Table 7f) for HSC, which at initial temperatures (i.e., 25 °C) did not converge with the UHPC of this research, tends to converge at the end of analysis. Normally the UHPC of this research (Table 7a) has a specific heat relatively higher in relation to the others concretes. It can be attributed to the lower permeability and dense microstructure of UHPC that requires more heat for evaporation of water.

3.2.2 Conductivity

Figure 7a plots the thermal conductivity of UHPC for various temperature ranges. Figure 7b and Table 8 show the comparison of these results with bibliography.

(a) UHPC (test data)   (b) UHPC (test data) and references
Figure 7 – Thermal elongation at high temperatures

Thermal conductivity variation in concrete with temperature is governed by the change in moisture levels in fire. Concrete moisture decreases with increasing temperature and therefore thermal conductivity decreases at high temperatures. At temperatures above 100°C, free water starts to evaporate, sometimes causing spalling. When the concrete temperature reaches about 300°C, the adsorbed water from the calcium silicate hydrate (C─S─H) gel and a part of the chemically bound water begin to evaporate. The concrete temperature further to 400°C causes decomposition of Ca(OH)2, converting it into CaO and H2O, increasing the moisture content of concrete. Further

increase in temperature beyond 500°C leads to decomposition of C─S─H and further deterioration of concrete and aggregate.

According to Figure 7b and Table 8, it can be seen that the UHPC in this research (Table 8a) are, respectively, 50.4%, 2.6% and 2.6% higher in relation to the NSC proposed by EN 1992-1.2 [18] (Table 8b and c) and NF EN 1992 [53] (Table 8d). Research by Kodur et al. (2020) [37] show that the UHPC had a conductivity 55% higher than those obtained in this research. After 300°C, the values between both researches tend to converge. In relation to the NSC proposed by the EN 1992-1.2, the UHPC tested by Kodur et al. (2020) were 133.8% higher. The notable variability in these results is understandable, and can be attributed to varying moisture content, cement type, aggregate, test conditions and measurements techniques used in each research, as explain by Kodur et al. (2020) [37], Kodur et al. (2019) [52], Bazant and Kaplan (1996) [54].

Table 8 – Thermal conductivity: correlation between UHPC and references

Temperature (°C)	UHPC Test Data	NSC EN 1992 (lower limit)	NSC EN 1992 (Upper limit)	NSC NF EN 1992	NSC (Shin et al., 2002)	HSC (Kodur Khaliq, 2011)	UHPC (Kodur et al., 2020)	HSC - Sili (Kodur and Sultan,2003)	HSC - Carbo (Kodur and Sultan,2003)
	(a)	(b)	(c)	(d)	(e)	(f)	(g)	(h)	(i)
25	2.00	1.33	1.95	1.95	2.19	2.42	3.11	1.97	1.97
100	1.83	1.23	1.77	1.77	-	2.17	2.19	1.89	1.87
200	1.64	1.11	1.55	1.11	-	1.84	1.88	1.78	1.74
300	1.24	1.00	1.36	1.00	-	1.51	1.53	1.67	1.61
400	1.20	0.90	1.19	0.90	-	1.18	1.18	1.56	1.41
500	1.10	0.82	1.04	0.82	1.28	1.30	1.40	1.45	1.21
600	1.00	0.75	0.91	0.75	-	1.10	1.40	1.34	1.00

4. CONCLUSIONS

The general conclusions of this paper are:

- The superior durability of UHPC proposes a concrete matrix almost impermeable to the chemical attack, as already demonstrated by the references. However, its impermeable matrix influences its fire performance, which may cause spalling;
- This research demonstrated that UHPC specimens tested before 700 days are susceptible to concrete spalling;
- The reduction in the compressive strength of UHPC starts at around 400°C;
- In relation to normal strength (NSC) and high strength concretes (HSC) and ultra-high strength concrete (UHSC), UHPC had the lowest mechanical strength loss (partial factor) for each temperature range;
- When compared to NSC (according to EN 1992-1.2 parameters), UHPC showed higher thermal diffusivity;
- In this sense, in relation to NSC, UHPC will have a higher average temperature. However, for each temperature range, it loses less strength than NSC;
- When compared to NSC and HSC, UHPC has the lowest thermal elongation;
- The density of UHPC has a more evident reduction in the range of 100 to 300°C, mainly due to dehydration of the compounds and volatilization of the PVA fibers;
- UHPC has a specific heat higher in relation to the others concretes (NSC, HSC). It can be attributed to the lower permeability and dense microstructure of UHPC that requires more heat for evaporation of water;
- Thermal conductivity of UHPC is also higher than NSC. Steel fibers can justify these results;

REFERENCES

[1.]   ASTM C1856. Standard Practice for Fabricating and Testing Specimens of Ultra High-Performance Concrete. ASTM International, West Conshohocken, United States (2017).

[2.]   Y Zhu, H Hussein, A Kumar, G Chen. A review: Material and structural properties of UHPC at elevated temperatures or fire conditions. Cement and Concrete Composites. (2021) V123. https://doi.org/10.1016/j.cemconcomp.2021.104212

[3.]   MX Xiong, JTR Liew. Mechanical behaviour of ultra-high strength concrete at elevated temperatures and fire resistance of ultra-high strength concrete filled steel tubes. Materials and Design (2016). v. 104, pp. 414-427. https://doi.org/10.1016/j.matdes.2016.05.050

[4.]   VKR Kodur, W Khaliq. Effect of Temperature on Thermal Properties of Different Types of High-Strength Concrete. Journal of Materials in Civil Engineering (ASCE) (2011) V.15, Issue 2. https://doi.org/10.1061/(ASCE)0899-1561(2003)15:2(101)

[5.]   M Li, CX Qian, W Sun. Mechanical properties of high-strength concrete after fire. Cement and Concrete Research (2004). V.34, Issue 6, pp.1001-1005. https://doi.org/10.1016/j.cemconres.2003.11.007

[6.]   CS Poon, ZH Shui, L Lam. Compressive behavior of fiber reinforced high-performance concrete subjected to elevated temperatures. Cement and Concrete Research (2004). V.34, Issue 12. https://doi.org/10.1016/j.cemconres.2004.02.011

[7.]   VKR Kodur, MA Sultan. Effect of Temperature on Thermal Properties of High-Strength Concrete. Journal of Materials in Civil Engineering (2003). V.15, Issue 2 https://doi.org/10.1061/(ASCE)0899-1561(2003)15:2(101)

[8.]   KY Shin, SB Kim, JH Kim, M Chung, PS Jung. Thermo-physical properties and transient heat transfer of concrete at elevated temperatures. Nuclear Engineering and Design (2002). V.212, pp.233-241. https://doi.org/10.1016/S0029-5493(01)00487-3

[9.]   R Ullah, Y Qiang, J Ahmad, NI Vatin, MA El-shorbagy MA. Ultra-High-Performance Concrete (UHPC): A State-of-the-Art Review. Materials (2022). V15, pp.4431. https://doi.org/10.3390/ma15124131

[10.]   AH Akca, NO Zihnioglu. High performance concrete under elevated temperatures. Construction and Building Materials (2013). V44, pp.317-328. https://doi.org/10.1016/j.conbuildmat.2013.03.005

[11.]   X Liang, C Wu, Y Su, Z Chen, Z Li. Development of ultra-high performance concrete with high fire resistance. Construction and Building Materials (2018). V. 179, pp. 400-412. https://doi.org/10.1016/j.conbuildmat.2018.05.241

[12.]   S Banerji, VKR Kodur. Effect of temperature on mechanical properties of ultra-high-performance concrete. Fire and Materials (2021). V.46, pp. 287-301 https://doi.org/10.1002/fam.2979

[13.]   G Choe, G Kim, N Gucunski, S Lee. Evaluation of the mechanical properties of 200 MPa ultra-high-strength concrete at elevated temperatures and residual strength of column. Construction and Building Materials (2015). V86, pp.159-168. https://doi.org/10.1016/j.conbuildmat.2015.03.074

[14.]   M Abid, X Hou, W Zheng, RR Hussain. Effect of fibers on high-temperature mechanical behavior and microstructure of reactive powder concrete. Materials (2019). V.12, pp.1-30. https://doi.org/10.3390/ma12020329

[15.]   S Sanchayan, SJ Foster. High temperature behaviour of hybrid steel–PVA fibre reinforced reactive powder concrete. Materials and Structures (2016). V.49, pp.769-782. https://doi.org/10.1617/s11527-015-0537-2

[16.]   C Laneyrie, AL Beaucour, MF Green, RL Hebert, B Ledesert, A Noumowe. Influence of recycled coarse aggregates on normal and high-performance concrete subjected to elevated temperatures. Construction and Building Materials (2016). V.111, pp. 368-378. https://doi.org/10.1016/j.conbuildmat.2016.02.056

[17.]   B Luo, C Deng, Y Luo (2022). Mechanical properties and microstructure of UHPC with recycled glasses after exposure to elevated temperatures. Journal of Building Engineering (2022). V.62, pp.105369. https://doi.org/10.1016/j.jobe.2022.105369

[18.] EN 1992-1.2. Eurocode 2: Design of concrete structures - Part 1-2: General rules - Structural fire design. Brussels, Belgium (2004).

[19.] ACI 216. Code Requirements for Determining Fire Resistance of Concrete and Masonry Construction Assemblies. American Concrete Institute (ACI). Farmington Hills, Michigan, United States (2014).

[20.] AS 3600. Concrete Structures. Australian Standard. Sydney, Australia (2018).

[21.] NZS 3101. Concrete structures standard. The design of concrete structures. Standards New Zealand. Wellington, New Zealand (2006).

[22.] NBR 15200. Design of reinforced concrete structures in case of fire. Brazilian Standard Association, Rio de Janeiro [in Portuguese] (2012).

[23.] J Du, W Meng, KH Khayat, Y Bao, P Guo, Z Lyu, A Abu-obeidah, H Nassif, H Wang. New development of ultra-high-performance concrete (UHPC). Composites Engineering (2021) V224. https://doi.org/10.1016/j.compositesb.2021.109220

[24.] K Wille, AE Naaman, GJ Parra-Montessinos. Ultra-High Performance Concrete with Compressive Strength Exceeding 150 MPa (22 ksi): A Simpler Way. ACI Materials Journal (2011). V.108, pp.46-34. https://doi.org/10.14359/51664215

[25.] K Habel, M Viviani, E Denarié, E Bruhwiller. Development of the mechanical properties of an Ultra-High Performance Fiber Reinforced Concrete (UHPFRC). Cement and Concrete Research (2006). V36, Issue 7, pp.1362-1370. https://doi.org/10.1016/j.cemconres.2006.03.009

[26.] X Zhang, X Wu, D Zhang, Q Huang, B Chen. Axial compressive behaviors of reinforced concrete composite column with precast ultra-high-performance concrete (UHPC) jacket. Journal of Building Engineering (2022). V.48, pp.103956. https://doi.org/10.1016/j.jobe.2021.103956

[27.] H Tian, Z Zhou, Y Wei, L Zhang. Experimental and numerical investigation on the seismic performance of concrete-filled UHPC tubular columns. Journal of Building Engineering (2022). V.43, pp. 103118. https://doi.org/10.1016/j.jobe.2021.103118

[28.] F Zhou, Q Su, Y Cheng, H Wu. A novel dynamic constitutive model for UHPC under projectile impact. Engineering Structures (2023). V. 280, pp.115711. https://doi.org/10.1016/j.engstruct.2023.115711

[29.] P Zhang, J Shang, Y Liu, J Shao, D Gao, Z Dong, SA Sheikh. Flexural behavior of GFRP bar-reinforced concrete beams with U-shaped UHPC stay-in-place formworks. Journal of Building Engineering (2022). V.45, pp. 103403. https://doi.org/10.1016/j.jobe.2021.103403

[30.] XY Zhang, MX Fan, YX Zhou, DD Ji, JH Li, R Yu. Development of a sustainable alkali activated ultra-high performance concrete (A-UHPC) incorporating recycled concrete fines. Journal of Building Engineering (2023). V.67, pp.105986. https://doi.org/10.1016/j.jobe.2023.105986

[31.] Y Li, X Zeng, Y Shi, K Yang, J Zhou, HA Umar, G Long, Y Xie. A comparative study on mechanical properties and environmental impact of UHPC with belite cement and portland cement. Journal of Cleaner Production (2023). V.380, pp.135003. https://doi.org/10.1016/j.jclepro.2022.135003

[32.] Y Cui, Y Li, Q Wang. Engineering performance and expansion mechanism of MgO expansion agent in ultra-high performance concrete (UHPC). Journal of Building Engineering (2023). V.68, pp.106079. https://doi.org/10.1016/j.jobe.2023.106079

[33.] SFPE. Handbook of fire protection engineering. Society of Fire Protection Engineers, 4th Ed., Cleveland (2008).

[34.] JJ Park, DY Yoo, S Kim, SW Kim. Benefits of synthetic fibers on the residual mechanical performance of UHPFRC after exposure to ISO standard fire. Cement and Concrete Composites (2019). V.104. https://doi.org/10.1016/j.cemconcomp.2019.103401

[35.] C Kahanji, F Ali, A Nadjai, N Alam. Effect of curing temperature on the behaviour of UHPFRC at elevated temperatures. Construction and Building Materials (2018). V182, pp.670-681. https://doi.org/10.1016/j.conbuildmat.2018.06.163

[36.] DX Xuan, ZH Shui. Rehydration activity of hydrated cement paste exposed to high temperature. Fire and Materials (2010) V.35, Issue 7. https://doi.org/10.1002/fam.1067

[37.] VKR Kodur, S Banerji, R Solhmirzaei. Effect of Temperature on Thermal Properties of Ultrahigh-Performance Concrete. ASCE Journal of Materials in Civil Engineering (2020). V.32. https://doi.org/10.1061/(ASCE)MT.1943-5533.0003286

[38.] J Yang, GF Peng, J Zhao, GS Shui. On the explosive spalling behavior of ultra-high performance concrete with and without coarse aggregate exposed to high temperature. Construction and Building Materials (2019). V.226, pp.932-944. https://doi.org/10.1016/j.conbuildmat.2019.07.299

[39.] NBR 16697. *Portland cement - Requirements*. Brazilian Standard Association, Rio de Janeiro [in Portuguese] (2018).

[40.] R Christ, BF Tutikian, PRL Helene. Proposition of Mixture Design Method for Ultra-High- Performance Concrete. ACI (American Concrete Institute) Materials Journal, (2022) V.119, pp.79-89. https://doi.org/10.14359/51734191

[41.] ASTM C470. Standard Specification for Molds for Forming Concrete Test Cylinders Vertically. American Society for Testing and Materials, West Conshohocken, United States (2016).

[42.] ASTM C39. Standard Test Method for Compressive Strength of Cylindrical Concrete Specimens. American Society for Testing and Materials, West Conshohocken, United States (2022).

[43.] ASTM C469. Standard Test Method for Static Modulus of Elasticity and Poisson's Ratio of Concrete in Compression. American Society for Testing and Materials, West Conshohocken, United States (2022).

[44.] ASTM C31. Standard Practice for Making and Curing Concrete Test Specimens in the Field. American Society for Testing and Materials, West Conshohocken, United States (2022).

[45.] ASTM C192. Standard Practice for Making and Curing Concrete Test Specimens in the Laboratory. American Society for Testing and Materials, West Conshohocken, United States (2020).

[46.] ASTM E1461-13. Standard Test Method for Thermal Diffusivity by the Flash Method. American Society for Testing and Materials, West Conshohocken, United States (2022).

[47.] RILEM TC 129-3 Test methods for mechanical properties of concrete at high temperatures: compressive strength. International Union of Laboratories and Experts in Construction, Materials, Systems and Structures. Cité Descartes, France (1995).

[48.] RILEM TC 129-5 Test methods for mechanical properties of concrete at high temperatures: modulus of elasticity. Cité Descartes, France (2000).

[49.] ASTM E228. Standard Test Method for Linear Thermal Expansion of Solid Materials with a Push-Rod Dilatometer. American Society for Testing and Materials, West Conshohocken, United States (2017).

[50.] G Manica, FL Bolina, BF Tutikian, M Oliveira, MA Moreira. Influence of curing time on the fire performance of solid reinforced concrete plates. Journal of Materials Research and Technology (2020). V.9, pp2506-2512. https://doi.org/10.1016/j.jmrt.2019.12.081

[51.] D Zang, Y Liu, KH Tan. Spalling resistance and mechanical properties of strain-hardening ultra-high performance concrete at elevated temperature. Construction and Building Materials (2021). V.266. https://doi.org/10.1016/j.conbuildmat.2020.120961

[52.] VKR Kodur, S Banerji, R Solhmirzaei. Test methods for characterizing concrete properties at elevated temperatures. Fire and Materials (2019). V.44, pp.381-395. https://doi.org/10.1002/fam.2777

[53.]   NF EN 1992-1.2. Design of concrete structures - Part 1-2: general rules - Structural fire design - National annex to NF EN 1992-1-2. France (2005).

[54.]   ZP Bazant, MF Kaplan. Concrete at temperatures: Material properties and mathematical models. Essex, UK: Longman Group (1996).

[55.]   FIB Bulletin 38. Fire design of concrete structures – materials, structures and modelling – state of art report. Fédération Internationale du Béton, 97p (2007).

NUMERICAL MODEL FOR CELLULAR STEEL BEAMS UNDER FIRE SITUATION SUBJECTED TO THE LATERAL-TORSIONAL BUCKLING

Caroline C. de Faria a,*; Hermes Carvalho b; Ricardo H. Fakury c; João Paulo C. Rodrigues d

ABSTRACT

The present study focuses on the development and validation of a numerical model to evaluate cellular steel beams subjected to the lateral-torsional buckling under fire situation. All sides of the beams are exposed to the standard ISO 834 fire curve. The beams are simply supported and subjected to uniform bending. Firstly, thermal and mechanical models are developed using ABAQUS *software*. The numerical models are validated by comparing their results to numerical and experimental results from the literature. The numerical thermal analysis is also compared with a simplified model, which uses analytical methods to determine the temperature at the flanges and the web. The proposed numerical model is used to obtain moment resistance curves for cellular beams at 200ºC, 300ºC, 400ºC, 500ºC, 600ºC, 700ºC, and 800ºC.

Keywords: Numerical model; Fire situation; Cellular steel beams; Lateral-torsional buckling.

1. INTRODUCTION

The lateral-torsional buckling (LTB) is a global limit state for steel members under flexure, which presents a lateral displacement and a torsion of the cross-section. For cellular steel beams, this limit state can be impacted by the cross-section discontinuity and the presence of web openings [1, 2]. The behavior of cellular steel beams subjected to the LTB has been extensively investigated at room temperature [1-7]. The LTB elastic critical moment and the moment gradient factor for cellular steel beams were investigated by [1, 2]. At room temperature, [3, 4] conducted experiments on cellular beams simply supported. Procedures to assess the LTB moment resistance at room temperature and fire situation can be found in [3-7] and [7, 9], respectively. Moreover, a series of numerical and experimental studies have been conducted to evaluate the behavior of cellular beams under fire situation [7-13].

In this study, a numerical model is developed and validated to evaluate cellular beams subjected to the LTB under fire situation. Thermal and mechanical finite element models are created using ABAQUS *software*. For the thermal models, the beams are exposed to the standard ISO 834 fire [14] at all sides. The thermal model is validated against numerical and experimental results from the literature [11-13]. The mechanical model is validated by comparing its results to the numerical and experimental results from [15], but considering the measured temperatures. Thereafter, the proposed numerical model is used to determine moment resistance curves for cellular steel beams at different temperatures [7].

ᵃ,* Department of Structural Engineering, Federal University of Minas Gerais (carolinecf@ufmg.br, linkedin.com/in/carolinefaria)**.**

ᵇ Department of Structural Engineering, Federal University of Minas Gerais (hermes@dees.ufmg.br).

ᶜ Department of Structural Engineering, Federal University of Minas Gerais (fakury@dees.ufmg.br)**.**

ᵈ Department of Structural Engineering, Federal University of Minas Gerais & Department of Civil Engineering, University of Coimbra (jpaulocr@dec.uc.pt)**.**

2. METHODOLOGY

2.1 Thermal model

The cellular steel beams were simulated using DS4 shell elements from the ABAQUS library for thermal analysis. The element size was a function of the geometry and taken as the minimum among 10 mm, $b_f/12$, $w/4$, and $H/24$, as depicted in Figure 1, where b_f and t_f are the flange width and thickness, respectively, t_w is the web thickness, H is equal to the beam height (d_g) minus the flange thickness, D is the opening diameter, and L_b is the beam length.
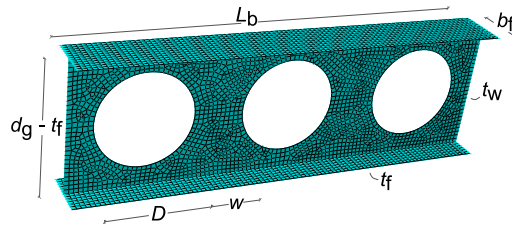

Figure 1: Geometry and mesh details

The unit mass of steel ρ_a was taken as 7850 kg/m³. Discrete points from the curves given in [16] were used to define the steel specific heat, c_a, and the thermal conductivity in the numerical models, as shown in Figure 2.
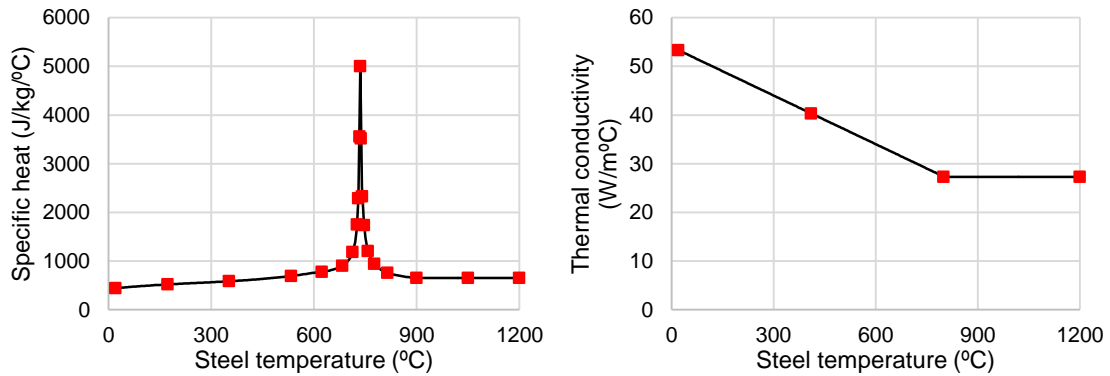
Figure 2: Steel thermal properties [16]

The numerical cross-section temperatures were obtained using the *Heat Transfer* method from ABAQUS. All sides of the beams were exposed to the ISO 834 fire [14], as illustrated in Figure 3. The time step of 5 s, the Stefan Boltzmann constant, and the absolute zero were assigned to the models. The convective heat flux coefficient and the emissivity were taken as 25 W.m^{-2}.K^{-1} and 0.7, respectively, unless stated otherwise.
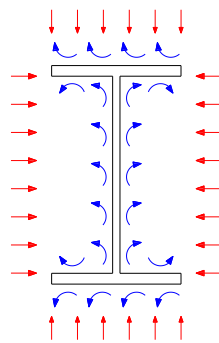
Figure 3: Radiative (red lines) and convective (blue lines) heat fluxes for beams with all sides exposed to fire

Although the numerical thermal model provides detailed information regarding the temperature at the elements of the cross-section at each time step, the size of the generated files and the convergence problems are obstacles to performing a comprehensive parametric study. Therefore, the numerical model was compared to a simplified model,

704

in which the average flange ($\theta_{f,a}$) and web ($\theta_{w,a}$) temperatures were calculated using Equation 1, considering the section factor, A/V, equal to $2/t_f$ and $2/t_w$, respectively. In this equation, $\Delta\theta_{a,t}$ is the increase in temperature, φ_t is the heat flux, and Δt is the time interval, which was taken as 1 s.

$$\Delta\theta_{a,t} = \frac{(A/V)}{c_a\rho_a} \varphi_t \, \Delta t \tag{1}$$

Two methods to include the fire effects in the mechanical models were evaluated:

(i) Method M1: the data generated from the numerical thermal analysis at time t_{target} was assigned to the beams, where t_{target} is the time in which the flange reaches the target temperature;

(ii) Method M2: no temperatures were assigned, instead the degenerated steel properties corresponding to the analytical temperatures at the time t_{target}, $\theta_{f,a}$ and $\theta_{w,a}$, were directly assigned to the flanges and the web, respectively.

2.2 Mechanical model

For the mechanical analysis, S4 shell elements were considered. The stress-strain model from [16] was used to describe the mechanical behavior of steel at elevated temperatures, as given in Figure 4. The Young's modulus of steel and the yield strength (f_y) at room temperature were taken as 200 GPa and 345 MPa, respectively, and the Poisson ratio was taken as 0.3.
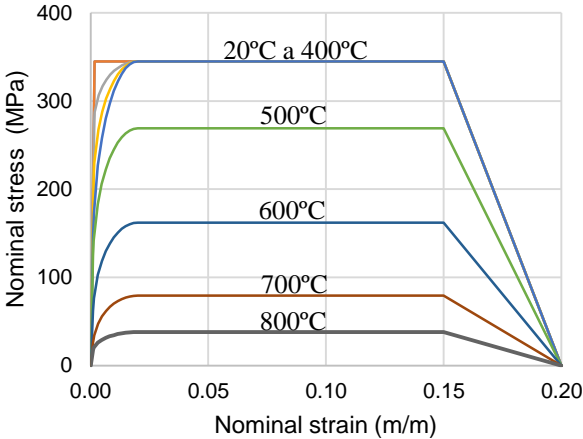
Figure 4: Steel mechanical properties at elevated temperatures

The cellular steel beams were simply supported, and subjected to uniform bending, which was accomplished by applying a pair of opposite-distributed loads at the upper and lower flanges, as shown in Figure 5. Torsional and out-of-plane displacements were restrained at both ends of the beams. Vertical displacements were prevented at the web at the ends, and the longitudinal displacement was restricted at one end.
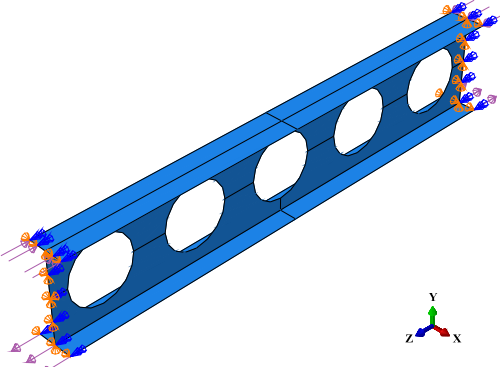
Figure 5: Loading and boundary conditions

Buckling analyses were performed to determine the elastic critical moment associated with the lateral-torsional buckling ($M_{cr,\theta,FEM}$). The moment resistance ($M_{Rk,\theta,FEM}$) was obtained through nonlinear static analysis, considering an initial imperfection with a sinusoidal shape and magnitude equal to $L_b/1000$. Residual stresses were not considered under fire situation.

The resistance curves for cellular beams were determined considering a fixed cross-section temperature at time t_{target}, using one of the two methods described in Section 2.1, and increasing the load until failure. In order to enable comparison among the different cross-sections evaluated, the flange temperature was taken as a reference. The following target flange temperatures were evaluated: 200ºC, 300ºC, 400ºC, 500ºC, 600ºC, 700ºC, and 800ºC.

3. RESULTS

3.1 Thermal model validation

The numerical model from Section 2.1 was validated by comparison with the experimental results from Bailey [11] and Mesquita *et al* [13], and a numerical model from Wang *et al* [12]. In order to represent the results from [11-13], some adjustments were made in the numerical models. Firstly, the models to represent the experiments from [11, 13] were exposed to fire on three sides. Secondly, the model from [13] accounted for the ceramic material at the top flange described in [13]. Finally, in the numerical model to simulate the results from [12], all the sides of the beams were exposed to the fire and the emissivity factor was taken as 0.5, as given in [12]. A comparison between the numerical thermal model (FEM) and the results from [11-13] is given in Figures 6, 7, and 8.

The numerical model overestimated the temperature evolution obtained by [11], but satisfactorily represented the experimental results from [13]. It can also be observed that the proposed model presented an excellent agreement with the numerical model of [12]. Therefore, due to the difficulty of controlling and measuring the temperature during the experiments, and the good agreement with [12], it was considered that the proposed thermal model can represent the temperature evolution in beams exposed to the standard fire.

The thermal numerical model was also compared to a simplified model. The temperatures obtained numerically and analytically for the flanges and the web components are shown in Figure 9. Figure 10 shows the moment resistances obtained considering method M1, which uses the numerical thermal analysis results, and method M2, which uses steel degenerated properties at the established target times. In these figures, the cellular beams were considered made from W 360x79 profile, where the ratio d_g/d_p between the cellular beam height and its parent section height was taken as 1.5. The opening diameter was equal to 0.7 d_g, the spacing between openings was taken as 0.186 m, the beam length varied from 1.6 m to 10 m, and the yield strength of steel was taken as 345 MPa. As can be seen, the temperatures obtained by the two methods presented an excellent agreement. Besides, the moment resistances presented differences of less than 3% for all cases evaluated. Therefore, due to its simplicity and coherent results, the method M2 was proposed to evaluate the moment resistance curves for cellular beams under fire situation.

Figure 6: Temperature evolution at points C7 and C16 of beam exposed to the ISO 834 fire [14] at three sides obtained experimentally [11] and numerically
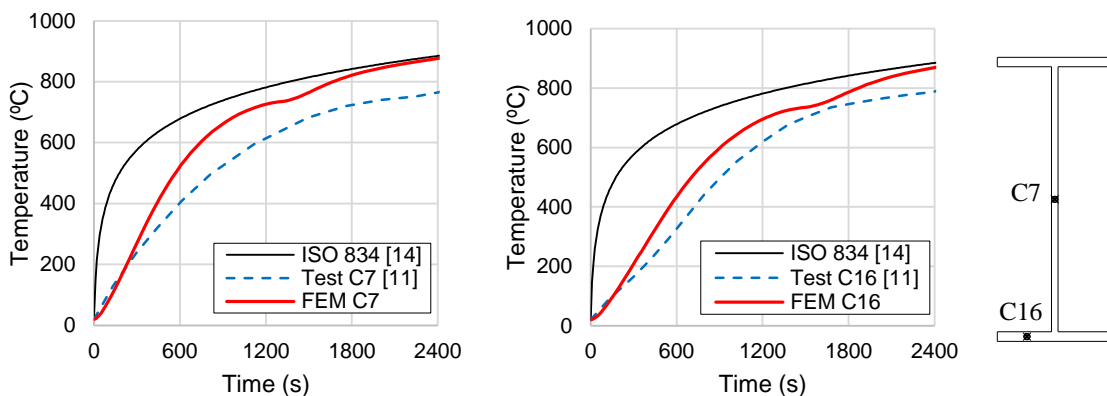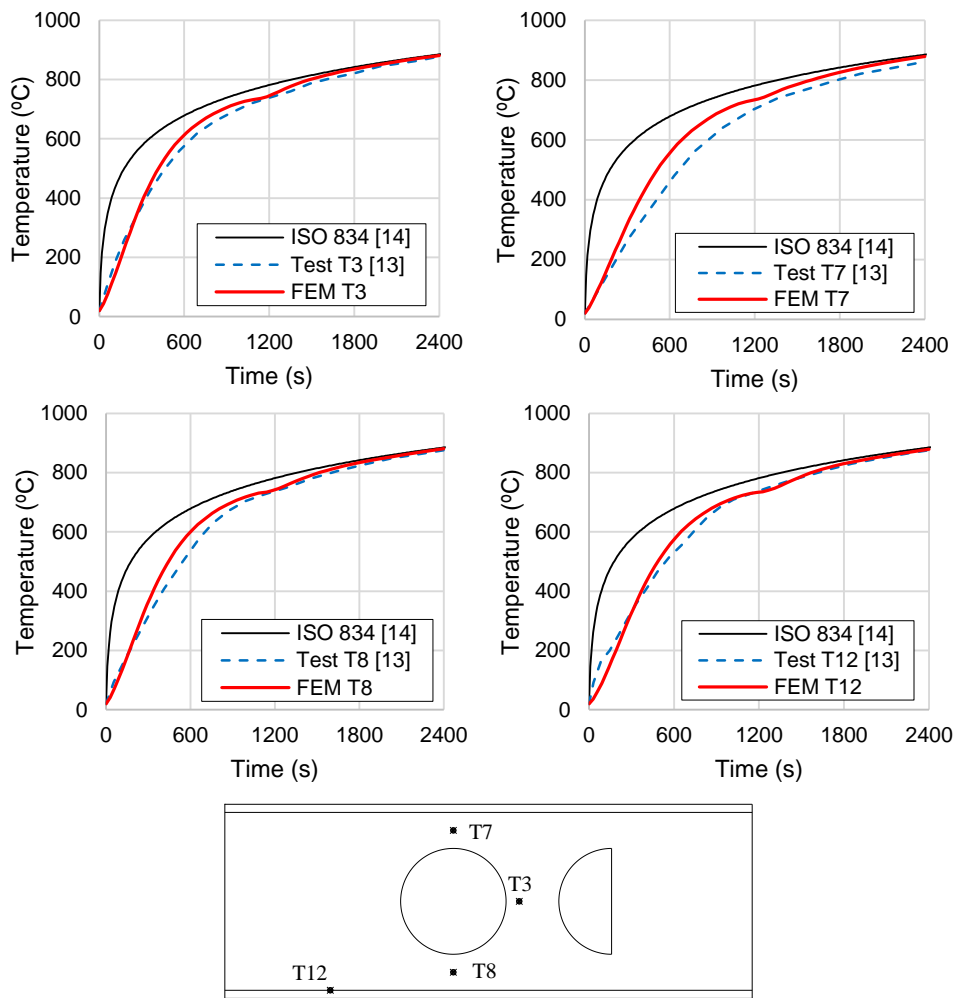
Figure 7: Temperature evolution at points T3, T7, T8, and T12 of beam exposed to the ISO 834 fire [14] at three sides obtained experimentally [13] and numerically
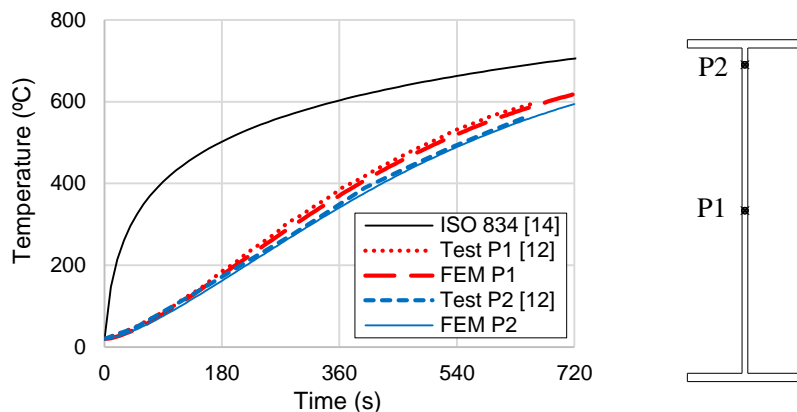
Figure 8: Temperature evolution at points P1 and P2 of beam exposed to the ISO 834 fire [14] at all sides obtained through numerical models
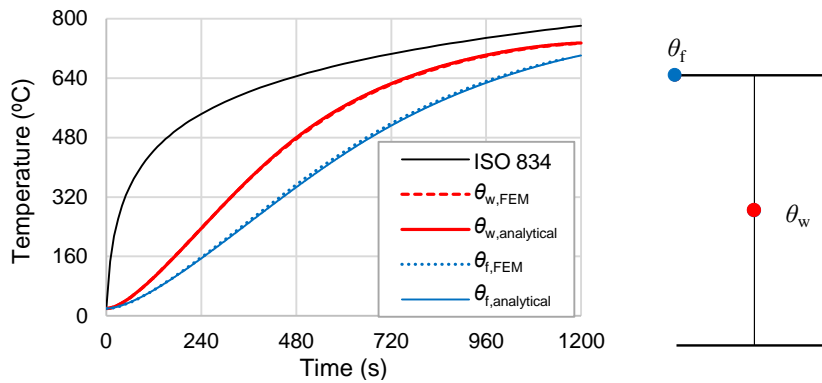
Figure 9: Flange and web temperatures obtained analytically and through the thermal numerical model
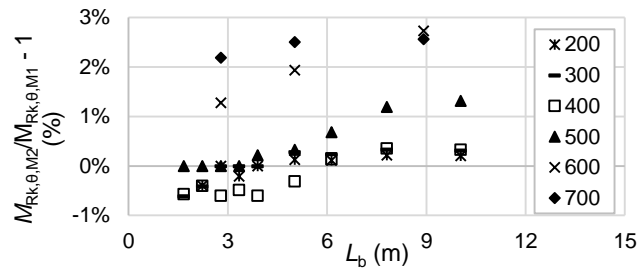
Figure 10: Moment resistance differences obtained using the methods M1 and M2

3.2 Mechanical model validation

The proposed numerical model was validated against three experiments and the numerical models from Prachar *et al* [15]. These authors evaluated steel beams subjected to lateral-torsional buckling at elevated temperatures. Initially, the authors aimed to reach a uniform temperature, but a temperature gradient was observed [15]. The proposed numerical model was used to simulate these experiments, but considering the average temperatures for the upper flange, web, and lower flange, as given in [15]. Figure 11 shows the moment resistance *versus* the mid-span vertical displacement obtained by [15] and through the proposed numerical model.

Overall, the numerical model from [15] and the proposed one were conservative compared to the experimental results, with moment resistance differences of -25%, -21%, and 4%, respectively, for tests 5, 6, and 7. The discrepancy between experimental and numerical results could be related to the temperature variation during the tests, the variation of temperature along the cross-section, boundary conditions problems, and the heating process [15]. Nevertheless, due to the complexity of experiments at elevated temperatures, it was considered that the proposed numerical model presented conservative and coherent results. Moreover, the proposed numerical model predicted the LTB failure and had an excellent agreement with the numerical model from [15]. Therefore, the proposed model was considered satisfactory for developing a parametric study.
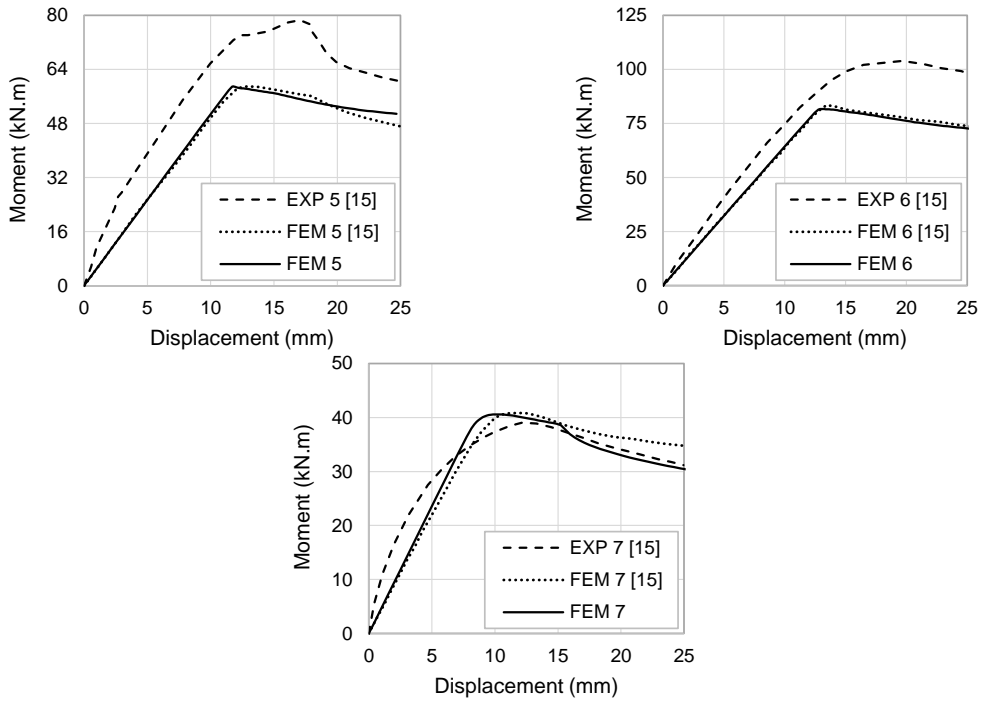
Figure 11: Moment resistance *versus* mid-span deflection obtained experimentally [15] and through numerical models

3.3 LTB resistance curves

In this study, the following target flange temperatures ($\theta_{f,target,i}$) were evaluated: 200ºC, 300ºC, 400ºC, 500ºC, 600ºC, 700ºC, and 800ºC. In total, twenty cross-sections were investigated [7]. For each cross-section geometry, the time in which the flange temperature reaches the current target value, $t_{target,i}$, was calculated using Equation 1 assuming the section factor equal to $2/t_f$. Afterward, the web temperature $\theta_{w,i}$ at time $t_{target,i}$ was determined using Equation 1, but considering the section factor equal to $2/t_w$. Then, the steel degenerated properties at temperatures $\theta_{f,target,i}$ and $\theta_{w,i}$ were determined using the EN 1993-1-2 provisions [16], and assigned to the numerical mechanical models. The loading, boundary conditions, and other details were given in Section 2.2.

Representative resistance curves for $\theta_{f,target}$ equal to 300ºC and 700ºC are depicted in Figure 12, where the LTB slenderness ($\bar{\lambda}_{LT,\theta}$) is given by:

$$\bar{\lambda}_{LT,\theta} = \sqrt{\frac{M_{y,\theta}}{M_{cr,\theta,FEM}}} \tag{2}$$

where $M_{y,\theta}$ is the section modulus (W_y) multiplied by the yield strength of steel corresponding to the target flange temperature.
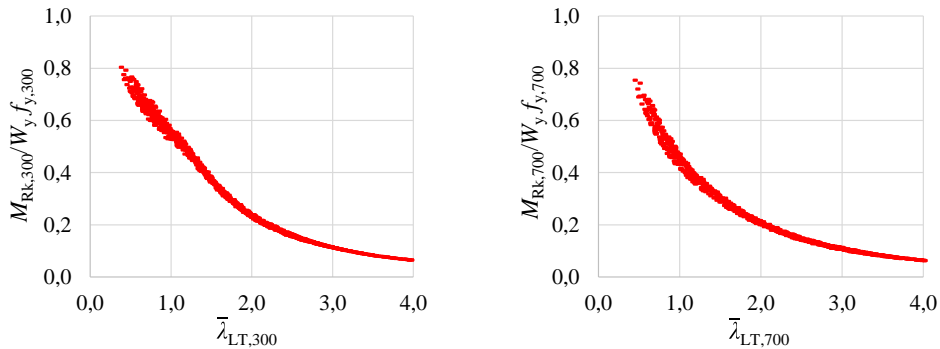
Figure 12: Moment resistance curves for cellular steel beams under uniform bending at elevated temperatures for the cases of (a) $\theta_{f,target}$ = 300ºC, and (b) $\theta_{f,target}$ = 700ºC

4. CONCLUSIONS

In this study, a numerical model was developed and validated to investigate the behavior of cellular steel beams subjected to lateral-torsional buckling (LTB) at elevated temperatures. The cellular beams were simply supported and subjected to uniform bending. Thermal and mechanical numerical models were created using ABAQUS *software*. Two methods to include the fire effect in the mechanical analysis were evaluated: M1 and M2, which considers, respectively, the results from the numerical thermal analysis and analytical temperatures determined according to [16].

Overall, the thermal model was able to represent the results from [11-13]. The mechanical model predicted the LTB failure, presenting reasonable agreement with the experimental results from [15], and excellent agreement with the numerical model from [15]. The methods M1 and M2 showed differences between the moment resistances of less than 3% for all cases investigated. Therefore, due to its simplicity, method M2 was proposed to perform the parametric study. Finally, representative moment resistance curves were given for cellular steel beams subjected to the LTB at elevated temperatures.

ACKNOWLEDGEMENTS

REFERENCES

[1] Sweedan, A. M. I (2011). *Elastic lateral stability of I-shaped cellular steel beams, Journal of Constructional Steel Research*, vol. 67, 2011, p. 151-163.

[2] El-Sawy, K. *et al* (2014). *Moment gradient factor of cellular steel beams under inelastic flexure*, *Journal of Constructional Steel Research*, vol. 98, 2014, p. 20-34.

[3] Boissonnade, N. *et al* (2014). *Design of cellular beams against lateral torsional buckling*, *Structures and Buildings*, vol. 167, no. SB7, 2014, p. 436-444.

[4] Sonck, D. & Belis, J. (2015). *Lateral-torsional buckling resistance of cellular beams, Journal of Constructional Steel Research*, vol. 105, 2015, p. 119-128.

[5] Panedpojaman, P. *et al* (2016). *Cellular beam design for resistance to inelastic lateral-torsional buckling, Thin-Walled Structures*, vol. 99, 2016, p. 182-194.

[6] Ferreira, F. P. V. *et al* (2019). *Lateral-torsional buckling of cellular beams according to the possible updating of EC3, Journal of Constructional Steel Research*, vol. 153, 2019, p. 222-242.

[7] Faria, C. C. *et al* (2021). *Lateral-torsional buckling resistance of cellular steel beams at room temperature and fire situation, Engineering Structures,* vol. 237, 2021, 15 p.

[8] Kotapati, V. K & Khatri, A. P (2022). *Performance of cellular steel beam under fire, Asian Journal of Civil Engineering,* vol. 23, 2022, p. 1267-1276.

[9] Ferreira, F. P. V. *et al* (2022). *Lateral–torsional buckling resistance prediction model for steel cellular beams generated by Artificial Neural Networks (ANN), Thin-Walled Structures*, vol. 170, 2022, 108592.

[10] Oribi, S. B. *et al* (2021). *Investigation of residual stresses on the fire resistance of unrestrained cellular beams, Ce/Papers*, vol. 4, 2021, p. 1386-1394.

[11] Bailey, C. (2004). *Indicative fire tests to investigate the behaviour of cellular beams protected with intumescent coatings, Fire Safety Journal*, vol. 39, 2004, p. 689-709.

[12] Wang, P. *et al* (2016). *Web-post buckling of fully and partially protected cellular steel beams at elevated temperatures in a fire, Thin-Walled Structures*, vol. 98, 2016; p. 29-38.

[13] Mesquita, L. *et al* (2015). *Intumescent Fire Protection of Cellular Beams,* X Congresso de Construção Metálica e Mista, Coimbra, 2015, p. 623-630.

[14] International Organization for Standardization (1999). *ISO 834: Fire resistance tests – Elements of building construction, Part 1: General requirements*. Switzerland, 25 p.

[15] Prachar, M. *et al* (2016). *Experiments of Class 4 open section beams at elevated temperature, Thin-Walled Structures*, vol. 98, 2016, p. 2-18.

[16] European Committee for Standardization (2005). *EN 1993-1-2: Design of steel structures. Part 1.2: General rules – Structural fire design*. Brussels, 81 p.

SELF-COMPACTING CONCRETE AT HIGH TEMPERATURE: A LITERATURE REVIEW

Alessandro Simas Franchetto[a]; Ana Júlia Smolinski Gouveia[b*]; Ângela Gaio Graeff[c]; Mônica Regina Garcez[d].

[a*] Laboratory of Testing and Structural Modeling, Post Graduation Program in Civil Engineering: Construction and Infrastructure, LEME/PPGCI/UFRGS, alessandrosimasfranchetto@gmail.com

[b] Laboratory of Testing and Structural Modeling, Post Graduation Program in Civil Engineering: Construction and Infrastructure, LEME/PPGCI/UFRGS, anajulia.gouveia@gmail.com

[c] Laboratory of Testing and Structural Modeling, Post Graduation Program in Civil Engineering: Construction and Infrastructure, LEME/PPGCI/UFRGS, angela.graeff@ufrgs.br

[d] Post Graduation Program in Civil Engineering: Construction and Infrastructure, PPGCI-UFRGS, monica.garcez@ufrgs.br

ABSTRACT

Although self-compacting concrete exhibits excellent mechanical properties and might be used in many civil engineering applications, it might suffer from fire exposure due to specific characteristics such as high compactness and low permeability. From this perspective, the main objective of this paper is to assess previous literature about self-compacting concrete exposed to high temperatures, addressing research developments to date and discussing the potential use of self-compacting concrete according to the existing information. Although there are several studies on the effects of high temperatures on conventional concrete, there is still a gap in research addressing the effects of high temperatures on self-compacting concrete, mainly due to the variability of mix proportions, use of waste substitutes for conventional materials, circumstances not simulated experimentally, the tested specimen geometry, the heating rate, the maximum exposure temperature, and the residence time. Moreover, the self-compacting composition can comprise non-pozzolanic fines, pozzolanic fines, and viscosity-modifying additives, which modify the mechanical behavior at high temperatures. Additionally, published research on self-compacting concrete evaluates mainly the occurrence of spalling, not addressing residual mechanical properties after exposure to high temperatures. The variability in the parameters assessed by different experimental programs makes it difficult to compare the results, fomenting further studies and discussions on the subject.

Keywords: self-compacting concrete; high temperature; fire; residual behavior.

1. INTRODUCTION

Concrete shows better high-temperature performance than steel and timber due to lower thermal conductivity and non-combustibility. The state-of-the-art reports that under elevated temperatures, the matrix of conventional concrete undergoes chemical transformations, water vaporization, dehydration of compounds, and decomposition reactions. These reactions lead to changes in the microstructure of the hardened matrix, the appearance of microcracks and differential thermal movements, which directly impact the compressive strength of concrete [1, 2, 3, 4, 5, 6, 7]. Regarding self-compacting concrete (SCC), the denser and more compact microstructure, with less connectivity among the pores, tends to make it more sensitive to high temperatures when compared to conventional concrete (CC) [8, 9].

Although there are several studies on the effects of high temperatures on CC, there is still a gap in research addressing the effects of high temperatures on SCC, mainly due to the variability of mixes, mortar content, water/cement ratio, use of waste materials, the geometry of tested specimens, heating rate, and residence time. Additionally, the little research related to SCC evaluates mainly the occurrence of spalling, not enough assessing the residual mechanical properties after exposure to high temperatures, and the variability among the assessed parameters leads to a difficulty in comparing the results presented in the literature. The different approaches adopted to design the SCC mixture, such as viscosity modifier additive and fine replacement by non-pozzolanic or pozzolanic material, may also influence the behavior under high temperatures.

From this perspective, the main objective of this paper is to assess previous literature about self-compacting concrete exposed to high temperatures, addressing research developments to date and discussing the potential use of self-compacting concrete according to the existing information. The review comprises a broad geographic scope, although most publications are from Europe, China, and India.

2. SELF-COMPACTING CONCRETE AT HIGH TEMPERATURE

SCC is considered a high-performance concrete with excellent workability in the fresh state and high resistance to segregation [10]. The high capacity to flow allows filling the formwork with the self-weight without any vibration, compaction, or external influence. The self-compacting characteristic improves the final surface finish, improves durability, eliminates vibration noise, and reduces labor costs. Consequently, the SCC has gained more space in the market, not only for special projects but also for application in residential and commercial buildings. SCC is usually prepared with higher cement and filler content and a lower water/cement ratio than CC, resulting in compressive strength and pore size distribution compatible with high-performance concrete [11].

There are different mix-proportioning methods (i.e.: Okamura Method, 1995; Japanese Ready-Mixed Concrete Association – JRMCA, 1998; Su *et al*. Method, 2001; Gomes Method, 2002; and Tutikian and Dal Molin Method, 2007) and a broad range of materials (i.e.: cement, coarse and fine aggregate, pozzolanic and non-pozzolanic fines, superplasticizer, and viscosity modifier additive) used to produce SCC, whose type, origin, granulometry, porosity, and reactivity may influence the SCC properties, especially under high temperatures. The mix-proportioning with different granulometric compositions used to improve aggregate packing and the different water/cement ratios govern the SCC compressive strength, porosity, and permeability, influencing the concrete performance under high temperatures. While the high porosity and interconnected channels of CC contribute to relieving high internal moisture pressure and, consequently, the risk of spalling, the denser microstructure and the less connected voids content tend to make SCC more sensitive to high temperature [8, 9, 11].

Although the behavior of CC under high temperatures is well reported in the literature [6, 12, 13, 14, 15] there is still a research gap on the effects of high temperature on the properties of SCC. Additionally, the few studies related to SCC evaluate mainly the occurrence of spalling, lacking discussions about residual mechanical properties and data scattering due to different parameters. The difficulty in comparing the results of different experimental programs can be attributed mainly to the different mix-proportions and circumstances under which the experiments are performed [8, 16, 17, 18, 19, 20, 21, 22, 23] as discussed in the following sections.

2.1 Mix-Proportion

Tables 01 and 02 highlight the variability of mix-proportions used to produce SCC. The cement content varies between 268 kg/m³ and 550 kg/m³, the water/cement ratio between 0.28 and 0.7, and the superplasticizer (SP) amount between 0.51% and 6.67%, resulting in mixtures with a compressive strength between 21.43 MPa and 97.93 MPa. Additionally, mix-proportions include viscosity modifier agent (VMA), polypropylene and steel fibers with variable contents. In some cases, the publications mention a reference CC whose results are compared with SCC produced with quite different materials (i.e.: fiber, filler, etc.), w/c ratio, and cement content, which may influence the assessment, especially under high temperature [18, 24, 25, 26].

The water/cement ratio influences the volume and size of the capillary pores and the pore interconnection, the main responsible for the permeability of the hardened cement paste [27]. The interconnected voids network allows water transport in the liquid and gaseous phases to the external environment [28]. Lower water/cement ratios may lead to concrete spalling at high temperatures [29].

SCC are usually designed with higher cement content, higher filler content, and lower water/binder ratio than CC high-performance concrete (HPC), resulting in higher compressive strength and finer pore size, both critical factors for the concrete at elevated temperatures [11].

The different variables investigated in the literature create difficulties in determining if the type of addition or the self- compacting characteristic is the most influencing factor for spalling.

2

Reference	Concrete	Compressive strength (MPa)	Cement Content (kg/m³)	w/c ratio	Fillers	SP (%)	VMA (%)	PP Fiber (%)
Person [24]	SCC	80	430	0.40	GF	1.00	-	-
	SCC	88	411	0.40	LS	1.20	-	-
	SCC	87	433	0.40	LS	1.85	-	0.09
	SCC	81	487	0.40	LS	1.70	-	0.17
	CC	75	518	0.40	-	2.00	-	-
	SCC	80	447	0.40	LS	2.20	-	-
	CC	75	436	0.40	-	0.60	-	-
	SCC	68	308	0.55	LS	1.50	-	-
	SCC	63	344	0.55	LS	1.75	-	0.09
	SCC	65	382	0.55	LS	2.00	-	0.17
	CC	63	346	0.55	-	0.57	-	-
	SCC	48	316	0.70	GF	1.65	-	-
	SCC	56	268	0.70	LS	3.50	-	-
	SCC	40	294	0.70	LS	1.64	-	0.09
	SCC	53	312	0.70	LS	2.00	-	0.17
	CC	41	278	0.70	-	-	-	-
Noumowé et al. [9]	CC	75	400	0.47	SF	2.00	-	-
	CC	79.1	400	0.47	SF	3.20	-	0.09
	SCC	81.3	400	0.49	SF and CF	3.40	-	-
	SCC	75.6	400	0.51	SF and CF	5.50	-	0.09
Uysal [30]	SCC	75	550	0.33	-	1.60	-	-
	SCC	72	495	0.37	LP	1.60	-	-
	SCC	67	440	0.41	LP	1.60	-	-
	SCC	62	385	0.47	LP	1.60	-	-
	SCC	74	495	0.37	BP	1.60	-	-
	SCC	77	440	0.41	BP	1.60	-	-
	SCC	75	385	0.47	BP	1.60	-	-
	SCC	76	495	0.35	MP	1.60	-	-
	SCC	79	440	0.37	MP	1.60	-	-
	SCC	70	385	0.39	MP	1.60	-	-
	SCC	74	550	0.33	-	1.60	-	0.09
	SCC	72	495	0.37	LP	1.60	-	0.09
	SCC	65	440	0.41	LP	1.60	-	0.09
	SCC	64	385	0.47	LP	1.60	-	0.09
	SCC	73	495	0.37	BP	1.60	-	0.09
	SCC	77	440	0.41	BP	1.60	-	0.09
	SCC	76	385	0.47	BP	1.60	-	0.09
	SCC	78	495	0.35	MP	1.60	-	0.09
	SCC	79	440	0.37	MP	1.60	-	0.09
	SCC	72	385	0.39	MP	1.60	-	0.09
Bamonte e Gambarova [8]	SCC	51	350	0.50	CF	1.20	-	-
	SCC	82	480	0.35	CF	2.00	-	-
	SCC	90	520	0.33	CF	2.00	-	-
Qadi et al. [31]	SCC	-	437.5	0.41	FA	1.85	-	-
	SCC	-	437.5	0.41	FA	1.85	-	0.05
	SCC	-	437.5	0.41	FA	1.85	-	0.10
	SCC	-	437.5	0.41	FA	1.85	-	0.15
Annerel e Taerwe [26]	SCC	-	400	0.48	LS	0.73	-	-
	CC	-	350	0.47	-	-	-	-
Tao et al. [32]	SCC	-	400	0.41	LS	1.39	-	0.04
	SCC	-	310	0.64	LS	1.30	-	-
	SCC	-	310	0.64	LS	1.92	-	0.04
Al-Kadi [33]	SCC	-	437.5	0.406	FA	1.85	-	-
	SCC	-	437.5	0.406	FA	1.85	-	0.05
	SCC	-	437.5	0.406	FA	1.85	-	0.1
	SCC	-	437.5	0.406	FA	1.85	-	0.15
Werner et al. [34]	SCC	61.4	330	0.53	-	1.68	-	-
	SCC	62.9	330	0.53	LS	1.14	-	-
	SCC	62.9	330	0.53	LS	1.04	-	-
	SCC	65.8	330	0.53	LS	1.22	-	-
	SCC	63.1	330	0.53	LS	0.93	-	-
Xargay et al. [35]	SCC	97.93	429.8	0.35	Slag	0.51	-	-
	SCC	76.76	425.5	0.35	Slag	0.51	-	0.04 PP and 2.61 Steel

PP – polypropylene, GF – glass filler, LS – limestone, SF – silica fume, CF – calcareous filler, LP – lime-stone powder, BP – basalt powder , MP – marble powder, FA – fly ash.

Table 02: Mix proportions for SCC

Reference	Concrete	Compressive strength (MPa)	Cement content (kg/m³)	w/c ratio	Filler	SP (%)	VMA (%)	PP Fiber (%)
Sideris [11]	CC	29.5	350	0.54	-	1.21	-	-
	CC	39.6	350	0.57	-	0.68	-	-
	CC	45.2	430	0.46	-	0.63	-	-
	CC	67	430	0.45	SF	0.95	-	-
	SCC	33.7	370	0.60	-	1.62	-	-
	SCC	43.4	350	0.57	-	1.66	-	-
	SCC	53.5	430	0.46	-	2.03	-	-
	SCC	73.2	430	0.48	SF	1.43	-	-
Anangnostopoulos et al. [18]	SCC	37.1	335	0.55	LS	1.63	-	-
	SCC	54	375	0.50	LS	1.88	-	-
	SCC	37.7	340	0.55	Slag	1.29	-	-
	SCC	53.5	375	0.50	Slag	1.74	-	-
	SCC	38.3	340	0.56	GF	1.16	-	-
	SCC	49	380	0.51	GF	1.17	-	-
	CC	36	330	0.55	-	1.00	-	-
	CC	52.7	375	0.50	-	1.00	-	-
Annerel e Taerwe [25]	SCC	63.3	400	0.48	LS	0.73	-	-
	CC	46	350	0.47	-	-	-	-
Pathak e Sidique [2]	SCC	40.68	500	0.38	-	2.00	-	-
	SCC	30.67	500	0.38	FA	1.82	-	-
	SCC	27	500	0.40	FA	1.80	-	-
	SCC	21.43	500	0.42	FA	1.72	-	-
Jansson e Boström [19]	SCC	44	410	0.52	LS	1.51	-	0.04
	SCC	45	430	0.52	LS	1.37	-	0.07
	SCC	37	355	0.65	LS	1.27	-	-
	SCC	47	380	0.52	LS	1.45	-	-
	SCC	55	420	0.40	LS	1.90	-	0.04
	SCC	67	420	0.40	LS	1.50	-	-
	SCC	72	420	0.40	LS	1.90	-	0.07
	SCC	67	420	0.40	-	-	-	-
Anand et al. [36]	SCC	24.69	360	0.43	FA	1.35	0.06	-
	SCC	36.97	405	0.37	FA	1.81	0.07	-
	SCC	48.24	479	0.31	FA	2.32	-	-
	SCC	58.99	525	0.28	FA	2.58	-	-
	SCC	22.13	360	0.47	SF	1.18	0.05	-
	SCC	34.15	405	0.41	SF	1.53	0.05	-
	SCC	45.26	479	0.35	SF	1.98	-	-
	SCC	56.09	525	0.31	SF	2.45	-	-
	SCC	26.95	360	0.44	MK	1.10	0.14	-
	SCC	37.2	405	0.38	MK	1.54	0.13	-
	SCC	49.6	479	0.32	MK	2.18	0.06	-
	SCC	60.07	525	0.29	MK	2.44	0.07	-
Sadrmomtazi et al. [37]	SCC	38	500	0.38	-	6.67	-	-
	SCC	43	500	0.38	-	6.67	-	0.3 steel
	SCC	41	500	0.38	-	6.67	-	0.5 steel
	SCC	53	425	0.38	FA	5.80	-	0.3 steel
	SCC	52	425	0.38	FA	6.16	-	0.5 steel
	SCC	50	350	0.38	FA	5.56	-	0.3 steel
	SCC	51	350	0.38	FA	5.95	-	0.5 steel
Guler et al. [23]	SCC	42	375	0.48	FA	1	-	-
	SCC	37	375	0.48	FA	1	-	0.3
	SCC	39	375	0.48	FA	1	-	0.3
	SCC	41	375	0.48	FA	1	-	0.3
	SCC	42	375	0.48	FA	1.5	-	0.6
	SCC	40	375	0.48	FA	1.5	-	0.6
	SCC	45	375	0.48	FA	1.5	-	0.6
	SCC	40	375	0.48	FA	2	-	1
	SCC	42	375	0.48	FA	2	-	1
	SCC	47	375	0.48	FA	2	-	1

PP – polypropylene, SF – silica fume, LS – Limestone, GF – glass filler, LS – limestone, FA – fly ash, MK – metakaolin.

Regarding CC and SCC with equivalent compressive strength, produced with similar water/cement ratio, Sideris [11] highlighted the higher compressive strength achieved for the SCC mixtures due to the more efficient particle packing and concluded that the spalling phenomena depend more on the water/cement content than the compaction

714

procedure. The water permeability was the same after the test in CC and SCC mixtures with similar strength classes and filler content.

Steel (ST), polyamide (PA), and polypropilene (PP) fibers are widely used as an attempt to mitigate spalling. SCC produced with PP fibers is reported in the literature as the most effective to protect concrete against fire effects [24, 38, 39]. Previous research reports that 0.05% PP by volume may reduce or even prevent explosive concrete fragmentation and significantly increase void content in the SCC microstructure [16, 33]. There are also reports mentioning a better correlation for 0.1% PP by volume in view of temperature control performance and relative residual compressive strength [40, 41]. Studies by Xargay *et al.* [35] concluded that SCC concrete produced with steel and PP fibers presents fewer surface cracks caused by temperature. However, as steel and PP fibers were used simultaneously, the test protocol does not allow the assessment of the effects of each fiber separately. Regarding the fiber content, positive effects on spalling resistance were observed with 1 kg/m³ to 1.5 kg/m³ of PP [19, 42, 43, 44, 45], attributed to the increase in pore connectivity after fiber melting.

2.2 Test specimen

The specimens' geometry used in experimental programs to assess high temperature in SCC is widely variable, as illustrated in Table 03, varying from cylindrical (φ10x20 cm, φ16x32 cm, φ15x30 cm, φ10.6x32 cm, φ7.5x15 cm) and prismatic (10x10x40 cm, 10x10x10 cm, 15x15x15 cm, 7.5x7.5x35cm) to columns, beams, and slabs, [9, 11, 22, 23, 24, 25, 36, 46, 47, 48].

Thus, it is not easy to compare the results of different publications within the state-of-the-art of SCC under high temperatures. Even test standards recommend specimens with different dimensions for each assessed property or aggregate size, for instance. Recognizing as standard test specimen diameters such as 150 mm, 100 mm, 80 mm and 60 mm, other diameters must be considered "nonstandard". The accepted slenderness for different tests are the following, modulus of elasticity between 3 and 4, thermal strain, transient creep, steady-state creep, creep recovery and shrinkage between 3 and 5, while for tensile strength it must have a length/diameter ratio of 2 ±0.5 in the cylindrical part which must be extended in order to allow the application of loads in the longitudinal direction. [49, 50, 51, 52, 53].

Tests performed by [19] have shown substantially lower spalling in reduced-size slabs (60x50x20 cm) compared to larger specimens (180x120x20 cm) under the same testing protocol. Additionally, it is essential to consider whether one or more specimen sides are exposed to the high temperature since it influences the moisture escape routes and can amplify the spalling effect [38, 42].

There are important differences between the analysis of specimens and structural elements, which are the geometry itself and the surface area exposed to fire/high temperature [38]. In real fire situations with reinforced concrete, it must also be considered that the geometry of the structure as well as the depth of the steel bars influence the spalling [39]. Some authors have concluded that the boundary of the specimen also affects the amount of spalling, and the spalling on the central exposed areas is larger than around the edges [38]. Jansson and Bostron [19] compared slab sizes and concluded that the design affects not only the probability of spalling but also its extent.

2.3 Curing and storage

Evaluating the curing process and, mainly, the storage or drying of specimens exposed to high temperatures is essential to understand the spalling phenomenon, given the protagonism of the moisture content [54], along with porosity and permeability. The spalling phenomenon can be related to high compressive stresses, to high heating rates, or high moisture content that may vary depending on the test protocol.

Different combinations of curing and storage are reported in the state-of-the-art of SCC under high temperatures. While some studies mention controlled humidity and temperature for 28 days, not specifying the temperature and/or humidity [21], others reference different curing and storage protocols (i.e.: curing room at 20°C and RH 95% [18, 35], curing room at 20°C and RH 65% [34]), which difficult comparative assessments.

There are also reports of different curing ages, 20°C water for 28 days [20, 43], lime-saturated water 28 days [46]; 20°C water for 89 days [2016], water-curing and air-cured after 5 days water-curing [24], wet (water tank) and dry (laboratory environment) [37].

Reference	Specimen geometry	Heating Rate (°C/min)	Maximum Temperature (°C)	Residence time (h)
Persson [24]	cylindrical/prismatic	4 and 8, HC, ISO 834	800	0.5
Stegmaier e Reinhardt [55]	prismatic	ISO 4102	-	-
Ye *et al.* [56]	-	10	950	-
Boström e Larsen [39]	prismatic	-	800	-
Noumowé *et al.* [9]	cylindrical/prismatic	0.5, ISO 834	400 e 600	-
Reinhardt e Stegmaier [54]	cylindrical	ISO 834	-	-
Annerel *et al.* [57]	prismatic	3.5	550	12.5
Boström e Jansson [38]	prismatic	ISO 834	-	-
Boström *et al.* [58]	prismatic	specific/ISO 834	1300	-
Dehn *et al.* [59]	prismatic	specific	1300	2
Jansson e Boström [60]	-	-	-	-
Tao *et al.* [61]	cylindrical	5	800	-
Sideris [11]	cylindrical/prismatic	5	700	1
Anagnostopoulos *et al.* [18]	cylindrical/prismatic	10	600	1
Liu *et al.* [44]	prismatic	10	500	-
Fares *et al.* [3]	cylindrical/prismatic	1	600	1
Jansson e Boström [62]	prismatic	HC	-	-
Lu *et al.* [63]	prismatic	-	920	-
Tao *et al.* [64]	cylindrical	8	700	-
Uygunoğlu e Topçu [65]	cylindrical/prismatic	5	100	-
Annerel e Taerwe [25]	cylindrical	5	500	12.5
Fares *et al.* [66]	cylindrical/prismatic	1	600	1
Helal e Heiza [67]	cylindrical/prismatic	-	600	2
Tao *et al.* [68]	cylindrical	5	800	-
Ali [17]	cylindrical/prismatic	2	800	2
Bakhtiyari *et al.* [69]	cylindrical/prismatic	10	1000	2
Ding *et al.* [45]	prismatic	6	900	3
Fares *et al.* [70]	-	1	600	1
Khaliq e Kodur [71]	cylindrical/prismatic	2 and 5	800	-
Annerel e Taerwe [26]	cylindrical	5	400	-
Bamonte e Gambarova [8]	cylindrical	1 and 2	600	-
Pathak e Siddique [2]	cylindrical/prismatic	1	300	1
Qadi *et al.* [31]	cylindrical	-	600	-
Tao *et al.* [32]	cylindrical	5, 10 and 15	600	-
Tao *et al.* [72]	cylindrical	5	800	-
Uysal e Tanyildizi [30]	prismatic	similar to RILEM	800	-
Anand *et al.* [73]	prismatic	specific	900	1.5
Aaslani e Samali [4]	-	-	800	-
Haddad *et al.* [74]	cylindrical/prismatic	specific	600	-
Jansson e Boström [19]	prismatic	HC e STD	-	-
Pistol *et al.* [75]	cylindrical	1	600	1
Sideris e Manita [42]	cylindrical/prismatic	5	600	1
Trezos e Sfikas [76]	prismatic	specific	900	-
Anand *et al.* [77]	cylindrical	specific	900	-
Ding *et al.* [78]	prismatic	ISO 834	600	-
Lomonte e Gambarova [79]	cylindrical/prismatic	similar to HC and ISO 834	750	-
Lura e Terrasi [80]	prismatic	ISO 834	-	-
Qadi e Al-Zaidyeen [41]	cylindrical/prismatic	5 and 10	600	-
Al-Kadi *et al.* [81]	cylindrical	-	600	-
Chung *et al.* [40]	prismatic	ISO 834	-	-
Fares *et al.* [46]	cylindrical/ prismatic	1 and ISO 834	400 e 600	1 and 2
Alhasanat *et al.* [16]	cylindrical	5 to 10	600	4
Al-Kadi *et al.* [33]	cylindrical/prismatic	-	600	-
Anand et al. [36]	cylindrical and prismatic	specific	900	-
Ding *et al.* [82]	prismatic	ISO 834	600	1.5
Muthusamy e Kolandasamy [83]	prismatic	2.5	800	1
Werner *et al.* [34]	cylindrical/prismatic	ISO 834	-	-
Al-Lami [84]	cylindrical and prismatic	70	700	-
Aslani e Kelin [85]	cylindrical	similar to ISO 834	900	1
Aslani e Ma [86]	cylindrical	similar to ISO 834	900	1
Ríos *et al.* [43]	cylindrical	10	700	6, 24, and 48
Xargay *et al.* [35]	cylindrical/prismatic	10	600	3
Aslani *et al.* [21]	cylindrical	5	900	-
Azarijafari *et al.* [87]	cylindrical/prismatic	1	700	1
Mahapatra e Barai [22]	cylindrical/prismatic	-	600	1
Jani *et al.* [48]	prismatic	HC	1100	-
Sadrmomtazi *et al.* [37]	cylindrical	5	600	2
Guler *et al.* [23]	prismatic	-	800	-
Mujedu *et al.* [47]	prismatic	2.7	1000	2
Franchetto [88]	cylindrical	1	1000	temperature function

716

6

Other examples of the wide curing and storage protocols there are the following studies: i) keeping the specimens for a specific period of time in a laboratory room under air-curing before heating: 24 h [16, 22], 7 days [37], 90 days (cured in ambient conditions) [48], 90 days [46], 102 days, RH 50-60% and 20+-2°C [84], 152 days, RH 95% and 20+-2°C [18], 180 days [54]; and ii) curing for 91 days underwater, as proposed by RILEM, at 20 ± 5 °C followed by 24 h at room temperature in a laboratory room before exposure to high temperatures [87]. Comprehensive reports indicate the period, temperature, and humidity of both curing and storage processes. Annerel and Taerwe [25], for instance, mentioned specimens cured for 28 days at 20 ± 1°C and 90% RH, followed by storage at 60% RH and 20 ± 1°C for about 29 months. Accelerated curing, described simply as oven drying [83] is another procedure described in the literature. As an example, Guler *et al.* [23] carried out tests in which specimens were cured for 28 days in an oven at 100 ± 5 °C for 24 h, followed by curing in a controlled chamber at 22 ± 1 °C up to 28 days [23]. It is worth noting that the results obtained from these quite different experiment protocols are not directly comparable.

It is important to register that RILEM [49, 50, 51, 52] recommendations regarding curing are first keeping specimens at 20+-2°C for 7 days, the first 24+-4 hours in their molds, followed by 6 days under conditions without moisture exchange, which can be achieved by several means. Then, two storage options are available until the test age: drying in air at 20+-2°C and RH of 50+-5% and non-drying conditions within sealed bags, molds, or wrapped in water diffusion tight and non-corrosive foil at 20+-2°C. Finally, the specimens should be tested after at least 90 curing days.

2.4 Heating rate

Table 3 shows the wide variety of heating rates used to evaluate the behavior of SCC under high temperatures. The following references illustrate this issue: 0.5°C/min [9], 1°C/min [2, 3, 87, 88], 1 to 2°C/min [8], 2,5°C/min [22], 2,7°C/min [47], 3.5°C/min [57], 4°C/min [24], 5°C/min [11, 25, 37], 4 to 6°C/min [54], 8°C/min [24], and 10 °C/min [18, 44]. The most frequent heating rates used in the literature are the one indicated by the ISO 834 curve or the fixed rate of 5°C/min.

In general, the spalling phenomenon is more pronounced at high heating rates. On the other hand, tests performed by Noumowé *et al.* [9] show severe spalling in high-strength SCC at a heating rate of 0.5°C/min, which might be explained by the denser cementitious matrix. Under this perspective, assessing residual properties of SCC based on tests performed using different heating rates may not be comparable.

The most frequent reason for using heating rates different than the ISO 834 and RILEM curves is related to limitations imposed by the available equipment used to perform the test, which contributes to the wide range of curves specified in the literature.

2.5 Maximum exposure temperature

The peak temperature adopted in most of the published research on SCC varies from 100°C to 1000°C [8, 9, 11, 23, 24, 47, 88].

The main reasons for adopting different maximum temperatures are diverse: the low capacity of the available furnace, the impossibility of programming complex heating rate curves, and the loss of mechanical properties due to microstructural decomposition at high temperatures. Bamonte and Gambarova [8] consider the target temperature of 600°C a suitable target since above this temperature, both the compressive strength and the elastic modulus rapidly decrease, and above 700°C calcination is activated. Annerel and Taerwe [25] justify maximum temperature choices of 175°C, 300°C, and 520°C as those corresponding to the total loss of free water, onset of strength loss, and decomposition of portlandite, respectively.

During the heating of concrete, several chemical reactions occur. At lower temperatures, however, free water evaporates, and at 105°C the water inside the chemical bonds of concrete also begins to evaporate. The loss of capillary and physically bound water develops between 80°C and 200°C, at 374°C there is the critical point of water, above which there is no free water, while the loss of chemically bound water continues up to 850°C. Around 200°C, dehydration of the C-S-H gel occurs with a reduction in volume, simultaneously with the expansion of the cement paste, causing an increase in porosity, microcracks and, consequently, an abrupt reduction in resistance to compression and penetration [90, 91]. From 420°C, the dehydration of portlandite crystals also generates shrinkage and microcracking [92]. At 573°C, the quartz aggregates undergo a phase change from α to β, causing a slight expansion that contributes to the deterioration of the cementitious matrix. The thermal effects increase between 500°C and 600°C, considered the critical temperature for the deleterious effects of high temperatures on concrete. The decomposition of C-S-H into $\beta - C2S$ (belite), βCS (wollastonite) and water close to 720°C causes paste

shrinkage and loss of concrete strength [27, 92]. Above 800°C the properties of concrete are negligible as there is a change from the hydraulic structure to a ceramic structure.

2.6 Residence time

The residence time, or steady-state phase, period in which the maximum temperature is maintained during testing, is another critical variable for assessing SCC at high temperatures. The RILEM test procedure [49, 50] suggests that the maximum temperature, determined as the average of three thermocouples positioned at specific points on the specimen, should be kept for 60±5 minutes.

Previous studies noticed large thermal gradients related to short residence times. Ye *et al.* [56] reported at 600°C gradient in thermocouples positioned only 30 mm away in the specimen depth in an experiment performed using the ISO 834 curve up to 950ºC. Fares *et al.* [46] used two heating rate curves to perform their experiments: ISO 834 and of the rate of 1°C/min, both up to 400°C. For the ISO 834 the residence time was 120 minutes, whilst for the 1ºC/min heating rate the residence time was 60 minutes.

As illustrated in Table 03, different residence times may be found in the literature, ranging from 0.5 to 24 hours [11, 18, 37, 47, 83, 85].

The residence time may also vary depending on the maximum testing temperature. Bamonte and Gambraova [2010], for instance, adopted 120-150 minutes for 200°C and 400°C and 240-270 minutes for 600°C, aiming at reaching uniform temperature within the specimen. In this context, Annerel and Taerwe [25] adopted a residence time of 750 minutes for maximum temperatures of 175°C, 300°C and 500°C. Franchetto [88] performed tests with thermocouples in order to verify the time required to reach uniform temperature within the specimen for each target temperature, adopting different periods between 35 and 435 minutes.

The different maximum temperatures and steady-state phases influence the residual compressive strength [89]. Longer residence times (6h, 24h, and 48h) are indifferent if the temperature is uniform within the specimen [43].

Thus, different conclusions regarding the behavior of SCC under high temperatures may be related to the different residence times used in the tests. As a way of simulating reality, it would be advisable to verify the temperature of the structure in a real fire situation, because although the simulation curves indicate temperatures generated by the fire, which extinguishes itself with the end of the combustible materials, it does not consider the period that the concrete remains heated, which is what residence time seeks to simulate.

2.7 Cooling protocol

The colling protocol is one of the test parameters least discussed and detailed in the reported literature, probably due to the difficulty in guaranteeing a constant cooling rate. In general, descriptions of the cooling procedure only mention the period and whether the furnace was kept open or closed. Sometimes, the only mention refers to specimens being cooled down to room temperature [46]. Some examples of cooling protocols to avoid thermal gradients are: i) specimens kept in the furnace closed until reaching ambient temperature [18, 23, 47, 56]; ii) slow cooling down for 24 hours not mentioning if inside or outside the oven [86]; iii) cooling rate of 1°C/min or 0.5°C/min in the furnace closed [24, 25]; and iii) specimens kept under air or sprayed water [36, 57].

The cooling protocol varies according to the maximum temperature, furnace size, and, mainly, the furnace thermal insulation [18]. RILEM [49] suggests that the cooling rate follows the same heating pattern.

3. CONCLUSIONS

Although SCC exhibits excellent mechanical properties and could be used in many applications, because of the high amount of fines, SCC might suffer from fire exposure and explosive concrete fragmentation if insufficient attention is paid due to low permeability and to pore distribution. From recent research on this cement-based composites under elevated temperatures and fire conditions, some conclusions are drawn:

1) The main outcome of this research relies on the fact that there is not a uniform method to investigate the behavior of SCC at high temperatures, since different experimental variables are used throughout the researches. Due to the variability of parameters adopted, it was found that it was difficult to compare existing results, currently making it difficult to reach a more general and definitive conclusion regarding SCC at high temperatures;

2) The main aim of adding steel, polyamide, or polypropilene fibers are widely used to mitigate spalling. SCC produced with PP fibers has the potential as the most effective to protect concrete against fire effects. Therefore, the melting point of polymer fibers seems a critical parameter, and the shape of fibers can also be carefully considered;

718

3) Fiber type, filler type, moisture content, pore-volume, and permeability affect the mass loss, tensile strength and fracture energy of SCCs under elevated temperatures;

4) Although RILEM exists to guide high temperature tests, it is just a procedure, which means that there is a lack of standardization of tests for high temperatures. Likewise, there is still no standard for SCC, making it difficult to compare results between studies.

ACKNOWLEDGEMENTS

REFERENCES

[1] Lima, R. C. A. (2005). *Investigação de Temperatura de Concretos em Temperaturas Elevadas*. Doctoral Thesis, Universidade Federal do Rio Grande do Sul, 257p.

[2] Pathak, N. & Siddique, R. (2012). *Properties of self-compacting-concrete containing fly ash subjected to elevated temperatures.* Construction And Building Materials, vol. 30, p. 274-280.

[3] Fares, H.; Noumowé, A. & Remond, S. (2009). *Self-consolidating concrete subjected to high temperature*. Cement And Concrete Research, vol. 39, no. 12, p. 1230-1238.

[4] Aaslani, F.; Samali, B. (2013). Constitutive relationships for self-compacting concrete at elevated temperatures. Materials And Structures, vol. 48, no. 1-2, p. 337-356.

[5] Zeiml, M.; Lackner, R.; Mang, H. A. (2008). *Experimental insight into spalling behavior of concrete tunnel linings under fire loading*. Acta Geotechnica, vol. 3, no. 4, p. 295-308.

[6] Mindeguia, J. C; Pimienta, P.; Noumowé, A.; Kanema, M. (2010). *Temperature, pore pressure and mass variation of concrete subjected to high temperature — Experimental and numerical discussion on spalling risk*. Cement And Concrete Research, vol. 40, no. 3, p. 477-487.

[7] Khoury, G. A.; Majorana, C. E.; Pesavento, F.; Schrefler, B. A. (2002). Modelling of heated concrete. Magazine Of Concrete Research, vol. 54, no. 2, p. 77-101.

[8] Bamonte, P. & Gambarova, P. G. (2012). *A study on the mechanical properties of selfcompacting concrete at high temperature and after cooling*, Materials and Structures, vol. 45, no. 9, p. 1375-1387.

[9] Noumowé, A.; Carré, H.; Daoud, A. & Toutanji, H. (2006). *High-Strength Self-Compacting Concrete Exposed to Fire Test*, Journal of Materials in Civil Engineering, vol. 18, n. 6, p. 754-758.

[10] Tutikian, B. (2004) Método para dosagem de concretos auto-adensáveis, Master, Universidade Federal do Rio Grande do Sul, 148p.

[11] Sideris, K. K. (2007). *Mechanical Characteristics of Self-Consolidating Concretes Exposed to Elevated Temperatures*, Journal Of Materials In Civil Engineering, vol. 19, no. 8, p. 648-654.

[12] Hertz, K.D. (2003). *Limits of spalling of fire-exposed concrete*. Fire Safety Journal, vol. 38, no. 2, p. 103-116.

[13] Mindeguia, J.C.; Pimienta, P.; Carré, H.; Laborderie, C. (2013). *Experimental analysis of concrete spalling due to fire exposure*. European Journal Of Environmental And Civil Engineering, vol. 17, no. 6, p. 453-466.

[14] Kodur, V.K.R.; Phan, L. (2007). *Critical factors governing the fire performance of high strength concrete systems.* Fire Safety Journal, vol. 42, no. 6-7, p. 482-488.

[15] Kakae, N.; Miyamoto, K.; Momma, T.; Sawada, S.; Kumagai, H.; Ohga, Y.; Hirai, H.; Abiru, T. (2017*). Physical and Thermal Properties of Concrete Subjected to High Temperature*. Journal Of Advanced Concrete Technology, vol. 15, no. 6, p. 190-212.

[16] Alhasanat, M. B.; Qadi, A. N. A.; Khashman, O. A. A. & Dahamsheh, A. (2016). *Scanning Electron Microscopic Evaluation of Self-Compacting Concrete Spalling at Elevated Temperatures*. American Journal Of Engineering And Applied Sciences, vol. 9, no. 1, p. 119-127.

[17] Ali, M. (2011). *Residual Mechanical Properties of Self-Compacting Concrete Exposed to Elevated Temperatures*. Engineering And Technology Journal, vol. 29, p. 1386-1390.

[18] Anagnostopoulos, N.; Sideris, K. K. & Georgiadis, A. (2008) *Mechanical characteristics of self-compacting concretes with different filler materials, exposed to elevated temperatures*, Materials And Structures, vol. 42, n. 10, p. 1393-1405.

[19] Jansson, R. & Boström, L. (2013). *Factors influencing fire spalling of self-compacting concrete*. Materials And Structures, vol. 46, no. 10, p. 1683-1694.

719

[20] Ding, Y.; Zhang, C.; Cao, M.; Zhang, Y. & Azevedo, C. (2016). *Influence of different fibers on the change of pore pressure of self-consolidating concrete exposed to fire*. Construction And Building Materials, vol. 113, p. 456-469.

[21] Aaslani, F.; Hamidi, F.; Ma, Q. (2019). *Fire Performance of Heavyweight Self-Compacting Concrete and Heavyweight High Strength Concrete*. Materials, vol. 12, no. 5, p. 822.

[22] Mahapatra, C. K. & Barai, S.V. (2019) *Temperature impact on residual properties of self-compacting based hybrid fiber reinforced concrete with fly ash and colloidal nano silica*, Construction and Building Materials, vol. 198, p. 120-132.

[23] Guler, S.; Akbulut, Z. F.; Siad, H.& Lachemi, M. (2021). *Effect of macro polypropylene, polyamide and steel fibers on the residual properties of SCC at ambient and elevated temperatures,* Construction and Building Materials, vol. 289, p. 123154.

[24] Persson, B. (2004). *Fire resistance of self-compacting concrete, SCC*, Materials and Structures, vol. 37, no. 9, p. 575-584.

[25] Annerel, E. & Taerwe, L. (2010). *Evolution of the strains of traditional and self-compacting concrete during and after fire*, Materials and Structures, vol. 44, no. 8, p. 1369-1380.

[26] Annerel, E. & Taerwe, L. (2012). *Strain model for traditional and self-compacting concrete during fire*. Fire And Materials, vol. 37, no. 3, p. 217-229.

[27] Mehta, P. K.; Monteiro, P. J. M. (2014). Concreto: estrutura, propriedades e materiais. Pini, 751 p.

[28] Silva Filho, L. C. P. (1994). *Durabilidade do concreto à ação de sulfatos: análise do efeito da permeação de água e da adição de microssílica, Master,* Universidade Federal do Rio Grande do Sul, 143 p.

[29] Ma, Q.; Guo, R.; Zhao, Z.; Lin, Z. & He, K. (2015). *Mechanical properties of concrete at high temperature—A review*. Construction And Building Materials, vol. 93, p. 371-383.

[30] Uysal, M. & Tanyildizi, H. (2012). *Estimation of compressive strength of self compacting concrete containing polypropylene fiber and mineral additives exposed to high temperature using artificial neural network*. Construction And Building Materials, vol. 27, no. 1, p. 404-414.

[31] Qadi, A. N. S. Al; Mustapha, K. N. B.; Naganathan, S. & Al-Kadi, Q. N. S. (2012). *Effect of polypropylene fibers on thermogravimetric properties of self-compacting concrete at elevated temperatures*. Fire And Materials, vol. 37, no. 3, p. 177-186.

[32] Tao, J.; Liu X.; Yuan, Y. & Taerwe, L. (2012) *Transient strain of self-compacting concrete loaded in compression heated to 700 °C*. Materials and Structures, vol. 46, no. 1-2, p. 191-201.

[33] Al-kadi, Q. ; Alhasanat, M. B. & Al-kadi, A. (2016). *Spalling Assessment of Self-Compacting Concrete with and Without Polypropylene Fibres at Elevated Temperatures*. Journal Of Engineering Research And Application, vol. 6, no. 6, p. 82-93, 2016.

[34] Werner, S.; Schmidt, W.; Pirskawetz, S. & Rogge, A. (2016). *Fire Spalling of Self-Compacting Concrete Mixtures with Different Limestone Powder Contents*, 8th International RILEM Symposium on Self-Compacting Concrete, Washington, p. 353-363.

[35] Xargay, H.; Folino, P.; Sambataro, L. & Etse, G. (2018). *Temperature effects on failure behavior of self-compacting high strength plain and fiber reinforced concrete*. Construction And Building Materials, vol. 165, p. 723-734.

[36] Anand, N.; Antony G. I & Prince A. G. (2016*). Influence of mineral admixtures on mechanical properties of self-compacting concrete under elevated temperature*. Fire And Materials, vol. 40, no. 7, p. 940-958.

[37] Sadrmomtazi, A.; Gashtil, S. H. & Tahmouresi, B. (2020). *Residual strength and microstructure of fiber reinforced self-compacting concrete exposed to high temperatures*, Construction and Building Materials, vol. 230, p. 116969

[38] Boström, L. & Jansson, R. (2007). *Fire spalling of self-compacting concrete*. 5Th International RILEM Symposium on Self-Compacting Concrete, Ghent, p. 741-745.

[39] Boström, L. & Larsen, C. K. (2006). *Concrete for Tunnel Linings Exposed to Severe Fire Exposure*, Fire Technology, vol. 42, no. 4, p. 351-362.

[40] Chung, C. H.; Lee, J. & Choi, S. H. (2015). *Temperature distribution within polypropylene fiber-mixed reinforced concrete slabs exposed to an ISO 834 standard fire*. Ksce Journal Of Civil Engineering, vol. 20, no. 5, p. 1878-1886.

[41] Qadi, A. & Al-ZAiadyeen, S. M. (2014). *Effect of fibre content and specimen shape on residual strength of polypropylene fibre self-compacting concrete exposed to elevated temperatures*. Journal Of King Saud University - Engineering Sciences, vol. 26, no. 1, p. 33-39.

[42] Sideris, K.K. & Manita, P. (2013). *Residual mechanical characteristics and spalling resistance of fiber reinforced self-compacting concretes exposed to elevated temperatures*. Construction And Building Materials, vol. 41, p. 296-302

[43] Ríos, J. D.; Cifuentes, H.; Leiva, C.; García, C. & Alba, M. D. (2018). *Behavior of High-Strength Polypropylene Fiber-Reinforced Self-Compacting Concrete Exposed to High Temperatures*. Journal Of Materials in Civil Engineering, vol. 30, no. 11.

[44] Liu, X.; Ye, G.; Schutter, G.; Yuan, Y. & Taerwe, L. (2008). *On the mechanism of polypropylene fibres in preventing fire spalling in self-compacting and high-performance cement paste*. Cement And Concrete Research, vol. 38, no. 4, p. 487-499.

[45] Ding, Y.; Azevedo, C.; Aguiar, J.B. & Jalali, S. (2011). *Study on residual behaviour and flexural toughness of fibre cocktail reinforced self-compacting high-performance concrete after exposure to high temperature*. Construction And Building Materials, vol. 1, no. 6, p. 21-31.

[46] Fares, H.; Toutanji, H.; Pierce, K. & Noumowé, A. (2015). *Lightweight Self Consolidating Concrete Exposed to Elevated Temperatures*, Journal of Materials In Civil Engineering, vol. 27, no. 12.

[47] Mujedu, K. A.; Ab-Kadir, M. A.; Sarbini, N. N. & Ismail, M. (2021). *Microstructure and compressive strength of self-compacting concrete incorporating palm oil fuel ash exposed to elevated temperatures*, Construction And Building Materials, vol. 274, p. 122025.

[48] Jani, N. M.; Nasif, M. S.; Shafiq, N. & Holt, I. (2020). *Experimental Investigation on the Effect of Varying Fiber Mix Proportion on the Mechanical and Thermal Performances of Fiber-Reinforced Self-Compacting Concrete under Hydrocarbon Fire Condition*, Applied Sciences, vol. 10, no. 13, p. 4586.

[49] RILEM TC 129-MHT (2000): Test methods for mechanical properties of concrete at high temperatures: Part 4: Tensile strength for service and accident conditions. Materials and Structures, vol. 33, p. 219-223.

[50] RILEM TC 129-MHT (1997): Test Methods for Mechanical Properties of Concrete at High Temperature: Part 6 – Thermal Strain. Materials and Structures, p. 17-21.

[51] RILEM TC 129-MHT (1998): Test methods for mechanical properties of concrete at high temperatures: Recommendations: Part 7: Transient Creep for service and accident conditions. Materials and Structures, vol. 31, p. 290-295.

[52] RILEM TC 129-MHT (2000): Test methods for mechanical properties of concrete at high temperatures: Part 8: Steady-state creep and creep recovery for service and accident conditions. Materials and Structures, vol. 33, p. 6-13.

[53] RILEM TC 129-MHT (2000): Test methods for mechanical properties of concrete at high temperatures: Part 9: Shrinkage for service and accident conditions. Materials and Structures, vol. 33, p. 224-228.

[54] Reinhardt, H. W. & Stegmaier, M. (2006). *Self-Consolidating Concrete in Fire*, ACIMaterials Journal, vol. 103, p. 130-135, 2006.

[55] Stegmaier, M. & Reinhardt H. W. (2004). *Fire behaviour of plain Self-Compacting Concrete (SCC)*, Otto Graf Journal, vol. 15, p. 33-42.

[56] Ye, G., Liu, X., De Schutter, G., Taerwe, L., & Yuan, Y. (2005). *Microstructure aspects of self-compacting concrete at elevated temperature*, 1st International Symposium on Design, Performance and Use of Self-consolidating concrete, Changsha, p.403-411.

[57] Annerel, E.; Taerwe, L. & Vandevelde, P. (2007). *Assessment of Temperature Increase and Residual Strength of SCC after Fire Exposure*, 5th International RILEM Symposium on Self-Compacting Concrete, Ghent, p. 715–720, doi:1854/11477.

[58] Boström, L.; Wickström, U. & Adl-zarrabi, B. (2007). *Effect of specimen size and loading conditions on spalling of concrete*. Fire And Materials, vol. 31, no. 3, p. 173-186.

[59] Dehn, F.; Nause, S. & Hauswaldt, S. (2007). *Fire Spalling behaviour of self-compacting concrete (SCC) for tunnel construction - Taking the Malmö Citytunnel as an example*. 5Th International RILEM Symposium on Self-Compacting Concrete, Ghent, v. 5, p. 1027-1034.

[60] Jansson, R. & Boström, L. (2007). *Fire spalling: Theories and experiments*. 5Th International RILEM Symposium on Self-Compacting Concrete, Ghent, p. 735-740.

[61] Tao, J. ; Xian, L. & Yong, Y. (2007). *High strength self-compacting concrete at elevated temperature*. 5Th International RILEM Symposium on Self-Compacting Concrete, Ghent, p. 1135-1144

[62] Jansson, R. & Boström, L. (2009). *The Influence of Pressure in the Pore System on Fire Spalling of Concrete*. Fire Technology, vol. 46, no. 1, p. 217-230.

[63] Lu, H.; Zhao, X. & Han, L. (2009). *Fire behaviour of high strength self-consolidating concrete filled steel tubular stub columns*. Journal Of Constructional Steel Research, vol. 65, no. 10-11, p. 1995-2010.

[64] Tao, J.; Liu, X.; Yuan, Y. & Taerwe, L. (2009). *Transient strain of self-compacting concrete exposed to high temperature*. 2Nd International Symposium on Design, Performance And Use Of Self Consolidating Concrete, Beijing, p. 628-638.

[65] Uygunoğlu, T. & Topçu, I. (2009). *Thermal expansion of self-consolidating normal and lightweight aggregate concrete at elevated temperature*. Construction And Building Materials, vol. 23, no. 9, p. 3063-3069.

[66] Fares, H.; Remond, S.; Noumowé, A. & Cousture, A. (2010). *High temperature behaviour of self-consolidating concrete*. Cement And Concrete Research, vol. 40, no. 3, p. 488-496.

[67] Helal, M. A. & Heiza, K. M. (2010). *Effect of Fire and High Temperature on the Properties of Self Compacted Concrete*. Cice 2010 - The 5Th International Conference on FRP Composites In Civil Engineering, Pequim, p. 433-439.

[68] Tao, J.; Yuan, Y. & Taerwe, L. (2010). *Compressive Strength of Self-Compacting Concrete during High-Temperature Exposure*. Journal Of Materials in Civil Engineering, vol. 22, no. 10, p. 1005-1011.

[69] Bakhtiyari, S.; Allahverdi, A.; Rais-ghasemi, M.; Zarrabi, B.A. & Parhizkar, T. (2011). *Self-compacting concrete containing different powders at elevated temperatures – Mechanical properties and changes in the phase composition of the paste*. Thermochimica Acta, vol. 514, no. 1-2, p. 74-81.

[70] Fares, H.; Remond, S.; Noumowé, A. & Cousture, A. (2011). *Microstructure et propriétés physico-chimiques de bétons autoplaçants chauffés de 20 à 600°C*. European Journal Of Environmental And Civil Engineering, vol. 15, no. 6, p. 869-888.

[71] Khaliq, W. & Kodur, V. (2011). *Thermal and mechanical properties of fiber reinforced high performance self-consolidating concrete at elevated temperatures*. Cement And Concrete Research, vol. 41, no. 11, p. 1112-1122.

[72] Tao, J.; Yuan, Y.; Taerwe, L. (2012). *Thermal stress-strain of self-compacting concrete in compression*. Fire And Materials, vol. 37, no. 3, p. 187-199.

[73] Anand, N. & Arulraj, G. P. (2013). *Effect of Grade of Concrete on the Performance of Self-Compacting Concrete Beams Subjected to Elevated Temperatures*. Fire Technology, vol. 50, no. 5, p. 1269-1284.

[74] Haddad, R. H.; Odeh, R. A.; Amawi, H. A. & Abaneh, A. N. (2013). *Thermal performance of self-compacting concrete: destructive and nondestructive evaluation*. Canadian Journal of Civil Engineering, vol. 40, no. 12, p. 1205-1214.

[75] Pistol, K. ; Weise, F. & Meng, B. (2013) *High temperature behaviour of self-compacting concrete with limestone powder*. Rheology And Processing Of Construction Materials – 7Th RILEM International Conference on Self-Compacting Concrete And 1St RILEM International Conference On Rheology And Processing Of Construction Materials, Paris, p. 221-228.

[76] Trezos, K. G. & Sfikas, I. P. (2013). *Residual bond stress of self-compacting concrete specimens after high temperature treatment*. Rheology And Processing Of Construction Materials – 7Th RILEM International Conference On Self-Compacting Concrete And 1St RILEM International Conference On Rheology And Processing Of Construction Materials, Paris, p. 163-170.

[77] Anand, N.; Arulraj, G. & Aravindhan, C. (2014). Stress-Strain Behaviour of Normal Compacting and Self Compacting Concrete Under Elevated Temperatures. Journal Of Structural Fire Engineering, vol. 5, no. 1, p. 63-76.

[78] Ding, Y.; Zhang, C.; Cao, M. & Haifeng, L. (2014). *Pore pressure of high-strength concrete and self-consolidating concrete at high temperature - a review. Third International Symposium on Design*, Performance And Use Of Self-Consolidating Concrete, Xiamen, p. 297-307.

[79] Lomonte, F; Gambarova, P. G. (2014). *Corner spalling and tension stiffening in heat-damaged R/C members: a preliminary investigation*. Materials And Structures, vol. 48, no. 11, p. 3657-3673.

[80] Lura, P. & Terrasi, G. P. (2014). *Reduction of fire spalling in high-performance concrete by means of superabsorbent polymers and polypropylene fibers*. Cement And Concrete Composites, vol. 49, p. 36-42.

[81] Al-kadi, Q. N. S.; Qadi, A. N. S. Al.; Mustapha, K. N. B.; Naganathan, S. & Muda, Z. B. C. (2015). *Coconut Fibre Effect on Fresh and Thermo Gravimetric Properties to Mitigate Spalling of Self-Compacting Concrete at Elevated Temperatures*. Open Journal Of Civil Engineering, vol. 05, no. 03, p. 328-338, 2015.

[82] Ding, Y.; Zhang, C.; Cao, M.; Zhang, Y. & Azevedo, Cecília. (2016). *Influence of different fibers on the change of pore pressure of selfconsolidating concrete exposed to fire*. Construction And Building Materials, vol. 113, p. 456-469.

[83] Muthusamy, S. & Kolandasamy, P. (2015). Lightweight self-compacting concrete at high temperatures. Journal Of The Croatian Association Of Civil Engineers, vol. 67, no. 4, p. 329-338.

[84] Al-Lami, M. S. (2017). *Effect of Elevated Temperature on Compressive Strength of Self Compacting Concrete Using Viscocrete and Silica Fume*, International Journal of Civil Engineering and Technology, vol. 8, no. 10, p. 405–413.

[85] Aslani, F. & Kelin, J. (2018). *Assessment and development of high-performance fibre-reinforced lightweight self-compacting concrete including recycled crumb rubber aggregates exposed to elevated temperatures*. Journal Of Cleaner Production, vol. 200, p. 1009-1025.

[86] Aslani, F. & Ma, G. (2018). *Normal and High-Strength Lightweight Self-Compacting Concrete Incorporating Perlite, Scoria, and Polystyrene Aggregates at Elevated Temperatures*. Journal Of Materials In Civil Engineering, vol. 30, no. 12.

[87] Azarijafari, H.; Amiri, M. J. T.; Ashrafian, A.; Rasekh, H.; Barforooshi, M. J & Berenjian, J. (2019). *Ternary blended cement: an eco-friendly alternative to improve resistivity of high-performance self-consolidating concrete against elevated temperature*. Journal Of Cleaner Production, vol. 223, p. 575-586.

[88] Franchetto, A. (2022). *Investigação das características físicas e propriedades residuais de concretos autoadensáveis expostos a altas temperaturas*, Master, Universidade Federal do Rio Grande do Sul, 238p.

[89] Qadir, S. S. (2015). *Strength and Behavior of Self Compacting Concrete with Crushed Ceramic Tiles as Partial Replacement for Coarse Aggregate and Subjected to Elevated Temperature*. International Journal of Engineering Technology, Management And Applied Sciences, vol. 4, no. 3, p. 278-286.

[90] Hager, I. (2013). Behaviour of cement concrete at high temperature. Bulletin Of The Polish Academy Of Sciences: Technical Sciences, vol. 61, no. 1, p. 145-154.

[91] Wang, G.; Zhang, C.; Zhang, B.; Li, Q.; Shui, Z.(2014). Study on the high-temperature behavior and rehydration characteristics of hardened cement paste. Fire And Materials, vol. 39, no. 8, p. 741-750.

[92] Fernandes, B.; Gil, A. M.; Bolina, F. L.; Tutikian, B. F. (2017). Microstructure of concrete subjected to elevated temperatures: physico-chemical changes and analysis techniques. Revista Ibracon de Estruturas e Materiais, vol. 10, no. 4, p. 838-863.

723

Research and Certification of Building Products

A PLAN FOR THE TEACHING OF FIRE SAFETY IN ARCHITECTURE AND URBANISM COURSES

Evandro C. Medeiros

Ângela G Graeff

ABSTRACT

After the fire at Nightclub Kiss, in 2013, in the city of Santa Maria (RS), which killed 242 people, Brazilian society once again discussed the need to promote Fire Safety (SCI) in such a way that tragedies like that would never happen again. In the academic world, proposals arose again for the creation of postgraduate courses (specialization), but also for introducing, in undergraduate courses of bachelor's degree in Architecture and Urbanism, and also in bachelor's courses in Engineering, concepts of Fire Safety (SCI) and a discipline with exclusive content on the subject, since graduates of these schools receive the possibility of effective action in the area, regardless of the adequate formation of their knowledge - often requiring postgraduate courses to correct this educational deficiency. This research analyzes a possibility of a pedagogical approach, aiming to transmit basic fundamentals of Fire Safety (SCI) during the graduation of the Architecture and Urbanism courses, in order to, in addition to supporting the implementation of the required discipline of exclusive content, or to the courses of post-graduation, mainly, to promote and make students aware of the related knowledge between the assumptions of Fire Safety (SCI) and Architecture and Urbanism.

Keywords: Safety. Fires. Architecture. Teaching. Project.

(a) Universidade Federal do Rio Grande do Sul - UFRGS (babu.arq@gmail.com).
(b) Universidade Federal do Rio Grande do Sul - UFRGS (angela.graeff@ufrgs.br).

1. INTRODUCTION

After the fire that took place in 2013 at the Kiss nightclub, in Santa Maria, Rio Grande do Sul, which took the lives of 242 people, the Brazilian population was taken by the feeling of doing something to prevent this from happening again. This tragedy resulted in several actions, in different areas of society, including the publication by the Brazilian Federal Government, of Law 13,425, in 2017, four years after the tragedy at the Kiss Nightclub, which determined in its article 8, the obligation that Architecture courses include in the disciplines taught content related to fire prevention and fighting [1].

In the parliamentary area, in 2015, two task forces were created in the National Congress, the Civil Firefighter Parliamentary Front (FBPC) and the Joint Parliamentary Front for Fire Safety (FPMSCI), and in the later, with the justification that there was the lack of professionals with specific knowledge to work in the area of Fire Safety (SCI) and, also, of infrastructure for training these professionals, proposals were presented that corresponded to actions of the education sector for Fire Safety (SCI), such as the creation of postgraduate courses (lato sensu) to train Fire Safety Specialists and the inclusion of fire safety topics in Engineering and Architecture courses.

On the other hand, the Fire Safety (SCI) bibliography showed, long before the Kiss nightclub fire, that the premises of Fire Safety (SCI) are already present in the areas of knowledge of courses such as Architecture and Urbanism, and that, invariably, the risk of fire arises at the same time that a certain statement of problem in architecture appears, that is, in the architectural project to be elaborated, as demonstrated by the academic works of Berto [2], from 1991, and Negrisolo [3], 2011. In this way, the proposal to do something to meet a demand, from the Kiss nightclub fire, seemed, initially, a new attempt to impose Fire Safety (SCI) on Architecture, without observing that some intrinsic relationships between the subjects had already been identified, as described by other authors, as they are unconditional in the relationship between Architecture and Fire Safety (SCI).

2. THE TEACHING OF PROJECT IN ARCHITECTURE

From the perspective that the risk of fire arises concomitantly with the architectural project, it is also necessary to understand, albeit tangentially, the teaching of architectural design, in such a way that the quality of the architectural solution is visualized, including the premises of the Fire safety. It should be noted that teaching, when referring to architectural design, has a very different meaning from other areas of learning, since, in addition to the links with professional practice, it is directly related to professional performance and the way of seeing architecture of those who teach it. For Malard [4], the problem is always prior to any observation or perception of the senses. Observation and perception help in the formulation of solution hypotheses and conjectures. The elimination of errors is done by the critical method.

According to Pahl apud Cunha [5], the more developed a culture, the stronger the need, and the greater the concern about rational processes of construction, as well as expression itself in architecture. That is, the approach to Fire Safety (SCI) in the analysis of the architectural solution should not only certify compliance with legislation or endorse performance criteria for the built object, but, above all, serve the analysis of architecture itself as a representation of a moment and of a culture that feeds back on its own history. Cunha [5], when reviewing the triad proposed by Vitrúvio, defines the place as the structuring element of the design conception, as it is the reference of the object's relations to the environment where it is inserted, including, here, the fulfillment of norms and regulations; the program as not just the division of the building into compartments according to their uses, but as the succession of vertical and horizontal planes according to the degrees of permeability and privacy of the spaces; technique represents the third element and no longer concerns only the structuring of the building, but, currently, the "valorization of the image of technological development, mainly from the valorization of architectural elements in the composition, such as the structure, with sculptural form or no, like the sun protection elements, like the shape of the roof, among other aspects" representing what distinguishes the building from the others.
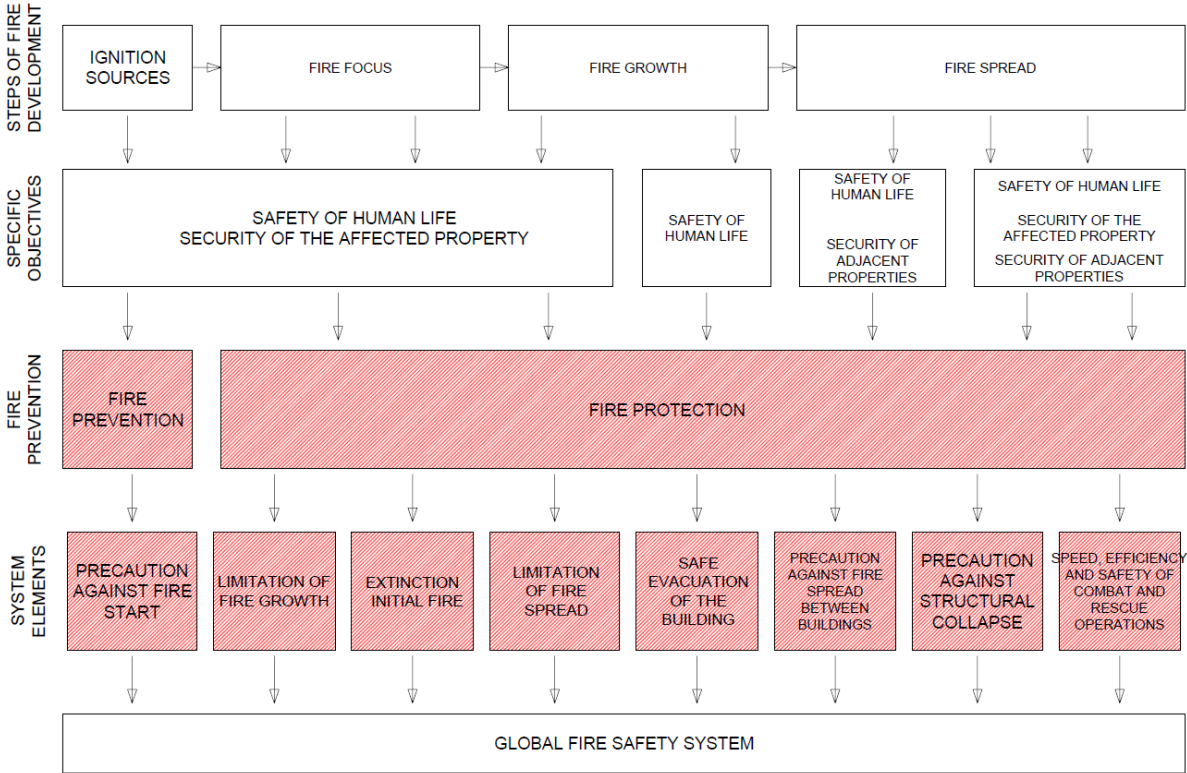
3. THE TEACHING OF FIRE SAFETY

Several authors already pointed out, before the Kiss Nightclub fire, in 2013, or the federal law of 2017, the need to introduce the theme of fire safety in undergraduate Architecture and Urbanism courses. Negrisolo even tested a methodology and concluded, in his publication, that "what and how to teach is not something that can be defined and remain static in any area of knowledge" [3].

Negrisolo [3] narrates his experience when presenting the theme of Fire Safety to students of two disciplines of the Architecture and Urbanism course, at the University of São Paulo, in 2011. It is important to highlight that this school, in that year, was the only one in country, according to the author, where there was a discipline dedicated to this subject, although optional and shared with two other themes, according to a survey carried out by the author to prepare his work, highlighting three aspects that should be improved, based on the evaluation of the students who were submitted to his teachings: "The approach on systems or subsystems, structure and façade; compartmentation/smoke control (fire containment); Technical Standards" [3].

The Global Fire Safety System (Figure 1), presented by Berto [2], demonstrates the stages of fire development, the objectives to be preserved, what is the object of prevention and what concerns combat, making it clear that the failure of prevention anticipates the need for combat, in such a way that preventive measures are essential in fire safety, as they prevent the emergence of a fire, combat the spread, protect human life, property and also the very system. Among the preventive measures, there are those related to the constructive aspects of the building and those related to the use of the building. In construction, in addition to the characteristics of the building materials, there are strategies originated by the architectural project, such as horizontal and vertical compartmentalization, risk isolation, protected circulations and safe escape routes, and the Fire Safety System itself, equipped with the measures of combat, is part of the prevention measures of the building.

Figure 01 - Global Fire Safety System

The overall fire safety system, for Berto [2], is fundamentally the architect's responsibility, due to the system's ability to interact with a large number of aspects directly associated with the architectural project.

4. THE TEACHING OF ARCHITECTURE PROJECT WITH SAFETY

From the conclusion that, briefly, preventing the emergence of fires is also a way to prevent its propagation and, at the same time, a form of combat, or, in which the presence of a combat system is also a form of prevention , there is a relationship with the way of thinking of the architect and thus, mutatis mutandis: "the designer develops his understanding of the problem through attempts to solve it, as if the analysis were done through synthesis. The problematization therefore comes together with the solution." [5][6]

Anticipating technical issues – in this case, from the area of fire safety – to the architectural project is doing fire safety and doing architecture, but, above all, it is fighting against the trivialization or malfunction of both.

"The architectural project must be prepared based on a thorough knowledge of the relationships they have with the provisions that give the building adequate levels of fire safety." [two]

"It is in the architectural design that the required compartmentalization and emergency stairs or, eventually, emergency elevators and refuge areas are foreseen. This is where the architectural details must be made compatible with the fire installations and with the dimensions of the structures calculated for the fire situation. In the project, the coatings and finishes of the building are defined. Finally, the architectural project of a building is fundamental for fire safety." [7]

From this perspective, it is imperative to define, therefore, which fire safety issues arise - and coexist - primarily, at the origin of architecture and urbanism projects, still in the definition of the architectural approach, constituting the basic notions of the matter, which must be presented to the students still in the disciplines where architectural design is taught, to, in addition to generating answers to technical questions, such as dimensioning that interfere in architecture, provide their use as strategies in architectural design, by adopting materials or compartmentalizations, for example. [6]

In this way, to begin with, students need to know and incorporate three expressions that, although they have subjective and relatively flexible concepts, from identification to qualification, at the same time, serve as assumptions, inflexible and unquestionable, and that must be present in the analysis of any architectural project, to provide safe conditions for human life, property, the economic chain and the environment. Thus, even during the graduation cycle, in the project ateliers, students must conceptualize, analyze and qualify the risk, prevention and combat – of fires.[6]

The risk arises and becomes constant at all stages of fire safety, as long as there are one or more architectural objects, in the case of unnatural fires: there is the risk of ignition, there is the risk of combustion, there is the risk of propagation, etc. Fire safety will act on this in two ways: prevention and, if this fails or is ineffective, through combat actions, as Berto [2] demonstrated in the Global Fire Safety System (Figure 1). [6]

5. A PLAN FOR EDUCATION OF FIRE SAFETY

5.1. 01st Stage - Basic Notions

In his thesis, Negrisolo [3] presents his preliminary proposal for the development of the discipline "Fire Safety and Architecture", whose first objective is "to provide architecture and urbanism students with knowledge of the fundamentals and techniques of fire safety".

By applying the reasoning described above, anticipating the problematization of the solution in order to qualify it, it is suggested the presentation/insertion of the basic notions of fire safety in the design studios during the presentation of the statement of the architecture exercise, aiming, not exactly the training of a professional to work in the security area, but of an architecture professional who is aware of the subject, as shown in Figure 02.

Figure 02 - Introduction to Fire Safety[6]
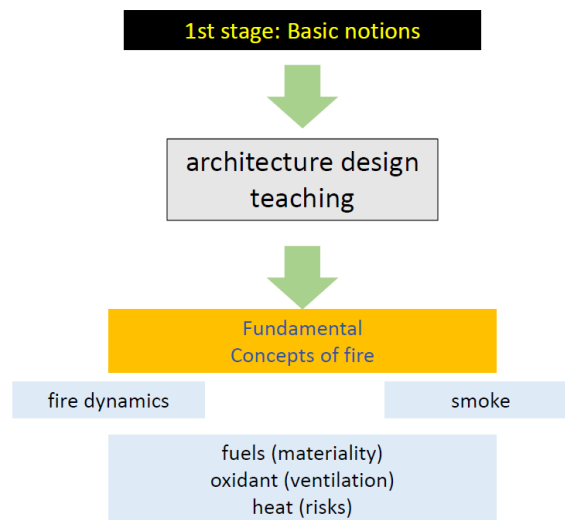
Divided into two stages, the introduction is a class on the most basic concepts of fire safety, so that students can identify possible fire risks and specific characteristics defined by the activity or use for which the building is proposed, as well as its user population, in a way that allows them to include, in the act of designing, in the different phases of the project and in the different systems of the building, characteristics and qualities of fire safety" [3].

5.2. Fire safety concepts applied to building architecture

In this chapter of the research, based on the elements that constitute the fire triangle (source, oxidant and fuel), the objective is to demonstrate the importance of some concepts of fire safety for students of Architecture and Urbanism courses, as previously described. The relationship with the triad proposed by Cunha [5] allows the concepts of fire safety to become elements of architecture, definitively. In a way, it can be said that the concepts below are directly related to the building's program and its construction technique, but one cannot forget that its solution will correspond to its influence on the place where the building is located.

5.2.1. Heat Sources

Knowing and assimilating the ignition processes means identifying, in a building, which heat sources need to receive adequate treatment, such as safe distances between them (air conditioning, refrigeration, substations and electrical generators, etc.).

5.2.2. Oxidizing:

With regard to the oxidizing agent, the best-known element is oxygen and, in this regard, its relationships with the architectural project refer to the geometric shape of the building: room dimensions, number of openings, walls, slabs, and partitions. horizontal and vertical of the environments, in short, the degree of ventilation of the building.

5.2.3. Fuels:

As for fuels, it is the materiality itself that constitutes the project, from the most basic elements of construction, structural or cladding elements, ceilings, floors, walls, facades, internal furniture, partitions, etc., which are responsible for starting , growth and spread of fire.

729

5.2.4. Smoke:

Another basic component of fire safety is smoke, directly related to fuels and present in all stages of a fire, from its origin, and considered by some authors the second leading cause of victims in fires, given the characteristics of the materials present. inside the buildings.

5.3. Step 2 – Designing the Fire Safe Architecture

Thus, in all workshops where architectural design is taught, throughout the Architecture course, a prior analysis should be made of preliminary solutions of the architectural solution (the conceptual diagram of the project), of the fire risks of what will be designed in atelier (theme), fire risks and possible measures aimed at fire safety, so that these can be conceptually incorporated into the data set for the exercise proposed to the students, as represented in Figure 03.

Figure 03 - Relationship between the architectural problem and Fire Safety[6]
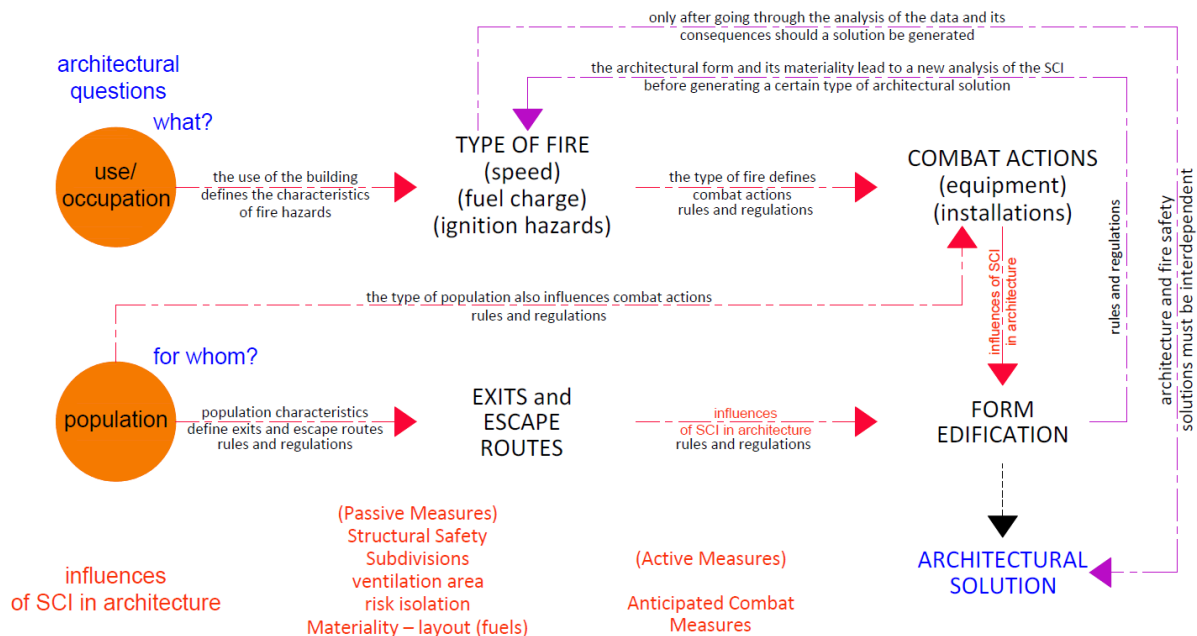
Although there is some complexity, this stage does not aim at training the student to become a professional specialist in fire safety, but the awareness of the matter and the formation of an analytical spirit, aiming to create the habit, in the student, of thinking about fire safety together with the architecture project and, this, cannot be in a single discipline, but in each architecture exercise – as it will be in your professional life. The student does not need to be a specialist in Fire Safety, but he can be induced to identify the relationships that arise from his project and concern fire prevention and fighting, in such a way that this will also be perpetuated in his practice as a professional.

Issues such as the identification of fire risks, by the architect, as well as the identification of the population that will use a certain architectural solution are essential, when designing in architecture, for defining accesses and exits in case of emergency. Likewise, incorporating issues such as the resistance and behavior of the materials used in the building in case of fire, and the influence of the building in a fire that reaches it, among others, are not fire safety issues (sci), but of knowing how to see and do Architecture.

It is also important to highlight that the routes in case of an emergency in a building do not have to be just an exit in case of fires; they can constitute a route solution within the building allied to the safety of its users, adding to

themselves a quality as an alternative. What cannot, ever, is that there are no alternatives to transit through the building without the safety condition being guaranteed.

5.4. Designing Fire Safety

In a second moment, it is necessary to effectively insert a discipline exclusive to fire safety, aiming at the training of professionals who will work in this area, so that they can identify, recognize, analyze, review and, if applicable, complement defined measures by the architectural project with other solutions or with other systems complementary to those identified in the elaboration of the architectural project, according to the scheme shown in Figure 04.

Figure 04 - Content of the Fire Safety discipline[6]
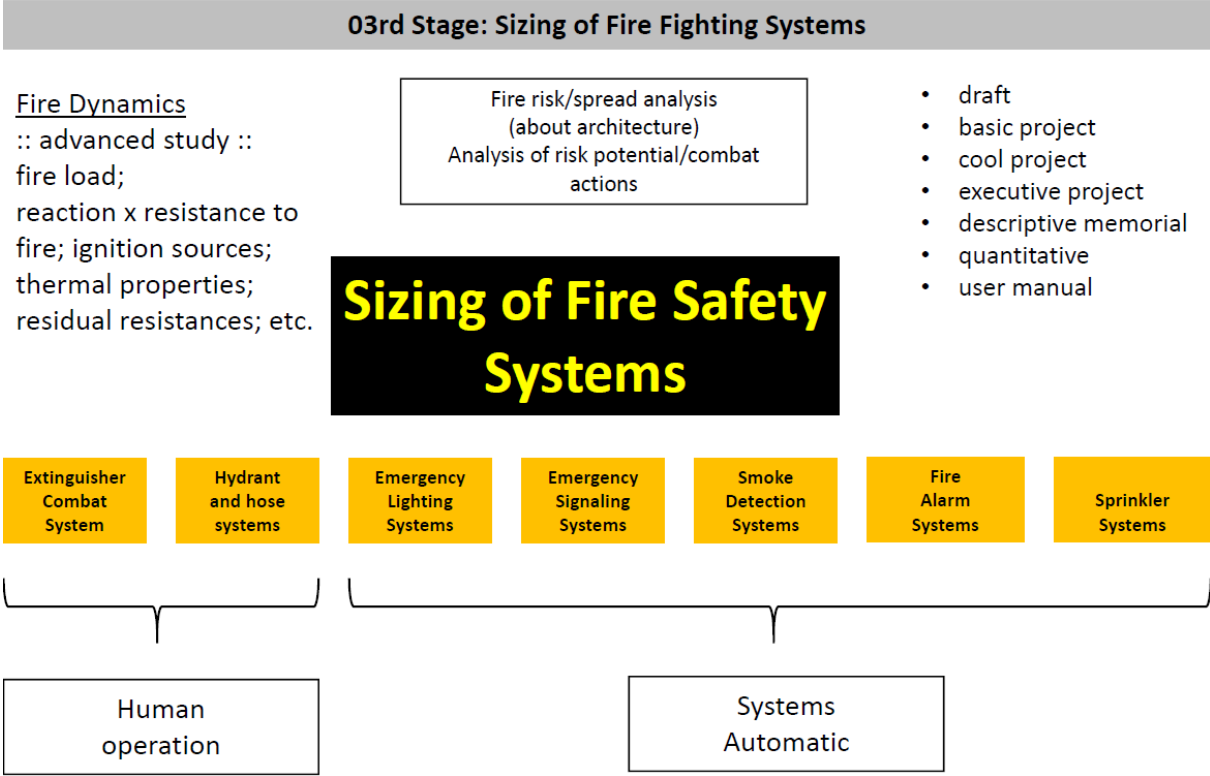
Thus, initial questions can be answered before any architectural idea sketch, being inserted no longer from the synthesis or pre-evaluation of the solution, but during the analysis and data collection - or in the formulation of the architectural object statement.

a) What heat sources will be installed due to the function of the building? (air conditioners, electrical transformers, generators, etc.);
b) Considering its operation, what type of fuel will exist inside the building? (fabrics, papers, furniture, dividers, etc.)
c) What are the characteristics of the users of this building? (total population of the building; distribution of the population in the building; degree of permanence of the population in the building; composition of the fixed and floating population; physical, psychological and cultural conditions of the population; age distribution of the population).
d) What are the external constraints? (distance to neighboring lots and buildings, access conditions, distance to fire stations, water sources) [6]

The effectiveness of this exclusive discipline requires compliance with the previous step, in order not only to avoid overlapping content or class hours being spent with basic learning later, but also, mainly, in fact, the teachings obey a constructive sequence. The main objective is to give the student the qualification to, in addition to giving a response to society, assimilate new knowledge to their performance and professional career, as well as their

complete preparation for an eventual specialization (postgraduate), where the formulation and resolution will take place. of improved technical tasks.

6. CONCLUSIONS

Fire safety is not a simple matter, with solutions isolated from architecture, and its concepts will be present in architectural projects as long as they constitute an intention, and should not be a restriction, a condition, but as a parameter of the quality of the architect's response to a problem and its performance, its responsibility and its professional ethics.

The fundamentals of fire safety must be present not as an objective, but as a demonstration of how much an architect masters his project in different uses - including unwanted ones, as in case of fire - and, also, how much he masters knowledge about the building, its materiality and functionality, recognizing its routes and the characteristics of its users.

Finally, with a view to training professionals capable of defining systems designed to prevent and fight fires in an exclusive discipline, the importance of the architectural project and the independence of subsequent learning are highlighted, as a strategy for teaching prevention and teaching firefighting in an orderly, continuous and effective manner.

7. AGRADECIMENTOS

I would like to thank my advisor and inspiration Angela Graeff, to all my colleagues on the specialization course in fire safety, and to all architects and urban planners who value architecture thinking safely.

8. REFERÊNCIAS

[1]   Brasil (2017). Lei nº 13.425. Diário Oficial da União, Atos do Poder Legislativo. 31 de Março de 2017, p. 1. (Diretrizes gerais sobre medidas de prevenção e combate a incêndio e a desastres em estabelecimentos, edificações e áreas de reunião de público).
[2]   BERTO, af e DEL CARLO, U (1991). Medidas de proteção contra incêndio: aspectos fundamentais a serem considerados no projeto arquitetônico dos edifícios. Dissertação de Mestrado, Universidade de São Paulo, 351 p.
[3]   NEGRISOLO, W (2011). Arquitetando a segurança contra Incêndio. Tese de Doutoramento em Tecnologia da Arquitetura, Universidade de São Paulo, 415 p.
[4]   MALARD, ML (2009). A lógica da invenção arquitetônica e a inversão ilógica do processo de projeto: alguns problemas na elaboração de um "projeto enxuto", Anais do 1 Simpósio Brasileiro de Qualidade do Projeto no Ambiente Construído, vol. 1. p. 200-210.
[5]   CUNHA, G. (2008). A tecnologia no processo de concepção arquitetônica contemporânea: análise de três obras de Norman Foster. Arquiteturarevista. Vol. 01, pp. 49-65.
[6]   MEDEIROS, EC (2020), Um plano para o ensino da segurança contra incêndios nas faculdades de Arquitetura e Urbanismo, Monografia de Especialização em Engenharia de Segurança contra Incêndio, Universidade Federal do Rio Grande do Sul, 27 p.
[7]   SILVA, Valdir Pignatta. (2014) Segurança Contra Incêndio em Edifícios - Considerações para o Projeto de Arquitetura. Blucher, p. 129.
.

Wildland/Urban Interface Fires

IMPACT OF HOUSE, PARCEL, AND COMMUNITY CHARACTERISTICS ON STRUCTURE SURVIVAL DURING A WILDLAND-URBAN INTERFACE WILDFIRE

Erica C. Fischer [a],* **Amy J. Metz** [b] **Abbie B. Liel** [c]

ABSTRACT

Housing loss within a community has societal, economical, and symbolic implications on the community in addition to substantially impacting post-wildfire recovery. There are many guides for parcel-level and house-level mitigation measures for wildfires to reduce the ignitability of the parcel and house. In addition, previous researchers have used post-wildfire housing data to investigate characteristics of the parcel or house that influence survivability during a wildfire. This paper summarizes research that used data from Louisville, Colorado after the 2021 Marshall Fire to further investigate parcel, house, and community-level characteristics that influenced housing survivability. The authors built upon previous research on the subject and furthered the field by considering factors that relate to firefighting abilities and urban planning. The authors performed developed a logistic regression model and evaluating the significance of each parcel, house, and community-level characteristic on how they influenced the ability of fhe model to accurately predict house survivability in Louisville, Colorado during the 2021 Marshall Fire. The results of this study showed that, similar to previous research, distance between houses or housing density and proximity of the house to vegetation (either on the property, open space, or forested land) are influential factors for predicting housing survivability during a WUI fire. However, this study also concluded that a wooden fence on the property or touching the house and the location of the house within an isolated community or within a cul-de-sac also influenced housing survivability, and these factors had not been previously considered in other studies.

Keywords: Wildfires, wildland urban interface, housing

1. INTRODUCTION

---

[a],* Oregon State University, 1491 SW Campus Way, Corvallis, OR 97331, USA (erica.fischer@oregonstate.edu), Corresponding author**.**

[b] Oregon State University (metzamy@oregonstate.edu).

[c] University of Colorado, Boulder (abbie.liel@oregonstate.edu)**.**

Housing has societal, economic, and symbolic significance that makes its loss in hazard events devastating and its role in post-disaster recovery pivotal. When a wildfire intrudes on a community, houses become fuel for the fire, thereby intensifying the wildfire. Due to the critical role housing plays during and after a wildfire, many agencies and researchers have used housing data collection methods to collect data on wildfire housing survivability. This data has been used to investigate the parameters or characteristics of houses that most influence survivability. However, much of these investigations have not included community characteristics or firefighting capabilities and their influence on housing damage.

To help negate the effects of wildfire on housing in communities, the National Fire Protection Agency (NFPA) developed FireWise USA, a program that provides resources to communities on mitigations measures at the house and parcel level through vegetation management and house hardening. Many of these recommendations were incorporated into the International Wildland Urban Interface (IWUI) Code [1], which has been adopted by many states. California not only adopted the IWUI Code, but developed a chapter of their building code, Chapter 7A, to address wildfire mitigation at the house parcel level.

This study uses data collected after the Marshall Fire, which began on December 30, 2021 in Boulder County, Colorado. In Colorado, building codes are adopted at the county level. At the time of the fire, none of the impacted communities had adopted the IWUI. The Marshall Fire ignited as a small grass fire near the intersection of Colorado 93 and Marshall Road in Boulder County, Colorado. The fire spread eastward through and was intensified by hurricane force winds with speeds ranging from 80 to 100 miles per hour and sustained winds of 50 – 60 miles per hour. Snowfall on December 31st provided firefighters with an opportunity to control the fire and the fire was considered fully contained by January 4, 2022. The Marshall Fire burned over 6,200 acres and destroyed 1,091 structures and damaged an additional 179 across unincorporated Boulder County, Louisville, and Superior. The origin of the fire is still under investigation.

2. BACKGROUND AND STATE-OF-THE-ART IN HOUSING DATA COLLECTION

Wildfire housing damage assessment methods intended to be implemented both pre- and post-wildfire have been developed. California Department of Forestry and Fire Protection (CALFire) performs damage inspections to determine why a house was damaged in a fire or what may have caused fire damage to a house. This survey includes characteristics of the house itself and the proximity of other combustible entities to the house (parcel-level). These specifically include:
- Where the fire may have started on or in the house,
- Visible signs of defensive actions,
- Roof construction materials,
- Eave style of the house,
- Size of the attic or location/presence of basement vents,
- Exterior siding material,
- Presence of a deck or porch and their construction material,
- Presence of fences attached to the house and their construction material,
- Distance between the house and any propane tank,
- Distance between the house and another structure (> 120 ft^2)

This survey is most useful when the house has partial damage, and these characteristics are visible to the inspector. It does not include any information about the proximity of vegetation to the house or any potential fire intensity visible during the inspection.

NFPA has developed a house and parcel-level wildfire risk assessment guide as part of NFPA 1144 that aims to assess how vulnerable a structure is to wildfire and provide recommendations to houseowners [2]. This assessment form is meant to be completed before a fire impacts a house. Both housing assessment forms consider combustible details of housing such as the eave configurations, attics, basement vents or crawl spaces, which are places embers or firebrands can be caught and cause ignition of the house. Both assessment forms also consider combustible materials of the house such as siding or roofing materials, as well as the presence of combustible materials near the house, such as propane tanks, fences, porches, decks. However, the NFPA assessment considers the presence of vegetation and the management of that vegetation around the house in addition to the presence of fire protection systems that can be used for defensive actions.

The mitigation practices that contribute most to house survivability or preventing house loss is still an active research topic. Researchers have performed in-depth studies on wildfire impact data with the goal of understanding which mitigation practices have a significant impact on increasing house survivability. Past research has considered house characteristics, such as year of construction [3], [4], window treatments [3], construction material of the siding [3], [5] and roof [3], [5], [6], and presence of vent covers [6].

House survivability can also be dependent upon parcel-level characteristics that previous researchers have considered such as distances between houses [4], [5], [7]–[10], to the nearest structure [4], [5], [9], or to the nearest fire impacted structure [4], [9]. The relationship between the house and vegetation is also considered, such as defensible space [3], [5], [6], [11] and vegetation overhanging the house [3], [4], [9], [11]. Other parcel-level characteristics considered are elevation of the property [7]–[10], [12], slope [3]–[5], [7]–[10], vegetation [9], [11], [12] and canopy cover [3], [4] on the property, neighbor's vegetation cover [11], and the distance to wildland vegetation [5], [13].

Community-level characteristics can also contribute to housing survivability during a wildfire. Researchers have examined different community-level characteristics, the most common of which is housing density [3], [4], [7]–[10], [13]. Housing density can also be examined through housing clusters where groups of houses are examined as a cluster and clusters have spatial separation through roads or open space [7], [10]. Lastly, housing density and proximity to wildland fuels can be examined through the WUI classifications to examine how the two work together to influence survivability [4], [12].

In general, there is a consensus in the research community that housing spatial arrangement and location are the most influential factors that affect the survivability of structures during a wildfire. However, authors have found varying results and influences within these categories. In addition, there is some variation in the conclusions of these studies and the data used to make these conclusions.

2.1 Housing characteristics

Vinyl window framing, stucco exterior construction, dual pane windows, and tile roofs have been shown to be the most influential housing characteristics that influenced survivability [3]. The window detailing was the most influential housing characteristic, followed by the roofing and exterior construction materials. Exterior construction material was the least influential of the housing characteristics and vegetation treatments on a property demonstrated to be just as influential as building construction materials. In addition, properties that did not have overhanging vegetation and did have defensible space performed just as well as those that had dual pane windows and vinyl window framing. These conclusions were also made by Syphard and Keeley [6], who concluded that eaves had the largest influence on housing survivability of all the housing characteristics followed by windowpanes and vent screens. However, in Northern CA, vent screens and exterior siding were the third most influential housing characteristics that influenced housing survivability in a wildfire. Knapp et al. [4] examined factors that influenced house survivability during the 2018 Camp Fire and concluded that more modern houses had a higher probability of survivability than older houses (pre-1990s).

2.2 Defensible space, vegetation, and slope

Defensible space was found to be a significant variable that influenced house survivability. Syphard et al. [11] concluded it was the variable that contributed most to the probability of house survivability. However, as slope increased, more defensible space was needed to increase survivability. This was further confirmed by the studies of Price and Bradstock [8], Alexandre et al. [10], and Knapp et al. [4].

Vegetation touching the house was the most influential vegetation variable [8] and had more of an influence than a nearby forest cover for the study performed by Penman et al. [9]. Similarly, garden cover and vegetation overhang also were more influential to housing loss than proximity to a nearby forest.

2.3 Housing density and proximity to areas of wildland fuels

In general, there is a consensus in the research community that housing spatial arrangement and location are the most influential factors that affect the survivability of structures during a wildfire. However, different researchers

have concluded varying results and influences within these categories. For example, Syphard et al. [7] and Syphard et al. [12] concluded that housing loss is more likely to occur in regions with low or moderate housing density. In particular, Syphard et al. [12] concluded that the majority of housing in California was lost due to wildfires in low- and moderate-density housing regions, specifically in intermix communities with high vegetation cover. This conclusion was further enforced by the results of the study performed by Alexandre et al. [10]. These assessments were based on aggregating all California wildfire housing loss data across decades, regardless of landscape or WUI type (e.g., intermix, interface) or weather. Knapp et al. [7] concluded that distance to the nearest destroyed structure and density of structures were the two factors that most influenced house survivability [4] in the Camp Fire, more so than the proximity to vegetation, However, unlike the Syphard et al. [3, 12] conclusions, Knapp et al. [7] concluded that smaller distances to a destroyed house and higher housing density negatively influenced house survivability. Knapp et al. [4] also concluded that distance to the nearest destroyed structure and density of structures were the two factors that most influenced house survivability followed by the distance to the next destroyed house. Further, Knapp et al. [4] concluded that WUI interface versus intermix showed to be a significant variable influencing house survivability with a higher survival rate in the intermix definition than in the interface. Houses built in more of a subdivision arrangement with wildland fuels nearby had a lower survivability rate. This goes against the results found by Syphard et al. [7] ,[12]. The next two factors that influenced survivability in the Camps Fire [7] were distance to the next destroyed house and canopy cover within 100 m of the house.

Studies of Australian fires concluded that increasing housing density increased the likelihood of house loss [8], [9]. This conclusion shows that the results of housing survivability studies can be specific to the region studied. Gibbons et al. [14] also concluded that when houses within housing clusters are spaced closely together, the ignition of one house in the cluster can cause the remainder of the houses to be destroyed. Penman et al. [9] further confirmed that proximity to another house that was impacted by the fire was the strongest variable in increasing the likelihood of housing loss because, as houses become closely spaced together, the defensible space around each house decreases. Meldrum et al. [5] further confirmed these results finding a strongly significant result with spatial clustering of structures indicating the effect of distance between houses as a factor to contribute to house survivability in addition distance to adjacent fuels. They concluded that it was not only the distance between houses, but distance to the nearest destroyed house post-fire: burned structures tend to be clustered indicating that the house is not only a recipient of the fire, but also an entity that can intensify or drive the fire behavior.

2.4 Gaps in knowledge and research objectives

The conclusions of the studies summarized in Sections 2.1 – 2.3 varied and the data used to make these conclusions also varied widely across the studies. Syphard et al. [3], [7], [11], [12] and Syphard and Keeley [6] examined data from decades of California wildfires, Alexandre et al. [10] used data throughout California and the Pacific Northwest and aimed to make conclusions with respect to climate. Price and Bradstock [8] and Penman et al. [9] used data from Australian fires to examine the influence of characteristics on house survivability. Knapp et al. [4] only used the data from the 2018 Camp Fire to develop conclusions on house survivability. Lastly, Meldrum et al. [5] only used data from the 2020 East Troublesome Fire in Colorado.

Previous research on house survivability during a wildfire has shown that spatial arrangement of housing and proximity of the house to large areas of wildland fuels are highly significant variables in predicting house survivability. However, even with the congregation of data across decades of fires, climates, and types of WUI communities (intermix versus interface) grass fires were specifically not included within the data of previous studies. In addition, these studies did not consider the proximity to firefighting resources or examine how spatial arrangement of housing might influence the ability of defensive actions such as firefighting. Relatively few of the studies have focused on community characteristics consistent with suburban communities.

The research summarized in this paper uses data collected after the 2021 Marshall Fire in Louisville, Colorado, to examine which housing, parcel, and community-level characteristics influence house survivability. Specifically, the research objective is to compare significant housing, parcel, and community characteristics that influenced house survivability during the 2021 Marshall Fire to previous housing assessment studies to draw broader conclusions about house survivability during a wildfire.

3. METHODS

3.1 Data Collection

The authors collected housing data after the Marshall Fire as members of the Geotechnical Extreme Event Reconnaissance (GEER) team that deployed to the impacted regions of the Marshall Fire January 24 – 29, 2022, approximately 3 weeks after the fire. Housing data was collected using three methods: (i) an in-field survey to collect housing data at the parcel level, (ii) remote data collection using publicly available housing websites (e.g. Zillow, Google Earth), and (iii) drone imagery (while in the field) to provide aerial imagery of the impacted regions. All of these data together incorporate characteristics of the house, parcel and community.

The in-field survey was administered through google forms. This platform allowed the team to easily make changes to the survey in the field if needed and share the form amongst team members in the field [15]. This form was used to evaluate 201 impacted houses, including 151 in Louisville. The data collected through the survey included the type of house (e.g., freestanding, townhouse, apartment building), the house's damage state (destroyed, damaged, not damaged), number of stories, visible damage, proximity to nearby destroyed structures, and distances to neighboring houses and their damage state. These data were prioritized for collection because of the significance of these factors in previous research. In practice, almost all houses were found to be destroyed or standing. Smoke damage was not considered [16]

Remote data collection supplemented the data obtained from the in-field survey and allowed the team to expand the data set to include all impacted houses. The addresses of impacted houses and their damage state (damaged or destroyed) were obtained from Boulder County's Office of Emergency Management. For all houses impacted, remote data was collected using Google Maps, Google Earth, Zillow. The remote data was validated with the data collected through the in-field survey. For the jurisdiction of Louisville, permitting data and tax records were also available to further supplement the information obtained. Table 1 summarizes the data collected via each remote data source. The most recent satellite images available were used in both Google Earth and Google Maps. Where the information reported on Zillow differed from tax records, the tax records data was used. Where discrepancies between the field measurements and the remote measurements occurred, the remote measurements were used because in many cases, in-field measurements had error built in due to the debris present at damaged or destroyed houses. The houses classified as standing in the data set were those with minor damage and any surviving houses in the fire damaged neighborhood. In total, the data set for Louisville is comprised of 452 destroyed houses and 78 standing.

Table 1. Data Collected with In-Field Survey and Remote Methods

Data Category	Data Collected	Data Source
House Characteristics	Damage state	In-field survey Boulder County OEM
	Presence of porch on house (Y/N) Porch material Presence of deck on house (Y/N) Deck material Visible vents	Google Earth (2021)
	Exterior cladding material Roof material	Zillow
	Construction type Square footage Number of stories	Zillow City of Louisville Tax Records
	Foundation temperature of destroyed houses	In-field survey
	Siding update occurred (Y/N) Date of siding update Material of siding update	City of Louisville Siding Permits
Parcel Characteristics	Distance to neighboring house (ft) Distance to auxiliary structures (ft)	In-field Survey Google Maps Satellite Imagery (2021)
	Parcel abutting open space (Y/N) Parcel containing or bordered by ditch (Y/N)	Google Maps Satellite imagery (2021)
	Fence present on property (Y/N) Fence Material Fence touching house (Y/N) Fire hydrant within view of house (Y/N) Elevation above sea level (m) Woody Vegetation within 5ft of house (Y/N) Vegetation types present on property Vegetation overhanging house (Y/N)	Google Earth (2021)
	Lot size (sq ft)	Zillow
Community Characteristics	Located in isolated neighborhood or cul-de-sac [d](Y/N) Neighborhood Density[e]	Google Maps Satellite imagery (2021)

3.2 Multivariate Logistic Regression Analysis

Initial trends in the data were assessed using the compiled raw data from in-person and remote sources. Each of the considered predictor variables were plotted against house outcome to assess if trends were present in the un-processed data. After predictor variable trends were noted, we normalized the data set using min-max normalization between 1 and 0.

A Logistic regression was utilized to estimate the probability of house survivability within the city of Louisville. A logistic regression was utilized because of the binary nature of wildfire damage on houses. Houses were either standing (survival = 1) or considered a complete loss (survival = 0). Multivariate logistic regression analysis was performed in python using the sklearn and statsmodels.api packages and the maximum likelihood method for estimating coefficients. The logistic regression model considered the full set of predictor variables to develop probability models. The logistic regression took the form shown in Equation 1.

$$Log\left[\frac{y}{1-y}\right] = \beta_0 + \beta_1 x_1 + \beta_2 x_2 + \beta_3 x_3 + \cdots + \beta_{n-1} x_{n-1} + \beta_n x_n \qquad (1)$$

For each case considered, the data provided was split randomly into training and test sets, with 70% of the data provided used as the training set. These data subsets were used to train and perform initial evaluation of the model.

---

[d] Isolated neighborhoods have 2 or less means of egress. Cul-de-sacs have one means of egress (i.e. dead-end street)

[e] Neighborhood density was calculated by determining the number of houses in a polygon placed over the neighborhood in question

Once trained, the full suite of predictor variables was used within the model to determine the overall accuracy, precision, and recall of the model and to develop a confusion matrix.

A stepwise Akaike Information Criteria (AIC) evaluation of the logistic regression model was performed to further refine the fit. This stepwise analysis was performed using stepAIC in R. StepAIC adds and/or removes predictor variables iteratively until a combination is found that gives the best value of the AIC. The fit of the model developed from the AIC analysis was assessed based on the probabilities generated. A threshold probability of greater than 0.5 is used to indicate survival from model predictions. These predictions were then used to create a confusion matrix for each case. Using this threshold, the models were reevaluated for accuracy, precision, and recall and each model's Brier Score and a Brier Skills Score for each was determined. The Brier Score is a measure of the mean square error of the probability forecasts and is commonly used in weather and climate applications. A score of 0 corresponds to a perfect model. The Brier Skills Score compares the regression model with a baseline model. The Brier Skills Score results in this study considered the baseline model to be a Brier Score of 0.15, which corresponds to the percentage of standing houses in the data set. Positive values indicate that the regression model is better than the baseline model, where a negative value would mean that it is worse.

4. RESULTS

4.1 Trends in housing data

Using the data gathered through both the in-field survey and remote methods, an initial analysis was performed on the raw data. This analysis was performed on all the impacted houses in Louisville. Of the houses that were destroyed in the Marshall Fire, 74% of the houses had wood frame construction. Based on the data available from remote sources, 20% of the houses destroyed by the Marshall Fire had roofs of fire-resistant material such as asphalt, composite, or metal, while 22% had fire-resistant cladding.

Houses impacted by the Marshall Fire ranged in size. In Louisville's jurisdiction, the average house size was 2,520 ft^2 and the median house size was 2,400 ft^2 and 41% of the houses destroyed by the Marshall Fire in Louisville had houses in the range of 2,000 – 2,999 ft^2. Most of the impacted houses were built between the years 1980 and 2000 (70%). Under Louisville's jurisdiction, all the houses destroyed by the Marshall Fire were built between 1981 and 2000.

The minimum average house spacing for the destroyed houses in Louisville was 15 ft. Of those houses destroyed in Louisville 95% had another house within the Firewise intermediate zone (5-30ft), respectively. In addition, in Louisville, the average distance to a destroyed house was also within the immediate zone with 24 ft and 30 ft, respectively. In general, it can be noted that spacing between houses in this study was strongly related to parcel size, with a Pearson correlation coefficient of 0.48. Houses on larger lots had greater spacing distance to the next nearest structure. In Louisville, 74% of the houses destroyed by the Marshall Fire had parcel sizes less than 10,000 ft^2, which corresponds to less than 0.23 acres. The remaining houses were located on parcels 10,000 – 19,999 ft^2 (0.23 – 0.46 acres).

While few houses themselves had other structures within in their immediate zone, many houses destroyed by the Marshall Fire had bushes, shrubbery, or trees within the immediate zone (0 – 5 ft) of the house. These types of vegetation can serve as additional fuel and help spread fire to the house itself. For Louisville, 40% had bushes or shrubbery within five feet of the house. In addition to vegetation on the parcel itself, many houses destroyed by the Marshall Fire were bordering open space lands. These lands were observed to be overgrown and prescribed burns for some of these spaces was scheduled for April 2021 [15]. In Louisville, 24% of the destroyed houses bordered open space.

Drainage ditches provide a conduit for fire to travel from open space onto properties. In Louisville, 8% of destroyed houses, respectively, have drainage ditches on the property or adjacent to the property. Houses in isolated communities or within a cul-de-sac have one path in and out for firefighting. This characteristic can create a vulnerability for firefighters during the fire. Of the houses destroyed, 91% of the houses in Louisville were located in such a neighborhood.

There were many anecdotal observations that wooden fences contributed to the fire spread throughout the community [15]. Within Louisville, 92% of the destroyed houses had fences and of those houses, 100% of them had wooden fences due to city and HOA covenants prescribing fencing regulations. Of the houses that were destroyed in Louisville, 87% of the houses had fences touching the houses. This detail provides a pathway for the fire to ignite the house itself. Similar to fences providing a pathway for the fire to reach the home, porches and decks also provide combustible material attached to the house and are suggested by the NFPA to be constructed of non-combustible material when in a WUI community. Of the houses that were destroyed by the Marshall Fire in Louisville, 77% of the houses had both a porch and a deck.

Vents provide a pathway for firebrands or embers to get into the home and start a fire within an attic space. Using Google Earth, the authors observed that 44% of the houses in Louisville had visible vents on the home. From local policies, the authors can assume that none of these vents have coverings; however, this was not ground truthed. The ability of firefighters to defend houses is impacted by the presence of fire hydrants. Of the houses that were destroyed by the Marshall Fire, 17% had a fire hydrant within view of the home.

4.2 Logistic Models for Housing Survivability

The multivariate logistic regression analysis produced an equation in the form as shown in Equation 1 such that each of the predictor variable coefficients and p-values are shown in Table 2 for the analysis when all variables were included in the model formulation (this is referred to as model 'a'). The variables with positive coefficient indicate that greater values for these variables result in a positive influence on housing survivability and conversely for the negative coefficients. For instance, the presence of open space adjacent to the property, a wooden fence touching the home, visible vents on the home, and location of the home within a cul-de-sac or isolated neighborhood negatively impact the survivability of the home. In contrast, a greater distance between houses, larger lot size, larger housing density, and fire hydrants within view of the home positively impact the probability of survival of the home. These results are consistent with the previous literature summarized in Section 2.

Table 2. Summary of predictor variable coefficients for each variable for model 'a'

Variable	Coefficient	p-value	Variable	Coefficient	p-value
Intercept	-3.7807	0.070*	Wooden Fence Touching Home	22.9784	1.00
			Fire Hydrant within View	0.0741	0.878
Distance to Nearest Home	0.5582	0.771	Porch	0.4471	0.324
Distance to Destroyed Home	17.0778	0.000*	Deck	0.2261	0.603
Elevation Above Sea Level	4.0400	0459	Visible Vents	-0.5249	0.159
Lot Size	1.3925	0.598	Woody Vegetation within Immediate Zone	0.5351	0.654
Home Square Footage	0.0362	0.983	Vegetation Overhanging Home	0.0848	0.878
Construction Year	13.1055	0.320	Fire Resistant Exterior	0.5128	0.327
Ditch Bordering Parcel	-19.3087	0.999	Fire Resistant Roof	-0.1796	0.626
Open Space Bordering Parcel	-0.7876	0.085*	Construction Type	50.1088	1.000
Fence on Parcel	-21.8816	1.00	Located in Isolated Neighborhood or Cul-de-sac	-2.1202	0.000*
Wooden Fence on Parcel	-1.5008	0.315	Neighborhood Density	2.1595	0.060*

*statistically significant $p < 0.10$

From the stepwise AIC analysis performed in R, the most impactful variables within Table 2 were distance to nearest destroyed structure, lot size, construction year, presence of a drainage ditch on or adjacent to the property, presence of a wooden fence on the property, wooden fence touching the house, construction type, whether the

house is located within an isolated neighborhood or on a cul-de-sac, and neighborhood density. These are a mix of house, parcel, and community characteristics. The coefficients for the optimized model are shown in Table 3 below.

Table 3. Summary of predictor variable coefficients for each variable for model 'b'

Variable	Coefficient	p-value	Variable	Coefficient	p-value
Intercept	-0.4835	0.583	Wooden Fence on Parcel	-16.9522	0.990
Distance to Nearest Destroyed	15.2176	4.15×10^{-7}	Wooden Fence Touching House	16.1605	0.991
Lot Size	4.2383	0.0453	Construction Type	40.4657	0.994
Construction Year	-4.1718	0.0508	Located in Isolated Neighborhood or Cul-de-sac	-1.8095	0.000787
Ditch Bordering Parcel	-15.8652	0.989	Neighborhood Density	1.0783	0.135

Some of these variables are consistent with the previous literature discussed in Section 2. The distance to nearest destroyed structure and proximity to large areas of vegetation were found to be a significant variable by previous researchers. However, previous researchers did not consider the presence of wooden fences touching the house or the type of community/neighborhood the house is located in. Particularly, within the towns, impacted by the Marshall Fire, wooden fences were prevalent on the properties. Wooden fences acted as fire conduits thereby providing opportunities for the fire to spread from one property to the next. Isolated communities or parcels located on a cul-de-sac provided challenges and safety concerns for firefighters throughout the Marshall Fire. As the fire intensified, many houses burning together created unsafe conditions for firefighters and from the data, this negatively influenced survivability. While firefighting data from the fire is largely anecdotal, the authors spoke to fire teams who confirmed this trend, and the team also observed abandoned hoses in some neighborhoods [15]. While previous researchers considered the proximity of fire hydrants to a house, they had not considered how the layout of communities created firefighting challenges.

Table 3 summarizes the predictive capacity of the model for both the survived houses and the destroyed houses. The model results shown in Table 4 were able to accurately predict 98.7 – 99.8% of the destroyed houses. The models were also able to reasonably predict the number of standing houses correctly with the best performance predicting 47.4% of the standing houses accurately. The Brier Skill Scores (BSS) for models (a) and (b) considering a base Brier Score of 0.15 (the proportion of standing houses in the data set) are shown in Table 4. These BSS values indicate that model (b) is most likely the most accurate of the models developed by the authors with the highest Brier Skill Score (0.387).

Table 4. Summary of different model ability to predict survivability of houses

Model	Model description	Brier Skill Score (Base Model = 0.15)	Percentage of Standing Correctly Predicted	Percentage of Destroyed Correctly Predicted
(a)	All Considered Predictor Variables	+0.260	32.1%	98.7%
(b)	Distance to Nearest Destroyed, Lot Size, Construction Year, Ditch Bordering, Fence on Parcel, Wooden Fence Touching, Construction Type, Isolated Neighborhood, Neighborhood Density	+0.387	47.4%	98.7%

The percentages shown in Table 4 were determined from each corresponding model's confusion matrix (Figure 1). These matrices show how the models classified the 530 houses in the data set in relation to the actual end state of the house. Since the outcome of is binary (0 = destroyed, 1 = survived), the matrices produced have four quadrants pertaining to prediction classification, with the true values falling on the vertical axes and predicted on the horizontal. True positive or correctly classified survived houses fall in the 1-1 quadrant. True negative or correctly classified destroyed houses fall in the 0-0 quadrant. The 0-1 quadrant represents misclassified standing houses, and the 1-0 quadrant represents misclassified destroyed houses. In all models, the amount of misclassified destroyed houses is an order of magnitude smaller than the number of misclassified standing houses.
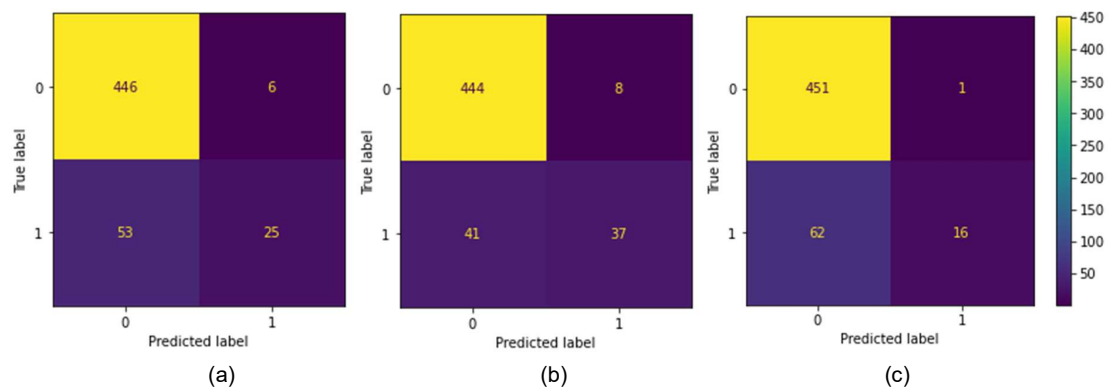
Figure 1: Confusion matrices corresponding to the models shown in Table 3

5. CONCLUSIONS

Housing data from Louisville, Colorado was utilized to develop a multivariant logistic regression model to predict the survivability of housing in Louisville due to the 2021 Marshall Fire and investigate the most influential variables that influence survivability. Data was collected using in-field methods and remote data collection methods that were validated against the in-field measurements.

The results of the analysis concluded that similar to previous post-fire housing analysis, distance between houses or housing density and proximity of the house to vegetation (either on the property, open space, or forested land) are influential factors for predicting housing survivability during a WUI fire. However, this study examined the influence of a wooden fence on the property or touching the house and the location of the house within an isolated community or within a cul-de-sac. These two variables were influential ($p < 0.1$) in accurately predicting the survivability of houses in Louisville during the Marshall Fire. These conclusions are significant because the Marshall Fire began as a grass fire and because Louisville is a suburban community, unlike some of the previously impacted WUI communities, which are more rural. These conclusions also demonstrate that WUI mitigation must examine more than what is occurring at the property level as the community layout (proximity of houses to open space, isolated communities, cul-de-sacs) itself can be influential for house survivability and that firefighting abilities were influential for house survivability within Louisville during the Marshall Fire. Future work in this area includes the analysis of all houses impacted by the Marshall Fire to evaluate differences between jurisdictions (Superior, Louisville, Unincorporated Boulder County).

ACKNOWLEDGEMENTS

REFERENCES

[1]   I. International Code Council, (2021). *2021 International Wildland-Urban Interface Code*, Second Print. International Code Council, Inc.

[2]   National Fire Protection Association, (2018). *NFPA 1144 Standard for Reducing Structure Ignition Hazards from Wildland Fire*.

[3]   A. D. Syphard, T. J. Brennan, and J. E. Keeley, (2017) *The importance of building construction materials relative to other factors affecting structure survival during wildfire*, International Journal of Disaster Risk Reduction, no. 21, pp. 140–147, doi: http://dx.doi.org/10.1016/j.ijdrr.2016.11.011.

[4]   E. Knapp, Y. Valachovic, S. L. Quarles, and N. G. Johnson, (2021). *Factors associated with single-family home survival in the 2018 Camp Fire, California*, Fire Ecology, pp. 1–27.

[5] J. R. Meldrum *et al.* (2022). *Parcel-Level Risk Affects Wildfire Outcomes: Insights from Pre-Fire Rapid Assessment Data for Homes Destroyed in 2020 East Troublesome Fire*. Fire, vol. 5, no. 24, doi: https://doi.org/10.3390/fire5010024.

[6] A. D. Syphard and J. E. Keeley, (2019). *Factors associated with structure loss in the 2013–2018 california wildfires*, Fire, vol. 2, no. 3, pp. 1–15, doi: 10.3390/fire2030049.

[7] A. D. Syphard, J. E. Keeley, A. B. Massada, T. J. Brennan, and V. C. Radeloff, (2012). *Housing arrangement and location determine the likelihood of housing loss due to wildfire*, PLoS ONE, vol. 7, no. 3, doi: 10.1371/journal.pone.0033954.

[8] O. Price and R. Bradstock, (2013). *Landscape Scale Influences of Forest Area and Housing Density on House Loss in the 2009 Victorian Bushfires*, PLoS ONE, vol. 8, no. 8. doi: 10.1371/journal.pone.0073421.

[9] S. H. Penman, O. F. Price, T. D. Penman, and R. A. Bradstock, (2019). *The role of defensible space on the likelihood of house impact from wildfires in forested landscapes of south eastern Australia*, International Journal of Wildland Fire, vol. 28, no. 1, pp. 4–14, doi: 10.1071/WF18046.

[10] P. M. Alexandre *et al.*, (2016). *Factors related to building loss due to wildfires in the conterminous United States*, Ecological Applications, vol. 26, no. 7, pp. 2323–2338, doi: 10.1002/eap.1376.

[11] A. D. Syphard, T. J. Brennan, and J. E. Keeley, (2014) *The role of defensible space for residential structure protection during wildfires*, International Journal of Wildland Fire, vol. 23, no. 8, pp. 1165–1175, doi: 10.1071/WF13158.

[12] A. D. Syphard, H. Rustigian-Romsos, and J. E. Keeley, (2021). *Multiple-scale relationships between vegetation, the wildland–urban interface, and structure loss to wildfire in California*, Fire, vol. 4, no. 1, doi: 10.3390/fire4010012.

[13] M. D. Caggiano, T. J. Hawbaker, B. M. Gannon, and C. M. Hoffman, (2020). *Building loss in wui disasters: Evaluating the core components of the wildland–urban interface definition*, Fire, vol. 3, no. 4, pp. 1–17, doi: 10.3390/fire3040073.

[14] P. Gibbons *et al.*, (2012). *Land management practices associated with house loss in wildfires*, PLoS ONE, vol. 7, no. 1, doi: 10.1371/journal.pone.0029212.

[15] E. Fischer *et al.*, (2022). *The 2021 Marshall Fire, Boulder County, Colorado*. doi: 10.18118/G6KT04.

[16] I. Hager, (2014) *Colour Change in Heated Concrete*, Fire Technology, vol. 50, no. 4, pp. 945–958, doi: 10.1007/s10694-012-0320-7.

Author Index

745

9 786500 825336